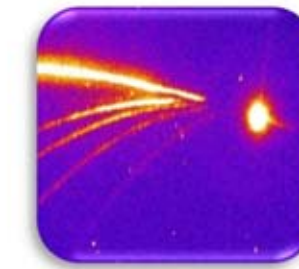
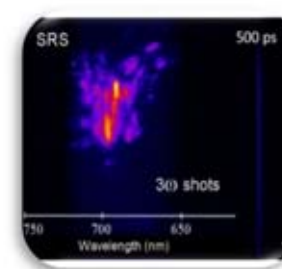
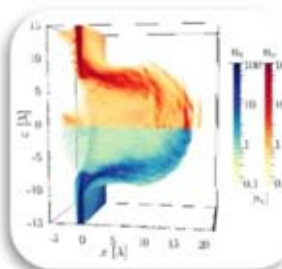
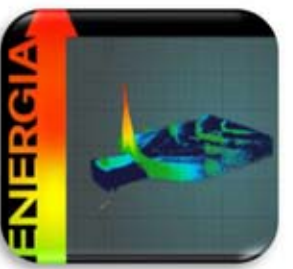
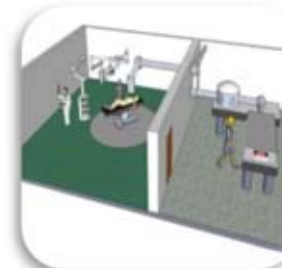
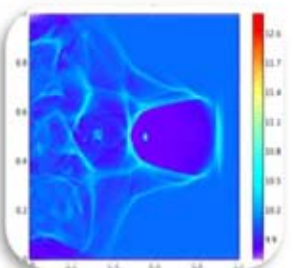
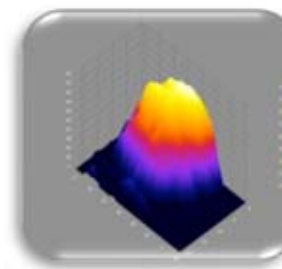
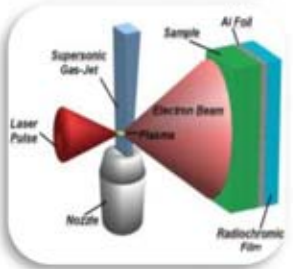
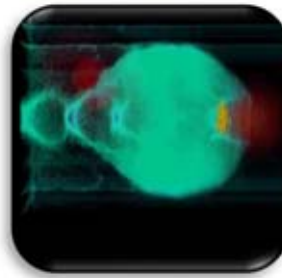


CONSIGLIO NAZIONALE DELLE RICERCHE

Istituto Nazionale di Ottica

INTENSE LASER IRRADIATION LABORATORY

Publications from January 2017 to October 2019



A collection of ILIL publications on recent activity on ultra-intense laser-plasma interactions, charged particles acceleration, ultra-short pulse X-ray generation and applications to Energy and Life Sciences

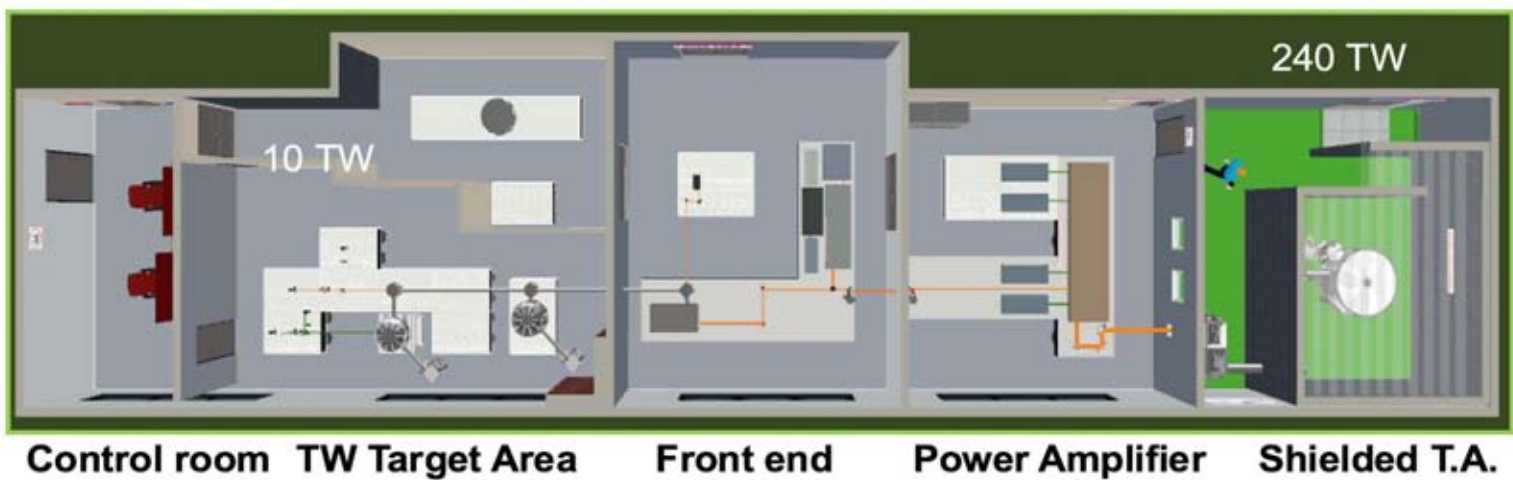
Pisa, November 2019

CONSIGLIO NAZIONALE DELLE RICERCHE

Istituto Nazionale di Ottica

INTENSE LASER IRRADIATION LABORATORY

Publications from January 2017 to October 2019



A collection of ILIL publications on recent activity on
ultra-intense laser-plasma interactions,
charged particles acceleration,
ultra-short pulse X-ray generation and applications to
Energy and Life Sciences

Pisa, November 2019

To the reader,

This report collects the publications of the ILIL Group since January 2017, for a total of 37 publications. As for the previous editions, this volume is a reference of the recent activity of the Group and the impact of completed research, in view of future directions.

The past three years were strongly characterized by the commissioning of the ILIL-PW installation, the sub-PW upgrade to the Intense Laser Irradiation Laboratory developed in the framework of the Italian Network for the Extreme Light Infrastructure (ELI-Italy), that was formally inaugurated in March 2018. This is an important event that marks the arrival point of a journey started in 2014, when the first step towards the new installation was taken. Since then an intense activity has progressed through the design of new lab upgrade, the refurbishment of the building and the installation of both the laser amplifier, the beam compression and transport line, and the interaction area with its radioprotection bunker. This effort has given to both CNR and the wider research community a unique experimental capability to perform an entirely new class of experimental studies on high intensity laser-plasma interaction and compact, plasma-based particle acceleration. Having the ILIL-PW as the pivot of the activity, the group carried out research along several main directions.

A first direction was signed by the EuPRAXIA project, a Horizon 2020 infrastructure initiative aimed at the design of a new infrastructure dedicated to high-quality plasma acceleration. In this streamline a strong activity was pursued that led to several publications concerning an original scheme for laser-driven plasma acceleration named ReMPI and an innovative design for a laser driver for the EuPRAXIA infrastructure. These results are now also part of the Conceptual Design Report of the project that is being published while we write.

A second main direction, strongly related to the ILIL-PW development, is related to the Light Ions beamline, an activity jointly developed with INFN, with the L3IA project, that also served as the first commissioning experimental activity of the new installation. High quality results were obtained and published, in this context, with important further developments planned.

In spite of the effort required for the ILIL-PW construction, the Group was constantly participating, also with a leading role, to the studies related to Inertial Confinement Fusion (ICF) towards Inertial Fusion Energy (IFE), with participation to several experimental campaign at major labs including the Vulcan laser at CLF (UK), the PALS laser in Czech Republic and the Gekko laser in Osaka (Japan). This is part of a continued effort to develop, also in the framework of a EURATOM funded program, a European approach to IFE based on the shock ignition scheme.

Finally, an area of major strategical developments of the Group looks at biomedical applications of novel particle and radiation beams generated by laser-plasma acceleration either for innovative radiotherapy approaches or for diagnostic purposes. This activity is gaining further interest especially in the context of the CNR Research Campus in which biomedical research is very active and the new installation is becoming a fundamental tool for such developments.

We are confident that the range of activities and the results discussed in this report will succeed in triggering interest in the reader and stimulate curiosity. At the same time colleagues from other labs and universities focusing on similar topics will find this report an easy tool to access our results and evaluate opportunities for collaboration.

Leonida A. Gizzi

People of the Intense Laser Irradiation Laboratory

(as of Nov. 2019)



Leonida A. GIZZI, Senior Research Staff
Head



Federica BAFFIGI, Technologist Staff (TD)
Laser System Operations



Fernando BRANDI, Research Staff
Experiments and Target Area Operation



Gabriele CRISTOFORETTI, Research Staff
Experiments & Data Analysis



Lorenzo FULGENTINI, Technologist Staff
Laser System Operation



Antonio GIULIETTI, Associate Researcher



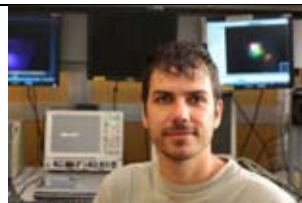
Petra KOESTER, Research Staff
Experiments and Lab Operations



Luca LABATE, Research Staff
Laser System, Coordinator



Sanjeev KUMAR, Post Doc
Experiments



Daniele PALLA, Post Doc
Experiments and Data Analysis



Davide TERZANI, Post Doc
Numerical Modelling



Gianluca CELLAMARE, Ph.D
Laser Development



Federico AVELLA, Physics Master student
Numerical modeling

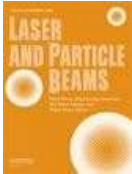


Paolo TOMASSINI, Consultant
Numerical Modelling

Publications of the ILIL group 2017 – 2019

<p>1. A. Zsedenyi, B. Farkas, G. N. Abdelrasoul, I. Romano, E. Gyukity-Sebestyen, K. Nagy, M. Harmati, G. Dobra, S. Kormondi, G. Decsi, I. B. Nemeth, A. Diaspro, <u>F. Brandi</u>, S. Beke, K. Buzas Gold nanoparticle-filled biodegradable photopolymer scaffolds induced muscle remodeling: in vitro and in vivo findings <i>Materials Science and Engineering C 72 (2017) 625–630</i> p.1</p>	
<p>2. <u>G. Cristoforetti</u>, A. Colartis, L. Antonelli, S. Atzeni, <u>F. Baffigi</u>, D. Batani, F. Barbato, G. Boutoux, R. Dudzak, <u>P. Koester</u>, E. Krouscky, <u>L. Labate</u>, Ph. Nicolai, O. Renner, M. Skoric, V. Tikhonchuk and <u>L. A. Gizzi</u> Experimental observation of parametric instabilities at laser intensities relevant for shock ignition <i>Europhysics Letters, 35001, 117 (2017), doi: 10.1209/0295-5075/117/35001</i> p.7</p>	
<p>3. C. Altana, S. Tudisco, G. Lanzalone, D. Mascali, A. Muoio, <u>F. Brandi</u>, <u>G. Cristoforetti</u>, P. Ferrara, <u>L. Fulgentini</u>, <u>P. Koester</u>, <u>L. Labate</u>, <u>D. Palla</u> and <u>L.A. Gizzi</u> Experimental investigation of ion production and acceleration mechanism in laser-produced plasma at moderate intensity for nuclear studies @ ELI-NP <i>Journal of Instrumentations (2017) 12, C04011</i> p.13</p>	
<p>4. <u>G. Cristoforetti</u>, P. Londrillo, P. K. Singh, <u>F. Baffigi</u>, G. D'Arrigo, Amit D. Lad, R. G. Milazzo, A. Adak, M. Shaikh, D. Sarkar, G. Chatterjee, J. Jha, M. Krishnamurthy, G. R. Kumar, <u>L. A. Gizzi</u> Transition from Coherent to Stochastic electron heating in ultrashort relativistic laser interaction with structured targets <i>Scientific Reports 7, (2017)</i> p.20</p>	
<p>5. <u>L. A. Gizzi</u>, D. Giove, C. Altana, <u>F. Brandi</u>, P. Cirrone, <u>G. Cristoforetti</u>, A. Fazzi, P. Ferrara, <u>L. Fulgentini</u>, <u>P. Koester</u>, <u>L. Labate</u>, G. Lanzalone, P. Londrillo, D. Mascali, A. Muoio, <u>D. Palla</u>, F. Schillaci, S. Sinigardi, S. Tudisco, G. Turchetti A New Line for Laser-Driven Light Ions Acceleration and Related TNSA Studies <i>Appl. Sci. 7, 984, 2017</i> p.28</p>	
<p>6. J. Babaei, <u>L. A. Gizzi</u>, P. Londrillo, S. Mirzanejad, T. Rovelli, S. Sinigardi, and G. Turchetti Rise time of proton cut-off energy in 2D and 3D PIC simulations <i>Phys. Plasmas 24, 043106 (2017)</i> p.38</p>	
<p>7. A. Walker et al., Horizon 2020 EuPRAXIA design study <i>Journal of Instrumentation, 12 (2017)</i> p.46</p>	

<p>8. A. Lapucci, M. Vannini, M. Ciofini, A. Pirr; M. Nikl. J. Li, L. Esposito, V. Biasini, J. Hostasa, T. Goto, G. Boulon, R. Maksimov; <u>L.A. Gizzi</u>, <u>L. Labate</u>, G. Toci Design and characterization of Yb and Nd doped transparent ceramics for high power laser applications: recent advancements <i>Proc. of SPIE vol. 10254: XXI International Symposium on High Power Laser Systems and Applications 2016, 102540E (2017)</i> p.54</p>	
<p>9. Balázs Farkas, Silvia Dante and <u>Fernando Brandi</u> Photoinitiator-free 3D scaffolds fabricated by excimer laser photocuring <i>Nanotechnology 28 (2017) 034001</i> p.60</p>	
<p>10. <u>A. Giulietti</u> Laser-driven particle acceleration for radiobiology and radiotherapy: where we are and where we are going <i>Proc. of SPIE vol. 10239, Medical Applications of Laser-Generated Beams of Particles IV: Review of Progress and Strategies for the Future, 1023904 (2017)</i> p.69</p>	
<p>11. Gourab Chatterjee, Prashant Kumar Singh, A. P. L. Robinson, D. Blackman, N. Booth, O. Culfa, R. J. Dance, <u>L. A. Gizzi</u>, R. J. Gray, J. S. Green, <u>P. Koester</u>, G. Ravindra Kumar, <u>L. Labate</u>, Amit D. Lad, K. L. Lancaster, J. Pasley, N. C. Woolsey, and P. P. Rajeev Micron-scale mapping of megagauss magnetic fields using optical polarimetry to probe hot electron transport in petawatt-class laser-solid interactions <i>Scientific Reports 7, 8347 (2017)</i> p.90</p>	
<p>12. Deep Sarkar, Prashant Kumar Singh, <u>G. Cristoforetti</u>, Amitava Adak, Gourab Chatterjee, Moniruzzaman Shaikh, Amit D. Lad, P. Londrillo, Giuseppe D'Arrigo, J. Jha, M. Krishnamurthy, <u>L. A. Gizzi</u>, and G. Ravindra Kumar Silicon nanowire based high brightness, pulsed relativistic electron source <i>APL . PHOTONICS 2, 066105 (2017)</i> p.98</p>	
<p>13. <u>Tomassini, P.</u>; De Nicola, S.; <u>Labate, L.</u>; Londrillo, P.; Fedele, R.; <u>Terzani, D.</u>; <u>Gizzi, LA.</u> The resonant multi-pulse ionization injection <i>Physics of Plasmas 24, 103120 (2017)</i> p.105</p>	
<p>14. <u>Tomassini, P.</u>; <u>Labate, L.</u>; Londrillo, P.; Fedele, R.; <u>Terzani, D.</u>; <u>Gizzi, LA.</u> High-Quality electron bunch production for high-brilliance Thomson Scattering sources <i>Proc. of SPIE vol. 10240, Laser Acceleration of Electrons, Protons, and Ions IV, UNSP 102400T (2017)</i> p.114</p>	
<p>15. <u>F. Brandi</u>, P. Marsili, F. Giammanco, F. Sylla, <u>L. A. Gizzi</u> Measurement of the particle number density in a pulsed flow gas cell with a second-harmonic interferometer <i>Journal of Physics: Conference Series 1079 (1), 012006 (2018).</i> p.132</p>	

<p>16. X. Chen, Y. Zhao, X. Li, Z. Xiao, Y. Yao, Y. Chu, B. Farkas, I. Romano, <u>F. Brandi</u>, J. Dai Functional Multichannel Poly (Propylene Fumarate) -Collagen Scaffold with Collagen-Binding Neurotrophic Factor 3 Promotes Neural Regeneration After Transected Spinal Cord Injury <i>Advanced Healthcare Materials</i> 7 (14), 1800315, (2018) p.138</p>	
<p>17. T. Pisarczyk, S.Yu. Gus'kov, R. Dudzak, O. Renner, D. Batani, T. Chodukowski, Z. Rusiniak, J. Dostal, N.N. Demchenko, M. Rosinski, P. Parys, M. Smid, Ph. Korneev, E. Krousky, S. Borodziuk, J. Badziak, L. Antonelli, <u>L.A. Gizzi</u>, <u>G. Cristoforetti</u>, <u>P. Koester</u>, Y. Maheut, L. Volpe, <u>F. Baffigi</u>, T. Levato, J. Skala, A. Zaras-Szydłowska, J. Trela, D. Mancelli, J. Ullschmied, M. Pfeifer, L. Juha, M. Krus, J. Hrebicek, T. Medrik, K. Jungwirth, M. Krupka and P. Pisarczyk Wavelength dependence of laser plasma interaction related to shock ignition approach <i>Laser and Particle beams</i> 36, 2018, 405-426 p.151</p>	
<p>18. G. Lanzalone, A. Muoio, C. Altana, M. Frassetto, L. Malferrari, D. Mascali, F. Odorici, S. Tudisco, <u>L.A. Gizzi</u>, <u>L. Labate</u>, S.M.R. Puglia, A. Trifirò Nuclear Reactions Studies in Laser-Plasmas at the forthcoming ELI-NP facilities <i>IOP Conf. Series: Journal of Physics: Conf. Series</i> 1014 (2018) 012006 p.173</p>	
<p>19. <u>L.A. Gizzi</u>, <u>P. Koester</u>, <u>L. Labate</u>, F. Mathieu, Z. Mazzotta, G. Toci, M. Vannini A viable laser driver for a user plasma accelerator <i>Nuclear Inst. and Methods in Physics Research, A</i> 909 (2018) 58–66 p.179</p>	
<p>20. <u>P. Tomassini</u>, S. De Nicola, <u>L. Labate</u>, P. Londrillo, R. Fedele, <u>D. Terzani</u>, F. Nguyen, <u>G. Vantaggiato</u>, <u>L.A. Gizzi</u> High-quality GeV-scale electron bunches with the Resonant Multi-Pulse Ionization Injection <i>Nuclear Inst. and Methods in Physics Research, A</i> 909 (2018) 1–4 p.188</p>	
<p>21. <u>L.A. Gizzi</u>, <u>F. Baffigi</u>, <u>F. Brandi</u>, <u>G. Bussolino</u>, <u>G. Cristoforetti</u>, A. Fazzi, <u>L. Fulgentini</u>, D. Giove, <u>P. Koester</u>, <u>L. Labate</u>, G. Maero, <u>D. Palla</u>, M. Romé, <u>P. Tomassini</u> Light Ion Accelerating Line (L3IA): Test experiment at ILIL-PW <i>Nuclear Inst. and Methods in Physics Research, A</i> 2018, 909, 160-163 p.192</p>	
<p>22. <u>L. Labate</u>, <u>G. Vantaggiato</u>, <u>L.A. Gizzi</u> Intra-cycle depolarization of ultraintense laser pulses focused by off-axis parabolic mirrors <i>High Power Laser Science and Engineering</i>, (2018), Vol. 6, e32 p.196</p>	

<p>23. <u>G. Cristoforetti</u>, L. Antonelli, S. Atzeni, <u>F. Baffigi</u>, F. Barbato, D. Batani, G. Boutoux, A. Colaitis, J. Dostal, R. Dudzak, L. Juha, <u>P. Koester</u>, A. Marocchino, D. Mancelli, Ph. Nicolai, O. Renner, J. J. Santos, A. Schiavi, M. M. Skoric, M. Smid, P. Straka, <u>L. A. Gizzi</u> Measurements of parametric instabilities at laser intensities relevant to strong shock generation <i>Physics of Plasmas</i> 25, 012702 (2018) p.204</p>	
<p>24. <u>L.A. Gizzi</u>, B. Marchetti, P.P. Rajeev Summary of WG7—High brightness power sources: From laser technology to beam drivers <i>Nuclear Inst. and Methods in Physics Research, A</i> 909 (2018) 450–451 p.216</p>	
<p>25. <u>G. Vantaggiato</u>, <u>L. Labate</u>, <u>P. Tomassini</u>, <u>L.A. Gizzi</u> Modelling of pulse train generation for resonant laser wakefield acceleration using a delay mask <i>Nuclear Inst. and Methods in Physics Research, A</i> 909 (2018) 114–117 p.218</p>	
<p>26. <u>L. A. Gizzi</u>, <u>P. Koester</u>, <u>L. Labate</u>, F. Mathieu, Z. Mazzotta, G. Toci and M. Vannini Lasers for Novel Accelerators <i>Proceedings of IPAC2019, Melbourne, Australia</i> p.222</p>	
<p>27. D. Batani, L. Antonelli, F. Barbato, G. Boutoux, A. Colaïtis, J.-L. Feugeas, G. Folpini, D. Mancelli, Ph. Nicolai, J. Santos, J. Trela, V. Tikhonchu, J. Badziak, T. Chodukowski, K. Jakubowska, Z. Kalinowska, T. Pisarczyk, M. Rosinski, M. Sawicka, <u>F. Baffigi</u>, <u>G. Cristoforetti</u>, F. D’Amato, <u>P. Koester</u>, <u>L.A. Gizzi</u>, S. Viciani, S. Atzeni, A. Schiavi, M. Skoric, S. Gus’kov, J. Honrubia, J. Limpouch, O. Klimo, J. Skala, Y.J. Gu, E. Krousny, O. Renner, M. Smid, S. Weber, R. Dudzak, M. Krus and J. Ullschmied Progress in understanding the role of hot electrons for the shock ignition approach to inertial confinement fusion <i>Nuclear Fusion</i> 59, 032012 (2019) p.226</p>	
<p>28. D. Panetta, <u>L. Labate</u>, L. Billeci, N. Di Lascio, G. Esposito, F. Faita, G. Mettievier, <u>D. Pala</u>, L. Pandola, P. Pisciotta, G. Russo, A. Sardo, <u>P. Tomassini</u>, P. A. Salvadori, <u>L. A. Gizzi</u> and P. Russo Numerical Simulation of Novel Concept 4D cardiac microtomography for small rodents based on all-optical Thomson scattering x-ray sources <i>Scientific Reports</i> 9, 8439, (2019). p.240</p>	
<p>29. <u>G. Cristoforetti</u>, L. Antonelli, D. Mancelli, S. Atzeni, <u>F. Baffigi</u>, F. Barbato, D. Batani, G. Boutoux, F. D’Amato, J. Dostal, R. Dudzak, E. Filippov, Y. J. Gu, L. Juha, O. Klimo, M. Krus, S. Malko, A. S. Martynenko, Ph. Nicolai, V. Ospina, S. Pikuz, O. Renner, J. Santos, V. T. Tikhonchuk, J. Trela, S. Viciani, L. Volpe, S. Weber, and <u>L. A. Gizzi</u> Time evolution of stimulated Raman scattering and two-plasmon decay at laser intensities relevant for shock ignition in a hot plasma <i>High Power Laser Science and Engineering</i>, 7, e51 (2019). p.252</p>	

<p>30. <u>D. Terzani</u> and <u>P. Londrillo</u> A fast and accurate numerical implementation of the envelope model for laser-plasma dynamics <i>Computer Physics Communications</i> 242 (2019) 49–59 p.266</p>	
<p>31. <u>F. Brandi</u> and <u>L. A. Gizzi</u> Optical diagnostics for density measurement in high-quality laser-plasma electron accelerators <i>High Power Laser Science and Engineering</i>, 7, e26 (2019) p.277</p>	
<p>32. <u>G. Toci</u>, <u>Z. Mazzotta</u>, <u>L. Labate</u>, <u>F. Mathieu</u>, <u>M. Vannini</u>, <u>B. Patrizi</u> and <u>Leonida A. Gizzi</u> Conceptual Design of a Laser Driver for a Plasma Accelerator User Facility <i>Instruments</i> 2019, 3, 40 p.288</p>	
<p>33. <u>Toci, G</u> ; <u>Gizzi, LA</u> ; <u>Koester, P</u>; <u>Baffigi, F</u>; <u>Fulgentini, L</u>; <u>Labate, L</u> ; <u>Hospodkova, A</u>; <u>Jary, V</u>; <u>Nikl, M</u>; <u>Vannini, M</u> InGaN/GaN multiple quantum well for superfast scintillation application: Photoluminescence measurements of the picosecond rise time and excitation density effect <i>Journal of Luminescence</i> 208 (2019) 119-124 p.307</p>	
<p>34. <u>Danson, CN</u> et al. Petawatt and exawatt class lasers worldwide <i>High Power Laser Science and Engineering</i> 7, e54 (2019) p.313</p>	
<p>35. <u>L. Antonelli</u> , <u>J. Trela</u>, <u>F. Barbato</u> , <u>G. Boutoux</u>, <u>Ph. Nicolaï</u>, <u>D. Batani</u>, <u>V. Tikhonchuk</u> , <u>D. Mancelli</u>, <u>A. Tentori</u>, <u>S. Atzeni</u> , <u>A. Schiavi</u> , <u>F. Baffigi</u>, <u>G. Cristoforetti</u>, <u>S. Viciani</u> , <u>L. A. Gizzi</u> , <u>M. Smid</u>, <u>O. Renner</u> , <u>J. Dostal</u> , <u>R. Dudzak</u> , <u>L. Juha</u>, and <u>M. Krus</u> Laser-driven strong shocks with infrared lasers at intensity of 1016 W/cm² <i>Phys. Plasmas</i> 26, 112708 (2019) p.367</p>	
<p>36. <u>Tomassini, P</u>; <u>Terzani, D</u>; <u>Baffigi, F</u>; <u>Brandi, F</u>; <u>Fulgentini, L</u>; <u>Koester, P</u>; <u>Labate, L</u>; <u>Palla, D</u>; <u>Gizzi, LA</u> High-quality 5 GeV electron bunches with resonant multi-pulse ionization injection <i>Plasma Physics and Controlled Fusion</i> 62, 1, 014010 (2020) p.380</p>	
<p>37. <u>L. A. Gizzi</u>, <u>R. Assmann</u>, <u>P. Koester</u>, <u>A. Giulietti</u> (Editors) Lecture Notes of the “Capri” Advanced Summer School <i>ISBN 978-3-030-25849-8; ISBN 978-3-030-25850-4 (e-book)</i> p.389</p>	

Publications



Gold nanoparticle-filled biodegradable photopolymer scaffolds induced muscle remodeling: *in vitro* and *in vivo* findings



Adam Zsedenyi^a, Balazs Farkas^b, Gaser N. Abdelrasoul^b, Ilaria Romano^b, Edina Gyukity-Sebestyen^c, Katalin Nagy^a, Maria Harmati^c, Gabriella Dobra^c, Sandor Kormondi^d, Gabor Decsi^a, Istvan Balazs Nemeth^e, Alberto Diaspro^b, Fernando Brandi^{b,f}, Szabolcs Beke^b, Krisztina Buzas^{a,c,g,*}

^a University of Szeged, Faculty of Dentistry, Tisza Lajos krt. 64, H-6720 Szeged, Hungary

^b Department of Nanophysics, Istituto Italiano di Tecnologia (IIT), Via Morego 30, 16163 Genova, Italy

^c Hungarian Academy of Sciences, Biological Research Centre, Temesvari krt. 62, H-67268 Szeged, Hungary

^d University of Szeged, Department of Traumatology, Semmelweis utca 6, H-6720 Szeged, Hungary

^e University of Szeged, Department of Dermatology and Allergology, Koranyi fasor 6, H-6720 Szeged, Hungary

^f Istituto Nazionale di Ottica (INO-CNR), Via Moruzzi 1, 56124 Pisa, Italy

^g Biological Research Centre Institute of Biochemistry H-6726 Szeged, Temesvari krt. 62. Hungary

ARTICLE INFO

Article history:

Received 15 August 2016

Accepted 27 November 2016

Available online 2 December 2016

ABSTRACT

Therapeutic stem cell transplantation bears the promise of new directions in organ and tissue replacement, but a number of its difficulties and perils are also well known. Our goal was to develop a method of transplantation by which the transplanted cells remain confined to the transplantation site and induce favorable processes. With the help of mask-projection excimer laser stereolithography, 3D hybrid nanoscaffolds were fabricated from biodegradable, photocurable PPF:DEF resin with incorporated gold nanoparticles (Au NPs). The scaffolds were tested *in vitro* and *in vivo* in order to find out about their biocompatibility and fitness for our purposes.

In vitro, macrophages and mouse autologous adipose stem cells (ASCs) were seeded over the hybrid scaffolds and non-hybrid (with Au NPs) scaffolds for 4 days. The hybrid nanocomposite greater stem cell dispersion and stem cell adhesion than PPF scaffolds without Au NPs, but such a difference was not seen in the case of macrophages. *In vivo*, stem cells, scaffoldings and scaffoldings covered in stem cells were transplanted under the back skin of mice. After 14 days, blood samples were taken and the affected skin area was excised. Cytokine and chemokine profiling did not indicate elevated immunomediators in the sera of experimental animals. Interestingly, the autologous-stem-cell-seeded hybrid nanocomposite scaffold induced muscle tissue regeneration after experimental wound generation *in vivo*. We could not observe such stem cell-induced tissue regeneration when no scaffolding was used.

We conclude that PPF:DEF resin nanoscaffolds with incorporated gold nanoparticles offer a safe and efficient alternative for the enhancement of local tissue remodeling. The results also support the idea that adipose derived stem cells are an optimal cell type for the purposes of regenerative musculoskeletal tissue engineering.

© 2016 Published by Elsevier B.V.

1. Introduction

Tissue Engineering (TE) is one of the most progressively developing disciplines [1–3], the development of which is largely stimulated by its biomedical potential. Throughout the last decade, various health issues have been successfully addressed utilizing a TE approach, such as bone regeneration [4] bladder [5] and muscle [6,7] augmentation/repair and also neuroregeneration [8,9].

The utility of polypropylene fumarate (PPF):diethyl fumarate (DEF) (7:3 w/w) biodegradable photocurable polymers in TE has already been widely investigated [10,11]. The results were promising, but further *in vivo* corroboration is still lacking.

Mask projection excimer laser stereolithography (MPEXSL) [12] makes it possible to fabricate 3D scaffolds in the nano range, including PPF:DEF nanocomposite scaffolds [13]. Such scaffolds act as a template for cell organization and tissue development in the tissue engineering process, and they are also biodegradable. Furthermore, to augment their efficiency, hybrid scaffolds can be fabricated by incorporating nanoparticles into the polymer resin, as recently reported by our group using [14] and gold [13] nanoparticles. The optical and physico-chemical properties of Au NPs have been intensively investigated,

* Corresponding author at: University of Szeged, Faculty of Dentistry, Tisza Lajos krt. 64, H-6720 Szeged, Hungary.

E-mail address: kr.buzas@gmail.com (K. Buzas).

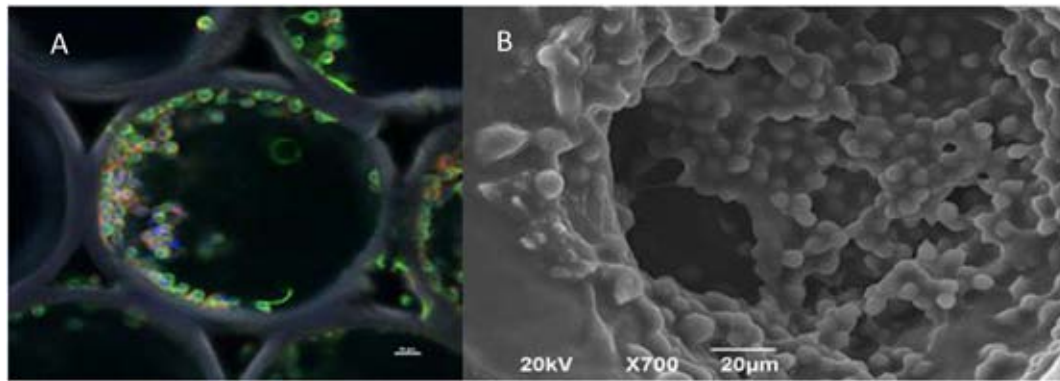


Fig. 1. Scaffold of 200 μm pore size, with Au nanoparticles and macrophages A) confocal microscopy, B) SEM.

along with their potential biomedical uses. Au NPs appear to be optimal candidates to be used as “transport vehicles” in scaffolds, due to their low inherent toxicity, tunable stability, switchable plasmonic optical properties and high surface area [15].

In this study, we conducted *in vitro* and *in vivo* experiments. The aim of our *in vitro* experiment was to investigate the interactions of the biodegradable Au NP hybrid scaffold with the adhesion and proliferation of mouse autologous adipose stem cells (ASCs) and macrophages as compared to non-hybrid PPF:DEF scaffolds.

In vitro, two different cell lines were used for the testing of the scaffolds. One of these, RAW 264.7, is a macrophage cell line of good proliferative potential and excellent adherence. In the other case, a primary cell culture also fit for real transplantation purposes was used (ASCs). In comparison with transformed cell lines, the adherence and proliferative potential of these cells is less well-defined. This way it was possible to test the biocompatibility of the scaffolds with both a stable and a sensitive system. During the *in vitro* experiments we managed to optimize the conditions for the proliferation and adherence of the stem cells.

The aim of the *in vivo* part of the study was to provide further support for our previous findings regarding the favorable biocompatibility of these scaffolds [13] - this time with the Au NP hybrids. To reach that end, stem cells, scaffoldings and scaffoldings covered in stem cells were transplanted under the back skin of mice. Inflammatory and allergic reactions upon transplantation are among the first signs of impending failure. The measurement of inflammatory cytokine and chemokine levels allows a sensitive detection of such processes, wherefore we utilized a proteome profiler capable of detecting 44 cytokines and chemokines.

The cytokine and chemokine profiling was followed by the histological analysis of the removed implant, which was important in two ways. First, histology verified the biodegradability of the polymer. Second, this way we could rule out tumor formation, which is a potential and dangerous side effect of stem cell transplantation. Finally, the results of the immunological profiling could be verified by the lack of inflammatory infiltration.

Interestingly, the autologous-stem-cell-seeded hybrid nanocomposite scaffold induced muscle tissue regeneration after experimental wound generation *in vivo*.

2. Materials and methods

2.1. Mask-projection excimer laser stereolithography (MPExSL)

MPExSL is a stereolithography process developed in our laboratory [15] based on excimer laser irradiation of a liquid photocrosslinkable resin. The geometry and physical properties of the scaffolds to be fabricated is selected by a set of interchangeable masks and different laser and resin parameters, such as the laser wavelength [15], number of laser pulses and/or pulse fluence [16,17], and the photoinitiator concentration [15]. The setup is described in detail in Beke et al. [15].

2.2. Polymer resin

The PPF:DED biodegradable photopolymer resin preparation is described in detail in our previous work [18]. The preparation of PPD:DEF–Au NP nanocomposites is described previously [13].

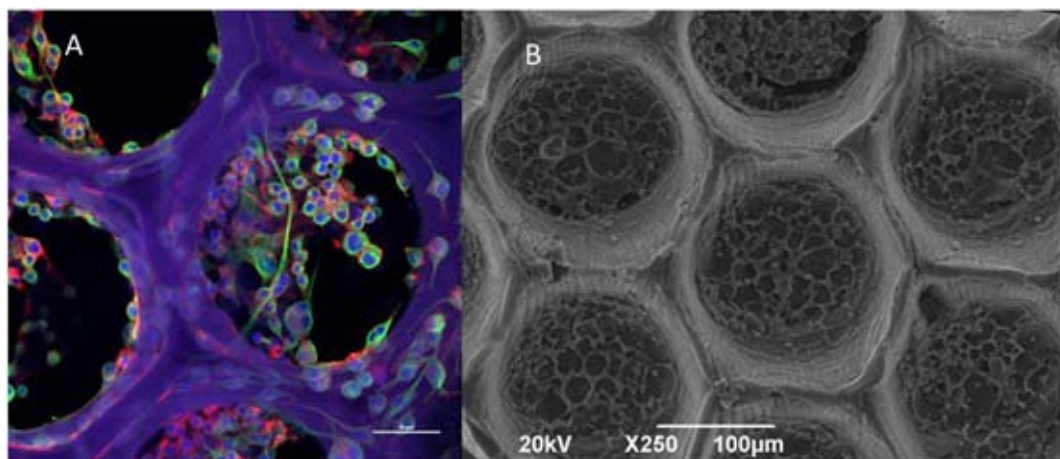


Fig. 2. Scaffold of 200 μm pore size, without Au nanoparticles and macrophages A) confocal microscopy, B) SEM.

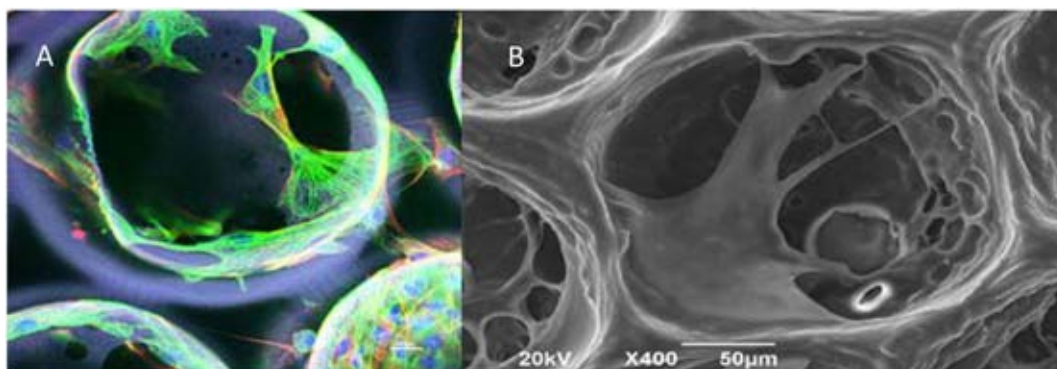


Fig. 3. Scaffold of 200 μm pore size, with Au nanoparticles and with mouse ASCs A) confocal, B) SEM.

To test the produced Au nanocomposite scaffolds, we used biodegradable scaffolds with 200 μm pore size and 5.52 μM Au nanoparticle [13].

2.3. Biological testing: cell culture, mouse model, histology, and cytokine/chemokine profile

The primary autologous adipose stem cells were isolated from 4 to 6 weeks old Balb/c mice (Charles River Laboratories International, Inc.). After cervical dislocation, the abdominal adipose tissue was removed. The tissue was put in 100 $\mu\text{g}/\text{ml}$ RPMI (Lonza, Cat. No.: BE12-115F) treated with kanamycin (Kanamycin sulfate from Streptomyces Kanamyceticus, Sigma K 1377-16), then digested in collagenase (Sigma) at 37 $^{\circ}\text{C}$. After 1 h, the cells were washed and cultured in a Petri dish for 2 weeks in MSC Medium (MesenCult, STEMCELL) with 10% fetal bovine serum, 100 U/ml penicillin, 100 U/ml streptomycin and 0.25 $\mu\text{g}/\mu\text{l}$ fungizone (Promocell) at 37 $^{\circ}\text{C}$, 5% CO_2 .

2.3.1. In vitro experiments

The photocured samples were sterilized with UV irradiation for 30 min and coated with 0.01% poly-L-lysine (MW 70,000–150,000 Da, Sigma) for 30 min at room temperature. Poly-L-lysine was removed and the scaffolds were dried under laminar box, and then incubated in Eagle's Minimum Essential Medium (EMEM, Lonza) with 10% fetal bovine serum, 100 U/ml penicillin, 100 U/ml streptomycin and 0.25 $\mu\text{g}/\mu\text{l}$

fungizone (Promocell) for 7 days at 37 $^{\circ}\text{C}$. At day seven, adipose-derived mesenchymal stem cells (ASC) isolated from Balb/c male mouse or macrophages (RAW 264.7) were seeded at 7×10^4 cells/ml in wells containing one scaffold each, and then incubated in humidified atmosphere with 5% CO_2 at 37 $^{\circ}\text{C}$ for 4 days. Cell-seeded-scaffolds with cells were prepared for Scanning Electron Microscope (SEM), and Confocal microscope (Nikon A1) examination. For the preparation for Confocal microscopy we used 4% paraformaldehyde and immune staining (Alpha tubulin, Phalloidin, Dapi). SEM samples were treated 0.1 M Sodium Cacodylate, and 1.2% Glutaraldehyde. Samples were dehydrated in ethanol of increasing concentration (50%, 70%, 80%, 90%, 96%, 100%) for 10 min each concentration and 100% Hexamethyldisilazane overnight.

2.3.2. In vivo experiments

The MPExSL-fabricated samples were sterilized with UV irradiation for 30 min and coated with 0.01% poly-L-lysine (MW 70,000–150,000 Da, Sigma) for 30 min at room temperature. Poly-L-lysine was removed and the scaffolds were dried under laminar box, and then incubated in Eagle's Minimum Essential Medium (EMEM, Lonza) with 10% fetal bovine serum, 100 U/ml penicillin, 100 U/ml streptomycin and 0.25 $\mu\text{g}/\mu\text{l}$ fungizone (Promocell) for 7 days at 37 $^{\circ}\text{C}$. The medium was changed every other day. At day seven, ASCs were seeded in MSC Medium at 5×10^4 cells/ml in wells containing one scaffold each, and then incubated in humidified atmosphere with 5% CO_2 at 37 $^{\circ}\text{C}$ for 7 days. After being covered with cells, the scaffolds were implanted

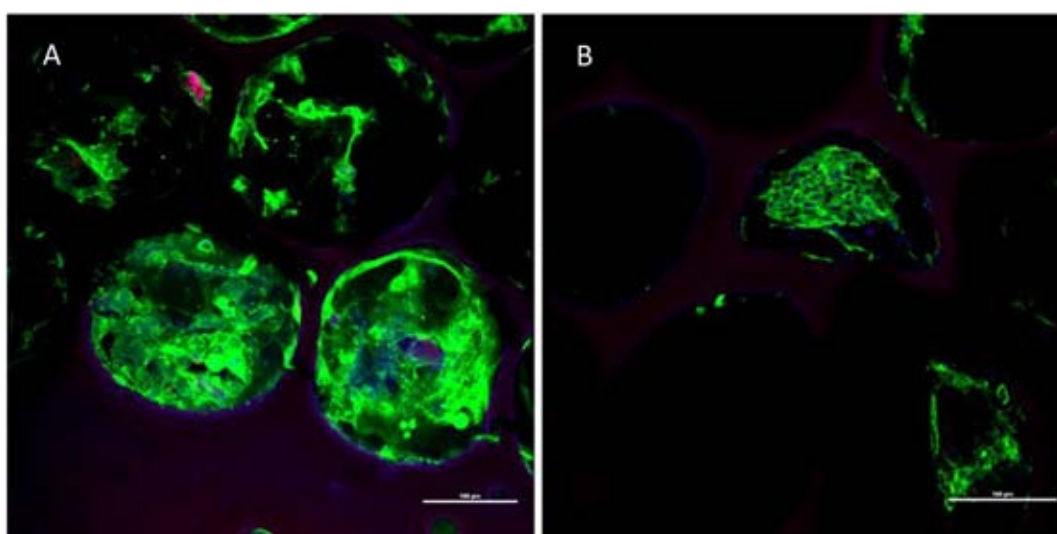


Fig. 4. ASC adhesion to a hybrid (A) and a normal (B) scaffold.

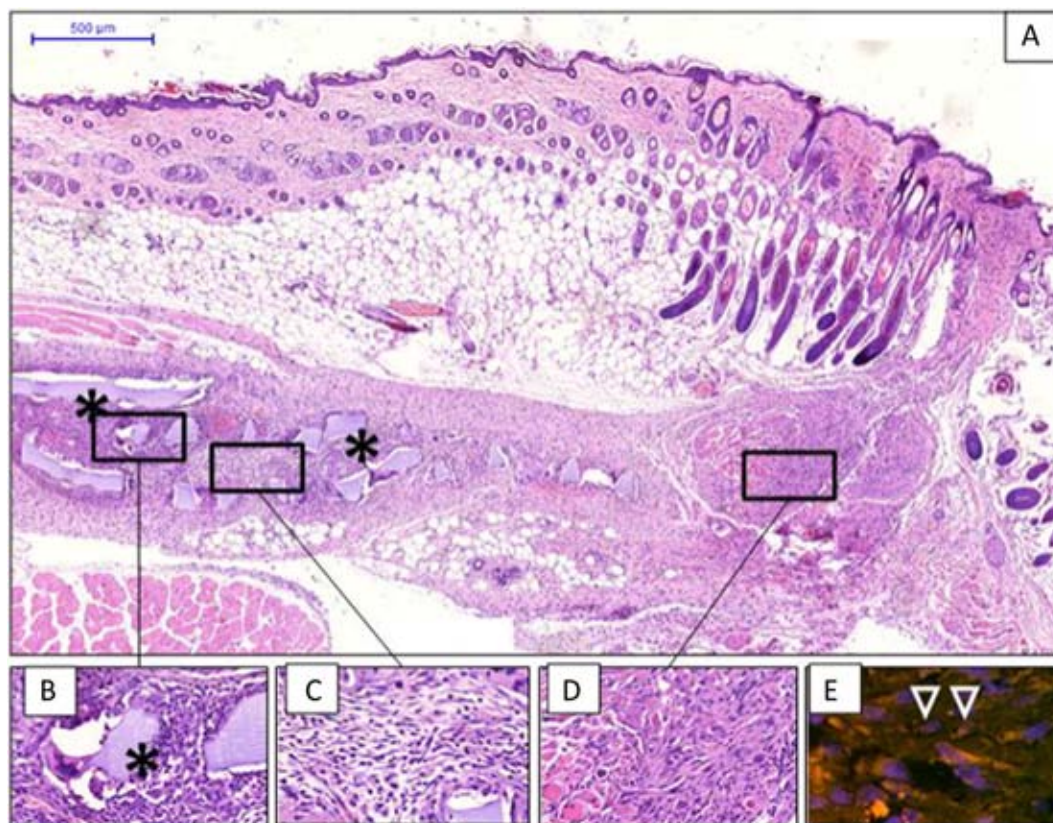


Fig. 5. Images of a section with ASC seeded Au filled scaffold (A, B, C). Viable mesenchymal cell colonies and striated muscle regeneration indicated by stem cells were seen in the scaffold specimen (D). The Y chromosome content of the transplanted stem cells was detected by the FISH technique, red dots indicated by arrowheads (E).

under the dorsal skin of 8 week old female Balb/c mice (Charles River Laboratories International, Inc.). The control group was injected with 5×10^4 ASCs. Three mice per group were implanted. 14 days after transplantation, the scaffolds and dorsal skin were removed and blood samples were collected. For cytokine and chemokine profile, collected blood samples were allowed to clot for 30 min at room temperature, then overnight at 4 °C. Serum samples were collected by centrifugation at 3000 rpm for 5 min and stored at -80 °C until the time of analysis. In case of a successful cell implantation, the presence or absence of selected mouse ASC was followed by histology. Specimens were fixed in 4% buffered paraformaldehyde and then embedded in paraffin blocks. Four-micrometer-thick sections were prepared and stained by conventional hematoxylin-eosin stain then coverslipped. The sections were visualized by scanning virtual microscope (3D Histech, Hungary). Inflammatory reactions were detected by cytokine and chemokine profiling.

Protein concentrations of the sera were measured by BCA Protein Assay (Thermo Scientific) and pooled samples were tested to simultaneously detect relative levels of different cytokines according to the manufacturer's instructions by Mouse Cytokine Array, Panel A (R&D Systems). Immunoreactive signals were detected using an LI-COR ODYSSEY Fc imager followed by analysis with Odyssey v1.2 software. All animal experiments were performed in accordance with national (1998. XXVIII; 40/2013) and European (2010/63/EU) animal ethics guidelines. The experimental protocols were approved by the Animal Experimentation and Ethics Committee of the Biological Research Centre of the Hungarian Academy of Sciences and the Hungarian National Animal Experimentation and Ethics Board (clearance number: XVI./03521/2011.)

For fluorescence *in situ* hybridization (FISH), chromosome X and Y control probe (Empire Genomics, Buffalo, NY, USA) was used to verify

the presence of the Y chromosome of the transplanted mouse adipose stem cells, according to the manufacturer's instructions.

3. Results

3.1. *In vitro* tests

Macrophages –a cell type of high adherence–could be seeded on the scaffold surface as shown in Fig. 1.

The Au-content of the polymer resin had no influence on the adherence of the macrophages (Fig. 2).

The adherence of ASCs, however, proved to be sensitive to the Au content. Adherence to the Au NP hybrid scaffold proved to be much better (Figs. 3, 4).

3.2. *In vivo* tests

The excised skin areas showed no visible signs of reactive inflammation (Fig. 5), and the cytokine profiling did not indicate inflammation either (Fig. 6).

Interestingly, we detected not only the implanted ASCs with X-Y chromosome but also cells containing Y and more than one X chromosomes, most likely resulting from regenerative cellular fusion between ASCs and stromal mesenchymal cells (Fig. 5A). This suggests that the biopolymers applied together with ASCs were able to initiate tissue repair in the appropriate tissue environment.

We could not detect ASC or ASC-derived tissue regeneration in ASC injected mice when scaffold support was not utilized (data not shown). In the histological sections of the group implanted with adipose stem cells, small residual biopolymer pieces of varying diameter (50–500 μm) were seen.

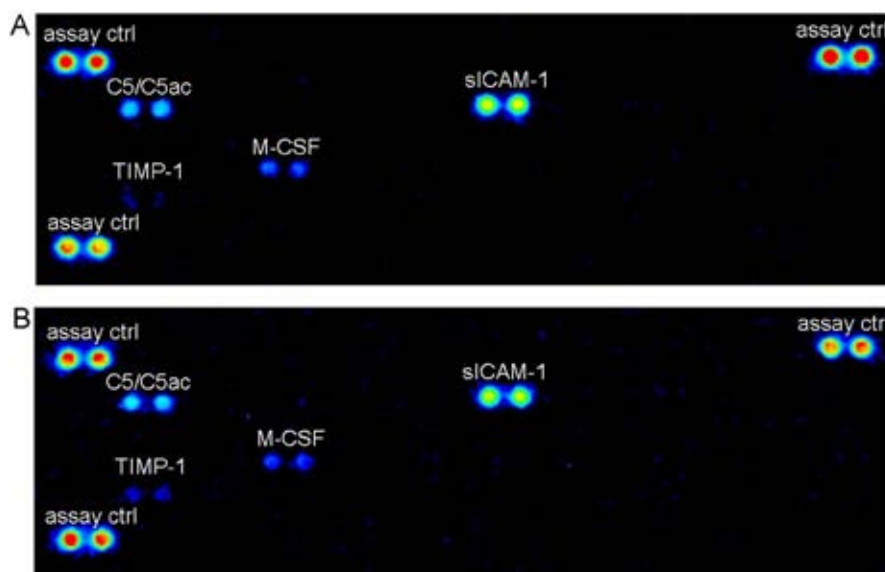


Fig. 6. Cytokine and chemokine proteome profiling detected C5 complement component, sICAM-1 adhesion molecule, M-CSF and TIMP-1 cytokines. The profiler did not indicate significant immune reaction to the ASC-seeded scaffolds (A) as compared to the control scaffold (B). This is supported by the lack of immune cell infiltration or relevant immune reaction against the ASC-seeded scaffold, as revealed by histology.

4. Conclusion

To use stem cells in the regenerative medicine is one of the most important challenge of tissue engineering. Stem cell implantation is the best way to regenerate different types of tissues based on pluripotency but the stem cells incorporated to the circulation could initiate cancerous transformation.

Biodegradable, photocurable polymer resin, polypropylene fumarate (PPF) along with Au NPs were utilized to synthesize a hybrid nanocomposite resin, that is directly exploitable in stereolithography (SL) processes. The resulting resin was used to fabricate nanocomposite scaffolds *via* mask projection excimer laser stereolithography.

In vitro studies helped to optimize scaffold structure, composition and cell culturing conditions for further *in vivo* experiments. We compared the colony-forming abilities of macrophages- as a highly adherent cell line- and the primary stem cell culture on different biomaterials. While the stable but transformed macrophage cell line was not especially sensitive to the Au-content of the polymer, the adherence and distribution of ASCs was definitely better on the Au hybrid polymer. This is important because of the potential value of these cells in regenerative tissue engineering.

Our results suggested to use Au-filled scaffolds to secure the optimal cell transfer. In the case of Au-filled scaffolds we have seen evenly distribution and adherence of stem cells.

As the potentially most dangerous sequela of the implantation of any foreign body is a violent immune response, monitoring immune reactions is of key importance. Neither immunological profiling nor histology revealed any sign of inflammatory or allergic reactions in our experimental animals. To our knowledge, we are the first to have proven that PPF:DEF Au NP scaffolds do not induce immune response in experimental animals.

These scaffolds provided an optimal surface for the adherence of ASCs and kept them in place, but an even more valuable observation was also made: ASCs induced muscle regeneration *in situ*, which was verified by the histological analysis and the FISH test. This in itself may not be new, as several publications have dealt with scaffold-derived muscle regeneration, but the preference of ASCs for this unique surface [13] make the Au NP nanocomposite- ASC system a really promising one for clinical applications.

Tumor formation is an ever-present danger of stem cell transplantation [19,20], but our system proved to be safe in this respect.

The use of the scaffold ensures that the cells are kept in place, and the chance of stem cells getting into the bloodstream is significantly reduced. The use of autologous stem cells reduces the risk of rejection [21], ensures better regeneration [22], and ASCs are readily available. ASCs are easy to harvest in a safe, minimally invasive way from almost any patient.

We conclude that PPF:DEF resin scaffolds with incorporated gold nanoparticles, especially in combination with ASCs carry the promise of a new, safe and efficient means of musculoskeletal tissue regeneration [2].

Acknowledgement

This research was funded by Hungarian Scientific Research Fund (OTKA K) 112493 and GINOP-2.3.2-15-2016-00001.

The authors would like to thank Gábor Braunitzer for his helpful comments.

References

- [1] H.T. Liao, C.T. Chen, Osteogenic potential: comparison between bone marrow and adipose-derived mesenchymal stem cells, *World. J. Stem. Cells.* 6 (3) (2014) 288–295, <http://dx.doi.org/10.4252/wjsc.v6.i3.288>.
- [2] A. Trumbull, G. Subramanian, E. Yildirim-Ayan, Mechanoresponsive musculoskeletal tissue differentiation of adipose-derived stem cells, *Biomed. Eng. Online* 15 (2016) 43, <http://dx.doi.org/10.1186/s12938-016-0150-9>.
- [3] R. Langer, J.P. Vacanti, Tissue engineering, *Science* 260 (1993) 920–926, <http://dx.doi.org/10.1126/science.8493529>.
- [4] A.M. Yousefi, P.F. James, R. Akbarzadeh, A. Subramanian, C. Flavin, H. Oudadesse, Prospect of stem cells in bone tissue engineering: a review, *Stem. Cells. Int.* (2016), Article ID 6180487, <http://dx.doi.org/10.1155/2016/6180487> (13 pages).
- [5] O. Lam Van Ba, S. Aharony, O. Loutochin, J. Corcos, Bladder tissue engineering: a literature review, *Adv. Drug Deliv. Rev.* 82–83 (2015) 31–37, <http://dx.doi.org/10.1016/j.addr.2014.11.013>.
- [6] J.M. Grasman, M.J. Zayas, R.L. Page, G.D. Pins, Biomimetic scaffolds for regeneration of volumetric muscle loss in skeletal muscle injuries, *Acta Biomater.* 25 (2015) 2–15, <http://dx.doi.org/10.1016/j.actbio.2015.07.038>.
- [7] J. Stern-Straeter, F. Riedel, G. Bran, K. Hörmann, U.R. Goessler, *Advances in skeletal muscle tissue engineering, In Vivo.* 21 (2007) 435–444.
- [8] A. Faroni, S.A. Mobasser, P.J. Kingham, A.J. Reid, Peripheral nerve regeneration: experimental strategies and future perspectives, *Adv. Drug Deliv. Rev.* 82–83 (2015) 160–167, <http://dx.doi.org/10.1016/j.addr.2014.11.010>.
- [9] V. Chiono, C. Tonda-Turo, Trends in the design of nerve guidance channels in peripheral nerve tissue engineering, *Prog. Neurobiol.* 131 (2015) 87–104, <http://dx.doi.org/10.1016/j.pneurobio.2015.06.001>.
- [10] J.W. Lee, K.S. Kang, S.H. Lee, J.Y. Kim, B.K. Lee, D.W. Cho, Bone regeneration using a microstereolithography-produced customized poly (propylene fumarate)/diethyl

- formate photopolymer 3D scaffold incorporating BMP-2 loaded PLGA microspheres, *Biomaterials* 32 (2011) 744e752, <http://dx.doi.org/10.1016/j.biomaterials.2010.09.035>.
- [11] P.X. Lan, J.W. Lee, Y.J. Seol, D.W. Cho, Development of 3D PPF/DEF scaffolds using micro-stereolithography and surface modification, *J. Mater. Sci. Mater. Med.* 20 (2009) 271–279, <http://dx.doi.org/10.1007/s10856-008-3567-2>.
- [12] B. Farkas, A. Zsedenyi, E. Gyukity-Sebestyen, I. Romano, K. Nagy, A. Diaspro, F.K. Brandi, K. Buzas, S. Beke, Excimer laser-produced biodegradable photopolymer scaffolds do not induce immune rejection in vivo, *JLMN* 10 (2015) 11–14, <http://dx.doi.org/10.2961/jlmn.2015.01.0002>.
- [13] G.N. Abdelrasoul, B. Farkas, I. Romano, A. Diaspro, S. Beke, Nanocomposite scaffold fabrication by incorporating gold nanoparticles into biodegradable polymer matrix: synthesis, characterization, and photothermal effect, *Mater. Sci. Eng. C Mater. Biol. Appl.* 56 (2015) 305–310, <http://dx.doi.org/10.1016/j.msec.2015.06.037>.
- [14] B. Farkas, M. Rodio, I. Romano, A. Diaspro, R. Intartaglia, S. Beke, Fabrication of hybrid nanocomposite scaffolds by incorporating ligand-free hydroxyapatite nanoparticles into biodegradable polymer scaffolds and release studies, *Beilstein J. Nanotechnol.* 6 (2015) 2217–2223, <http://dx.doi.org/10.3762/bjnano.6.227>.
- [15] S. Beke, B. Farkas, I. Romano, F. Brandi, 3D scaffold fabrication by mask projection excimer laser stereolithography, *Opt. Mater. Express.* 4 (2014) 2032–2041, <http://dx.doi.org/10.1364/OME.4.002032>.
- [16] S. Beke, F. Anjum, L. Ceseracciu, I. Romano, A. Athanassiou, A. Diaspro, F. Brandi, Rapid fabrication of rigid biodegradable scaffolds by excimer laser mask projection technique: a comparison between 248 and 308 nm, *Laser Phys.* 23 (3) (2013) 035602 <https://www.researchgate.net/publication/257416197>.
- [17] B. Farkas, I. Romano, L. Ceseracciu, A. Diaspro, F. Brandi, S. Beke, Four-order stiffness variation of laser-fabricated photopolymerbiodegradable scaffolds by laser parameter modulation, *Mater. Sci. Eng. C Mater. Biol. Appl.* 55 (2015) 14–21, <http://dx.doi.org/10.1016/j.msec.2015.05.0540928-493>.
- [18] S. Beke, F. Anjum, H. Tsushima, L. Ceseracciu, E. Chierregatti, A. Diaspro, A. Athanassiou, F. Brandi, Towards excimer-laser-based stereolithography: a rapid process to fabricate rigid biodegradable photopolymer scaffolds, *J. R. Soc. Interface* 9 (2012) 3017–3026, <http://dx.doi.org/10.1098/rsif.2012.0300>.
- [19] H.C. Li, C. Stoicov, A.B. Rogers, J. Houghton, Stem cells and cancer: evidence for bone marrow stem cells in epithelial cancers, *World J. Gastroenterol.* 12 (3) (2006) 363–371, <http://dx.doi.org/10.3748/wjg.v12.i3.363>.
- [20] T.E. Werbowetski-Ogilvie, M. Bossé, M. Stewart, A. Schnerch, V. Ramos-Mejia, A. Rouleau, T. Wynder, M.J. Smith, S. Dingwall, T. Carter, C. Williams, C. Harris, J. Dolling, C. Wynder, D. Boreham, M. Bhatia, Characterization of human embryonic stem cells with features of neoplastic progression, *Nat. Biotechnol.* 27 (2009) 91–97, <http://dx.doi.org/10.1038/nbt.1516>.
- [21] L.A. Vonk, T.S. de Windt, I.C. Slaper-Cortenbach, D.B. Saris, Autologous, allogeneic, induced pluripotent stem cell or a combination stem cell therapy? Where are we headed in cartilage repair and why: a concise review, *Stem. Cell Res. Ther.* 6 (2015) 94, <http://dx.doi.org/10.1186/s13287-015-0086-1>.
- [22] D. Currò, G. Mancardi, Autologous hematopoietic stem cell transplantation in multiple sclerosis: 20 years of experience, *Neurol. Sci.* 37 (2016) 857–865, <http://dx.doi.org/10.1007/s10072-016-2564-3>.

Experimental observation of parametric instabilities at laser intensities relevant for shock ignition

G. CRISTOFORETTI¹, A. COLAÏTIS², L. ANTONELLI³, S. ATZENI³, F. BAFFIGI¹, D. BATANI^{2,4}, F. BARBATO⁵, G. BOUTOUX², R. DUDZAK⁶, P. KOESTER¹, E. KROUSKY⁶, L. LABATE¹, PH. NICOLAÏ², O. RENNER⁷, M. SKORIC⁸, V. TIKHONCHUK² and L. A. GIZZI¹

¹ *Intense Laser Irradiation Laboratory, INO CNR (National Council of Research) - Pisa, Italy*

² *Université de Bordeaux, CNRS, CEA, CELIA (Centre Lasers Intenses et Applications) - Talence, France*

³ *Dipartimento SBAI, Università di Roma "La Sapienza" - Rome, Italy*

⁴ *National Research Nuclear University MEPhI, Department of Plasma Physics - Moscow, Russia*

⁵ *Empa Swiss Federal Laboratories for Materials Science and Technology - Dübendorf, Switzerland*

⁶ *Prague Asterix Laser System - Prague, Czech Republic*

⁷ *Institute of Physics & ELI Beamlines, ASCR - Prague, Czech Republic*

⁸ *Vinca Institute of Nuclear Sciences - Belgrade, Serbia*

received 11 January 2017; accepted in final form 15 March 2017
published online 31 March 2017

PACS 52.38.-r – Laser-plasma interactions

PACS 52.38.Dx – Laser light absorption in plasmas (collisional, parametric, etc.)

PACS 52.65.-y – Plasma simulation

Abstract – We report measurements of parametric instabilities and hot electron generation in a laser intensity regime up to 6×10^{15} W/cm², typical of the shock ignition approach to inertial fusion. Experiments performed at the PALS laboratory in Prague show that the incident laser energy losses are dominated by Stimulated Brillouin Scattering (SBS) rather than by Stimulated Raman Scattering (SRS) or Two-Plasmon Decay (TPD). Results are compared to hydrodynamics simulations using a code that includes self-consistent calculations of non-linear laser plasma interactions and accounts for the laser intensity statistics contained in the beam speckles. Good agreement is found for the backscattered SRS light, and for temperature and flux of hot electrons. The effect of high-intensity speckles on backscattered SRS is also underlined numerically and experimentally.

Copyright © EPLA, 2017

Introduction. – Shock Ignition (SI) [1–6] is a promising approach to Inertial Confinement Fusion (ICF) [7–9], that relies on the separation of the compression and ignition phases. Since the target is not meant to be ignited by the pressure-volume work of the imploding capsule, it can be assembled at lower velocities [1] with lower intensity nanosecond laser pulses ($I \approx 5 \times 10^{14}$ W/cm²). This reduces the risks associated to hydrodynamic instabilities during the compression. The ignition of the hotspot relies on an intense laser pulse (I up to $\approx 10^{16}$ W/cm²), generating a pressure $P > 300$ Mbar at the ablation layer which drives a strong shock into the target. The final fuel assembly is non-isobaric resulting in higher target gains than in conventional hotspot ignition. This scheme is compatible with present-day “NIF-like” laser technology [2,10,11] and, therefore, a full-scale demonstration of SI could be realized in the next decade.

The success of the SI concept depends mainly on the coupling of the laser spike with the extended corona surrounding the imploding shell, where an efficient laser absorption, able to generate a strong shock wave (> 300 Mbar), is needed. In recent experiments carried out at OMEGA laser [12,13] in spherical irradiation geometry, at laser intensities relevant for SI ($I \sim 6 \times 10^{15}$ W/cm²), a peak ablation pressure close to 400 Mbar was inferred, which constitutes a significant breakthrough toward the demonstration of the feasibility of the SI scheme. Despite this step forward, the physics of laser-plasma interaction in this highly non-linear regime, is still largely unknown and needs dedicated investigations.

Notably, laser-plasma interaction at $I\lambda^2 > 10^{14}$ W μ m²/cm² is strongly non-linear. Parametric instabilities (Stimulated Brillouin Scattering (SBS), Stimulated Raman Scattering (SRS), and Two-Plasmon

Decay (TPD)) may arise [14–17], with the unwanted effects of reflecting a large part of incident laser light and generating Hot Electrons (HEs). Further, laser filamentation may alter compression uniformity and enhance the growth of parametric instabilities [18].

The presence of HEs is usually detrimental in ICF because they may preheat the target, making compression more difficult. In the SI scheme, HEs are generated at the end of the compression phase, when the shell areal density is high. As a result, they do not affect target compression and might even improve the shock pressure provided their kinetic energy is not too large [1,12,13,19]. However, recent studies using a hydrodynamic model incorporating HEs effects [20] suggest that the highest energy HEs may prevent hotspot ignition by preheating the fuel and by driving an inner-shell interface ablation that increases the hotspot mass prior to the ignitor shock arrival [21]. As such, the characterization of HEs generated in the SI regime is a key physical issue that must be carried out.

While integrated SI experiments require spherical geometry, many underlying processes can be investigated in planar geometry, which offers the advantage of a simpler scheme and an easier approach to diagnostics. In this letter, we report experimental results in the intensity range $(2\text{--}6) \times 10^{15} \text{ W/cm}^2$, obtained using the Prague Asterix Laser System (PALS) [22], and simulation results obtained with the radiative-hydrodynamic code CHIC [23] that includes a description of the non-linear laser-plasma interaction. While in previous work [24] we investigated hydrodynamics and shock propagation, here we focus on the impact of laser-plasma instabilities and their role in the generation of hot electrons. Although plasma conditions are significantly different from those envisaged in a real SI reactor, in particular density scale length and electron temperature are lower than expected, we think that the data reported here can contribute to draw a picture of the growth of parametric instabilities in this interaction regime. Our work shows that the impact of parametric instabilities in the SI regime is controlled by local intensities and plasma conditions, varying on the scale of speckle dimensions, which can drive non-linear and kinetic effects. An accurate modeling of the local interaction is therefore needed in order to allow mastering the interaction and hence the processes bringing to successful shock ignition.

Experimental set-up. – The PALS iodine laser delivers pulses with wavelength $\lambda_0 = 1.3 \mu\text{m}$ and duration $\tau = 300 \text{ ps}$ [22]. In the experiment we used an *auxiliary* pulse delivering $\approx 30 \text{ J}$ and the *main* pulse delivering up to 300 J , both smoothed with Random Phase Plates (RPP) to produce a uniform irradiation. The auxiliary pulse was operating at the fundamental frequency and focused to $I \approx 7 \times 10^{13} \text{ W/cm}^2$ in an extended spot (full width at half-maximum, FWHM = $900 \mu\text{m}$) to create an approximately planar plasma. The main pulse, delayed up to 1.2 ns with respect to the auxiliary pulse, was converted

to 3ω ($\lambda_0 = 438 \text{ nm}$) and focused by an $F/2$ lens to create a strong shock. The beam profile in the laser waist and the effective energy enclosed in it were accurately measured by imaging and calorimetric techniques. A spot size of $100 \mu\text{m}$ FWHM provided an envelope peak intensity on the target up to $I_{max} = 6 \times 10^{15} \text{ W/cm}^2$. Local intensity in laser speckles can however exceed this value by a factor up to one order of magnitude. By changing the delay between the pulses we tuned the density scale length $L = n_e/(dn_e/dx)$ of the preformed plasma. According to hydrodynamic simulations, L varies from 50 to $150 \mu\text{m}$ in the underdense plasma during the interaction with the main pulse. These values are in agreement with interferometric measurements conducted both in the visible [25] and in the X-ray domain [26].

Three-layer targets were used. The front layer was parylene-C plastic ($\text{C}_8\text{H}_7\text{Cl}$) of various thicknesses, mimicking a low- Z ICF ablator material. High-resolution X-ray spectroscopy of chlorine ions allowed getting the plasma temperature [26]. Underneath plastic, two tracer layers of Ti and Cu ($10 \mu\text{m}$ each) were placed. X-ray spectroscopy of Ti and Cu K_α radiation, originating from collisions with hot electrons, was used to estimate their average energy and flux. K_α emission was measured with a CCD working in single-photon regime and with two spherically bent quartz (422) and (203) crystals providing a 2D spatial distribution of K_α intensity on the target surface [27]. Both K_α and X-ray spectrometers used Kodak AA400 films as detectors.

The backscattered radiation from SRS and SBS was collected through the focusing lens of the main beam and measured by two calorimeters. On the same line, backscattered radiation was spectrally analyzed by a broadband spectrometer, allowing the detection of radiation both in the range $\omega_0/2 < \omega < \omega_0$, originating from SRS at $n_e < n_c/4$, and at $\omega \approx \omega_0/2$, originating from SRS/TPD occurring at $n_e \approx n_c/4$. Besides, the $3/2\omega_0$ harmonic of the laser frequency, generated by the mixing of laser light with electron plasma waves (EPWs) produced by TPD, was collected inside the vacuum chamber and sent to a UV spectrometer and a calorimeter.

Experimental results. –

X-ray spectroscopy. X-ray spectra, showing well-resolved He- and Li-like lines from Cl ions, were compared with SPECT3D [28] predictions, providing a time-integrated temperature of $\approx 700\text{--}850 \text{ eV}$ in the overdense plasma near the ablation surface ($n_e \approx 3n_{cr} \approx 2 \times 10^{22} \text{ cm}^{-3}$) [26]. This temperature is in a good agreement with hydrodynamic simulations and, as expected, is lower than in the underdense region ($n_e \approx n_c/4$), as inferred from the $\omega_0/2$ spectra (see below).

Calorimetry. Back-reflected light is dominated by wavelengths near $\lambda \approx 438 \text{ nm}$, carrying 5–15% of the incident energy and originating from SBS and laser light reflected at the critical density. The light backscattered by SRS, in the $630\text{--}750 \text{ nm}$ range, is $\sim 0.02\text{--}0.2\%$ of the laser

energy. The energy backscattered in both spectral ranges increases when the delay rises from 0 to 1200 ps, growing by a factor 2 and 5, respectively. Indeed, larger delays produce longer scale length plasmas, resulting in larger gain for instabilities. The estimated energy scattered in half-harmonics is $\sim 0.5\%$ of laser light. These values are larger than what reported in our previous paper [24] due to a more accurate characterization of the laser intensity profile in the focal plane. Our new evaluation is closer to data from other experiments [2]. The use of an integrating sphere also showed the presence of light scattered outside the lens focusing cone.

Two-plasmon decay. Emission of $3/2\omega_0$ and $\omega_0/2$ harmonics was detected, giving evidence that a fraction of laser radiation reaches the $n_c/4$ surface. Both components show a doublet structure (see fig. 1), related to the frequency difference of plasma waves produced by TPD instability $|\delta\omega|/\omega_0 = (9/4)(v_e^2/c^2)\kappa$, where $\kappa = \mathbf{k}_e \cdot \mathbf{k}_0/k_0^2 - 1/2$, \mathbf{k}_e is the blue EPW wave vector and v_e is the electron thermal velocity. The $3/2\omega_0$ harmonic ($\lambda = 292$ nm) blue peak is weaker than the red one, due the fact that the blue EPW must be reflected at the critical density before coupling to the laser light.

Spectra of the $\omega_0/2$ harmonic ($\lambda = 876$ nm) agree with the results of other experiments [29,30], showing a broad blue-shifted peak (labeled 1), a sharp red-shifted peak (2), and a less evident small bump at even higher wavelengths (3), which in ref. [30] is referred to as a supplementary peak. The blue peak 1 has a shift similar to peak 3, and approximately 3 times the shift of the narrow red peak 2. Also the width of peak 1 is larger (~ 3.6 times) than that of peak 2, suggesting a different origin. The sharp red-shifted peak 2 is associated to hybrid TPD/SRS instability [31], as in ref. [30], where the laser wave decays into a forward EPW with wave vector $\mathbf{k}_e \approx \mathbf{k}_0$ ($\kappa = 1/2$) and in a backward partly electrostatic and partly electromagnetic wave. Peaks 1 and 3 are associated to TPD waves and are produced by Inverse Resonance Absorption (IRA) or Raman Downscattering (RD) of laser light [32]. In the IRA process, an EPW with $k_\perp/k_0 < 0.1$ is converted into a photon near its turning point. Considering that blue EPWs propagate inward the density gradient, *i.e.*, toward their turning point, it is expected that the $\omega_0/2$ blue peak is more intense than the red one, that is originated by outgoing EPWs and need additional processes (*e.g.*, Langmuir decay instability) to reverse their direction and be converted into photons. In the RD process, conversely, a laser photon is downscattered by a plasmon produced by TPD. The matching conditions for this process however need that the laser photon is rescattered at a proper angle or that the photon is produced by stimulated Brillouin scattering, as shown in detail in refs. [30,32]. So, both IRA and RD need particular coupling conditions, and many authors have speculated on the prevalence of the one or the other in different experiments. Here, both coupling conditions can be fulfilled

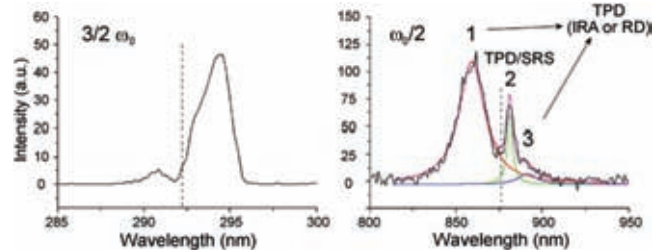


Fig. 1: (Colour online) Typical $3/2\omega_0$ and $\omega_0/2$ spectra, obtained at 5×10^{15} W/cm².

near $n_c/4$, where filamentation, turbulence, cavitation and laser photon scattering can occur.

According to ref. [30], the shift of the narrow peak 2 in the $\omega_0/2$ spectrum provides a reliable estimate of plasma temperature not being affected by the observation angle, filamentation or cavitation [33]. By setting $\kappa = 1/2$, we find that the plasma temperature increases from 1.35 to 1.68 keV when I_{max} rises from 2.4 to 3.7×10^{15} W/cm². This agrees with hydrodynamic simulations and with the Landau cutoff of SRS produced at densities $n_e < n_c/4$.

Interestingly, the frequency shift of the peaks of $3/2\omega_0$ emission, $\overline{\Delta\omega}/\omega_0 \approx 1.1 \times 10^{-2}$, is equal to that of peaks 1 and 3 of the $\omega_0/2$ spectrum, suggesting that the EPWs responsible for these harmonics are the same ($k_e \approx 2.9k_0$). For a plasma temperature $T_e \approx 1.5$ keV, we get $k_e\lambda_D \approx 0.27$, indicating that these EPWs are close to the Landau cutoff.

Stimulated Raman scattering. Typical SRS spectra are shown in fig. 2(a), revealing a backscattered emission in the spectral range 630–750 nm. Wave number matching conditions locate backward SRS in the 0.09–0.16 n_c density range, well below $n_c/4$. The short-wavelength limit corresponds to the expected Landau cutoff ($k\lambda_D \approx 0.27$) for the electron temperature of ~ 1.5 keV.

Spectra also exhibit complex and non-reproducible features, where intensity, spectral bandwidth and complexity strongly increase with the laser intensity and the delay. Since the intensity threshold for SRS in a non-uniform plasma scales inversely with the density scale-length L , and the SRS growth rate γ_0^2 is proportional to the laser intensity I , we then plotted the spectrally integrated intensity I_{SRS} vs. the product $I \cdot L$ (fig. 2(b)). Given the time and space dependence of laser intensity, we considered the laser intensity I_{av} averaged over one standard deviation in time and space ($I_{av} = I_{max}/1.366$). L values for the different shot conditions (intensity, delay) were taken from hydrodynamic simulations. Figure 2(b) shows a typical SRS feature of exponential growth leveling off at saturation, which is hidden in the plot as a function of laser intensity alone (not shown here). This is the indication that the density gradient is indeed decisive in determining the SRS growth.

According to ref. [34], the SRS threshold intensity I_{th} in inhomogeneous plasmas is given by

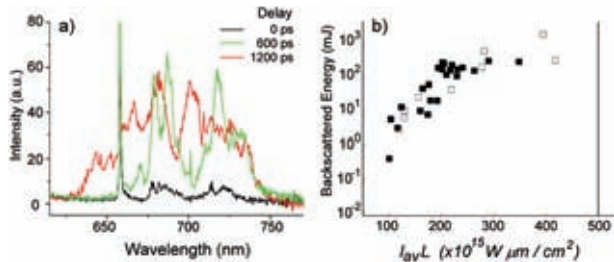


Fig. 2: (Colour online) (a) Backscattered SRS emission spectra obtained with laser intensity $I \approx 4 \times 10^{15} \text{ W/cm}^2$ and different delays between prepulse and main pulse (0, 600, and 1200 ps). The spike at 657 nm is a laser harmonic. (b) Backscattered SRS energy *vs.* the product $I_{av} \cdot L$, where I_{av} is the average laser intensity. Full squares are experimental data and empty squares hydrodynamic simulations. The vertical line represents the SRS threshold.

$v_0^2/c^2 > 4|k_e - k_0|/k_e^2 L$, where v_0 is the quiver velocity of an electron in the laser field.

This condition implies that $I_{th} \cdot L = 500 \times 10^{15} \text{ W}\mu\text{m/cm}^2$ (vertical line in fig. 2(b)), corresponding to a threshold intensity I_{th} between 4.5×10^{15} and $8 \times 10^{15} \text{ W/cm}^2$, depending on the density scale length, which is above the intensity in all our shots. This suggests that SRS is originated into the laser speckles, and the intensity statistics across the RPP-smoothed laser beam is essential for explaining our results. Based on the focusing geometry and focal volume size, the number of speckles can be estimated to be $\approx 10^5$. Assuming an exponential speckle intensity distribution $f(I) \propto \exp(-I/I_{av})/I_{av}$ typical for RPP-smoothed beams [35], intensities up to $\sim 8\text{--}10I_{av}$ can be achieved. Moreover, the most intense speckles can undergo self-focusing further contributing to the SRS emission. At the lowest laser intensities, only speckles with intensities at least ≥ 5 times the average intensity can drive SRS. Conversely, at higher laser intensities, also speckles with intensity marginally higher than I_{av} can play a role. Therefore, when the laser intensity increases, SRS reflectivity increases as the result both of the larger intensity in a single speckle, and of the increasing number of speckles above I_{thres} . This trend is confirmed by numerical simulations as explained in detail below (empty symbols in fig. 2(b)). Nevertheless, the growth observed in the experiment is smaller than that expected by the Rosenbluth gain [36]. This suggests that damping and kinetic effects lead to saturation of SRS inside the speckles. The importance of kinetic mechanisms in SRS saturation is also suggested by the spectral broadening shown in fig. 2(a), increasing with intensity and delay. This can be related to temporal reflectivity bursts and pulsations in non-linear saturation of anomalous SRS, as found in kinetic (PIC) simulations [33,37].

Hot electrons. HEs flux and average energy were obtained by Cu K_α and Ti K_α spectroscopy. The reduction of the K_α yield obtained by increasing the plastic thickness allowed the penetration depth of HEs to be calculated and

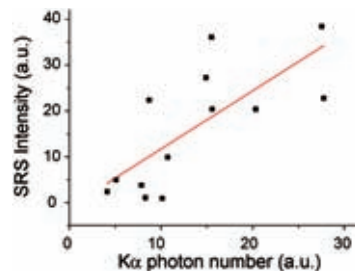


Fig. 3: (Colour online) Correlation between K_α photon number, generated from collisions with hot electrons, and SRS intensity.

hence their average energy. Another approach for estimating the HE energy is to consider the ratio between Cu K_α and Ti K_α emissions on the same shot, which is more accurate since this value does not depend on the absolute number of generated hot electrons. Monte Carlo simulations performed with the GEANT4 [38] and PENELOPE [39] codes were used for evaluating the hot-electron temperature, by using the electron stopping range tables [40]. Assuming an exponential distribution for hot electrons $\sim \exp(-E/T_{hot})$, the average energy (“temperature”) is found to be $T_{hot} = 25 \pm 8 \text{ keV}$ and the energy conversion $\sim 0.1\% \pm 0.05\%$ of the incident laser energy. Such values are in agreement with data obtained from plasmas with similar temperature and density scale length values, where SRS is the main source of HEs [41]. Also, the HE energy is close to what can be estimated from the phase velocity of the SRS-driven plasma waves in the density region $0.09\text{--}0.16 n_c$, which is $T_{SRS} \sim 17\text{--}20 \text{ keV}$. These arguments suggest that HEs are mainly generated by SRS, and only marginally by TPD. This conclusion is also supported by the coarse correlation between Cu K_α photon number and SRS signal (fig. 3).

Numerical simulations. – Simulations have been carried out using the radiative-hydrodynamic code CHIC [23]. In addition to laser refraction, diffraction, resonant and collisional absorption, the code takes into account SRS and TPD processes and generation of HEs, by means of appropriate scaling laws using the local and instantaneous values of laser intensity and plasma parameters [20]. Since SBS was not included in the model, the related reflected energy was subtracted from the incident pulse. The LPI-generated HEs are transported into the plasma using a reduced model based on the angular scattering approximation [42,43], validated against kinetic simulations. This coupled approach allows accounting for the interplay between HEs energy deposition, hydrodynamics and competition between LPI processes.

In this code, laser propagation is described using a new model based on stochastically distributed Gaussian beamlets [44]. This allows reproducing the laser intensity envelope and, to a significant extent, the speckles in the focal spot. Typically, the model is able to reproduce realistic intensity distributions up to $4\text{--}5I_{av}$ but not the

speckles of higher intensity, a limitation imposed by the mesh size. According to the expected intensity distribution in the speckles, the energy fraction contained in speckles above $5I_{av}$ (noted χ_5) is only 0.67%. Nonetheless, these high-intensity speckles may play an important role in our experimental conditions (fig. 2(b)). We addressed this issue in the simulations by maximizing the energy fraction χ_5 , within the limits of the laser propagation model. This was obtained by refining the Lagrangian mesh to allow for smaller scale variations of the intensity distribution. Mesh refinement in the code allowed to reach values of $\chi_5 \approx 0.3\%$. The difference between this value and that expected in the experiment ($\chi_5 \approx 0.67\%$) was compensated by using a value of SRS threshold lower than the calculated one by a factor of 2. The same mesh resolution and modified threshold were then used for all simulations.

In order to test the validity of our model, we ran simulations at intensities well below the modified threshold ($I_{av} = 2.1 \times 10^{15} \text{ W/cm}^2$). An increase of χ_5 from 0.02% to 0.06% and 0.3% with reduced SRS threshold resulted in a SRS signal increase from the noise level (*i.e.*, no SRS predicted) to 0.003% and 0.008% of the incident laser energy. The latter value reasonably matches the experimental results, while the increasing trend of SRS with χ_5 clearly shows the impact of the intensity statistics on the SRS level.

Simulations accounting for the speckle statistics were carried out in our experimental conditions, where the envelope laser intensity is significantly lower than the SRS threshold. A good agreement is obtained (empty squares in fig. 2(b)) confirming the importance of accurate modeling of the speckle statistics.

A general picture of the interaction can be drawn by inspecting simulation results obtained at a laser intensity of $4 \times 10^{15} \text{ W/cm}^2$ and with a 600 ps delay between the pulses. A large fraction of the pulse energy is collisionally absorbed ($\sim 70.5\%$) while a small amount ($\sim 1.3\%$) is resonantly absorbed at the critical surface. The resonant absorption produces electrons with an average energy of $\sim 3 \text{ keV}$, which are therefore indistinguishable from the thermal electrons. SRS and TPD appear slightly later. The time-integrated SRS reflectivity is $\sim 0.25\%$, in good agreement with the experiment. Both TPD and SRS produce forward emitted HEs, with conversion efficiencies of $\sim 0.35\%$ and 0.07% of the laser energy, respectively. The temperature of hot electrons from TPD ($\approx 66 \text{ keV}$) is higher than that of electrons from SRS ($\approx 17 \text{ keV}$), as expected. The measured HEs temperature is between these two values but definitely closer to SRS. The discrepancy in HE production from TPD in the simulation suggests that, in the experiment, TPD is damped or saturated by kinetic effects. Since in our model, parametric instabilities are described by scaling laws, saturation processes specific for our conditions (*e.g.*, cavitation phenomena or damping of daughter waves into small speckles) are probably underestimated.

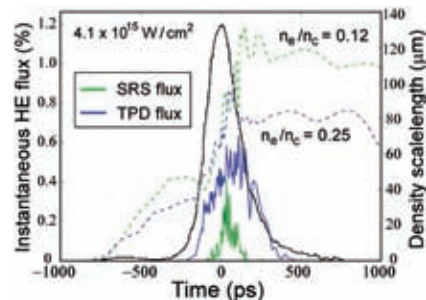


Fig. 4: (Colour online) Instantaneous HE flux as a function of time for SRS (green) and TPD (blue). Density scale lengths computed at $n_c/4$ and $0.12n_c$ are also shown (dashed blue and green lines, respectively). The peak intensity of the laser pulse is indicated as a gray line.

The evolution of the density scale length at $n_e \approx 0.12n_c$ and $n_e \approx n_c/4$, indicative, respectively, of the layers where SRS and TPD are active, is shown in fig. 4 alongside the laser/HE energy conversion efficiencies. SRS is maximum after the laser peak, when the scalelength becomes large enough while the laser intensity remains high. The plasma temperature is similar in both layers and varies with time from 0.5 to 2.8 keV at the laser peak. This is in good agreement with the time-integrated estimate based on TPD splitting ($T_e \approx 1.68 \text{ keV}$ at $I = 3.7 \cdot 10^{15} \text{ W/cm}^2$). In the overdense region, the plasma temperature is lower, in agreement with X-ray spectroscopy results.

Summary and conclusions. – In the present experiment, backscattering is dominated by SBS and laser reflection (5–15%) while the contribution from SRS, occurring at $0.09\text{--}0.16n_c$ near the Landau cutoff, is of the order of 0.1%. While the level of SBS agrees with other experiments carried out under similar interaction conditions, SRS backscatter appears at least an order of magnitude lower [12,41,45]. This can be maybe explained by the longer plasma scale lengths obtained in other works and/or by the low $f/\#$ of our focussing system, that combined with the phase plate, results in small speckles, inhibiting filamentation and damping the SRS growth.

The latter seems confirmed by the spectral modulation of SRS spectra and the reflectivity saturation observed at the highest laser intensities/delays explored, which suggests the occurrence of kinetic effects suppressing the growth of EPWs inside the speckles. The correlation of SRS reflectivity and K_α emission and the measured HE temperature (25 keV) suggest that HEs are mainly generated by SRS, similarly to conclusions of recent experiments in spherical geometry [12,41]. The presence of half-harmonics confirms the TPD at $n_c/4$.

Hydrodynamic simulations well reproduce SRS levels and the plasma temperature from the experiment, while TPD is overestimated, probably because saturation mechanisms are underestimated. The agreement of simulated and experimental SRS reflectivities points out the need

of correctly modeling the speckle intensity statistics for reproducing LPI in laser-fusion experiments.

This work was supported by the European Union under the Laserlab program of the 7th FP and the COST Action MP1208, by the Czech Ministry of Education, Youth and Sports, projects LC528 and LM2010014, by the Italian MIUR (contract PRIN 2012AY5LEL), by the EUROfusion Consortium (grant agreement 633053), by the Sapienza project C26A15YTMA and by the ELI project CZ.02.1.01/0.0/0.0/15 008/0000162 from European Regional Development Fund. SciTech Precision supplied targets. The authors are grateful the PALS staff for help in running the experiments.

REFERENCES

- [1] BETTI R. *et al.*, *Phys. Rev. Lett.*, **98** (2007) 155001.
- [2] BATANI D. *et al.*, *Nucl. Fusion*, **54** (2014) 054009.
- [3] PERKINS L. J. *et al.*, *Phys. Rev. Lett.*, **103** (2009) 045004.
- [4] RIBEYRE X. *et al.*, *Plasma Phys. Control. Fusion*, **51** (2009) 015013.
- [5] ATZENI S. *et al.*, *Plasma Phys. Control. Fusion*, **53** (2011) 035010.
- [6] ATZENI S. *et al.*, *Nucl. Fusion*, **54** (2014) 054008.
- [7] NUCKOLLS J. *et al.*, *Nature*, **239** (1972) 139.
- [8] LINDL J., *Phys. Plasmas*, **2** (1995) 3933.
- [9] ATZENI S. and MEYER-TER-VEHN J., *The Physics of Inertial Fusion* (Clarendon-Oxford) 2004.
- [10] THEOBALD W. *et al.*, *Plasma Phys. Control. Fusion*, **51** (2009) 124052.
- [11] ANDERSON K. S. *et al.*, *Phys. Plasmas*, **20** (2013) 056312.
- [12] THEOBALD W. *et al.*, *Phys. Plasmas*, **22** (2015) 056310.
- [13] NORA R. *et al.*, *Phys. Rev. Lett.*, **114** (2015) 045001.
- [14] KRUEER W. L., *The Physics of Laser Plasma Interactions* (Addison-Wesley, Redwood City, Cal.) 1988.
- [15] SEKA W. *et al.*, *Phys. Fluids*, **27** (1984) 2181.
- [16] AFSHAR-RAD T. *et al.*, *Phys. Rev. Lett.*, **68** (1992) 942.
- [17] TANAKA K. *et al.*, *Phys. Rev. Lett.*, **48** (1982) 1179.
- [18] GIULIETTI A. *et al.*, *Phys. Rev. E*, **59** (1999) 1038.
- [19] RIBEYRE X. *et al.*, *Phys. Plasmas*, **20** (2013) 062705.
- [20] COLAÏTIS A. *et al.*, *Phys. Rev. E*, **92** (2016) 041101.
- [21] COLAÏTIS A. *et al.*, *Phys. Plasmas*, **23** (2016) 072703.
- [22] JUNGWIRTHV K. *et al.*, *Phys. Plasmas*, **8** (2001) 2495.
- [23] BREIL J. *et al.*, *Comput. Fluids*, **46** (2011) 161.
- [24] BATANI D. *et al.*, *Phys. Plasmas*, **21** (2014) 032710.
- [25] PISARCZYK T. *et al.*, *Phys. Plasmas*, **21** (2014) 012708.
- [26] ŠMÍD M. *et al.*, *Acta Polytech.*, **53** (2013) 233.
- [27] MORACE A. and BATANI D., *Nucl. Instrum. Methods A*, **623** (2010) 797.
- [28] MACFARLANE J. J. *et al.*, *High Energy Density Phys.*, **3** (2007) 181.
- [29] SEKA W. *et al.*, *Phys. Plasmas*, **16** (2009) 052701.
- [30] SEKA W. *et al.*, *Phys. Fluids*, **28** (1985) 2570.
- [31] AFEYAN B. B. and WILLIAMS E. A., *Phys. Rev. Lett.*, **75** (1995) 4218.
- [32] BERGER R. L. and POWERS L. V., *Phys. Fluids*, **28** (1985) 2895.
- [33] KLIMO O. and TIKHONCHUK V. T., *Plasma Phys. Control. Fusion*, **55** (2013) 095002.
- [34] FORSLUND D. W. *et al.*, *Phys. Fluids*, **18** (1975) 1002.
- [35] ROSE H. A. and DUBOIS D. F., *Phys. Fluids B*, **5** (1993) 590.
- [36] ROSENBLUTH M. N., *Phys. Rev. Lett.*, **29** (1972) 565.
- [37] KLIMO O. *et al.*, *Plasma Phys. Control. Fusion*, **56** (2014) 055010.
- [38] SEMP AU J. *et al.*, *Nucl. Instrum. Methods B*, **132** (1997) 377.
- [39] AGOSTINELLI S. *et al.*, *Nucl. Instrum. Methods A*, **506** (2003) 250.
- [40] <http://physics.nist.gov/PhysRefData/Star/Text/ESTAR.html>.
- [41] THEOBALD W. *et al.*, *Phys. Plasmas*, **19** (2012) 102706.
- [42] LI C. K. and PETRASSO R. D., *Phys. Rev. E*, **70** (2004) 067401.
- [43] SOLODOV A. A. and BETTI R., *Phys. Plasmas*, **15** (2008) 042707.
- [44] COLAÏTIS A. *et al.*, *Phys. Rev. E*, **89** (2014) 033101.
- [45] BATON S. D. *et al.*, *Phys. Rev. Lett.*, **108** (2012) 195002.

THE 3RD ELIMED WORKSHOP MEDICAL AND MULTIDISCIPLINARY APPLICATIONS
OF LASER-DRIVEN ION BEAMS AT ELI-BEAMLINES
7–9 SEPTEMBER 2016,
LABORATORI NAZIONALI DEL SUD, CATANIA, ITALY

Experimental investigation of ion production and acceleration mechanism in laser-produced plasma at moderate intensity for nuclear studies @ ELI-NP

C. Altana,^{a,b,1} S. Tudisco,^a G. Lanzalone,^{a,c} D. Mascali,^a A. Muoio,^{a,d} F. Brandi,^{e,f}
G. Cristoforetti,^e P. Ferrara,^e L. Fulgentini,^e P. Koester,^e L. Labate,^e D. Palla^{e,g,h} and
L. Gizzi^{e,g}

^aINFN-LNS, Laboratori Nazionali del Sud, Via Santa Sofia 62, 95123 — Catania, Italy

^bDip. di Fisica e Astronomia — Università di Catania, Via Santa Sofia 64, 95123 — Catania, Italy

^cUniversità degli Studi di Enna “Kore”, Via delle Olimpiadi, 94100 — Enna, Italy

^dUniversità di Messina, Viale F.S. D’Alcontres 31, 98166 — Messina, Italy

^eCNR-INO — Intense Laser Irradiation Laboratory, Via G. Moruzzi 1, 56124 — Pisa, Italy

^fIstituto Italiano di Tecnologia, Via Morego 30, 16163 — Genova, Italy

^gINFN — Sezione di Pisa, Largo B. Pontecorvo 3, 56127 — Pisa, Italy

^hDipartimento di Fisica, Università di Pisa, Largo B. Pontecorvo 3, 56127 — Pisa, Italy

E-mail: altana@lns.infn.it

ABSTRACT: High-power lasers allow to produce plasmas extremely appealing for the nuclear physics studies. An intense scientific program is under preparation for the experiments that will be conducted at the Extreme Light Infrastructure for Nuclear Physics (ELI-NP) in Magurele, Romania. Among the several planned activities, we aim to study low-energy fusion reactions and nuclear structure in a plasma environment. In this work, we discuss the results of some preliminary tests related to the experimental set-up, which is in phase of preparation, for the conduction of this scientific program at ELI-NP. Tests have been performed at ILIL laboratory in Pisa, where a Terawatt laser is installed. The goal of this experimental campaign was a systematic experimental investigation of ion production and acceleration mechanism that occur in laser-produced plasma at moderate intensity, $I=10^{18}$ – 10^{22} W/cm². We particularly focus the attention to identify the role of the target composition: surface contaminants versus volume contribution.

KEYWORDS: Ion identification systems; Plasma diagnostics - charged-particle spectroscopy; Spectrometers

¹Corresponding author.

Contents

1	Introduction	1
2	The target normal sheath acceleration	2
3	Experimental apparatus	3
4	Results and discussion	3
5	Conclusions	5

1 Introduction

High-power lasers have proven being capable to produce high-energy γ , charge particles and neutrons, and to induce all kinds of nuclear reactions. For the first time, at ELI-NP, it will enter into new domains of power and intensities: 10 PW and $>10^{23}$ W/cm². The future availability of such intense beams at high repetition rates will give the unique opportunity to investigate nuclear reactions and fundamental interactions under the extreme plasma conditions [1] where it is expected that the physical properties of nuclear matter (structure, lifetimes, reaction mechanisms, etc.) could be drastically changed inside the plasma [2]. On the other hand, these studies represent one of the largest, most difficult and challenging research areas today; the implications could cover others fields, from quantum physics to cosmology, astrophysics, etc.

We have proposed the construction of a general-purpose experimental apparatus in order to investigate these research topics: by using colliding plasma plumes [3], it will be possible to study the electron-screening effects [4] at low-energy fusion reactions, in a wide variety of cases and configurations, and the structure of the weakly bound nuclear states (see for instance the papers of Hoyle [5], Afimov [6], etc.).

The apparatus can be schematized in three main sections [2]: the interaction zone, the charged particles detection-wall and the neutrons detection-wall. In the interaction zone, two plasmas are produced and collide with each other. The basic interaction principle is the following: a first high-power laser pulse impinges on a primary solid thin target producing, through the TNSA (Target Normal Sheath Acceleration) acceleration scheme, a plasma. This plasma collides with a secondary plasma, produced through the interaction of another laser pulse on a supersonic gas jet (made for example by ⁴He, H, D₂, ³He etc.). By using this configuration, we intend to minimize the “plasma-plasma friction”, i.e. the energy dissipation of the collision between fast-flowing and gas-jet plasmas. Moreover this configuration allows to work in a more “classical” nuclear physics experimental scheme (i.e. projectiles on a fixed target).

Moreover, in order to reconstruct the reaction kinematic, the construction of two highly-segmented detection systems for neutrons and charged particles is required.

The charged particles detection-wall will be realised by Silicon Carbide (SiC) detectors [7]. SiC have been proven recently to have excellent properties: high energy and time resolution, resistance to radiation damage, insensible to visible light, etc. Such detectors are able to work in a time of flight (ToF) configuration or in single particle detection mode.

For these studies, the “ideal” neutron detection module should have high efficiency, good gammas versus neutrons discrimination, excellent timing for the energy reconstruction in time of flight of neutrons. In addition, it should be able to work in hard environmental conditions, i.e. in the laser-matter interaction area. All these aspects may be met by configuration based on new PPO-Plastic scintillator [8] coupled with a Silicon Photomultiplier [9] and a totally digital read-out system.

2 The target normal sheath acceleration

Thanks to the unique opportunities provided by ELI-NP (high repetition rate and Petawatt laser beams), by operating at around 10^{18} W/cm² (typically TNSA regime) with large focal spot, it will be possible to ensure the production of a very large flux of ions and plasma with optimized energy distributions for our nuclear purpose. Such conditions ensure the possibility to study, in a plasma environment, the nuclear reactions at very low cross-section.

TNSA was intensively studied in the last years; experiments [10] and models [11] show that this acceleration scheme works very well for the surface protons acceleration. Protons and ions flows are expected expanding along a cone, whose axis is normal to the target surface [12]. The observed energy distributions present an exponential shape [13] with a high-energy cut-off, linearly depending on the laser intensity [10] and scaling with the atomic number.

A simple description of the TNSA mechanism is the following: laser driven electrons penetrate the foil, escape at the rear side of the target inducing a strong longitudinal electric field (\sim TV/m), which ionizes atoms in the surface layer and accelerates them in the target normal direction. Typically, this field accelerates simultaneously several ion species, but suffers of two drawbacks. The first is related to the fact that only a thin layer of ions on the back surface of the foil is accelerated. This is called “surface acceleration” and it is less efficient with respect to the “volumetric acceleration”, which is originated by the bulk material. The second drawback arises from acceleration of contaminants layers (hydrocarbon, water, etc.) present on both sides of the target foils. The protons of contaminant layer are accelerated at first, due to their lower charge-to-mass ratio, thus shielding the region behind the front and inhibiting the acceleration of heavier ions.

Several experiments have demonstrated that, even though the thickness of the contaminant is only few nanometers, this is sufficient to damp the acceleration of heavier ions [14, 15]. Other experiments, in which hydrogen-rich contaminant layers were removed from the target, either by thermal heating [16, 17] by an argon-ion sputter gun [18, 19] or using a secondary laser to ablate the surface [20, 21], have showed more efficient acceleration of the bulk target material.

Target cleaning is technologically challenging, therefore the aim of this work is to understand if heavier ions can be efficiently accelerated in the TNSA regime when contaminants are present.

A systematic experimental investigation to identify the role of surface contaminants and volume contribution was carried out by using a Thomson parabola Spectrometer (TPS) with adequate charged species discrimination capability in order to detect the energy spectra of individual ion species.

3 Experimental apparatus

The preliminary tests for studies of nuclear reactions at ELI-NP [22] have been performed at the Intense Laser Irradiation Laboratory (ILIL) in Pisa. A Ti:Sapphire laser system, which delivers 40 fs - 800 nm pulses with energy on target up to 450 mJ, was employed. The ILIL laser pulse exhibits an ASE (Amplified Spontaneous Emission) contrast greater than 10^{10} and a ps contrast of 10^5 at 1ps before the peak pulse. The beam is focused on the target at an angle of incidence of 15° using an off-axis parabolic mirror; the corresponding maximum intensity at the target position was up to 2×10^{19} W/cm². Furthermore the target was mounted on a three-axis translation stage system and centered respect a 640 mm diameter interaction chamber.

Deuterated plastic (CD₂) 10 μ m thick foil was used as a target. The choice of this material is based on two points. Since the target is composed of deuteron and carbon atoms, protons are certainly originated from surface impurities. Moreover, after protons, deuterons are the ions with smallest atomic mass, thus they are more easily detectable than heavier ions.

To investigate ions acceleration [23] in laser-matter interaction, at TNSA regime, a Thomson Parabola Spectrometer was employed. It was placed normally to the target rear side, housed in a separate vacuum chamber, operating at a pressure of 10^{-6} Torr, and differentially pumped with respect to the main target chamber. Details about TPS are given elsewhere [24]. The ions position is detected using an imaging system consisting of a micro-channel plate coupled to a phosphor screen, 75 mm in diameter (MCP-PH), and an EMCCD camera.

4 Results and discussion

Deuterated plastic targets were irradiated by changing the focal conditions in order to investigate the behaviour of the accelerated ions.

Typical energy spectra for the all detected species (protons, deuterons and carbons of different charge states) are shown in figure 1. As expected from TNSA mechanism, broad Maxwellian-like shapes are produced (i.e. a linear drop is observed in the semilog-scale). Since during the measurements we focused our attention on highest energies values, the electric and magnetic fields have been chosen in such a way to have a broad high-energy region. For this reason, due to the MCP dimension, protons and deuterons at lower energies were cut in the spectra.

Our goal was to investigate the behaviour of superficial protons acceleration versus deuterons bulk emission. Therefore, the cut-off energies of the two ion species were obtained from energy spectra in different laser focus conditions. The results are plotted in figure 2.

Protons and deuterons cut-off energies exhibit an opposite trend: where protons exhibit a maximum, corresponding to the best focus, deuterons show a minimum. Therefore, the contribution of surface seems to prevail in the optimal z-focus, while in off-focus positions the two contributions (surface and bulk target) tend to equalize [25]. Focus conditions were monitored by means of a pin-diode, plotted in same graph of figure 2, and giving information about X-rays flux.

Protons and deuterons spectra were also integrated in order to obtain information about the total yield, in arbitrary units, as reported in table I. The mean values were estimated among different focus condition, because we did not observe significant changes within the error by changing the focusing conditions.

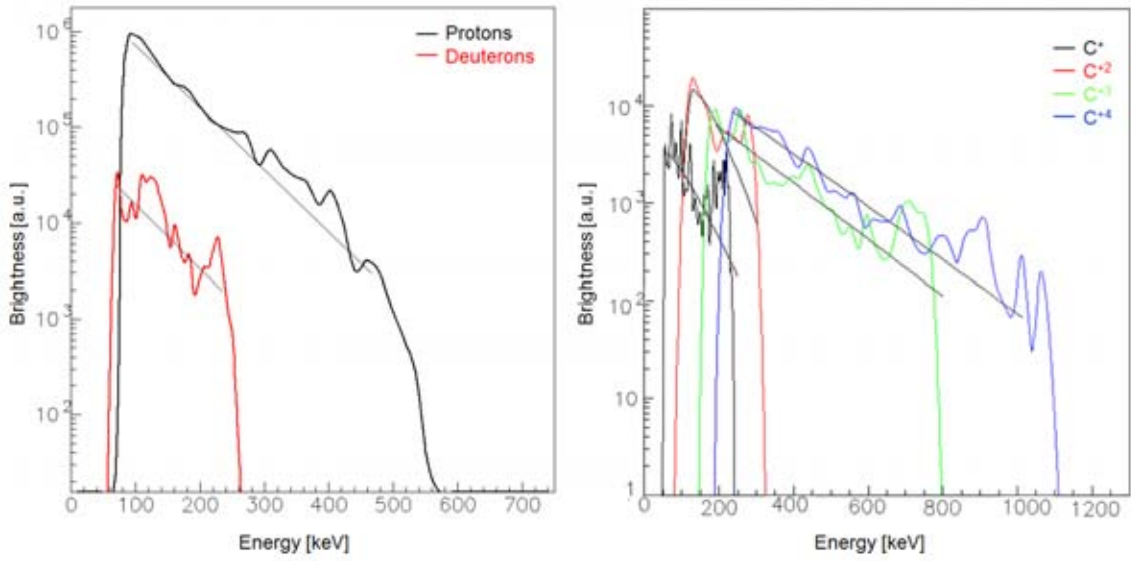


Figure 1. Left — Comparison between protons and deuterons spectra. Right — Comparison among (C^+, C^{+2}, C^{+3} and C^{+4}) spectra showing the Coulomb shift. Maxwellian fits are also plotted.

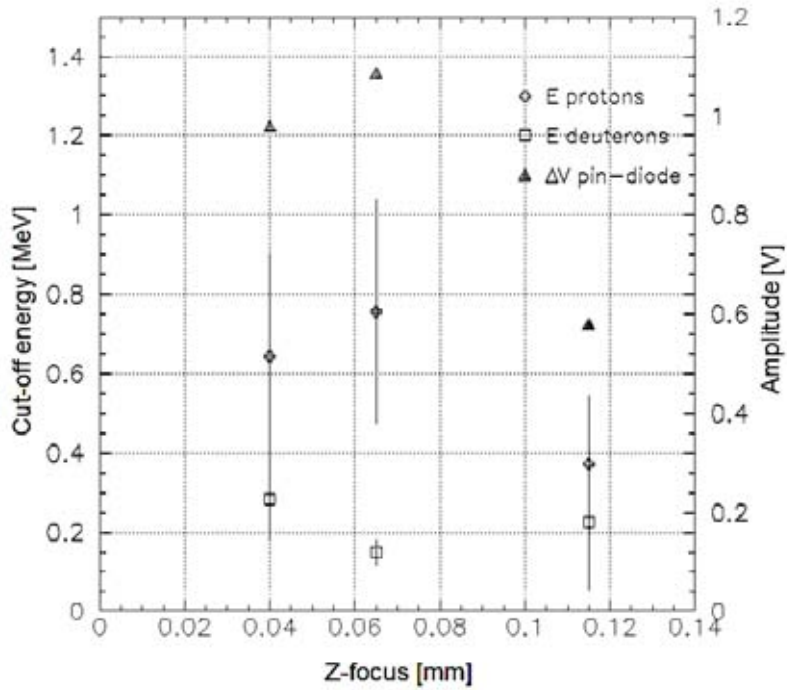


Figure 2. Trend of the maximum energy values at the cut_off versus z-focus, for a CD_2 target.

Table 1. Mean protons and deuterons yield.

Protons yield (a.u.)	$1.26 \times 10^7 \pm 5.78 \times 10^6$
Deuterons yield (a.u.)	$1.61 \times 10^5 \pm 7.67 \times 10^4$

We can conclude that at 0° , where TP has been placed, the surface contribution (in terms of number of protons) is dominant compared to deuterons bulk emission. The total yields, both for protons and deuterons, have not dependence from focus laser condition.

Concerning the carbons energy spectra, as can be noticed, each spectrum shows a different energy threshold, which is shifted at higher energies relying to the different charge state; while the total yield seams behaving vary similarly to that of deuterons.

5 Conclusions

Experimental investigations on ions production and acceleration mechanism in laser-produced plasma at moderate intensity were performed with a TPS as preliminary test of the configuration that is under preparation for the nuclear physics activity at ELI-NP.

In order to identify the role of the surface versus bulk contribution a CD_2 target was irradiated. Data show that ion acceleration originates from a complex scenario set by the laser-target interaction conditions. It is possible to argue that protons, coming from the surface contaminant layer, feel earlier the accelerating electric field due to their lower charge-to-mass ratio, and consequently shield the deuterons. Therefore, protons are accelerated at higher velocities, while the deuterons are accelerated from the remaining shielded electric field at relatively lower velocities.

More complex to explain it is the energy cut-off dependence on focus condition. The two species could be emitted with different angular distributions. Since the TPS is placed at 0° respect the target emission, it is possible that deuterons are accelerated at larger angles. Therefore, when the beam is defocused, a larger target surface is hit, consistent with the higher deuterons cut-off energies.

Interesting results coming also from the carbons data, where an energy shift (several thresholds) has been observed as a function the different charge states.

References

- [1] D. Mascali et al., *Calculation of fusion rates at extremely low energies in laser plasmas*, *Proc. IAU* **274** (2010) 44.
- [2] F. Negoita et al., *Laser driven nuclear physics at ELI-NP*, *Rom. Rep. Phys.* **68** (2016) S37.
- [3] D. Mascali et al., *Colliding laser-produced plasmas: a new tool for nuclear astrophysics studies*, *Radiat. Effects Defects Solids* **165** (2010) 730.
- [4] S. Cherubini et al., *Cross-section of $^8\text{Li}(\alpha, n)^{11}\text{B}$: inhomogeneous big bang nucleosynthesis*, *Eur. Phys. J. A* **20** (2004) 355.
- [5] F. Hoyle, *On nuclear reactions occuring in very hot stars. I. The synthesis of elements from carbon to nickel*, *Astrophys. J. Suppl.* **1** (1954) 121.
- [6] V. Efimov, *Few-body physics: giant trimers true to scale*, *Nature Phys.* **5** (2009) 533.
- [7] A. Muoio et al., *Silicon carbide detectors study for NUMEN project*, *EPJ Web Conf.* **117** (2016) 10006.
- [8] N. Zaitseva et al., *Plastic scintillators with efficient neutron/gamma pulse shape discrimination*, *Nucl. Instrum. Meth. A* **668** (2012) 88.

- [9] E. Sciacca et al., *Arrays of Geiger mode avalanche photodiodes*, *IEEE Photon. Technol. Lett.* **18** (2006) 1633.
- [10] A. Macchi et al., *Ion acceleration by superintense laser-plasma interaction*, *Rev. Mod. Phys.* **85** (2013) 751.
- [11] M. Passoni and M. Lontano, *Theory of light-ion acceleration driven by a strong charge separation*, *Phys. Rev. Lett.* **101** (2008) 115001.
- [12] M. Borghesi et al., *Multi-MeV proton source investigations in ultraintense laser-foil interactions*, *Phys. Rev. Lett.* **92** (2004) 055003.
- [13] T. Dzelzainis et al., *The TARANIS laser: a multi-Terawatt system for laser-plasma investigations*, *Laser Particle Beams* **28** (2010) 451.
- [14] M. Zepf et al., *Proton acceleration from high-intensity laser interactions with thin foil targets*, *Phys. Rev. Lett.* **90** (2003) 064801.
- [15] P. McKenna et al., *Effect of target heating on ion-induced reactions in high-intensity laser-plasma interactions*, *Appl. Phys. Lett.* **83** (2003) 2763.
- [16] P. McKenna et al., *Characterization of proton and heavier ion acceleration in ultrahigh-intensity laser interactions with heated target foils*, *Phys. Rev. E* **70** (2004) 036405.
- [17] B.M. Hegelich et al., *Laser acceleration of quasi-monoenergetic MeV ion beams*, *Nature* **439** (2006) 441.
- [18] M. Allen et al., *Direct experimental evidence of back-surface ion acceleration from laser-irradiated gold foils*, *Phys. Rev. Lett.* **93** (2004) 265004.
- [19] D.T. Ofermann et al., *Observations of proton beam enhancement due to erbium hydride on gold foil targets*, *Phys. Plasmas* **16** (2009) 093113.
- [20] J.C. Fernandez et al., *Laser-ablation treatment of short-pulse laser targets: toward an experimental program on energetic-ion interactions with dense plasmas*, *Laser Part. Beams* **23** (2005) 267.
- [21] S.M. Pfotenhauer et al., *Spectral shaping of laser generated proton beams*, *New J. Phys.* **10** (2008) 033034.
- [22] G. Lanzalone et al., *Study of nuclear reactions in laser plasmas at future ELI-NP facility*, *EPJ Web Conf.* **117** (2016) 05008.
- [23] C. Altana et al., *Investigation of ion acceleration mechanism through laser-matter interaction in femtosecond domain*, *Nucl. Instrum. Meth. A* **829** (2016) 159.
- [24] F. Schillaci et al., *Calibration and energy resolution study of a high dispersive power Thomson Parabola Spectrometer with monochromatic proton beams*, *2014 JINST* **9** T10003.
- [25] S. Tudisco et al., *Investigation on target normal sheath acceleration through measurements of ions energy distribution*, *Rev. Sci. Instrum.* **87** (2016) 02A909.

SCIENTIFIC REPORTS

OPEN

Transition from Coherent to Stochastic electron heating in ultrashort relativistic laser interaction with structured targets

G. Cristoforetti¹, P. Londrillo², P. K. Singh³, F. Baffigi¹, G. D'Arrigo⁴, Amit D. Lad³, R. G. Milazzo⁴, A. Adak³, M. Shaikh³, D. Sarkar³, G. Chatterjee³, J. Jha³, M. Krishnamurthy³, G. R. Kumar³ & L. A. Gizzi^{1,5}

Relativistic laser interaction with micro- and nano-scale surface structures enhances energy transfer to solid targets and yields matter in extreme conditions. We report on the comparative study of laser-target interaction mechanisms with wire-structures of different size, revealing a transition from a *coherent particle heating* to a *stochastic plasma heating* regime which occurs when migrating from micro-scale to nano-scale wires. Experiments and kinetic simulations show that large gaps between the wires favour the generation of high-energy electrons via laser acceleration into the channels while gaps smaller than the amplitude of electron quivering in the laser field lead to less energetic electrons and multi-keV plasma generation, in agreement with previously published experiments. Plasma filling of nano-sized gaps due to picosecond pedestal typical of ultrashort pulses strongly affects the interaction with this class of targets reducing the laser penetration depth to approximately one hundred nanometers. The two heating regimes appear potentially suitable for laser-driven ion/electron acceleration schemes and warm dense matter investigation respectively.

Relativistic interaction of an ultrashort laser pulse with micro- or nano-structured targets has recently stimulated a large interest for possible application in many fields, including Inertial Confinement Fusion¹, laser-driven ion/electron acceleration^{2,3} or warm dense matter creation⁴. The reason for such an interest lies in a more efficient absorption of the laser energy, if compared to a flat target. In the more favourable cases⁵ absorption can be as high as 90% and the enhancement in absorption is mainly due to the extended penetration depth of laser light into the nanostructured target compared to the collisionless skin depth of a flat target, resulting in a much longer interaction time.

Depending on the target geometry, improved laser-plasma coupling can result in volumetric heating of dense matter up to extreme temperatures⁴, stronger X-ray emission⁶ and/or efficient generation and guiding of energetic electrons/ions^{7–12}.

A pioneering work in this area is that of Murnane *et al.*¹³ where gold gratings and gold nanoclusters were introduced to enhance target absorptivity. Gordon *et al.*¹⁴ and Kulcsar *et al.*¹⁵, then showed a significant enhancement of X-ray emission by using nanostructured surfaces. Since then several target geometries have been tested both in experiments and in numerical simulations, in a wide range of laser intensities from 10^{14} to 10^{22} W/cm², including wires/nano-brush^{4,6,11,12}, nano-spheres^{2,16}, gratings¹⁷, nano-holes¹⁸, nano/microtubes^{3,7}. However, in spite of the considerable amount of experimental data, a satisfactory knowledge of the key control parameters is still missing, thereby limiting the exploitation of this class of targets for applications. This is also due to the many experimental parameters affecting the Laser Target Interaction regime of published experiments, the most relevant being the morphology of the nanostructures and the laser temporal contrast ratio (i.e. the ratio of the peak intensity to the pedestal intensity), often poorly known.

¹Intense Laser Irradiation Laboratory at INO-CNR, Via G. Moruzzi 1, Pisa, Italy. ²INAF-Osservatorio astronomico Bologna, Bologna, Italy. ³Tata Institute of Fundamental Research, Homi Bhabha Road, Colaba, Mumbai, 400005, India. ⁴Istituto per la Microelettronica e Microsistemi, CNR, Catania, Italy. ⁵INFN, Pisa Section, Largo B. Pontecorvo 3, Pisa, Italy. Correspondence and requests for materials should be addressed to G.C. (email: Gabriele.cristoforetti@cnr.it)

Received: 28 October 2016

Accepted: 31 March 2017

Published online: 05 May 2017

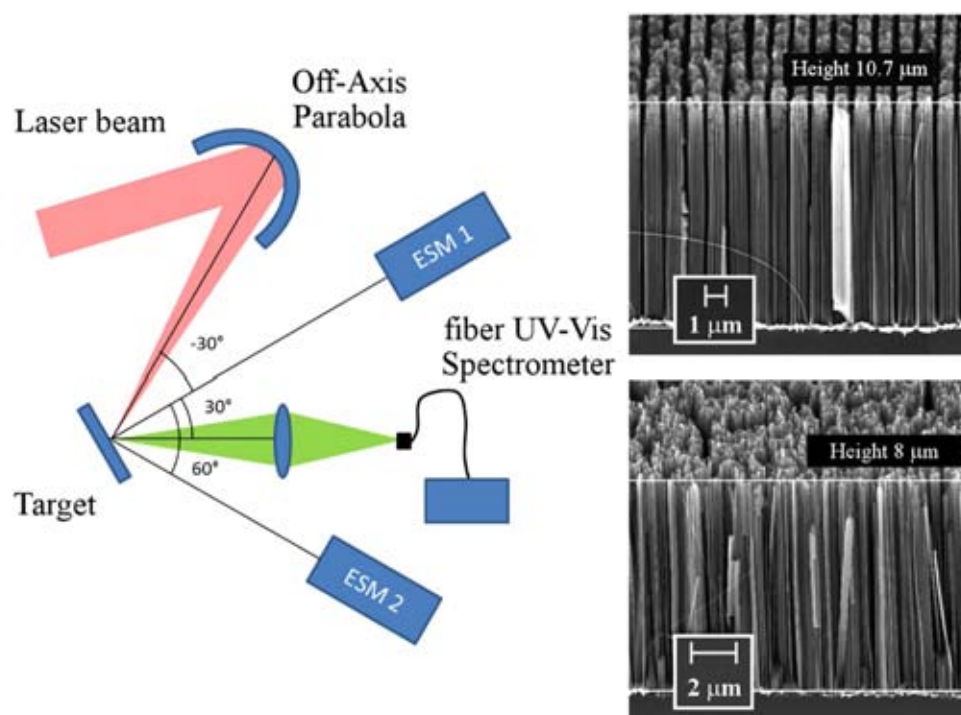


Figure 1. Experimental setup (left). SEM images of MicroWires (MW) (right top) and of NanoWires (NW) (right bottom) targets.

The critical role played by the geometry of the structures can be easily understood by comparing their characteristic dimensions with the typical scales affecting the interaction process such as the collisionless skin depth, the spatial excursion of quivering electrons in the laser field, the laser wavelength and the density scale-length, usually in the range between 10 nm and 1 μm . It is therefore reasonable to expect that when the dimensions of the structures fall below such values, the interaction will change dramatically. From an experimental viewpoint an ideal investigation path would require a parametric study of the interaction by changing gradually the target geometry. Because of the limitations in making suitable targets with tuneable structure dimensions, this approach is not feasible. Furthermore, in spite of the major recent enhancements of the temporal contrast of laser systems, experiments at high laser intensities are always systematically affected by premature plasma formation that can modify the target prior to the time of peak intensity. In fact, while ns-scale amplified spontaneous emission can be suppressed to levels below plasma formation threshold, the inherent picosecond pedestal will inevitably affect the interaction, giving rise to a preformed plasma with a characteristic scale-length specific of each laser system and partially dependent on target materials. Just as an example, for a relativistic pulse of peak intensity of 10^{19} W/cm², a contrast of 10^6 just a few ps before the laser peak can produce a pre-plasma with a scale-length of the order of 100 nm, which can be larger than the gap between the structures in the target. Moreover, the plasma formation threshold of nanostructured targets is usually much lower than that of flat targets, because of the higher absorption efficiency¹⁹.

In this paper we show the effects of nanostructure dimensions on the interaction at relativistic intensities, using silicon wires targets. Nano-sized wires/gaps and micro-sized wires separated by hundreds of nanometers are used to investigate absorption and hot electron generation via dedicated experiments and two dimensional particle-in-cell (2D PIC) simulations. In the experiments, laser target interaction is investigated by characterizing the hot electrons emitted in the backward direction and by systematically comparing the resulting electron spectra with those obtained by using a flat silicon target. Compared with forward escaping fast electrons, backward emitted hot electrons (BWE) are not affected by the interaction with the bulk target substrate and the refluxing inside it, so their properties can be easily referred to the interaction region and modelled by PIC codes. We show that wires gap and size significantly affect laser interaction with the electrons; while nano-wires/gaps, strongly affected by any residual pre-plasma, feature an efficient laser absorption via low-energy, few keV electrons and rapidly generate a hot dense plasma, micro-wires/gaps yield a cooler plasma and a high-energy electron component.

Experimental setup

The experiment was carried out at the Tata Institute of Fundamental Research TIFR laboratory in Mumbai, using a Ti:Sapphire CPA laser system that delivers 800 nm, 25 fs laser pulses at a maximum energy of 600 mJ (~ 20 TW).

The p-polarized laser beam was focussed on the target with an incidence angle of 30° to an elliptical spot of $\sim 10 \times 15 \mu\text{m}$ FWHM by means of an $f/2.5$ off-axis parabolic mirror (Fig. 1). The temporal profile of the laser pulse was measured by a third order cross-correlation technique and showed a contrast value of the main peak with

respect to the ns-long amplified spontaneous emission (ASE) of $\sim 3 \times 10^9$ and with respect to a 3 ps pedestal of $\sim 10^6$. The laser irradiance on the target at the best focus was varied in the range $I\lambda^2 = (1.5-3) \cdot 10^{18} \text{ W } \mu\text{m}^2 \text{ cm}^{-2}$ ($a_0 = 1-1.4$).

Spectra of hot electrons emitted at angles of 0° and 60° were measured by two absolutely calibrated electron spectrometers (ESMs) as sketched in Fig. 1. The ESMs consisted of a 0.1 T dipole magnet and an image plate and detected electrons in the energy range (0.1–7.0) MeV.

Three types of silicon targets were used including optically polished FS (Flat Silicon), NanoWires (NW) and MicroWire (MW) targets. Scanning Electron Micrographs (SEM) of the targets are shown in Fig. 1. The MW targets consisted of pillars of length $\sim 10 \mu\text{m}$ and 800 nm diameter regularly distributed on a Si surface in a grid and separated by 200 nm gaps (fill factor = 0.64). The lateral walls of the pillars were partially ragged by the fabrication process. The NW targets were formed by nanowires of length $\sim 8 \mu\text{m}$ and diameter $\sim 10-20 \text{ nm}$, randomly distributed onto a Si surface, separated by 10–50 nm, resulting in a fill factor in the range 0.04–0.2. The MW and NW targets used in our study, therefore, differ both in the size of the wires and of the gaps.

Light scattered in the specular direction was collected and analysed by a compact spectrometer (350–800 nm) via an optical fiber to monitor the occurrence of three-halves harmonic ($\lambda \sim 533 \text{ nm}$), which is here used a signature of preplasma formation¹⁹.

Results

Preplasma and target structures. The formation of a preplasma before the arrival of the main laser peak can damage the structures on the target surface and fill the gaps between them, strongly affecting the interaction of the main peak. A meaningful understanding and modelling of the experimental observations therefore requires a careful characterization of such a preplasma, experimentally or by means of numerical simulations. A mean to accomplish this task is to monitor the formation of three-halves laser harmonic in the emission spectra.

The $(3/2)\omega_0$ emission arises from the mixing of laser light with electron plasma waves produced by two-plasmon decay (TPD) instability²⁰. TPD occurs in the underdense plasma at an electron density $n_e/4$, n_c being the critical density, and needs a sufficiently large density scalelength $L_{pp} = n_e/(dn_e/dx)$ to grow, usually $L_{pp} > \lambda_0$ for ultrashort laser irradiation^{21,22}. Therefore, the detection of $3/2\omega_0$ emission can be used as an indirect indicator of the presence of a pre-plasma¹⁹. At the lowest laser irradiance explored here ($I\lambda^2 = 1.5 \cdot 10^{18} \text{ W } \mu\text{m}^2 \text{ cm}^{-2}$), the $3/2\omega_0$ harmonic was never detected in our experiment, suggesting that $L_{pp} \ll \lambda_0$ during the main peak interaction, as expected, considering the large ASE contrast. A short pre-plasma in the nm range is however expected to be generated by the ps pedestal that overcomes the plasma formation threshold. The order of magnitude of L_{pp} can be estimated by assuming that the pre-plasma formation occurs 3 ps before the peak of the pulse, where the contrast ratio is approximately 10^6 , and successively expands at the ion-acoustic wave speed. Considering a pre-plasma temperature $\approx 10 \text{ eV}$ and $Z = 3$, as given by hydrodynamic simulations, we obtain $L_{pp} \approx 35 \text{ nm}$. This value is in the range of the separation of the NWs (10–50 nm) suggesting that tiny structures with gaps of tens of nanometers are likely to be strongly affected by such a small, ubiquitous pre-plasma. In contrast, the laser interaction with MW targets is expected to be marginally perturbed by this effect.

Energy spectra of hot electrons. Energy spectra of hot electrons for the MW target irradiated at $I\lambda^2 = 1.5 \cdot 10^{18} \text{ W } \mu\text{m}^2 \text{ cm}^{-2}$ detected in the direction normal to the target are shown in Fig. 2a. They show a significantly larger flux with respect to the flat target. Also the temperature T_{hot} , calculated by fitting the spectra with an exponential distribution, is found to be as high as 180 keV for MW targets and 36 keV for flat targets, showing a dramatic five-fold increase. Similar results were obtained from spectra measured at 60° from the target normal.

To check the role of a short pre-plasma on the observed rise of hot electrons, we repeated the measurements at twice the laser irradiance, where a larger L_{pp} would be expected. At $I\lambda^2 = 3 \cdot 10^{18} \text{ W } \mu\text{m}^2 \text{ cm}^{-2}$, a broad and weak $3/2\omega_0$ emission centred at $\sim 535 \text{ nm}$ was detected for MW targets while it was not detected in FS targets. This result suggests that gaps between MWs could be partially filled by underdense plasma during the ps pedestal. In these circumstances, $3/2\omega_0$ emission could be explained by the occurrence of TPD instability along the plasma channels between the wires. Electron spectra measured with MW at $I\lambda^2 = 3 \cdot 10^{18} \text{ W } \mu\text{m}^2 \text{ cm}^{-2}$ reveal a less efficient generation of high-energy electrons characterized by a lower T_{hot} (Fig. 2a). This suggests that the damage of the wire-structure over the surface, associated to the partial filling of the gaps, results in a less efficient laser-plasma coupling and electron acceleration.

Measurements carried out with NW targets did not show any $3/2\omega_0$ emission at any laser irradiance in the range explored. BWE spectra exhibit an amount of hot electrons larger than that generated with a FS target, as shown in Fig. 2b for $I = 3 \cdot 10^{18} \text{ W } \mu\text{m}^2 \text{ cm}^{-2}$. However, the enhancement of both flux and temperature of hot electrons is smaller than the values observed for MW targets, particularly for electrons measured in the normal direction. At $\theta = 0^\circ$, the amount of hot electrons is approximately 30 times higher than for a FS target, while T_{hot} is approximately the same in the measurement uncertainty. The ESM at $\theta = 60^\circ$ yielded a larger total flux and a higher temperature of 70 keV, revealing anisotropic generation of hot electrons (Fig. 2b).

Kinetic simulations and interaction mechanisms. *MicroWire Targets.* Fully kinetic PIC numerical simulations were carried out using the Aladyn²³ code in 2D Cartesian geometry. The simulated MW target was designed using realistic sizes, $l_y = 800 \text{ nm}$ for solid material and $dl_y = 200 \text{ nm}$ for the gap size. The main pulse impinges on the tip of nanostructures at $t = 48 \text{ fs}$. Calculated spectra of high-energy BW electrons for MW and FS targets are reported in Fig. 2c for $a_0 = 1$. Spectra account for BW electrons ($p_x < 0$) in front of the target, (i.e. integrated over all the emission angles) at time $t = 100 \text{ fs}$, i.e. 52 fs after the main peak impinges on the tip of MWs.

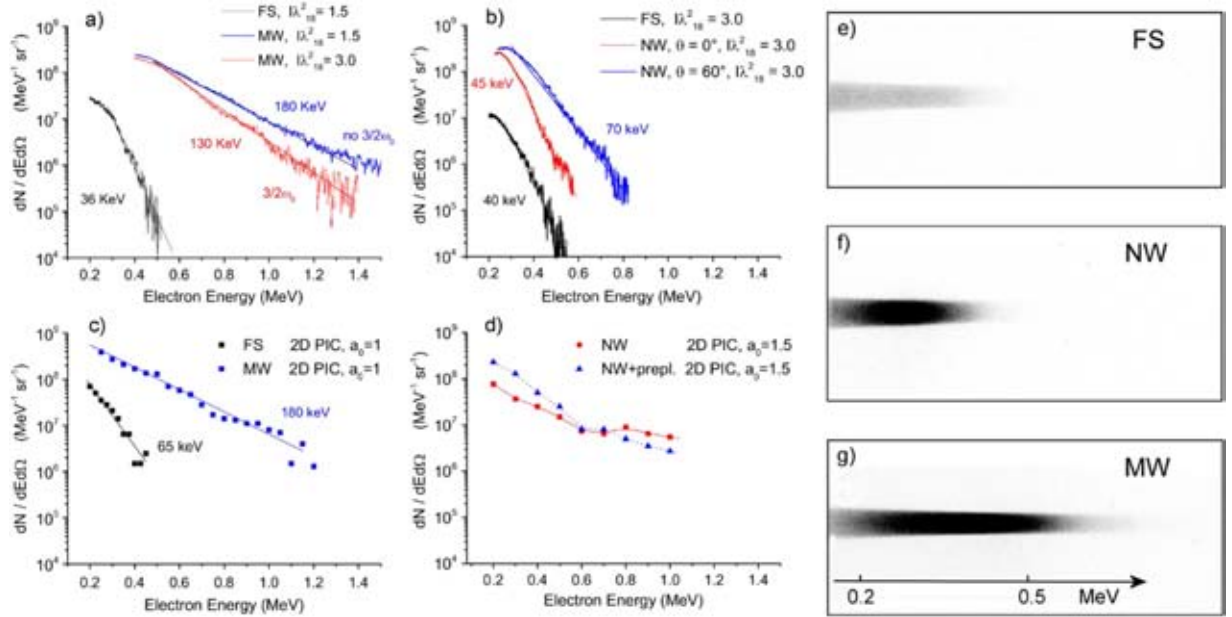


Figure 2. Experimental (a,b) and simulated (c,d) spectra of BW hot electrons and raw traces on the imageplate for the different targets (e,f,g). (a) FS and MW targets ($\theta = 0^\circ$), $I\lambda^2 = 1.5 \cdot 10^{18} \text{ W } \mu\text{m}^2 \text{ cm}^{-2}$ and $I\lambda^2 = 3 \cdot 10^{18} \text{ W } \mu\text{m}^2 \text{ cm}^{-2}$; (b) FS ($\theta = 0^\circ$) and NW ($\theta = 0^\circ$ and 60°) targets, $I\lambda^2 = 3 \cdot 10^{18} \text{ W } \mu\text{m}^2 \text{ cm}^{-2}$; (c) FS and MW targets, 2D PIC at $a_0 = 1$, $t = 100 \text{ fs}$; (d) NW targets, 2D PIC at $a_0 = 1.5$, $t = 100 \text{ fs}$. The 2D PIC spectrum obtained by filling the gaps between NWs with a pre-plasma of density $10 n_c$ is also reported; (e,f,g) $I\lambda^2 = 3 \cdot 10^{18} \text{ W } \mu\text{m}^2 \text{ cm}^{-2}$; $\theta = 0^\circ$. For a fruitful comparison of the simulated with the experimental spectra the number of electrons given by 2D simulations has been rescaled by a factor given by the extension of the 2D box in the Z direction and by the solid angle.

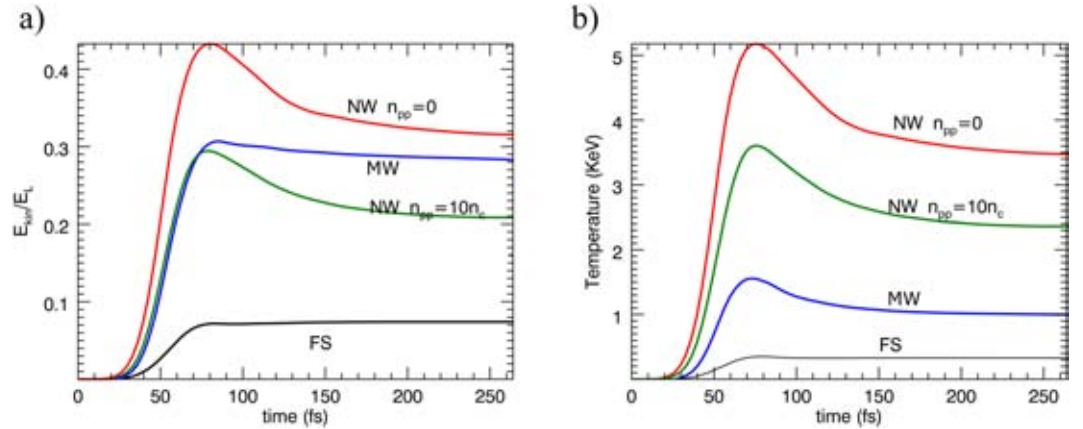


Figure 3. (a) Energy absorbed by electrons and (b) electron heating, obtained by 2D PIC simulations. The temperature here is calculated as the kinetic temperature averaged over all the electrons into the interaction region, corresponding to a box having a transverse size equal to two times the laser waist and a depth of a 400 nm into the wires.

Simulated spectra show a fair quantitative agreement with experimental spectra measured in the corresponding conditions (Fig. 2a, $I\lambda^2 = 1.5 \cdot 10^{18} \text{ W } \mu\text{m}^2 \text{ cm}^{-2}$) for the MW target, while T_{hot} for FS target is to some extent overestimated.

The simulation results provide us with an effective description of the interaction mechanism. The laser pulse penetrates several microns beyond the tip of the MWs, which results in a significant enhancement of laser absorption ($\alpha \approx 0.3$) with respect to a planar surface ($\alpha \approx 0.07$) (Fig. 3a). Since the skin depth is much smaller than the wire diameter, the structures are progressively eroded by the laser pulse. At the end of the interaction ($t \sim 100 \text{ fs}$), however, MWs are still well visible, with the gap channels filled by a $2\text{--}10 n_c$ plasma and a skin depth layer of $30\text{--}50 \text{ nm}$, at the MW lateral wall, at a plasma density $\approx 60 n_c$. At this time, the core of MWs has an electron density of $100\text{--}150 n_c$ and a temperature of around 0.8 keV , likely resulting from cold electron return currents or from

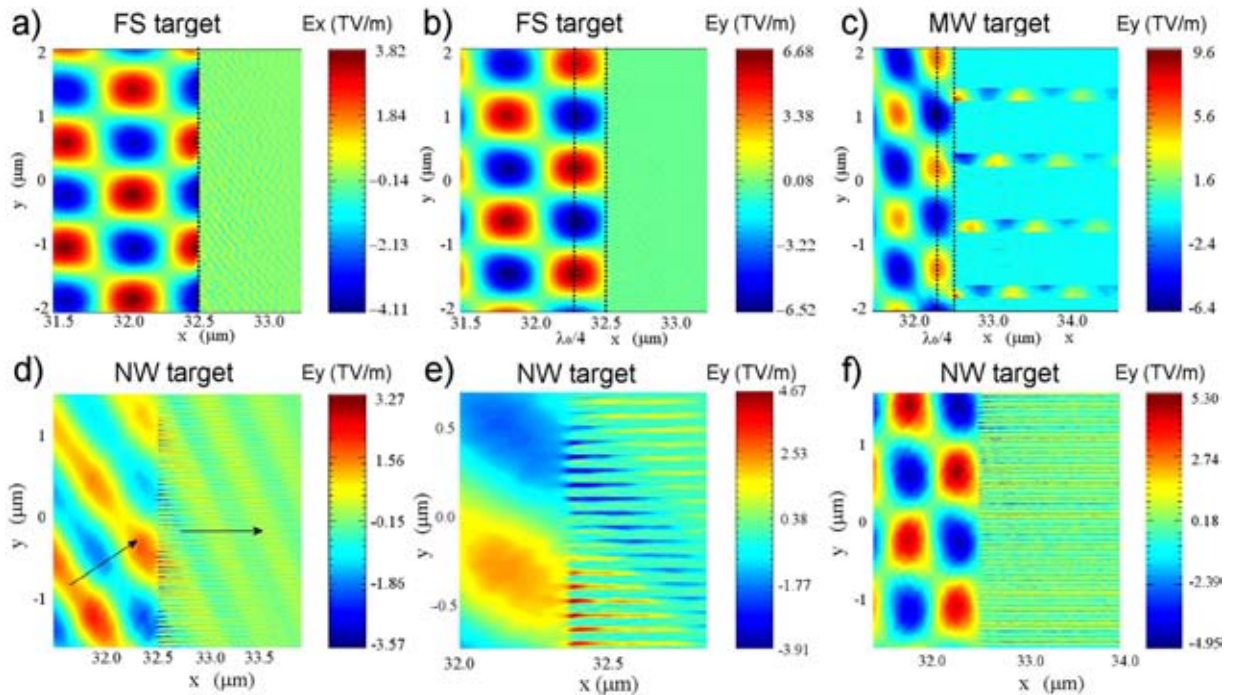


Figure 4. EM field structure for FS (a,b), MW (c) and NW (d) (with no preplasma) targets at the time when peak intensity reaches the target surface ($t = 48$ fs). In (e) field enhancement for NW target. (f) EM field structure for NW target in the trailing part of the laser pulse ($t = 66$ fs).

electrons accelerated in the gap channels and penetrating the wire. These results suggest that the core is in a warm dense matter regime at the end of the interaction.

According to our simulations, electrons retain almost completely the absorbed energy where only 10% of it is transferred to ions at 200 fs after the laser peak. The large absorption results in a plasma temperature $T_e \approx 1.6$ keV, significantly higher than the value obtained for FS targets $T_e \approx 300$ –400 eV.

To gain insight into hot electron generation, it is helpful to observe the spatial distribution of the electromagnetic field in FS and MW targets (Fig. 4). For a FS target, p -polarization results in a combination of stationary and travelling components. An electric field E_x (~ 3.4 TV/m at $t = 50$ fs) near the surface, travelling in the y direction, extracts electrons from the target, according to Brunel's model²⁴ (Fig. 4a). The higher electric field $\sim 2E_{0y}$ (~ 6 TV/m) is however localized at a distance $\approx \lambda_0 \cos(30^\circ)/4 \approx 175$ nm from the surface, produced by the interference of incident and reflecting light and resulting in a standing-wave (SW) pattern along the x direction (Fig. 4b). The maximum energy that an electron reaches in vacuum is therefore $\sim E_{\max} \approx (\sqrt{1 + (2a_0)^2} - 1) \cdot m_e c^2 \approx 590$ keV, which is much higher than the electron mean oscillation energy in the laser field²⁵. This estimation, similar to the one used by May *et al.*²⁶ and Kemp *et al.*²⁷ for the interaction at normal incidence on a steep overdense target, is in a qualitative agreement with maximum electron energies obtained in our simulated and experimental spectra.

For a MW target, the standing-wave pattern in the x direction is still present in front of the target; however, because of the larger absorption of the surface, the reflected wave is weaker and therefore the E_y maximum field is slightly lower (~ 5 TV/m) than in a FS target (Fig. 4c). A travelling EM field (non SW) propagates into the channels and is responsible for high-energy electron generation. The transverse E_y field extracts the electrons from the wire, which successively quiver across the density gradient according to relativistic $J \times B$ force. Since the amplitude of oscillations is smaller than the channel size, many electrons quiver coherently without reaching the neighbouring wire and acquire a net kinetic energy re-entering into the wire or entering an overdense region. A close look to the p_x vs p_y phase space at the beginning of the interaction (Fig. 5a) shows evidence of a coherent forward acceleration along the channels (central peak) and at angles corresponding to $J \times B$ quivering. A similar mechanism of forward acceleration of electrons along micro-sized channels was previously discussed by Jiang *et al.*¹¹, although at a much higher laser intensity $\sim 10^{21}$ W cm⁻². Although most of the hot electrons are accelerated forward, Fig. 5a shows the presence of some backward hot electrons, of similar energy, whose trajectories are probably bent and randomized by magnetic fields. The expected temperature of hot electrons accelerated in underdense plasma is that expressed by the Wilks ponderomotive scaling²⁸ $T_{\text{hot}} \approx (\sqrt{1 + a_0^2} - 1) \cdot m_e c^2 \approx 194$ keV, which is in a good agreement with both experimental and numerical results.

NanoWire targets. NW targets were modelled by considering wires of 20 nm separated by 40 nm gaps. In contrast to the experimental targets, wires are here regularly distributed onto the surface. As shown in Fig. 2d for a pulse with amplitude $a_0 = 1.5$, the number of generated BW HEs is slightly smaller than the experimental value and their energy distribution, integrated over the entire emission angles, scarcely reproduces the experimental

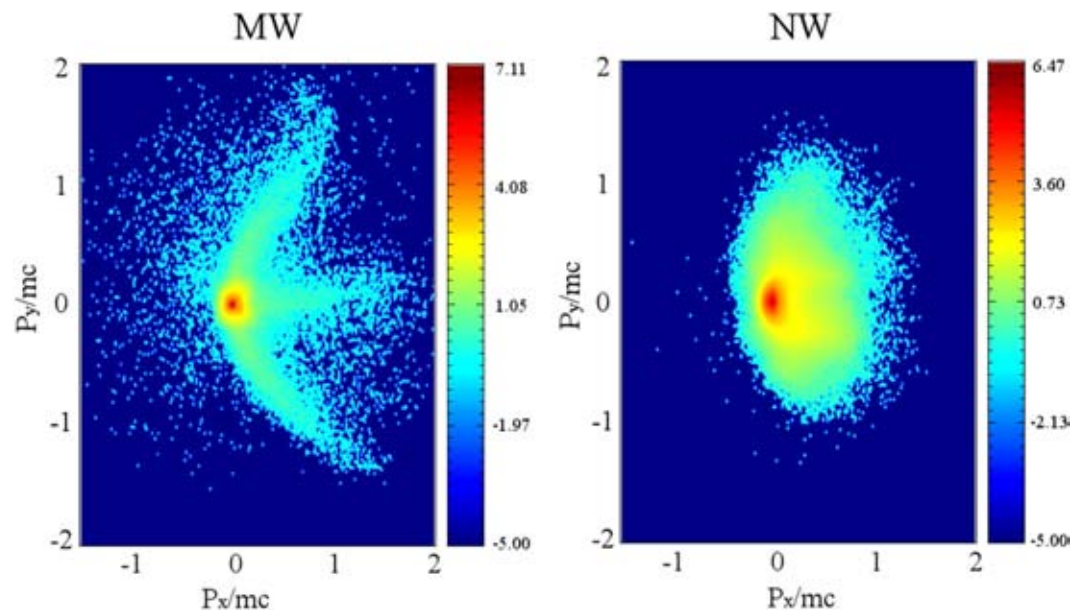


Figure 5. Distribution in logarithmic scale of electron momenta P_x vs. P_y in the leading part of the laser pulse ($t = 40$ fs).

one ($I = 3 \cdot 10^{18} \text{ W } \mu\text{m}^2 \text{ cm}^{-2}$). PIC spectra, in fact, exhibit a lower amount of electrons with energy $E \leq 500 \text{ keV}$ and a tail of higher-energy electrons $E \geq 800 \text{ keV}$, emitted in the normal direction, which is not observed in the experiment. The situation does not appreciably change by varying the fill factor of the structures. The discrepancy with experimental data can be reduced by considering the presence of a tiny preplasma, which rapidly fills the nm-scale gaps and reduces the laser penetration into the target. The effect of preplasma was tested by numerical simulations by partially filling the gaps with a pre-plasma density of $n_{pp} = 10 n_c$ and $n_{pp} = 20 n_c$. In Fig. 2d the BWE spectrum obtained for a preplasma $n_{pp} = 10 n_c$ is reported. The growth of pre-plasma density produces a progressive reduction of the high-energy tail of BW electrons emitted normally to the target, and in the corresponding growth of electrons with energy $E \leq 500 \text{ keV}$, resulting in a better agreement with the experimental spectrum (blue curve in Fig. 2d). In particular, the temperature of hot electrons with $E \leq 500 \text{ keV}$ decreases from 170 keV in the case where the preplasma is not present to 110 keV and 90 keV for $n_{pp} = 10 n_c$ and $n_{pp} = 20 n_c$, respectively, approaching the value obtained for a flat target. The flux of hot electrons obtained with a preplasma is in agreement with the experimental results and remains at levels considerably higher than those obtained for a flat target.

A picture of laser target interaction can again be drawn by observing the EM field distribution of the 2D simulations. In case of no initial pre-plasma into the channels, the laser initially enters between the wires (Fig. 4d). A strong spatial modulation like a fine toothed-comb, with an evident field enhancement, is present at the target surface (Fig. 4e), resulting in a much more efficient laser absorption than in a FS target. The large absorption at this time hinders the formation of a clear SW pattern along x direction in front of the target.

PIC simulations show however that in the trailing part of the pulse the gaps are partially filled by the plasma, expanding preferentially between the wires rather than in front of the target. At this time, no coherent EM field is observed between the wires (Fig. 4f). The larger laser reflection now results in a clear SW pattern in front of the target, even if the maximum EM field is lower than for a FS target.

In the actual interaction, a tenuous pre-plasma is already present between the wires at the arrival of the main peak making the initial evolution of the fields similar to that observed above in the trailing part of the pulse. The SW-pattern accompanied by a substantial absence of pre-plasma in front of the target, results in the generation of hot electrons with an energy distribution similar to that obtained for a FS, as observed in the normal direction. Here, however, their flux is enhanced by the larger absorption (Fig. 3b) resulting in a larger amount of electrons reaching the SW accelerating fields. The oscillating EM field across the comb teeth, attenuated by the pre-plasma presence, could result in the generation of hot electrons propagating mainly along the surface or at larger angles, as experimentally observed, even if an accurate investigation of hot electron trajectory, accounting for magnetic fields, is here needed. Laser interaction with the wires can be inferred by looking at the phase plot of electron momenta into the interaction layer (Fig. 5b). Similar to the MW, the electrons are extracted by the wires and accelerated by the laser field, but given the small gap between wires, the energy gain of the electrons is limited by the collision with neighbouring wires and their trajectories are randomized. In this way, electrons are stochastically heated to a higher bulk electron temperature and the high-energy tail of forward hot electrons has a much lower temperature than that obtained with a MW target. The target depth where the stochastic heating occurs, however, decreases with the density of the preplasma present into the gaps approaching the interaction conditions obtained by using a flat homogeneous target. For $n_{pp} = 10 n_c$ the laser penetration depth reduces approximately to one hundred nanometers resulting also in a reduction of the total laser absorption, from $\alpha \approx 0.5$ ($n_{pp} = 0$) to

$\alpha \approx 0.29$. In spite of the fact that the pre-plasma filling the gaps reduces the laser absorption to levels similar or lower than for MW, the energy is now shared by a lower number of bulk electrons, due to the lower fill factor of the target and to the lower temperature of HE. Therefore, NW targets results in higher plasma temperature, going from $T_e \approx 5.2 \text{ keV}$ for $n_{pp} = 0$ to $T_e \approx 3.6 \text{ keV}$ for $n_{pp} = 10 n_c$, calculated in an interaction layer of thickness 400 nm and 100 nm, respectively. These values are in agreement with multi-keV temperatures obtained by Purvis *et al.*⁴, who irradiated Au and Ni nanowires with a relativistic high-contrast laser at $I = 5 \cdot 10^{18} \text{ W cm}^{-2}$. Simulations also show that the abrupt leak of electrons from the nanowire, due to the quivering in the laser EM field, drives its Coulomb explosion, resulting in a considerable and rapid transfer of energy to ions. This energy constitutes 35–40% of the total energy absorbed at 200 fs after the peak of the pulse.

The different interaction regime envisaged for MW and NW targets suggests that a suitable tailoring of the surface can enhance its performance, depending on the desired aim. Additional preliminary results obtained by a parametric investigation with 2D PIC simulations indicate that laser absorption rises for smaller NW sizes and for larger gaps, while keeping the other parameter fixed. Larger values of laser absorption are therefore obtained for smaller fill factors, reaching values $\alpha > 0.9$ for a few-tens of nanometers tiny wires separated by hundreds of nanometers gaps. In this case, only a small fraction of the laser energy is reflected by the tip of the NWs while most of it penetrates between the wires and is absorbed by multiple reflection scattering. Moreover, since the skin depth is only a few tens nanometers, the increase of NW size beyond this value does not provide an increment of electrons capable of absorbing the laser light. These preliminary indications, however, do not account for the possible presence of a tiny preplasma among the wires nor for the effects of 3D geometry on the laser interaction, and therefore need an accurate validation which is out of the scope of the present work.

Conclusions and Outlook

In conclusion, our comparative study shows for the first time the role of key geometrical parameters in relativistic laser interaction with nanostructured targets. Size and separation of wires were found to be governing parameters in setting the interaction regime while taking into account realistic laser contrast. Gaps between structures play a key role in determining the energy distribution of hot electrons. Larger gaps lead to high-energy hot electrons, generated by coherent laser acceleration into the channels while small gaps give rise to a stochastic heating of the electrons inhibiting the formation of high-energy hot electrons in favour of the formation of a hot, dense plasma. In the first case, the enhanced generation of hot electrons makes targets with large gaps potentially suitable for ion acceleration. In contrast, smaller gaps result in hot plasmas with temperatures reaching several keV, making these targets suitable for warm dense matter investigation and strong shock generation. These targets are however very sensitive to even tiny amount of pre-plasma generated by high-contrast laser pulses, which contribute to prevent efficient acceleration of electrons but also tend to reduce the volumetric character and the efficiency of laser absorption.

Methods

Particle In Cell simulations were carried out using the Aladyn²⁰ code in 2D Cartesian geometry. The intensity of a *p*-polarized laser pulse was modeled by a Gaussian profile in the transverse coordinate with focal spot of 10 μm FWHM. The time profile on the focal plane was given by $I(t) = I_0 \cos^4(\pi t/2\tau)$ where $2\tau = 70 \text{ fs}$ corresponds to a pulse length $\tau_{\text{FWHM}} = 25 \text{ fs}$. The laser pulse enters in the computational (*X*, *Y*) box from the left edge, with incidence angle $\alpha = 30^\circ$ with respect to the target normal. The sizes of the numerical box were set to $L_x = 40 \mu\text{m}$ and $L_y = 50 \mu\text{m}$ and the grid cell to $dx = dy = 10 \text{ nm}$, assuring reasonable space-time resolution. The initial density of Si^{4+} ions was set to $n_{\text{Si}} = 4.3 \cdot 10^{22} \text{ cm}^{-3}$, corresponding to a plasma electron density $n_e = 100 n_c = 1.74 \cdot 10^{23} \text{ cm}^{-3}$. In the PIC code, 256 (macro) electrons per cell were used. During dynamical laser-plasma interaction, field ionization using the ADK model has been activated. At the intensities here considered, Si ions increases ionization levels from the initial $Z = 4$ to a final $Z = 8$ – 10 .

References

1. Sentoku, Y. *et al.* Laser light and hot electron micro focusing using a conical target. *Phys. Plasmas* **11**, 3083–3087, doi:10.1063/1.1735734 (2004).
2. Klimo, O. *et al.* Short pulse laser interaction with micro-structured targets: simulations of laser absorption and ion acceleration. *New J. Phys.* **13**, 053028, doi:10.1088/1367-2630/13/5/053028 (2011).
3. Ji, L. L. *et al.* Towards manipulating relativistic laser pulses with micro-tube plasma lenses. *Sci. Rep.* **6**, 23256, doi:10.1038/srep23256 (2016).
4. Purvis, M. A. *et al.* Relativistic plasma nanophotonics for ultrahigh energy density physics. *Nat. Photonics* **7**, 796–800, doi:10.1038/nphoton.2013.217 (2013).
5. Cao, L. *et al.* Enhanced absorption of intense short-pulse laser light by subwavelength nanolayered target. *Phys. Plasmas* **17**, 043103, doi:10.1063/1.3360298 (2010).
6. Zhao, Z. *et al.* Acceleration and guiding of fast electrons by a nanobrush target. *Phys. Plasmas* **17**, 123108, doi:10.1063/1.3507292 (2010).
7. Chatterjee, G. *et al.* Macroscopic transport of Mega-ampere electron currents in aligned carbon-nanotube arrays. *Phys. Rev. Lett.* **108**, 235005, doi:10.1103/PhysRevLett.108.235005 (2012).
8. Singh, P. K. G. *et al.* Efficient generation and guiding of megaampere relativistic electron current by silicon Nanowires. *Appl. Phys. Lett.* **100**, 244104, doi:10.1063/1.4729010 (2012).
9. Singh, P. K. *et al.* Enhanced transport of relativistic electrons through nanochannels. *Phys. Rev. ST Accel. Beams* **16**, 063401, doi:10.1103/PhysRevSTAB.16.063401 (2013).
10. Jiang, S. *et al.* Effects of front-surface target structures on properties of relativistic laser-plasma electrons. *Phys. Rev. E* **89**, 013106, doi:10.1103/PhysRevE.89.013106 (2014).
11. Jiang, S. *et al.* Microengineering laser plasma Interactions at relativistic intensities. *Phys. Rev. Lett.* **116**, 085002, doi:10.1103/PhysRevLett.116.085002 (2016).

12. Tian, Y. *et al.* MeV surface fast electron emission from femtosecond laser pulses interacting with planar and nanowire targets. *Plasma Phys. Control. Fusion* **56**, 075021, doi:10.1088/0741-3335/56/7/075021 (2014).
13. Murnane, M. M. *et al.* Efficient coupling of high-intensity subpicosecond laser pulses into solids. *Appl. Phys. Lett.* **62**, 1068–1070, doi:10.1063/1.108797 (1993).
14. Gordon, S. P. *et al.* X rays from microstructured targets heated by femtosecond lasers. *Opt. Lett.* **19**, 484–6, doi:10.1364/OL.19.000484 (1994).
15. Kulcsar, G. *et al.* Intense Picosecond X-Ray Pulses from Laser Plasmas by Use of Nanostructured “Velvet” Targets. *Phys. Rev. Lett.* **84**, 5149–52, doi:10.1103/PhysRevLett.84.5149 (2000).
16. Sumeruk, H. A. *et al.* Control of strong-laser-field coupling to electrons in solid targets with wavelength-scale spheres. *Phys. Rev. Lett.* **98**, 045001, doi:10.1103/PhysRevLett.98.045001 (2007).
17. Ceccotti, T. *et al.* Evidence of resonant surface-wave excitation in the relativistic regime through measurements of proton acceleration from grating targets. *Phys. Rev. Lett.* **111**, 185001, doi:10.1103/PhysRevLett.111.185001 (2013).
18. Chakravarty, U. *et al.* Enhancement of K_{α} emission through efficient hot electron generation in carbon nanotubes on intense laser pulse irradiation. *J. Appl. Phys.* **112**, 053301, doi:10.1063/1.4749575 (2012).
19. Cristoforetti, G. *et al.* Investigation on laser–plasma coupling in intense, ultrashort irradiation of a nanostructured silicon target. *Plasma Phys. Control. Fusion* **56**, 095001, doi:10.1088/0741-3335/56/9/095001 (2014).
20. Giulietti, D. *et al.* Three half harmonic generation in laser-plasma interaction: evidence for plasmon propagation. *Il Nuovo Cimento* **13**, 845–858, doi:10.1007/BF02457172 (1991).
21. Veisz, L. *et al.* Three-halves harmonic emission from femtosecond laser produced plasmas with steep density gradients. *Phys. Plasmas* **11**, 3311–3323, doi:10.1063/1.1748174 (2004).
22. Tarasevitch, A. *et al.* 3/2 harmonic generation by femtosecond laser pulses in steep-gradient plasmas. *Phys. Rev. E* **68**, 026410, doi:10.1103/PhysRevE.68.026410 (2003).
23. Benedetti, C., Sgattoni, A., Turchetti, G. & Londrillo, P. ALADyn: A high-accuracy PIC code for the Maxwell–Vlasov equations. *IEEE Trans. Plasma Sci.* **36**, 1790–1798, doi:10.1109/TPS.2008.927143 (2008).
24. Brunel, F. Not-so-resonant, resonant absorption. *Phys. Rev. Lett.* **59**, 52–55, doi:10.1103/PhysRevLett.59.52 (1987).
25. Liseykina, T., Mulser, P. & Murakami, M. Collisionless absorption, hot electron generation, and energy scaling in intense laser-target interaction. *Phys. Plasmas* **22**, 033302, doi:10.1063/1.4914837 (2015).
26. May, J. *et al.* Mechanism of generating fast electrons by an intense laser at a steep overdense interface. *Phys. Rev. E* **84**, 025401, doi:10.1103/PhysRevE.84.025401 (2011).
27. Kemp, G. E. *et al.* Coupling of laser energy into hot-electrons in high-contrast relativistic laser-plasma interactions. *Phys. Plasmas* **20**, 033104, doi:10.1063/1.4794961 (2013).
28. Wilks, S. C. & Krueer, W. L. Absorption of ultrashort, ultra-intense laser light by solids and overdense plasmas. *IEEE J. Quantum Electron.* **33**, 1954–1968, doi:10.1109/3.641310 (1997).

Acknowledgements

We acknowledge the National Research Council of Italy for the support in the framework of the Short Term Mobility program 2014. GRK acknowledges partial support from a J.C. Bose Fellowship grant (JCB-037/2010) from the Department of Science and Technology, Government of India. This work was partially supported by the MIUR-PRIN 2012 (Contract No. PRIN2012AY5LEL) and by the INFN L3IA project (CN5).

Author Contributions

G.Cr., A.D.L., A.A., M.S., D.S., G.Ch., J.J., P.K.S. performed the experiment. G.D. and G.M. prepared the targets. G.Cr. carried out the data analysis and prepared the figures. P.L. carried out the kinetic PIC simulations. G.Cr. wrote the manuscript with inputs from G.R.K. and L.A.G. L.A.G., G.R.K. and M.K. provided overall guidance. All authors participated in the discussion and reviewed the manuscript.

Additional Information

Competing Interests: The authors declare that they have no competing interests.

Publisher's note: Springer Nature remains neutral with regard to jurisdictional claims in published maps and institutional affiliations.



Open Access This article is licensed under a Creative Commons Attribution 4.0 International License, which permits use, sharing, adaptation, distribution and reproduction in any medium or format, as long as you give appropriate credit to the original author(s) and the source, provide a link to the Creative Commons license, and indicate if changes were made. The images or other third party material in this article are included in the article's Creative Commons license, unless indicated otherwise in a credit line to the material. If material is not included in the article's Creative Commons license and your intended use is not permitted by statutory regulation or exceeds the permitted use, you will need to obtain permission directly from the copyright holder. To view a copy of this license, visit <http://creativecommons.org/licenses/by/4.0/>.

© The Author(s) 2017

Perspective

A New Line for Laser-Driven Light Ions Acceleration and Related TNSA Studies

Leonida Antonio Gizzi ^{1,2,*}, Dario Giove ³, Carmen Altana ^{4,5}, Fernando Brandi ^{1,6}, Pablo Cirrone ⁵, Gabriele Cristoforetti ¹, Alberto Fazzi ⁷, Paolo Ferrara ¹, Lorenzo Fulgentini ¹, Petra Koester ¹, Luca Labate ^{1,2}, Gaetano Lanzalone ^{5,8}, Pasquale Londrillo ⁹, David Mascali ⁵, Annamaria Muoio ⁵, Daniele Palla ^{1,2,10}, Francesco Schillaci ^{5,11}, Stefano Sinigardi ⁹, Salvatore Tudisco ⁵  and Giorgio Turchetti ⁹

¹ Intense Laser Irradiation Laboratory (ILIL), Istituto Nazionale di Ottica (INO), Consiglio Nazionale delle Ricerche (CNR), Via G. Moruzzi 1, 56124 Pisa, Italy; fernando.brandi@ino.it (F.B.); gabriele.cristoforetti@cnr.it (G.C.); paolo.ferrara@ino.it (P.F.); lorenzo.fulgentini@ino.it (L.F.); petra.koester@ino.it (P.K.); luca.labate@ino.it (L.L.); daniele.palla@ino.it (D.P.)

² Istituto Nazionale di Fisica Nucleare (INFN) Sezione di Pisa, Largo Pontecorvo 3, 56127 Pisa, Italy

³ Istituto Nazionale di Fisica Nucleare, Laboratorio Acceleratori e Superconduttività Applicata (INFN-LASA), Via Fratelli Cervi 201, 20090 Segrate, Italy; dario.giove@mi.infn.it

⁴ Dipartimento di Fisica e Astronomia, Università degli Studi di Catania, 95123 Catania, Italy; altana@lns.infn.it

⁵ Laboratori Nazionali del Sud, INFN, Via S. Sofia, 95125 Catania, Italy; pablo.cirrone@lns.infn.it (P.C.); gaetano.lanzalone@unikore.it (G.L.); davidmascali@lns.infn.it (D.M.); muoio@lns.infn.it (A.M.); schillacif@lns.infn.it (F.S.); tudisco@lns.infn.it (S.T.)

⁶ Istituto Italiano di Tecnologia, Via Morego 30, 16163 Genova, Italy

⁷ Dipartimento di Energia, Politecnico di Milano and INFN, Sezione di Milano, via Lambruschini 4, 20156 Milano, Italy; alberto.fazzi@polimi.it

⁸ Università degli Studi di Enna Kore, Via delle Olimpiadi, 94100 Enna, Italy

⁹ Dipartimento di Fisica e Astronomia, Università di Bologna and INFN, Sez. di Bologna, 40126 Bologna, Italy; pasquale.londrillo@oabo.inaf.it (P.L.); sinigardi@bo.infn.it (S.S.); giorgio.turchetti@bo.infn.it (G.T.)

¹⁰ Dipartimento di Fisica, Università di Pisa, 56124 Pisa, Italy

¹¹ Institute of Physics Czech Academy of Science, ELI-Beamlines, Za Radnicí 835, 252 41 Dolní Břežany, Czech Republic

* Correspondence: la.gizzi@ino.it; Tel.: +39-050-315-2257

Received: 4 August 2017; Accepted: 6 September 2017; Published: 25 September 2017

Abstract: In this paper, we present the status of the line for laser-driven light ions acceleration (L3IA) currently under implementation at the Intense Laser Irradiation Laboratory (ILIL), and we provide an overview of the pilot experimental activity on laser-driven ion acceleration carried out in support of the design of the line. A description of the main components is given, including the laser, the beam transport line, the interaction chamber, and the diagnostics. A review of the main results obtained so far during the pilot experimental activity is also reported, including details of the laser-plasma interaction and ion beam characterization. A brief description of the preliminary results of a dedicated numerical modeling is also provided.

Keywords: ultra-intense laser-matter interaction; laser-driven ion acceleration

1. Introduction

The development of novel ion acceleration techniques based on ultra-intense lasers has been developing rapidly in the past decades due to the dramatic progress of laser systems capable of delivering increasingly higher power laser pulses. Based on these developments, laser-driven

acceleration is now moving from pure scientific exploration to applications. As described in details in several recent review papers, the primary process known as Target Normal Sheath Acceleration (TNSA) [1] is a robust mechanism to accelerate light ions from laser interaction with thin foil targets with exceptional properties including high brightness and high spectral cut-off, high directionality and laminarity, as well as short pulse duration. The process has been explored for a wide range of laser and target parameters in addition to target specifications [2], and has proven to be reliable and relatively easy to implement to accelerate light ions such as protons, deuterons, boron, carbon, oxygen, to energies up to several tens of MeV using large laser systems producing sub-ps pulses with tens or hundreds of Joules per pulse. The main challenges of the current research on TNSA include the control of acceleration parameters, namely cut-off energy, beam divergence, charge, and emittance. At the same time, experimental investigation is also being dedicated to target optimization and engineering, looking at different properties of surface, geometry, and conductivity. Finally, post-acceleration control is being tackled with special attention to selection, collimation [3], and, eventually, injection in secondary acceleration structures, even using miniature target-driven guiding devices [4].

Indeed, ions beams produced with TNSA are ideal for applications where high ion flux is required with relatively large energy spread. Examples of applications include injectors for high power ion beams, neutron generation [5] for high power ion beams, and probes for fast evolving phenomena like the ultrafast charging of laser-heated samples [6]. Additionally, laser-driven ion beams have been proposed for space radiation studies and electronic components testing [7]. A more specific application with potential impact on industry and cultural heritage is the proton-induced X-ray emission spectroscopy (PIXE), which may be applicable with currently achievable TNSA performances and may strongly benefit from the compactness of a multi-MeV laser-driven ion source [8]. For these applications to emerge, the operation of laser-driven ion acceleration should be practical and reliable. In this context, the operation of a compact, high-intensity proton beam line at 10 MeV has been demonstrated recently [9]. However, for practical applications, compact, Joule-scale laser systems in the sub-100 fs domain [10] are much more attractive [11] for their higher repetition rate, potentially reaching the 100 Hz or even the kHz range with diode-pumping [12], which may allow future laser-driven accelerators to reach a repetition rate in the kHz range. Here, we describe a new initiative aimed at the construction of an all-optical accelerator line for light ions using a multi-J class, femtosecond laser system. The line for laser-driven light ions acceleration (L3IA) project has the purpose of establishing an outstanding beam-line operation of a laser-plasma source in Italy, taking advantage of the results achieved so far in this field by the precursor experimental campaigns [13] and numerical modeling. The beam-line will operate at a newly developed sub-petawatt (PW) scale laser installation to enter the parameter range of ion acceleration currently being explored by leading European laboratories in this field, and will provide an advanced test facility for the development and exploitation of laser-driven ion sources. The beam-line development is linked to a strong research and development programme with clear goals, deliverables, and objectives, implementing the required laser-plasma technology and beam diagnostics and control techniques.

2. Materials and Methods: The ILIL-PW Laser Facility

The L3IA will be established at the Intense Laser Irradiation Laboratory and will be based at INO-CNR where the ILIL-PW laser installation features a >200 TW laser system, a beam transport line, and a multi-purpose interaction area with radiation shielding. An overview of the ILIL-PW facility is shown in Figure 1, while a summary of the main laser parameters is given in the table of Table 1. The 10-Hz front-end is shown schematically in Figure 2, with the oscillator producing 15 fs pulses at approximately 6 nJ. A “booster” unit amplifies the oscillator pulse to the 10 μ J level and is followed by a stretcher that delivers a chirped pulse with a duration of 600 ps to the regenerative amplifier. The mJ energy pulse is further amplified by a 5-pass amplifier followed by a 4-pass amplifier, finally delivering 600 mJ at 800 nm. The output pulses of the front-end are then transported to the final 4-pass amplifier, pumped by four Nd:YAG lasers (Titan6 by Amplitude Technologies) delivering a total of

24 J pulses at 532 nm at a maximum rep-rate of 5 Hz. The 800-nm pulse is thus amplified up to >7 J and compressed down to <25 fs. Pulse duration control is achieved through standard techniques based on acousto-optical devices placed in the front-end to achieve control of spectral gain, phase, and amplitude. The pulse energy losses due to acousto-optics devices are compensated in the amplification stages. Pump fluence throughout the front-end system is kept below 1 J/cm² to operate well below the Ti:Sa crystal damage threshold [14], yielding a typical energy extraction efficiency of less than 30%.

The compressed pulse is then transported under vacuum to the octagonal interaction chamber via two remotely controlled, beam steering chambers. The beam is then focused on a target by an F/3 Off-Axis Parabolic (OAP) mirror to an intensity in excess of 10²⁰ W/cm². The interaction chamber is equipped with a remotely controlled motorized target mount with a sub-micrometer resolution capable of XYZ translation and azimuthal rotation around the vertical axis.

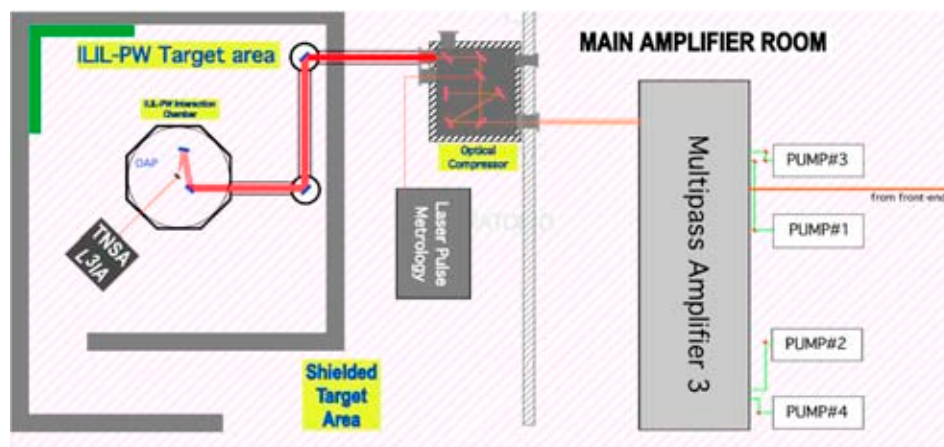


Figure 1. Schematic view of the ILIL-PW facility at INO, including the main amplifier room, the shielded target area, and the laser-driven light ions acceleration (L3IA) dedicated line. OAP: Off-Axis Parabolic.

The target mount was designed to enable a 100-mm range of positioning and withstand a load of up to 500 N in all directions of motion. These specifications ensure that the scanning of targets up to 100 mm × 100 mm can be accomplished, enabling a large number of laser shots to be fired on a given target (typically up to 10³) before target replacement is required.

Table 1. Summary table of the ILIL-PW laser parameters including the front-end and the full system after the two-step facility upgrade.

MAIN BEAM	Front-end	1st Phase	2nd Phase
Wavelength (nm)	800	800	800
Pump Energy (J)	1.8	12	24
Pulse Duration (fs)	40	30	25
Energy Before Compression (J)	0.6	4.7	7.9
Energy After Compression (J)	0.4	>3	>5
Rep. Rate (Hz)	10	1	2
Max intensity on target (W/cm ²)	2 × 10 ¹⁹	2 × 10 ²⁰	4 × 10 ²⁰
Contrast@100ps	>10 ⁹	>10 ⁹	>10 ¹⁰
Beam Diameter (mm)	36	100	100

The output from the front-end can be compressed independently to deliver 450 mJ in a 30 fs pulse with an M² < 1.5 to a separate interaction chamber, which is used for the pilot experimental activity. Cross-correlation measurement of the laser pulse show [15] that the front-end laser contrast

remains above 10^{10} up to 10 ps before the peak of the pulse, and decreases to 10^6 , 1 ps before the peak of the pulse.

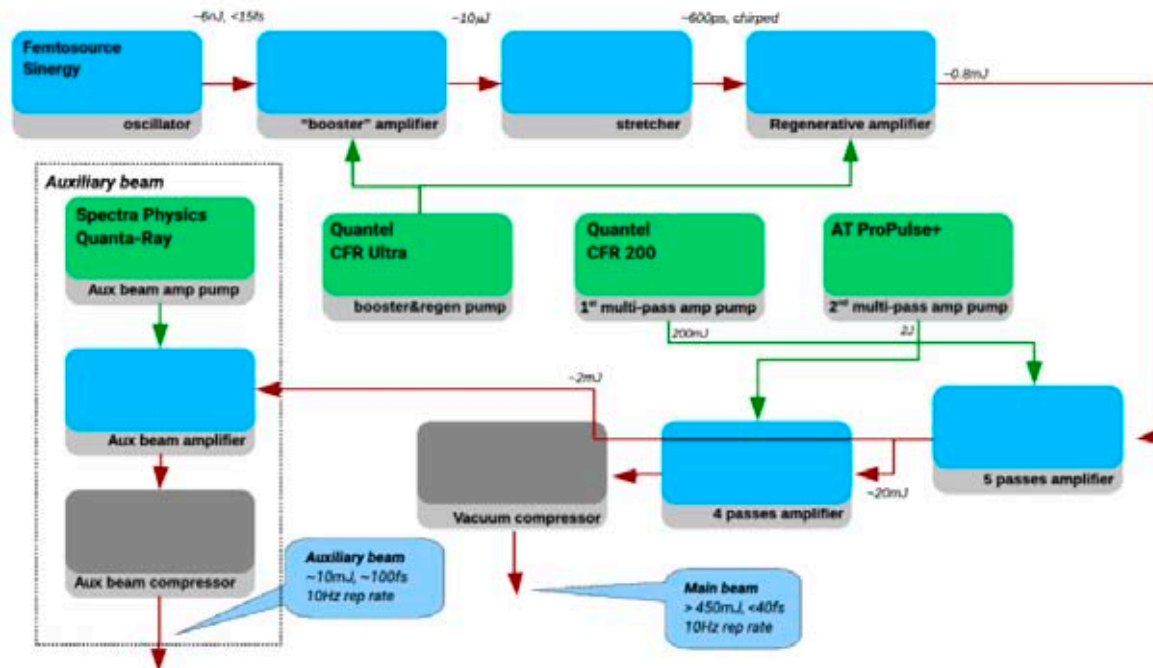


Figure 2. Schematic view of the laser front-end, including the 10 TW compressor.

3. L3IA Development Plan

The L3IA project aiming at the development of the ion acceleration line includes a complete set of work-packages, including the interface with the ILIL-PW hosting facility, and the beam line scheme comprising targets, laser beam focusing, and diagnostic devices dedicated to both the laser-plasma interaction and the ion beam detection and characterization. Numerical modeling is also included, with the specific tasks of providing basic predictive simulations for the baseline parameters of the beam line as well as allowing for the investigation of advanced target and laser configurations. Provision is also made for specific application cases, including radiobiological testing and cultural heritage applications.

In fact, the project develops in two stages that build on the laser upgrade phases described in Table 1. The first phase will establish TNSA operation at a cut-off energy >6 MeV, using standard thin foil targets optimized for the laser performances, with particular attention paid to the available laser contrast. The second phase will be mainly dedicated to the control and enhancement of the laser contrast, to enable the use of targets with nano-structured targets [16] to enhance laser absorption as recently investigated by our collaboration. Moreover, the higher contrast will allow sub-micron thickness targets to be used to increase the cut-off energy, as originally demonstrated by T. Ceccotti and co-workers [17]. In fact, our pilot experimental activity summarized below shows that the existing laser contrast gives rise to plasma formation with a micrometer spatial scale, which limits the use of this kind of target. Based on this enhancement of the laser performance, and on the additional increase of laser pulse energy described in Table 1, the second phase of the project is expected to establish TNSA operation at a cut-off energy >12 MeV. Along with these source developments, the project also includes post-acceleration manipulation of the accelerated ions, with collection, collimation, and energy selection and transport. Based on the output from the beam characterization phase, we will tune post-acceleration devices to obtain the highest collection and the highest throughput of protons to the sample for pilot applications including radiobiology and PIXE studies. Our foreseen applications have been selected on the basis of compatibility with the inherent properties of the

TNSA-accelerated beam of protons, namely large energy spread and large peak current. Our setup will include a vacuum-air interface to access the beam in air and provide sample exposure at standard pressure and temperature. A quantitative design of this transport line is currently in progress and will be the subject of future publications.

4. Results: Numerical Investigation of TNSA Regime

Numerical simulations were carried out using the ALaDyn code [18] following the prospects outlined in the table of Table 1. We considered a laser pulse with a duration of $\tau = 25\text{--}40$ fs full width half maximum (FWHM) and a Gaussian focal spot $D_f = 7.5$ μm , with an energy per pulse in the range of $E_L = 0.4\text{--}6$ J. The corresponding peak intensity ranges from 2×10^{19} to 5×10^{20} and the normalized intensity $a_0 = 0.85(I\lambda^2/10^{18} \text{ W/cm}^2)^{1/2}$ ranges from 3 to 15. Some simulations with higher intensity were also considered. The lower intensity value corresponds to the front-end laser operation, which has been extensively explored [15,19,20] and was found to be fully consistent with the above scaling. In the simulations, the laser impinges with different angles $\theta = 0^\circ, 10^\circ, 15^\circ, 30^\circ$ on a fully ionized, CH_2 slab with a thickness $l_{\text{th}} = 2\text{--}2.5$ μm and electronic density $n_e = 100n_c = 1.74 \times 10^{23} \text{ cm}^{-3}$. No effects originating from pre-plasma due to finite pre-pulse are taken into account. The first outcome of Particle In Cell (PIC) investigation summarized in Figure 3 shows a significant dependence of proton acceleration on the laser incidence angle, but only at lower intensities $a_0 < 5$. In this range, going from incidence $\theta = 0^\circ$ to $\theta = 30^\circ$, the proton cut-off energy increases by 40%. At higher intensities, $a_0 > 10$, this factor drops to only a few percentage points.

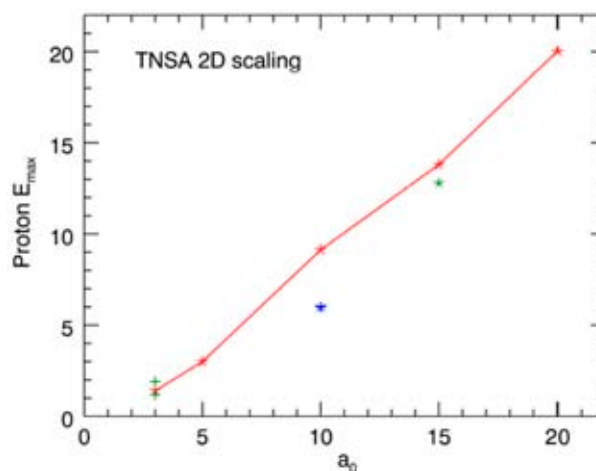


Figure 3. Calculated protons cut-off energy (MeV) at different laser intensities with strength parameter $a_0 = 3\text{--}20$. Data on the red line all refer to laser pulse duration $\tau = 30$ fs, incidence angle $\theta = 10^\circ$, and target thickness $l_{\text{th}} = 2$ μm . Different data at $a_0 = 3$, $E_{\text{max}} = [1.2, 1.4, 1.82]$ MeV refer to different incidence angles ($\theta = 0\text{--}30^\circ$). The lower value at $a_0 = 10$ refers to a larger $l_{\text{th}} = 2.5$ target thickness, whereas the lower value at $a_0 = 15$ refers to a lower $\tau = 25$ fs pulse duration. TNSA: Target Normal Sheath Acceleration.

In PIC simulations, systematic parametric scans are necessarily restricted to 2D geometry. The main difficulty to extract useful quantitative information on proton acceleration is that 2D TNSA models give a logarithmic increase with time of the $E_m(t)$ energy. The choice of a definite time at which to stop the simulation to evaluate the final proton energy is therefore intrinsically arbitrary. To overcome this limitation, a method has been introduced [21] that allows a unique proton energy, the so-called asymptotic E value, to be extracted using only the information on the growth rate of energy in a finite time range. The results reported in Figure 3 were consistent with this approach, which enabled a more detailed description of the intensity and angular dependence of TNSA cut-off energy.

5. Results: Pilot Experimental Activity

The pilot experimental activity presented here was carried out using the laser pulse at the output of the front-end. The pulse was compressed in a separate compressor chamber and focused, at an angle of incidence of 15° or 30° , using an $f/4.5$ off-axis parabolic mirror (OAP), in a spot size of $6.2 \mu\text{m}$ (FWHM), giving a nominal intensity on the target of about 2×10^{19} ($a_0 = 3$). A schematic view of the pilot experimental setup is given in Figure 4. Special attention was dedicated in the experimental campaign to the target integrity prior to the arrival of the main pulse on the target, which strongly depends on the temporal profile of the laser pulse [22].

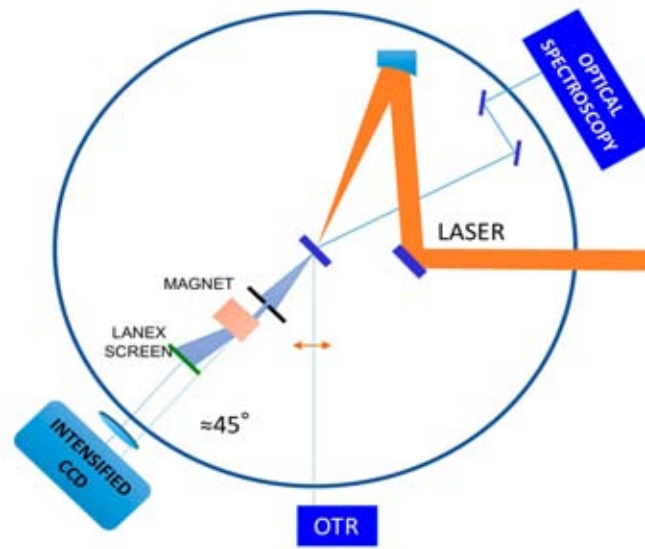


Figure 4. Schematic view of the experimental setup showing the main diagnostics, including the optical spectroscopy of the specular reflection, the rear side optical imaging, and the magnetic electron spectrometer of the forward escaping electrons. A Thomson Parabola ion spectrometer was used in place of the electron spectrometer to detect forward accelerated ions. CCD: Charge Coupled Device; TR: Optical Transition Radiation.

To this purpose, we used optical spectroscopy of the light scattered in the specular direction to monitor the generation of second harmonic emission, $2\omega_L$, and $(3/2)\omega_L$ of the incident laser light. These components of the scattered radiation are associated with the coupling of the laser light at the critical density and at the quarter critical density, respectively [23]. In fact, the formation of even a very small pre-plasma before of the arrival of the main pulse can provide suitable conditions for the growth of stimulated instabilities including the Stimulated Raman Scattering and the Two Plasmon Decay. Electron plasma waves at $\omega_L/2$ generated by the instabilities can couple non-linearly with incident laser light and give rise to $(3/2)\omega_L$ emission. This emission is therefore a signature of the presence of even a small pre-plasma. Second harmonic emission in the specular direction is instead generated by the non-linear interaction of the main laser pulse at the critical density [24]. Therefore, second harmonic emission can be taken as a signature of the presence of a critical density layer in the plasma at the time of interaction of the main pulse, a prerequisite for the interaction with an over-dense target and the occurrence of TNSA. In our experiments, in spite of the increase of the $(3/2)\omega_L$ intensity, the intensity of the $2\omega_L$ emission remained significant, indicating that the laser contrast in the best focus was sufficient to ensure the survival of the target rear surface and, therefore, the proper onset of the TNSA accelerating field.

Another crucial issue in this class of experiments is the control of the irradiation intensity on the target, which is complicated by the typically very short depth of focus of the focusing optics. These circumstances make the irradiation intensity very sensitive to small changes in the position of

the target relative to the best focus. Also, small changes in the thermal lensing in the laser amplifiers may lead to changes in the position of the best focus which, if not compensated for, can change irradiation conditions. To this purpose, as shown in Figure 4, optical imaging of the rear side of the target at 45° from the target normal was performed to detect Optical Transition Radiation (OTR) generated from electrons crossing the target rear surface as a marker of optimum focusing conditions. OTR intensity is also very sensitive to the sharpness of the density transition across the rear surface [25], and is therefore a useful additional indicator of the integrity of the target rear surface.

We also measured fast electron emission from the target rear side in the forward direction. Forward escaping fast electrons were detected and analyzed using a permanent magnet electron spectrometer with a detection range from 1 MeV to 5 MeV. Measurements were carried out with the target placed either at the best focus position or $100\ \mu\text{m}$, corresponding to two Rayleigh lengths, away from the best focus towards the off-axis parabola. As shown in Figure 5, clear forward electron emission was detected in the condition of best focus while no electron emission was detectable out of focus. These circumstances were confirmed by the rear side images, which clearly show optical emission (OTR) strongly correlated with the forward escaping fast electrons. In addition, OTR images (not shown here) taken for different target materials and thicknesses exhibited similar spectral and angular properties. These measurements enabled us to confirm that a simple optical imaging of the target rear side gives accurate shot-by-shot information of the optimum laser focusing on the target and of the quality of the target rear surface.

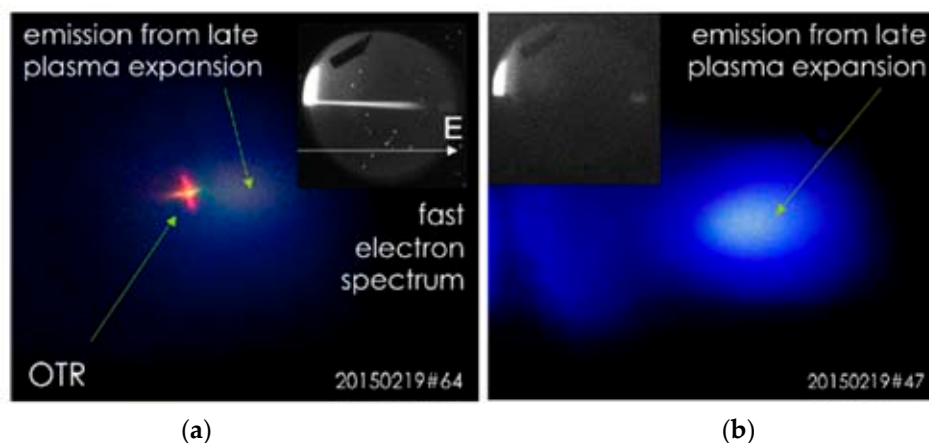


Figure 5. (a) Rear side optical imaging showing Optical Transition Radiation from fast electrons from laser irradiation of $10\text{-}\mu\text{m}$ thick Al foil at the best focus position. The insert shows the raw spectrum of fast electrons obtained with a permanent magnet spectrometer. (b) Same image, but with the target displaced by two Rayleigh lengths ($100\ \mu\text{m}$).

6. Results: Ion Detection

Concerning ion detection, a range of diagnostics was used in our experiments to measure ion acceleration, including radio-chromic films (GAF), CR39, Thomson Parabola, and Time of Flight (TOF) diamond detectors. Normally, Thomson Parabola, and TOF detectors were used simultaneously so that a cross-comparison of the signals obtained from the two devices was possible. This was done in view of a possible use of the diamond detector for on-line direct detection of accelerated ions during normal beamline operation. A detailed discussion of all these measurements with different detectors is given elsewhere [15,19]. Here, we focus our attention on the interpretation of the TOF signal in particular. The plot of Figure 6a shows the TOF signal obtained with the diamond detector from the irradiation of a $5\ \mu\text{m}$ thick Mylar target and with a laser angle of incidence on the target of 30° . The detector was placed at a distance of $30\ \text{cm}$ and was filtered using a $12\ \mu\text{m}$ thick Al foil. The strong peak at $-10\ \text{ns}$

was originally attributed to a combination of X-rays and fast electrons reaching the detector soon after the interaction.

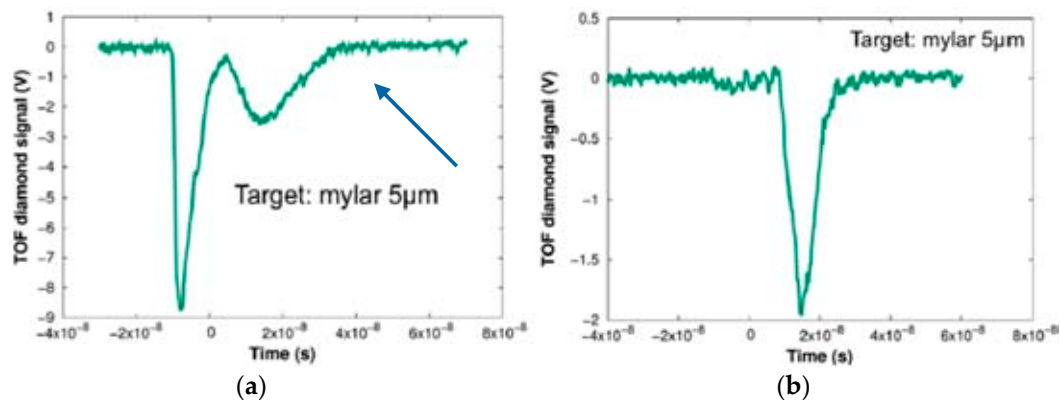


Figure 6. (a) Raw signal of the diamond Time of Flight (TOF) detector showing the ion signal from the irradiation of a 5 μm thick Mylar target corresponding to ions between 1.9 MeV and 0.8 MeV. $T = 0$ is arbitrary in this plot. The strong emission at $T = -10$ ns is the signal due to fast electrons. (b) Same measurement as (a), but with magnetic shielding in front of the diamond detector. The blue arrow indicate the onset of the ion signal corresponding to the cut-off energy.

This peak is followed by the actual ion signal that, as shown by the blue arrow, starts at 4 ns, namely, 15 ns after the starting of the photo-peak. Taking into account the TOF distance and assuming a signal predominantly due to protons that have the highest charge-to-mass ratio, calculations yield a high energy cut-off of approximately 2 MeV. A similar measurement carried out placing a magnetic dipole with a 1T magnetic field in front of the diamond detector is shown in Figure 6b. This measurement shows that the peak at -10 ns is strongly reduced, leaving a clean proton signal, indicating that the peak was due to the presence of fast electrons that are stopped by the strong magnetic field. Incidentally, the measurements of Figure 6 were obtained at the 30° angle of incidence, which is comparable to the maximum energy of 1.9 MeV obtained [15] on the $10 \mu\text{m}$ Al target at a 15° angle of incidence, indicating that such a change in the angle of incidence does not lead to significant changes of the interaction conditions. This is consistent with the numerical simulation results of Figure 3 where, for similar values of laser intensity, no significant dependence on the angle of incidence was expected. A more systematic investigation is planned to confirm the observed behavior with the angle of incidence and target thickness.

7. Conclusions

In summary, we described the L3IA project dedicated to the establishment of a new laser-driven light ions acceleration line based on the physical mechanism known as Target Normal Sheath Acceleration. The project takes advantage of the ongoing ILIL-PW upgrades at the Intense Laser Irradiation Laboratory, providing a sub-PW class laser combined with a new interaction area. The L3IA initiative was developed after major research and development advances in laser-driven ion acceleration in the TNSA regime, carried out during the past few years and dedicated to the establishment of the key scientific and technological aspects required for a reliable operation of the acceleration line. In particular, significant effort has been dedicated to the control of the underlying physical processes that play a role in the complex dynamics of TNSA: non-linear optical scattering occurring at the plasma interface as a quantitative marker of plasma formation; optical transition radiation imaging and fast electron energy measurements as a critical indicator of laser focusing quality; and finally, direct measurement of the ions cut-off energy. Pilot exploration of basic target parameters such as target material and thickness shows results well in line with expected values from dedicated numerical simulations and published results in this regime. All these aspects provide a

quite complete characterization of the laser-target interaction regime in our experimental conditions and a reference set of ion acceleration data for the upcoming upgrade of the laser installation that is expected to soon provide a >20-fold increase in the laser power.

Acknowledgments: We acknowledge financial contribution from the CNR ELI-Italy Network funded by the MIUR for the upgrade of the ILIL-PW installation. The L3IA is a project of the INFN CSN5. This work is also partially supported by the MIUR-PRIN 2012 (Contract No. PRIN2012AY5LEL).

Author Contributions: Leonida Antonio Gizzi, Dario Giove, Fernando Brandi, Pablo Cirrone, Gabriele Cristoforetti, Alberto Fazzi, Petra Koester, Luca Labate and Salvatore Tudisco conceived, designed and realized the experimental setup. Leonida Antonio Gizzi, Dario Giove, Carmen Altana, David Mascali, Fernando Brandi, Francesco Schillaci, Gabriele Cristoforetti, Pasquale Londrillo, Alberto Fazzi, Stefano Sinigardi, Giorgio Turchetti, Paolo Ferrara, Lorenzo Fulgentini, Petra Koester, Luca Labate, Gaetano Lanzalone, Annamaria Muoio, Daniele Palla and Salvatore Tudisco performed the experiments and the data acquisition and participated to the data analysis; Lorenzo Fulgentini and Luca Labate were in charge of laser control; all authors contributed to the interpretation of the data; Leonida Antonio Gizzi wrote the paper.

Conflicts of Interest: The authors declare no conflict of interest. The founding bodies had no role in the design of the study; in the collection, analyses, or interpretation of data; in the writing of the manuscript, and in the decision to publish the results.

References

1. Snavely, R.A. Intense high-energy proton beams from petawatt-laser irradiation of solids. *Phys. Rev. Lett.* **2000**, *85*, 2945–2948. [[CrossRef](#)] [[PubMed](#)]
2. Daido, H.; Nishiuchi, M.; Pirozhkov, A.S. Review of laser-driven ion sources and their applications. *Rep. Prog. Phys.* **2012**, *75*, 056401. [[CrossRef](#)] [[PubMed](#)]
3. Romano, F.; Schillaci, F.; Cirrone, G.A.P.; Cuttone, G.; Scuderi, V.; Allegra, L.; Amato, A.; Amico, A.; Candiano, G.; Luc, G.D.; et al. The ELIMED transport and dosimetry beamline for laser-driven ion beams. *Nucl. Instrum. Methods Phys. Res. Sect. A Accel. Spectrom. Detect. Assoc. Equip.* **2016**, *829*, 153–158. [[CrossRef](#)]
4. Kar, S.; Ahmed, H.; Prasad, R.; Cerchez, M.; Brauckmann, S.; Aurand, B.; Cantono, G.; Hadjisolomou, P.; Lewis, C.L.S.; Macchi, A.; et al. Guided post-acceleration of laser-driven ions by a miniature modular structure. *Nat. Commun.* **2016**, *7*, 10792. [[CrossRef](#)] [[PubMed](#)]
5. Roth, M.; Schollmeier, M. Ion Acceleration—Target Normal Sheath Acceleration. In Proceedings of the CERN Conference, Geneva, Switzerland, 23–29 November 2014; C14-11-23, pp. 231–270. [[CrossRef](#)]
6. Ahmed, H.; Kar, S.; Cantono, G.; Nersisyan, G.; Brauckmann, S.; Doria, D.; Gwynne, D.; Macchi, A.; Naughton, K.; Willi, O.; et al. Investigations of ultrafast charge dynamics in laser-irradiated targets by a self probing technique employing laser driven protons. *Nucl. Instrum. Methods Phys. Res. Sect. A Accel. Spectrom. Detect. Assoc. Equip.* **2016**, *829*, 172–175. [[CrossRef](#)]
7. Hidding, B.; Königstein, T.; Willi, O.; Rosenzweig, J.; Nakajima, K.; Pretzler, G. Laser-plasma-accelerators—A novel, versatile tool for space radiation studies. *Nucl. Instrum. Methods Phys. Res. Sect. A Accel. Spectrom. Detect. Assoc. Equip.* **2011**, *636*, 31–40. [[CrossRef](#)]
8. Barberio, M.; Veltri, S.; Scisciò, M.; Antici, P. Laser-Accelerated Proton Beams as Diagnostics for Cultural Heritage. *Sci. Rep.* **2017**, *7*, 40415. [[CrossRef](#)] [[PubMed](#)]
9. Busold, S.; Schumacher, D.; Deppert, O.; Brabetz, C.; Kroll, F.; Blažević, A.; Bagnoud, V.; Roth, M. Commissioning of a compact laser-based proton beam line for high intensity bunches around 10 MeV. *Phys. Rev. Spec. Top. Accel. Beams* **2014**, *17*, 031302. [[CrossRef](#)]
10. Macchi, A.; Borghesi, M.; Passoni, M. Ion Acceleration by Superintense Laser Pulses. *Rev. Mod. Phys.* **2013**, *85*, 751–793. [[CrossRef](#)]
11. Noaman-ul-Haq, M.; Ahmed, H.; Sokollik, T.; Yu, L.; Liu, Z.; Yuan, X.; Yuan, F.; Mirzaie, M.; Ge, X.; Chen, L.; et al. Statistical analysis of laser driven protons using a high-repetition-rate tape drive target system. *Phys. Rev. Accel. Beams* **2017**, *20*, 041301. [[CrossRef](#)]
12. Mason, P.; Divoky, M.; Ertel, K.; Pilar, J.; Butcher, T.; Hanus, M.; Banerjee, S.; Phillips, J.; Smith, J.; De Vido, M.; et al. Kilowatt average power 100 J-level diode pumped solid state laser. *Optica* **2017**, *4*, 438–439. [[CrossRef](#)]
13. Agosteo, S.; Anania, M.P.; Caresana, M.; Cirrone, G.A.P.; de Martinis, C.; Side, D.D.; Fazzi, A.; Gatti, G.; Giove, D.; Giulietti, D.; et al. The LILIA (laser induced light ions acceleration) experiment at LNF. *Nucl. Instrum. Methods Phys. Res. Sect. B-Beam Interact. Mater. At.* **2014**, *331*, 15–19. [[CrossRef](#)]

14. Canova, F.; Chambaret, J.-P.; Mourou, G.; Sentis, M.; Uteza, O.; Delaporte, P.; Itina, T.; Natoli, J.-Y.; Commandre, M.; Amra, C. Complete characterization of damage threshold in titanium doped sapphire crystals with nanosecond, picosecond, and femtosecond laser pulses. *Proc. SPIE*. **2005**, 599123. [[CrossRef](#)]
15. Gizzi, L.A.; Altana, C.; Brandi, F.; Cirrone, P.; Cristoforetti, G.; Fazzi, A.; Ferrara, P.; Fulgentini, L.; Giove, D.; Koester, P.; et al. Role of laser contrast and foil thickness in target normal sheath acceleration. *Nucl. Instrum. Methods Phys. Res. Sect. A Accel. Spectrom. Detect. Assoc. Equip.* **2016**, *829*, 144–148. [[CrossRef](#)]
16. Cristoforetti, G.; Londrillo, P.; Singh, P.K.; Baffigi, F.; D'Arrigo, G.; Lad, A.D.; Milazzo, R.G.; Adak, A.; Shaikh, M.; Sarkar, D.; et al. Transition from Coherent to Stochastic electron heating in ultrashort relativistic laser interaction with structured targets. *Sci. Rep.* **2017**, *7*, 1479. [[CrossRef](#)] [[PubMed](#)]
17. Ceccotti, T.; Lévy, A.; Popescu, H.; Réau, F.; D'Oliveira, P.; Monot, P.; Geindre, J.P.; Lefebvre, E.; Martin, P. Proton Acceleration with High-Intensity Ultrahigh-Contrast Laser Pulses. *Phys. Rev. Lett.* **2007**, *99*, 185002. [[CrossRef](#)] [[PubMed](#)]
18. Benedetti, C.; Sgattoni, A.; Londrillo, P. Aladyn: A High-Accuracy PIC Code for the Maxwell–Vlasov Equations. *IEEE Trans. Plasma Sci.* **2008**, *36*, 1790–1798. [[CrossRef](#)]
19. Altana, C.; Muoio, A.; Lanzalone, G.; Tudisco, S.; Brandi, F.; Cirrone, G.A.P.; Cristoforetti, G.; Fazzi, A.; Ferrara, P.; Fulgentini, L.; et al. Investigation of ion acceleration mechanism through laser-matter interaction in femtosecond domain. *Nucl. Instrum. Methods Phys. Res. Sect. A Accel. Spectrom. Detect. Assoc. Equip.* **2016**, *829*, 159–162. [[CrossRef](#)]
20. Tudisco, S.; Altana, C.; Lanzalone, G.; Muoio, A.; Cirrone, G.A.P.; Mascali, D.; Schillaci, F.; Brandi, F.; Cristoforetti, G.; Ferrara, P.; et al. Investigation on target normal sheath acceleration through measurements of ions energy distribution. *Rev. Sci. Instrum.* **2016**, *87*, 02A909. [[CrossRef](#)] [[PubMed](#)]
21. Babaei, J.; Gizzi, L.A.; Londrillo, P.; Mirzanejad, S.; Rovelli, T.; Sinigardi, S.; Turchetti, G. Rise time of proton cut-off energy in 2D and 3D pic simulations. *Phys. Plasmas* **2017**, *24*, 043106. [[CrossRef](#)]
22. Baffigi, F.; Cristoforetti, G.; Fulgentini, L.; Giulietti, A.; Koester, P.; Labate, L.; Gizzi, L.A. X-ray conversion of ultra-short laser pulses on a solid sample: Role of electron waves excited in the pre-plasma. *Phys. Plasmas* **2014**, *21*, 072108. [[CrossRef](#)]
23. Gizzi, L.A. Advances in X-ray Studies of Ultraintense Laser-Plasma Interactions. In *Progress in Ultrafast Intense Laser Science*; Yamanouchi, K., Giulietti, A., Ledingham, K., Eds.; Springer: New York, NY, USA, 2010; Volume 98, pp. 123–138.
24. Gizzi, L.A.; Giulietti, D.; Giulietti, A.; Audebert, P.; Bastiani, S.; Geindre, J.P.; Mysyrowicz, A. Simultaneous measurements of hard X-rays and second-harmonic emission in fs laser-target interactions. *Phys. Rev. Lett.* **1996**, *76*, 2278. [[CrossRef](#)] [[PubMed](#)]
25. Bellei, C.; Davies, J.; Chauhan, P.K.; Najmudin, Z. Coherent transition radiation in relativistic laser–solid interactions. *Plasma Phys. Control. Fusion* **2012**, *54*, 035011. [[CrossRef](#)]



© 2017 by the authors. Licensee MDPI, Basel, Switzerland. This article is an open access article distributed under the terms and conditions of the Creative Commons Attribution (CC BY) license (<http://creativecommons.org/licenses/by/4.0/>).

Rise time of proton cut-off energy in 2D and 3D PIC simulations

J. Babaei,¹ L. A. Gizzi,² P. Londrillo,³ S. Mirzanejad,¹ T. Rovelli,⁴ S. Sinigardi,^{4,a)} and G. Turchetti⁵

¹Department of Physics, Faculty of Basic Sciences, University of Mazandaran, P.O. Box 47415-416, Babolsar, Iran

²ILIL, Istituto Nazionale di Ottica, CNR Pisa and INFN Sezione di Pisa, Italy

³INAF Osservatorio Astronomico di Bologna, Via Ranzani 1, 40127 Bologna, Italy

⁴Dipartimento di Fisica e Astronomia, Università di Bologna and INFN Sezione di Bologna, Via Irnerio 46, I-40126 Bologna (BO), Italy

⁵Dipartimento di Fisica e Astronomia, Università di Bologna, Via Irnerio 46, I-40126 Bologna (BO), Italy

(Received 1 December 2016; accepted 22 March 2017; published online 17 April 2017)

The Target Normal Sheath Acceleration regime for proton acceleration by laser pulses is experimentally consolidated and fairly well understood. However, uncertainties remain in the analysis of particle-in-cell simulation results. The energy spectrum is exponential with a cut-off, but the maximum energy depends on the simulation time, following different laws in two and three dimensional (2D, 3D) PIC simulations so that the determination of an asymptotic value has some arbitrariness. We propose two empirical laws for the rise time of the cut-off energy in 2D and 3D PIC simulations, suggested by a model in which the proton acceleration is due to a surface charge distribution on the target rear side. The kinetic energy of the protons that we obtain follows two distinct laws, which appear to be nicely satisfied by PIC simulations, for a model target given by a uniform foil plus a contaminant layer that is hydrogen-rich. The laws depend on two parameters: the scaling time, at which the energy starts to rise, and the asymptotic cut-off energy. The values of the cut-off energy, obtained by fitting 2D and 3D simulations for the same target and laser pulse configuration, are comparable. This suggests that parametric scans can be performed with 2D simulations since 3D ones are computationally very expensive, delegating their role only to a correspondence check. In this paper, the simulations are carried out with the PIC code ALaDYN by changing the target thickness L and the incidence angle α , with a fixed $a_0 = 3$. A monotonic dependence, on L for normal incidence and on α for fixed L , is found, as in the experimental results for high temporal contrast pulses. *Published by AIP Publishing.* [<http://dx.doi.org/10.1063/1.4979901>]

I. INTRODUCTION

The acceleration of protons by intense laser pulses is still the subject of active experimental investigation. The most consolidated regime is the Target Normal Sheath Acceleration (TNSA), where the electrons, heated by a laser, diffuse and leave the target, creating an electric field which accelerates the surface protons present in the contaminants. The comparison with current particle-in-cell (PIC) simulations is still affected by uncertainties. Indeed, the energy spectra are found to be exponential with a cut-off

$$\begin{cases} dN/dE = (E_{\max}/T) e^{-E/T} & \text{for } E < E_{\max} \\ dN/dE = 0 & \text{for } E > E_{\max}, \end{cases}$$

but the cut-off energy E_{\max} and the average energy T (proton temperature) depend on time. In 2D PIC TNSA simulations, a monotonic rise of E_{\max} with time is observed, whereas in 3D PIC, a slow trend towards a possible saturation to an asymptotic value is usually observed. As a consequence, a comparison of 2D (two dimensional) and 3D (three dimensional) simulations is difficult since the laws of the cut-off energy rise with time $E_{\max}(t)$ appear to be different.

Although the different asymptotic dependence on t for E_{\max} for 2D and 3D PIC simulations is well known, its origin

has not been investigated. Empirical rules, based on a choice of t related to laser pulse duration τ_L , have been proposed, and the ratio between the 3D and 2D cut-off energies has been suggested to be $\sim 2/3$. To our knowledge, no model was proposed to explain this behaviour. A logarithmic growth of the proton energy was shown to occur in a plasma vacuum expansion model, but no relation with PIC simulations was suggested. A comparison of 2D and 3D simulations was presented in the literature for a model of composite targets (foam+metal target),¹ but the problem of the different asymptotic behaviour of E_{\max} was not addressed. Another systematic study, using 2D and 3D simulation, was presented for thin solid targets down to the transparency limit and for near critical targets.² In both cases, the acceleration regime is not TNSA, the way the cut-off energies in 2D and 3D are determined is not specified, and a model to relate them is not proposed.

In this paper, we try to give a phenomenological answer to this question, by proposing two empirical laws for $E_{\max}(t)$, which are suggested by a model first proposed by Schreiber *et al.*,³ to describe the dependence of the cut-off energy from the laser pulse duration.

Schreiber's model refers to a 3D configuration, and we worked out its 2D version obtaining an analytic approximation to the cut-off energy dependence on time. Both in 2D and 3D, the cut-off energy $E_{\max}(t)$ depends only on two parameters, the rise time t^* , and the asymptotic energy E_{∞} .

^{a)}sinigardi@bo.infn.it

This model assumes that the hot electron cloud leaves the rear side of the target, creating a surface density of positive charge, whose electric field accelerates the protons belonging to the contaminants. For a Gaussian laser pulse of waist R , we have considered a 2D model in which the surface charge is located on a strip, with the infinite length and height $2R$, and a 3D model in which the surface charge is located on a disc of radius R . In our model, the laser is assumed to have normal incidence on the target and in Figure 1, we sketch the geometric configurations.

The numerical analysis presented here refers to a laser pulse with $\tau = 40$ fs and $a_0 = 3$. This choice was made because, recently, systematic experiments with such a laser pulse were carried out at ILIL in Pisa.⁴ Furthermore, several experiments with similar parameters, which ensure that the acceleration regime is TNSA, are present in the literature. For an overview on the physics of the proton acceleration by high intensity lasers and related experiments, we refer to recent reviews.^{5–7} In the intensity range that we have considered, experimental results concerning the dependence on the target thickness, the incidence angle, and the temporal contrast are reported in many papers.^{8–14} When the contrast is very high, the cut-off energy varies monotonically with target thickness and if the contrast were infinite, this behaviour should be observed, until the radiation pressure becomes dominant by approaching the relativistic transparency limit. When the contrast is finite, as in experiments, a maximum in the cut-off energy E_{\max} is reached by decreasing the metal foil thickness. Further reducing it, a rapid decrease to zero of E_{\max} is observed due to the increasing damage on the foil

induced by the prepulse. A significant dependence on the incidence angle is also observed, and typically, the proton cut-off energy increases with the angle up to a maximum value because the electrons are heated more efficiently.⁶

In our model, the preplasma is neglected (the temporal contrast is assumed as infinite). Because of this choice, the Amplified Spontaneous Emission (ASE) prepulse is not permitted. On the other hand, a prepulse coming from compression artefacts (ps time scale) can be tolerated when comparing our simulation results with experiments, as long as the plasma preformed on the illuminated side of the target has a scale length much shorter than the laser wavelength.

The 2D and 3D simulations were carried out with the ALaDyn code,¹⁵ and the asymptotic cut-off energy E_{∞} was determined by a best-fit procedure on its time dependence, following the laws obtained from the electrostatic model, which just depend on two parameters: the asymptotic cut-off energy E_{∞} and the rise time t^* , i.e., the time at which the energy starts to rise.

Beyond the good agreement of the asymptotic cut-off energies obtained from 2D and 3D simulations, the monotonic dependence on the incidence angle and the target thickness was found to be in qualitative agreement with the experimental results for high contrast pulses.

In our 3D simulations, the transverse section of the computational box is the same as the target, whose extension is comparable with the focal spot (four times bigger) measured by the waist. As a consequence, a leakage of electrons from the computational box occurs and when the fraction of lost electrons becomes appreciable, typically for ct significantly above $100 \mu\text{m}$, the simulation loses reliability. That is why we stop our analysis at this time. Increasing the box size would enable us to go further but without adding any insightful detail.

Our method allows us to limit the simulation even to $ct = 60 \sim 80 \mu\text{m}$ using small boxes since the results are already stable and comparable with 3D results. Here, we present the results for a single laser pulse and various target thicknesses, to assess the validity of our model, even though we have started a more extensive exploration by varying the laser duration, its intensity, and the metal target electron density. A detailed analysis of the dependence of E_{∞} and t^* on laser and target parameters will give us a better insight, but, from the encouraging results obtained so far, we can conclude that the simple method we propose here appears to be adequate to extract the asymptotic cut-off energy from PIC simulations.

II. THE 3D CASE

Starting from the 3D case and considering a laser pulse which propagates along the z axis, we choose an electrostatic potential which vanishes at $z = 0$, where a uniform charge density σ , within a disc of radius R , is located. This potential is given by

$$V(\zeta) = 2\pi R \sigma \left(\sqrt{1 + \zeta^2} - \zeta - 1 \right) \quad \zeta = \frac{z}{R}.$$

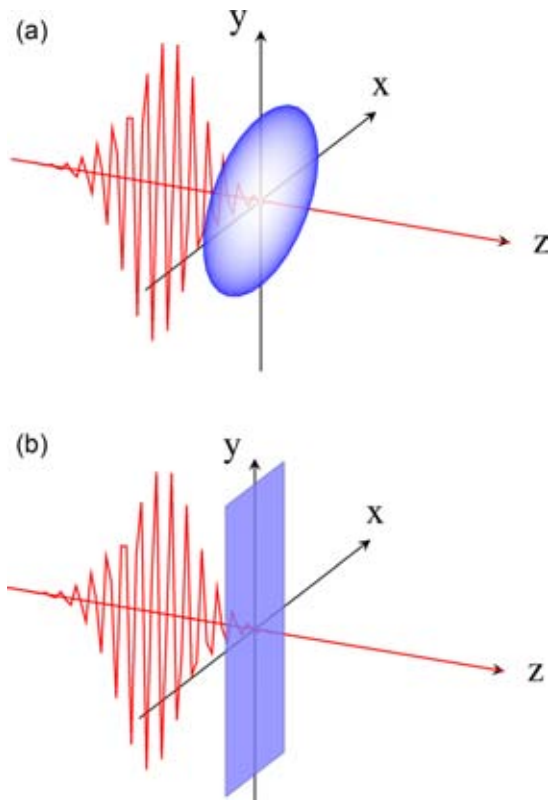


FIG. 1. Schematic representation of the configurations used to compute the accelerating field: 3D (top) and 2D (bottom).

Asymptotically, for $z \rightarrow \infty$, it behaves as $V=Q/z$, where $Q = \pi R^2 \sigma$ is the charge on the disc. A particle initially at rest accelerates, and the law of motion is obtained from energy conservation. Since $V(0)=0$, we have

$$m \frac{v^2}{2} + eV(z) = 0 \quad v = \dot{z}.$$

Letting $v_\infty = \dot{z}(\infty)$, the kinetic energy of the particle, after integrating the equation of motion, is

$$E(t) \simeq E_\infty \left(1 - \frac{t^*}{t}\right)^2 \quad t > t^* = \frac{R}{4v_\infty},$$

where

$$E_\infty = m \frac{v_\infty^2}{2} = 2\pi e R \sigma.$$

Since this is an asymptotic law, we may assume that $E(t)=0$ for $t < t^*$. Notice that E is the highest energy reached at time t , namely, $E = E_{\max}$.

III. THE 2D CASE

In this case, we have an infinite strip along the y axis with uniform charge density σ on $-R < x < R$. A potential that vanishes at $z=0$ is given by

$$V(z) = 4R\sigma \left(-\zeta \arctan \frac{1}{\zeta} + \log \frac{1}{\sqrt{1+\zeta^2}} \right) \\ \simeq -4R\sigma \log(1+\zeta),$$

where we defined $\zeta = z/R$. To obtain this result, it is simpler to compute first the electric field $\mathcal{E}_x = 4\sigma \arctan(1/\zeta)$, whose asymptotic behaviour is $4\sigma/\zeta$. As a consequence, a potential having this asymptotic behaviour and which vanishes at the origin is $\hat{V} \simeq -4R\sigma \log(1+\zeta)$. The potential in this case diverges logarithmically, and consequently, the particle accelerates indefinitely. We approximate the potential energy with

$$e\hat{V}(z) = -E_\infty \log(1+\zeta), \quad E_\infty \equiv m \frac{v_\infty^2}{2} = 4eR\sigma.$$

We may then easily solve the equations of motion from energy conservation, assuming the proton are initially at rest in the origin as for the 3D case. The result is (see the [Appendix](#) for more details)

$$E(t) = E_\infty \log\left(\frac{t}{t^*}\right) \quad t \geq t^* = \frac{R}{v_\infty}.$$

Again, since this is an asymptotic law, we may assume that $E(t)=0$ for $t < t^*$.

IV. COMPARISON WITH PIC SIMULATIONS

Even though the models we propose are very simple, we tried to see whether the predicted asymptotic laws for $E(t)$ hold for PIC simulations. The answer is positive, at least for

targets consisting of a uniform foil whose thickness is in the micrometer range, covered by a thin layer of contaminants. For this type of targets, the fits, both for 2D and 3D PIC simulations, are surprisingly accurate. However, the asymptotic energy E_∞ and the time scale t^* in 2D and 3D must be considered fitting parameters, even though the results we obtain have the correct order of magnitude with respect to the theoretical results.

The law to be fitted for 2D simulations is

$$\begin{cases} E_{\max}^{(2D)}(ct) = 0 & \text{for } t < t^{*(2D)} \\ E_{\max}^{(2D)}(ct) = E_\infty^{(2D)} \log \frac{ct}{ct^*} & \text{for } t > t^{*(2D)}. \end{cases}$$

We perform a linear fit by defining $y=E$ and $x = \log ct$ so that the previous law becomes

$$y = a + bx, \quad E_\infty^{(2D)} = b, \quad ct^{*(2D)} = e^{-a/b}.$$

The law to be fitted for 3D simulations is

$$\begin{cases} E_{\max}^{(3D)}(ct) = 0 & \text{for } t < t^{*(3D)} \\ E_{\max}^{(3D)}(ct) = E_\infty^{(3D)} \left(1 - \frac{ct^{*(3D)}}{ct}\right)^2 & \text{for } t > t^{*(3D)}. \end{cases}$$

We can perform a linear fit by defining $y = \sqrt{E}$ and $x = 1/ct$ so that the previous law becomes

$$y = a + bx, \quad E_\infty^{(3D)} = a^2, \quad ct^{*(3D)} = -\frac{b}{a}.$$

V. RESULTS FOR 2D SIMULATIONS

We have considered the following model: the laser pulse has wavelength $\lambda = 0.8 \mu\text{m}$, intensity $I = 2 \times 10^{19} \text{W/cm}^2$, waist $6.2 \mu\text{m}$, and P-polarization and its duration is 40 fs. The corresponding normalized vector potential is $a_0 = 3$. The target is a uniform Al foil of thickness L varying between 0.5 and $8 \mu\text{m}$, having a layer of hydrogen on the rear (nonilluminated) side, with a fixed thickness of $0.08 \mu\text{m}$.

The ionization levels are Al^{9+} and H^+ , and it is fixed throughout the simulation. The electron densities have been chosen as $n_e^{\text{Al}} = 100 n_c$ and $n_e^{\text{H}} = 10 n_c$. For an Al foil, whose thickness is in the range of $0.5\text{--}8 \mu\text{m}$, we expect that the process is dominated by TNSA (we are far above the transparency limit). The collisions have been neglected in our simulations.

In [Figure 2](#), we show the results obtained from 2D simulations for $0.5 \mu\text{m} \leq L \leq 8 \mu\text{m}$, by plotting $E_{\max}(ct)$ in a linear and a logarithmic scale for ct with the corresponding fits. In [Table I](#), we quote the results of the fit: we notice that $E_\infty^{(2D)} \simeq E(ct = 50)$. In [Figure 3](#), we resume the dependence of the cut-off energy on the thickness. In [Figure 4](#), we show the results of 2D simulations obtained when the incidence angle is small but different from zero: the logarithmic growth in ct is still present, and the linear fits are quite good; see also [Table II](#), where the numeric values for $\alpha = 5^\circ$, 10° , and 15° , and a target thickness of $L = 2 \mu\text{m}$ are shown.

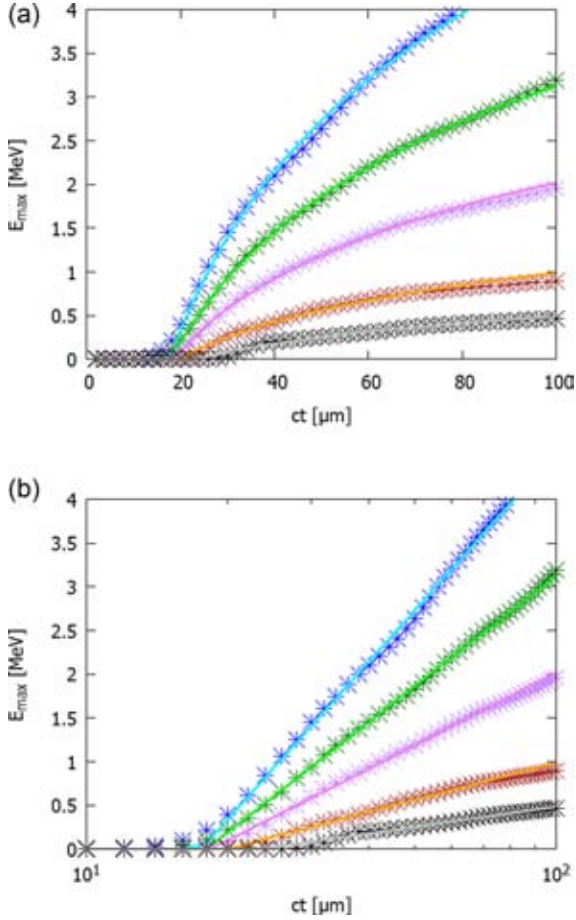


FIG. 2. (Top) Cut-off energy E_{\max} versus ct in the range $10 \leq ct \leq 100 \mu\text{m}$ obtained from a PIC simulation (stars) and comparison with the fit (continuous line) for targets of various thicknesses L . Blue (cyan), $L = 0.5 \mu\text{m}$; dark green (green), $L = 1 \mu\text{m}$; purple (violet), $L = 2 \mu\text{m}$; brown (orange), $L = 4 \mu\text{m}$; and black (grey), $L = 8 \mu\text{m}$. (Bottom) The same as the upper panel but on a logarithmic scale for ct , which clearly shows the linearity and the accuracy of the fit.

TABLE I. Fitting parameters for 2D simulations with zero incidence angle and target thicknesses $0.5 \leq L \leq 8 \mu\text{m}$. The chosen intervals for fitting are $ct_1 = 20 \mu\text{m}$ and $ct_2 = 80 \mu\text{m}$.

L	$E_{\max}(ct=50)$	$E_{\infty}^{(2D)}$	$ct^{*(2D)}$	σ_E	σ_{ct}
0.5	2.64	2.62	17.5	0.05	0.03
1	1.82	1.82	18.0	0.02	0.15
2	1.19	1.19	18.4	0.02	0.2
4	0.58	0.61	19.9	0.02	0.5
8	0.25	0.33	23.3	0.02	0.9

VI. RESULTS FOR 3D SIMULATIONS

We present now the results for some 3D simulations, precisely with $L = 0.5, 1,$ and $2 \mu\text{m}$. In Figure 5, we show the curves corresponding to a linear fit to $\sqrt{E(t)}$ versus $1/ct$. The asymptotic values $E_{\infty}^{(3D)}$ and the fitting curves up to $ct = 100 \mu\text{m}$ are shown in the upper panel of Figure 5.

We notice that, even though the extrapolated data from the 2D and 3D simulations are not the same, the correspondence is quite reasonable. In Table III, the numerical results are quoted, and in any case, the discrepancy does not exceed

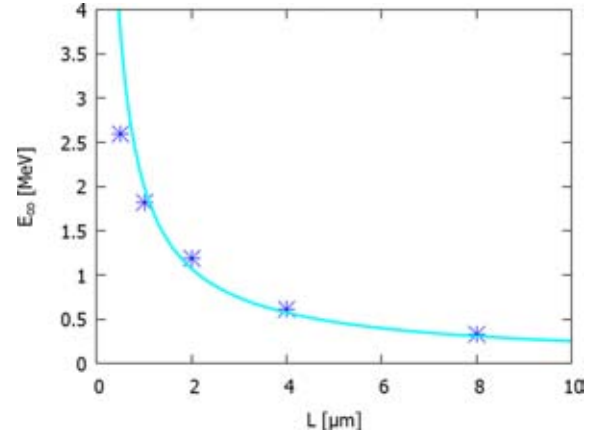


FIG. 3. Comparison of the extrapolated cut-off energy for 2D PIC simulations (blue stars) for different target thicknesses $L = 0.5, 1, 2, 4,$ and $8 \mu\text{m}$ and a fit with the curve $E_{\max} = 1/L^{0.9}$ (cyan line).

20%. We may observe that the energy for $ct = 50 \mu\text{m}$ in the 2D simulation is very close to the extrapolated value, due to the logarithmic growth, but in 3D, at $ct = 50 \mu\text{m}$, the energy value is less than one half of the extrapolated value E_{∞} , due to the slower rise. In this case, there is an asymptotic limit,

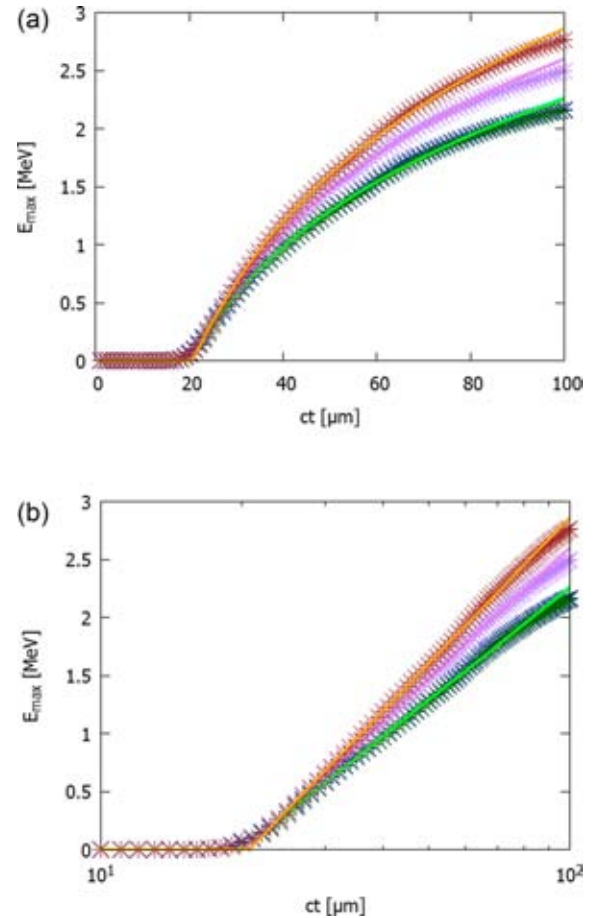


FIG. 4. (Top) Comparison of the 2D PIC solution with a small incidence angle α . The figure shows E_{\max} versus ct , with the stars corresponding to the PIC simulation and the curves to the fit for various angles: $\alpha = 5^\circ$, dark green (green); $\alpha = 10^\circ$, purple (violet); and $\alpha = 15^\circ$, brown (orange). (Bottom) The same data are plotted with a logarithmic scale for ct , which shows how the data stay on a line and the accuracy of the linear fit (Table II).

TABLE II. Fitting parameters for 2D simulations for three different incidence angles $\alpha = 5^\circ, 10^\circ,$ and 15° and target thickness $L = 2 \mu\text{m}$. The chosen intervals for fitting are $ct_1 = 20 \mu\text{m}$ and $ct_2 = 80 \mu\text{m}$, and the fitting errors are quoted.

α	$E_{\text{max}}(ct = 50)$	$E_{\infty}^{(2D)}$	$ct^{*(2D)}$	σ_E	σ_{ct^*}
5	1.28	1.40	19.9	0.01	0.1
10	1.47	1.62	20.1	0.01	0.1
15	1.59	1.82	20.7	0.02	0.15

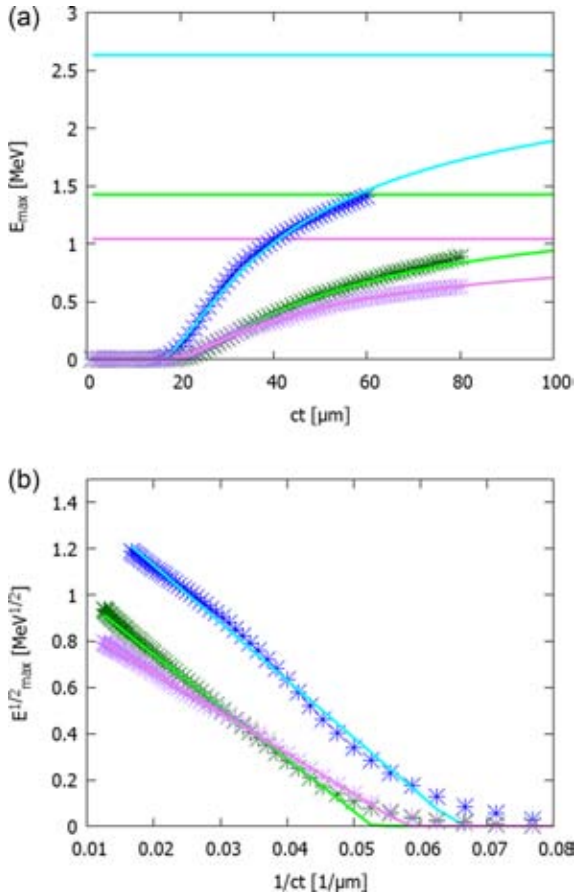


FIG. 5. (Top) Results for a 3D PIC simulation for E_{max} versus ct (stars) compared with the linear fit of $\sqrt{E_{\text{max}}}$ as a function of $1/ct$ (continuous lines, and the asymptotic values $E_{\infty}^{(3D)}$ are also shown), for different target thicknesses: $L = 0.5 \mu\text{m}$, blue (cyan); $L = 1 \mu\text{m}$, dark green (green); and $L = 2 \mu\text{m}$, purple (violet). (Bottom) Plot of $\sqrt{E_{\text{max}}}$ versus $1/ct$, which shows their linearity, with the corresponding linear fit.

TABLE III. Fitting parameters for 3D simulations for zero incidence angle and three different target thicknesses $L = 0.5, 1,$ and $2 \mu\text{m}$. The chosen intervals for fitting are $ct_1 = 20 \mu\text{m}$ and $ct_2 = 60 \mu\text{m}$, and the fitting errors are quoted.

L	$E_{\text{max}}(ct = 50)$	$E_{\infty}^{(3D)}$	$ct^{*(3D)}$	σ_E	σ_{ct^*}
0.5	1.25	2.63	15.3	0.01	0.2
1	0.56	1.43	18.9	0.02	0.1
2	0.44	1.04	17.3	0.01	0.1

which is reached quite far, when $ct > 200 \mu\text{m}$. Such a large value is computationally too expensive to be attained, but a correct extrapolation is still possible with data just up to $ct \leq 50 \mu\text{m}$.

The comparison with the experimental results is a challenging task: in Figure 6, we show the results of some experiments whose laser pulse has the same P-polarization, with a duration and intensity very close to the ones considered here and whose target has the same structure, namely, a metal foil plus contaminants. The cut-off energy increases as the target thickness is reduced, until the effect of finite contrast prevails inverting the trend. The results of various experiments differ by more than a factor two, but the decreasing trend is similar, and the same behaviour can be seen in the 2D and 3D PIC simulations.

VII. CONCLUSIONS

The asymptotic value of the cut-off energy of protons, which is what is measured in experiments, is difficult to extract from PIC simulations. Indeed, the 2D results do not exhibit a saturation, whereas the 3D results show that a saturation might be reached, despite at a large time ($ct > 200 \mu\text{m}$), which is computationally too expensive to be reached. We propose here a simple recipe based on the model described by Schreiber *et al.*,³ which assumes that the acceleration of protons present in the contaminants is due to the positive surface charge created on the rear target, thanks to the escape of the electrons. In the 3D version, the charged spot is circular with a radius R comparable with laser waist. The rise in time of the cut-off energy can be analytically computed. We have formulated an analogous 2D model where the charge is on an infinite strip of height $2R$, and we obtain a simple asymptotic expression for the rise in time of the cut-off energy, which does not saturate but exhibits a logarithmic growth, just as in 1D models of the vacuum expansion of plasmas.¹⁶ The analytical results suggest two phenomenological laws, which depend on the asymptotic energy E_{∞} and the time t^* at which the acceleration begins. The fits to the 2D and 3D results coming from PIC simulations are quite good, and the statistical uncertainties $\sigma_{E_{\infty}}/E_{\infty}$ and σ_{ct^*}/ct^* are quite small (a few percent).

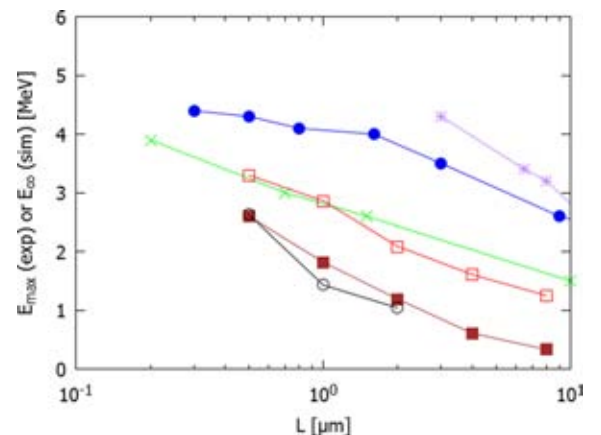


FIG. 6. Plot of E_{max} versus L on a logarithmic scale from various experiments with a laser pulse having $a_0 \sim 3$ and a metal target: the Ceccotti experiment (45° incidence angle) from Ref. 9 (blue circles), Neely experiment (30°) from Ref. 12 (green crosses), and Flacco experiment (45°) from Ref. 14 (purple stars). These data are compared with the results of our 2D PIC simulation at zero degree incidence (filled red squares) and at 30° incidence (empty red squares) and 3D PIC simulation at zero degree incidence (empty black circles).

The extrapolated values $E_{\infty}^{(2D)}$ and $E_{\infty}^{(3D)}$, computed for different target thicknesses, are comparable, and moreover, they can be fully calculated fitting the results obtained before $ct \leq 50\text{--}60 \mu\text{m}$, which is a distance reachable also in 3D numerical simulations. There is no need to let simulations run longer since the fit can already be correctly obtained. The fitting appears to be satisfactory also for small incidence angles, even though the model was developed for normal incidence.

To conclude, we believe that, for the targets that we have analysed, in which the protons are only on the thin layer above the bulk, the proposed phenomenological model is adequate to avoid the arbitrariness in the choice of the time at which the asymptotic cut-off energy is chosen in numerical simulations. In addition, the parametric explorations, which can be carried out only in 2D, may have a quantitative value, with an adequate extrapolation, rather than being of purely qualitative nature. The results we have presented refer to a specific intensity and a range of target thicknesses chosen in order to fulfil the applicability conditions of the model.

ACKNOWLEDGMENTS

The work was done within the L3IA INFN Collaboration, which the authors would like to thank.

APPENDIX: ASYMPTOTIC CUT-OFF ENERGY ANALYTICAL ESTIMATES

Let us consider a target which is infinitely extended along the plane xy and delimited by the planes $z = -L$ and $z = 0$. We can consider a circular radius r_L which we assume to be the spot of the laser pulse propagating along z . The electrons are heated and diffused by the laser itself. Supposing that they diverge with angle θ , the electrons will leave the plane $z = 0$ from a disc of radius

$$R = r_L + L \tan \theta.$$

We assume that the target is a metallic foil and that the protons are in the contaminants deposited on the plane $z = 0$. The electrons, which are heated, diffuse and cross the $z = 0$ boundary, leaving the target and inducing on it a positive charge density $\sigma(t)$, which we suppose varies slowly with t . If Qe is the total number of positive charge on the surface, the density is

$$\sigma = \frac{Qe}{\pi R^2}. \quad (\text{A1})$$

This is the geometry for the 3D case, which we shall treat analytically.

We consider another geometry in which the electrons on the plane $z = L$ leave the rectangle $|x| \leq R$, $|y| \leq L$ of area $4LR$. In this case, the density is given by

$$\sigma = \frac{Qe}{4RL}. \quad (\text{A2})$$

The intensity defined as the power per unit surface is assumed to be the same for both geometries.

A. The 3D case: Charge density on a disk

Using cylindrical coordinates and computing the potential, we have

$$\begin{aligned} V(z) &= 2\pi\sigma \int_0^R r dr \frac{1}{\sqrt{r^2 + z^2}} = \pi\sigma \int_0^R dr^2 \frac{1}{\sqrt{z^2 + r^2}} \\ &= 2\pi\sigma \left[\sqrt{z^2 + R^2} - z \right]. \end{aligned}$$

Introducing the dimensionless variable $\zeta = z/R$, we have

$$V(\zeta) = 2\pi R\sigma \left[\sqrt{1 + \zeta^2} - \zeta \right].$$

Since $V(0) = 2\pi R\sigma$, we redefine the potential by subtracting it.

$$\hat{V}(\zeta) = V(\zeta) - V(0) = 2\pi R\sigma \left[\sqrt{1 + \zeta^2} - \zeta - 1 \right]. \quad (\text{A3})$$

The potential energy is given by $eV(\zeta)$. We notice that we have

$$\begin{cases} \hat{V}(z) \simeq -2\pi\sigma z & \text{for } z \rightarrow 0 \\ \hat{V}(z) \simeq \frac{eQ}{z} - \frac{2Qe}{R} & \text{for } z \rightarrow \infty. \end{cases}$$

Letting $v = z$ and assuming $v(0) = 0$, i.e., that the protons are initially at rest on the surface $z = 0$, we can apply the energy conservation

$$m \frac{v^2}{2} + eV(\zeta) \equiv E + eV(\zeta) = 0.$$

Calling v_{∞} , the speed reached at infinite distance

$$E_{\infty} = m \frac{v_{\infty}^2}{2} = -eV(\infty) = \frac{2Qe^2}{R} = 2\pi e R \sigma,$$

we can define

$$-eV(\zeta) = 2\pi e R \sigma s(\zeta) = m \frac{v_{\infty}^2}{2} s(\zeta),$$

where from Equation (A3)

$$s(\zeta) = 1 + \zeta - \sqrt{1 + \zeta^2}.$$

As a consequence, we have

$$E = E_{\infty} s(\zeta), \quad v = v_{\infty} \sqrt{s(\zeta)}. \quad (\text{A4})$$

We introduce the new variables

$$X = \sqrt{s}, \quad \tau = t \frac{v_{\infty}}{R}.$$

Then, we have

$$\frac{d\zeta}{d\tau} = \frac{v}{v_{\infty}} = \sqrt{s(\zeta)}. \quad (\text{A5})$$

We might solve this equation with initial condition $\zeta(0) = 0$. We rather solve the equation for X

$$\frac{dX}{d\tau} = \frac{dX}{ds} \frac{ds}{d\zeta} \frac{d\zeta}{d\tau} = \frac{1}{2} \frac{ds}{d\zeta}. \quad (\text{A6})$$

Let us notice that

$$\frac{dX}{d\tau} = \frac{1}{2} \left(1 - \frac{\zeta}{\sqrt{1+\zeta^2}} \right) = \frac{1}{2} \left(1 + \frac{\zeta}{1-s} \right)^{-1}.$$

Inverting $s = s(\zeta)$, we have $\zeta = (2s - s^2)/(2(1 - s))$, and finally replacing this in the r.h.s. of the last equation, we obtain

$$\frac{dX}{d\tau} = \left(1 + \frac{1}{(1-s)^2} \right)^{-1} = \left(1 + \frac{1}{(1-X^2)^2} \right)^{-1}.$$

The results are obtained with integration by parts

$$\begin{aligned} \tau &= X + \int_0^X \frac{du}{(1-u^2)^2} \\ &= X - \frac{1}{2} \frac{d}{d\alpha} \int_0^X \frac{1}{\alpha^2 - u^2} \Big|_{\alpha=1} \\ &= X + \frac{1}{2} \frac{X}{1-X^2} + \frac{1}{4} \log \frac{1+X}{1-X}. \end{aligned}$$

Asymptotically, for $\tau \rightarrow \infty$, we have $X \rightarrow 1$

$$\tau \sim \frac{1}{4(1-X)}, \quad X \simeq 1 - \frac{1}{4\tau}.$$

The energy asymptotic behaviour is given by $E/E_\infty = s = X^2$, and consequently for $t \rightarrow \infty$

$$E \simeq E_\infty \left(1 - \frac{1}{4\tau} \right)^2.$$

B. The 2D case: Charge on slab

We consider the slab $|x| \leq R$ and $|y| \leq L$ on the rear surface $z=0$, where the density is given by Eq. (A2). The potential is given by

$$\begin{aligned} V(z) &= \sigma \int_{-R}^R dx \int_{-L}^L \frac{dy}{\sqrt{x^2 + y^2 + z^2}} \\ &= 4\sigma \int_0^R dx \int_0^{L/\sqrt{x^2+z^2}} \frac{du}{\sqrt{1+u^2}} \\ &= 4\sigma \int_0^R dx \operatorname{arsinh} \left(\frac{L}{\sqrt{x^2+z^2}} \right). \end{aligned} \quad (\text{A7})$$

Since $4\sigma = eQ/(LR)$, we first consider the limit $L \rightarrow 0$, which corresponds to the density $\sigma(z) = eQ/(2R)\delta(y)$, and the result, letting $\zeta = z/R$, is

$$V(z) = \frac{eQ}{R} \int_0^R dx \left(\frac{1}{\sqrt{x^2+z^2}} \right) = \frac{eQ}{R} \operatorname{arsinh} \frac{1}{\zeta}.$$

Recalling that $\operatorname{arsinh}(u) = \log(u + \sqrt{1+u^2})$, we see that $V(\zeta) \sim \log(2/\zeta)$ for $\zeta \rightarrow 0$, whereas it vanishes as $1/\zeta$ for $\zeta \rightarrow \infty$. As a consequence, we cannot have V vanishing at $\zeta=0$ with a subtraction. Indeed, if we compute $V(0)$, we will see that it diverges as $\log(1/L)$ for $L \rightarrow 0$ (see Eq. (A10)). We wish to define a potential which vanishes at $z=0$: as a consequence, in the definition, we have to subtract $V(0)$. This can be done for any finite value of L and also for $L \rightarrow \infty$. In order to compute $V(0)$ for a given non vanishing L , we set $\xi = x/L$; integrating by parts, we obtain

$$\begin{aligned} V(0) &= \frac{eQ}{R} \int_0^{R/L} d\xi \operatorname{arsinh} \frac{1}{\xi} \\ &= \frac{eQ}{R} \left[\xi \operatorname{arsinh} \frac{1}{\xi} \Big|_0^{R/L} + \int_0^{R/L} \frac{d\xi}{\sqrt{1+\xi^2}} \right] \\ &= \frac{eQ}{R} \left[\frac{R}{L} \operatorname{arsinh} \frac{L}{R} + \operatorname{arsinh} \frac{R}{L} \right]. \end{aligned} \quad (\text{A8})$$

We see that $V(0)$ is finite for any $L > 0$, that it diverges as $\log(1/L)$ for $L \rightarrow 0$, and that it vanishes for $L \rightarrow \infty$. We redefine the potential as

$$\begin{aligned} \hat{V}(z) &= V(z) - V(0) \\ &= \frac{eQ}{RL} \int_0^R dx \left[\operatorname{arsinh} \left(\frac{L}{\sqrt{x^2+z^2}} \right) - \operatorname{arsinh} \frac{L}{x} \right]. \end{aligned}$$

Let us consider the asymptotic behaviour of $V(z)$, for $z \rightarrow \infty$, for L having any fixed finite value. To this end, we recall that, when $u = L/\sqrt{x^2+z^2} \rightarrow 0$, we can approximate arsinh with its Taylor expansion $\operatorname{arsinh}(u) = u - u^3/6 + O(u^5)$; retaining only the first term, we have

$$V(z) = \frac{eQ}{R} \int_0^{R/z} \frac{du}{\sqrt{1+u^2}} = \frac{eQ}{R} \operatorname{arsinh} \frac{R}{z} \simeq \frac{eQ}{z}.$$

We consider now the limit $L \rightarrow \infty$: here, it is evident that $V(0)=0$. Moreover, starting from Equation (A7) and computing the electric field, we have

$$\begin{aligned} \mathcal{E}_z &= -\frac{\partial V}{\partial z} = 4\sigma \int_0^R dx \frac{1}{\sqrt{1+\frac{L^2}{x^2+z^2}}} \frac{Lz}{(x^2+z^2)^{3/2}} \\ &= 4\sigma \int_0^R \frac{dx}{z} \frac{1}{1+\frac{x^2}{z^2}} \frac{1}{\left(1+\frac{x^2+z^2}{L^2}\right)^{1/2}}. \end{aligned}$$

If we take the limit for $L \rightarrow \infty$, we recover the following result

$$\mathcal{E}_z = 4\sigma \arctan \frac{R}{z}, \quad \mathcal{E}_z \sim \frac{4\sigma R}{z} \quad \text{for } z \rightarrow \infty. \quad (\text{A9})$$

As a consequence, the potential behaves as $V(z) \simeq -4\sigma R \log(R/z)$ for $z \rightarrow \infty$. We compute exactly the potential corresponding to Eq. (A9), introducing again the dimensionless variable $\zeta = z/R$

$$\begin{aligned}
V(z) &= -4\sigma \int_0^z \arctan \frac{R}{z'} dz' \\
&= 4R\sigma \left(-\zeta \arctan \frac{1}{\zeta} + \log \frac{1}{\sqrt{1+\zeta^2}} \right), \quad (\text{A10})
\end{aligned}$$

where manifestly $V(0) = 0$.

The potential now diverges for $z \rightarrow \infty$, but we still use the energy conservation

$$E + eV = 0, \quad E = -eV = E_\infty s(\zeta),$$

where we put, in analogy with the 3D,

$$\begin{aligned}
E_\infty &\equiv m \frac{v_\infty^2}{2} = 4eR\sigma \\
s(\zeta) &= \zeta \arctan \frac{1}{\zeta} - \log \frac{1}{\sqrt{1+\zeta^2}}
\end{aligned}$$

and Eq. (A5) holds for the coordinate ζ . As in the 3D case, we introduce the coordinate $X = \sqrt{s}$ and Eq. (A6) holds. In order to simplify the analysis, we replace $s(\zeta)$, defined by Eq. (A8), with $s(\zeta) = \log(1 + \zeta)$ which has the same asymptotic behaviour at $\zeta = 0$ and $\zeta \rightarrow \infty$. Finally, we have

$$\frac{dX}{d\tau} = \frac{1}{2} \frac{1}{1+\zeta} = \frac{e^{-s}}{2} = \frac{1}{2} e^{-X^2}.$$

The solution reads

$$\tau = 2 \int_0^X e^{u^2} du = e^{X^2} \left[\frac{1}{X} + \frac{1}{2X^3} + O\left(\frac{1}{X^5}\right) \right].$$

Retaining only the first term, we invert the equation

$$x^2 = \log \tau + \log x, \quad x^2 = \log \tau + \frac{1}{2} \log \log \tau + \dots$$

The results is given by

$$E = E_\infty \left[\log \tau + \frac{1}{2} \log \log \tau \right] \quad \tau = t \frac{v_\infty}{R},$$

and neglecting the loglog term, we get the required result.

¹A. Sgattoni, P. Londrillo, A. Macchi, and M. Passoni, "Laser ion acceleration using a solid target coupled with a low-density layer," *Phys. Rev. E* **85**, 036405 (2012).

²E. d'Humières, A. Brantov, V. Yu. Bychenkov, and V. T. Tikhonchuk, "Optimization of laser-target interaction for proton acceleration," *Phys. Plasmas* **20**(2), 023103 (2013).

³J. Schreiber, F. Bell, F. Grüner, U. Schramm, M. Geissler, M. Schnürer, S. Ter-Avetisyan, B. M. Hegelich, J. Cobble, E. Brambrink, J. Fuchs, P. Audebert, and D. Habs, "Analytical model for ion acceleration by high-intensity laser pulses," *Phys. Rev. Lett.* **97**, 045005 (2006).

⁴L. A. Gizzi, C. Altana, F. Brandi, P. Cirrone, G. Cristoforetti, A. Fazzi, P. Ferrara, L. Fulgentini, D. Giove, P. Koester, L. Labate, G. Lanzalone, P. Londrillo, D. Mascali, A. Muoio, D. Palla, F. Schillaci, S. Sinigardi, S. Tudisco, and G. Turchetti, "Role of laser contrast and foil thickness in target normal sheath acceleration," *Nucl. Instrum. Methods Phys. Res., Sect. A* **829**, 144–148 (2016).

⁵M. Borghesi, J. Fuchs, S. V. Bulanov, A. J. Mackinnon, P. K. Patel, and M. Roth, "Fast ion generation by high-intensity laser irradiation of solid targets and applications," *Fusion Sci. Technol.* **49**(3), 412–439 (2006); available at [http://pure.qub.ac.uk/portal/en/publications/fast-ion-generation-by-highintensity-laser-irradiation-of-solid-targets-and-applications\(77a8bf2e-c4a8-4d49-a44a-10bbda2388a7\)/export.html](http://pure.qub.ac.uk/portal/en/publications/fast-ion-generation-by-highintensity-laser-irradiation-of-solid-targets-and-applications(77a8bf2e-c4a8-4d49-a44a-10bbda2388a7)/export.html).

⁶A. Macchi, M. Borghesi, and M. Passoni, "Ion acceleration by super-intense laser-plasma interaction," *Rev. Mod. Phys.* **85**, 751–793 (2013).

⁷H. Daido, M. Nishiuchi, and A. S. Pirozhkov, "Review of laser-driven ion sources and their applications," *Rep. Prog. Phys.* **75**(5), 056401 (2012).

⁸S. Fritzier, V. Malka, G. Grillon, J. P. Rousseau, F. Burgy, E. Lefebvre, E. d'Humières, P. McKenna, and K. W. D. Ledingham, "Proton beams generated with high-intensity lasers: Applications to medical isotope production," *Appl. Phys. Lett.* **83**(15), 3039–3041 (2003).

⁹T. Ceccotti, A. Lévy, H. Popescu, F. Réau, P. D'Oliveira, P. Monot, J. P. Geindre, E. Lefebvre, and Ph. Martin, "Proton acceleration with high-intensity ultrahigh-contrast laser pulses," *Phys. Rev. Lett.* **99**, 185002 (2007).

¹⁰K. Zeil, S. D. Kraft, S. Bock, M. Bussmann, T. E. Cowan, T. Kluge, J. Metzkes, T. Richter, R. Sauerbrey, and U. Schramm, "The scaling of proton energies in ultrashort pulse laser plasma acceleration," *New J. Phys.* **12**(4), 045015 (2010).

¹¹I. Spencer, K. W. D. Ledingham, P. McKenna, T. McCanny, R. P. Singhal, P. S. Foster, D. Neely, A. J. Langley, E. J. Divall, C. J. Hooker, R. J. Clarke, P. A. Norreys, E. L. Clark, K. Krushelnick, and J. R. Davies, "Experimental study of proton emission from 60 fs, 200 mJ high-repetition-rate tabletop-laser pulses interacting with solid targets," *Phys. Rev. E* **67**, 046402 (2003).

¹²D. Neely, P. Foster, A. Robinson, F. Lindau, O. Lundh, A. Persson, C.-G. Wahlström, and P. McKenna, "Enhanced proton beams from ultrathin targets driven by high contrast laser pulses," *Appl. Phys. Lett.* **89**(2), 021502 (2006).

¹³A. Yogo, H. Daido, S. V. Bulanov, K. Nemoto, Y. Oishi, T. Nayuki, T. Fujii, K. Ogura, S. Orimo, A. Sagisaka, J.-L. Ma, T. Zh. Esirkepov, M. Mori, M. Nishiuchi, A. S. Pirozhkov, S. Nakamura, A. Noda, H. Nagatomo, T. Kimura, and T. Tajima, "Laser ion acceleration via control of the near-critical density target," *Phys. Rev. E* **77**, 016401 (2008).

¹⁴A. Flacco, F. Sylla, M. Veltcheva, M. Carrié, R. Nuter, E. Lefebvre, D. Batani, and V. Malka, "Dependence on pulse duration and foil thickness in high-contrast-laser proton acceleration," *Phys. Rev. E* **81**, 036405 (2010).

¹⁵P. Londrillo, A. Marocchino, A. Sgattoni, and S. Sinigardi, *ALADyn* (Zenodo, 2016).

¹⁶P. Mora, "Plasma expansion into a vacuum," *Phys. Rev. Lett.* **90**, 185002 (2003).

Horizon 2020 EuPRAXIA design study

P A Walker¹, P D Alesini², A S Alexandrova^{3,4}, M P Anania², N E Andreev^{5,6}, I Andriyash⁷, A Aschikhin¹, R W Assmann¹, T Audet⁸, A Bacci⁹, I F Barna¹⁰, A Beaton¹¹, A Beck¹², A Beluze¹³, A Bernhard¹⁴, S Bielawski¹⁵, F G Bisesto², J Boedewadt¹, F Brandi¹⁶, O Bringer¹⁷, R Brinkmann¹, E Bründermann¹⁴, M Büscher¹⁸, M Bussmann¹⁹, G C Bussolino¹⁶, A Chance¹⁷, J C Chanteloup¹³, M Chen²⁰, E Chiadroni², A Cianchi²¹, J Clarke^{3,22}, J Cole²³, M E Couprie⁷, M Croia², B Cros⁸, J Dale¹, G Dattoli²⁴, N Delerue²⁵, O Delferriere¹⁷, P Delinikolas¹¹, J Dias²⁶, U Dorda¹, K Ertel²⁷, A Ferran Pousa^{1,28}, M Ferrario², F Filippi², J Fils^{17,29}, R Fiorito^{3,4}, R A Fonseca²⁶, M Galimberti²⁷, A Gallo², D Garzella¹⁷, P Gastinel¹⁷, D Giove⁹, A Giribono², L A Gizzi^{16,30}, F J Grüner^{28,31}, A F Habib¹, L C Haefner³², T Heinemann^{1,11,28}, B Hidding^{3,11}, B J Holzer³³, S M Hooker^{34,35}, T Hosokai³⁶, A Irman¹⁹, D A Jaroszynski¹¹, S Jaster-Merz^{1,28}, C Joshi³⁷, M C Kaluza^{38,39}, M Kando⁴⁰, O S Karger²⁸, S Karsch⁴¹, E Khazanov⁴², D Khikhlikha⁴³, A Knetsch²⁸, D Kocon⁴³, P Koester¹⁶, O Kononenko¹, G Korn⁴³, I Kostyukov⁴², L Labate^{16,30}, C Lechner¹, W P Leemans⁴⁴, A Lehrach¹⁸, F Y Li¹¹, X Li¹⁷, V Libov²⁸, A Lifschitz⁴⁵, V Litvinenko^{46,47}, W Lu⁴⁸, A R Maier^{28,31}, V Malka⁴⁵, G G Manahan¹¹, S P D Mangles²³, B Marchetti¹, A Marocchino⁴⁹, A Martinez de la Ossa²⁸, J L Martins²⁶, F Massimo⁴⁵, F Mathieu¹³, G Maynard⁸, T J Mehrling¹, A Y Molodozhentsev⁴³, A Mosnier¹⁷, A Mostacci^{2,49}, A S Mueller¹⁴, Z Najmudin²³, P A P Nghiem¹⁷, F Nguyen²⁴, P Niknejadi¹, J Osterhoff¹, D Papadopoulos¹³, B Patrizi⁵⁰, R Pattathil²⁷, V Petrillo⁹, M A Pocsai¹⁰, K Poder¹, R Pompili², L Pribyl⁴³, D Pugacheva^{5,6}, S Romeo², A R Rossi⁹, E Roussel⁷, A A Sahai²³, P Scherkl¹¹, U Schramm¹⁹, C B Schroeder⁴⁴, J Schwindling¹⁷, J Scifo², L Serafini⁹, Z M Sheng^{11,20}, L O Silva²⁶, T Silva²⁶, C Simon¹⁷, U Sinha²⁶, A Specka¹², M J V Streeter⁵¹, E N Svystun¹, D Symes²⁷, C Szwaj¹⁵, G Tauscher¹, A G R Thomas⁵¹, N Thompson^{3,22}, G Toci⁵⁰, P Tomassini¹⁶, C Vaccarezza², M Vannini⁵⁰, J M Vieira²⁶, F Villa², C-G Wahlström⁵², R Walczak^{34,35}, M K Weikum^{1,11}, C P Welsch^{3,4}, C Wiemann¹⁸, J Wolfenden^{3,4}, G Xia^{3,53}, M Yabashi⁵⁴, L Yu²⁰, J Zhu¹, A Zigler⁵⁵

1 Deutsches Elektronen-Synchrotron, 22607 Hamburg, Germany

2 INFN, Laboratori Nazionali di Frascati, 00044 Frascati, Rome, Italy

3 Cockcroft Institute, Warrington WA4 4AD, UK

4 University of Liverpool, Liverpool L69 7ZE, UK

5 IHT, Moscow, 125412, Russia

6 Moscow Institute of Physics and Technology, Dolgoprudny, 141701, Russia

7 Synchrotron SOLEIL, Gif-sur-Yvette 91192, France

8 LPGP, CNRS, Univ. Paris-Sud, Université Paris-Saclay, 91405 Orsay, France

9 INFN, Sezione di Milano, Milan, Italy

10 Wigner Research Centre for Physics, Budapest, Hungary

11 SUPA, Department of Physics, University of Strathclyde, Glasgow G4 0NG, UK

12 LLR, CNRS, Ecole Polytechnique, Palaiseau and Université Paris Saclay, France

13 LULI, Ecole Polytechnique, CNRS, CEA, UPMC, 91128 Palaiseau, France



- 14 Karlsruhe Institute of Technology, 76131 Karlsruhe, Germany
- 15 PHLAM, UMR-CNRS 8523, Université de Lille, France
- 16 CNR Istituto Nazionale di Ottica, 56124 Pisa, Italy
- 17 CEA, IRFU, SACM, Université Paris Saclay, F-91191 Gif-sur-Yvette, France
- 18 Forschungszentrum Jülich, 52428 Jülich, Germany
- 19 Helmholtz Institute Dresden-Rossendorf, 01328 Dresden, Germany
- 20 Shanghai Jiao Tong University, Shanghai 200240, P. R. China
- 21 University of Rome Tor Vergata, 00173 Rome, Italy
- 22 STFC Daresbury Laboratory, Sci-Tech Daresbury, Warrington, U.K.
- 23 John Adams Institute, Blackett Laboratory, Imperial College London, UK
- 24 ENEA, Centro Ricerche Frascati, 00044 Frascati, Rome, Italy
- 25 LAL, CNRS/IN2P3 Univ. Paris Sud, Orsay, and Université Paris Saclay, France
- 26 GoLP/Instituto de Plasmas e Fusão Nuclear, Instituto Superior Técnico, Universidade de Lisboa, Lisbon, Portugal
- 27 Central Laser Facility, RAL, Didcot, Oxfordshire OX11 0QX, UK
- 28 Universität Hamburg, 22761 Hamburg, Germany
- 29 GSI Helmholtzzentrum für Schwerionenforschung, 64291 Darmstadt, Germany
- 30 INFN, Sezione di Pisa, Italy
- 31 Center for Free Electron Laser Science, 22607 Hamburg, Germany
- 32 Lawrence Livermore National Laboratory, Livermore, CA 94550, United States
- 33 CERN, 1211 Geneva 23, Switzerland
- 34 John Adams Institute, Oxford University, UK
- 35 University of Oxford, Oxford OX1 2JD, UK
- 36 Osaka University, Osaka Prefecture, 565-0871, Japan
- 37 University of California Los Angeles, Los Angeles, CA 90095, USA
- 38 Helmholtz Institute Jena, 07743 Jena, Germany
- 39 Institut für Optik und Quantenelektronik, 07743 Jena, Germany
- 40 KPSI-QST, Kyoto 619-0215, Japan
- 41 Ludwig-Maximilians-Universität München, 80802 Munich, Germany
- 42 IAP RAS, Nizhnij Novgorod, 603155, Russia
- 43 ELI-Beamlines, Dolni Brezany, Czech Republic
- 44 Lawrence Berkeley National Laboratory, Berkeley, CA 94720, USA
- 45 LOA, ENSTA-CNRS-École Polytechnique UMR 7639, Palaiseau F-91761, France
- 46 Brookhaven National Laboratory, Upton, NY 11973, USA
- 47 Stony Brook University, Stony Brook, NY 11794, USA
- 48 Tsinghua University, Beijing, 100084, P. R. China
- 49 Sapienza, University of Rome, 00161, Rome, Italy
- 50 CNR Istituto Nazionale di Ottica, I-50019 Sesto Fiorentino, Italy
- 51 Lancaster University, Lancaster LA1 4YB, UK
- 52 Lund University, 223 62 Lund, Sweden
- 53 University of Manchester, Manchester M13 9PL, UK
- 54 RIKEN SPring-8 Center, Hyogo, 679-5148, Japan
- 55 Hebrew University of Jerusalem, Jerusalem, Israel

E-mail: andreas.walker@desy.de

Abstract. The Horizon 2020 Project EuPRAXIA (“European Plasma Research Accelerator with eXcellence In Applications”) is preparing a conceptual design report of a highly compact and cost-effective European facility with multi-GeV electron beams using plasma as the acceleration medium. The accelerator facility will be based on a laser and/or a beam driven plasma acceleration approach and will be used for photon science, high-energy physics (HEP)

detector tests, and other applications such as compact X-ray sources for medical imaging or material processing. EuPRAXIA started in November 2015 and will deliver the design report in October 2019. EuPRAXIA aims to be included on the ESFRI roadmap in 2020.

1. Introduction

The EuPRAXIA collaboration is the first plasma accelerator collaboration on this scale bringing together 16 European partner laboratories and additional 22 associated partners from the EU, Israel, China, Japan, Russia and the USA [1]. EuPRAXIA is structured into 14 working packages each headed by two work package leaders from different institutions. Eight work packages receive EU funding and their topics include: plasma and laser simulations (WP2), plasma accelerator structures (WP3), laser design (WP4), conventional beam physics (WP5), FEL radiation (WP6), and a table-top test beam for HEP and other applications (WP7). Two further EU work packages work on the management of the collaboration (WP1) and the outreach to the public (WP8). In-kind work packages (WP9 - WP14) include additional approaches: beam driven plasma acceleration PWFA (WP9), hybrid acceleration schemes (WP14), alternative radiation generation (WP13) and alternative laser sources such as fiber lasers (WP10). WP11 and WP12 connect to prototyping on plasma-based FEL's and facility access for experiments until 2019. Industry partners Amplitude Technologies, Thales and TRUMPF Scientific take part in the scientific advisory board and contribute their experience towards a successful completion of the design report.

2. Plasma acceleration

Scientists, medical doctors and engineers have used radio-frequency (RF) based particle accelerator beams for ninety years to probe nature, to produce new particles, to generate light of exquisite quality or to irradiate tumors. The accelerators are of outstanding quality, but have grown in size and cost due to the materials used for construction, which can only sustain accelerating fields of around 100 MV/m before electrical breakdown occurs. Plasma accelerators are not subject to these electrical breakdown limits and the accelerating field reaches 100 GV/m, three orders of magnitude larger than in an RF accelerator. As a consequence, the size of plasma accelerators can potentially be quite small, reducing kilometer scale machines to the meter scale. A new generation of cost-efficient and compact accelerators could open completely new usages of particle accelerators, for example in hospitals and universities. This requires suitable stability and repetition rates.

The great potential of plasma waves for particle acceleration was first recognized by Veksler [2] and Tajima and Dawson [3]. The longitudinal plasma waves can be excited by both electron beams (plasma wakefield acceleration, PWFA) or intense laser pulses (laser wakefield acceleration, LWFA) and are well suited for accelerating charged particles to relativistic energies [4]. Electron beams that are accelerated inside a plasma accelerator structure can originate from the background plasma within the plasma accelerator structure itself ("internal injection") or from an accelerator that is situated in front of the plasma accelerator structure ("external injection"). Within the last two decades, the beam quality of LWFA accelerators has significantly improved [5-13] and the current peak energy lies at 4.2 GeV [14]. Using these beams, various types of X-ray radiation such as betatron, synchrotron, and undulator radiation down to the water-window wavelengths were produced [15-21]. While several tens of laboratories use laser systems to accelerate electrons, few laboratories have the electron beam needed for beam-driven plasma acceleration [22-28]. FACET at SLAC achieved energy doubling within a single electron beam in 2007 [24] and energy was transferred successfully from a drive beam to a witness bunch in 2014 [25].

In the EuPRAXIA study, both laser driven and beam driven approaches as well as combined plasma acceleration schemes - using LWFA-produced beams as drivers of PWFA stages [29, 30] - are taken into consideration. The final EuPRAXIA design report in 2019 will include various configurations of a possible EuPRAXIA facility. Depending on available budget and the targeted science case, one of these options, or a combination of options, might be the best choice. The design report will compare size, cost, and performance on a common basis. The first iteration of the design goals were defined in

October 2016 [31] and from these, the initial goal parameters for the 5 GeV electron beam at the entrance of the undulator are shown in Table 1. The agreed possible configurations are:

Configuration 1: LWFA with internal injection;

Configuration 2: LWFA with external injection from an RF accelerator;

Configuration 3: LWFA with external injection from a laser plasma injector;

Configuration 4: PWFA with an RF electron beam; and

Configuration 5: PWFA with LWFA produced electron beam (hybrid schemes).

In addition to the 5 GeV electron beam, the facility aims to provide a medical imaging X-ray source as well as FEL radiation ultimately concentrating in the range between 1 nm and 0.1 nm. TW laser pulses synchronized to the electron and X-ray radiation will be available in the user areas. Parameter tables for medical imaging and a table-top test beam for HEP and other applications are currently being finalized.

3. Laser and electron beam drivers

The laser used in the LWFA cases is being studied in work package 4 (WP4) with colleagues from Thales and Amplitude industry. WP4 reviewed current laser systems in 2016 [32] and proposed preliminary specifications of the EuPRAXIA laser, the so-called “100 cube” laser challenge (an energy of 100 Joule, a pulse length of 100 fs (FWHM), and a repetition rate of 100 Hz, with a contrast of 10^{10} at 10 ps). The present work towards this challenging goal disfavors a complete Ti:Sa laser system and is considering a diode-pumped solid-state laser pumping scheme. A second laser system, used for the plasma injector [33], will operate at lower energy and shorter pulse length.

Design work on the drive beam for the PWFA case is being performed in WP5. One option under discussion is that both configuration 2 (LWFA) and 4 (PWFA) use at low energy the same S-band injector and RF linac [34]. The simulated transverse phase space of a possible electron drive beam for a PWFA application is shown in Figure 1. This electron beam has an energy of 548 MeV, a peak beam current of 1 kA, transverse normalized emittances of $1 \mu\text{rad m}$ and an energy spread of below 0.07%. After acceleration through S-band and X-band structures, the beam is focused by both conventional, electro-magnets, and permanent quadrupole magnets before entering the plasma.

Table 1. Target values for the 5 GeV electron beam parameters at the entrance of the undulators [31].

Quantity	Symbol	Value
Particle type	e	Electrons
Energy	E	5 GeV
Charge	Q	30 pC
Bunch length (FWHM)	τ	10 fs
Peak current	I	3 kA
Repetition rate	f	10 Hz
Number of bunches	N	1
Total energy spread (RMS)	σ_E/E	1%
Slice energy spread (RMS)	$\sigma_{E,S}/E$	0.1%
Trans. Norm. emittance	$\epsilon_{N,x}, \epsilon_{N,y}$	$1 \mu\text{rad m}$
Alpha function	α_x, α_y	0
Beta function	β_x, β_y	5 m
Trans. beam size (RMS)	σ_x, σ_y	$22 \mu\text{m}$
Trans. divergence (RMS)	$\sigma_{x'}, \sigma_{y'}$	$4.5 \mu\text{rad}$

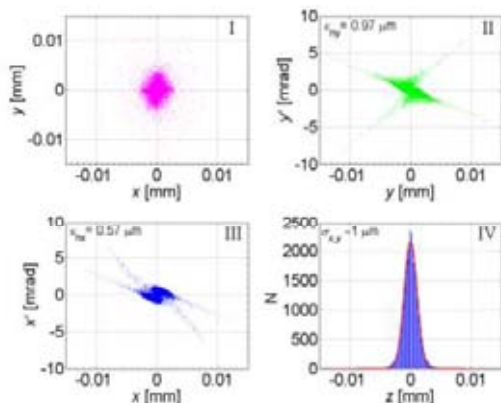


Figure 1. Preliminary simulation results for the transverse phase space of a possible PWFA drive beam (configuration 4) with an energy of 548 MeV, a peak beam current of 1 kA, transverse normalized emittances of $1 \mu\text{rad m}$ and an energy spread of below 0.07%.

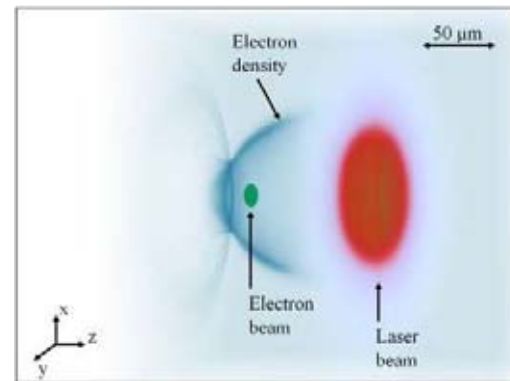


Figure 2. PIC simulation [36] of a LWFA case (configuration 2). The laser pulse (red) propagates the plasma (electron density shown in blue) from left to right and excites a wakefield, which accelerates electrons (shown in green) from 0.1 to 1 GeV in 2.5 cm.

4. Plasma accelerator structure

Components necessary for the design of the plasma accelerator structure were reviewed by WP3 in 2017 [35] in which published experimental results were examined and compared not only in terms of achieved electron properties, but also regarding their reliability, stability, or scalability to larger electron energy, or repetition rate. The proposed criteria from [35] for selecting a specific plasma accelerator structure will be used to decide which types of plasma accelerator will ultimately be incorporated into the design report.

Figure 2 shows a particle-in-cell (PIC) simulation [36, 37] performed with the OSIRIS code [38] in which a 1 PW laser traverses a plasma accelerator structure of $1.2 \cdot 10^{17} \text{cm}^{-3}$ electron density. The externally injected electron beam (initially: energy $E = 100 \text{ MeV}$; relative energy spread $\sigma_E/E = 0.1\%$; transverse emittance $\varepsilon_{N,x} = 1 \mu\text{rad m}$) exits the plasma after 2.5 cm with an energy of 1 GeV ($\sigma_E/E = 1.5\%$; $\varepsilon_{N,x} = 1 \mu\text{rad m}$). While emittance is well preserved, the energy spread is significantly increased due to the sizable variation of the accelerating field along the injected bunch. Beam loading techniques

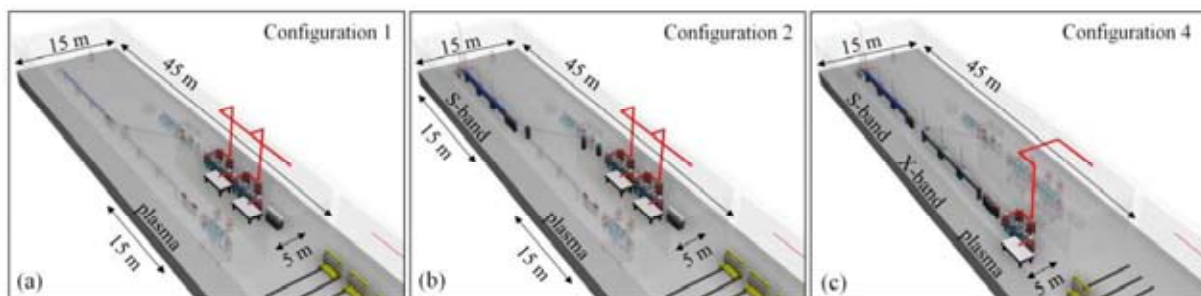


Figure 3. The preliminary layout of the EUPRAXIA accelerator tunnel is shown [43]. All RF and laser infrastructure is being supplied from the level above (not shown). Undulators (yellow) are shown in the bottom right corners. (a) Configuration 1: LWFA with internal injection. Two plasma stages are included which are supplied with two laser beams (red). (b) Configuration 2: LWFA with external injection from an RF accelerator. The RF gun and three S-band structures are shown in front of a dogleg which transports the electrons to the two plasma stages. (c) Configuration 4: PWFA. Using the same infrastructure of RF gun and S-band structure, the PWFA case uses additional X-band structures to accelerate beams to several hundred MeV before using it inside a single plasma accelerator stage.

will be used in order to compensate this gradient on the accelerating field and minimize the induced energy spread [39-42]. After completion of 1 GeV simulations with conservation of all beam qualities, simulations of the 5 GeV beam will continue.

5. Layout considerations

The preliminary layout of the EuPRAXIA accelerator tunnel [43] is shown in Figure 3, excluding user areas. Configurations 1, 2, and 4 are visualized. In the current layout, laser and RF infrastructure are situated on the level above the accelerator level floor (not shown). If individual configurations were built separately, the area for the accelerator tunnel for configuration 1, 2, 3, and 4 are 75 m², 175 m², 150 m², and 225 m², respectively and configuration 1 to 4 can incorporate configuration 5. Hence the footprint of the accelerator tunnel can be up to 5 times smaller than in conventional accelerator facilities. EuPRAXIA is a site-independent design study. Potential sites will be included in the design report and EuSPARC (Frascati, Italy), SINBAD (Hamburg, Germany), CILEX (Paris, France), CLF (Didcot, UK) and ELI (Prague, Czech Republic) have been discussed as potential sites.

6. Summary

The EuPRAXIA collaboration is preparing a conceptual design report for a multi-GeV plasma-based accelerator with outstanding beam quality. The facility design aims to include FEL radiation in the soft (to hard) X-ray range, a table-top test beam for HEP detectors and industry, and a compact X-ray source for medical imaging. Synchronized TW laser beams will be available in the user areas. Both laser and electron beams are considered as power sources for the plasma accelerator. EuPRAXIA will prepare a proposal to be included on the ESFRI roadmap in 2020 as an innovative European research infrastructure. Ultimately, EuPRAXIA will: use the world-wide leading high power lasers from European industry, drive laser innovation in the connected companies, provide for the first time usable electron beam quality from a plasma accelerator, and serve pilot users from science, engineering, medicine and industry.

References

- [1] European Plasma Research Accelerator with eXcellence In Applications <http://www.eupraxia-project.eu>
- [2] Veksler V 1956 Coherent principle of acceleration of charged particles *Proc. of the CERN Symposium on High Energy Accelerators and Pion Physics* Geneva Switzerland
- [3] Tajima T and Dawson J M 1979 Laser electron-accelerator *Phys. Rev. Lett.* **43**(4):267–270
- [4] Esarey E *et al.* 2009 Physics of laser-driven plasma based electron accelerators *Rev. Mod. Phys.* **81**:1229–1285
- [5] Modena A *et al.* 1995 Electron acceleration from the breaking of relativistic plasma waves *Nature* **377**:606 – 608
- [6] Umstadter D *et al.* 1996 Laser injection of ultrashort electron pulses into wakefield plasma waves *Phys. Rev. Lett.* **76**(12):2073–2076
- [7] Malka V *et al.* 2002 Electron acceleration by a wake field forced by an intense ultrashort laser pulse *Science* **298**(5598):1596–1600
- [8] Mangles S P D *et al.* 2004 Monoenergetic beams of relativistic electrons from intense laser plasma interactions *Nature* **431**(7008):535–538
- [9] Faure J *et al.* 2004 A laser-plasma accelerator producing monoenergetic electron beams *Nature* **431**(7008):541–544
- [10] Geddes C G R *et al.* 2004 High-quality electron beams from a laser wakefield accelerator using plasma-channel guiding *Nature* **431**(7008):538–541
- [11] Leemans W P *et al.* 2006 GeV electron beams from a centimetrescale accelerator *Nat. Phys.* **2**(10):696–699
- [12] Wang X *et al.* 2012 Petawatt-laser-driven wakefield acceleration of electrons to 2 GeV in 1017cm³ plasma *Proc. AIP* 1507(1):341–344

- [13] Assmann R W *et al.* 2014 Accelerator Physics Challenges towards a Plasma Accelerator with Usable Beam Quality *Proc. of 5th International Particle Accelerator Conference* Dresden Germany
- [14] Leemans W P *et al.* 2014 Multi-GeV Electron Beams from Capillary-Discharge-Guided Sub-petawatt Laser Pulses in the Self-Trapping Regime *Phys. Rev. Lett.* **113** 245002
- [15] Kneip S *et al.* 2009 Near-GeV acceleration of electrons by a nonlinear plasma wave driven by a self-guided laser pulse *Phys. Rev. Lett.* **103**:035002
- [16] Fuchs M *et al.* 2009 Laser-driven soft-X-ray undulator source *Nature Physics* **5** 826 – 829
- [17] Maier A R 2012 Stabilized Water-Window X-Ray Pulses from a Laser-Plasma Driven Undulator *PhD thesis* Ludwig-Maximilians-Universität München
- [18] Lambert G *et al.* 2012 Progress on the generation of undulator radiation in the UV from a plasma-based electron beam *Proc. FEL Conf.* Nara Japan
- [19] Cipiccia S *et al.* 2012 A tuneable ultra-compact high-power, ultra-short pulsed, bright gamma-ray source based on bremsstrahlung radiation from laser-plasma accelerated electrons *Journal of Applied Physics* **111**(6):063302
- [20] Anania M P *et al.* 2014 An ultrashort pulse ultra-violet radiation undulator source driven by a laser plasma wakefield accelerator *Applied Physics Letters* **104** 264102
- [21] Khrennikov K *et al.* 2015 Tunable all-optical quasimonochromatic Thomson X-ray source in the nonlinear regime *Phys. Rev. Lett.* **114**(19):195003
- [22] Chen P 1985 Acceleration of Electrons by the Interaction of a Bunched Electron Beam with a Plasma *Phys. Rev. Lett.* **54** 693
- [23] Wang S *et al.* 2001 Observation of spontaneous emitted X-ray betatron radiation in beam-plasma interactions *Proc. of 19th IEEE PAC* Chicago IL USA
- [24] Blumenfeld I *et al.* 2007 Energy doubling of 42 GeV electrons in a metre-scale plasma wakefield accelerator *Nature* **445** 741
- [25] Litos M *et al.* 2014 High-efficiency acceleration of an electron beam in a plasma wakefield accelerator *Nature* **515** 7525:92-5
- [26] Ferrario M *et al.* 2013 SPARC_LAB present and future *Nuclear Instruments and Methods in Physics Research B* **309** 183–188
- [27] Aschikhin A *et al.* 2016 The FLASHForward facility at DESY *Nucl. Instrum. Meth.* Vol. **806** 175-183
- [28] Kasilnikov M *et al.* 2012 Experimentally minimized beam emittance from an L-band photoinjector *Phys. Rev. ST Accel. Beams* **15** 100701
- [29] Hidding B *et al.* 2010 Monoenergetic Energy Doubling in a Hybrid Laser-Plasma Wakefield Accelerator *Phys. Rev. Lett.* **104** 195002
- [30] Martinez de la Ossa A *et al.* 2013 High-Quality Electron Beams from Beam-Driven Plasma Accelerators by Wakefield-Induced Ionization Injection *Phys. Rev. Lett.* **111** 245003
- [31] Walker P A *et al.* 2016 *Report defining preliminary study concept* EuPRAXIA Deliverable Report 1.2
- [32] Gizzi L A *et al.* 2016 *Benchmarking of existing technology and comparison with the requirements* EuPRAXIA Deliverable Report 4.1
- [33] Cros B *et al.* 2017 Electron injector for multi-stage laser-driven plasma accelerators *presented at the 8th Int. Particle Accelerator Conf.* Copenhagen Denmark WEPVA001
- [34] Chiadroni E *et al.* 2016 *Preliminary RF accelerator specifications* EuPRAXIA Milestone Report 5.2
- [35] Cros B *et al.* 2017 *Design for an electron injector and a laser plasma stage proposed* EuPRAXIA Milestone Report 3.1
- [36] Ferran Pousa A *et al.* 2017 VisualPIC: A New Data Visualizer and Post-Processor for Particle-in-Cell Codes *presented at the 8th Int. Particle Accelerator Conf.* Copenhagen Denmark TUPIK007
- [37] Mosnier A *et al.* 2017 *Report designing baseline designs* EuPRAXIA Deliverable Report 2.1

- [38] Fonseca R A *et al.* 2002 *OSIRIS: A Three-Dimensional, Fully Relativistic Particle in Cell Code for Modeling Plasma Based Accelerators* Sloot P.M.A., Hoekstra A.G., Tan C.J.K., Dongarra J.J. (eds) Computational Science — ICCS 2002. ICCS 2002. Lecture Notes in Computer Science vol 2331 Springer Berlin Heidelberg
- [39] Katsouleas T *et al.* 1987 Beam loading in plasma accelerators *Particle Accelerators* **22**:81–99
- [40] Tzoufras M *et al.* 2008 Beam loading in the nonlinear regime of plasma-based acceleration *Phys. Rev. Lett.* **101**:145002
- [41] Rechatin C *et al.* 2009 Observation of Beam Loading in a Laser-Plasma Accelerator *Phys. Rev. Lett.* **103**:194804
- [42] Schroeder C B *et al.* 2013 Beam loading in a laser-plasma accelerator using a near-hollow plasma channel *Physics of Plasmas* **20** 123115
- [43] Walker P A *et al.* 2017 Space considerations and possible layouts for future plasma accelerator facilities in the context of EuPRAXIA *presented at the 8th Int. Particle Accelerator Conf.* Copenhagen Denmark TUPIK012

Acknowledgments

This work was supported by the European Union's Horizon 2020 research and innovation programme under grant agreement No. 653782.

Design and characterization of Yb and Nd doped transparent ceramics for high power laser applications: recent advancements

A. Lapucci^{1,*}, M. Vannini¹, M. Ciofini¹, A. Pirri², M. Nikl³, J. Li⁴, L. Esposito⁵, V. Biasini⁵, J. Hostasa⁵, T. Goto⁶, G. Boulon⁷, R.N. Maksimov^{8,9}, L. Gizzi¹, L. Labate¹, G. Toci¹

1 - Istituto Nazionale di Ottica, CNR, Italy

2 - Istituto di Fisica Applicata "Nello Carrara", CNR, Sesto F.no, Italy

3 - Institute of Physics, Academy of Sciences, Prague, Czech Republic

4 - Shanghai Institute of Ceramics, Chinese Academy of Sciences, Shanghai, China

5 - Istituto di Scienza e Tecnologia dei Materiali Ceramici, CNR, Faenza, Italy

6 - Institute for Materials Research (IMR), Tohoku University, 980-8577, Sendai, Japan

7 - Institute Light Matter (ILM), CNRS-University Lyon1, 69622 Villeurbanne, France

8 - Institute of Electrophysics, Ural Branch of RAS, Ekaterinburg 620016, Russia

9 - Ural Federal University "B.N. Yeltsin", Ekaterinburg 620002, Russia

ABSTRACT

We report a review on our recent developments in Ytterbium and Neodymium doped laser ceramics, along two main research lines. The first is the design and development of Yb:YAG ceramics with non uniform doping distribution, for the management of thermo-mechanical stresses and for the mitigation of ASE: layered structures have been produced by solid state reactive sintering, using different forming processes (spray drying and cold press of the homogenized powders, tape cast of the slurry); samples have been characterized and compared to FEM analysis. The second is the investigation of Lutetium based ceramics (such as mixed garnets LuYAG and Lu₂O₃); this interest is mainly motivated by the favorable thermal properties of these hosts under high doping. We recently obtained for the first time high efficiency laser emission from Yb doped LuYAG ceramics. The investigation on sesquioxides has been focused on Nd-doped Lu₂O₃ ceramics, fabricated with the Spark Plasma Sintering method (SPS). We recently achieved the first laser emission above 1 W from Nd doped Lu₂O₃ ceramics fabricated by SPS.

Keywords: Laser ceramics, Nd:YAG, Yb:YAG, Lu₂O₃ sesquioxide, Layered ceramics, SPS method.

1. INTRODUCTION

Important advances have been recently achieved in the field of solid state laser materials through the development of transparent ceramics. The first breakthrough was obtained by A. Ikesue¹, who obtained substantially equivalent laser output from Nd³⁺:YAG crystal transparent ceramic, overcoming the problems related to scattering. Laser performances of commercial YAG ceramics are currently fully comparable with their crystalline equivalents²⁻⁵. In our recent work on in Yb and Nd doped laser ceramics we aimed our investigations along two main lines. The first is the design and development of Yb:YAG ceramics with non uniform doping distribution, for the management of thermo-mechanical stresses and for the mitigation of ASE and re-absorption processes. Layered structures have been produced by Solid State Reactive Sintering (SSRS), using forming processes such as spray drying and cold press of the homogenized powders, or tape cast of the slurry. Composite structures have been characterized and compared to FEM analysis⁶. The second line is the investigation of ceramics with new compositions based on Lutetium, with Yb and Nd doping. The interest on Lu-based materials as laser hosts is mainly motivated by their thermal properties: in hosts such as LuAG, LuYAG and Lu₂O₃ doped with Nd³⁺, Er³⁺, Yb³⁺ the thermal conductivity remains fairly constant⁷ even at high doping level, because of the small atomic weight difference between Lu³⁺ and the substituting ion. Conversely, the thermal conductivity of YAG significantly decreases with doping, due to the larger difference between the atomic weight of the doping ion and of the Y³⁺. These features are very important in high power laser scaling up. A higher thermal conductivity favors the transport of heat from the active medium pumped regions to the heat sink and reduces peak temperatures and temperature

* antonio.lapucci@ino.it; phone +39.055.2308226; fax +39.055.2337755; www.ino.it

gradients, reducing thermally induced stresses and allowing higher pump power densities on the active medium. All these advantages can improve the performances of High Power/High Energy Diode Pumped ceramic sources^{8,9}. In this framework we also investigated mixed garnets ((Lu_xY_{1-x})₃Al₅O₁₂, LuYAG) doped with Yb, obtaining for the first time laser emission from these ceramics, with a high efficiency and relatively broad tuning range^{10,11}. The investigation on Nd-doped Lu₂O₃ ceramics, fabricated at the Tohoku University (Japan) by the Spark Plasma Sintering (SPS) method¹²⁻¹⁴ resulted in the first extraction of powers above 1 W.

2. LASER CERAMICS WITH NON-UNIFORM DOPING DISTRIBUTIONS

The control in the distribution of the doping enables to mitigate the thermal and thermo-mechanical effects (e.g. thermal lens, stress-induced depolarization, surface deformations) deriving from the laser pumping process. These effects can degrade the performance of the laser source, eventually leading to a catastrophic failure of the laser active element under high pump power densities. Finally, a suitable non uniform doping distribution can reduce Amplified Spontaneous Emission (ASE) effects with respect to an uniform doping. To evaluate this approach we analyzed both numerically and experimentally end-pumped active media a layered, non uniform doping distribution.

2.1 Design and numerical analysis of Yb:YAG end-pumped layered systems

To study the behavior of ceramic layered structure with different doping levels we developed a 3D numerical analysis of the slab optical properties as a consequence of the thermal load induced by the pump process, based on on Finite Element Mesh (FEM) analysis⁶. The model allows both longitudinal and transverse variations of the parameters, enabling to estimate thermal distributions and thermo-mechanical stresses in spatially structured active media.

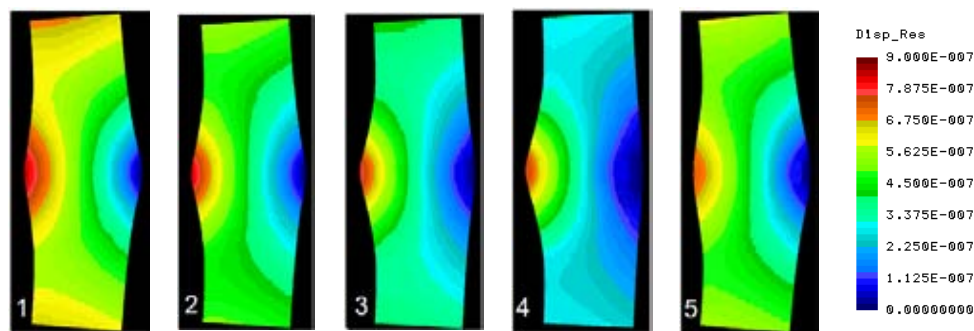


Figure 1. Surface deformation in an axial cross-section for five differently structured layered samples (see Ref.6) under the same thermal load in a ring cooling geometry.

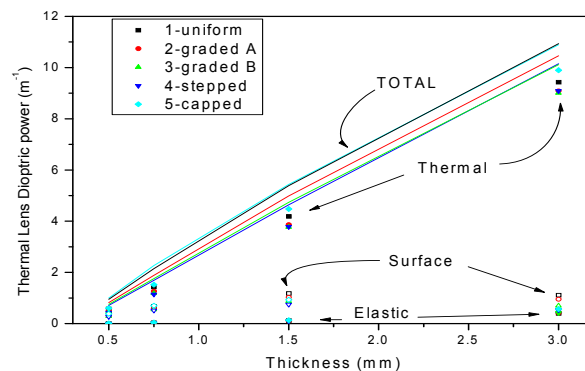


Figure 2. Thermal lens contributions (thermal, stress induced and surface deformation) as a function of the thickness for a given diameter of the active volume.

We concentrated on end pumped disc-like systems with longitudinally varying doping concentrations, both with ring-cooling and face-cooling. Our analysis included uniform active media, graded active media, stepped active media (with doped-undoped interfaces). The FEM thermo-mechanical simulation produces the internal temperature and stress distribution. The effects on the refractive index (thermal lens and depolarization estimations) are determined with a

tensor post-processing calculation. Fig.1 shows an example of the deformation of five differently doped samples under the same total thermal load. Interestingly, a longitudinal doping variation doesn't affect the thermal lens as long as the cooling is substantially radial⁶ (differently from disk or slab systems with high aspect ratios) as summarized in Fig.2.

2.2 Experimental characterization of Yb:YAG end-pumped layered systems

The numerical simulations were validated by means of experimental measurements of thermal lens (TL) on uniform and structured samples produced with the spray-drying method. All the experiment refer to a single sided standard end-pumping scheme¹⁵. The layer thicknesses and doping levels of the tested samples are summarized in Table 1. The TL effect in the different samples was characterized using the setup shown in Figure 3. This was done both on lasing and non lasing samples, to show possible differences in the thermal load. The samples are end pumped by a fiber coupled diode laser (pump spot 480 μm diameter @1/e²). The TL is evaluated by measuring the wavefront distortion of a probe beam emitted by a HeNe laser, using a Shack-Hartmann sensor. The dioptric power of the TL is proportional to the absorbed power, with a linear coefficient *C* reported in Table 5. A more detailed description of the TL evaluation and its dependence on the probe beam aperture is given elsewhere¹⁵. TL measurements show little differences between the various samples, given the substantially radial heat flow of our cooling geometry. These experimental tests substantially confirm the predictions of our numerical analysis. This validation allows us to our model it to other geometries and doping distributions. This will be illustrated in the following section for a second case study.

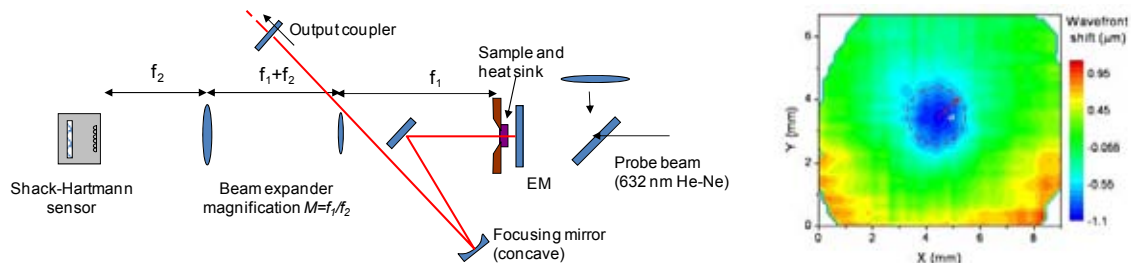


Figure 3. (Left) Experimental set up for the thermal lens measurements; (Right) Example of wavefront deformation map.

Table 1. Thermal lens dioptric power Coefficient *C* (dioptric power per Watt of absorbed pump radiation).

Sample	Doping levels	Layer Thickness [mm]	<i>C</i> (Laser on)	<i>C</i> (Laser off)
Uniform (Ceramic)	10 %	1.25	0.889	0.919
Uniform (Crystal)	8%	2	0.959	0.988
Stepped (Ceramic)	(0,10,0)%	(0.6-1.2-0.6)	0.870	1.003
Capped (ceramic)	(0,10)%	(1.6-2.0)	1.138	1.166

Table 2. Parameters of the samples used in the efficiency comparison experiments. SD. Samples made by cold pressing of spray dried powders; TC: samples made by tape casting and thermal compression.

Sample n.	Yb doping % <i>at.</i>	Total thickness (mm)	Individual layers thickness (mm)	Laser slope efficiency
SD-1	0-10	3.4	1.5 (0% Yb) -1.9 (10 % Yb)	58.1 %
SD-2	1-3-5-7	2.0	0.5	19.5 %
TC-1	0-10	1.9	1.0 (0% Yb) - 0.9 (10% Yb)	52.2 %
TC-2	1-3-5-7	2.0	0.5	43.8 %

Laser efficiency measurements have been performed to compare samples produced with different methods. Table 2 summarizes the properties and the laser efficiencies of samples produced at ISTECH with the Spray-Drying (SD)¹⁶ and Tape-Casting (TC)¹⁷ methods. These results show a substantial equivalence of the two methodologies in the case of a small number of layers (2) while they indicate a relevant quality degradation when a larger number of layers is used. Tape casting seems more suited for this kind (large number of thin layers) of devices.

2.3 Numerical analysis of Yb:Lu₂O₃ layered systems

We repeated a numerical analysis campaign for samples with the same geometries but based on different hosts. YAG was compared to Lu₂O₃ and Sc₂O₃ which, as mentioned above, present higher thermal conductivity than YAG, under relatively high Yb³⁺ doping levels (see table 3). Therefore for Lu₂O₃ hosts we obtained lower maximum temperatures and lower deformations (thus thermal lens and depolarization), as summarized in Fig.4.

Table 3. Parameters of the different hosts compared in our numerical simulations.

Parameter	YAG	Lu ₂ O ₃	Sc ₂ O ₃
Doping	10%, 0%	4.5%, 0%	3.0%, 0%
Absorption coeff. (cm ⁻¹)	5 (10% Yb), 0 (0% Yb)	5 (4.5% Yb), 0 (0% Yb)	5 (3.0% Yb), 0 (0% Yb)
Thermal Cond. [W/(mK)]	6.7 (10% Yb), 10.7 (0% Yb)	11.9 (4.5% Yb), 12.5 (0% Yb)	7.0 (3.0% Yb), 16.5 (0% Yb)
Thermal exp. Coeff. [K ⁻¹]	8 x 10 ⁻⁶	5.5 x 10 ⁻⁶	6.7 x 10 ⁻⁶
Young Modulus	0.280 x 10 ¹² Pa	0.178 x 10 ¹² Pa	0.221 x 10 ¹² Pa
Poisson Number	0.28	0.28	0.28

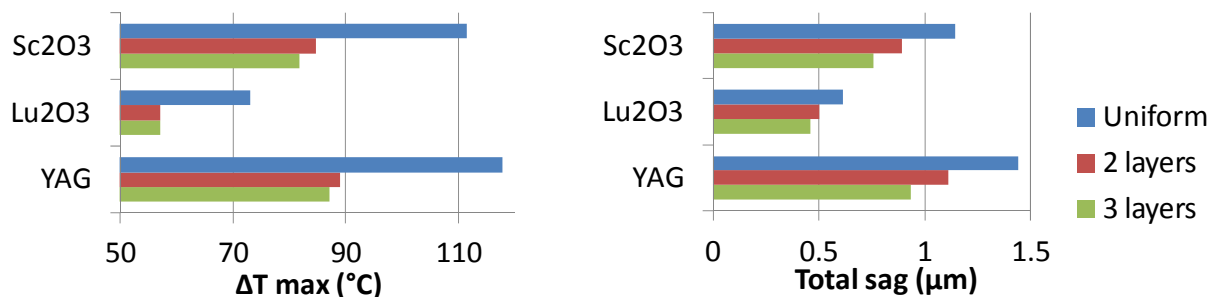


Figure 4. Summary of max internal temperature increase and max sag of layered samples based on different hosts.

3. OTHER HOST FORMULATIONS AND PREPARATION PROCEDURES

Our recent activities in the developments of laser ceramics also included the investigation on alternative material preparation routes, and different formulations. In particular, we investigated the use of laser ablated nanopowders as a starting materials for the production of Nd:YAG ceramics. The other formulations under study included Nd:Lu₂O₃ fabricated by means of the SPS method, and mixed garnet with formulation Yb:LuYAG.

3.1 Nd:YAG ceramics produced from laser ablated powders

Transparent Nd:YAG ceramics were prepared at the Institute of the Electrophysics (Russia) by the SSRS method using nanopowders of 1 at.% Nd:Y₂O₃ and Al₂O₃ synthesized by laser ablation. A pre-calcining step and addition of tetraethyl orthosilicate were found crucial for the quality of the samples fabricated from such nanoparticles¹⁸. The transmittance of a 2-mm-thick Nd:YAG ceramic was 83.6% at 1064 nm, very close to the theoretical. Output power of 4.9 W (slope efficiency 52.7%) was obtained from Nd:YAG ceramic with quasi- CW end pumping at 805 nm (Fig. 5).

3.2 Nd:Lu₂O₃ ceramics produced by SPS

SPS is a new sintering technique that has been successfully applied to the fabrication of Lu₂O₃ transparent ceramics for laser applications. 1% Nd doped samples were prepared at the at the Tohoku University, Sendai (Japan)¹⁹. SPS is comparatively simple and it requires less time than the conventional sintering methods (usually tens of minutes instead of several hours) and lower processing temperatures^{12, 13}. This is particularly attractive for sesquioxides because these materials are very difficult to grow as single crystal, due to their very high melting temperature (e.g. 2490 °C for Lu₂O₃). For these samples the sintering phase required about 90 min (plus cooling), with a peak processing temperature of 1450°. Laser output from these ceramics was already reported by us²⁰ using an experimental set up similar to that shown of Fig. 5 (a); recently, we obtained a maximum output power above 1 W with a maximum slope efficiency of 12.9% (fig. 5 c).

3.3 Yb:LuYAG ceramics

Besides the problem of the high processing temperature mentioned above, the fabrication of Lu-based hosts such as Lu₂O₃ and LuAG has the disadvantage of the high cost of the high purity Lu₂O₃ powder required for both the ceramics and the crystals; to overcome these problems, the mixed garnet resulting from solid solutions of LuAG and YAG, i.e. (Lu_xY_{1-x})₃Al₅O₁₂ (Lutetium-Yttrium Aluminum Garnet, LuYAG) was recently proposed [21], as crystals and ceramics. Due to the partial substitution of Lu with Y, it requires a lower quantity of Lu³⁺, it has a lower melting point than LuAG and Lu₂O₃, and a fairly high thermal conductivity (7.8 W/m•K [22]). Recently, we have demonstrated for the first time the laser action for Yb:LuYAG ceramics with 15% Yb doping and various Y/Lu balances [23, 24]. Samples were

prepared at the Shanghai Institute of Ceramics (SIC-CAS, China) by reactive sintering; a detailed spectroscopic analysis was carried out at the Institute of Physics of the Czech Academy of Sciences (Prague). Laser tests were carried out at INO-CNR using a longitudinally pumped cavity (Fig. 6). Remarkable laser emission results were achieved, with maximum output power of 8.2 W, 7.3 W and 8.7 W for Y/Lu balance 25/75, 50/50 and 75/25 respectively, at 1030 nm, with a maximum absorbed pump power of about 16 W; the slope efficiency and the optical-to-optical efficiencies approached or exceeded 60% and 50% respectively.

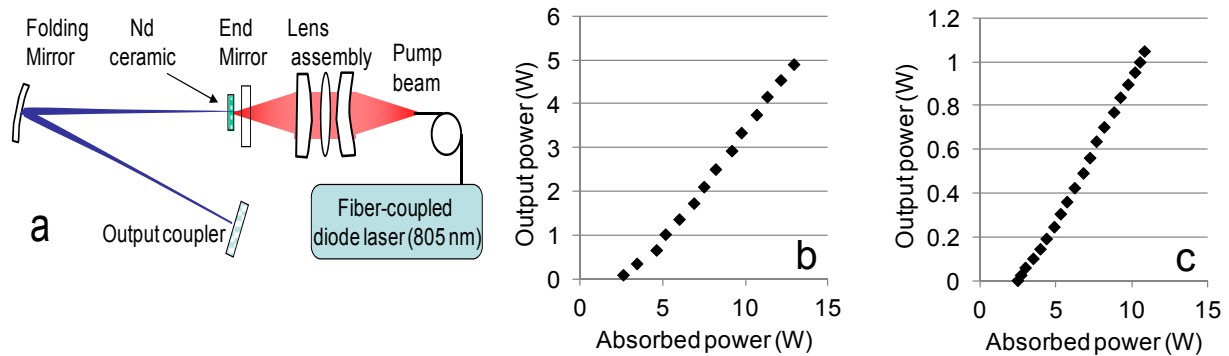


Figure 5. (a) Experimental set-up for the laser test on the Nd-doped ceramics. (b, c) Output power vs. absorbed pump power for the Nd:YAG and Nd:Lu₂O₃ (output coupler reflectivity respectively 80% and 98%). QCW pumping, duty factor 12.5%.

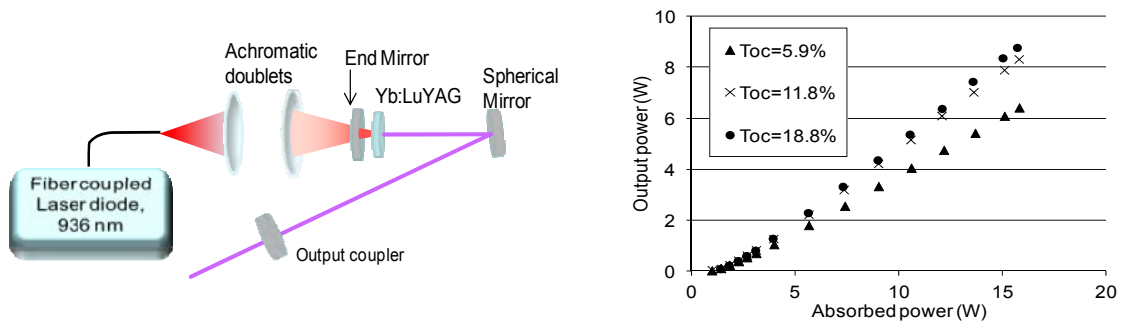


Figure 6. (Left) Experimental set-up for the laser test on the Yb:LuYAG ceramics, (Right) Output power vs. absorbed pump power for the sample with Y/Lu=75/25 (QCW pumping, pump duty factor 20%; Toc: output coupler transmission).

4. CONCLUSIONS

We have investigated, both numerically and experimentally, the performance of ceramic active media with various host compositions and with structured design. In particular end-pumped discs with a layered structure with varying doping level have been thoroughly analyzed. These structured ceramics appear promising in appropriate geometrical configurations, and thus are intended to be applied in the construction of High Power Diode Pumped Solid State Laser (DPSSL) or High Energy pulsed systems working in high repetition-rate pulsed regimes.

REFERENCES

- [1] Ikesue A., Furusato I., Kamata K. J., "Fabrication of Polycrystal line, Transparent YAG Ceramics by a Solid-State Reaction Method", *J. Am. Ceram. Soc.* 78 225–228 (1995).
- [2] Nakamura S., Yoshioka H., Matsubara Y., Ogawa T., and Wada S., "Broadly Tunable Yb³⁺-Doped Y₃Al₅O₁₂ Ceramic Laser at Room Temperature", *Jpn. J. Appl. Phys.* 48, 060205-1-060205-3 (2009)
- [3] Esposito L., Piancastelli A., Costa A.L., Serantoni M., Toci G., Vannini M., "Experimental features affecting the transparency of YAG ceramics" *Opt. Mat.* 33 (5), 713 (2011)
- [4] Alderighi D., Pirri A., Toci G., Vannini M., Esposito L., Costa A. L., Piancastelli A., Serantoni M., "Characterization of Yb:YAG ceramics as laser media", *Opt. Mater.* 33, 205, (2010)

- [5] Pirri A., Alderighi D., Toci G., Vannini M., "High-efficiency, high-power and low threshold Yb³⁺:YAG ceramic laser", *Opt. Express* 17 (25), 23344 (2009).
- [6] Ferrara P., Ciofini M., Esposito L., Hostaša J., Labate L., Lapucci A., Pirri A., Toci G., Vannini M., Gizzi L.A., "3-D numerical simulation of Yb: YAG active slabs with longitudinal doping gradient for thermal load effects assessment", *Opt. Express*, **22**, 5, 5375 (2014)
- [7] Gaumé, R., Viana, B., Vivien, D., Roger, J. P., & Fournier, D. A simple model for the prediction of thermal conductivity in pure and doped insulating crystals. *Applied physics letters*, 83(7), 1355-1357. (2003).
- [8] Lapucci, A., and Ciofini M., "Efficiency optimization for a diode-pumped Nd: YAG ceramic slab laser." *Appl. Opt.* **44** (20) 4388-4393 (2005).
- [9] Lapucci, A., Ciofini, M., Vannoni, M., Sordini, A. "High efficiency, diode pumped Nd: YAG ceramics slab laser with 230 W continuous-wave output power", *Appl. Opt.*, **51** (18), 4224-4231 (2012)
- [10] Toci G., Pirri A., Li J., Xie T., Pan Y., Babin V., Beitlerova A., Nikl M., and Vannini M., "First laser emission of Yb_{0.15}:(Lu_{0.5}Y_{0.5})₃Al₅O₁₂ ceramics," *Opt. Express* **24**, 9611-9616 (2016)
- [11] Pirri A., Toci G., Li J., Xie T., Pan Y., Babin V., Beitlerova A., Nikl M., and Vannini M., "Spectroscopic and laser characterization of Yb_{0.15}:(Lu_xY_{1-x})₃Al₅O₁₂ ceramics with different Lu/Y balance," *Opt. Express* **24**, 17832-17842 (2016)
- [12] An L., Ito A., Goto T., "Fabrication of Transparent Lutetium Oxide by Spark Plasma Sintering" *J. Amer. Ceramics Soc.* 94 (2011) 695-698.
- [13] An L., Ito A., Goto T., "Two-step pressure sintering of transparent lutetium oxide by spark plasma sintering" *J. Europ. Ceramics Soc.* 31 (9) (2011) 1597-1602.
- [14] Toci G., Vannini M., Ciofini M., Lapucci A., Pirri A., Ito A., T. Goto T., Yoshikawa A., Ikesue A., Alombert-Goget G., Guyot Y., Boulon G., "Nd³⁺-doped Lu₂O₃ transparent sesquioxide ceramics elaborated by the Spark Plasma Sintering (SPS) method. Part 2: First laser output results and comparison with Nd³⁺-doped Lu₂O₃ and Nd³⁺-Y₂O₃ ceramics elaborated by a conventional method", *Opt. Mater.*, 41, 12 (2015)
- [15] Lapucci, A., Ciofini, M., Esposito, L., Ferrara, P., Gizzi, L. A., Hostaša J., Labate L., Pirri A., Toci G., Vannini, M. "Characterization of Yb: YAG active slab media based on a layered structure with different doping." *Proc. SPIE 8780, High-Power, High-Energy, and High-Intensity Laser Technology; and Research Using Extreme Light: Entering New Frontiers with Petawatt-Class Lasers, 87800J* (May 7, 2013);
- [16] Esposito L., Hostaša J., Piancastelli A., Toci G., Alderighi D., Vannini M., Epicier T., Malchère A., Alombert-Goget G., Boulon G., "Multilayered YAG-Yb:YAG ceramics: manufacture and laser performance", *J. Mater. Chem. C*, **2**, 10138-10148 (2014)
- [17] Hostaša J., Esposito L., Biasini V.; Piancastelli A.; Vannini M., Toci G. Layered Yb:YAG ceramics produced by two different methods: processing, characterization and comparison ", *Proc. SPIE 9726, Solid State Lasers XXV: Technology and Devices, 97261M* (March 16, 2016).
- [18] Osipov V.V., Maksimov R.N., Shitov V.A., Lukyashin K.E., Toci G., Vannini M., Ciofini M., Lapucci A., "Fabrication, optical properties and laser outputs of Nd:YAG ceramics based on laser ablated and pre-calcined powders", in press on *Opt. Mater* (accepted June 12, 2016), DOI 10.1016/j.optmat.2016.06.021
- [19] Alombert-Goget G, Guyot Y, Guzik M, Boulon G, Ito A, Goto T, Yoshikawa A and Kikuchi M "Nd³⁺-doped Lu₂O₃ transparent sesquioxide ceramics elaborated by the Spark Plasma Sintering (SPS) method. Part 1: Structural, thermal conductivity and spectroscopic characterization" *Opt. Mater.* 41 3 (2015)
- [20] Toci G, Vannini M., Ciofini M, Lapucci A., Pirri A., Ito A., Goto T., Yoshikawa A., Ikesue A., Alombert-Goget G., Guyot Y., Boulon G., "Nd³⁺-doped Lu₂O₃ transparent sesquioxide ceramics elaborated by the Spark Plasma Sintering (SPS) method. Part 2: First laser output results and comparison with Nd³⁺-doped Lu₂O₃ and Nd³⁺-Y₂O₃ ceramics elaborated by a conventional method", *Opt. Mater.* **41**, (2015).
- [21] S. Cheng, X. Xu, D. Li, D. Zhou, F. Wua, Z. Zhao, and J. Xu, "Growth and spectroscopic properties of Yb:Lu_{1.5}Y_{1.5}Al₅O₁₂ mixed crystal," *Opt. Mater.* **33**, 112-115 (2010).
- [22] Y. Kuwano, K. Suda, N. Ishizawa, and T. Yamada, "Crystal growth and properties of (Lu,Y)₃Al₅O₁₂, " *J. of Cryst. Growth* 260, 159–165 (2004).
- [23] Toci G., Pirri A., Li J., Xie T., Pan Y., Babin V., Beitlerova A., Nikl M., and Vannini M., "First laser emission of Yb_{0.15}:(Lu_{0.5}Y_{0.5})₃Al₅O₁₂ ceramics," *Opt. Express* **24**, 9611-9616 (2016)
- [24] Pirri A., Toci G., Li J., Xie T., Pan Y., Babin V., Beitlerova A., Nikl M., and Vannini M., "Spectroscopic and laser characterization of Yb_{0.15}:(Lu_xY_{1-x})₃Al₅O₁₂ ceramics with different Lu/Y balance," *Opt. Express* **24**, 17832-17842 (2016)

Photoinitiator-free 3D scaffolds fabricated by excimer laser photocuring

Balázs Farkas¹, Silvia Dante¹ and Fernando Brandi^{1,2}

¹Department of Nanophysics, Istituto Italiano di Tecnologia (IIT), Via Morego 30, 16163 Genova, Italy

²Istituto Nazionale di Ottica (INO), Consiglio Nazionale delle Ricerche (CNR), Via Moruzzi 1, 56124-Pisa, Italy

E-mail: fernando.brandi@ino.it

Received 7 July 2016, revised 11 October 2016

Accepted for publication 27 October 2016

Published 9 December 2016



CrossMark

Abstract

Photoinitiator-free fabrication of poly(ethylene glycol) diacrylate (PEGDA) scaffolds is achieved using a novel three-dimensional (3D) printing method called mask projected excimer laser stereolithography (MPEXSL). The spatial resolution of photoinitiator-free curing is suitable for 3D layer-by-layer fabrication with a single layer thickness well controllable at tens to hundreds of microns using 248 nm wavelength for the irradiation. The photoinitiator-free scaffolds are superior compared to their counterparts fabricated by using photoinitiator molecules, showing a higher level of biocompatibility. A release of toxic chemicals from the photoinitiator containing scaffolds is proven by cell proliferation tests. In contrast, no toxic release is found from the photoinitiator-free scaffolds, resulting in the very same level of cell proliferation as the control sample. The demonstration of photoinitiator-free PEGDA scaffolds enables the fabrication of 3D scaffolds with the highest level of biocompatibility for both *in vitro* and *in vivo* applications.

 Online supplementary data available from stacks.iop.org/NANO/28/034001/mmedia

Keywords: photoinitiator-free, scaffolds, poly(ethylene glycol) diacrylate, 3D printing, excimer laser, photocuring, stereolithography

(Some figures may appear in colour only in the online journal)

1. Introduction

In regenerative medicine, any possible immune reaction towards foreign matter implanted in the hosting body is of great concern [1, 2]. Potential inflammation could hinder the efficiency of intended healing/self repair, potentially leading to the complete failure of the implanting process. *Biocompatibility*—high tolerance of the body towards the material—should be fulfilled by the foreign matter, determining that cells must grow, function normally, and migrate onto the implants [3, 4].

Tissue engineering (TE)—an interdisciplinary field consisting of physics, chemistry, biology and medicine—was conceived mainly to avoid this aforementioned detrimental effect when outside matter is implanted into a body for healing purposes. Various highly biocompatible *biomaterials* were proposed, tested and extensively researched over recent decades, ranging from organic [5–7] to inorganic [8–11]

sources, from metals [12, 13] and ceramics [14, 15] to polymers [5–11].

Apart from materials though, the TE strategy itself—the methodology of how the healing process is conducted—also determines the success of tissue regeneration: the porous 3D ‘carrier’ structures or *scaffolds* used routinely in TE have to provide an appropriate environment for the regeneration of tissues, and eventually serve as the delivery system for the implanted cells [10–14, 16–18]. Scaffolds must also mediate cellular migration and maintenance of the cells by the local presentation of physical and structural cues. Thus, the design of and control over the physical and chemical properties of these artificially made extracellular matrices is one of the main pillars of an effective scaffold-based TE strategy, and this has been studied extensively in recent years [16–18].

The work presented here aims at investigating the fabrication of scaffolds obtained by photocuring poly(ethylene glycol) diacrylate (PEGDA) using a 3D printing process

named mask projection excimer laser stereolithography (MPEXSL) [19–24], which is based on the use of UV pulsed excimer laser radiation.

PEG is US Food and Drug Administration (FDA) approved for a variety of applications, and its photocurable derivative, PEGDA, is commercially available and already a widely utilized polymer in regenerative medicine research; for instance, to investigate the engineering of tissues including bone [25], cartilage [26], cornea [27] and peripheral nerve [28]. PEGDA has been successfully applied in combination with two-photon polymerization using femtosecond near-infrared lasers to fabricate TE scaffolds with high spatial resolution [29, 30]. It is a non-toxic material generating minimal immunogenic response [31, 32], and it has also been photocured in the presence of living organisms [33].

The MPEXSL technique expands the traditional photolithography approach widely used for the production of two-dimensional (2D) microchips in the semiconductor industry, and brings it to the third dimension by applying a layer-by-layer procedure. In the present study, we investigate the effect on the spatial resolution (layer thickness) and biocompatibility (toxicity) of the laser parameters (laser pulse repetition rate, number of laser pulses applied and laser energy delivered per unit surface, i.e. the laser pulse fluence), as well as photoinitiator (PI) molecules generally added to the photopolymer resin to enable the stereolithography process. In the case of photocuring-based 3D printing processes the biocompatibility of the produced structures depends on the components of the photopolymer resin used (polymer and PI molecules), as well as on the effect of the photocuring process on the resin itself apart from solidification (e.g. new residual molecules being formed upon irradiation). Specifically, the presence of PI molecules is a constant source of possible toxic effects. To tackle this problem, the main research path up to now has been the detailed investigation of the effect of such PI molecules and their residues on the biological systems [34–39].

Here, we introduce an alternative way to completely eliminate issues related to the use of PI molecules, and thus generate highly biocompatible 3D scaffolds by employing the MPEXSL technique. In fact, we hypothesize that PEGDA can be photocured by pulsed excimer laser radiation even without the use of PI due to the presence of the two terminating acrylate groups which can be photo-crosslinked under irradiation with UV light [40–43]. Acrylate groups possess a UV absorption band which is peaked around 200 nm, and therefore short UV wavelength (<220 nm) has been used to photo-crosslink the acrylate group without the use of PI by continuous light irradiation. However the use of pulsed laser irradiation with a high peak intensity may activate an efficient photo-crosslinking process with longer wavelength photons as well provided that sufficient optical absorption is present. Such an effect would lead to a photoinitiator-free (PI-free) photocuring procedure, which is highly desired especially when *in vivo* applications are considered, since no chance emerges for toxic PI molecules/residuals to be released from the constructs. Up to now no stereolithographic method (based either on single photon absorption or on the more

sophisticated multi-photon absorption version) has yet demonstrated the possibility of producing PI-free 3D scaffolds.

Significantly, we find that the use of excimer laser pulses (≤ 300 nm) does enable photocuring of PEGDA *without the use of any PI molecules*. The demonstration of such PI-free PEGDA 3D scaffolds fabricated by MPEXSL opens the way for the production of highly biocompatible implants, with high potential impact in TE and regenerative medicine applications.

2. Experimental section

2.1. The fabrication process

MPEXSL is a 3D printing method relying on a layer-by-layer building up process where the layers are defined/cured by image projection using a pulsed excimer laser [18–23]. The MPEXSL system used in the present study is described in detail in [21], and here only a general presentation is given for clarity.

Two pulsed excimer lasers, with a pulse duration of 20 ns, are used in the experiments: a KrF laser at 248 nm (COMPexPro-110, Coherent), and a XeCl laser at 308 nm (COMPexPro-110, Coherent). A motorized mask holder can be used to select a mask (out of five), even during fabrication, leading to complex constructs. The mask consists of chromium on quartz photomasks used for optical lithography in which the desired pattern is written using a laser writer. Furthermore, the shape of the scaffold (e.g. the diameter) can be modified by means of an iris placed in front of the mask holder in order to select a sub-portion of the mask. Laser pulse energy, and therefore the single pulse fluence, is adjusted by a motorized variable attenuator, and a CCD camera is used to on-line image the resin surface and monitor the fabrication process. The laser pulse fluence applied to the resin is estimated by measuring the laser pulse energy at the mask position and then considering the demagnification factor of 4 and the energy losses of the optical projection system. In figure 1 the various irradiation methods used during the experiments are schematically reported. For single layer photocuring two irradiation configurations are used: (i) in thin layers (<1 mm), the resin is sandwiched in between two thin quartz slides (see figure 1(a)); (ii) in thick layers (>1 mm) a quartz slide is left to float on the surface of the resin contained in a cup (see figure 1(b)). In both cases the fabricated structures remained attached to the quartz slide through which the irradiation occurs. For 3D constructs, the layer-by-layer method is adopted, as schematically reported in figure 1(c).

All the structures produced were obtained by static irradiation applying the desired number of laser pulses at a pulse repetition rate of 20 Hz if not stated otherwise. The sample holder can be moved in the horizontal plane in order to change the irradiation point in the resin. The entire process, comprising laser pulse repetition rate, pulse energy setting, mask selection and sample stage movements, is controlled with a PC using a simple and easily programmable routine.

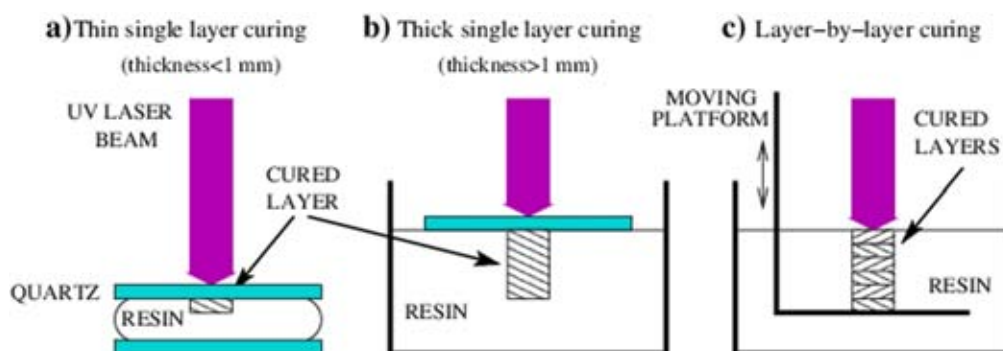


Figure 1. Irradiation conditions used in the experiments: (a) single layer curing for thickness <1 mm; (b) single layer curing for thickness >1 mm; (c) layer-by-layer fabrication.

The post-fabrication treatment of all produced samples is four-times soaking (15 min each cycle) and rinsing using Milli-Q water, then drying in a desiccator for 30 min. Therefore all produced parts consist of the insoluble structures after the post-fabrication treatment.

2.2. The UV sensitive liquid resin

The PEGDA (average Mn 700) as well as the PI utilized in this study (IRGACURE 2959) were ordered from Sigma Aldrich. PEGDA is used as it is, i.e. not diluted in water.

Three variants of the PEGDA resin were tested, depending on PI concentration used: 1% w/w, 2% w/w and '0%', i.e. PI-free.

2.3. Material and scaffolds characterization

UV-vis spectroscopy was performed with a photo-spectrometer (Varian, Cary 6000i) using a quartz cuvette in order to measure the penetration depth of UV light inside PEGDA.

Curing depth measurements were carried out by a stylus profiler (Veeco Dektak 150) with 1 mg of load on the tip for samples with a thickness <1 mm, while magnified optical inspection and a caliper were used for samples with a thickness >1 mm.

Mechanical characterization of the produced structures was performed by means of nanoindentation (Micro Materials Ltd NanoTest). The tests were done using a Berkovich tip with a maximum load of 0.6 mN, a dwell time at maximum load of 30 s, loading and unloading periods of 30 s and 15 s, respectively. The samples were measured at 16 different points (in a 4×4 matrix, distance between points $50 \mu\text{m}$). Young's modulus is calculated through the Oliver and Pharr method each time. Eventually, the stiffness for one sample is acquired by calculating the mean value of these aforementioned 16 measurements.

Electron microscopy imaging was performed with a scanning electron microscope (SEM) JEOL JSM-6490 (JEOL, Tokyo, Japan) operating at 15 kV. Samples were previously sputter coated with a 10 nm thick gold film using a Cressington 208HR coating system (Cressington Scientific Instruments Inc., Watford, UK).

2.4. Toxicity tests

Tests were conducted to investigate the possible release of toxic agents from the scaffolds, with and without PI. In order to do so, fabricated scaffolds were sterilized under a fume hood using the hood's in-built UV lamp for 60–90 min. The sterile samples were transferred into a multi-well and the wells were filled with 2 ml of Dulbecco's Eagle Medium (DMEM, Euroclone) mixed with 5% fetal bovine serum (FBS, Euroclone). The samples were kept into the incubator for 3 days. This immersion procedure was performed in order to check if toxic material was released into the culture medium. The treated DMEM was then used in cell proliferation tests conducted using an ACEA Biosciences xCELLigence system, equipped with E-plate 16. The device allows the real-time monitoring of cell viability, based on electrical impedance read out. All the gold electrodes were coated with poly-D-lysine (PDL, Sigma-Aldrich, mw 70.000–120.000) by adding $100 \mu\text{l}$ of a 0.1 mg ml^{-1} aqueous solution to each of the 16 wells of a single plate for 24 h. The wells were then rinsed with sterilized water and left to dry.

After the drying, the wells were filled with $100 \mu\text{l}$ DMEM+FBS for background measurement, then Chinese hamster ovarian cells (CHO) in $100 \mu\text{l}$ of DMEM were added to the wells. For the control sample fresh DMEM was employed. Cell density was 1000 or 2000 cells μl^{-1} .

The device was kept in the incubator and left to run for 7 days. Sampling of the cell proliferation was done every 30 min by reading out the impedance of the electrodes, and converting it to a dimensionless parameter, named Cell Index (C.I.). The C.I. matrix was then processed by Microcal's Origin.

Pilot cell seeding tests on the produced scaffolds were conducted using CHO cells. The cells were seeded on the scaffolds immersed in DMEM for 3 days. Before cell seeding, scaffolds were sterilized under a UV hood. Further, the scaffolds were left for 2 h in poly-D-lysine aqueous solution (0.1 mg ml^{-1}), rinsed and left to dry. Finally, fresh DMEM was added into the wells, CHO cells were seeded at a density of 10 000 cells μl^{-1} and left to grow in the incubator (37°C , 5% of CO_2) for 7 days *in vitro* (DIV 7). At DIV 7 cells were fixed in PFA 4%, and cell nuclei were stained with DAPI.

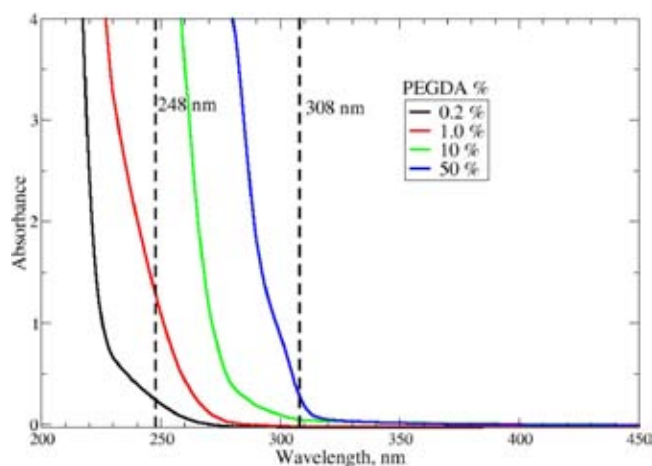


Figure 2. UV–vis absorption spectra of PEGDA for various concentrations in deionized water: the vertical dashed lines indicate the position of the two laser wavelength used in the experiments.

3. Results and discussion

3.1. Material characterization

3.1.1. UV–vis spectroscopy of PEGDA. The UV–vis absorption spectra of PEGDA obtained with different concentration in Milli-Q deionized water are shown in figure 2. It is found that the two excimer lasers wavelengths used fall within the UV absorption band of PEGDA, the 308 nm wavelength being on the very low energy edge of such an absorption band. The UV absorption band is due to the excitation of the acrylic group and can lead to a direct photochemical activation of the acrylic carbon bonds through internal conversion in the singlet state followed by inter-system crossing to the triplet state [42]. This photochemical activation of the carbon bond results in the cross-linking of the acrylic groups between adjacent PEGDA molecules and therefore in efficient photocuring of the polymer resin even without the use of any PI molecules. The specific absorption values at the two laser wavelengths used (highlighted by the vertical dashed lines) allowed estimating the penetration depth in pure PEGDA (see figure S1 in the online supporting information): 35 μm at 248 nm, and 8 mm at 308 nm. Indeed the longer 308 nm wavelength is at the very edge of the UV absorption band resulting in a large penetration depth, while there is significant absorption at 248 nm leading to a short penetration depth which indicates the feasibility of layer-by-layer 3D fabrication even without the use of any PI.

3.1.2. PEGDA photocuring WITHOUT photoinitiator (PI-free). To fabricate the appropriate pillars (reported in figure 3) the PI-free PEGDA resin was sandwiched between a glass holder and a quartz plate (see schematic in figure 1(a)). This irradiation method could only be used with the 248 nm laser. Since the penetration depth in PI-free PEGDA for 308 nm light is several mm another irradiation method was used: a glass cup was filled with pure PEGDA and a thin quartz sheet was positioned floating on top of the liquid uncured resin while irradiation was performed through the

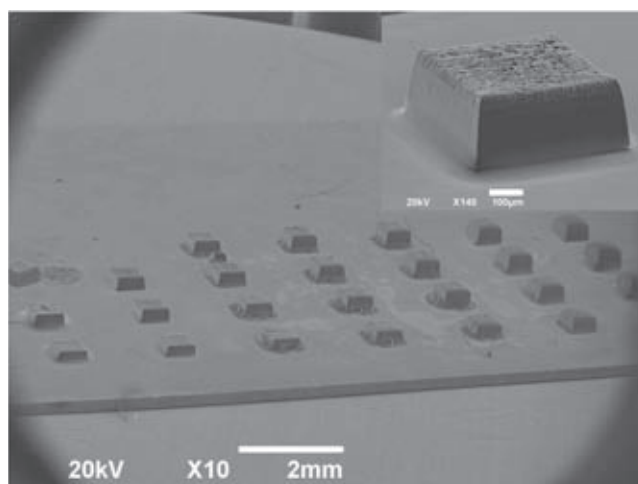


Figure 3. SEM image of typical PI-free PEGDA structures obtained with 248 nm laser and used for profilometry and nanoindentation measurements. The substrate is the quartz slide used during irradiation as shown in figure 1(a).

quartz (see schematic in figure 1(b)). In both cases the irradiation was performed using a simple aperture mask and static irradiations varying the single laser pulse fluence and the total number of laser pulses delivered for each irradiation. The result is an array of pillars (as shown in figure 3) that remained attached to the quartz after the post-fabrication treatment and that were subsequently used for profilometry and nanoindentation tests. Therefore the cured depth measured is the height of the pillars after post-fabrication treatment, i.e. the insoluble cured part.

The curing depth data, shown in figure 4, demonstrate that at 248 nm the single layer thickness can be tuned in the tens to hundreds of micron range, while mm thickness is achieved at 308 nm. This fact reflects the smaller penetration depth in PEGDA at 248 nm compared to 308 nm, leading to the viability of PI-free 3D constructs fabricated with a KrF excimer laser. It is noted that the curing depth obtained at 248 nm is actually larger compared to the light penetration depth at the same wavelength. This fact indicates that there may be significant photo-bleaching during the irradiation, which leads to an effective larger penetration depth of the light [44]. In contrast, when using 308 nm light the achieved pillar height is in the order of the penetration depth, i.e. several mm, and no photo-bleaching is observed. However, it has to be noted that for such long penetration depth the projected image goes out of focus within the resin volume and the actual fluence decreases a lot deep within the resin, leading to a much reduced curing efficiency for thick structures.

In general, the longer the crosslinking time the lower the spatial resolution, and this is also the case for PI-free photocuring: both the lateral and vertical resolution get degraded when longer irradiations are performed (see figure S2 in the online supplementary data). The spatial resolution is estimated in the few micrometer-scale for short irradiation times (i.e. small number of laser pulses) and increases to tens of micrometers for long irradiation times. It is also noted that

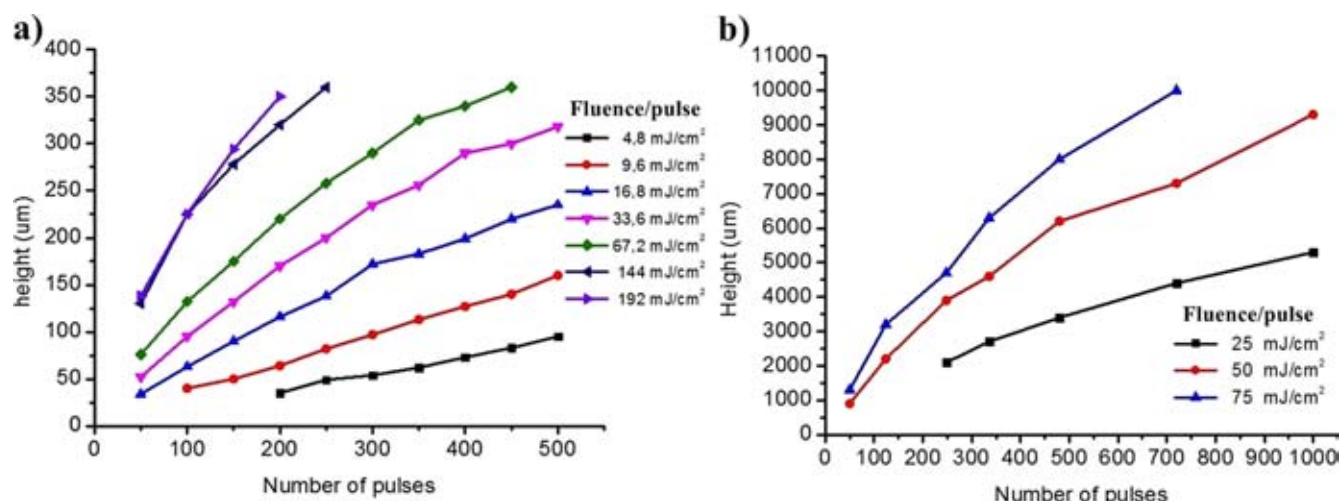


Figure 4. Curing depth, i.e. height of PI-free PEGDA pillars, as a function of the number of laser pulses applied for various single laser pulse fluences: (a) for 248 nm and (b) for 308 nm.

for long irradiation times the top part of the pillars has a 'dome' structure which most probably arises from the non-uniform illumination occurring when the image goes out of focus at long curing depth, decreasing the spatial resolution. However, in 3D fabrication the layers are usually ~ 100 micron thick resulting in sharp edges and micrometer-scale resolution, well suited for tissue engineering scaffolds (see figure S3 in the online supplementary data).

A selection of the same kind of 2D samples used for curing depth measurements was used to perform mechanical characterization of the PI-free PEGDA when various laser fabrication parameters were used. The results are presented in tables 1 and 2 in the online supplementary data file for 248 nm and 308 nm laser light, respectively. No striking difference could be detected between the samples: all have stiffness around 0.1 GPa. In the case of irradiation at 248 nm with a high fluence per pulse ($>100 \text{ mJ cm}^{-2}$) there is a decrease of the Young's modulus up to a factor of 4, which is an indication of possible photodegradation of the material.

3.1.3. PEGDA photocuring with photoinitiator. Adding PI to the PEGDA resin leads to a lower light penetration depth due to the increased optical absorption. From the UV-vis absorption spectra of the PI reported in the data sheet it is estimated that the penetration depth at 1% concentration in PEGDA is a couple of hundred microns at 308 nm and some tens of microns at 248 nm. The curing depth experiments were performed with 308 nm light, and 1% and 2% PI concentration in pure PEGDA. The use of 248 nm light would instead lead to a very small layer thickness hampering application of the layer-by-layer 3D printing and was therefore not tested. The measured curing depths in PEGDA with 1% and 2% PI at 308 nm reported in figure 5 are in agreement with the penetration depth in the photo-resins.

The reduced curing depth (tens to hundreds of microns) compared with PI-free photocuring at 308 nm makes layer-

by-layer fabrication possible with the MPExSL setup coupled with the XeCl laser.

3D layered structures with 1% and 2% PI were fabricated for mechanical testing: circular scaffolds of 2 mm diameter made from five layers, fabricated with six different repetition rates (i.e., 1, 5, 10, 20, 40 and 60 Hz) and two different fluences (2 mJ cm^{-2} and 8 mJ cm^{-2}). The profilometry data of figure 5 are used to find the appropriate number of pulses for the 2 mJ cm^{-2} fluence (seven pulses) and 8 mJ cm^{-2} fluence (two pulses), so each layer's thickness would be adjusted to $\sim 100 \mu\text{m}$. Overlap between layers was set to $20 \mu\text{m}$. The nanoindentation data (reported in table 2 of the online supplementary data) show a Young's modulus in the range of tens of MPa without major disparity between the two resins' compositions. There is an indication of lower modulus at higher fluences which may be an indication of some photodegradation during the irradiation.

3.2. Scaffold fabrication

The fabrication capability of the MPExSL system in conjunction with PEGDA can be seen in figure 6 where a gallery of various scaffolds is shown. The single layer multi-channel conduit in figure 6(a) is a PI-free scaffold fabricated using a dotted mask (see left panel in figure S4 in the online supplementary data) with 248 nm light and delivering 500 laser pulses at a fluence of 33 mJ cm^{-2} . In figure 6(b) a 3D multi-layer multi-channel conduit PI-free scaffold is reported; it was fabricated using a dotted mask with 248 nm light and delivering 100 laser pulses per layer at a fluence of 67.2 mJ cm^{-2} . The 3D multi-layer star-shaped multi-channel conduit scaffold reported in figure 6(c) was fabricated from PEGDA and 1% PI using 308 nm light and delivering seven laser pulses per layer at a fluence of 2 mJ cm^{-2} . The shape of this last scaffold was obtained alternating two star-shaped masks (see right panel in figure S4 of the online supplementary data), one of which resulted in a laterally open structure, as highlighted in the inset of figure 6(c).

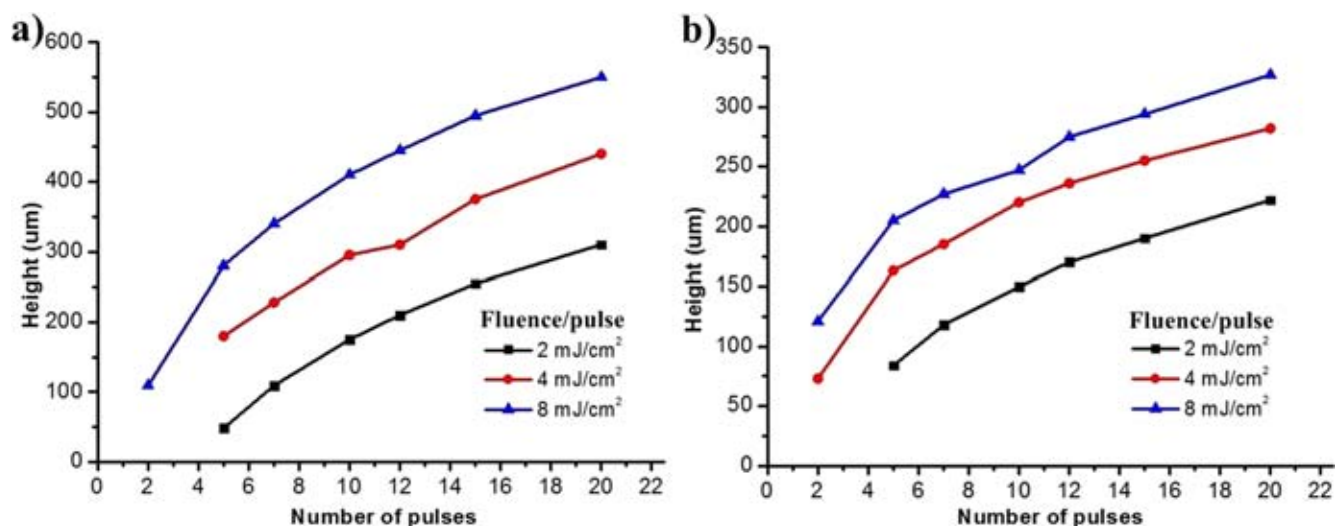


Figure 5. Curing depth of PEGDA at 308 nm irradiation: (a) 1% and (b) 2% PI.

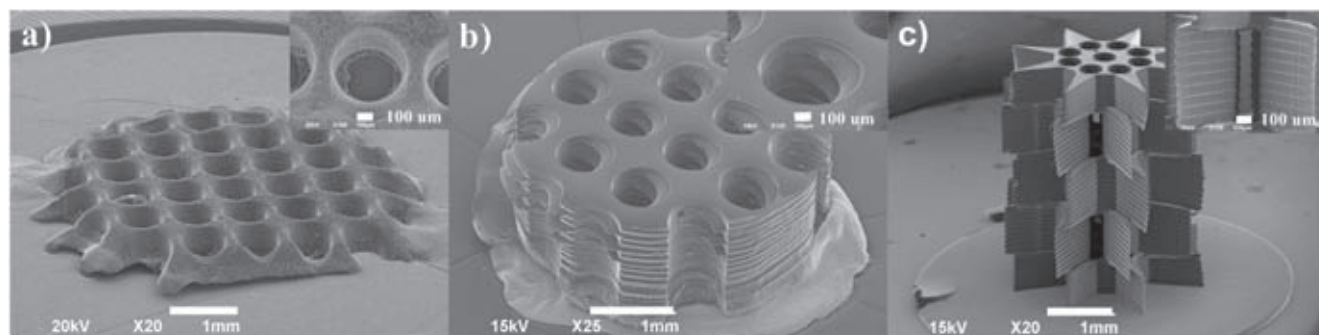


Figure 6. SEM images of PEGDA scaffolds produced by MPEXSL: (a) single layer multi-channel conduit PI-free scaffold fabricated with 248 nm light and 500 laser pulses at a fluence of 33 mJ cm^{-2} ; (b) multi-layer multi-channel conduit PI-free scaffold fabricated with 248 nm light and 100 laser pulses per layer at a fluence of 67.2 mJ cm^{-2} ; (c) star-shaped multi-layer multi-channel open conduit fabricated with 1% PI, 308 nm light, and seven laser pulses per layer at a fluence of 2 mJ cm^{-2} . In the insets, a highlight of each scaffold is reported. The scale bar in the insets is 100 micron.

3.3. Toxicity test

From the results previously presented it is clear that various PEGDA resin compositions (PI-free, 1% PI and 2% PI) with different lasers and laser parameters (248 nm KrF excimer, 308 nm XeCl excimer) can be used to achieve physically identical scaffolds. This offers a good basis to compare the biocompatibility of these cured resins, focusing on the possible release and toxicity of the added PI. Thus, identical circular scaffolds were fabricated from PI-free, 1% and 2% PI resins. In order to achieve the same physical properties (i.e. layer thickness), the 1% and 2% samples were fabricated with the XeCl, while the PI-free samples were made by the KrF laser. Layer thickness was adjusted to be $\sim 110 \mu\text{m}$, which corresponded to 300 pulses at 16.8 mJ cm^{-2} for irradiation at 248 nm, and seven pulses at 2 mJ cm^{-2} fluence for irradiation at 308 nm. Sample diameter was 4 mm.

As mentioned above, the samples were kept in DMEM for several days. A control well containing only DMEM and no scaffold was also included. After 7 days of soaking, the media were removed and used for the indirect toxicity test

further described. The scaffolds themselves were used for pilot cell seeding tests.

Initially, UV-vis spectroscopy was conducted to detect traces of PI in the soaking media (data not shown), with fresh DMEM used as comparison. The results show a slight difference in the absorbance only with the DMEM which had the 1% and 2% PI samples soaked in: from around 400 nm, the absorbance increased slightly, ramping up quickly in the UV. This corresponds well to the absorption properties of IRGACURE 2959.

In order to investigate the effect of PI release in the DMEM, the media were put under testing in an xCELLigence system for cell proliferation and viability tests [45]. This real-time and label free method has become an established tool to assess cell viability in the presence of toxic agents [46, 47]. The testing was repeated twice, with different cell numbers, i.e. with 10 000 and with 20 000 cells, leading to the results shown in figure 7. The C.I. stabilizes to the same value when cells reach confluency, independent of the initial cell numbers. In all experiments, the C.I. should always be compared at a given time to the positive (fresh DMEM) and the negative

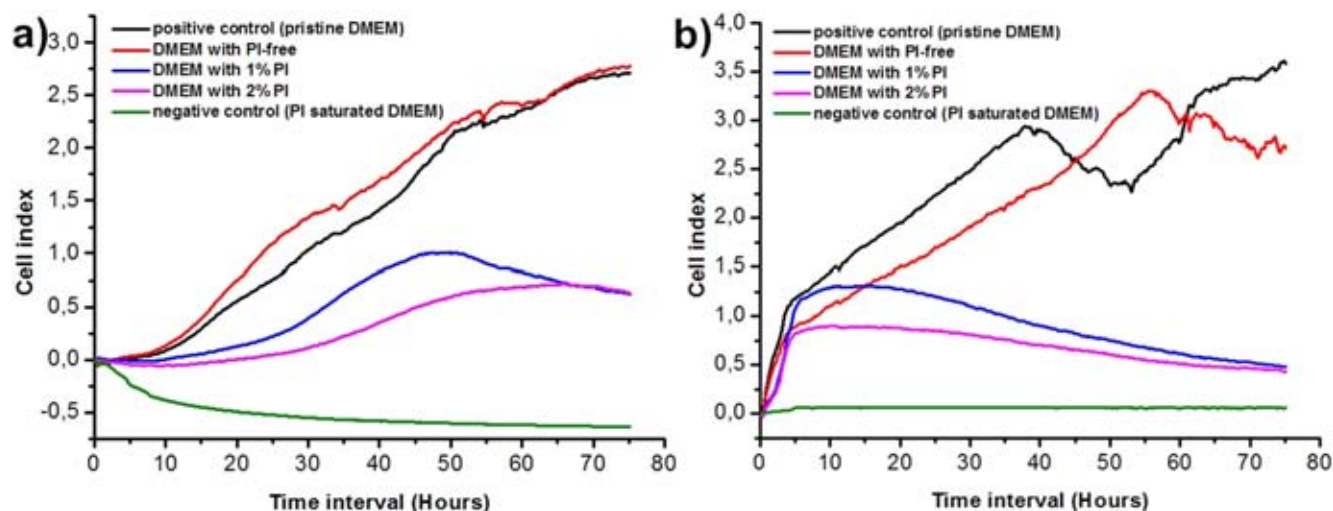


Figure 7. xCELLigence measurements with two different cell numbers: (a) 10 000; (b) 20 000. In both cases, the C.I. drops for PI samples and stabilizes in 3–4 days. The PI-free sample does not affect its environment.

(DMEM saturated with PI) control. The images acquired from the cells in the wells are reported in figure S5 in the online supplementary data.

Both experiments lead to the same results, showing a distinct difference in the behavior of the DMEM regarding its pre-treatment: the DMEM kept in contact with PI-containing samples is toxic for the cells, leading to a decrease in the C.I. over time, whilst the DMEM of the PI-free scaffold behaves identically to the pristine (albeit, not fresh) DMEM showing a high C.I. and, subsequently, high cell proliferation. The negative control group with DMEM saturated with IRGACURE 2959 leads to zero C.I., i.e. immediate cell death and detachment from the electrode surface. These results are in accordance with the UV–vis spectra and show the toxic effect of the PI released from the scaffolds during their soaking period. Importantly, it also demonstrates that no toxic substances are created during the PI-free excimer laser photocuring of PEGDA when 248 nm light is used.

In a pilot experiment to test possible reduced toxicity of the scaffolds after aging in DMEM, the specimens used for the indirect toxicity test based on xCELLigence were used as substrates for cell seeding. The experiment was conducted in triplicate. The growth of CHO cells was monitored for several days, and, as shown in figure S6 in the online supplementary data, only the PI-free scaffolds showed at the end a uniform coverage of cells. In contrast, no cells were proliferating on the PI-containing scaffolds (data not shown), indicating that even after aging in DMEM the PI scaffolds retained some toxic agents.

4. Conclusions and outlook

We report an investigation of the photocuring process of PEGDA using excimer laser and we compare the results obtained without using PI molecules with the results obtained with a typical PI molecule. The possibility of curing PEGDA without the use of any PI molecules is demonstrated using

excimer lasers, which enables the fabrication of PI-free 3D PEGDA scaffolds for the first time to the best of our knowledge. Irradiation with a KrF laser at 248 nm results in tens to hundreds of micron thick layers, which enables the implementation of layer-by-layer fabrication resulting in 3D scaffolds. In contrast, XeCl irradiation (at 308 nm) of the PI-free PEGDA leads to a few mm layer thickness, not suitable for layer-by-layer 3D fabrication. The long penetration depth of 308 nm light in PEGDA can be reduced by the use of absorbing molecules or nanoparticles, which could lead to the fabrication of (nano)composite and bio-active PI-free scaffolds. As expected, adding PI to the PEGDA resin decreases both the curing depth as well as the amount of total energy necessary for the curing, resulting in a slightly higher spatial resolution.

Nanoindentation tests revealed a Young's modulus in the order of 100 MPa for PI-free structures and 10 MPa for PI-containing structures. In general, a lower modulus is found in the case of irradiation with a high fluence per pulse ($>100 \text{ mJ cm}^{-2}$), which may be an indication of photo-degradation of the hydrogel. Further dedicated studies are necessary to investigate this phenomenon.

Using a cell proliferation assay we demonstrate that the PI-free scaffolds do not release any toxic substance once submerged in culture medium for several days, whereas the scaffolds containing the photoinitiator molecules have adverse effects on cell proliferation once submerged in the culture medium. Therefore the use of PI for the fabrication of TE scaffolds should be avoided whenever possible. At the same time, PI-free scaffolds fabricated using a 248 nm excimer laser do not release any toxic substance in the culture medium, resulting in high biocompatibility, potentially representing the perfect environment for both *in vitro* and *in vivo* applications.

In some 3D bioprinting methodologies cells can be embedded into the biomaterial [48–51]. In principle, the use of short wavelength UV light from excimer lasers may limit the inclusion of live cells during fabrication, decreasing the

viability of the cells upon irradiation [52, 53]. The precise assessment of such effect requires dedicated systematic experiments, specific for each cell line to be used.

In perspective, the demonstration of PI-free photocuring of PEGDA by short wavelength UV laser pulses can have a strong impact on the fabrication of high-resolution highly biocompatible 3D scaffolds to be used in TE. Specific quantum mechanical calculations are necessary to comprehend the exact molecular path way behind the PI-free curing of PEGDA with excimer laser radiation at 248 nm and 308 nm, as has been done for other acrylate molecules [37, 38]. Such calculations, as well as experimental investigations would be highly desirable also for other acrylate-based polymers used in TE, e.g. collagen-based gelatin methacrylate (GelMA) [54] and methacrylated glycole chitosan (MGC) [55, 56]. A systematic investigation on the PI-free curing dynamics with IR spectroscopy would also help to highlight and optimize the curing process.

Besides the static irradiation performed in the present study, it is feasible to implement a direct write approach in which each layer is cured by moving the laser beam and/or the resin cup during irradiation in order to produce the desired pattern. This methodology would increase the versatility of the printing system *albeit* at the expenses of production time.

Finally, apart from the use of MPEXSL for the fabrication of 3D scaffolds via the layer-by-layer photocuring method, we foresee a systematic investigation of PI-free PEGDA photocuring via two-photon absorption using visible femto-second laser pulses (e.g. at about 500 nm, second-harmonic of the Nd-based and Yb-based lasers), which would enable a direct laser writing PI-free 3D printing process.

Acknowledgments

This work received funding support from the European Union (FP7-NMP-2013-EU-China), grant agreement no. 604263 (NEUROSCAFFOLDS).

References

- [1] Wooley P H, Nasser S and Fitzgerald R H 1996 The immune response to implant materials in humans *Clin. Orthop. Relat. R.* **326** 63–70
- [2] Merritt K and Rodrigo J J 1996 Immune response to synthetic materials—sensitization of patients receiving orthopaedic implants *Clin. Orthop. Relat. R.* **326** 71–9
- [3] Junker R, Dimakis A, Thoneick M and Jansen J A 2009 Effects of implant surface coatings and composition on bone integration: a systematic review *Clin. Oral. Implan. Res.* **20** 185–206
- [4] Zhang B G X, Myers D E, Wallace G G, Brandt M and Choong P F M 2014 Bioactive coatings for orthopaedic implants—recent trends in development of implant coatings *Int. J. Mol. Sci.* **15** 11878–921
- [5] Galbis J A and Garcia-Martin M G 2010 Carbohydrates in sustainable development II *Topics in Current Chemistry* (Berlin: Springer) **295** 147–76
- [6] Shanmugasundaram O L 2012 Development and characterization of cotton and organic cotton gauze fabric coated with biopolymers and antibiotic drugs for wound healing *Indian J. Fibre Text* **37** 146–50 (<http://nopr.niscair.res.in/handle/123456789/14264>)
- [7] Sell S A, McClure M J, Garg K, Wolfe P S and Bowlin G L 2009 Electrospinning of collagen/biopolymers for regenerative medicine and cardiovascular tissue engineering *Adv. Drug. Deliver. Rev.* **61** 1007–19
- [8] Müller W E, Schröder H C, Shen Z, Feng Q and Wang X 2013 Inorganic polymers: morphogenic inorganic biopolymers for rapid prototyping chain *Prog. Mol. Subcell. Biol.* **54** 235–59
- [9] Müller W E, Wang X and Schöder H C 2013 *Biomedical Inorganic Polymers* (Berlin: Springer)
- [10] Rezwan K, Chen Q Z, Blaker J J and Boccaccini A R 2006 Biodegradable and bioactive porous polymer/inorganic composite scaffolds for bone tissue engineering *Biomaterials* **27** 3413–31
- [11] Li X M, Cui R R, Sun L W, Aifantis K E, Fan Y B, Feng Q L, Cui F Z and Watari F 2014 3D-printed biopolymers for tissue engineering application *Int. J. Polym. Sci.* **2015** 829145
- [12] Bose S, Roy M and Bandyopadhyay A 2012 Recent advances in bone tissue engineering scaffolds *Trends Biotechnol.* **30** 546–54
- [13] Alavi S H and Kheradvar A 2012 Metal mesh scaffold for tissue engineering of membranes *Tissue Eng. Part C Methods* **18** 293–301
- [14] Li J, Baker B A, Mou X, Ren N, Qiu J, Boughton R I and Liu H 2014 Biopolymer/calcium phosphate scaffolds for bone tissue engineering *Adv. Health. Mater.* **3** 469–84
- [15] Zhou H and Lee J 2011 Nanoscale hydroxyapatite particles for bone tissue engineering *Acta Biomater.* **7** 2769–81
- [16] Chan B P and Leong K W 2008 Scaffolding in tissue engineering: general approaches and tissue-specific considerations *Eur. Spine. J.* **17** (Suppl 4) 467–79
- [17] Carletti E, Motta A and Migliaresi C 2011 3D cell culture: methods and protocols *Methods in Molecular Biology* (Totowa, NJ: Humana Press) **695** 17–39
- [18] Bajaj P, Schweller R M, Khademhosseini A, West J L and Bashir R 2014 3D biofabrication strategies for tissue engineering and regenerative medicine *Annu. Rev. Biomed. Eng.* **16** 247–76
- [19] Beke S, Anjum F, Tsushima H, Ceseracciu L, Chiergatti E, Diaspro A, Athanassiou A and Brandi F 2012 Towards excimer-laser-based stereolithography: a rapid process to fabricate rigid biodegradable photopolymer scaffolds *J. R. Soc. Interface* **9** 3017–26
- [20] Beke S, Anjum F, Ceseracciu L, Romano I, Athanassiou A, Diaspro A and Brandi F 2013 Rapid fabrication of rigid biodegradable scaffolds by excimer laser mask projection technique: a comparison between 248 and 308 nm *Laser Phys.* **23** 035602
- [21] Beke S, Farkas B, Romano I and Brandi F 2014 3D scaffold fabrication by mask projection excimer laser stereolithography *Opt. Mater. Express* **4** 2032–41
- [22] Farkas B, Romano I, Ceseracciu L, Diaspro A, Brandi F and Beke S 2015 Four-order stiffness variation of laser-fabricated photopolymer biodegradable scaffolds by laser parameter modulation *Mat. Sci. Eng. C* **55** 14–21
- [23] Abdelrasoul G N, Farkas B, Romano I, Diaspro A and Beke S 2015 Nanocomposite scaffold fabrication by incorporating gold nanoparticles into biodegradable polymer matrix: synthesis, characterization, and photothermal effect *Mat. Sci. Eng. C* **56** 305–10
- [24] Brandi F, Anjum F, Ceseracciu L, Barone A C and Athanassiou A 2011 Rigid biodegradable photopolymer structures of high resolution using deep-UV laser photocuring *J. Micromech. Microeng.* **21** 054007
- [25] Tan F, Xu X D, Deng T, Yin M, Zhang X Z and Wang J W 2012 Fabrication of positively charged poly(ethylene

- glycol)-diacrylate hydrogel as a bone tissue engineering scaffold *Biomed. Mater.* **7** 055009
- [26] Musumeci G, Loreto C, Carnazza M L, Strehin I and Elisseeff J 2011 OA cartilage derived chondrocytes encapsulated in poly(ethylene glycol) diacrylate (PEGDA) for the evaluation of cartilage restoration and apoptosis in an *in vitro* model *Histol. Histopathol.* **26** 1265–78
- [27] Kadakia A, Keskar V, Titushkin I, Djalilian A, Gemeinhart R A and Cho M 2008 Hybrid superporous scaffolds: an application for cornea tissue engineering *Crit. Rev. Biomed. Eng.* **36** 441–71
- [28] Pateman C J, Harding A J, Glen A, Taylor C S, Christmas C R, Robinson P P, Rimmer S, Boissonade F M, Claeysens F and Haycock J W 2015 Nerve guides manufactured from photocurable polymers to aid peripheral nerve repair *Biomaterials* **49** 77–89
- [29] Qin X H, Gruber P, Markovic M, Plochberger B, Klotzsch E, Stampfl J, Ovsianikov A and Liska R 2014 Enzymatic synthesis of hyaluronic acid vinyl esters for two-photon microfabrication of biocompatible and biodegradable hydrogel constructs *Polym. Chem-Uk* **5** 6523–33
- [30] Torgersen J, Qin X H, Li Z Q, Ovsianikov A, Liska R and Stampfl J 2013 Hydrogels for two-photon polymerization: a toolbox for mimicking the extracellular matrix *Adv. Funct. Mater.* **23** 4542–54
- [31] Mazzoccoli J P, Feked D L, Baskaran H and Pintauro P N 2010 Mechanical and cell viability properties of crosslinked low- and high-molecular weight poly(ethylene glycol) diacrylate blends *J. Biomed. Mater. Res.* **93A** 558–66
- [32] Lynn A D, Kyriakides T R and Bryant S J 2010 Characterization of the *in vitro* macrophage response and *in vivo* host response to poly(ethylene glycol)-based hydrogels *J. Biomed. Mater. Res.* **93A** 941–53
- [33] Torgersen J *et al* 2012 Photo-sensitive hydrogels for three-dimensional laser microfabrication in the presence of whole organisms *J. Biomed. Opt.* **17** 105008
- [34] Ovsianikov A, Malinauskas M, Schlie S, Chichkov B, Gittard S, Narayan R, Lobler M, Sternberg K, Schmitz K P and Haverich A 2011 Three-dimensional laser micro- and nano-structuring of acrylated poly(ethylene glycol) materials and evaluation of their cytotoxicity for tissue engineering applications *Acta Biomater.* **7** 967–74
- [35] Li Z Q, Torgersen J, Ajami A, Muhleder S, Qin X H, Husinsky W, Holthoner W, Ovsianikov A, Stampfl J and Liska R 2013 Initiation efficiency and cytotoxicity of novel water-soluble two-photon photoinitiators for direct 3D microfabrication of hydrogels *RSC Adv.* **3** 15939–46
- [36] Bail R, Patel A, Yang H, Rogers C M, Rose F R A J, Segal J I and Ratchev S M 2013 The effect of a type I photoinitiator on cure kinetics and cell toxicity in projection-microstereolithography *Proc. Cirp.* **5** 222–5
- [37] Geurtsen W, Lehmann F, Spahl W and Leyhausen G 1998 Cytotoxicity of 35 dental resin composite monomers/additives in permanent 3T3 and three human primary fibroblast cultures *J. Biomed. Mater. Res.* **41** 474–80
- [38] Williams C G, Malik A N, Kim T K, Manson P N and Elisseeff J H 2005 Variable cytocompatibility of six cell lines with photoinitiators used for polymerizing hydrogels and cell encapsulation *Biomaterials* **26** 1211–8
- [39] Ovsianikov A *et al* 2014 Laser photofabrication of cell-containing hydrogel constructs *Langmuir* **30** 3787–94
- [40] Elsner C, Boulares-Pender A, Hahnel M, Konieczny R, Kuhnel C and Buchmeiser M R 2009 Photoinitiator-free plasma-induced polymerization and microstructuring of acrylate-based coatings on 3D substrates *Macromol. Mater. Eng.* **294** 422–31
- [41] Huang L, Li Y, Yang J, Zeng Z and Chen Y 2009 Self-initiated photopolymerization of hyperbranched acrylates *Polymer* **50** 325–4333
- [42] Bauer F, Decker U, Naumov S and Riedel C 2014 Photoinitiator-free UV curing and matting of acrylate-based nanocomposite coatings: III. *Prog. Org. Coat.* **77** 1085–94
- [43] Scherzer T, Knolle W, Naumov S and Prager L 2005 Investigations on the photoinitiator-free photopolymerization of acrylates by vibrational spectroscopic methods *Macromol. Symp.* **230** 173–82
- [44] Prager L, Wennrich L, Knolle W, Naumov S and Prager A 2012 Absorption of acrylates and polysilazanes in the far UVC and the VUV regions *Mater. Chem. Phys.* **134** 235–42
- [45] Ke N, Wang X B, Xu X and Abassi Y A 2011 Mammalian Cell Viability: Methods and Protocols (Totowa, NJ: Humana Press) **740** 33–43
- [46] Garcia S N, Gutierrez L and McNulty A 2013 Real-time cellular analysis as a novel approach for *in vitro* cytotoxicity testing of medical device extracts *J. Biomed. Mater. Res. A* **101** 2097–106
- [47] Meindl C, Absenger M, Roblegg E and Frohlich E 2013 Suitability of cell-based label-free detection for cytotoxicity screening of carbon nanotubes *Biomed. Res. Int.* **2013** 564804
- [48] Durst C A, Cuchiara M P, Mansfield E G, West J L and Grande-Allen K J 2011 Flexural characterization of cell encapsulated PEGDA hydrogels with applications for tissue engineered heart valves *Acta Biomater.* **7** 2467–76
- [49] Wang Z, Abdulla R, Parker B, Samanipour R, Ghosh S and Kim K 2015 A simple and high-resolution stereolithography-based 3D bioprinting system using visible light crosslinkable bioinks *Biofabrication* **7** 045009
- [50] Zhang Y S *et al* 2016 Bioprinting 3D microfibrillar scaffolds for engineering endothelialized myocardium and heart-on-a-chip *Biomaterials* **110** 45–59
- [51] Huang J, Wang L, Xiong C and Yuan F 2016 Elastic hydrogel as a sensor for detection of mechanical stress generated by single cells grown in three-dimensional environment *Biomaterials* **98** 103–12
- [52] de Gruijl F R, van Kranen H J and Mullenders L H 2001 UV-induced DNA damage, repair, mutations and oncogenic pathways in skin cancer *J. Photochem. Photobiol. B Biol.* **63** 19–27
- [53] Sinha R P and Häder D P 2002 UV-induced DNA damage and repair: a review *Photochem. Photobiol. Sci.* **1** 225–36
- [54] Gauvin R, Chen Y C, Lee J W, Soman P, Zorlutuna P, Nichol J W, Bae H, Chen S C and Khademhosseini A 2012 Microfabrication of complex porous tissue engineering scaffolds using 3D projection stereolithography *Biomaterials* **33** 3824–34
- [55] Amsden B G, Sukarto A, Knight D K and Shapka S N 2007 Methacrylated glycol chitosan as a photopolymerizable biomaterial *Biomacromolecules* **8** 3758–66
- [56] Romano I, Ayadi F, Rizzello L, Summa M, Bertorelli R, Pompa P P, Brandi F, Bayer I S and Athanassiou A 2015 Controlled antiseptic/eosin release from chitosan-based hydrogel modified fibrous substrates *Carbohydr. Polym.* **131** 306–14

Laser-driven particle acceleration for radiobiology and radiotherapy: where we are and where we are going

Antonio Giulietti*

Intense Laser Irradiation Laboratory, Istituto Nazionale di Ottica[†]
CNR Campus, via Moruzzi 1, 56124 Pisa (Italy)

ABSTRACT

Radiation therapy of tumors progresses continuously and so do devices, sharing a global market of about \$ 4 billions, growing at an annual rate exceeding 5%. Most of the progress involves tumor targeting, multi-beam irradiation, reduction of damage on healthy tissues and critical organs, dose fractioning. This fast-evolving scenario is the moving benchmark for the progress of the laser-based accelerators towards clinical uses. As for electrons, both energy and dose requested by radiotherapy are available with plasma accelerators driven by lasers in the power range of tens of TW but several issues have still to be faced before getting a prototype device for clinical tests. They include capability of varying electron energy, stability of the process, reliability for medical users. On the other side hadron therapy, presently applied to a small fraction of cases but within an exponential growth, is a primary option for the future. With such a strong motivation, research on laser-based proton/ion acceleration has been supported in the last decade in order to get performances suitable to clinical standards. None of these performances has been achieved so far with laser techniques. In the meantime a rich crop of data have been obtained in radiobiological experiments performed with beams of particles produced with laser techniques. It is quite significant however that most of the experiments have been performed moving bio samples to laser labs, rather moving laser equipment to bio labs or clinical contexts. This give us the measure that laser community cannot so far provide practical devices usable by non-laser people.

Keywords: Laser-driven particle accelerators, radiobiology, radiotherapy, dosimetry, radiation safety

1. INTRODUCTION

It is time to check state of the art and perspective of laser technologies addressed at implementing compact particle accelerators for biological researches and clinical uses. During a recent editorial work¹ I realized that the expectation level for this novel technology is quite high in a broad community of scientists, including laser, plasma and nuclear physicists, medical physicists, radiation biologists, radiologists and radiotherapists. Contributions from each one of these classes of expertise become highly desirable today to actually state where we are, where we should move and how. Physicists involved in the particle acceleration with laser techniques can provide not only the state of the art of laser-driven electron, proton and ion accelerators most suitable for biological studies and future clinical therapies, but also a deep insight into the most advanced experiments and novel ideas. It will come out that laser produced particles have been used in a variety of physical schemes to generate secondary sources of high-energy photons, another kind of ionizing radiation, the most used in radiation therapy of tumors. In turn, photons of tens of MeV have been used to produce, via photonuclear reactions, radionuclides of interest for the nuclear medicine. In addition, high-resolution ultrafast radiography has been performed with particles accelerated by laser². On the other hand, radiotherapists can update our knowledge about the most advanced devices and protocols, very effective, they actually use in a hospital: the novel practice in radiotherapy of tumors is the benchmark (continuously moving forward) for the laser-driven technologies. While a number of biologists are systematically investigating the response of living matter to the particle bunches produced by lasers, some others are already speculating on how this new opportunity can extend and empower the most recent concepts of radiobiology. The action of such kind of radiation can be followed for the first time on femtosecond time scale and nanometric spatial scale. The novel acceleration technologies, based on the interaction of ultrashort intense laser pulses with matter, delivering sub-picosecond pulses of ionizing radiation, also demand a general renewing

* antonio.giulietti@ino.it

[†] www.ino.it

of dosimetry³ and safety protocols. Both absolute and relative dosimetry are currently re-considered, in the framework of international standards⁴. While suitable existing devices are examined, including radiochromic foils, ionization chambers and Faraday cups, novel concepts for ad hoc detectors are introduced and need to be carefully investigated. Dosimetric simulations with Monte Carlo methods, in particular with the GEANT4 toolkit provide a precious support to this effort. Also radiological safety has to be reconsidered while thinking to transfer technologies based on high power lasers in a clinical context. It is not the same issue as with conventional accelerators delivering a well defined type of particle with an almost monoenergetic spectrum. We are dealing now with a mix of radiological products delivered by laser-matter interaction, at a given but changeable intensity, with a variety of materials acting as accelerating media. Of course this kind of problems have already been faced in high-power laser facilities devoted to studies on laser-matter interactions and in particular to particle acceleration, but for a medical facility the safety of patients and personnel is paramount, then also doses from any secondary radiation and any kind of other hazards have to be carefully minimized⁵.

Though the rate of survivals increases regularly year by year, cancer is still the first cause of death everywhere. The number of *new* cases of cancer in the world is estimated to have been about 14 millions in the year 2012, with an expectation of more than 20 millions in 2020⁶. About 50% of cases are treated with radiation therapies, possibly in combination with surgery and/or chemotherapy, with an emerging problem for the access of low- and middle-income countries (LMIC) to radiation therapy⁷, particularly to the more expensive hadron therapy. Among these treatments, more than 90% use RF-driven linear accelerators of electrons (RF-Linac). Other techniques include internal radiation (brachytherapy) and proton-ion beams (hadron therapy). In most cases electrons delivered by a RF-linac are not used directly on the tumor but converted into photons (hard X-rays) by bremsstrahlung through a suitable target. In some case electrons are used directly, either to cure superficial tumors or in the Intra-Operative Radiation Therapy (IORT) which can be applied during surgical operation of a tumor^{8,9}. Radiation therapy techniques evolve and progress continuously and so do accelerators and dose delivering devices, which share a global market of about \$ 4 billions, growing at an annual rate exceeding 5%¹⁰. Most of the progress involves precision in tumor targeting, multi-beam irradiation, reduction of damage on healthy tissues and critical organs, fractionation of dose delivering for a more effective cure¹¹. Among these novel techniques and protocols of treatment, particularly effective appears the so-called Cyberknife. This technique uses a multitude of small beams which creates a large dose gradient resulting in the delivery of high dose to the tumor while minimizing the dose to adjacent healthy tissues¹².

Basically, requested electron kinetic energy ranges from 4 to 25 MeV, but rarely energy above 15 MeV is used. Required dose/rate usually ranges from 1 to 10 Gy/min. These two ranges of performances are presently well fulfilled by plasma accelerators driven by ultrashort laser pulses of “moderate” peak power, i.e. tens of TW, operating within high efficiency laser-plasma interaction regimes at a pulse repetition rate of the order of tens of Hz¹³. However further work has to be done on laser acceleration in order to reach the clinical standard in terms of the electron output stability and reproducibility. Several tasks have to be afforded before proceeding to a technical design of a laser-driven linac prototype for clinical tests. A first task is the optimization of both laser and gas-jet (or other possible targets) as well as their coupling (involving mechanical stability and optical design). Another task is the energy control of the electron bunch to provide different electron energies on clinical demand. These goals would require a complex scientific and technological investigation addressed to both the laser system, in order to make it as stable, simple and easy to use as possible, and the physics of the acceleration process, in order to get the highest possible efficiency, stability and output control. We may nevertheless try and list some of the expected advantages of future Laser-linac’s for clinical uses. Laser technology strongly reduces size and complexity of the acceleration section (Mini-linac) of the device; it also totally decouples the “driver” from the acceleration section: we can imagine in a hospital a single high power laser plant in a dedicated laser-room (with no need for radioprotection) which delivers pulses to a number of accelerators located in several treatment or operating rooms, suitably radioprotected. Laser managing and maintenance can proceed independently from the managing and maintenance of the Mini-linac’s. Each Mini-linac could be easily translated and rotated according to the given radiotherapy plan. Current studies could prove that the extreme dose-rate per pulse delivered by the Laser-linac would reduce the total dose for a therapeutic effect. This latter of course would be a major advantage of laser-driven radiotherapy.

The original idea of Laser Wake-Field Acceleration¹⁴ and the advent of the decisive CPA laser technology¹⁵ originated one of the most appealing scientific case of the last decades. Since then, a number of schemes for laser driven acceleration of electrons in plasmas have been proposed and studied, some of which have been successfully tested till very recently^{16,17}. New experimental records have been reported in the recent literature, in terms of the maximum

electron energy achieved, the minimum energy spread, as well as maximum collimation, stability, and so on. These records are in general obtained with lasers of outstanding performances and/or with very sophisticated methods hardly applicable for practical uses. On the other hand, several labs are intensively working on scientific and technological innovations aimed at demonstrating that reliable laser-based devices can be built which are able to produce electron beams fulfilling requirements of specific applications. A major task is addressed to the possible clinical use of electron laser-linac's and their potential advantages with respect to the existing RF-linacs operating today for millions of daily hospital treatments in the world.

This is the context in which the exciting progress of laser-driven electron acceleration try to make this technique competitive with existing RF-based devices involved in 90% of tumor treatments with radiation therapy. It has to be said however that hadron therapy, presently limited to a few percent of global treatments, is by far the most desirable way for the future to treat many tumors with ionizing radiation. This is due to the peculiar character of energy deposition of hadrons in a medium: treating a tumor at a given depth, monoenergetic protons or ions of suitable kinetic energy deliver most of the dose in a thin layer (Bragg peak) around the tumor site, while either electrons or gamma rays leave lot of their energy inside healthy tissues, before and after the tumor, with possible damages on these latter tissues. It has to be said, this drawback for electron-based clinical devices has been strongly reduced with modern configurations allowing multi-beam irradiations at different angles^{11,12}. Nevertheless, hadron therapy still remains a primary option for the future of radiotherapy, 70 years after its first conceptual proposition¹⁸ followed by pioneering experimental tests¹⁹. Since then, hadron therapy was occasionally performed inside accelerator facilities devoted to high energy physics, until the opening (1990) of a first clinical center equipped with a proton accelerator facility at Loma Linda Hospital in California (USA). In the last decades both the number of centers and the number of treated patients grew almost exponentially worldwide as shown in Figure 1²⁰. More than 137,000 patients were treated with this therapy worldwide from beginning up to 2014, including 15,000 in 2014, 86% of which were treated with protons and 14% with carbon ions or with other particles.



Figure 1. Growth of hadron therapy in treatment centers and treated patients worldwide (image from Reference 20).

Though the total number of treatments is still a small fraction of the total number of radiation treatments, this impressive growth demanded a huge capital investment which could be afforded only by medical institutions from rich countries[‡]. RF-based ion accelerators have faced an impressive progress, mostly in the synchrotron configuration (Figure 2 shows an overview of the CNAO synchrotron) but typical acceleration gradients still remain of the order of 1MeV/m, so that the typical diameter of an accelerator ring is several tens of meters for energies of clinical interest, namely $E \approx 100-400$

[‡] As a matter of fact, a global survey from the the Particle Therapy Co-Operative Group updated at the end of 2015, attributes 27 operating facilities to USA, 23 to European countries, 17 to Japan, 4 to China, 4 to Russia, 2 to Canada, 2 to South Korea, 1 to South Africa.

MeV/u, with severe costs involved²¹. Additional high costs and large spaces are requested by the very heavy gantry systems necessary to guide the particle beam onto the patient body from the right direction(s) and focus it with a millimeter precision²². According to a recent review²³, the seven major commercial companies operating in the field are able to deliver systems (based on either Cyclotron or Synchrotron technologies) with “superb reliability records”. The same companies are actively engaged in reducing size and cost for the next generation of devices. In fact, size and cost (both for construction and maintenance) of such facilities are presently the major drawbacks for a wider diffusion of hadron therapy.



Figure 2. The CNAO Synchrotron, Pavia, Italy.

With such a strong motivation, research on laser-based proton acceleration has been considerably supported in the last decade, mostly in the direction of achieving the challenging performances requested by the clinical standards. A usable device for cancer therapy needs to produce 200-250 MeV protons and /or 400-450 MeV/u carbon ions. In order to really profit of the Bragg peak, no more than 1% energy bandwidth is requested. Further, to release a dose of therapeutic interest in a reasonable time, more than 10^{10} particle/s have to reach the tissue under treatment. None of these performances has been achieved so far with laser techniques. Some of them seem still hard to achieve with existing lasers or even with the next generation lasers, at least in a configuration practically usable in a hospital context. Someone can define today the goal of laser-driven ion therapy as an “unrealistic expectation”²³ but the impressive crop of knowledge²⁴, the preliminary successful biological tests already performed²⁵ and some exciting new ideas²⁶ strongly encourage the community of laser-driven ion acceleration in its serious effort aimed at that long-term goal.

Historically, ion acceleration in plasmas was proposed before the invention of optical lasers, as early as 1956²⁷ and initially tested with electrons propagating in plasmas. Apart from initial observations related to fusion studies with infrared CO₂ lasers, the laser driven ion acceleration studies with optical lasers could really start only after some decisive breakthrough towards high peak power lasers, like mode-locking (ML) for picosecond pulses and chirped pulse amplification (CPA) for femtosecond pulses¹⁵. About 1-MeV ions were produced in the early Nineties with picosecond laser pulses²⁸. Subsequently, a continuous progress towards higher kinetic energies was continuously driven by both innovation in laser technology and better comprehension of the complex physics involved in the ion acceleration processes. Several proposals raised for a variety of schemes of laser-matter interaction at ultra-high (ultra-relativistic) intensities able to drive protons and light ions to near-relativistic energies. Most of them can be attributed either to *target normal sheath acceleration* (TNSA) or *radiation pressure dominated acceleration* (RPDA). This matter has been recently discussed by Borghesi and Macchi²⁴.

In a general view, considering the present state of the art, we can say that laser-driven acceleration to kinetic energies suitable for radiotherapy of cancer is well consolidated in the case of electrons and bremsstrahlung photons (with bunches delivering the requested dose). Effort is being invested towards achievement of corresponding energies for protons and light ions. In the case of electrons most of the work to be still done, in order to achieve clinical standards, has to address the control of the electron energy, as well as stability and reliability of the laser-linac. In the case of protons

and light ions the work to be done still includes the identification of an acceleration regime able to produce particles of suitable energy (and energy spread) in bunches delivering the right dose.

However, there is a major scientific issue which deserves to be addressed from now, concerning potential radiobiological effects of the extremely different duration of bunches produced by laser with respect to bunches produced by conventional accelerators. A factor exceeding 1,000,000 is involved, from μs to sub-ps timescale. The ultrashort duration of laser-produced particle bunches may involve unexpected consequences for cancer therapy. In fact, it is not known if delivering the same dose with particles of the same kinetic energy but at much higher instantaneous dose-rate may lead to a different tissutal effects with possible consequences on therapeutic strategy and protocols²⁹. From the physical point of view we can expect that the extreme particle density we can produce in a bunch with laser acceleration could behave “collectively” and/or lead to non-linear effects which cannot be described by the usual single-particle Monte Carlo simulation. In other words it is possible that each ultradense bunch of electrons could produce not only the statistic sum of the effects of each low-LET particle but also some high-LET effect due to the total charge involved. If this would be true, the biological action could not only concern DNA but also some structural cellular feature, like membrane. This major issue, in turn, calls for a dedicated research on radiobiological effects to be performed with the ultrashort particle bunches produced by laser technology. It is evident that such a research also has a high conceptual value since it enables, for the first time, the investigation of very early processes occurring in the timescales of physical, chemical, biological responses of the living matter to ionizing radiation³⁰. Investigation of very early effects arising from ultrashort ionizing pulses at nanometric scale become possible in a framework of advanced *femtochemistry*. This opportunity move also the interest of biologists, aimed at improving the “OMIC” approach to radiation therapy³¹. Finally, it has be be pointed out that the use of laser in combination of an electron beam is capable of creating collimated energy-specific (and energy-tunable) X-rays and γ -rays via the laser Compton scattering process³². Such high-energy quasi-monochromatic photon source can be very useful in radiation oncology.

2. HADRON THERAPY AND LASER-INDUCED ION ACCELERATION

In the year 1932, E. O. Lawrence (see Figure 3) and his group at University of California - Berkeley were able to accelerate protons to 1 MeV kinetic energy into their Cyclotron, based on a 11 inch magnet. Interestingly, his brother, Dr. John Lawrence, from University's Medical Physics Laboratory, already collaborated with him in studying medical and biological applications of the cyclotron, and himself became a consultant to the Institute of Cancer Research. The Cyclotron technology faced a decade of enthusiastic increase in proton energies with Nobel Prize assigned to E.O. Lawrence in 1939³³ till it was realized that energy was limited by the relativistic effect of the mass growth with velocity. The era started of synchro-cyclotrons and synchrotrons, basically the same big machines in operation today in the hadron therapy facilities.

Just after WWII, in his decisive paper¹⁸, Robert Wilson from Harvard noticed that “The accelerators now being constructed or planned will yield protons of energies above 125 Mev (million electron volts) and perhaps as high as 400 Mev. The range of a 125 Mev proton in tissue is 12 cm., while that of a 200 Mev proton is 27 cm. It is clear that such protons can penetrate to any part of the body.” and “the specific ionization or dose is many times less when the proton enter the tissue at high energy than it is in the last centimeter of the path where the ion is brought to rest.” All the future of the Hadron Therapy was simply depicted in these two sentences. More than 10 years later, John Lawrence published his first clinical study (see Figure 4) on “Proton irradiation of the pituitary” which opened the gate to all the subsequent works slowly leading to the present therapeutic protocols.

While discussing the progress of Laser-induced Ion Acceleration (LIA) towards its application to cancer therapy and possibly complaining about its delays, Figure 5 should be carefully considered. The Radio-Frequency (RF) approach to ion acceleration asked some 25 years before getting kinetic energies suitable to deep tumor irradiation, almost 30 years to produce significant clinical tests. Since then, 30 years were spent to experiment on samples and treat a few thousands patients worldwide inside nuclear laboratories in order to setup suitable protocols and reliable statistics. More than 60 years after the first cyclotron a huge device was built for the first time in a Hospital and devoted to patient treatment.

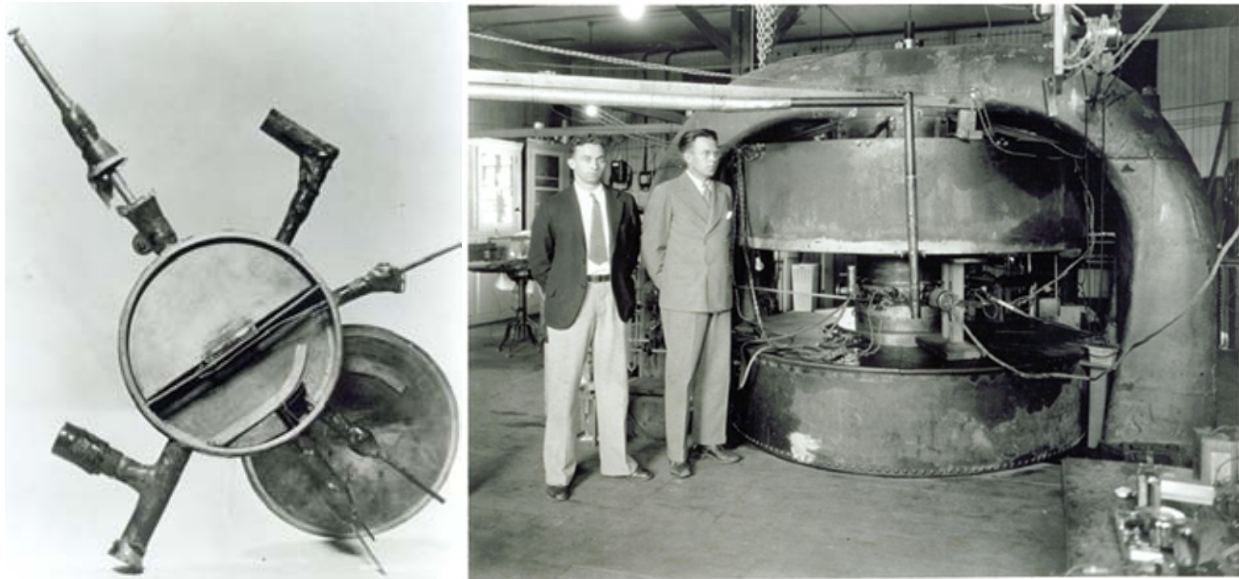


Figure 3. Left: the first 4" Lawrence cyclotron (1930). Right: Lawrence standing close to his 27" cyclotron (1933) at UC-Berkeley.

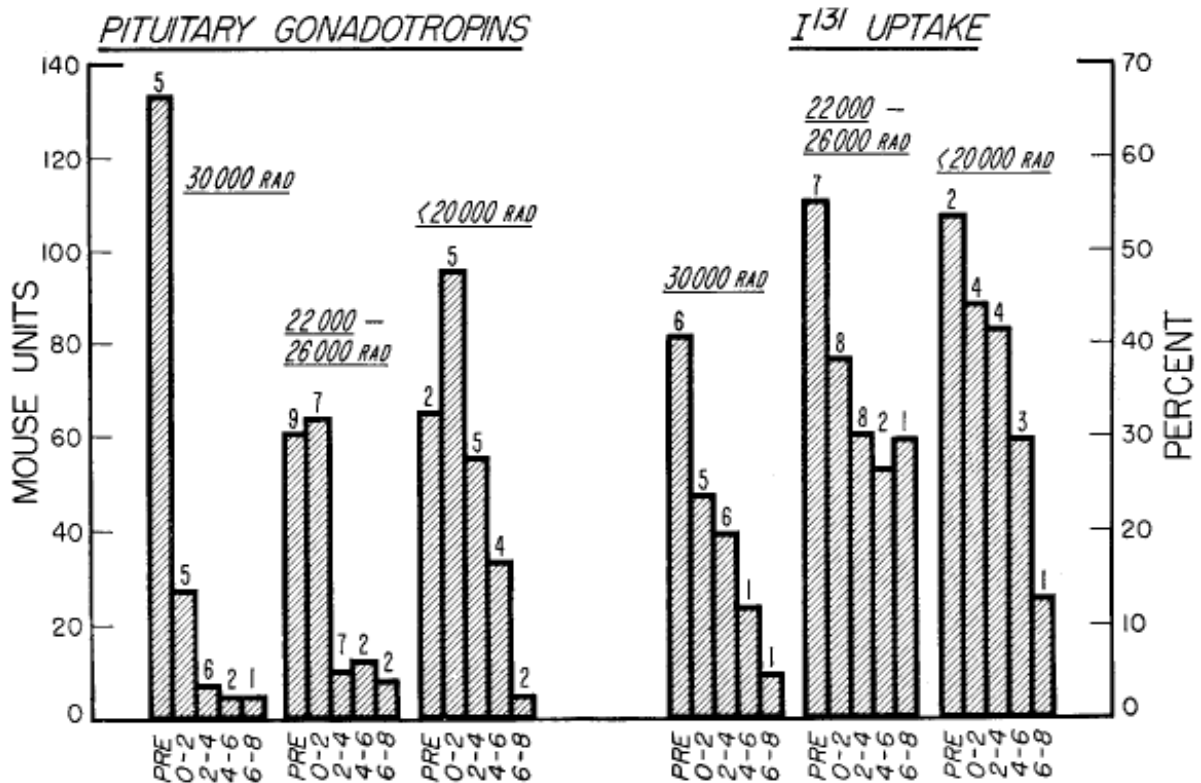


FIG. 4. Decrease in pituitary gonadotropins and I¹³¹ uptake for months after start of irradiation; grouping is according to three treatment levels—30,000 rads, 22,000 to 26,000 rads, and less than 20,000 rads.

Figure 4. Taken from the historic paper of Ref. 19.

Only 10 years later both the numbers of installed clinical facilities and treated patient showed a really fast growth rate with a weak but sensible decrease in the last few years, possibly due to the global economical crisis. Presently the

number of treatments performed with ions are a few percent of the total radiation treatments, while the ordinary X-ray radiotherapy based on electron linacs covers more than 90% of the cases. The story of LIA and its steps towards medical application is obviously shifted forward of several decades and could conventionally start with the invention of lasers delivering short pulses and more exactly when those pulses reached a suitable power, namely early Nineties. Whether the progress towards the medical application is comparable to the one performed by RF accelerators in a comparable period of time is hard to say, also because physical processes to be studied and applied were well assessed in the RF case, while laser acceleration in plasmas created from a variety of targets involves a number of physical processes and regimes almost never explored so far, whose modeling requires sophisticated, not always fully reliable, numerical calculations. This complex matter has been reviewed recently by several authors^{24,34,35} in the framework of the physics of laser-matter interaction at extreme intensities³⁶.

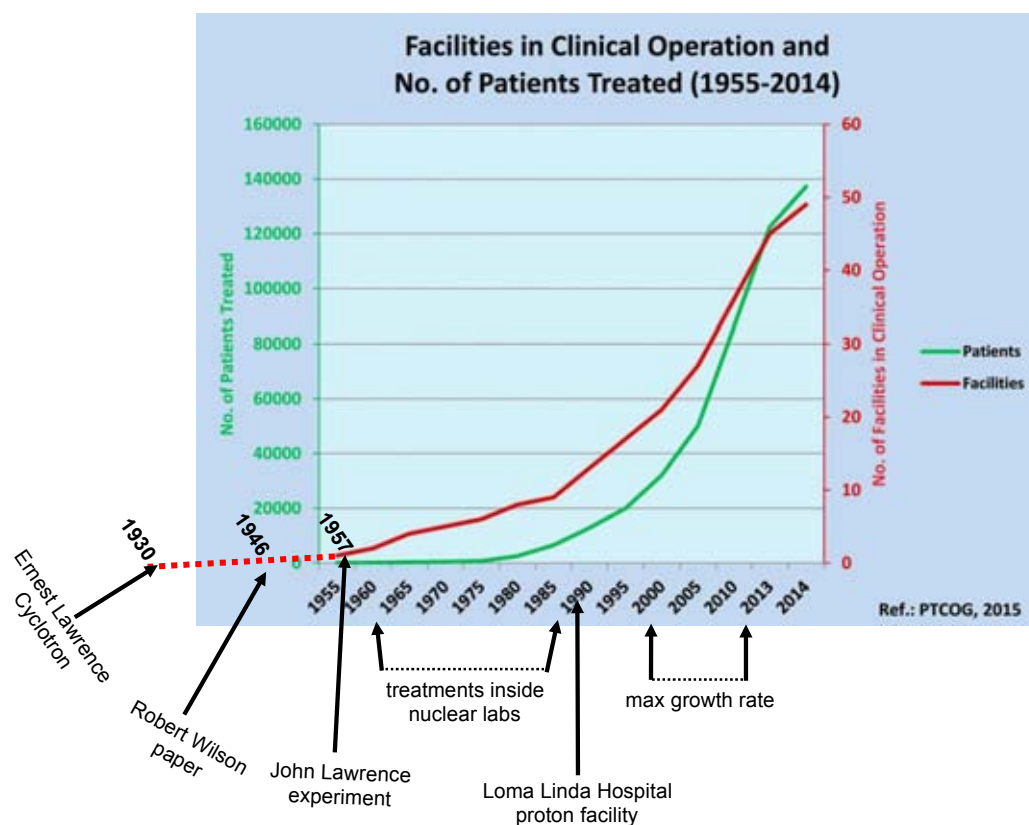


Figure 5. Milestones on the hadron therapy road.

Target Normal Sheath Acceleration (TNSA) is by far the most studied acceleration mechanism also in view of medical applications. Typical proton spectra produced via TNSA are exponential-like up to a cut-off energy which has been so far well below 100 MeV with the largest available lasers. 67 MeV protons were obtained at LANL using a) 80 J pulse energy and b) hollow-cone microtargets³⁷ a record result but both experimental features are not suitable for a Hospital device. The more suitable *table-top* lasers, typically having a few joule energy, presently allow to reach up to few tens of MeV. The use of targets with limited mass³⁸ or surface structuring³⁹ has recently moved the cut-off towards higher energies.

A few years ago the exploitation of radiation pressure in laser plasma interaction at ultra-high intensity emerged from simulations as a brilliant solution to get quasi-monochromatic bunches of energetic ions⁴⁰. The regime of Radiation

Pressure Acceleration (RPA) is usually split in two, namely Hole Boring (HB) and Light Sail (LS), depending on the thickness of the foil used as interaction target. The HB regime applies to thicker targets where the radiation pressure pushes as a piston the interaction surface causing its recession and the steepening of the density profile. A first experiment used a CO₂ infrared laser ($\lambda \approx 10 \mu\text{m}$), for which $n_c \approx 10^{19} \text{ cm}^{-3}$, at a density approaching n_c , using circularly polarized pulses at intensities up to $10^{16} \text{ W cm}^{-2}$. A high-charge proton bunch, whose spectrum peaked at 1 MeV was obtained⁴¹, with a substantial agreement with theory. Production of ion energies useful for medical applications requires substantial advances in CO₂ laser technology⁴². Optical lasers ($\lambda \approx 1 \text{ mm}$) require the development of targets with suitable density values and profiles, by engineering high density gas jets⁴³ or using low-density foams⁴⁴. Differently from most of the acceleration regimes, the presence of a low-density plasma produced by the laser prepulse in front of solid targets may favor HB acceleration. The LS regime applies when very thin foil targets are used and the whole mass of the irradiated portion of the foil is pushed by radiation pressure. The LS's scaling with pulse energy for ultrashort pulses is quite promising²⁴, and quasi-monochromatic spectra are expected. However, first experimental investigations (see Ref. 45 and references therein) showed some promising results but also a number of optimization and stability issues. Recently, extremely intense and sharp rising fs pulses were focused on thin foils covered by a few-micron Carbon nanotube foam in order to induce self-focusing and self steepening of the pulse at a plasma density close to n_c . Enhanced acceleration of carbon ions (up to $\bullet 20 \text{ MeV}$ energy per nucleon) with RPA-LS features has been obtained⁴⁶.

Collisionless shock acceleration (CSA) has been invoked as the mechanism leading to the generation of highly monoenergetic proton spectra (up to $\bullet 20 \text{ MeV}$ energy) in the interaction of CO₂ laser pulses with gaseous hydrogen jet targets⁴⁷. The laser pulse was a sequence of 3 ps pulses with peak intensity $I \approx 6 \cdot 10^{16} \text{ W cm}^{-2}$. The energy spread of less than 1% is the narrowest one observed in laser-plasma acceleration experiments. However, the number of accelerated protons is very low, apparently about three orders of magnitude lower than produced via HB acceleration in similar laser and target conditions⁴¹. Simulations⁴⁷ suggest that CSA could scale with laser intensity in order to produce $> 100 \text{ MeV}$ protons, although this will require at least substantial upgrades in the laser system to allow an increase by two orders of magnitude in intensity. Demonstrating CSA with optical lasers requires the development of target media with suitable density profiles. Although often confused in the literature, HB and CSA are different processes, the latter being effective in the presence of hot electrons. As stated above, a very relevant difference is the number of ions accelerated per shot. In CSA, such number must be low in order to preserve a monoenergetic spectrum.

A few experiments have investigated ion acceleration during the interaction with underdense gas jet targets, which would be suited to high repetition rate operation. In these experiments, ion acceleration typically occurs in the radial direction with respect to the laser propagation axis, as the result of the drilling of a low-density channel (see e.g. Ref. 48 and references therein); such uncollimated ion emission has low brilliance and is not ideal for applications. Collimated, longitudinal ion emission from a gas jet has been observed by focusing a 40-fs laser pulse at $7 \cdot 10^{17} \text{ W cm}^{-2}$, achieving a surprisingly high cut-off of 20 MeV⁴⁹. The interpretation of these results is still not well assessed. It has to be mentioned that next generation lasers might allow a super-relativistic regime of efficient acceleration in underdense plasmas which has been foreseen theoretically almost two decades ago⁵⁰. Once the quiver velocity reaches a given value, the electron mass equals the rest mass of proton, so that protons stick to electrons and are accelerated in a "snow-plow" mode with high efficiency. The simulations of Ref. 50 show that hundreds of MeV ions, collimated by self-generated magnetic fields, may be generated. Finally, for laser intensities above the relativistic transparency threshold for ultrathin targets, it is also possible to remove target electrons completely in a region with a size of the order of the focal radius. In such conditions, ions undergo a Coulomb explosion, i.e. they are accelerated by the electrostatic field generated by themselves which is the highest field attainable for a given target size. Differently from the same process undergoing in clusters⁵¹, Coulomb explosion in thin foils accelerates ions in a preferential direction⁵².

Excluding the case of HB acceleration, in all the ion acceleration schemes a crucial role is played by the *laser pulse contrast*⁵³, more exactly by the ratio between the main pulse peak *power* and the power associated with the light emitted by the laser chain *before* the main pulse itself. In Figure 5 the emitted power vs. time is sketched in a log-log diagram. Though all the early emission is often indicated as *prepulse*, the actual prepulse (left hand peak in Figure 5) is an ultrashort pulse, similar to the main pulse but much weaker, leaking from the electro-optical shutter out of the oscillator. This prepulse usually carries a negligible amount of energy (and power). More dangerous is the *amplified spontaneous emission* (ASE), also called *ASE pedestal*, which lasts typically a few nanosecond and then carries a considerable amount of energy, comparable with the main pulse energy if the contrast is worse than 10^6 . In most of the previous experiments

on laser-driven proton acceleration this *ns*-contrast had to be increased above 10^9 , with several means, including the “plasma mirror” technique⁵⁴. Early emission a few picosecond before the main pulse involves the *ps*-contrast which is

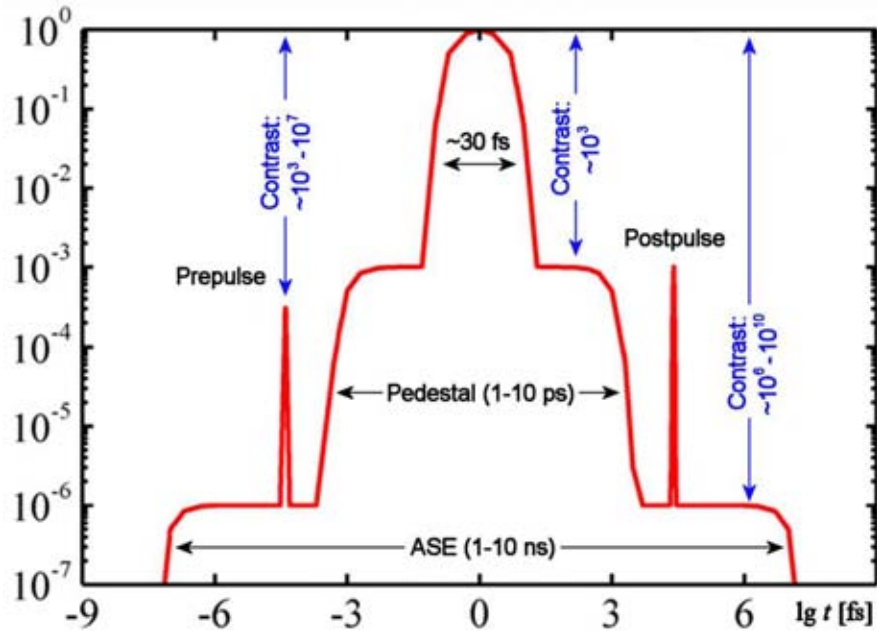


Figure 5. Time evolution of parasitic laser emission before and after the main pulse (image from Ref. 53).

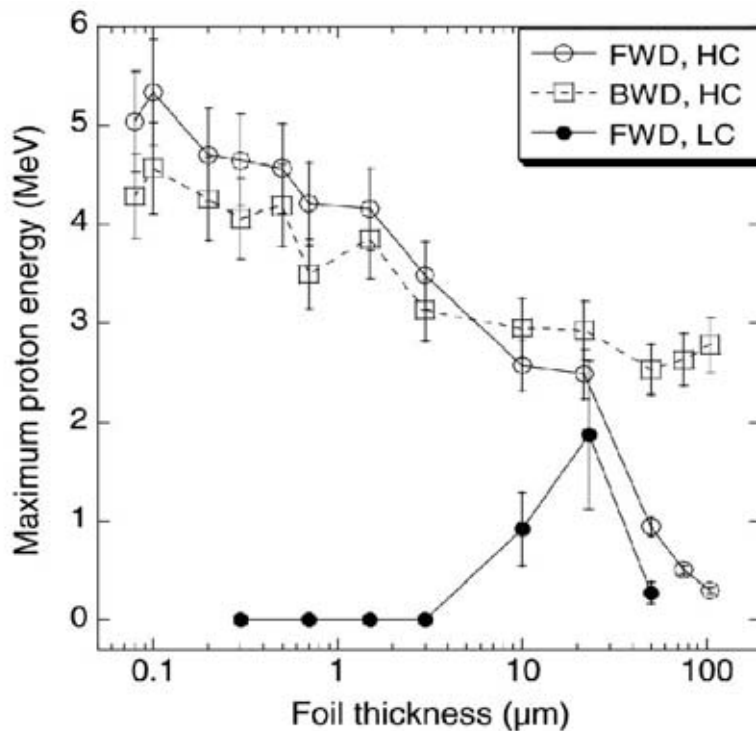


Figure 6. Proton energy vs. foil thickness for high-contrast (HC) and low-contrast (LC) laser pulses (image from Ref. 55).

usually 3-4 orders of magnitude worse than the ASE-contrast, but carries much less energy. It can be nevertheless dangerous as well. It can be reduced only assuring high quality and accuracy in the optical compression of the stretched amplified pulse at the end of the laser chain. A critical feature of the pre-pulse problem is that most of the undesired effects depend on the absolute value of the pre-pulse energy and power and not from the value of the contrast. In other words, increasing the laser power, as requested by most of the advanced schemes of acceleration, the contrast has to be increased correspondingly. This technical point deserves a special attention for the future of laser-driven ion accelerators. A clear example of the relevance of ultrashort laser pulse contrast was provided by the crucial experiment performed by Ceccotti et al. on thin targets⁵⁵, as shown in Figure 6.

Back to the ion accelerators presently operating in clinical background, their census at the end of the year 2015 was about 80 worldwide, possibly they raised close to one hundred today. Though the spectrum of these devices is quite rich and varied, most of them deliver only protons and are based on standard design of cyclotrons, still the true “workhorse” of the proton therapy of tumors. Nevertheless synchrotron, the first machine implemented in a hospital at Loma Linda, is gaining positions in the race, also for his capability of accelerating both protons and C ions, like in the case of CNAO machine shown in Figure 2. A number of alternative devices are under intensive study and test, including the fixed-field alternating-gradient accelerators, proton linacs and dielectric wall accelerators. In the meantime also cyclotrons and synchrotrons are facing a true revolution in their design, in some case already introduced in the market. Most of novelties are due or linked to the use of superconductive materials in the construction of magnets both for the circular machines and for dipoles and quadrupoles assembled in the gantries, with a significant reduction of their weight and footprint. As for the actual costs reduction, the scenario is still controversial. An excellent, concise review of the status of the art in this field has been published recently⁵⁶.

Try to compete *just now* with such a rich offer of clinical solutions would be frustrating for the Laser-induced Ion Acceleration (LIA) community. Nevertheless crude pessimism²³ has to be rejected. It is clear that the possible application of LIA to Ion Beam Therapy (IBT) is still far away and that a long term research and development effort is needed to evaluate its real potential. Several projects are currently active worldwide⁵⁷. For sure a great deal of innovation is required at each stage of the design of a future LIA-IBT facility, once standard beam parameters and reliability will be reached. Strict monoenergeticity may not be required a priori for IBT since the energy spectrum must be modulated in order to obtain the optimal “spread-out Bragg peak” distribution for an optimal dose delivery over the tumor region. Methods to obtain directly such distribution from the native spectrum of laser-accelerated ions have been investigated⁵⁸. The possible success of LIA as an option for IBT also relies on exploiting the peculiar properties of laser-driven ion beams. One of the main advantages would be the option of optical transport to the treatment rooms rather than transporting and steering high energy ion beams with large magnets, so that all costs related to ion beam transport and radiation shielding on the way to the treatment room are removed. Such scenario would benefit further from the development of a compact beam handling system in replacement of the massive and costly gantries used in existing hadrontherapy facilities. Optical control combined with the dose concentration in small-duration bunches may have potential for the irradiation of moving targets⁵⁹, which is a major challenge for the IBT of specific organs. Further progress in laser design, not necessarily towards higher pulse energies, together with ideation of new laser coupling and related processes could provide unexpected solutions. In particular production of few-cycle pulses of high energy seems to be a promising option. The recent proposal of a single-cycle high power fiber laser⁶⁰ has triggered a new acceleration scheme²⁶.

Laser-driven ion sources have progressively revealed to be a unique tool for radiobiological studies, for several good reasons. First there is now a variety of facilities, differing each other by relevant features, allowing a broad range of investigations on biological samples with a degree of availability and flexibility unthinkable with ordinary accelerators either operating in nuclear labs or hospitals. Second, the particle energy provided presently by most of the laser-plasma devices ranges between 1 MeV and a few tens of MeV. Though it is too low for therapy of deep tumors, this range of energy includes the energy of particles at Bragg peaks for any kind of tissues. By using thin layers of sensible tissue or cultures, including tumor cells and ill tissues, it is possible to investigate the radiological action straight in the condition occurring around the Bragg region, i.e. the region of therapeutical interest. Third, the particle bunches provided by laser techniques can deliver on sample an unprecedented dose-rate, several orders of magnitude higher than any other device, so allowing to study unexplored regimes of very high specific dose. In this condition each cell can be reached by a number $\gg 1$ of particles in a time period much shorter than any DNA repairing time. It is also possible investigate the

occurrence of non-linear or collective effects induced by such “dense” ionizing radiation. The high dose rate is partly due to the high charge attainable with laser techniques but mostly to the ultra-short duration of the bunches. This latter feature actually is the fourth good reason for using laser acceleration, since it could allow for the first time to investigate very early processes in the complicate chain of physical, chemical and biological effects leading to either cure of tumors or damage of healthy tissues.

This unique opportunity has also triggered the advance of specific dosimetry^{61,62}. In single shot irradiations, on-cell dose rates of the order of 10^9 Gy s⁻¹ have been estimated⁶³ from measurements. Such values are some nine orders of magnitude higher than with conventional means. It is therefore important to assess the biological effect of laser-driven ions with respect to conventional ion beams used in IBT and to other sources of radiation. To this aim, the Relative Biological Effectiveness (RBE) has been measured in several experiments. Two fundamental experiments^{64,65} by Yogo et al. at JAEA lab in Japan with • 2 MeV laser-accelerated protons found a RBE value of 1.2 ± 0.1 , comparable to that of protons from conventional accelerators⁶⁶ having a similar value of Linear Energy Transfer (LET). Those experiments were also relevant for their sophisticated set-up of magnets allowing to separate the protons from electrons and photons, deflect the proton beam first towards an energy selecting pinhole, then towards the sample as shown in Figure 7.

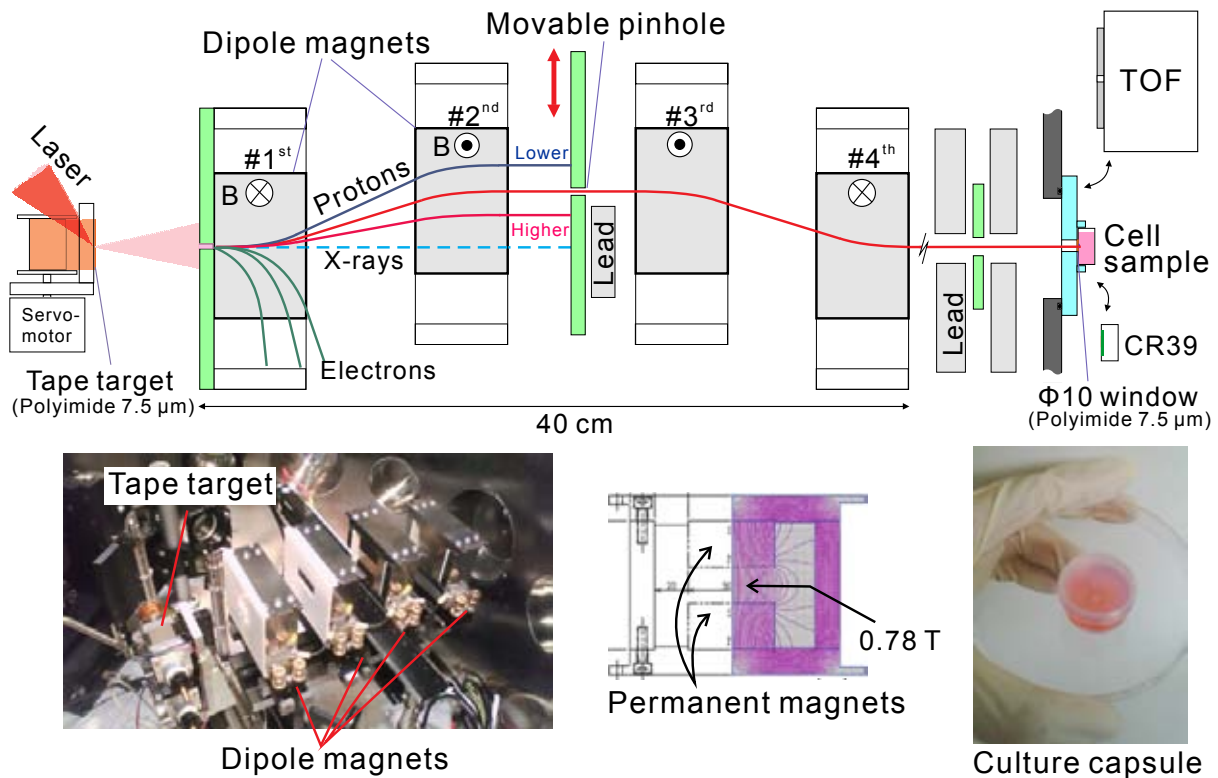


Figure 7. Layout and details describing the second Yogo's experiment⁶⁴ equipped with Energy-Selection System (image from Ref. 25).

Another interesting biological application of energetic protons and ions produced with laser techniques is radiography². In fact, the unique properties of protons, multicharged ions and electron beams generated by high-intensity laser-matter interactions, particularly in terms of spatial quality and temporal duration, have opened up a totally new area of high-resolution radiography. Laser-driven radiographic sources obtained by irradiation of clustered gases were proved to be particularly effective, leading to large-field high-contrast images with 1 μm spatial resolution. Faenov et al.⁶⁷ produced $> 10^{18}$ multicharged carbon and oxygen ions per laser shot by irradiating CO₂ clusters from a gas-jet. The ion energy was measured to be ≥ 300 KeV. With such rather divergent but uniform ion beam, ionography of a spider net revealed submicron details, as shown in Fig. 7.

Finally, isotope production by proton-induced nuclear reactions has been achieved with Laser-induced Ion Acceleration and then proposed as a way to produce radionuclides and positron emitters for medical diagnostics⁶⁸. Short-lived positron emitters are of great interest for medical imaging Positron Emission Tomography (PET) and are commonly produced using \bullet 20 MeV protons or deuterons from cyclotrons, i.e. in an energy range currently well accessible with LIA. Reported values of the integrated activity produced using “table-top” femtosecond lasers typically operating at 10 Hz are some two orders of magnitude lower than required for use in PET⁶⁹. Higher activities and a large number of emitters were produced with larger lasers, but their low repetition rate makes them unsuitable for application in PET. On the basis of the extrapolation of present results and additional theoretical and simulation work⁷⁰, the activity values required for PET may be reached with table-top lasers (typically delivering a few Joules, 20-30 fs pulses tightly focused to achieve intensities of \bullet 10^{20} W cm⁻²) working at kHz rate. A recent work reports on laser-driven deuteron beams optimized for isotope production⁷¹. Nuclear reactions driven by proton or deuteron beams are also of interest for production of neutrons, which has been observed either from direct laser interaction with deuterated targets⁷² or by means of a secondary target, i.e. in a “pitcher-catcher” configuration⁷³.

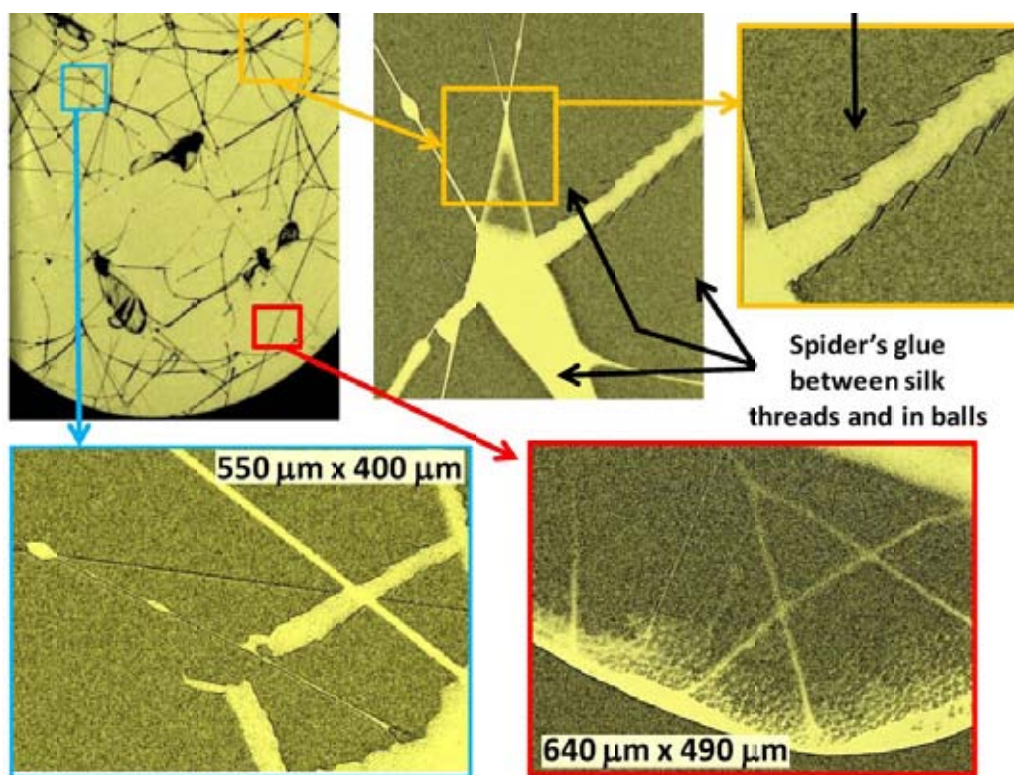


Figure 7. Ion Microscopy with Carbon and Oxygen ions produced by laser interaction with a CO₂ clustered jet: contact image of a spider web and magnified details showing high resolution (image from Ref. 67).

3. CURRENT RADIATION THERAPY AND LASER-DRIVEN ELECTRON ACCELERATION

As already noticed in the Introduction, more than 90% of radiation treatments on tumors are presently based on the use of RF-driven linear accelerators of electrons, mostly after conversion of relativistic electrons into hard X-rays. Since the first trials at the end of the 19th Century, the progress of this medical technique was so vast and deep that cannot be resumed here. There is now a variety of advanced devices and protocols for Hospital practice whose very sophisticated features allow high precision irradiation of the tumor with a minimized detrimental effects on healthy tissues and critical organs. Among them Stereotactic Radiotherapy (SRT)¹² offers a method for delivering high doses of radiation in a single

or limited number of fractions to a small volume encompassing the tumor while minimizing the dose to adjacent normal structures due to a large dose gradient and therefore reducing the risk of sequelae. It uses a multitude of small beams requiring extremely precise control of position and movement of the linear accelerator. Moreover, SRT needs a real-time image-guided technique that tracks the target during treatment allowing an automatic reset based on the acquired image. SRT enables hypo-fractionated treatments, i.e strong doses delivered in a small number of fractions, due to its high level of accuracy.

If we limit our consideration to energy and dose, present table-top laser driven electron accelerators can be already considered as competitors of the RF-linac's. In fact, most of the performances usually asked to electron bunches, including energy range and delivered dose have been achieved. Collimation, monochromaticity, pointing stability, etc. are requested at a moderate levels already available with laser techniques, while the main effort has still to be addressed to efficiency, stability and reliability of the process in order to provide clinically acceptable devices. As far as the efficiency is concerned, in an experiment performed at CEA-Saclay (France) a regime of electron acceleration of high efficiency was found, using a 10 TW laser and a supersonic jet of Helium¹³. This *table-top* accelerator delivered high-charge (nC), reproducible, fairly collimated, and quasimonochromatic electron bunches, with peak energy in the range 10–45 MeV. In Figure 8 a typical cross section of the relativistic electron beam at 25 MeV is shown, after deconvolution of experimental data from the SHEEBA radiochromic film stack device⁷⁴.

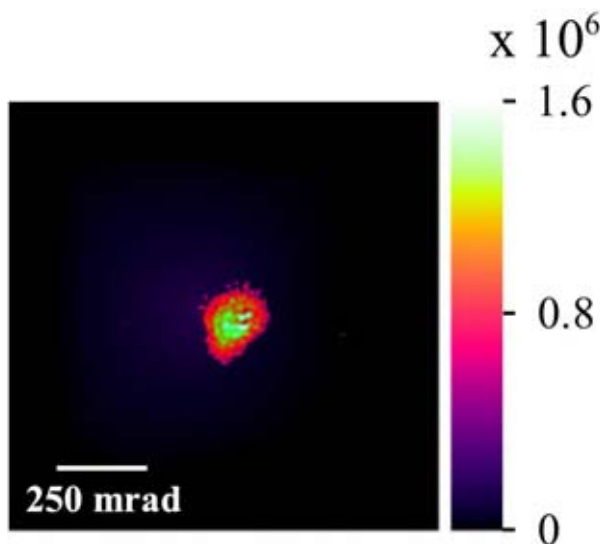


Figure 8 . 25-MeV electron beam cross section (image from Ref. 13).

3D particle-in-cell simulation performed with the numerical code CALDER⁷⁵ revealed that the unprecedented efficiency of this accelerator was due to the achievement of a physical regime in which multiple electron bunches are accelerated in the gas-jet plasma during the action of each laser shot. With this experiment, laser driven electron acceleration approached the threshold of suitability for medical uses, in particular for Intra-Operative Radiation Therapy (IORT) of tumors^{8,9}. Comparison of the main parameters of electron bunches produced by a commercial RF Hospital accelerator for IORT treatment and those of the that laser driven accelerator is shown in the Table 1. Notice that, while main clinical parameters, including mean current and released energy (proportional to the dose) are comparable, bunch duration is 10⁶ times shorter and consequently the peak current (proportional to max the dose-rate) 10⁶ times higher. In the same experiment electron bunches of ≈ 40 MeV were converted, via bremsstrahlung in a tantalum foil, into gamma rays with a strong component in the range 10-20 MeV, which matches the Giant Dipole Resonance of nuclei. This gamma rays could in turn activate a foil of gold according to the nuclear reaction $^{197}\text{Au}(\gamma,n)^{196}\text{Au}$. The number of radioactive gold atoms produced in this way was measured¹³. This achievement opens the way to table-top laser-driven nuclear physics and production of radio-isotopes for medical uses.

Linac	IORT-NOVAC7	LIAC	Laser-Linac (experimental)
<i>Company</i>	<i>(SORDINA SpA)</i>	<i>(Info & Tech Srl)</i>	<i>(CEA-Saclay)</i>
<i>Max Electron Energy</i>	<i>10 MeV</i>	<i>12 MeV</i>	<i>45 MeV</i>
<i>Available Energies</i>	<i>(3, 5, 7, 9 MeV)</i>	<i>(4, 6, 9, 12 MeV)</i>	<i>(5 to 45 MeV)</i>
<i>Peak current</i>	<i>1.5 mA</i>	<i>1.5 mA</i>	> 1.6 KA
<i>Bunch duration</i>	<i>4 μs</i>	<i>1.2 μs</i>	< 1 ps
<i>Bunch charge</i>	<i>6 nC</i>	<i>1.8 nC</i>	<i>1.6 nC</i>
<i>Repetition rate</i>	<i>5 Hz</i>	<i>5-20 Hz</i>	10 Hz
<i>Mean current</i>	<i>30 nA @5Hz</i>	<i>18 nA @10Hz</i>	16 nA @10Hz
<i>Released en. in 1 min.</i>	<i>18 J @ 9 MeV</i>	<i>14 J @12 MeV</i>	21 J @20 MeV

Table 1. Comparison between commercial RF-linac's and the experimental Laser-linac (table from Ref. 53).

As already said in the Introduction, in most cases electrons delivered by a RF-linac currently used in Hospitals, are not sent directly on the tumor but previously converted into photons (hard X-rays) by bremsstrahlung through a suitable target. Of course this is possible also for electrons of comparable energy currently produced in high-power laser labs. Laser-driven electron accelerators would be then ready and produce X-rays for clinical uses provided a suitable stability, uniformity and reproducibility of the electron bunches will be reached. The Laser-driven Electron Accelerator for Radiotherapy of Cancer (LEARC) project⁷⁶ aims at speeding up the transfer of a novel laser-based technology to radiotherapy of cancer. The first point to be addressed is to make the driving laser, suitable for efficient acceleration, as reliable and easy to use as possible, with a duty cycle allowing an effective medical use. Second, the laser beam transport to the mini-linac located close to the patient has to be optimized. Third, the most important point, provide the mini-linac with an acceleration process stable and reproducible at each laser shot, also at high repetition rates. This task needs the detailed investigation of both known and novel acceleration schemes and then the optimization of both laser and target parameters. Gas jets are the most investigated targets so far and a special effort will be devoted in making them fully operative at high repetition rate. But other targets can be considered and studied to produce the plasma acceleration path, including gas cells and thin foil stripes. A crucial and difficult task is to deliver electrons of the requested energy and change their energy on demand. Several experiments proved this possibility at some extent but the methods used are hardly transferable in a clinical device which exclude continuous tuning or frequent re-tuning of its components. It has to be recognized that ultrashort laser systems and laser-plasma interactions are not easy to handle and put under complete control.

It is also interesting to consider electrons of energies outside the energy range between 1 and 25 MeV currently provided by commercial accelerators for radiation therapy. Both extremes of sub-relativistic and very high energy electrons (VHEE) are presently studied in view of specific applications. Recently, outstanding performances were obtained with sub-MeV electron bunches produced by the LESM laser-plasma device⁷⁷. This source delivers ultrashort bunches of electrons with kinetic energy around 300 keV, uniformly over a large solid angle. The device is presently setup for radiobiological tests covering a previously untested energy range. Each bunch combines high charge with short duration and sub-millimeter range into a record instantaneous dose rate, as high as 10^9 Gy/s. Both such a high dose rate and high level of Relative Biological Effectiveness, attached to sub-MeV electrons, make this source very attractive for radiobiological tests on thin samples of living cells in similar way as discussed in the previous section for sub-relativistic protons. On the opposite side, very high energy electrons (VHEEs) with energies in the range 150-250 MeV, which penetrate deeply into tissue where the dose can be absorbed within the tumor volume with a relatively small penumbra have been proposed for radiation therapy of tumors a few years ago⁷⁸. Electrons in this range of energy can be produced with plasma acceleration driven by laser of hundreds of TW. Parameters of bunches of such an energy and their dosimetry is under active investigation^{79,80}.

Electron average energy	260 keV
Spectral shape	exponential
Bunch divergence	20° FWHM
Bunch charge	> 100 pC
Repetition rate	up to 10 Hz
Bunch duration on the sample	3.5 ps
Peak current	> 100A
Non-uniformity on sample	< 10% (over 25 shots)
Stopping power in water	2.49 MeV cm ² /g
Range in water	0.68 mm
Dose per pulse	3.5 ± 0.3 mGy
Peak dose rate	10 ⁹ Gy/s
Average dose rate	35 mGy/s

Table 2 Main features of the laser-driven sub-relativistic electron sources LESM (table from Ref. 77).

Secondary sources of high-energy photons are another exciting by-product of laser-driven electron acceleration. They include the above mentioned bremsstrahlung sources and betatron sources originated during the laser wakefield process itself by the strong restoring forces acting on the electron bunches. Further, the electron beam produced by laser-driven acceleration can be sent to collide with another powerful laser pulse and produce energetic photons by Compton scattering^{32,81}. Generation of radiation via Thomson scattering of a laser pulse by energetic counter-propagating electrons was initially proposed in 1963^{82,83} as a quasi monochromatic and polarized photons source. With the development of ultra intense lasers the interest on this process has grown and the process is now being exploited as a bright source of energetic photons from UV to gamma-rays and atto-second sources in the full nonlinear regime. In view of medical application, tuneability of the X-ray photon energy may be an important option of an *all-optical* laser-based Thomson source. Recent experiments performed by Sarri et al.⁸⁴ and Liu et al.⁸⁵ obtained photons of several tens of MeV and opened a new phase of these studies.

We mentioned in the previous Section radiography performed with protons and ions. A similar technique has been used also with electron beams produced by laser-driven accelerators⁸⁶. The laser-driven electron sources included interaction with both ordinary and clustered gas jets⁸⁷. Figure 9 shows an example of test samples and their electron radiography obtained from a laser-produced electron beam. Resolution in this case was better than 60 μm, but 10 μm can be achieved.



Figure 9. The sample (left) and its own electron radiograph. Overall size: 35 mm x 48 mm (image from Ref. 83).

Radiobiological studies with relativistic electrons generated by laser-plasma interactions, including evaluation of their RBE, have been performed in the last decade. Results have been also compared with RBE of electrons produced with conventional RF-linac's^{88,89}. Very recently, a multidisciplinary team of scientists performed an RBE evaluation of electrons from a laser-driven accelerator impinging on several cell lines (including tumor tissues). The experiment included measurements of Micronucleus Frequency, Telomere Shortening and Cell Viability (see Figure 10). The same cell lines were also irradiated with standard reference X-rays and electrons from a RF-linac for IORT. The three series of results were compared, giving comparable values within the error bars, except for a single cell line for which the laser-produced electron bunches resulted slightly more effective⁹⁰.

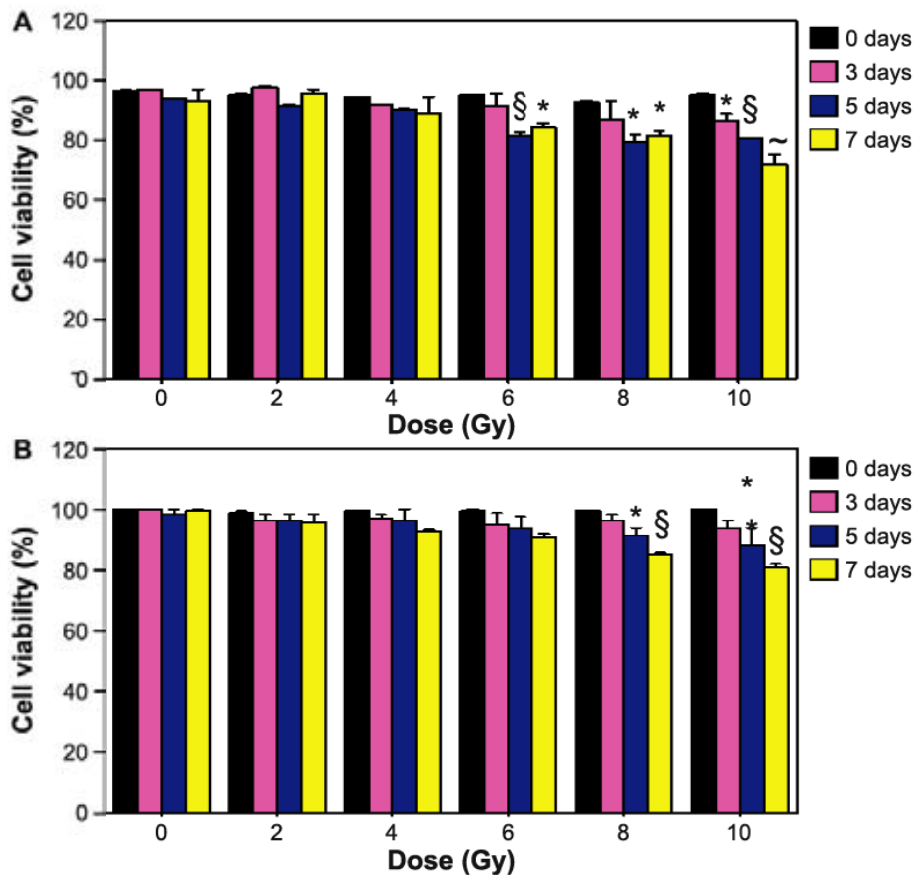


Figure 10. Cell Viability assay in a human cancer cell line after A: exposure to laser-generated electrons and B: conventional accelerated particle beams. All values are expressed as mean \pm SD of three independent experiments. Statistical differences SD were assessed for each dose compared to negative control (* $P \leq 0.05$; § $P \leq 0.01$; ~ $P \leq 0.001$) (image from Ref. 90).

Current studies on biological effects of laser-produced electron bunches need a strong support of a) dosimetry, suitably revised in order to take into account the unprecedented features of these bunches, mainly in terms of duration and instantaneous dose rate³; b) simulation, mostly with a correct application of the Monte Carlo code based on GEANT4 toolkit⁹¹.

Great deal of research has being devoted to the comprehension of biophysical events triggered by an initial energy deposition inside the first ionization tracks. Ultrashort electron bunches delivered by laser-driven plasma accelerators and secondary femtosecond photon sources are suitable for the development of high energy radiation femtochemistry (HERF)³⁰ in the prethermal regime of secondary low energy electrons and for a real-time imaging of radiation-induced biomolecular alterations at the nanoscopic scale. It would be possible then to correlate early radiation events triggered by ultrashort radiation sources with the molecular approach of Relative Biological Effectiveness (RBE)⁹².

4. A PERSPECTIVE VIEW

The story began more than 120 years ago (see Figure 11). Since then, a continuous progress was made in understanding several kinds of ionizing radiation, produce that radiation in form of photons, electrons and ions, use it for many purposes, first of all for medical applications. More than 50 years ago powerful lasers proved to be another source of ionizing radiation and laser-produced dense plasmas opened a vaste field of novel physics to be investigated. Some 38 years ago¹⁴ a brilliant theory suggested how to use ultrashort laser pulses to accelerate particles in plasmas, whenever they could get enough power and 32 years ago¹⁵ the way was opened to reach that power. Since then, and mostly in the

last 25 years, the community of scientists working on laser-driven particle acceleration grew up and many great, somehow unexpected results were obtained.

On A New Kind of Rays*

Wilhelm Konrad Röntgen

1. A discharge from a large induction coil is passed through a Hittorf's vacuum tube, or through a well-exhausted Crookes' or Lenard's tube. The tube is surrounded by a fairly close-fitting shield of black paper; it is then possible to see, in a completely darkened room, that paper covered on one side with barium platinocyanide lights up with brilliant fluorescence when brought into the neighborhood of the tube, whether the painted side or the other be turned towards the tube. The fluorescence is still visible at two metres distance. It is easy to show that the origin of the fluorescence lies within the vacuum tube.

2. It is seen, therefore, that some agent is capable of penetrating black card-

Figure 11. The *incipit* of the 1895 Roentgen paper

This is “from where” we come. This short-review paper try to provide the community with some elements to understand “where we are” and maybe a few indication on “where to go”. For sure the scientific crop of these enthusiastic years was considerable, in laser and plasma physics, radiation physics, radiation biology. How far we are from setting up a prototype device for clinical use is hard to say. Maybe a little closer for electrons (and then photons), a little farer for proton/ions. For sure there is no reason for giving this exciting navigation up, since we have progress of knowledge as our lighthouse: successful landing may be not so far.

ACKNOWLEDGEMENT

Author is deeply grateful to Toshi Tajima for his magistral teaching and friendly support. Author also acknowledges financial support by the ELI-Italy project funded by the Italian Ministry of Research and University. The author also thanks the whole team at the Intense Laser Irradiation Laboratory of INO-CNR in Pisa for reference information and for the continuing enlightening discussions on the subject.

REFERENCES

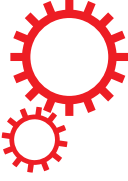
- [1] Giulietti, A. (Editor) “Laser-Driven Particle Acceleration Towards Radiobiology and Medicine” Springer Series on “Biological and Medical Physics, Biomedical Engineering”, ISBN 978-3-319-31563-8, Springer International Publishing AG Switzerland (2016).
- [2] Faenov, A. Ya., Pikuz, T.A., Kodama, R., Chapter 11 in Ref. [1] (2016).
- [3] Labate, L., Lamia, D., Russo, G., Chapter 9 in Ref. [1] (2016).
- [4] International Atomic Energy Agency, Absorbed Dose Determination in External Beam Radiotherapy: An International Code of Practice for Dosimetry Based on Standards of Absorbed Dose to Water, IAEA Technical Reports Series no. 398 - IAEA, Vienna (2000).
- [5] Simons, A., Chapter 5 in Ref. [1] (2016).
- [6] IARC, Cancer Fact Sheets, Globocan, <http://globocan.iarc.fr/>
- [7] Rodin, D. et al., *The Lancet Oncology* **15**, 378 (2014).
- [8] Veronesi, U. et al., *Ann. Oncol.* **12**, 997 (2001).
- [9] Beddar, A.S. et al., *Med. Phys.* **33**, 1476 (2006).
- [10] <http://www.businesswire.com/news/home/20140313005577/en/Research-Markets-External-Beam-Radiation-Therapy-Devices>.
- [11] Baskar, R. et al., *Int. J. Med. Sci.* **9**, 193 (2012).
- [12] Mouttet-Audouard, R., Lacornerie, T., and Lartigau, E., Chapter 3 in Ref. [1] (2016).
- [13] Giulietti, A. et al., *Phys. Rev. Lett.* **101**, 105002 (2008).
- [14] Tajima, T., Dawson, J., *Phys. Rev. Lett.* **43**, 267 (1979).
- [15] Strickland, D. and Mourou, G., *Opt. Commun.* **56**, 219 (1985).
- [16] Jeong, T. M., and Lee, J., Chapter 6 in Ref. [1] (2016).
- [17] Chen, M., and Shen, Z.-M., Chapter 7 in Ref. [1] (2016).
- [18] Wilson, R. R., *Radiology* **47**, 487 (1946).
- [19] Lawrence, J., *Cancer* **10**, 795 (1957).
- [20] Jermann, M., *Int. J. Particle Ther.* **2**, 50 (2015).
- [21] Goitein, M. A., Lomax, J. and Pedroni, E. S., *Phys. Today* **55**, 45 (2012).
- [22] Schippers, M., “Beam Delivery System for Particle Therapy”, in “Proton and Ion Carbon Therapy”, C.-M. Charlie Ma and Tony Lomax Editors, CRC Press (Boca Raton, FL) page 43 (2013).
- [23] Linz, U., and Alonso, J., *Phys. Rev. Accelerators and Beams* **19**, 124802 (2016).
- [24] Borghesi, M. and Macchi, A., Chapter 10 in Ref. [1] (2016).
- [25] Yogo, A., Chapter 11 in Ref. [1] (2016).
- [26] Tajima, T., Chapter 13 in Ref. [1] (2016).
- [27] Veksler, V.I., *Proc. CERN Symp. on High Energy Accel. and Pion Physics (Geneva, Switzerland) Vol. 1*, 80 (1956).
- [28] Fews, A. P., Norreys, P. A., Beg, F. N., Bell, A. R., Dangor, A. R., Danson, C. N., Lee, P., and Rose, S. J., *Phys. Rev. Lett.* **73**, 1801 (1994).
- [29] Bulanov S.S. et al., *Med. Phys.* **35**, 1770 (2008).
- [30] Gauduel, Y.A., Chapter 2 in Ref. [1] (2016).
- [31] Minafra, L., Bravatà, V., Cammarata, F. P., Forte, G. I., Chapter 4 in Ref. [1] (2016).
- [32] Gizzi, L.A., Chapter 8 in Ref. [1] (2016).
- [33] Lundqvist, S. (Editor), *Nobel Lectures in Physics (1922-1941)*, pag. 425, World Scientific Publishing Co.,

Singapore (1998).

- [34] Macchi, A., Borghesi, M., Passoni, M., *Rev. Mod. Phys.* **85**, 751 (2013).
- [35] Daido, H., Nishiuchi, M., and Pirozhkov, A. S., *Rep. Prog. Phys.* **75**, 056401 (2012).
- [36] Mulser, P. and Bauer, D., *High Power Laser-Matter Interaction*, Springer Tracts in Modern Physics (Springer, New York), Vol. **238** (2010).
- [37] Gaillard, S.A., et al, *Phys. Plasmas* **18**, 056710 (2011).
- [38] Zeil, K., et al., *Plasma Physics and Controlled Fusion* **56**, 084004 (2014).
- [39] T. Ceccotti, T., et al., *Phys. Rev. Lett.* **111**, 185001 (2013).
- [40] Macchi, A., Cattani, F., Liseykina, T.V., Cornolti, F., *Phys. Rev. Lett.* **94**, 165003 (2005).
- [41] Palmer, C.A.J., et al., *Phys. Rev. Lett.* **106**, 014801 (2011).
- [42] Bravy, B.G., et al., *Opt. Express* **20**, 25536 (2012).
- [43] Sylla, F., et al, *Review of Scientific Instruments* **83**, 033507 (2012).
- [44] Zani, A., et al., *Carbon* **56**, 358 (2013).
- [45] Kar, S., et al., *Plasma Physics and Controlled Fusion* **55**, 124030 (2013).
- [46] Bin, J.H., et al., *Phys. Rev. Lett.* **115**, 064801 (2015).
- [47] Haberberger, D., et al., *Nat. Phys.* **8**, 95 (2012).
- [48] Lifschitz, A., et al., *New Journal of Physics* **16**, 033031 (2014).
- [49] Fukuda, Y., et al., *Phys. Rev. Lett.* **103**, 165002 (2009).
- [50] Esirkepov, T., et al., *JETP Letters* **70**, 82 (1999).
- [51] Ditmire, T. et al., *Nature* **386**, 54 (1997).
- [52] Bulanov, S.S., et al., *Phys. Rev. E* **78**, 026412 (2008).
- [53] Giulietti, A., et al., *Laser-Plasma Particle Sources for Biology and Medicine*, in *Progress in Ultrafast Intense Laser Science XII*, K. Yamanouchi et al. (eds.), Springer Series in Chemical Physics 112, DOI 10.1007/978-3-319-23657-5_8, Springer Int. Pub. Switzerland (2015).
- [54] Perry, M. D., et al., *Opt. Lett.* **24**, 160 (1999).
- [55] Ceccotti, T., et al., *Phys. Rev. Lett.* **99**, 185002 (2007).
- [56] Owen, H., Lomax, A., Jolly, S., *NIMA* 809, 96 (2016).
- [57] Ledingham, K.W.D., Bolton, P.R., Shikazono, N., Ma, C.M.C., *Applied Sciences* **4**, 402 (2014).
- [58] Yoo, S., et al., *Australasian Physical and Engineering Sciences in Medicine* **37**, 635 (2014).
- [59] Hofmann, K.M., Schell, S., Wilkens, J.J., *Journal of Biophotonics* **5**, 903 (2012).
- [60] Mourou, G., Brocklesby, B., Tajima, T., & Limpert, J., *Nature Photonics* **7**, 258 (2013).
- [61] Fiorini, F., et al., *Phys.Med. Biol.* **56**, 6969 (2011).
- [62] Zeil, K., et al., *Applied Physics B* **110**, 437 (2013).
- [63] Doria, D., et al., *AIP Advances* **2**, 011209 (2012).
- [64] Yogo, A., et al., *Appl. Phys. Lett.* **94**, 181502 (2009).
- [65] Yogo, A., et al., *Appl. Phys. Lett.* **98**, 053701 (2011).
- [66] Folkard, M., *Int. J. Rad. Biol.* **69**, 729 (1996).
- [67] Faenov, A. Ya., et al., *Appl. Phys. Lett.* **95**, 101107 (2009).
- [68] Spencer, I., et al., *Nucl. Inst. Meth. Phys. Res. B* **183**, 449 (2001).
- [69] Fujimoto, M. K., et al., *Rev. Sci. Instrum.* **80**, 113301 (2009).
- [70] Lefebvre, E., d'Humières, E., Fritzier, S., Malka, V., *J. Appl. Phys.* **100**, 113308 (2006).
- [71] Maksimchuk, A., et al., *Applied Physics Letters* **102**, 191117 (2013).
- [72] Zulick, C., et al., *Appl. Phys. Lett.* **102**, 124101 (2013).
- [73] Roth, M., et al., *Phys. Rev. Lett.* **110**, 044802 (2013).
- [74] Galimberti, M., et al., *Rev. Sci. Instrum.* **76**, 053303 (2005).
- [75] Lefebvre, E., et al., *Nucl. Fusion* **43**, 629 (2003).
- [76] Baffigi, F., et al., *The LEARC Concept: Laser-driven Electron Accelerator for Radiotherapy of Cancer*, INO-CNR Internal Report (2014). Available at: www.ilil.ino.it
- [77] Labate, L., et al., *Journal of Physics D: Applied Physics* **49**, 275401 (2016).
- [78] DesRosiers, C., Moskvina, V., Bielajew, A., Papiez, L., *Phys. Med. Biol.* **45**, 1781 (2000).
- [79] Moskvina, V., et al., *Medical Physics*. **39**, 3813 (2012).
- [80] Subiel, A., et al., *Phys. Med. Biol.* **59**, 5811 (2014).
- [81] Gizzi, L. A., et al., *IEEE Trans. PLASMA Sci.* **39**, 2954 (2011).
- [82] Milburn, R. H., *Phys. Rev. Lett.* **10**, 75 (1963).

- [83] Bemporad, C., Milburn, R. H., Tanaka, N., and Fotino, M., Phys. Rev.B **138**, 1546 (1965).
- [84] Sarri, G., et al., Phys. Rev. Lett. **113**, 224801 (2014).
- [85] Liu C., et al., Optics Letters **39**, 4132 (2014).
- [86] Bussolino, G.C. et al., J. Phys. D. Appl. Phys. **46**, 245501 (2013).
- [87] Koester, P., et al., Laser and Particles Beams **33**, 331 (2015).
- [88] Laschinsky, L., et al., J. Radiat. Res. **53**, 395 (2012).
- [89] Labate L., et al., Proc SPIE **8779** (2013).
- [90] Andreassi, M.G., et al, Radiation Research **186**, 245 (2016).
- [91] Lamia D., et al., Nucl. Instrum. Methods Phys. Res. A **786**,113 (2015).
- [92] Gauduel, Y.A., Journal of Instrumentation **12**, C02048 (2017).

SCIENTIFIC REPORTS



OPEN

Micron-scale mapping of megagauss magnetic fields using optical polarimetry to probe hot electron transport in petawatt-class laser-solid interactions

Gourab Chatterjee^{1,6}, Prashant Kumar Singh¹, A. P. L. Robinson², D. Blackman³, N. Booth², O. Culfa³, R. J. Dance^{3,4}, L. A. Gizzi⁵, R. J. Gray⁴, J. S. Green², P. Koester⁵, G. Ravindra Kumar¹, L. Labate⁵, Amit D. Lad¹, K. L. Lancaster^{2,3}, J. Pasley^{2,3}, N. C. Woolsey³ & P. P. Rajeev²

The transport of hot, relativistic electrons produced by the interaction of an intense petawatt laser pulse with a solid has garnered interest due to its potential application in the development of innovative x-ray sources and ion-acceleration schemes. We report on spatially and temporally resolved measurements of megagauss magnetic fields at the rear of a 50- μm thick plastic target, irradiated by a multi-picosecond petawatt laser pulse at an incident intensity of $\sim 10^{20} \text{ W/cm}^2$. The pump-probe polarimetric measurements with micron-scale spatial resolution reveal the dynamics of the magnetic fields generated by the hot electron distribution at the target rear. An annular magnetic field profile was observed ~ 5 ps after the interaction, indicating a relatively smooth hot electron distribution at the rear-side of the plastic target. This is contrary to previous time-integrated measurements, which infer that such targets will produce highly structured hot electron transport. We measured large-scale filamentation of the hot electron distribution at the target rear only at later time-scales of ~ 10 ps, resulting in a commensurate large-scale filamentation of the magnetic field profile. Three-dimensional hybrid simulations corroborate our experimental observations and demonstrate a beam-like hot electron transport at initial time-scales that may be attributed to the local resistivity profile at the target rear.

An intense laser pulse focussed on a solid target can generate relativistic electron currents reaching mega-ampere levels^{1–3}. The generation and transport of these hot electron currents through the solid are central to a number of potential applications including the development of novel x-ray sources⁴ and alternate particle acceleration schemes⁵. For instance, the hot electron distribution at the target rear seeds the growth of the sheath fields responsible for target-normal-sheath-acceleration and plays an important role in determining the laminarity and spatial uniformity of the proton and ion emission profiles⁶ – a principal parameter in deciding the viability of such intense-laser-based energetic ion sources for their diverse applications in medical imaging and ion therapy⁵. In addition, in the fast ignition variant of inertial confinement fusion, the generation and collimated transport of the ignitor electron pulse is crucial to the energy transfer from the point of laser-coupling to the imploded fuel hot-spot. Self-divergence of the hot electron beam results in inefficient heating of the fuel, imposing impractical demands on the ignitor laser pulse in terms of energy and intensity³. Consequently, various experimental techniques^{7–12} corroborated by numerical simulations^{13–16} have been designed to investigate hot electron transport by employing a variety of diagnostics such as rear-side optical self-emission^{7,10}, and proton radiography^{8,12}. The hot

¹Tata Institute of Fundamental Research, Homi Bhabha Road, Mumbai, 400005, India. ²Central Laser Facility, STFC Rutherford Appleton Laboratory, Chilton, Didcot, OX11 0QX, UK. ³York Plasma Institute, University of York, Heslington, York, YO10 5DQ, UK. ⁴SUPA, Dept. of Physics, University of Strathclyde, Glasgow, G4 0NG, UK. ⁵Intense Laser Irradiation Laboratory (ILIL), INO-CNR, Pisa, Italy. ⁶Present address: Max Planck Institute for the Structure and Dynamics of Matter, Luruper Chaussee, 22761, Hamburg, Germany. Correspondence and requests for materials should be addressed to P.P.R. (email: rajeev.pattathil@stfc.ac.uk)

Received: 18 November 2016

Accepted: 17 July 2017

Published online: 21 August 2017

electron transport process is inherently transient and confined to micron-scales, and therefore warrants diagnostics with a *simultaneous spatio-temporal resolution* capable of capturing the rapidly evolving dynamics of the hot electron distribution¹⁷.

Mapping the evolution of the magnetic fields produced by the hot electron currents streaming into the solid target can open a window to the complex dynamics of the hot electron currents in the solid target. These magnetic fields, with magnitudes approaching gigagauss levels^{18, 19}, are pivotal in determining the propagation of the hot electron currents that generate them, leading to a complex interplay between the hot electron currents and the magnetic fields.

In order to study the influence of the target material in the hot electron transport process, one needs to measure the magnetic fields set up at the rear surface of the target²⁰. The spatial profile of the magnetic fields at the target rear is determined by the spatial profile of the hot electron currents evolved through their transport across the bulk of the target. Detailed measurements of these magnetic fields enable one to make detailed inferences about transport in the bulk target as well as detailed comparisons with numerical models. To understand the dynamics of hot electron transport, a simultaneous spatio-temporal characterisation of the magnetic fields at the target rear is therefore required.

Previous magnetic field measurements have mostly been limited to the laser-irradiated front surface of the target. For instance, the X-wave cutoff of laser-generated harmonics²¹ provides a measure of the magnetic fields at the critical surface at the target front. Faraday rotation of an external probe^{22, 23}, provides temporal snapshots of the magnetic fields in the underdense plasma, albeit integrated along the transverse density profile. Proton deflection²⁴ can also provide time-resolved magnetic field measurements¹⁷, albeit, in principle, integrated through the thickness of the target. Although studying the proton beam profile at various energies can shed light on the profile of the hot electron distribution at different instants of time, the temporal resolution of this technique may be limited by the duration of the proton pulse and its time of flight along with the energy resolution in its measurement.

Here, we present an optical polarimetry technique that can be a complementary diagnostic, providing spatially and temporally resolved snapshots of hot electron transport through solids. We employ a time-delayed optical probe, reflected off the critical surface at the target rear, for the simultaneous spatial and temporal mapping of the magnetic fields at the target rear. The magnetic fields induce a change in the polarization state of the probe beam. Since the magnetic fields are mostly azimuthal in nature, they induce an ellipticity in the reflected probe due to the Cotton-Mouton effect^{24–26}. The polarimetric measurements, localized at the target rear and spatially resolved along the transverse plane, map the picosecond-scale temporal evolution of the magnetic fields at the target rear, produced by the hot electron transport through the target. Consequently, this technique provides a generic recipe of magnetic field measurement, influenced only by the hot electron distribution at the target rear, and in principle with a spatial resolution decided by the diffraction-limited optical resolution of the probe imaging setup, and a temporal resolution limited by the laser pulsewidth.

This paper presents the first spatio-temporally resolved magnetic field measurements at the target rear for a multi-picosecond, petawatt driver laser pulse using optical pump-probe Cotton-Mouton polarimetry, yielding new insights into the principal characteristics of hot electron transport through solid targets under fast-ignition relevant irradiation conditions. We observed signatures of a relatively smooth hot electron transport in 50- μm thick plastic (CH) targets until ~ 5 ps after the incidence of the main interaction pulse, mirrored in the annular magnetic field profile measured at the target rear. At later time-scales of ~ 10 ps, however, a diffused and filamented magnetic field profile was observed. At these time-scales, the dynamics in the plasma sheath at the rear of the target^{27, 28}, including refluxing¹², influence the measurements, along with the filamentation in the hot electron distribution¹. Most notably, our experimental observations identify an initial regime where the transport is relatively smooth in a material that is non-conducting at room temperature. This conforms to the proton radiography measurements by Quinn *et al.*¹², but is contrary to the generic description of such targets typically associated with a highly structured hot electron transport, as opposed to metals that are characterized by a smooth hot electron beam profile^{8–10}, inferred from time-integrated measurements. Our experiments aim at resolving this apparent contradiction by a spatio-temporally resolved study of hot electron transport through solids and are supported by the results of three-dimensional (3D) hybrid simulations that elucidate the dynamic role played by the transient temperature-dependent local resistivity profile of the target.

Results

The experiment was performed at the Rutherford Appleton Laboratory using the Vulcan Petawatt laser, delivering more than 400 J on target at a central wavelength of 1.053 μm over a pulse duration of 2.5 ps and at an irradiance of $\sim 4 \times 10^{20}$ W/cm². A schematic of the experimental setup is shown in Fig. 1. The magnetic fields were inferred from a pump-probe polarimetric diagnostic^{24–26}, employing a linearly-polarized, time-delayed and frequency-doubled ($\lambda = 526$ nm) probe pulse, derived from the main interaction pulse, and focused to the rear of the target at near-normal incidence. The polarimetric measurements indicated that the predominant polarization change consisted of an induced ellipticity in the probe due to the azimuthal nature of the self-generated magnetic fields according to the Cotton-Mouton effect. The Faraday rotation of the normally incident probe due to any axial component of the magnetic field was found to be below the threshold of detection.

Figure 2 presents the magnetic field profiles at the rear of a 50- μm thick CH target at different instants of time. At a negative time delay of 10 ps (that is, for the probe reaching the target 10 ps before the main interaction pulse), a null magnetic field profile was obtained (Fig. 2a), indistinguishable from the background. This measurement defines the noise level for the magnetic field and shows that the probe as well as the prepulse does not induce any perturbative effects on the magnetic field measurements reported here.

Figure 2b and c show the magnetic field profiles at 5 ps and 10 ps after the main interaction pulse respectively. The magnetic field reaches local peak values of ~ 50 MG at a temporal delay of 5 ps. The most significant

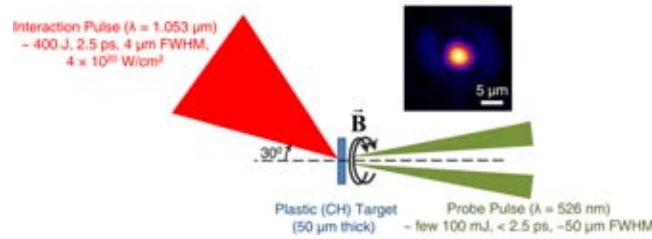


Figure 1. Schematic of the experimental setup, showing the main interaction pulse generating the magnetic fields (B) in the plastic (CH) target, which are probed at the target rear by a time-delayed probe pulse. The inset shows the typical transverse profile of the focal spot of the main interaction pulse on the target.

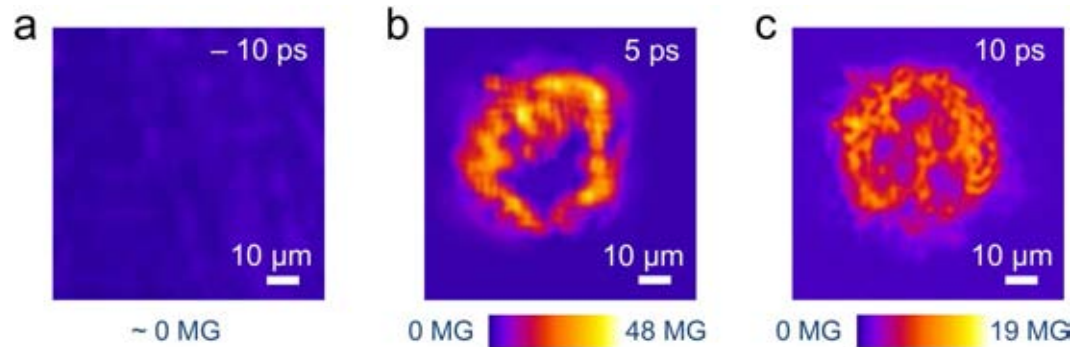


Figure 2. The magnetic field profile at the rear of a 1 mm × 1 mm, 50- μ m thick plastic (CH) target at a temporal delay of (a) -10 ps, (b) 5 ps and (c) 10 ps after the main interaction pulse (negative delay indicates that the probe reached the target before the main interaction pulse). The spatial resolution of the optical imaging setup was $< 10 \mu\text{m}$ and the error in the estimation of the peak magnetic field is ± 5 MG. A null magnetic field profile at negative time-delays defines the noise level of the measurement and serves as a ‘control’ measurement. An annular magnetic field profile can be observed at 5 ps, indicating a relatively smooth hot electron distribution. However, at 10 ps, a large-scale filamentation of the hot electron distribution at the target rear can be observed.

feature in the profile, however, is the annular distribution of the magnetic field with a central hollow (Fig. 2b), observed repeatedly in our experiments. Qualitatively similar magnetic field profiles with a central hollow were also observed for 100- μ m thick CH targets at 5 ps. Such an annular magnetic field profile at the target rear^{13–15}, is indicative of a beam-like distribution of the hot electrons exiting the target²⁹. In contrast, the magnetic field profile 10 ps after the main interaction pulse (Fig. 2c) shows a diffused magnetic field profile with pronounced filamentation. At these time-scales, the hot electron distribution can be filamented inside a CH target^{1, 2, 8–10}, which can be further influenced by the dynamics in the rear-side sheath^{12, 27, 28}.

The magnetic fields observed at the target rear are generated in conjunction with the sheath field, which is set up when the hot electron beam generated at the target front impinges on the rear surface of the target²⁰. As the hot electron beam has a finite transverse extent, so will the sheath field at early times. This leads to a significant net $\nabla \times \mathbf{E}$, which generates a large magnetic field ($\partial \mathbf{B} / \partial t$), an analysis of which is given in ref. 30. A simplistic order-of-magnitude estimate of the magnitude of these fields identifies their mechanism of generation, as follows. Typically, $B \sim E_{\text{sheath}} / c$, and as E_{sheath} is of the order of a few TV/m⁵ we see that $B > 10$ MG, which agrees with the magnitude of the magnetic fields observed in our experiments.

Detailed simulations were carried out using ZEPHYROS^{31, 32}, a 3D hybrid code, to probe the hot electron transport process in the CH target. The simulations assume that the energy is deposited into the target and investigate the propagation of the hot electrons, following the energy deposition. The measured magnetic fields are established when the sheath field first forms at the target rear surface, which occurs following the first transit of the hot electrons through the target. Consequently, early time-scales are the most significant, and hence running the simulations up to 0.7 ps was found to capture most of the relevant physics (given magnetic diffusion time-scales are significantly longer than the experimental time-scales for our experimental parameters). The qualitative outcome of the simulations was found to be quite robust and independent of varying the energy deposition time or the initial angular divergence of the hot electron beam.

The results of the simulations are shown in Fig. 3, where Fig. 3a and b give the longitudinal and transverse snapshots of the electron distribution 0.7 ps after the interaction, as the electrons propagate through the target. It is clear that, although the electrons diverge as they pass through the target, the distribution remains beam-like at initial time-scales, as shown in Fig. 3a. The transverse hot electron density profile at the rear surface (Fig. 3b) illustrates this clearly, indicating a relatively smooth hot electron distribution. Such a hot electron distribution should give rise to an annular magnetic field profile²⁹. Had the beam fragmented into several beamlets due to resistive filamentation¹ in the bulk of the target, a more complex, fragmented magnetic field profile would have emerged. It

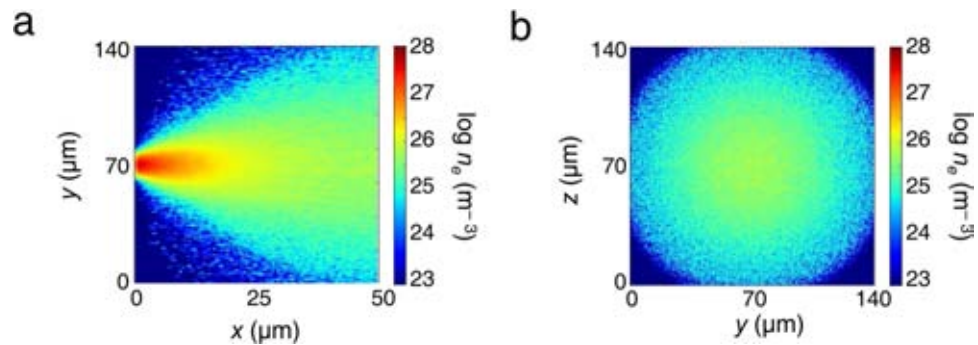


Figure 3. Results of the ZEPHYROS simulations at 0.7 ps, showing the (a) longitudinal and (b) transverse profiles of the electron density n_e . These simulations corroborate the experimentally observed collimated hot electron transport pattern through the target at early time-scales.

is therefore reasonable to interpret our experimental results in Fig. 2 as providing evidence of minimal fragmentation at early time-scales, corresponding to a beam-like hot electron distribution and an annular magnetic field profile. In contrast, later time-scales are characterized by a fragmented magnetic field profile due to the onset of large-scale filamentation, further affected by the sheath-field dynamics at the target rear^{12, 27, 28}.

Discussion

Hot electron distribution at the rear of a solid target is rather well-documented in literature^{1, 2, 7–10, 12–16, 33–35}; targets that are non-conducting at room temperature (such as CH and glass) are typically associated with a highly filamented hot electron transport, as opposed to the rather smooth beam-like hot electron propagation in metals, supported by various *time-integrated* measurements^{8, 10, 34}. Fuchs *et al.*⁸ reported on the smooth proton distribution obtained on a radiochromic film by the illumination of a $\sim 50\text{-}\mu\text{m}$ thick gold (Au) foil with an intense laser ($\sim 2 \times 10^{19}\text{ W/cm}^2$, 350 fs), in stark contrast with the “proton caustics” and filaments observed for polished glass (SiO_2) targets or alternatively, CH targets or layered Au + CH targets of thicknesses varying in the range (50–100) μm . Similar distinctions were also made by Manclossi *et al.*¹⁰, who contrasted the smooth optical emission from the rear of aluminum (Al) targets with the highly filamented emission from the CH targets, with thicknesses ranging from 10 to 100 μm , when irradiated with 40 fs pulses at an incident intensity of $6 \times 10^{19}\text{ W/cm}^2$. However, Quinn *et al.*¹² recently quantified the non-uniformity in the spatial profile of the proton beam emitted from the rear of Al as well as CH and SiO_2 targets as a function of the target thickness varying between 50 and 1200 μm , under irradiation conditions similar to those in our experiment ($5 \times 10^{20}\text{ W/cm}^2$, 1 ps). While the non-uniformity parameter was found to increase significantly with increasing thickness for the CH and SiO_2 targets, it was found to be fairly similar for 50- μm thick CH and Al targets. This is a clear departure from the previously established understanding that hot electron transport in metals (such as Al) is less prone to filamentation, compared to materials such as CH. It is questionable whether this material dependence should be universal, as the details of the interaction should also depend on local target conditions, most notably the local resistivity profile. This naturally elicits an extensive spatio-temporally resolved investigation. Our experimental inferences that the hot electron distribution remains relatively smooth and almost beam-like even in a CH target for at least a few picoseconds following the incidence of the main interaction pulse are in broad agreement with the experimental results of Quinn *et al.*¹². For a better understanding of the hot electron transport process, additional simulations were carried out, comparing the resistivity of CH with that of Al – an excellent conductor – as a function of the temperature, which is the key dynamic parameter deciding the local resistivity profile.

Figure 4a shows the background electron temperature contour plot in the CH target along the longitudinal $x - y$ plane, 0.7 ps after the interaction. The saturated area in the figure close to the interaction represents regions with temperatures greater than 100 eV. As can be seen, the temperature remains above 20 eV throughout most of the hot electron distribution. At these temperatures, the resistivity of CH can be lower than Al. Figure 4b shows the resistivity of CH (green) and Al (red) as a function of temperature, using the Lee-More resistivity model³⁶. Although CH is more resistive than Al at lower temperatures, this is not so above 20 eV. As the temperature remains above 20 eV throughout most of the hot electron distribution in the CH target soon after the laser irradiation, a high degree of filamentation is not expected at early time-scales, consistent with our experimental observations. At later time-scales, the hot electron distribution and consequently the magnetic field profile suffer from filamentation, owing to a fall in the temperature, which may be further affected by the dynamics of the evolving sheath field structure at the target rear^{12, 27, 28}.

Recent experiments by Scott *et al.*²⁷ demonstrated the effect of Weibel instability, evolving as a function of the scale-length of the rear-side plasma. This was experimentally achieved by a controlled, time-delayed prepulse incident on 45- μm thick graphite foils and 5- and 25- μm thick Au foils at an intensity of $4 \times 10^{18}\text{ W/cm}^2$, the evolution of the Weibel instability being imprinted on the accelerated proton beam at the target rear particularly at time-scales of several tens of picoseconds. Similar results have also been recently reported by Göde *et al.*²⁸, where strong spatial modulations of the proton beam profile were observed for a micron-scale solid-density hydrogen jet at an intensity of $5 \times 10^{20}\text{ W/cm}^2$, attributed to Weibel-like instabilities in the rear-side plasma, particularly near the critical density. In light of the above experiments, it is plausible that Weibel-like filamentary instabilities in the micron-scale rear-surface plasma may play a pivotal role in inducing the filamentary structures we observe in the

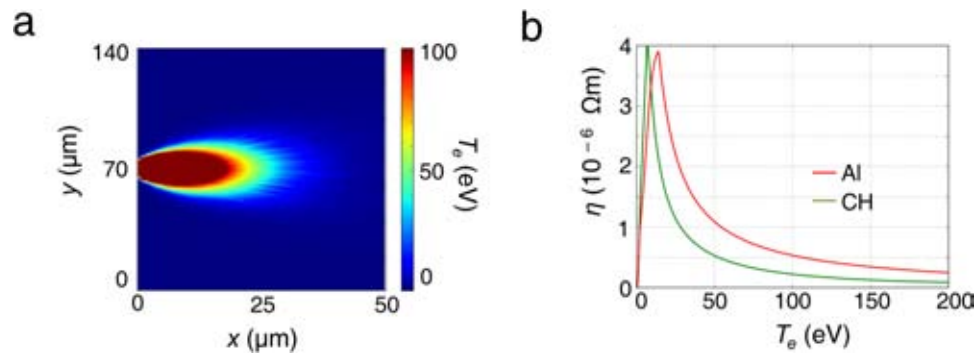


Figure 4. (a) Temperature (T_e) contours in the $x - y$ plane along the longitudinal direction in the CH target, 0.7 ps after the interaction. (b) Resistivities of CH (green) and Al (red) as a function of bulk temperature. The saturated region indicates temperatures greater than 100 eV. The simulations indicate that CH is more resistive than Al at lower temperatures, although this is not true above 20 eV. Most of the CH target reaches temperatures above 20 eV and consequently, a high degree of filamentation is not expected in the CH target at these early time-scales, consistent with our experimental observations.

rear-surface magnetic field profile at later time-scales of ~ 10 ps, in addition to the resistive filamentation¹ induced in the bulk of the target. Such filamentary instabilities hosted in the rear-surface sheath are not prominent at earlier time-scales of a few picoseconds, as observed in our magnetic field measurements at initial time-scales, and consistent with measurements by Scott *et al.*²⁷

In conclusion, we have explored the magnetic fields at the rear of solid targets, generated by hot electrons originating from the intense laser-solid interaction at the target front surface. The optical polarimetry we employed is a sensitive technique that enables us to resolve the dynamics of hot electron propagation with high spatial and temporal resolution. As a result, we infer snapshots of the hot electron distribution through a CH target at different time-scales and identify an interaction regime in terms of local temperature where the transport can be smooth and beam-like. The hot electron distribution not only depends on the initial conductivities of the materials but also on how the conductivity changes with temperature. In fact, the local temperature or resistivity inside the solid is inherently transient and is expected to be a complex function of the distance from the interaction point, local lattice configurations³⁷ and laser parameters like intensity, pulsewidth and contrast³⁸. It is therefore essential to have a diagnostic that can unravel the complex dynamics of hot electron propagation through solids in order to optimise it. This is of critical importance in developing novel sources for energetic ions and engineering innovative techniques for long-range energy transport³⁹. The experimental snapshots presented here highlight the complexity in the phenomenon and suggest that it is highly transient in nature, yet amenable to accurate and detailed measurement. This measurement technique would enable us to extend these studies to obtain a full spatio-temporal understanding and a potential control of the hot electron transport process that is so central in intense-laser-plasma research; further investigations to that end are under way.

Methods

Experimental setup. The p -polarized interaction (pump) laser pulse was focused on the target by an $f/3$ off-axis parabolic mirror at an angle of incidence of 30° . Measurements at low intensities using a microscope objective normal to the target plane estimated the focal spot to be $4 \mu\text{m}$ (FWHM), containing about 30% of the laser energy in the focal volume, resulting in an estimated peak intensity of $\sim 4 \times 10^{20} \text{ W/cm}^2$. The amplified spontaneous emission (ASE) contrast was measured to be 10^{10} at 1 ns and the contrast was better than 10^8 at 100 ps.

The target surface was examined with a white-light interferometer, with a resolution < 50 nm, and no micron-scale initial granularity of the target surface was observed.

A linearly-polarized, time-delayed and frequency-doubled ($\lambda = 526$ nm) probe pulse, extracted from the main interaction pulse, was focused to a $50\text{-}\mu\text{m}$ diameter spot on the target rear at near-normal incidence ($\sim 3^\circ$). The probe energy was suitably attenuated to a few hundred mJ to allow detection of the probe above the plasma emission as well as transition radiation in the charge-coupled-devices (CCDs), while ensuring that the probe is non-intrusive and non-perturbative with regard to the magnetic field measurement (as indicated by Fig. 2a).

The magnetic fields induce a birefringence in the plasma at the target rear, resulting in a change in the polarization state of the incident probe. Briefly, the phase difference between the ordinary O -wave and the extra-ordinary X -wave of the external probe, reflected from the critical surface and the X -wave cutoff respectively, induces an ellipticity in the probe, which can be expressed in terms of the differences between the refractive indices of the O - and X -waves in accordance with the Appleton-Hartree formula. Since the refractive index of the X -wave depends on the ambient magnetic field via the cyclotron frequency, the ellipticity induced in the probe can be uniquely mapped on to the magnetic field experienced by the probe^{24,25}.

An optical streak camera was employed to synchronize the probe pulse with the main interaction pulse, the synchronization being limited by the pulsewidth of 2.5 ps. All temporal delays between the probe and the main interaction pulse mentioned are peak-to-peak measurements of the streak camera. A complete characterization of the polarization of the reflected probe was performed by measuring all the Stokes' parameters (s_1, s_2, s_3) of the reflected probe, using high-extinction-ratio polarizers, quarter-wave-plates and CCDs, coupled with interference filters. In particular, a polarizer aligned parallel to the incident polarization gave $I_1 = I_0(1 + s_1)/2$, whereas a

polarizer aligned at an angle of 45° to the incident polarization gave $I_2 = I_0(1 + s_2)/2$, where I_0 is the intensity of the reflected probe. In addition, a quarter wave-plate, along with a polarizer aligned at an angle of 45° with respect to the quarter-wave-plate, gave $I_3 = I_0(1 + s_3)/2$. The Faraday rotation ψ and the induced ellipticity χ were then measured from the Stokes' parameters since $s_1 = \cos 2\chi \cos 2\psi$, $s_2 = \cos 2\chi \sin 2\psi$ and $s_3 = \sin 2\chi$ ^{25,40}.

The amplitude of the magnetic fields at the target rear depends on the scale-length of the rear-side plasma. Consequently, 1D radiation hydrodynamics simulations using the HYADES code⁴¹ were performed to obtain the scale-length of the plasma density profile at the target rear, assuming that the target rear was volume-heated to a temperature consistent with that observed for similar targets in previous experiments under similar conditions^{42,43}. These simulations were run for a CH target for the time-period (1-10) ps following the main interaction pulse and the expansion velocity of the critical surface was found to be fairly constant at 9×10^6 cm/s during the simulation period equivalent to a scale-length of $< 1 \mu\text{m}$ at 10 ps at the target rear, consistent with shadowgraphy measurements). The exponential scale-lengths were obtained from the plasma density profiles near the critical density of the reflected probe. The error bar in the temperature was taken into account while calculating the error bar in the magnetic field. The fact that a 100 eV change in the temperature resulted in only 1-2 MG change in the magnetic field indicates that the magnetic field magnitude is not too sensitive to the scale-length of the rear-side plasma for our experimental conditions and consequently, an approximate target-rear expansion velocity calculated by the 1D radiation hydrodynamics simulation suffices.

Simulation details. ZEPHYROS is a 3D hybrid code, where the hot electron population is treated as macro-particles, while the background electrons and ions are treated as a two-temperature fluid. A detailed description of the methods and approximations may be found in refs 44–46. The generation and evolution of the magnetic field \mathbf{B} is represented by the well-known equation⁴⁵:

$$\frac{\partial \mathbf{B}}{\partial t} = \eta \nabla \times \mathbf{j}_f + \nabla \eta \times \mathbf{j}_f + \frac{\eta}{\mu_0} \nabla^2 \mathbf{B} - \frac{1}{\mu_0} \nabla \eta \times \mathbf{B},$$

where η is the local resistivity (a function of the background temperature), \mathbf{j}_f is the fast electron current density and μ_0 is the permeability of free space.

The ZEPHYROS simulations were performed using a $100 \times 280 \times 280$ box with a cell size of $0.5 \times 0.5 \times 0.5 \mu\text{m}^3$ up to 0.7 ps. The electrons were injected from a region in the center of the $x=0$ plane so as to model laser irradiation at 4×10^{20} W/cm². A laser-to-hot-electron conversion efficiency of 30% was assumed⁴⁷. The transverse 'laser spot' profile was chosen to be a Gaussian function with an FWHM of $4 \mu\text{m}$. The hot electron energy distribution used was an exponential distribution ($\propto \exp(-\varepsilon/\bar{\varepsilon})$) with the mean energy, $\bar{\varepsilon}$, determined by the Wilks' ponderomotive scaling⁴⁸. The angular distribution of the hot electrons was considered to be $\propto \cos^2 \theta$, where θ is the divergence angle. The background material used was CH at an initial temperature of ~ 1 eV. The resistivity of CH was determined using the Lee-More model³⁶, which was found to be most appropriate for our experimental conditions⁴⁹. The x -boundaries of the simulation box were reflective to allow refluxing⁵⁰, but the transverse boundaries were open.

Data Availability. Data associated with research published in this paper can be accessed at <http://dx.doi.org/10.5286/edata/706>.

References

- Gremillet, L., Bonnaud, G. & Amiranoff, F. Filamented transport of laser-generated relativistic electrons penetrating a solid target. *Phys. Plasmas* **9**, 941 (2002).
- Tikhonchuk, V. T. Interaction of a beam of fast electrons with solids. *Phys. Plasmas* **9**, 1416 (2002).
- Robinson, A. P. L. *et al.* Theory of fast electron transport for fast ignition. *Nucl. Fusion* **54**, 054003 (2014).
- Murnane, M. M., Kapteyn, H. C., Rosen, M. D. & Falcone, R. W. Ultrafast x-ray pulses from laser-produced plasmas. *Science* **251**, 531 (1991).
- Macchi, A., Borghesi, M. & Passoni, M. Ion acceleration by superintense laser-plasma interaction. *Rev. Mod. Phys.* **85**, 751 (2013).
- Gizzi, L. A. *et al.* Role of resistivity gradient in laser-driven ion acceleration. *Phys. Rev. ST Accel. Beams* **14**, 011301 (2011).
- Santos, J. J. *et al.* Fast electron transport in ultraintense laser pulse interaction with solid targets by rear-side self-radiation diagnostics. *Phys. Rev. Lett.* **89**, 025001 (2002).
- Fuchs, J. *et al.* Spatial uniformity of laser-accelerated ultrahigh-current MeV electron propagation in metals and insulators. *Phys. Rev. Lett.* **91**, 255002 (2003).
- Stephens, R. B. *et al.* k_α fluorescence measurement of relativistic electron transport in the context of fast ignition. *Phys. Rev. E* **69**, 066414 (2004).
- Manicacci, M. *et al.* Study of ultraintense laser-produced fast-electron propagation and filamentation in insulator and metal foil targets by optical emission diagnostics. *Phys. Rev. Lett.* **96**, 125002 (2006).
- Yuan, X. H. *et al.* Effect of self-generated magnetic fields on fast-electron beam divergence in solid targets. *New J. Phys.* **12**, 063018 (2010).
- Quinn, M. N. *et al.* Refluxing of fast electrons in solid targets irradiated by intense, picosecond laser pulses. *Plasma Phys. Control. Fusion* **53**, 124012 (2011).
- Honda, M., Meyer-ter-Vehn, J. & Pukhov, A. Collective stopping and ion heating in relativistic-electron-beam transport for fast ignition. *Phys. Rev. Lett.* **85**, 2128 (2000).
- Pukhov, A. Three-dimensional simulations of ion acceleration from a foil irradiated by a short-pulse laser. *Phys. Rev. Lett.* **86**, 3562 (2001).
- Sentoku, Y. *et al.* Three-dimensional particle-in-cell simulations of energetic electron generation and transport with relativistic laser pulses in overdense plasmas. *Phys. Rev. E* **65**, 046408 (2002).
- Califano, F., Del Sarto, D. & Pegoraro, F. Three-dimensional magnetic structures generated by the development of the filamentation (Weibel) instability in the relativistic regime. *Phys. Rev. Lett.* **96**, 105008 (2006).

17. Sarri, G. *et al.* Dynamics of self-generated, large amplitude magnetic fields following high-intensity laser matter interaction. *Phys. Rev. Lett.* **109**, 205002 (2012).
18. Sudan, R. N. Mechanism for the generation of 10^9 G magnetic fields in the interaction of ultraintense short laser pulse with an overdense plasma target. *Phys. Rev. Lett.* **70**, 3075 (1993).
19. Wagner, U. *et al.* Laboratory measurements of 0.7 GG magnetic fields generated during high-intensity laser interactions with dense plasmas. *Phys. Rev. E* **70**, 026401 (2004).
20. Davies, J. R., Bell, A. R. & Tatarakis, M. Magnetic focusing and trapping of high-intensity laser-generated fast electrons at the rear of solid targets. *Phys. Rev. E* **59**, 6032 (1999).
21. Tatarakis, M. *et al.* Measurements of ultrastrong magnetic fields during relativistic laser–plasma interactions. *Phys. Plasmas* **9**, 2244 (2002).
22. Stamper, J. A. & Ripin, B. H. Faraday-rotation measurements of megagauss magnetic fields in laser-produced plasmas. *Phys. Rev. Lett.* **34**, 138 (1975).
23. Borghesi, M., MacKinnon, A. J., Bell, A. R., Gaillard, R. & Willi, O. Megagauss magnetic field generation and plasma jet formation on solid targets irradiated by an ultraintense picosecond laser pulse. *Phys. Rev. Lett.* **81**, 112 (1998).
24. Hutchinson, I. H. *Principles of Plasma Diagnostics* (Cambridge University Press, New York, 1987).
25. Segre, S. E. A review of plasma polarimetry – theory and methods. *Plasma Phys. Control. Fusion* **41**, R57 (1999).
26. Sandhu, A. S. *et al.* Laser-generated ultrashort multimegagauss magnetic pulses in plasmas. *Phys. Rev. Lett.* **89**, 225002 (2002).
27. Scott, G. G. *et al.* Diagnosis of Weibel instability evolution in the rear surface density scale lengths of laser solid interactions via proton acceleration. *New J. Phys.* **19**, 043010 (2017).
28. Göde, S. *et al.* Relativistic electron streaming instabilities modulate proton beams accelerated in laser-plasma interactions. *Phys. Rev. Lett.* **118**, 194801 (2017).
29. Jackson, J. D. *Classical Electrodynamics* 3rd ed. p. 175 (Wiley, New York, 1999).
30. Ridgers, C. P., Sherlock, M., Evans, R. G., Robinson, A. P. L. & Kingham, R. J. Superluminal sheath-field expansion and fast-electron-beam divergence measurements in laser-solid interactions. *Phys. Rev. E* **83**, 036404 (2011).
31. Ramakrishna, B. *et al.* Laser-driven fast electron collimation in targets with resistivity boundary. *Phys. Rev. Lett.* **105**, 135001 (2010).
32. Robinson, A. P. L., Key, M. H. & Tabak, M. Focusing of relativistic electrons in dense plasma using a resistivity-gradient-generated magnetic switchyard. *Phys. Rev. Lett.* **108**, 125004 (2012).
33. Clark, E. L. *et al.* Measurements of energetic proton transport through magnetized plasma from intense laser interactions with solids. *Phys. Rev. Lett.* **84**, 670 (2000).
34. Wei, M. S. *et al.* Observations of the filamentation of high-intensity laser-produced electron beams. *Phys. Rev. E* **70**, 056412 (2004).
35. Jaeckel, O. *et al.* All-optical measurement of the hot electron sheath driving laser ion acceleration from thin foils. *New J. Phys.* **12**, 103027 (2010).
36. Lee, Y. T. & More, R. M. An electron conductivity model for dense plasmas. *Phys. Fluids* **27**, 1273 (1984).
37. McKenna, P. *et al.* Effect of lattice structure on energetic electron transport in solids irradiated by ultraintense laser pulses. *Phys. Rev. Lett.* **106**, 185004 (2011).
38. Ovchinnikov, V. M. *et al.* Effects of preplasma scale length and laser intensity on the divergence of laser-generated hot electrons. *Phys. Rev. Lett.* **110**, 065007 (2013).
39. Chatterjee, G. *et al.* Macroscopic transport of mega-ampere electron currents in aligned carbon-nanotube arrays. *Phys. Rev. Lett.* **108**, 235005 (2012).
40. Chatterjee, G., Singh, P. K., Adak, A., Lad, A. D. & Kumar, G. R. High-resolution measurements of the spatial and temporal evolution of megagauss magnetic fields created in intense short-pulse laser-plasma interactions. *Rev. Sci. Instrum.* **85**, 013505 (2014).
41. HYADES is a commercial product of Cascade Applied Sciences, email: larsen@casinc.com.
42. Lancaster, K. L. *et al.* Temperature profiles derived from transverse optical shadowgraphy in ultraintense laser plasma interactions at $6 \times 10^{20} \text{ W cm}^{-2}$. *Phys. Plasmas* **16**, 056707 (2009).
43. Culfa, O. *et al.* Plasma scale-length effects on electron energy spectra in high-irradiance laser plasmas. *Phys. Rev. E* **93**, 043201 (2016).
44. Davies, J. R., Bell, A. R., Haines, M. G. & Guerin, S. M. Short-pulse high-intensity laser-generated fast electron transport into thick solid targets. *Phys. Rev. E* **56**, 7193 (1997).
45. Davies, J. R. How wrong is collisional Monte Carlo modeling of fast electron transport in high-intensity laser-solid interactions? *Phys. Rev. E* **65**, 026407 (2002).
46. Davies, J. R. Electric and magnetic field generation and target heating by laser-generated fast electrons. *Phys. Rev. E* **68**, 056404 (2003).
47. Levy, M. C., Wilks, S. C., Tabak, M., Libby, S. B. & Baring, M. G. Petawatt laser absorption bounded. *Nature Commun.* **5**, 4149 (2014).
48. Wilks, S. C., Kruer, W. L., Tabak, M. & Langdon, A. B. Absorption of ultra-intense laser pulses. *Phys. Rev. Lett.* **69**, 1383 (1992).
49. MacLellan, D. A. *et al.* Annular fast electron transport in silicon arising from low-temperature resistivity. *Phys. Rev. Lett.* **111**, 095001 (2013).
50. McKeever, K. *et al.* Fast-electron refluxing effects on anisotropic hard-x-ray emission from intense laser-plasma interactions. *Phys. Rev. E* **91**, 033107 (2015).

Acknowledgements

The authors acknowledge the excellent experimental support provided by the Vulcan/Experimental Science staff at CLF. G.R.K. acknowledges financial support from DAE, (Govt. of India) and a J.C. Bose grant (DST, Govt. of India) and G.C. and P.K.S. acknowledge support from the “Strong Field Science” program (11P-1401) of DAE (Govt. of India) operated by TIFR. EPSRC support for the Fusion Doctoral Training Network is also gratefully acknowledged. P.K., L.L. and L.A.G. acknowledge financial support from MiUR project PRIN-2012AY5LEL. R.J.G. and R.J.D. acknowledge the grant EP/J003832/1. Part of this work was supported by the Newton-Bhabha Funds.

Author Contributions

P.P.R. was the principal investigator of the experiment, with A.P.L.R., L.A.G., G.R.K., J.P. and N.C.W. as co-investigators. G.C. and P.K.S. conducted the magnetic-field experiments, assisted by N.B., O.C., R.J.D., R.J.G., J.S.G., P.K., L.L. and K.L.L. The results were analysed by G.C., assisted by A.D.L. ZEPHYROS simulations were performed by A.P.L.R. and HYADES simulations by D.B. and J.P. The manuscript was written by G.C., P.P.R. and A.P.L.R. along with discussions with R.J.G. All authors contributed to the discussion and reviewed the manuscript.

Additional Information

Competing Interests: The authors declare that they have no competing interests.

Publisher's note: Springer Nature remains neutral with regard to jurisdictional claims in published maps and institutional affiliations.



Open Access This article is licensed under a Creative Commons Attribution 4.0 International License, which permits use, sharing, adaptation, distribution and reproduction in any medium or format, as long as you give appropriate credit to the original author(s) and the source, provide a link to the Creative Commons license, and indicate if changes were made. The images or other third party material in this article are included in the article's Creative Commons license, unless indicated otherwise in a credit line to the material. If material is not included in the article's Creative Commons license and your intended use is not permitted by statutory regulation or exceeds the permitted use, you will need to obtain permission directly from the copyright holder. To view a copy of this license, visit <http://creativecommons.org/licenses/by/4.0/>.

© The Author(s) 2017

Silicon nanowire based high brightness, pulsed relativistic electron source

Deep Sarkar,^{1,a} Prashant Kumar Singh,¹ G. Cristoforetti,^{2,a} Amitava Adak,¹ Gourab Chatterjee,¹ Moniruzzaman Shaikh,¹ Amit D. Lad,¹ P. Londrillo,² Giuseppe D'Arrigo,³ J. Jha,¹ M. Krishnamurthy,⁴ L. A. Gizzi,² and G. Ravindra Kumar^{1,a}

¹Tata Institute of Fundamental Research, Mumbai, India

²ILIL, National Institute of Optics, CNR, Pisa, Italy

³CNR-Institute for Microelectronics and Microsystems, Catania, Italy

⁴Tata Institute of Fundamental Research, Hyderabad, India

(Received 28 March 2017; accepted 22 May 2017; published online 9 June 2017)

We demonstrate that silicon nanowire arrays efficiently emit relativistic electron pulses under irradiation by a high-intensity, femtosecond, and near-infrared laser ($\sim 10^{18}$ W/cm², 25 fs, 800 nm). The nanowire array yields fluxes and charge per bunch that are 40 times higher than those emitted by an optically flat surface, in the energy range of 0.2–0.5 MeV. The flux and charge yields for the nanowires are observed to be directional in nature unlike that for planar silicon. Particle-in-cell simulations establish that such large emission is caused by the enhancement of the local electric fields around a nanowire, which consequently leads to an enhanced absorption of laser energy. We show that the high-intensity contrast (ratio of picosecond pedestal to femtosecond peak) of the laser pulse (10^{-9}) is crucial to this large yield. We extend the notion of surface local-field enhancement, normally invoked in low-order nonlinear optical processes like second harmonic generation, optical limiting, etc., to ultrahigh laser intensities. These electron pulses, expectedly femtosecond in duration, have potential application in imaging, material modification, ultrafast dynamics, terahertz generation, and fast ion sources. © 2017 Author(s). All article content, except where otherwise noted, is licensed under a Creative Commons Attribution (CC BY) license (<http://creativecommons.org/licenses/by/4.0/>). [<http://dx.doi.org/10.1063/1.4984906>]

I. INTRODUCTION

Ultrashort, relativistic electron bunches are created when an intense laser pulse interacts with a solid. Such electrons are emitted both at the target front and rear and carry information on laser absorption by the target and electron transport in the hot, dense matter, created by the propagation^{1–5} of these electron bunches. Nanostructures are versatile in their ability for efficient light coupling to solids at low incident intensities, thereby enhancing various processes, namely, second harmonic generation,⁶ surface-enhanced Raman spectroscopy (SERS),^{7,8} optical limiting,⁹ multi-photon emission, etc. It is of considerable practical interest to explore if nanostructures facilitate such enhancement at ultra-high laser intensities in view of the potential application of the high-energy electron bunches¹⁰ in the studies on ultrafast electron microscopy and as sources of high-energy X-rays,¹¹ THz radiation,¹² and fast ion beams.^{13,14} These radiation sources are indispensable tools for ultrafast imaging,¹⁵ spectroscopy,¹⁶ cancer therapy,^{17,18} and material science.¹⁹ Studies have shown that increased X-ray emission is achieved when moderately high-intensity (10^{16} W/cm²), femtosecond laser pulses interact with nanostructures.²⁰ It is still an open question whether such enhancements occur at higher intensities²¹ since the structures may be damaged by the rising edges of the high-intensity pulse and may not survive long enough to interact with the peak intensity.

^aElectronic addresses: deep.sarkar@tifr.res.in; gabriele.cristoforetti@cnr.it; and grk@tifr.res.in



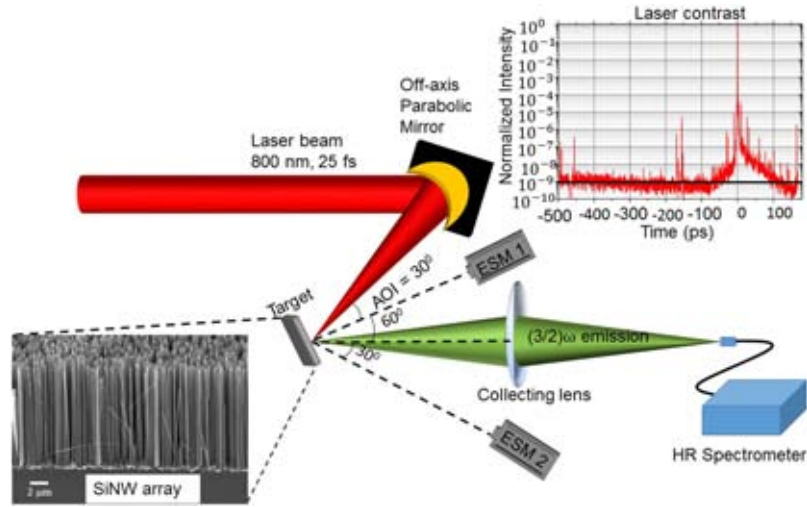


FIG. 1. Schematic for the experimental setup. The laser beam is focused on the target with an ($f/2.5$) off-axis parabola (OAP). Electron Spectrometers (ESM) are used for the measurement of the electron energy spectrum. The $(3/2)\omega$ emission from plasma is captured using a high-resolution, compact UV-visible spectrometer. (Inset) SEM image of the SiNW array and laser intensity profile.

In order for the laser pulse to “see” the nanostructures on the target, the structural dimensions must be of the same order as the characteristic length scales affecting the interaction—for instance, the collisionless skin depth, the quiver amplitude of the electrons oscillating in the laser field, the laser wavelength, and the pre-plasma density scale length. If the nanostructure dimensions are well below these length scales, the laser pulse would effectively “see” a plane target and the enhanced coupling due to structuring can no longer be expected. It is, however, difficult to experimentally investigate the nature of the interaction by tuning the target parameters owing to the difficulty inherent in the fabrication of structured targets with tunable dimensions. Another important factor determining the nature of the laser-matter interaction and the efficiency of laser absorption is the temporal structure of the laser pulse. The possibility of an early onset of ionization and the formation of a plasma prior to the arrival of the main peak is the result of such a low-intensity pedestal of several picoseconds accompanying the main peak. This can damage the structures well before the main peak of the pulse arrives. Another challenging aspect of the problem is the fact that the ablation threshold for nanostructured targets is much lower than the plane targets due to their higher absorption efficiency.²²

In this letter, we show that silicon nanowire (SiNW) arrays²³ enhance the interaction with high contrast, high-intensity laser pulses, and generate high-flux relativistic electron pulses in the energy range of 0.2–0.5 MeV. The flux is also found to be dependent on the emission direction—a feature not observed in the planar case. We demonstrate local light field enhancement, normally observed at low intensities of light, in the regime of ultrahigh intensities²⁴ (10^{18} W/cm²). Silicon nanowires were fabricated using a bottom-up approach with random silver deposition and silicon etching in two separate steps. In the first step, the samples were immersed in a solution of 0.005M AgNO₃ and 4.8M HF for 160 s to promote the silver nanocluster deposition on the Si (100) surface, and in the next step, they were immersed in a second solution of 0.1M H₂O₂ and 4.8M HF for 30 min to activate the silicon etching. A Scanning Electron Microscope (SEM) image of the nanowire arrays used for the experiment is shown in the inset of Fig. 1. The nanowires were ~ 8 μm in length and ~ 10 – 20 nm in diameter, randomly distributed on the surface with inter-wire separation ~ 10 – 50 nm, giving a fill factor in the range of 0.04–0.2.

II. EXPERIMENT

The experiments were carried out using the 100 TW Ti:Sapphire chirped pulse amplification²⁵ laser system at the Tata Institute of Fundamental Research (TIFR), Mumbai. As shown in Fig. 1,

the laser beam (800 nm, 25 fs) was focused on the target in p-polarization at an incidence angle of 30° to a spot size of $10 \mu\text{m} \times 15 \mu\text{m}$ (full width at half maximum) by an ($f/2.5$) off-axis parabolic mirror. The intensity on the target was varied in the range $I\lambda^2 = (1.5\text{--}3) \times 10^{18} \text{ W } \mu\text{m}^2 \text{ cm}^{-2}$.

The ratio of the main peak intensity to the pedestal intensity, known as pulse contrast, is measured by third order cross-correlation techniques and is shown in the inset of Fig. 1. The contrast ratio of the main peak with respect to the nanosecond-long pedestal (due to amplified spontaneous emission) was $\sim 10^{-9}$, while it was $\sim 10^{-6}$ at 3 ps before the main peak.

The plasma created at the target surface was probed by electron and optical spectrometers. A high-resolution, fiber-coupled spectrometer [$\Delta\lambda = (350\text{--}800) \text{ nm}$] measured the emission spectrum along the specular direction, sent to it through a fiber. This was aimed at detecting the three-halves harmonic emission ($\lambda \sim 532 \text{ nm}$) and second harmonic emission ($\lambda \sim 400 \text{ nm}$), the former resulting from the Two Plasmon Decay (TPD)²² instability in the under-dense ($n < n_c$) plasma region at a layer of density $\frac{n_c}{4}$. Since TPD requires an appreciable pre-plasma scale length ($\sim \lambda_{\text{laser}}$) to grow,^{26,27} the detection of the $(3/2)\omega_0$ signal could be used to indicate the presence of a pre-plasma. However, no such $(3/2)$ harmonic emission was observed for the nanowire arrays at any laser irradiance, indicating that these structures survived during the irradiation of pre-pulse.

To measure the spectra of the relativistic electrons, two magnet-based electron spectrometers (ESM)²⁸ were placed at angles of 0° and 60° with respect to the target normal (shown in Fig. 1) at distances of 22 cm ($\theta = 0^\circ$) and 21.5 cm ($\theta = 60^\circ$), respectively. The laser-generated electrons are made to pass through a narrow collimating aperture of diameter $\sim 2 \text{ mm}$ before it reaches the detector plate.

III. RESULTS AND DISCUSSION

In our experiments, we characterize the electrons emitted at the front of the target and compare their spectra with those obtained for a plane silicon target. The electrons at the front are chosen for

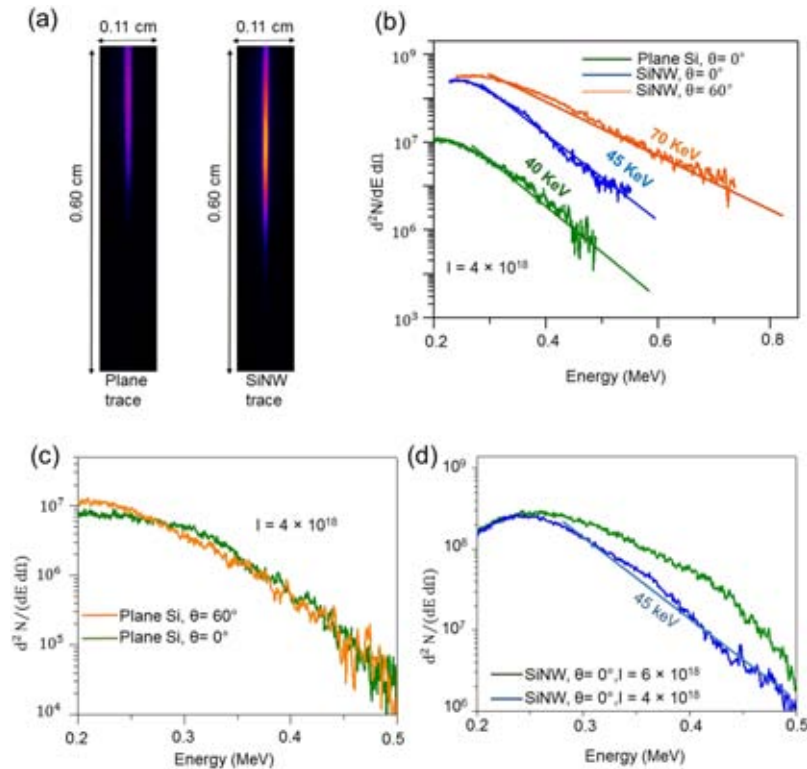


FIG. 2. (a) Front side ESM traces for plane Si and SiNW. (b) Electron energy spectra for plane ($\theta = 0^\circ$) and SiNW target ($\theta = 60^\circ$). (c) Electron energy spectra for plane Si for $\theta = 0^\circ$ and $\theta = 60^\circ$. (d) Energy spectra for SiNW at $\theta = 0^\circ$ for two different intensities. All intensity values are in units of W/cm^2 .

the analysis as they do not interact with the bulk of the target and hence can be compared more easily with the simulation results.

Energy spectra of the relativistic electrons emitted from nanowire targets revealed a much higher total yield compared to the plane silicon case, as shown in Fig. 2. The electron temperature for the nanowire arrays (70 keV) is also observed to be higher than that of a plane silicon target (40 keV), although along the target normal direction (45 keV), the enhancement is within the limits of the measurement uncertainty. The flux enhancement along 0° is 20 times while that along $\theta = 60^\circ$ is 40 times, indicating an anisotropic distribution of the relativistic electrons. Since the charge yield per bunch is linearly related to the flux ($Q = e \times \text{flux}$), the charge enhancement factor remains the same (along 0° , 2.4 pC for flat and 58 pC for nanowires; along $\theta = 60^\circ$, 2.6 pC for flat and 114 pC for nanowires). These data indicate a clear anisotropy in the case of the nanowire arrays.

IV. COMPUTATIONAL ANALYSIS

To comprehend these experimental results and have a closer look at the underlying mechanisms, fully kinetic particle-in-cell (PIC) simulations with the Aladyn code²⁹ in the 2D Cartesian geometry were carried out. The laser pulse was modeled by a Gaussian beam profile in the transverse coordinate with a FWHM spot size of $10 \mu\text{m}$. The temporal profile on the focal plane was of the form $I(t) = I_0 \cos^4(\pi t/2\tau)$, where $2\tau = 70$ fs corresponding to a pulse duration of $\tau_{\text{FWHM}} = 25$ fs. The laser pulse entered into the computational (X, Y) box from the left edge, with an incidence angle of 30° with respect to the target normal. The dimensions of the numerical box were set to $L_X = 40 \mu\text{m}$ and $L_Y = 50 \mu\text{m}$ while the grid cell dimensions were set to $dx = dy = 10$ nm, thus allowing for reasonable space-time resolution. The initial density of Si^{4+} ions was set to $n_{\text{Si}} = 4 \times 3 \times 10^{22} \text{ cm}^{-3}$, corresponding to the plasma electron density $n_e = 100 n_c = 1 \times 74 \times 10^{23} \text{ cm}^{-3}$. 256 (macro) electrons were used per cell in the PIC code. In modeling the laser-plasma interaction, field ionization using the Ammosov-Delone-Krainov (ADK) model was used. For the intensities considered here, the degree of ionization of Si ions increases from the initial $Z = 4$ to a final $Z = (8-10)$.

In the case of plane silicon, p-polarization of the laser produces a mixing of a traveling wave structure (traveling parallel to the target surface) and a standing wave pattern along the x-direction.

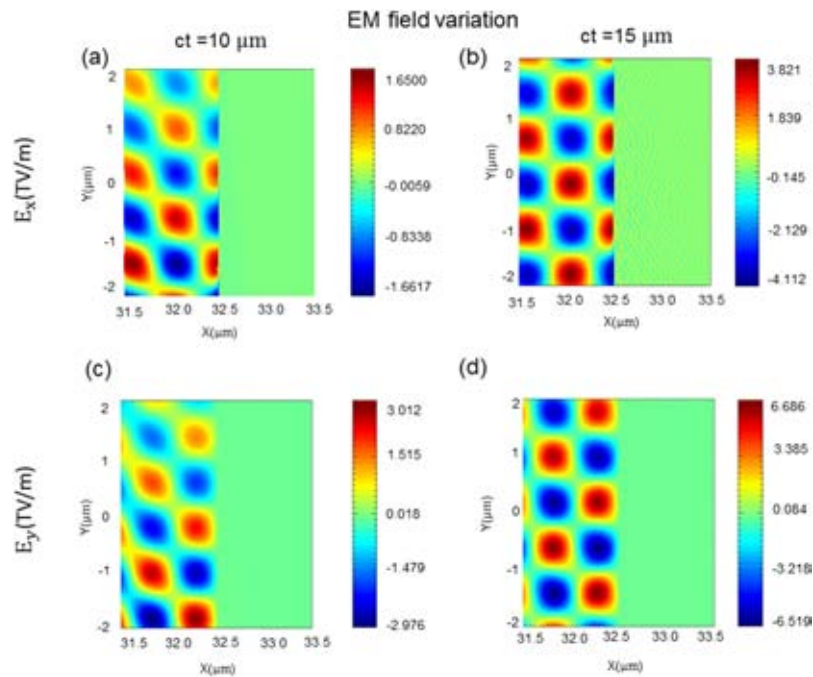


FIG. 3. Simulations for the EM field variations across the plane Si targets. The peak of the laser pulse impinges at $t = 48$ fs, corresponding to $ct = 15 \mu\text{m}$ [(b) and (d)]. Therefore $ct = 10 \mu\text{m}$ [(a) and (c)] corresponds to $t = 30$ fs.

This is well visible by observing the electromagnetic (EM) fields at two different times, corresponding to the leading part and peak of the pulse, showing that the horizontal nodes move in the y -direction while the vertical nodes are located at fixed distances from the target surface (Fig. 3); the electric field E_X (~ 3.4 TV/m at $t = 48$ fs) is maximum at the target surface and results in the extraction of electrons from the target. The larger electric field $2E_{0Y}$ (~ 6 TV/m), on the other hand, is localized far from the surface, at a distance $\approx \lambda_0 \cos(30^\circ)/4 \approx 175$ nm. This field is produced by the interference of the incident and the reflected laser and can accelerate the electrons to energies much higher than their mean oscillation energies in the laser electric field. Since the quiver amplitude of electrons $x_{\text{quiver}} \approx \frac{v_0 \lambda_0}{4c} \sim 150$ nm, where $\frac{v_0}{c} = \sqrt{\frac{a_0^2}{a_0^2 + 1}}$, a few electrons are able to make it to the point of maximum

E_Y , upon which they are accelerated at the maximum energy $E_{\text{max}} \approx (\sqrt{1 + 2a_0^2} - 1)m_e c^2 \approx 590$ keV. This model, similar to that introduced by May³⁰ and Kemp³¹ for the interaction at normal incidence on a steep, overdense target, is in qualitative agreement with the maximum energy electrons obtained in the simulations and the experiment.

The nanowires were modeled by wires of size 20 nm separated by a gap of 40 nm. Unlike the real target, the nanowires in the model have a regular distribution on the surface. For a pulse with a normalized vector potential $a_0 = 1.4$, the PIC spectra for the front electrons exhibit a low flux of electrons with energy $E \leq 500$ keV and a high-energy tail with $E \geq 800$ keV in the normal direction (red curve, Fig. 4), features not observed in the experiment. Interestingly, the high energy tail strongly reduces on letting the 2D PIC simulations account for the formation of low density plasma in the channels prior to the arrival of the main pulse due to the temporal structure of the laser beam (blue curve, Fig. 4). This suggests that the high energy electrons are possibly generated by direct laser acceleration (DLA) into the channel gaps. This hypothesis is strengthened by performing 3D PIC simulations. In the 3D geometry, due to the low fill factor, the channels are no longer present and DLA becomes less efficient, resulting also in a reduction of high energy electrons (black curve, Fig. 4). Both the pre-plasma and 3D geometry, therefore, contribute to inhibit DLA acceleration, making the PIC spectra approach the experimental ones.

The observation of the spatial EM field distribution shows that, for negligible plasma formation prior to the main pulse, the laser initially penetrates the gap between the wires; owing to the formation of a strong spatial modulation resembling a fine tooth-comb at the target surface [Fig. 5(a)] there is an evident field enhancement resulting in large absorption of the laser energy. Due to the strong reduction of laser light reflection, there is no clear formation of a standing wave pattern and the EM field at the target front has the nature of a traveling wave along the incidence direction [Fig. 5(a)]. Similarly, due to the absence of the plasma between the channels, laser light travels between the wires, as visible in the figure. The situation is very different in the trailing part of the pulse, when the partial filling of the gaps by the plasma inhibits laser propagation into the target and

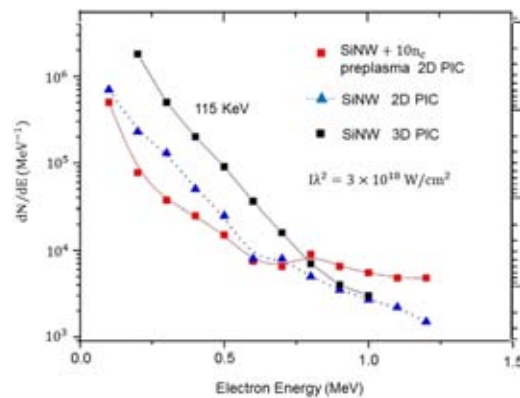


FIG. 4. 2D and 3D PIC electron energy spectra for the SiNW targets with no pre-plasma and in the presence of a pre-plasma of density $10 n_c$.

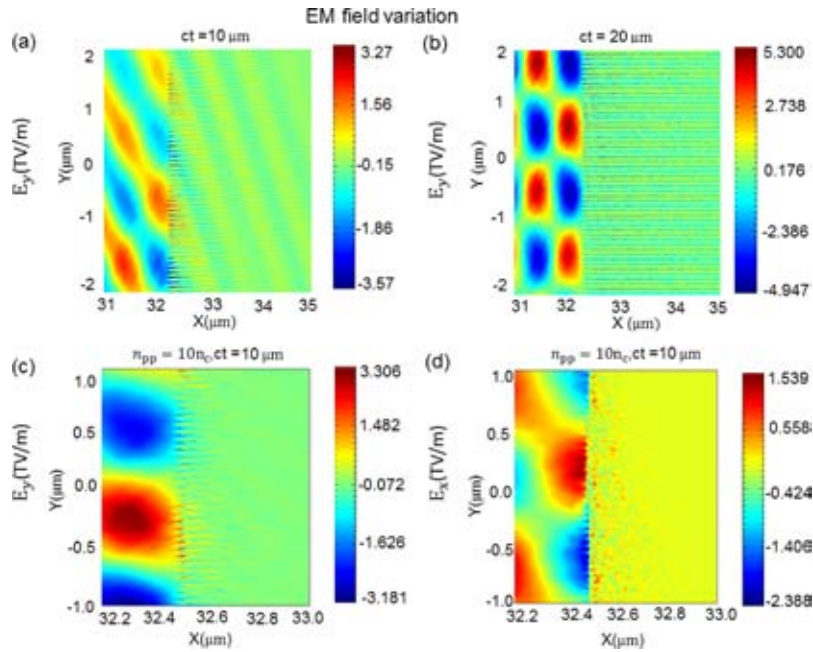


FIG. 5. Simulation figures of the EM field pattern in the nanowires in the absence [(a) and (b)] and presence [(c) and (d)] of the pre-plasma. Here $ct = 10$ and $20 \mu\text{m}$ correspond to $t = 30$ and 66 fs, respectively, and refer to early and late times of interaction.

the electrostatic fields between the wires are produced by charge separation [Fig. 5(b)]; owing to a large reflection at this time, a clear standing wave pattern is visible in front of the target along the x -direction [Fig. 5(b)].

In the real situation, a tenuous, low density plasma prior to the arrival of the main peak is already present between the wires due to the structure of the laser pulse. A strong spatial modulation and field enhancement, in the form of a fine-toothed comb [Fig. 5(c)], is however still present in a layer of approximately 100 nm leading to a more efficient laser absorption than in the case of the plane silicon target. The standing wave pattern at the target front gives rise to relativistic electrons with an energy distribution similar to that for plane silicon; however, the flux is higher in this case due to larger absorption. In this case, the EM field between the wires is prevalingly along the y direction [Fig. 5(c)], while the E_x component is inhibited by the pre-plasma [Fig. 5(d)]. This could result in the propagation of hot electrons primarily at larger angles, in agreement with the anisotropic distribution observed, even if an accurate investigation of the hot electron trajectory, accounting for magnetic fields, is required. The extent to which the electrons extracted from the wires can be accelerated by the laser field depends upon the closeness of the nanowires, as the oscillating phase is lost (upon reaching the neighboring wire) for separations less than the quiver amplitude. We therefore expect an optimization of the electron acceleration by tuning the gap between the nanowires.³²

V. CONCLUSION

In summary, we show silicon nanowire arrays to be an extremely efficient absorber of laser energy and capable of generating relativistic electron pulses in the energy range of 0.2 – 0.8 MeV with a 30 times higher yield than that of the plane surface. Particle-in-cell (PIC) simulations of the interaction process reveal the role of the temporal structure of the laser pulse in the acceleration mechanism. It is seen that in the presence of an appreciable picosecond pedestal, the nanowire gaps are rapidly filled with the pre-plasma which hinders direct laser acceleration (DLA) of the electrons into the channels. Such relativistic electron beams show potential for applications in the study of ultrafast processes in biology, chemistry, and condensed matter physics.

ACKNOWLEDGMENTS

G.R.K. acknowledges support from the J. C. Bose Fellowship Grant (No. JCB-037/2010) from the Department of Science and Technology, Government of India. We also acknowledge the National Research Council of Italy for the support in the framework of the Short Term Mobility program 2014. This work was partially supported by the MIUR-PRIN 2012 (Contract No. PRIN2012AY5LEL) and by the INFN L3IA Project (No. CN5).

- ¹ L. Gremillet, F. Amiranoff, S. Baton, J.-C. Gauthier, M. Koenig, E. Martinolli, F. Pisani, G. Bonnaud, C. Lebourg, C. Rousseaux, C. Toupin, A. Antonicci, D. Batani, A. Bernardinello, T. Hall, D. Scott, P. Norreys, H. Bandulet, and H. Pépin, *Phys. Rev. Lett.* **83**, 5015(1999).
- ² G. Chatterjee, P. K. Singh, S. Ahmed, A. P. L. Robinson, A. D. Lad, S. Mondal, V. Narayanan, I. Srivastava, N. Koratkar, J. Pasley, A. K. Sood, and G. R. Kumar, *Phys. Rev. Lett.* **108**, 235005 (2012).
- ³ P. K. Singh, G. Chatterjee, A. D. Lad, A. Adak, S. Ahmed, M. Khorasaninejad, M. M. Adachi, K. S. Karim, S. S. Saini, A. K. Sood, and G. Ravindra Kumar, *Appl. Phys. Lett.* **100**, 244104 (2012).
- ⁴ I. Dey, A. Adak, M. Shaikh, G. Chatterjee, D. Sarkar, A. D. Lad, and G. Ravindra Kumar, *Opt. Express* **24**, 28419 (2016).
- ⁵ A. Adak, P. K. Singh, A. D. Lad, G. Chatterjee, M. Dalui, P. Brijesh, A. P. L. Robinson, J. Pasley, and G. Ravindra Kumar, *Appl. Phys. Lett.* **109**, 174101 (2016).
- ⁶ Y. Zhang, N. K. Grady, C. Ayala-Orozco, and N. J. Halas, *Nano Lett.* **11**, 5519 (2011).
- ⁷ C. E. Talley, J. B. Jackson, C. Oubre, N. K. Grady, C. W. Hollars, S. M. Lane, T. R. Huser, P. Nordlander, and N. J. Halas, *Nano Lett.* **5**, 1569 (2005).
- ⁸ K. Kneipp, Y. Wang, H. Kneipp, L. T. Perelman, I. Itzkan, R. R. Dasari, and M. S. Feld, *Phys. Rev. Lett.* **78**, 1667 (1997).
- ⁹ G. Ispasoiu, L. Balogh, O. P. Varnavski, D. A. Tomalia, and T. Goodson III, *J. Am. Chem. Soc.* **122**, 11005 (2000).
- ¹⁰ M. A. Purvis, V. N. Shlyaptsev, R. Hollinger, C. Bargsten, A. Pukhov, A. Prieto, Y. Wang, B. M. Luther, L. Yin, S. Wang, and J. J. Rocca, *Nat. Photonics* **7**, 796 (2013).
- ¹¹ S. Mondal, I. Chakraborty, S. Ahmad, D. Carvalho, P. K. Singh, A. D. Lad, V. Narayanan, P. Ayyub, G. R. Kumar, J. Zheng, and Z. M. Sheng, *Phys. Rev. B* **83**, 035408 (2011).
- ¹² D. K. Polyushkin, E. Hendry, E. K. Stone, and W. L. Barnes, *Nano Lett.* **11**, 4718 (2011).
- ¹³ D. Margarone, O. Klimo, I. J. Kim, J. Prokúpek, J. Limpouch, T. M. Jeong, T. Mocek, J. Pšikal, H. T. Kim, J. Proška, K. H. Nam, L. Štolcová, I. W. Choi, S. K. Lee, J. H. Sung, T. J. Yu, and G. Korn, *Phys. Rev. Lett.* **109**, 234801 (2012).
- ¹⁴ S. Bagchi, P. Prem Kiran, M. K. Bhuyan, S. Bose, P. Ayyub, M. Krishnamurthy, and G. Ravindra Kumar, *Appl. Phys. Lett.* **90**, 141502 (2007).
- ¹⁵ F. Légaré, K. F. Lee, A. D. Bandrauk, D. M. Villeneuve, and P. B. Corkum, *J. Phys. B: At., Mol. Opt. Phys.* **39**, S503 (2006).
- ¹⁶ E. R. Keim, M. L. Polak, J. C. Owrutsky, J. V. Coe, and R. J. Saykally, *J. Chem. Phys.* **93**, 3111 (1990).
- ¹⁷ S. V. Bulanov and V. S. Khoroshkov, *Plasma Phys. Rep.* **28**, 453 (2001).
- ¹⁸ V. Malka, J. Faure, Y. A. Gauduel, E. Lefebvre, A. Rousse, and K. T. Phuoc, *Nat. Phys.* **4**, 447 (2008).
- ¹⁹ S. Cabrini, A. Carpentiero, R. Kumar, L. Businaro, P. Candeloro, M. Prasciolu, A. Gosparini, C. Andreani, M. De Vittorio, T. Stomeo, and E. Di Fabrizio, *Microelectron. Eng.* **78–79**, 11 (2005).
- ²⁰ P. P. Rajeev, P. Taneja, P. Ayyub, A. S. Sandhu, and G. R. Kumar, *Phys. Rev. Lett.* **90**, 115002 (2003).
- ²¹ S. Jiang, A. G. Krygier, D. W. Schumacher, K. U. Akli, and R. R. Freeman, *Eur. Phys. J. D* **68**, 283 (2014).
- ²² G. Cristoforetti, A. Anzalone, F. Baffigi, G. Bussolino, G. D'Arrigo, L. Fulgentini, A. Giuliotti, P. Koester, L. Labate, S. Tudisco, and L. A. Gizzi, *Plasma Phys. Controlled Fusion* **56**, 95001 (2014).
- ²³ L. Hu and G. Chen, *Nano Lett.* **7**, 3249 (2007).
- ²⁴ P. P. Rajeev, P. Ayyub, S. Bagchi, and G. R. Kumar, *Opt. Lett.* **29**, 2662 (2004).
- ²⁵ D. Strickland and G. Mourou, *Opt. Commun.* **55**, 447 (1985).
- ²⁶ A. Tarasevitch, C. Dietrich, C. Blome, K. Sokolowski-Tinten, and D. von der Linde, *Phys. Rev. E* **68**, 26410 (2003).
- ²⁷ L. Veisz, W. Theobald, T. Feuerer, H. Schillinger, P. Gibbon, and P. Sauerbrey, *Phys. Plasmas* **9**, 3197 (2002).
- ²⁸ K. A. Tanaka, T. Yabuuchi, T. Sato, R. Kodama, Y. Kitagawa, T. Takahashi, Y. Honda, and S. Okuda, *Rev. Sci. Instrum.* **76**, 13507 (2004).
- ²⁹ C. Benedetti, A. Sgattoni, G. Turchetti, and P. Londrillo, *IEEE Trans. Plasma Sci.* **36**, 1790 (2008).
- ³⁰ J. May, J. Tonge, F. Fiuza, R. A. Fonseca, L. O. Silva, C. Ren, and W. B. Mori, *Phys. Rev. E* **84**, 25401 (2011).
- ³¹ G. E. Kemp, A. Link, Y. Ping, D. W. Schumacher, R. R. Freeman, and P. K. Patel, *Phys. Plasmas* **20**, 33104 (2013).
- ³² G. Cristoforetti, P. Londrillo, P. K. Singh, F. Baffigi, G. D'Arrigo, A. D. Lad, R. G. Milazzo, A. Adak, M. Shaikh, D. Sarkar, G. Chatterjee, J. Jha, M. Krishnamurthy, G. R. Kumar, and L. A. Gizzi, *Sci. Rep.* **7**, 1479 (2017).

The resonant multi-pulse ionization injection

Paolo Tomassini,^{1,a)} Sergio De Nicola,^{2,3} Luca Labate,^{1,4} Pasquale Londrillo,⁵
 Renato Fedele,^{2,6} Davide Terzani,^{2,6} and Leonida A. Gizzi^{1,4}

¹Intense Laser Irradiation Laboratory, INO-CNR, 56124 Pisa, Italy

²Dip. Fisica Università di Napoli Federico II, 80126 Napoli, Italy

³CNR-SPIN, Napoli, 80126 Napoli, Italy

⁴INFN, Sect. of Pisa, 56100 Pisa, Italy

⁵INAF, 40129 Bologna, Italy

⁶INFN, Sect. of Napoli, 80126 Napoli, Italy

(Received 17 August 2017; accepted 14 September 2017; published online 5 October 2017)

The production of high-quality electron bunches in Laser Wake Field Acceleration relies on the possibility to inject ultra-low emittance bunches in the plasma wave. In this paper, we present a new bunch injection scheme in which electrons extracted by ionization are trapped by a large-amplitude plasma wave driven by a train of resonant ultrashort pulses. In the Resonant Multi-Pulse Ionization injection scheme, the main portion of a single ultrashort (e.g., Ti:Sa) laser system pulse is temporally shaped as a sequence of resonant sub-pulses, while a minor portion acts as an ionizing pulse. Simulations show that high-quality electron bunches with normalized emittance as low as $0.08 \text{ mm} \times \text{mrad}$ and 0.65% energy spread can be obtained with a single present-day 100TW-class Ti:Sa laser system. *Published by AIP Publishing.* <https://doi.org/10.1063/1.5000696>

I. INTRODUCTION

High-quality Laser Wake Field Accelerated (LWFA) electron bunches are nowadays requested for several applications including free electron lasers,^{1–3} X/γ sources,^{4–8} and staged acceleration.^{9–13} While performances of self-injected bunches generated in the so-called bubble regime^{14,15} continue to improve, other promising injection schemes, including injection via density downramp,^{16–20} colliding pulses injection,^{21–23} and ionization injection,^{24–32} are under active theoretical and experimental investigation.

Evolution of the ionization injection, based on the use of two laser pulses (either with the same or different wavelengths), was proposed in Refs. 33–36. In the two-color ionization injection,³⁴ the main pulse that drives the plasma wave has a long wavelength, five or ten micrometers, and a large normalized amplitude $a_0 = eA/mc^2 = 8.5 \times 10^{-10} \sqrt{I\lambda^2} > 1$, being I and λ the pulse intensity in W/cm^2 and the wavelength in μm . The second pulse (the “ionization pulse”) possesses a large electric field though its normalized amplitude is low. This is achieved by doubling the fundamental frequency of a Ti:Sa pulse. While the main pulse cannot ionize the electrons in the external shells of the contaminant species due to its long wavelength, the electric field of the ionization pulse is large enough to generate newborn electrons that will be trapped in the bucket. This opens the possibility of using gas species with relatively low ionization potentials, thus enabling separation of wake excitation from particle extraction and trapping.

Two color ionization injection is in fact a flexible and efficient scheme for high-quality electron bunch production. The main drawbacks of the two color ionization injection are the current lack of short ($T < 100 \text{ fs}$) 100TW-class laser

systems operating at large ($\approx 10 \mu\text{m}$) wavelength and lasers synchronization jitter issues. These limitations make the two-color scheme currently unpractical for application to LWFA-based devices requiring high quality beams.

In this paper, we propose a new injection configuration (Fig. 1) (we will refer to it as Resonant Multi-Pulse Ionization injection, ReMPI) that overcomes these limitations and opens the way to a reliable generation of high quality Laser Wakefield accelerators. The breakthrough of our ReMPI scheme consists in the replacement of the long wavelength high peak power driving pulse of the two-color scheme with a short wavelength, resonant multi-pulse laser driver. In fact, due to the resonant enhancement of the ponderomotive force, a properly tuned train of pulses^{37–39} is capable of driving plasma waves with larger amplitude than a single pulse with the same energy. In such a way, given the much lower intensity of the driving pulses, it is possible to match the conditions of *both* particle trapping and unsaturated ionization of the active atoms level. Notably, such a driver can be obtained via temporal shaping techniques from a *single*, linearly polarized, standard CPA laser pulse. A minor fraction of the same pulse can be frequency doubled

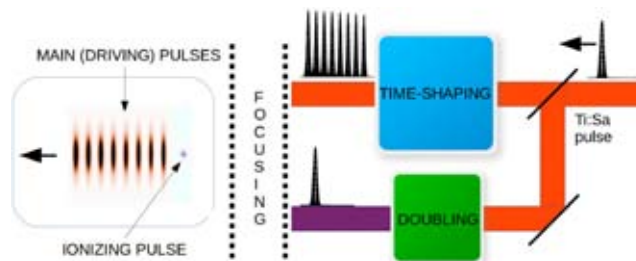


FIG. 1. Resonant Multi-Pulse Ionization injection scheme. A small fraction of a single Ti:Sa laser pulse is frequency doubled and will constitute the ionizing pulse. The main portion of the pulse is temporally shaped as a train of resonant pulses that will drive a large amplitude plasma wave.

^{a)}paolo.tomassini@ino.it

(or tripled) and used as the ionizing pulse. Recently,^{40,41} exciting experimental results on the generation of such a time shaped pulses demonstrate that a multi pulse scheme is obtainable with present day technology.

The paper is organized as follows. In Sec. II, we recall the resonant multi-pulse wakefield excitation comparing it with typical single pulse excitation conditions. In Sec. III, we set-up trapping conditions for electrons extracted in a plasma wave driven by a resonant train of pulses designed for a state-of-the-art 250TW Ti:Sa laser system. In Sec. IV, we will discuss in detail the process of electron extraction by a linearly polarized ultraintense pulse. We carried out extensive numerical simulations to evaluate applicability and robustness of the scheme. In Sec. V, we will report on the simplest case of un-guided pulses designed for a state-of-the-art 250TW Ti:Sa laser system. Finally, Sec. VI is devoted to discussion of the results obtained by our simulations. In the Appendices details on the ADK ionization model will be found, along with a description of the hybrid fluid/kinetic QFluid code used for the simulations.

II. THE MULTI-PULSE LWFA

The excitation of plasma waves using multiple laser pulses rather than a single, higher energy one was first studied, from a theoretical viewpoint, by Umstadter *et al.*³⁷ and Dalla and Lontano.³⁸ In this Multi Pulse (MP) option, the Langmuir wave is gradually excited by means of a resonant train of pulses. The Self-Modulated LWFA process (see, among others Refs. 42 and 43), is, for instance, based on such a kind of multi pulse excitation, each short pulse resulting from the self-modulation of a single, long laser pulse with length exceeding the plasma wavelength λ_p .

In a linear regime, the resonant enhancement of the ponderomotive force effect takes place when the pulse-to-pulse delay T_{delay} matches the plasma wave period. When the plasma wave amplitude is relatively high, both the optimal pulse-to-pulse delay T_{delay} and pulse duration can change (even significantly)^{37,38} from the simpler case of constant delay $T_{delay} = \lambda_p/c$ given by the linear theory. In that case, a parametric scan for T_{delay} is needed to obtain an efficient resonant regime. On the experimental side, the Multi-Pulse acceleration can be achieved either starting from a set of pulses generated by different laser systems (e.g., from fiber lasers³⁹ to reach kHz repetition rates) or, as considered in the present paper, from a single pulse passing through a time-shaping device.^{40,41}

It is worth noting that, for the excitation of the plasma wave, an optimized train of pulses is more efficient than a single laser pulse with the same duration and delivered energy. As an illustrative example, a comparison between the two cases is shown in Fig. 2 where we report the line outs of the on-axis longitudinal electric field in the cases of excitations by either a single driving pulse or an optimized eight-pulses driving train with the same total energy as the single pulse. Simulations reported were performed with the ALaDyn PIC code⁴⁴ in 2D slice geometry and with the QFluid code⁴⁵ (see also Appendix B) in 2D cylindrical geometry. The QFluid code is the cold-fluid/kinetic code that

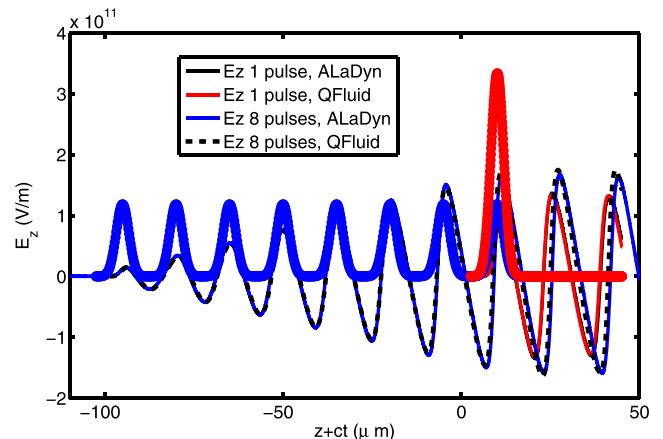


FIG. 2. Single-pulse vs eight-pulses train comparison. Pulses (moving through the left) with a duration of 10fs and a waist size of 25 μm are focused in a $n_e = 5 \times 10^{18} \text{ cm}^{-3}$ plasma. The single-pulse (red thick line) with a peak intensity of $5.9 \times 10^{18} \text{ W/cm}^2$ drives a plasma wave whose maximum accelerating gradient is 20% less than that of the wave excited by the eight-pulses train having the same delivered energy and intensity $7.4 \times 10^{17} \text{ W/cm}^2$. A numerical scan of the pulse-to-pulse-delay has been performed to obtain the resonance condition. QFluid and PIC (ALaDyn 2D) simulation are in excellent agreement.

solves the plasma dynamics in a 2D cylindrical geometry by means of the Quasi Static Approximation.⁴⁶ Electron macroparticles move kinetically in a full 3D dynamics depicted by the longitudinal E_z and radial E_r electric field, the azimuthal magnetic field B_ϕ and ponderomotive forces due to laser pulses. The main laser pulse train propagates following the envelope evolution equation with the second time derivative included,⁴⁷ while the evolution of the ionization pulse follows the Gaussian pulse evolution prescription. For our purposes, in the absence of non-fluid plasma behavior, strong longitudinal background gradients and radial anisotropies, QFluid returns the same results of a 3D PIC code with much less demanding computation time/resources. In the simulations of Fig. 2, each pulse has a duration of 10fs and a waist size of 25 μm and is focused in a plasma having density of $n_e = 5 \times 10^{18} \text{ cm}^{-3}$. According to these plots, the eight-pulses train is capable of exciting a plasma wave whose electric field gradient is approximately 20% larger than the peak accelerating gradient of the single pulse.

III. TRAPPING CONDITIONS IN REMPI

To set conditions of particles trapping in the plasma wave, we will focus on a configuration where the longitudinal ponderomotive force dominates over the radial wakefield force, with a train of driving pulses having waist $w_{0,d}$ exceeding the plasma wavelength λ_p . In the 1D limit, the Hamiltonian of a passive particle in the plasma wave is⁴⁸ $H = (1 + u_z^2)^{1/2} - \beta_{ph} u_z - \phi$, where β_{ph} is the wave phase velocity (transverse contribution to the Lorentz factor has been neglected since relatively low values of the pulse amplitudes will be considered here). The separatrix Hamiltonian H_s decomposes the phase space in a sequence of periodic buckets, so trapping of newborn electrons occurs if the particle Hamiltonian satisfies $H \leq H_s$, i.e., if

$$\phi_e \geq 1 - 1/\gamma_{ph} + \phi_{min} \quad (1)$$

ϕ_e being the normalized electrostatic potential at particle extraction and ϕ_{min} the minimum potential. Equation (1) clearly states that the trapping condition relies on wave phase velocity and on wake electrostatic potential, i.e., on plasma density and normalized electric field $E_{norm} = E_z/E_0$ solely, where $E_0 = mc\omega_p/e$. The exact solution of the fully nonlinear wave equation in the 1D limit gives us a relationship between the normalized electric field and maximum/minimum potential⁴⁸ $\phi_{max,min} = E_{norm}^2/2 \pm \beta_{ph} \sqrt{(1 + E_{norm}^2/2)^2 - 1}$.

Trapping starts when Eq. (1) holds, i.e., when electrons reach the end of the bucket with the same speed as the wake phase speed ($v = \beta_{ph}c$). Since these electrons will not be accelerated further, we will refer to this condition as a “weak trapping condition”

$$2\beta_{ph} \sqrt{(1 + E_{norm}^2/2)^2 - 1} \geq 1 - 1/\gamma_{ph}. \quad (2)$$

Moreover, electrons that reach the speed of the wake before they experience the maximum accelerating field will dephase in the early stage of acceleration. As a consequence, a “strong trapping condition” can be introduced in such a way that electrons move with $v = \beta_{ph}c$ when they are in phase with the maximum longitudinal accelerating field. In this case the potential at $E_z = E_{max}$ is null, so we get

$$E_{norm}^2/2 + \beta_{ph} \sqrt{(1 + E_{norm}^2/2)^2 - 1} \geq 1 - 1/\gamma_{ph}. \quad (3)$$

Trapping analysis (see Fig. 3) reveals that efficient trapping occurs in a nonlinear wave regime since $E_{norm} \approx 0.5$, but far from the deep-nonlinear regime, E_{norm} being well below the longitudinal wavebreaking limit $E_{norm} \ll E_{WB}/E_0 = \sqrt{2(\gamma_{ph} - 1)} \gg 1$.⁴⁹ Such an analysis is confirmed by our simulations and it is useful to set trapping threshold values for peak pulse normalized amplitude $a_{0,d}$ in single or multi-pulse schemes.

If a plasma density of $n_e = 5 \times 10^{17} \text{ cm}^{-3}$ is selected, a matched set of parameters for the driving train gives each pulse duration of $T_d = 30$ fs FWHM, with a minimum waist $w_{0,d} = 45 \mu\text{ m}$ (the same parameters set will be used in the 250 TW state-of-the-art simulation, see below). Results of a set of QFluid simulations with a scan of the maximum accelerating field versus pulse normalized amplitude and the number of pulses in the driving train is reported in Fig. 3 (bottom). Three delivered energies of 2.5 J, 5.0 J, and 7.5 J have been considered and, for any of them, a single-pulse, two, four and eight-pulses trains have been simulated. As shown in Fig. 3 (bottom), for a fixed total delivered laser energy, as the number of pulses in the train increases the maximum accelerating gradient of the wave increases due to a resonance enhancement of the wave. Moreover, from Fig. 3 (top and bottom), we can infer that the weak-trapping threshold Eq. (2) is reached with a single-pulse of normalized amplitude exceeding $a_{0,d} = 1.6$, while in the case of an eight-pulses train, weak-trapping threshold normalized amplitude is reduced to $a_{0,d} = 0.5$.

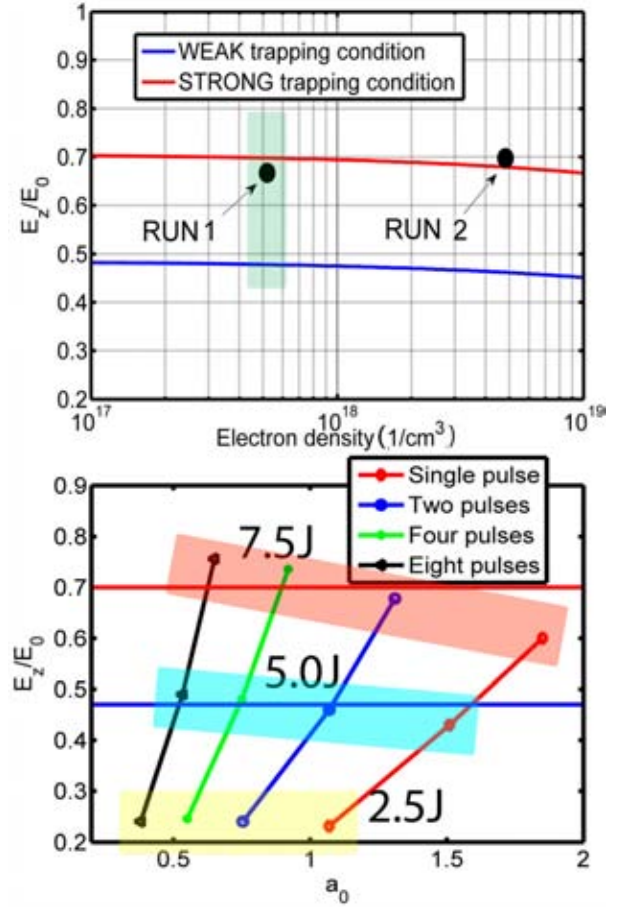


FIG. 3. Trapping conditions. Blue lines: weak trapping threshold; red lines: strong trapping condition. Top: trapping conditions in a 1D nonlinear limit vs plasma density from 1D analytical expression Eqs. (2) and (3). RUN 1,2 refer to the working points of the state-of-the-art simulation (Sec. V) and the simulation in Appendix B, respectively. Bottom: scan of maximum accelerating normalized fields as in the RUN 1 setup ($T_d = 30$ fs, $n_e = 5 \times 10^{17} \text{ cm}^{-3}$, $w_{0,d} = 45 \mu\text{ m}$) as a function of pulse amplitude and the number of pulses in the train. The cases of a single pulse and two, four and eight-pulses trains with three different delivered energies of 2.5 J, 5.0 J and 7.5 J have been considered. A numerical scan with QFluid of the pulse-to-pulse delay has been performed to obtain the resonance condition for each number of pulses.

IV. IONIZATION DYNAMICS IN LINEAR POLARIZATION

Ultraintense laser pulses possess electric fields large enough to make tunneling as the dominant ionization mechanism (i.e., Keldysh parameter⁵⁰ $\gamma_K = \sqrt{2U_I/mc^2}/a_0 \ll 1$) so the Ammosov-Delone-Krainov (ADK) ionization rate⁵¹ (see also Ref. 52 for a general discussion about the strong laser field ionization) can be assumed to evaluate electron extraction from the initial level (see the Appendix). Ionization potential of 6th electron from nitrogen is $U_I^{6th} = 552 \text{ eV}$ and efficient extraction of 6th electron of nitrogen requires $a_0 \approx 1.7$ for a few tens of femtoseconds long pulses at $\lambda = 0.8 \mu\text{ m}$. On the other hand, Argon can be ionized from the 8th level to 9th level ($U_I^{9th} = 422.5 \text{ eV}$) at a much lower intensity, where $a_0 \approx 0.8$ and $a_0 \approx 0.4$ with $\lambda = 0.8 \mu\text{ m}$ and $\lambda = 0.4 \mu\text{ m}$, respectively.

We point out that a detailed description of ionization dynamics is crucial not only to correctly estimate the number

of bunch electrons but (more importantly) to get a precise measure of the transverse phase space covered by newborn electrons. In the linear polarization case, most of the electrons are ejected when the local electric field is maximum, i.e., when the pulse normalized amplitude a_e (the normalized amplitude at the extraction time) is null. These electrons will leave the pulse with a negligible quivering mean momentum along the polarization axis x . If newborn electrons leave the atom when electric field is not exactly at its maximum, a non null transverse momentum $u_x = p_x/mc = -a_e$ is acquired, a_e being the local pulse potential at the extraction time. Moreover, ponderomotive forces introduce an axisymmetric contribution to particle transverse momentum. Following Ref. 53, we can write an expression for the *rms* momentum along the x direction as a function of the pulse amplitude *envelope* at the extraction time a_{0e}

$$\sigma_{u_x} \cong \Delta \cdot a_{0e} = \sqrt{a_{0e}^3/a_c}, \quad (4)$$

where $a_c = 0.107(U_I/U_H)^{3/2}\lambda$ is a critical pulse normalized amplitude and $\Delta = \sqrt{a_{0e}/a_c}$ [see Eqs. (7) and (10) in Ref. 53]. Equation (4) gives us an accurate estimate of the minimum transverse momentum obtainable by the ionization process.

Trapping analysis with a standard *single* driving pulse shows that nitrogen could be used in a simplified ionization injection (as suggested in Ref. 34). Since efficient ionization threshold for N^{6+} is $a_{0,d} \approx 1.7$ for $\lambda_d = 0.8 \mu\text{m}$, a small interval of $1.6 < a_{0,d} < 1.7$ for the pulse normalized amplitude is suitable for both trapping and ionization purposes. Such a simplified scheme could be useful either for demonstration purposes or to obtain a controlled injection for good-quality bunches without ultra-low emittance requirements. A two-pulses driver is a far better choice since an optimal pulse normalized amplitude $1.1 < a_{0,d} < 1.3$ allows us to strongly inhibit driver pulses ionization. Using argon ($Ar^{8+} \rightarrow Ar^{9+}$) as a contaminant instead of nitrogen gives us a drastic reduction of transverse particle momentum since the ionization level is saturated with an ionizing pulse with normalized amplitude above $a_{0,i} = 0.4$ at $\lambda_i = 0.4 \mu\text{m}$. Multi-pulse ionization injection with argon; however, requires trains with at least four pulses since the normalized pulse amplitude should not exceed $a_{0,d} = 0.8$ at $\lambda_d = 0.8 \mu\text{m}$ (see Fig. 3).

V. STATE-OF-THE-ART 250 TW SIMULATION

The reported simulation (RUN 1) of our Resonant Multi-Pulse Ionization injection is based upon a linearly polarized Ti:Sa laser pulse that is initially split into the ionizing pulse and the eight-pulses driver train, each sub-pulse being 30 fs FWHM in duration and delivering 895 mJ of energy, with a maximum pulse amplitude $a_{0,d} = 0.64$ and minimum waist size $w_{0,d} = 45 \mu\text{m}$. In the present working point, consisting of a relatively low number of pulses that drive a weakly nonlinear plasma wave, the optimal pulse-to-pulse delay used for the simulation $T_{delay} = 1.015 \times \lambda_p/c$ differs of a most a few percent from the linear one.

The uniform plasma electron density is set to $n_e = 5 \times 10^{17} \text{ cm}^{-3}$ (plasma wavelength is $\lambda_p = 46.9 \mu\text{m}$), obtained

with a pure argon pre-ionized up to the 8th level. The frequency doubled component (the “ionizing pulse”) with wavelength $\lambda_i = 0.4 \mu\text{m}$, amplitude $a_{0,i} = 0.41$ and duration $T_i = 38 \text{ fs}$ is focused with a waist $w_{0,i} = 3.5 \mu\text{m}$. The QFluid simulation (see Fig. 4) has been performed in a moving cylinder having a radius $4 \times w_0$ with a resolution of $\lambda_p/100$ and $\lambda_p/200$ in the radial and longitudinal coordinates, respectively.

Electrons extracted in the bulk of the ionizing pulse move suddenly backwards in the wake reaching the peak of the accelerating gradient of relative intensity $E_{norm} = E_z/E_0 = 0.685$, i.e., very close to the strong-trapping condition (see Fig. 3). Even though the driving pulse sequence generates a marginal further ionization of Ar^{8+} with a maximum percentage ionization of about 3%, such a dark current will not be trapped in the wake (particles are extracted away from the optimal extraction point of maximum potential ϕ_{max}) and so it will have no detrimental effect on beam quality. Moreover, the short Rayleigh length $Z_R = \pi w_{0,i}^2/\lambda_i \approx 100 \mu\text{m}$ ensures a sudden truncation of beam charging that turns into a small rms absolute energy spread $\Delta E \approx E_{norm} \times E_0 \times Z_R \approx 5 \text{ MeV}$ and extracted charge $Q = 3.8 \text{ pC}$.

At the end of beam charging, i.e., after about $200 \mu\text{m}$ of propagation, the *rms* bunch length is $0.56 \mu\text{m}$ and the transverse normalized emittance is $\epsilon_{n,x} = 0.070 \text{ mm} \times \text{mrad}$ in the polarization direction x and $\epsilon_{n,y} = 0.016 \text{ mm} \times \text{mrad}$ along the y direction. Afterwards, the *quasi-matched* beam

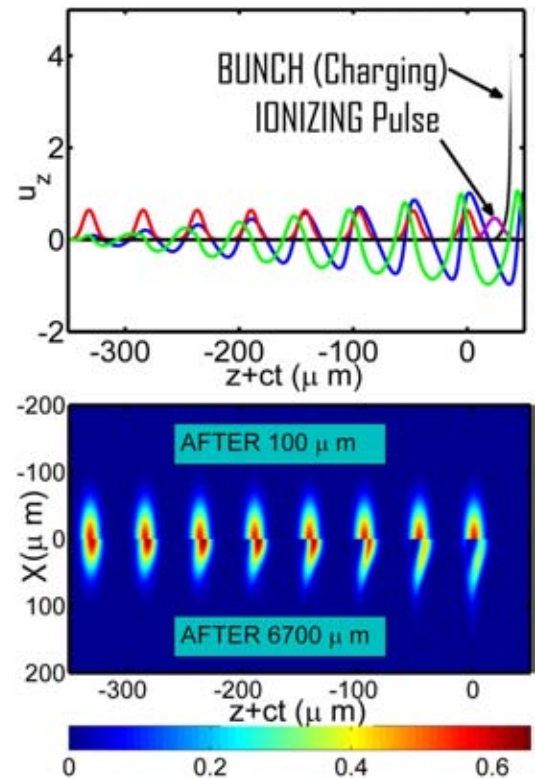


FIG. 4. QFluid Snapshot after $100 \mu\text{m}$ of propagation and after 6.5 mm . Top: (after $100 \mu\text{m}$) lineout of the pulses amplitudes (red/purple lines), accelerating gradient (blue line) fluid longitudinal momentum (green line) and extracted particle’s longitudinal phase-space. Electrons ejected by the driving pulse train do not comply with trapping conditions and move as a (quasi) fluid. Bottom: laser pulse amplitude comparison after $100 \mu\text{m}$ (upper) and after 6.5 mm (lower).

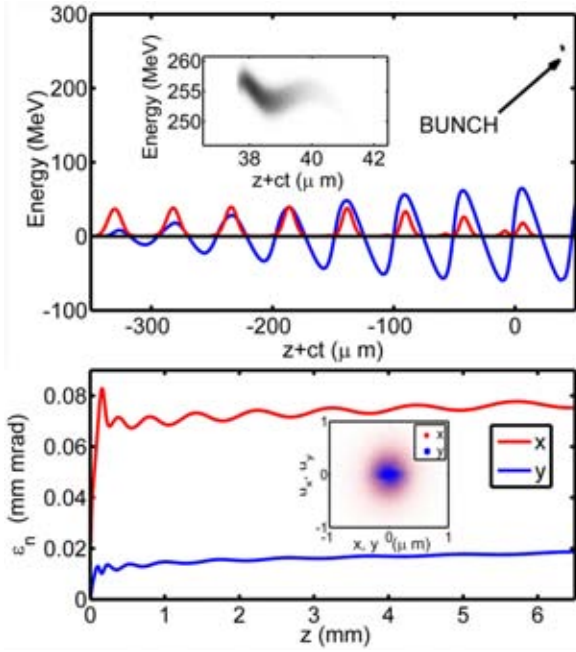


FIG. 5. Bunch quality. Top: Final longitudinal position-energy distribution. Blue and red lines represent the accelerating gradient and pulse amplitude on axis on a.u., respectively. Inset: zoom of the longitudinal phase space. Bottom: Normalized emittance in mm \times mrad as bunch moves into the wake. Inset: final transverse phase space.

experiences damped betatron oscillations with a converging beam radius of $0.4 \mu\text{m}$ that generates an emittance growth of about 10% as simulation ends (see Fig. 5).

Since in the weak nonlinear regime there is no electron density cavitation as in the bubble regime, beam loading might be a serious limit for beam quality. In the current working point, however, beam loading is present but exerts a tiny perturbation (of about 1%) of the longitudinal field on the bunch core, as it is evident in Fig. 6. We expect, therefore, that the transverse asymmetry of the bunch ($\sigma(x) \approx 2\sigma(y)$) arising from the initial transverse momentum will generate asymmetric beam loading effects but with very low amplitude.

At the end of the 6.5 mm long extraction/acceleration phase, the bunch has mean energy 265 MeV, with final

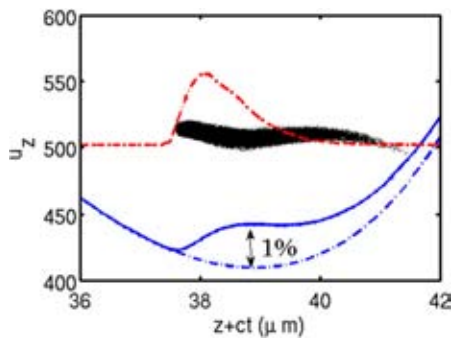


FIG. 6. Beam loading effect at the end of the simulation. The longitudinal phase space of the beam is shown along with the (on axis) beam density (red line), accelerating field (full blue line), and reference field without beam-loading (dashed blue line). Beam loading makes a decrease of the longitudinal field of about 1% at most.

normalized emittances of $0.076 \text{ mm} \times \text{mrad}$ (x axis) and $0.018 \text{ mm} \times \text{mrad}$ (y axis), with an *rms* energy spread 0.65% and the peak current of about 1 kA. These extremely low values of emittance and energy spread show that the proposed Resonant Multi-Pulse Ionization injection scheme is ideal for the generation of very high quality accelerated bunches.

VI. CONCLUSIONS

We described a new, ultra-low emittance, LWFA injector scheme that uses a Resonant train of pulses to drive plasma waves having amplitude large enough to trap and accelerate electrons extracted by ionization. The train of pulses is obtained by temporal shaping of an ultrashort pulse. Unlike the original two-color ionization injection, a *single* laser system (e.g., Ti:Sa) can be therefore employed to both drive the plasma wave and extract newborn electrons by ionization. Simulations consistently show that the main processes, including extraction of electrons due to the ionizing pulse, their trapping in the bucket and subsequent acceleration can be controlled by tuning electron density and laser intensity. Simulations also show a negligible contribution of spurious electrons extracted directly by the driver pulses. Simulations carried out under different plasma conditions show feasibility of the scheme with state-of-the-art-lasers making ReMPI suitable either for direct interaction (e.g., Thomson Scattering or FEL) or as ultra-low emittance injector for GeV-scale energy boosting.

Very recently Cowley *et al.*⁴¹ reported on very encouraging results about the feasibility of their time-shaping setup, with the demonstration of efficient excitation of the plasma wave via Multi-Pulse LWFA. The ReMPI scheme could be tested with two pulses in the train at first, with nitrogen as a contaminant species. In order to obtain very good-quality electron bunches; however, argon should be preferred and in this case more than four pulses in the train are necessary as shown in Sec. III.

ACKNOWLEDGMENTS

The research leading to these results has received funding from the European Union's Horizon 2020 Research and Innovation Program under Grant Agreement No. 653782–EuPRAXIA. The authors also acknowledge financial support from the ELI-ITALY Network funded by CNR. They would like to thank CNAF-INFN for access to computational resources. Finally, the authors acknowledge support from Manuel Kirchen from Hamburg University for his help about the FB-PIC code.

APPENDIX A. ADK IONIZATION RATE

In this paper, we use the following formulation of the instantaneous ADK ionization rate in the tunneling regime:⁵¹

$$w_{ADK}(|m|) = C \times \rho_{ADK}^{n(|m|)} \times \exp(-1/\rho_{ADK}), \quad (A1)$$

where $n(|m|) = -2n^* + |m| + 1$, C is a coefficient depending on the atomic numbers and ionization energy U_I ($U_H = 13.6\text{eV}$)

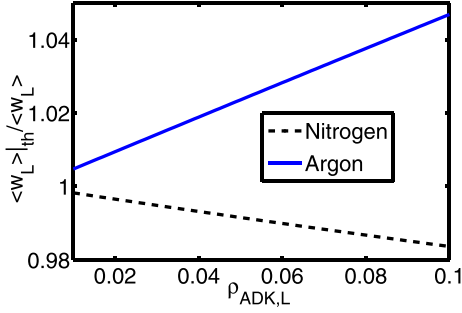


FIG. 7. Comparison between the numerical estimation of the mean-cycled ADK rate and the widely used analytical result of Eq. (A4) for Ar^{9+} and N^{6+} final states.

$$C = \frac{1}{4\pi} \left(\frac{U_I}{U_H} \right)^{3/2} 3^{(2n^* - |m| - 1)} \left[\frac{4e^2}{n^{*2} - l^{*2}} \right]^{n^*} \left[\frac{n^* - l^*}{n^* + l^*} \right]^{l^* + \frac{1}{2}}, \quad (\text{A2})$$

and $\rho_{ADK} = 3/2(E/E_{at})(U_H/U_I)^{3/2}$, where $E_{at} = 0.514$ TV/m and E the atomic and the local electric fields, respectively. The effective quantum numbers are $n^* = Z\sqrt{U_H/U_I}$ and $l^* = n_0^* - 1$, n_0^* being referred to the lower state with the same l . A critical electric field $E_c = 2/3E_{at}(U_I/U_H)^{3/2}$, giving a scale of a short-time scale ionization, can be introduced. By expressing E/E_c using vector potentials, we get $a/a_c = \rho_{ADK} = 9.37(U_H/U_I)^{3/2}a/\lambda$ which is nothing but the square of Δ parameter in Refs. 53 and 54.

In the circularly polarized pulse case, the electric field rotates within each cycle still retaining the same intensity, so in the tunnelling regime the mean-cycled ionization rate coincides with the instantaneous rate of Eq. (A1)

$$\langle w_c \rangle = w_{ADK}. \quad (\text{A3})$$

In the linearly polarized pulse case, the mean over a cycle can be performed analytically after a Taylor expansion of the leading exponential term. The well-known result (rewritten in our notation) is

$$\langle w_L \rangle = w_{ADK}(\rho_{ADK,0}) \times \left(\frac{2}{\pi} \rho_{ADK,0} \right)^{1/2}, \quad (\text{A4})$$

where $\rho_{ADK,0}$ is the peak value of $\rho_{ADK} = a/a_c$ within the cycle. A numerical estimation of the mean-cycled rate confirms the validity of Eq. (A4) with errors below 4% in the ionization rates, for ρ_{ADK} parameters in the range of interest for ionization injection techniques (see Fig. 7).

APPENDIX B: QFLUID CODE

The 2D *cylindrical*, cold-fluid/kinetic code QFluid solves the plasma dynamic by means of the Quasi Static Approximation.⁴⁶ Electron macroparticles move kinetically in a full 3D dynamics depicted by the longitudinal E_z and radial E_r electric field, the azimuthal magnetic field B_ϕ and ponderomotive forces due to laser pulses. The main laser pulse train propagates following the envelope evolution equation with the second time derivative included.⁴⁷ Particle extraction from atoms/ions is simulated with an ADK rate including the mean over a pulse cycle, while newborn particles are finally ejected with a random transverse momentum u_\perp , whose rms value

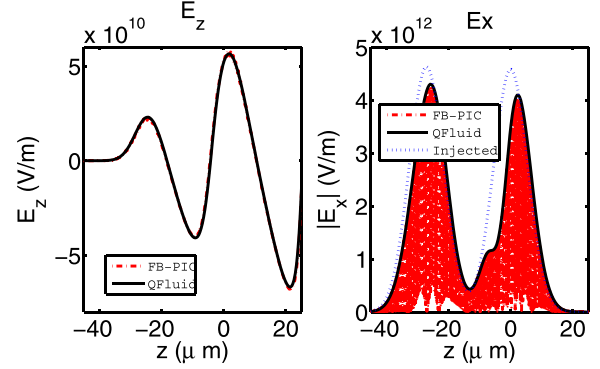


FIG. 8. FB-PIC vs QFluid in a two-pulses driver configuration with nitrogen. Snapshot after $700 \mu\text{m}$ of propagation into a plasma with background density of $n_e = 1.5 \times 10^{18} \text{cm}^{-3}$. Left: longitudinal electric field on axis. Right: pulse electric field (FB-PIC) and its amplitude (QFluid). The injected pulse amplitude (blue dotted line) has been shown for reference.

depends on the polarization of the pulses. For a linear polarization (as for the ionizing pulse), we assigned $\sigma_{ix} \cong \Delta \cdot a_{0e} = \sqrt{a_{0e}^3/a_c}$ [see Eq. (4)], while for the circular polarization each extracted particle is associated to a random extraction phase ϕ_e so as $u_x = a_{0e} \times \cos(\phi_e)$, $u_y = a_{0e} \times \sin(\phi_e)$. Benchmark of QFluid with a multi-pulse setup has been obtained in a nonlinear regime with ALaDyn⁴⁴ (used here in either a 3D with laser envelope configuration or a 2D slice with a full-PIC pulse evolution) and with FB-PIC (quasi-3D PIC).⁵⁵ The comparison of QFluid with FB-PIC is focused on a 2-pulses driver scheme with nitrogen as atomic species. The selected working point consists of linearly polarized pulses of duration $T_d = 30$ fs, minimum waist size $w_{0,d} = 12 \mu\text{m}$ and amplitude $a_{0,d} = 1.2$ delayed by a plasma wavelength ($\lambda_p = 27 \mu\text{m}$ with $n_e = 1.5 \times 10^{18} \text{cm}^{-3}$). FB-PIC simulations were performed with two azimuthal modes, i.e., possible deviation from perfect azimuthal symmetry were included.

The comparison between FB-PIC and QFluid simulation (see Fig. 8) shows a perfect superposition between the codes output, notwithstanding the nontrivial evolution of the pulses due to both nonlinear effects and the variation of the susceptibility due to the wake.

The first QFluid and ALaDyn comparison shown here has been focused on an eight-pulses driver train with argon as atomic species, with selected working point as the same as the state-of-the-art setup. To fasten the 3D PIC simulation, ALaDyn has been equipped with an envelope pulse solver. The ALaDyn/envelope code implements a fully 3D PIC scheme for particle motion whereas the laser pulses are represented by the envelope model proposed in Ref. 56.

Once again (see Fig. 9), QFluid outcomes deviate at most of a few percent from those of a 3D PIC (full 3D in this case).

Finally, a full-PIC (not in envelope approximation) in 2D slice geometry vs QFluid comparison, including the bunch extraction and trapping, will be presented (RUN 2). To save computational time, a high-density setup has been simulated. A train of eight 10fs linearly polarized Ti:Sa pulses impinge

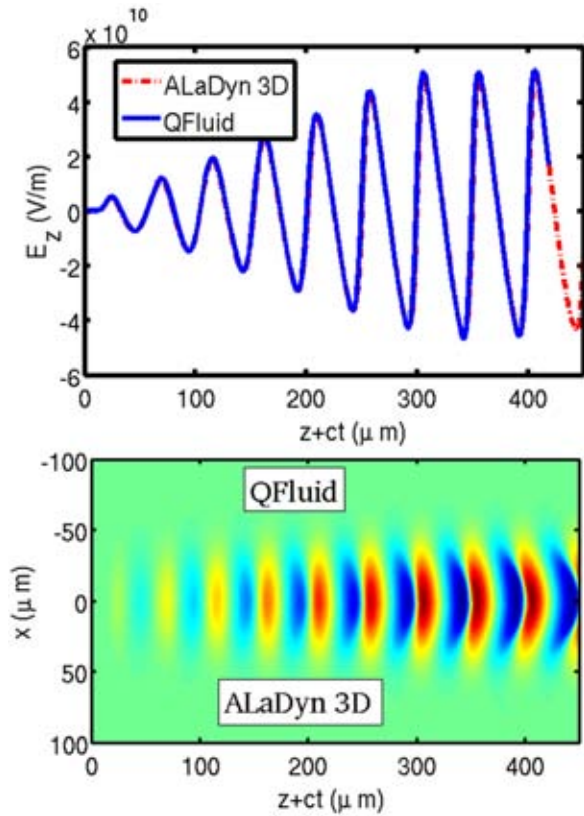


FIG. 9. ALaDyn vs QFluid in an eight-pulses setup with argon (state-of-the-art run parameters). Top: Snapshot of the on-axis longitudinal electric field after 1 mm of propagation. Bottom: radial maps of $E_{norm} = E_z/E_0$ for Qfluid (upper side) vs ALaDyn (lower side).

onto a preformed plasma of Ar^{8+} with density $5 \times 10^{18} \text{ cm}^{-3}$. The driver pulse train has a waist size $w_{0,d} = 25 \mu\text{m}$ and a normalized amplitude $a_{0,d} = 0.589$, having a pulse delay of a single plasma period $T_p = 2\pi/\omega_p$. We use a relatively large focal spot with $w_{0,d} > \lambda_{p,d} = 14.8 \mu\text{m}$, so as to reduce the effects of the missing third dimension in the PIC simulations. The frequency doubled ionizing pulse is injected with a delay of $1.5 \times T_p$ in the vicinity of its focus with a waist $w_{0,i} = 3.5 \mu\text{m}$ and possesses a peak pulse amplitude of $a_{0,i} = 0.41$. PIC simulations were performed with a $170 \times 150 \mu\text{m}^2$ box in the longitudinal and transverse directions with a resolution of $\lambda_d/40$ and $\lambda_d/10$, respectively. QFluid simulations were carried out in the same (cylindrical) box size with resolution $\lambda_p/70$ and $\lambda_p/35$ in the longitudinal and radial coordinates, respectively.

The final snapshot of both simulations, after $300 \mu\text{m}$ propagation in the plasma is shown in Fig. 10, where the injected electron bunch just at the end of the charging phase is visible (black and blue dots). Due to the large ponderomotive forces (that scale as $a_{0,i}^2/w_{0,i}$, see Eq. (23) in Ref. 53), bunch transverse *rms* momentum (0.26 mc for QFluid and 0.27 mc for ALaDyn, respectively) shows an increase of about a factor of 2 from the value expected by Eq. (4).

We finally stress that QFluid cannot face with the plasma exit of the generated bunch since the Quasi Static Approximation requires a steady plasma density within the box. A PIC code will be used in a future work to simulate the plasma exit, too.

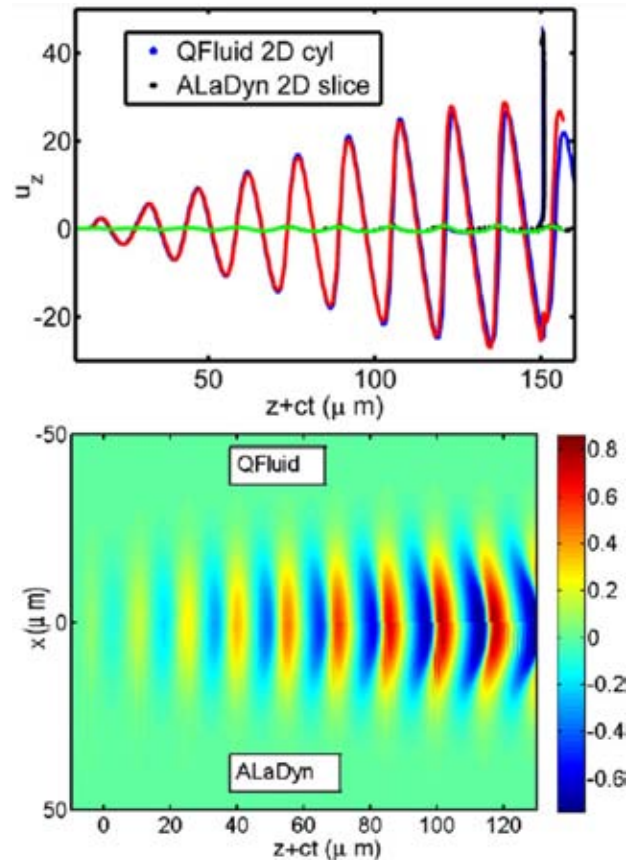


FIG. 10. 2D-slice ALaDyn and QFluid in RUN 2 setup. QFluid and ALaDyn PIC results after $300 \mu\text{m}$ of propagation. Top: (on-axis) ALaDyn phase space of particles (black dots), QFluid phase space of particles (blue dots), ALaDyn accelerating field (blue line, a.u.), and QFluid accelerating field (red line, a.u.). The green line represents fluid momentum of QFluid output. Bottom: Longitudinal electric field $E_{norm} = E_z/E_0$ from QFluid (upper) and ALaDyn (lower).

¹K. Nakajima, “Few femtosecond, few kiloampere electron bunch produced by a laser–plasma accelerator,” *Nat. Phys.* **4**, 92–93 (2008).

²V. Petrillo, M. P. Anania, M. Artioli, A. Bacci, M. Bellaveglia, E. Chiadroni, A. Cianchi, F. Ciocci, G. Dattoli, D. D. Giovenale, G. D. Pirro, M. Ferrario, G. Gatti, L. Giannessi, A. Mostacci, P. Musumeci, A. Petralia, R. Pompili, M. Quattromini, J. V. Rau, C. Ronsivalle, A. R. Rossi, E. Sabia, C. Vaccarezza, and F. Villa, “Observation of time-domain modulation of free-electron-laser pulses by multi-peaked electron-energy spectrum,” *Phys. Rev. Lett.* **111**, 114802 (2013).

³A. Loulergue, M. Labat, C. Evain, C. Benabderrahmane, V. Malka, and M. E. Couprie, “Beam manipulation for compact laser wakefield accelerator based free-electron lasers,” *New J. Phys.* **17**, 023028 (2015).

⁴E. Esarey, S. K. Ride, and P. Sprangle, “Nonlinear Thomson scattering of intense laser pulses from beams and plasmas,” *Phys. Rev. E* **48**, 3003 (1993).

⁵P. Tomassini, A. Giuliotti, D. Giuliotti, and L. A. Gizzi, “Thomson back-scattering x-rays from ultra-relativistic electron bunches and temporally shaped laser pulses,” *Appl Phys. B* **80**, 419–436 (2005).

⁶S. Corde, K. Ta Phuoc, G. Lambert, R. Fitour, V. Malka, A. Rousse, A. Beck, and E. Lefebvre, “Femtosecond x rays from laser-plasma accelerators,” *Rev. Mod. Phys.* **85**, 1 (2013).

⁷V. Petrillo, A. Bacci, C. Curatolo, I. Drebot, A. Giribono, C. Maroli, A. R. Rossi, L. Serafini, P. Tomassini, C. Vaccarezza, and A. Variola, “Polarization of $x-\gamma$ radiation produced by a Thomson and Compton inverse scattering,” *Phys. Rev. Spec. Top.-Accel. Beams* **18**, 110701 (2015).

⁸D. Micieli, I. Drebot, A. Bacci, E. Milotti, V. Petrillo, M. Rossetti Conti, A. R. Rossi, E. Tassi, and L. Serafini, “Compton sources for the observation of elastic photon-photon scattering events,” *Phys. Rev. Spec. Top.-Accel. Beams* **19**, 093401 (2016).

- ⁹A. Döpp, E. Guillaume, C. Thaurya, A. Lifschitz, K. Ta Phuoc, and V. Malka, "Energy boost in laser wakefield accelerators using sharp density transitions," *Phys. Plasmas* **23**, 056702 (2016).
- ¹⁰S. Steinke, J. Van Tilborg, C. Benedetti, C. G. R. Geddes, J. Daniels, K. K. Swanson, A. J. Gonsalves, K. Nakamura, B. H. Shaw, C. B. Schroeder, E. Esarey, and W. P. Leemans, "Staging of laser-plasma accelerators," *Phys. Plasmas* **23**, 056705 (2016).
- ¹¹T. L. Audet, F. G. Desforges, A. Maitrallain, S. D. Dufrenoy, M. Bougeard, G. Maynard, P. Lee, M. Hansson, B. Auran, A. Persson, I. G. González, P. Monot, C.-G. Wahlström, O. Lundh, and B. Cros, "Electron injector for compact staged high energy accelerator," *Nucl. Instrum. Methods Phys. Res., Sect. A* **829**, 304–308 (2016).
- ¹²G. Golovin, S. Banerjee, S. Chen, N. Powers, C. Liu, W. Yan, J. Zhang, P. Zhang, B. Zhao, and D. Umstadter, "Control and optimization of a staged laser-wake field accelerator," *Nucl. Instrum. Methods Phys. Res., Sect. A* **830**, 375–380 (2016).
- ¹³Z. Zhang, W. Li, J. Liu, W. Wang, C. Yu, Y. Tian, K. Nakajima, A. Deng, R. Qi, C. Wang, Z. Qin, M. Fang, J. Liu, C. Xia, R. Li, and Z. Xu, "Energy spread minimization in a cascaded laser wakefield accelerator via velocity bunching," *Phys. Plasmas* **23**, 053106 (2016).
- ¹⁴J. Faure, Y. Glinec, A. Pukhov, S. Kiselev, S. Gordienko, E. Lefebvre, J.-P. Rousseau, F. Burgy, and V. Malka, "A laser-plasma accelerator producing monoenergetic electron beams," *Nature* **431**, 541 (2004).
- ¹⁵G. R. Plateau, C. G. R. Geddes, D. B. Thorn, M. Chen, C. Benedetti, E. Esarey, A. J. Gonsalves, N. H. Matlis, K. Nakamura, C. B. Schroeder, S. Shiraishi, T. Sokollik, J. van Tilborg, C. Toth, S. Trotsenko, T. S. Kim, M. Battaglia, T. Stöhlker, and W. P. Leemans, "Low-emittance electron bunches from a laser-plasma accelerator measured using single-shot x-ray spectroscopy," *Phys. Rev. Lett.* **109**, 064802 (2012).
- ¹⁶S. Bulanov, N. Naumova, F. Pegoraro, and J. Sakai, "Particle injection into the wave acceleration phase due to nonlinear wake wave breaking," *Phys. Rev. E* **58**, R5257 (1998).
- ¹⁷H. Suk, N. Barov, J. B. Rosenzweig, and E. Esarey, "Plasma electron trapping and acceleration in a plasma wake field using a density transition," *Phys. Rev. Lett.* **86**, 1011–1014 (2001).
- ¹⁸P. Tomassini, M. Galimberti, A. Giulietti, D. Giulietti, L. A. Gizzi, L. Labate, and F. Pegoraro, "Production of high-quality electron beams in numerical experiments of laser wakefield acceleration with longitudinal wave breaking," *Phys. Rev. Spec. Top.-Accel. Beams* **6**, 121301 (2003).
- ¹⁹C. G. R. Geddes, E. Cormier-Michel, E. Esarey, K. Nakamura, G. R. Plateau, C. B. Schroeder, C. Toth, D. L. Bruhwiler, J. R. Cary, and W. P. Leemans, "Plasma gradient controlled injection and postacceleration of high quality electron bunches," in *Proceedings of the Thirteenth Advanced Accelerator Concepts Workshop* (2008), p. 1086.
- ²⁰A. Buck, J. Wenz, J. Xu, K. Khrennikov, K. Schmid, M. Heigoldt, J. M. Mikhailova, M. Geissler, B. Shen, F. Krausz, S. Karsch, and L. Veisz, "Shock-front injector for high-quality laser-plasma acceleration," *Phys. Rev. Lett.* **110**, 185006 (2013).
- ²¹E. Esarey, R. F. Hubbard, W. P. Leemans, A. Ting, and P. Sprangle, "Electron injection into plasma wakefields by colliding laser pulses," *Phys. Rev. Lett.* **79**, 2682 (1997).
- ²²H. Kotaki, I. Daito, M. Kando, Y. Hayashi, K. Kawase, T. Kameshima, Y. Fukuda, T. Homma, J. Ma, L. M. Chen *et al.*, "Electron optical injection with head-on and counter-crossing colliding laser pulses," *Phys. Rev. Lett.* **103**, 194803 (2009).
- ²³M. Chen, E. Esarey, C. G. R. Geddes, E. Cormier-Michel, C. B. Schroeder, S. S. Bulanov, C. Benedetti, L. L. Yu, S. Rykovanov, D. L. Bruhwiler, and W. P. Leemans, "Electron injection and emittance control by transverse colliding pulses in a laser-plasma accelerator," *Phys. Rev. Spec. Top.-Accel. Beams* **17**, 051303 (2014).
- ²⁴M. Chen, Z.-M. Sheng, Y.-Y. Ma, and J. Zhang, "Electron injection and trapping in a laser wakefield by field ionization to high-charge states of gases," *J. Appl. Phys.* **99**, 056109 (2006).
- ²⁵A. Pak, K. A. Marsh, S. F. Martins, W. Lu, W. B. Mori, and C. Joshi, "Injection and trapping of tunnel-ionized electrons into laser-produced wakes," *Phys. Rev. Lett.* **104**, 025003 (2010).
- ²⁶C. McGuffey, A. G. Thomas, W. Schumaker, T. Matsuoka, V. Chvykov, F. J. Dollar, G. Kalintchenko, V. Yanovsky, A. Maksimchuk, K. Krushelnick *et al.*, "Ionization induced trapping in a laser wakefield accelerator," *Phys. Rev. Lett.* **104**, 025004 (2010).
- ²⁷C. Thaury, E. Guillaume, A. Lifschitz, K. Ta Phuoc, M. Hansson, G. Grittani, J. Gautier, J.-P. Goddet, A. Tafzi, O. Lundh, and V. Malka, "Shock assisted ionization injection in laser-plasma accelerators," *Sci. Rep.* **5**, 16310 (2015).
- ²⁸C. E. Clayton, J. E. Ralph, F. Albert, R. A. Fonseca, S. H. Glenzer, C. Joshi, W. Lu, K. A. Marsh, S. F. Martins, W. B. Mori, A. Pak, F. S. Tsung, B. B. Pollock, J. S. Ross, L. O. Silva, and D. H. Froula, "Self-guided laser wakefield acceleration beyond 1 gev using ionization-induced injection," *Phys. Rev. Lett.* **105**, 105003 (2010).
- ²⁹M. Chen, E. Esarey, C. B. Schroeder, C. G. R. Geddes, and W. P. Leemans, "Theory of ionization-induced trapping in laser-plasma accelerators," *Phys. Plasmas* **19**, 033101 (2012).
- ³⁰M. Zeng, M. Chen, L. L. Yu, W. B. Mori, Z. M. Sheng, B. Hidding, D. A. Jaroszynski, and J. Zhang, "Multichromatic narrow-energy-spread electron bunches from laser-wakefield acceleration with dual-color lasers," *Phys. Rev. Lett.* **114**, 084801 (2015).
- ³¹M. Zeng, J. Luo, M. Chen, W. B. Mori, Z.-M. Sheng, and B. Hidding, "High quality electron beam acceleration by ionization injection in laser wakefields with mid-infrared dual-color lasers," *Phys. Plasmas* **23**, 063113 (2016).
- ³²T. L. Audet, M. Hansson, P. Lee, F. G. Desforges, G. Maynard, S. Dobosz Dufrenoy, R. Lehe, J.-L. Vay, B. Auran, A. Persson, I. Gallardo González, A. Maitrallain, P. Monot, C.-G. Wahlström, O. Lundh, and B. Cros, "Investigation of ionization-induced electron injection in a wakefield driven by laser inside a gas cell," *Phys. Plasmas* **23**, 023110 (2016).
- ³³N. Bourgeois, J. Cowley, and S. M. Hooker, "Two-pulse ionization injection into quasilinear laser wakefields," *Phys. Rev. Lett.* **111**, 155004 (2013).
- ³⁴L.-L. Yu, E. Esarey, C. B. Schroeder, J.-L. Vay, C. Benedetti, C. G. R. Geddes, M. Chen, and W. P. Leemans, "Two-color laser-ionization injection," *Phys. Rev. Lett.* **112**, 125001 (2014).
- ³⁵L.-L. Yu, E. Esarey, C. B. Schroeder, J.-L. Vay, C. Benedetti, C. G. R. Geddes, M. Chen, and W. P. Leemans, "Ultra-low emittance electron beams from two-color laser-ionization injection," *AIP Conf. Proc.* **1777**, 040019 (2016).
- ³⁶X. L. Xu, Y. P. Wu, C. J. Zhang, F. Li, Y. Wan, J. F. Hua, C.-H. Pai, W. Lu, P. Yu, and W. B. Mori, "Low emittance electron beam generation from a laser wakefield accelerator using two laser pulses with different wavelengths," *Phys. Rev. Spec. Top.-Accel. Beams* **17**, 061301 (2014).
- ³⁷D. Umstadter, E. Esarey, and J. Kim, "Nonlinear plasma waves driven by optimized laser pulse trains," *Phys. Rev. Lett.* **72**, 1224 (1994).
- ³⁸S. Dalla and M. Lontano, "Large amplitude plasma wave excitation by means of sequences of short laser pulses," *Phys. Rev. E* **49**, R1819 (1994).
- ³⁹S. M. Hooker, R. Bartolini, S. P. D. Mangles, A. Tunnermann, L. Corner, J. Limpert, A. Seryi, and R. Walczak, "Multi-pulse laser wakefield acceleration: A new route to efficient, high-repetition-rate plasma accelerators and high flux radiation sources," *J. Phys. B* **47**, 234003 (2014).
- ⁴⁰R. J. Shalloo, L. Corner, C. Arran, J. Cowley, G. Cheung, C. Thornton, R. Walczak, and S. M. Hooker, "Generation of laser pulse trains for tests of multi-pulse laser wakefield acceleration," *Nucl. Instrum. Methods Phys. Res., Sect. A* **829**, 383–385 (2016).
- ⁴¹J. Cowley, C. Thornton, C. Arran, R. J. Shalloo, L. Corner, G. Cheung, C. D. Gregory, S. P. D. Mangles, N. H. Matlis, D. R. Symes, R. Walczak, and S. M. Hooker, "Excitation and control of plasma wakefields by multiple laser pulse," *Phys. Rev. Lett.* **119**, 044802 (2017).
- ⁴²K. Nakajima, D. Fisher, T. Kawakubo, H. Naknishi, A. Ogata, Y. Kato, Y. Kitagawa, R. Kodama, K. Mima, H. Shiraga *et al.*, "Observation of ultra-high gradient electron acceleration by a self-modulated intense short laser pulse," *Phys. Rev. Lett.* **74**, 4428–4431 (1995).
- ⁴³A. Modena, Z. Najmudin, A. E. Dangor, C. E. Clayton, K. A. Marsch, C. Joshi, V. Malka, C. B. Darrow, and C. Danson, "Observation of raman forward scattering and electron acceleration in the relativistic regime," *IEEE Trans. Plasma Sci.* **24**, 289 (1996).
- ⁴⁴C. Benedetti, A. Sgattoni, G. Turchetti, and P. Londrillo, "ALaDyn: A high-accuracy pic code for the Maxwell Vlasov equations," *IEEE Trans. Plasma Sci.* **36**, 1790 (2008).
- ⁴⁵P. Tomassini and A. R. Rossi, "Matching strategies for a plasma booster," *Plasma Phys. Controlled Fusion* **58**, 034001 (2016).
- ⁴⁶P. Sprangle, E. Esarey, and A. Ting, "Nonlinear theory of intense laser-plasma interaction," *Phys. Rev. Lett.* **64**, 2011–2014 (1990).
- ⁴⁷P. Sprangle, E. Esarey, and J. Krall, "Self-guiding and stability of intense optical beams in gases undergoing ionization," *Phys. Rev. E* **54**, 4211 (1996).
- ⁴⁸E. Esarey and M. Pilloff, "Trapping and acceleration in nonlinear plasma waves," *Phys. Plasmas* **2**, 1432 (1995).
- ⁴⁹A. I. Akhiezer and R. V. Polovin, "Theory of wave motion of an electron plasma," *Sov. Phys.-JETP* **3**, 696–705 (1956).

- ⁵⁰L. V. Keldysh, "Ionization in the field of a strong electromagnetic wave," *Zh. Eksp. Thor. Fiz.* **47**, 1945 (1964). [*Sov. Phys. JETP* **20**, 1307 (1965)].
- ⁵¹V. P. Krainov, W. Xiong, and S. L. Chin, "An introductory overview of tunnel ionization of atoms by intense lasers," *Laser Phys.* **2**, 4 (1992).
- ⁵²V. S. Popov, "Tunnel and multiphoton ionization of atoms and ions in a strong laser field (Keldysh theory)," *Phys. Usp.* **47**, 855–885 (2004).
- ⁵³C. B. Schroeder, J.-L. Vay, E. Esarey, S. Bulanov, C. Benedetti, L.-L. Yu, M. Chen, C. G. R. Geddes, and W. P. Leemans, "Thermal emittance from ionization-induced trapping in plasma accelerators," *Phys. Rev. Spec. Top.-Accel. Beams* **17**, 101301 (2014).
- ⁵⁴J.-W. Geng, L. Qin, M. Li, W.-H. Xiong, Y. Liu, Q. Gong, and L.-Y. Peng, "Nonadiabatic tunneling ionization of atoms in elliptically polarized laser fields," *J. Phys. B: At. Mol. Opt. Phys.* **47**, 204027 (2014).
- ⁵⁵R. Lehe, M. Kirchen, I. A. Andriyash, B. B. Godfrey, and J.-L. Vay, "A spectral quasi-cylindrical and dispersion-free Particle-In-Cell algorithm," *Comput. Phys. Commun.* **203**, 66–82 (2016).
- ⁵⁶P. Mora and T. M. Antonsen, Jr., "Kinetic modeling of intense, short laser pulses propagating in tenuous plasmas," *Phys. Plasmas* **4**, 217 (1997).

High-Quality electron bunch production for high-brilliance Thomson Scattering sources

Paolo Tomassini¹, Luca Labate^{1,3}, Pasquale Londrillo⁴,
Renato Fedele², Davide Terzani² and Leonida A. Gizzi^{1,3}

¹*Intense Laser Irradiation Laboratory, INO-CNR, Pisa (Italy)**

²*Dip. Fisica Universita' di Napoli Federico II (Italy)*

³*INFN, Pisa, (Italy) and*

⁴*INAF Bologna (Italy)*

Abstract

Laser Wake Field accelerated electrons need to exhibit a good beam-quality to comply with requirements of FEL or high brilliance Thomson Scattering sources, or to be post-accelerated in a further LWFA stage towards TeV energy scale. Controlling electron injection, plasma density profile and laser pulse evolution are therefore crucial tasks for high-quality e-bunch production. A new bunch injection scheme, the Resonant Multi-Pulse Ionization Injection (RMPII), is based on a single, ultrashort Ti:Sa laser system. In the RMPII the main portion of the pulse is temporally shaped as a sequence of resonant sub-pulses, while a minor portion acts as an ionizing pulse. Simulations show that high-quality electron bunches with energies in the range $265\text{MeV} - 1.15\text{GeV}$, normalized emittance as low as $0.08\text{ mm}\cdot\text{mrad}$ and 0.65% energy spread can be obtained with a single 250 TW Ti:Sa laser system. Applications of the e-beam in high-brilliance Thomson Scattering source, including $1.5 - 26.4\text{ MeV}$ γ sources with peak brilliance up to $1 \cdot 10^{28}\text{ ph}/(\text{s} \cdot \text{mm}^2 \cdot \text{mrad}^2 \cdot 0.1\% \text{ bw})$, are reported.

* paolo.tomassini@ino.it

I. INTRODUCTION

Ultra-high brilliance $UV/X/\gamma$ ray sources including Free Electron Lasers [1–3] and Thomson/Compton scattering sources [4, 5, 7–9], as well as multi-stage schemes in LWFA acceleration [10–12] require high-quality electron bunches. Controlled self-injection schemes as density downramp injection [15–19], colliding pulses injection [20–22] and ionization injection [23–28], are therefore under active theoretical and experimental investigation.

In the two-colour ionization injection [29–31] two laser systems are needed. The main pulse that drives the plasma wave has a long wavelength, five or ten micrometers, and a large amplitude $a_0 = eA/mc^2 = 8.5 \cdot 10^{-10} \sqrt{I\lambda^2} > 1$, being I and λ pulse intensity in W/cm^2 and wavelength in μm . The second pulse (the “ionization pulse”) is constituted by a frequency doubled Ti:Sa pulse. While the main pulse cannot further ionize the electrons in the external shells of the of the large Z contaminant species due to its large wavelength, the electric field of the ionization pulse is large enough to generate newborn electrons that will be trapped in the bucket. This opens the possibility of using gas species with relatively low ionization potentials, thus enabling separation of wake excitation from particle extraction and trapping. Two colour ionization injection is therefore a flexible and efficient scheme for high-quality electron bunch production. The main drawbacks of the two colour ionization injection are the current lack of availability of short ($T < 100$ fs) 100TW-class laser systems operating at large ($\approx 10\mu m$) wavelength and lasers synchronization jitter issues. These limitation make the two-colour scheme currently unpractical for application to LWFA-based devices requiring high quality beams.

A new injection scheme, the Resonant Multi-Pulse Ionization Injection [32], is derived from two-colour ionization and it has the possibility to be operative with present-day single Ti:Sa laser systems. Simulations show that such a scheme is capable of generating ultra-low emittance GeV-scale bunches that can be employed in High-Brilliance Thomson Scattering sources.

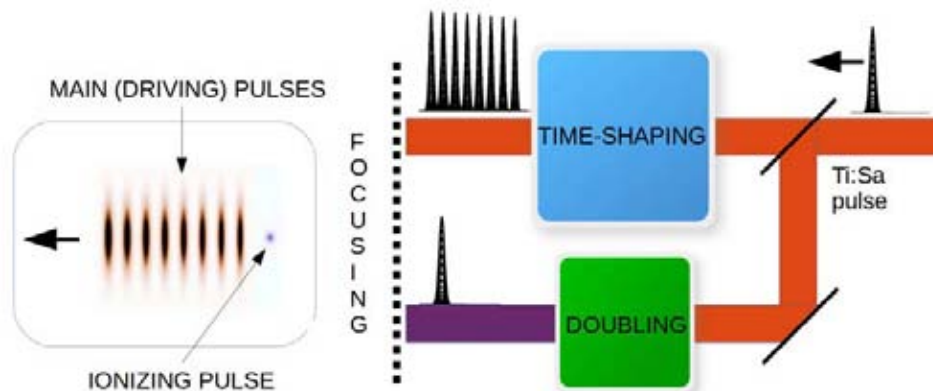


Figure 1. Multi-Pulse ionization injection scheme. A small fraction of a single Ti:Sa laser pulse is frequency doubled and will constitute the ionizing pulse. The main portion of the pulse is temporally shaped as a train of resonant pulses that will drive a large amplitude plasma wave.

II. THE RESONANT MULTI-PULSE IONIZATION INJECTION

A new ionization injection scheme, the Resonant Multi-Pulse ionization injection [32], has been recently proposed to overcome the (current) limitation of two-colour ionization injection. In the Resonant Multi-Pulse scheme only one short-wavelength laser system (e.g a Ti:Sa) is needed. The long wavelength driving pulse of the two-colour scheme is replaced by a short wavelength, resonant multi-pulse laser driver. Such a driver can be obtained via temporal shaping techniques from the *single*, linearly polarized, standard CPA laser pulse. A minor fraction of the same pulse is frequency doubled and used as ionizing pulse. Due to the resonant enhancement of the ponderomotive force, a properly tuned train of pulses is capable of driving amplitude waves larger than a single pulse with the same energy [33, 34]. Noticeably, since the peak intensity of the driver is reduced by a factor equal to the number of train pulses, it is also possible to match the conditions of *both* particle trapping and unsaturated ionization of the active atoms level. Recently [35] new experimental results on the generation of such a time shaped pulses demonstrate that a multi pulse scheme is obtainable with present day technology.

Trapping analysis with a standard *single* pulse shows [32] that Nitrogen could be used in

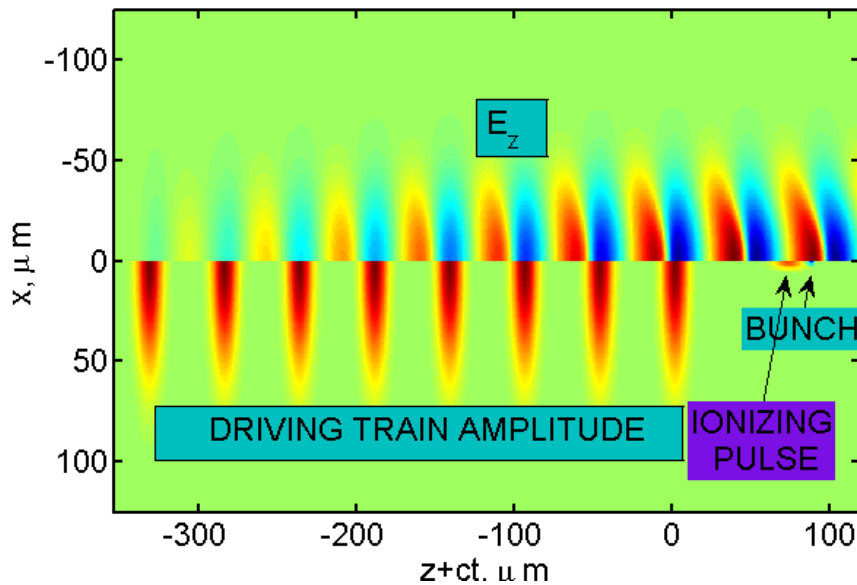


Figure 2. Pulse amplitude , bunch density and accelerating gradient after $100 \mu m$ of propagation.

a simplified ionization injection (as suggested in [29]). Since efficient ionization threshold for N^{6+} is $a_0 \approx 1.7$ for $\lambda = 0.8 \mu m$, a two-pulses driver is an optimal choice since pulse amplitude in the range $1.1 < a_0 < 1.3$ allows us to strongly inhibit driver pulses ionization. Using Argon ($Ar^{8+} \rightarrow Ar^{9+}$) as a contaminant instead of Nitrogen gives us a drastic reduction of transverse particle momentum. Multi-pulse ionization injection with Argon requires trains with at least four pulses since ionization level is saturated with amplitude above $a_0 = 0.8$ at $\lambda = 0.8 \mu m$.

A. Flat background density simulation

The following QFluid [40] simulation of our Resonant Multi-Pulse Ionization Injection is based upon a Ti:Sa laser pulse that is initially split into the ionizing pulse and the eight-pulses driver train, each sub-pulse being $30 fs$ FWHM in duration and delivering $895 mJ$ of energy, with a maximum pulse amplitude $a_0 = 0.64$ and minimum waist size $w_0 = 45 \mu m$. Plasma electron density is set to $n_e = 5 \cdot 10^{17} cm^{-3}$ (plasma wavelength is $\lambda_p = 46.9 \mu m$),

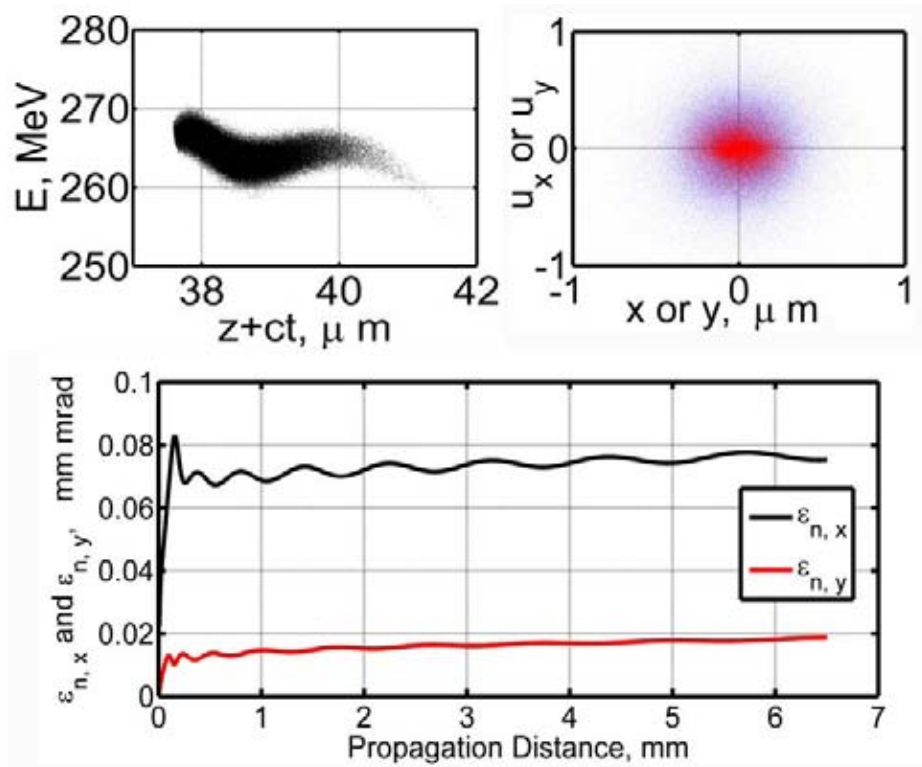


Figure 3. 265MeV simulation. Bunch quality as simulation ends. Top left: Longitudinal position-energy distribution. Top left: Transverse distribution (blue dots for x component and red dots for y component). Bottom: normalized emittance as the bunch propagates into the plasma.

obtained with a pure Argon pre-ionized up to level 8^{th} . The frequency doubled component ($\lambda_{ion} = 0.4 \mu\text{m}$) with amplitude $a_{0,ion} = 0.41$ and duration $T_{ion} = 38 \text{ fs}$ is focused with a waist $w_{0,ion} = 3.5 \mu\text{m}$. The simulation (see Figs. 2 and 3) has been performed in a moving cylinder having a radius $4 \cdot w_0$ with a resolution of $\lambda_p/100$ and $\lambda_p/200$ in the radial and longitudinal coordinates, respectively.

Electrons extracted in the bulk of the ionizing pulse move suddenly backwards in the wake reaching the peak of the accelerating gradient. The short Rayleigh length $Z_R = \pi w_{0,ion}^2 / \lambda_{ion} \approx 100 \mu\text{m}$ ensures a sudden truncation of beam charging that turns into a small rms absolute energy spread $\Delta E \approx E_{norm} \cdot E_0 \cdot Z_R \approx 5 \text{ MeV}$ and extracted charge $Q = 3.8 \text{ pC}$.

At the end of beam charging, i.e after about $200\ \mu\text{m}$ of propagation, the *rms* bunch length is $\sigma_l = 0.56\ \mu\text{m}$ and the transverse normalized emittance is $\epsilon_{n,x} = 0.070\ \text{mm}\cdot\text{mrad}$ in the polarization direction x and $\epsilon_{n,y} = 0.016\ \text{mm}\cdot\text{mrad}$ along the y direction. Afterwards, the *quasi-matched* beam experiences dumped betatron oscillations with converging beam radius of $\sigma_t = 0.3\ \mu\text{m}$ that generate an emittance growth of about 10% as simulation ends (see Fig. 3). At the end of the $6.5\ \text{mm}$ long extraction/acceleration phase the bunch has mean energy $265\ \text{MeV}$, with final normalized emittances of $0.076\ \text{mm}\cdot\text{mrad}$ (x axis) and $0.018\ \text{mm}\cdot\text{mrad}$ (y axis) , with an *rms* energy spread 0.65% and peak current exceeding $2\ \text{KA}$. These extremely low values of emittance and energy spread show that the proposed Resonant Multi-Pulse Ionization Injection scheme is ideal for the generation of very high quality accelerated bunches.

B. Preformed plasma-channel simulation

To extend the acceleration length a pulse guiding technique is necessary since low-density plasmas don't allow for pulse self-guiding at those pulse powers. A possible setup consists of a gas-jet containing pure Argon (for bunch injection) and a $5\ \text{cm}$ long capillary waveguide filled with Helium (for energy boosting). The driver pulses are focused close to the entrance of the capillary and enter into the guide with a matched radius $w_m = w_0$ and radial density profile

$$n_e(r) = n_{axis} \left[1 + \eta \frac{1.1 \cdot 10^{20}}{n_{axis} w_0^2} \left(\frac{r}{w_0} \right)^2 \right], \quad (1)$$

being n_{axis} the on-axis plasma density. The η factor accounts for weakly nonlinear corrections and in the case of short pulses ($T \ll 2\pi/\omega_p$ can be evaluated as [43] $\eta \cong 1 - \frac{1}{16}(a_0\omega_p T)^2 \cdot (1 + 4.6 \cdot 10^{-21} n_e w_0^2)$, which is very close to unity in our simulations.

Plasma background density is flat in the injector stage with nominal density of $3.5 \cdot 10^{17}\ \text{cm}^{-3}$. At the end of the $4\ \text{mm}$ long gas-jet, a contiguous capillary with preformed plasma having a channel with center density of $3.3 \cdot 10^{17}\ \text{cm}^{-3}$ is placed. Transition scale to the first to the second stage has been set to $L_{trans} = 2\ \text{mm}$. The driver pulse train

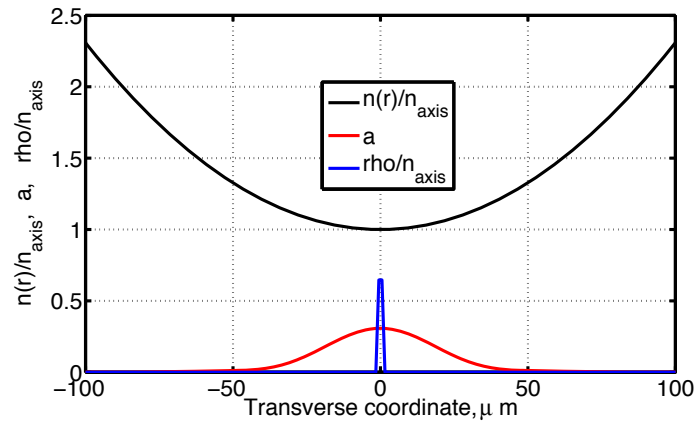


Figure 4. 1GeV simulation. Plasma radial density (black), pulse amplitude (red) and bunch density (blue) inside the plasma channel.

enters the gas jet with a waist $w = 45 \mu\text{m}$ with minimum waist $w_0 = 40 \mu\text{m}$ placed 3.2 mm after plasma entrance. At the end of the gas jet the driver pulses train has waist close the minimum value and enters into the channel with a matched size. The ionizing pulse has minimum waist $w_0 = 4 \mu\text{m}$, a bit higher than the pulse of the 265 MeV case to compensate for the lower atomic density so as to extract 4.6 pC of charge. Due to the defocusing effect of the wake, at the end of the 3.5 cm of propagation the rear part of the train is partially disrupted (See Fig. 5).

The final electron bunch has energy 1.15 GeV and energy spread 0.81 % *rms*. While normalized emittance is the same of the lower energy bunch (0.08 $\text{mm} \cdot \text{mrad}$ and 0.02 $\text{mm} \cdot \text{mrad}$ in x and y directions, respectively), the present bunch is spatially more compact than the 265 MeV one. Transverse size has been reduced down $0.2 \mu\text{m}$ by transverse wakefield forces while longitudinal size has been strongly reduced down $0.25 \mu\text{m}$ by having selected an injection phase closer to the maximum of the accelerating force (see Table 1).

III. POSSIBLE APPLICATION IN ULTRA HIGH BRILLIANCE SOURCES

The ultra-low emittance bunches reported above have ideal application in either X/γ Thomson/Compton scattering sources or FEL sources. The Thomson Scattering process is

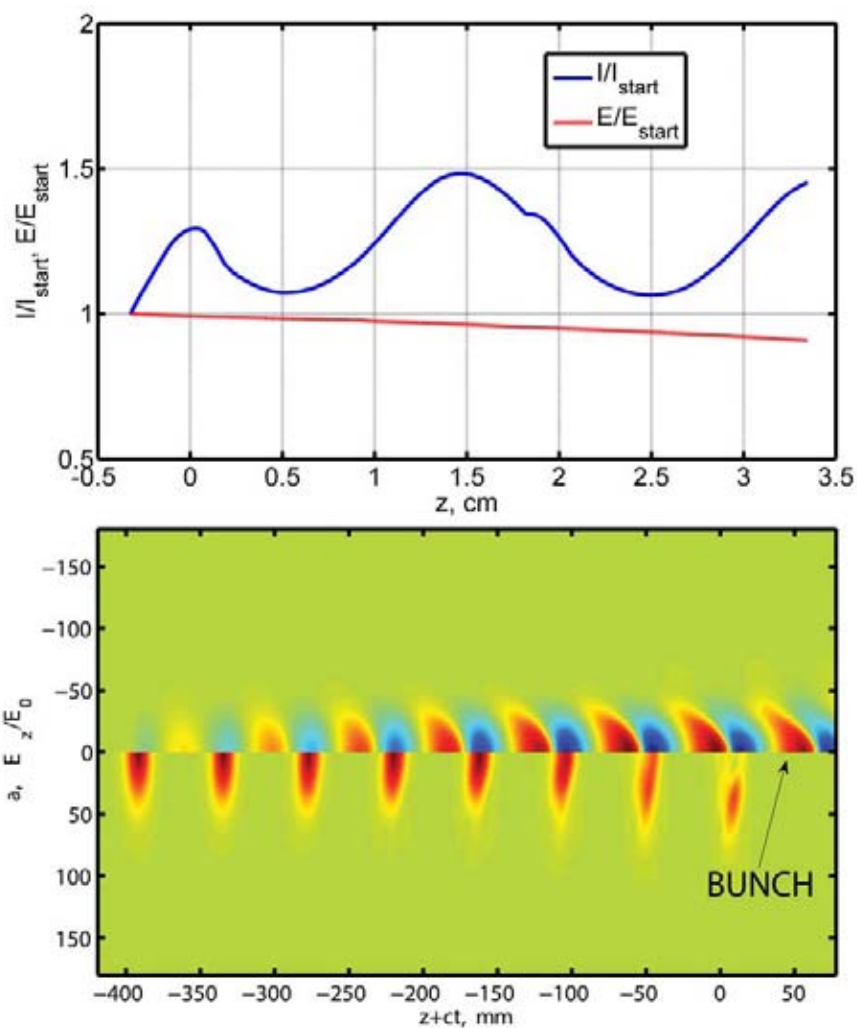


Figure 5. 1 GeV simulation. Top: Pulses peak amplitude and total delivered energy as the train propagates into the plasma. Bottom: final snapshot of the longitudinal electric field and pulse(s) amplitude.

the classical limit of Compton Scattering, i.e. the limit of negligible quantum recoil of the electron when it absorbs one (or more) photons. This is the case when a Ti:Sa laser pulse impinges onto a bunch with energy below tens of GeV's [4, 5]. Relativistic effects generate a blue-shift of the scattered radiation

Bunch	E, GeV	σ_E/E	Q, pC	$\sigma_l, \mu m$	$\sigma_t, \mu m$	$\epsilon_{nx}, \mu m \cdot rad$
A	0.265	0.65 %	3.8	0.56	0.30	0.078
B	1.15	0.81%	4.6	0.25	0.22	0.080

Table I. Bunches A and B quality

$$\lambda_{rad} = \lambda_0(1 + \tilde{\theta}^2 + a_0^2/2)/(4\gamma^2) \quad (2)$$

and its collimation into a cone of aperture $\theta \approx 1/\gamma$, being λ_0 the wavelength of the counterpropagating laser pulse and $\tilde{\theta}$ the angle from the scattered photon and the incoming electron [5, 6]. Nonlinear Thomson Scattering occurs when quivering velocity approaches c so as magnetic field induces non harmonic components in electrons trajectories, i.e. when more than one photon is absorbed. Main signatures of nonlinear features are harmonic generation and redshift associated to spectral broadening [4, 5]. In quasi-monochromatic X/γ sources, therefore, a linear or weakly-nonlinear regime is preferable.

A possible sub-micromer γ source is obtained either with a single laser-system setup or with a two-laser systems setup. In the former case the counterpropagating pulse is a portion of the Ti:Sa pulse that generates the electron beam, while in the latter the pulse is generated by a dedicated laser system. In both cases the counterpropagating pulse should have a significantly larger duration than the beam driver pulse in order to reduce unwanted nonlinear effects.

In the following simulations a single laser system setup is assumed. The counterpropagating pulse has length $T = 1ps$ and delivers 1 J of energy in a spot of waist $w_0 = 15 \mu m$. Since pulse amplitude is well below unity ($a_0 = 0.23$) a weakly-nonlinear regime is reached so the energy spread of the collected radiation mainly depends upon electron beam quality and acceptance angle. Following [5, 6] we can write an expression for the expected energy spread once the normalized acceptance $\Psi = \theta_{max} \cdot \gamma$ has been fixed

$$(\delta E/E)_{FWHM} \approx \Psi^2 + 2(\delta\gamma/\gamma)_{rms} + \delta u_{\perp}^2, \quad (3)$$

PEAK ENERGY	ENERGY SPREAD	COLLECTED PHOTONS PER SHOT	DURATION
1.5 MeV	4.8 % rms	$1.3 \cdot 10^6$ ph	1.9 fs
ACCEPTANCE ANGLE	SOURCE SURFACE	SPECTRAL DENSITY	BRILLIANCE
0.65 mrad	$0.4 \mu\text{m}^2$	$12 \frac{\text{ph}}{\text{eVbw}}$	$9 \cdot 10^{26} \frac{\text{ph}}{\text{s} \cdot \text{mm}^2 \cdot \text{mrad}^2 \cdot 0.1\% \text{bw}}$

Table II. Thomson Scattering Source parameters list (bunch A)

it is therefore commonplace to set the normalized acceptance to a value close to $\Psi \approx [2(\delta\gamma/\gamma)|_{rms} + \delta u_{\perp}^2]^{1/2}$, value that can be adjusted after source optimization.

A. TS source from the 265 MeV bunch A

The low-energy bunch A energy spread and transverse momentum are $(\delta\gamma/\gamma)|_{rms} = 6.5 \cdot 10^{-3}$ and $\delta u_{\perp} = 0.32$, respectively, so from Eq. 3 we get $\Psi \approx 0.25$. We expect that the energy spread of the γ source will not decrease by reducing the accepted normalized below $\Psi \approx 0.25$. To collect the maximum number of photons still maintaining the energy spread as low as possible we perform parameters optimization in the range $0.2 < \Psi < 0.5$. The number of scattered photons roughly scales as Ψ^2 for $\Psi \ll 1$, therefore an optimization of the source leads to the best compromise between the flux and the energy spread on the basis of the application of the generated radiation. Here we suppose that the emphasis is on a limit energy spread of 10% FWHM. Simulations of the Thomson Scattering process were performed with the Thomson Scattering Simulation Tool (TSST) [6] with a sample of 1000 bunch macroparticles. In Figure 6a a scan of the energy spread and the number of collected photons as a function of the acceptance is reported. From Figure 6a we infer that, having selected a goal energy spread of 10%, the optimal normalized acceptance is $\Psi = 0.28$, that corresponds to an acceptance of $\theta_{max} = 0.56$ mrad and a flux of $N_{ph} = 1.3 \cdot 10^6$ collected photons per shot.

The angular/spectral distribution of the γ radiation exhibits strong anisotropy due to the different *rms* transverse momenta along *x* and *y* directions ($0.31 mc$ and $0.14 mc$, respectively). Finally, the integrated spectrum (Fig. 6 c) has peak energy of 1.5 MeV, *rms*

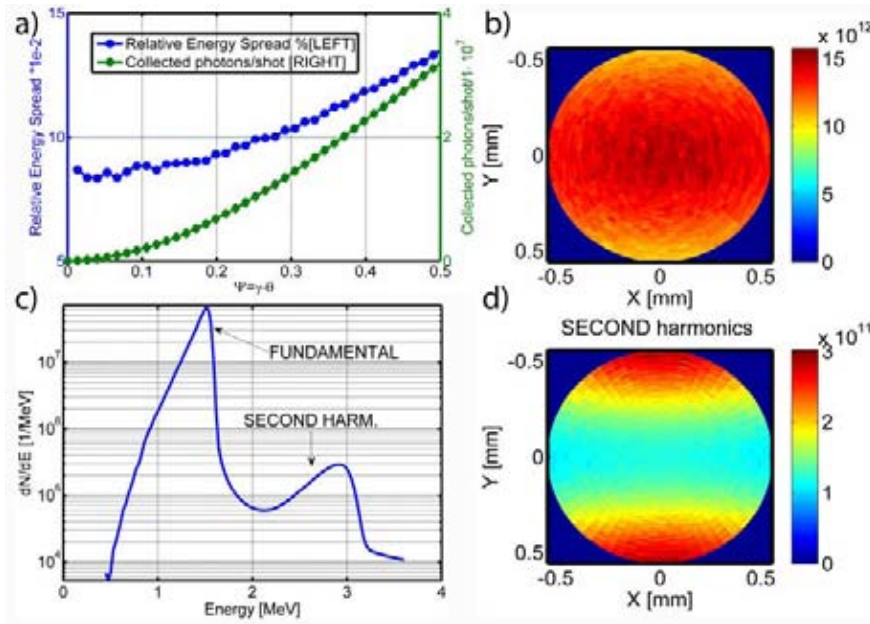


Figure 6. Thomson Source optimization and output from the 265 MeV bunch. a) Scan of the radiation energy spread (blue dots) and number of collected photons (green diamonds) vs acceptance angle. b) and d) Yield on a screen 1m downstream of the fundamental and second harmonics. c) Integrated spectrum (log scale).

energy spread of 4.8 % and FWHM energy spread 10%. The source emits ultrashort bursts of γ radiation, with *rms* duration $\delta t_\gamma \approx \sigma_l/c = 1.9 \text{ fs}$ within a spot of size $S = \pi \sigma_t^2 = 0.4 \mu\text{m}^2$.

To compute peak brilliance of the source, we evaluated the number of photons emitted close to the peak with energy spread within 0.1 %, resulting in $N_{ph}/(0.1\%bw) = 2.9 \cdot 10^4$. Peak brilliance is

$$B = \frac{N_{ph}/0.1\%bw}{\delta t_\gamma(s) S(\text{mm}^2) \theta_{max}^2(\text{mrad}^2)} = 9 \cdot 10^{26} \text{ph}/(s \cdot \text{mm}^2 \cdot \text{mrad}^2 \cdot 0.1\%bw) \quad (4)$$

which is orders of magnitude more than brilliance reported in Thomson scattering experiments with LWFA generated electrons [44, 45].

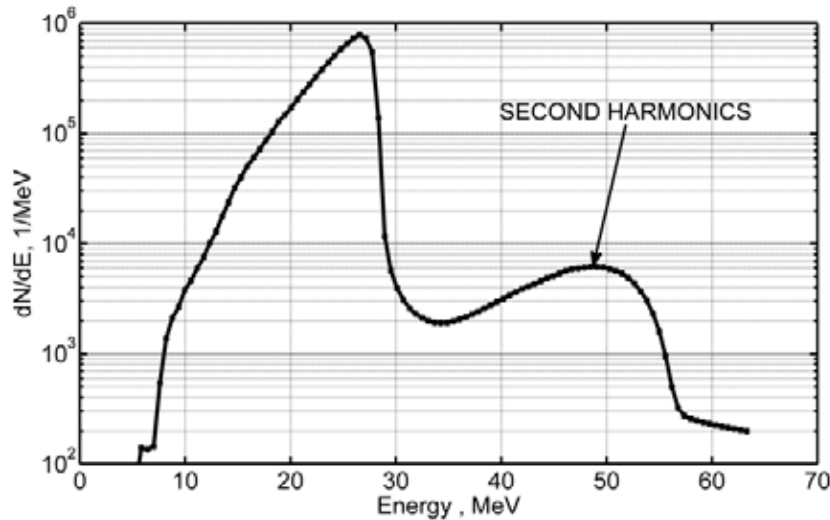


Figure 7. Integrated spectrum of the γ rays emitted by the TS source driven by bunch B within an acceptance angle of 0.21 mrad .

B. TS source from the 1GeV bunch B

Though the 1GeV bunch possesses the same emittance as the 265MeV one, we expect that the minimum energy spread of the TS source obtainable with the bunch B is higher than the previous case. This is because during the post-acceleration phase focusing forces reduced the transverse size roughly by a factor 1.5. The transverse momentum spread along x and y directions are now $0.37 mc$ and $0.21 mc$, respectively. From Eq. 3 we can estimate the minimum energy spread as $(\delta E/E)_{min} \approx 2(\delta\gamma/\gamma)_{rms} + \delta u_{\perp}^2 \approx 0.2$. After source optimization with goal energy spread of 20% FWHM, the selected normalized acceptance is $\Psi = \gamma \cdot \theta_{max} = 0.45$, corresponding to a geometrical acceptance of 0.21 mrad . The TSST simulation, obtained with the same laser parameters of the previous case, results in a sub-fs bursts of γ radiation with *rms* duration $\delta t_{\gamma} = 0.8 \text{ fs}$ within a spot of size $S = 0.14 \mu\text{m}^2$, with peak energy 26.4 MeV (see Fig. 7) and a flux of $N_{ph} = 4.6 \cdot 10^6$ collected photons per shot.

As expected, the energy spread of this source is roughly as double as that of the 1.5 MeV source, with the peak of $N_{ph}/(0.1\%bw) = 4.9 \cdot 10^4$ photons emitted within 0.1 % spread.

PEAK ENERGY	ENERGY SPREAD	COLLECTED PHOTONS PER SHOT	DURATION
26.4 MeV	9.8 % rms	$4.6 \cdot 10^6$ ph	0.8 fs
ACCEPTANCE ANGLE	SOURCE SURFACE	SPECTRAL DENSITY	BRILLIANCE
0.21 mrad	$0.14 \mu\text{m}^2$	$1.6 \frac{\text{ph}}{\text{eVbw}}$	$1 \cdot 10^{28} \frac{\text{ph}}{\text{s} \cdot \text{mm}^2 \cdot \text{mrad}^2 \cdot 0.1\% \text{bw}}$

Table III. Thomson Scattering Source parameters list (bunch B)

Nevertheless, since source size is considerably smaller than the case A, peak brilliance is one order of magnitude higher $B = 1 \cdot 10^{28} \text{ph}/(\text{s} \cdot \text{mm}^2 \cdot \text{mrad}^2 \cdot 0.1\% \text{bw})$.

IV. CONCLUSIONS

We employed the new RMPII injection scheme to (numerically) generate two electron bunches with outstanding quality and compactness. Bunch A has been obtained with a flat density profile and reaches the energy of 265 MeV prior laser pulse(s) defocusing. Bunch B has been generated with the REMPII scheme and further accelerated into a plasma channel for pulse guiding, obtaining a final energy of 1.15 GeV with a similar beam quality. High-brilliance Thomson Scattering sources have been investigated with the classical nonlinear TSST code, showing that a sub-fs γ ray source with brilliance $B = 1 \cdot 10^{28} \frac{\text{ph}}{\text{s} \cdot \text{mm}^2 \cdot \text{mrad}^2 \cdot 0.1\% \text{bw}}$ can be obtained with this setup. A future work will be focused on the another natural application of those high-quality bunches, i.e. Free Electron Laser drivers.

V. ACKNOWLEDGMENTS

Authors wish to thank Vittoria Petrillo and Luca Serafini for their unvaluable discussions about FEL and Thomson Scattering. The research leading to these results has received funding from the European Union's Horizon 2020 research and innovation programme under

- [1] K. Nakajima, "Few femtosecond, few kiloampere electron bunch produced by a laser-plasma accelerator"; *Nature Physics* 4, 92 - 93 (2008).
- [2] V. Petrillo, M. P. Anania, M. Artioli, A. Bacci, M. Bellaveglia, E. Chiadroni, A. Cianchi, F. Ciocci, G. Dattoli, D. Di Giovenale, G. Di Pirro, M. Ferrario, G. Gatti, L. Giannessi, A. Mostacci, P. Musumeci, A. Petralia, R. Pompili, M. Quattromini, J. V. Rau, C. Ronsivalle, A. R. Rossi, E. Sabia, C. Vaccarezza, and F. Villa, "Observation of Time-Domain Modulation of Free-Electron-Laser Pulses by Multip peaked Electron-Energy Spectrum"; *Phys. Rev. Lett.* 111, 114802 (2013).
- [3] A Loulergue, M Labat, C Evain, C Benabderrahmane, V Malka and M E Couprie, "Beam manipulation for compact laser wakefield accelerator based free-electron lasers", *New J. Phys.* 17, 023028 (2015).
- [4] E. Esarey, S. K. Ride, and P. Sprangle, "Nonlinear Thomson scattering of intense laser pulses from beams and plasmas", *Phys. Rev. E* 48, 3003 (1993).
- [5] P. Tomassini, A. Giulietti D. Giulietti and L. A. Gizzi, "Thomson backscattering X-rays from ultra-relativistic electron bunches and temporally shaped laser pulses", *Appl Phys. B* 80, 4, pp 419-436 (2005).
- [6] P. Tomassini, A. Bacci, J. Cary, M. Ferrario, A. Giulietti, D. Giulietti, L.A. Gizzi, L. Labate, L. Serafini, V. Petrillo, C. Vaccarezza, "Linear and Nonlinear Thomson Scattering for Advanced X-ray Sources in PLASMONX", *IEEE-Trans. Plasma Sci.* 36, 4, 1782 (2008)
- [7] S. Corde, K. Ta Phuoc, G. Lambert, R. Fitour, V. Malka, A. Rousse, A. Beck, and E. Lefebvre, "Femtosecond x rays from laser-plasma accelerators", *Rev. Mod. Phys.* 85, 1 (2013);
- [8] V. Petrillo, A. Bacci, C. Curatolo, I. Drebot, A. Giribono, C. Maroli, A. R. Rossi, L. Serafini, P. Tomassini, C. Vaccarezza, and A. Variola, "Polarization of x-gamma radiation produced by a Thomson and Compton inverse scattering", *Phys. Rev. ST-AB* 18, 110701 (2015);

- [9] D. Micieli, I. Drebot, A. Bacci, E. Milotti, V. Petrillo, M. Rossetti Conti, A. R. Rossi, E. Tassi, and L. Serafini, "Compton sources for the observation of elastic photon-photon scattering events", *Phys. Rev. ST-AB* 19, 093401 (2016).
- [10] A. Döpp, E. Guillaume, C. Thaurya), A. Lifschitz, K. Ta Phuoc, and V. Malka, "Energy boost in laser wakefield accelerators using sharp density transitions", *Phys. Plasmas* 23 (5), 056702 (2015).
- [11] T.L. Audet, F.G. Desforges, A. Maitrallain, S. Dobosz Dufrénoy, M. Bougeard, G. Maynard, P. Lee, M. Hansson, B. Aurand, A. Persson, I. Gallardo González, P. Monot, C.-G. Wahlström, O. Lundh, B. Cros, "Electron injector for compact staged high energy accelerator", *NIM A* 829, 304-308 (2016).
- [12] G. Golovin, S. Banerjee, S. Chen, N. Powers , C. Liu, W. Yan, J. Zhang, P. Zhang, B. Zhao, D. Umstadter, "Control and optimization of a staged laser-wake field accelerator", *NIM A* 830, 375-380 (2016).
- [13] J. Faure, Y. Glinec, A. Pukhov, S. Kiselev, S. Gordienko, E. Lefebvre, J.-P. Rousseau, F. Burgy, V. Malka, "A laser plasma accelerator producing monoenergetic electron beams", *Nature* 541, 431(2004).
- [14] G. R. Plateau, C. G. R. Geddes, D. B. Thorn, M. Chen, C. Benedetti, E. Esarey, A. J. Gonsalves, N. H. Matlis, K. Nakamura, C. B. Schroeder, S. Shiraishi, T. Sokollik, J. van Tilborg, Cs. Toth, S. Trotsenko, T. S. Kim, M. Battaglia, Th. Stöhlker, and W. P. Leemans, "Low-Emittance Electron Bunches from a Laser-Plasma Accelerator Measured using Single-Shot X-Ray Spectroscopy", *Phys. Rev. Lett.* 109, 064802 (2012).
- [15] S. Bulanov, N. Naumova, F. Pegoraro, and J. Sakai, "Particle injection into the wave acceleration phase due to nonlinear wake wave breaking", *Phys. Rev. E* 58 , R5257 (1998).
- [16] H. Suk, N. Barov, J.B. Rosenzweig and E. Esarey, "Plasma Electron Trapping and Acceleration in a Plasma Wake Field Using a Density Transition", *Phys. Rev. Lett.* 86, 1011-1014 (2001).
- [17] P. Tomassini, M. Galimberti, A. Giulietti, D. Giulietti, L. A. Gizzi, L. Labate, and F. Pegoraro, "Production of high-quality electron beams in numerical experiments of laser wakefield acceleration with longitudinal wave breaking", *Phys. Rev. ST Accel. Beams* 6 , 121301 (2003).

- [18] C. G. R. Geddes, E. Cormier-Michel, E. Esarey, K. Nakamura, G. R. Plateau, C. B. Schroeder, Cs. Toth, D. L. Bruhwiler, J. R. Cary, and W. P. Leemans, "Plasma gradient controlled injection and postacceleration of high quality electron bunches", Proceedings of the Thirteenth Advanced Accelerator Concepts Workshop, 1086 (2008).
- [19] A. Buck, J. Wenz, J. Xu, K. Khrennikov, K. Schmid, M. Heigoldt, J. M. Mikhailova, M. Geissler, B. Shen, F. Krausz, S. Karsch, and L. Veisz, "Shock-Front Injector for High-Quality Laser-Plasma Acceleration", Phys. Rev. Lett. 110, 185006 (2013).
- [20] E. Esarey, R. F. Hubbard, W. P. Leemans, A. Ting, and P. Sprangle, "Electron Injection into Plasma Wakefields by Colliding Laser Pulses", Phys. Rev. Lett. 79, 2682 (1997).
- [21] H. Kotaki, *et al.*, "Electron Optical Injection with Head-On and Countercrossing Colliding Laser Pulses", Phys. Rev. Lett. 103, 194803 (2009).
- [22] M. Chen, E. Esarey, C. G. R. Geddes, E. Cormier-Michel, C. B. Schroeder, S. S. Bulanov, C. Benedetti, L. L. Yu, S. Rykovanov, D. L. Bruhwiler, and W. P. Leemans, "Electron injection and emittance control by transverse colliding pulses in a laser-plasma accelerator", Phys. Rev. ST Accel. Beams 17, 051303 (2014).
- [23] Min Chen, Zheng-Ming Sheng, Yan-Yun Ma, and Jie Zhang, "Electron injection and trapping in a laser wakefield by field ionization to high-charge states of gases", Jour. Appl. Phys. 99, 056109 (2006).
- [24] A. Pak, K. A. Marsh, S. F. Martins, W. Lu, W. B. Mori, and C. Joshi, "Injection and Trapping of Tunnel-Ionized Electrons into Laser-Produced Wakes", PRL 104, 025003 (2010).
- [25] C. E. Clayton, J. E. Ralph, F. Albert, R. A. Fonseca, S. H. Glenzer, C. Joshi, W. Lu, K. A. Marsh, S. F. Martins, W. B. Mori, A. Pak, F. S. Tsung, B. B. Pollock, J. S. Ross, L. O. Silva, and D. H. Froula, "Self-Guided Laser Wakefield Acceleration beyond 1 GeV Using Ionization-Induced Injection", Phys. Rev. Lett. 105, 105003 (2010).
- [26] M. Chen, E. Esarey, C. B. Schroeder, C. G. R. Geddes, and W. P. Leemans, "Theory of ionization-induced trapping in laser-plasma accelerators", Phys. Plasmas 19, 033101 (2012).
- [27] M. Zeng, M. Chen, L. L. Yu, W. B. Mori, Z. M. Sheng, B. Hidding, D. A. Jaroszynski, and J. Zhang, "Multichromatic Narrow-Energy-Spread Electron Bunches from Laser-Wakefield

- Acceleration with Dual-Color Lasers", *Phys. Rev. Lett.* 114, 084801 (2015).
- [28] T. L. Audet, M. Hansson, P. Lee, F. G. Desforges, G. Maynard, S. Dobosz Dufrénoy, R. Lehe, J.-L. Vay, B. Aurand, A. Persson, I. Gallardo González, A. Maitrallain, P. Monot, C.-G. Wahlström, O. Lundh, and B. Cros, "Investigation of ionization-induced electron injection in a wakefield driven by laser inside a gas cell", *Phys. Plasmas* 23 023110 (2016).
- [29] L.-L. Yu, E. Esarey, C. B. Schroeder, J.-L. Vay, C. Benedetti, C. G. R. Geddes, M. Chen, and W. P. Leemans, Two-Color Laser-Ionization Injection, *Phys. Rev. Lett.* 112, 125001 (2014).
- [30] L.-L. Yu, E. Esarey, C. B. Schroeder, J.-L. Vay, C. Benedetti, C. G. R. Geddes, M. Chen, and W. P. Leemans, "Ultra-low emittance electron beams from two-color laser-ionization injection", *Advanced Accelerator Concepts 2014 AIP Conf. Proc.* 1777, 040019-1–040019-5; doi: 10.1063/1.4965621.
- [31] X.L. Xu et al, "Low emittance electron beam generation from a laser wakefield accelerator using two laser pulses with different wavelengths", *Phys.Rev.ST Accel.Beams* 17 061301 (2014)
- [32] P. Tomassini, L. Labate, P. Londrillo, R. Fedele, D. Terzani and L. A. Gizzi, "Resonant Multi Pulse Ionization Injection", submitted (2017)
- [33] D. Umstadter, E. Esarey, and J. Kim, "Nonlinear Plasma Waves Resonantly Driven by Optimized Laser Pulse Trains", *Phys. Rev. Lett.* 72, 1224 (1994).
- [34] S M Hooker, R Bartolini, S P D Mangles, A Tunnermann, L Corner, J Limpert, A Seryi and R Walczak, "Multi-pulse laser wakefield acceleration: a new route to efficient, high-repetition-rate plasma accelerators and high flux radiation sources", *J. Phys. B* 47, 234003 (2014).
- [35] R.J. Shalloo, L. Corner, C. Arran, J. Cowley, G. Cheung, C. Thornton, R. Walczak, S.M. Hooker, "Generation of laser pulse trains for tests of multi-pulse laser wakefield acceleration", *NIM A* 829, 1, 383-385 (2016).
- [36] E. Esarey and M. Pilloff, "Trapping and acceleration in nonlinear plasma waves", *Phys. Plasmas* 2, 1432 (1995).
- [37] V.P. Krainov, W. Xiong, S.L. Chin, "An introductory overview of tunnel ionization of atoms by intense lasers", *Laser Physics* 2, 4 (1992).

- [38] C. B. Schroeder, J.-L. Vay, E. Esarey, S. Bulanov, C. Benedetti, L.-L. Yu, M. Chen, C. G. R. Geddes, and W. P. Leemans, "Thermal emittance from ionization-induced trapping in plasma accelerators", *Phys. Rev. ST AB* 17, 101301 (2014).
- [39] C. Benedetti, A. Sgattoni, G. Turchetti and P. Londrillo, "ALaDyn: A High-Accuracy PIC Code for the Maxwell-Vlasov Equations", *IEEE Trans. On Pl. Science* 36, 4 (2008).
- [40] P. Tomassini and A.R. Rossi, "Matching strategies for a plasma booster", *Plasma Phys. Control. Fusion* 58 034001 (2016).
- [41] P. Sprangle, E. Esarey and A. Ting, "Nonlinear Theory of Intense Laser-Plasma Interaction", *Phys. Rev. Lett* 64, 2011-2014 (1990).
- [42] P. Sprangle, E. Esarey, and J. Krall, "Self-guiding and stability of intense optical beams in gases undergoing ionization", *Phys. Rev. E* 54, 4211 (1996).
- [43] W. Lu, M. Tzoufras, C. Joshi, F. S. Tsung, W.B. Mori, J. Vieira, R.A. Fonseca, L.O. Silva, *Phys. Rev. ST Accel. Beams* 10, 061301 (2007)
- [44] G. Sarri, D. J. Corvan, W. Schumaker, J. M. Cole, A. Di Piazza, H. Ahmed, C. Harvey, C. H. Keitel, K. Krushelnick, S. P. D. Mangles, Z. Najmudin, D. Symes, A. G. R. Thomas, M. Yeung, Z. Zhao, and M. Zepf, "Ultrahigh Brilliance Multi-MeV γ -Ray Beams from Nonlinear Relativistic Thomson Scattering", *Phys. Rev. Lett.* 113, 224801 (2014).
- [45] Changhai Yu et al, "Ultrahigh brilliance quasi- monochromatic MeV γ -rays based on self-synchronized all-optical Compton scattering", *Sci Rep.* 6 29518 (2016).

Measurement of the particle number density in a pulsed flow gas cell with a second-harmonic interferometer

F Brandi^{1,2}, P Marsili³, F Giammanco³, F Sylla⁴ and LA Gizzi¹

¹ Intense Laser Irradiation Laboratory (ILIL), Istituto Nazionale di Ottica (CNR-INO), Via Moruzzi 1, 56124 Pisa, Italy

² Istituto Italiano di Tecnologia (IIT), Via Morego 30, 16163 Genova, Italy

³ Dipartimento di Fisica, Università degli Studi di Pisa, Largo B. Pontecorvo 3, 56127 Pisa, Italy

⁴ SourceLAB SAS, 86 rue de Paris, 91400 Orsay, France

E-mail: fernando.brandi@ino.cnr.it

Abstract.

A high-sensitivity high-speed second-harmonic interferometer is used to monitor the particle number density inside a pulsed flow gas cell designed for laser wakefield acceleration. The interferometer can precisely follow the particle density temporal evolution therefore offering a practical way to control in real-time the target density during laser-plasma interaction. The presented results are relevant for the evaluation of density diagnostic tools for flow gas cells used as laser-plasma acceleration stages.

1. Introduction

The demonstration of laser wakefield acceleration (LWFA) of electrons to the GeV level [1, 2] opens the way for the application of LWFA-based accelerators and high photon energy radiation sources [3] within user oriented facilities with superior beam quality and reliability necessary for actual high-level applications, as envisaged within the EuPRAXIA project [4]. The transition from fundamental research to actual implementation must go along with a full control and tailoring of the laser-plasma based accelerator, and specifically of the plasma free-electron density. In LWFA the plasma in the gas target is created either by the laser pulse itself or pre-generated by an electric discharge or by a second laser pulse.

Gaseous targets used in LWFA are: *i) supersonic gas jets* that are easy to implement, allow for a good control over the peak particle number density [5], but produce density profiles that can vary shot-to-shot due to reproducibility of valve operation over time and turbulent flow, and prevent high repetition rate operation due to pulsing capability. *ii) Capillary discharges* that provides guiding of the laser up to centimeters, thus increasing the acceleration length [1], but can get damaged during usage and may require somehow sophisticated density diagnostics methods [6] which pose technical challenges; *iii) flow gas cells* that are very good candidates to avoid the above mentioned limitations, allowing for a stable and controllable laser-plasma interaction even at high repetition rate along with easily tunable accelerator length [7–14]. Flow gas cells are also suitable to be implemented in multi-stage accelerators [15, 16], which



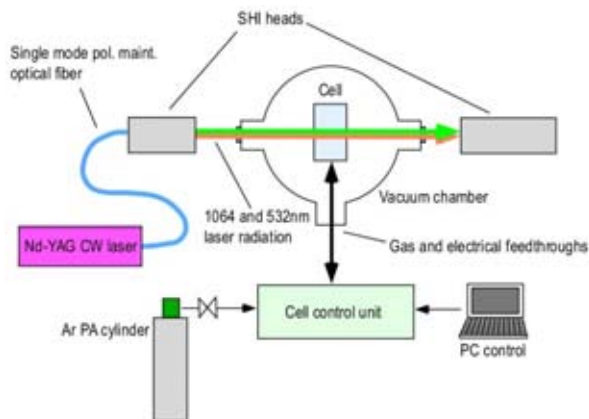


Figure 1. Schematic of the experimental apparatus.

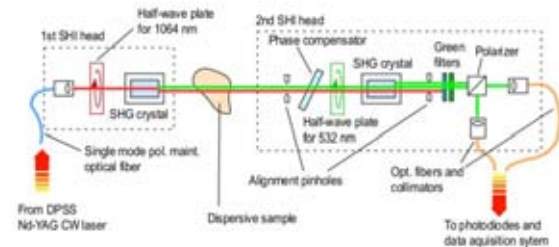


Figure 2. Schematic of the second-harmonic interferometer.

is important in the perspective of designing and implementing LWFA-based facilities. In this context the reliable and robust measurement and control of the free-electron density is a crucial aspect, and interferometry plays a major role as diagnostic tool being non-invasive and versatile. Typical two-arm interferometers [17] suffer from a high sensitivity to environmental conditions which limits their use outside the laboratory environment. Nomarski and folded two-arm interferometers provide better stability compared to standard two-arm interferometers, are widely used in research laboratories [18–21], and provide an interferogram from which the phase is retrieved applying image analysis software and phase-unwrapping algorithms. The lengthy data analysis limit their use in real-time measurements, while they may be suitable for off-line measurements during alignment and tuning of the laser-plasma accelerator stages.

When stability and ease of implementation matters, an alternative robust interferometric method is the second-harmonic interferometer (SHI), also called dispersion interferometer [22]. The SHI is a single-arm, two-color interferometer, which is sensitive to the change of refractive index between the fundamental and second-harmonic wavelength, measured phase shift given by $\Delta \phi = \frac{4\pi}{\lambda} \int_L \Delta n(\lambda) dl = \frac{4\pi}{\lambda} L \overline{\Delta n}(\lambda)$, where $\Delta n(\lambda) = n(\lambda) - n(\lambda/2)$, $n(\lambda)$ is the refractive index, λ is the wavelength, and L the optical path in the sample. Being a fully common-path interferometer the SHI is insensitive to vibration when compared with typical two-arm interferometers, which allows long term stable operation even in a harsh environment [23].

In this work, the latest results on the use of a high-speed ($\sim \mu s$) and high-sensitivity ($\sim mrad$) SHI based on a CW Nd:YAG laser to measure the particle number density inside a pulsed flow gas cell in vacuum are presented.

2. Experiment

Fig.1 shows a schematic block diagram of the experimental apparatus. The cell (model SL-ALC, SourceLAB) is placed in a cylindrical vacuum chamber, evacuated by a turbo-molecular pump to 10^{-5} mbar. The gas cell comprises two 600 μm -diameter apertures to allow the gas to flow in the vacuum chamber, two lateral glass windows at $L = 35$ mm to enable transverse interferometry. When the gas pulse flows out of the cell the pressure in the chamber increases shortly, not exceeding however values of the order of 10^{-2} mbar. The vacuum chamber is equipped with three KF50 vacuum flanges on the lateral surface. Two lie opposite along a diameter and are used to mount BK7 optical precision windows, anti-reflection coated for 1064 nm and 532 nm wavelengths, providing entrance and exit of the interferometer beams. The third flange hosts the gas and electrical feedthroughs between the cell and the controller. The argon gas at 2

bar enters the control unit which then sends a gas puff to the cell at a pre-set pressure and duration. It is noted that if the cell would be continuously feed with gas or long gas pulses were used, the effect from back-ground density build up in the chamber would become visible during the interferometric measurement. Such effect was not revealed for the gas pressure and pulse length used. In case longer pulses and/or higher pressures would be needed the vacuum system (chamber plus pump) would have to be adequately scaled in order to avoid density build up in the interaction chamber.

Fig. 2 shows a detailed sketch of the fully fiber-coupled SHI interferometer used in the experiment [24–26], which is here briefly described. The radiation of a CW DPSS Nd-YAG laser is sent to the first interferometer head using a single mode polarization maintaining optical fiber. The laser light emerging from the fiber is collimated to a diameter of 1 mm. A half-wave plate is used to adjust the polarization, in order to ensure an optimal harmonic generation in the first type-I SHG crystal. Both the 1064 nm and 532 nm beams leave the first head and are sent collinearly through the cell. In the cell the two components suffer a de-phasing due to the gas dispersion and proportional to the gas number density. The transmitted beams enter the second head where a half-wave plate rotates the second-harmonic polarization by an angle of 90° leaving the fundamental beam polarization unchanged. A tilted glass slab adds a controlled de-phasing acting as a compensator, in order to tune the phase difference to an optimal working point. In a second type-I SHG crystal the 1064 nm beam is duplicated again. Following the filtering out of the residual 1064 nm beam, the two 532 nm beams with crossed polarizations enter a polarizing cube oriented by an angle of 45° , where the two beams are mixed giving rise to two complementary interference patterns. The beams emerging from the beam-splitter cube are finally collected by two fiber optic cables and sent to photodiodes, directly connected to ultra low-noise transimpedance amplifiers. The output signals are acquired by a 15 MHz USB digitizing oscilloscope controlled by a LabView software which calculates in real-time the ratio between the difference and the sum of the digitalized signals. The recorded quantity is equal to $V \sin(\Delta\phi + \phi_0) + \alpha$ [24], where $\phi_0 \ll 1$ is the off-set phase that can be controlled acting on the phase compensator, V is the fringe visibility, and $\alpha \ll 1$ is related to the detector responsivities. The visibility is directly obtained by scanning the phase compensator over half-fringe [25, 27] and it is $V = 0.9$.

3. Results

The Gladstone-Dale relation between the refractive index n and the number density N , i.e., $(n - 1) \propto N$, is used to obtain the particle number density from the measured phase by the equation $\bar{N} = \frac{\lambda}{4\pi L} \frac{N_0}{\Delta n_0} \Delta\phi = 1.63 \Delta\phi \times 10^{19} \text{ cm}^{-3}$, where $N_0 = 2.69 \times 10^{19} \text{ cm}^{-3}$ is the Loschmidt constant and $\Delta n_0 = 4 \times 10^{-6}$ the difference of the refractive index of argon at 1064 nm and 532 nm [28].

The results of the systematic measurements for a 100 ms gas pulse at various values of the pre-set backing pressure are reported in Fig. 3. The zero point represents the time when the trigger is sent to the cell's controller. In less than 100 ms from the trigger the filling up of the cell starts and lasts for about 100 ms. Then the gas density in the cell drops exponentially with a decay time of ~ 0.9 s.

In Fig. 4 a comparison between 100 ms and 500 ms long gas pulses is shown for two values of the backing pressure. As expected the filling up of the cell lasts longer for the longer gas pulse and the achieved peak density value is larger by a factor ~ 1.5 .

Fig. 5 shows the values of the peak density value obtained in the experimental conditions investigated, while the dashed-line indicates the density estimated from the ideal gas law at the preset backing pressure and ambient temperature, reported as reference.

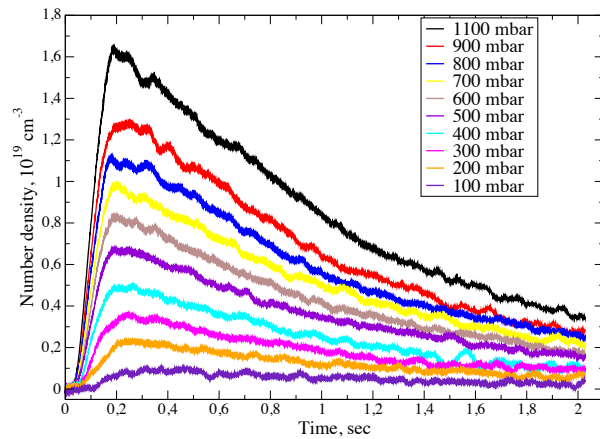


Figure 3. Time evolution of the average particle number density for a 100 ms gas pulse at various backing pressure settings.

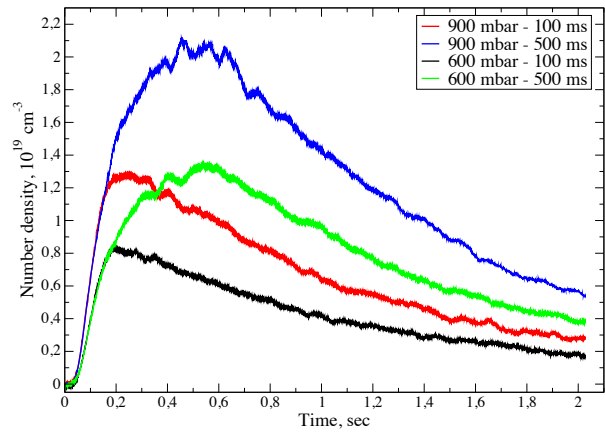


Figure 4. Time evolution of the average particle number density for a 100 ms and 500 ms gas pulse at two backing pressure settings.

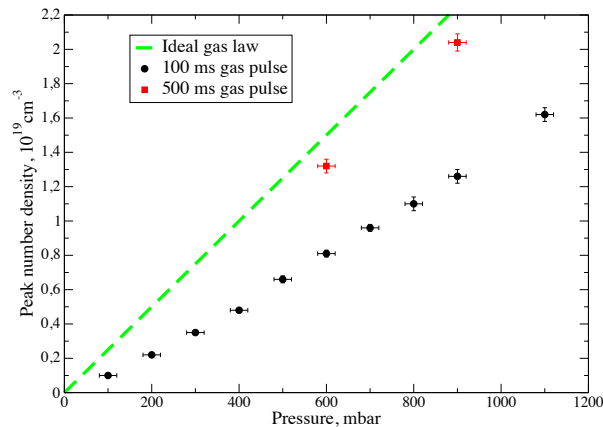


Figure 5. Peak value of the particle number density for 100 ms and 500 ms gas pulse at various backing pressure settings.

4. Conclusions

A second-harmonic interferometer is used to monitor in real-time the particle number density in a commercial pulsed flow gas cell designed for LWFA. It is found that diagnostic method is successful in measuring the density temporal evolution inside the cell from the filling up to the evacuation in the range up to 10^{19} cm^{-3} . The achieved peak value is less than what estimated from the ideal gas law especially for the shortest gas pulse, therefore characterization and continuous monitoring of the gas density is necessary in order to tune and control the laser-plasma interaction process inside the cell. The experiment performed and the results obtained are important towards the implementation of gas cells as laser-plasma based acceleration stages in a fully controlled and user oriented particle accelerator facility, as that envisaged within the EuPRAXIA design study project.

It is noted that the SHI presented can be used also to measure the particle density for other gases typically used in LWFA, like H_2 and He. The difference between the refractive indices at 1064 nm and 532 nm in hydrogen and helium at STP are 2.8×10^{-6} and 2.2×10^{-7} respectively [28]. Therefore, the measurement can be performed with hydrogen instead of argon. In case of helium, the expected phase shift at STP is ~ 90 mrad, therefore the SHI with a noise level down to less than 1 mrad [24] is capable of measuring He number density within the cell in the order of 10^{17} cm^{-3} .

In perspective, the development of a 2D imaging version of the SHI would allow to monitor

samples with non-uniform and/or non-cylindrically symmetric spatial density distribution, like gas jets from square nozzles and/or with shock fronts. There are reports in the literature about 2D second-harmonic interferometry [29–31] however more research and development activity is necessary to validate the imaging SHI methodology as viable diagnostics for LWFA gas target.

Acknowledgments

FB and LG acknowledge the financial support from the European Unions Horizon 2020 research and innovation programme Grant Agreement No 653782 EuPRAXIA, and from the Istituto Italiano di Tecnologia (convenzione operativa IIT CNR-INO prot. n. 0010983, 26/11/2013).

References

- [1] Leemans W P *et al.* 2014 Multi-GeV Electron Beams from Capillary-Discharge-Guided Subpetawatt Laser Pulses in the Self-Trapping Regime *Phys. Rev. Lett.* **113** 245002
- [2] Hyung T K *et al.* 2017 Stable multi-GeV electron accelerator driven by waveformcontrolled PW laser pulses *Sci. Rep.* **7** 10203
- [3] Gizzi L A *et al.* 2009 An integrated approach to ultraintense laser sciences: The PLASMON-X project *Eur. Phys. J. Spec. Top.* **175** 3-10
- [4] Walker P A *et al.* 2017 Horizon 2020 EuPRAXIA design study *J. Phys.: Conf. Ser.* **874** 012029
- [5] Brandi F and Giammanco F 2011 Temporal and spatial characterization of a pulsed gas jet by a compact high-speed high-sensitivity second-harmonic interferometer *Opt. Express* **19** 25479–87
- [6] Daniels J, Tilborg J van, Gonsalves A J, Schroeder C B, Benedetti C, Esarey E and Leemans W P 2015 Plasma density diagnostic for capillary-discharge based plasma channels *Phys. Plasmas* **22** 073112
- [7] Osterhoff J *et al.* 2008 Generation of Stable, Low-Divergence Electron Beams by Laser-Wakefield Acceleration in a Steady-State-Flow Gas Cell *Phys. Rev. Lett.* **101** 085002
- [8] Corde S *et al.* 2013 Observation of longitudinal and transverse self-injections in laser-plasma accelerators *Nature Comm.* **4** 1501
- [9] Aniculaesei C, Kim H T, Yoo B J, Oh K H and Nam C H 2018 Novel gas target for Laser Wakefield Accelerators *Rev. Scient. Instrum.* **89** 025110
- [10] Kononenco O *et al.* 2016 2D hydrodynamic simulations of a variable length gas target for density down-ramp injection of electrons into a laser wake field accelerator *Nucl. Instr. Meth. Phys. A* **829** 125-9
- [11] Audet T L *et al.* 2016 Electron injector for compact staged high energy accelerator *Nucl. Instr. Meth. Phys. A* **829** 304-8
- [12] Lee P, Maynard G, Audet T L, Cros B, Lehe R and Vay J-L 2016 Electron injector for compact staged high energy accelerator *Phys. Rev. Accel. Beams* **19** 112802
- [13] Audet T L *et al.* 2016 Investigation of ionization-induced electron injection in a wakefield driven by laser inside a gas cell *Phys. Plasmas* **23** 023110
- [14] Vargas M *et al.* 2014 Improvements to laser wakefield accelerated electron beam stability, divergence, and energy spread using three-dimensional printed two-stage gas cell targets *Appl. Phys. Lett.* **104** 174103
- [15] Pollock B B *et al.* 2011 Demonstration of a narrow Energy Spread, ~ 0.5 GeV Electron Beam from a Two-stage Laser Wakefield Accelerator *Phys. Rev. Lett.* **107** 045001
- [16] Liu J S *et al.* 2011 All-Optical Cascaded Laser Wakefield Accelerator Using Ionization-Induced Injection *Phys. Rev. Lett.* **107** 035001
- [17] Gizzi L A *et al.* 2006 Femtosecond interferometry of propagation of a laminar ionization front in a gas *Phys. Rev. E* **74** 036403
- [18] Feister S, Nees J A, Morrison J T, Frische K D, Orban C, Chowdhury E A and Roquemore W M 2014 A novel femtosecond-gated, high-resolution, frequency-shifted shearing interferometry technique for probing pre-plasma expansion in ultra-intense laser experiments *Rev. Scient. Instrum.* **85** 11D602
- [19] Park J, Baldis H A and Chen H 2016 The implementation and data analysis of an interferometer for intense short pulse laser experiments *High Power Laser Science and Engineering* **4** E26, doi:10.1017/hpl.2016.21
- [20] Kalal M, Slezak O, Martinkova M and Rhee Y J 2010 Compact Design of a Nomarski Interferometer and Its Application in the Diagnostics of Coulomb Explosions of Deuterium Clusters *Journal of the Korean Physical Society* **56** 287-94
- [21] Ruiz-Camacho J, Beg F N and Lee P 2007 Comparison of sensitivities of Moire deflectometry and interferometry to measure electron densities in z-pinch plasmas. *J. Phys. D: Appl. Phys.* **40** 2026-32
- [22] Hopf F, Tomita A, and Al-Jumaily G 1980 Second-harmonic interferometers *Opt. Lett.* **5**, 386–8

- [23] Brandi F, Giammanco F, Harris W S, Roche T, Trask E and Wessel F J 2009 Electron density measurements of a field-reversed configuration plasma using a novel compact ultrastable second-harmonic interferometer *Rev. Sci. Instrum.* **80** 113501
- [24] Brandi F and Giammanco F 2007 Versatile second-harmonic interferometer with high temporal resolution and high sensitivity based on a continuous-wave Nd:YAG laser *Opt. Lett.* **32** 2327–29
- [25] Brandi F and Giammanco F, 2008 Harmonic interferometry in the visible and UV, based on second- and third-harmonic generation of a 25 ps mode-locked Nd:YAG laser *Opt. Lett.* **33** 2071–73
- [26] Brandi F, Giammanco F, Conti F, Sylla F, Lambert G and Gizzi LA 2016 Note: Real-time monitoring via second-harmonic interferometry of a flow gas cell for laser wakefield acceleration *Rev. Sci. Instrum.* **87** (8) 086103
- [27] Brandi F, Marsili P and Giammanco F 2008 Compact high-speed high-sensitivity second-harmonic interferometer for electron density measurement in AIP conference proceedings: Burning plasma diagnostics, **988**, 132–5
- [28] Velsko S P and Eimerl D 1986 Precise measurements of optical dispersion using a new interferometric technique *Appl. Opt.* **25**, 1344–49
- [29] Minoshirna K and Matsumoto H 1997 In-situ measurements of shapes and thicknesses of optical parts by femtosecond two-colour interferometry *Opt. Commun.* **138** 6–10
- [30] Abraham E, Minoshima K and Matsumoto H 2000 Femtosecond laser-induced breakdown in water: time-resolved shadow imaging and two-color interferometric imaging *Opt. Commun.* **176** 441–452
- [31] Jobs, F C and Bretz N L 1997 A prototype imaging second harmonic interferometer. *Rev. Scient. Instrum.* **68** 709

Functional Multichannel Poly(Propylene Fumarate)-Collagen Scaffold with Collagen-Binding Neurotrophic Factor 3 Promotes Neural Regeneration After Transected Spinal Cord Injury

Xi Chen, Yannan Zhao, Xing Li, Zhifeng Xiao, Yuanjiang Yao, Yun Chu, Balázs Farkas, Ilaria Romano, Fernando Brandi,* and Jianwu Dai*

Many factors contribute to the poor axonal regrowth and ineffective functional recovery after spinal cord injury (SCI). Biomaterials have been used for SCI repair by promoting bridge formation and reconnecting the neural tissue at the lesion site. The mechanical properties of biomaterials are critical for successful design to ensure the stable support as soon as possible when compressed by the surrounding spine and musculature. Poly(propylene fumarate) (PPF) scaffolds with high mechanical strength have been shown to provide firm spatial maintenance and to promote repair of tissue defects. A multichannel PPF scaffold is combined with collagen biomaterial to build a novel biocompatible delivery system coated with neurotrophin-3 containing an engineered collagen-binding domain (CBD-NT3). The parallel-aligned multichannel structure of PPF scaffolds guide the direction of neural tissue regeneration across the lesion site and promote reestablishment of bridge connectivity. The combinatorial treatment consisting of PPF and collagen loaded with CBD-NT3 improves the inhibitory microenvironment, facilitates axonal and neuronal regeneration, survival of various types of functional neurons and remyelination and synapse formation of regenerated axons following SCI. This novel treatment strategy for SCI repair effectively promotes neural tissue regeneration after transected spinal injury by providing a regrowth-supportive microenvironment and eventually induces functional improvement.

1. Introduction

Spinal cord injury (SCI) is a severe and irreversible central nervous system (CNS) injury with varying degrees of damage and loss of motor and sensory functions below the injury level.^[1] Numerous mechanisms underlie the deficient axonal regrowth and poor functional recovery that occur post-SCI, including an absence of neurotrophic factors to protect neurons and to stimulate intrinsic neuronal regeneration-related responses,^[2] the lack of growth-permissive substrates to support axon elongation through the lesion area,^[3] the production of various myelin-associated and extracellular matrix-derived inhibitory molecules including Nogo, oligodendrocyte myelin glycoprotein (OMgp), and chondroitin sulfate proteoglycans (CSPGs),^[4] and the occurrence of a range of secondary effects including vascular damage, scar formation, and inflammation.^[4a,5] Given that even apparently minor displacement of spinal tissue can result in severing of axons and loss of function, the

Dr. X. Chen, Prof. J. Dai
Institute of Combined Injury
State Key Laboratory of Trauma
Burns and Combined Injury
Chongqing Engineering Research Center for Nanomedicine
Chongqing Engineering Research Center for Biomaterials
and Regenerative Medicine
College of Preventive Medicine
Army Medical University (Third Military Medical University)
30th Gaotanyan street, Chongqing 400038, China
E-mail: jwdai@genetics.ac.cn

Dr. Y. Zhao, Dr. X. Li, Dr. Z. Xiao, Prof. J. Dai
State Key Laboratory of Molecular
Developmental Biology
Institute of Genetics and Developmental Biology
Chinese Academy of Sciences
Beijing 100101, China

 The ORCID identification number(s) for the author(s) of this article can be found under <https://doi.org/10.1002/adhm.201800315>.

DOI: 10.1002/adhm.201800315

Dr. Y. Yao, Prof. J. Dai
Department of Neurobiology
Chongqing Key Laboratory of Neurobiology
Army Medical University (Third Military Medical University)
30th Gaotanyan street, Chongqing 400038, China

Dr. Y. Chu
Division of Nanobiomedicine
Suzhou Institute of Nano-Tech and Nano-Bionics
Chinese Academy of Sciences
Suzhou 215123, China

Dr. B. Farkas, Dr. I. Romano, Dr. F. Brandi
Istituto Italiano di Tecnologia
Via Morego 30, Genova 16163, Italy
E-mail: fernando.brandi@cnr.ino.it

Dr. F. Brandi
Istituto Nazionale di Ottica
Consiglio Nazionale delle Ricerche
Via Moruzzi 1, Pisa 56124, Italy

complex nature of SCI poses a significant challenge for clinical treatment.^[6]

Various biomaterials have been used for promoting SCI repair. Biomaterials play therapeutic effects by providing a bridge between the two damaged spinal cord ends, reconnecting the neural tissue within the lesion site, hindering scar formation and the inflammatory process, reconstituting the conductive circuits of the nerve, reducing glutamate and calcium ions in cerebrospinal fluid, protecting neurons of spinal cord from apoptosis and finally enhancing locomotion recovery after spinal cord injury.^[7] Neural tissue engineering studies have paid much attention to the essential parameters for biomaterial design such as biocompatibility, biodegradability, porosity and permeability.^[8] Mechanical properties are especially crucial for successful transplantation of biomaterial, because the grafted biomaterial should not only be able to direct axonal regeneration prior to complete biodegradation, but also must be strong enough to bear normal forces from the spine and surrounding muscles.^[9] The mechanical properties of biomaterials such as hydrogel scaffolds may influence the growth rates of regenerated nerve fibers.^[10] The results of studies of neurite extension in 3D cultures reinforce that the mechanical properties of biomaterials play an important role in their ability to facilitate axonal regrowth.^[10b,11] The fast biodegradation rate and low mechanical strength of some natural materials have limited their use as biomaterials, and modification by crosslinking techniques and optimization of the material composition are required to improve their mechanical properties and to enable tissue bridging and to achieve optimal results.^[8,12]

Poly (propylene fumarate) (PPF) polymer is a photo-cross-linkable or chemically cross-linkable biomaterial with biocompatibility and absorbability.^[13] Synthetic PPF can be manufactured into various shapes and sizes and plays a therapeutic role when implanted in vivo either as an injectable biomaterial or in prefabricated scaffolds possessing high mechanical strength.^[14] Porous PPF scaffolds have been extensively used in both bone and blood vessel regeneration tissue engineering studies, where they provide structural maintenance and suitably filling up tissue defects.^[13,15] A recent study showed that PPF-based scaffolds can be coated with growth factors, including basic fibroblast growth factor (FGF-2), platelet-derived growth factor (PDGF-BB), or epidermal growth factor, which enhances the conventional application of PPF coated with bone morphogenetic protein alone.^[16] There has been little research into the potential use of PPF-based biomaterial for CNS injury repair. However, in SPL201 cells, a conditionally immortalized Schwann cell precursor line that myelinates axons could be cultured on cross-linked PPF discs which did not cause cytotoxicity and significantly improved cell attachment and proliferation, suggesting that PPF-based biomaterial may be used for neural damage repair.^[17]

Collagen, with desirable attributes including low antigenicity, excellent biocompatibility and biodegradability when grafted in vivo, has been used widely as a biomaterial for spinal cord repair.^[18] Linear ordered collagen scaffold is a nerve guidance material with excellent tissue compatibility and low antigenicity in vivo,^[19] and when coated with myelin-associated inhibitor antibodies, it facilitates bridge establishment, synapse formation and locomotor enhancement.^[19,20] Furthermore, 3D

collagen biomaterials combined with neurotrophic factors promoted neurite outgrowth in vitro and nerve fiber regrowth.^[4b] Previous studies have shown that collagen biomaterial-based therapies for SCI induced numerous regenerative axons with myelination and functional recovery in canine models, and improvement of sensory function in lower limbs of humans without adverse events such as infection, allergic reaction, and aggravation of neurological status.^[21]

Neurotrophin-3 (NT3) has neuroprotective and neurotrophic roles in neurons and neural grafts, and promotes long-distance axonal extension and reconstitution of neural connectivity through the lesion site after severe SCI.^[22] The results from several studies of CNS injury have indicated that effective controlled delivery of growth factor could limit the initial burst release of growth factors from biomaterials and enable the local delivery of growth factors with a sustained dosage over a prolonged time.^[23] NT3 with an engineered collagen-binding domain (CBD-NT3) specifically binds to collagen biomaterials and retains high neurotrophic bioactivity when cultured with dorsal root ganglia neurons.^[24] And collagen scaffolds exhibit controlled release of CBD-NT3 that promotes nerve fiber regeneration followed by hind limbs movement recovery after SCI.^[24,25] In this study, we combined PPF with collagen biomaterial to establish biocompatible delivery system which may form a more stable spatial support without deformation in a short period and has higher mechanical properties than collagen alone. Combined with collagen and CBD-NT3, the functional parallel-aligned multichannel PPF scaffold was made for directing neural tissue regeneration across the lesion site through the porous structures, rebuilding bridge connectivity and accelerating axonal regrowth between the two spinal cord stumps after transection injury. The multichannel PPF scaffolds were produced by excimer laser photocuring,^[26] specifically using the novel 3D printing methodology Mask Projection Excimer laser StereoLithography (MPExSL),^[27] which is capable of high production yield of well-shaped 3D scaffolds with micrometer resolution. Within the combinatorial approach here adopted, collagen also acted as an effective cell attachment platform, along which neural lineage cells including neurons and oligodendrocytes could regenerate. Controlled-releasing CBD-NT3 loaded onto the collagen biomaterial provided continued neurotrophin and promoted survival of various types of functional neurons. This novel treatment strategy for SCI repair, combining biomaterials with growth factor, resulted in electrophysiological and locomotor improvements, and has potential for use in clinical therapy in the future.

2. Results

2.1. Characterization of PPF-Collagen Scaffold with Collagen-Binding NT3 and Promotion of Neurite Outgrowth In Vitro by CBD-NT3

The prepared functional PPF scaffolds with regular lateral prisms consisted of an ≈ 4 mm deep \times 5 mm diameter columnar structure with 24 equal-sized pores (**Figure 1A**). After the PPF scaffold was sectioned into pieces, it exhibited a uniform parallel-aligned porous structure and the pores could be

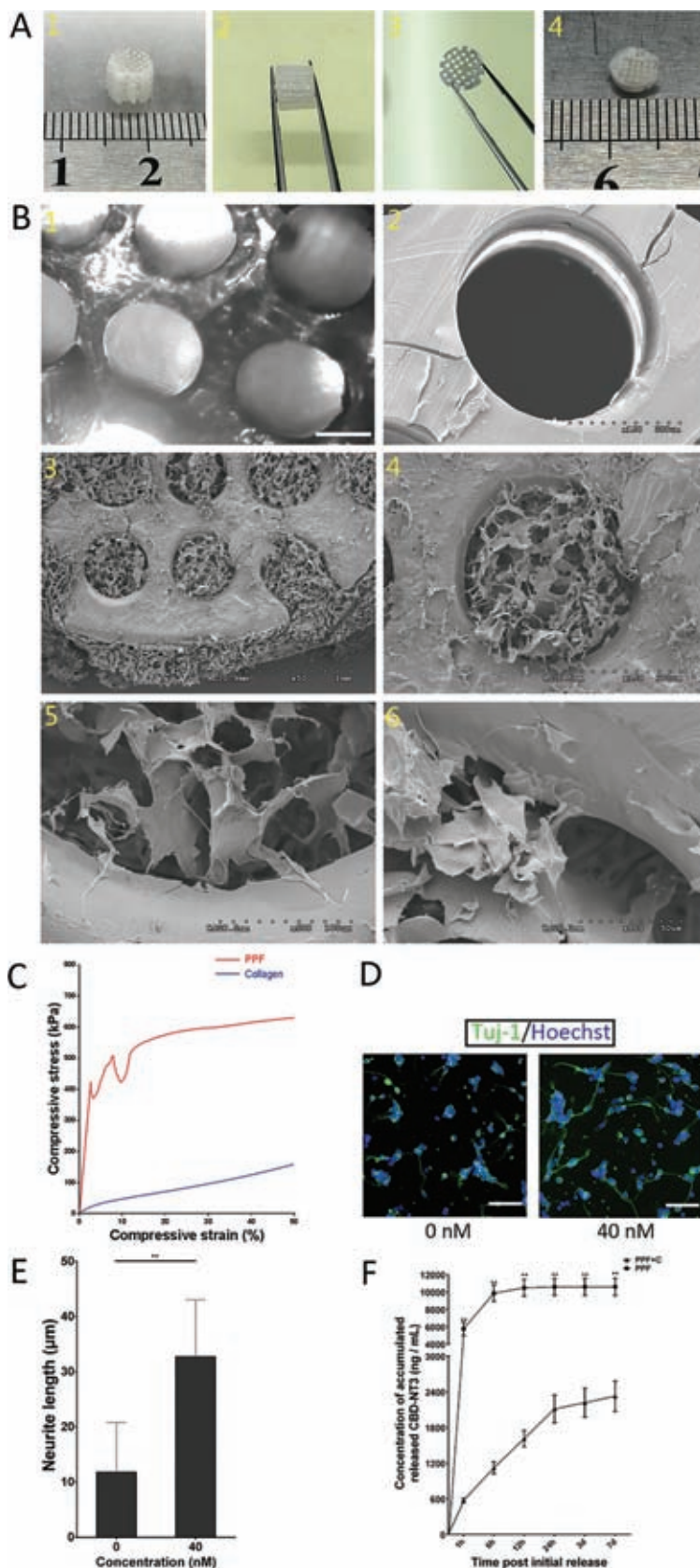


Figure 1. A–C) Macroscopic and scanning electron microscope images and mechanical properties of functional parallel-aligned multichannel PPF combined

combined with collagen biomaterial (Figure 1A). The presence of multiple rounded channels in the PPF biomaterial was confirmed by examination under an optical microscope (Figure 1B).

PPF scaffold samples with or without collagen were freeze-dried and sprayed with gold powder for scanning electron microscopy (SEM) characterization. Similar to the results described above, SEM analysis showed the homogeneous porous structure of the PPF scaffold with a smooth surface inside. Surprisingly, the collagen coating penetrated into each channel of the PPF scaffold while maintaining its intrinsic ordered structure (Figure 1B). Images captured at higher magnification revealed that collagen firmly adhered to the side walls of the PPF scaffold (Figure 1B).

The mechanical properties of the PPF and collagen biomaterial were examined. Acquisition and analysis to compressive press showed the results within compressive strain of 50%. The maximum compressive stress of the PPF scaffold at 2.68% strain (423.2 ± 5.7 kPa) was considered the compressive failure stress, and this was markedly higher (21.7-fold) than that of collagen (19.44 ± 3.2 kPa) at the same strain (Figure 1C). The elastic modulus of the PPF scaffold was 15.78 MPa, which was significantly higher than that of the collagen biomaterial (0.725 MPa). These findings indicated stronger and more stable mechanical properties of PPF compared with collagen, and supported the idea for establishment of a molecule

with collagen. D,E) Neurite outgrowth of CGNs cultured with CBD-NT3 in vitro. (A) PPF scaffold combined with or without collagen. (1), (2) Columnar and porous structure of PPF scaffold with a diameter of 5 mm. Sliced PPF (3) with a thickness of 1 mm shows uniform parallel-aligned porous structure that sustains its shape when combined with collagen (4). (B) Optical and scanning electron micrographs of PPF samples with or without collagen. (1) PPF scaffold with multiple rounded channels observed under an optical microscope. Scale bars represent 250 μm. (2) A channel of PPF scaffold showed rounded structure. (3)–(6) Collagen biomaterials filled into every channel of the PPF scaffold and well attached to inner surfaces of porous structure. (C) Assessment of mechanical properties of PPF and collagen determined by measuring compressive stress at various levels of compressive strain. The observation of significantly higher stresses of PPF compared with collagen under the same level of strain led to the idea for establishment of a stable molecular delivery platform combining the two biomaterials. (D) Representative fluorescence micrographs of dissected CGNs cultured in vitro with CBD-NT3 or PBS control. Neurons were identified by immunofluorescence using antibodies directed against Tuj-1 (green) and cell nuclei were stained with Hoechst (blue). Scale bars represent 50 μm. (E) Quantification of length of neurite outgrowth of dissected CGNs cultured with 40×10^{-9} M CBD-NT3 or PBS control indicated that CBD-NT3 facilitated longer neurite outgrowth in vitro than the control treatment ($n = 3$ samples per group). (F) Elisa assay of concentration of released CBD-NT3 at 1 h, 6 h, 12 h, 24 h, 3 d, 7 d after initial release. Data are presented as mean \pm standard error of the mean. Error bars indicate the SD from three different experiments ($n = 4$ scaffolds per group). * $p < 0.05$, ** $p < 0.01$.

delivery platform combining PPF and collagen, which was predicted to be more stable than collagen biomaterial alone.

Both CBD-NT3 and NT3 provide neurotrophic stimulus for neurons, however, when tightly bound to collagen biomaterial, CBD-NT3 promotes survival of more neurons and elicits longer neurite outgrowth than NT3.^[24] Isolated rat cerebellar granule neurons (CGNs) were cultured in 48-well plates with 40×10^{-9} M CBD-NT3 to confirm the bioactivity of CBD-NT3. In wells containing CBD-NT3, neurons exhibited neurite outgrowth, and under neurotrophic stimulus, these neurons extended significantly longer nerve fibers in wells with CBD-NT3 than in wells with PBS ($p < 0.01$, Figure 1D,E), verifying the bioactivity of CBD-NT3. Furthermore, we evaluated the release of CBD-NT3 from PPF and combinatorial scaffold in vitro by ELISA assay (Figure 1F). The released CBD-NT3 was detected at 1 h, 6 h, 12 h, 24 h, 3d, 7d after initial release. The results of accumulated concentration of released CBD-NT3 indicated that within short period (12 h) after initial release, most CBD-NT3 could be released rapidly from PPF scaffold. In contrast, CBD-NT3 loaded onto combinatorial scaffold exhibited more stable controlled releasing in vitro. It suggested that collagen significantly enhanced binding ability of CBD-NT3 to combinatorial scaffold and effectively achieved controlled releasing of CBD-NT3.

2.2. Transplantation of PPF-Collagen Scaffold with CBD-NT3 Reduced Glial and Fibrotic Scar Formation in the Lesion Center Following SCI

In the rat complete transection SCI model, PPF scaffold, PPF-collagen scaffold or PPF-collagen scaffold loaded with CBD-NT3 were implanted into the injury sites, and SCI rats without scaffold implantation were used as a negative control (Figure 2A). At 12 weeks posttransplantation, the spinal cords of the four groups were harvested. Macroscopic observations indicated spinal cord tissue in the lesion site of control group was severely destroyed after injury and morphology of damaged tissue was clearly different from that of host tissues (Figure 2B). In contrast, there were good connectivity and integration of injured spinal cords with host tissues after treatment in the PPF+C group and PPF+C+NT3 group (Figure 2B).

Next, we examined whether reduced scar formation resulted in the good spinal cord connectivity observed in the PPF+C+NT3 group compared with the other groups. Glial scars secrete a series of inhibitory molecules and are one of the main barriers to regeneration of damaged axons after CNS injury.^[28] After transected spinal cord injury, control group exhibited obvious GFAP-positive astrocytic scar formation in the lesion area while there were fewer GFAP-positive areas in injury site of three scaffold groups (Figure S1A, Supporting Information). The number of GFAP-positive astrocyte in lesion center of control group were much greater than those of other groups (Figure S1B,C, Supporting Information, $p < 0.01$). There were least number of GFAP-positive astrocyte in lesion center of PPF+C+NT3 group (Figure S1B,C, Supporting Information, $p < 0.01$). Within the inhibitory microenvironment following SCI, one family of molecules, the chondroitin sulfate proteoglycans (CSPGs), has a significant role in limiting the reparative response and CSPG

deposits are regarded as a substantial barrier.^[4c] CS-56 staining was used to indicate CSPG expression at the lesion site. After transected SCI, the abundance of CS-56-positive signals at the lesion site in the control group was significantly higher than in the scaffold implantation groups ($p < 0.01$, Figure 2C,D). Among the three transplant therapy groups, the functional PPF-collagen scaffold with CBD-NT3 showed the greatest effect in reduction of CSPG deposits ($p < 0.01$, Figure 2D). All primary antibodies used in this study were listed in Table 1.

Fibrotic scarring, characterized by excessive deposition of extracellular matrix (ECM) molecules, is another important constituent of scar tissue that inhibits axons growing past the lesion site after SCI.^[29] Furthermore, fibrotic scar is produced by fibroblasts that invade into the lesion area from adjacent meningeal and perivascular cells. The main extracellular matrices derived from those invading fibroblasts contain fibronectin, laminin, and type IV collagen.^[30] Given collagen was used as a major component of the combinatorial scaffolds, laminin was labeled to represent the accumulation of fibrotic scarring in the damaged area. Laminin-positive signals were detected at the lesion sites of rats in all groups, with the highest number of laminin-positive signals (81 ± 5.1) at the damage site of the control group (without any treatment). The number of laminin-positive signals in the control group was statistically significantly higher than those of all the other groups ($p < 0.01$, Figure 2E,F), and the laminin-positive signals were distributed across almost the whole injury site in the control group (Figure 2E). The PPF+C+NT3 group showed a significant reduction in the number of laminin-labeled cells (31 ± 3.9) compared with the other two groups with transplantation of PPF scaffolds ($p < 0.01$, Figure 2F). When combined with collagen, the grafted PPF scaffold exhibited significantly less laminin-positive fibrotic scar formation than PPF used alone ($p < 0.05$, Figure 2F). These results demonstrated that transplantation of a PPF scaffold promoted neural connectivity and integration of damaged tissues to host spinal cord with reduction of scar formation, which was enhanced when combined with collagen. The PPF scaffold combined with collagen and CBD-NT3 prevented production of regeneration-inhibitory molecules under CBD-NT3 neurotrophic stimulation.

2.3. Treatment with PPF Combined with Collagen and CBD-NT3 Increased Production of Newly Generated and Mature Neurons and Facilitated axonal Regrowth at the Lesion Site

We used β -III tubulin (Tuj-1), a marker of neuronal precursors, to examine the production of new neurons in the lesion area. The results showed that Tuj-1-positive neural tissue regenerated into the lesion site, and the regenerated neurons in the PPF+C+NT3 group effectively established a neuronal bridge between the two stumps following transection SCI (Figure 3A). We also found regrowth of several Tuj-1-positive tissue strips across the lesion area in the three groups in which functional PPF scaffold was implanted, illustrating guided nerve regeneration through the parallel-aligned multichannel structures of the porous PPF scaffold (Figure 3A). Furthermore, although Tuj-1-positive neurons were detected in all groups, the number of Tuj-1-positive neurons in the PPF+C+NT3 group was statistically significantly higher than those in the other three

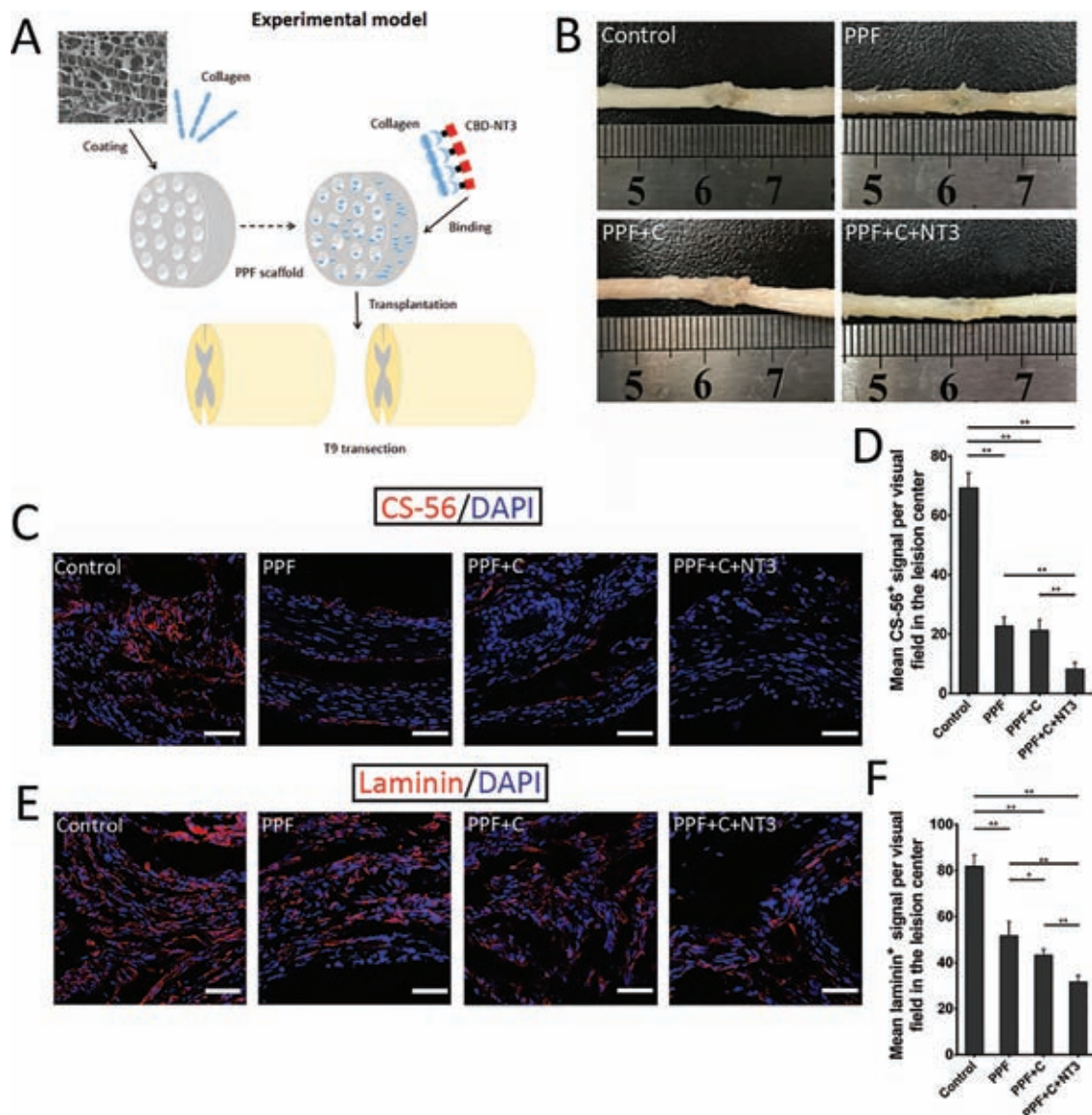


Figure 2. Functional PPF scaffold combined with collagen and bioactive CBD-NT3 facilitated neural tissue connection with inhibition of scar formation. A) Schematic diagram of experimental model of combinatorial treatment with PPF, collagen and CBD-NT3. B) Macroscopic observation of spinal cord tissues containing injury sites at 12 weeks postsurgery. Spinal cord tissue in the PPF+C+NT3 group had the greatest connectivity and integration with normal spinal cord. C) Confocal images of CS-56-positive signals (red) in the injury site of each group indicated abundant chondroitin sulfate proteoglycans (CSPGs) deposited within the lesion area after transected spinal cord injury (SCI) without any therapy ($n = 6$ animals per group). Scale bars represent $50 \mu\text{m}$. D) Quantification of mean CS-56-positive signal per visual field in the lesion center of each group. The PPF+C+NT3 therapy resulted in the greatest improvement to the microenvironment after SCI with a statistically significant decrease in chondroitin sulfate proteoglycans. E) Representative images of laminin-labeled signals (red) in the lesion centers in each group indicating fibrotic scar deposition following SCI ($n = 6$ animals per group). Scale bars represent $50 \mu\text{m}$. F) Quantification of mean laminin-positive signals per visual field in the lesion center of each group. Functional PPF scaffold combined with collagen and bioactive CBD-NT3 significantly inhibited formation of fibrotic scarring. Data are presented as mean \pm standard error of the mean. * $p < 0.05$, ** $p < 0.01$.

groups ($p < 0.01$, Figure 3B,C), while the number of Tuj-1-positive neurons in both the PPF and PPF+C groups were significantly higher than that of the control group ($p < 0.05$, Figure 3C). These results demonstrated that new neurons were generated in the lesion center following transplantation of PPF scaffolds after SCI, while the combinatorial treatment of PPF combined with collagen and CBD-NT3 exerted the greatest therapeutic effect.

The survival or generation of mature neurons was determined under conditions with or without PPF treatment. Rats of

the PPF+C+NT3 group exhibited the largest number of Map2-positive mature neurons at the middle of damage area compared with other groups ($p < 0.01$, Figure 3D,E). The PPF+C and PPF groups also exhibited promotion of neural regeneration, because the quantity of mature neurons in these two groups was also significantly greater than that of the control group ($p < 0.01$, Figure 3D,E). The curative effect of PPF combined with collagen was much greater than implantation of PPF alone, based on the statistically significant differences in the numbers

Table 1. Primary antibodies.

Antibody	Species	Source	Catalog number	Dilution
Anti- β III tubulin (Tuj-1)	Rabbit	Abcam	Ab18207	1:500
Anti-neurofilament (NF)	Rabbit	Abcam	Ab8135	1:500
	Mouse	Abcam	Ab7795	1:500
Anti-serotonin (5-HT)	Rabbit	Immunostar	20080	1:500
Anti-Choline acetyltransferase (ChAT)	Rabbit	Abcam	Ab6168	1:500
Anti-GABA	Rabbit	Sigma	A2052	1:500
Anti-Tyrosine Hydroxylase (TH)	Rabbit	Abcam	Ab112	1:500
Anti-Map2	Rabbit	Abcam	Ab11267	1:500
Anti-Chondroitin Sulfate (CS56)	Mouse	Abcam	Ab11570	1:500
Anti-myelin-associated glycoprotein (MAG)	Mouse	Abcam	Ab89780	1:200
Anti-Synaptophysin (Syn)	Rabbit	Abcam	Ab32594	1:200
Anti-Laminin	Rabbit	Sigma	L9393	1:500

of mature neurons ($p < 0.01$, Figure 3E). These results indicated that PPF-based treatment could facilitate production of mature neurons, and when coated with CBD-NT3 that provides continuous neurotrophic effects and binding to collagen, the functional PPF scaffold biomaterial enhances survival of existing neurons and production of NSCs-derived mature neurons.

The immunofluorescence staining results also showed that neurofilament (NF)-positive signals were present in the lesion centers of rats in all groups after transected SCI (Figure 3F and Figure S2, Supporting Information). The PPF+C+NT3 group exhibited significantly more NF-positive signals than the other three groups, which indicated that it had the greatest amount of axonal regeneration ($p < 0.01$, Figure 3F,G), while the numbers of NF-positive signals in both the PPF and PPF+C group were higher than that of the control group, but were not significantly different from each other ($p > 0.05$, Figure 3G).

2.4. Implantation of PPF Scaffold Combined with Collagen and CBD-NT3 into SCI Lesion Site Promoted Functional Axonal Regeneration Along with Myelination and Synapse Formation of Regenerated Axons

As observed above that we had found numerous regenerative axons in PPF+C+NT3 group, we further examined whether the numerous regenerative axons observed in the PPF+C+NT3 group were functional neurons. We detected that 5-HT-positive motor neurons had regenerated into the lesion area and co-labeled with NF-positive axons (Figure 4A,B), indicating the regrowth of serotonergic axons into the lesion site. Next, we used ChAT antibody to label spinal cord motor neurons and motor axons. ChAT-labeled motor neurons were abundant in the injury center in the PPF+C+NT3 group after SCI and observation at higher magnification showed distinct colocalization of NF-positive axons with ChAT-positive neurons, indicating the regeneration of cholinergic neurons and axons (Figure 4C,D). Two types of sensory neurons, GABA-positive and TH-positive neurons, were also observed in the lesion area, and parts of these neurons showed double labeling with regenerated axons, indicating effective regeneration of gamma-aminobutyric acid-energetic and dopaminergic axons

(Figure 4E–H). These findings suggested that the combination of PPF and collagen formed a stable delivery platform, which closely bound with and enabled controlled release of CBD-NT3 in vivo, and this combinatorial treatment consisting of a PPF scaffold with collagen and CBD-NT3 directed axonal regrowth and accelerated the regeneration of various functional neurons and axons into the injured area after severe SCI.

To confirm the remyelination, myelination and synapse formation of the abundant regenerated axons in the PPF+C+NT3 group, we double-stained for NF with myelin-associated glycoprotein (MAG) or synaptophysin (Syn). In the damage center, plentiful MAG-positive myelin co-localized with NF-positive axons and clear double labeling of regenerated axons and myelin was observed at higher magnification (Figure 4I,J). Additionally, Syn-positive signals also existed in the NF-positive axon-enriched area of the lesion site, and multiple synapse formations onto regenerated axons were detected at higher magnification (Figure 4K,L). These results demonstrated that there was not only abundant functional neuronal axon regrowth in the PPF+C+NT3 group, but also that these regenerated axons were effectively myelinated, accompanied by remyelination in the lesion site and the formation of synapses.

2.5. Combinatorial Treatment Consisting of PPF Scaffold and Collagen Loaded with CBD-NT3 Induced Improvement of Electrophysiology and Locomotor Function Recovery After Transected Spinal Cord Injury

To measure enhancement of motor function, electrophysiological tests were carried out. Before SCI, animals receiving electrophysiological stimulation exhibited an average cortical motor-evoked potential (MEP) with a latent period of 2.6 ms and an amplitude of 6.95 mV, which was completely eliminated immediately after transected SCI (Figure 5A). At 12 weeks postinjury and transplant treatments, the latencies of MEPs in all groups were not restored to normal levels ($p < 0.01$, Figure 5A,B), however, the latencies of potentials in the PPF+C+NT3 group were shorter compared with those in the control group ($p < 0.05$, Figure 5B), suggesting an enhancement

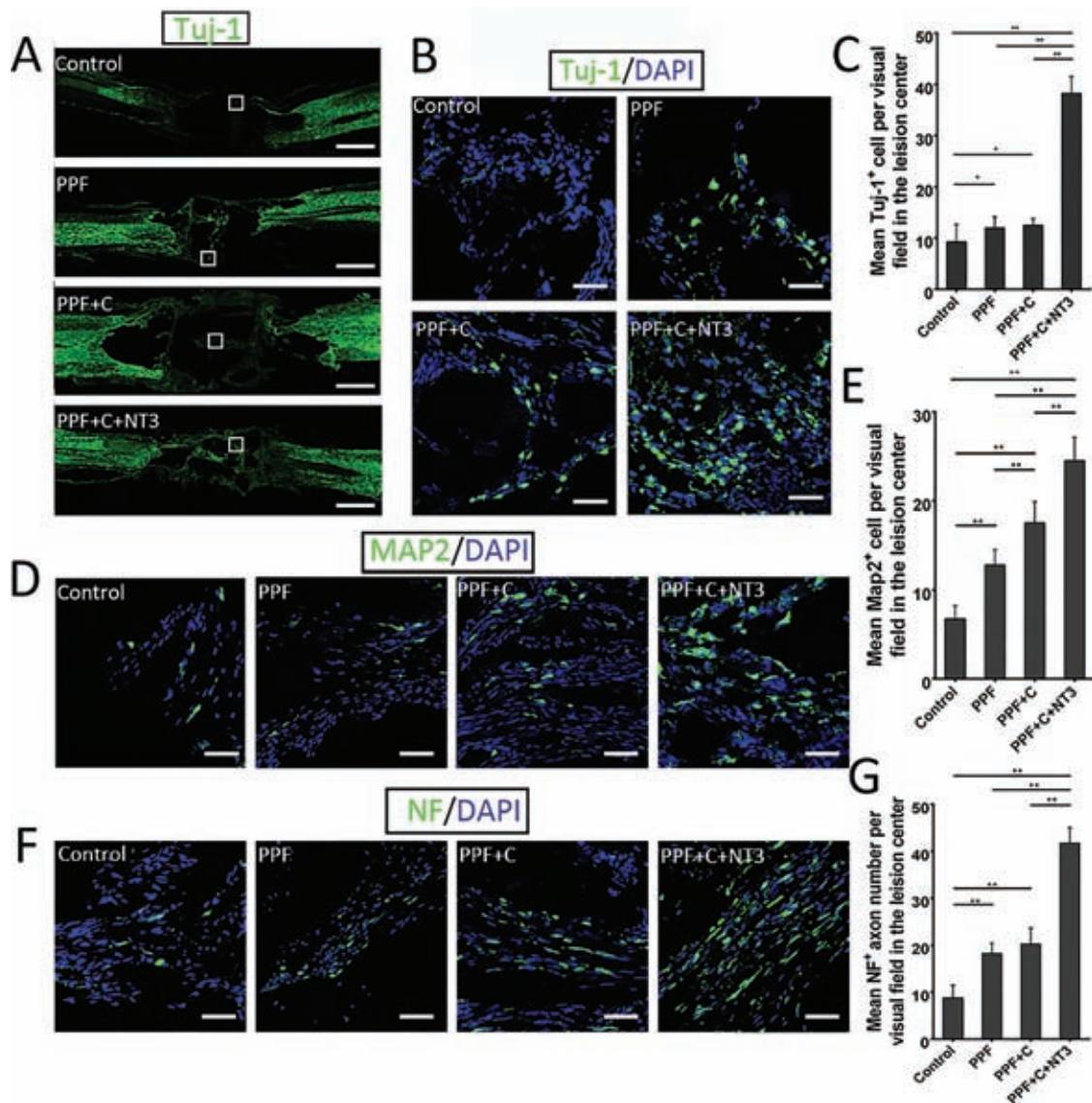


Figure 3. Transplantation of functional PPF scaffolds combined with collagen and CBD-NT3 promoted production of newly generated and mature neurons and axonal regrowth in the lesion areas of rats after spinal cord injury (SCI) ($n = 6$ animals per group). A) Confocal images labeled with anti-Tuj-1 (green) in the lesion areas, indicating that the largest number of Tuj-1-positive neurons across the injury site that established connections with the two cut ends occurred in the PPF+C+NT3 group. Scale bars represent 1 mm. B) Higher magnification images of areas indicated by white boxes in (A), showing significantly more Tuj-1-positive neurons in the lesion center of PPF+C+NT3 group than those of other groups. Scale bars indicate 50 μm . C) Quantification of Tuj-1-positive cells in the lesion center of each group. The number of newly generated neurons was much higher in the lesion site of the PPF+C+NT3 group compared with those of other groups, while PPF and PPF+C treatment displayed similar therapeutic effects. D) Representative immunofluorescence micrographs of Map2-positive signals (green) in the lesion center showed more Map2-positive neurons in the lesion center of the PPF+C+NT3 group than those of other groups. Scale bars represent 50 μm . E) Quantification of Map2-positive mature neurons in the middle of damage sites of each group showed the highest number of mature neurons was present in the lesion center of the PPF+C+NT3 group, suggesting that this treatment group had the greatest protective and neurotrophic effect to host or endogenous NSCs-derived mature neurons. F) Representative images of neurofilament (NF)-positive axons (green) regenerated into the lesion center at 12 weeks after SCI. Scale bars represent 50 μm . G) Quantification of number of NF-positive axons in the injury center demonstrated the highest number of regenerated axons in the PPF+C+NT3 group. Data are presented as mean \pm standard error of the mean. $**p < 0.01$.

of the latency. The amplitudes of MEPs in all groups did not recover to normal levels within the time period of the study, indicating severe damage of bioelectric conduction after transected SCI ($p < 0.01$, Figure 5A,C). Surprisingly, the amplitude in the PPF+C+NT3 group ($20.7 \pm 1.53 \mu\text{V}$) was statistically significantly larger than those in the PPF+C ($14.0 \pm 2.83 \mu\text{V}$), PPF

($14.3 \pm 1.41 \mu\text{V}$) and control group ($13.3 \pm 0.58 \mu\text{V}$) ($p < 0.01$, Figure 5C). These data suggest that the abundant myelination and synapse formation in regenerated axons described above contributes to reconstruction of neuronal relays in the lesion area, eventually resulting in electrophysiological improvement in animals in the PPF+C+NT3 group.

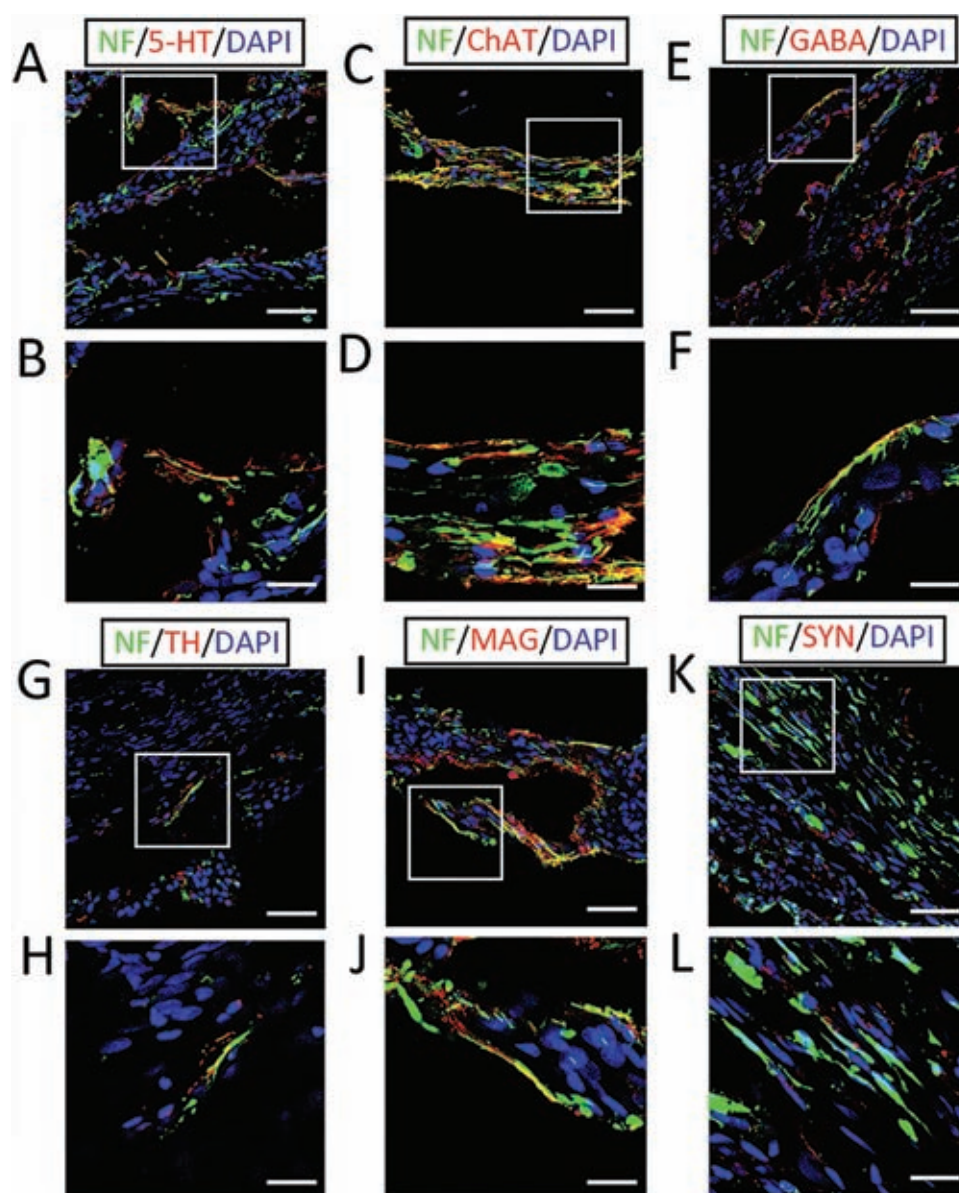


Figure 4. The combination of PPF scaffold with collagen and CBD-NT3 (PPF+C+NT3) induced generation of various functional neurons, and myelination and synapse formation of regenerative axons in the middle of lesion area of rats following transected spinal cord injury (SCI). A,C,E,G) Representative micrographs of serotonergic (5-HT), cholinergic (ChAT), gamma-aminobutyric acid-energetic (GABA), and dopaminergic (TH) neurons, respectively, produced in the middle of lesion area of rats in the PPF+C+NT3 group. Scale bars represent 50 μm . B,D,F,H) Higher magnification images of areas indicated by white boxes in (A), (C), (E), and (G), respectively, show various regenerated motor and sensory neurons in the lesion site following SCI and PPF+C+NT3 treatment. Scale bars represent 20 μm . I) Representative immunofluorescence image of double-labeled NF (green)/MAG (myelin-associated glycoprotein) (red) in the middle of lesion site indicated efficient remyelination in the regenerated axon-abundant area of rats in the PPF+C+NT3 group. Scale bar represents 50 μm . K) Representative immunofluorescence image of double staining with NF/Syn (synaptophysin) showed multiple Syn-positive (red) signals colocalized with regenerated axons within the damage center of SCI rats receiving implantation of PPF loaded with collagen and CBD-NT3. Scale bar represents 50 μm . J,L) Higher magnification images of areas indicated by white boxes in (I) and (K), respectively, which revealed effective myelination of nerve fibers and synapse formation of regenerated axons in the lesion center after PPF+C+NT3 treatment. Scale bars indicate 20 μm .

The Basso–Beattie–Bresnahan (BBB) test was applied weekly to evaluate behavioral recovery after SCI. At 1 week after SCI, rats in all groups exhibited undetectable locomotion restoration with BBB scores of 0 (Figure 5D). During the period of 2–12 weeks postsurgery, rats in the PPF+C+NT3 group showed the greatest locomotion recovery, with BBB scores of 2–8, which were statistically significantly higher than those in the other

three groups ($p < 0.01$, Figure 5D). BBB scores of rats in the PPF+C group were significantly higher than those in control group during 7–12 weeks post surgeries ($p < 0.05$, Figure 5D). BBB scores of the PPF+C+NT3 group plateaued at 10–12 weeks postinjury at levels of 8–9, meaning that there was at least sweeping of lower limbs with no weight support.^[31] These findings indicated that the animals subjected to transected spinal

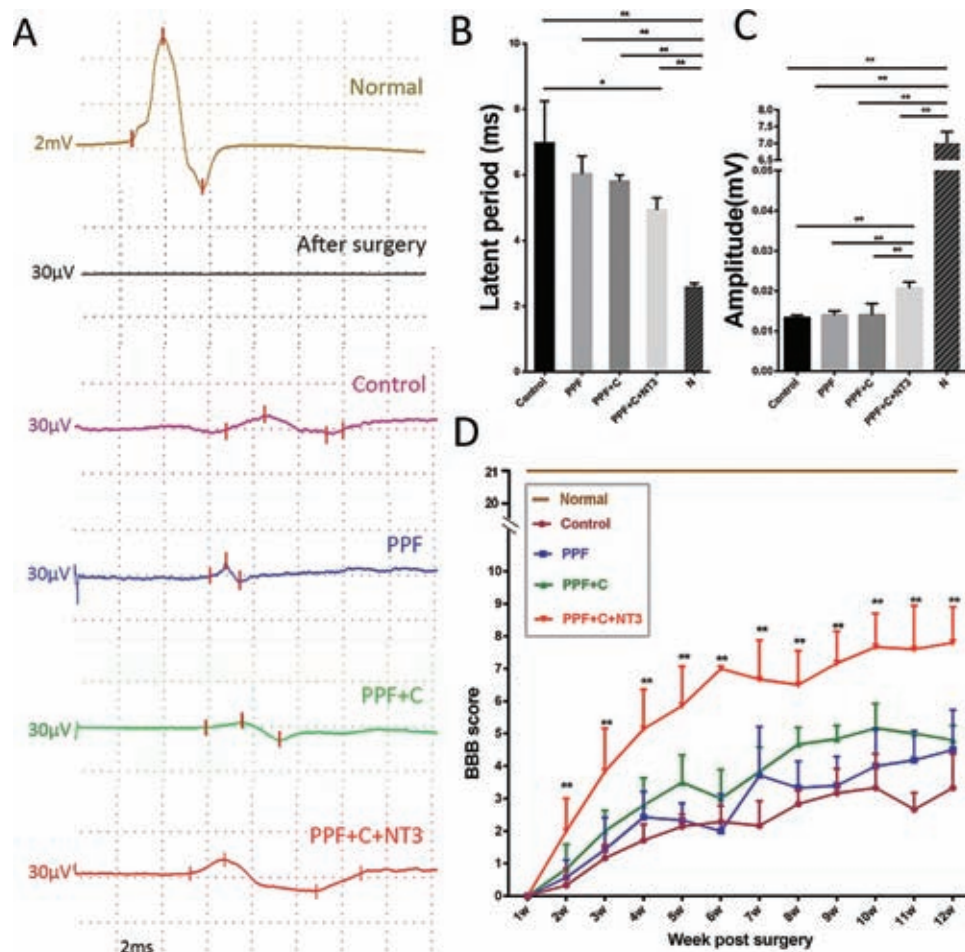


Figure 5. Combinatorial treatment consisting of functional PPF scaffold, collagen and CBD-NT3 (PPF+C+NT3) enhanced electrophysiological and locomotor recovery following spinal cord injury (SCI) ($n = 6$ animals per group). A) Schematic diagrams of motor-evoked potentials (MEPs) of untreated rats and rats in SCI, PPF, PPF+C and PPF+C+NT3 groups at 12 weeks postinjury. B) Quantification of latencies of MEPs in each group at 12 weeks postinjury, showing that latency in PPF+C+NT3 was closest to the normal level, suggesting a partial restoration. C) Quantification of amplitudes of MEPs in each group at 12 weeks postinjury, indicating that the greatest electrophysiological improvement occurred in the PPF+C+NT3 group with statistically significantly larger amplitudes than the control group and other treatment groups. D) Weekly BBB scores of rats in each group during the first 12 weeks after surgery. From 2 to 12 weeks postsurgery, rats in the PPF+C+NT3 group exhibited distinctly better locomotor function recovery than the control group and other treatment groups, although this did not reach the normal level. Data are presented as mean \pm standard error of the mean. * $p < 0.05$, ** $p < 0.01$.

cord injury together with combinatorial treatment of functional PPF scaffold with collagen and CBD-NT3 showed restored effective hindlimb motor function, including significant movement ability in the three predominant joints.

3. Discussion

Numerous complex biological processes contribute to the poor capacity for spontaneous regeneration after SCI. Formation of an inhibitory microenvironment following SCI results in failure of effective axonal regrowth even when there are small numbers of damaged axons caused by incomplete contusion.^[32] In complete transection or spinal cord removal injury, the loss of all motor and sensory axonal tracts eliminates the possibility of translesion regeneration and restoration within a week, posing a significant challenge for treatment.^[33] It is necessary to combine different biomaterials to integrate their respective

advantages and provide multiple therapeutic effects.^[34] In addition, a recent study reported that multichannel agarose scaffolds combined with brain-derived neurotrophic factor (BDNF) could induce motor axon regeneration into a severe injured spinal cord and organize linearly axons regrowth.^[35] In the present study, we used a 3D printing approach based on stereolithography to fabricate parallel-aligned multichannel PPF scaffolds that enhanced the mechanical properties of a molecular delivery platform loaded with collagen. We confirmed the superior mechanical properties of the PPF scaffold compared with collagen. Specially, the uniform pores and parallel-aligned structure of the PPF scaffold provided guided channels for regeneration of neural tissues along the axial direction of spinal cord. Collagen biomaterials greatly filled into each channel and adhered to inner structures of pores in scaffold, promoting attachment of NSCs or new neurons and inducing axonal regeneration as regrowth-permissive matrix. A recent study reported an aid for peripheral nerve repair using

nerve conduits prepared by 405 nm micro-stereolithography.^[36] However, they did not reported that these single-channel conduits possessed biodegradability. We are the first, to our knowledge, to have implanted a combinatorial scaffold comprising also multichannel biodegradable stereolithographically 3D scaffolds for repair of CNS injury. A previous research using similar technology in present study has reported the degradation of PPF material *in vitro*.^[37] The weight of PPF material decreased by about 30% after degrading for 90 d.^[37] The data indicates that PPF scaffold is a kind of degradable biomaterial *in vitro*. However, the degradation in PBS is significantly different from body fluid in SCI sites.^[37] In our present study, we found the most of this biodegradable PPF scaffold degraded at 12 weeks post-surgery. And we further weighed these small PPF residues (11.8 ± 2.8 mg) compared with mass of 1-mm PPF scaffold (70 ± 2.6 mg). Mass decay of PPF scaffold ranged from 79.20% to 87.10%.

We have also focused on the utilization of a CBD to enhance the collagen-binding ability of growth factors. CBD-fused proteins can bind tightly to native and insoluble collagen, limiting the likelihood of them being washed away or diluted and preventing their rapid diffusion in the extracellular fluids, thus enabling enhanced aggregation onto the collagen-based biomaterial.^[38] Moreover, CBD-fusion has been reported to have no impact on the bioactivity of growth factors.^[39] In fact, CBD-fused growth factors have been shown to elicit greater biological effects than native growth factors *in vitro*, enabling collagen-based biomaterials to be developed as sustained-release delivery system.^[4b,25,39] CBD-NT3 is bioactive and promotes neurite outgrowth *in vitro*, and controlled release of CBD-NT3 coated on a delivery platform exhibits continual neurotrophic effects and contributes to an improved microenvironment following SCI for 2–3 d,^[40] assisting neural regeneration in the lesion center. In this study, we found that within short period (12 h) after initial release, plentiful CBD-NT3 could be released rapidly from PPF scaffold. Combinatorial scaffold exhibited more stably controlled releasing for CBD-NT3 loaded *in vitro*. We speculate the release of CBD-NT3 in the SCI sites might be rapid than in PBS, because the sustained flow of cerebrospinal fluid and the degradation of scaffold. But the release rate of CBD-NT3 in PPF+C scaffold might still be much slower than in PPF (Figure 1F).

Ependymal cells of the central canal in the adult spinal cord are considered to be potential endogenous NSCs, and they are able to be induced to proliferate and differentiate after traumatic SCI.^[41] Previous studies have revealed robust proliferation of activated endogenous NSCs in the lesion center and initiation of migration of these NSCs from the central canal within 3 d after SCI.^[42] In the present study, there were likely abundances of endogenous NSCs in uninjured segments adjacent to lesion site in short term after transected spinal cord injury. At the lesion site, we observed the highest number of newly generated neurons in the PPF+C+NT3 group, suggesting that controlled release of CBD-NT3 could offer neurotrophs and neuroprotection to the host spinal cord neurons, sparing endogenous NSCs after SCI and likely further directing neural differentiation of NSCs within 2–3 d postsurgery. Moreover, in all three PPF treatment groups, Tuj-1-positive signals across the lesion area demonstrated that parts of likely activated endogenous NSCs and sparing NSCs might be able to attach to the porous biomaterials

and proliferate, migrate and differentiate along the pores or channels, potentially contributed to regeneration of neural tissue bridges that connect the two transected spinal cord ends. Actually, part of Tuj-1-positive neuron might be deprived from other sources, such as survived or uninjured host neurons. Additional production of sprouting from surviving neurons in the spinal cord induced with treatment was another important reason for effective neural regeneration. Collagen enhanced attachment of NSCs or neurons and CBD-NT3 further promoted surviving of host neural tissues and regeneration of neural tissues across the lesion site. The maximum number of mature neurons was also observed in the injury center of the PPF+C+NT3 group, which could be explained by effects of CBD-NT3 on survival of likely endogenous NSC-derived neurons and of host sparing neurons. Surprisingly, the combinatorial treatment involving PPF, collagen and CBD-NT3 also resulted in a decrease in deposition of inhibitory molecules and reduction of scar tissue formation (Figure 2C,E), resulting in improved neural connection and integration between damaged and host spinal cord (Figure 2B). These results indicate that coated onto collagen, the tissue regeneration-permissive matrix, neurotrophic CBD-NT3 contributes to provide a supportive microenvironment for neural regeneration and further vastly amplifies therapeutic effect of PPF+C+NT3 treatment, supporting the idea that optimal repair of SCI is likely to involve combined treatment strategies.

In addition to finding higher numbers of regenerated axons in the PPF+C+NT3 group than in the other groups, we confirmed functional neuronal regeneration and colocalization with regenerated axons in the lesion area. These findings indicated that the addition of CBD-NT3 soon after injury clearly enhanced the neural regeneration response. The generation and regrowth of various types of functional motor and sensory neurons in the PPF+C+NT3 group corresponded with improved functional assessment outcomes (Figure 5D). Plentiful regrowth of axons into the lesion site represented potential reestablishment of neural connections. The remyelination in axon-abundant areas and myelination of newly generated axons that benefited bioelectric conduction, together with detectable synapse formation on the regenerated axons, indicating potential rebuilding of neural relays. Regrowth of axons across lesion area and reestablishment of neural relays potentially underlied the improvement of electrophysical function with restored latency and enhanced amplitude of MEP in PPF+C+NT3 group (Figure 4I,J and 5B,C).^[43] However, a limitation of our study was that we did not perform retrograde or anterograde tracing which might better evaluate regrowth of axonal tracts across lesion site and reestablishment of neural relays.

A recent study has revealed numerous and long-distance axonal regeneration beyond the transected spinal cord injury site with effective myelination, synapse formation and expression of neurotransmitters resulting in significant improvement of electrophysiological and locomotor recovery,^[22a] demonstrating the formation of new functional neural relays to support functional restoration. In the present study, remyelination and synapse formation in the regenerated axon-abundant area of the PPF+C+NT3 group was associated with eventual improvement of electrophysiology and locomotion. These functional recoveries indicated the potential establishment of new neuronal circuits.

4. Conclusion

In this study, we prepared parallel-aligned multichannel PPF with high mechanical strength and successfully combined this with collagen biomaterial, creating a novel molecule delivery platform with stable spatial support *in vivo*. When coated with bioactive CBD-NT3 (PPF+C+NT3) and implanted into transected spinal cord, the treatment showed effective neurotrophs and protection of neural tissues, inducing axonal regrowth and functional neuron regeneration. PPF+C+NT3 also promoted myelination and synapse formation of these regenerated axons. The porous structure of the delivery platform provided attachment and channels for host endogenous NSCs, which achieved migration, proliferation and differentiation under this improved microenvironment, along with reduction of CSPG deposits and fibrotic scarring, contributing to neuronal regeneration. The anatomical outcomes corresponded with the enhancement of functional assays that showed significantly better electrophysiological and locomotor recovery in rats receiving treatment combining PPF with collagen and CBD-NT3 that could be beneficial to clinical research in the future.

5. Experimental Section

Ethics: All experimental procedures were performed in accordance with Chinese Ministry of Public Health (CMPH) Guide and the Guide for the Care and Use of Laboratory Animals from the National Institutes of Health.

Preparation of Poly(Propylene Fumarate) Scaffold: To synthesize PPF, fumaric acid was heated in access of propylene glycol at 145 °C, with overhead mechanical stirrer under chemical hood, a Barrette trap was connected beneath the condenser and water was collected as by-product.^[44] After 17 h of reaction the temperature was increased to 185 °C for 5 h and then cooled to room temperature. The PPF was then dissolved in dichloromethane, repeated for three times. The synthesized PPF was blended with diethyl fumarate (DEF) at a ratio of 70:30 (PPF:DEF), and with the photoinitiator bis-acyl phosphine oxide Irgacure 819 at a concentration of 1.0% wt/wt. The photoinitiator was first dissolved in ethanol, then after complete dissolution DEF was added, and finally PPF was added. The solution was then stirred under hood for 3 d. The 3D multichannel scaffolds were produced using MPEXSL following the procedure presented in.^[27,45] Briefly, the surface of the photocurable PPF-based resin is irradiated with 308 nm light pulses from an excimer XeCl laser (COMPexPro-110, Coherent) using a mask projection system. The resin surface is cured only on the irradiated part, thus creating a solid layer with 500 µm channels. The layer thickness is defined by the number of laser pulses applied, and in the present case was 120 µm. The 3D scaffolds were created layer-by-layer, i.e., recasting fresh resin on top of the cured layer and repeating the laser irradiation, with 20 micron overlap between adjacent layers. The final size of the cylindrical scaffolds is 5 mm in diameter and few mm long.

Combining of Collagen onto PPF Scaffolds: Prepared porous PPF biomaterials were steeped in 75% alcohol for 24 h and then washed 10 times with sterile water. The PPF biomaterials were placed on a sterile surface and gently cut into several uniform 1-mm thick pieces. After drying, one piece was placed into each well of a 96-well plate, and the remaining pieces were stored in sterile tubes. Each PPF-containing well was then filled by injection of prefabricated collagen biomaterial prepared as previously described,^[18] and the plate was centrifuged for 10 min at 5000 rpm. Plates were frozen at -80 °C for 48 h followed by 24 h of freeze-drying. The dried and stable combinatorial biomaterials were cut into 1 mm thick pieces and stored in sterile tubes.

Test of Mechanical Properties: For measurement of mechanical properties, 1 mm thick pieces of PPF or collagen were placed in a materials-testing machine (Instron 3365) with 30 mm diameter plates at room temperature. The mechanical sensor was used with a 10-N load cell and the upper plate was lowered at a rate of 3 mm min⁻¹. Compressive strain and compressive pressure data were collected.

Protein Bioactivity Assessment: CBD-NT3 was purified as previously described.^[24,25] Briefly, the coding sequence of CBD, TKKTLRT, was fused to human NT3, into which a His-linker and pET-28a were inserted, producing engineered CBD-NT3. Then CGNs were cultured with CBD-NT3 to estimate its bioactivity. Briefly, CGNs were isolated from 5 d old Sprague Dawley rats and the cerebellums were dissected in trypsin solution (0.25% in PBS buffer) and seeded on 48-well plates with 40 × 10⁻⁹ M CBD-NT3 or PBS as a control. After culture for 24 h, neurons were fixed in 4% paraformaldehyde at 4 °C for 20 min, and incubated in DPBS containing 5% bovine serum albumin with 0.1% Triton X-100 for 1 h at RT. The neurons were incubated with βIII tubulin primary antibody overnight at 4 °C and incubated with corresponding secondary antibody for 1 h at RT. Cell nuclei were then stained with Hoechst 33342 and neurite outgrowth of CGNs was visualized under a Zeiss 200 fluorescence microscope (Carl Zeiss). The mean length of the neurite outgrowths per field was assessed using the accessory software of AxioVision (Zeiss Microscopy GmbH, Germany).

ELISA Assay: Four 1 mm PPF scaffolds and four 1 mm combinatorial scaffolds were loaded with Sug CBD-NT3 and 200 µL PBS was added to detect CBD-NT3 releasing from the scaffold at room temperature. The released CBD-NT3 was detected at 1 h, 6 h, 12 h, 24 h, 3 d, 7 d after initial release, respectively. All samples were measured with Human NT-3 DuoSet Elisa plate (R&D System, USA). The results were quantified at 450 nm using an ELISA reader (Molecular Devices, USA).

Surgery Processing: Animals were anesthetized by intraperitoneal injection of sodium pentobarbital. A 1.5 cm midline incision was made on the back to expose the T8–T10 vertebrae. Laminectomy was performed at the T9 vertebral level using a #11 surgical blade. A 1 mm long transection of the T9 spinal cord was made and the lesion site was irrigated with normal saline followed by control of bleeding with gelatin sponge. Rats were randomly divided into four groups: (1) control group, no treatment after 1 mm long transected spinal cord injury; (2) PPF group, a 1 mm thick piece of PPF prepared as described above was transplanted into the transection site immediately after SCI; (3) PPF + Collagen (PPF + C) group, a 1 mm thick piece of combinatorial biomaterial containing PPF and collagen bound with 20 µL of PBS was implanted into the lesion site after SCI; (4) PPF + Collagen + CBD-NT3 (PPF + C + NT3) group, a piece of combinatorial biomaterial loaded with 20 µL of CBD-NT3 (5 µg) was implanted into the transected lesion gap after SCI. The muscle and skin layers were then closed with sutures.

Electrophysiology: Twelve weeks after surgery, animals in each group were intraperitoneally anesthetized with sodium pentobarbital and cortical motor-evoked potentials (cMEPs) were measured using the Keypoint bichannel-evoked potential/electromyography system (9033A07, Dantec Company, Copenhagen, Denmark) as previously described.^[46] Briefly, two steel stimulating electrodes were inserted into the cranial surface of the motor cortex behind the anterior fontanel. Two recording electrodes and one reference electrode were inserted into the contralateral gastrocnemius muscle at a depth of 2 mm and dorsal skin at a depth of 3 mm. Then, a cMEP was recorded following a single stimulation with intensity of 45 mA.

Behavioral Assessment: The BBB 21-point open field locomotion rating scale was applied weekly following surgeries.^[31] Hind limb movements of each animal were assessed by two independent observers blinded to group identity.

Mass Decay Test of Scaffold: PPF scaffolds were weighed and four animals underwent operations with PPF as described above. At 12 weeks post surgeries, several remanant little PPF residues were taken out from each animal carefully. Obvious connective tissues on PPF were cleared away by using microforceps and PPF residues were added with 100 U mL⁻¹ collagenase (Invitrogen, USA) for 4 h at 37 °C to clear the rest of connective tissues. Washed with PBS for 5 times, PPF residues were dried at room temperature and weighed.

Statistical Analysis: All statistical analyses were conducted using the statistical software SPSS19.0. Data were presented as means \pm standard deviations. Multiple group comparisons were performed using one-way analysis of variance. Two-group comparisons were performed by applying Student's *t*-test. Statistically significant differences were represented as * *p*-value < 0.05 and ** *p*-value < 0.01.

Supporting Information

Supporting Information is available from the Wiley Online Library or from the author.

Acknowledgements

X.C. and Y.Z. contributed equally to this work. This work was supported by grants from the National Key R&D Program of China (2017YFA0104704 and 2016YFC1101500), Key Research Program of the Chinese Academy of Sciences (Grant No. ZDRW-ZS-2016-2), Youth Innovation Promotion Association CAS (2015077 and 2016096), and the European Union (FP7-NMP-2013-EU-China call, grant agreement no. 604263 – NEUROSCAFFOLDS).

Conflict of Interest

The authors declare no conflict of interest.

Keywords

collagen, neural regeneration, poly(propylene fumarate) scaffolds, spinal cord injury, stereolithography

Received: March 25, 2018

Revised: May 11, 2018

Published online:

- [1] T. Hagg, M. Oudega, *J. Neurotrauma* **2006**, *23*, 264.
- [2] a) L. L. Jones, M. Oudega, M. B. Bunge, M. H. Tuszynski, *J. Physiol.* **2001**, *533*, 83; b) K. Kadoya, S. Tsukada, P. Lu, G. Coppola, D. Geschwind, M. T. Filbin, A. Blesch, M. H. Tuszynski, *Neuroendocrinology* **2009**, *64*, 165.
- [3] M. B. Bunge, *Neuroscientist* **2001**, *7*, 325.
- [4] a) M. T. Fitch, J. Silver, *Exp. Neurol.* **2008**, *209*, 294; b) X. Li, J. Han, Y. Zhao, W. Ding, J. Wei, J. Li, S. Han, X. Shang, B. Wang, B. Chen, Z. Xiao, J. Dai, *Acta Biomater.* **2016**, *30*, 233; c) J. R. Siebert, A. Conta Steencken, D. J. Osterhout, *BioMed Res. Int.* **2014**, *2014*, 845323.
- [5] T. B. Jones, E. E. McDaniel, P. G. Popovich, *Curr. Pharm. Des.* **2005**, *11*, 1223.
- [6] C. Profyris, S. S. Cheema, D. Zang, M. F. Azari, K. Boyle, S. Petratos, *Neurobiol. Dis.* **2004**, *15*, 415.
- [7] a) A. E. Haggerty, M. Oudega, *Neurosci. Bull.* **2013**, *29*, 445; b) M. Wang, P. Zhai, X. Chen, D. J. Schreyer, X. Sun, F. Cui, *Tissue Eng., Part B* **2011**, *17*, 177; c) B. Q. Lai, M. T. Che, B. L. Du, X. Zeng, Y. H. Ma, B. Feng, X. C. Qiu, K. Zhang, S. Liu, H. Y. Shen, J. L. Wu, E. A. Ling, Y. S. Zeng, *Biomaterials* **2016**, *109*, 40; d) D. Liu, J. Chen, T. Jiang, W. Li, Y. Huang, X. Lu, Z. Liu, W. Zhang, Z. Zhou, Q. Ding, H. A. Santos, G. Yin, J. Fan, *Adv. Mater.* **2018**, *30*, e1706032; e) D. Liu, T. Jiang, W. Cai, J. Chen, H. Zhang, S. Hietala, H. A. Santos, G. Yin, J. Fan, *Adv. Healthcare Mater.* **2016**, *5*, 1513.
- [8] S. Kubinova, E. Sykova, *Regener. Med.* **2012**, *7*, 207.
- [9] B. Shrestha, K. Coykendall, Y. Li, A. Moon, P. Priyadarshani, L. Yao, *Stem Cell Res. Ther.* **2014**, *5*, 91.
- [10] a) R. K. Willits, S. L. Skornia, *J. Biomater. Sci., Polym. Ed.* **2004**, *15*, 1521; b) T. W. Carone, J. M. Hasenwinkel, *J. Biomed. Mater. Res., Part B* **2006**, *78*, 274.
- [11] A. P. Balgude, X. Yu, A. Szymanski, R. V. Bellamkonda, *Biomaterials* **2001**, *22*, 1077.
- [12] M. Tsintou, K. Dalamagkas, A. M. Seifalian, *Neural Regener. Res.* **2015**, *10*, 726.
- [13] R. Mishra, B. M. Roux, M. Posukonis, E. Bodamer, E. M. Brey, J. P. Fisher, D. Dean, *Biomaterials* **2016**, *77*, 255.
- [14] a) C. C. Wu, L. H. Hsu, S. Sumi, K. C. Yang, S. H. Yang, *J. Biomed. Mater. Res., Part B* **2017**, *105*, 2232; b) J. M. Walker, E. Bodamer, O. Krebs, Y. Luo, A. Kleinfehn, M. L. Becker, D. Dean, *Biomacromolecules* **2017**, *18*, 1419; c) D. Dean, W. Jonathan, A. Siblani, M. O. Wang, K. Kim, A. G. Mikos, J. P. Fisher, *Virtual Phys. Prototyping* **2012**, *7*, 13.
- [15] M. Dadsetan, T. Guda, M. B. Runge, D. Mijares, R. Z. LeGeros, J. P. LeGeros, D. T. Silliman, L. Lu, J. C. Wenke, P. R. Brown Baer, M. J. Yaszemski, *Acta Biomater.* **2015**, *18*, 9.
- [16] R. Mishra, R. S. Sefcik, T. J. Bishop, S. M. Montelone, N. Crouser, J. F. Welter, A. I. Caplan, D. Dean, *Tissue Eng., Part C* **2016**, *22*, 904.
- [17] S. Wang, D. H. Kempen, N. K. Simha, J. L. Lewis, A. J. Windebank, M. J. Yaszemski, L. Lu, *Biomacromolecules* **2008**, *9*, 1229.
- [18] X. Li, S. Liu, Y. Zhao, J. Li, W. Ding, S. Han, B. Chen, Z. Xiao, J. Dai, *Adv. Funct. Mater.* **2016**, *26*, 5835.
- [19] Q. Han, W. Jin, Z. Xiao, H. Ni, J. Wang, J. Kong, J. Wu, W. Liang, L. Chen, Y. Zhao, B. Chen, J. Dai, *Biomaterials* **2010**, *31*, 9212.
- [20] X. Li, Z. Xiao, J. Han, L. Chen, H. Xiao, F. Ma, X. Hou, X. Li, J. Sun, W. Ding, Y. Zhao, B. Chen, J. Dai, *Biomaterials* **2013**, *34*, 5107.
- [21] a) S. Han, B. Wang, W. Jin, Z. Xiao, X. Li, W. Ding, M. Kapur, B. Chen, B. Yuan, T. Zhu, H. Wang, J. Wang, Q. Dong, W. Liang, J. Dai, *Biomaterials* **2015**, *41*, 89; b) Z. Xiao, F. Tang, J. Tang, H. Yang, Y. Zhao, B. Chen, S. Han, N. Wang, X. Li, S. Cheng, G. Han, C. Zhao, X. Yang, Y. Chen, Q. Shi, S. Hou, S. Zhang, J. Dai, *Sci. China: Life Sci.* **2016**, *59*, 647; c) Y. Zhao, F. Tang, Z. Xiao, G. Han, N. Wang, N. Yin, B. Chen, X. Jiang, C. Yun, W. Han, C. Zhao, S. Cheng, S. Zhang, J. Dai, *Cell Transplant.* **2017**, *26*, 891.
- [22] a) P. Lu, Y. Wang, L. Graham, K. McHale, M. Gao, D. Wu, J. Brock, A. Blesch, E. S. Rosenzweig, L. A. Havton, B. Zheng, J. M. Conner, M. Marsala, M. H. Tuszynski, *Cell* **2012**, *150*, 1264; b) K. Kadoya, P. Lu, K. Nguyen, C. Lee-Kubli, H. Kumamaru, L. Yao, J. Knackert, G. Poplawski, J. N. Dulin, H. Strobl, Y. Takashima, J. Biane, J. Conner, S. C. Zhang, M. H. Tuszynski, *Nat. Med.* **2016**, *22*, 479.
- [23] a) S. J. Taylor, S. E. Sakiyama-Elbert, *J. Controlled Release* **2006**, *116*, 204; b) N. K. Mohtaram, A. Montgomery, S. M. Willerth, *Biomed. Mater.* **2013**, *8*, 022001.
- [24] J. Fan, Z. Xiao, H. Zhang, B. Chen, G. Tang, X. Hou, W. Ding, B. Wang, P. Zhang, J. Dai, R. Xu, *J. Neurotrauma* **2010**, *27*, 1671.
- [25] X. Li, J. Han, Y. Zhao, W. Ding, J. Wei, S. Han, X. Shang, B. Wang, B. Chen, Z. Xiao, J. Dai, *ACS Appl. Mater. Interfaces* **2015**, *7*, 13960.
- [26] a) F. Brandi, F. Anjum, L. Ceseracciu, A. C. Barone, A. Athanassiou, *J. Micromech. Microeng.* **2011**, *21*, 054007; b) S. Beke, F. Anjum, H. Tsushima, L. Ceseracciu, E. Chierigatti, A. Diaspro, A. Athanassiou, F. Brandi, *J. R. Soc., Interface* **2012**, *9*, 3017; c) S. Beke, F. Anjum, L. Ceseracciu, I. Romano, A. Athanassiou, A. Diaspro, F. Brandi, *Laser Phys.* **2013**, *23*, 035602.
- [27] S. Beke, B. Farkas, I. Romano, F. Brandi, *Opt. Mater. Express* **2014**, *4*, 2032.
- [28] J. Silver, J. H. Miller, *Nat. Rev. Neurosci.* **2004**, *5*, 146.
- [29] a) C. Soderblom, X. Luo, E. Blumenthal, E. Bray, K. Lyapichev, J. Ramos, V. Krishnan, C. Lai-Hsu, K. K. Park, P. Tsoufias, J. K. Lee, *J. Neurosci.* **2013**, *33*, 13882; b) A. E. Haggerty, M. M. Marlow, M. Oudega, *Neurosci. Lett.* **2017**, *652*, 50.

- [30] H. Kawano, J. Kimura-Kuroda, Y. Komuta, N. Yoshioka, H. P. Li, K. Kawamura, Y. Li, G. Raisman, *Cell Tissue Res.* **2012**, 349, 169.
- [31] D. M. Basso, M. S. Beattie, J. C. Bresnahan, *Exp. Neurol.* **1996**, 139, 244.
- [32] P. Assinck, G. J. Duncan, B. J. Hilton, J. R. Plemel, W. Tetzlaff, *Nat. Neurosci.* **2017**, 20, 637.
- [33] J. R. Siebert, A. M. Eade, D. J. Osterhout, *BioMed Res. Int.* **2015**, 2015, 752572.
- [34] a) B. Xu, Y. Zhao, Z. Xiao, B. Wang, H. Liang, X. Li, Y. Fang, S. Han, X. Li, C. Fan, J. Dai, *Adv. Healthcare Mater.* **2017**, 6; b) S. M. Amr, A. Gouda, W. T. Koptan, A. A. Galal, D. S. Abdel-Fattah, L. A. Rashed, H. M. Atta, M. T. Abdel-Aziz, *J. Spinal Cord Med.* **2014**, 37, 54.
- [35] M. Gao, P. Lu, B. Bednark, D. Lynam, J. M. Conner, J. Sakamoto, M. H. Tuszynski, *Biomaterials* **2013**, 34, 1529.
- [36] C. J. Pateman, A. J. Harding, A. Glen, C. S. Taylor, C. R. Christmas, P. P. Robinson, S. Rimmer, F. M. Boissonade, F. Claeysens, J. W. Haycock, *Biomaterials* **2015**, 49, 77.
- [37] P. Ferraro, S. Scaglione, R. Barenghi, S. Beke, L. Ceseracciu, I. Romano, F. Sbrana, P. Stagnaro, F. Brandi, M. Vassalli, M. Ritsch-Marte, S. Grilli, D. Stifter, *Proc. SPIE* **2013**, 8792, 87920H.
- [38] a) B. Chen, H. Lin, J. Wang, Y. Zhao, B. Wang, W. Zhao, W. Sun, J. Dai, *Biomaterials* **2007**, 28, 1027; b) W. Zhao, B. Chen, X. Li, H. Lin, W. Sun, Y. Zhao, B. Wang, Y. Zhao, Q. Han, J. Dai, *J. Biomed. Mater. Res., Part A* **2007**, 82, 630; c) Q. Shi, W. Gao, X. Han, X. Zhu, J. Sun, F. Xie, X. Hou, H. Yang, J. Dai, L. Chen, *Sci. China: Life Sci.* **2014**, 57, 232.
- [39] H. Lin, B. Chen, W. Sun, W. Zhao, Y. Zhao, J. Dai, *Biomaterials* **2006**, 27, 5708.
- [40] W. Liang, Q. Han, W. Jin, Z. Xiao, J. Huang, H. Ni, B. Chen, J. Kong, J. Wu, J. Dai, *Biomaterials* **2010**, 31, 8634.
- [41] a) L. K. Hamilton, M. K. Truong, M. R. Bednarczyk, A. Aumont, K. J. Fernandes, *Neuroscience* **2009**, 164, 1044; b) S. Lacroix, L. K. Hamilton, A. Vaugeois, S. Beaudoin, C. Breault-Dugas, I. Pineau, S. A. Levesque, C. A. Gregoire, K. J. Fernandes, *PLoS One* **2014**, 9, e85916.
- [42] a) Y. Qin, W. Zhang, P. Yang, *J. Neurosci. Res.* **2015**, 93, 391; b) X. Li, Y. Zhao, S. Cheng, S. Han, M. Shu, B. Chen, X. Chen, F. Tang, N. Wang, Y. Tu, B. Wang, Z. Xiao, S. Zhang, J. Dai, *Biomaterials* **2017**, 137, 73.
- [43] Z. Xiao, B. Chen, J. Dai, *J. Spine* **2016**, 57, 005.
- [44] P. X. Lan, J. W. Lee, Y. J. Seol, D. W. Cho, *J. Mater. Sci.: Mater. Med.* **2009**, 20, 271.
- [45] B. Farkas, S. Dante, F. Brandi, *Nanotechnology* **2016**, 28, 034001.
- [46] N. Wang, Z. Xiao, Y. Zhao, B. Wang, X. Li, J. Li, J. Dai, *J. Tissue Eng. Regener. Med.* **2018**, 12, e1154.

Wavelength dependence of laser plasma interaction related to shock ignition approach

Research Article

Cite this article: Pisarczyk T *et al.* (2018). Wavelength dependence of laser plasma interaction related to shock ignition approach. *Laser and Particle Beams* 1–22. <https://doi.org/10.1017/S0263034618000447>

Received: 1 October 2018

Revised: 11 October 2018

Accepted: 13 October 2018

Key words:

Absorption mechanisms; fast electrons; femtosecond interferometry; inertial fusion; resonant absorption; shock ignition; shockwave

Author for correspondence:

T. Pisarczyk, Institute of Plasma Physics and Laser Microfusion, 01-497 Warsaw, Poland, E-mail: tadeusz.pisarczyk@ifpilm.pl

T. Pisarczyk¹, S.Yu. Gus'kov^{2,3}, R. Dudzak^{4,5}, O. Renner^{4,5}, D. Batani^{3,6}, T. Chodukowski¹, Z. Rusiniak¹, J. Dostal^{5,4}, N.N. Demchenko², M. Rosinski¹, P. Parys¹, M. Smid⁴, Ph. Korneev^{2,3}, E. Krousky^{4,5}, S. Borodziuk¹, J. Badziak¹, L. Antonelli⁸, L. Gizzi⁷, G. Cristoforetti⁷, P. Koester⁷, Y. Maheut⁶, L. Volpe⁷, F. Baffigi⁷, T. Levato⁷, J. Skala⁵, A. Zaras-Szydłowska¹, J. Trela⁷, D. Mancelli⁶, J. Ullschmied⁴, M. Pfeifer^{4,5}, L. Juha^{4,5}, M. Krus^{4,5}, J. Hrebicek^{4,5}, T. Medrik^{4,5}, K. Jungwirth⁴, M. Krupka⁵ and P. Pisarczyk⁹

¹Institute of Plasma Physics and Laser Microfusion, 01-497 Warsaw, Poland; ²P. N. Lebedev Physical Institute of RAS, 119991 Moscow, Russian Federation; ³National Research Nuclear University MEPhI, 115409 Moscow, Russian Federation; ⁴Institute of Physics, Czech Academy of Sciences, 182 21 Prague, Czech Republic; ⁵Institute of Plasma Physics, Czech Academy of Sciences, 182 00 Prague, Czech Republic; ⁶Universite Bordeaux, CNRS, CEA, CELIA, Talence, France; ⁷Universita di Roma La Sapienza, Rome, Italy; ⁸York Plasma Institute, University of York, York, UK and ⁹Warsaw University of Technology, ICS, 00-661 Warsaw, Poland

Abstract

This paper provides a summary of recent research connected with the shock ignition (SI) concept of the inertial confinement fusion which was carried out at PALS. In the experiments, Cu planar targets coated with a thin CH layer were used. Two-beam irradiation experiment was applied to investigate the effect of preliminary produced plasma to shock-wave generation. The 1ω or 3ω main beam with a high intensity $>10^{15}$ W/cm² generates shock wave, while the other 1ω beam with the intensity below 10^{14} W/cm² creates CH pre-plasma simulating the pre-compressed plasma related to SI. Influence of laser wavelength on absorbed energy transfer to shock wave was studied by means of femtosecond interferometry and measuring the crater volume. To characterize the hot electron and ion emission, two-dimensional (2D) K_{α} -imaging of Cu plasma and grid collector measurements were used. In single 1ω beam experiments energy transport by fast electrons produced by resonant absorption made a significant contribution to shock-wave pressure. However, two-beam experiments with 1ω main beam show that the pre-plasma is strongly degrading the scalelength which leads to decreasing the fast electron energy contribution to shock pressure. In both the single 3ω beam experiments and the two-beam experiments with the 3ω main beam, do not show any clear influence of fast electron transport on shock-wave pressure. The non-monotonic behavior of the scalelength at changing the laser beam focal radius in both presence and absence of pre-plasma reflects the competition of plasma motion and electron heat conduction under the conditions of one-dimensional and 2D plasma expansion at large and small focal radii, respectively.

Introduction

Iodine laser PALS provides excellent opportunities for a comparative study of the interaction of laser radiation with different wavelengths. These possibilities were used in experiments (Gus'kov *et al.*, 2004, 2006) to study the effect of laser-accelerated fast electrons on the efficiency of energy transfer to a shock wave in a flat target. These investigations using Cu massive planar targets irradiated by the laser beam with different wavelengths (first and third harmonics of the iodine laser) and different intensities were carried out. As diagnostics the three-frame interferometry, in combination with the diagnostics characterizing electrons, ion emission, and the crater formation efficiency, was applied. These experiments as the very first ones have shown increasing contribution of fast electrons to energy transfer to shock wave with growing intensity and wavelength of laser radiation. To determine the role of the fast electrons in the laser energy transport to shock wave next experiments were performed with the PALS iodine laser, delivering a 300 ps duration pulse at intensities of 1–50 PW/cm² using the first (1315 nm) and third (438 nm) harmonics radiation (Kalinowska *et al.*, 2012; Gus'kov *et al.*, 2014). In these experiments massive targets of Al and Cu have been irradiated at various focal spot radii of the laser beam, R_L , to identify the mechanisms of laser absorption and to determine their influence on the absorbed energy transfer to the target. The mass of the ablated solid material as well as the fraction of the laser energy deposited in the plasma have been

determined by using a three-frame interferometer and by measuring the volume of the crater created on the solid surface. In order to identify the absorption mechanisms, the N_e/V_{cr} parameter has been introduced for the first time. This parameter shows how many electrons participate in creation of the crater volume unit (1 cm^3). These experiments have shown a strong influence of the wavelength and the intensity of the laser beam on the efficiency of the laser energy transfer to a massive target, independent of its material. Two-dimensional (2D) numerical simulations, including fast electron transport (Gus'kov *et al.*, 2004) as well as theoretical analysis based on an analytical model (Pisarczyk *et al.*, 2015), confirmed the experimental results and demonstrated conclusively that in the case of 1ω beam, intensities of $10\text{--}50\text{ PW/cm}^2$, the dominant ablation mechanism is the heating by fast electrons generated at the resonant absorption. For the maximum laser energy of 580 J and intensity of 50 PW/cm^2 , the ablative pressure reaches about 180 Mbar in spite of 2D expansion of the target corona. However, for 3ω , the ablation pressure originates from thermal electron conductivity heating, and its value of about 50 Mbar is several times lower in comparison with the 1ω case. To confirm these possibilities in the generation of the high-ablative pressure in the case of the first harmonic as well as, to identify other absorption mechanisms of the laser irradiation in the case of the third harmonic which are responsible for the laser energy transport with participation of fast electrons, the further experiments at PALS for the conditions corresponding to the shock ignition (SI) conception were carried out (Koester *et al.*, 2013; Batani *et al.*, 2014; Pisarczyk *et al.*, 2014).

In these experiments, the SI conditions were simulated by two-beam irradiation of two-layer targets, consisting of massive Cu and a $25\text{ }\mu\text{m}$ thick layer of light plastic (CH) material. The first 1ω beam with energy of $40\text{--}70\text{ J}$ produced pre-plasma imitating the corona of the pre-compressed inertial confinement fusion (ICF) target that is a spherical target designed for creation of inertially confined thermonuclear plasma under action of pulsed energy driver. The spike-driven shock wave was generated by the main pulse (1ω or 3ω) with the intensity of radiation in the range of $1\text{--}50\text{ PW/cm}^2$. In the paper of Pisarczyk *et al.* (2014), the influence of pre-plasma on parameters of the shock wave was determined from the crater volume measurements and from the electron density distribution measured by three-frame interferometry. The ignited shock wave was generated by the main pulse with energy of 200 J (either at 1ω or 3ω). The 1ω pulse with the energy of 50 J produced pre-plasma, imitating the corona of the pre-compressed ICF target. Similarly in the paper of Pisarczyk *et al.* (2015), experiments with a single 1ω beam confirmed the enhanced efficiency of energy transfer to shock wave associated with fast electrons transporting energy to the dense plasma region. However, two-beam experiments have shown a significantly decreasing efficiency of the 1ω radiation energy transmission to the solid part of the target in comparison with the case without pre-plasma. The presence of pre-plasma creates poor conditions for resonant absorption and, therefore, for the laser energy conversion to fast electrons. The significantly smaller effectiveness of the energy transfer to the shock wave is clearly seen on both the crater volumes and the density gradient data. However, these experiments have not provided data indicating alteration of the fast electron generation due to resonant absorption by any other mechanism connected with parametric plasma instabilities in the pre-plasma.

Investigations of the fast electron generation connected with parametric plasma instabilities and their influence on the generation of a strong shock wave are presented in Koester *et al.* (2013).

Similarly in the previous PALS experiments (Pisarczyk *et al.*, 2014) pre-plasma was created by the 1ω auxiliary beam with an intensity about 10^{13} W/cm^2 which was achieved by enlarging the focal spot diameter to $900\text{ }\mu\text{m}$. A strong shock was generated by the 3ω laser beam at intensities in the range of $10^{15}\text{--}10^{16}\text{ W/cm}^2$ at various delays with respect to the first beam. As main diagnostics X-ray spectroscopy and calorimetry of the backscattered radiation were applied. The fast electron production is characterized through 2D imaging of the K_α emission. Information on the shock pressure is obtained using shock breakout chronometry and measurements of the craters produced by the shock in a massive target. The preliminary results show a low level of backscattered radiation ($<10\%$) mainly due to simulated Brillouin scattering. The conversion efficiency into kinetic energy of suprathermal electrons was inferred to be well below 1% and the experimental results indicate that the suprathermal electrons are predominantly generated through the simulated Raman scattering process. The mean energy of the suprathermal electron population was estimated to be $\approx 50\text{ keV}$. The shock pressure inferred from our measurements is in the range of $60\text{--}100\text{ Mbar}$ for the highest laser intensities. To know better development of the parametric plasma instabilities additional two-beam experiments were carried out at PALS (Batani *et al.*, 2014). In these experiments different kinds of targets were used. To estimate the average energy of fast electrons, Cu massive targets with plastic layers of different thicknesses in front of the Cu layer were used. To allow X-ray spectroscopic measurements, the parylene ($\text{C}_8\text{H}_7\text{Cl}$) plastic layer with Cl was applied. To measure the velocity of shock wave by shock chronometry, two-layer targets with $25\text{ }\mu\text{m}$ plastic (parylene-C) on the laser side, and $25\text{ }\mu\text{m}$ Al (with an additional $10\text{ }\mu\text{m}$ Al step) on the rear, were used. The targets were illuminated with the 1ω auxiliary beam delivering 30 J , and the 3ω main beam delivering up to 250 J , with a delay of up to 1.2 ns with respect to the auxiliary beam. As in previous experiments, the auxiliary beam was focused with an intensity of 10^{13} W/cm^2 in an extended focal spot diameter to create an approximately one-dimensional (1D) plasma. To produce uniform irradiation the beam was smoothed with a random phase plate. These investigations confirmed that using the third harmonic of the PALS laser as a main beam, one can generate a strong shock with the ablative pressure reaching 90 Mbar . It should be noted that it is indeed the highest pressure measured so far in this kind of experiment, showing a clear progress in approaching a SI relevant regime. Higher pressures (up to 180 Mbar) are inferred when a much larger focal spot is used.

In hitherto studies performed at PALS (described above) connected with the SI concept, the three-frame interferometry was applied. This diagnostic system worked with the second or third harmonic of the iodine laser featuring approximately 350 ps pulse, identical by its duration to the main plasma-generating laser pulse. With such relation between the diagnostic and the main laser pulse duration, this system could not allow for detailed-enough plasma probing taking into account the expansion velocities of the order of 10^8 cm/s corresponding to the fast component of the ablation plasma generated in the initial stage of the plasma expansion. Under such conditions blurring of interference fringes close to the critical density region, caused by plasma movement and/or oscillations, did not allow for measurement of the maximal reachable concentration given by the wavelength of the diagnostic laser.

From the point of view of the "shock ignition" research, particularly interesting is the initial phase of the expansion related to the interaction of the laser pulse with plasma generated by

the rising parts of the laser pulse itself. In this phase the above-mentioned processes of anomalous absorption appear which are responsible for the generation of fast electrons, and there are electric and magnetic fields created. They result both from the motion of electrons and the effects of various phenomena and processes occurring in the non-homogeneous plasma, such as spontaneous magnetic fields associated with the effect of crossed gradients of temperature and electron concentration. These fields can significantly modify the plasma parameters and fast transport of electrons from their source to the ablation zone (surface) and influence the formation of the shock-wave ablation pressure.

It should be emphasized that the studies of the early phase of the expansion of the ablation plasma (including the interaction of the laser pulse with the plasma produced by it) have not been the subject of detailed research so far, because it requires the use of very high resolution time diagnostics. A multi-frame interferometric system irradiated by the use of a Ti:Sa femtosecond laser with a pulse duration of about 40 fs turned out to be particularly useful diagnostics in these studies. Due to the application of the femtosecond interferometry in the research on SI carried out on PALS, for the first time information about the time changes of the electron density distributions in ablative plasma during the laser pulse interaction with plasma created by it was obtained. The space-time electron density distributions allowed determining such parameters of the ablation plasma as: the axial density profile, the scalelength, the maximal density gradient, the linear density, and the total electron number in different expansion times in the ablative plasma. Information obtained from femtosecond interferometry in combination with parameters of the electron and ion emission obtained by means of the spectroscopic measurements in the X-ray range and the grid collectors, they proved to be extremely useful from the point of view of identification of absorption mechanisms of the laser irradiation by the ablative plasma, and which are responsible for the energy transport to the shock wave, in particular of the energy carried by fast electrons.

This paper is summary of the last investigations performed in experiments at PALS related to the SI concept of the ICF (Pisarczyk *et al.*, 2015, 2016) in which comprehensive measurements involving the multi-frame femtosecond interferometry as the main diagnostic were carried out.

This paper is structured as follows. In Section “Experimental setup”, the experimental setup is presented which includes description and operation of the three-frame interferometer as well as the way of synchronization of the Ti:Sa diagnostic laser with the PALS iodine laser. Results of the interferometric and the crater volume measurements with use of both 1ω and 3ω of the PALS laser to create the igniting shockwave are presented in Section “Ablation and energy transfer to shock wave”. The N/V_{cr} parameter (defined in Gus'kov *et al.*, 2014; Pisarczyk *et al.*, 2014) was determined to identify of the possible absorption mechanisms of the laser radiation for different wavelengths that generate a shockwave and to assess their influence on the energy transport to the shock wave under conditions without pre-plasma as well as with pre-plasma simulating the SI concept. In Section “Fast electron emission”, measurements characterizing the electron and ion emission are presented. Obtained quantitative information about the population and the energy of the fast electrons from the 2D imaging of the K_α emission, clearly demonstrate the differences between 1ω and 3ω which were used for creation of a shockwave, both without pre-plasma and with pre-plasma presence. The influence of pre-plasma for various irradiation conditions is shown on the angular distributions of ions obtained

with the use of the grid collectors. Section “Ion emission measurements” concerns the results of 2D numerical simulations (2DSS). Summary of the obtained results is presented in Section “2D numerical modeling of laser-plasma interaction in different wavelength experiments”.

Experimental setup

The experiments were performed using the double planar targets, Figure 1a, consisting of a massive Cu plate coated with a thin CH layer, which was irradiated by the 1ω or 3ω PALS laser beam at the energy of 250 J.

To imitate the SI conditions, the lower-intensity auxiliary 1ω beam with the energy of 40 J and angle of incidence $\alpha = 25^\circ$ created CH-pre-plasma that was irradiated by the main beam with a delay of 1.2 ns, thus generating the shock wave in the massive part of the target. Both beams were equipped with phase plates to generate homogeneous irradiation of the target surface. As the fundamental option of measurements, two-beam experiments for different irradiation conditions of the targets depending on the focal spot radius were realized. The investigations were carried out at different intensities of the main 1ω and 3ω beams controlled by varying the focal spot radius in a range of 50–200 μm and keeping the laser energy fixed. To better characterize of the pre-plasma influence on the laser energy transport to the massive part of the target and the fast electron emission parameters, the results of two-beam experiments have been compared with the single-beam experiments (without pre-plasma) for the same irradiation condition as in the case of two-beam experiments when the pre-plasma was created.

The multiframe interferometric investigations of the ablative plasma with the femtosecond resolution and the measurements of the crater creation efficiency were the main source of information about absorption mechanisms responsible for the laser energy transport process to the shock wave generated in the solid target.

The optical scheme of the three-frame interferometric system which was used in measurements is presented in Figure 2. The optical delay line is an integral part of this system and it enables space-time separation of the diagnostic beam into three independent channels.

Transmission of mirrors in the delay line is selected in such a way to ensure the same intensity for each channel of the interferometer. The construction of the delay line enables to change the time distance between frames in the range of 0.3–3 ns. Moreover, the diagnostic beam that irradiates this line is synchronized in such a manner that the first frame is recorded in a required moment of the plasma expansion (related to the maximum intensity of the laser beam which creates the plasma). Each interferometric channel is equipped with its own independent interferometer of the folding-wave type (Kasperczuk *et al.*, 1993; Borodziuk *et al.*, 2005) and with a charge-coupled device camera (RM-4200GE) enabling registration of interferograms with the high-spatial resolution (2048 \times 2048 pixels with a size of 7.3 μm) and the 12-bit dynamics. Cameras are connected to a computer through a Gigabit Ethernet interface and controlled by a custom-build application PALS Vision GigEV, which is capable of pre-treatment of images (modification of the Fourier spectra, correction of histograms, correction of colors, calibration, etc.). In the case of high-quality interferograms, electron density distribution may be obtained after the laser shot with on-the-fly mode. For more detailed analysis of interferograms, specialized software (created at IPPLM) is used.

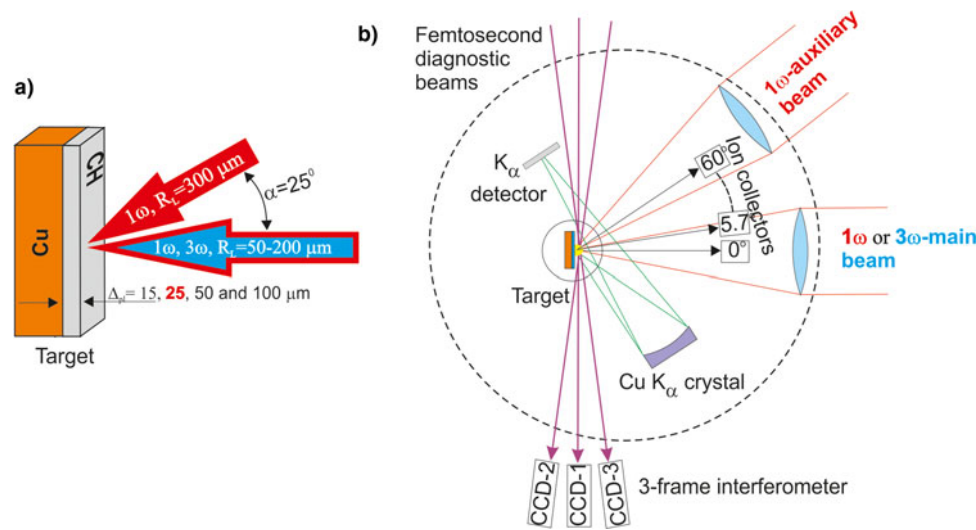


Fig. 1. Experimental set-up: (a) the construction and the geometry of irradiation of the two-layer target and (b) the location of the diagnostics on the PALS experiment.

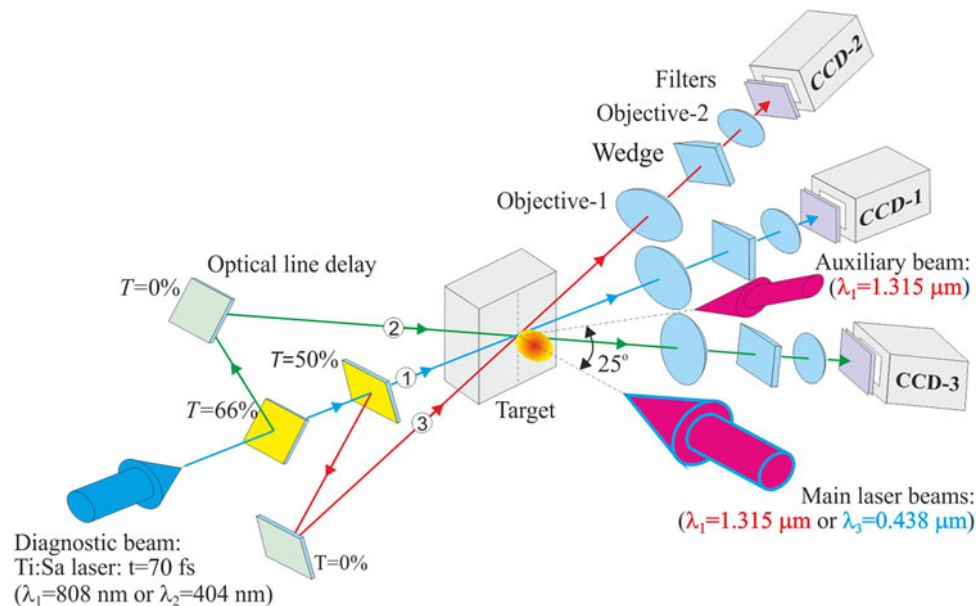


Fig. 2. Three-frame interferometric system.

To implement this three-frame interferometric system for the plasma investigation in the femtosecond regime, the method of the electronic synchronization between the Ti:Sa and the PALS laser described in Dostal *et al.* (2017) has been developed. This method enables plasma probing in selected times of plasma expansion (related to the maximum intensity of the main pulse) with the accuracy of ± 100 ps.

To characterize the fast electron and ion emission, measurements were carried out using the following diagnostic sets:

- 2D imaging of the emission of Cu K_{α} line using spectrograph with a spherical crystal type (211) to determine the distribution of fast electron population and their energy; for this purpose experiments with use of two-layer targets, covered by the polyethylene layers of different thickness: $\Delta_{p1} = 15, 25, 50,$ and $100 \mu\text{m}$ were carried out and

- the grid collectors to measure the angular distributions of the ion emission, as a source of information about the ablative plasma electron temperature, the average energy of fast electrons and the geometry of the ablative plasma expansion.

The location of the all diagnostics used in the PALS experiment is shown in Figure 1b.

Ablation and energy transfer to shock wave

Interferometric measurements. 1ω -experiments

The main aim of the femtosecond interferometry was obtaining interferograms with a high-time resolution, to observe temporal changes of the electron density distributions during the laser pulse interaction with a target. These electron density distributions are necessary to obtain information about the changes of

the maximal density gradient and the density scalelength which are very important from the point of view of identification of the absorption mechanism, because they are responsible for the laser energy transport to the shock wave generated in the massive part of the two-layer target.

Therefore, to know the electron density of the ablative plasma in the period which included the main pulse interaction with a target, three-frames were recorded successively with the time distance of 400 ps and the first frame was recorded before the main laser pulse in the range of -400 to 200 ps relative to the maximum intensity of the main laser beam. Tens of interferograms were obtained for different conditions of irradiation of two-layer targets. Only interferograms obtained under the same conditions were analyzed.

On the basis of electron density distributions, the maximum density gradient and the density scalelength have been calculated. To obtain the information about these parameters, an exponential fitting of the experimental axial density profiles has been applied: $n_e(z) = n_0 e^{-z/L}$ (Pisarczyk *et al.*, 2014). The parameters of this function determine the maximum electron density gradient in the opacity zone: $(dn_e/dz)_{z=0} = -n_0/L$, where L is the density scalelength and n_0 is the maximum electron density. The time sequences of interferograms obtained for different expansion times during the interaction of the main laser pulse with the double target and at different irradiation conditions by changing the dimensions of the focal spot radius on the target were analyzed. The comparison of the electron density distributions of the ablative plasma and axial density profiles and the scalelength corresponding to these distributions obtained in the absence of the pre-plasma at different focal spot radii and for different times of the plasma stream expansion is presented in Figure 3. The time delays of each individual frame relate to the maximal intensity of the main pulse. As it results from Figure 3, the electron density distributions demonstrate the quasi-spherical character of the expansion for the small focal spot radius with the characteristic minimum of the density on the axis. When increasing the focal spot radius of the laser beam, the plasma stream expansion becomes more axial. It is seen from both the time sequence of the density distributions and the axial profiles related to larger focal spot radii: $R_L = 150$ and $200 \mu\text{m}$. This change in the character of the ablative plasma expansion (from spherical to axial) by the relevant scalelengths is demonstrated.

The comparison of the electron density distributions of the ablative plasma and axial density profiles as well as the scalelength corresponding to these distributions obtained in the pre-plasma presence at different focal spot radii and for different times of the plasma stream expansion is presented in Figure 4.

The electron density distributions indicate that the light plasma with a higher pressure, being generated from the thin plastic layer by an auxiliary beam, limits the radial expansion of the central plasma created by the main laser beam. The radial limitation favors the axial character of the plasma expansion particularly in the case of larger focal spot radii. The radial limitation results in the growth of the electron density on the axis and in the increase of the scalelength. This is clearly demonstrated by the axial density profiles and the scalelength values in Figure 4.

In contrast, when the pre-plasma is not created, the density scalelength of the ablative plasma is considerably greater. A detailed comparison of the ablative plasma expansion in the case of absence and presence of the pre-plasma is presented in Figure 5. This figure shows the maximal density gradient, the scalelength, and the maximal density for three characteristic times of

the expansion: 0, 300, and 600 ps related to the maximum intensity of the main laser beam. Single values corresponding to the chosen expansion times have been determined by approximating the experimental data.

Figure 5a shows that in the case of without the pre-plasma, the density gradient increases with the decreasing R_L for the focal spot radii smaller than $150 \mu\text{m}$. The largest growth of the density gradient corresponds to the maximum laser pulse intensity ($t = 0$). The density gradient achieves a value of about $1 \times 10^{22}/\text{cm}^4$ for the minimum focal spot radius ($R_L = 50 \mu\text{m}$) and this gradient corresponds to the minimal density scalelength $L = 160 \mu\text{m}$. It can be explained by the fact that for the time of the ablative plasma expansion $t = 0$, the favorable conditions for high energy fast electron generation due to resonant absorption occur. This effect is responsible for the energy transfer to the shock wave generated in a solid target. As follows from Figure 5a, the density gradient also increases with increasing the focal spot radii above $150 \mu\text{m}$. However, this growth is connected with a transition to predominating 1D expansion of the ablative plasma at large focal spot radii (Gus'kov *et al.*, 2014).

In the case of pre-plasma presence (Fig. 5b), the density gradient falls in the whole range of the focal spot radii and the expansion time includes the maximum intensity of the laser pulse and ensuing 600 ps. The scalelength is increased by approximately two times as compared with the case of with the pre-plasma absence. At the maximum laser intensity $t = 0$ and the minimal focal spot radius $R_L = 50 \mu\text{m}$, the scalelength grows to a level of about $L = 330 \mu\text{m}$. This proves that in the presence of the pre-plasma, the effect of energy transfer by fast electrons becomes smaller. The presence of the extended pre-plasma leads to decreasing density gradients of the plasma created by the action of the main beam.

Crater volume measurements. 1 ω -experiments

The crater volume and the interferometric measurements are very useful combination and they can provide essential information about mechanisms of the laser radiation absorption using the ratio N/V_{cr} , where N is the total electron number in the plasma plume, and V_{cr} is the crater volume in cm^3 . This parameter defines how many numbers of thermal electrons are participating in the creation of a crater volume unit (1cm^3). To obtain information about the N/V_{cr} parameter, the craters and interferograms obtained for the same irradiation conditions of two-layer targets were taken into account. Data about the total electron number obtained from the interferometric measurements (presented in the previous paragraph) in Figure 6 are shown. The time changes of the total number of electrons for different focal spot radii in the case of pre-plasma absence are shown in Figure 6a, while Figure 6b shows the time changes in the case of the presence of pre-plasma. As it results from the presented dependences in figures below, the total number of electrons increases during the laser pulse interaction with target, both in the cases of the absence and presence of the pre-plasma. As expected, in the case of two-beam irradiation (with pre-plasma) the total number of electrons is larger than the single-beam irradiation (without pre-plasma) and it increases with increasing of the focal spot radius.

The examples of photographs of the crater replicas and their shapes in mutually perpendicular cross-sections obtained in the case of the absence and presence of the pre-plasma for the same irradiation conditions as for the interferograms are presented in Figure 7. For measuring the crater volume the method described in the paper of Pisarczyk *et al.* (2014) was applied.

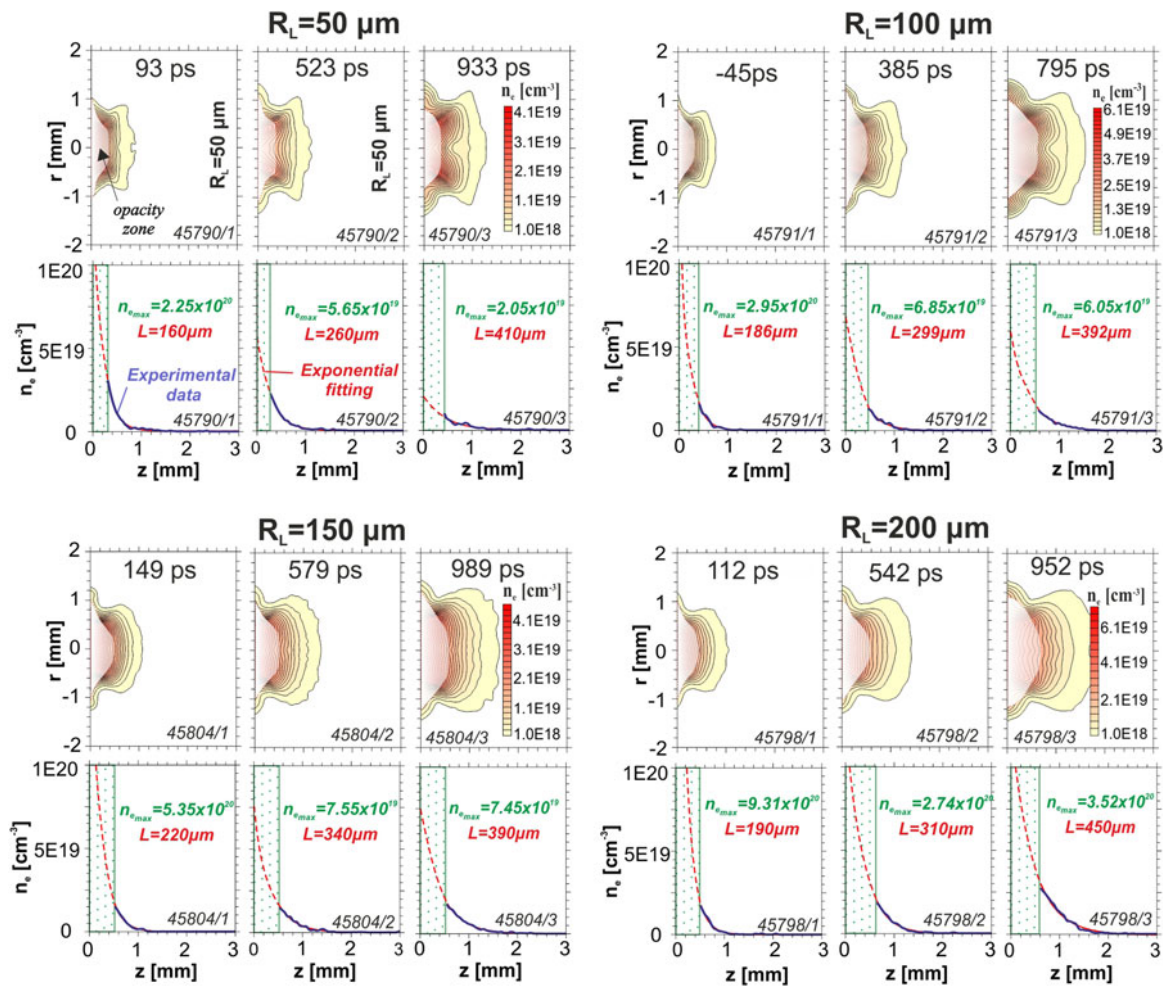


Fig. 3. Electron density distributions illustrating the time evolution of the ablative plasma expansion during the laser pulse interaction with the target at different focal spot radii in the pre-plasma absence.

Considering that the time of the crater formation is longer than the duration of the laser pulse, the N/V_{cr} parameter was evaluated only for the expansion time $t = 600$ ps, that is after the end of the main laser pulse, when both the ablation process and the processes related to absorption of laser radiation have ended. Figure 8 presents a comparison of N/V_{cr} parameter, the crater volume V_{cr} , total number of electrons N , and obtained for the target irradiation without and with the pre-plasma.

As it results from Figure 8, in the case of pre-plasma absence, the crater volumes and the N/V_{cr} parameter demonstrate the increased efficiency of the crater creation with the decreasing focal spot radius in the range of $R_L < 150$ μm . According to our previous papers (Gus'kov *et al.*, 2014; Pisarczyk *et al.*, 2014), this corresponds directly to the energy transfer into the target by fast electrons generated due to resonant absorption. However, the crater creation efficiency also grows in the range of the focal spot radii larger than $R_L = 150$ μm . When the beam radius exceeds this value, the fast electron temperature decreases (with decreasing the laser intensity) and the role of the fast electron energy transfer in the ablation process becomes smaller than the role of thermal conductivity. In this case, the crater volume growth is due to decreasing the transverse expansion of the laser-produced plasma. This is confirmed by interferometric results, which show an increasing density gradient (see Fig. 5a), that is

connected with the axial (1D) expansion of the ablative plasma, which predominates in the case of the 1ω radiation and $R_L > 150$ μm . Therefore, the transverse plasma expansion decreases, the pressure increases and hence, the efficiency of the energy transformation to the shock wave also increases. According to Borodziuk *et al.* (2004a, b) the largest crater in the massive Cu target is created by means of the 1ω laser beam focused on the focal spot radius about 300 μm .

At the pre-plasma presence, Figure 8b, the crater volume decreases to the level about 3×10^{-5} cm^3 , and this value does not depend on the focal spot radius of the main laser beam. A comparison with Fig. 8a indicates that in the presence of pre-plasma, the effect of the fast electron energy transfer on the solid target is suppressed. The experimental data stating the rate of the electron number growth in the presence of pre-plasma (Fig. 8) are approximately by a factor of 1.5 larger in comparison with the case of pre-plasma absence. It can be explained by the fact that in this case the absorption coefficient (according to results of numerical simulation presented below) is two times higher than that in the case of pre-plasma absence. The rate of 8×10^{25} electrons per s can provide the number of electrons equal to approximately 1.2×10^{16} and 3.6×10^{16} . These values are about two times smaller than the data of Fig. 8, which is ascribed to the contribution of the electrons from the pre-plasma.

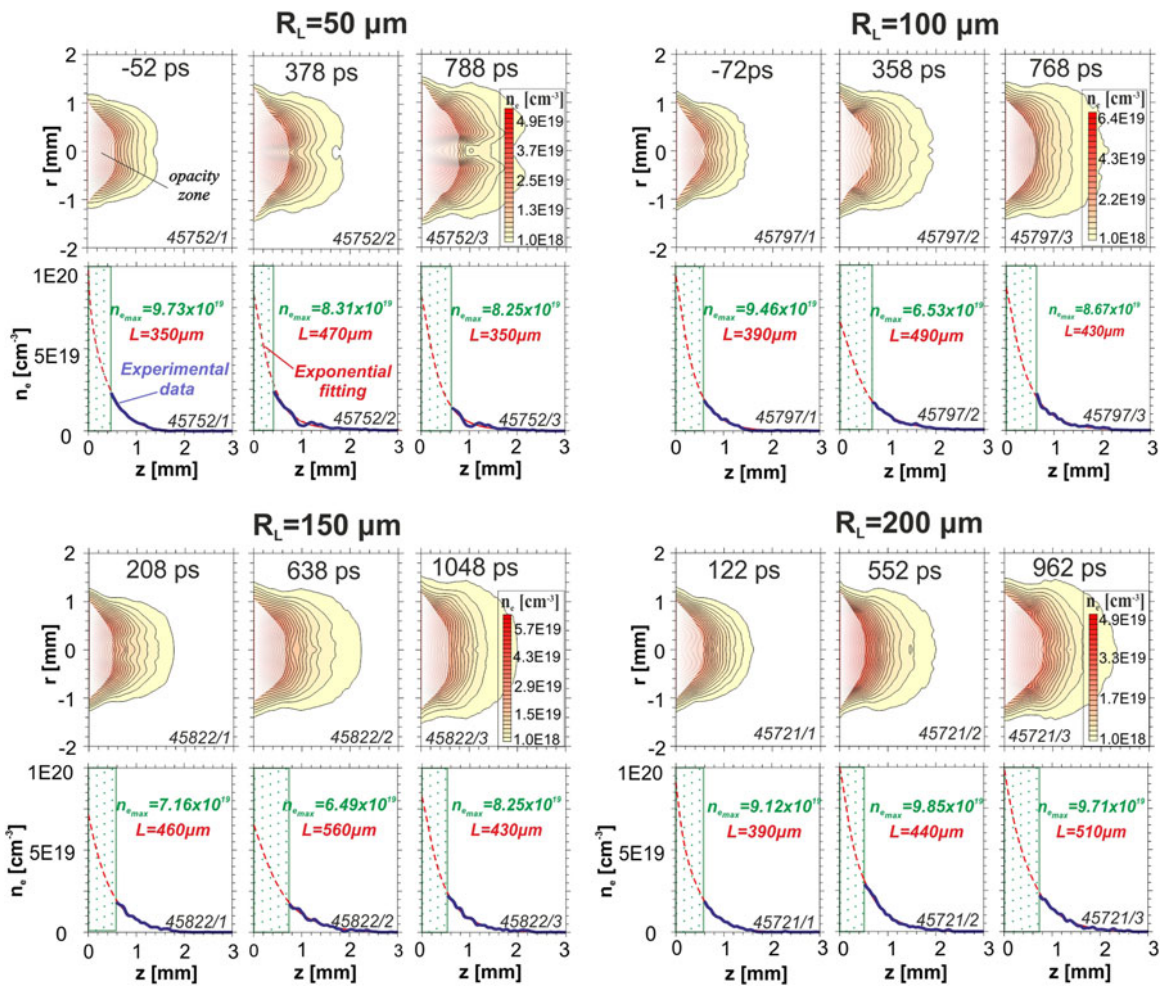


Fig. 4. Electron density distributions illustrating the time evolution of the ablative plasma expansion during the laser pulse interaction with the target at different focal spot radii in the presence pre-plasma.

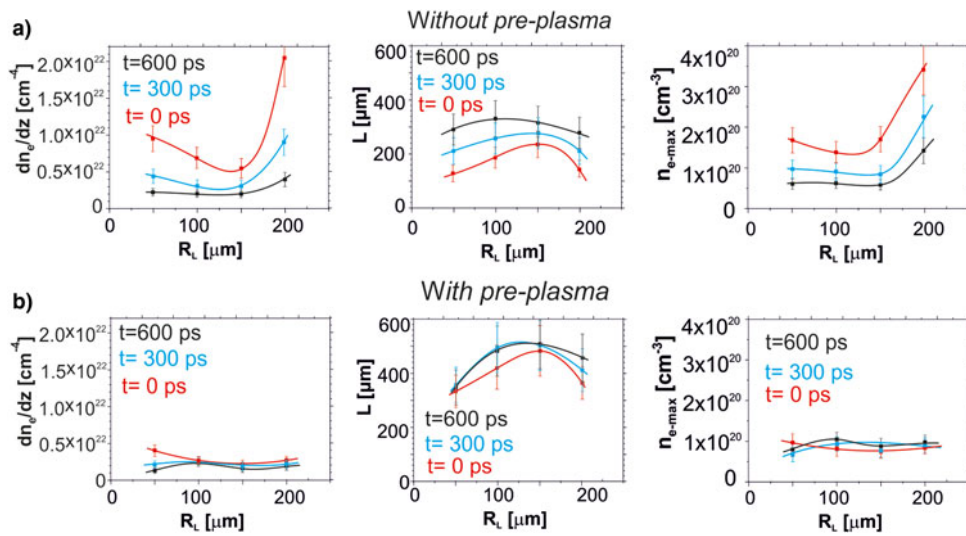


Fig. 5. Comparison of the maximal density gradient, the scalelength, and the maximal density obtained in the cases of absence and presence of the pre-plasma.

To conclude, according to the temporary changes of the gradient determined from interferometric measurements the temporal changes of the N/V_{cr} parameter confirm that electrons produced

in time $t = 0$ provide the largest contribution to the creation of the craters, corresponding to the maximum of the main laser pulse intensity.

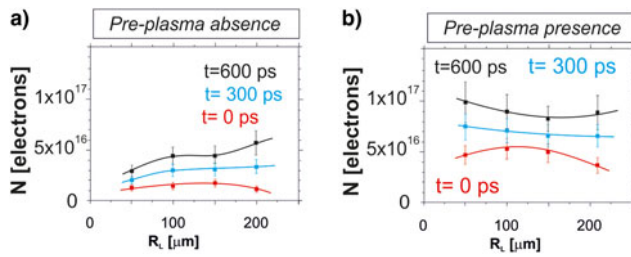


Fig. 6. Comparison of the changes of total number of electrons in the cases of absence (a) and presence of the pre-plasma (b) for three characteristic times of the expansion.

Interferometric measurements. 3ω -experiments

To simulate the SI conditions the third harmonic ($\lambda_3 = 438$ nm) iodine laser beam with the intensity of radiation in the range of $1\text{--}20$ PW/cm² corresponding to changes of parameter $I\lambda_3^2$ of $2 \times 10^{14}\text{--}4 \times 10^{15}$ Wm²/cm². The desired intensity of the main beam has been achieved at a constant laser energy at the level of about 200 J by changing the focal spot radius of the laser beam impinging the target in range of $R_L = 50\text{--}200$ μm . As in the experiments with the first harmonic of the iodine laser, to simulate the SI conditions two-beam irradiation of two-layer targets (Fig. 1) consisting of a planar massive part with Cu, covered by a 25 μm layer of polyethylene was applied. The pre-plasma, which simulates the pre-compressed plasma in a real inertial fusion experiment, was created by means of the first harmonic laser beam with an energy of about 40 J, defocused to the focal spot radius $R_L = 300$ μm . Analogously as in the 1ω -experiment, the main 3ω pulse was delayed by 1.2 ns relative to the pulse creating the pre-plasma. Obtaining information about the temporal changes of the density scalelength (L) and the maximal density gradient (dn_e/dz) on the basis of the space-time electron density distributions was the main aim of investigations using the femto-second interferometry.

The summary comparison of the electron density distributions and the axial density profiles of the ablative plasma obtained in the absence of pre-plasma at different focal spot radii and for different times of the plasma stream expansion is presented in Figure 9. The time delay of each individual frame relates to the maximal intensity of the main pulse. On each individual frame the information about the maximal electron density in near of the target and the scalelength using by the exponential fitting the axial density profiles is given.

As results from the temporal changes of the electron density distributions and the axial density profiles, the axial expansion increases with increasing the focal spot radius and leads to an increase in the electron density on the axis at later times of the laser pulse interaction with a target. It is in contrast to temporal changes of electron density in the case of the 1ω -experiments, where the electron density on the axis decreases with the expansion time due to the spherical expansion. Consequently, a larger electron density on the axis in the vicinity of the target for the 3ω case leads to a decrease of the scalelength due to the greater axial expansion of the ablation plasma. This scalelength is on the level of $L = 200$ μm and it is almost two times smaller compared with the scalelength in the case of the 1ω -experiments.

The comparison of temporal sequences of electron density distributions of the ablative plasma obtained in the presence of pre-plasma at different focal spot radii is presented in Figure 10. As it results from Figure 10, both the equidensity lines of electron

density and the space density profiles demonstrate that the light plasma with a higher pressure, being generated from a thin plastic layer by the auxiliary beam, limits radial expansion of the central plasma created by the main laser beam. The radial limitation favors the axial character of the plasma expansion particularly in the case of larger focal spot radii. These changes in the character of the ablative plasma expansion, caused both by the increasing focal spot radius and the radial expansion limitation by pre-plasma, lead to an increase in the electron density on the axis and to the elongation of the plasma stream at later times of its expansion. However, despite the increase in the electron density on the axis, the strong elongation of the plasma stream causes an increase of the scalelength. As it results from Figure 10, in the case of pre-plasma presence the scalelength is about two times larger than that when the pre-plasma is not created.

The detailed comparison of the ablative plasma expansion in the cases of absence and presence of pre-plasma is presented in Figure 11. This figure shows the maximal density gradient, the scalelength, and the maximal density for three characteristic times of expansion: 0, 300, and 600 ps in relation to the maximum intensity of the main laser beam. Single values corresponding to chosen expansion times have been determined by interpolation of the experimental data.

From Figure 11a it results that in the case of without pre-plasma the highest density gradient values correspond to the maximum laser pulse intensity ($t = 0$). Its maximum value is about $5 \times 10^{22}/\text{cm}^4$ for the focal spot radius R_L equal to 100 μm and it corresponds to the minimal scalelength $L = 100$ μm .

Such value of the scalelength is approximately the same in the whole range of the changes of the focal spot radius. For later times of plasma expansion, the density gradient decreases rapidly, reaching a value five times smaller (at $t = 600$ ps) in comparison with the maximum value, while the scalelength increases to a value about 300 μm at the same expansion time of the ablative plasma.

An increase of the focal spot radius above $R_L = 100$ μm leads to a decrease of the density gradient and to small changes in the scalelength. Further increasing the focal spot radius (above $R_L = 150$ μm) increases the density gradient, reducing the scalelength a little, which is the result of the increasing role of 1D expansion of the ablative plasma for larger focal spot radii (Gus'kov *et al.*, 2014; Pisarczyk *et al.*, 2015).

However, the presence of pre-plasma, Figure 11b, degenerates neither the maximal density gradient nor the scalelength of electron density, unlike the case of the first harmonics main beam generating igniting shock wave (Pisarczyk *et al.*, 2015). As it results from Figure 11b, the strong limitation of the radial expansion of the 3ω ablative plasma by the external light plastic pre-plasma which is created by means of the 1ω auxiliary laser beam, leads to an increase in the electron density on the axis, and, consequently to an increase in the density gradient. The largest density gradient occurs during the intensity peak of the main laser beam ($t = 0$), for the smallest focal spot radius ($R_L = 50$ μm) and its value is about $7 \times 10^{22}/\text{cm}^4$, which is even a bit higher than in the absence of pre-plasma. However, this gradient drops rapidly, both as a function of the expansion time and focal spot radius. It should be noted also that the plasma stream formed in the presence of pre-plasma is characterized by a greater scalelength than in its absence. As it results from Fig. 11b, the smallest density scalelength, $L = 220$ μm , corresponds to the maximum laser pulse intensity ($t = 0$) and minimal focal spot radius. With the increase in the focal spot radius, the scalelength increases

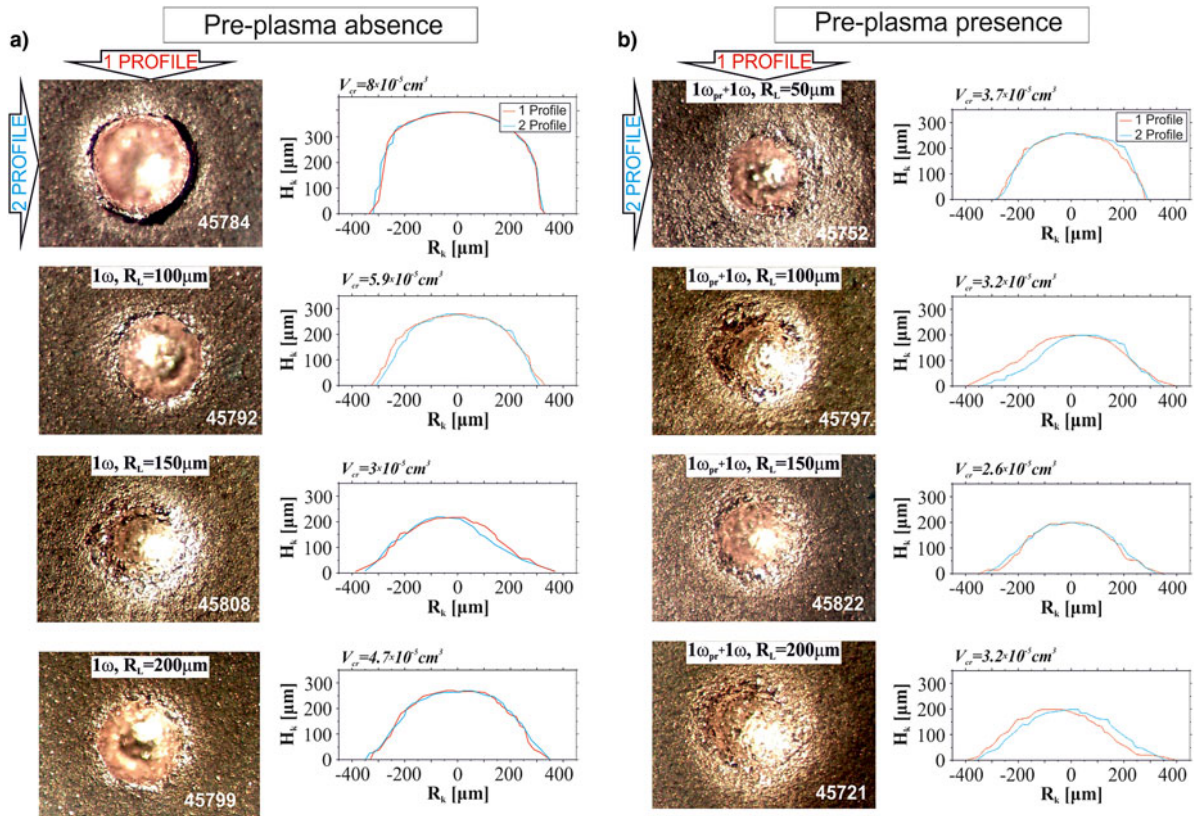


Fig. 7. The craters and their shapes in two cross-sections for different focal spot radii obtained in cases absence (a) and presence (b) of the pre-plasma.

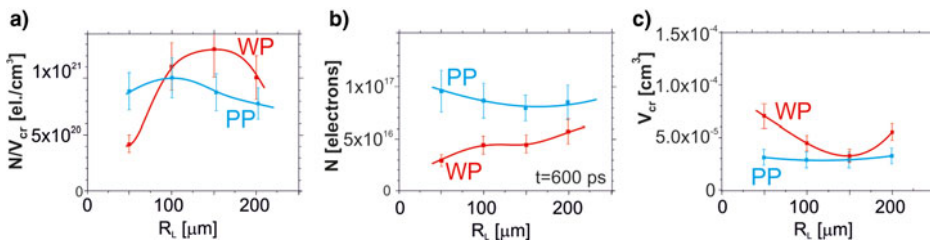


Fig. 8. Comparison of: (a) N/V_{cr} parameter, (b) the crater volumes, and (c) the total electron number obtained in the case of absence (WP) and presence (PP) of the pre-plasma.

monotonously, reaching a value of one and a half time greater (about $L = 340 \mu\text{m}$) than in the case of without pre-plasma. For later times of ablative plasma expansion the changes of scalelength as a function of focal spot radius are very similar to those for the initial phase of expansion. This proves the stabilizing influence of the pre-plasma on the central plasma created by the main 3ω beam.

In previous experiments carried out with the first harmonic main pulse (Pisarczyk *et al.*, 2015), a significant effect of energy transfer by fast electrons on the formation of plasma density and temperature distributions was found and, as a result, also on the formation of ablation pressure and laser energy transfer to shock wave. In the absence of pre-plasma the fast electron energy transport deep into the corona at a high-laser intensity (at small radii of laser beam) was more effective than the electron thermal conductivity and led to a significant increase in the ablation density in comparison with the low critical plasma density corresponding to the first harmonic radiation. This explains the measured rather high values of electron density gradient of about $10^{22}/\text{cm}^4$ at the small beam radii. The generation of fast electrons is due to a significant contribution of resonant mechanism of laser light absorption. The presence of pre-plasma

significantly worsened both the conditions for generation of fast electrons and the effectiveness of the energy transfer by them, that was manifested by a significant decrease (two to four times) of the density gradient.

The results of the experiments with the third harmonic main pulse, presented here, do not reveal the influence of energy transfer by fast electrons on the plasma formation. The non-monotonic dependence of the density gradient on the laser beam focal spot radius in both the presence and absence of pre-plasma is determined by the competition of the processes of plasma motion and electron heat conduction under the conditions of 1D and 2D expansion at large and small values of the focal spot radius, respectively. The significant increase in the density gradient in the case of the third harmonic main pulse in comparison with the first harmonic one is due to the ninefold excess of the critical plasma density.

Crater volume measurements. 3ω -experiments

The N/V_{cr} parameter has been determined taking into account the total electron number obtained from the interferometric

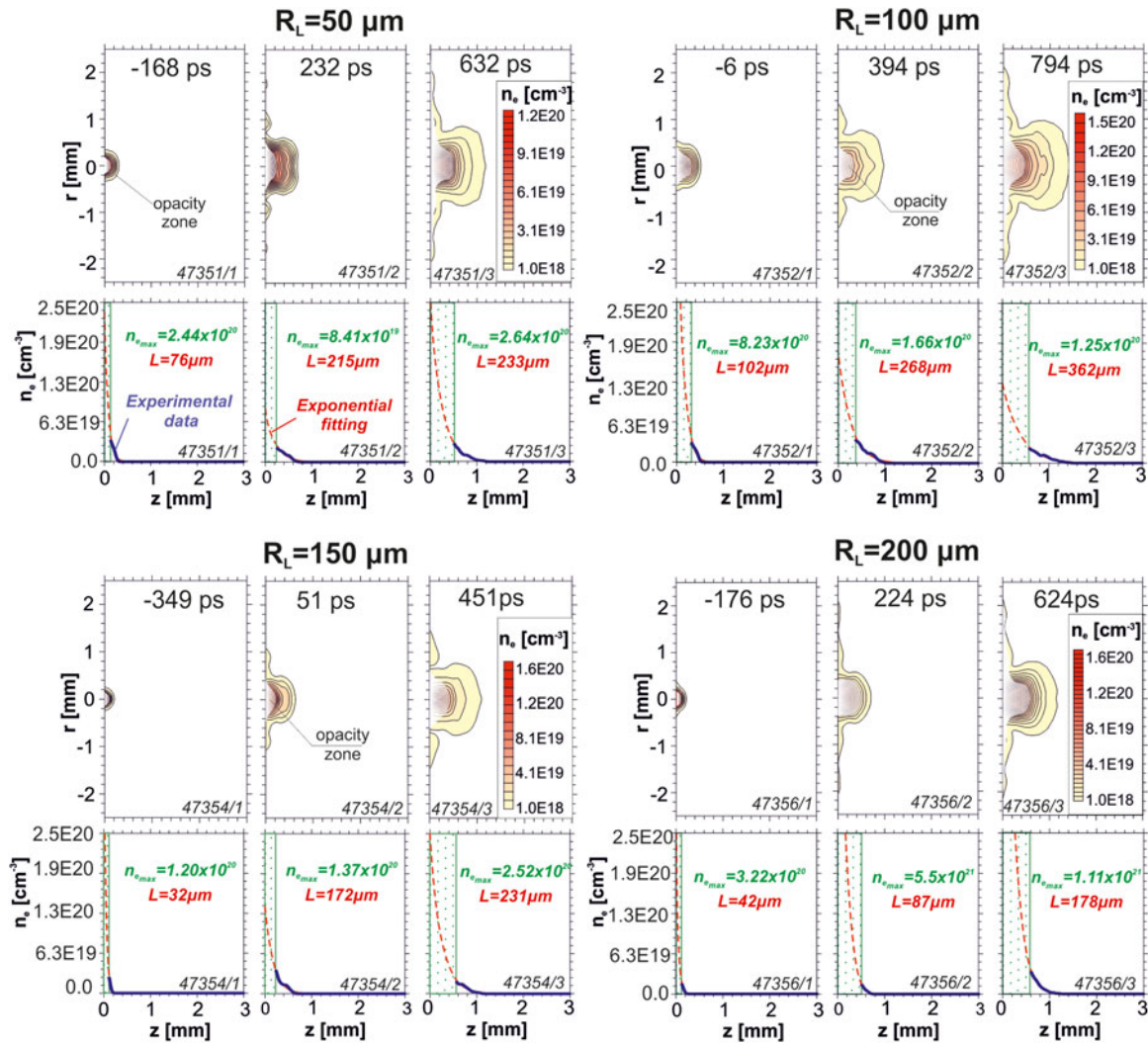


Fig. 9. Electron density distributions illustrating the time evolution of the ablative plasma expansion during the laser pulse interaction with the target at different focal spot radii in the pre-plasma absence.

measurements and the crater volume values obtained for the same experimental conditions for which interferograms were registered. A comparison of temporal changes of the total electron number in the case of absence and presence of pre-plasma is presented in Figure 12. As it follows from Figure 12, the total electron number in the plasma streams increases both with the expansion time and the focal spot radii. For measuring the volume of craters which were obtained together with interferometry, a digital microscope (HIROX-KH-8700 model) from the Institute of Optoelectronics of Military University of Technology (MUT) was used. This microscope enables determination of the crater parameters in the selected cross-sections with micron accuracy and their visualization.

The N/V_{cr} parameter was evaluated only for the expansion time $t = 600$ ps, that is after the end of the main laser pulse, when both the ablation process and processes related to absorption of laser radiation were completed. The results of calculations of the N/V_{cr} parameter, the total electron number N , and the crater volumes V_{cr} , for the different options of irradiation of two-layer targets are shown in Figure 13.

First of all, it should be noted that in comparison with the results of 1ω main pulse experiments (Pisarczyk *et al.*, 2015), in the 3ω case the crater volume increases significantly less with decreasing radius in the region of its low value, $R_L < 100$ μm . This indicates that in the case of the 3ω radiation the strong effect of energy transfer by fast electrons deep into a dense plasma, observed in the case of the 1ω case, is absent. As a result, at 3ω only one transport mechanism works, namely that caused by the electron thermal conductivity. This fact leads to just a weak growth in the crater volume with increasing laser intensity with decreasing beam radius. Furthermore, the crater volume in the case of the third harmonic main pulse is six to eight times larger in comparison with the case of the 1ω main pulse. This is due to a more efficient energy transfer to shock waves due to a larger ablation pressure associated with a significantly (ninefold) higher critical plasma density in the case of the third harmonic radiation. The presence of pre-plasma, which increases the corona mass and therefore the number of electrons N , slightly reduces the crater volume by reducing the efficiency of energy transfer by electron conductivity. At the same time, the decrease in the ratio N/V_{cr} in the case of both the absence and presence of pre-plasma

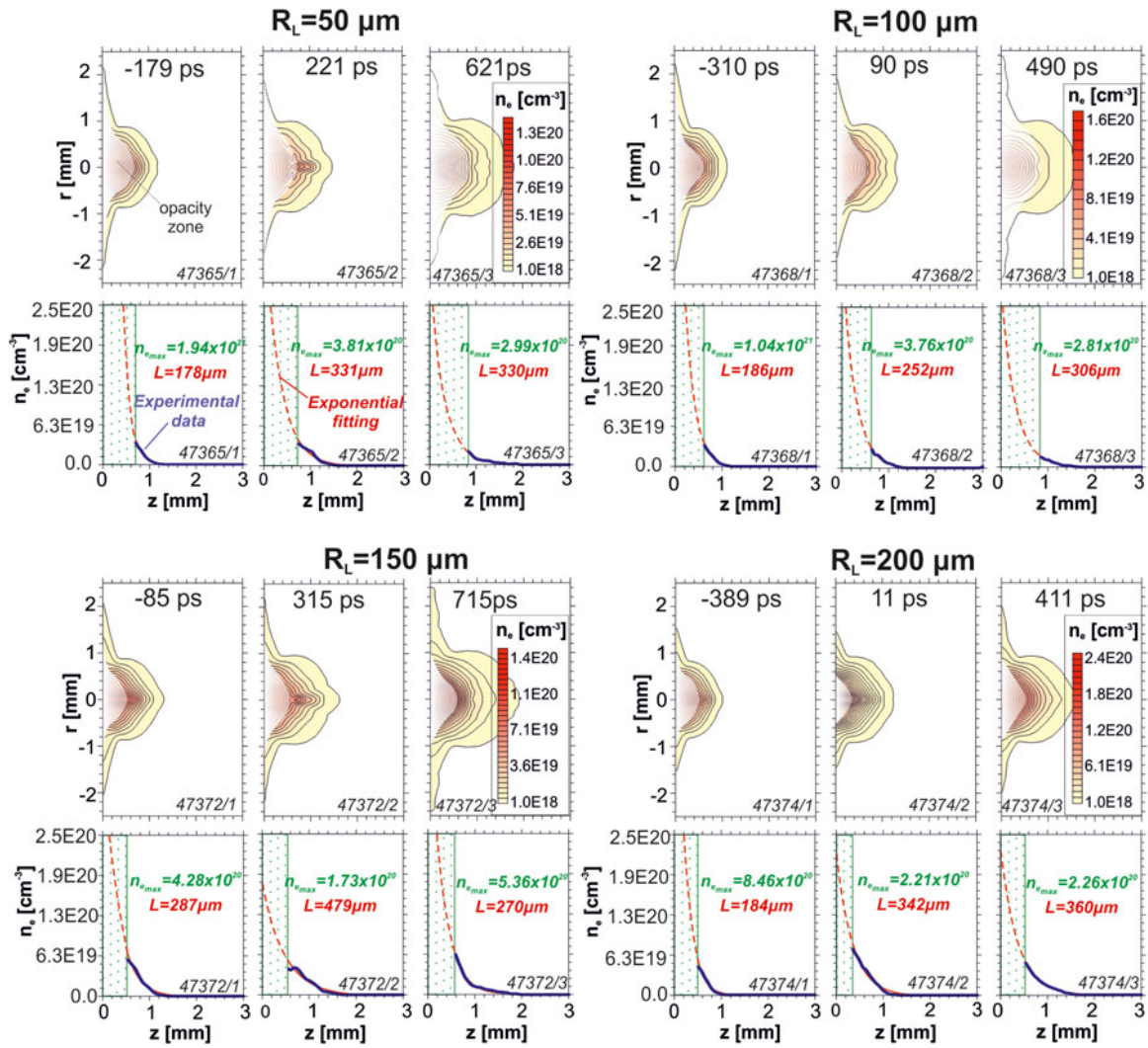


Fig. 10. Electron density distributions illustrating the time evolution of the ablative plasma expansion during the laser pulse interaction with the target at different focal spot radii in the pre-plasma presence.

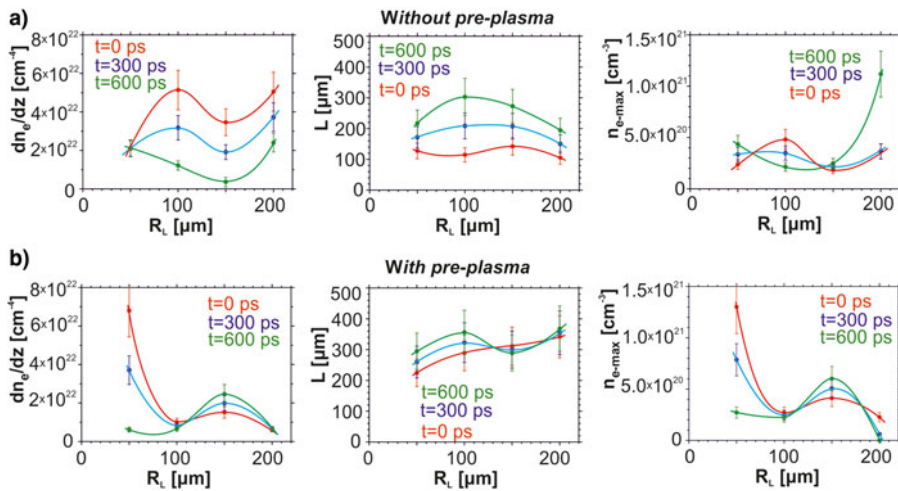


Fig. 11. Comparison of the maximal density gradient, the scaleglength, and the maximal density obtained in the cases of absence and presence of the pre-plasma.

shows that in the absence of fast electron energy transfer, when the electron conductivity is the dominant mechanism of energy transfer, the most favorable conditions for the energy transfer to

shock wave correspond to the plane expansion of plasma at large values of the beam radius (Gus'kov *et al.*, 2014; Pisarczyk *et al.*, 2014).

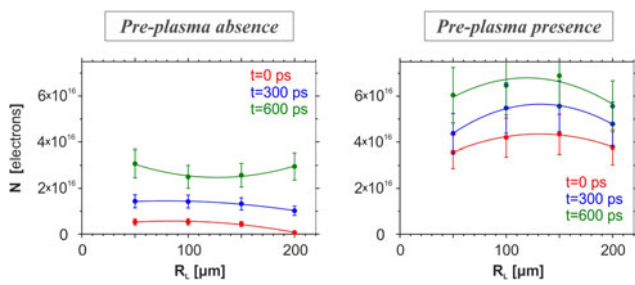


Fig. 12. Comparison of the changes of the total electron number in the cases of absence and presence of pre-plasma for three characteristic times of plasma expansion.

Fast electron emission

K_{α} -emission. 1ω -experiments

To characterize in more detail the impact of the pre-plasma on the laser energy transport and the formation of ablation pressure, the interferometry and crater volume measurements were complemented by measurements of the fast electron emission. The collected data were used to determine the population and energy of hot electrons (HE), as well as the conversion efficiency of the laser energy into HE for different irradiation conditions of the two-layer target is shown in Figure 1. The X-ray images were recorded using a spherically-bent crystal of quartz (422), Figure 14, which was setup as an imaging mode monochromator (with the Bragg angle $\theta_B = 88.2^\circ$ and magnification of $c/a = 1.73$) to provide a distribution of the 2D-spatially resolved Cu K_{α} emission along the target surface (Smid *et al.*, 2013; Pisarczyk *et al.*, 2015; Renner *et al.*, 2016).

The time-integrated K_{α} signals attenuated by transmission through filters consisting of 10 μm of Cu, 20 μm of Al, and 40 μm of mylar were obtained with the Kodak AA400 X-ray film. The recorded images were digitized with a calibrated table-top scanner, recalculated to optical densities and to intensities of the impinging radiation by using the characteristic curve of the film.

The research was carried out using the 1ω main laser beam with the energy at the level of 250 J. The intensities of the radiation impinging onto the target were varied by changing the laser energy or the focal spot radius in range of $R_L = 50\text{--}200\ \mu\text{m}$. To determine the energy of the fast electrons, the two-layer targets with different thicknesses of the plastic ($\Delta_{pl} = 15; 25; 50; \text{and } 100\ \mu\text{m}$) have been used. Typical images obtained when focusing the variable energy laser beam on focal spots with radii $R_L = 50$ and $100\ \mu\text{m}$ are presented in Figure 15. As is obvious from Figure 15, the intensity of the K_{α} signal increases with the decreasing focal spot size and with the increasing energy of the laser beam.

The 2D-resolved records contain information on the emitting area and intensity of the K_{α} emission generated in cold copper material by fast electrons. The quantitative evaluation of this data was based on assumption of the Maxwellian energy distribution of supra-thermal electrons impacting on the double layer target and an exponential decay of the photon emission I with the increasing thickness x of the plastic layer $I(x) = A \times \exp(-x/L)$, where L is an attenuation coefficient. The experimental data were interpreted by using Monte Carlo simulations of the electron and photon transport performed with the PENELOPE code (Salvat *et al.*, 2009). Assuming characteristic temperature T_{HE} of Maxwellian HE distribution, the trajectories of electrons propagating into the target were calculated both in the plastic and Cu

layers, the generation of K_{α} emission inside the Cu layer and its propagation and absorption in the target was taken into account. A set of simulations was performed for different T_{HE} values and various plastic thicknesses. Each simulation calculated the probability $dp/d\Omega(\Psi)$ that one electron produces a K_{α} photon escaping the target in a unit solid angle at the given polar angle Ψ . These probabilities were further used in interpretation of the experimental data and in derivation of the sought interaction characteristics, for example, the exponential attenuation of the fast-electron-generated photon emission due to different-thickness surface plastic layers. The calculated dependence of the attenuation coefficient L on the supra-thermal electron energy is shown in Figure 16. The final experimental results were obtained *via* fitting the photon fluxes spatially integrated over 2D-resolved images with simulations. To determine the energy of fast electrons E , the Cu K_{α} emission was measured at targets with different thickness plastic layers. Results of these measurements are presented in Figure 17 showing the dependence of the detected photon fluxes on the thickness of the surface plastic layer Δ_{pl} in the absence and presence of the pre-plasma.

All the data were taken when irradiating the target by the 1ω beam focused on the focal spot with a radius of $R_L = 50\ \mu\text{m}$. In addition to the useful K_{α} signal and the film noise, the recorded images captured a non-negligible amount of the continuum radiation emitted primarily by the plastic layer covering the Cu substrate. This radiation has independently been measured using self-supporting plastic foils and subtracted from the recorded images, but the uncertainty estimate has significantly increased due to the fluctuation of the background signal.

Consequently, the shown error bars indicate mainly uncertainties in the background subtraction. The number of incident photons refers to photon fluxes impinging on the film-pack, that is, when processing the recorded images, the signal attenuation in filters covering the film was taken into account. The dependences plotted in Figure 17 demonstrate the decrease of the Cu K_{α} photon fluxes with the increasing thickness of plastic. The best-fit values of the attenuation coefficient L and the HE energy E are also indicated in Figure 17. The fitted scalelength is about $L = 30\ \mu\text{m}$ without the pre-pulse and $L = 29\ \mu\text{m}$ for the case of the plasma presence. The simulations show that for scalelengths $L < 50\ \mu\text{m}$, the relation is very close to $T_{HE} \text{ (keV)} \approx L \text{ (}\mu\text{m)}$. Thus we can state that the energies of the fast electrons for 1ω for both cases with and without pre-pulse are close each other and about $T_{HE} = 29\ \text{keV}$.

The effect of the pre-plasma on the total number of detected Cu K_{α} photons in dependence on the laser intensity, that is, on the focal spot radius, is shown in Figure 18. All these data fitted with the second degree polynomial were measured at Cu targets coated with 25 μm of plastic. As it results from Figure 18 in the case of the pre-plasma presence, the K_{α} emission decreases strongly with R_L . The interferometric and spectroscopic measurements seem to confirm that the presence of the pre-plasma reduces the contribution of fast electrons in the energy transfer process to the Cu massive target.

To estimate the conversion of the laser energy into fast electrons, the number of detected photons $N_{K_{\alpha}}$ was related to the number of HEs N_{HE} propagating through the target using the expression:

$$N_{HE} = \frac{N_{PH}}{(4\pi r dp/d\Omega)} \quad (1)$$

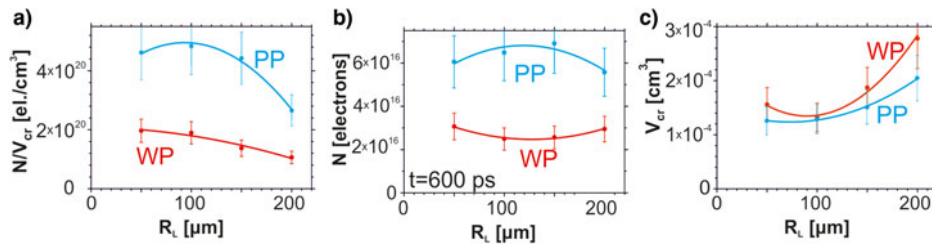


Fig. 13. Comparison of the crater volumes V_{cr} and N/V_{cr} parameter obtained in the cases of absence and presence of pre-plasma.

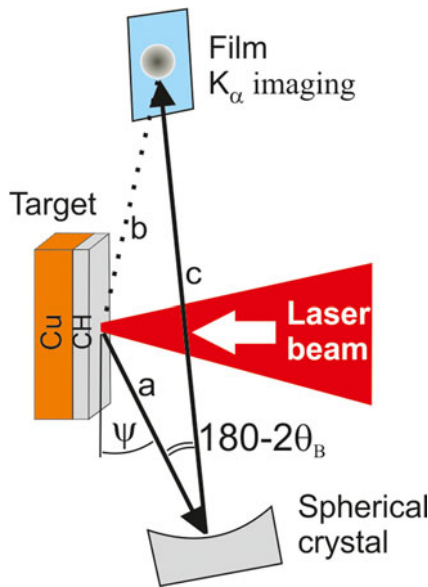


Fig. 14. The scheme of the measurement of Cu K_{α} emission.

where $r = 8.3 \times 10^{-7}$ is the ray tracing constant relating the fraction of photons impinging on the detector to the number of photons isotropically emitted from the cold copper into the full solid angle 4π within the Cu $K_{\alpha,1,2}$ profile (Smid *et al.*, 2013). This assumption is well justified for copper targets coated with 25 μm of plastic where the frequency shifted satellite emission generated by fast electrons in the heated copper can be neglected. By taking into account the average energies E presented in Figure 17, the found values of N_{HE} were further related to the conversion efficiency η of the laser energy into HEs. In the current experiment, the typical numbers of fast electrons N_{HE} propagating through the target were within the range of $1-5 \times 10^{12}$. The conversion efficiencies calculated as the ratio of the total energy carried by fast electrons entering the target to the energy of the main 1ω laser beam in the presence/absence of pre-plasma are shown in Figure 19.

K_{α} -emission. 3ω -experiments

Analogously to experiments using the 1ω main laser beam, similar studies were performed to determine the characteristics of fast electrons under irradiation of two-layer targets by the 3ω laser beam. The main aim of these measurements was to investigate the influence of the plasma formation on the fast electron generation in the presence and absence of the pre-plasma.

The experiment was carried out with the laser energy of about 200 J and various intensities resulting from changes of the focal spot radius of laser beam on the target in the range of $R_L = 50-$

200 μm . To determine the energy of fast electrons, two-layer targets with different thicknesses of the plastic ($\Delta_{pl} = 15, 25, 50,$ and $100 \mu\text{m}$) were again used.

The imaging setup was the same as in the previous section “ K_{α} -emission. 1ω -experiments” (Fig. 14). The time-integrated K_{α} signals attenuated by transmission through filters consisting of 10 μm of Cu, 20 μm of Al, and 40 μm of mylar were obtained with the Kodak AA400 X-ray film. The recorded images were digitized with a calibrated table-top scanner. Then the experimental data were interpreted by using the methodology presented in the previous section.

The results of the measurements showing the effect of the pre-plasma on the total number of photons detected as a function of the thickness of the surface plastic layer Δ_{pl} in the absence and presence of the pre-plasma are shown in Figure 20.

This figure demonstrates attenuation of the Cu K_{α} photon fluxes with the increasing thickness of the plastic and a significant increase of the emission in the presence of the pre-plasma. The best-fit values of the attenuation coefficient L and the HE energy E are also indicated in Figure 20. The characteristic energy of fast electrons produced in the case of the single-beam irradiation of the targets equals to 37 keV, while in the pre-plasma presence the value of E is almost two times higher.

The effect of the pre-plasma on the total number of the detected Cu K_{α} photons in dependence on the laser intensity, that is, on the focal spot radius, is shown in Figure 21.

All these data fitted with the second degree polynomial were measured using Cu targets coated with 25 μm of plastic. While the number of detected Cu K_{α} photons (and consequently also the production of HEs) increases only slightly with the focal spot radius in the pre-plasma absence, the presence of the pre-plasma results in a distinct growth of the fast electron population peaking at $R_L \approx 150 \mu\text{m}$. Obviously the increased scalelength of the ablative plasma in the presence of the pre-plasma increases both the production and the energy of fast electrons.

To estimate the conversion of the laser energy into fast electrons, the number of detected K_{α} photons was related to the number of HEs N_{HE} propagating through the target using expression (1). By taking into account the average energies E presented in Figure 20, the found values of N_{HE} were further related to the conversion efficiency η of the laser energy into HEs. As in the case of the 1ω -experiments (see previous section), the typical numbers of fast electrons N_{HE} propagating through the target were within the range of $1-5 \times 10^{12}$.

The conversion efficiencies calculated as the ratio of the total energy carried by fast electrons entering the target to the energy of the main 3ω laser beam in the presence/absence of pre-plasma are shown in Figure 22. The conversion efficiencies are grouped near four laser intensities $1 \times 10^{16}, 2.5 \times 10^{15}, 1 \times 10^{15},$ and $6 \times 10^{14} \text{ W/cm}^2$ corresponding to focal spot radii of 50, 100, 150, and 200 μm , respectively. The found values of η are considerably scattered and do not display any distinct dependence on the laser

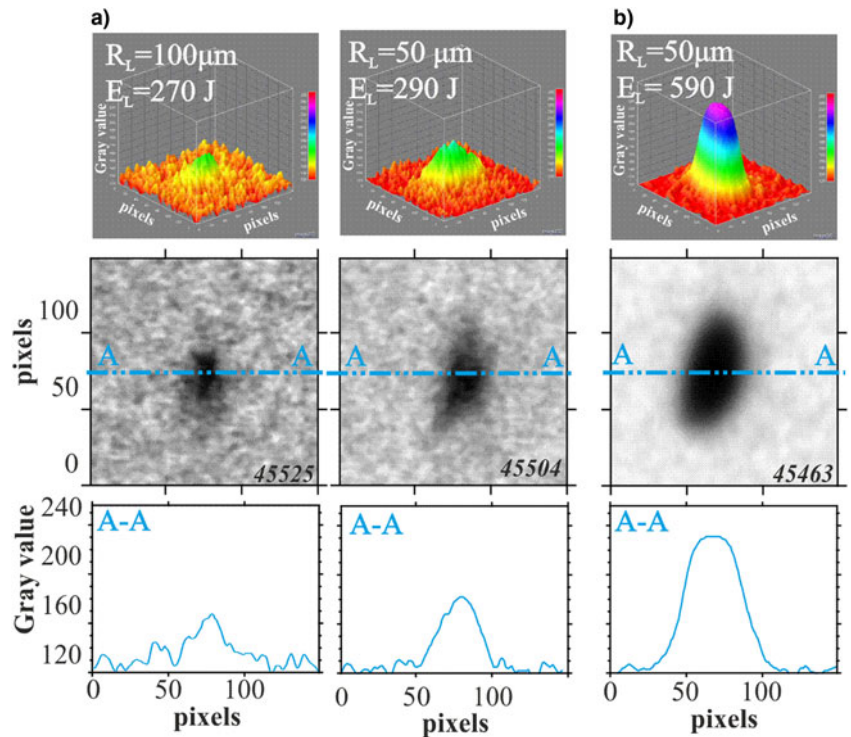


Fig. 15. Images of the K_{α} obtained in the case of without pre-plasma at the minimal focal spot radii for different laser energies: (a) 290 J and (b) 590 J.

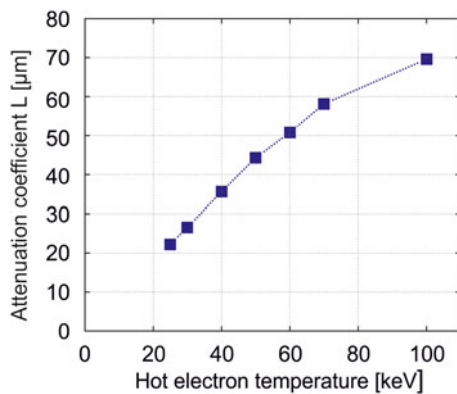


Fig. 16. Dependences of the attenuation coefficient L as a function of fast electron energy.

intensity. On the other hand, the presence of pre-plasma increases their average values (1.2×10^{-4} in the pre-plasma absence and 3.5×10^{-4} in its presence) by a factor of approximately 2.9.

Under given conditions of the target irradiation, the observed laser energy conversion to fast electrons is rather small in both cases of the pre-plasma presence and absence. This conversion efficiency is too small for fast electrons to provide major impact on the laser-produced plasma evolution as well as on the processes of the laser energy deposition and pressure formation in experiments using the 3ω main pulse.

Ion emission measurements

Ion emission. 1ω -experiments

The ion diagnostics applied in the PALS experiment consisted of the ion collectors which were installed at different angles (from 0

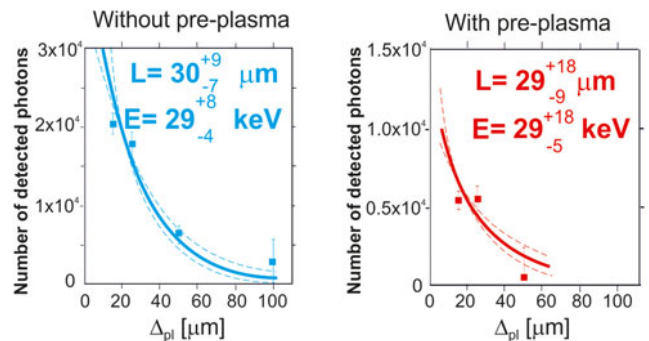


Fig. 17. Dependences of the K_{α} on thickness of plastic for the cases of absence and presence of the pre-plasma.

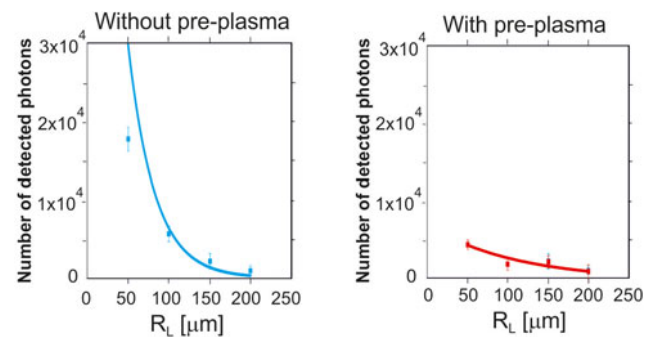


Fig. 18. The influence of pre-plasma presence on the total population of photons depending on the focal spot radius of the laser beam.

to 60°) at the distance of 40 cm from the target. The collected ion current was emitted from the two-layer targets (see Fig. 1a). The sorted oscillograms illustrating temporary changes of the ion-

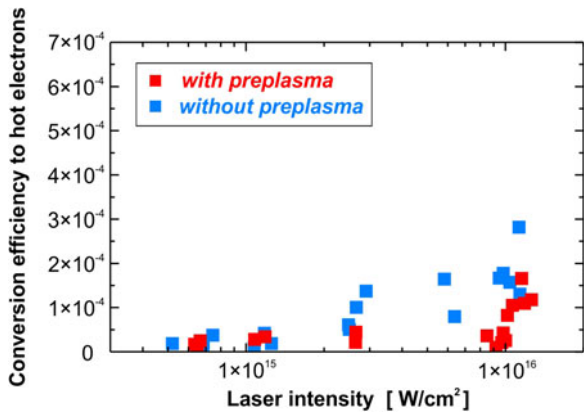


Fig. 19. Conversion efficiency of the energy of 1ω main laser beam into the total energy carried by fast electrons as a function of the laser beam intensity.

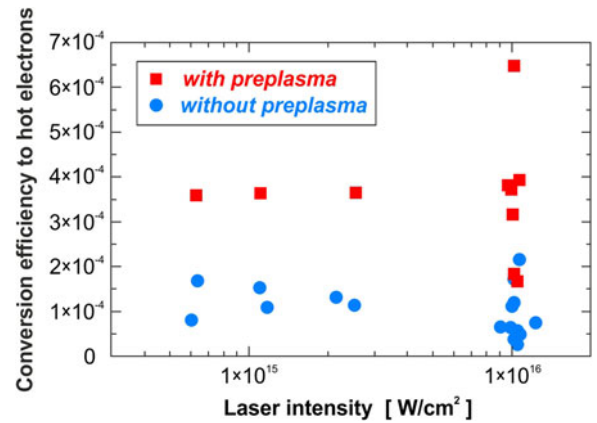


Fig. 22. Conversion efficiency of the 3ω main laser beam energy in the total energy carried by fast electrons as a function of laser beam intensity.

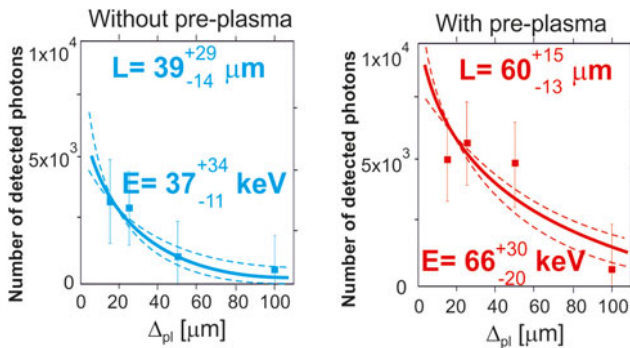


Fig. 20. Results of the 2D fast electron emission imaging showing the influence of the pre-plasma on the total population of photons, depending on the plastic layer thickness in the two-layer target in the cases of absence and presence of pre-plasma.

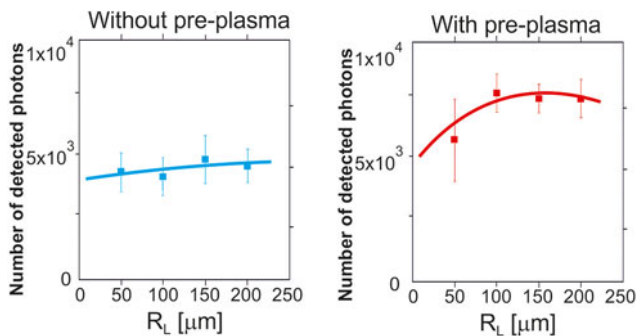


Fig. 21. Results of 2D fast electron emission imaging, showing the influence of pre-plasma on the total population of photons depending on the focal spot radius of laser beam under the conditions of absence and presence of pre-plasma.

collector signals provided by this diagnostic system are presented in Figure 23a. In the left column there are results obtained without the application of the pre-pulse and in the right column the results obtained with the pre-pulse application. The basic difference in the subsequent experimental series is in the focal radius which ranged from 50 to 200 μm . The parameters of the laser beam were at the same level for all experimental series (about 250 J in the main beam and about 40 J in the pre-pulse). The diagrams show the time dependence of the ion-collector signals as a function of time for different angles and focal diameters. The

main conclusions following from these results may be summarized as below:

- The number of thermal ions (the second-delayed peak) in the case of pre-plasma presence is two to three times larger than that observed in the case of pre-plasma absence for all the beam radii. It means that the absorption coefficient in the case of pre-plasma presence is two to three times larger than in the case of pre-plasma absence. This conclusion is confirmed by the results of 2DSs presented in the next section.
- In the case of pre-plasma presence, fast ions (the first peak) are generated at all radii of the laser beam. Since the fast ions are generated in the field of fast electrons, this means that in the presence of pre-plasma also the fast electrons are generated at all laser beam radii. This conclusion agrees with the results of 2DSs predicting high efficiency of resonant absorption of laser radiation for all the radii of laser beam in the presence of pre-plasma.
- In the case of pre-plasma absence, fast ions are generated only at the radii of 100 and 50 μm . It is in agreement with the results on fast electrons generation from interferometric and X-ray spectroscopic measurements presented above.
- The time of the second peak equals to about 0.7 μs ; it is approximately the same for the cases both with and without pre-plasma and for all radii of the laser beam.
- The time of the first peak (0.15 μs) is significantly shorter than that of the second peak which indicates that the energies of fast ions are much higher than those of thermal ions.

The ion-collector data not sorted according to the ion types give a possibility to determine only the scales of temperature of the plasma plume and average energy of fast electrons. Taking the time of the second peak as 0.7 μs , the average velocity of thermal ions as $(3T/2m_p)^{1/2}$ (in the $A/Z=2$ approximation) and the distance between the target and collector equals to 40 cm, we obtain that the value of plasma temperature, averaged over space and time, is approximately equals to 2.1 keV.

This value is obviously larger than the time-averaged temperature obtained from X-ray spectroscopy measurements, since the latter corresponds to the relatively cold part of plasma torch near the ablation surface. Now, taking the average velocity of fast ions as $(E_h = m_p)^{1/2}$ (where the energy of fast ions was, approximately, expressed through the average energy of fast electrons E_h as ZE_h)

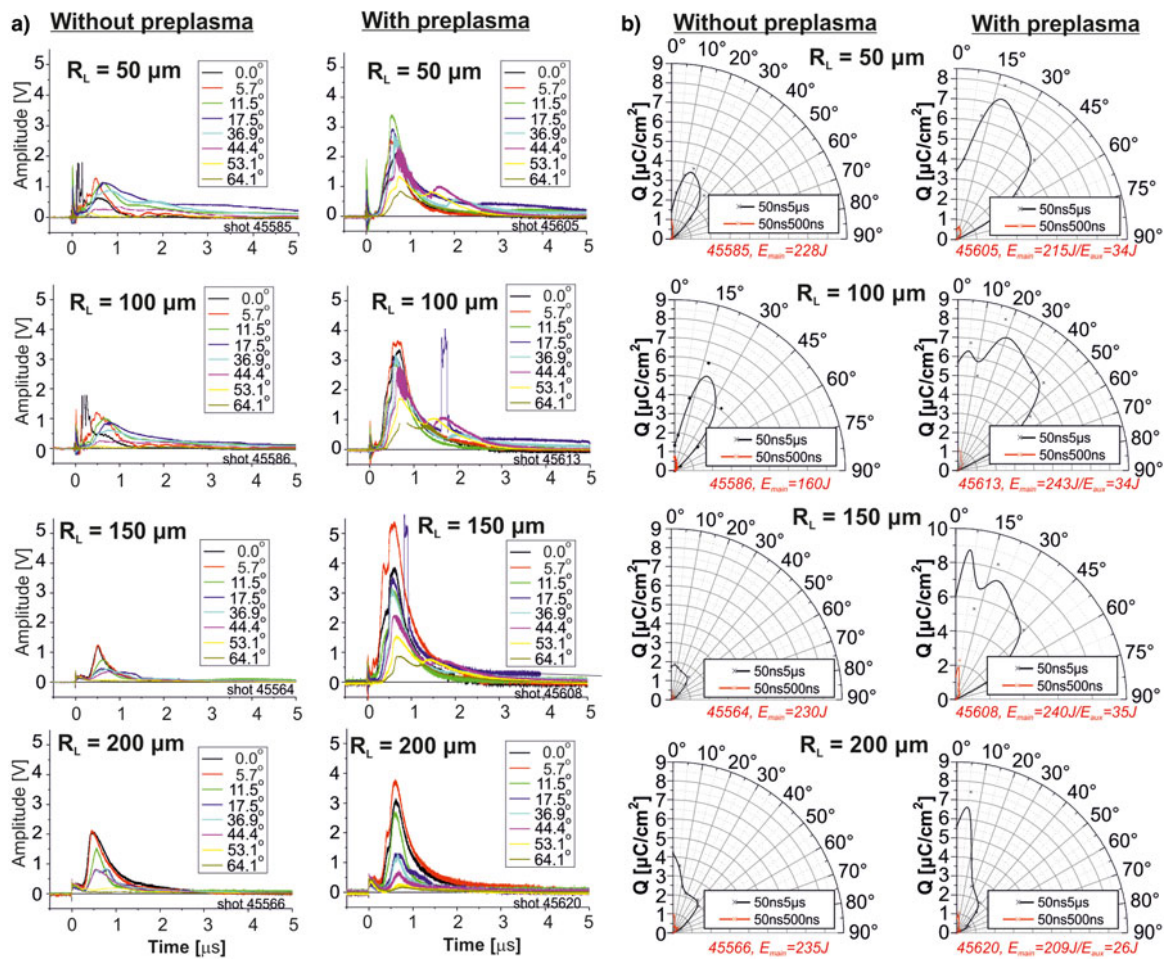


Fig. 23. Influence of the pre-plasma on: (a) the ion-collector signals measured at different angles and (b) angle distributions of the ion charge density for different focal spot radii.

and the time of the second peak as $0.15 \mu\text{s}$, we obtain the average energy of fast electrons approximately equal to 70 keV .

Figure 23b shows the plots of charge distributions for each experimental series, calculated on the basis of integration of the charge of both thermal ions (of time-of-flight ranging in $50\text{--}500 \text{ ns}$).

When comparing the results from the two columns depicted in Figure 23b, it can be seen that when increasing the focal diameter, the ions are better collimated which is manifested in a distinct plasma “jet”. When the pre-pulse configuration is applied together with the $200 \mu\text{m}$ focus diameter, the jet is well visible and the whole group of the pre-pulse series has considerably larger integrated charges than those obtained without the pre-pulse.

Ion emission. 3ω -experiments

The ion diagnostics applied in the PALS experiment consisted of several ion collectors installed at different angles (from 0 to 60°) at the distance of 40 cm from the target. The collected ion current was emitted from two-layer targets (see Fig. 1a). Some of the selected results provided by this diagnostic system are presented in Figure 24a and 24b.

In the left column there are the results obtained without application of pre-pulse and in the right column – those obtained with it. The parameters of the 3ω laser beam were at the same level for all the presented measurements (about 200 J in the main beam

and about 40 J in the pre-pulse). Figure 24a shows the ion-collector signals for different angles and focal spot radii. All the signals for the case of both pre-plasma absence and presence correspond to thermal ions only and do not contain any response related to fast ions. It is in contrast to the results of our previous experiments carried out with the 1ω main beam, where strong signals related to fast ions were measured for the case of pre-plasma absence at high main beam intensities of $0.5\text{--}2 \times 10^{16} \text{ W/cm}^2$ (Pisarczyk *et al.*, 2015).

It should be also noted that in the case of the 1ω beam the collector signals referring to thermal ions were more than two times less compared with the 3ω -experiment for both the cases of pre-plasma absence and presence. It means that in the case of 3ω beam the absorption of laser light is significantly higher than that for the 1ω beam. According to the results of numerical simulations presented in the next paragraph, the absorption efficiency for 3ω is $0.7\text{--}0.8$, while for 1ω (Pisarczyk *et al.*, 2015) it was $0.4\text{--}0.5$. Other conclusions deduced from the ion-collector measurements (Fig. 24a) may be summarized as below:

- The number of thermal ions in the case of pre-plasma presence is approximately $1.2\text{--}1.5$ times larger than that observed in the case of pre-plasma absence for all the focal spot radii.
- The signal of fast ions is not measurable, which confirms the results of previous paragraphs concerning the negligible effect of fast electron generation.

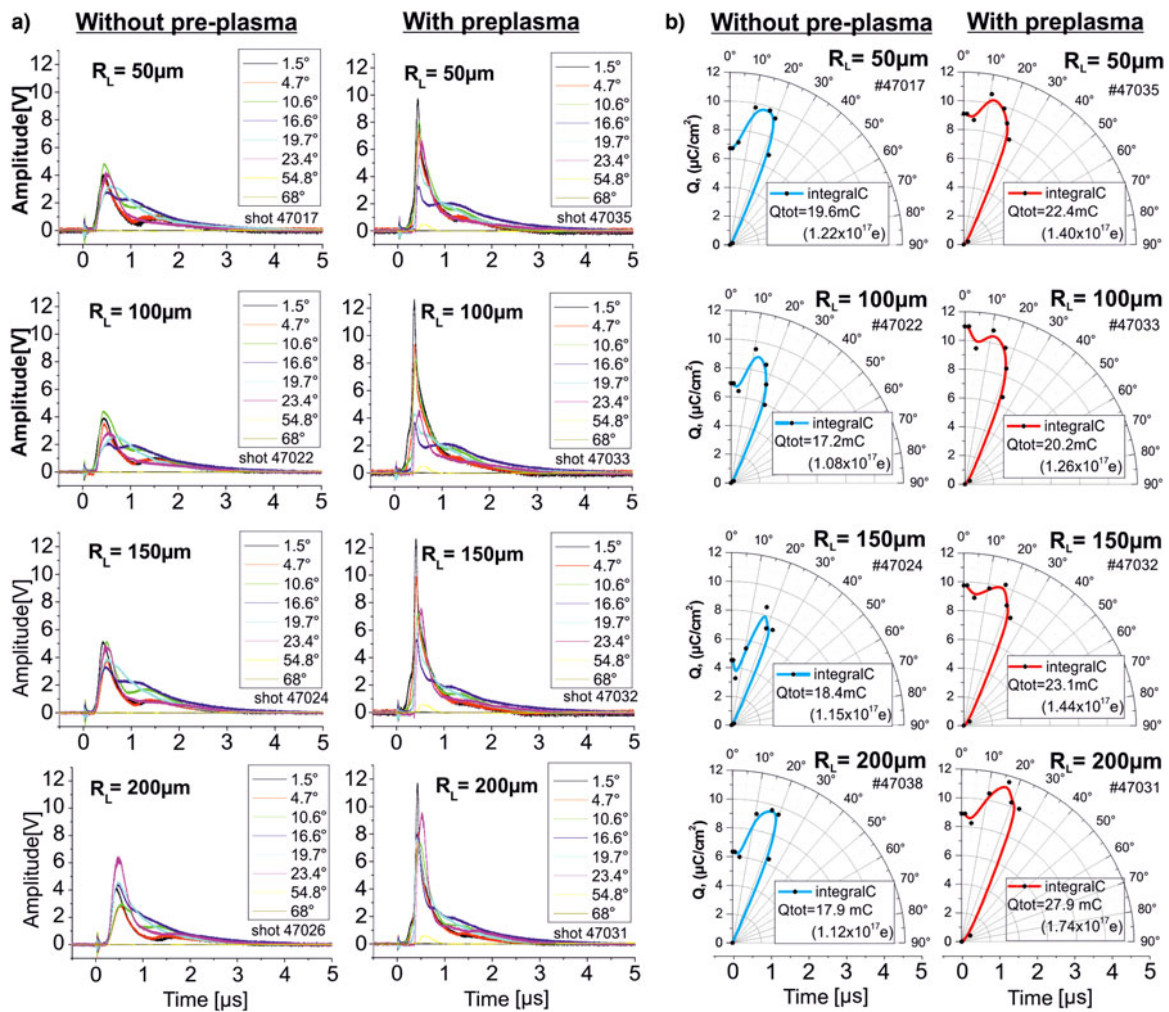


Fig. 24. Influence of the pre-plasma on: (a) the ion-collector signals measured at different angles and (b) angle distributions of the ion charge density for different focal spot radii.

- Thermal ion signals peak practically at the same time for both the cases of pre-plasma presence and absence, at about 0.5 μs , which is smaller by a factor of 1.4–1.6 in comparison with the case of 1ω main pulse (Pisarczyk *et al.*, 2015). It means that the temperature of plasma produced by 3ω beam is higher than that generated by the 1ω beam. This correlates well with the increase of absorption efficiency for the shorter wavelengths revealed by numerical simulations.
- The ion-collector data, not separated with respect to the ion type, give a possibility to determine only the scales of temperature of the plasma plume and average energy of fast electrons. Taking the time of the second peak as 0.5 μs , the average velocity of thermal ions as $(3T/2m_p)^{1/2}$ (in the $A/Z = 2$ approximation) and the distance between target and collector equals to 40 cm, we obtain that the value of plasma temperature, averaged in space and time, is approximately equal to 3–4 keV.

Figure 24b shows the plots of charge distributions for each experimental series, calculated on the basis of integration of the charge of thermal ions (for the time-of-flight ranging from 50 to 500 ns). It can be seen that in the case of the pre-plasma presence, the ion charge density on the axis is higher compared with the case when the pre-plasma is absent.

2D numerical modeling of laser–plasma interaction in different wavelength experiments

1ω laser beam interaction

To obtain more information about the ablative plasma expansion and the fast electrons emission, the 2D-simulations were carried out using the 2D hydrodynamic code ATLANT-HE (Lebo *et al.*, 2004) from Lebedev Physical Institute in Moscow. 2D numerical code allows modeling of the following processes: the laser radiation refraction in the plasma, inverse bremsstrahlung and resonance absorption of laser radiation, generation of fast electrons due to the resonance absorption, and the fast electron energy transfer *via* Coulomb collisions. The aim of the numerical calculations was to obtain information about:

- the temporal evolution of 2D spatial distributions of the electron density as well as electron temperature of the ablation plasma;
- the fractions of the laser energy absorbed in the plasma by resonant and inverse bremsstrahlung mechanisms as well as
- the energy of fast electrons.

The calculation details are explained in our recent paper (Gus'kov *et al.*, 2014). To model the experimental conditions, the

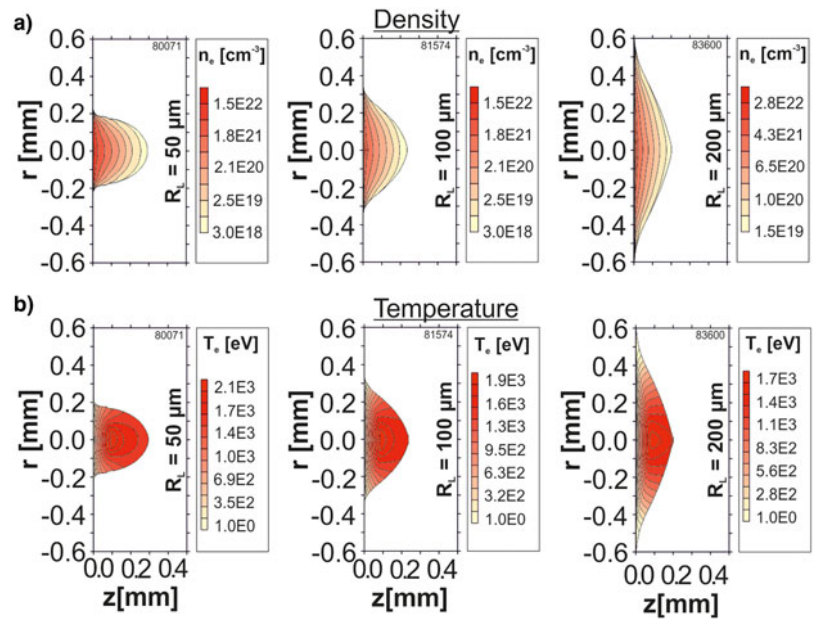


Fig. 25. The density (a) and temperature (b) distributions in the ablative plasma created by the main laser beam at the maximum of the laser pulse intensity.

computations were performed for the 1ω radiation of the main laser beam with the energy of 250 J and three values of the focal spot radius: 50, 100, and 200 μm .

In the case of a two-beam experiment referring to the SI concept, the pre-plasma was created by the auxiliary 1ω laser beam with the energy of 40 J focused on the focal spot radius $R_L = 300 \mu\text{m}$ and preceding by 1.2 ns the main laser pulse. For the case of pre-plasma absence, the 2D calculations of the density and temperature corresponding to the maximum laser intensity are presented in Figure 25. In contrast to the experimental results shown in Figure 3, these density distributions do not show any growth of the axial character of plasma expansion with the increasing focal spot radii.

As demonstrated in Figure 25, the growth of the focal spot radius leads to the increased transverse dimension of the ablative plasma. The distribution of the electron density and temperature of the pre-plasma produced by the auxiliary laser beam is shown in Figure 26.

This distribution corresponds to time $t = 400$ ps, that is, to the end of the pulse. 2D distributions of the density and temperature characterizing the process of the interaction of the main beam with the pre-plasma created by the auxiliary laser beam are presented in Figure 27.

Compared with the situation when the pre-plasma is not created, the density scalelength of the ablative plasma is considerably larger. Comparison of the experimental data with the 2DS is presented in Table 1. This comparison has been performed in the range of the electron density smaller than $10^{20}/\text{cm}^3$ as determined from the femtosecond interferometry. Table 1 indicates that there is a satisfactory agreement between experimental and numerical data in the case of pre-plasma presence. In the case of pre-plasma absence, the qualitative character is the same, but the observed and simulated scalelength values differ considerably. The large values of experimental scalelengths result from the action of the temporally extended beam profile which is characteristic for the PALS laser and contributes to the creation of the low density plasma even in the case of pre-pulse absence.

A long pedestal (even about 1 ns long) of the pulse is not taken into account in numerical simulations. In the case of pre-plasma

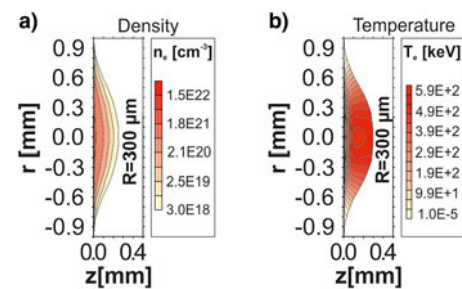


Fig. 26. Distributions of the density (a) and temperature (b) in pre-plasma for the expansion moment of $t = 400$ ps.

presence, the contribution of the pre-pulse is significantly smaller compared with the pre-plasma itself. This is why the experimental and numerical scalelengths agree well in the case of the pre-plasma presence. In Table 2 the numerical simulations of the total (δ_{total}), the resonant (δ_{res}) and the inverse bremsstrahlung δ_{ib} absorption coefficients are compared for the cases of the pre-plasma absence and presence.

This comparison demonstrates the significantly larger total absorption coefficient in the case of pre-plasma presence compared with the case of the pre-plasma absence. The excess is, approximately, of the factor of 3 for the beam radius of 50 μm and the factor of 2 for the beam radius of 100 μm . This explains the ion-collector measurements, where the number of thermal ions in the case of pre-plasma presence is by a factor of 2–3 larger in comparison with the case of pre-plasma absence. The maximal temperature (occurring near the region of the plasma critical density) obtained by numerical simulations falls within the interval of 2–3 keV which agrees well with the evaluation based on ion-collector data. The pre-plasma provides better conditions for resonant absorption of the laser energy. For the beam radius of 50–100 μm , the resonant absorption coefficient is equal to $\delta_{\text{res}} = 0.32$ – 0.23 in the case of pre-plasma presence and to $\delta_{\text{res}} = 0.06$ – 0.09 in the case of pre-plasma absence. The maximal energies of fast electrons are about 140–120 keV. This value relates to the electrons

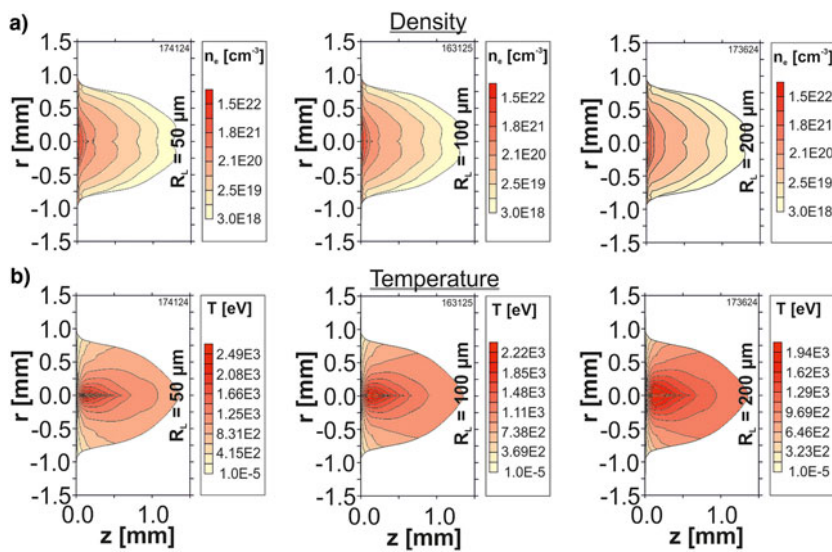


Fig. 27. The density (a) and temperature (b) distributions after the time delay of $t = 1.2$ ns relate to the auxiliary laser pulse, created when affecting the main laser beam with a pre-plasma.

Table 1. Comparison of the experimental L with the 2DS in the cases of presence and absence of pre-plasma

R_L (μm)	L (μm)			
	1ω		$1\omega + 1\omega$	
	Exp.	2D	Exp.	2D
50	125	30	326	320
100	190	36	420	346
200	140	34	365	296

which two times crossed the region of plasma resonance after their reflection from external plasma boundary.

These estimates are very close to the values evaluated from the ion-collector data. This evaluation gives the value of 70 keV of the average fast electron energy, that corresponds to the maximal energy of 140 keV. According to the numerical modeling presented in Gus'kov *et al.* (2014), the increased efficiency of the resonance absorption in the case of pre-plasma results probably from a better fitting of the angles between the individual laser beams and the direction of the density gradient near the critical surface (these angles are closer to optimum angles because of a smaller scalelength).

3 ω laser beam interaction

2DSs of the ablative plasma created by the 3 ω main laser beam were carried out using the 2D hydrodynamic code ATLANT-HE, which was described in section “1 ω laser beam interaction”. Analogously as in the 1 ω experiment to compare the experimental results obtained by femtosecond interferometry and fast electron measurements with 2DSs was the main task, in order to formulate final conclusions about the laser energy transport to the shock wave with the participation of fast electrons.

To model the experimental conditions, the computations were performed for the 3 ω radiation of the main laser beam with the energy of 200 J and three values of the focal spot radius: 50, 100, and 200 μm . In the case of two-beam experiment, the pre-

plasma was created by an auxiliary 1 ω laser beam of energy of 40 J, focused on a focal spot radius R_L of 300 μm and preceding the main laser pulse by 1.2 ns.

For the case of pre-plasma absence, the 2D calculations of the density and temperature show that the increase of focal spot radius leads to an increase of transverse size and a decrease of axial size of expanding plasma. Due to that, the angles between the directions of density gradient and the normal to the target surface decrease and the geometry of expansion is close to a planar one. Similarly as for the 1 ω -experiments (without pre-plasma), the 2D calculations of the density and temperature do not show any growth of the axial character of plasma expansion with the increasing focal spot radii (Pisarczyk *et al.*, 2015).

A satisfactory agreement of calculations with the experiment was obtained in the case of laser beam interaction with a two-layer target (Fig. 1) in the presence of pre-plasma. A comparison of the axial density profiles and L in the ablative plasma, in the cases of both pre-plasma absence and presence, is presented in Figure 28. As it results from Figure 28, the scalelength of the ablative plasma in the case of the pre-plasma presence is considerably larger in comparison with the situation when the pre-plasma is not created.

A more detailed comparison of the experimental data with the 2DS is presented in Tables 3 and 4. As in the 1 ω -experiments presented in the previous chapter, the comparison of the experimental and simulation data has been performed in the range of the electron density smaller than $10^{20}/\text{cm}^3$. Table 3 shows a satisfactory agreement between experimental and numerical data in the case of pre-plasma presence. In the case of pre-plasma absence, the qualitative character is the same but the observed and simulated L values differ considerably. The large values of experimental L result from the action of the temporarily extended beam profile which is characteristic for the PALS laser and contributes to creation of a low density plasma even in the case of pre-pulse absence. It was explained in the previous section.

In Table 4 the numerical simulations of the total (δ_{total}), resonant (δ_{res}), and inverse bremsstrahlung (δ_{ib}) absorption coefficients are compared for the cases of pre-plasma absence and presence.

From Table 4 it results that in the case of absence of pre-plasma, the total absorption increases with the increasing focal spot radius from 0.593 to 0.876. In contrast, the fraction of resonant absorption decreases from 0.0883 to 0.0697 staying small.

Table 2. Comparison of numerical simulations of the total δ_{total} , resonant δ_{res} , and inverse bremsstrahlung δ_{ib} absorption coefficients in the cases of pre-plasma absence and presence

R_L (μm)	$50\ 1\omega$	$1\omega + 1\omega$	$100\ 1\omega$	$1\omega + 1\omega$	$200\ 1\omega$	$1\omega + 1\omega$
δ_{total}	0.21	0.64	0.29	0.57	0.42	0.59
δ_{ib}	0.15	0.31	0.19	0.34	0.25	0.39
δ_{res}	0.06	0.32	0.09	0.23	0.17	0.21
$E_{h(\text{max})}$ (keV)	143	152.8	129	144	121	114
T_{emax} (keV)	2.48	3.27	2.20	2.99	1.92	2.31

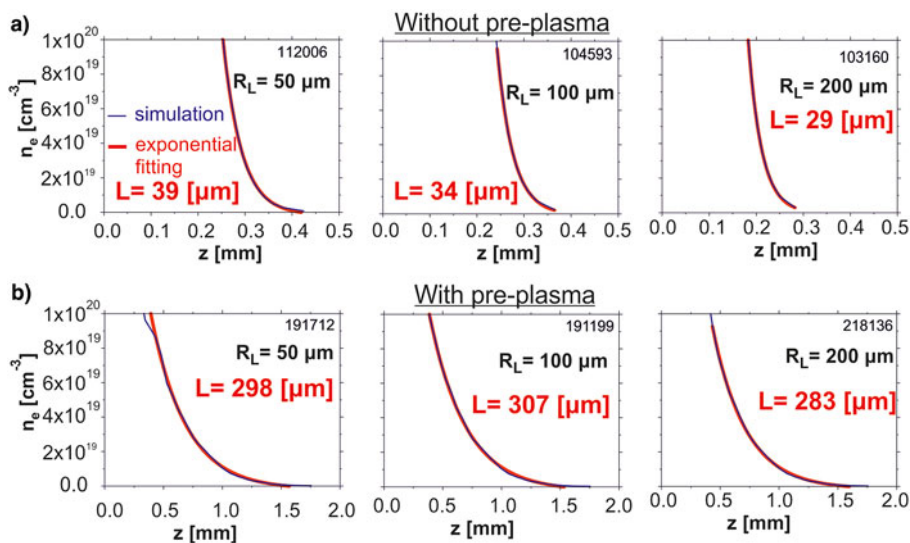


Fig. 28. Comparison of the axial density profiles and the scale-length obtained in the cases of: (a) absence and (b) presence of pre-plasma.

Table 3. Comparison of the experimental values L with the 2DS in the cases of presence and absence of pre-plasma

R_L (μm)	L (μm)			
	3ω		$1\omega + 3\omega$	
	Exp.	2D	Exp.	2D
50	125	39	220	298
100	115	34	290	307
200	100	29	340	283

The average energy of fast electrons $E_{h(\text{max})}/2$ is about 30–35 keV for both the cases with and without pre-plasma. The average fast electron energy is close to the experimental values obtained from Cu K_α line measurements in the experiment without a pre-plasma. The pre-pulse has a small effect on these quantities and does not alter their dependence on the radius of the main beam. These results differ significantly from the case of the 1ω main pulse which was presented in section “ 1ω laser beam interaction” [see Table 2 and the paper of Pisarczyk *et al.*, (2015)].

Numerical simulations show that without pre-plasma, the total absorption is considerably larger for 3ω than that of the 1ω main pulse. This is confirmed by the data from ion-collector measurements. The fraction of the resonance absorption is about the same. The pre-plasma has a small effect on absorption in the

3ω case and strong effect in the case of 1ω . In the case with pre-plasma, for the 3ω main pulse the fraction of resonance absorption (and hence the energy contained in the fast electrons) is several times smaller than that for the 1ω main pulse. This is confirmed by ion-collector measurements, too. The average energy of fast electrons generated by resonant absorption is approximately two times smaller in the case of the 3ω main pulse (30–35 keV) as compared with the 1ω main pulse (50–70 keV) (Pisarczyk *et al.*, 2015).

Conclusion

1ω-experiment

Summing up the comparison of the experimental and numerical data we can claim that:

- Based on the interferometric results, measurements of the crater volume, spectroscopic determination of the temperature, and density near the ablation surface, and imaging *via* K_α emission, there is a good reason to conclude that the presence of pre-plasma leads to a decrease in the energy transfer efficiency of the main 1ω laser beam to a solid target by means of fast electrons. In the same time, 2DSs show that the presence of pre-plasma makes the conditions of resonant absorption of the laser radiation more favorable, increases the fraction of the laser energy absorbed by resonant mechanism, and hence increases the energy contained in the fast electron stream.

Table 4. Comparison of numerical simulations of the total δ_{total} , resonant δ_{res} , and inverse bremsstrahlung δ_{ib} absorption coefficients in the cases of pre-plasma absence and presence

R_L (μm)	50		100		200	
	3ω	$1\omega + 3\omega$	3ω	$1\omega + 3\omega$	3ω	$1\omega + 3\omega$
δ_{total}	0.593	0.553	0.751	0.691	0.876	0.789
δ_{ib}	0.505	0.462	0.655	0.592	0.806	0.716
δ_{res}	0.0883	0.091	0.0963	0.0993	0.0697	0.0733
$E_{\text{h(max)}}$ (keV)	69.4	73.8	62.3	69.6	58.2	54.8
T_{emax} (keV)	3.67	3.91	2.81	3.27	2.09	2.58

- The results of the interferometric measurements, as well as the results of 2DSs, show that the presence of pre-plasma decreases the axial density gradient.
- The decrease of the contribution of the fast electron energy transfer to a solid target when increasing the laser energy converted to fast electrons can be explained by the deterioration of the conditions of energy transfer by fast electrons in the presence of pre-plasma. There are two reasons for such a decline:
 - a large divergence of streaming fast electrons which are generated far from the target surface in the presence of pre-plasma and
 - the effect of plasma density gradient at the irradiated target boundary on the efficiency of energy transfer from the streaming fast electrons to the shock wave. Such an effect was predicted and numerically investigated in Nicolai *et al.* (2014).

3ω -experiment

The performed investigations show that by using the third-harmonic main pulse the laser energy conversion into the energy of fast electrons is very small – the fraction of fast electron energy does not exceed a few tenths of a percent of laser energy both in the absence and in the presence of pre-plasma. This conclusion deduced from K_α -emission measurements and numerical simulations is confirmed by the measurements of ion yield and volumes of laser-produced craters, which characterizes the amount of energy transferred to shock waves. The measurements of ion signals show virtually no contribution of the fast ion component. The crater volume measurements, in combination with femtosecond interferometry, both in the cases of pre-plasma presence and absence, show that the target ablation and evolution of laser-produced plasma are determined by energy transfer *via* electron conductivity under conditions of 1D or 2D matter expansion without any appreciable effect of energy transfer by fast electrons. Both the maximal volume of the crater (the maximum energy of the shock wave) and the minimal N/V_{cr} parameter corresponds to the greatest radius of the focal spot at which the negative effect of 2D-expansion of plasma is minimal and, as a result, the ablation pressure is maximal (Gus'kov *et al.*, 2004, 2014). This result holds for the experiments both in absence and presence of pre-plasma. With the decrease of focal spot radius the negative effect of 2D-plasma expansion increases and the crater volume decreases. This is in contrast with experiments with the first-harmonic main pulse, in which increasing the intensity of long-wavelength radiation leads to such a significant generation of fast electrons by the resonance mechanism and to such a strong effect of the fast electron energy transfer in the target depth that its contribution to the shock generation is significant and the crater volume

strongly increases with decreasing the focal spot radius (Gus'kov *et al.*, 2004, 2006, 2014).

Acknowledgements. This work has been carried out within the framework of the EUROfusion Enabling Research Project: AWP17-ENR-IFE-CEA-01 “Preparation and Realization of European Shock Ignition Experiments” and has received funding from the Euratom research and training programme 2014–2018 under grant agreement no. 633053. The views and opinions expressed herein do not necessarily reflect those of the European Commission. The work was also supported by the European Union LASERLAB IV project (Grant Agreement No. 654148), by the Russian Foundation for Basic Research under the Project No. 17-02-00059, by the MEFPh Academic Excellence Project (contract no. 02.a03.21.0005, 27.08.2013), by the Czech Ministry of Education, Youth and Sports, project LD14089 and projects LM2010014 and LM2015083 (PALS RI), and by the Czech Science Foundation, Project No. P205/11/P712. The authors also acknowledge support from the project High Field Initiative (HiFI) (CZ.02.1.01/0.0/0.0/15 003/0000449) and ELI Tools for Advanced Simulation (ELITAS) (CZ.02.1.01/0.0/0.0/16013/0001793), both from European Regional Development Fund. Finally, the authors are grateful to the PALS staff for help in running the experiments.

Author ORCIDs.  Tadeusz Pisarczyk <http://orcid.org/0000-0002-1109-7683>.

References

- Batani D, Antonelli L, Atzeni S, Badziak J, Baffigi F, Chodukowski T, Consoli F, Cristoforetti G, De Angelis R, Dudzak R, Folpini G, Giuffrida L, Gizzi LA, Kalinowska Z, Koester P, Krousky E, Krus M, Labate L, Levato T, Maheut Y, Malka G, Margarone D, Marocchino A, Nejd J, Nicolai P, O'Dell T, Pisarczyk T, Renner O, Rhee YJ, Ribeyre X, Richetta M, Rosinski M, Sawicka M, Schiavi A, Skala J, Smid M, Spindloe C, Ullschmied J, Velyhan A and Vinci T (2014) Generation of high pressure shocks relevant to the shock-ignition intensity regime. *Physics of Plasmas* **21**, 032710.
- Borodziuk S, Kaspercuk A, Pisarczyk T, Gus'kov SYu, Ullschmied J, Kralikova B, Rohlena K, Skala J, Kalal M and Pisarczyk P (2004a) Investigation of plasma ablation and crater formation processes in the Prague Asterix Laser System laser facility. *Optica Applicata* **34**, 31–42.
- Borodziuk S, Kaspercuk A, Pisarczyk T, Demchenko NN, Guskov SYu, Rozanov VB, Kalal M, Limpouch J, Ullschmied J, Kondrashov VN and Pisarczyk P (2004b) Application of the 3-frame interferometry and the crater replica method for investigation of laser accelerated macroparticles interacting with massive targets in the pals experiment. *Optica Applicata* **34**, 385–403.
- Borodziuk S, Demchenko NN, Gus'kov SYu, Jungwirth K, Kalal M, Kaspercuk A, Kondrashov VN, Krousky E, Limpouch J, Masek K, Pisarczyk P, Pisarczyk T, Pfeifer M, Rohlena K, Rozanov VB, Skala J and Ullschmied J (2005) High power laser interaction with single and double layer targets. *Optica Applicata* **35**, 242–262.
- Dostal J, Dudzak R, Pisarczyk T, Pfeifer M, Huynh J, Chodukowski T, Kalinowska Z, Krousky E, Skala J, Hrebicek J, Medrik T, Golasowski J,

- Juha L and Ullschmied J (2017) Synchronizing single-shot high-energy iodine photodissociation laser PALS and high-repetition-rate femtosecond Ti:sapphire laser system. *Review of Scientific Instruments* **88**, 045109.
- Gus'kov SYu, Borodziuk S, Kalal M, Kasperczuk A, Kralikova B, Krousky E, Limpouch J, Masek K, Pisarczyk P, Pisarczyk T, Pfeifer M, Rohlena K, Skala J and Ullschmied J (2004) Shock wave generation and crater formation in solids by a short laser pulse interaction. Generation of shock waves and formation of crater in a solid material irradiated by a short laser pulse. *Quantum Electronics* **34**, 989–1003.
- Gus'kov SYu, Kasperczuk A, Pisarczyk T, Borodziuk S, Kalal M, Limpouch J, Ullschmied J, Krousky E, Masek K, Pfeifer M, Rohlena K, Skala J and Pisarczyk P (2006) Efficiency of ablative loading of material upon the fast-electron transfer of absorbed laser energy. *Quantum Electronics* **36**, 429–434.
- Gus'kov SYu, Demchenko NN, Kasperczuk A, Pisarczyk T, Kalinowska Z, Chodukowski T, Renner O, Smid M, Krousky E, Pfeifer M, Skala J, Ullschmied J and Pisarczyk P (2014) Laser-driven ablation through fast electrons in pals experiment at the laser radiation intensity of 1–50 PW/cm². *Laser and Particle Beams* **32**, 177–195.
- Kalinowska Z, Kasperczuk A, Pisarczyk T, Chodukowski T, Gus'kov SYu, Demchenko NN, Ullschmied J, Krousky E, Pfeifer M, Rohlena K, Skala J and Pisarczyk P (2012) Investigations of mechanisms of laser radiation absorption at PALS. *Nukleonika* **57**, 227–230.
- Kasperczuk A, Makowski J, Paduch M, Tomaszewski K, Wereszczynski Z, Wolowski J and Wyzgal J (1993) Application of fast three-frame interferometry to investigation of laser plasma. *Proceedings of SPIE* **2202**, 449.
- Koester P, Antonelli L, Atzeni S, Badziak J, Baffigi F, Batani D, Cecchetti CA, Chodukowski T, Consoli F, Cristoforetti G, De Angelis R, Folpini G, Gizzi LA, Kalinowska Z, Krousky E, Kucharik M, Labate L, Levato T, Liska R, Malka G, Maheut Y, Marocchino A, O'Dell T, Parys P, Pisarczyk T, Raczka P, Renner O, Rhee YJ, Ribeyre X, Richetta M, Rosinski M, Ryc L, Skala J, Schiavi A, Schurtz G, Smid M, Spindloe C, Ullschmied J, Wolowski J and Zaras A (2013) Recent results from experimental studies on laser–plasma coupling in a shock ignition relevant regime. *Plasma Physics and Controlled Fusion* **55**, 124045.
- Lebo IG, Demchenko NN, Iskakov AB, Limpouch J, Rozanov VB and Tishkin VF (2004) Simulation of high-intensity laser plasma interactions by use of the 2D Lagrangian code ATLANT-HE. *Laser and Particle Beams* **22**, 267–273.
- Nicolai PH, Feugeas JL, Toutati M, Ribeyre X, Gus'kov SYu and Tikhonchuk V (2014) Deleterious effects of nonthermal electrons in shock ignition concept. *Physical Review E* **89**, 033107.
- Pisarczyk T, Gus'kov SYu, Kalinowska Z, Badziak J, Batani D, Antonelli L, Folpini G, Maheut Y, Baffigi F, Borodziuk S, Chodukowski T, Cristoforetti G, Demchenko NN, Gizzi LA, Kasperczuk A, Koester P, Krousky E, Labate L, Parys P, Pfeifer M, Renner O, Smid M, Rosinski M, Skala J, Dudzak R, Ullschmied J and Pisarczyk P (2014) Pre-plasma effect on energy transfer from laser beam to shock wave generated in solid target. *Physics of Plasmas* **21**, 012708.
- Pisarczyk T, Gus'kov SYu, Renner O, Demchenko NN, Kalinowska Z, Chodukowski T, Rosinski M, Parys P, Smid M, Dostal J, Badziak J, Batani D, Volpe L, Krousky E, Dudzak R, Ullschmied J, Turcicova H, Hrebicek J, Medrik T, Pfeifer M, Skala J, Zaras-Szydłowska A, Antonelli L, Maheut Y, Borodziuk S, Kasperczuk A and Pisarczyk P (2015) Pre-plasma effect on laser beam energy transfer to a dense target under conditions relevant to shock ignition. *Laser and Particle Beams* **33**, 221–236.
- Pisarczyk T, Gus'kov SYu, Renner O, Dudzak R, Dostal J, Demchenko NN, Smid M, Chodukowski T, Kalinowska Z, Rosinski M, Parys P, Badziak J, Batani D, Borodziuk S, Gizzi LA, Krousky E, Maheut Y, Cristoforetti G, Antonelli L, Koester P, Baffigi F, Ullschmied J, Hrebicek J, Medrik T, Pfeifer M, Skala J and Pisarczyk P (2016) Short wavelength experiments on laser pulse interaction with extended pre-plasma at the pals-installation. *Laser and Particle Beams* **34**, 94–108.
- Renner O, Smid M, Batani D and Antonelli L (2016) Suprathermal electron production in laser-irradiated Cu targets characterized by combined methods of X-ray imaging and spectroscopy. *Plasma Physics and Controlled Fusion* **58**, 075007.
- Salvat F, Fernandez-Varea JM and Sempau J (2009) Penelope-2008: A code system for Monte Carlo simulation of electron and photon transport. *Workshop Proceedings – Barcelona Spain June-3 July 2008*, ISBN 978-92-64-99066-1.
- Smid M, Antonelli L and Renner O (2013) X-ray spectroscopic characterization of shock-ignition-relevant plasmas. *Acta Polytechnica* **53**, 233.

Nuclear Reactions Studies in Laser-Plasmas at the forthcoming ELI-NP facilities

G. Lanzalone^{1,2,*}, A. Muoio^{1,4}, C. Altana^{1,3}, M. Frassetto⁵, L. Malferrari⁵, D. Mascali¹, F. Odorici⁵, S. Tudisco¹, L. A. Gizzi^{6,7}, L. Labate^{6,7}, S. M. R. Puglia¹, A. Trifirò^{4,8}

¹ Istituto Nazionale di Fisica Nucleare - Laboratori Nazionali del Sud – Via S. Sofia 62, 95123 Catania, Italy

² Università degli Studi di Enna “Kore” – Via delle Olimpiadi, 94100 Enna, Italy

³ Dipartimento di Fisica e Astronomia, Università degli Studi di Catania – Via S. Sofia 64, 95123 Catania, Italy

⁴ Dipartimento di Scienze MIFT, Università degli Studi di Messina – Viale F.S. D’Alcontres 31, 98166 Messina, Italy

⁵ Istituto Nazionale di Fisica Nucleare – Sezione di Bologna – Viale B. Pichat 6/2, 40127 Bologna, Italy

⁶ Istituto Nazionale di Ottica CNR - Via G. Moruzzi, 1 – 56124 Pisa, Italy

⁷ Istituto Nazionale di Fisica Nucleare, Sezione di Pisa, Largo Bruno Pontecorvo 3 - 56127 Pisa, Italy

⁸ Istituto Nazionale di Fisica Nucleare, Sezione di Catania - Via S. Sofia 64, 95123 Catania, Italy

*Corresponding author e-mail : Gaetano.Lanzalone@lns.infn.it

Abstract. This work aim to prepare a program of studies on nuclear physics and astrophysics, which will be conducted at the new ELI-NP Laser facility, which actually is under construction in Bucharest, Romania. For the arguments treated, such activity has required also a multidisciplinary approach and knowledge in the fields of nuclear physics, astrophysics, laser and plasma physics join with also some competences on solid state physics related to the radiation detection. A part of this work has concerned to the experimental test, which have been performed in several laboratories and in order to study and increase the level of knowledge on the different parts of the project. In particular have been performed studies on the laser matter interaction at the ILIL laboratory of Pisa Italy and at the LENS laboratory in Catania, where (by using different experimental set-ups) has been investigated some key points concerning the production of the plasma stream. Test has been performed on several target configurations in terms of: composition, structure and size. All the work has been devoted to optimize the conditions of target in order to have the best performance on the production yields and on energies distribution of the inner plasma ions. A parallel activity has been performed in order to study the two main detectors, which will constitute the full detections system, which will be installed at the ELI-NP facility.

1. Introduction

Given its nature, the plasma state is characterized by a complexity that far exceeds the one exposed by the solid, liquid, and gaseous states. Correspondingly, the physical properties of nuclear matter (structure, reaction mechanisms, lifetimes, etc.) could change inside the plasma. Thus, the study of



Content from this work may be used under the terms of the [Creative Commons Attribution 3.0 licence](https://creativecommons.org/licenses/by/3.0/). Any further distribution of this work must maintain attribution to the author(s) and the title of the work, journal citation and DOI.

these properties represents one of the most far ranging, difficult and challenging research areas today. Implications can cover also others fields, from quantum physics to cosmology, astrophysics, etc.

One of the crucial topics related to nuclear reactions in the ultra-low energy regime is the electron screening, which prevents a direct measurement of the bare nucleus cross section at the energies of astrophysical interest. Since in the laboratory interacting particles are in the form of neutral atoms, molecules or ions, in direct experiments at very low beam energy, electron clouds partially screen the nuclear charges thus reducing the Coulomb suppression. This results in an enhancement of the measured cross section compared with the bare nucleus one. The electron screening effect is significantly influenced by the target conditions and composition. In this context, it is of particular importance the measurement of cross-sections at extremely low energetic domains including plasmas effect, i.e. in an environment that under some circumstances and assumptions can be considered as "stellar-like". A further key point is connected with the fact that in such environment nuclear reactions can be triggered also by the excited states of the interacting nuclei. Thus, determining the appropriate experimental conditions that set the role of the excited states in the stellar environment can strongly contribute to the development of nuclear astrophysics [1]. The study of direct measurements of reaction rates in plasma offers this chance.

The future availability of high-intensity laser facilities [2,3] capable of delivering tens of peta-watts of power into small volumes of matter at high repetition rates will give the unique opportunity to investigate nuclear reactions and fundamental interactions under extreme plasma conditions, including also the influence of huge magnetic and electric fields, shock waves, intense fluxes of γ and X rays originating during plasma formation and expansion stages.

A laser is a unique tool to produce plasma and very high fluxes of photons and particles beams in very short duration pulses. Both aspects are of great interest for fundamental nuclear physics studies. In a plasma, the electron-ion interactions may modify atomic and nuclear level properties. This is of prime importance for the population of isomeric states and for the issue of energy storage in nuclei. Nuclear properties in the presence of very high electromagnetic fields, nuclear reaction rates or properties in hot and dense plasmas are new domains of investigation. Furthermore, with a laser it is possible to produce electric and magnetic fields strong enough to change the binding energies of electronic states. If nuclear states happen to decay via internal conversion (IC) through these perturbed states, a modification of their lifetimes will be seen. The excitation of nuclear levels by means of energy transfer from the atomic part to the nuclear part of an atom is the subject of a large number of investigations. Their goal is to find an efficient mechanism to populate nuclear isomers in view of further applications to energy storage and development of lasers based on nuclear transitions. In addition, other new topics can be conveniently explored such as three-body fusion reactions as those predicted by Hoyle [4,5].

Several Laser facilities are under construction around the world to push the physics beyond the actual level of knowledge. Among of these, the Extreme Light Infrastructure for Nuclear Physics at Magurele (Bucharest) in Romania, will be the only one devoted to Nuclear Physics studies.

ELI-NP [2] will be made up of a very high intensity laser system, consisting of two 10 PW laser arms able to reach intensities of 10^{23} W/cm² and electrical fields of 10^{15} V/m, and very short wavelength γ beams with very high brilliance (10^{13} γ /s) and energy up to 19.5 MeV. This combination allows for three types of experiments: stand-alone high power laser experiments, stand-alone γ beam experiments and combined experiments of both facilities. Here the low repetition rate (1/min) of the high power laser requires the same low repetition rate for the γ beam in combined experiments. While the standalone γ beam will be used with typically 120 kHz, the low repetition mode requires few very intense γ pulses. With the high power laser we do not plan to interact with nuclear dynamics directly, but we use the laser for ion acceleration or to produce relativistic electron mirrors followed by a coherent reflection of a second laser beam in order to generate very brilliant X-ray or γ beams. We plan to use these beams later to produce exotic nuclei or to perform new γ spectroscopy experiments in the energy or time domain. The production of heavy elements in the Universe, a central question of astrophysics, will be studied within ELI-NP in several experiments.

In this article some of the activities, related to the project of study of nuclear astrophysics at ELI-NP will be discussed. A brief introduction is given to present the main open problems on nuclear

astrophysics and the opportunity offered by the laser matter interaction scheme. Afterwards, it is shown a short presentation of ELI-NP project and the studies performed to prepare the future activities and test on plasma and nuclear detectors. Finally, some results of the tests performed on the new targets are presented and discussed.

2. Open problems on nuclear astrophysics

Accurate measurements of nuclear reaction rates of proton and alpha burning processes are essential for the correct understanding of many astrophysical processes, such as stellar evolutions, supernova explosions and Big Bang nucleosynthesis, etc. To this aim direct and indirect measurements of the relevant cross sections have been performed over the years. Since in the laboratory interacting particles are in the form of neutral atoms, molecules or ions, in direct experiments at very low beam energy, electron clouds partially screen the nuclear charges thus reducing the Coulomb suppression [6]. This results in an enhancement of the measured cross section compared with the bare nucleus one [7]. The electron screening effect is significantly affected by the target conditions and composition [8]; it is of particular importance the measurement of cross-sections at extremely low energetic domains including plasmas effect, i.e. in an environment that under some circumstances and assumptions can be considered as "stellar-like" (for example, for the study of the role played by free/bounded electrons on the Coulombian Screening can be done in dense and warm plasmas). Electron screening prevents a direct measurement of the bare nucleus cross section at the energies of astrophysical interest. In the last decade, the bare cross section has been successfully measured in certain cases by using several indirect methods [9]. Habitually, astrophysical appropriate reactions are performed in laboratories with both target and projectile in their ground state. However, at temperatures higher than about 10^8K , an important role can be also played by the excited states, as already deeply discussed in the innovative theoretical work of Bahcall and Fowler [10]. In that case, the authors studied the influence of low lying excited ^{19}F states on the final $^{19}\text{F}(\text{p},\alpha)$ reaction, predicting an increase of a factor of about 3 in reaction rate at temperatures of about 1-5 GK.

Thus determining the appropriate experimental conditions that allow the role of the excited states in the stellar environment could strongly contribute to the development of nuclear astrophysics. The study of direct measurements of reaction rates in plasma offers this chance. In addition others new topics can be conveniently explored such as three body fusion reactions as those predicted by Hoyle [4], lifetime changes of unstable elements [11] or nuclear and atomic levels [12] in different plasma environments; other fundamental physics aspects like non-extensive statistical thermodynamics [13] can be investigated in order to validate/confute the general assumption of local thermal equilibrium that is traditionally done for plasmas. The future availability of high-intensity laser facilities capable of delivering tens of peta-watts of power (e.g. ELI-NP) into small volumes of matter at high repetition rates will give the unique opportunity to investigate nuclear reactions and fundamental interactions under extreme conditions of density and temperature that can be reached in laser generated plasmas [14], including the influence of huge magnetic and electric field, shock waves, intense fluxes of X and γ -ray originated during plasma formation and expansion stages.

To investigate these research topics, we are proposing the construction of a general-purpose experimental set-up, where it will be possible to study the electronic screening problem in a wide variety of cases and configurations with different purposes [4,5,15]. Through the laser-target interaction, we aim at producing plasmas containing mixtures of $^{13}\text{C} + ^4\text{He}$ and $^7\text{Li} + \text{d}$ appropriate to investigate inner-plasma thermo-nuclear reactions. The $^{13}\text{C}+^4\text{He}$ reaction is of key interest for the investigation of the helium burning process in advanced stellar phases [16]. The $^7\text{Li}(\text{d},\text{n})^4\text{He}$ reaction was recently addressed by Coc et al. [17] as one of the most important reactions affecting the CNO abundances produced during the primordial nucleosynthesis (BBN). Very few experimental data exist, and authors consequently assume a constant S-factor ranging between two extreme hypotheses values.

Also, we propose to investigate the $^{11}\text{B}(^3\text{He}, \text{d})^{12}\text{C}^*$ reaction in a plasma. Nucleonic matter displays a quantum-liquid structure, but in some cases finite nuclei behave like molecules composed of clusters of protons and neutrons. To perform the proposed experiments, providing relevant data concerning the aforementioned reactions and others, we aim to take advantage from the excellent and unique

performance of the ELI-NP [2] facility and realize an experimental setup where two laser beams generate two colliding plasmas. The reaction products (neutrons and charged particles) will be detected through a new generation of plastic scintillators wall and through a new silicon carbides wall. The use of colliding plasma plumes appropriate for nuclear physics studies was suggested few years ago at LNS [14] and recently adopted also by other research teams [18]. One of the possible schemes may be the following: a first laser pulse imping on a ^{13}C , ^7Li or ^{11}B solid thin target (few micro-meters) producing, through the well-known TNSA [19] (Target Normal Sheath Acceleration) acceleration scheme, boron, carbon or lithium plasma. The rapidly streaming plasma impacts on a secondary plasma, prepared through the interaction of a second laser pulse on a gas jet target (made by ^4He , D_2 or ^3He). TNSA [19] was intensively studied in the last years; experiments [20] and models [21] show that this acceleration scheme works very well in the intensity domain between 10^{18} - 10^{20} W/cm^2 . The produced ions expand along a cone, whose axis is normal to the target surface, with a relatively low emittance [22].

3. Experimental Set-Up

The project will take advantage from the excellent and unique performance of the ELI-NP facility to create two colliding plasmas using two separate laser beams. The use of colliding plasma plumes suitable for nuclear physics studies [23] was proposed few years ago [14] and recently adopted to achieve such goal [18]. The idea is the following: a first laser pulse impinging on a ^{13}C , ^7Li or ^{11}B solid thin target (few micro-meters) produces, through the TNSA (Target Normal Sheath Acceleration) [20] acceleration scheme, boron, carbon or lithium plasma. In view of this, an extensive experimental investigation programme is in progress, aiming at the optimization of targets and interaction configuration [24,25]. The rapidly streaming plasma impacts on a secondary plasma, prepared through the interaction of a second laser pulse on a gas jet target (made by ^4He , D_2 or ^3He). The proposed activity requires also the construction of a highly segmented detection system for neutrons and charged particles. The segmentation is required for the reconstruction of the reactions kinematic. The ideal neutron detection module for these studies must exhibit: high efficiency, good discrimination of gammas from neutrons, good timing performance for ToF (Time of Flight) neutron velocity reconstruction. In addition, it must be able to work in hard environmental conditions, like the ones established in the laser-matter interaction area. All these aspects may be met by configuration based on $50 \times 50 \times 50 \text{ mm}^3$ PPO-Plastic scintillator plus a SiPM [26] read-out and a totally digital acquisition of the multi-hit signals. Concerning the charged particle detector, an R&D activity was funded by INFN on Silicon Carbide [27]. In this framework we aim to realize a wall of detectors. The SiC detectors have been proven recently to have excellent properties [28,29]: high energy and time resolution, resistance to radiation, low sensitivity to visible light, etc. The use of segmented SiC detectors would be very helpful for the study of nuclear reactions where only the position and energy measurement of light charged particles can give access to the desired information. In conclusion, we present in this contribution the research project that our collaboration will conduct in the next years @ELI-NP. More details about these activities are reported in reference [2].

4. Experimental Investigation on acceleration mechanisms and target.

A experimental campaign aiming at investigating the ion acceleration mechanisms through laser-matter interaction in femtosecond domain has been carried out at the Intense Laser Irradiation Laboratory (ILIL-Pisa, Italy) [30] facility with a laser intensity of up to $2 \cdot 10^{19} \text{ W}/\text{cm}^2$. In recent years, laser ion acceleration has gained much interest focusing on fast ions emitted from a solid target by intense laser irradiation [31,32]. Protons and heavier ions can be accelerated up to tens MeV per nucleon via various mechanisms such as target normal sheath acceleration (TNSA) [19,20,33,34], radiation pressure acceleration (RPA) [35-39], and break-out afterburner acceleration (BOA) [40-42]. Our work concerns the TNSA regime, in which an intense laser pulse is focused ($> 10^{18} \text{ W}/\text{cm}^2$) on different micrometers thick foil target.

In this context, we carried out a systematic experimental investigation to identify the role of target properties in TNSA, with special attention to target thickness and dielectric properties. We used a full range of ion, optical, and X-ray diagnostics to investigate laser-plasma interaction and ion

acceleration. We focus on the results obtained using a Thomson Parabola Spectrometer (TPS). In the TPS, often used in such experiments, ions with different charge-to-mass ratios are separated into distinct parabolas. This allows to extract information for each ion species when several ions are generated simultaneously in a given solid angle. In the paper [43] we discuss the energy spectra of light-ions depending on structural characteristics of the target. Surface and volume contributions to the ion acceleration have been clearly identified by using a unique target configuration consisting of a thin CD₂ foil. Preliminary results show that protons and deuterons temperatures show opposite trend, suggesting a complex interplay between surface and volume acceleration [43].

More experimental campaign [44] aiming at investigating the ion acceleration in laser-driven plasma with the production of a quasi-monoenergetic beam has occurred. At the LENS (Laser Energy for Nuclear Science) laboratory of INFN-LNS in Catania, experimental measures were carried out; the features of LENS are: Q-switched Nd:YAG laser with 2 J laser energy, 1064 nm fundamental wavelengths, and 6 ns pulse duration. Measures demonstrate that at the reached values of fluence even when using ns lasers, quasi-mono-energetic protons and aluminum ion beams can be generated. The presented results [45] represent a very stable and reproducible phenomenon. The production of mono-energetic protons from aluminum target was predicted by our previous work that correlated the spectrum to the initial proton distribution on the target. Preliminary results show the production of multi-charged ions having very narrow energy spreads [45-46]. The presented results are no singular manifestations, but represent a very stable and reproducible phenomenon. The production of quasi mono-energetic Alⁿ from aluminum target was predicted by our previous work [47] that correlated the spectrum to the initial ions distribution on the target. A linear dependence between the energy of the laser and the energy of the mono-peaks of ions produced is evident.

Also, we investigate the effects of innovative nanostructured targets [48] based on Ag nanowires on laser energy absorption in the ns time domain. The tested targets were realized at INFN-Bologna by anodizing aluminium sheets in order to obtain layers of porous Al₂O₃ of different thicknesses, on which nanowires of various metals are grown by electro-deposition with different heights. Targets were then irradiated by using a Nd:YAG laser at different pumping energies. Advanced diagnostic tools were used for characterizing the plasma plume and ion production. As compared with targets of pure Al, a huge enhancement (of almost two order of magnitude) of the X-ray flux emitted by the plasma has been observed when using the nanostructured targets, with a corresponding decrease of the "optical range" signal, pointing out that the energetic content of the laser produced plasma was remarkably increased. Signs of plasma stagnation, of great interest for carrying out inner-plasma studies, have been found [48]. Special targets, based on Co, Ni and Fe NWs, with high absorbance in the VIS and NIR range, have been irradiated with the same laser LENS. From preliminary results [49], a higher X-ray intensity was observed for all samples compared to bulk-Al, with about a ten-fold increase for Co NWs and around a five-fold increase for Ni and Fe NWs. Further tests are needed to explain such a difference among metals, which cannot be accounted in terms of different atomic numbers. Moreover, there are strong indications that plasma conditions for NWs targets are quite different from those obtained for bulk targets. This indication could be very promising, since it could open the possibility to study specific nuclear reactions in plasma, at high rates. Concerning the results on the plasma temperature analysis, NWs and the bulk-Al target seams have close temperatures. This scenario is consistent with the indication that plasma conditions for NWs targets are quite different from those obtained for bulk targets, at least in terms of plasma density and/or plasma stagnation [14]. If confirmed, these results could be very useful for nuclear physics studies, because can contribute to the increasing of the total reaction events.

All these experimental observations, although in a preliminary stage of analysis, provide a quite complete characterisation of the laser–target interaction regime in our experimental conditions and a reference set of data for the upcoming ELI-NP facility installation.

5. References

- [1] Rolfs C E et al. 1988 *Cauldrons in the cosmos: nuclear astrophysics*. (Chicago: University of Chicago Press. Harvard 18th ed.)

- [2] Negoita F et al. 2016 *Romanian Reports in Physics* **68** S37
- [3] Zamfir N V 2014 *N. Eur. Phys. J. Spec. Top.* **6** 223
- [4] Hoyle F 1946 *Monthly Notices of the Royal Astronomical Society* **106** 343
- [5] Hoyle F. 1954 *The Astrophysical Journal Supplement Series* **1** 121
- [6] Salpeter E E 1954 *Aust. J. Phys.* **7(3)** 373
- [7] Angulo C 1999 *Nucl. Phys. A* **656** 3
- [8] Lipoglavšček M 2010 *Eur. Phys. J. A* **44** 71
- [9] Spitaleri C et al. 2011 *Phys. Atom. Nucl.* **74** 1725
- [10] Bahcall N A 1969 *Fowler Astrophysical Journal* **157** 645
- [11] Limata B N 2006 *Eur. Phys. J. A* **27s01** 193
- [12] Hannachi F et al. 2007 *Plasma Phys. Control. Fusion* **49** B79
- [13] Tsallis C 2009 *Introduction to Nonextensive Statistical Mechanics (New York: Springer-Verlag)*
- [14] Mascali D et al. 2010 *Rad. Eff. and Def. in Sol.* **165** 730
- [15] Efimov V 2009 *Nature Phys.* **5** 533
- [16] Meyer B 1994 *Annu. Rev. Astron. Astrophys.* **32** 153
- [17] Coc A et al. 2010 *Astrophysical Journal* **744** 158
- [18] Labaune C et al. 2013 *Nature Comm.* **4** 2506
- [19] Macchi A et al. 2013 *Reviews of Modern Physics* **85** 751
- [20] Macchi A 2013 *A Superintense Laser-Plasma Interaction Theory Primer (Netherlands: SpringerBriefs in Physics)*
- [21] Passoni M et al. 2008 *Phys. Rev. Lett.* **101** 115001
- [22] Borghesi M et al. 2004 *Phys. Rev. Lett.* **92** 055003
- [23] Lanzalone G et al. 2016 *EPJ Web of Conferences* **117** 05008
- [24] Tudisco S et al. 2015 *Rev. Sci. Instrum.* **87** 02A909
- [25] Gizzi L A et al. 2011 *Phys.Review ST Acc. Beams* **14** 011301
- [26] Privitera S et al. 2008 *Sensors* **8(8)** 4636
- [27] Muoio A et al. 2016 *EPJ Web of Conferences* **117** 10006
- [28] Moll M 2003 *NIM in Physics Research A* **511** 97
- [29] Sandeep K et al. 2013 *NIM A* **728** 97
- [30] Gizzi L A et al. 2017 *Appl. Sci.* **7(10)** 984
- [31] Clark E L et al. 2000 *Phys. Rev. Lett.* **85** 1654
- [32] Hegelich O M et al. 2002 *Phys. Rev. Lett.* **85** 085002
- [33] Fuchs J et al. 2006 *Nature Physics* **2** 48
- [34] Passoni M et al. 2010 *New J. Phys.* **12** 045012
- [35] Esirkepov T et al. 2004 *Phys. Rev. Lett.* **92** 175003
- [36] Robinson A P L et al. 2008 *New J. Phys.* **10** 013021
- [37] Robinson A P L et al. 2009 *Plasma Phys. Control. Fusion* **51** 024004
- [38] Macchi A et al. 2010 *New J. Phys.* **12** 045013
- [39] Qiao B et al. 2012 *Phys. Rev. Lett.* **108** 115002; Kar S. et al. 2012 *ibid.* **109** 185006
- [40] Yin L et al. 2006 *Laser Part. Beams* **24** 291
- [41] Yin L et al. 2011 *Phys. Rev. Lett.* **107** 045003
- [42] Gizzi L A et al. 2011 *Phys. Rev. ST Accel. Beams* **14** 011301
- [43] Tudisco S et al. 2016 *Review of Scientific Instruments* **87** 02A909
- [44] Altana C et al. 2016 *Review of Scientific Instruments* **87** 02A914
- [45] Muoio A et al. 2016 *Nuclear Instruments and Methods in Physics Research A* **829** 141
- [46] Altana C et al. 2016 *Nuclear Instruments and Methods in Physics Research A* **829** 159
- [47] Mascali D et al. 2012 *EPL(Europhysics Letters)* **100** 45003
- [48] Lanzalone G et al. 2016 *Review of Scientific Instruments* **87** 02B324
- [49] Muoio A et al. 2017 *Journal of Instrumentation* **12** C03076

Contents lists available at [ScienceDirect](https://www.sciencedirect.com)

Nuclear Inst. and Methods in Physics Research, A

journal homepage: www.elsevier.com/locate/nima

A viable laser driver for a user plasma accelerator

L.A. Gizzi^{a,*}, P. Koester^a, L. Labate^a, F. Mathieu^b, Z. Mazzotta^b, G. Toci^c, M. Vannini^c^a Intense Laser Irradiation Laboratory, Istituto Nazionale di Ottica, CNR, Pisa, Italy^b Ecole Polytechnique, CNRS, Palaiseau, France^c Istituto Nazionale di Ottica, CNR, Firenze, Italy

A B S T R A C T

The construction of a novel user facility employing laser-driven plasma acceleration with superior beam quality will require an industrial grade, high repetition rate petawatt laser driver which is beyond existing technology. However, with the ongoing fast development of chirped pulse amplification and high average power laser technology, options can be identified depending on the envisioned laser–plasma acceleration scheme and on the time scale for construction. Here we discuss laser requirements for the EuPRAXIA infrastructure design and identify a suitable laser concepts that is likely to fulfill such requirements with a moderate development of existing technologies.

1. Introduction

Laser-driven plasma accelerators for user applications will require high repetition rate laser drivers capable of petawatt peak power and kW average laser power. The worldwide scenario for this kind of technology is rapidly evolving and new concepts are emerging with the promise of addressing medium and long term objectives of laser–plasma acceleration [1] and future plasma-based particle colliders. However, scaling the technology of existing high peak power lasers based on Chirped Pulse Amplification (CPA) [2] to higher average power remains challenging. Pulsed high energy solid state lasers have demonstrated continuous operation at energies of approximately 100 J and repetition rates up to 10 Hz (e.g., RAL's DiPOLE100 [3] and the LLNL HAPLS [4]). Solid-state lasers with peak power in the petawatt class [5] and pulse energies exceeding 10 J have reached an average power of tens of watts (BELLA [6]), with HAPLS aiming at 300 W. In order to address user-level requirements, average power of ultrafast lasers will have to increase by one or two orders of magnitude.

In this scenario, the EuPRAXIA infrastructure design study [7] aims at delivering a full concept for a compact, user-oriented, plasma accelerator with superior beam quality to enable free electron laser operation in the X-ray range and other developments of advanced compact radiation sources. In its current configuration, the infrastructure relies on three main laser systems to drive plasma acceleration in different configurations, including the 150 MeV injector, the 1 GeV injector/accelerator and 5 GeV accelerator stage.

A pulse duration as short as 30 fs is required for the first two configurations with an energy per pulse as high as 100 J for the 5 GeV accelerator configuration. A repetition rate ranging from a minimum

of 20 Hz up to 100 Hz is envisioned to fulfill user operation. To achieve its goals the infrastructure will therefore require a laser driver ranging from 1 kW to 10 kW average laser power and petawatt peak power. As shown in Fig. 1, such specifications are beyond current demonstrated performances but, as discussed here, they may be reached with incremental developments of current technology, although full accomplishment may require step changes based on novel technologies.

Several technologies are developing which aim at high repetition rate, higher average power levels and energy-efficient configurations. Fiber laser technology is currently offering the best wall-plug efficiency for a laser, now exceeding 50% in CW mode, and solutions based on the coherent combination of a very large number of fiber amplifiers is being developed [8,9]. Such a technology is particularly suited and cost-competitive for applications requiring low energy per pulse and higher repetition rate, as technology is really optimized for repetition rate of 10 kHz and above.

Direct Chirped Pulse Amplification (DCPA) using lasing media that can be pumped directly with diodes may offer higher efficiency and higher rep-rate. DCPA concepts currently under development, including Yb:YAG and Yb:CaF provide effective solution for 100 fs or longer pulses, while for shorter pulses like those envisioned for EuPRAXIA, new amplifying media are needed capable of a larger bandwidth. Recently, big aperture Tm:YLF (BAT) concept has been proposed [10] that offers significant lifetime advantage over Yb doped materials for multi-pulse extraction and becomes very efficient for kHz repetition rates and above. Moreover, the BAT architecture may allow amplification of shorter pulse duration than Yb based systems and would be more efficient for wakefield excitation due to the longer plasma wavelength of $\lambda \approx 1.9\mu\text{m}$.

* Corresponding author.

E-mail address: la.gizzi@ino.cnr.it (L.A. Gizzi).<https://doi.org/10.1016/j.nima.2018.02.089>

Received 8 December 2017; Received in revised form 17 January 2018; Accepted 19 February 2018

Available online 27 March 2018

0168-9002/© 2018 Published by Elsevier B.V.

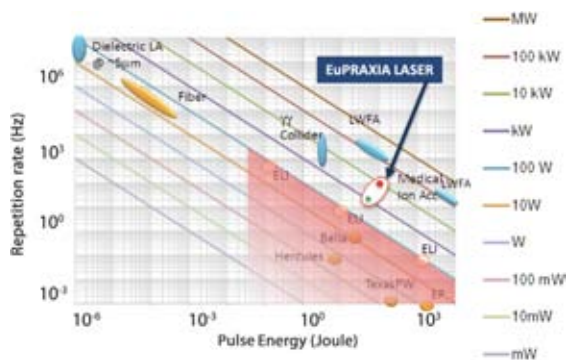


Fig. 1. The main EuPRAXIA laser specifications for the minimum mandatory configuration (green dot) and the best effort specifications (red dot). (For interpretation of the references to color in this figure legend, the reader is referred to the web version of this article.)

The EuPRAXIA laser design focuses on a relatively short time-scale for construction of the infrastructure. In view of this, the laser design relies primarily on the most established laser technologies currently available, namely those that are likely to be scaled to the required specifications starting from existing prototypes. Titanium Sapphire technology pumped by 0.5 μm , diode-pumped solid state (DPSSL) lasers, provides a relatively safe ground, with major industrial endeavor in place, on which the required developments can also build. As discussed here, technologies addressing some of the most critical aspects related to the high average power operation, primarily pump sources, but also cooling strategies for the amplifying media and for the compressor diffraction gratings, are reaching a readiness level that can make it reasonably possible their deployment in the required time scale.

2. Preliminary laser design

The baseline architecture of the EuPRAXIA laser relies on Ti:Sa technology and includes the most advanced components implemented so far in industrial systems plus leading edge technologies to conceive operation of the demanding detailed specification. Simultaneous operation of the three main laser systems and auxiliary laser beams for diagnostics and photocathode laser are considered, with a common oscillator. As shown in Fig. 2, each laser chain includes a front-end, amplification sections, a propagation area and a compressor, with final transport to the target.

As for the front-end, in order for the spectral amplitude/phase to be adjusted independently, three separated systems are envisaged, sharing the same oscillator and a common architecture. Each of these front-end will deliver stretched pulses with 1 J energy to the subsequent amplification stages.

2.1. Front-end

The architecture adopted here is similar to several state of the art front-end systems available also as a commercial solution [e.g. Amplitude Technologies, 100 Hz]. After a common oscillator, shared among the three systems, a first CPA stage is devoted to the amplification of the pulse at the 1mJ level, which is required to efficiently pump an XPW stage immediately downstream. The resulting pulse, with typical energy of the order of 10–100 μJ is then seeded into the main CPA chain. The energy is then increased up to the >1 J level, needed by the subsequent amplification stages, by means of a regenerative amplifier and two multipass amplifiers, all running at 20 Hz (P0 level) or 100 Hz (P1 level).

Table 1

Main requirements of the laser drivers for the injector at 150 MeV (top), the injector at 1 GeV (middle) and the accelerator at 5 GeV (bottom), and for the mandatory (P0) and best effort (P1) performance levels.

Laser 1 - Injector 150 MeV			
Parameter	Label	P0	P1
Wavelength (nm)	λ_1	800	800
Maximum energy on target (J)	E_{target}	5	7
Maximum output energy (J)	E_{out}	8.8	12.5
Energy tuning resolution (% of targeted value)	δE	7	5
Total output energy (including diagnostic beams)	E_{tot}	7	10
Pulse length (FWHM) (fs)	τ_1	30	20
Repetition rate (Hz)	f_1	20	100
Requirement on energy stability (RMS) %	$\sigma_{<E>}$	1	0.6
Laser 2 - Injector 1 GeV			
Parameter	Label	P0	P1
Wavelength (nm)	λ_2	800	800
Maximum energy on target (J)	E_{target}	15	30
Maximum output energy (J)	E_{out}	18.8	37.5
Energy tuning resolution (% of targeted value)	δE	7	5
Shortest pulse length (FWHM) (fs)	τ_2	30	20
Repetition rate (Hz)	f_2	20	100
Requirement on energy stability (RMS) %	$\sigma_{<E>}$	1	0.6
Laser 3 - Driver 5 GeV			
Parameter	Label	P0	P1
Wavelength (nm)	λ_3	800	800
Maximum energy on target (J)	E_{target}	50	100
Maximum output energy (J)	E_{out}	62.5	125
Energy tuning resolution (% of targeted value)	δE	7	5
Shortest pulse length (FWHM) (fs)	τ_3	60	50
Repetition rate (Hz)	f_3	20	100
Requirement on energy stability (RMS) %	$\sigma_{<E>}$	1	0.6

2.2. Power amplification

The amplification stages of the different beamlines will rely on Chirped Pulse Amplification in Ti:Sapphire, pumped by frequency doubled solid state Nd or Yb based lasers with emission in the range 515–532 nm. This technology is already well established for the amplification of ultrashort pulses down to a duration of <20 fs, and with energies >100 J. The most challenging point in the design of the required system is mainly related to the high pulse repetition rate, resulting in high average pump power requirements and thus setting a severe thermal load on the amplification stages. Indeed, petawatt lasers systems typically run in single shot mode or up to 1 Hz, whereas the EuPRAXIA uses a pulse repetition rate from 20 to 100 Hz.

A preliminary design of the amplification stages was carried out considering the cooling requirements as one of the main and most demanding design drivers. Combination of conductive cooling through the crystal mounts and convective cooling in air of the amplifying crystal, the most commonly used cooling techniques in low repetition rate systems, may result insufficient for high repetition rate operation at the required energy levels. In order to minimize pump power requirements and thermal dissipation needs, a detailed analysis was carried out of all the factors affecting the conversion from pump energy to energy on target, including extraction efficiency, transport and compression.

Another driver in the design study was the modularity of the laser system. As pointed out before, some different plasma injection and amplification configurations are currently under consideration, resulting in a set of laser amplification chain systems with different requirements. These laser systems can be considered as consisting of a limited set of base modules that can be used alone, or built in multi-stage amplification chains, with minor adaptations. In view of an industrial development, this approach will help to reduce costs and development time.

A schematic layout of power amplification sections for each laser system is given in Fig. 3. Here the modules AMP1 and AMP2 have the

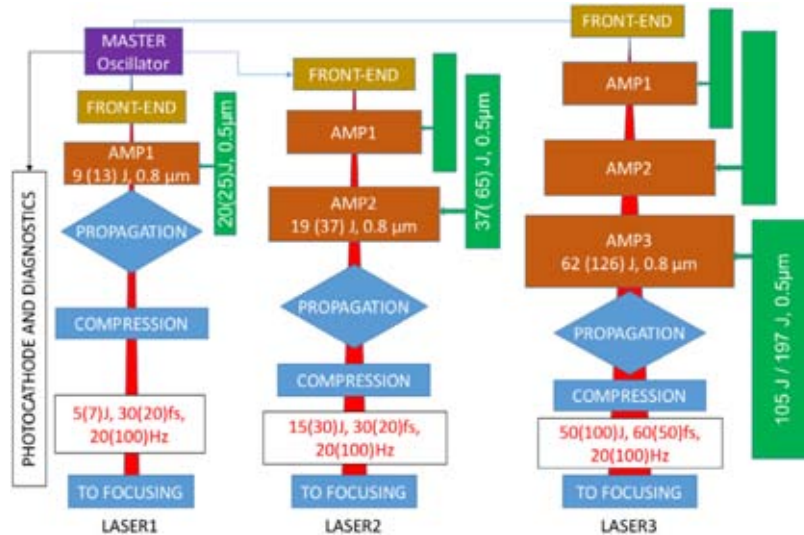


Fig. 2. General layout of the EuPRAXIA laser, including the main blocks, from the common master oscillator, to the front-end, the power amplifiers, the propagation and the compressor. The main specifications of the system before and after the compression stage are also specified. The main pumping units are also included with the respective specifications at 0.5 μm wavelength.

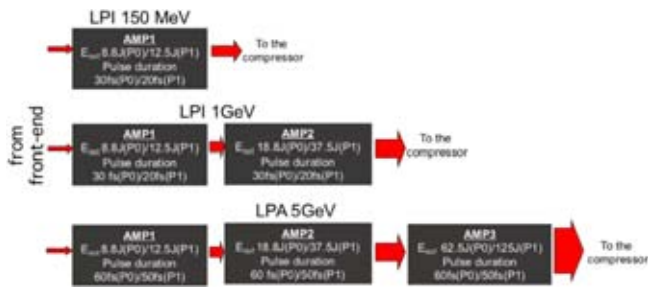


Fig. 3. Layout of the power amplification sections of the three laser lines.

same structure and they operate on the same input/output and pump energies, although they operate on pulses with different bandwidth, due to the different compressed pulse duration. The module AMP3 is the final energy booster specific for the 5 GeV accelerator.

Water cooling at room temperature of thin disk shaped crystals may be a suitable solution. This approach has been recently proposed [11] to achieve high repetition rate operation in multi-PW Ti:Sapphire laser systems, and it is currently under development in the frame of the ELI-ALPS related activities. Another possible approach is the cooling of the crystals (shaped as thin slabs) with a high speed gas flow at cryogenic temperatures, as used for instance in the DIPOLE system (see for instance [12,13]). This technology is currently demonstrated up to 10 Hz and an average pump power of 4.65 kW. With respect to water cooling this approach is more complex, and its cooling capability are limited by the smaller heat capacity of the flowing gas with respect to water.

Finally, the scalability of the technical solutions has also been considered as a guideline in the preliminary design study. The EuPRAXIA specifications for the various laser systems currently foresees two performance levels. The first one (PO) is considered as a (relatively) conservative performance, achievable with reasonable incremental developments of currently available laser technologies; the second one (P1) is more challenging, and it will require a more considerable technological effort.

Based on these considerations power amplifiers were designed with attention to the individual modules and the respective dimensioning, in terms of pump energy, size and doping of the crystals, beam cross

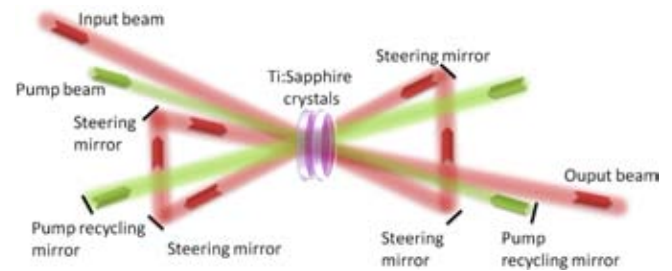


Fig. 4. Schematic representation of a 3-pass amplification stage, in transmission geometry. The two pump beams are counter-propagating in the crystal, and after the first pass each one is back-reflected in the crystal for a second pass. The gain medium is considered to be split in two identical crystals.

sections. Output energies, output pulse width, output beam profile, sensitivity to parameters, requirements on input pulse/beam were calculated using numerical simulations. Finally, cooling requirements and water cooling architectures have been investigated and a preliminary assessment of the thermal behavior of the different modules was made including thermal aberrations.

2.3. Module dimensioning

The three laser modules described above were dimensioned by means of numerical simulations using the code MIRO developed by CEA [14], using the built-in amplification model for Ti:Sapphire. The simulations were validated by comparison with real laser systems [15–17]. These case studies were considered relevant because the operating parameters of these systems are similar in terms of pump fluence, single pass gain and output energies. As a baseline design, all the amplifying modules feature a multi-pass amplification architecture, between 4 to 6 passes, depending on the stage, and a two-side injection of the pump beams. A conceptual scheme is shown in Fig. 4, for a 4 pass layout.

As it will be described in details below, for thermal management reasons, the amplifying crystal will not be monolithic, but it will be divided in few identical sub-crystals (typically 2), face cooled by a liquid flow, to increase the available cooling surface. This fractioning of the crystal has no impact on the overall energy amplification performances.

In all the simulations, the seed pulse was assumed to have a Gaussian spectral shape, with a bandwidth corresponding to the desired pulse duration FWHM (assumed at the Fourier limit) with a stretched duration of 500 ps FWHM and a Gaussian temporal shape, regardless its bandwidth and compressed pulse duration, as a result of the stretching before the amplification. The pump beam and the injected beam were assumed to have a super-Gaussian power distribution profile with index 8; pump and seed beam diameters were chosen so that the seed beam is slightly narrower than the pump beam, in order to have a more uniform gain profile. Each pump beam is assumed to pass twice in the amplifying crystal.

The amplifying crystals were considered cylindrical, with a clear aperture larger than the pump beam of about 10 mm and a standard orientation, that is with the c axis perpendicular to the propagation direction and parallel to the polarization of the amplified beam. Doping level of the crystals has been chosen to have a high absorption (>90%) of the pump pulses, on a double pass configuration. The absorption data with respect to doping level were derived from commercial materials datasheets (see for instance [18] [GT 2013]). Pumping wavelength was assumed 532 nm. In case of different pumping wavelength (e.g. 514 nm or 527 nm) the pumping energy levels must be scaled with the ratio (532 nm)/ λ_{pump} , to ensure the same pump photon flux. The doping level of the crystals must be revised accordingly. Passive losses (e.g. at the optical interfaces, on the mirrors or due to volume scattering) were not considered in this phase.

The transverse gain G_T was estimated on the basis of the pump fluence, crystal size and doping using analytical formulas (see for instance [16,19]). It is assumed that the crystal lateral faces will be surrounded by an absorbing, index matching liquid, or by an absorbing coating to prevent the onset of parasitic lasing (PL) effects. Considering that the residual diffuse reflection coefficient achievable at the crystal surfaces by these means is of the order of 10^{-3} [17] an estimated threshold level for the suppression of the PL effects is $G_T \ll 10^3$. Moreover, to reduce the transverse gain the amplifying crystals were pumped from both sides. To mitigate parasitic lasing, Extraction During Pumping (EDP) was implemented. Typically, a two-step pumping was adopted, with different pump energy repartition between the two pumping steps. The transverse gain was calculated for each passage, on the basis of the residual stored energy and the injected energy, by means of the Frantz–Nodvick formulas [20]. The sensitivity of the output energy to the pump and seed pulse energy was determined by calculating the variation output energy obtained with small variations in the pump and seed energy; the relevant slopes were then calculated by linear interpolation. These slopes will be denoted as S_{seed} and S_{pump} below.

As an example we focus here on the output of the amplifier module AMP3 which is the most demanding in terms of size and specifications. The AMP3 module is based on a 6 pass amplification scheme, with re-pumping before the 3rd pass as EDP scheme. It is assumed that this stage is injected by the whole output energy available from AMP2. A summary of the output parameters is given in Table 2. As it can be seen, the calculated output energy (62.4 J) matches the requirements.

A set of output plots is shown in Fig. 5 including the pulse energy as a function of the number of passes, the input and output spectra and beam fluence profiles, for the P0 performance (top) and P1 performance (bottom). In the case of P0 performance level, due to the relatively long output pulse duration requirements (compressed output pulse duration 60 fs FWHM) the input pulse bandwidth is 18.7 nm FWHM, corresponding to a compressed pulse duration (to the Fourier Transform limit) of 50 fs. This leaves 10 fs of margin for incomplete recompression. The red shift of the amplified pulse peak was found 1 nm with respect to the input pulse, so that the input pulse spectrum must be peaked at 799 nm to have an output spectrum peaked at 800 nm. The spectral bandwidth at the output is 18.8 nm, with a negligible broadening with respect to the input pulse as shown in Fig. 5. Regarding the output beam shape, the FWHM of the output beam remains substantially unchanged with respect to the input beam as it can be seen in the top-right plot of Fig. 5.

Table 2

Main output parameters of the AMP3 module for the P0 and P1 level of performances as obtained from numerical simulations.

Output	P0	P1
Crystal clear aperture \varnothing (cm)	16	16
Doping level (%Wt.)	0.03	0.03
Pump energy (J)	105	197
Pump fluence at crystal surfaces (J/cm ²)	0.51	0.95
Seed pulse energy (J)	18.8	37.5
Output energy (J)	62.4	126.0
Output beam diameter (FWHM) (cm)	12.8	13.0
EDP scheme (1st pass, 3rd pass)	65%, 35%	65%, 35%
S_{pump} ($\Delta E_{\text{out}}/\Delta E_{\text{pump}}$)	0.53	0.54
B integral	0.17	0.22
Crystal thickness (cm, overall)	3.2	3.2
Absorption coefficient (cm ⁻¹)	0.47	0.47
Pump beam diameter (FWHM) (cm)	14.0	14.0
Absorbed pump energy	96%	96%
Seed beam diameter (FWHM) (cm)	12.8	12.8
Extraction efficiency	41.5%	44.9%
Output beam peak fluence (J/cm ²)	0.49	1.08
Max G_T (before 1st pass)	~18	~20
S_{seed} ($\Delta E_{\text{out}}/\Delta E_{\text{seed}}$)	1.64	1.4

For the P1 performance, the upscaling of the output performances is achieved by increasing the pump pulse energy, but leaving unchanged the geometrical parameters. The number of passes is reduced to 4 due to the higher energy of injection. The main parameters are resumed in the right column of Table 2. As it can be seen, the calculated output energy (126 J) matches the required level as given in Table 1. The pulse energy as a function of the number of passes is shown in the bottom-left plot of Fig. 5. Due to the higher pump fluence and energy, the transverse gain is higher as well as the B integral, but both values are well within safety limits. The pulse bandwidth is larger than in the case of the P0 specification, because the required compressed pulse duration is smaller (50 fs FWHM). In this case a input pulse bandwidth of 23.3 nm FWHM, corresponds to a compressed pulse duration (to the Fourier Transform limit) of 40 fs. This leaves 10 fs of margin for incomplete recompression. The red shift of the amplified pulse peak was found 3 nm with respect to the input pulse, so that the input pulse spectrum must be peaked at 797 nm to have an output spectrum peaked at 800 nm. The spectral bandwidth remains substantially unchanged as shown in the bottom-center plot of Fig. 5. Regarding the output beam shape, the FWHM diameter of the output beam increases to 12.4 cm, due to the amplification of the beam wings, as it can be seen in the bottom-right plot of Fig. 5.

3. Pump lasers

As outlined above, pump laser requirements are a critical aspect of our design. Our approach was to minimize pump laser needs while optimizing extraction efficiency and relying on efficient transport and compressor throughput and optimized second harmonic conversion efficiency of pump lasers. The compressor throughput was assumed to be 80%, achievable with a single grating reflectivity better than 95%. Such a value is not far from current commercial grating technology providing gold coated gratings with demonstrated reflectivity between 90% and 94% at 800 nm. We also assume a conversion efficiency from 1 μm pump energy to 0.5 μm of 70%, a conservative value if compared to the 80% conversion efficiency demonstrated recently [De Vido, 2016]. Based on these assumptions, we obtain average IR pump power requirements ranging from 0.5 kW for the first amplifier module AMP1 at 20 Hz, to approximately 30 kW for the last amplifier module AMP3 at 100 Hz. The corresponding total pulse energies at 0.5 μm range from 20 J to 200 J, resulting in a IR pump pulse energy ranging from 27 J to 280 J. The survey of suitable pump lasers capable of delivering these performances was based on an extensive evaluation of currently available technologies. Moreover, a similar analysis was carried out in

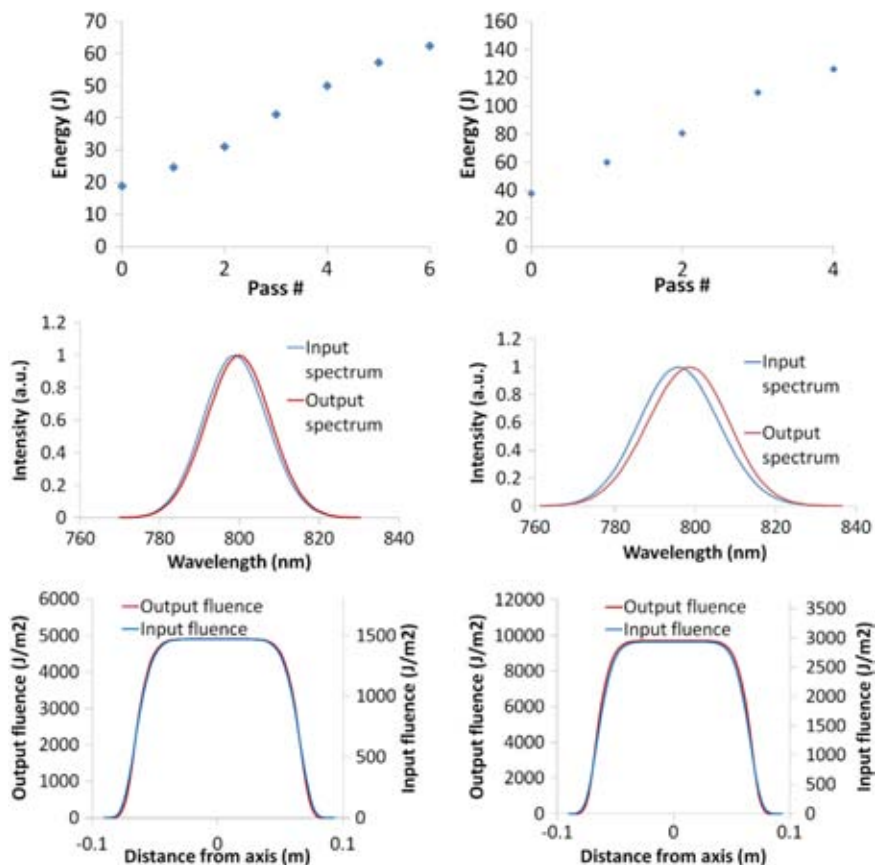


Fig. 5. Pulse energy as a function of the number of passes for the AMP3 module (top); Input and output spectrum for the AMP3 module (middle); Input and output beam fluence profile for the AMP3 module at P0 performance level (bottom). The two profiles have been scaled to have the same graphical appearance. Note that the horizontal scale is in m and the vertical scale is in J/m^2 ($=10^4 \text{ J}/\text{cm}^2$). The top set refers to the P0 performance level while the bottom set refers to the P1 performance level.

the framework of the k-BELLA project (W.Leemans, EAAC 2017). These investigations consistently suggest that diode pumped Yb based systems are emerging as candidates to sustain the envisaged average power. At the same time, Nd based systems also proved to be capable of rep-rated operation at average power levels relevant for our aims. At this stage we can identify three different technologies for the three EuPRAXIA lasers, all based on diode pumping or adaptable to diode pumping and all having been demonstrated at a sufficient average power level to give confidence on their technical feasibility.

4. Thermal management

The levels of thermal load considered here range for 200 W for the smaller energy amplifier module to 10 kW for the maximum laser energy (AMP3) at the highest performance level (P1). We envisage two cooling techniques for the Ti:Sapphire crystal, namely cooling with water flow and cooling with He flow at cryogenic temperatures. Water cooling of thin Ti:Sapphire crystal disks has been recently tested on a small scale system [Cvykow 2016] and scaling up to kW levels have been studied by Nagymihaly et al. [Nagymihaly 2017]. Thin disk (TD) technology may offer the possibility for Ti:Sa crystals to be used in high average output power systems because the longitudinal direction of heat extraction greatly reduces thermal lensing; scalability can be obtained by segmenting the required crystal length in thinner slices, each one individually cooled. The general scheme of this approach is shown in Figs. 6–8. The surface of the disks is cooled by a high speed flow (several m/s) of water at room temperature. The water flow is confined between the crystal surface and an optical window. The crystal can be cooled from both sides: in this case the use of counterpropagating water flows ensures a more uniform temperature profile across the disk aperture.

Cooling with gas flow at cryogenic temperatures is a technique currently under advanced development for high average power, diode pumped Yb:YAG lasers, using a multi-slab architecture. This technique has been adopted for the realization of DiPOLE Yb:YAG amplifiers, targeting the generation of 10 J and 100 J ns laser pulses at a repetition rate of 10 Hz [12,13,21]. It has also been applied to the development of an Yb:CaF₂ high energy amplifier [22]. Cooling is obtained by a He gas flow with temperature in the range 125–175 K, 5–10 bar of pressure and a flow velocity around 25 m/s. For several reasons, water cooling of thin disks is considered as the candidate technology for the cooling of the amplification stages. In fact, water cooling at near room temperature is easier to implement than gas cooling at cryogenic temperature and the cooling capability achievable with the water flow is higher than with the gas flow, due to the much higher heat capacity of the cooling fluid. Indeed, heat removal rates per unit surface, expressed by the average Heat Transfer Coefficient, HTC) are about 1 order of magnitude higher for water cooling than for gas cooling; this is particularly relevant in view of the scaling up of the system toward high average power levels. In order to achieve a sufficient heat removal rate, gas cooling requires a large heat exchange surface. This implies that the gain medium is usually split in several slabs, increasing the occurrence of parasitic reflections at interfaces, which can be detrimental for the pulse contrast. Conversely, for a given overall gain length water cooling allows using a smaller number of thicker slabs thus reducing the risk of parasitic reflections. A potential drawback of the water cooling technique is that the turbulences and temperature gradients in the water flow can induce aberrations in the laser beams. This can be critical in particular in the schemes where the amplified beam crosses the cooling flow.

Nonetheless, a similar approach has already been experimented in some high power laser sources. For instance Fu et al. [23] have recently

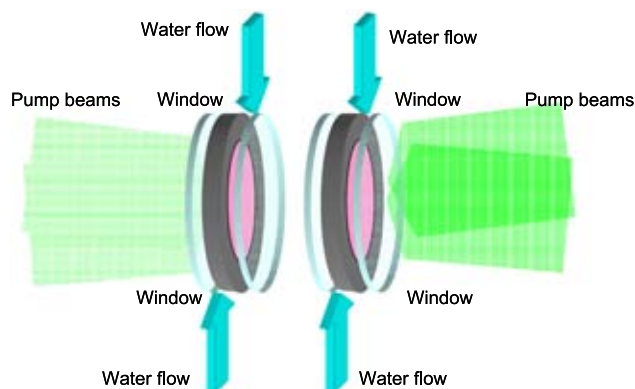


Fig. 6. Schematics of the twin thin disk crystal assembly. Each crystal is individually cooled by two counterpropagating water flows, confined by an optical window. The outer ring of the crystal features an absorbing region or edge coating for ASE and parasitic lasing suppression. Pump beams are also represented.

proposed a 3 kW CW liquid cooled Nd:YAG laser. Multiple Nd:YAG slabs are face cooled by a flow of deuterated water (D_2O) which is crossed by the laser beam. Here D_2O is used instead of H_2O because of the absorption at 1064 nm of H_2O , but it should not be needed at 800 nm. A similar cooling scheme was adopted by Wang et al. [24] for a 7 kW Nd:YAG laser system. Also in this case the gain medium is split in several slabs, face cooled by a high speed D_2O flow crossed by the laser beam. It must be noticed that both devices are oscillators and not multi-pass amplifiers. This is an even more critical arrangement because the effect of the aberrations induced by the flow turbulences are accumulated over the high number of intra-cavity passes. Finally, a similar approach was demonstrated to be effective in the so-called Disk Amplifier Head (DAH) used in the P-series by Amplitude Technology. A possible alternative, that was also considered in the design, is the use of a reflection geometry where the laser beam is reflected on the back side of the amplifying crystal. In this case the crystal is fluid cooled on its back side only, so that the laser beam does not cross the cooling fluid flow. This eliminates the problem of the fluid turbulences affecting the propagation of the laser beam, at the price of a reduction of the available cooling surface. This geometry was experimented for instance by V. Cvhykov et al. [25] for a Ti:Sapphire amplifier.

In the case of the transmission scheme with two crystals with half-length is depicted in Fig. 6 the heat removal capability of the system is doubled with respect to a single crystal and a relatively low crystal doping level can be used, easing parasitic lasing suppression.

For the preliminary evaluation of thermal effects, it was assumed that about 50% of the absorbed pump energy is dissipated as heat in the crystals (heat efficiency factor = 0.5). The thermomechanical behavior of the crystals was modeled using a commercial software package, i.e. LAS-CAD (ver. 3.6.1) developed by LAS-CAD GmbH (www.las-cad.com). The software features several numerical tools for the modeling of solid state laser systems. Among them, a Finite Element Analysis (FEA) module was extensively used for the purposes of this preliminary design. The FEA thermal modeling was used to calculate the spatial temperature distribution in the gain material resulting from the heat input due to the pump absorption and from the cooling at the surfaces. The stress mechanical modeling was then used to calculate the stress distribution and the deformation distribution in the crystal, induced by the thermal expansion.

The thermal aberrations were calculated by computing the Optical Path Difference (OPD) distribution across the crystal aperture. Total OPD is made of two main contributions, namely the variation in the optical path length due to the variation of the refractive index with temperature integrated along the crystal length L and the variation in

the crystal thickness due to thermal expansion and thermally induced stresses. Thermally induced birefringence [26] was not considered and the dependence of the thermal and mechanical parameters of the Ti:Sapphire from the temperature was neglected, as well as the slight anisotropy of some parameters in the orientation with respect to the crystalline axes.

For the thermal modeling of the AMP3 module, the crystal was assumed to have an overall diameter of 18 cm, with a cooled surface diameter of 16 cm. The absorption coefficient for the pump radiation was assumed to be 0.47 cm^{-1} .

The plots of Fig. 7 shows the average temperature distribution for the P1 levels of performance for the single slab and for the thin slab with half of the thickness. In the single crystal configuration, a peak temperature of about $100 \text{ }^\circ\text{C}$ was found, which is probably too high, with a surface temperature around $40 \text{ }^\circ\text{C}$. On the other hand, the split (thin) crystal configuration features a much lower peak temperature of only $40.8 \text{ }^\circ\text{C}$ that has a positive impact in terms of overall thermal aberrations. The analysis of the thermal aberrations shows that the maximum OPD for the thin crystal is $7 \text{ }\mu\text{m}$, a factor of 3 smaller than in the case of the thick crystal. Similarly, the dioptric power of the equivalent spherical thermal for the thin crystal is $2.7\text{E}-3$, i.e. approximately 30% of the thick crystal case. In general it appears that water cooling at high flow speed is a promising approach for the thermal management of the amplification stages, provided a cooling scheme based on the splitting of the crystal in twin gain elements is adopted to mitigate thermal aberrations.

5. Candidate pumping units

Several systems are emerging in the current scenario of diode-pumped solid state lasers for high average power. Among these, three configurations have demonstrated performances relevant to our specifications. Based on an end-pumped stack of ceramic Yb:YAG slabs, the DiPOLE system is a diode-pumped, solid state laser amplifier architecture cooled by a flow of low-temperature, high-pressure helium gas [Ertel, 2011]. This technology was recently demonstrated at the 1 kW level, showing 100 J output energy at 10 Hz, 1030 nm with $>60 \text{ J}$ expected conversion @ 515 nm [21]. This architecture and gain material exhibit reduced reabsorption loss and increased absorption and emission cross-sections in Yb:YAG, with a low quantum defect due to the very close pump and emission wavelengths being 940 nm and 1030 nm, respectively. These advantages enable efficient energy extraction and potential scalability to high average power. ceramic Yb:YAG, ceramic Nd:YAG and glass Nd:YAG. Several laser systems based on this amplifier technology have already been constructed and successfully operated. These lasers produce pulses of ns duration, 1030 nm wavelength, multi-J energy and a repetition rate of 10 Hz. Frequency doubling to 515 nm, required for pumping of Ti:sapphire amplifiers, has also been successfully demonstrated. Performance demonstrated so far includes generation of 105 J, 10 ns, 1030 nm pulses at 10 Hz and frequency doubling of 7 J pulses at 10 Hz with 82% conversion efficiency. Recent progress [27] also shows the possibility of increasing the output energy of an existing system to 150 J at 1030 nm and demonstrating frequency doubling at the 100 J level, with an expected output $>100 \text{ J}$ at 515 nm. Based on these considerations, DiPOLE-like architecture could provide the necessary building blocks for pump lasers up to Laser 2 at P0 with some moderate energy scaling and staggering of two 10 Hz units to match the required 20 Hz repetition rate. Delivering pump pulses at 100 Hz at the $>100 \text{ J}$ energy level using the current DiPOLE amplifier design is likely to need new approaches, such as liquid cooling and room temperature operation. These new approaches, whilst requiring substantial up-front investment, have the potential to significantly reduce the number of lasers, and therefore the cost, required for a given amount of average power.

Using Ceramic Nd:YAG, the P60 is a commercial system produced by Amplitude Technologies as a part of the P-series systems, using an improved “active mirror” configuration, the so-called Disk Amplifier

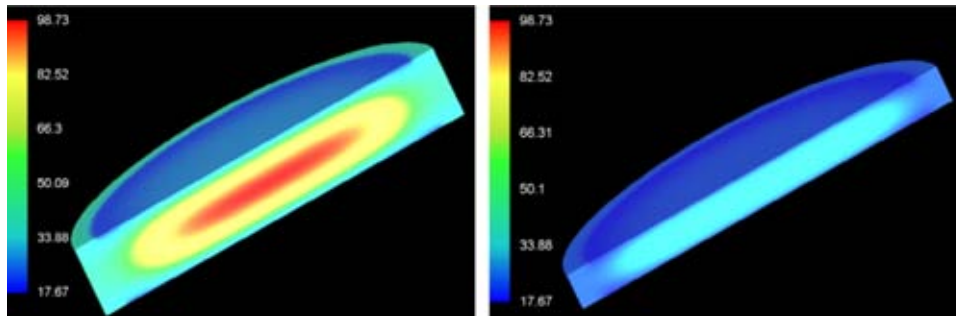


Fig. 7. Temperature distribution (in °C) at the performance level P1, for a single crystal amplifier (left) with thickness 3.2 cm and for one of the two crystals with thickness 1.6 cm (right). Diameter of the crystal is 18 cm in both cases.

Heads (DAH). Currently delivered with flash lamp pumping, conversion to diode pumping has been developed by Amplitude and a preliminary design has been produced. The general architecture of the P60 includes a seeder, followed by 6 identical Nd:YAG DAH amplifiers. The main features of the system are (1) enhanced and simple thermal management without cryogenic cooling with longitudinal liquid cooling in gain/heat load distributed disks; (2) compatibility with diode pumping, (3) compact footprint 1.5×4.8 m and beam specifications suitable for Ti:Sa pumping. The demonstrated performances include >70 J at 1064 nm with a 0.41% RMS shot-to-shot stability and 75% SHG efficiency with 5–6 ns Gaussian temporal pulse @ 2.8 J/cm² incident fluence with a 65 mm diameter and 18 mm thick LBO type I crystal. These values indicate that an array of a limited number of P60-like systems could deliver the required pump energy for Laser 1 and Laser 2. Laser 3 will require additional development to reach the >100 J level after SHG so that an array of up to 4–5 units would provide sufficient pump energy. The DPSSL version of the P60 is envisaged to operate at an ultimate rep. rate of 100 Hz. However, current heat load performances would already enable 3.5 kW average power with 75 J per pulse (IR) at 50 Hz with no risk. In fact, the thermal load extraction capability demonstrated in disk amplifiers with flashlamps pumping is similar to the heat load at 50 Hz with diode pumping. Moreover, diodes with required brilliance and Power supplies are existing and qualified. One important issue concerns the lifetime of diodes for high rep rate. Assuming a diode lifetime 2 billions shots at 2% duty cycle, diodes should be replaced every 700 days at 8/24H operation at 100 Hz rep-rate and every 1400 days at 8/24H operation at 50 Hz rep-rate.

Based on a diode pumped, He cooled Nd:glass with cooled ASE edge cladding, the HAPLS system developed by the LLNL for the ELI Beamlines can operate at >100 J output energy demonstrated @ 3.3 Hz, 1053 nm, with 0.7% RMS stability and 80 J SHG energy @ 526.5 nm. Ramping up to 10 Hz, 200 J (IR) design limit is currently in progress. In the HAPLS system, the diode pumped system is used to pump a Ti:Sa system to deliver 30 J in 30 fs at 10 Hz. This technology is derived from Inertial Fusion Energy Laser architectures and can be aperture scaled to single aperture, kilojoule, >100 kW output. Based on the data obtained from the design, construction, and operation of this laser system, is envisaged that increasing the repetition rate by 10 times to 100 Hz is possible.

Summarizing the current and expected performances of kW-scale DPSSL pumping systems currently available, we can conclude that the three selected systems are in a highly advanced development stage. All of them have demonstrated performances required to fulfill part, if not all of the pumping needs of the main EuPRAXIA lasers P0 Specifications. Some of these technologies are being considered independently for scaled operation at higher rep rate and higher energy per pulse, making them good candidate for pump lasers to reach the P1 specifications. However, a significant targeted development will be needed to address scaling of candidate systems at the desired 100 Hz repetition rate.

6. Output energy stability

Energy fluctuations of both the input pulse and of the pump energy determine the occurrence of fluctuations in the output energy. Moreover, when the individual stages are assembled in an amplification chain, the fluctuations in the earlier stages influences the output energy. This effect tightens the requirements on the stability of the front-end and on the stability of the pump sources. The evaluation of the fluctuation of the output energy, determined by the fluctuations in the pump and seed energy, was carried out on the basis of the results of the simulations described above.

It was assumed that each different stage is pumped by one or more identical pump laser, with an energy output of about 60 J at 515–532 nm. This reflects the expected performances of possible pump lasers. Given an absolute energy fluctuation level for each individual pump source, assumed identical for all the modules in the pump laser array, and assuming again that the fluctuations of the individual sources are statistically uncorrelated, we find the overall absolute pump energy fluctuation as shown in Fig. 8 for the case of Laser 3. In general, the results of the analysis shown above indicate that (i) the front-end energy fluctuations have a relatively small impact on the overall system stability, which is mainly influenced by the fluctuations of the pump sources; (ii) as far as the P0 performance level is concerned, the requirement of the overall output stability $<1\%$ allows a fluctuation of the individual pump source up to about 0.8% (up to 1.1% in the case of Laser 3); (iii) concerning the P1 performance level, a stability of the individual pump module of 0.6% RMS should be sufficient to attain an overall stability level in the output energy of $<0.7\%$.

7. Beam transport control

Another very challenging task in the EuPRAXIA laser design is the transport to the interaction chamber after amplification and here we briefly discuss the main issues currently under scrutiny. The use of the most effective technologies is foreseen, as shown in the conceptual diagram of Fig. 9, including adaptive optics, spatial filters, cooled grating technology for the compressor and compact focusing optics.

The main challenges are certainly the thermal and spectral issues in the compressor, and the pointing stability at the interaction plane. As for the compression, EuPRAXIA needs a compressor able to handle around 10 W/cm² in a $\sim 10^{-6}$ mbar vacuum. Regardless of the grating technology, cooling of the gratings will most likely be necessary. Moreover, depending on the laser beamline, wide bandwidth acceptance will be needed. In the current state of the art, studies about thermal issues on the gratings are only in their primordial stage. At LLNL [Alessi, 2016] measurements were carried out of surface deformations of gold gratings at hundreds of Watts average power. As a baseline, in EuPRAXIA we foresee the use of gold gratings, where a cooling strategy in vacuum is being studied in deep detail. Nevertheless, new grating technologies are emerging, like hybrid gratings with metal and multilayer dielectric coatings or new configurations for pure multilayer dielectric gratings,

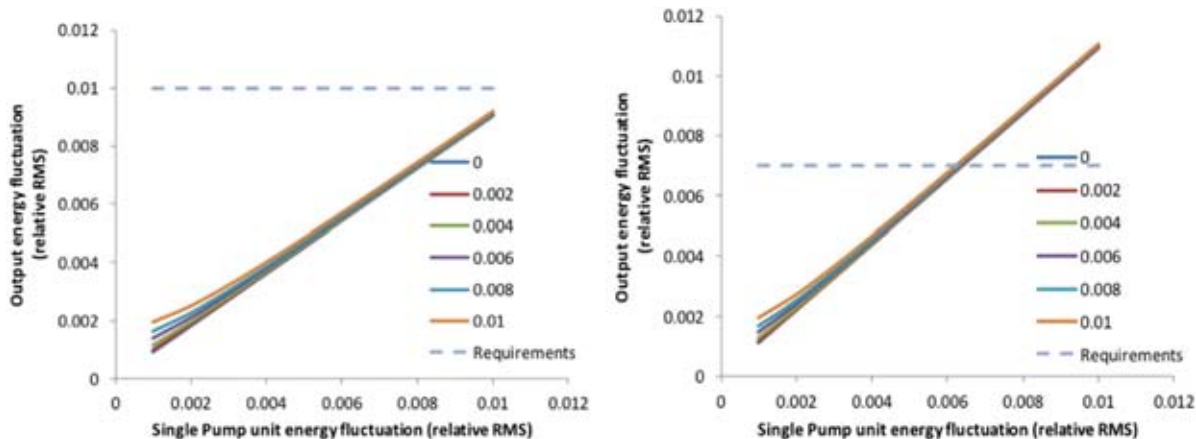


Fig. 8. Relative variation of the output energy (relative RMS) for the Laser3, as a function of the relative fluctuations of the output energy of the individual pump unit. The different curves in the graphs correspond to different relative energy fluctuation levels (RMS) of the seed pulse generated by the front-end. Left graph correspond to the P0 performance level, right graph corresponds to the P1 performance level.

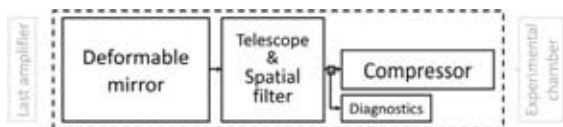


Fig. 9. Schematic view of the main beam transport components from the last amplifier to the interaction chamber.

to increase the compressor global spectral acceptance and work at 800 nm central wavelength. Research in this direction is very active, so technology of these novel solutions will likely reach readiness for EuPRAXIA construction time scale.

Regarding pointing stability, in general, the requirements depend on the specific application involving superposition of two laser focal spots or a laser focal spot and an electron beam in the focal region, as in external injection or Thomson scattering [28,29], or the matching of one or more laser focal spots with plasma targets [30]. From the point of view of intensity in a given position in the focal spot, specifications aim at less than 10% for Laser 1 and 2 and below 5% for Laser 3, which call for high stability for the performance of the amplification chain as discussed above. From the mechanical point of view, Laser 3 is the most demanding requiring 1 μrad (or less) pointing stability. These specifications will require a major design effort, still under investigation. In general, pointing stability will be affected by the whole system and several strategies can be considered. Active stabilization of PW-scale lasers using closed loops between stability detection on the interaction point and crucial transport optics are being tested recently [31]. At the same time, passive stabilization acting on building specification and adopting self-stabilizing optics mounts, are also being considered.

8. Conclusions

The design of the EuPRAXIA laser driver is, by all means, a very challenging task. The required laser performances are unique in the current world wide scenario and dramatic developments are ongoing on several aspects, including architectures and components. Guided by the physics requirements and taking into account the expected time-scale for the construction of the EuPRAXIA infrastructure, we selected our enabling technology, define a preliminary architecture and conceive our initial layout. Our concept combines most, if not all, of the highly advanced and proven technologies and aims at delivering performances well beyond those of existing systems or systems currently under construction. With this design, EuPRAXIA will provide a credible step towards a reliable operation of a laser-driven plasma accelerator,

giving the opportunity to the EU laser industry to gain momentum and setting the basis for another step-change in high power laser based sciences and applications.

Acknowledgments

The research leading to these results has received funding from the EU Horizon 2020 Research and Innovation Program under Grant Agreement No. 653782 EuPRAXIA. This project has received funding from the CNR funded Italian research Network ELI-Italy (D.M. n. 631 08.08.2016). We gratefully acknowledge P. Mason and K. Ertel of the Central Laser Facility, A. Bayramian, C. Siders and C. Haefner of the Lawrence Livermore National Laboratory, and F. Falcoz of Amplitude Technologies for fruitful discussion on the laser developments.

References

- [1] T. Tajima, J.M. Dawson, Laser electron accelerator, *Phys. Rev. Lett.* 43 (1979) 267–270.
- [2] D. Strickland, G. Mourou, Compression of amplified chirped optical pulses, *Opt. Commun.* 55 (6) (1985) 447–449.
- [3] P. Mason, M. Divoký, K. Ertel, J. Pilař, T. Butcher, M. Hanuš, S. Banerjee, J. Phillips, J. Smith, M.D. Vido, A. Lucianetti, C. Hernandez-Gomez, C. Edwards, T. Mocek, J. Collier, Kilowatt average power 100j-level diode pumped solid state laser, *Optica* 4 (4) (2017) 438–439.
- [4] E.F. Sistrunk, T. Spinka, A. Bayramian, P. Armstrong, S. Baxamusa, S. Betts, D. Bopp, S. Buck, K. Charron, J. Cupal, R. Demaret, R. Deri, J.-M.D. Nicola, M. Drouin, A. Erlanson, S. Fulkerson, C. Gates, J. Horner, J. Horacek, J. Jarboe, K. Kasl, D. Kim, E. Koh, L. Koubikova, R. Lanning, J. Lusk, W. Maranville, C. Marshall, D. Mason, P. Mazurek, J. Menapace, P. Miller, J. Naylon, J. Nissen, J. Novak, D. Peceli, P. Rosso, K. Schaffers, T. Silva, D. Smith, J. Stanley, R. Steele, C. Stolz, S. Telford, J. Thoma, D. VanBlarcom, J. Weiss, P. Wegner, B. Rus, C. Haefner, All diode-pumped, high-repetition-rate advanced petawatt laser system (hapls), in: *Conference on Lasers and Electro-Optics, Optical, Society of America*, 2017, p. STh1L2.
- [5] C. Danson, D. Hillier, N. Hopps, D. Neely, Petawatt class lasers worldwide, *High Power Laser Sci. Eng.* 3 (2015) e3.
- [6] K. Nakamura, H.S. Mao, A.J. Gonsalves, H. Vincenti, D.E. Mittelberger, J. Daniels, A. Magana, C. Toth, W.P. Leemans, Diagnostics, control and performance parameters for the bella high repetition rate petawatt class laser, *IEEE J. Quantum Electron.* 53 (4) (2017) 1–21.
- [7] P.A. Walker, P.D. Alesini, A.S. Alexandrova, M.P. Anania, N.E. Andreev, Horizon 2020 EuPRAXIA design study, *J. Phys. Conf. Ser.* 874 (2017) 1–8.
- [8] J.L. Dortz, A. Heilmann, M. Antier, J. Bourderionnet, C. Larat, I. Fsaifes, L. Daniault, S. Bellanger, C.S. Boisson, J.-C. Chanteloup, E. Lallier, A. Brignon, Highly scalable femtosecond coherent beam combining demonstrated with 19 fibers, *Opt. Lett.* 42 (10) (2017) 1887–1890.
- [9] A. Klenke, M. Müller, H. Stark, J. Limpert, A. Tünnermann, Compact integration of coherent beam combination for high power femtosecond fiber laser systems, in: *Laser Congress 2017 (ASSL, LAC)*, Optical Society of America, 2017, p. JTu2A21.
- [10] C. Haefner, High efficiency, diode pumped petawatt lasers for the next generation particle accelerators and secondary sources, in: *European Advanced Accelerator Concept*, Elba, Italy, 2017.

- [11] R.S. Nagymihaly, et al., Liquid-cooled ti:sapphire thin disk amplifiers for high average power 100-tw systems, *Opt. Express* 25 (2017) 6664–6677.
- [12] S. Banerjee, et al., High-efficiency 10 j diode pumped cryogenic gas cooled yb:YAG multislabs amplifier, *Opt. Lett.* 37 (2012) 2175.
- [13] S. Banerjee, et al., 100 j-level nanosecond pulsed diode pumped solid state laser, *Opt. Lett.* 51 (2016) 2089–2092.
- [14] O. Morice, Miró: complete modeling and software for pulse amplification and propagation in high-power laser systems, *Opt. Eng.* 42 (2003) 1530–1541.
- [15] L.A. Gizzi, D. Giove, C. Altana, F. Brandi, P. Cirrone, G. Cristoforetti, A. Fazzi, P. Ferrara, L. Fulgentini, P. Koester, L. Labate, G. Lanzalone, P. Londrillo, D. Mascali, A. Muoio, D. Palla, F. Schillaci, S. Sinigardi, S.T. Id, G. Turchetti, A new line for laser-driven light ions acceleration and related tnsa studies, *App. Sci.* 7 (10) (2017) 984.
- [16] Y. Chu, et al., High-contrast 2.0 petawatt ti:sapphire laser system, *Opt. Express* 21 (2013) 29231.
- [17] S. Chu, et al., Parasitic lasing suppression in large-aperture ti:sapphire amplifiers by optimizing the seed pump time delay, *Laser Phys. Lett.* 10 (2013) 055302.
- [18] U. Althechna, Ti:Sapphire Crystal White Paper, Tech. Rep., 2017. <http://www.althechna.com>.
- [19] K. Ertel, et al., Ase suppression in a high energy titanium sapphire amplifier, *Opt. Express* 16 (2008) 8030.
- [20] L.M. Frantz, et al., Theory of pulse propagation in a laser amplifier, *J. Appl. Phys.* 34 (1963) 2346.
- [21] P. Mason, et al., Scalable design for a high energy cryogenic gas cooled diode pumped laser amplifier, *Appl. Opt.* 54 (2015) 4227.
- [22] M. Siebold, et al., Penelope: a high peak- power diode-pumped laser system for laser-plasma experiments, in: *High-Power, High-Energy, and High-Intensity Laser Technology; and Research using Extreme Light: Entering New Frontiers with Petawatt-Class Lasers*, Vol. 8780, International Society for Optics and Photonics, 2013, p. 878005.
- [23] X. Fu, P. Li, Q. Liu, M. Gong, 3kw liquid-cooled elastically-supported nd:YAG multi-slab cw laser resonator, *Opt. Express* 22 (15) (2014) 18421–18432.
- [24] K. Wang, B. Tu, C. Jia, J. Shang, X. An, Y. Liao, Z. Xu, J. Guo, J. Yi, Y. Yu, H. Su, Q. Gao, X. Wang, W. Liu, K. Zhang, 7kw direct-liquid-cooled side-pumped nd:YAG multi-disk laser resonator, *Opt. Express* 24 (13) (2016) 15012–15020.
- [25] V. Chvykov, R.S. Nagymihaly, H. Cao, M. Kalashnikov, K. Osvay, Design of a thin disk amplifier with extraction during pumping for high peak and average power ti:sa systems (edp-td), *Opt. Express* 24 (4) (2016) 3721–3733.
- [26] P. Ferrara, M. Ciofini, L. Esposito, J. Hostaša, L. Labate, A. Lapucci, A. Pirri, G. Toci, M. Vannini, L.A. Gizzi, 3-d numerical simulation of yb:YAG active slabs with longitudinal doping gradient for thermal load effects assessment, *Opt. Express* 22 (5) (2014) 5375–5386.
- [27] M. De Vido, et al., Characterisation of adhesive-free bonded crystalline yb:YAG for high energy laser applications, *Opt. Mater. Express* 7 (2017) 425.
- [28] L.A. Gizzi, A. Bacci, S. Betti, C.A. Cecchetti, M. Ferrario, A. Gamucci, A. Giulietti, D. Giulietti, P. Koester, L. Labate, T. Levato, V. Petrillo, L. Serafini, P. Tomassini, C. Vaccarezza, An integrated approach to ultraintense laser sciences: The plasmon-x project, *Eur. Phys. J. Spec. Top.* 175 (1) (2009) 3–10.
- [29] P. Tomassini, A. Bacci, J. Cary, M. Ferrario, A. Giulietti, D. Giulietti, L.A. Gizzi, L. Labate, L. Serafini, V. Petrillo, C. Vaccarezza, Linear and nonlinear thomson scattering for advanced x-ray sources in plasmonx, *IEEE Trans. Plasma Sci.* 36 (4) (2008) 1782–1789.
- [30] S. Steinke, J. van Tilborg, C. Benedetti, C.G.R. Geddes, J. Daniels, K.K. Swanson, A.J. Gonsalves, K. Nakamura, B.H. Shaw, C.B. Schroeder, E. Esarey, W.P. Leemans, Staging of independent laser plasma accelerators, *AIP Conf. Proc.* 1812 (1) (2017) 020003.
- [31] M. Galimberti, B. Parry, D. Shepherd, C. Gregory, R. Pattathil, Fast beam pointing stabilization for high power laser system, in: *7th International Conference on Charged and Neutral Particles Channeling Phenomena Channeling*, 2016.



Contents lists available at ScienceDirect

Nuclear Inst. and Methods in Physics Research, A

journal homepage: www.elsevier.com/locate/nima

High-quality GeV-scale electron bunches with the Resonant Multi-Pulse Ionization Injection



P. Tomassini ^{a,*}, S. De Nicola ^{b,f}, L. Labate ^{a,c}, P. Londrillo ^d, R. Fedele ^{e,f}, D. Terzani ^{a,e,f}, F. Nguyen ^g, G. Vantaggiato ^a, L.A. Gizzi ^{a,c}

^a Intense Laser Irradiation Laboratory, INO-CNR, Pisa, Italy,

^b SPIN-CNR, Sect. of Napoli, Italy

^c INFN, Sect. of Pisa, Italy

^d INAF, Bologna, Italy

^e Dip. Fisica Università di Napoli Federico II, Italy

^f INFN, Sect. of Napoli, Italy

^g ENEA, Nuclear Fusion and Safety Technologies Department, Frascati, Italy

ABSTRACT

Recently a new injection scheme for Laser Wake Field Acceleration, employing a single 100-TW-class laser system, has been proposed. In the Resonant Multi-Pulse Ionization injection (ReMPI) a resonant train of pulses drives a large amplitude plasma wave that traps electrons extracted from the plasma by further ionization of a high-Z dopant (Argon in the present paper). While the pulses of the driver train have intensity below the threshold for the dopant's ionization, the properly delayed and frequency doubled (or more) ionization pulse possesses an electric field large enough to extract electrons, though its normalized amplitude is well below unity. In this paper we will report on numerical simulations results aimed at the generation of GeV-scale bunches with normalized emittance and *rms* energy below 80 nm × rad and 0.5%, respectively. Analytical consideration of the FEL performance for a 1.3 GeV bunch will be also reported.

1. Introduction

The Resonant Multi-Pulse Ionization injection (ReMPI) scheme is derived from the so-called “two-color ionization injection”. In the two-color ionization injection [1,2] two laser systems are needed. The main pulse that drives the plasma wave has a long wavelength, five or ten micrometers, and a large normalized amplitude $a_0 = eA/mc^2 = 8.5 \cdot 10^{-10} \sqrt{I\lambda^2} > 1$, being I and λ pulse intensity in W/cm² and wavelength in μm . The second pulse (the “ionization pulse”) is a frequency doubled Ti:Sa pulse with wavelength 400 nm. While the main pulse cannot further ionize the electrons in the external shells of the large Z dopant due to its large wavelength, the electric field of the ionization pulse is large enough to generate newborn electrons that will be trapped in the bucket. This opens the possibility of using gas species with relatively low ionization potentials, thus enabling separation of wake excitation from particle extraction and trapping. Two color ionization injection is therefore a flexible and efficient scheme for high-quality electron bunch production. The main drawbacks of the two color ionization injection are the current lack of availability of short ($T < 100$ fs) 100 TW-class laser systems operating at large ($\approx 10\mu\text{m}$) wavelength and lasers synchronization jitter issues. These limitation make the two-color

scheme currently unpractical for application to LWFA-based devices requiring high quality beams.

The Resonant Multi-Pulse Ionization injection [3] has the possibility to be operating with present-day *single* Ti:Sa laser systems. Simulations show that such a scheme is capable of generating ultra-low emittance GeV-scale bunches with easily tunable length and final energy.

2. The Resonant Multi-Pulse ionization injection

In the Resonant Multi-Pulse ionization injection scheme (see Fig. 1) only one short-wavelength laser system (e.g a Ti:Sa) is needed. The long wavelength driving pulse of the two-color scheme is replaced by a short wavelength, resonant multi-pulse laser driver. Such a driver can be obtained via temporal shaping techniques from the *single*, linearly polarized, standard CPA laser pulse, while the minor fraction of the Ti:Sa CPA pulse is frequency doubled and used as an ionizing pulse.

Due to the resonant enhancement of the ponderomotive force, a properly tuned train of pulses is capable of driving amplitude waves larger than a single pulse with the same energy [4,5]. Noticeably, since the peak intensity of the driver is reduced by a factor equal to the number of train pulses, it is also possible to match the conditions of *both*

* Corresponding author.

E-mail address: paolo.tomassini@ino.it (P. Tomassini).

<https://doi.org/10.1016/j.nima.2018.03.002>

Received 15 November 2017; Received in revised form 14 February 2018; Accepted 1 March 2018

Available online 26 March 2018

0168-9002/© 2018 Elsevier B.V. All rights reserved.

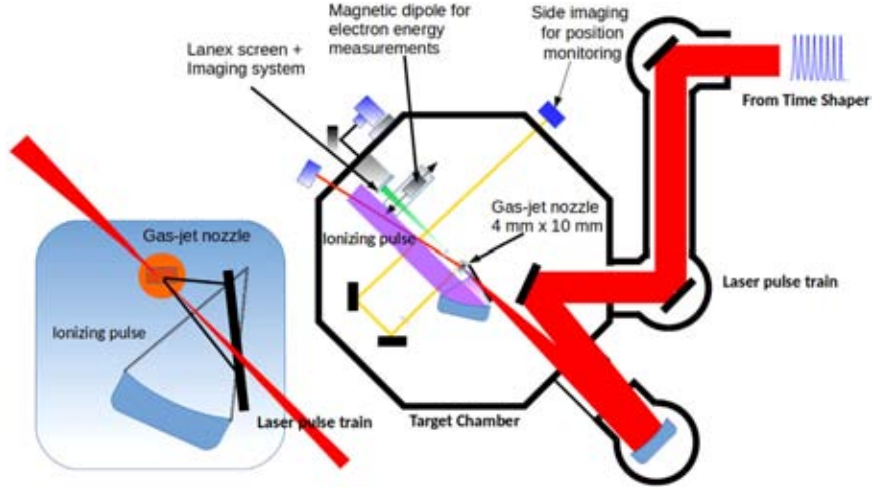


Fig. 1. Multi-Pulse ionization injection scheme. A small fraction of a single Ti:Sa laser pulse is frequency doubled and, after focusing with a low $F/\#$ paraboloid, will constitute the ionizing pulse. The main portion of the pulse is temporally shaped as a train of resonant pulses that will drive a large amplitude plasma wave. Inset: the ionizing pulse focusing is achieved by using a mirror with a hole for the driving pulse passage.

particle trapping and unsaturated ionization (i.e. with low ionization percentage) of the active atoms level. Recently [6] new experimental results on the generation of such a time shaped pulses demonstrate that a multi pulse scheme is obtainable with present day technology and that plasma waves can be excited with this scheme [7]. Using Argon ($\text{Ar}^{8+} \rightarrow \text{Ar}^{9+}$ with ionization potential $U_I = 422.5 \text{ eV}$) as a dopant gives us the possibility to obtain bunches with tens of $\text{nm} \times \text{rad}$ of normalized emittance. Multi-pulse ionization injection with Argon requires trains with more than four pulses since ionization level is saturated with amplitude above $a_0 = 0.8$ at $\lambda = 0.8 \mu\text{m}$ (see Fig. 3 in [3]).

3. 1.3 GeV beam simulation

We report on a long acceleration length (of about 4 cm) simulation performed in a 2D cylindrical geometry with QFluid [8] (see also the Appendix in [3]). The Ti:Sa laser system generates pulses that will pass through a beam splitter. The major portion of each pulse is time shaped as a train of resonant eight sub-pulses having FWHM duration of $T = 30 \text{ fs}$ each, with peak power of $200/8 \text{ TW}$. The driving train is subsequently focused down to a spot of $w_0 = 45 \mu\text{m}$ waist onto a capillary filled with Argon, obtaining a sequence of pulses with peak intensity and normalized amplitude of $I = 7.9 \times 10^{17} \text{ W/cm}^2$ and $a_0 = 0.6$, respectively. The frequency doubled pulse from the minor portion of the Ti:Sa pulse delivers 13 mJ and is focused with a minimum waist of $w_{0,\text{ion}} = 3.6 \mu\text{m}$. On-axis plasma background density is set to $n_{\text{axis}} = 5 \times 10^{17} \text{ cm}^{-3}$ and is obtained by assuming full ionization of Argon up to level eight (ionization potentials of Ar^{n+} are below 144 eV for $n \leq 8$ so Argon ionization up to Ar^{8+} is achieved within the first cycles of the pulse).

To obtain a so long acceleration length pulse guiding technique is necessary since low-density plasmas do not allow for pulse self-guiding at those pulse powers. The driver pulses are focused close to the entrance of the capillary (or gas-cell) and enter into the guide with a matched radius $w_m = w_0$ and radial density profile

$$n_e(r) = n_{\text{axis}} \left[1 + \eta \frac{1.1 \cdot 10^{20}}{n_{\text{axis}} w_0^2} \left(\frac{r}{w_0} \right)^2 \right]. \quad (1)$$

The η factor accounts for weakly nonlinear corrections and in the case of short pulses ($T \ll 2\pi/\omega_p$) can be evaluated as [9]

$$\eta \cong 1 - \frac{1}{16} (a_0 \omega_p T)^2 \cdot (1 + 4.6 \cdot 10^{-21} n_e w_0^2),$$

which is very close to unity in our simulations.

Simulation has been performed onto a moving cylinder of radius $160 \mu\text{m}$, length $430 \mu\text{m}$ and a resolution in both radial and longitudinal

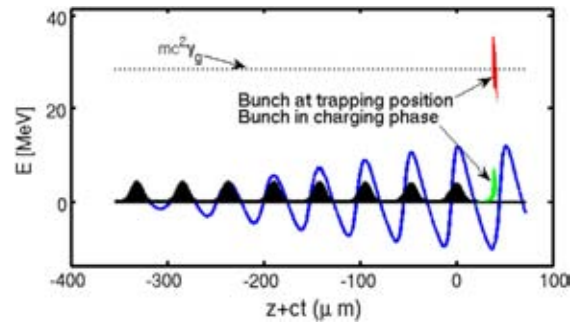


Fig. 2. Line-out of the longitudinal electric field (blue line, a.u.) and pulse amplitude of the driver train at the early stage of bunch trapping. Green dots show the longitudinal phase space of the bunch after $100 \mu\text{m}$ of propagation. The horizontal dotted line shows the energy at the trapping point (γ_g is the Lorentz factor of the pulse train) and the red dots represent the longitudinal phase-space of the bunch at the trapping point (i.e. $\langle \gamma \rangle = \gamma_g$). (For interpretation of the references to color in this figure legend, the reader is referred to the web version of this article.)

directions of 150 nm . Due to the tight focusing of the ionization pulse that diffracts in a scale $Z_{r,\text{ion}} = \pi \times w_{0,\text{ion}}^2 / \lambda_{\text{ion}} \approx 100 \mu\text{m}$, the bunch population grows and saturates (bunch charging phase) in about $150 \mu\text{m}$ (see Fig. 2, green dots representing the longitudinal phase-space of the bunch in the charging phase) and the extracted bunch is trapped after $\approx 600 \mu\text{m}$ of propagation of the ionizing pulse (see red dots in Fig. 2) in a phase of the bucket intermediate between the weak-trapping and the strong-trapping conditions (see Eqs. 2 and 3 in Ref. [3]).

The driver pulses evolution through the 3.7 cm of plasma shows a twofold behavior. Though peak intensity is remarkably stable (see the black line in Fig. 3), and no visible self-steepening occurs (we are well below the threshold for the onset of self-steepening since $a_0 \times (c \times T) \times k_p \approx 0.8$ and according to [10] the growth of self-steepening occurs if $a_0 \times (c \times T) \times k_p > (32 \times \log(2) / (\pi - 1))^{1/2} \approx 3.2$) sub-pulses of the rear part of the train propagate in the wake generated by all the preceding pulses, thus being partially exposed to the defocusing effect of the wake. As a final effect, a radial breathing of the rear pulses occurs with possible off-axis maxima of the local intensity, as it is apparent in Fig. 4 (bottom).

The final electron bunch of charge 4.3 pC has energy 1.3 GeV , energy spread 0.49% rms and normalized emittance of 0.08 mm mrad and 0.04 mm mrad in x (laser polarization) and y directions, respectively.

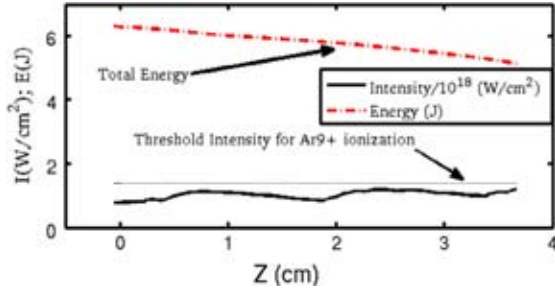


Fig. 3. Evolution of the total energy (red line) and peak intensity (black line). The horizontal dotted line represents the intensity threshold for further ionization of the 9th level of Argon.

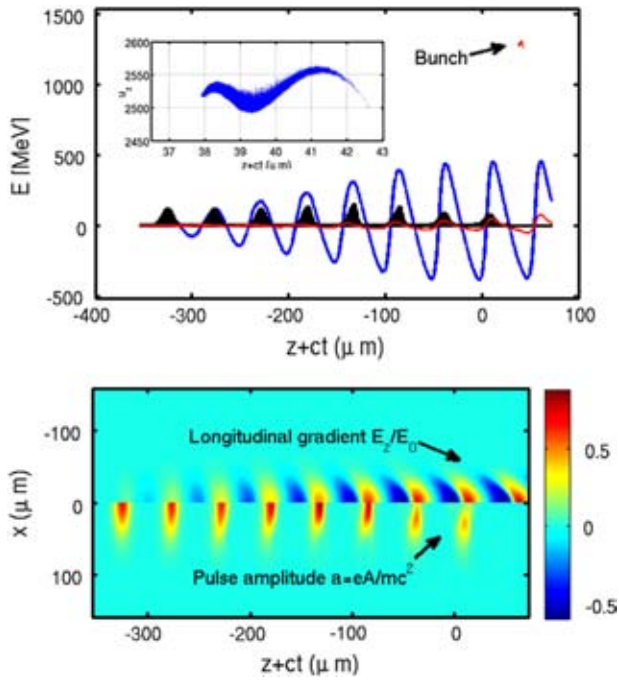


Fig. 4. Top: longitudinal phase space of the electron bunch after 3.7 cm of propagation (red dots). The blue line shows the electric field on axis (a.u.), while the red line represents the transverse focusing force at a radius close to the beam radius (a.u.). Bottom 2D maps of the longitudinal normalized electric field E_z/E_0 and of the normalized laser amplitude. (For interpretation of the references to color in this figure legend, the reader is referred to the web version of this article.)

After 3.7 cm of propagation the electron bunch is still far from dephasing (see Fig. 4 top) and almost 70% of laser energy is still available for further energy boost. However, while normalized emittance looks stable in the last 3 cm (see Fig. 5) due to the matched-beam configuration, the relative energy spread finds its minimum at 3.7 cm and rapidly increases with further acceleration up to percent level. For high-quality oriented application, therefore, such an earlier truncation of particle acceleration limits the overall energy conversion efficiency of the scheme (at the present working point). We finally stress the remarkably low value of 0.2% for the slice energy spread (with slice thickness of $0.05\mu\text{m}$).

The simulation ends when the pulses and the bunch are close to the plasma exit. Due to the use of the quasistatic approximation, QFluid cannot face with rapidly varying longitudinal plasma densities so we will be forced to use a different code to face with the plasma exit stage.

The ReMPI scheme uses a single laser system (a Ti:Sa in the present paper) so the driving train and the ionization pulse have no relative

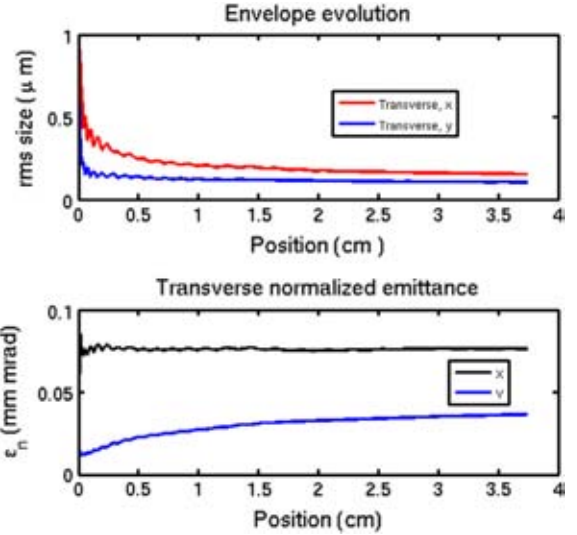


Fig. 5. Transverse rms size (top) and normalized emittance (bottom) in x (pulse polarization) and y directions.

timing jitter. This opens the possibility of fine tuning the ionization-to-driver delay according to the requested bunch energy or length. The fine-tuning of the bunch duration is easily obtainable just by selecting the appropriate ionization-to-driver delay t_d . Numerical simulations (supported by the theory in 1D) show that the minimum bunch length is obtained when the ionization pulse is placed at the position of maximum potential (zero longitudinal electric field) and the trapped bunch is placed at the position of maximum accelerating gradient (i.e. exactly at the strong-trapping point). Starting from that configuration and further delaying the ionization pulse, the final bunch length increases. The fulfillment of the weak-trapping condition for the whole set of bunch electrons makes an upper limit of the bunch duration. Both the minimum and maximum obtainable values depend on the working point. In the current setup bunch lengths that can be obtained by simply delaying the ionization pulse are in the range $360\text{ as} < t_{rms} < 2.2\text{ fs}$. Optimization of the bunch length/energy tuning strategy is ongoing [11].

4. Estimates of FEL performance

In this section we will report on analytical results obtained with the 1.3 GeV bunch, having supposed an emittance preserving beamline to transport the bunch from the accelerator stage to the undulator. We stress, therefore, that the following results do not constitute the final stage of a start-to-end simulation but just the expected outcomes of FEL radiation in the case of a quality-preserving optics.

For an electron beam of energy $E_{beam} = \gamma m_e c^2$, the resonance condition for the wavelength of the emitted radiation, in a planar undulator, is

$$\lambda = \frac{\lambda_u}{2\gamma^2} \left(1 + \frac{K^2}{2} \right) \quad (2)$$

where λ_u is the period of longitudinal variation of the on-axis magnetic field for a planar undulator and K is the undulator parameter defined as:

$$K = \frac{eB\lambda_u}{2\pi mc} \quad (3)$$

B being the peak value of the on-axis magnetic field and e, m_e and c respectively the electron charge, the electron mass and the speed of light.

The efficiency of energy transfer from electrons to the electric field and so the gain of the process are summarized by the FEL Pierce

Table 1

Performance estimates of a Free Electron Laser driven by the electron beams discussed in the text.

Bunch parameters	
Beam energy [GeV]	1.3
Long. beam size (rms) σ_L [μm]	0.655
Current intensity [A]	785
Norm. emittance [$\text{mm} \times \text{mrad}$]	0.08
Slice energy spread σ_E/E (%)	0.22
Common FEL parameters	
Undulator magnetic field [T]	1
Undulator period [cm]	1.4
Deflection parameter	1.3
Output FEL parameters	
FEL wavelength [nm]	2.0
Twiss β [m]	6.16
Pierce parameter ρ	0.0018
inh. broad. gain length [m]	0.702
Saturation power [MW]	861
Saturation length [m]	17.7
Coherence length [μm]	0.05
Sat. power with slippage [MW]	826

parameter ρ ,

$$\rho = \frac{1}{4\pi\gamma} \sqrt[3]{2\pi \frac{J}{I_0} (\lambda_u K f_b(K))^2} \quad (4)$$

where $f_b(K) = J_0(\xi) - J_1(\xi)$ is the planar undulator Bessel correction factor, of argument

$$\xi = \frac{K^2}{4(1 + K^2)}$$

and $I_0 = 17$ kA the Alfvén current. The current is expressed in terms of the bunch root mean squared (rms) time duration σ_τ and of the bunch charge Q_b as

$$I[\text{A}] = \frac{Q_b[\text{C}]}{\sigma_\tau[\text{s}] \sqrt{2\pi}}. \quad (5)$$

The current density J given by

$$J \left[\frac{\text{A}}{\text{m}^2} \right] = \frac{Q_b[\text{C}]}{\sigma_\tau[\text{s}] \sigma_x[\text{m}] \sigma_y[\text{m}] (2\pi)^{3/2}} \quad (6)$$

where $\sigma_{x,y}[\text{m}]$ is the rms transverse size of the electron beam.

The gain length, determining the FEL growth rate, can be expressed in terms of ρ as follows

$$L_g = \frac{\lambda_u}{4\pi \sqrt{3\rho}}. \quad (7)$$

The Pierce parameter gives an estimate of the natural bandwidth of the FEL, $\Delta\omega/\omega \simeq \rho$ and rules also the power at saturation that writes

$$P_S \simeq \sqrt{2\rho} P_E \quad (8)$$

P_E being the electron beam power, linked to the peak current and energy by the relation $P_E = E_{beam} I$. Then, the length of the undulator section needed to reach the saturated laser power – the saturation length – is

$$L_S = 1.066 L_g \ln \left(\frac{9P_S}{P_0} \right) \quad (9)$$

where P_0 is the input seed power.

The effect of inhomogeneous broadening due to significant energy spread and emittance can be embedded in the previous formulas [12,13]: both contribute to increase the gain and saturation length. Furthermore, since the longitudinal beam size becomes comparable to the coherence length, slippage corrections are taken into account resulting in an effective saturation power. Table 1 shows the results obtained using simple and analytical scaling laws [12,13] to describe the

FEL signal pulse evolution in terms of saturation length and saturation power accounting for the beam emittance, the energy spread and the slippage corrections for the reported beam.

5. Conclusions

We employed the new ReMPII scheme to (numerically) generate a 1.3 GeV electron bunch with outstanding quality ($\sigma_E/E|_{\text{slice}} = 0.22\%$, $\epsilon_n = 80$ nm and compactness by using a single Ti:Sa laser system and a preformed plasma channel of length 3.7 cm. To operate with the ReMPII scheme a small portion of the Ti:Sa pulse has been frequency doubled and tightly focused on the target to further ionize the dopant and extract electron from the background. The main portion passed through a time shaping device and after focusing by a large F/# paraboloid constituted the driving pulse(s) of the plasma wave. The scheme takes advantage of the virtual absence of jitter between the ionizing and driving pulses due to the usage of a single laser system. This opens the possibility to precisely determine both the bunch length and energy of the final bunch. In the current setup numerical simulations show that bunches with duration from 360 as up to 2.2 fs can be generated.

Analytical results of FEL performance, based on a 2.2 fs long bunch, show that powerful 2 nm X radiation of peak power exceeding 0.8 GW can be generated with state-of-the-art undulator parameters, provided that quality-preserving beam optics from plasma exit to the undulator is employed.

Acknowledgments

We thank Giuseppe Dattoli for his help and suggestions in estimating the FEL performance with the electron beams discussed in the text. The research leading to these results has received funding from the European Union's Horizon 2020 research and innovation program under Grant Agreement No 653782-EuPRAXIA. We also acknowledge financial support from the ELI-ITALY Network funded by CNR (ELI- Nuclear Physics (FOE) D.M.n. 631 del 08.08.2016).

References

- [1] L.-L. Yu, E. Esarey, C.B. Schroeder, J.-L. Vay, C. Benedetti, C.G.R. Geddes, M. Chen, W.P. Leemans, Two-color laser-ionization injection, *Phys. Rev. Lett.* 112 (2014) 125001.
- [2] L.-L. Yu, E. Esarey, C.B. Schroeder, J.-L. Vay, C. Benedetti, C.G.R. Geddes, M. Chen, W.P. Leemans, Ultra-low emittance electron beams from two-color laser-ionization injection, in: *Advanced Accelerator Concepts 2014 AIP Conf. Proc.*, Vol. 1777, pp. 040019-1–040019-5. <http://dx.doi.org/10.1063/1.4965621>.
- [3] P. Tomassini, S. De Nicola, L. Labate, P. Londrillo, R. Fedele, D. Terzani, L.A. Gizzi, The resonant multi-pulse ionization injection, *Phys. Plasmas* 24 (10) (2017). <http://dx.doi.org/10.1063/1.5000696>.
- [4] D. Umstadter, E. Esarey, J. Kim, Nonlinear plasma waves resonantly driven by optimized laser pulse trains, *Phys. Rev. Lett.* 72 (1994) 1224.
- [5] S.M. Hooker, R. Bartolini, S.P.D. Mangles, A. Tunnermann, L. Corner, J. Limpert, A. Seryi, R. Walczak, Multi-pulse laser wakefield acceleration: a new route to efficient, high-repetition-rate plasmas and high flux radiation sources, *J. Phys. B* 47 (2014) 234003.
- [6] R.J. Shalloo, L. Corner, C. Arran, J. Cowley, G. Cheung, C. Thornton, R. Walczak, S.M. Hooker, Generation of laser pulse trains for tests of multi-pulse laser wakefield acceleration, *Nucl. Instrum. Methods A* 829 (1) (2016) 383–385.
- [7] J. Cowley, C. Thornton, C. Arran, R.J. Shalloo, L. Corner, G. Cheung, C.D. Gregory, S.P.D. Mangles, N.H. Matlis, D.R. Symes, R. Walczak, S.M. Hooker, Excitation and control of plasma wakefields by multiple laser pulse, *Phys. Rev. Lett.* 119 (2017) 044802.
- [8] P. Tomassini, A.R. Rossi, Matching strategies for a plasma booster, *Plasma Phys. Control. Fusion* 58 (2016) 034001.
- [9] W. Lu, M. Tzoufras, C. Joshi, F.S. Tsung, W.B. Mori, J. Vieira, R.A. Fonseca, L.O. Silva, *Phys. Rev. ST Accel. Beams* 10 (2007) 061301.
- [10] J. Vieira, F. Fiuza, L.O. Silva, M. Tzoufras, W.B. Mori, Onset of self-steepening of intense laser pulses in plasmas, *New. J. Phys.* 12 (2010) 045025.
- [11] P. Tomassini, et al., in preparation.
- [12] G. Dattoli, P.L. Ottaviani, S. Pagnutti, Booklet for FEL design. Available at http://fel.enea.it/booklet/pdf/Booklet_for_FEL_design.pdf.
- [13] G. Dattoli, A. Renieri, A. Torre, *Lectures on Free Electron Laser Theory and Related Topics*, World Scientific, Singapore, 1993.



Contents lists available at ScienceDirect

Nuclear Inst. and Methods in Physics Research, A

journal homepage: www.elsevier.com/locate/nima

Light Ion Accelerating Line (L3IA): Test experiment at ILIL-PW

L.A. Gizzi^{a,b,*}, F. Baffigi^a, F. Brandi^a, G. Bussolino^{a,b}, G. Cristoforetti^a, A. Fazzi^c,
L. Fulgentini^a, D. Giove^d, P. Koester^a, L. Labate^{a,b}, G. Maero^e, D. Palla^a, M. Romé^e,
P. Tomassini^a

^a Intense Laser Irradiation Laboratory, INO-CNR, Pisa, Italy

^b INFN, Sez. Pisa, Italy

^c Dipartimento di Energia, Politecnico di Milano and INFN, Sezione di Milano, Italy

^d INFN-LASA, Segrate, Italy

^e Università di Milano and INFN Sez. Milano, Italy

ARTICLE INFO

Keywords:

Ultraintense lasers

Laser–plasma acceleration

Target normal sheath acceleration

Ion detection

ABSTRACT

The construction of a novel Laser-driven Light Ions Acceleration Line (L3IA) is progressing rapidly towards the operation, following the recent upgrade of the ILIL-PW laser facility. The Line was designed on the basis of the pilot experimental activity carried out earlier at the same facility to define design parameters and to identify main components including target control and diagnostic equipment, also in combination with the numerical simulations for the optimization of laser and target parameters. A preliminary set of data was acquired following the successful commissioning of the laser system > 100 TW upgrade. Data include output from a range of different ion detectors and optical diagnostics installed for qualification of the laser–target interaction. An overview of the results is given along with a description of the relevant upgraded laser facility and features.

1. Introduction

Novel acceleration techniques based on ultraintense lasers are evolving rapidly from scientific exploration to applications, relying on established and extensively investigated [1] acceleration processes like the Target Normal Sheath Acceleration (TNSA) [2].

Examples of applications include injectors for high power ion beams, neutron generation [3], probes for fast evolving phenomena like the ultrafast charging of laser-heated samples [4], space radiation studies and electronic components testing [5]. Applications with potential impact on industry and cultural heritage like the proton-induced X-ray emission spectroscopy (PIXE) may be applicable with currently achievable TNSA performances and may strongly benefit from the compactness of a multi-MeV laser-driven ion source [6].

Laser-based applications requiring multi MeV ions are being developed for industrial use, in view of the ongoing evolution of the next generation of Joule-scale laser drivers in the sub-100 fs domain, which may become attractive [7] for their higher repetition rate, potentially reaching the 100 Hz or even the kHz range. In fact, with the ongoing transition to an extensive use of diode-pumping in high power lasers [8], high repetition rate and higher efficiency TNSA drivers may soon be

available enabling laser-driven high average power sources to become finally commercially available.

At the same time, great attention is being dedicated to the control of acceleration parameters to enhance TNSA performances, including energy cut-off, beam divergence, charge, emittance. Target optimization and engineering, looking at different properties of surface, geometry and conductivity are becoming crucial in this effort, with nano-structured targets emerging as a potential breakthrough in table-top laser-driven ion sources development [9]. Finally, post acceleration is being tackled with special attention to selection, collimation [10] and injection in secondary acceleration structures, even using miniature target-driven guiding devices [11].

Here we describe the preliminary results of the commissioning experiment of a new Line for Laser-driven Light Ions Acceleration (L3IA) with the purpose of establishing an outstanding beam-line operation of a laser–plasma source in Italy taking advantage of the results achieved so far in this field by the precursor activity [12] and based upon experimental campaigns and numerical modeling. The beam-line will operate in the parameter range of ion acceleration currently being explored by leading European laboratories in this field and will provide an advanced test facility for the development of laser-driven ion sources.

* Corresponding author at: Intense Laser Irradiation Laboratory, INO-CNR, Pisa, Italy.
E-mail address: la.gizzi@ino.cnr.it (L.A. Gizzi).

<https://doi.org/10.1016/j.nima.2018.03.016>

Received 8 December 2017; Received in revised form 14 February 2018; Accepted 7 March 2018

Available online 27 March 2018

0168-9002/© 2018 The Authors. Published by Elsevier B.V. This is an open access article under the CC BY-NC-ND license (<http://creativecommons.org/licenses/by-nc-nd/4.0/>).

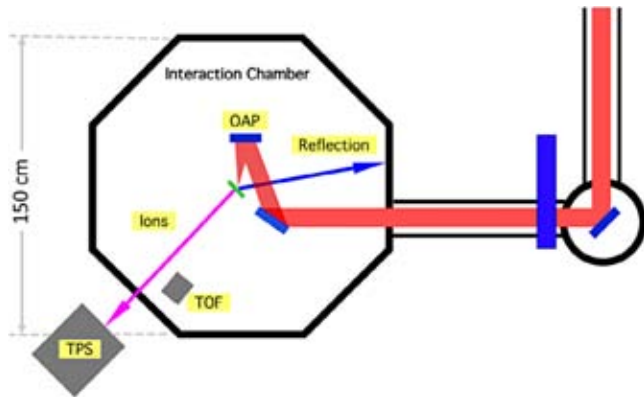


Fig. 1. Schematic experimental setup showing the octagonal target chamber, the off-axis parabola and the main diagnostics.

The project includes a complete set of work-packages, including the interface with the ILIL-PW facility, the beam line scheme comprising targets, laser beam focusing, and diagnostic devices dedicated to both the laser–plasma interaction and the ion beam detection and characterization. Numerical modeling is also included, with the specific tasks of providing basic predictive simulations for the baseline parameters of the beam line and also allowing investigation of advanced target and laser configurations. Provision is also made for specific application cases, including radiobiological testing and cultural heritage applications.

2. Experimental set up

The experiment was carried out at the Intense Laser Irradiation Laboratory using the ILIL-PW Ti:Sa laser and interaction facility with laser pulse parameters related to the phase 1 configuration described in Ref. [13]. Preliminary results obtained using the laser pulse at the output of the front-end can be found in Ref. [13]. In the same reference, an overview of the ILIL-PW facility and a summary of the main laser parameters are also presented. In the experiment presented here the pulse duration was 30 fs and the pulse energy was 3 J on target.

A schematic view of the experimental set up is given in Fig. 1. The 100 mm diameter laser beam was focused by an F/4.5 Off-Axis Parabolic (OAP) mirror with an angle of incidence of 15° . The focal spot was elliptical, with an average diameter of $4.4 \mu\text{m}$ (FWHM) and an intensity in excess of $1.6 \times 10^{20} \text{ W/cm}^2$ ($a_0 = 8.6$). The target was mounted in a remotely controlled motorized support with a sub-micrometer resolution, capable of XYZ translation and azimuthal rotation around the vertical axis.

As shown in Fig. 2, the target mount consisted of a solid steel frame machined to leave access to the surface of the foil from both sides through a set of $500 \mu\text{m}$ diameter holes with conical aperture to allow oblique laser incidence on target. The whole mount was designed to enable a 100-mm range of positioning and withstand a load of up to 500 N in all directions of motion. These specifications ensure that the scanning of targets up to $100 \text{ mm} \times 100 \text{ mm}$ can be accomplished, enabling a large number of laser shots to be fired on a given target before target replacement is required. In the measurements discussed here the target consist of a $10 \mu\text{m}$ Al foil.

Special attention was dedicated, during the experiment, to establish target integrity at the time of arrival of the main pulse on target which strongly depends on the temporal profile of the laser pulse [14]. A cross-correlation curve of the laser pulse taken with the Sequoia (Amplitude Technologies) is shown in Fig. 3. According to this plot, the laser contrast is greater than 10^7 up to 10 ps before the peak of the pulse. A detailed modeling of laser–target interaction with such a laser temporal profile is in progress, but we can anticipate that with the measured laser

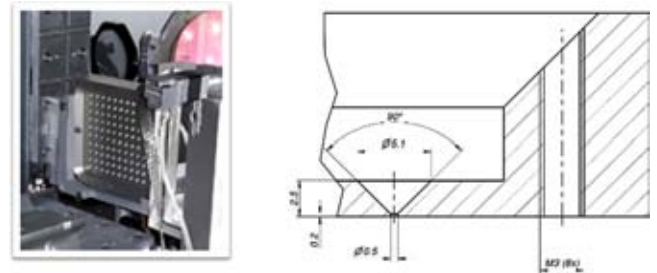


Fig. 2. (left) Target mount showing the $500 \mu\text{m}$ hole array. (right) Detail showing the conical hole geometry.

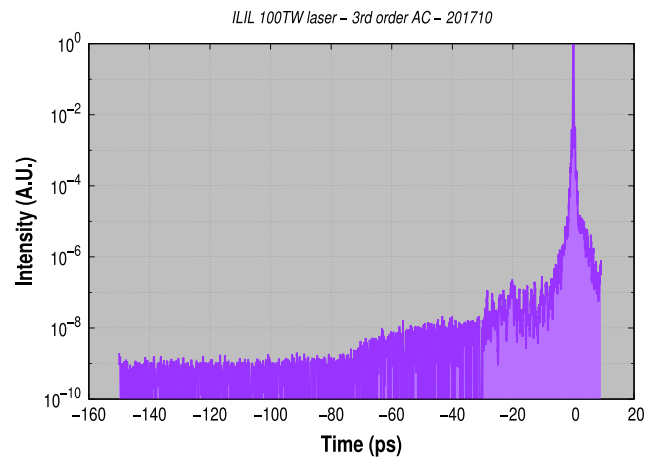


Fig. 3. Cross-correlation curve of the laser pulse.

contrast, no major pre-plasma formation occurs, ensuring bulk target survival at the peak of the pulse.

These circumstances were further confirmed by optical spectroscopy of the light scattered in the specular direction, collected shot by shot using a F/5 collecting lens placed in vacuum to collimate scattered light outside the target chamber. Light was then attenuated using neutral filters and rejecting filters at 800 nm and focused on the tip of a fiber coupled to a spectrometer. This set up enabled detection of second harmonic emission, $2\omega_L$, and $(3/2)\omega_L$ of the incident laser light scattered in the specular direction. Such components are associated to the coupling of the laser light at the critical density and at the quarter critical density respectively [15].

In fact, the formation of even a very small pre-plasma before of the arrival of the main pulse can provide suitable conditions for the growth of stimulated instabilities including the Stimulated Raman Scattering and the Two Plasmon Decay (see [6] and references therein). Electron plasma waves at $\omega_L/2$ generated by the instabilities can couple non-linearly with the incident laser light and give rise to $(3/2)\omega_L$ emission. This emission is therefore a signature of the presence of even a small pre-plasma.

Second harmonic emission in the specular direction is generated by the non-linear interaction of the main laser pulse at the critical density [16]. Therefore, second harmonic emission can be taken as a signature of the presence of a critical density layer in the plasma at the time of interaction of the main pulse, a prerequisite for the interaction with an over-dense target and the occurrence of TNSA.

As shown by Fig. 4, in our experiments, in spite of the increase of the $(3/2)\omega_L$ intensity compared to the previous experimental campaign at 10 TW [13], the intensity of the $2\omega_L$ emission remains always significant, indicating that the laser contrast in the best focus is sufficient to ensure survival of an overdense target.

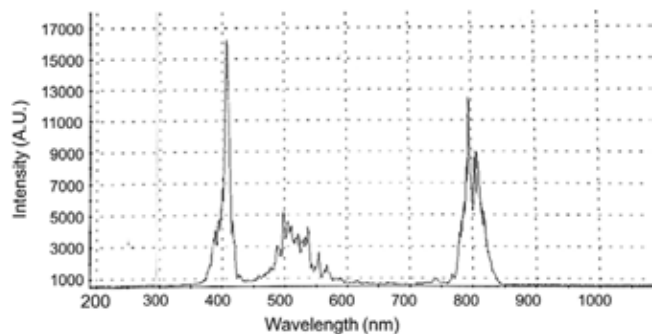


Fig. 4. A typical spectrum obtained with the target placed near the best focus. The second harmonic component at 400 nm is used to monitor the survival of the target at the peak of the pulse.

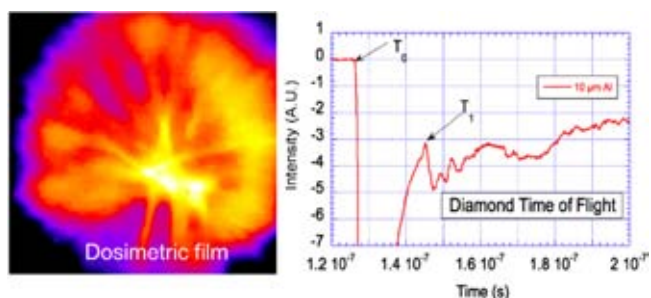


Fig. 5. (left) The signal from the GAFchromic™ EBT-3 film placed at 100 mm from the target rear surface. (right) Signal of the diamond Time of Flight (TOF) showing the ion signal from the irradiation of a 10 μm thick aluminium target. $T = 0$ is arbitrary in this plot. The strong emission in the range $t = [T_0 - T_1]$ is the signal due to fast electrons. For $t > T_1$ the signal is due to ions detection.

3. Results and discussion

A range of diagnostics were used in our experiments to measure ion acceleration, including radio-chromic films (GAF), CR39, Thomson Parabola, and Time of Flight (TOF) diamond detectors. Thomson Parabola Spectrometer (TPS) and a TOF detector were used simultaneously so that a cross-comparison of the signals obtained from the two devices was possible. This was done in view of a possible use of the diamond detector for on-line direct detection of accelerated ions during normal operation. A detailed discussion of all these measurements with different detectors is given elsewhere [17,18]. Here, we focus our attention on the presentation of the preliminary results of TOF and TPS signals obtained during the currently operating L3IA phase 1 configuration.

A typical GAF image obtained with a 10 μm thick Al target is shown in Fig. 5(left), showing an intense on-axis spot, surrounded by a broader signal.

Fig. 5(right) shows the plot of the TOF signal obtained with the diamond detector from the irradiation of the same 10 μm thick Al target. The TOF detector was placed at a distance of 60 cm from the target rear side and was filtered using a 12 μm thick Al foil. The strong peak between $t = T_0$ and $t = T_1$ is attributed to a combination of X-rays and fast electrons reaching the detector soon after the interaction [13,17]. This peak is then followed by the actual ion signal that starts at $t = T_1$. Taking into account the TOF distance and assuming a signal predominantly due to protons that have the highest charge-to-mass ratio, calculations yield a high energy cut-off of approximately 5 MeV.

For the same aluminium shot, the raw TPS spectrogram is also presented in Fig. 6, showing the parabolic traces of protons and carbons with different ionization states. As we can see, the assumption that the TOF ion signal is predominantly due to protons is consistent with

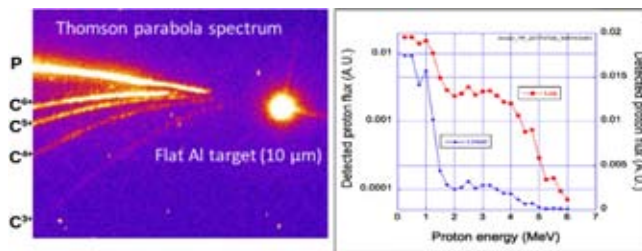


Fig. 6. Image of the Thomson Parabola Spectrometer (TPS) spectrogram from a 10-μm thick aluminium target showing protons and carbon ions with different charge states. The proton spectrum is also reported (right) in logarithmic scale showing the proton cut-off energy of 6 MeV.

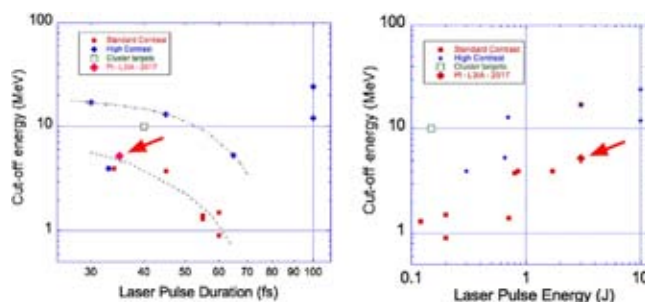


Fig. 7. Summary of data from published TNSA experiments (after [1]) showing measured dependence upon laser pulse duration (left) and laser pulse energy (right). The arrows indicate the cutoff energy of our experiment.

the TPS signal showing a bright proton signal. The analysis of the TPS proton spectrum is presented in Fig. 6(right). The measured proton cut-off energy considering the minimum detectable signal above noise is 6 MeV. The TPS measurement is in agreement with the TOF estimate that is done at a higher signal level. The possibility of using our TOF detector for a reliable, online shot to shot proton energy evaluation is therefore confirmed.

It is interesting to compare the measured cut-off energy with published results obtained in similar interaction conditions. A summary of published results relevant for our experimental conditions, taken from [1], is displayed in Fig. 7 as a function of laser pulse duration (left) and laser pulse energy (right) showing the cut-off of our experiment for comparison. These plots show that the cut-off energy measured in our experiment is in agreement or even exceeds the cut-off values measured in similar experiments with standard contrast (no plasma mirror).

Our preliminary results from this commissioning experiment meet the expectations from first phase of L3IA as anticipated [13], enabling foreseen applications. Further increase of ion energy and flux will require fine tuning of laser pulse parameters and target optimization.

4. Conclusions

In summary, we described the preliminary data obtained during an experiment dedicated to the commissioning of the new laser-driven light ions acceleration line (L3IA). Our experiment shows proton acceleration cut-off energies up to 6 MeV which are in a perfect agreement with intensity scaling established by previous measurements in similar interaction conditions. Our data demonstrate overall laser and target performances of our setup in line with project specification planned for Phase 1.

Acknowledgments

This project has received funding from the CNR funded Italian research Network ELI-Italy (D.M. n.631 08.08.2016) and from the L3IA

INFN Experiment of CSN5. We gratefully acknowledge support from the Central Laser Facility for in kind contribution to the experimental set up described in this experiment.

References

- [1] H. Daido, M. Nishiuchi, A.S. Pirozhkov, Review of laser-driven ion sources and their applications, *Rep. Progr. Phys.* 75 (2012) 056401.
- [2] R.A. Snavely, Intense high-energy proton beams from petawatt-laser irradiation of solids, *Phys. Rev. Lett.* 85 (2000) 2945–2948.
- [3] M. Roth, M. Schollmeier, Ion acceleration — target normal sheath acceleration, in: *Proceedings of the CERN Conference, Geneva, Switzerland, 23–29 November 2014*, C14-11-23, pp. 231–270, <http://dx.doi.org/10.5170/CERN-2016-001.231>.
- [4] H. Ahmed, S. Kar, G. Cantono, G. Nersisyan, S. Brauckmann, D. Doria, D. Gwynne, A. Macchi, K. Naughton, O. Willi, et al., Investigations of ultrafast charge dynamics in laser-irradiated targets by a self probing technique employing laser driven protons, *Nucl. Instrum. Methods Phys. Res. A* 829 (2016) 172–175.
- [5] B. Hidding, T. Königstein, O. Willi, J. Rosenzweig, K. Nakajima, G. Pretzler, et al., Laser-plasma accelerators — A novel, versatile tool for space radiation studies, *Nucl. Instrum. Methods Phys. Res. A* 636 (2011) 31–40.
- [6] M. Barberio, S. Veltri, M. Scisciò, P. Antici, Laser-accelerated proton beams as diagnostics for cultural heritage, *Sci. Rep.* 7 (2017) 40415.
- [7] M. Noaman-ul Haq, H. Ahmed, T. Sokollik, L. Yu, Z. Liu, X. Yuan, F. Yuan, M. Mirzaie, X. Ge, L. Chen, et al., Statistical analysis of laser driven protons using a high-repetition-rate tape drive target system, *Phys. Rev. Accel. Beams* 20 (2017) 041301.
- [8] P. Mason, M. Divoky, K. Ertel, J. Pilar, T. Butcher, M. Hanus, S. Banerjee, J. Phillips, J. Smith, M. De Vido, et al., Kilowatt average power 100 J-level diode pumped solid state laser, *Optica* 4 (2017) 438–439.
- [9] M. Blanco, M.T. Flores-Arias, C. Ruiz, M. Vranic, Table-top laser-based proton acceleration in nanostructured targets, *New J. Phys.* 19 (3) (2017) 033004.
- [10] F. Romano, F. Schillaci, G.A.P. Cirrone, G. Cuttone, V. Scuderi, L. Allegra, A. Amato, A. Amico, G. Candiano, G.D. Luc, et al., The ELIMED transport and dosimetry beamline for laser-driven ion beams, *Nucl. Instrum. Methods Phys. Res. A* 829 (2016) 153–158.
- [11] S. Kar, H. Ahmed, R. Prasad, M. Cerchez, S. Brauckmann, B. Aurand, G. Cantono, P. Hadjisolomou, C.L.S. Lewis, A. Macchi, G. Nersisyan, A.P.L. Robinson, A.M. Schroer, M. Swantusch, et al., Guided post-acceleration of laser-driven ions by a miniature modular structure, *Nature Commun.* 7 (2016) 10792.
- [12] S. Agosteo, M.P. Anania, M. Caresana, G.A.P. Cirrone, C. de Martinis, D.D. Side, A. Fazzi, G. Gatti, D. Giove, D. Giulietti, et al., The LILIA (laser induced light ions acceleration) experiment at LNF, *Nucl. Instrum. Methods Phys. Res. B* 331 (2014) 15–19.
- [13] L.A. Gizzi, D. Giove, C. Altana, F. Brandi, P. Cirrone, G. Cristoforetti, A. Fazzi, P. Ferrara, L. Fulgentini, P. Koester, L. Labate, G. Lanzalone, P. Londrillo, D. Mascali, A. Muoio, D. Palla, F. Schillaci, S. Sinigardi, S. Tudisco, G. Turchette, A new line for laser-driven light ions acceleration and related TNSA studies, *Appl. Sci.* 7 (2017) 984.
- [14] F. Baffigi, G. Cristoforetti, L. Fulgentini, A. Giulietti, P. Koester, L. Labate, L.A. Gizzi, X-ray conversion of ultra-short laser pulses on a solid sample: Role of electron waves excited in the pre-plasma, *Phys. Plasmas* 21 (2014) 072108.
- [15] L.A. Gizzi, in: K. Yamanouchi, A. Giulietti, K. Ledingham (Eds.), *Advances in X-ray Studies of Ultraintense Laser-Plasma Interactions*, in: *Progress in Ultrafast Intense Laser Science*, vol. 98, Springer, New York, NY, USA, 2010, pp. 123–138.
- [16] L.A. Gizzi, D. Giulietti, A. Giulietti, P. Audebert, S. Bastiani, J.P. Geindre, A. Mysyrowicz, Simultaneous measurements of hard X-rays and second-harmonic emission in fs laser-target interactions, *Phys. Rev. Lett.* 76 (1996) 2278.
- [17] L.A. Gizzi, C. Altana, F. Brandi, P. Cirrone, G. Cristoforetti, A. Fazzi, P. Ferrara, L. Fulgentini, D. Giove, P. Koester, et al., Role of laser contrast and foil thickness in target normal sheath acceleration, *Nucl. Instrum. Methods Phys. Res. A* 829 (2016) 144–148.
- [18] C. Altana, A. Muoio, G. Lanzalone, S. Tudisco, F. Brandi, G.A.P. Cirrone, G. Cristoforetti, A. Fazzi, P. Ferrara, L. Fulgentini, et al., Investigation of ion acceleration mechanism through laser-matter interaction in femtosecond domain, *Nucl. Instrum. Methods Phys. Res. A* 829 (2016) 159–162.

Intra-cycle depolarization of ultraintense laser pulses focused by off-axis parabolic mirrors

Luca Labate^{1,2}, Gianluca Vantaggiato¹, and Leonida A. Gizzi^{1,2}

¹Istituto Nazionale di Ottica, Consiglio Nazionale delle Ricerche, via Moruzzi 1, 56124 Pisa, Italy

²Istituto Nazionale di Fisica Nucleare, Sezione di Pisa, largo B. Pontecorvo 3, 56127 Pisa, Italy

(Received 15 January 2018; revised 19 February 2018; accepted 29 March 2018)

Abstract

A study of the structure of the electric and magnetic fields of ultraintense laser pulses focused by an off-axis parabolic mirror is reported. At first, a theoretical model is laid out, whose final equations integration allows the space and time structure of the fields to be retrieved. The model is then employed to investigate the field patterns at different times within the optical cycle, for off-axis parabola parameters normally employed in the context of ultraintense laser–plasma interaction experiments. The results show that nontrivial, complex electromagnetic field patterns are observed at the time at which the electric and magnetic fields are supposed to vanish. The importance of this effect is then studied for different laser polarizations, f numbers and off-axis angles.

Keywords: laser-driven particle acceleration; laser focusing; off-axis parabolic mirrors; ultrashort laser pulses

1. Introduction

Off-axis parabolic (OAP) mirrors have now become an essential tool to focus ultrashort laser pulses down to micrometre size spots, thus allowing relativistic intensities ($\gtrsim 10^{18} \text{ W} \cdot \text{cm}^{-2}$) to be reached. Indeed, focusing by means of OAP, which basically enables to get rid of the nonlinear and dispersive effects occurring in refractive optics, is currently pursued on basically all of the 10 TW–1 PW scale laser facilities worldwide (see Ref. [1] for instance and references therein), providing intensities on target up to $\sim 10^{21} \text{ W} \cdot \text{cm}^{-2}$. The usage of OAP is also envisaged as essential to get tight focusing of the next generation >10 PW scale lasers in order to reach an intensity on target in the 10^{22} – $10^{24} \text{ W} \cdot \text{cm}^{-2}$ range, thus allowing strong field quantum electrodynamics (QED) phenomena such as radiation reaction, vacuum polarization and pair production to be investigated^[2, 3].

On the other hand, the wealth of physical processes involved in laser–matter interaction at relativistic or ultra-relativistic intensity requires a detailed knowledge of the spatial and temporal structure of the electromagnetic field in the focal region. For instance, laser–plasma interaction processes depending on the laser polarization, such as, among others, the ones involved in proton acceleration, via

either target normal sheath acceleration or radiation pressure acceleration (see Refs. [4, 5] and references therein), or the excitation of parametric instabilities^[6–8], are normally modelled using focused pulses with an ideal space and time structure. The detailed study of the structure of the electromagnetic field of beams focused by means of parabolic surfaces was initially undertaken in the field of optical microscopy, and thus devoted to the investigation of on-axis reflecting parabolic surfaces. The earliest works were essentially based on geometric optics approaches^[9]; in Ref. [10] a mixed method is used, based on geometric propagation from the paraboloid surface to a spherical surface, which is then used, in turn, as a boundary surface for a vector diffraction treatment based on the Stratton–Chu^[11, 12] theory. The first studies based on a direct numerical integration of diffraction integrals, for either off-axis^[13] or on-axis^[14, 15] parabolic mirrors, date back to the early 2000s. Such approaches, made possible by the availability of advanced numerical integration schemes and increasingly powerful simulation platforms, were driven by the need for tight focusing in applications such as confocal microscopy (see Ref. [16] for instance). Beside theoretical/numerical studies^[14, 15, 17], different focusing configurations were also experimentally investigated^[18–20].

Motivated by the widespread diffusion of OAP mirrors as optical devices to focus ultrashort laser pulses, a growing attention is being devoted by the community active in the field of ultraintense laser–matter interaction to the experimental

Correspondence to: L. Labate, Istituto Nazionale di Ottica, Consiglio Nazionale delle Ricerche, via Moruzzi 1, 56124 Pisa, Italy.
Email: luca.labate@ino.cnr.it

characterization of the intensity pattern in the focal region of high-intensity beams. This is a crucial issue even in light of the strong wavefront aberrations which can be expected to occur in $\gtrsim 10$ TW laser systems, unless wavefront correction techniques are applied. In particular, the available intensity in the focal plane has been studied for 100 TW scale systems both with^[21] and without^[22] correcting the wavefront distortions by means of adaptive mirrors. More recently, the study of the aberrations induced by a not ideal OAP alignment was undertaken from a theoretical as well as an experimental point of view^[23, 24]. In Ref. [24], in particular, a theoretical model was developed, based on a full vector diffraction treatment, to study parameters such as the maximum intensity and Strehl ratio in the focal region of an OAP in the presence of small misalignments. These parameters are of particular importance in the context of laser–matter interaction at ultrahigh intensity.

These latter studies did not account for the ultrashort duration of the pulse; in other words, no time dependence was considered. As it is known since the first works dealing with the focusing of ultrashort pulses by lenses^[25], the envelope of the focused pulse takes on a rather complex structure in the far-field region, so that analytical frameworks able to predict the detailed electromagnetic field behaviour of an ultrashort pulse focused by an OAP would be desirable. However, as it can be easily realized, such treatments are rather involved, due to both the ultrashort duration (also implying large bandwidth) and the structure of the boundary surface (that is, the reflecting OAP surface).

A theory enabling the study of the far field of femtosecond pulses focused by a parabolic mirror, although in an on-axis configuration, was recently presented in Ref. [26], aimed at investigating the ultimate intensity achievable under very tight focusing ($f/\# < 1$) with the next generation $\gtrsim 10$ PW systems. In particular, the authors first develop a theoretical treatment based on vector diffraction theory for a monochromatic wave upon reflection from the on-axis parabolic surface; based on that, the fields in the focal region of a femtosecond pulse are then calculated using a coherent superposition of monochromatic beams with suitable spectral amplitude and phase relationships. A different approach was more recently proposed in Ref. [27]. The method provides an equation (for a hertz-type vector potential) with the same structure of a unidirectional pulse propagation equation, which can be thus numerically solved using standard beam propagation methods. The reflection from an on-axis parabolic surface is taken into account using suitable initial conditions for the beam to be propagated. By comparison with full vector diffraction calculations the authors find out that their method gives pretty accurate results down to $f/\# \sim 2-3$, while a 2-step method, involving the numerical integration of a diffraction integral, has to be used for smaller f numbers.

The works reported in Refs. [26, 27] both account for a time dependence of the focused ultrashort pulse at an

envelope level. Recently, a group working in the field of terahertz radiation reported on an experiment in which the electric and magnetic fields of a THz beam focused with a 90° OAP mirror were characterized with sub-cycle time resolution^[28, 29]. In particular, the authors observed a loss of the original polarization structure and the formation of what they call electromagnetic divergence and rotation at the time of the optical cycle at which the fields are supposed to vanish. In Ref. [28] the authors also develop a simple and approximate model; although not directly applicable to their experimental results, due to its validity strictly holding only for high f numbers, this model predicts the observed loss of the original polarization. An approximate theoretical description of the electric field in the focal region has been also recently proposed by the same authors^[30]. Indeed, the first guess that the original beam polarization could not be preserved due to off-axis focusing dates back to Ref. [31], where a theoretical model is presented predicting that the polarization of a beam focused by an off-axis ellipsoidal mirror exhibits a (smooth) spatial dependence in the focal plane. However, this observation only concerned the time averaged pattern of the polarization direction and did not describe any change occurring at a sub-cycle level.

In this paper, we first present, in Section 2, an exact theoretical model allowing the electric and magnetic fields of a laser beam (with a super-Gaussian transverse profile) focused by an OAP to be calculated. Unlike previous works, our framework is based on a full vector diffraction treatment and also retains a time dependence of the fields as provided by their initial phases, thus allowing the electromagnetic field pattern to be retrieved at any given time within the optical cycle. Using this model and solving the resulting integrals by numerical calculations, we study then, in Section 3.1, the field maps at different times, showing that, as a result of the off-axis focusing, electric (magnetic) fields are generated, during the optical cycle, along directions different from the original polarization direction (or original magnetic field direction, respectively). In order to assess the importance of this unusual and unexpected effect, basically resulting in a generation of intra-cycle cross polarization, we carry out a parametric study as a function of the OAP f number and focal length; we also show how this phenomenon depends upon the original pulse polarization direction with respect to the OAP geometry. Finally, in Section 4, after mentioning some possible consequences of this intra-cycle depolarization in the context of laser–plasma interaction, we draw some conclusions and outline some future work.

2. Theoretical model

As typical in the field of ultrashort laser beam focusing, we consider in our model an OAP mirror whose boundary, projected onto a plane orthogonal to the (parent) paraboloid axis, is a circle. In other words, the mirror boundary results from the intersection of a revolution paraboloid surface and

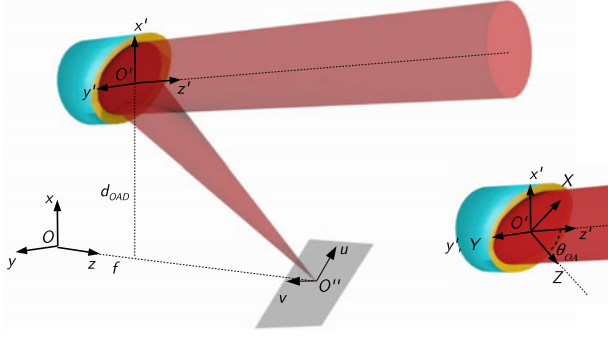


Figure 1. Sketch showing the systems of coordinates used throughout the text.

a cylinder with axis parallel to the paraboloid axis (we denote the distance between the two axes as d_{OAD}). The axis of the cylinder intersects the OAP surface at a point which from now on we will refer to as the ‘OAP centre’. Figure 1 provides some conventions used in the following. In particular, the system of Cartesian orthogonal coordinates $Oxyz$ is centred on the parent paraboloid vertex and is oriented in such a way that the parabola focus and the OAP centre (O' in Figure 1) are located at the points $\mathbf{x}_f = (0, 0, z_f)$, with $z_f = f > 0$, and $\mathbf{x}_c = (d_{OAD}, 0, d_{OAD}^2/4f)$, respectively. The meridional (sagittal) plane is thus the plane $x-z$ ($y-z$). The OAP surface (S_{OAP}) is therefore identified by the equation

$$z = \frac{1}{4f}(x^2 + y^2) = a(x^2 + y^2) = s(x, y) \cdot f \quad (1)$$

together with the condition $(x - d_{OAD})^2 + y^2 \leq (d/2)^2$, where d is the OAP diameter (we have defined $a = 1/4f$ and $s(x, y) = (x^2 + y^2)/4f^2$, which will be useful in the following). We can also introduce the so-called off-axis angle ϑ_{OA} , defined by $\tan \vartheta_{OA} = d_{OAD}/(f - ad_{OAD}^2)$. In the following, two further systems of coordinates will be used, both having the origin at the OAP centre (see the inset of Figure 1): the system $O'x'y'z'$, which is obtained from $Oxyz$ with just a translation, and the system $O'XYZ$, which encompasses a further rotation of an angle $-\vartheta_{OA}$ around the y -axis (Z lies thus along the direction of the ray reflected from the OAP centre, which will be occasionally called the ‘central ray’ in the following).

We now consider a monochromatic beam, with a super-Gaussian transverse profile, incident along the $-z'$ direction; its electric and magnetic fields can thus be written, in the $O'x'y'z'$ system, as

$$\mathbf{E}(\mathbf{x}', t) = A'(x', y')(\cos \delta \hat{\mathbf{e}}_{x'} + \sin \delta \hat{\mathbf{e}}_{y'}) \times e^{-ik(z'-z'_0)} e^{-i\omega t} \equiv \mathbf{E}_{\text{inc}}(\mathbf{x}') e^{-i\omega t}, \quad (2)$$

$$\mathbf{B}(\mathbf{x}', t) = A'(x', y')(\sin \delta \hat{\mathbf{e}}_{x'} - \cos \delta \hat{\mathbf{e}}_{y'}) \times e^{-ik(z'-z'_0)} e^{-i\omega t} \equiv \mathbf{B}_{\text{inc}}(\mathbf{x}') e^{-i\omega t}, \quad (3)$$

with

$$A'(x', y') = A_0 \exp \left\{ -\frac{1}{2} \left[\left(\frac{x'}{\sigma_x} \right)^2 + \left(\frac{y'}{\sigma_y} \right)^2 \right]^n \right\}, \quad (4)$$

n being the super-Gaussian order of the spatial profile of the beam. In equations (2) and (3) we have assumed that the phase of the incoming beam is equal to zero at $t = 0$ on a reference plane $z' = z'_0$, with $z'_0 > 0$ (also, we have implicitly ruled out any deviation from a perfect planar wavefront). The angle δ was introduced in order to account for different polarization directions; in particular, $\delta = 0$ ($\delta = \pi/2$) corresponds to a polarization in the meridional (sagittal) plane.

We are now interested in the time-dependent behaviour of the electromagnetic fields in the focal region upon reflection off the OAP surface. As it is well known, the problem can be formally factorized into the time and space domains, and a suitable diffraction approach can be used to deal with this latter domain. As a consequence, we can write the field at the point \mathbf{x}_P at time t as $\mathbf{E}(\mathbf{x}_P, t) = \mathbf{E}_{SC}(\mathbf{x}_P) e^{-i\omega t}$ (a similar equation holds for \mathbf{B}), where the spatial part has to be calculated using a suitable diffraction formulation; in our case, we use a full vector diffraction approach based on the Stratton–Chu theory (hence the subscript SC). As recently discussed in Ref. [32], the Stratton–Chu approach allows, generally speaking, beams with sharper transverse profiles to be dealt with, with respect to a more direct approach based on Green’s theorem applied to each field. It can be shown (see for instance our recent paper^[24]) that, assuming a perfect (100%) reflection, the boundary fields (on the OAP surface) appearing in the Stratton–Chu theory can be related to the incident fields, and the resulting integrals read

$$\mathbf{E}_{SC}(\mathbf{x}_P) = \frac{1}{2\pi} \int_{OAP} [ik(\hat{\mathbf{n}} \times \mathbf{B}_{\text{inc}})G + (\hat{\mathbf{n}} \cdot \mathbf{E}_{\text{inc}})\nabla G] dA, \quad (5)$$

$$\mathbf{B}_{SC}(\mathbf{x}_P) = \frac{1}{2\pi} \int_{OAP} [(\hat{\mathbf{n}} \cdot \nabla G)\mathbf{B}_{\text{inc}} - (\mathbf{B}_{\text{inc}} \cdot \nabla G)\hat{\mathbf{n}}] dA. \quad (6)$$

Here G is the Green function for the Helmholtz equation, $G = \exp(ik|\mathbf{x} - \mathbf{x}_P|)/|\mathbf{x} - \mathbf{x}_P| \equiv \exp(ik|\mathbf{u}|)/|\mathbf{u}|$, with $\mathbf{u} = \mathbf{x} - \mathbf{x}_P$. The integrals are of course carried out over the OAP surface.

Using as parameters of the OAP surface just the x, y coordinates of each point, we can write the (inward) normal to the surface as $\hat{\mathbf{n}} = (-x/2f, -y/2f, 1)/\sqrt{1 + s(x, y)}$ and the area element as $dA = \sqrt{1 + s(x, y)} dx dy$. The incident fields in the above integrals must be expressed in the system $Oxyz$ and can be easily retrieved from equations (2) and (3); the electric field, for instance, can be written as $\mathbf{E}_{\text{inc}}(\mathbf{x}) = A(x, y)(\cos \delta \hat{\mathbf{e}}_x + \sin \delta \hat{\mathbf{e}}_y) e^{ikp(\mathbf{x})}$. Here $p(\mathbf{x})$ is the optical path from the point $(x, y, z_0 = ad_{OAD}^2 + z'_0)$ on the reference plane to the point $(x, y, a(x^2 + y^2))$ on the OAP surface (notice that we are assuming $z_0 > a(x^2 + y^2)$, $\forall x, y \in S_{OAP}$).

The transverse field amplitude is obtained as $A(x, y) = A'(x - d_{OAD}, y)$.

On substituting all these expressions into equations (5) and (6) one thus gets, after some cumbersome algebra, the following equations for the (time-dependent) electric and magnetic field components focused by the OAP:

$$E_j(\mathbf{x}_P, t) = e^{-i\omega t} \frac{i}{\lambda} \int_{\text{OAP}} A(x, y) e^{ik(p(\mathbf{x})+u(\mathbf{x}, \mathbf{x}_P))} \times g^{(E_j)}(\mathbf{x}, \mathbf{x}_P) dx dy, \quad (7)$$

$$B_j(\mathbf{x}_P, t) = e^{-i\omega t} \frac{i}{\lambda} \int_{\text{OAP}} A(x, y) e^{ik(p(\mathbf{x})+u(\mathbf{x}, \mathbf{x}_P))} \times \frac{1}{u^2} \left(1 - \frac{1}{iku}\right) g^{(B_j)}(\mathbf{x}, \mathbf{x}_P) dx dy, \quad (8)$$

with $j = x, y, z$. In these expressions $u = u(\mathbf{x}, \mathbf{x}_P) = |\mathbf{u}| = |\mathbf{x} - \mathbf{x}_P|$ and the functions $g^{(E_j)}(u(\mathbf{x}, \mathbf{x}_P))$, $g^{(B_j)}(u(\mathbf{x}, \mathbf{x}_P))$ can be written as

$$g^{(E_x)} = \frac{1}{u} \cos \delta - \left(1 - \frac{1}{iku}\right) \frac{1}{u^2} \times \left(\frac{x}{2f} \cos \delta + \frac{y}{2f} \sin \delta\right) (x - x_P), \quad (9)$$

$$g^{(E_y)} = \frac{1}{u} \sin \delta - \left(1 - \frac{1}{iku}\right) \frac{1}{u^2} \times \left(\frac{x}{2f} \cos \delta + \frac{y}{2f} \sin \delta\right) (y - y_P), \quad (10)$$

$$g^{(E_z)} = \frac{1}{u} \left(\frac{x}{2f} \cos \delta + \frac{y}{2f} \sin \delta\right) - \left(1 - \frac{1}{iku}\right) \frac{1}{u^2} \times \left(\frac{x}{2f} \cos \delta + \frac{y}{2f} \sin \delta\right) (z - z_P), \quad (11)$$

and

$$g^{(B_x)} = \left(-\frac{x}{2f} \cos \delta - \frac{y}{2f} \sin \delta\right) (y - y_P) + (\sin \delta)(z - z_P), \quad (12)$$

$$g^{(B_y)} = \left(\frac{x}{2f} \cos \delta + \frac{y}{2f} \sin \delta\right) (x - x_P) - (\cos \delta)(z - z_P), \quad (13)$$

$$g^{(B_z)} = -(\sin \delta)(x - x_P) + (\cos \delta)(y - y_P). \quad (14)$$

The real part of the fields, which we are going to use in the following, can be easily calculated from the above equations. In particular, it can be readily verified that

$$E_{j,r}(\mathbf{x}_P, t) = -\frac{1}{\lambda} \int_{\text{OAP}} \left[g_r^{(E_j)} \sin(kv - \omega t) + g_i^{(E_j)} \cos(kv - \omega t) \right] A(\mathbf{x}) dx dy, \quad (15)$$

$$B_{j,r}(\mathbf{x}_P, t) = -\frac{1}{\lambda} \int_{\text{OAP}} g^{(B_j)} \frac{1}{u^2} \left[\sin(kv - \omega t) + \frac{1}{ku} \cos(kv - \omega t) \right] A(\mathbf{x}) dx dy, \quad (16)$$

where we have defined $v \equiv v(\mathbf{x}, \mathbf{x}_P) \equiv p(\mathbf{x}) + u(\mathbf{x}, \mathbf{x}_P)$, $g_r^{(E_j)}(\mathbf{x}, \mathbf{x}_P) = \text{Re}(g^{(E_j)}(\mathbf{x}, \mathbf{x}_P))$ and $g_i^{(E_j)}(\mathbf{x}, \mathbf{x}_P) = \text{Im}(g^{(E_j)}(\mathbf{x}, \mathbf{x}_P))$ (notice that the functions $g^{(B_j)}$ are real valued). Equations (15) and (16), along with the expressions for the $g^{(E_j)}$ and $g^{(B_j)}$ functions (9)–(11) and (12)–(14), allow the time-dependent electric and magnetic field values at any space–time point to be calculated. It is worth to point out that, although not providing a closed expression, and thus requiring a numerical approach to be solved, no approximation or Taylor expansion has been used in our treatment, so that they retain the validity of the original Stratton–Chu formulation as detailed in Ref. [14].

In the field of high-intensity laser–matter interaction, one is in general interested in the study of the field components along longitudinal and transverse directions with respect to the focused beam propagation direction, that is the direction along $O'O''$ in Figure 1. With our conventions, this basically requires the knowledge of the field components in the system of coordinates $O'XYZ$; it is readily verified that these components can be retrieved from the components in the $Oxyz$ system, provided by the integrals (15) and (16), using the obvious transformation $\mathbf{F}^{(O'XYZ)} = \mathcal{R}(\vartheta_{OA})\mathbf{F}^{(Oxyz)}$, where $\mathcal{R}(\vartheta_{OA})$ is the matrix accounting for the rotation of an angle ϑ_{OA} around the y -axis.

In the following discussion, we use the coordinates u and v shown in Figure 1 to label the directions on a plane orthogonal to the central ray.

3. Intra-cycle behaviour of the electromagnetic fields

3.1. General discussion

In this section, we discuss some general features of the electric and magnetic fields in the focal plane of the OAP, starting from a numerical integration of equations (15) and (16) at different times during the optical cycle. The numerical integration was performed using a multi-dimensional adaptive integration scheme based on the algorithm described in Ref. [33]. For the sake of the following discussion, we used a beam with $\lambda = 800$ nm and with a transverse amplitude profile given by formula (4) with $n = 4$ and $A_0 = 1$; we also consider a rotationally symmetric beam ($\sigma_x = \sigma_y = \sigma$) and set the value of σ so as to have a beam with an intensity full width at half-maximum (FWHM) of 40 mm. The integration algorithm was implemented in a C++ code; with the above parameters, the integration required for each field component (at a given point and time) took typically a few hundreds of milliseconds to complete on a (Linux based) desktop PC equipped with a pretty standard CPU.

As said above, we are interested here in the field behaviour on the focal plane at different times of the optical cycle. For the sake of conciseness, from now on we will refer to the time at which the electric and magnetic fields at the centre of the observation plane (that is, at the point which the central

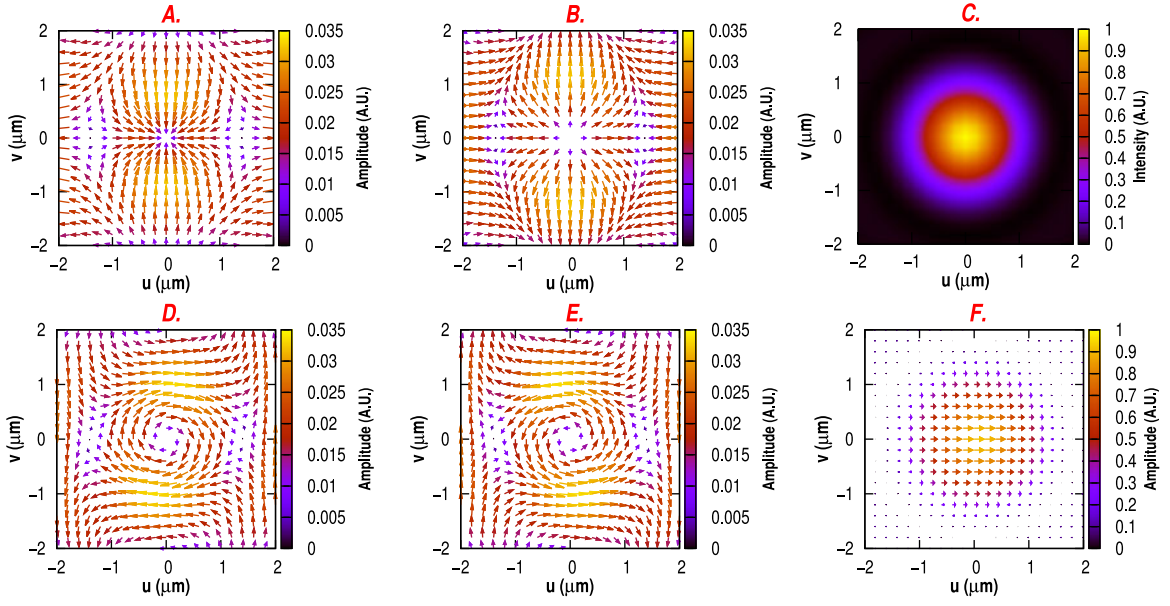


Figure 2. Left and middle columns: pattern of the E (top – plots A and B) and B (bottom – plots D and E) vector fields at t_0 and $t_0 + T/2$ for an $f/2$, $\vartheta_{OA} = 40^\circ$ OAP. Right column: intensity (top – plot C) and E field pattern (bottom – plot F) at t_{max} . The beam incident on the OAP is supposed to be polarized along x (or u , corresponding to $\delta = 0^\circ$).

ray is supposed to pass through) take on their maximum amplitude as t_{max} ; conversely, we refer to the time at which both fields are supposed to vanish as t_0 .

The bottom right plot of Figure 2 (plot F) shows the direction and amplitude (normalized to 1) of the electric field (in the focal plane) at t_{max} , for a beam polarized along x ($\delta = 0$ in equations (2) and (3)) and focused by an OAP with $f/\# = 2$ and $\vartheta_{OA} = 40^\circ$. As expected, the electric field is directed along the u direction. The top right plot (plot C) shows, for the sake of a visual aid in considering the importance of the effects we are going to discuss, the intensity of the focused beam.

The first (left) column of Figure 2 shows the direction and amplitude of the electric (plot A) and magnetic (plot D) fields at t_0 . Here, a not obvious effect can be observed. Indeed, both the electric and magnetic fields actually only vanish in the surroundings of the central point, while a complex pattern is observed out of this point. Looking at the colour scale of these plots, one can see that the nonzero field components reach typical values of a few percent of those at t_{max} ; we will discuss later how the importance of this effect depends upon the OAP parameters such as the f number and the off-axis angle.

The middle column of Figure 2 shows the E and B field patterns at the other minimum within the optical cycle, that is at $t_0 + T/2$, being T the radiation period. As it is rather predictable, the field patterns are similar to those encountered at t_0 , with the sign of the fields reversed.

It is interesting to look, at this point, at the behaviour of the fields for times very close to t_0 . Figure 3 shows the E -field pattern for the times $t_0 - T/200$ (top) and $t_0 + T/200$ (bottom) (this time span corresponds to a few tens of attoseconds for a

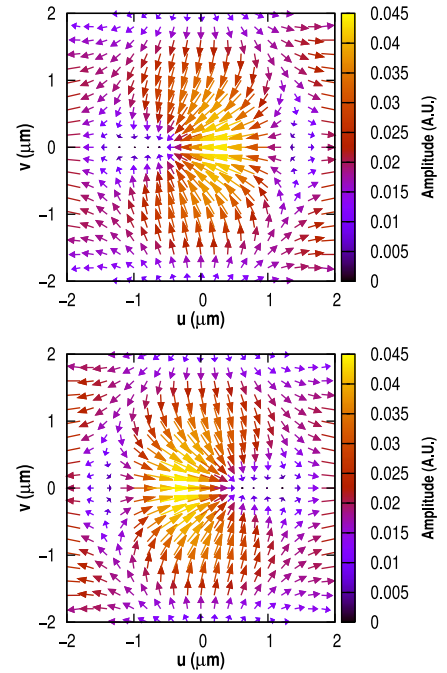


Figure 3. Pattern of the E vector field at the times $t_0 - T/200$ (top) and $t_0 + T/200$ (bottom), for an $f/2$, $\vartheta_{OA} = 40^\circ$ OAP.

typical infrared laser beam). As it can be easily realized from this Figure, the region where the field actually vanishes does describe a sort of sweep along the meridional (x - z) plane. In other words, for a small neighbour of the points in the meridional plane, a time instant exists, close to t_0 , at which the field is zero; this time instant corresponds to t_0 only for the focal point.

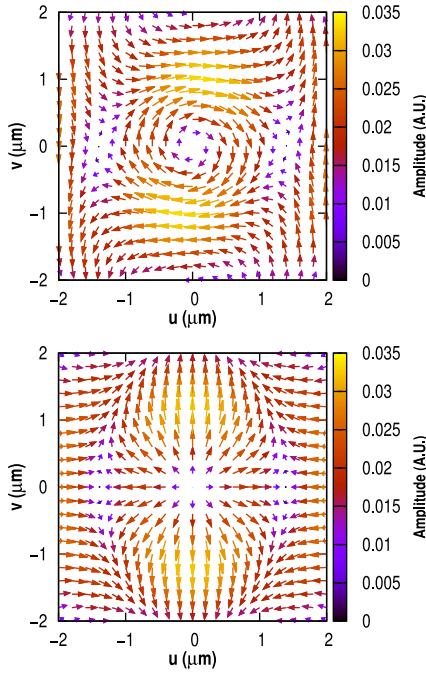


Figure 4. E (top) and B (bottom) field patterns at t_0 for an $f/2$, $\vartheta_{OA} = 40^\circ$ OAP, with an incident beam polarized along y (or v , corresponding to $\delta = 90^\circ$).

The pattern of E and B is interchanged when an incident beam polarized along y is considered; this can be seen in Figure 4, which shows the electric and magnetic field patterns at t_0 for the same OAP and beam parameters as the ones considered in Figure 2 but with $\delta = 90^\circ$. Finally, as shown in Figure 5, the situation is somewhat intermediate for a beam incident on the OAP with a polarization at 45° with respect to the x - z plane; in this case, the typical convergent/divergent pattern seen for the E field (in the case $\delta = 0^\circ$) or for the B field (in the case $\delta = 90^\circ$) is not encountered any more. However, it should be observed that the typical maximum amplitude of the fields at t_0 , which is of the order of a few percent of that at t_{max} , does not depend on the beam polarization.

It is worth to observe that a longitudinal electric field component is also appearing at t_0 . Figure 6 shows a density map of the ratio of the longitudinal component E_z to the transverse component $|E_{tr}| = \sqrt{|E_u|^2 + |E_v|^2}$, calculated at t_0 . As it can be realized by comparing with the top left plot of Figure 2, a longitudinal field component appears in the regions where the transverse field component $|E_{tr}|$ is smaller (except for the neighbour of the central point).

Notice that in Figure 6 we have restricted our attention to a region of interest (ROI) over which the focused beam intensity keeps at a level greater than 0.1 of its maximum; in other words, we have only considered points (u, v) such that $I(u, v) \geq 0.1 I_{max}$ and forced to a zero value all the points outside this ROI. Beside enabling a better readability of the plots, this procedure allows us to only consider a spatial region where the field observed at t_0 has enough magnitude

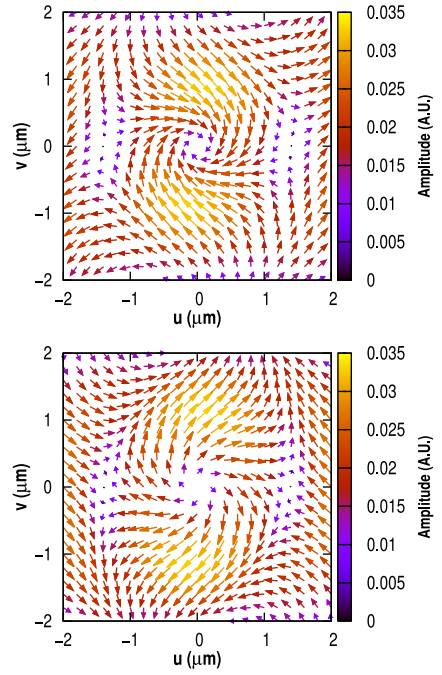


Figure 5. E (top) and B (bottom) field patterns at t_0 for an $f/2$, $\vartheta_{OA} = 40^\circ$ OAP, with an incident beam polarized at 45° with respect to x (or u , corresponding to $\delta = 45^\circ$).

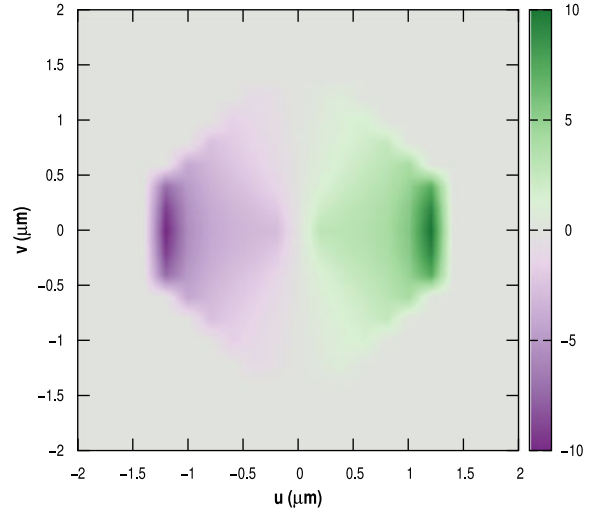


Figure 6. Map of the ratio (calculated at t_0) of the E field longitudinal component E_z to the transverse component $|E_{tr}|$, for an $f/2$, $\vartheta_{OA} = 40^\circ$ OAP and a beam polarized along x .

to potentially lead to nonnegligible physical effects in real laser-plasma interaction experiments. Unless otherwise specified, this procedure will be adopted in the following discussion.

3.2. Depolarization dependence upon the OAP parameters

We are now interested in investigating how the anomalous field patterns observed at the time t_0 depend upon the OAP

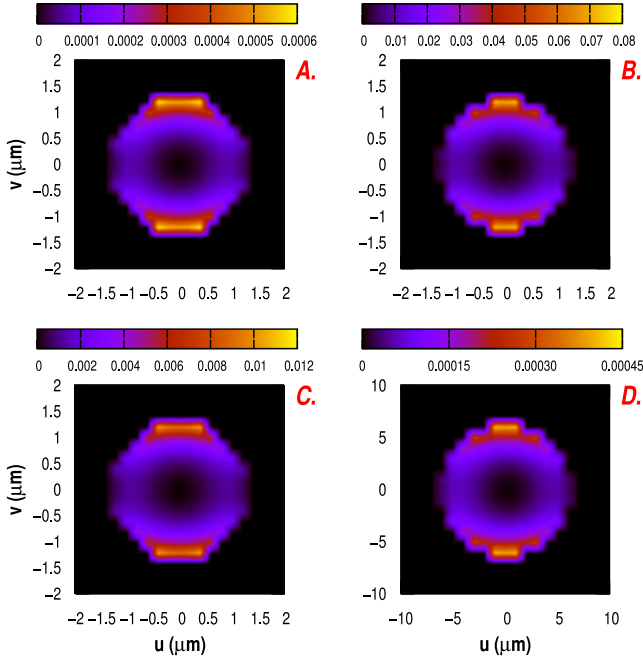


Figure 7. Maps of the ratio of $|E_{tr}|^2$ at t_0 to the corresponding value at t_{max} , calculated for a beam polarized along x ($\delta = 0^\circ$) and focused with the following OAPs: $f/2$, $\vartheta_{OA} = 10^\circ$ (plot A), $f/2$, $\vartheta_{OA} = 90^\circ$ (plot B), $f/2$, $\vartheta_{OA} = 40^\circ$ (plot C), $f/10$, $\vartheta_{OA} = 40^\circ$ (plot D).

parameters, namely the f number and the off-axis angle. To this purpose, we first look at the ratio of the square modulus of the electric field transverse component ($|E_{tr}|^2 = |E_u|^2 + |E_v|^2$) at t_0 to the corresponding quantity at t_{max} . Notice that for this discussion, we restrict our attention to the E field, since similar results obviously hold for the B field.

Figure 7 shows the maps (restricted to the ROI defined above) of this ratio for an increasing off-axis angle ϑ_{OA} (top row) and for an increasing f number (bottom row). In particular, the top row shows the maps of $|E_{tr}|^2|_{t_0}/|E_{tr}|^2|_{t_{max}}$ for an $f/2$ OAP with $\vartheta_{OA} = 10^\circ$ (plot A) and $\vartheta_{OA} = 90^\circ$ (plot B). It can be seen that the amplitude of the field obtained at t_0 is strongly dependent on the off-axis angle. In fact, by integrating the equations (15) and (16) for an on-axis parabola we find that the fields at t_0 almost vanish across all the plane; the effects observed at t_0 are thus a consequence of the off-axis focusing scheme. Analogously, the maps in the bottom row of Figure 7 show that the $f/\#$ plays a role as well: tighter focusing causes larger field components to appear at t_0 .

As it is clear from Figure 7, the (relative) magnitude of the anomalous fields at t_0 is not uniform across the ROI. For a quantitative assessment of the dependence upon the $f/\#$ and ϑ_{OA} of the observed phenomena, we thus need a spatially averaged quantity; we can consider, for instance, the integral of the square modulus of the transverse E field averaged over the ROI using the local intensity as a weight:

$$\langle |E_{tr}|^2 \rangle := \frac{\int_{ROI} |E_{tr}|^2 I(u, v) du dv}{\int_{ROI} I(u, v) du dv}.$$

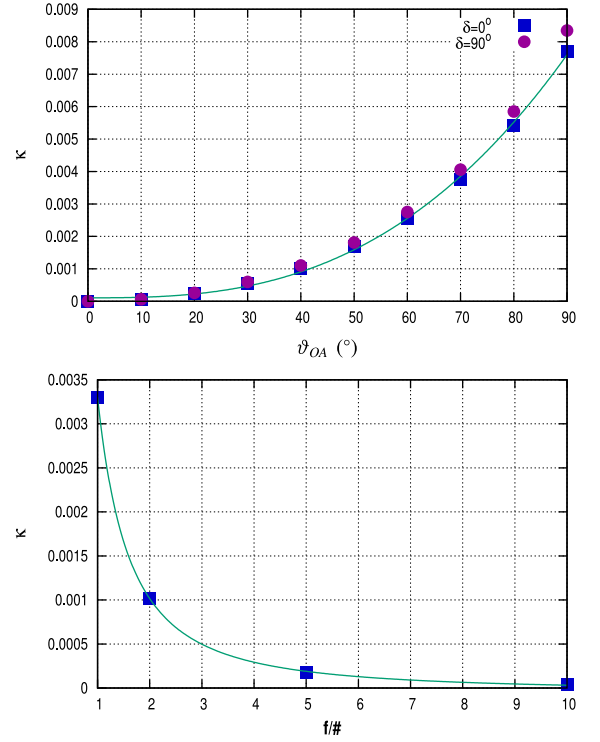


Figure 8. Plots of the κ parameter (defined in the text) vs. the off-axis angle ϑ_{OA} (top) and the $f/\#$ (bottom). In the first plot, data for both the x ($\delta = 0^\circ$) and y ($\delta = 90^\circ$) polarizations are shown, while only the data for the x polarizations are shown in the second plot. The results of fits with functions of the form given in equation (17) are also shown for the case $\delta = 0^\circ$.

In particular, we define the parameter κ as the ratio of this quantity at t_0 to the corresponding value at t_{max} : $\kappa := \langle |E_{tr}|^2 \rangle|_{t_0} / \langle |E_{tr}|^2 \rangle|_{t_{max}}$. In Figure 8 we plot the κ parameters as a function of the off-axis angle (top) and of the f number (bottom). Fitting the data, the following scaling laws can be obtained for the x polarization:

$$\kappa \propto (\vartheta_{OA})^\alpha, \quad \kappa \propto \frac{1}{(f/\#)^\beta}, \quad (17)$$

with $\alpha \simeq 2.75$ and $\beta \simeq 1.66$. Finally, we notice that a weak difference between the two orthogonal polarizations of the incoming beam ($\delta = 0^\circ$ and $\delta = 90^\circ$) can be observed; the corresponding α value for the y polarization is $\alpha \simeq 2.77$.

4. Conclusions and open issues

Starting from an exact time-dependent, vector diffraction based model developed on purpose, we have studied the electromagnetic field behaviour, at different times within the optical cycle, of a beam focused by an OAP mirror. In particular, we have investigated the electric and magnetic field patterns across planes orthogonal to the beam propagation direction.

A behaviour far from trivial was found, in the focal region, at the time (t_0) at which the electric and magnetic fields

are supposed to vanish; actually, this zero field value only occurs in a small neighbour of the focus, while a complex electromagnetic field pattern exists at farther points. Such a complex pattern basically results in the appearance of field components orthogonal to the original polarization (or magnetic field) direction; furthermore, longitudinal field components (that is, directed along the original propagation direction) can also appear.

What seems to be relevant for laser–matter interaction experiments at relativistic intensities is the fact that the amplitude of these ‘anomalous’ electric and magnetic fields can reach, depending on the focusing conditions, values of a few percent of the maximum values expected during the optical cycle. Beside the boundaries of the beam, where the intensity (and thus the field amplitude) drops down to negligible values, this may occur, under some circumstances, even within a transverse spatial region where the field values are supposed to be high enough so as to potentially lead to nonnegligible effects on the laser–matter interaction dynamics.

As mentioned in the Introduction, such effects are to be possibly expected for laser–plasma interaction processes dependent on the laser polarization, in particular when tight focusing is employed, such as proton acceleration via either target normal sheath acceleration or radiation pressure acceleration. On the other hand, according to our results, the phenomena discussed in this paper are expected to be negligible at high f numbers, so that, for instance, no departure from an ‘ideal’ laser beam is expected to occur in the context of Laser WakeField Acceleration experiments, where long focal length OAPs are commonly employed in order to sustain a long laser beam propagation.

As a final remark we observe that, in order to theoretically investigate possible effects in the laser–matter interaction at ultrahigh intensity, a full knowledge of the temporal dynamics of the field patterns discussed here would be needed. The discussion of a theory allowing such a study to be carried out is beyond the scope of the current paper and will be reported elsewhere. According to preliminary investigations carried out by numerically calculating the field integrals given above at different times close to the time t_0 and studying the resulting patterns, we can estimate that the features observed around this time have typical timescales of the order of 10^{-2} of the pulse cycle.

Acknowledgements

We acknowledge support from the EU’s Horizon 2020 research and innovation programme through the project ‘Eu-PRAXIA’ (grant agreement No. 653782), from the Italian Ministry of Education, University and Research (MIUR) through the PRIN project ‘Preclinical Tool for Advanced Translational Research with Ultrashort and Ultraintense x-ray Pulses’ (prot. 20154F48P9) and from the MIUR through the research network funding ELI-Italy (‘Attoseconds’).

References

1. C. Danson, D. Hillier, N. Hopps, and D. Neely, *High Power Laser Sci. Eng.* **3**, e3 (2015).
2. G. A. Mourou, T. Tajima, and S. V. Bulanov, *Rev. Mod. Phys.* **78**, 309 (2006).
3. A. Di Piazza, C. Müller, K. Z. Hatsagortsyan, and C. H. Keitel, *Rev. Mod. Phys.* **84**, 1177 (2012).
4. H. Daido, M. Nishiuki, and A. S. Pirozhkov, *Rep. Prog. Phys.* **75**, 056401 (2012).
5. A. Macchi, M. Borghesi, and M. Passoni, *Rev. Mod. Phys.* **85**, 751 (2013).
6. F. Baffigi, G. Cristoforetti, L. Fulgentini, A. Giulietti, P. Köster, L. Labate, and L. A. Gizzi, *Phys. Plasmas* **21**, 071208 (2014).
7. G. Cristoforetti, A. Anzalone, F. Baffigi, G. Bussolino, G. D’Arrigo, L. Fulgentini, A. Giulietti, P. Köster, L. Labate, S. Tudisco, and L. A. Gizzi, *Plasma Phys. Controll. Fusion* **56**, 095001 (2014).
8. L. Labate, M. Galimberti, A. Giulietti, D. Giulietti, P. Köster, P. Tomassini, and L. A. Gizzi, *Appl. Phys. B* **86**, 229 (2007).
9. J. E. Howard, *Appl. Opt.* **18**, 2714 (1979).
10. C. J. R. Sheppard, A. Choudhury, and J. Gannaway, *IEE J. Microwaves Opt. Acoust.* **1**, 129 (1977).
11. J. A. Stratton and L. J. Chu, *Phys. Rev.* **56**, 99 (1939).
12. J. D. Jackson, *Classical Electrodynamics*, 3rd ed. (Wiley, 1998).
13. P. Argujio, M. S. Scholl, and G. Paez, *Appl. Opt.* **40**, 2909 (2001).
14. P. Varga and P. Török, *J. Opt. Soc. Am. A* **17**, 2081 (2000).
15. P. Varga and P. Török, *J. Opt. Soc. Am. A* **17**, 2090 (2000).
16. M. A. Lieb and A. J. Meixner, *Opt. Express* **8**, 458 (2001).
17. A. April and M. Piché, *Opt. Express* **18**, 22128 (2010).
18. J. Stadler, C. Stanciu, C. Stupperich, and A. J. Meixner, *Opt. Lett.* **33**, 681 (2008).
19. A. Drechsler, M. A. Lieb, C. Debus, A. J. Meixner, and G. Tarrach, *Opt. Express* **9**, 637 (2001).
20. R. Dorn, S. Quabis, and G. Leuchs, *Phys. Rev. Lett.* **91**, 233901 (2003).
21. S.-W. Bahk, P. Rousseau, T. A. Planchon, V. Chvykov, G. Kalintchenko, A. Maksimchuk, G. A. Mourou, and V. Yanovsky, *Appl. Phys. B* **80**, 823 (2005).
22. L. Liu, H. Peng, K. Zhou, X. Wang, X. Wang, X. Zeng, Q. Zhu, X. Huang, X. Wei, and H. Ren, *Proc. SPIE* **5856**, 646 (2005).
23. R. Heathcote, R. J. Clarke, T. B. Winstone, and J. S. Green, *Proc. SPIE* **8844**, 884409 (2013).
24. L. Labate, P. Ferrara, L. Fulgentini, and L. A. Gizzi, *Appl. Opt.* **55**, 6506 (2016).
25. M. Kempe and W. Rudolph, *Phys. Rev. A* **48**, 4721 (1993).
26. T. M. Jeong, S. Weber, B. Le Garrec, D. Margarone, T. Mocek, and G. Korn, *Opt. Express* **23**, 11641 (2015).
27. A. Couairon, O. G. Kosareva, N. A. Panov, D. E. Shipilo, V. A. Andreeva, V. Jukna, and F. Nesa, *Opt. Express* **23**, 31240 (2015).
28. K. Shibata, M. Takai, M. Uemoto, and S. Watanabe, *Phys. Rev. A* **92**, 053806 (2015).
29. M. Takai, K. Shibata, M. Uemoto, and S. Watanabe, *Appl. Phys. Express* **9**, 052206 (2016).
30. K. Shibata, M. Uemoto, M. Takai, and S. Watanabe, *J. Opt.* **19**, 035603 (2017).
31. J. A. Murphy, *Int. J. Infrared Millimeter Waves* **8**, 1165 (1987).
32. J. Peatross, M. Berrondo, D. Smith, and M. Ware, *Opt. Express* **25**, 13990 (2017).
33. J. Bernstein, T. O. Espelid, and A. Genz, *ACM Trans. Math. Soft.* **17**, 437 (1991).

Measurements of parametric instabilities at laser intensities relevant to strong shock generation

G. Cristoforetti,¹ L. Antonelli,² S. Atzeni,² F. Baffigi,¹ F. Barbato,³ D. Batani,⁴ G. Boutoux,⁴ A. Colaitis,⁴ J. Dostal,^{5,6} R. Dudzak,^{5,6} L. Juha,^{5,8} P. Koester,¹ A. Marocchino,^{2,7} D. Mancelli,^{4,8} Ph. Nicolai,⁴ O. Renner,^{6,5} J. J. Santos,⁴ A. Schiavi,² M. M. Skoric,⁹ M. Smid,⁶ P. Straka,⁶ and L. A. Gizzi¹

¹Intense Laser Irradiation Laboratory, INO-CNR, 56124 Pisa, Italy

²Dipartimento SBAI, Università di Roma "La Sapienza," 00185 Roma, Italy

³Empa Swiss Federal Laboratories for Materials Science and Technology, 8600 Dübendorf, Switzerland

⁴Université Bordeaux, CNRS, CEA, CELIA, UMR 5107, F-33405 Talence, France

⁵Institute of Plasma Physics, Czech Academy of Sciences, 182 00 Prague 8, Czech Republic

⁶Institute of Physics, Czech Academy of Sciences, 182 21 Prague 8, Czech Republic

⁷Laboratori Nazionali di Frascati, 00044 Frascati, Rome, Italy

⁸Donostia International Physics Center (DIPC), 20018 Donostia/San Sebastian, Basque Country, Spain

⁹National Institutes of Natural Sciences, 105-0001 Tokyo, Japan

(Received 21 September 2017; accepted 18 December 2017; published online 8 January 2018)

Parametric instabilities at laser intensities in the range $(2\text{--}6) \times 10^{15}$ W/cm² (438 nm, 250 ps, 100–300 J) have been investigated in planar geometry at the Prague Asterix Laser System facility via calorimetry and spectroscopy. The density scalelength of the plasma was varied by using an auxiliary pulse to form a preplasma before the arrival of the main laser beam and by changing the delay between the two pulses. Experimental data show that Stimulated Brillouin Scattering (SBS) is more effective than Stimulated Raman Scattering (SRS) in degrading laser-plasma coupling, therefore reducing the energy available for the generation of the shock wave. The level of the SBS backscatter and laser reflection is found to be in the range between 3% and 15% of the incident laser energy, while Backward SRS (BRS) reflectivity ranges between 0.02% and 0.2%, depending on the delay between the pulses. Half-integer harmonic emission is observed and provides a signature of Two Plasmon Decay (TPD) occurring around the quarter of the critical density. Data analysis suggests that SRS is driven in beam speckles with high local intensity and occurs in bursts, particularly at higher laser intensities, due to the presence of kinetic mechanisms saturating the SRS growth in the speckles. Time-resolved measurements also show that BRS occurs in the trailing part of the laser pulse, when the plasma has a longer density scalelength. Our measurements also indicate that hot electrons are predominantly produced by SRS rather than TPD. *Published by AIP Publishing.* <https://doi.org/10.1063/1.5006021>

I. INTRODUCTION

Shock ignition (SI) is a promising two-step scheme of Inertial Confinement Fusion (ICF), where a strong converging shock wave is launched at the end of the compression phase to ignite the fuel.^{1–4} Both the compression of the DT pellet and the igniting shock wave can be produced by a single tailored laser pulse, consisting of a ns long peak at moderate intensity lower than 10^{15} W/cm² followed by a short intense spike (300–500 ps) at intensity between 10^{15} and 10^{16} W/cm². The SI approach may allow ignition with a low-velocity implosion, reducing the growth of the Rayleigh-Taylor Instability. In addition, SI is robust with respect to non-uniform spike irradiation and shock synchronization, as predicted by hydrodynamic simulations^{5,6} and leads to high gain,⁷ possibly enabling ignition at moderate laser energies, which are already available at Laser Megajoule (LMJ)⁸ and National Ignition Facility (NIF) facilities.⁹ In this context, an extensive preparatory study has been carried out also in the framework of the HiPER project¹⁰ and is now aiming at full scale demonstration at one of the above facilities.

The success of the SI concept depends mainly on the coupling of the laser spike with the extended corona surrounding the imploding shell, where an efficient laser absorption, which is able to generate a strong shock wave (>300 Mbar), is needed. In recent experiments carried out at the OMEGA laser^{11,12} in spherical irradiation geometry, at laser intensities relevant for SI ($I \sim 6 \times 10^{15}$ W/cm²), a peak ablation pressure close to 400 Mbar was inferred, which constitutes a significant breakthrough towards the demonstration of the feasibility of the SI scheme. Despite this step forward, the physics of the laser-plasma interaction in this highly non-linear regime is still largely unknown and needs dedicated investigations. In particular, the growth of parametric instabilities such as Stimulated Brillouin Scattering (SBS), Stimulated Raman Scattering (SRS), and Two-Plasmon Decay (TPD), and their interplay, can be considerable, and laser filamentation can further enhance their role in the interaction. These processes can significantly degrade laser-plasma coupling due to a strong reflection of light (SBS and SRS), resulting in the absorption of laser energy in rarefied regions of the corona, far from the ablation layer. Moreover, TPD and SRS generate electron plasma waves that lead to suprathermal electrons via damping.

Such electrons, depending on their energy,^{2,11–15} may preheat the fuel or affect the shock pressure.

In the last few decades, parametric instabilities have been deeply investigated in conditions suitable for direct-drive and indirect-drive schemes¹⁶ of ICF. The majority of these studies, therefore, refers to an interaction regime significantly different from that envisaged for the SI scheme, with laser intensities a factor 10 lower, leaving the interaction regime of interest for SI almost unexplored. The extrapolation of these studies to SI conditions is made complex by the high nonlinearity of parametric instabilities in this regime. After a rapid boost, instabilities can show a saturation due to non-linear effects limiting the growth of electron plasma waves (EPWs) or ionic acoustic waves (IAWs) in the interaction region. EPW decay via Langmuir Decay Instability^{17,18} and ponderomotive trapping of thermal electrons in the EPW field are classical examples of phenomena, leading to EPW saturation. More recently, other nonlinear mechanisms, such as bowing and filamentation of EPW into laser speckles,^{19,20} collective speckle effects,²¹ or instability cascades, have been suggested. All these mechanisms produce a phase detuning of the waves, which in many cases results in consecutive stages of damping and excitation of instabilities, in a burst-like, chaotic behavior.^{22,23} A fully kinetic approach is therefore needed to model processes as non-local heat transport or Landau damping in the kinetic regime.^{19,24,25}

Recently, several attempts have been made to model laser-plasma interactions in SI conditions with fully kinetic massively parallel PIC codes. According to Riconda *et al.*²⁶ and Klimo *et al.*,^{27,28} most of the laser energy is absorbed at densities lower than $n_c/4$, where n_c is the critical density for the main beam, and the reflectivity due to parametric instabilities, temporally bunched in trains of bursts, can span from the percent level to 30%–50% of the laser energy. Simulations show the importance of kinetic effects, leading to ps- or subps-long bursts of SRS and SBS, where SRS sometimes occurs in the inflationary regime, and to non-Maxwellian distributions of electron energies. Simulations also reveal the importance of modelling 2D and 3D effects such as filamentation, laser spraying, cavitation, or side-scattered EPW/light. Unfortunately, 2D numerical simulations carried out in the density range 0.01–0.3 n_c are at present limited to a few picoseconds of the interaction, which is much shorter than the ignition spike and which is inadequate to model processes having a small growth rate, such as filamentation. While particle in cell simulations (of the Vlasov-Fokker-Planck equation) are limited to a few picoseconds due to their computation costs, a series of reduced-hydrodynamic models are being investigated to partially take into account some effects that might influence the nanosecond plasma evolution, such as the nonlocal electron transport,²⁹ the growth of parametric instability, the generation of fast electrons,³⁰ and the influence of self-induced magnetic fields.³¹

A few experiments carried out at OMEGA^{11,12,32,33} and LULI facilities^{34–36} investigated the laser plasma interaction at SI intensities. The overall energy scattered by SRS/SBS in these experiments is disparate, in a range going from a few percent up to ~40%–50% of the incident energy, strongly dependent on the irradiation geometry and on the laser

intensity. SRS back-reflectivity is found to be around 10% in all the experiments, rising to ~20% when side-scattered light is also considered.³⁵ SRS reflectivity shows a larger range of variability, going from a few percent in planar irradiation experiments^{33–35} up to ~36% in spherical geometry.^{11,32} SI experiments at the OMEGA laser also suggest that SRS is the dominant mechanism of generation of hot electrons (HE), showing a conversion efficiency as high as ~9% of the laser energy in the case of spherical irradiation. Furthermore, they suggest that HE can significantly contribute to the shock formation by increasing the ablation pressure by ~30%.⁹ Both the variability of SRS and its effects on the fuel compression call for additional investigation. In particular, the dependence of SRS threshold and saturation on the beam speckle size needs further attention.

In this paper, we report and discuss experimental data obtained in a series of experiments carried out in a planar geometry at the Prague Asterix Laser System (PALS)³⁷ at intensities of interest for the Shock Ignition interaction regime. The overall description of the diagnostics used and an overview of the experimental results obtained, including the measured pressure of the shock wave, are reported elsewhere.^{38–42} Here, we focus on the laser plasma interaction and in particular, on the Stimulated Raman Scattering and Two Plasmon Decay instabilities. Despite our density scalelength (~100 μm) and the electron temperature (~1.5–2 keV) being lower than those envisaged in a real SI scenario, the data reported here provide a comprehensive study of the growth of parametric instabilities at a laser intensity relevant for SI where very little experimental data exist and where, as discussed above, a strong nonlinearity and interplay between different processes are expected to play a dominant role.

II. EXPERIMENTAL SETUP

A basic scheme of the experimental setup relevant to the results discussed here is shown in Fig. 1, while the complete setup is described elsewhere.³⁸

The interaction beam, frequency converted into the 3rd harmonic ($\lambda_0 = 438 \text{ nm}$) of the fundamental laser frequency and with a duration of 250 ps (FWHM), was smoothed by means of a Random Phase Plate (RPP) and focused on the target at normal incidence by an $f/2$ optical system. The beam profile in the focal spot and the effective energy enclosed in it were accurately measured by imaging and calorimetric techniques. RPP resulted in a Gaussian beam profile of ~100 μm (FWHM) and peak intensity in the range between 2 and $6 \times 10^{15} \text{ W/cm}^2$, depending on the energy of the laser shot.

In some shots, an auxiliary beam (not shown in Fig. 1) at the fundamental wavelength ($\lambda_0 = 1314 \text{ nm}$ and FWHM $\approx 250 \text{ ps}$) and incident at 30° with respect to the target normal impinged on the target before the main pulse and generated an extended preplasma, mimicking the corona at the end of the compression phase in the shock ignition scheme. The auxiliary beam had a focal spot diameter of ~900 μm (FWHM), i.e., much larger than the focal spot of the main beam, to reduce 2D effects during the interaction, resulting in a laser intensity of $\sim 7 \times 10^{13} \text{ W/cm}^2$. The delay

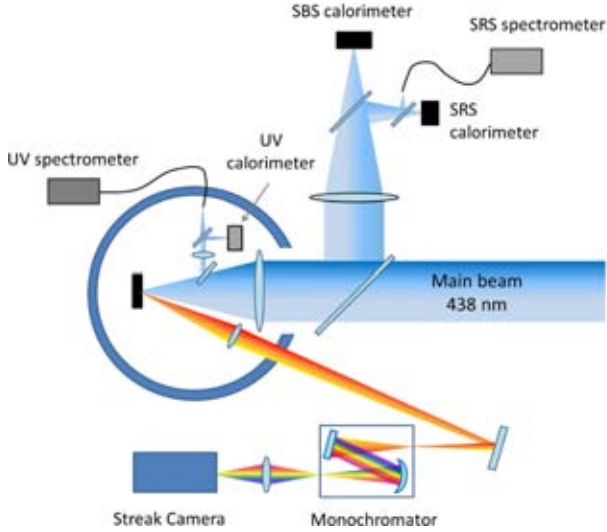


FIG. 1. Experimental setup used for the investigation of parametric instabilities.

between the peaks of auxiliary and main pulses was varied in the range between 0 and 1200 ps to change the density scale-length of the preplasma.

Thin multilayer targets consisting of a layer of plastic (C_8H_7Cl , parylene-C) with thicknesses ranging from 10 to $180 \mu m$ on the irradiated side, one or two tracer layers (5 to $10 \mu m$) of Cu and Ti and in some shots a $25 \mu m$ -thick Al layer on the rear side, were used. The low-Z material on the front played the role of the ICF ablator material, while chlorine ions allowed the plasma temperature to be measured via high-resolution X-ray spectroscopy. Both the spectra and the energy of the light backscattered during the laser plasma interaction were found not to depend on the thickness of the plastic layer nor on the presence of the Al layer. Therefore, these features of the targets are here disregarded. The layers of Cu and Ti were used as markers of hot electrons via K_α photon emission, which was detected using a CCD operating in the single-photon regime⁴³ and using two spherically bent quartz (422) and (203) crystal imaging spectrometers. Both K_α and X-ray spectrometers used Kodak AA400 films as detectors. A Bremsstrahlung spectrometer using k -edge and differential filtering (14 filters of increasing Z from Al to Pb) was also used with Imaging Plates to measure the x-ray fluence and, indirectly, infer a slope temperature for the hot electron distribution.⁴⁴ This spectrometer was looking at the front side of the target at $\sim 30^\circ$ from the laser axis.

The backscattered radiation originating from SRS and SBS/laser reflection was collected by the focusing lens and measured using two calorimeters. On the same line, the radiation was spectrally dispersed by a compact, fiber Vis-IR spectrometer ($\Delta\lambda_{res} \approx 1 \text{ nm}$), enabling the investigation of backscattered light up to $\omega_0/2$ ($\lambda \sim 876 \text{ nm}$), originating from SRS at densities lower than $n_c/4$ and SRS/TPD instabilities occurring near $n_c/4$. Such spectral resolution, however, did not allow the contribution of SBS to be separated from that of laser reflection in the backscattered emission at $\lambda \sim 438 \text{ nm}$. Light at $3/2\omega_0$ harmonics of laser frequency ($\lambda \sim 292 \text{ nm}$), originating from TPD, was collected inside the vacuum

chamber and sent to a UV spectrometer ($\Delta\lambda_{res} \approx 0.3 \text{ nm}$) and a calorimeter. Raman scattered light was also collected at a slightly larger angle than the focusing cone ($\approx 20^\circ$), spectrally dispersed by a monochromator, and relayed onto the entrance slit of a Hamamatsu C7700 Streak Camera. A spectral range of 100 nm was detected on the camera at a maximum temporal resolution of 8 ps.

III. INTERACTION CONDITIONS

The interaction conditions of the main pulse, with and without the auxiliary pulse, were modelled via hydrodynamic simulations performed with the codes DUED⁴⁵ and CHIC.⁴⁶ Figure 2 shows the instantaneous values of temperature and density scalelength $L = n_e/(dn_e/dx)$ at densities $n_c/4$ and $0.12 n_c$ for a laser intensity of $I_{max} = 2.9 \times 10^{15} \text{ W/cm}^2$ and a delay of 600 ps between auxiliary and main pulses. The $n_c/4$ and $0.12 n_c$ densities are the plasma regions where TPD and Backward SRS (BRS) are driven in the present experiment.

Figure 2(a) shows that the density scalelength rapidly increases during the pulse. The values of the scalelength at $n_c/4$ and $n_c/12$ are in the range between 20 and $80 \mu m$ and

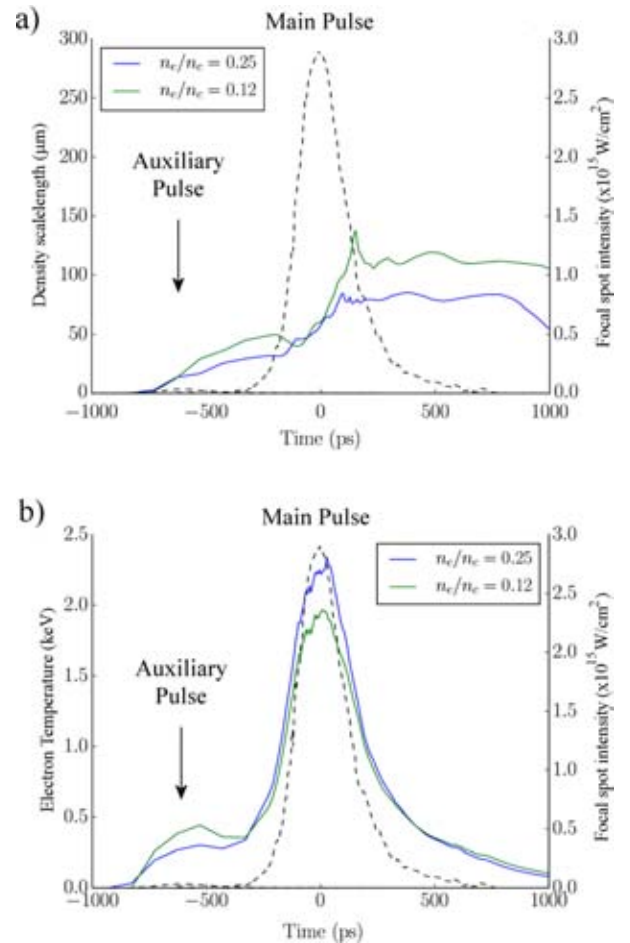


FIG. 2. Instantaneous values of the density scalelength (a) and temperature (b) computed at $n_c/4$ and $0.12 n_c$ by the CHIC code for a laser intensity $I_{max} = 2.9 \times 10^{15} \text{ W/cm}^2$ and a delay of 600 ps with respect to the auxiliary pulse. The intensity of the laser pulse is indicated as a gray dashed line and corresponds to the right-hand side ordinate axis.

between 40 and 150 μm , respectively, depending on the time and on the delay between the pulses. The scalelength increases with the delay between main and auxiliary pulses, showing a saturation at the longest delays explored. The preplasma scalelength given by the simulations is also in agreement with the 2D plasma density profiles measured by interferometric techniques (*monitor online*)³⁸ and X-ray laser (XRL) deflectometry.³⁹

According to Fig. 2(b), simulations show a time-dependent temperature, reaching maximum values between 1.9 keV and 2.5 keV, slightly depending on the laser intensity and density region, in the range of densities 0.10–0.25 n_c . According to the simulations, the temperature of the plasma during the main peak irradiation does not significantly depend on the delay between the pulses, with variations lower than 10%, but is determined by the energy of the main pulse. Spatially resolved X-ray spectra (not displayed here), showing well resolved He- and Li-like lines from Cl ions, were compared with SPECT3D predictions,⁴⁷ providing a temperature averaged over time of ≈ 700 –850 eV for all shots. Such values, however, refer to a plasma overdense region, for which hydrodynamic simulations predict temperatures of ≈ 800 –1000 eV at the time of the main laser peak. The time-averaged value of the temperature of the preplasma produced by the auxiliary pulse was also inferred by Cl X-ray spectroscopy. In this case, a value of ~ 175 eV was obtained for the underdense region, which is lower than the peak value of ~ 300 –400 eV obtained by simulations.

IV. CALORIMETRY

Here, we present the results of backscattered energy, namely, calorimetric measurements of the energy backscattered into the cone of the focusing lens. As already presented in Koester *et al.*,³⁸ backscattering is dominated by light around 438 nm, due to SBS and laser reflection, and ranges between 3% and 15% of the incident laser energy [Fig. 3(a)]. On the other hand, SRS gives rise to backscattered light in the 630–750 nm spectral range, consisting of $\sim 0.02\%$ –0.2% of laser energy [Fig. 3(b)]. Both these values show a clear increasing trend with the auxiliary-main pulse delay, where SBS and SRS reflectivities grow by factors 2 and 5, respectively, when the delay increases from 0 to 1200 ps. A similar trend is found for the intensity of scattered light in the spectral range 600–800 nm due to SRS [Fig. 3(b)]. This behavior can be explained by considering the inhomogeneity of the plasma which determines the convective gain of these instabilities. Regarding the trend in Fig. 3(a), hydrodynamic simulations show that the amount of backscattered laser light does not increase with the delay between the pulses; therefore, we expect that the trend observed is mainly determined by the growth of SBS instability with the delay. In our interaction conditions, however, the SBS threshold and the convective gain are mainly ruled by the gradient of the expansion velocity rather than by the density scalelength.⁴⁸ By using the approximate SBS threshold taken from Krueer⁴⁹ and the profiles obtained by hydrosimulations for shots without the auxiliary pulse, we find that the SBS threshold in the underdense plasma, which is determined by

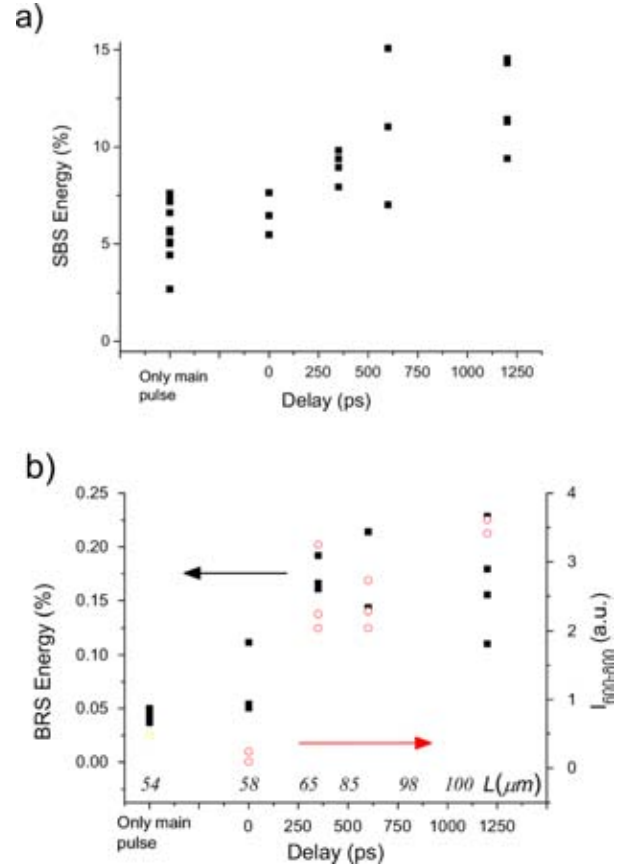


FIG. 3. (a) Energy backscattered by SBS and laser backscatter ($\lambda = 438$ nm). (b) SRS energy (black squares) and spectral intensity $I_{600-800}$ integrated in the range 600–800 nm (red circles) versus the delay auxiliary-main pulse for $I_{max} \approx (3.5-6) \times 10^{15}$ W/cm². The values of the density scalelength calculated by the code DUED in proximity of the laser peak ($I_{max} \approx 5 \times 10^{15}$ W/cm²) and at a density $n_e = 0.12 n_c$ are also reported for fixed values of auxiliary-main pulse delay.

the velocity gradients, is $I_{thres} \sim (1-2) \times 10^{15}$ W/cm², while the threshold calculated by considering the density gradient is an order of magnitude lower. Due to the poor spectral resolution, however, we were unable to determine accurately the plasma density region where SBS is driven. Hydrodynamic simulations including the auxiliary pulse clearly show that the gradient of the expansion velocity is strongly reduced in the underdense plasma, therefore lowering the SBS threshold and correspondingly boosting the instability gain. This can possibly explain the experimental results plotted in Fig. 3(a).

Figure 3(b), on the other hand, can be easily explained by considering that larger delays produce longer plasmas, resulting in larger gain for the SRS, whose threshold is strongly affected by the density scalelength in the plasma. In order to clarify the relationship between the auxiliary-main pulse delay and the density gradient, the values of the density scalelength calculated by the code DUED in the proximity of the laser peak ($I_{max} \approx 5 \times 10^{15}$ W/cm²) and at a density $n_e = 0.12 n_c$ are reported in Fig. 3(b) for fixed values of the delay.

Calorimetric measurements of $3/2\omega_0$ and $\omega_0/2$ emission, obtained by using an approximate isotropic distribution,

give a conversion efficiency ($\eta_{3/2}$) of around 0.5% of incident energy and a corresponding value $\eta_{1/2}$ in the range $(0.4-2) \times 10^{-2}\%$, i.e., a negligible loss of laser energy. Since the actual angular dependence is not known, such values have to be considered only as an order of magnitude.

V. HALF-INTEGER HARMONICS OF LASER FREQUENCY

Typical $\omega_0/2$ ($\lambda = 876$ nm) and $3/2\omega_0$ ($\lambda = 292$ nm) spectra are shown in Fig. 4. Both spectra exhibit an energy splitting around the harmonic wavelength, which is related to the frequency difference of plasma waves produced by TPD instability at $n_e \approx n_c/4$.

The frequency shift of TPD blue and red EPWs from the central frequency $\omega_0/2$ can be expressed by

$$|\delta\omega|/\omega_0 = \frac{9}{4} (v_{th}^2/c^2) \kappa, \quad (1)$$

where $\kappa = \mathbf{k}_B \cdot \mathbf{k}_0/k_0^2 - 1/2$, k_B is the blue EPW wavevector, and v_{th} is the thermal velocity.⁵⁰

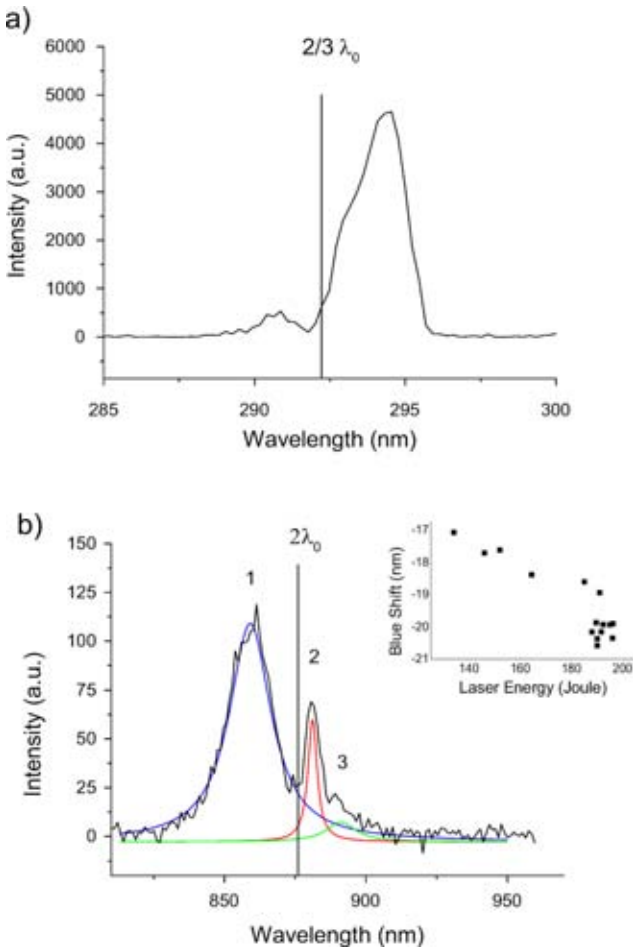


FIG. 4. Typical $3/2 \omega_0$ and $\omega_0/2$ spectra, obtained at $I_{max} \approx 5 \times 10^{15}$ W/cm² (black lines). Vertical lines indicate the position of the nominal laser harmonics. Red, green, and blue lines in (b) show the peaks resulting by fitting the spectrum using 3 Lorentzian peaks. The inset in (b) shows a plot of the shift of the blue peak 1 vs. the energy of the laser pulse. Adapted with permission from Cristoforetti *et al.*, *Europhys. Lett.* **117**, 35001 (2017), Copyright 2017 EPL Association.⁶⁵

The well-defined structure of $\omega_0/2$ [Fig. 4(b)] agrees with the relevant literature on the topic.^{51,52} Besides the evident blue- and red-shifted peaks (labelled 1 and 2, respectively), a less evident bump at longer wavelengths (peak 3) is visible, which we identify as a supplementary peak, as in Seka *et al.*⁵¹ The blue peak has a shift from the nominal $2\lambda_0$ wavelength and a width significantly larger than the red peak 2, approximately 3 and 3.6 times, respectively. Conversely, the shift of peak 1 is similar to the shift of the weak peak 3. The different frequency shift of peaks 1 and 3 ($\overline{\Delta\omega_{1,3}}/\omega_0 = 1.1 \times 10^{-2}$) and peak 2 ($\overline{\Delta\omega_2}/\omega_0 = 3.4 \times 10^{-3}$) indicates that the EPWs responsible for them have different wavevectors and a different origin. This is possible since TPD instability in an inhomogeneous plasma can generate different EPWs in the range allowed by the Landau damping.

Both frequency shifts increase with laser energy, as visible in the inset of Fig. 4(b) for the blue peak. In previous works,⁵¹ the sharp peak 2 was observed at laser intensities higher than TPD threshold but much lower than SRS threshold. For this reason, this is usually associated with a hybrid TPD/SRS instability rather than with a pure absolute SRS instability, where a pump electromagnetic wave decays in a forward electrostatic wave with $k \approx k_0$ (as TPD and SRS) and in a backward partly electrostatic and partly electromagnetic wave⁵³ in the proximity of the $n_c/4$ surface (here, $n_e/n_c \approx 0.24$). According to Seka *et al.*,⁵¹ the shift of this peak in the $\omega_0/2$ spectrum, differently from $3/2\omega_0$ splitting, is well applicable for the estimation of the plasma temperature because it is not affected by the angle of observation or by geometrical effects, such as filamentation, cavitation, or 2D profiles. By using Eq. (1) with $\kappa = 1/2$, we obtain a plasma temperature which increases from 1.35 keV to 1.68 keV when I_{max} rises from 2.4×10^{15} to 3.7×10^{15} W/cm². This value agrees with plasma temperature given by simulations, considering that it is calculated from time-integrated measurements; moreover, as shown below, it agrees with the Landau cutoff of the Raman spectrum produced at densities $n_e < n_c/4$.

According to the literature,⁵² the broad peak 1 and the small peak 3 can be generated by Inverse Resonance Absorption (IRA) or by Raman Downscattering (RD) of a laser photon. In the IRA process, an EPW with $k_{\perp}/k_0 < 0.1$ is converted into a photon near its turning point; therefore, blue and red peaks are originated by conversion of blue and red EPWs, respectively. In the RD process, conversely, a laser photon is down-scattered by an EPW produced by TPD, so that blue and red peaks are generated by scattering with red and blue EPWs, respectively. Both IRA and RD need particular matching conditions,^{51,54} and many authors have speculated on the prevalence of the one or the other in different experiments. Here, both coupling conditions can be fulfilled near $n_c/4$, where filamentation, turbulence, cavitation, and laser photon scattering can occur. For these reasons, it is here not possible to definitively exclude neither IRA nor RD. We note however that a blue shift $\Delta\lambda_B \approx 20$ nm implies $\kappa \approx 1.7$, indicating the involvement of EPWs with wavevector $k_e \approx 2.3k_0$. By taking a plasma temperature $T_e \approx 1.5$ keV, as estimated above, we obtain $k_e\lambda_D \approx 0.27$,

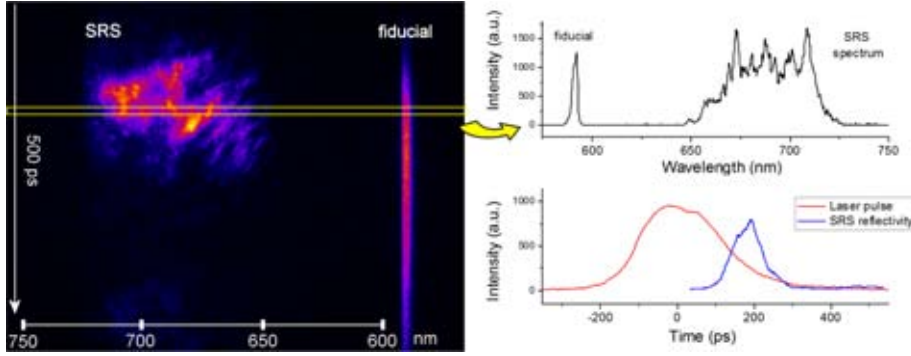


FIG. 5. (left) Time-resolved SRS spectrum obtained at a laser intensity of $I_{max} \approx 3.4 \times 10^{15}$ W/cm² and no auxiliary pulse. The acquisition time window, spanning the vertical axis, is 500 ps. (top-right) SRS spectrum emitted in the selected time window of $\Delta t = 20$ ps, as shown on the left. (bottom-right) Temporal profiles of the laser pulse and SRS emission.

indicating that EPWs originating from the broad peaks 1 and 3 are located near the Landau cutoff at densities $n_e/n_c \approx 0.21 - 0.22$. According to the linear theory,⁵⁵ TPD driven in such a low density region is expected to occur in a convective regime, as previously found both in experiments and numerical calculations.^{51,56,57} Such modes could be generated by ion density fluctuations driven by the ponderomotive force of the EPWs driven at $n_c/4$, which successively propagate down to lower densities.⁵⁸ By using 2D PIC simulations with the OSIRIS code, Yan *et al.* showed that after a linear growth stage, such modes could be coupled with the SRS/TPD mode near the $n_c/4$ surface via plasma waves and pump-depletion, giving rise to an intermittent burst-like pattern of the instability.²²

Three-half harmonic peaks are due to the coupling of laser photons with TPD EPWs. The blue peak is much weaker than the red one, which can be explained by the fact that the blue EPW must be reflected at its critical density in order that the $3/2\omega_0$ blue peak is observed in the backscattering direction.⁵⁰ Otherwise, the blue peak can be generated by the EPW resulting from the Langmuir Decay Instability of the primary TPD wave, as shown by Russel and DuBois.⁵⁹ The frequency shift of blue and red peaks is $\Delta\omega_{3/2}/\omega_0 \approx 1.09 \times 10^{-2}$, i.e., similar to that of peaks 1 and 3 of the $\omega_0/2$ spectrum, suggesting that EPWs responsible for these harmonics are the same, located near the Landau cutoff.

The splitting of half harmonic spectra shows that TPD (including hybrid TPD/SRS instability) dominates on absolute SRS at the quarter critical density. This is in a qualitative agreement with 2D IC simulations by Weber and Riconda,⁶⁰ performed with values of temperature and density scalelength similar to our experiment. Simulations referring to hotter plasmas in SI conditions^{27,28} indicate instead a large contribution of absolute SRS at $n_c/4$.

VI. BACKWARD STIMULATED RAMAN SCATTERING

The SRS instability driven at densities lower than $n_c/4$ gives rise to light scattered in the spectral range $\omega_0/2 < \omega < \omega_0$. All the emission spectra measured in our experiment exhibit peaks in the 630–750 nm spectral range, as shown in the time resolved spectrum in Fig. 5, obtained with a laser intensity of $I_{max} \approx 3.4 \times 10^{15}$ W/cm² and no auxiliary pulse. The same figure reports also a typical spectrum lineout and the temporal profile of the SRS emission compared to the laser pulse (discussed below). The emission has a

complex and not reproducible spectral structure, with an overall bandwidth usually increasing with the delay between auxiliary and main pulses [Fig. 6(a)]. The intensity of this emission grows with laser energy, for a fixed delay, showing a saturation for $\Delta t = 1200$ ps [Fig. 6(b)].

We associate these peaks to Backward Stimulated Raman Scattering (BRS) occurring in the underdense plasma. Matching conditions and a plasma temperature of ~ 1.5 keV, taken as an effective value during the laser peak, imply that BRS is excited in the density range of 0.10–0.15 n_c and drives forwardly directed EPWs with wave-vector $k_e = 1.37\text{--}1.52 \omega_0/c$. The lower wavelength cutoff of the

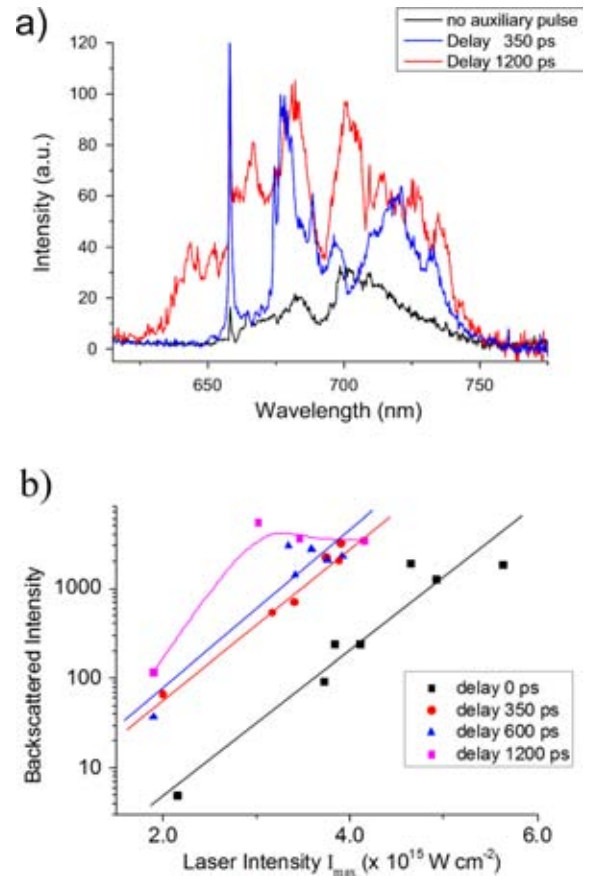


FIG. 6. (a) SRS spectra obtained with a laser intensity of $I_{max} \approx (3.5\text{--}5.5) \times 10^{15}$ W/cm² and delays between auxiliary and main pulses of 350 and 1200 ps, compared with the spectrum obtained without the auxiliary pulse. (b) Curves of growth of SRS intensity for different values of the auxiliary-main pulse delay.

emission ($n_e/n_c = 0.10$) corresponds to a value of $k_e \lambda_D \approx 0.27$, which agrees with a cutoff due to Landau damping of plasma waves; this value, indirectly, confirms the value of the plasma temperature in the underdense plasma estimated above.

A. SRS threshold and role of speckles

Stimulated Raman Scattering is driven by local values of the laser intensity. An investigation of SRS threshold in the present experiment must therefore account for the distribution of e.m. fields in the micro-scale. The use of a Random Phase Plate on the laser beam results in the reduction of the longitudinal and transverse spatial coherence length,⁶¹ yielding small speckles of size $l_{\perp} \approx 2F\lambda_0 = 1.6 \mu\text{m}$ and length $l_{\parallel} \approx 8F^2\lambda_0 \sim 14 \mu\text{m}$ (F is the f -number of the system). Taking into account the expected laser intensity distribution in the speckles and the number of speckles expected in the focal volume ($\approx 10^5$), the maximum local laser intensity should reach $\sim 8\text{--}10 I_{\text{max}}$. Speckle dimensions and intensity distribution control both filamentation and parametric instabilities occurring during the interaction. Here, ponderomotive self-focusing of the most intense speckles with $I > (2\text{--}3) \times 10^{16} \text{ W/cm}^2$ is expected to occur at densities relevant for SRS and TPD processes, while for lower intensity speckles, filamentation is inhibited by their small dimensions.

The threshold of SRS instability in speckles depends on many factors, including their possible filamentation and collective effects between speckles. The issue becomes much more complex in the kinetic regime ($k_e \lambda_D > 0.2$), where the non-linear Landau damping effect, depending on the electron trapping in EPW and on their side loss across filaments, plays an important role. Here, BRS threshold is basically estimated by considering the main damping effects of electron plasma waves. In inhomogeneous density profiles, the main source of damping is usually the limited resonance region where matching conditions are satisfied. The length l of this region is set by imposing $\int_0^l \kappa dx \approx 1/2$, where $\kappa = k_0 - k_s - k_e$ is the wavenumber mismatch of the interacting waves. Here, assuming a linear density profile in the resonant region, we calculate $l \sim 1.5 \mu\text{m} \approx 3.4 \lambda_0$, resulting in an effective damping rate of $\nu_s/l = 4 \times 10^{-2} \omega_0$ for the scattered e.m. wave and of $\nu_e/l = 1.53 \times 10^{-3} \omega_0$ for the EPW, where ν_s and ν_e are the group velocities of the two waves.

Relying on classical theory, the growth of convective SRS can be expressed by $I_{\text{SRS}} = I_{\text{noise}} \exp(2\pi\lambda)$ with the Rosenbluth parameter $\lambda = \gamma_0^2/\kappa' |v_e v_s| = (\gamma_0 l/\nu_s)(\gamma_0 l/\nu_e)$, where γ_0 is the homogenous growth rate, and the two terms in brackets correspond to the number of e-folds in length l of the scattered e.m. wave and of EPW, respectively.⁶² It is useful to plot the value of spectrally integrated intensity I_{SRS} versus the product $I \cdot L$ where laser intensity I is proportional to γ_0^2 and density scalelength L is proportional to $1/\kappa'$ (see, e.g., Liu *et al.*⁶³). Given the time and space dependences of laser intensity, we here considered the intensity I_{av} averaged over one standard deviation in time and space ($I_{\text{av}} = I_{\text{max}}/1.366$). Density scalelength values L were taken from the DUED and CHIC hydrodynamic simulations for different shot conditions (intensity and delay).

We observe that this representation—shown in the plot of Fig. 7—strongly reduces the scatter of points as compared to what obtained in the graph of I_{SRS} vs. I [Fig. 6(b)] and therefore seems to effectively account for both the effects of laser intensity and density scalelength; besides, the approaching of points supports the hypothesis that the Rosenbluth parameter, via the product $I \cdot L$, is the parameter determining the SRS threshold and growth in our experiment. Figure 7 also shows that the BRS emission rapidly grows for smaller $I_{\text{av}} \cdot L$ values and tends to saturate at larger values.

According to Liu *et al.*,⁶³ the threshold for BRS in inhomogeneous plasmas, obtained by considering wavenumber mismatch conditions, can be calculated by $\nu_0^2/c^2 > 1/k_0 L$, where ν_0 is the quiver velocity of an electron in the e.m. laser field. The threshold is therefore $I_{\text{BRS}} = (4.5\text{--}8) \times 10^{15} \text{ W/cm}^2$ depending on the auxiliary-main pulse delay. It is worth noting that in Fig. 7, the threshold is represented by the red vertical line $I_{\text{thres}} \cdot L = 500 \times 10^{15} \text{ W} \mu\text{m cm}^{-2}$, showing that SRS threshold is above the laser intensity in all our shots. Such a value can be inaccurate for several reasons, among them the effect of Landau damping to be considered in the kinetic regime, the damping due to the side-loss of electrons across the speckle edge, and the possible flattening of the density profile due to filamentation of speckles, which all need 3D fully kinetic simulations to be correctly estimated. The calculated threshold, however, suggests that local intensity in speckles, higher than the envelope laser intensity, is needed to drive BRS. At the lowest laser intensities, only speckles with intensities five times higher than I_{av} can drive BRS. Conversely, at higher laser intensities, also speckles with local intensity marginally higher than I_{av} can play a role.

This picture is further supported by considering other EPW damping processes, beyond the escape of the EPW from the resonance region. Considering the present interaction conditions ($T_e = 1.5 \text{ keV}$, $\lambda_{\text{SRS}} = 690 \text{ nm}$, $n_e/n_c \approx 0.12$, and speckle size, $l_{\perp} \approx 1.6 \mu\text{m}$), Landau and side-loss⁶⁴ damping rates are $\gamma_L \approx 5 \times 10^{-4} \omega_0$ and $\gamma_{\text{SL}} \approx 2\nu_{\text{th}}/l_{\perp} = 1.5 \times 10^{-3} \omega_0$, while collisional damping ν_{ei} is an order of magnitude lower. It is

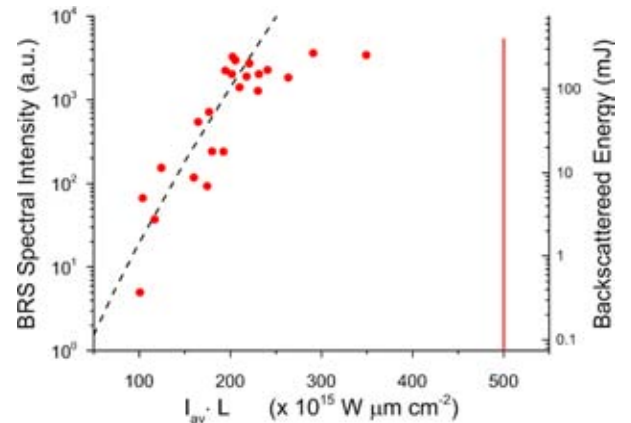


FIG. 7. BRS intensity versus the product $I_{\text{av}} \cdot L$ appearing in the Rosenbluth parameter, where I_{av} is the laser intensity averaged over one standard deviation in time and space. The dashed line represents the rate of BRS expected from Rosenbluth theory, calculated for single pulse irradiation.

therefore evident that side loss of electrons, due to the low $f/\#$ number of focusing optics, could be more effective in limiting the convective gain than the Landau damping of EPWs, affecting the saturation of SRS. This picture however changes when the SRS is driven at $n_e/n_c \approx 0.09\text{--}0.10$, i.e., near the Landau cutoff, where the Landau damping grows and can become predominant. When taking into account both convection out of the resonance region and side loss damping of EPWs, BRS threshold shifts to values near $I_{thres} \cdot L = 950 \times 10^{15} \text{ W } \mu\text{m cm}^{-2}$ (with a slight dependence on L), which implies an even stronger role of high intensity speckles. A more accurate investigation of the effect of high intensity speckles on the BRS amplification in the present data can be found in the study by Cristoforetti *et al.*,⁶⁵ where the experimental results are compared to those obtained by the radiative-hydrodynamic code CHIC. In addition to laser refraction and diffraction, the code also accounted for the laser intensity statistics contained in the beam speckles and included self-consistent calculations of non-linear laser plasma interactions.³⁰ The results of the simulations clearly show that a correct modeling of the speckle intensity statistics into the beam allows the experimentally observed SRS reflectivity to be explained.

B. Saturation and kinetic effects

Figures 6(b) and 7 show a rapid BRS growth and a saturation at higher intensities and scalelengths, visible, in particular, at delays of 600 and 1200 ps. SRS growth with $I_{av} \cdot L$ is expected to be a combined effect of the larger intensity in single speckles and of the increasing number of speckles overcoming I_{thres} . The comparison of the experimental SRS intensities with the SRS growth predicted by the classical Rosenbluth growth rate,⁶² shown in Fig. 7, reveals that the convective theory well reproduces the experiment for $I_{av} \cdot L < 240 \times 10^{15} \text{ W } \mu\text{m cm}^{-2}$, i.e., before that, the SRS saturation becomes evident. The expected SRS growth rate, displayed by the dashed line in Fig. 7, is obtained by considering single pulse irradiation and supposing that the SRS signal observed at $I_{av} \cdot L = 100 \times 10^{15} \text{ W } \mu\text{m cm}^{-2}$ is originated by speckles immediately above the threshold. The gain here is not calculated from thermal noise but just fitting the points at lower intensities. It is worth to remark that the predicted curve does not include the fact that an increasing number of speckles contributes to BRS intensity for larger values of I_{av} , which would make the curve steeper than that plotted in the graph,

increasing the discrepancy with experimental results, in particular in the saturation region. The SRS saturation observed at the highest $I_{av} \cdot L$ values suggests that damping and kinetic effects lead to saturation of SRS into the speckles.

A similar growth followed by a rapid saturation has also been found in experiments carried out at the Trident laser facility¹⁷ aimed at investigating SRS occurring in single hot spots and in PIC simulations in the kinetic regime reported in the literature.^{19,66–68} In these works, the saturation is due to a nonlinear frequency detuning occurring in large EPWs excited in the BRS process.^{69,70} The frequency shift can be due to ponderomotive and electron trapping effects as, for example, in bowing and filamentation of plasma waves in speckles.^{19,66} It was found^{23,67,68,71,72} that the nonlinear phase detuning results also in a non-stationary Raman saturation, in the form of a transition from a strongly modulated quasi-periodic to intermittent chaotic regime, with an increasing laser intensity.^{23,73} Since the SRS saturation is not mainly determined by Landau damping but rather by convective and side loss effects, we do not expect inflationary SRS or autoresonance⁷⁴ effects due to the ponderomotive trapping of electrons to be relevant for SRS growth, as discussed by Vu *et al.*⁶⁴

The occurrence of kinetics mechanisms in BRS saturation in the present experiment is suggested by the chaotic character of spectra in Fig. 6(a). Intensity dependent incoherent spectral broadening could be, in fact, attributed to nonlinear saturation of BRS with large bursts and quasi-periodic pulsations in intensity, as observed in kinetic simulations.^{71,72} According to theory and PIC simulations, kinetic mechanisms are expected to result in non-stationary SRS saturation and reflectivity bursts of the duration of the order of the ps or lower.^{21,72,73} Time-resolved BRS spectra in the saturation region ($I_{av} \cdot L > 240 \times 10^{15} \text{ W } \mu\text{m cm}^{-2}$) with high temporal resolution ($\Delta t = 8 \text{ ps}$) show evidence of emission bursts, as shown in Fig. 8. The temporal lineout of streak images reveals that the typical time duration of emission bursts is $\text{FWHM} \approx 8\text{--}10 \text{ ps}$, i.e., limited by the time resolution of the streak-camera. This is consistent with numerical PIC results and confirms the presence of kinetic mechanisms in the SRS saturation regime.

C. Timing of SRS emission

As pointed out above, the temporal evolution of SRS reflectivity exhibits a burst-like behavior and a considerable

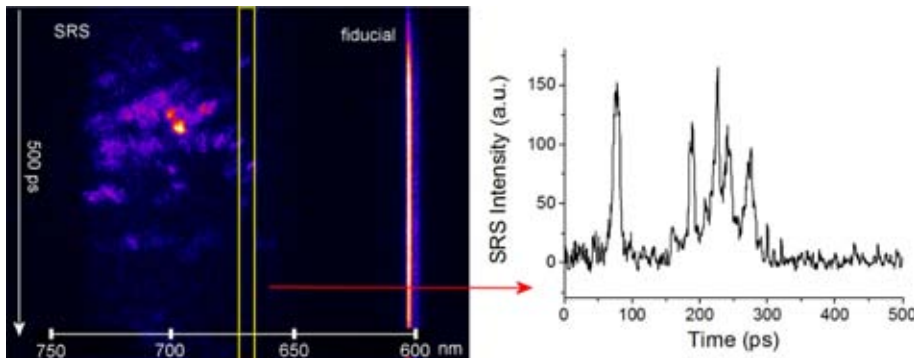


FIG. 8. (Left) Time-resolved SRS spectrum in the saturation region ($I_{av} \cdot L = 280 \times 10^{15} \text{ W } \mu\text{m cm}^{-2}$) obtained with a laser intensity of $I_{max} \approx 4.5 \times 10^{15} \text{ W/cm}^2$ and no auxiliary pulse is shown. The acquisition time window, spanning in the vertical axis, is 500 ps, and the time resolution is $\approx 8 \text{ ps}$. (Right) The time profile of SRS emission in the spectral range $\lambda = 670 \pm 3 \text{ nm}$.

delay with respect to the peak of the laser pulse, as shown in Fig. 5. The delay between BRS and laser peaks, measured only in the case of shots without the auxiliary pulse, was $\sim 190\text{--}220$ ps. The reflectivity due to Stimulated Raman Scattering is observed at even longer times, up to 300 ps after the laser peak, when laser intensity is very low. In order to understand this trend, hydrodynamic simulations with the radiative-hydrodynamic code CHIC were carried out. As in the study by Cristoforetti *et al.*,⁶⁵ simulations included self-consistent calculations of Stimulated Raman Scattering and generation of hot electrons by appropriate scaling laws using the local and instantaneous values of laser intensity and plasma parameters. The laser temporal profile measured shot by shot in the PALS control room was used in the simulations.

Simulation results obtained for $I_{max} \approx 3.7 \times 10^{15}$ W/cm² and no auxiliary pulse are shown in Fig. 9. Here, the code was not optimized to reproduce the speckles with the highest laser intensity. For this reason, local laser intensity barely overcomes the SRS threshold in a few regions of the laser spot, which explains the low value of the hot electron flux obtained. Consistent with our experimental findings, simulations show that SRS is driven in the trailing part of the laser pulse, here at ~ 180 ps after the peak of the pulse. Such a value is understood by looking at the temporal growth of the density scalelength in the plasma, which progressively increases during the laser pulse and reaches the maximum value when the laser pulse is over. Moreover, as shown in Fig. 2(b), the plasma temperature significantly decreases in the trailing part of the pulse, resulting in a considerable reduction of Landau and side loss damping rates and then in a corresponding lowering of the SRS threshold. These facts explain why the optimal conditions for SRS onset occur in the tail of the laser pulse.

VII. HOT ELECTRONS

A suprathermal electron propagating into the target gives rise to Cu K_α and Ti K_α emission when it crosses Cu and Ti tracer layers. X-ray spectroscopy of Cu K_α and Ti K_α

emission is therefore here used as a diagnostics of hot electrons. The flux and average energy of HEs were here estimated by measuring the reduction of the Cu K_α and Ti K_α signals when the thickness of the plastic layer was increased. By considering the electron stopping range in different layers (tabulated in ESTAR database of NIST⁷⁵), this value allowed us to calculate the penetration depth of hot electrons and hence their average energy. Monte Carlo simulations performed with the GEANT4⁷⁶ and PENELOPE⁷⁷ codes were used to reproduce the experimental results. Assuming an exponential distribution for hot electron energy $\sim \exp(-E/T_{hot})$, a temperature $T_{hot} = 20 \pm 10$ keV and an energy HE conversion $\varepsilon_{HE} \sim 0.14\% \pm 0.03\%$ were obtained. Such distribution well fitted the K_α signal obtained for all shots with the exception of those using plastic layers of 125 μm and overall 180 μm . In these shots, the measured K_α emission was higher than expected. This suggests that energetic HEs, with a temperature of $T_{hot} > 100$ keV, are also generated during the interaction. Another approach for estimating hot electron energy is considering the ratio between Cu K_α and Ti K_α emission on the same shot. This value does not depend on the absolute number of generated hot electrons, which may vary shot by shot, making this diagnostic more accurate. The HE temperature obtained with this method was $T_{hot} = 25 \pm 5$ keV, and the energy conversion was $\varepsilon_{HE} \sim 0.1\% \pm 0.05\%$ of the incident laser energy. Hot electron energy was also measured by using a bremsstrahlung cannon, resulting in a temperature of $T_{hot} = 19 \pm 3$ keV, in agreement with the previous values referring to the colder temperature.

The measured temperature of ~ 20 keV is close to that obtained for hot electrons generated by BRS ($T_{hot} \approx 28$ keV) in the 1D PIC simulations of Klimo *et al.*²⁷ Although the simulation time (≈ 80 ps) is shorter than our laser pulse, the explored range of intensities (2.4–24 PW/cm²) and the pre-plasma scalelength (150 μm) are similar to those of the present experiment. In these simulations, however, SRS occurs at densities closer to the quarter critical density, which determines the phase velocity of plasma waves induced by Raman and thus the energy of the hot electrons. Conversely, those simulations turn out in a prevailing component of hot electrons with a lower energy of ≈ 10 keV, which are accelerated in cavities seeded at quarter-critical density by SRS and TPD. In the present work, this low-energy hot electron component is not observed.

The Cu K_α intensities measured using a CCD working in the single-photon regime suggest a correlation between the BRS backscattered intensity and the K_α photon number, as shown in Fig. 10. This supports a scenario in which hot electrons are mainly generated by breaking of EPW induced by BRS.

The energy of the electrons generated by BRS in the density region 0.10–0.15 n_c , obtained by considering the phase velocity $v_{ph} = \omega_e/k_e$ of the driven EPW, is $\approx 17\text{--}20$ keV, which is in good agreement with the measured value. This again supports the conclusion that such hot electrons, which are the main component, are produced by BRS.

Assuming that the $\omega_0/2$ spectra loosely reflect the frequencies of TPD EPWs, hot electrons of different energies

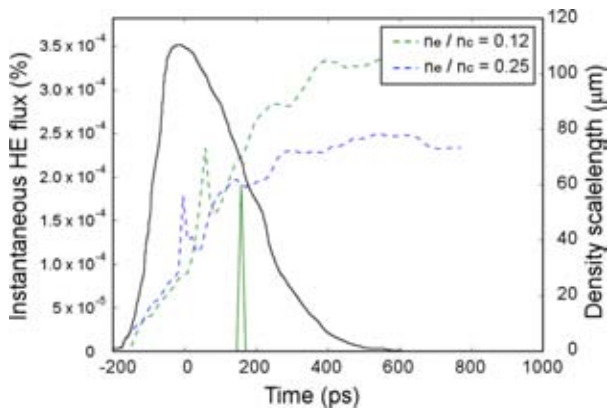


FIG. 9. Simulation results for $I_{max} \approx 3.7 \times 10^{15}$ W/cm² and no auxiliary pulse: instantaneous hot electron flux driven by BRS as a function of time (green) and density scalelengths computed at $n_e/4$ and $0.12 n_c$ (dashed blue and green lines, respectively). The intensity of the laser pulse is shown as a black line.

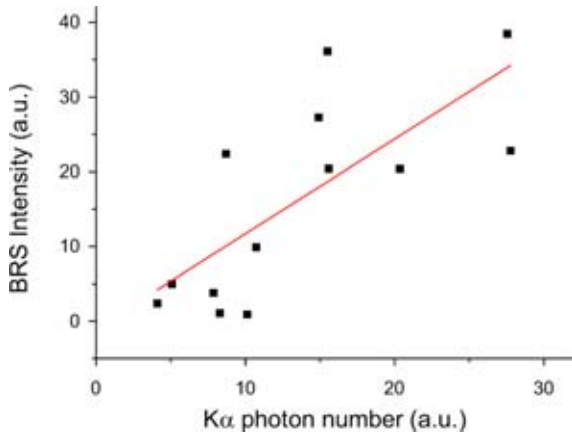


FIG. 10. Correlation between BRS intensity and Cu K_α photon number measured with the CCD working in the single photon regime. Reproduced with permission from Cristoforetti *et al.*, *Europhys. Lett.* **117**, 35001 (2017). Copyright 2017 EPL Association.⁶⁵

could be generated by the convective modes near the Landau damping and by the hybrid SRS/TPD modes near the $n_c/4$ surface. EPWs in low density regions ($n_e/n_c \approx 0.21 - 0.22$) are expected to easily trap thermal electrons due to their low phase velocity ($v_{ph} \approx 4v_{th}$), resulting however in low-energy hot electrons ($T_e \approx 10$ keV). A Maxwellian component in the electron distribution at this low temperature was however not clearly observed in our measurements. High frequency hybrid modes, on the other hand, could in principle generate much hotter electrons ($T_e > 100$ keV), but their flux is expected to be limited by the small number of thermal electrons that can be trapped at so large EPW phase velocities ($v_{ph} \approx 10.5v_{th}$). By means of 2D PIC and fluid simulations, Yan *et al.*⁵⁸ recently showed that the amount of these high-energy hot electrons can be significantly enhanced by a staged acceleration of electrons from the low density region ($n_e/n_c \approx 0.21 - 0.22$), generated by convective modes, to the high density region ($n_e/n_c \approx 0.24 - 0.25$) where hybrid SRS/TPD modes operate. Such high-energy electrons, which could be deleterious in SI for the possible pre-heating of the compressed fuel, could explain the K_α signal measured for the target with large plastic thickness (125 and 180 μm). Since the electrons generated by hybrid SRS/TPD modes are expected to be energetic and strongly peaked in the forward direction, the generated Bremsstrahlung emission is expected to be mainly emitted in the forward direction.⁷⁸ This could explain why their contribution was not detected by the Bremsstrahlung spectrometer, which was looking at the irradiated side of the target.

VIII. CONCLUSIONS

The impact of parametric instabilities at laser intensities relevant for shock ignition in a planar irradiation geometry has been investigated by both calorimetry and spectroscopy. Measurements show that the main mechanisms reducing the pulse energy transfer to the plasma are Stimulated Brillouin Scattering and laser reflection with reflectivities in the lens cone of 3%–15% of laser energy. The energy backscattered by Stimulated Raman Scattering is lower than 1%. Both

$3/2\omega_0$ and $\omega_0/2$ harmonics are measured, indicating that that a fraction of laser energy reaches the $n_c/4$ surface and drives TPD and hybrid TPD/SRS instabilities.

Stimulated Raman Scattering is driven at densities compatible with classical Landau cutoff ($n_e = 0.10 - 0.15 n_c$) in the trailing part of the laser pulse, where the scalelength of the plasma is larger. It results in the generation of a low flux ($\sim 0.1\%$) of low-energy ($T_{hot} \sim 20$ keV) hot electrons. Measurements also suggest the presence of a component of high energy hot electrons ($T_{hot} > 100$ keV), which could be possibly generated by the hybrid TPD/SRS instability. BRS is driven in the speckles generated by the RPP, where local intensity is much higher than the envelope value. The BRS gain, its spectral modulations, and the observation of reflectivity bursts suggest the occurrence of nonlinear and kinetic effects into the speckles, affecting EPW growth and resulting in the Raman saturation. BRS extent is much lower than that measured in other experiments relevant for SI,^{11,32,34,35} which is partly explainable by the lower plasma scalelength.

ACKNOWLEDGMENTS

We would like to thank Professor S. Hueller for the fruitful discussions and valuable suggestions on the interpretation of Stimulated Raman Scattering data. We would like to acknowledge financial support from the LASERLAB-EUROPE Access to Research Infrastructure activity within the EC's seventh Framework Program (Grant Agreement No. 284464).

We also acknowledge the support of Eurofusion Project (No. AWP17-ENR-IFE-CEA-01). We acknowledge financial contribution from the MIUR funded PRIN Project (No. 2012AY5LEL). Participation of O.R. and M.S. in this research was partly supported by the ELI project (No. CZ.02.1.01/0.0/0.0/15_008/0000162) and High Field Initiative (No. CZ.02.1.01/0.0/0.0/15_003/0000449). Participation of F.B. to this research was supported by the CNR funded Italian research Network ELI-Italy. S. Atzeni acknowledges financial support from the project Sapienza 2016 (No. 257584). The PALS staff acknowledges financial support from the Czech Ministry of Education (LM2015083 and EF16_013/0001552) and Czech Science Foundation (17-05076S). We acknowledge SciTech Precision and Rutherford Appleton Laboratory Target Fabrication Group for the supplied targets. Finally, we thank the technical staff of PALS for help in running the experiments.

¹R. Betti, C. D. Zhou, K. S. Anderson, L. J. Perkins, W. Theobald, and A. A. Solodov, *Phys. Rev. Lett.* **98**, 155001 (2007).

²L. J. Perkins, R. Betti, K. N. LaFortune, and W. H. Williams, *Phys. Rev. Lett.* **103**, 045004 (2009).

³S. Atzeni, X. Ribeyre, G. Schurtz, A. J. Schmitt, B. Canaud, R. Betti, and L. J. Perkins, *Nucl. Fusion* **54**, 054008 (2014).

⁴D. Batani, S. Baton, A. Casner, S. Depierreux, M. Hohenberger, O. Klimo, M. Koenig, C. Labaune, X. Ribeyre, C. Rousseaux, G. Schurtz, W. Theobald, and V. T. Tikhonchuk, *Nucl. Fusion* **54**, 054009 (2014).

⁵S. Atzeni, A. Schiavi, and A. Marocchino, *Plasma Phys. Controlled Fusion* **53**, 035010 (2011).

⁶A. Marocchino, S. Atzeni, and A. Schiavi, *Phys. Plasmas* **21**, 012701 (2014).

⁷X. Ribeyre, G. Schurtz, M. Lafon, S. Galera, and S. Weber, *Plasma Phys. Controlled Fusion* **51**, 015013 (2009).

- ⁸A. Casner, T. Caillaud, S. Darbon, A. Duval, I. Thfouin, J. P. Jadaud, J. P. LeBreton, C. Reverdin, B. Rosse, R. Rosch, N. Blanchot, B. Villette, R. Wrobel, and J. L. Miquel, *High Energy Density Phys.* **17**, 2–11 (2015).
- ⁹E. I. Moses, R. N. Boyd, B. A. Remington, C. J. Keane, and R. Al-Ayat, *Phys. Plasmas* **16**, 041006 (2009).
- ¹⁰B. Canaud, S. Laffite, V. Brandon, and M. Temporal, *Laser Part. Beams* **30**, 183 (2012).
- ¹¹W. Theobald, R. Nora, W. Seka, M. Lafon, K. S. Anderson, M. Hohenberger, F. J. Marshall, D. T. Michel, A. A. Solodov, C. Stoeckl, D. H. Edgell, B. Yaakobi, A. Casner, C. Reverdin, X. Ribeyre, A. Shvydky, A. Vallet, J. Peebles, F. N. Beg, M. S. Wei, and R. Betti, *Phys. Plasmas* **22**, 056310 (2015).
- ¹²R. Nora, W. Theobald, R. Betti, F. J. Marshall, D. T. Michel, W. Seka, B. Yaakobi, M. Lafon, C. Stoeckl, J. Delettrez, A. A. Solodov, A. Casner, C. Reverdin, X. Ribeyre, A. Vallet, J. Peebles, F. N. Beg, and M. S. Wei, *Phys. Rev. Lett.* **114**, 045001 (2015).
- ¹³R. Betti, W. Theobald, C. D. Zhou, K. S. Anderson, P. W. McKenty, S. Skupsky, D. Shvarts, V. N. Goncharov, J. A. Delettrez, and P. B. Radha, *J. Phys.: Conf. Ser.* **112**, 022024 (2008).
- ¹⁴A. R. Bell and M. Tzoufras, *Plasma Phys. Controlled Fusion* **53**, 045010 (2011).
- ¹⁵Ph. Nicolai, J. L. Feugeas, T. Nguyen-bui, V. Tikhonchuk, L. Antonelli, D. Batani, and Y. Maheut, *Phys. Plasmas* **22**, 042705 (2015).
- ¹⁶R. K. Kirkwood, J. D. Moody, J. Kline, E. Dewald, S. Glenzer, L. Divo, P. Michel, D. Hinkel, R. Berger, E. Williams, J. Milovich, L. Yin, H. Rose, B. MacGowan, O. Landen, M. Rosen, and J. Lindl, *Plasma Phys. Controlled Fusion* **55**, 103001 (2013).
- ¹⁷D. S. Montgomery, J. A. Cobble, J. C. Fernández, R. J. Focia, R. P. Johnson, N. Renard-LeGalloudec, H. A. Rose, and D. A. Russell, *Phys. Plasmas* **9**, 2311 (2002).
- ¹⁸S. Depierreux, J. Fuchs, C. Labaune, A. Michard, H. A. Baldis, D. Pesme, S. Hüller, and G. Laval, *Phys. Rev. Lett.* **84**, 2869 (2000).
- ¹⁹L. Yin, B. J. Albright, H. A. Rose, K. J. Bowers, B. Bergen, D. S. Montgomery, J. L. Kline, and J. C. Fernández, *Phys. Plasmas* **16**, 113101 (2009).
- ²⁰L. Yin, B. J. Albright, K. J. Bowers, W. Daughton, and H. A. Rose, *Phys. Rev. Lett.* **99**, 265004 (2007).
- ²¹L. Yin, B. J. Albright, H. A. Rose, D. S. Montgomery, J. L. Kline, R. K. Kirkwood, P. Michel, K. J. Bowers, and B. Bergen, *Phys. Plasmas* **20**, 012702 (2013).
- ²²R. Yan, J. Li, and C. Ren, *Phys. Plasmas* **21**, 062705 (2014).
- ²³M. M. Skoric, M. S. Jovanovic, and M. R. Rajkovic, *Phys. Rev. E* **53**, 4056 (1996); M. M. Skoric and M. M. Jovanovic, *AIP Conf. Proc.* **318**, 380 (1994).
- ²⁴H. X. Vu, D. F. DuBois, and B. Bezzerides, *Phys. Plasmas* **9**, 1745 (2002).
- ²⁵S. Depierreux, V. Yahia, C. Goyon, G. Loisel, P.-E. Masson-Laborde, N. Borisenko, A. Orekhov, O. Rosmej, T. Rienecker, and C. Labaune, *Nat. Commun.* **5**, 4158 (2014).
- ²⁶C. Riconda, S. Weber, V. T. Tikhonchuk, and A. Héron, *Phys. Plasmas* **18**, 092701 (2011).
- ²⁷O. Klimo and V. T. Tikhonchuk, *Plasma Phys. Controlled Fusion* **55**, 095002 (2013).
- ²⁸O. Klimo, J. Psikal, V. T. Tikhonchuk, and S. Weber, *Plasma Phys. Controlled Fusion* **56**, 055010 (2014).
- ²⁹A. Marocchino, M. Tzoufras, S. Atzeni, A. Schiavi, P. D. Nicolai, J. Mallet, V. Tikhonchuk, and J. L. Feugeas, *Phys. Plasmas* **20**, 022702 (2013).
- ³⁰A. Colaitis, G. Duchateau, X. Ribeyre, Y. Maheut, G. Boutoux, L. Antonelli, Ph. Nicolai, D. Batani, and V. Tikhonchuk, *Phys. Rev. E* **92**, 41101 (2015).
- ³¹A. Marocchino, S. Atzeni, and A. Schiavi, *New J. Phys.* **17**, 043052 (2015).
- ³²W. Theobald, R. Nora, M. Lafon, A. Casner, X. Ribeyre, K. S. Anderson, R. Betti, J. A. Delettrez, J. A. Frenje, V. Yu. Glebov, O. V. Gotchev, M. Hohenberger, S. X. Hu, F. J. Marshall, D. D. Meyerhofer, T. C. Sangster, G. Schurtz, W. Seka, V. A. Smalyuk, C. Stoeckl, and B. Yaakobi, *Phys. Plasmas* **19**, 102706 (2012).
- ³³M. Hohenberger, W. Theobald, S. X. Hu, K. S. Anderson, R. Betti, T. R. Boehly, A. Casner, D. E. Fratanduono, M. Lafon, D. D. Meyerhofer, R. Nora, X. Ribeyre, T. C. Sangster, G. Schurtz, W. Seka, C. Stoeckl, and B. Yaakobi, *Phys. Plasmas* **21**, 022702 (2014).
- ³⁴C. Goyon, S. Depierreux, V. Yahia, G. Loisel, C. Baccou, C. Courvoisier, N. G. Borisenko, A. Orekhov, O. Rosmej, and C. Labaune, *Phys. Rev. Lett.* **111**, 235006 (2013).
- ³⁵S. D. Baton, M. Koenig, E. Brambrink, H. P. Schlenvoigt, C. Rousseaux, G. Debras, S. Laffite, P. Loiseau, F. Philippe, X. Rybeyre, and G. Schurtz, *Phys. Rev. Lett.* **108**, 195002 (2012).
- ³⁶S. Depierreux, P. Loiseau, D. T. Michel, V. Tassin, C. Stenz, P. E. Masson-Laborde, C. Goyon, V. Yahia, and C. Labaune, *Phys. Plasmas* **19**, 012705 (2012).
- ³⁷J. Ullschmied, *Radiat. Eff. Defect Solids* **170**, 278–289 (2015).
- ³⁸P. Koester, L. Antonelli, S. Atzeni, J. Badziak, F. Baffigi, D. Batani, C. A. Cecchetti, T. Chodukowski, F. Consoli, G. Cristoforetti, R. De Angelis, G. Folpini, L. A. Gizzi, Z. Kalinowska, E. Krousky, M. Kucharik, L. Labate, T. Levato, R. Liska, G. Malka, Y. Maheut, A. Marocchino, P. Nicolai, T. O'Dell, P. Parys, T. Pisarczyk, P. Raczka, O. Renner, Y. J. Rhee, X. Ribeyre, M. Richetta, M. Rosinski, L. Ryc, J. Skala, A. Schiavi, G. Schurtz, M. Smid, C. Spindloe, J. Ullschmied, J. Wolowski, and A. Zaras, *Plasma Phys. Controlled Fusion* **55**, 124045 (2013).
- ³⁹D. Batani, L. Antonelli, S. Atzeni, J. Badziak, F. Baffigi, T. Chodukowski, F. Consoli, G. Cristoforetti, R. De Angelis, R. Dudzak, G. Folpini, L. Giuffrida, L. A. Gizzi, Z. Kalinowska, P. Koester, E. Krousky, M. Krus, L. Labate, T. Levato, Y. Maheut, G. Malka, D. Margarone, A. Marocchino, J. Nejdil, Ph. Nicolai, T. O'Dell, T. Pisarczyk, O. Renner, Y. J. Rhee, X. Ribeyre, M. Richetta, M. Rosinski, M. Sawicka, A. Schiavi, J. Skala, M. Smid, Ch. Spindloe, J. Ullschmied, A. Velyhan, and T. Vinci, *Phys. Plasmas* **21**, 032710 (2014).
- ⁴⁰T. Pisarczyk, S. Yu. Gus'kov, Z. Kalinowska, J. Badziak, D. Batani, L. Antonelli, G. Folpini, Y. Maheut, F. Baffigi, S. Borodziuk, T. Chodukowski, G. Cristoforetti, N. N. Demchenko, L. A. Gizzi, A. Kasperczuk, P. Koester, E. Krousky, L. Labate, P. Parys, M. Pfeifer, O. Renner, M. Smid, M. Rosinski, J. Skala, R. Dudzak, J. Ullschmied, and P. Pisarczyk, *Phys. Plasmas* **21**, 012708 (2014).
- ⁴¹J. Badziak, L. Antonelli, F. Baffigi, D. Batani, T. Chodukowski, G. Cristoforetti, R. Dudzak, L. A. Gizzi, G. Folpini, F. Hall, Z. Kalinowska, P. Koester, E. Krousky, M. Kucharik, L. Labate, R. Liska, G. Malka, Y. Maheut, P. Parys, M. Pfeifer, T. Pisarczyk, O. Renner, M. Rosinski, L. Ryc, J. Skala, M. Smid, C. Spindloe, J. Ullschmied, and A. Zaras-Szydłowska, *Laser Part. Beams* **33**, 561 (2015).
- ⁴²L. Antonelli, P. Koester, G. Folpini, Y. Maheut, F. Baffigi, G. Cristoforetti, L. Labate, T. Levato, L. A. Gizzi, F. Consoli, R. De Angelis, Z. Kalinowska, T. Chodukowski, M. Rosinski, P. Parys, T. Pisarczyk, P. Raczka, L. Ryc, J. Badziak, J. Wolowski, M. Smid, O. Renner, E. Krousky, M. Pfeifer, J. Skala, J. Ullschmied, P. Nicolai, X. Ribeyre, G. Schurtz, S. Atzeni, A. Marocchino, A. Schiavi, C. Spindloe, T. O'Dell, Y. J. Rhee, M. Richetta, and D. Batani, *J. Phys.: Conf. Ser.* **688**, 012003 (2016).
- ⁴³L. Labate, T. Levato, M. Galimberti, A. Giuliotti, D. Giuliotti, M. Sanna, C. Traino, M. Lazzeri, and L. A. Gizzi, *Nucl. Instrum. Methods Phys. Res., A* **594**, 278–282 (2008).
- ⁴⁴C. D. Chen, J. A. King, M. H. Key, K. U. Akli, F. N. Beg, H. Chen, R. R. Freeman, A. Link, A. J. Mackinnon, A. G. MacPhee, P. K. Patel, M. Porkolab, R. B. Stephens, and L. D. Van Woerkom, *Rev. Sci. Instrum.* **79**, 10E305 (2008).
- ⁴⁵S. Atzeni, A. Schiavi, F. Califano, F. Cattani, F. Cornolti, D. Del Sarto, T. Liseykina, A. Macchi, and F. Pegoraro, *Comput. Phys. Commun.* **169**, 153–159 (2005); S. Atzeni, *Comput. Phys. Commun.* **43**, 107–124 (1986).
- ⁴⁶J. Breil, S. Galera, and P. H. Maire, *Comput. Fluids* **46**, 161 (2011).
- ⁴⁷J. J. MacFarlane, I. E. Golovkin, P. Wang, P. R. Woodruff, and N. A. Pereyra, *High Energy Density Phys.* **3**, 181 (2007).
- ⁴⁸J. Myatt, A. V. Maximov, W. Seka, R. S. Craxton, and R. W. Short, *Phys. Plasmas* **11**, 3394 (2004).
- ⁴⁹W. L. Krueer, in *The Physics of Laser Plasma Interactions, Frontiers in Physics*, Vol. 73, edited by D. Pines (Addison-Wesley, Redwood City, CA, 1988).
- ⁵⁰R. E. Turner, D. W. Phillion, B. F. Lasinski, and E. M. Campbell, *Phys. Fluids* **27**, 511 (1984).
- ⁵¹W. Seka, B. B. Afeyan, R. Boni, L. M. Goldman, R. W. Short, K. Tanaka, and T. W. Johnston, *Phys. Fluids* **28**, 2570 (1985).
- ⁵²W. Seka, D. H. Edgell, J. F. Myatt, A. V. Maximov, R. W. Short, V. N. Goncharov, and H. A. Baldis, *Phys. Plasmas* **16**, 052701 (2009).
- ⁵³B. B. Afeyan and E. A. Williams, *Phys. Rev. Lett.* **75**, 4218 (1995).
- ⁵⁴R. L. Berger and L. V. Powers, *Phys. Fluids* **28**, 2895 (1985).
- ⁵⁵R. Yan, A. V. Maximov, and C. Ren, *Phys. Plasmas* **17**, 052701 (2010).
- ⁵⁶W. Seka, J. F. Myatt, R. W. Short, D. H. Froula, J. Katz, V. N. Goncharov, and I. V. Igumenshchev, *Phys. Rev. Lett.* **112**, 145001 (2014).
- ⁵⁷C. Z. Xiao, Z. J. Liu, C. Y. Zheng, and X. T. He, *Phys. Plasmas* **23**, 022704 (2016).

- ⁵⁸R. Yan, C. Ren, J. Li, A. V. Maximov, W. B. Mori, Z.-M. Sheng, and F. S. Tsung, *Phys. Rev. Lett.* **108**, 175002 (2012).
- ⁵⁹D. A. Russell and D. F. DuBois, *Phys. Rev. Lett.* **86**, 428 (2001).
- ⁶⁰S. Weber and C. Riconda, *High Power Laser Sci. Eng.* **3**, e6 (2015).
- ⁶¹D. Batani, C. Bleu, and Th. Lower, *Eur. Phys. J. D* **19**, 231–243 (2002).
- ⁶²M. N. Rosenbluth, *Phys. Rev. Lett.* **29**, 565 (1972).
- ⁶³C. S. Liu, M. N. Rosenbluth, and R. B. White, *Phys. Fluids* **17**, 1211 (1974).
- ⁶⁴H. X. Vu, D. F. DuBois, and B. Bezzerides, *Phys. Plasmas* **14**, 012702 (2007).
- ⁶⁵G. Cristoforetti, A. Colaitis, L. Antonelli, S. Atzeni, F. Baffigi, D. Batani, F. Barbato, G. Boutoux, R. Dudzak, P. Koester, E. Krousky, L. Labate, Ph. Nicolai, O. Renner, M. Skoric, V. Tikhonchuk, and L. A. Gizzi, *Europhys. Lett.* **117**, 35001 (2017).
- ⁶⁶L. Yin, B. J. Albright, K. J. Bowers, W. Daughton, and H. A. Rose, *Phys. Plasmas* **15**, 013109 (2008).
- ⁶⁷S. Miyamoto, K. Mima, M. M. Škorić, and M. S. Jovanović, *J. Phys. Soc. Jpn.* **67**, 1281 (1998).
- ⁶⁸C. Riconda and S. Weber, *High Power Laser Sci. Eng.* **4**, e23 (2016).
- ⁶⁹G. J. Morales and T. M. O’Neal, *Phys. Rev. Lett.* **28**, 417 (1972).
- ⁷⁰R. L. Dewar, *Phys. Fluids* **15**, 712 (1972).
- ⁷¹K. Estabrook and W. Kruer, *Phys. Fluids* **26**, 1892 (1983).
- ⁷²T. Kolber, W. Rozmus, and V. T. Tikhonchuk, *Phys. Fluids B* **5**, 138 (1993).
- ⁷³M. M. Skoric, L. Nikolic, and S. Ishiguro, *J. Plasma Phys.* **79**, 1003 (2013); M. M. Skoric, L. Nikolic, L. Hadzievski, D. Batani, S. Ishiguro, and K. Mima, *J. Phys.: Conf. Ser.* **688**, 012112 (2016).
- ⁷⁴T. Chapman, S. Huller, P. E. Masson-Laborde, A. Heron, D. Pesme, and W. Rozmus, *Phys. Rev. Lett.* **108**, 145003 (2012).
- ⁷⁵See <http://physics.nist.gov/PhysRefData/Star/Text/ESTAR.html> for Estar database.
- ⁷⁶J. Sempau, E. Acosta, J. Barò, J. M. Fernandez-Varea, and F. Salvat, *Nucl. Instrum. Method, B* **132**, 377 (1997).
- ⁷⁷S. Agostinelli, J. Allison, K. Amako, J. Apostolakis, H. Araujo, P. Arcel, M. Asaig, D. Axen, S. Banerjee, G. Barrand *et al.*, *Nucl. Instrum. Method, A* **506**, 250 (2003).
- ⁷⁸S. Von Goeler, J. Stevens, S. Bernabei, M. Bitter, T. K. Chu, P. Efthimion, N. Fisch, W. Hooke, K. Hill, J. Hosea, F. Jobs, C. Karney, J. Mervine, E. Meservey, R. Motley, P. Roney, S. Sesnic, K. Silber, and G. Taylor, *Nucl. Fusion* **25**(11), 1515 (1985).

Contents lists available at [ScienceDirect](https://www.sciencedirect.com)

Nuclear Inst. and Methods in Physics Research, A

journal homepage: www.elsevier.com/locate/nima

Summary of WG7—High brightness power sources: From laser technology to beam drivers

Leonida A. Gizzi^{a,*}, Barbara Marchetti^b, Pattathil P. Rajeev^c^a Istituto Nazionale di Ottica, Consiglio Nazionale delle Ricerche, Pisa, Italy^b DESY, Notkestrasse 85, 22607 Hamburg, Germany^c Central Laser Facility, Rutherford Appleton Laboratory, STFC, Chilton, Didcot, UK

ARTICLE INFO

Keywords:

High average power laser technology
Laser drivers
Laser wakefield acceleration

ABSTRACT

In this paper we summarize the contributions presented during the Working Group 7 (WG7) sessions, dedicated to high brightness power sources. In this context we have tackled several topics of high relevance to novel accelerators, including laser technology for laser driven accelerators, the state of the art of high peak and average power lasers, the laser beam quality, contrast and stability. A number of novel results were presented especially in the area of laser beam characterization and control, advanced laser concepts, target control and electron beam diagnostics currently under development at a range of labs engaged in the development of advanced accelerator concepts.

© 2017 Published by Elsevier B.V.

1. Introduction

Many novel acceleration techniques, such as the Laser Driven Plasma Wakefield Acceleration (LWFA) [1], rely on the use of high repetition-rate, high peak power laser drivers. In this working group special attention was given to the use of such driver lasers in view of future user applications.

In the current framework, aimed at the establishment of a reliable operation of LWFA, the high power lasers used to reach high acceleration gradients in the plasma also need to exhibit high repetition rates in order to drive applications; the laser control also needs to be improved through the implementation of feedback systems. All this leads to high average power lasers capable of delivering kW scale output on the target.

The control and the characterization of many parameters of the laser, such as its longitudinal shape and transverse contrast also are fundamental for controlling the wake-field generated in the plasma, which influences the quality of the accelerated electron bunches. These are some of the key areas where development is needed to finally deliver reliable operation of laser drivers as envisaged in the EuPRAXIA project [2].

2. Overview of research topics

Feedback Control. The feedback control of the spatio-temporal properties of high-intensity laser pulses allows the optimization of the output

parameters of an experiment by tuning the shape of the input laser. More specifically D. Symes (STFC) reported about the optimization of soft X-rays emission from electrons generated via LWFA thanks to the optimization of the laser shape by changing the dazzler settings of the 5 Hz Gemini laser. This approach clearly showed, possibly for the first time, that spatio-temporal laser stability plays a major role in the stability of the acceleration process and active control of these features will finally enable a major improvement on the quality of the accelerated electron bunches.

Characterization of the Contrast and Wavefront Control. The transverse properties of the laser beam have a strong impact on the properties of the wake-field generated in the plasma. Moreover the lack of control of the laser wavefront can potentially damage the plasma capillary. A research carried out at LUX, a collaboration between ELI-beamlines, the University of Hamburg and DESY investigates effects of laser beam propagation. The laser wavefront is controlled via a closed loop including a deformable mirror and a wavefront sensor. V. Leroux presented the status of the investigations concerning the laser wavefront at the target position, showing detailed characterization of actual laser specs at interaction point and a first investigations of effects of rep-rated operation on transport line.

At LMU in Munich a new concept has been developed for the measurement of the 2D spatial and temporal intensity distribution of

* Corresponding author.

E-mail address: la.gizzi@ino.cnr.it (L.A. Gizzi).

an high power laser at the focus. M. Speicher reported about the working principle of the method, that relies on optical probing of the dynamically generated plasma at a mm-thin foil. Experimental data were also presented that demonstrate the possibility to extract details of laser pulse temporal evolution on target.

Extended propagation in Plasmas. In the AWAKE experiment at CERN the laser is used to ionize a rubidium vapor source along a 10 m distance. J. Moody has reported about how the depletion of the laser in the plasma chamber can be controlled by using pulses with sufficient energy and intensity, thus allowing achieving sufficiently homogeneous ionization of the vapor along the complete chamber length. This is also an excellent example of the use of fiber pump laser technology at the multi-TW level to achieve laser stability, both shot-by-shot and on a long term operation.

Increasing Laser Brightness. Laser beam Circulators are used to potentially increase the laser brightness. K. Cassou presented the status of the realization and alignment of a laser beam circulator [3] used in the ELI-Nuclear Physics Project. The laser brightness needs to be increased right before the interaction point of the laser with the ELI electron beam aimed to produce X-rays. The construction of such a system is especially challenging because of the very precise surface manufacture requirement of the mirrors and high precision of their parallelism. Among the highlights of the presentation we mention the progress of the collaboration towards a successful implementation of self-alignment algorithms for alignment at interaction point.

Effects of Laser Properties in Plasmas and LWFA Experiments. The laser pulse propagating in the plasma experiences many changes in the longitudinal energy distribution such as e.g. laser depletion. M. Streeter reported about how the experimental characterization of the Gemini laser at the Central Laser Facility has enabled the understanding of the mechanisms influencing laser evolution in the plasma. A model well representing this phenomenon has been included in simulations and a good fit of the experimental data has been achieved. This is an example of investigation in which the role of laser and plasma properties on LWFA is clearly identified.

At SPARC-LAB the FLAME laser is being used for a variety of experiments such as LWFA, TNSA (i.e. proton acceleration by thin metal target), Compton Scattering etc. M.P. Anania presented an overview of the current status of the different experiments, ranging from high intensity, high density plasmas for generation of energetic ions to extended propagation in gases for LWFA. A. Curcio focused on recent SPARC-LAB experimental results concerning phase-space reconstruction [4] of low emittance electron beams in the plasma by measuring simultaneously the electron beam and the betatron radiation spectra. This novel single-shot measurement proves to be able to provide useful limits for the estimation of the electron bunch emittance in plasmas and may be

considered as a method for *on-line* monitoring of shot-by-shot variations of LWFA performance.

Perspectives for High Power and High Repetition rate Lasers On this topic an overview of the US developments was given by W. Leemans (LBNL) who reported on a recent workshop *Laser Technology for k-BELLA and Beyond* [5] held at LBNL in May 2017, focused on the identification of the key technologies for achieving, in the next decades, high (PW) peak power and high (kW and beyond) repetition rates, for applications in advanced accelerators concepts. Six technical approaches were presented based on Ti:sapphire lasers, TM:YLF lasers and fiber lasers. The issues connected to the longevity of the materials, such as heat load and carbon deposition on gratings or non-linear crystals and mirrors were also addressed. In general, this was one of the key subjects of the Working Group 7 that generated significant discussion during the whole workshop.

3. Conclusions

We have summarized the topics and the emerging issues that have been discussed during the WG7 sessions of the workshop concerning development of laser power sources and their control in laser-driven acceleration.

Presentations clearly show that a major effort is ongoing in many laboratories world-wide to address the issues connected to the laser control for application in novel acceleration techniques. Also the strategy for fulfilling the requirements for stable acceleration in short and medium term has been addressed and discussed. Significant progress has been achieved in this direction in the most recent years and we believe that these topics will attract significantly higher attention in the near future. It is therefore extremely important for the future editions of the EAAC workshop to encourage participation of key contributors in these fields, from high average power lasers development to laser characterization and control, from laser–plasma interactions to beam diagnostics.

References

- [1] T. Tajima, J.M. Dawson, Laser electron accelerator, *Phys. Rev. Lett.* 43 (1979) 267–270. <http://dx.doi.org/10.1103/PhysRevLett.43.267>.
- [2] P.A. Walker, P.D. Alesini, A.S. Alexandrova, M.P. Anania, N.E. Andreev, *Horizon 2020 EuPRAXIA design study*, *J. Phys. Conf. Ser.* 874 (2017) 1–8.
- [3] K. Dupraz, K. Cassou, N. Delerue, P. Fichot, A. Martens, A. Stocchi, A. Variola, F. Zomer, A. Courjaud, E. Mottay, F. Druon, G. Gatti, A. Ghigo, T. Hovsepian, J.Y. Riou, F. Wang, A.C. Mueller, L. Palumbo, L. Serafini, P. Tomassini, Design and optimization of a highly efficient optical multipass system for γ -ray beam production from electron laser beam Compton scattering, *Phys. Rev. ST Accel. Beams* 17 (2014) 033501. <http://dx.doi.org/10.1103/PhysRevSTAB.17.033501>.
- [4] A. Curcio, Trace-space reconstruction of low-emittance electron beams through betatron radiation in laser-plasma accelerators, *Phys. Rev. Accel. Beams* 20(1) <http://dx.doi.org/10.1103/PhysRevAccelBeams.20.012801>.
- [5] W. Leemans, *Report of Workshop on Laser Technology For k-bella and Beyond*. Tech. Rep., Lawrence Livermore National Laboratory, 2017.



Modelling of pulse train generation for resonant laser wakefield acceleration using a delay mask

G. Vantaggiato^a, L. Labate^{a,b,*}, P. Tomassini^a, L.A. Gizzi^{a,b}

^a Intense Laser Irradiation Laboratory, INO-CNR, Pisa, Italy

^b Istituto Nazionale di Fisica Nucleare, Sez. Pisa, Italy

ARTICLE INFO

Keywords:

Laser wakefield acceleration
Multi-pulse generation

ABSTRACT

A new method for the generation of a train of pulses from a single high-energy, ultra short pulse is presented, suited for Resonant Multi-Pulse Ionization injection (Tomassini, 2017). The method is based on different transverse portion of the pulse being delayed by a “mask” sectioned in concentric zones with different thicknesses, in order to deliver multiple laser pulses. The mask is placed right before the last focusing parabola. A hole in the middle of the mask lets part of the original pulse to pass through to drive electron injection. In this paper a full numerical modelling of this scheme is presented. In particular we discuss the spatial and temporal profile of the pulses emerging from the mask and how they are related to the radius and thickness of each section.

1. Introduction

Future applications of Laser WakeField Acceleration (LWFA), such as FELs and new generation of particle colliders, require high-quality electron bunches. The main approach consists in injecting low-emittance electron bunches in the plasma wave. Among the different models proposed, the Resonant Multi-Pulse Ionization injection (ReMPI) [1] relies on the plasma wake being excited by a train of pulses produced from a single high-energy, ultra short laser pulse. The theory of plasma wave excitation by a pulse train was presented in [2,3] (and more recently discussed in [4]); the scheme takes advantage of the coherent sum of the wakefields produced by each pulse of the train (the pulses being separated in time by a plasma period) to excite a plasma wave with suitable amplitude. In Fig. 1 a QFluid [5] plasma simulation shows a comparison between this scheme and the classic LWFA. In this example a train of 8 pulses equally separated by a plasma period, each with duration of 10 fs and peak intensity of 7.4×10^{17} W/cm², travels through a plasma with $n_e = 5 \times 10^{18}$ cm⁻³ exciting a wave with a longitudinal accelerating field 20% higher than the one generated by a single pulse moving through the same plasma with duration of 10 fs, peak intensity of 5.9×10^{18} W/cm² and the same delivered energy of the train. The advantage of the resonant scheme is that the reduced peak intensity of each train pulse enables controlled particle trapping conditions. Finally, a fraction of the original pulse is frequency doubled in order to provide separated ionization injection.

The generation of the pulse train from a single laser pulse has been widely investigated, using stacked Michelson interferometers [6,7], a

linear array of birefringent plates [8] and spectral filtering of a chirped pulse [9,10]. All these techniques require challenging alignments and big optical elements due to the energy involved.

In this work we present a relatively easy-to-implement method of train generation, employing a structured transmission mask which allows different portions of the original beam to be delayed by different thicknesses of the transmissive layers. Such a simple configuration makes our technique suitable to produce pulse trains with existing laser systems and small laboratories. We developed a complete characterization of both spatial and temporal profile of the train pulses using vector diffraction theory and nonlinear time dependent analysis of pulse propagation, respectively.

2. Description of the experimental method and space and time characterization of the pulse train

As shown in Fig. 2 we consider a single high-energy pulse, with a super-gaussian transverse profile, impacting on a concentric-sectioned mask placed just before the last focusing Off-Axis Parabola (OAP). Each section's thickness d_i is chosen to match the time delay of the emerging ring pulses with the plasma period. Then these rings are focused on the plasma target and results in a multi-pulse driver for the wakefield.

For a first case study we designed a delay mask suitable for the already mentioned ReMPI scheme. This mask (Fig. 3(a)) delivers a 4-pulses train while the hole in the middle allows the so-called “ionization pulse” to pass through. This pulse, with relatively low energy (~100 mJ),

* Correspondence to: Istituto Nazionale di Ottica - CNR, via Moruzzi 1, 56124 Pisa, Italy.
E-mail address: luca.labate@ino.it (L. Labate).

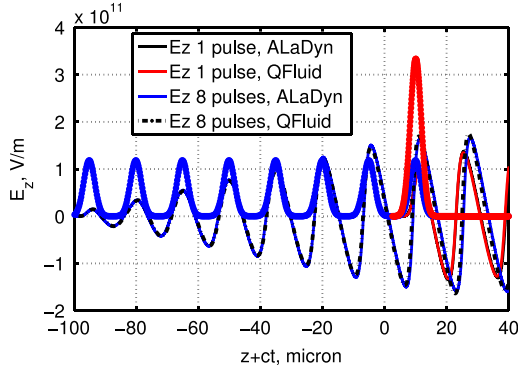


Fig. 1. Comparison of wakefield excitation by a single pulse or a pulse train. In these plasma simulations pulses moving through the left are considered. The thin lines indicate the plasma wake. In this example a train of 8 pulses equally separated by the plasma period drives a wave (thin blue) whose maximum accelerating gradient is 20% more than that of the wave excited by the single pulse (thin red) with the same delivered energy. (For interpretation of the references to colour in this figure legend, the reader is referred to the web version of this article.)
Source: Figure from [1].

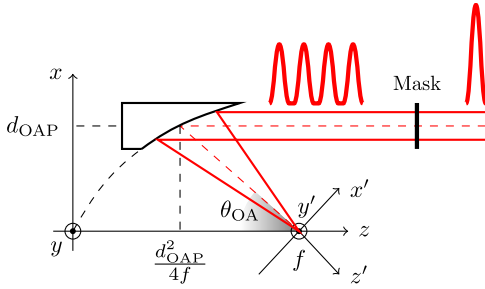


Fig. 2. Geometrical model. Cartesian coordinate system with the origin in the paraboloid vertex. The laser comes from the right and splits in 4 rings separated in time that will be focused on the focal plane $x'y'$.

can be produced in many ways. For instance, a pick up mirror can be used (upstream of the delay mask) and a suitable delay line can be set up, together with a frequency doubling crystal; a second small mirror can be used to re-insert the pulse into the main path. Since this paper is mostly concerned with the generation of the pulse train, we defer to another paper a deeper discussion of this issue.

The internal and external radii of each section are initially set in order to carry the same energy, i.e. each region has the same area (considering that the whole mask lies in the flat region of the super-gaussian transverse profile, as in Fig. 3(b)). Therefore i th radius is calculated as $r_i = \sqrt{i}r$ with r being the central hole radius.

2.1. Study of the spatial properties of the train pulses

Each pulse of the train is spatially characterized by its electrical field at the focal plane $x'y'$ of the OAP. The calculations are performed in the framework of the Stratton–Chu vector diffraction theory. Time dependence is intentionally omitted in this analysis and contour effects are negligible in the far-field calculation. We consider a super-gaussian transverse profile and linear polarization along the x axis for the incoming beam that, with reference to the coordinate system depicted in Fig. 2, is written as

$$E(\mathbf{x}) = \exp \left[-\frac{1}{2} \left(\left(\frac{x - d_{\text{OAP}}}{\sigma_x} \right)^2 + \left(\frac{y}{\sigma_y} \right)^2 \right) \right], \quad (1)$$

with $\sigma_x \equiv \sigma_y = \text{FWHM}/2(\ln 2)^{1/8}$, FWHM being the transverse size of the beam impinging on the mask, as represented in Fig. 3(b). Following the

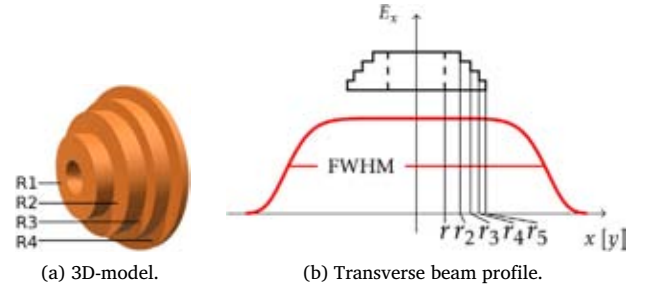


Fig. 3. Mask and beam. The incoming beam with a super-Gaussian transverse profile impacts normally on the mask and emerges as 4 rings time-separated. Sections with the same area give rise to pulses carrying the same energy. The hole in the middle is due to the necessity in ReMPI model to use part of the original pulse for ionization injection.

same formulation of [11] for the electric field at each point \mathbf{x}_p of the focal plane we get

$$E_j(\mathbf{x}_p) = -\frac{1}{\lambda} \int_{\text{OAP}} E(\mathbf{x}) \left(g_j^{(r)}(\mathbf{x}, \mathbf{x}_p) \sin(kv(\mathbf{x}, \mathbf{x}_p)) + g_j^{(i)}(\mathbf{x}, \mathbf{x}_p) \cos(kv(\mathbf{x}, \mathbf{x}_p)) \right) dx dy, \quad (2)$$

where λ is the laser wavelength, k the wave vector and $v = u(\mathbf{x}, \mathbf{x}_p) + p(\mathbf{x})$ with $u = |\mathbf{x} - \mathbf{x}_p|$ being the distance from the surface point \mathbf{x} to the point \mathbf{x}_p ; $p = (d_{\text{OAP}}^2 - x^2 - y^2)/4f$ is the difference of optical path with respect to the OAP centre. $g_j^{(r)}$ and $g_j^{(i)}$ are the real and imaginary part, respectively, of the complex g_j functions that can be written as:

$$g_x = \frac{1}{u} - \frac{x}{2f} \left(1 - \frac{1}{iku} \right) \frac{x - x_p}{u^2} \quad (3a)$$

$$g_y = -\frac{x}{2f} \left(1 - \frac{1}{iku} \right) \frac{y - y_p}{u^2} \quad (3b)$$

$$g_z = \frac{1}{u} \frac{x}{2f} - \frac{x}{2f} \left(1 - \frac{1}{iku} \right) \frac{x - x_p}{u^2}. \quad (3c)$$

In order to finally calculate the electric field we perform the numerical integration in Eq. (2) using a C++ code we developed. In particular, integrating on the portion of the OAP selected by a certain ring we get the intensity map of the corresponding train pulse.

Here we present a numerical case with the following parameters: original laser pulse FWHM = 40 mm (see Fig. 3(b)), $F/5$, $\theta_{\text{OA}} = 25^\circ$, $\lambda = 800$ nm and $r = 5$ mm. In Fig. 4 we plot the intensity maps at the focal plane of each train pulse. The maps show that the same-energy condition results in the same intensity peak for every pulse. In Fig. 5 we plot the line-out on the x' axis of the intensity for a better visualization. Spot sizes are also rather similar although diffraction effects become more important for external regions. Further studies will investigate the effects of these small differences on the excited plasma wave. We stress that these results are strictly related to the imposed conditions; working in parallel with plasma simulation can underline which one of these properties is most important or which are the best conditions to match in order to refine the mask.

2.2. Study of the temporal properties of the train pulses

A time dependent numerical approach including both linear and nonlinear interaction processes was undertaken in order to investigate the temporal behaviour of the generated pulse train. To this purpose we used the Mirò software [12]. In what follows we refer to a case study aimed at a practical implementation of the ReMPI scheme.

The time distance between each pulse of the train depends solely on the group velocity. In order to resonantly excite the plasma wave the pulse separation has to match the plasma period; the thickness of each section can be set according to this requirement.

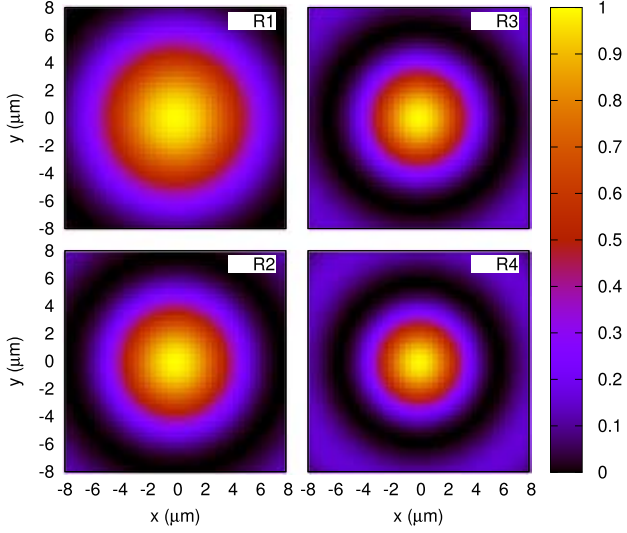


Fig. 4. Intensity maps in arbitrary units at the focal plane. Each map is normalized by the same I_{\max} value. Transverse profile of the focused rings is shown. Intensity peak is the same for each pulses and spot sizes are comparable.

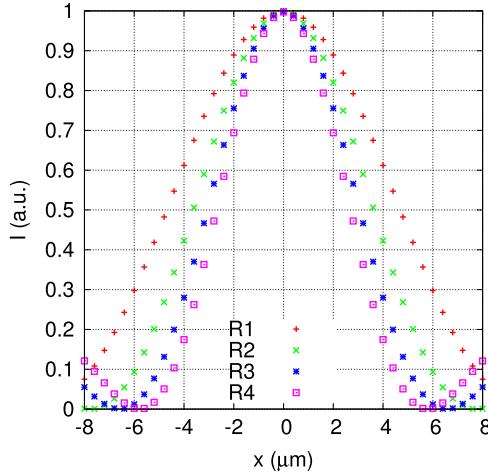


Fig. 5. Intensity line-out. Each plot is normalized by the same I_{\max} value. Sections with same area and incident energy result in the same peak intensity but different spot size. Diffraction effects are more relevant in the external rings.

Considering a slab of fused silica, chosen for its low GVD property, with an initial electron density of 10^{18} cm^{-3} , we get a difference in thickness between consecutive regions Δd of $71.52 \mu\text{m}$. With modern manufacturing technology it is possible to produce self-standing fused silica slabs, suited for the used parameters, with a minimum thickness of $500 \mu\text{m}$; the second column of [Table 1](#) shows the resulting values for the thickness of each ring.

The effects of the propagation through the mask on the time and spectral shape was simulated, using the Mirò code with the quasi-1D numerical scheme, for a pulse with 1 J energy and a duration (FWHM of the intensity) of 30 fs; different runs were carried out for each thickness d_i , corresponding to each mask's regions.

Since we are dealing with ultra short, intense laser pulses, both nonlinear and dispersive (up to the second order) effects were taken into account in these simulations. The results obtained for the final duration (that is, the pulse duration after passing through the mask) are reported in the third column of [Table 1](#); as it can be seen, a difference in duration between the pulses emerging from the inner ring and the outer one of approximately 10% arises as a consequence

Table 1

Train pulses duration. Considering an initial pulse with a duration of 30 fs we simulated the GVD-related time broadening, namely the FWHM of the intensity, of the train pulse emerging from each region with the corresponding thickness d_i . The fourth column shows the duration broadening for an initial pulse with a $-1 \times 10^{27} \text{ s}^{-2}$ frequency chirp.

Region	d_i (μm)	FWHM (fs)	FWHM _c (fs)
1	714	38.5	35.6
2	643	37.2	34.6
3	571	36.0	33.7
4	500	34.8	32.8

of the propagation. Preliminary QFluid plasma simulations show that this broadening is utterly acceptable in terms of wake excitation. It is possible to mitigate this effect by adding a tiny chirp to the incoming beam; for instance, a negative frequency chirp of the order of 10^{27} s^{-2} results in the durations reported in the fourth column of [Table 1](#). We notice that these results also suggest a low impact of the nonlinear effects occurring as a consequence of the propagation through the mask. Finally, we mention that the estimated B -integral after the mask is of order of 10^{-1} ; this confirms that the thicknesses considered here can be safely tolerated in any practical situation.

3. Conclusions

We presented an experimental method to generate a pulse train starting from a single high-energy femtosecond pulse and using a delay mask made up by concentric rings with different thicknesses.

Diffraction effects were studied and numerical approach was developed to study the transverse profile of each train pulse allowing a fine tuning of the rings' size for the optimization of the ReMPI scheme. We showed that pulse duration broadening is not a concern for typical plasma parameters of LWFA. Further combined optical and plasma simulations are needed to improve tuning of the mask in order to enhance multi-pulse wake excitation and provide a valid experimental set up.

Acknowledgements

This project has received funding from the European Union's Horizon 2020 research and innovation programme under grant agreement No. 653782 (EuPRAXIA project), and from the MIUR funded Italian research Network ELI-Italy (D.M.n. 631/16). We also acknowledge funding from the Italian MIUR through the PRIN project "Preclinical Tool for Advanced Translational Research with Ultrashort and Ultraintense X-ray Pulses" (prot. 20154F48P9).

References

- [1] P. Tomassini, S. De Nicola, L. Labate, P. Londrillo, R. Fedele, D. Terzani, L.A. Gizzi, The resonant multi-pulse ionization injection, *Phys. Plasmas* 24 (2017) 103120.
- [2] D. Umstadter, E. Esarey, J. Kim, Nonlinear plasma waves resonantly driven by optimised laser pulse trains, *Phys. Rev. Lett.* 72 (8) (1994) 1224–1227.
- [3] D. Umstadter, J. Kim, E. Esarey, E. Dodd, T. Neubert, Resonantly laser-driven plasma waves for electron acceleration, *Phys. Rev. E* 51 (5) (1995) 3484–3497.
- [4] S.M. Hooker, R. Bartolini, S. P.D. Mangles, A. Tunnermann, L. Corner, J. Limpert, A. Seryi, R. Walczak, Multi-pulse laser wakefield acceleration: A new route to efficient, high-repetition-rate plasma accelerators and high flux radiation sources, *J. Phys. B* 47 (2014) 234003.
- [5] P. Tomassini, A.R. Rossi, Matching strategies for a plasma booster, *Plasma Phys. Control. Fusion* 58 (3) (2016) 034001.
- [6] C.W. Siders, J.L.W. Siders, A.J. Taylor, S.G. Park, A.M. Weiner, Efficient high-energy pulse-train generation using a 2n-pulse michelson interferometer, *Appl. Opt.* 37 (22) (1998) 5302–5305.
- [7] J. Cowley, C. Thornton, C. Arran, R.J. Shalloo, L. Corner, G. Cheung, C.D. Gregory, S.P.D. Mangles, N.H. Matlis, D.R. Symes, R. Walczak, S.M. Hooker, Excitation and control of plasma wakefields by multiple laser pulses, *Phys. Rev. Lett.* 119 (2017) 044802.

- [8] B. Dromey, M. Zepf, M. Landreman, K. O'Keefe, T. Robinson, S.M. Hooker, Generation of a train of ultrashort pulses from a compact birefringent crystal array, *Appl. Opt.* 46 (22) (2007) 5142–5146.
- [9] T. Robinson, K. O'Keefe, M. Landreman, S.M. Hooker, M. Zepf, B. Dromey, Simple technique for generating trains of ultrashort pulses, *Appl. Opt.* 32 (15) (2007) 2203–2205.
- [10] R.J. Shalloo, L. Corner, C. Arran, J. Cowley, G. Cheung, C. Thornton, R. Walczak, S.M. Hooker, Generation of laser pulse trains for tests of multi-pulse laser wakefield acceleration, *Nucl. Instrum. Methods Phys. Res. A* 829 (2016) 383–385.
- [11] L. Labate, P. Ferrara, L. Fulgentini, L.A. Gizzi, Effects of small misalignments on the intensity and strehl ratio for a laser beam focused by an off-axis parabola, *Appl. Opt.* 55 (23) (2016) 6506–6515.
- [12] O. Morice, Miro: Complete modeling and software for pulse amplification and propagation in high-power laser systems, *Opt. Eng.* 42 (6) (2003) 1530–1541.

LASERS FOR NOVEL ACCELERATORS

L. A. Gizzi[†], P. Koester, L. Labate, Istituto Nazionale di Ottica, CNR, Pisa, Italy
 F. Mathieu, Z. Mazzotta¹, Ecole Polytechnique, CNRS, Palaiseau, France
 G. Toci, M. Vannini, Istituto Nazionale di Ottica, CNR, Sesto Fiorentino (FI), Italy
¹now at ARCNL, University of Amsterdam, The Netherlands

Abstract

Novel accelerator schemes are rapidly emerging in the wake of laser-plasma acceleration research and involve advanced high-power laser drivers for their operation. Significant progress has been made in laser performance during the past decade, including repetition rate, average and peak power, and footprint, making these systems attractive for many applications, including novel accelerators. Here we discuss laser driver requirements for the proposed novel accelerator schemes, examine emerging technologies and introduce a viable laser driver concept for a first generation of plasma accelerators.

INTRODUCTION

After two decades of dramatic developments in laser-plasma acceleration [1,2,3,4,5] following the original idea of Tajima and Dawson[6], enabled by the invention of CPA lasers [7] and the diffusion of high ultrashort pulse lasers worldwide [8], record electron energy in the lab is now approaching the 10 GeV [9]. As a consequence, concepts for a new generation of industrial, high gradient accelerators based on highly advanced laser-plasma acceleration schemes are emerging rapidly.

Among these, the European H2020 project named EuPRAXIA[10] aims at the realization of a European Plasma Research Accelerator with eXcellence In Applications and is delivering a conceptual design of a plasma based electron beam accelerator to final energies between 1 and 5 GeV, with bunch duration of a few fs, transverse emittance of about 1 mm-mrad and relative energy spread reaching from a few % down to a few 10^{-3} total and few 10^{-4} in a 1 micro-meter slice of the beam. The EuPRAXIA specifications [11] approach the regime of modern X-ray free-electron lasers (FELs) and fulfil basic requirements for a 5 GeV plasma accelerator stage of a linear collider.

The EuPRAXIA concept, like other similar programmes world-wide, builds upon ultrashort pulse laser drivers [12] with kW average power and up to petawatt-scale peak power, with a repetition rate ideally up to 1 kHz and beyond. Such laser systems are not currently available, but the scenario for enabling technologies is evolving rapidly. Indeed, new architectures are emerging with the promise of addressing medium and long-term objectives of laser-plasma acceleration and future plasma-based particle colliders. Scaling the technology of existing high peak power lasers to higher average power, while maintaining key technological performance requirements, is challenging and required high average power pump laser sources. Pulsed high energy solid state lasers have

demonstrated continuous operation at 100J scale energy per pulse and repetition rates up to 10 Hz, like the DI-POLE laser [13] and the industrial P60 [14]. Solid-state lasers with peak power in the petawatt class and pulse energies exceeding 10 J have reached an average power of tens of watts, like the BELLA system [15], with HAPLS aiming at 300 W[16]. It is therefore clear that a one order of magnitude or higher improvement in the average power of ultrafast lasers is needed to meet laser requirements for novel plasma accelerators.

TECHNOLOGY PATHS

Motivated by endeavours like the kBELLA project (LBNL, US)[17] and also by EuPRAXIA [10], new concepts are emerging which are now entering the design and prototyping demonstration phase for intermediate average power levels and may offer solution for kHz and higher rep-rate systems. Depending on the required laser parameters, the time to construction and the expected performance, several approaches can be identified starting from laser technologies currently available and evaluating their scalability to the required specifications. In the following, a brief description of the leading technologies is given, sorted according to their efficiency, outlining pros and cons in the perspective of designing a driver for a laser-plasma accelerator.

Titanium Sapphire

Currently used in almost all the laser-plasma acceleration laboratories and facilities, Ti:Sapphire based technology is certainly the most advanced and mature. Featuring a broad gain bandwidth, Titanium doped Al_2O_3 (Ti:Sa), allows for the amplification of a few tens of fs pulses. It is therefore perfectly suited for the laser pulse duration targeted by current LWFA driver parameters, at a wavelength of about 800 nm. On the other hand Ti:Sapphire must be pumped in the visible, typically between 500 and 550 nm, commonly obtained by frequency doubled Q-switched Nd:YAG lasers. The wall-plug efficiency of the whole system is usually quite low, in particular when flash lamp pumped Nd:YAG lasers are used. Moreover, the high (~ 34%) quantum defect between the pump and the fluorescence photon energy imposes a high thermal load on the gain medium. These elements make the operation at high average power quite challenging. Replacement of flash lamp, with diode-pumped solid state (DPSSL) lasers provides a significant improvement in wall-plug efficiency, with major European industrial endeavour in place. In very recent years, demonstration of

[†] la.gizzi@ino.cnr.it

innovative concepts and the construction of DPSSL prototypes are leading to kW average power pump lasers, possibly scalable to multi-kW [13,14].

The lack of diode pumps capable of pumping directly the Ti:Sa, forces us to use diode-pumped Nd lasers. This double-step impacts on the overall efficiency of the system, eventually limiting further scalability. Also, high-energy laser systems will require large aperture gain elements and, since Ti:Sa can only be produced as a single crystal, the size of the gain element is another limitation.

Direct Pumping Chirped Pulse Amplification

Other technologies are developing which aim at more efficient configurations removing the double-step in the pumping architecture, with direct pumping of the ultrafast amplifier with diodes. This is a mandatory step to deliver higher repetition rate and higher average power levels. Direct Chirped Pulse Amplification using lasing media that can be pumped directly with diodes offer an ideal alternative solution for higher efficiency and higher rep-rate. Direct CPA concepts under consideration have been explored in detail and some issues have been identified, including the minimum achievable pulse duration and the scaling of listed architectures.

Examples of Direct CPA are Yb based systems like Yb:YAG and Yb:CaF₂: with respect to the Ti:Sapphire, Yb based gain media have many advantages in terms of pumping efficiency: they allow direct pumping by semiconductor lasers at 930-970 nm, without further wavelength conversion stages. Moreover, the quantum defect between the pump photon energy and the laser photon energy is rather low (around 10%) because the emission wavelength (usually 1030-1050 nm, depending on the host) is close to the pumping wavelength. This reduces the thermal load on the gain medium and thus the power dissipation requirements. Both these elements are advantageous for a high average power operation regime.

The main drawback of the Yb-based gain media is the reduced gain bandwidth, that makes it difficult to achieve pulse duration of 100 fs or less for high-energy pulses, whereas operation in the range 100-200 fs is more easily achieved. Another potential drawback is that in Yb doped media the saturation fluence of the laser transition often largely exceeds the damage threshold of the host so that amplification stages cannot operate in saturation. Finally, several hosts allow doping with Yb, and this provides some flexibility in the choice of the gain media parameters (e.g. emission spectrum, but also thermal conductivity and thermo-optical parameters). Besides, several hosts can be fabricated with ceramics technologies, which can more easily allow large gain elements.

Another promising concept of direct CPA, with enhanced potential performance at very high rep rate is based on the Tm:YLF gain media which offers significant lifetime advantage over the well-established Yb doped materials traditionally used for diode pumped fiber and bulk systems. When operated in the multi-pulse extraction, it is as efficient at >70% at rep-rates > 1 kHz, while

at 100 Hz is still capable of $\approx 20\%$ efficiency. Among the host materials, YLF offers several attractive properties, including a negative dn/dT , low linear and nonlinear refractive index, and natural birefringence. The Tm dopant in YLF emits laser radiation at $\sim 1.9 \mu\text{m}$, and has a long upper-state lifetime (15 ms). It can be pumped with commercially-available, technologically-mature, high-brightness CW laser diodes at 800 nm. Also, Tm:YLF is commercially available in boule sizes consistent with 300 kW average power operation of a 30J compressed at 10 kHz or up to 160J at lower repetition rates [17].

Another robust and well established architecture is based on Nd:glass. Some high energy systems adopt Nd:glass as gain medium for the final power amplification stages. Nd-doped glasses provide a gain bandwidth suitable for the generation and amplification of pulses in the 100 fs time range. Large gain elements can be produced with glasses more easily than with crystal growth technologies. Moreover, Nd:glasses can be directly pumped with diode lasers, which is advantageous for the overall efficiency and power dissipation requirements of the pump system. On the other hand, even though the thermally dissipated pump power fraction is moderate (around 20%), the operation at high average power levels of Nd:glass bulk amplifiers is limited by the poor thermal conductivity of the glass host.

An additional alternative method for the amplification of high peak power pulses is based on parametric light amplification in nonlinear optical crystals, namely Optical Parametric Chirped Pulse Amplification (OPCPA) [18,19]. Instead of using ordinary laser media based on the excitation/deexcitation of an atomic transition, the amplification is based on optical difference frequency generation in nonlinear crystals. With respect to standard amplification, OPCPA has several specific features that can be potentially advantageous: first, it can reach a very high amplification factor of chirped pulses: up to 3-4 orders of magnitude per pass in terms of energy. Moreover, the parametric gain exists only when the pump pulse is present, so that the amplification process inherently acts as a temporal contrast gate, enabling high temporal contrast pulses. Finally, the process is non dissipative, because the energy difference between the pump (highest energy) photon and the amplified signal (lower energy photon) is emitted as a third photon (the so called idler) and it is not dissipated into the crystal, as it happens in stimulated emission process. Therefore, the parametric amplification process imposes a much lower thermal load on the amplified medium with respect to the amplification based on the emission from atomic transitions. The amplification of high energy pulses requires large aperture crystals: this limits the choice of the possible nonlinear materials, mainly to KDP, DKDP and LBO.

Other Concepts

Finally, a very promising approach that has attracted a major attention for its potential compactness and the strong link with the industrial world of telecommunica-

Content from this work may be used under the terms of the CC BY 3.0 licence (© 2019). Any distribution of this work must maintain attribution to the author(s), title of the work, publisher, and DOI

tions is based on Fiber laser technology, which is currently offering the best wall-plug efficiency for a laser, now exceeding 50% in CW mode. For high peak power architectures, solutions based on the coherent combination [20] of a very large number of fiber amplifiers is being developed and prototype developments are in progress. Studies show that this technology is really optimized for repetition rate of 10 kHz and above and will be particularly suited and cost-competitive if laser driver parameters are going to evolve towards small energy (J level) per pulse and higher repetition rate (>1kHz) .

INDUSTRIAL DRIVER

In the perspective of a short term approach, a driver for a plasma accelerator capable of outstanding parameters, like those required by the EuPRAXIA laser, should be based on components with a high Technology Readiness Level, ideally sourcing from a lab environment where specific technology have been explored in depth. Ti:Sa technology is certainly an excellent platform that leads to the required specifications by scaling existing systems. As anticipated, scaling still requires innovative solutions for high repetition rate, DPSSL pump lasers and thermal management in both the amplifier and the whole transport chain from the compressor to the target plasma.

As anticipated, kW scale lasers suitable for pumping Ti:Sa in the 10-20 Hz range repetition rate are just emerging with industrial systems like the P60 [14] or prototypes like the DIPOLE [13], and can be integrated in advanced Ti:Sa amplifiers design, provided a geometry with efficient cooling ensures heat removal from the amplifier head. This is an important conceptual aspect of laser design that has impact on both the complexity and the compactness of the final system. As shown in Fig.1, transmission and reflection geometries of the amplifier head are considered in this context.

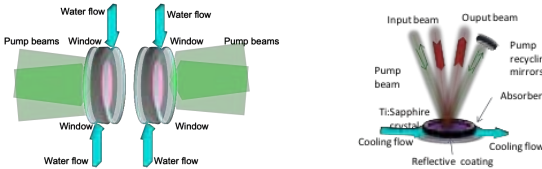


Figure 1: Possible conceptual configurations of an amplifier head, the core of a laser driver where efficient heat exchange between the gain material and the heat sink is crucial to enable high average power operation.

Indeed, in currently explored designs, heat exchange sets the limit of accessible average power to $\approx 1\text{kW}$, leaving options for a 10 Hz system at 100 J energy per pulse. Higher repetition rate, namely 100 Hz at 10 J or possibly 1kHz at 1J pulse energy, are also possible, provided higher repetition rate, high power diode laser operation can be achieved. Also, a modest increase (2X) of the average power performance is accessible using multiple pump units simultaneously. This approach, while inevitably increasing the complexity of the pumping geometry, has the advantage of increasing the robustness of the driver operation against failure of individual components.

FRYPLM2

2

Higher rep-rate will require developments to increase the repetition rate of currently available high power diode lasers and to enhance thermal management in the amplifier head [21]. Yb:YAG and Yb:CaF₂ are both candidates as gain media, however major numerical modelling and experimental data is needed to demonstrate the path to commercial availability of diode pump sources needed for a reliable kHz driver.

TRANSPORT AND STABILITY

The general layout of the driver delivery to target plasma includes a number of components that ensure control and stability of the wakefield generation. Indeed, experimental studies are currently focusing attention of the role of driver beam quality, namely focal spot intensity distribution, energy and pointing stability, that are key factors behind the stability of the accelerated electron bunch.

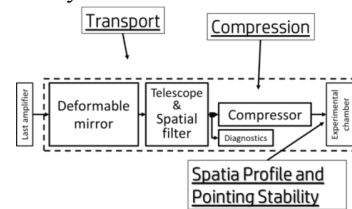


Figure 2: Schematic layout of the post-amplification section required to deliver the driver beam to the target plasma and to maintain control of the beam quality.

The block diagram of Fig.2 shows the main components required to gain angular, spatial and temporal control of the driver. Scaling these components to the beam size and average power currently required is a very challenging task that calls for a significant development. Spatial beam diagnostics in the focal plane are necessary in order to measure and improve the beam spatial quality, in a closed loop with the deformable mirror, and in order to estimate the beam intensity achieved during the acceleration experiment. Requirements on beam pointing stability are highly demanding, with pointing accuracy well below the μrad to ensure no impact on the pointing instability of the accelerated electron bunch, typically set by the acceleration process. Here a combination of pointing detector and active pointing control is envisaged in the full scale implementation of the driver.

CONCLUSIONS

First generation of high quality laser-plasma accelerator design is progressing rapidly and needs a new generation of ultrashort pulse laser drivers, with high average power and high stability. A range of candidate technology paths is being considered and will develop according to time-scale for implementation and required driver performance. Evolution of widely explored Ti:Sa based system may provide viable short term solution for kW scale drivers with rep-rate up to the kHz, while higher rep-rate, high average power solutions will build on newer, more efficient technology and high efficient direct DPSS CPA laser technology.

MC7: Accelerator Technology

T25 Lasers

This is a preprint — the final version is published with IOP

ACKNOWLEDGEMENTS

This work was supported by the European Union's Horizon 2020 research and innovation programme under grant agreement No. 653782. LAG, LL, and PK also acknowledge financial support from the CNR funded Italian Research Network ELI-Italy.

REFERENCES

- [1] A. Modena et al. "Electron acceleration from the breaking of relativistic plasma waves", *Nature* 377, 606 (1995). doi: 10.1038/377606a0
- [2] S.P.D.Mangles et al., "Monoenergetic beams of relativistic electrons from intense laser-plasma interactions", *Nature*, 431, 535 (2004). doi:10.1038/nature02939
- [3] C. G. R. Geddes, et al., "High-quality electron beams from a laser wakefield accelerator using plasma-channel guiding", *Nature* 431, 538–541 (2004). doi:10.1038/nature02900
- [4] J. Faure, et al. "A laser-plasma accelerator producing monoenergetic electron beams", *Nature* 431, 541–544 (2004). doi:10.1038/nature02963
- [5] W. P. Leemans et al., "Multi-GeV Electron Beams from Capillary-Discharge-Guided Subpetawatt Laser Pulses in the Self-Trapping Regime", *Phys. Rev. Lett.* 113, 245002 (2014). doi: 10.1103/PhysRevLett.113.245002
- [6] T. Tajima and J. M. Dawson, "Laser Electron Accelerator", *Phys. Rev. Lett.* 43, 267 (1979).
- [7] D. Strickland, G. Mourou, "Compression of amplified chirped optical pulses", 56, 219 (1985). doi: 10.1016/0030-4018(85)90120-8.
- [8] C. Danson et al., "Petawatt class lasers worldwide", *High Power Laser Science and Engineering*, 3, e3 (2015). doi:10.1017/hpl.2014.52
- [9] A. J. Gonsalves et al., "Petawatt Laser Guiding and Electron Beam Acceleration to 8 GeV in a Laser-Heated Capillary Discharge Waveguide", *Phys. Rev. Lett.* 122, 084801 (2019). doi: 10.1103/PhysRevLett.122.084801
- [10] P A Walker et al, "Horizon 2020 EuPRAXIA design study", *J. Phys.: Conf. Ser.* 874 012029 (2017);
- [11] M. Ferrario et al., "Recent Results at the SPARCLAB Facility", in *Proc. 3rd Int. Particle Accelerator Conf. (IPAC'12)*, New Orleans, LA, USA, May 2012, paper WEPPP017, pp. 2758-2760.
- [12] L.A.Gizzi et al., "A viable laser driver for a user plasma accelerator", *NIM, A* 909, 56 (2018). doi:10.1016/j.nima.2018.02.089
- [13] P. Mason et al., "Kilowatt average power 100 J-level diode pumped solid state laser", *Optica* 4, 438 (2017). doi:10.1364/OPTICA.4.000438
- [14] S Kühn et al., *J. Phys. B: At. Mol. Opt. Phys.* 50, 132002 (2017). doi:10.1088/1361-6455/aa6ee8
- [15] K.Nakamura et al., "Diagnostics, Control and Performance Parameters for the BELLA High Repetition Rate Petawatt Class Laser", *IEEE Journal of Quantum Electronics*, 53, 1200121 (2017). doi: 10.1109/JQE.2017.2708601
- [16] E. Sistrunk et al., "All Diode-Pumped, High-repetition-rate Advanced Petawatt Laser System (HAPLS)", *Proceedings of the Conference on Lasers and Electro-Optics* (2017). doi: 10.1364/CLEO_SI.2017.STh1L.2
- [17] Report of Workshop on Laser Technology for k-BELLA and Beyond, Workshop held at Lawrence Berkeley National Laboratory (2017)
- [18] I. Ross et al., "Generation of terawatt pulses by use of optical parametric chirped pulse amplification", *Applied Optics*, 39, 15, 2422 (2000). doi: 10.1364/AO.39.002422
- [19] J. Bromage et al., "Technology development for ultraintense all-OPCPA systems", *High Power Laser Science and Engineering*, 7, e4 (2019). doi: 10.1017/hpl.2018.64
- [20] A. Heilmann et al., "Coherent beam combining of seven fiber chirped-pulse amplifiers using an interferometric phase measurement", *Optics Express*, 26, 31542 (2018). doi:10.1364/OE.26.031542
- [21] P. Ferrara et al., "3-D numerical simulation of Yb:YAG active slabs with longitudinal doping gradient for thermal load effects assessment", *Optics Express* 22, 5375 (2014).doi: 10.1364/OE.22.005375

Progress in understanding the role of hot electrons for the shock ignition approach to inertial confinement fusion

D. Batani^{1,a}, L. Antonelli², F. Barbato¹, G. Boutoux^{1,b}, A. Colaïtis¹, J.-L. Feugeas¹, G. Folpini¹, D. Mancelli¹, Ph. Nicolai¹, J. Santos¹, J. Trela¹, V. Tikhonchuk^{1,9}, J. Badziak³, T. Chodukowski³, K. Jakubowska³, Z. Kalinowska³, T. Pisarczyk³, M. Rosinski³, M. Sawicka³, F. Baffigi⁴, G. Cristoforetti⁴, F. D'Amato⁴, P. Koester⁴, L.A. Gizzi⁴, S. Viciani⁴, S. Atzeni⁵, A. Schiavi⁵, M. Skoric⁶, S. Gus'kov^{7,a}, J. Honrubia⁸, J. Limpouch⁹, O. Klimo^{9,10}, J. Skala⁹, Y.J. Gu^{10,11}, E. Krousky¹⁰, O. Renner^{10,11}, M. Smid¹⁰, S. Weber¹⁰, R. Dudzak^{10,11}, M. Krus^{10,11} and J. Ullschmied^{10,11}

¹ Université Bordeaux, CNRS, CEA, CELIA (Centre Lasers Intenses et Applications), UMR 5107, F-33405 Talence, France

² York Plasma Physics Institute, Department of Physics, University of York, Heslington, York YO10 5DD, United Kingdom of Great Britain and Northern Ireland

³ Institute of Plasma Physics and Laser Microfusion, Warsaw, Poland

⁴ INO-CNR, Pisa and Florence, Italy

⁵ Dipartimento SBAI, Università di Roma 'La Sapienza', Roma, Italy

⁶ Vinca Institute of Nuclear Sciences, Belgrade, Serbia

⁷ P. N. Lebedev Physical Institute of RAS, 119991 Moscow, Russian Federation

⁸ ETSI Aeronautica & Espacio, Universidad Politecnica de Madrid, Plaza Cardenal Cisneros 3, E-28040 Madrid, Spain

⁹ Czech Technical University in Prague, FNSPE, Prague, Czech Republic

¹⁰ Institute of Physics of ASCR, ELI-Beamlines, Na Slovance 2, Prague, Czech Republic

¹¹ Institute of Plasma Physics of the ASCR, PALS, Za Slovankou 3, 182 00, Prague, Czech Republic

E-mail: dimitri.batani@u-bordeaux.fr

Received 1 May 2018, revised 31 October 2018

Accepted for publication 14 November 2018

Published 18 December 2018



CrossMark

Abstract

This paper describes the results of a series of experiments conducted with the PALS laser at intensities of interest for the shock ignition approach to inertial fusion. In particular, we addressed the generation of hot electrons (HE) (determining their average energy and number), as well as the parametric instabilities which are producing them. In addition, we studied the impact of HE on the formation and dynamics of strong shocks.

Keywords: hot electrons, shock ignition, parametric instabilities, shock generation, preheating, diagnostics

(Some figures may appear in colour only in the online journal)

^a Department of Plasma Physics, National Research Nuclear University MEPhI, Moscow, Russia Federation.

^b CEA, DAM, DIF, F-91297 Arpajon, France.

1. Introduction

The so-called ‘shock ignition’ [1–4] approach (SI) to inertial confinement fusion has been proposed by researchers at the University of Rochester [1] (and somehow anticipated in [5]) as an alternative to the conventional indirect-drive, central-hotspot approach currently investigated at NIF [6]. SI is a direct-drive scheme, and relies on the separation of the phases of target compression and ignition. Compression is achieved similarly to the conventional direct-drive approach with lasers at intensity a few times $10^{14} \text{ W cm}^{-2}$ and pulse duration ≈ 10 ns (with temporal shaping). The ignition phase is triggered by a high intensity laser spike ($\approx 10^{16} \text{ W cm}^{-2}$, lasting several hundred ps) launching a very strong shock (≥ 0.3 GBar at the ablation front). The convergence of the shock at target centre heats the compressed fuel creating conditions for the onset of nuclear reactions.

A critical issue for SI concerns the role of hot electrons (HE) generated by the interaction of the intense laser spike. HE can either be detrimental or beneficial to SI, depending on their quantity and energy spectrum. HE generation and transport under SI relevant conditions must then be experimentally studied, and properly described within the hydrodynamics simulation codes which will be used for designing full-scale SI experiments.

In the conventional approach to ICF, HE are detrimental since they can preheat the cold fuel in the imploding shell making its compression more difficult. In SI, HE are produced by the final high-intensity laser spike that creates the very strong shock. At such late time the accumulated target areal density $\langle \rho r \rangle$ is already quite large and can prevent the HE, depending on their energy, from passing through the compressed shell and to reaching the fuel in the centre. On the contrary they may deposit their energy in the denser part of the plasma providing an extra pressure, which may be the critical factor in reaching the needed sub-Gbar pressures. Therefore, in contrast to the classical scenario, HE may improve laser-target coupling and hence be beneficial to SI. This result was indeed anticipated in several theoretical [7–10] and numerical [11] works.

Recent experiments at Omega facility indicate that pressure of 0.3 GBar has indeed been obtained [12, 13]. This is an important result; however, it is not clear to what extent HE contributed to such a pressure.

At the same time, while studying HE, it is natural to study the impact of parametric instabilities since HE are indeed produced by Stimulated Raman scattering (SRS) and two plasmon decay (TPD). These two instabilities produce HE with different energy and angular spectra and at different times and locations of interaction. TPD electrons are typically much hotter and can then be more dangerous since they can produce preheating. Therefore, it is essential to study when and by what mechanisms HE are produced.

Current experiments in inertial fusion are most performed at the maximum intensity of $\approx 10^{15} \text{ W cm}^{-2}$, while the intensity regime around $10^{16} \text{ W cm}^{-2}$ is quite unexplored. Parametric instabilities are well studied and of relatively minor concern at intensities of $\approx 10^{15} \text{ W cm}^{-2}$, but extrapolating results of

these experiments to higher intensities is not justified. Indeed, at higher intensities SRS and TPD are expected to be in a strongly nonlinear regime and affected by kinetic effects (such as Landau damping, see section 4), depending critically on plasma conditions. SRS and Stimulated Brillouin scattering (SBS) can reflect a large part of incident laser radiation causing a decrease of absorption. Moreover, laser beam filamentation may ease the onset of parametric instability and affect the uniformity of energy deposition. Therefore, parametric instabilities need to be studied not only as sources of HE, but also since they may alter the laser-plasma coupling.

In this context, we have conducted a series of experiments at the PALS (Prague Asterix Laser System) Laboratory in Prague [14]. Earlier experiments [15–17] have recently been complemented with experiments realized in the framework of the Eurofusion Enabling Research Project «Preparation and Realization of European Shock Ignition Experiments». The laser PALS was chosen, as it is the only laser system in Europe that can deliver energies of the order of 0.5 kJ in a duration of about 300 ps, with the additional advantage of allowing irradiation at 1ω (1314 nm) or at 3ω (438 nm). We highlight that pulse duration of the order of a few hundred ps is just what is needed for SI. In addition, an auxiliary laser beam is available which allows creating an extended plasma corona before the arrival of the main pulse. Although due to the limited available energy, the density scale-lengths are shorter and the corona temperature lower than those envisaged for full-scale SI, these conditions can be considered as a first significant step toward really SI-relevant parameters.

The use of PALS allowed us to perform a unique set of high intensity interaction experiments (10^{15} – $10^{16} \text{ W cm}^{-2}$; see details below), at both 1ω and 3ω , in a well-characterized experimental configuration.

It is worth noticing that while the conventional approach to ICF relies on using short wavelength lasers converted to 3ω , in SI one could envisage using a final spike at 2ω or even 1ω . In addition, measurements at 1ω are needed to validate advanced hydrodynamics codes in a wider range of parameters. In particular, we are interested in testing simplified models which are able to take into account the role of parametric instabilities in the frame of a fluid code.

2. Experimental set-up and diagnostics

PALS is an iodine laser system, which can deliver energies ≈ 0.5 kJ in a duration ≈ 300 ps. It can be operated either at 1ω (1314 nm) or at 3ω (438 nm). In our experiments, the PALS laser was focused onto multi-layered targets in order to simultaneously study the generation of a strong shock and the production of HE. Phase Plates were used at both irradiation wavelengths, allowing for a uniform and well-known intensity profile. The focal spot had a nominal Gaussian profile with FWHM of $100 \mu\text{m}$. However, dedicated experiments on the spatial distribution of the laser energy showed that, when phase plates are used, the nominal Gaussian spot is superimposed to a larger energy ‘plateau’ and that about only 55% of the laser energy is actually delivered within the $100 \mu\text{m}$ spot,

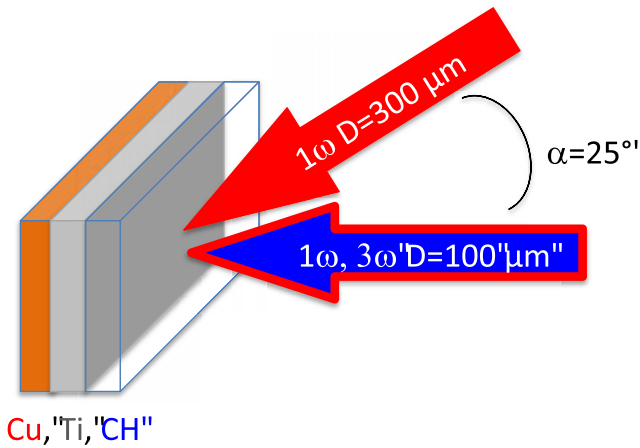


Figure 1. Typical scheme of targets used for characterization of hot-electron generation at PALS. The two laser pulses are also represented. The main pulse (horizontal in the figure) is focused onto a spot of 100 micron diameter, the auxiliary pulse onto a 300 micron spot.

both at 1ω and 3ω irradiation. Peak laser intensities on target were up to $6 \times 10^{15} \text{ W cm}^{-2}$ at 3ω and $2 \times 10^{16} \text{ W cm}^{-2}$ at 1ω , when RPP are used.

The auxiliary laser beam, with energy up to 80 J at 1ω , and focused onto a spot of $300 \mu\text{m}$ (again smoothed with phase plate) was used to create a plasma corona with a flat radial profile and relatively long axial scale-length (50–100 micrometres, depending on the delay between auxiliary pulse and main pulse).

We used multi-layered targets with an interaction layer of plastics (either polyethylene or polyurethane) followed by one or more ‘tracer layers’ (typically Ti and Cu, see figure 1). The HE generated in the interaction propagated in the plastic layer (low-Z, to mimic the low-Z ablator of ICF targets) and then reached the tracer layers. Here the collisions of the HE with the atoms result in creation of holes in inner electronic shells and their subsequent filling via radiative transitions. In particular, the $2p \rightarrow 1s$ K-shell fluorescence from the relatively cold target material (usually referred to as $K\alpha$ emission) provides a direct tool for HE investigation. In some cases, the plastic layer was doped with Cl allowing for diagnostics of plasma conditions through x-ray spectroscopy.

The use of plastic layers with different thicknesses (from 10 to $180 \mu\text{m}$) allowed obtaining information on both shock-waves dynamic (through shock chronometry) and HE energy spectrum. The information on the energy spectrum is obtained by analysing $K\alpha$ emission from targets with plastic layer of different thickness. Indeed, HE propagate through the target depending on their initial energy. For given laser parameters, the intensity of $K\alpha$ radiation depends on the number of HE reaching the tracer layer and on their residual energy. When a double tracer layer was present, a comparison of the relative intensities of Cu and Ti $K\alpha$ emissions was used to get information on the HE energy spectrum. This is a widely-used technique [18–20] for the characterization of HE. We performed both imaging of the $K\alpha$ sources using spherically bent crystals [21] and x-ray spectroscopy [22]. This enables the separation

of the contribution of $K\alpha$ emission from the continuum radiation in the same spectral range [23].

The K-shell spectra emitted from the Ti tracer layer were observed at an angle of 65° to the target surface by using the x-ray spectrometer equipped with the crystal of quartz (211) spherically bent to a radius of 150 mm. The spectrometer was aligned to cover the photon energy range of 4.4–4.8 keV and provided the 1D spatial resolution at magnification of $M = 0.53$. The spectra were recorded on x-ray film Kodak Industrex AA 400 or imaging plate BAS-MS (IP). Characteristic curves of these detectors were recalibrated using a Fe-55 source. This set-up allowed achieving spectral resolution $E/\Delta E$ of 5000, and spatial resolution along the target surface of $11 \mu\text{m}$ (using the film) or $104 \mu\text{m}$ (using IP). The spectral records were calibrated with respect to a ray-traced dispersion relation of the experimental geometry and crosschecked via tabulated dominant Ti K-shell transitions.

The transfer function of the x-ray spectrometer was calculated using a detailed quantitative ray-tracing analysis [24]. This procedure accounted for all relevant geometric factors (source-to-crystal and crystal-to-detector distances, crystal and detector dimension, and bending-broadened reflection curves of the crystal). The computed transfer characteristics of the spectrometer relate one photon impinging on the detector to $T_F = 1.2 \times 10^7$ photons emitted from the source over the whole solid angle. The fluorescence yields were taken into account to calculate the photon production probability for a given electron. This allowed to finally determine the relation between the relation of K-shell photons to HEs by using the spatially integrated signal recorded on the detector within the above-mentioned photon energy range 4450–4650 eV. It is also worth noticing that in our conditions the generation of $K\alpha$ photons due to photo-pumping from the x-rays produced in the plasma corona is negligible. This is due to the relatively low temperature and to the relatively low emission of x-rays (since the ablator is low-Z).

As for the emission from the Cu tracer layers, 2D-resolved (time-integrated) images of the Cu $K\alpha$ source were recorded with a quartz crystal (422) spherically bent to a radius of 380 mm. Images were recorded on x-ray film Kodak Industrex AA400, digitized with a scanner providing spatial resolution of $5.3 \mu\text{m}$, and converted to incident photon fluxes by using the film calibration curve and filter transmission.

The combination of Cu $K\alpha$ radiation (photon energy 8047.8 eV) and of the crystal interplanar spacing $2d = 0.154 \text{ nm}$ results in quasi-normal incidence configuration with a Bragg angle at the centre of the crystal $\theta_B = 88.15^\circ$. The range of photon energies reflected from the crystal surface is limited to 3.86 eV, which is comparable to the FWHM width of the cold Cu $K\alpha_1$ emission (2.29 eV). The signal collected by the crystal therefore corresponds only to a fraction of the K-shell emission due to HEs. To take this effect into account, the recorded signal was complemented to the information obtained via high-resolution spectroscopy.

Cu K-shell spectra were observed at an angle of 10° to the target surface by using the x-ray spectrometer equipped with the crystal of quartz (223) spherically bent to a radius

of 150 mm. The spectrometer was aligned to cover the photon energy range of 7.9–8.5 keV and provided 1D spatial resolution of 14 μm in the direction of the target normal. The spectra were again recorded on x-ray film, calibrated with respect to the dispersion relation of the experimental geometry and cross-checked via tabulated dominant Cu K-shell transitions ($K\alpha$ doublet, resonance w and intercombination y line of He-like Cu). The recorded signal was converted to an absolute intensity taking into account crystal reflectivity and filter transmission.

In addition to using $K\alpha$ diagnostics, we also characterized HE by detecting the hard x-ray emission with a bremsstrahlung cannon [25, 26]. This hard x-ray spectrometer, placed inside the experimental chamber, allowed inferring the high-energy bremsstrahlung-produced photon distribution and hence indirectly estimating the HE energy distribution. The detector was made of a stack of 14 IP's separated by filters, leading to different transmission curves for each IP. Incident bremsstrahlung spectra (and then HE 'temperatures') were obtained with the help of GEANT4 Monte Carlo simulations using the measured doses released in the IP's, as well the IP sensitivities [27].

The simultaneous use of the three diagnostics provides higher confidence in obtained results.

The onset of parametric instabilities was studied by measuring the back-reflected radiation [28, 29]. We measured both the time-resolved emitted spectra and the reflected energy in the different spectral regions, by suitable spectroscopic and calorimetric tools. Details on the setup can be found in [29].

Finally, in order to study shock propagation, we used a shock chronometry diagnostics based on streaked optical pyrometry. The target rear-side is imaged on the slit of a streak camera, recording self-emission in the visible range of the electro-magnetic spectrum [30–32]. This allows to determine shock transit time through the sample. Shock pressure is then inferred by using hydrodynamic simulations reproducing the experimental shock breakout time.

3. Hot electron characterization

We characterized HE generation by either comparing Cu $K\alpha$ and Ti $K\alpha$ emission, or by studying the dependence of Ti $K\alpha$ emission on the thickness of the plastic layer. As described in the previous section we used three different diagnostics simultaneously.

- (i) $K\alpha$ imaging, using a spherically bent Bragg crystal, providing an image of the $K\alpha$ source. The signal was processed and integrated spatially to provide the total $K\alpha$ yield. The drawback of this diagnostics is its very narrow bandwidth, which implies the possibility of losing a part of the $K\alpha$ signal whenever matter is significantly ionized and heated producing a shift of the $K\alpha$ emission (indeed in ionized atoms the screening effect of electrons on nuclear charge is reduced, causing a shrink of the energy levels).
- (ii) X-ray spectroscopy, centered on the $K\alpha$ line. This diagnostic complements imaging data, since it can easily

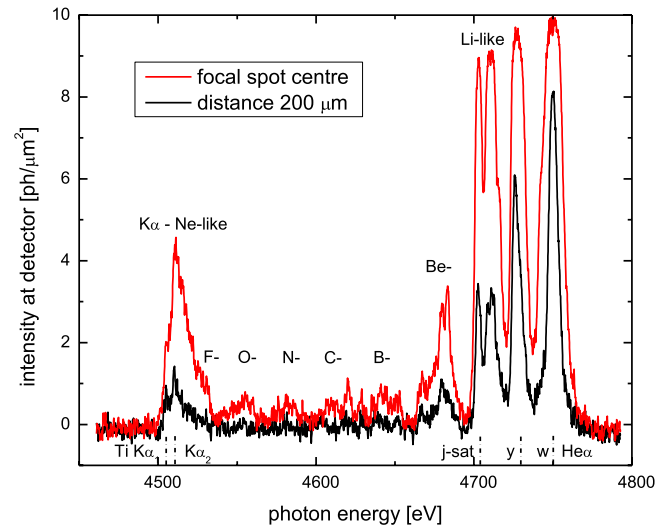


Figure 2. Ti K-shell spectra emitted from the central part of the laser focal spot and from its periphery.

detect the shift of $K\alpha$ emission. In addition, it allows estimating the continuum due to bremsstrahlung emission which may also partially superimpose to the $K\alpha$ signal (iii) Bremsstrahlung cannon, allowing measuring the hardest x-rays generated by HE propagation inside the target.

An example of the Ti K-shell spectra emitted from the non-coated 5 μm -thick Ti foil irradiated by the 1ω -beam, is presented in figure 2. The spectra emitted from the central part of the laser focal spot and from its periphery are governed, respectively, by the inner-shell $K\alpha$ emission (singly ionized up to B-like Ti), and by line transitions in highly ionized atoms (Be- up to He-like w and y lines).

Detailed interpretation of these spectral features depends on two factors, namely hot electron (HE) production as a driving force, and the heated, variable-temperature target material as a diagnostic medium. Modelling of relevant spectra was performed using the collisional-radiative atomic code FLYCHK [33]. The synthesized spectra proved that the occurrence of singly-ionized Ti $K\alpha_{1,2}$ to B-like transitions in the photon energy range up to approximately 4650 eV is due to HE interaction with Ti at bulk temperature $T \leq 200$ eV. At higher bulk temperatures, the K-shell emissivity is instead governed by thermal emission and the effect of HEs is of secondary importance. Consequently, when studying HE generation, only the photon fluxes recorded in the spectral range of 4450–4650 eV were taken into account, corresponding to the range between $K\alpha$ and B-like Ti emission (see figure 2). The number of these photons was then related to HE population via Monte-Carlo simulations. We used GEANT4 combined to the PENELOPE physics library [34, 35] to simulate HE propagation and K-shell emission inside the studied targets. Note that K-shell ionization cross sections are provided by PENELOPE, which is known to reproduce experimental data rather well [23]. The use of a Monte-Carlo code assumes that HEs propagate through cold materials. Moreover, only collisional effects are treated in GEANT4, which means that collective effects such as self-consistent magnetic and electrostatic fields are fully ignored. Indeed, such a Monte-Carlo

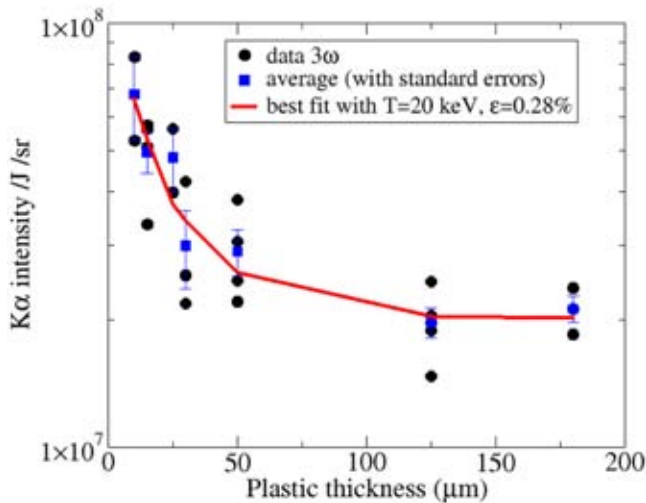


Figure 3. Ti $K\alpha$ emission versus thickness of plastic overlayer. 3ω irradiation, intensity of $3 \times 10^{15} \text{ W cm}^{-2}$.

Table 1. HE characteristics at 3ω and 1ω irradiation deduced from the χ^2 minimization procedure. We assumed an exponential distribution for the HE energy, described as $\exp(-E/T_{\text{hot}})$. Here ϵ is the laser-to-electrons conversion efficiency.

	$3\omega, E_{\text{laser}} = 200 \text{ J}$ $I = 3 \times 10^{15} \text{ W cm}^{-2}$	$1\omega, E_{\text{laser}} = 650 \text{ J}$ $I = 10^{16} \text{ W cm}^{-2}$
T_{hot} (keV)	20_{-8}^{+15}	38_{-12}^{+57}
ϵ (%)	$0.28_{-0.06}^{+0.28}$	$5.32_{-0.26}^{+6.90}$

approach does not intend to fully model the experiment, but it is used as a benchmark for interpreting data. The resulting photon fluxes detected in dependence on the plastic coating thickness is given in figure 3.

Figure 3 shows the $K\alpha$ intensity versus target thickness, at 3ω and laser intensity of about $3 \times 10^{15} \text{ W cm}^{-2}$. The black scattered points represent the measured fluxes while the blue squares are the average values at each thickness. The associated error bars are defined as $\text{SE} = \text{SD}/\sqrt{n}$, where SD is the standard deviation of the sample and n is the number of data points. The red line in figure 3 is the result of the Monte–Carlo simulation using an HE exponential energy distribution [$\approx \exp(-E/T_{\text{hot}})$], with temperature $T_{\text{hot}} \approx 20 \text{ keV}$, which was the one that better approximates the experimental data.

The results obtained following this procedure are reported in table 1, at both 1ω and 3ω .

The data in table 1 imply that the HE temperature is in both cases in agreement with theoretical estimates for the HE generation from SRS, obtained by considering the phase velocity $v_{\text{ph}} = \omega_e/k_e$ of the driven plasma waves in the density regions obtained by experimental spectra [28]. Also, the conversion efficiency is much larger at 1ω , as expected, due to the much larger impact of parametric instabilities. Figure 3 also shows the presence of some $K\alpha$ emission even from targets with plastic layer thickness of 125 and 180 μm . This implies a non-negligible number of electrons with energy higher than

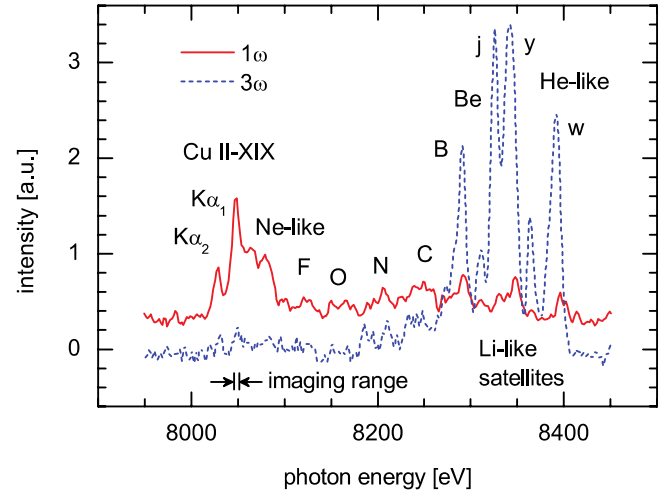


Figure 4. X-ray spectra emitted from Cu targets (no coating) subject to 1ω and 3ω laser radiation.

100 keV, since only electrons with such an energy can cross 125 μm of plastic. This $K\alpha$ contribution could be due to HE produced by TPD or other mechanisms.

Figure 4 shows Cu spectra obtained from bare Cu targets. These clearly demonstrate the effect of the wavelength dependence of laser plasma coupling: at 1ω the typical density of the interaction region (\approx critical density) is lower and the target temperature is higher (both due to the higher intensity and to the lower density). This results in an increased emission of inner shell electronic transitions in less ionized atoms ($K\alpha$ transitions in single-ionized Cu II overlapped by Cu III up to Cu XIX emission). At 3ω , instead, Cu K-shell emission is governed by the resonance line transitions in highly ionized atoms and their satellites (the so-called quasi-optical transitions). Complementary spectral structure observed between $K\alpha$ and He α lines belongs to emission from Li-like to Ne-like copper ions.

In addition to high-resolution x-ray spectroscopic investigation, the bremsstrahlung cannon also allowed inferring the high-energy photon distribution and hence indirectly estimate the HE energy distribution. Typical results from this diagnostic are shown in figure 5.

Raw cannon data were analysed by using Monte Carlo simulations. Best results were systematically obtained using a single exponential photon energy distribution, $\exp(-E/T_\gamma)$, and are given in table 2 (notice: the value in the figure, 18 keV, differs from that in the table, 20 keV, because this last one is the average over different shots)

The inferred Bremsstrahlung spectra give direct information on the HE distribution, since in first approximation $T_\gamma \approx T_{\text{hot}}$. The data in table 2 confirm, within error bars, the values of HE temperature obtained using $K\alpha$ spectroscopy and $K\alpha$ imaging (table 1). They also confirm that HE conversion efficiency is much larger at 1ω than at 3ω .

The lack of a higher energy component in bremsstrahlung emission could be explained as follows. At high electron energies bremsstrahlung emission is strongly peaked in the

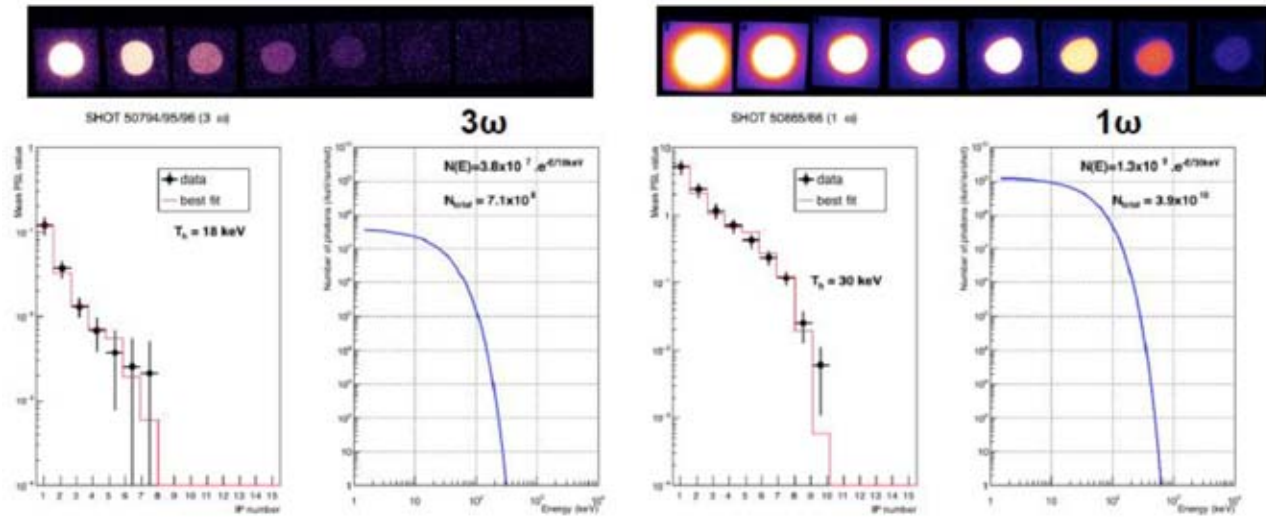


Figure 5. Raw data (each circle corresponds to the signal recorded on a single IP) and related fit and deduced photon spectrum at 3ω (left panel) and 1ω (right panel) irradiation.

Table 2. Bremsstrahlung emission characteristics at 3ω and 1ω irradiation deduced from BSC data. ‘Temperature’ of the photon distribution and number of emitted photons per unit solid angle.

	$3\omega, E_{\text{laser}} = 200 \text{ J}$	$1\omega, E_{\text{laser}} = 650 \text{ J}$
	$I = 3 \times 10^{15} \text{ W cm}^{-2}$	$I = 10^{16} \text{ W cm}^{-2}$
T_γ (keV)	20 ± 6	30 ± 9
N_γ (/sr)	$7 \cdot 10^8 \pm 2 \cdot 10^8$	$4 \cdot 10^{10} \pm 1 \cdot 10^{10}$

direction of motion of the HE beam, and the bremsstrahlung cannon might simply be outside the lobe of emission of the highest energy electrons.

4. Parametric instabilities

In 3ω shots, back-reflectivity was dominated by SBS and laser reflection, accounting for 3%–15% of laser energy [28, 29]. Poor spectral resolution, however, did not allow separating SBS contribution from laser reflection. The energy backscattered by SRS was lower than 0.2% and exhibited an increasing trend with the auxiliary-main pulse delay [29]. DUED hydrodynamic simulations [36] showed that the delay between auxiliary and main pulses affected the interaction conditions mainly by modifying the density scalelength of the plasma, increasing from 50 to 100 μm as the pulse delay increased from 0 to 1200 ps, while the plasma temperature remained roughly the same in the regions of interest for instabilities. Considering that larger delays produce longer plasmas, the trend of SRS with the time delay confirmed that SRS gain and threshold were mainly limited by inhomogeneity effects and had a convective character.

Emission spectra showed broad and non-reproducible peaks in the spectral range 630–750 nm (figure 6), implying that SRS was driven at densities 0.10–0.15 n_{cr} , well below the $n_{\text{cr}}/4$ region. By considering the electrons moving with the phase velocity of plasma waves at these densities, HE generated by SRS are expected to have a temperature about

18 keV [37] which is in agreement with the main component measured in the experiment; such an agreement suggested that SRS was the main source of HE in the present experiment. Considering that the low-density limit of the SRS unstable region ($n_e/n_{\text{cr}} \approx 0.1$) corresponds to $k_e \lambda_D \approx 0.27$ for a temperature $T_e = 1.5 \text{ keV}$ (as estimated from the CHIC and DUED hydro-simulations at the time of SRS onset), it is clear that the low-density edge of SRS region was limited by Landau damping.

At slightly higher densities ($n_e/n_{\text{cr}} \approx 0.12$), where SRS emission was maximal, the instability was mostly limited by the length of the resonance region l where the k -matching is satisfied, which determined also the SRS threshold. In the present experiment $l \approx 1.5 \mu\text{m} \approx 3.4 \lambda_0$, as usually calculated by imposing $\int_0^l k dk \approx 1/2$ where $\kappa = k_0 - k_s - k_e$ is the wave-number mismatch of the interacting waves [37], resulting in a SRS threshold $I_{\text{SRS}} = (4.5\text{--}8) \times 10^{15} \text{ W cm}^{-2}$ [38]. It can be calculated that such a threshold almost doubles when other damping factors of EPWs are taken into account, as for example Landau damping and side-loss of electrons from the speckles. It is therefore evident that in all the shots the laser intensity was lower than the SRS threshold. However, the intensity in laser speckles can be much higher than the envelope intensity. Therefore, the statistics of local intensity in speckles should be considered to explain the experimental results. An accurate investigation of these effects is reported in [28], where the experimental results were compared to those calculated by the radiative-hydrodynamic code CHIC. As described in section 5, the code was modified to account for the local intensity in the beam speckles and included self-consistent calculations of non-linear laser plasma interactions, by using suitable scaling laws [39]. The results clearly showed that a correct modelling of the speckle intensity statistics into the beam allows the experimentally observed SRS reflectivity to be explained.

Interesting details on SRS were also retrieved from time resolved measurements (figure 6). Streaked spectra showed

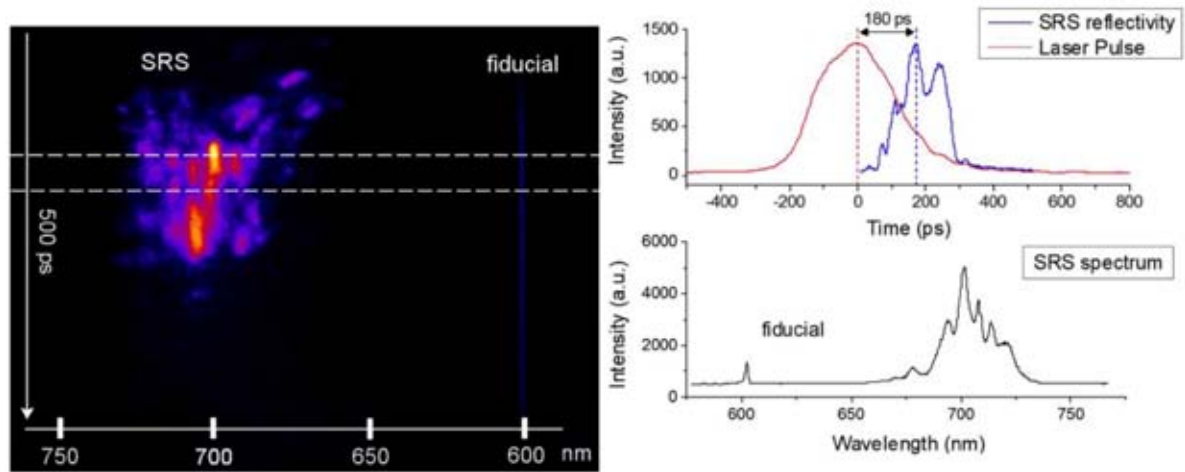


Figure 6. (left) time-resolved SRS spectrum obtained at 3ω laser intensity $I \approx 4.1 \times 10^{15} \text{ W cm}^{-2}$ and no auxiliary pulse. The acquisition time window, spanning the vertical axis, is 500 ps; (centre) temporal profiles of laser pulse and SRS emission; (right) SRS spectrum emitted in the selected time window in the image.

that SRS was driven in the trailing part of the laser pulse, with a time delay of the SRS peak from the laser peak around 200 ps. This can be understood by considering that density scale-length progressively increased during laser irradiation and reached the maximum value at a time of 300–400 ps after the laser peak. Since the convective SRS gain, through the Rosenbluth parameter [40], is proportional to the product of laser intensity and density scalelength, the instability maximized at a certain time after the laser peak. In addition, plasma temperature was expected to fall after the laser peak. Therefore, at the time of SRS onset, both Landau damping and side-loss of electrons from the speckles, due to thermal motion, were significantly reduced.

Streak camera measurements with higher temporal resolution ($\Delta t \approx 8 \text{ ps}$) also revealed a bursty behaviour of SRS, where the duration of the measured emission spikes was limited by time resolution (see figure 8 in [29]). In agreement with numerical PIC simulations, this confirmed the presence of kinetic mechanisms ruling SRS emission, where large electron plasma waves (EPW) were repeatedly driven and successively damped by nonlinear frequency detuning, due to ponderomotive and electron trapping effects.

Both $3/2 \omega_0$ and $\omega_0/2$ harmonics were detected, indicating that a fraction of laser energy reached the $n_{cr}/4$ surface; the splitting of these spectra also suggested the prevalence of TPD over absolute SRS in this density region of the plasma. Due to the linear dependence of TPD threshold on the plasma temperature, it is in fact expected that in the $n_{cr}/4$ region SRS starts to dominate on TPD at temperatures higher ($T_e > 4 \text{ keV}$) than that obtained in our experiment. At the same time, our low temperature ($T_e < 2 \text{ keV}$) results in a Landau damping rate significantly lower than in realistic full-scale shock-ignition plasmas and allows SRS to develop convectively in lower density regions, as experimentally observed. A more careful analysis of the half harmonic spectra revealed that different instabilities were driven in different plasma regions near $n_{cr}/4$: while TPD was convectively driven at low densities $\approx 0.21\text{--}0.22 n_{cr}$ near the Landau cut-off ($k_e \approx 2.3k_0$,

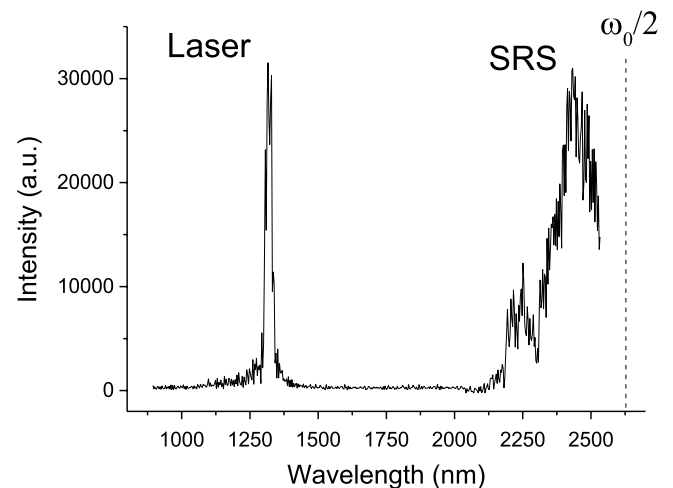


Figure 7. Time-integrated SRS spectrum obtained at 1ω and laser intensity $I \approx 2 \times 10^{16} \text{ W cm}^{-2}$.

$k_e \lambda_D \approx 0.27$ for $T_e = 1.5 \text{ keV}$), hybrid TPD/SRS was present near $n_{cr}/4$ ($n_e \approx 0.24 n_{cr}$, $k_e \approx k_0$). The EPWs driven by the latter process could in principle give rise to very energetic HE ($T_{hot} > 100 \text{ keV}$), which could therefore explain the $K\alpha$ emission measured for plastic thickness of 125 and 180 μm (figure 3). However, their flux is expected to be limited by the small number of thermal electrons that can be trapped at so large EPW phase velocities, unless a staged acceleration of electrons from low-density regions occurred, as suggested by Yan *et al* [41].

Also in 1ω shots, back-reflected energy was dominated by SBS and laser reflection, consisting of 12%–18% of laser energy. Measurements showed that light backscattered in the lens cone by SRS was here higher than in 3ω shots, around 0.5%–5% of laser energy, which can be explained by the higher $I\lambda^2$ factor (~ 18 times than in 3ω shots) and by the larger size of speckles, which reduced the side-loss of electrons. This value however did not include light in the spectral range 2550–2650 nm, which could not be measured by our calorimetric/spectroscopic apparatus. Time-integrated IR

spectra showed that backscattered light covered the spectral range 2200–2550 (which was the upper wavelength limit of the detector) and was peaked around 2400–2450 nm (figure 7). By considering a plasma temperature $T_e \approx 3\text{--}4\text{ keV}$, as given by CHIC hydro-simulations, emission spectra indicated that backward SRS was excited mainly at densities $n_e \approx 0.185 n_{cr}$ and extended down to $\sim 0.12 n_{cr}$. It is worth noting that EPWs excited at $n_e \approx 0.185 n_{cr}$ in a plasma with temperature $\sim 4\text{ keV}$ are expected to generate HE with $T_{hot} \approx 40\text{ keV}$, which is close to the values obtained by $K\alpha$ spectroscopy and Bremsstrahlung x-ray spectra.

Time-integrated spectral measurements in the visible range exhibited integer harmonics up to $4\omega_0$, denoting non-linear laser interaction near critical density, and half-integer harmonics up to $7/2\omega_0$, indicating Thomson scattering of laser light and integer harmonics with EPWs driven by SRS and TPD. The analysis of half-harmonics suggested the presence of SRS down to low densities ($< 0.1 n_{cr}$), which was made possible by the occurrence of side-scattering SRS, maybe in inflationary regime, resulting in a reduction of the Landau damping, as shown by PIC simulations at high laser intensity [42]. However, the amount of side-scattered reflected light could not be quantified.

5. LPI and HE model for advanced hydrodynamic simulations

Modelling nonlinear laser-plasma interaction (LPI) and the laser-plasma-electron coupling on hydrodynamic scales poses severe difficulties related to the accurate description of the laser intensity in plasmas and the consistent description of HE sources from the laser propagation model. These limitations are related to the use of geometrical optics, which implies a ray-tracing description of the wave field and does not allow for robust evaluations of the laser intensity in plasma. We have developed an approach to hydrodynamic modelling that relies on paraxial complex geometrical optics (PCGO) [43] to describe the laser propagation in plasma using randomly distributed Gaussian optical beamlets. It is coupled to a model for the HE source and reduced HE transport model that describes electron propagation and computes energy deposition. The model for HE transport is based on the angular scattering approximation [44], adapted to two-dimensional (2D), transversally Gaussian, multigroup HE beams of arbitrary angular distribution. We consider the simultaneous and concurrent acceleration of HE by resonant absorption (RA), SRS, and TPD. This coupled LPI-HE model has been implemented in the CHIC arbitrary Lagrangian-Eulerian radiative hydrodynamic code [45], and is computed inline, i.e. within hydrodynamic time steps.

The reduced electron transport model is derived from the kinetic Vlasov–Fokker–Planck equation by considering electron-ion and electron–electron collisions. The HE distribution function is decomposed on the basis of spherical harmonics at first order, and the mean scattering angle is expressed as a function of the curvilinear electron beam coordinate. Assuming the HE beam propagates along a straight line, the

energy loss is induced by bound electrons, free electrons, and plasmons. Scattering on background electrons and ions widens the beam as a significant process in ICF conditions. Each HE beam is described by an exponential distribution function in energy that is logarithmically discretized in a series of mono-energetic beamlets. This multigroup model for HE transport in plasmas has been validated with a reference code [46] for various cases in homogeneous and inhomogeneous plasmas. The free parameters defining a given HE source are the initial energy flux, mean temperature, angular distribution, and direction. Those parameters are determined with intensive PIC simulations.

The characterization of HE sources from parametric instabilities is inherently challenging. Theoretical works have demonstrated that the temperature of TPD-HEs is not related to the EPW's phase velocity at the quarter critical density ($n_{cr}/4$), because electrons undergo an acceleration stage. Time-dependent scaling laws for the flux and the temperature as a function of laser intensity were proposed from extensive PIC simulations in the $10^{15}\text{--}10^{16}\text{ W cm}^{-2}$ intensity range with $\lambda = 351\text{ nm}$ and in plasmas of electron temperature $\approx 2\text{ keV}$. The steady-state values of these scaling laws are used within CHIC to define HE sources from TPD. The EPWs excited by TPD have privileged directions at $\pm 45^\circ$ with respect to the pump. Shared pump wave processes and plasma density modulations have been shown to be significant in ICF regimes and spread the optimal angle of forward HE emission in various directions in that cone. We assume that the multiplicity of configurations for the pump and daughter waves produces a uniform HE emission in the -45° to $+45^\circ$ cone with respect to the PCGO ray direction. This spread is obtained by superimposing electron beamlets at various angles. HEs from TPD are emitted at $n_{cr}/4$, both forward and backward.

Contrary to the TPD process, the energy of SRS-induced HE is correlated with the phase velocity of the EPW at its resonance point and not with the laser intensity driving SRS (I_{SRS}). Conversely, the number of HEs scales with I_{SRS} . The asymptotic HE flux is set to 12.5% of the pump intensity (I_{SRS}), which is the maximum number of forward HEs that SRS can drive in a steady state. The shape of the flux function is chosen to be similar to that of TPD, and rearranged to correspond to experimental estimates. The relative pump intensity is defined with respect to the absolute instability threshold in inhomogeneous plasma and at $n_{cr}/4$. In order to account for the Raman gap observed in experiments, we assume that SRS takes place at plasma densities lower than $n_{cr}/4$. Experiments have shown that SRS-driven HEs are directional with respect to the laser drive. Consequently, HE sources from SRS are initialized in the direction of the pump wave with no initial angular spread, although a 'global' spread arises due to the different direction of laser Gaussian optical beamlets in the plasma.

6. Shock dynamics

We performed several experiments on shock wave dynamics. In two previous experiments [15–17], we studied shock transit

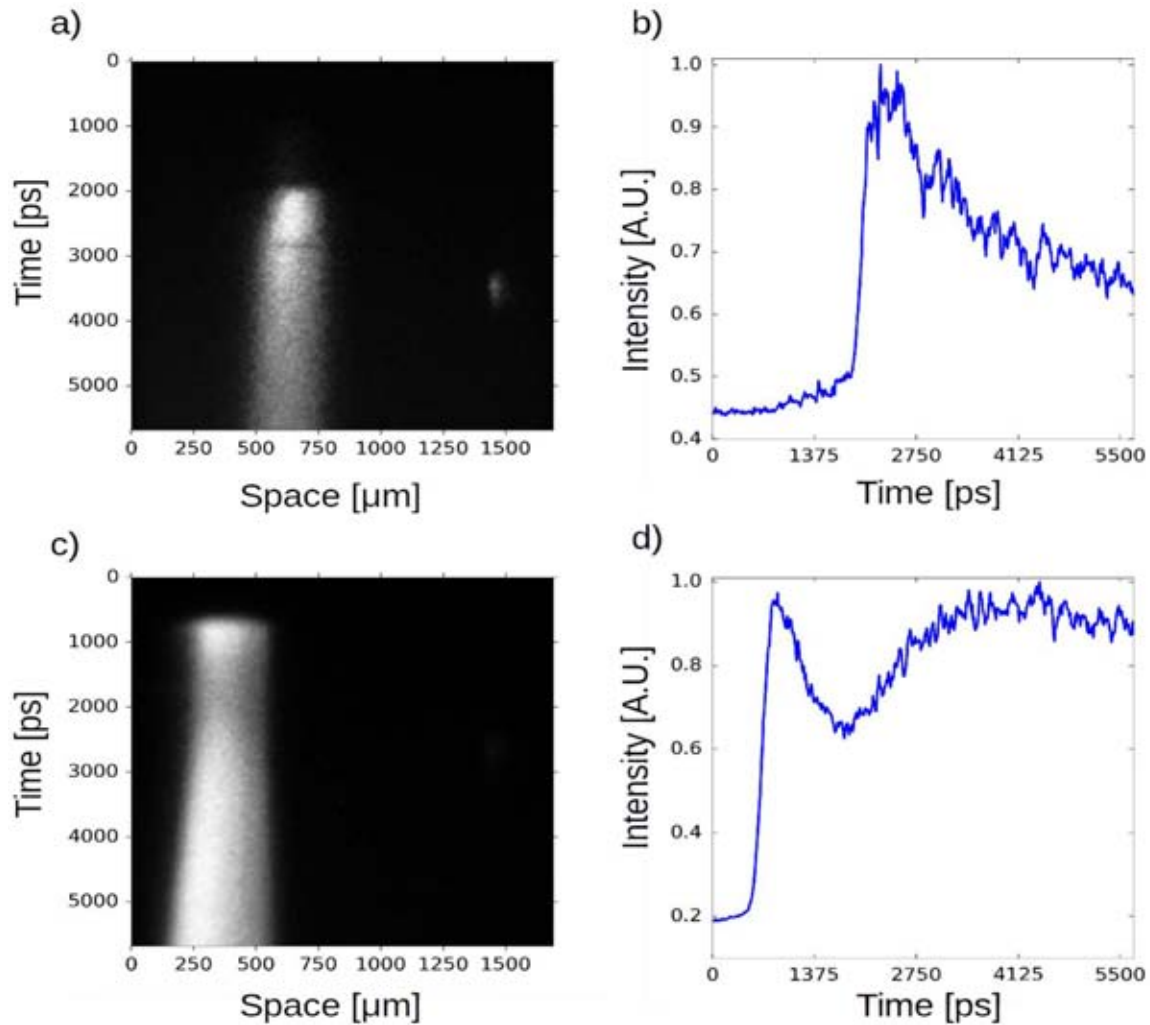


Figure 8. Streak images and intensity versus time lineout: (a) and (b) shot at 3ω and $I = 3 \times 10^{15} \text{ W cm}^{-2}$ and lineout at space coordinate $x = 625 \mu\text{m}$. (c) and (d) 1ω ; $I = 10^{16} \text{ W cm}^{-2}$, $x = 300 \mu\text{m}$ in (d). Thickness of the plastic layer: $50 \mu\text{m}$ in both cases.

time versus laser intensity, at 3ω . Targets with approximately the same thickness ($25 \mu\text{m}$ of plastic and $5\text{--}10 \mu\text{m}$ of higher-Z tracer) were used. Recently, we studied transit time versus target thickness at both 3ω and 1ω . We kept laser energy (and then intensity) fixed: about 110 J in the nominal spot at 3ω and 300 J at 1ω . Figure 8 shows streaked images of two shots at 3ω and 1ω . Both shots were performed using $50 \mu\text{m}$ plastic thickness. For the 3ω case we observe a very low preheating signal before shock breakout. Moreover, the shock breakout ramp is steep, which suggests that the preheating did not dramatically affect the Ti layer. In the shot at 1ω , instead, the preheating signal is comparable with the shock breakout signal. In addition, the rise of the shock breakout signal is significantly affected by preheating.

Experiments showed the expected trends for shock breakout times (and hence shock velocity and drive pressure) versus both laser intensity and target thickness. However, shock break-out times always turned out to be significantly longer than expected from simple models and pure hydrodynamics simulations, as reported in [15] (see, in particular, figure 5). A summary of data is presented in figure 9, showing shock

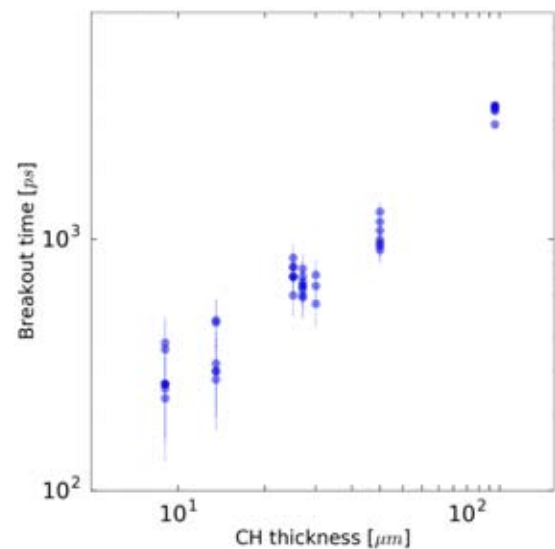


Figure 9. PALS experiment. Laser pulse at 3ω and intensity $I = 3 \times 10^{15} \text{ W cm}^{-2}$. Targets: plastic layer and $10 \mu\text{m}$ Ti layer. The figure shows shock breakout times versus thickness of the plastic layer.

break-out times versus target thickness, for 3ω shots. Detailed analysis and comparison with simulations will be discussed in a forthcoming publication.

In discussing the comparison between experiments, simulations, and simple scaling laws, we proceeded by steps, which allowed revealing the importance of the different processes.

- (i) First we carefully characterized the laser focal spot which was imaged at high (although not full) energy on the streak camera used for shock chronometry operated in focus mode, after inserting appropriate filter on the beam to reduce the laser intensity. This resulted to be approximately Gaussian with a FWHM of $100\ \mu\text{m}$ consistently with the design of the used phase plate. However, we also needed to take into account the real energy deposited on target within the nominal focal spot size. This required dedicated measurements in which the laser beam was focused on pin-holes of different diameters and we measured the energy going through the pinholes. Results showed that the nominal focal spot is superimposed to a larger energy ‘plateau’ and that about only 55% of the laser energy is actually deposited within the spot. This reduction of the effective energy was always taken into account in our evaluation of the laser intensity on targets and in following simulations.
- (ii) Then, we performed 2D simulations with purely hydrodynamic models, i.e. by neglecting any effect due to LPI and HE. We found that the experimental break out times could be approximately recovered by DUED and CHIC simulations with laser intensity reduced by a factor about 2. (Notice that instead hydrosimulations correctly reproduce recent experiments on shock propagation conducted at lower intensities by Batoni *et al* [47] and by Hohenberger *et al* [48]). From the simulations that reproduced the experimental break-out times we could infer a laser-induced peak ablation pressure of about 90 Mbar at intensity of the order of $(0.5\text{--}1) \times 10^{16}\ \text{W cm}^{-2}$. This pressure is much lower than the 200–300 Mbar predicted at these laser intensities from well-known, simple 1D scaling laws relating shock pressure to intensity $[p(\text{Mbar}) = 40 (I/\lambda)^{2/3}]$, with the intensity in units of $10^{15}\ \text{W cm}^{-2}$ and the wavelength in μm ; see equation (47) of [49].
- (iii) We understood that shock pressure during laser interaction is strongly affected by the spot size. In our experiments, the distance between the laser absorption layer and the ablation region ($\approx 60\ \mu\text{m}$) is comparable to spot size. Pressure therefore decreases due to the lateral energy flow in the overcritical region. To evaluating such an effect, we performed simulations with the same intensity but increased focal spot size, approaching a 1D ideal case. This considerably reduced the lateral flow and increased the pressure generated. For instance, for the case previously cited, the maximum pressure increases by a factor of ≈ 2 to ≈ 180 Mbar. The effect and the pressure increase were similar for all investigated laser intensities. Notice that this effect significantly contributes to the discrepancy between 1D scaling laws and inferred

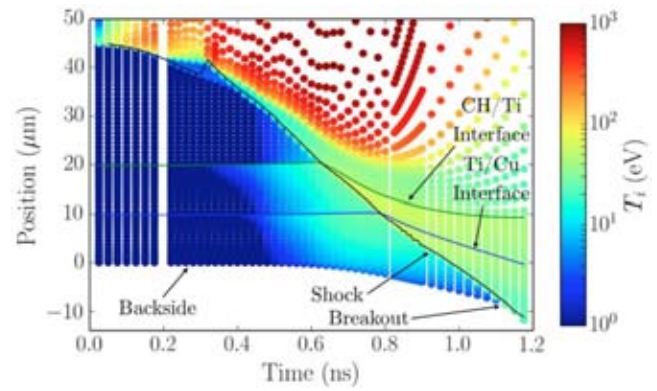


Figure 10. Evolution of ion temperature (eV, Log-scale) inside an irradiated CH/Ti/Cu target as a function of time (ns) and depth in the target (μm), along the laser axis. The solid lines show the locations of the tracer interfaces.

pressure, but cannot explain the discrepancy between 2D hydro simulation and experimental data.

- (iv) Next, we run simulations using the PCGO description including the generation of HE but without considering their effect on hydrodynamics. Here the main difference with normal hydro simulations is that we have a better description of laser absorption. Collisional absorption is modelled more precisely, and RA and effects of parametric instabilities are taken into account. For a typical run at 3ω , 1.3% of the laser energy is resonantly absorbed at the critical surface layer, early in the interaction, thus increasing the shock pressure and velocity. SRS and TPD start slightly later generating HE with temperatures and fluxes (averaged in time and space over the laser profile) of $\approx 40\ \text{keV}$ and $\approx 1\%$ of laser energy, respectively. These values are of the same order of magnitude and not too far from those experimentally measured taking into account experimental error bars (see section 3 ‘HE characterisation’). In the 3ω case the overall effect is a slight reduction of absorbed laser energy and hence a very small decrease of shock pressure and increase of shock breakout time. The integrated reflectivity in the simulation is 28%, in good agreement with the experimental measurements of $25 \pm 10\%$. However, such simulations still predict a shock breakout time much shorter than the experimental timings.
- (v) Finally, we performed simulations using the full multiscale LPI-HE model. In this case, SRS and TPD-generated HE beams gradually preheat the bulk of the target both in front and behind of the shock to a few tens of eV, as illustrated in figure 10. Preheating of the dense cold target raises the plasma pressure at a nearly constant density, thus increasing the shock velocity which scales as $\sqrt{P/\rho}$. However, HE preheating also rises the local sound velocity, thus significantly decreasing target compression during laser drive, i.e. the shock strength. Although the shock strength is lower, the local pressure increase leads to a post-shock pressure that is higher with HEs, up to 40% with respect to simulations without HEs, depending on the targets. Simultaneously to the bulk pre-

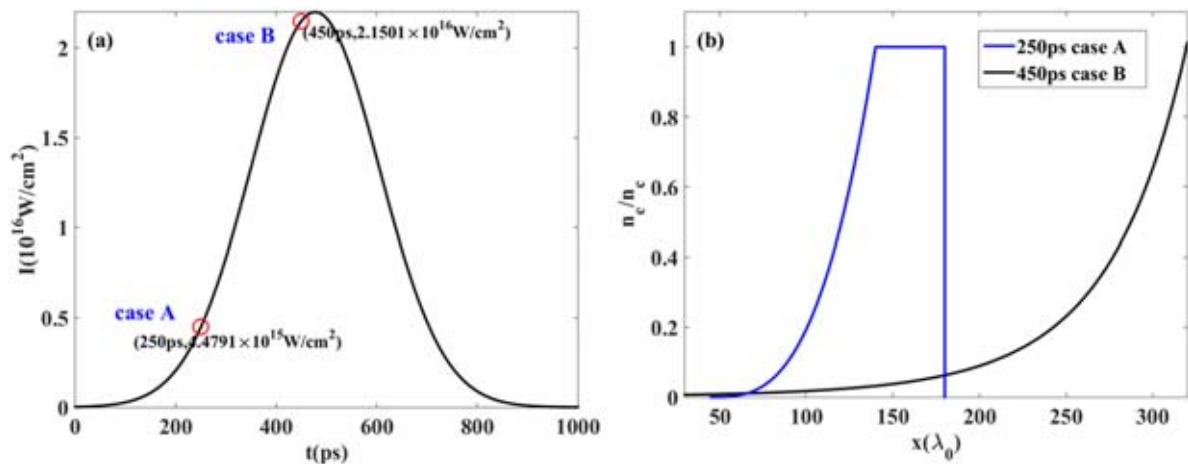


Figure 11. (a) Temporal profile of the laser intensity and the selected simulation case A and B. (b) Initial electron density distributions for the two simulation cases.

heat, LPI-generated HEs that reach the target rear surface heat it to several eV, thus initiating a backside plasma expansion that delays the shock breakout. For instance, in the case shown in figure 10, the shock breaks out at $t = 1.2$ ns, versus $t = 0.9$ ns in a simulation not accounting for preheating. This effect contributes, at least partly, to explaining the discrepancy between experimental and simulated shock breakout times and simulated ones. It also suggests that pressures are underestimated when analysing experiments with pure hydro simulations.

The results obtained at 1ω ($\lambda = 1314$ nm) generally show the same trends. At 1ω , preheating is clearly visible in the streak camera images (see figure 8) as an early signal before shock breakout. However, the laser to HE conversion efficiency is much higher, when compared to experimental results (as those in table 1). This is not a surprise since the scaling laws used to define HE sources from TPD and SRS have mainly been derived from experiments at 3ω . Such overestimation produces a stronger target heating and a bigger expansion before shock breakout as compared to experimental results.

7. PIC simulations for LPI

The radiation hydrodynamic simulations of the PALS experiment, with laser wavelength $\lambda_0 = 1.314$ μm and a plane CH target, have been compared with kinetic simulations for several selected time moments within the laser pulse. The goal of these kinetic simulations is to evaluate how the laser plasma nonlinear microscopic interaction processes, omitted in the hydrodynamic model, are modifying the global plasma characteristics. The kinetic simulations are performed with the relativistic electromagnetic code EPOCH [50] in planar 2D geometry. Absorbing boundary conditions were applied for both electromagnetic fields and particles. Two representative instants are selected, during the laser pulse, as shown in figure 11(a). Case A corresponds to a relatively low intensity of 4×10^{15} W cm^{-2} at time $t = 250$ ps, while case B corresponds to the pulse maximum at time $t = 450$ ps with the

intensity 2×10^{16} W cm^{-2} . As kinetic simulations consider a relatively small plasma volume of 50 laser wavelengths in the transverse direction, the laser pulse is assumed to be a plane wave with 1 ps rise time following a constant intensity corresponding to red circles in figure 11(a). Each simulation is run for about 10 ps until a quasi-stationary state has been reached that can be compared with the corresponding macroscopic data. The initial conditions for the kinetic simulations are obtained from hydrodynamics simulations with the code CHIC (see above), which provides density (figure 11(b)) and temperature distributions of the corona at the corresponding time moments. In the kinetic simulations, only part of the plasma with minimum and maximum densities of 1% and 100% of the critical density was considered. Spatial resolution $\delta x = \lambda_0/50$ and time step $\delta t = 0.08\omega_0^{-1}$ were chosen to resolve the Debye length, where $\omega_0 = 2\pi c/\lambda_0$ is the laser frequency. The simulation box length was $180 \lambda_0$ for case A and $350 \lambda_0$ for case B. Case A corresponds to density scale length of $29 \lambda_0$, electron temperature of 2.7 keV, ion temperature of 155 eV and average ion charge of 3.5. Case B corresponds to density scale length of $47 \lambda_0$, electron temperature 4.3 keV, ion temperature 245 eV and the same ion charge of 3.5.

The simulations converge to a quasi-steady state after 5–10 ps where a comparison with the hydro simulations and experiment can be made. Kinetic simulations show that the energy balance is dominated by SBS backscattering in early interaction, case A. The reflectivity saturates at that time at the level of 40% (figure 12(a)) and the average electron temperature increases from 2.3 to 4 keV. A high SBS reflectivity is explained by a low ion temperature and consequently a very low damping of ion acoustic waves [37, 51–54]. Consequently, SBS saturated on a rather high level. Conversely, SRS is very weak at that time because the secondary Langmuir decay instability (LDI) has a very low threshold and quickly saturates the SRS growth. The maximum SRS reflectivity is about 3% and on average this is about 1%. These values are of the order of magnitude of the measured HE energy fraction. The energy spectra of the electrons are presented in figure 12(b). In the case A, the HE temperature is in the range of 50–70 keV. The analysis of the energy transmitted through the right boundary

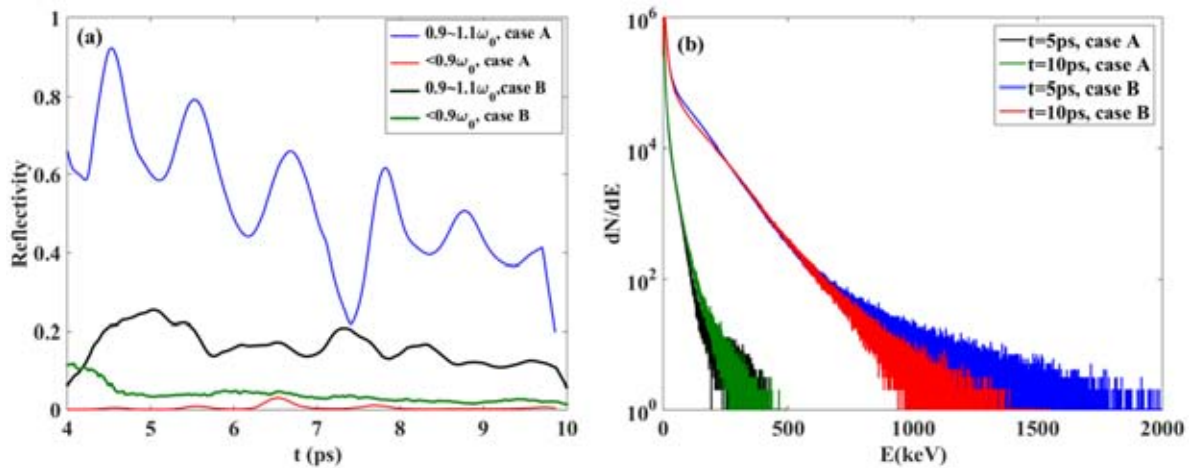


Figure 12. (a) The reflectivity with the different frequency domain to distinguish SRS and SBS. (b) The electron energy spectra for the two cases with different simulation time.

of the simulation box shows that the energy flux is dominated by thermal electrons and contribution of SRS-generated HE with energies above 50 keV is less than 4%.

With the increase of intensity in later interaction stage (case B), the bulk electrons are heated to the temperature of 6.2 keV and SRS attains a level of a few percent (figure 12(a)). Inspection of the plasma wave activity shows that it is localized near the quarter critical density region. However, the backward SBS still dominates reflectivity, which decreases to the level of 15% (figure 12(a)). A part of absorbed energy is transferred to HE generation. In case B, the HE temperature is in the range of 70–130 keV (figure 12(b)). SRS is identified as the major source of electron heating and HE generation. These HE contribute to about 40% to the energy flux transported from the corona to the dense plasma.

The presented results of kinetic simulations significantly contribute to shed light on the laser plasma interaction and are a unique tool to explain the experimental data. In our case, they confirm that SBS dominates light reflectivity; considering the progressive reduction of SBS with time, as suggested by simulations, the back-reflected energy tends to approach the value that was measured in the experiment. PIC data also show that SRS increases with time, reaching reflectivity values around a few percent, and that it is the main driving source of HE. All these features roughly agree with the experiment, even if for the moment they also show a significant discrepancy for what concern the plasma temperature, which in the PIC simulations is much higher than from experimental data or hydro simulations.

Finally, the HE conversion efficiencies by SRS and TPD found by the numerical simulations are in good agreement with the predictions of hydrodynamic simulations. This confirms that the nonlinear laser plasma interaction package implemented in the hydrodynamic code provides quite reasonable results. Concerning the HE temperature, a meaningful quantitative comparison between numerical simulations and experimental data is quite difficult, since HE energy distributions significantly change with time while the experiment only provides time-averaged values. However, further comparisons between numerical simulations and experimental data will

allow to improve the code predictive capabilities and to extend its domain of validity.

8. Conclusions

We have reported a wide study of the physical processes occurring in laser plasma interactions under conditions approaching those relevant to SI (but, of course, with lower electron temperature and significantly shorter plasma density gradient scale-lengths). A combination of several high-resolution diagnostics in optical and x-ray domains and advanced numerical simulations with radiation hydrodynamic and particle-in-cell codes allows to predict the plasma characteristics and identify the nonlinear processes of HE generation and transport. Generally we found a good agreement between the results obtained by advanced hydrodynamics simulations with experimental results in the UV domain of laser wavelengths ($\lambda \sim 0.35-0.45 \mu\text{m}$). For the case of 1ω irradiation, our experimental results thus provide indications on improving the performance of existent numerical tools in the IR domain. PIC simulations confirm several experimental results like the fact that SBS dominates light reflectivity, that SRS increases with time, reaching reflectivity values around a few percent, and that it is the main driving source of HE. Future works and comparisons between numerical simulations and experimental data will allow to improve the predictive capabilities of both PIC and advanced hydrocodes.

Future studies should be dedicated to reaching a better control of parametric processes and mitigation of the undesirable effects from HE, while maintaining their capacity of increasing shock strength.

Acknowledgment

This work has been carried out within the framework of the EUROfusion Enabling Research Project: AWP17-ENR-IFE-CEA-01 «Preparation and Realization of European Shock Ignition Experiments» and has received funding from the Euratom research and training programme 2014–2018

under grant agreement No 633053. The views and opinions expressed herein do not necessarily reflect those of the European Commission.

The work was also supported by the European Union under the Laserlab program, by the Competitiveness Program of NRNU MEPhI, Russia, and by the Czech Ministry of Education, Youth and Sports, projects LD14089, LM2015083 and LM2010014. The authors also acknowledge targeted support of Large Infrastructures, ELI Beamlines Project LQ1606 of the National Programme of Sustainability II and ELI Tools for Advanced Simulation (ELITAS) (CZ.02.1.01/0.0/0.0/16 013/0001793) from European Regional Development Fund. Finally, the authors are grateful the PALS staff for help in running the experiments.

ORCID iDs

S. Gus'kov  <https://orcid.org/0000-0003-3523-546X>

O. Renner  <https://orcid.org/0000-0003-4942-2637>

J. Limpouch  <https://orcid.org/0000-0001-9234-7172>

S. Weber  <https://orcid.org/0000-0003-3154-9306>

References

- [1] Betti R., Zhou C.D., Anderson K.S., Perkins L.J., Theobald W. and Solodov A.A. 2007 Shock ignition of thermonuclear fuel with high areal density *Phys. Rev. Lett.* **98** 155001
- [2] Perkins L.J., Betti R., LaFortune K.N. and Williams W.H. 2009 Shock ignition: a new approach to high gain inertial confinement fusion on the national ignition facility *Phys. Rev. Lett.* **103** 045004
- [3] Batani D. et al 2014 Physics issues for shock ignition *Nucl. Fusion* **54** 054009
- [4] Atzeni S., Ribeyre X., Schurtz G., Schmitt A.J., Canaud B., Betti R. and Perkins L.J. 2014 Shock ignition of thermonuclear fuel: principles and modelling *Nucl. Fusion* **54** 054008
- [5] Shcherbakov V.A. 1983 *Sov. J. Plasma Phys.* **9** 240
- [6] Lindl J., Landen O., Edwards J., Moses E. and NIC Team 2014 Review of the national ignition campaign 2009–2012 *Phys. Plasmas* **21** 020501
- [7] Piriz A.R., Rodriguez Prieto G., Tahir N.A., Zhang Y., Liu S.D. and Zhao Y.T. 2012 Ablation driven by hot electrons generated during the ignitor laser pulse in shock ignition *Phys. Plasmas* **19** 122705
- [8] Betti R. et al 2008 *J. Phys. Conf. Ser.* **112** 022024
- [9] Bell A.R. and Tzoufras M. 2011 *Plasma Phys. Control. Fusion* **53** 045010
- [10] Gus'kov S., Ribeyre X., Touati M., Feugeas J.-L., Nicolai Ph. and Tikhonchuk V. 2012 Ablation pressure driven by an energetic electron beam in a dense plasma *Phys. Rev. Lett.* **109** 255004
- [11] Nicolai Ph., Feugeas J.-L., Nguyen-bui T., Tikhonchuk V., Antonelli L., Batani D. and Maheut Y. 2015 Effect of nonthermal electrons on the shock formation in a laser driven plasma *Phys. Plasmas* **22** 042705
- [12] Nora R. et al 2015 Gigabar spherical shock generation on the OMEGA laser *Phys. Rev. Lett.* **114** 045001
- [13] Llor Aisa E., Ribeyre X., Duchateau G., Nguyen-Bui T., Tikhonchuk T.V., Colaitis A., Betti R., Bose A. and Theobald W. 2017 The role of hot electrons in the dynamics of laser-driven, strong converging shock *Phys. Plasmas* **24** 112711
- [14] Jungwirth K. et al 2001 The prague asterix laser system *Phys. Plasmas* **8** 2495
- [15] Batani D. et al 2014 Generation of high pressure shocks relevant to the shock-ignition intensity regime *Phys. Plasmas* **21** 032710
- [16] Antonelli L. et al 2011 Laser-plasma coupling in the shock-ignition intensity regime *Acta Technica* **56** T57–69
- [17] Koester P. et al 2013 *Plasma Phys. Control. Fusion* **55** 124045
- [18] Hall T. 1998 Fast electron deposition in laser shock compressed plastic targets *Phys. Rev. Lett.* **81** 1003
- [19] Martinolli E., Koenig M., Amiranoff F., Baton S.D., Gremillet L., Santos J.J., Hall T.A., Rabec-Le-Gloahec M., Rousseaux C. and Batani D. 2004 Fast electron heating of a solid target in ultra high intensity laser pulse interaction *Phys. Rev. E* **70** 055402(R)
- [20] Pisani F. et al 2000 Experimental evidence of electric inhibition in the propagation of fast electrons in solid matter *Phys. Rev. E* **62** R5927
- [21] Morace A. and Batani D. 2010 Spherically bent crystal for x-ray imaging of laser produced plasmas *Nucl. Instrum. Methods Phys. Res. A* **623** 797
- [22] Martinolli E., Koenig M., Boudenne J.M., Perelli-Cippo E., Batani D. and Hall T.A. 2004 Conical crystal spectrograph for high brightness X-ray Kalpha spectroscopy in subpicosecond laser-solid interaction *Rev. Sci. Instrum.* **75** 2024
- [23] Renner O., Šmíd M., Batani D. and Antonelli L. 2016 Suprathermal electron production in laser-irradiated Cu targets characterized by combined methods of x-ray imaging and spectroscopy *Plasma Phys. Control. Fusion* **58** 075007
- [24] Podorov S.G. et al 2001 *J. Phys. D: Appl. Phys.* **34** 2363
- [25] Rhee Y.J. et al 2016 Spectral tomographic analysis of Bremsstrahlung x-rays generated in a laser-produced plasma *Laser Part. Beams* **34** 645–54
- [26] Chen C.D. et al 2008 *Rev. Sci. Instrum.* **79** 10E305
- [27] Boutoux G. et al 2016 Validation of modelled imaging plates sensitivity to 1–100 keV x-rays and spatial resolution characterisation for diagnostics for the ‘PETawatt aquitaine laser’ *Rev. Sci. Instrum.* **87** 043108
- [28] Cristoforetti G. et al 2017 Experimental observation of parametric instabilities at laser intensities relevant for Shock ignition *Europhys. Lett.* **117** 35001
- [29] Cristoforetti G. et al 2018 Stimulated Raman Scattering and Two Plasmon Decay instabilities in laser-plasma interaction regime relevant to shock ignition *Phys. Plasmas* **25** 012702
- [30] Koenig M., Faral B., Boudenne J.M., Batani D., Bossi S. and Benuzzi A. 1994 Use of optical smoothing techniques for shock wave generation in laser produced plasmas *Phys. Rev. E* **50** R3314
- [31] Koenig M., Faral B., Boudenne J.M., Batani D., Bossi S., Benuzzi A., Remond C., Perrine J., Temporal M. and Atzeni S. 1995 Relative consistency of Equation of State by laser driven shock waves *Phys. Rev. Lett.* **74** 2260
- [32] Batani D., Löwer Th., Hall T., Benuzzi A. and Koenig M. 2003 Production of high quality shocks for equation of state experiments *Eur. Phys. J. D* **23** 99
- [33] Chung H.K. et al 2005 *High Energy Density Phys.* **1** 3
- [34] Agostinelli S. et al 2003 Geant4—a simulation toolkit *Nucl. Instrum. Methods Phys. A* **506** 250
- [35] Salvat F., Fernandez-Varea J.M., Acosta E. and Sempau J. 2001 PENELOPE, A Code System for Monte Carlo Simulation of Electron and Photon Transport *Proc. Workshop/Training Course, OECD/NEA (5–7 November 2001)* NEA/NSC/DOC(2001)19

- [36] Atzeni S. *et al* 2005 Fluid and kinetic simulations of inertial confinement fusion plasmas *Comput. Phys. Commun.* **169** 153
- [37] Estabrook K. and Kruer W.L. 1983 *Phys. Fluids* **26** 1892
- [38] Liu C.S., Rosenbluth M.N. and White R.B. 1974 *Phys. Fluids* **17** 1211
- [39] Colaitis A., Duchateau G., Ribeyre X., Maheut Y., Boutoux G., Antonelli L., Nicolai Ph., Batani D. and Tikhonchuk V. 2015 *Phys. Rev. E* **92** 41101
- [40] Rosenbluth M.N. 1972 *Phys. Rev. Lett.* **29** 565
- [41] Yan R., Ren C., Li J., Maximov A.V., Mori W.B., Sheng Z.-M. and Tsung F.S. 2012 *Phys. Rev. Lett.* **108** 175002
- [42] Riconda C., Weber S., Tikhonchuk V. and Heron A. 2011 *Phys. Plasmas* **18** 092701
- [43] Colaitis A. *et al* 2014 *Phys. Rev. E* **89** 033101
- [44] Li C.K. and Petrasso R.D. 2004 *Phys. Rev. E* **70** 067401
- [45] Breil J. *et al* 2011 *Comput. Fluids* **46** 161
- [46] Touati M. *et al* 2014 *New J. Phys.* **16** 073014
- [47] Baton S.D. *et al* 2012 *Phys. Rev. Lett.* **108** 195002
- [48] Hohenberger M. 2014 *Phys. Plasmas* **21** 022702
- [49] Lindl J.D. 1995 Development of the indirect-drive approach to inertial confinement fusion and the target physics basis for ignition and gain *Phys. Plasmas* **2** 3933
- [50] Arber T.D. *et al* 2015 *Plasma Phys. Control. Fusion* **57** 113001
- [51] Klimo O. *et al* 2014 *Plasma Phys. Control. Fusion* **56** 055010
- [52] Weber S. *et al* 2012 *Phys. Rev. E* **85** 016403
- [53] Riconda C. and Weber S. 2016 *High Power Laser Sci. Eng.* **4** e23
- [54] Weber S. and Riconda C. 2015 *High Power Laser Sci. Eng.* **3** e6

SCIENTIFIC REPORTS

OPEN

Numerical simulation of novel concept 4D cardiac microtomography for small rodents based on all-optical Thomson scattering X-ray sources

Daniele Panetta¹, Luca Labate^{2,3}, Lucia Billeci¹, Nicole Di Lascio¹, Giuseppina Esposito⁴, Francesco Faita¹, Giovanni Mettivier⁴, Daniele Palla², Luciano Pandola⁵, Pietro Pisciotta^{5,6}, Giorgio Russo^{5,6}, Antonio Sarno⁴, Paolo Tomassini², Piero A. Salvadori¹, Leonida A. Gizzi^{2,3} & Paolo Russo⁴

Accurate dynamic three-dimensional (4D) imaging of the heart of small rodents is required for the preclinical study of cardiac biomechanics and their modification under pathological conditions, but technological challenges are met in laboratory practice due to the very small size and high pulse rate of the heart of mice and rats as compared to humans. In 4D X-ray microtomography (4D μ CT), the achievable spatio-temporal resolution is hampered by limitations in conventional X-ray sources and detectors. Here, we propose a proof-of-principle 4D μ CT platform, exploiting the unique spatial and temporal features of novel concept, all-optical X-ray sources based on Thomson scattering (TS). The main spatial and spectral properties of the photon source are investigated using a TS simulation code. The entire data acquisition workflow has been also simulated, using a novel 4D numerical phantom of a mouse chest with realistic intra- and inter-cycle motion. The image quality of a typical single 3D time frame has been studied using Monte Carlo simulations, taking into account the effects of the typical structure of the TS X-ray beam. Finally, we discuss the perspectives and shortcomings of the proposed platform.

Small rodents, like rats and mice, are the most useful and validated animal models for the study of cardiovascular diseases (CVD), and especially of myocardial ischemia (MI) and heart failure (HF)^{1,2}. Surgical models of acute myocardial infarction (MI) and postischemic HF in rats are well validated and commonly employed^{3,4}. Imaging technologies are of key importance for quantitative simultaneous evaluation of regional and global changes in myocardial contractility and perfusion; for this reason, great efforts have been made in the last two decades to implement scanners for the study of small laboratory animals, able to meet the high spatial and temporal resolution required by this type of animal model^{5–7}. Limitations of current preclinical imaging scanners in terms of spatio-temporal resolution pose constraints on the accurate quantification of regional myocardial function/perfusion in small animal models of MI and HF. Due to the complex and fast three-dimensional motion of the heart, the identification of early regional dysfunction based on 3D strain and strain rate analysis would require real volumetric imaging at sub-millimeter spatial resolution and time-resolved imaging with more than 20–50 time frames per cardiac cycle⁸. High temporal resolution modalities such as micro magnetic resonance (micro-MRI) or micro-ultrasonography (micro-US) only allow multi-slice, non-isotropic (stacked 2D) imaging. On the other hand, micro-computed tomography (micro-CT) and micro-single photon emission tomography (micro-SPECT) with double ECG/respiratory gating do allow isotropic

¹Consiglio Nazionale delle Ricerche, Istituto di Fisiologia Clinica, 56124, Pisa, Italy. ²Consiglio Nazionale delle Ricerche, Istituto Nazionale di Ottica, 56124, Pisa, Italy. ³INFN, Sezione di Pisa, 56127, Pisa, Italy. ⁴Università di Napoli Federico II, Dipartimento di Fisica "Ettore Pancini", 80126, Napoli, Italy. ⁵INFN, Laboratori Nazionali del Sud, 95123, Catania, Italy. ⁶Consiglio Nazionale delle Ricerche, Istituto di Bioimmagini e Fisiologia Molecolare, 90015, Cefalù, Italy. Daniele Panetta and Luca Labate contributed equally. Correspondence and requests for materials should be addressed to D.P. (email: daniele.panetta@ifc.cnr.it) or L.L. (email: luca.labate@ino.cnr.it)

X-ray source	Spot size	Pulse duration	Allows in-line phase contrast	Prosp. gating	Retros. gating	Notes	refs
Minifocus tubes	30–200 μm	Continuous			•	Temporal resolution limited by the max. frame rate of X-ray detectors	47,66
Medical tubes	300–800 μm	>5 ms		•	•	Only with low magnification/ Sub-optimal spectral quality for small animal imaging	48,67
Carbon nanotube field emission X-ray tubes	>100 μm	>100 μs		•	•		68
Synchrotron hard X-ray beamlines (3rd generation)	Parallel beam	10–100 ps	•		•	4D CT <i>in-vivo</i> studies so far only applied to lung imaging/ few facilities	69,70
RF-based Thomson scattering	>40 μm	10–20 ps	•		•	No cardiac 4D imaging studies reported so far	13
All-optical Thomson scattering (this work)	<10 μm	<100 fs	•		•		—

Table 1. Main parameters of X-ray sources suitable for application in 4D μCT of the mouse heart.

fully 3D imaging, even though cine-mode dynamic reconstructions are limited to 10 time frames per cardiac cycle or less^{9,10}. In particular, dynamic micro-CT (4D μCT) appears promising for morphofunctional imaging of the cardiac biomechanics, due to its high spatial resolution and good discrimination of myocardial walls, ventricular cavities and lung tissue upon use of suitable blood-pool contrast agents. Several 4D μCT scanner designs have been validated by different investigators in the last decade, using either retrospective or prospective ECG gating. A full review of the existing systems and methods for 4D cardiac μCT imaging is beyond the scope of this paper; for a list of the most relevant works, see the papers cited in Table 1 and references therein.

Over the past few years, a novel kind of X-ray source, based upon the Thomson scattering (TS) of optical photons off relativistic electron bunches, has been intensively studied and developed worldwide^{11,12}. For instance, a TS X-ray source based on conventional RF LINAC and miniaturized electron storage ring has been recently commercialized by Lyncean Technologies Inc. and used for dynamic phase contrast imaging of the lung of living mice¹³. From a practical point of view, the striking feature of a TS X-ray source lies in the possibility to produce radiation in the hard X-ray region using electrons with a much lower energy, usually in the range of a few tens up to a few hundreds of MeV, than that required in synchrotron or free-electron lasers (FEL) machines, due to the much favourable scaling of the emitted photon energy with the electron γ factor¹¹. This, in turn, results in much smaller footprint and more affordable costs. The peak brightness of TS sources can exceed $10^{20}\text{ph}/(\text{s mm}^2 \text{mrad}^2 0.1\% \text{BW})$ ^{14,15}, only a couple of orders of magnitude smaller than that of 3rd generation light sources currently in operation (see for instance¹⁶). A TS source delivering photon beams in the hard X-ray region typically features an RF LINAC, accelerating electrons up to a few hundreds of MeV, and a pulsed laser system, providing optical photon beams with energy up to $\lesssim 1$ J/pulse and duration $\lesssim 1$ ps (the “scattering beam”). The typical footprint of such machines is of the order of a few tens up to ~ 100 meters, which is typical of medium scale research infrastructures. On the other hand, laser-driven electron accelerators has been witnessing an impressive development over the past decade, making it an ideal candidate for replacing RF LINACs for applications in medicine and biology^{17–19}, due to the reduced footprint and costs and the higher electron energy achievable using small scale devices. This kind of accelerator is based on the so-called Laser WakeField Acceleration (LWFA) process in a plasma (see^{20,21} for recent reviews); due to the very high field gradient which can be established in the accelerating plasma wave (up to 3 orders of magnitude higher than in a typical RF LINAC), electron bunches with energy up to the few GeVs level can be accelerated over a few up to a few tens of millimeters distances²², which is why LWFA sources have been dubbed “table-top” accelerators.

Based on this electron acceleration process, secondary X/ γ -ray emission have been studied and successfully demonstrated²³ over the past few years; several pilot application experiments have also been reported recently²⁴, exploiting either the so-called betatron oscillation of the electrons into the accelerating plasma wave^{25,26} or the Thomson scattering mechanism^{27,28}. Both these kinds of novel concept sources allow an extremely small spot size (down to $\lesssim 1$ μm) and an ultrashort pulse duration (down to the femtosecond range) to be achieved at the same time^{11,29}. Static (3D) microtomographic applications have been demonstrated using betatron radiation from laser-driven electron accelerators^{26,30}, even though the mean photon energy around 10–30 keV appears lower than optimal when working with living mice or rats, especially when using iodine-based contrast agents. While betatron sources can only deliver broadband photon spectra, Thomson scattering sources have the potential to produce narrow band X-ray beams, depending ultimately on the energy spread of the primary electron bunch. Since LWFA acceleration of electrons with low energy spread has already been demonstrated, all-optical TS sources offer a very promising route to get monochromatic radiation in the diagnostic energy range using table-top devices. Such “all-optical” X-ray sources are recognized as the most promising compact alternative to 3rd and 4th generation X-ray sources, providing ultrashort pulses and high peak brightness while keeping reasonable size and costs. The potential of these sources as a future replacement of current vacuum-tube technology in diagnostic and therapeutic regime is currently being investigated^{18,19}.

In this paper, we investigate the use of an all-optical TS source for X-ray 4D μCT . Our analysis will make it clear that such a kind of source meets all the requirements for such an application, namely: (a) the possibility to image out a sample of $\sim 2 \times 5 \text{ cm}^2$ typical size, with a voxel size down to ~ 100 μm ; (b) the possibility of getting a

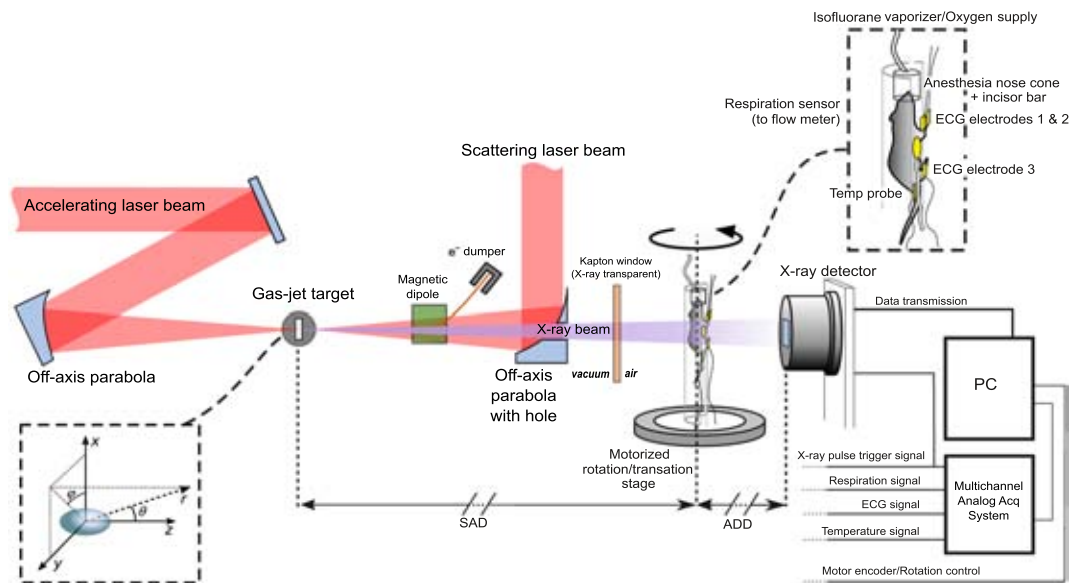


Figure 1. Conceptual scheme of the laser-based 4D μ CT scanner prototype for cardiac imaging of small rodents.

radiography with a single X-ray pulse (i.e., laser shot), which translates into a number of photons $\sim 10^3/\text{px}$, on a typical detector with $\sim 100\text{--}200\ \mu\text{m}$ pixel size; (c) an X-ray pulse duration $\lesssim 100\ \mu\text{s}$ (this point will be better deepened later); (d) an energy spectrum suitable to small animal imaging using iodine-based contrast agents (i.e., with a major part of the emission at $\gtrsim 33\ \text{keV}$ energy, corresponding to the iodine K -edge); a repetition rate $\gtrsim 10\ \text{Hz}$, so as to keep the overall μCT duration limited to few tens of minutes. As it will be shown later, a laser-driven TS source also features a high spatial coherence, due to its source size being in the order of few micrometers, which makes it very attractive for phase contrast imaging. In order to demonstrate all these features, we rely on start-to-end simulations to get insights of issues such as pulse duration, photon statistics and energy spectrum using a realistic kinetic behaviour of cardiac wall implemented in a numerical 4D mouse chest phantom, as well as radiation dose and total duration of the experiment involving the living animal. First, a general overview of the envisioned TS 4D μCT device will be given, including the results of a simulation of the spectral and spatial features of an all-optical X-ray source. Afterwards, the simulation results of a full retrospectively gated acquisition following the foreseen data acquisition scheme is presented. An account is also made of the expected final image quality and of the dosimetric issues, as resulting from Monte Carlo simulations using the actual photon distribution of a TS source. The main pro's and con's of our approach are then discussed.

Design of the Laser-Based 4D μCT Scanner Prototype

Prototype layout. A conceptual layout of the proposed 4D μCT scanner based on an all-optical TS source is shown in Fig. 1. Due to the inability (at least using simple setups) to put the TS source on a rotating gantry, the animal is placed on a cradle rotating around a vertical axis. The animal support is equipped with a physiological monitoring system (ECG, respiration, temperature), and a nose cone for gas anesthesia. The source-to-axis distance (SAD) and axis-to-detector distance (ADD) are kept flexible in our design; however, a sufficiently long ADD would enable the interesting spatial coherence properties of a TS source to be exploited for phase contrast imaging, although this issue will not be discussed here. All the physiological signals are acquired in a common time reference along with the laser pulse trigger and the image sequence grabbed by the X-ray detector. A/D sampling rate $> 2\ \text{kHz}$ will be used for physiological signals, in order to ensure off-line identification of the R peaks of the ECG with sub-ms temporal precision (see Supplementary Materials). A conceptual sketch of the laser-driven X-ray source based on Thomson scattering is shown on the left side of Fig. 1. In detail, an ultrashort laser pulse (the “driving” pulse) is focused onto a gas-jet target, under vacuum, at a relativistic intensity²⁸. The LWFA accelerated electron beam is set to collide with a second (“scattering”) laser beam just after having been accelerated (typically, for a well matched LWFA stage, at the exit of the gas-jet target). We defer until the next subsection a deeper presentation of the physical parameters of this source. We just observe here that, although requiring a complex setup (in order, for instance, to spatially and temporally overlap the accelerated electron bunch and the scattering laser pulse), the experimental apparatus envisioned here has been already demonstrated to be accessible, even on a routine basis, in a small scale laboratory (see for instance³¹ and refs therein).

The temporal rebinning scheme for tomographic acquisitions is fully described in the Supplementary Materials. Due to the extremely short duration of each pulse ($\sim 10^{13}$ times shorter than typical R-R interval in small animals), the likelihood that two different pulses will overlap in the same time bin of the cardiac cycle is negligible; hence, the maximum number of non-overlapping time bins will only depend on the total number of pulses acquired (i.e., constrained by the total absorbed dose and the total duration of the experiment). We believe that this extremely short pulse duration will open new possibilities in the field of cardiac imaging of small rodents,

Thomson scattering X-ray source parameters		Imaging simulation parameters	
Electron bunch		SAD	1000 mm
Size	2 μm \times 2 μm (tr), 3 μm (long)	ADD	1500 mm
Divergence	10 mrad	Magnification	2.5
Bunch charge	100 pC	Detector size (transverse \times axial)	50 \times 25 mm ²
Mean energy	~50 MeV	Detector pixel size	250 μm
Energy spread	\lesssim 20% rms	X-ray pulse duration	0
Scattering laser pulse		Total n. of X-ray pulses (for the entire 4D reconstruction)	6000 to 24000
Duration	500 fs (chirped)	Unattenuated no. photons per 250 μm pixel	5000
Energy	1 J	Unattenuated no. photons per 50 μm pixel	200
Central wavelength	800 nm	Size of the cubic voxel in tomographic reconstructions	100 μm
Spot size	20 μm		
a_0	~0.24		
X-ray source			
Duration	~10 fs		
Source transverse size	2 μm \times 2 μm		
No. of photons within 10 mrad per laser shot	$\sim 9.8 \times 10^7$		

Table 2. *Left column:* main parameters relevant for the operating regime of the X-ray source; the electron bunch and scattering laser pulse figures were used as input of the Thomson scattering simulation code TSST. More parameters related to a possible LWFA regime able to provide the required electron bunch are given in the Supplementary Materials. *Right column:* parameters of the numerical simulation with the 4D mouse chest phantom (SAD: Source to axis distance; ADD: Axis to detector distance).

overcoming limitations of the current 4D μCT systems with typical reconstruction windows of 5–10 ms per cardiac phase due to the constraints on pulse duration of conventional X-ray tubes and temporal resolution of X-ray detectors. Cooled scientific grade CCD or CMOS optically coupled or directly bonded to scintillators/phosphor screens appear the most adequate detection systems for the proposed application²⁶.

The Thomson Scattering Source. In this subsection, we will briefly discuss the main features of the all-optical Thomson scattering source envisioned for the advanced 4D μCT scanner and we provide some relevant figures of the photon beam. As a preliminary observation, we stress that the main figures considered here for both the electron bunch (e.g., total charge per bunch, energy spectrum and divergence/emittance) and the scattering laser beam (e.g., pulse energy, duration and focal spot size) have been demonstrated to be achievable with existing (although state-of-the-art) laser systems. In particular, according to the current, consolidated literature on experimental achievements in the field of LWFA, the usage of a 100 TW class laser system could be suitable for the application discussed in this paper. As anticipated above, a 10 Hz rep rate can be safely considered a standard value for such a class of lasers. The Thomson scattering source was modelled using the TSST code³², which provides the number of photons emitted in selected energy and solid angle bins over the desired ranges, once the parameters of the electron bunch (energy spectrum, spatial distribution and divergence, bunch charge), of the scattering laser pulse (central wavelength, duration and energy) and the geometry of the interaction are known. Details on the simulation code will be provided in the Methods.

The parameters of the LWFA bunch and the scattering laser beam used as input of the TSST simulation for the application discussed here are shown in Table 2 (left column). The scattering laser pulse, although picked off from the same laser chain as the main one, is stretched up to 500 fs duration³³. We notice here that we took into account a “not so small” energy spread, which ultimately affects the spectral width of the X-ray photon beam²⁹. Our choice for the energy spread is motivated by the ambition to keep the experimental setup of the X-ray source as simple as possible. Advanced schemes have been recently reported which allow remarkably lower energy spreads to be attained (such as, for instance, the usage of colliding pulses³⁴ or the so-called ReMPI scheme³⁵). However, these schemes either result, at the moment, in a rather low bunch charge (which is an essential parameter for the final photon flux³⁶) or require a complex setup. Generally speaking, a trade-off does in fact exist between the possibility to get a monochromatic photon beam and the number of photons per laser shot. Here we require that a single image (that is, an image with an average number of photons/pixel as the one shown in the right column in Table 2) might be obtained using a single laser pulse. To this purpose, an electron bunch charge of ~100 pC must be accelerated on each shot. Provided that the required energy spread is not too small (~15–20% rms), as it is in our case, such charge figures have been being reported in the literature over the past few years (see for instance³⁷ or³⁸). We also report in the Supplementary Materials on Particle-In-Cell (PIC) simulations, performed using the FBPIC code³⁹, showing a possible LWFA regime delivering such bunches. We point out that, although all-optical TS sources may potentially provide X-ray beams with smaller spectral width, the rather large width considered here

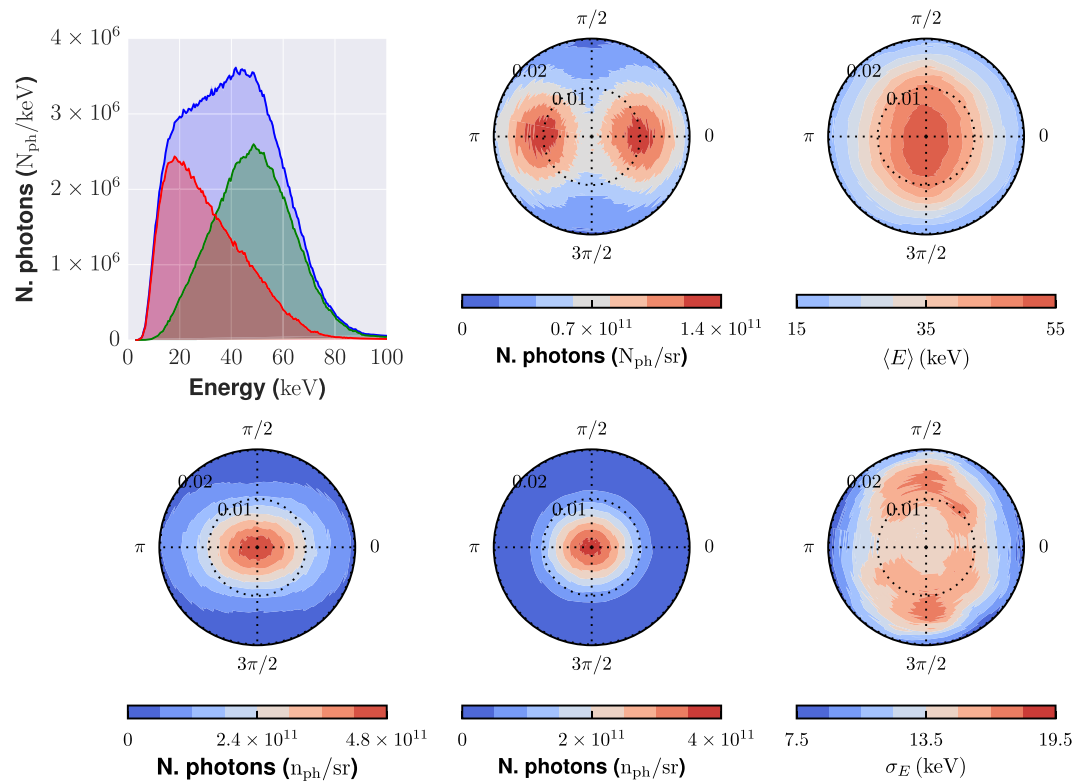


Figure 2. Spectral and angular distributions of the X-ray photons from the all-optical Thomson scattering source as retrieved using the TSST simulation code. The polar (ϑ) and azimuthal (φ) angles are defined in Fig. 1. *Left column, top:* photon spectra integrated over the whole polar angle $0 \leq \vartheta \leq 20$ mrad (blue curve), over the polar range $0 \leq \vartheta \leq 10$ mrad (green curve) and over the polar range $10 \leq \vartheta \leq 20$ mrad (red curve). *Left column, bottom:* angular distribution of the X-ray photons (integrated over the whole energy range). *Middle column:* photon angular distributions, taking into account only “low-energy” photons ($0 \leq E_{ph} \leq 40$ keV), *top*, or “high-energy” photons ($40 \leq E_{ph} \leq 80$ keV), *bottom*. *Right column:* Angular map of the average photon energy (*top*) and of the photon energy standard deviation (*bottom*). The angular maps span an azimuthal (φ , as shown in Fig. 1) range $0 \leq \varphi \leq 2\pi$ and a polar angle (ϑ) range $0 \leq \vartheta \leq 20$ mrad.

is not a limiting factor for the application discussed in this work; this issue will be addressed below using Monte Carlo simulations.

The X-ray source features a transverse size of around $2 \mu\text{m}$ FWHM. The X-ray pulse duration, in the TS geometry considered here, is comparable to the electron bunch duration, and thus is in the sub-10 fs range^{40,41}. Figure 2 shows, in the left column, the spectrum of the X-ray photon beam (top) and the photon angular distribution (bottom) as calculated using the TSST code. In the TS linear regime used here the spectrum extends up to the energy corresponding to the so-called fundamental harmonics, $E_x \simeq 4\bar{\gamma}^2 E_L$, being $\bar{\gamma}$ the average γ factor of the electron bunch and $E_L = \hbar\omega_L$ the photon energy of the scattering beam³³. As it is usual for a TS source, there is an angular dependence of the energy spectrum; this can be observed looking at the three curves in the first (top left) plot, which shows the photon spectrum integrated over different polar angle intervals. In particular, higher energy photons are predominantly emitted at smaller polar angles ($0 \leq \vartheta \leq 10$ mrad), while relatively low energy photons appear at angles $\vartheta > 10$ mrad. The angular distribution is rather elongated along the x ($\varphi=0$) direction; this corresponds to the polarization direction of the scattering laser beam. The anisotropy is mostly typical of lower energy photons, as it can be realized looking at the plots in the middle column, which show the angular distribution for “low” energy ($0 \leq E_{ph} \leq 40$ keV) and high ($40 \leq E_{ph} \leq 80$ keV) energy photons, respectively. The right column shows the average photon energy (top) and the energy standard deviation (bottom) as a function of the emission angles. For the sake of the application discussed in this paper, we choose our μCT geometry (basically SAD and ADD) in order to only rely on photons emitted within $\vartheta \leq 10$ mrad. Over such a range, the average photon energy is between 35 and 50 keV, and the standard deviation is of about 15 keV. We carried out extensive simulations in order to highlight possible effects of this real spectral/angular photon distributions on the quality of the final image; we will discuss this issue below.

Results

The ability of the system just described to reconstruct 4D images of the heart of the living animal was demonstrated by mean of analytical simulation of projection data with synthetic additive Poisson noise. The parameters of the idealized 4D numerical phantom are reported in the Supplementary Materials. The main parameters of the analytical simulation are reported in Table 2 (right column). In the Supplementary Material, additional simulations are reported to highlight the beneficial effect of ultrashort pulse duration on the proposed application. The peak myocardial wall velocity during

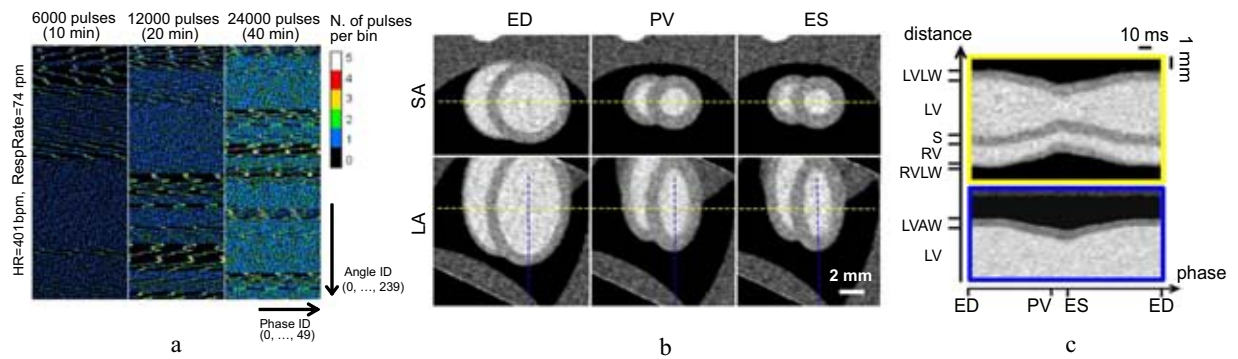


Figure 3. (a) 2D histograms showing the distribution of the X-ray pulses on the phase/angle diagram for the simulated acquisition of the dynamic phantom. Histograms are binned in 50 cardiac phase bins and 240 angular bins. Dark areas show missing data due to transitory coherence between the cardiac motion and the X-ray pulse sequence. (b) Reoriented short-axis and long-axis images of the mouse heart (only three of the 50 reconstructed phases are shown) obtained by iterative reconstruction from the sequence of 12000 pulses. (c) M-mode-like image of the reoriented heart, obtained along the dashed lines shown in (b) for all the 50 reconstructed time frames. For all images, the voxel size is $100\ \mu\text{m}$ and the temporal binning (frame duration) is 3 ms, calculated as the mean R-R interval divided by the number of reconstructed frames per cycle. ED: end-diastole; PV: peak myocardial velocity; ES: end-systole; SA: short axis; LA: long axis; LV: left ventricle; LVLW: left ventricle lateral wall; LVAW: left ventricle apical wall; RV: right ventricle; RVLW: right ventricle lateral wall; S: septum. FBP: filtered backprojection; SIRT: simultaneous iterative reconstruction technique.

systole was set to 45 mm/s in this simulation, based on micro-ultrasound measurements (see Supplementary Materials) and on previous studies on murine kinetics of cardiac contraction^{42,43}. At this velocity, the wall displacement at systole is $>400\ \mu\text{m}$ over an integration time of 10 ms, which is a typical X-ray pulse duration or detector integration time for conventional 4D μCT instrumentation. In order to get near blur-free imaging, the wall displacement should not exceed $\sim 50\ \mu\text{m}$, i.e., half of the reconstruction voxel size which can be set to $100\ \mu\text{m}$ without compromising morpho-functional cardiac measurements in mice. Hence, the required temporal resolution is in the order of 1 ms or lower. However, due to constraints on experiment duration (number of pulses required) and radiation dosimetry, a more realistic requirement for robust 3D strain/strain rate analysis is to set the temporal binning around 2–3 ms per cardiac phase as already done with high-field MRI on rats⁸. Such requirements can be relaxed for the other phases of the cardiac cycle. In this work, we have set the temporal binning to 3 ms throughout the entire cardiac cycle.

4D cardiac imaging results with realistic cardiopulmonary motion. A simulation was performed using the retrospectively gated acquisition strategy specifically foreseen for our 4D μCT prototype. Due to the real X-ray pulse duration expected for the TS source, in the order of a few up to ~ 10 femtoseconds, we have neglected the finite pulse duration in this simulation ($\Delta T_{\text{pulse}} = 0$ ms). We have generated a time series of 2D X-ray projections at constant repetition rate of 10 Hz of the 4D numerical phantom. Using real ECG and respiration waveforms previously acquired on mice and rats in our laboratory (see Supplementary Materials), each 2D projection was generated at a specific cardiac and respiratory phase; an average heart rate of 401 bpm and respiration rate of 74 respiratory acts per minute were used. A total number of pulses ranging from 6000 to 24000 over a full rotation of 360° was employed. As shown in Fig. 3a, these pulse sequences covered almost uniformly the whole cardiac cycle on most angular bins, allowing good flexibility in the choice of the subsequent temporal binning. In most cases, transitory coherence between the X-ray repetition rate and the cardiac motion was observed, randomly inducing missing data at specific ranges of projection angles and cardiac phases (Fig. 3a). Such missing data is a common source of streak artifacts in retrospectively gated acquisitions when analytical reconstruction (such as filtered backprojection) is performed. To reduce these artifacts, we employed the simultaneous iterative reconstruction technique (SIRT)⁴⁴. Figure 3b shows the reconstructed heart obtained by SIRT at end-diastole (ED) and end-systole (ES), after 300 iterations from the acquisition sequence of 12000 pulses and reoriented in short-axis (SA) and long-axis (LA). With an average R-R time of ~ 150 ms, we have obtained a temporal sampling of 3 ms by rebinning the projection data in 50 temporal frames. The selected respiratory window was 10%–90% (relative to the peak inspiration time), so that only 9632 projections out of a total of 12000 were employed in the reconstruction. M-mode-like reconstructions of the cardiac wall along two perpendicular directions are shown in Fig. 3c.

In order to highlight the advantage of using X-ray pulses much shorter than obtainable in conventional micro-CT instrumentation, we have also performed additional simulations without adding noise, by varying the duration of the X-ray pulse and of the reconstruction window. The simulations were performed on the end systolic phase ($v = 25$ mm/s) and at the phase of peak velocity ($v = 45$ mm/s) which is the most demanding phase in terms of spatial resolution when a 3D strain rate analysis is to be performed. The results are shown in Fig. 4. Even for this relatively coarse voxel size (100 micron), the RMSE error is nearly doubled when a pulse duration of 3 ms is used instead of ultra-short pulses, for a reconstruction time window of 1 ms. When using typical pulse duration obtainable in conventional micro-CT instrumentation ($\Delta T_{\text{pulse}} = 5$ –10 ms), the image quality degradation is evident even from a qualitative point of view, especially for the phase of peak velocity. No apparent differences can be found for pulse duration of 1 ms or below, due to the large (but realistic) voxel size used in this simulation.

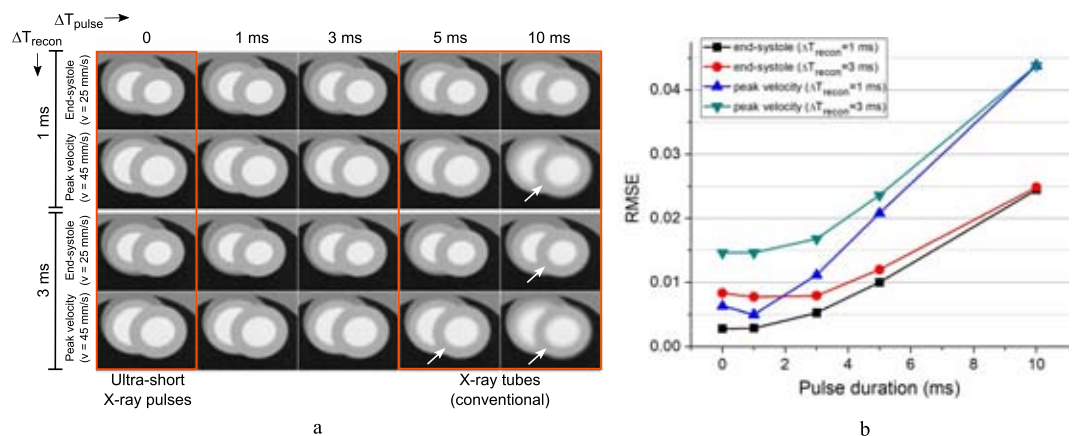


Figure 4. Noiseless simulation showing the motion blurring for different duration of the reconstruction window ΔT_{recon} and the X-ray pulse ΔT_{pulse} reconstructed at end-systole ($v = 25$ mm/s) and at time of peak myocardial velocity ($v = 45$ mm/s). **(a)** Reconstructed images in the transaxial plane (xy); the white arrows indicate settings leading to non negligible motion blurring. All images have been reconstructed by FBP with a voxel size of $100 \mu\text{m}$ from 240 projections per cardiac phase, taken at 1.5° sampling interval. **(b)** RMSE analysis relative to a reconstruction of the same ROI obtained with a fixed reconstruction window of negligible duration, $\Delta T_{recon} = 1 \mu\text{s}$ (reference image not shown).

Dosimetry and image quality assessment using Monte Carlo simulations with TS spectrum and fluence.

In order to assess the possible effects of the peculiar spectral and angular features of the TS X-ray beam on the quality of the final image for the kind of study proposed here, Monte Carlo simulations of the photon transport through a standard phantom and of the energy deposition on a conventional (phosphor screen based) X-ray detector were carried out, using the TS source photon distribution provided by the TSST code. These simulations also allowed a dosimetric study of the envisioned CT device to be performed. The phantom was made up by an 18 mm diameter water cylinder; at its center, a smaller cylinder, with diameter 5 mm, was supposed to be filled with an iodinated contrast agent with 3 mgI/mL. The source-to-phantom and the source-to-detector distances were set as in the analytical simulation (see Table 2, right column). Further details on these simulations are reported in the Methods Section and in the Supplementary Materials (examples of the synthetic images retrieved are also shown there).

Figure 5a shows a 3D density map of the dose deposition inside the phantom by a single laser shot (that is, according to the TSST simulation discussed above, considering $\sim 10^8$ photons per shot). A cubic averaging volume with a side length of 0.5 mm was used to reconstruct a raster image from this single-shot dosimetric simulation. The average phantom dose delivered with a single laser shot was $11.7 \mu\text{Gy}$; the entrance surface dose was $11.3 \mu\text{Gy}$.

For each X-ray pulse, we have measured the energy deposition onto a $100 \mu\text{m}$ thick Gadox ($\text{Gd}_2\text{O}_2\text{S}$) phosphor screen⁴⁵, with pixel size and active area as in Table 2. We ran a total of 240 projections over 360° (i.e., similar to the average number of projections per cardiac phase employed in the simulations shown above in Fig. 3b,c), with uniform angular sampling step of 1.5° . Each view was corrected with a flat field, which, in turn, was obtained by averaging 100 independent projections with no phantom in the field of view. A few projection images produced with the Monte Carlo code are reported in the Supplementary Material. A SIRT algorithm with 300 iteration was used to reconstruct the CT volume, with an isotropic voxel size of $100 \mu\text{m}$ as already done in the previous subsection. Figure 5b shows transverse and axial slices of the tomographic reconstruction; an increasing trend of the average reconstructed value toward the phantom periphery is observed, primarily due to the beam hardening effect. Due to the relatively higher energy spread at the FOV periphery (see Fig. 2), this effect was more evident on the slice reconstructed at $z = 5$ mm, where the average CT number in water increased from 59 HU at $r = 3$ mm to 192 HU at $r = 7.7$ mm (denoting by $r = \sqrt{x^2 + y^2}$ the radial distance from the slice center). An increasing trend of the image noise toward the FOV periphery is also observed. In the midplane ($z = 0$), the image noise in water increased from 395 HU at $r = 3$ mm to 501 HU at $r = 7.7$ mm. This is due to the decreasing average photon energy and photon fluence away from the central beam axis (see Fig. 2). For the same reasons, the average signal and noise of the iodine insert increased from 1189 ± 383 HU at the midplane to 1410 ± 478 HU at $z = 5$ mm. The average and standard deviation of contrast to noise ratio (CNR) of the iodine insert was 3.0 ± 0.3 . This is fully compatible with a subsequent image post-processing and ventricle segmentation for morphometric analysis.

Discussion and Perspectives

A compact imaging platform based on an all-optical laser-based Thomson scattering X-ray source has been conceived, designed and fully simulated by means of analytical and Monte Carlo simulations. To the best of the authors' knowledge, no studies (numerical or experimental) have been conducted so far on the possible use of all-optical Thomson scattering ultrashort X-ray sources for the specific task of cardiac 4D imaging of the small rodent. As discussed above, none of the current standard imaging modalities devoted to dynamic

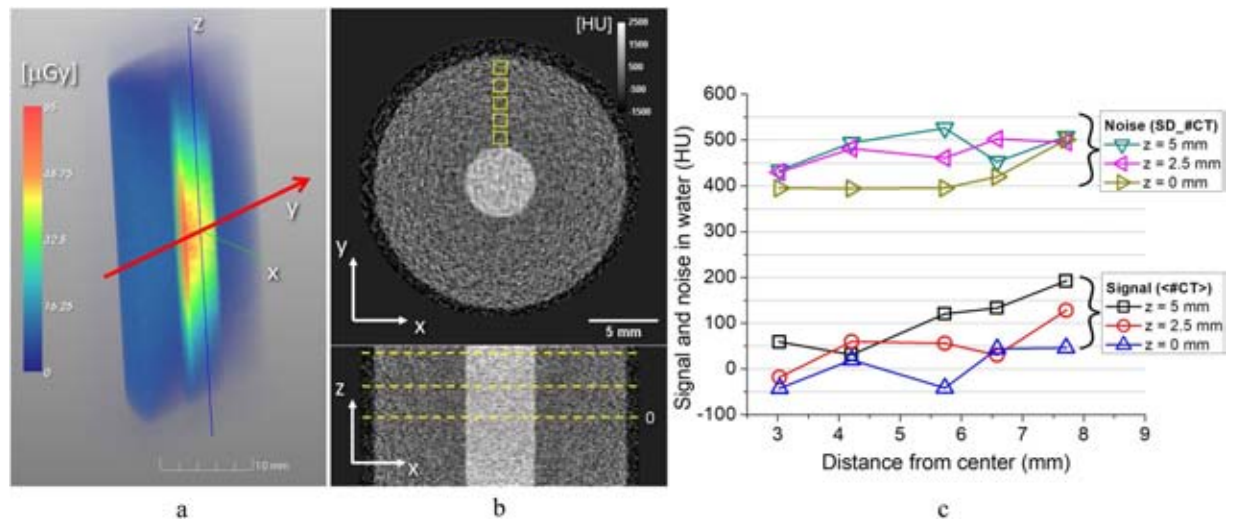


Figure 5. (a) Volume rendering of the 3D distribution of the X-ray dose delivered by a single laser shot to the water phantom with iodine insert (see text). For visualization purposes, a virtual cutting on the yz plane has been made on this rendering. The red arrow (y axis) shows the main direction of propagation of the X-ray beam for the selected laser shot. (b) Transverse (top) and coronal (bottom) slices of the tomographic reconstruction of the same phantom in (a). All images are reconstructed with a SIRT algorithm, 300 iterations, and with an isotropic voxel of $100\ \mu\text{m}$. (c) Average reconstructed values (signal) and noise in water at several radial and axial positions. The radial positions of the ROI's are depicted as yellow squares in (b), whereas the axial positions are shown as dashed lines in the coronal image (only $z = 0$ is marked).

morphofunctional quantification of small animal heart can achieve, at the same time, isotropic 3D spatial resolution in the order of $100\ \mu\text{m}$ and temporal resolution in the order of (or better than) 1 ms, as required for robust 3D cardiac strain and strain rate analysis in small animals. This gap is due to limitations of both current technology of compact X-ray sources (i.e., available in small-scale laboratories) and readout speed of high resolution X-ray detectors. Laser-based TS sources, as discussed in this paper, appear the most promising alternative to 3rd and 4th generation synchrotron sources, providing extremely short pulse duration, high spatial coherence and relatively small footprint and cost^{15,46}, and thus paving the way for the spread of X-ray sources with spatial and temporal features boasted so far only by large scale infrastructures.

We have demonstrated here that, using the proposed 4D μCT prototype based on TS source, it is feasible to obtain motion blur free 3D images of the mouse heart at isotropic voxel size of $100\ \mu\text{m}$ with wall velocities up to 45 mm/s, which is generally higher than what practically found in mice and rats, especially under deep anesthesia⁴². An attractive feature of our TS-based 4D μCT prototype is that, due to the extremely short duration of the X-ray source, no time overlap can occur between X-ray pulses at any phase of the cardiac cycle; this means that the reconstructed time bin duration T_{recon} can be set to an arbitrarily short duration without any overlap of adjacent phases, provided that a sufficient amount of projections per angle is acquired for each phase. Hence, the only practical limit to the temporal resolution is given by the radiation dose and the experiment duration. The temporal precision of R-peak identification on the ECG signal, along with the correlation between ECG and cardiac motion periodicity, could also play a role in the final temporal resolution of long gated acquisitions with the proposed system. These latter limitations are currently disregarded in conventional 4D μCT , as they can only have an effect when sub-ms temporal resolution is pursued. The estimated radiation dose after 12000 x-ray pulses generated during the simulated retrospectively gated acquisition was $\lesssim 150\ \text{mGy}$. This value is comparable to or lower than doses reported on similar works using conventional sources^{9,47–49}. Even though the focus of this paper was not on accurate dosimetry, the GEANT4 simulation toolkit has been already shown to be accurate in dosimetric calculations at low photon energy⁵⁰. Employing as many dose-lowering setup parameters as possible is beneficial in the proposed setup to push the temporal resolution of the system close to its fundamental limit, which is related to the synchronization between each laser pulse and the actual phase in the R-R interval. The employment of SIRT reconstruction, besides its beneficial effect in the suppression of streak artifacts from irregular angular sampling, played also a beneficial role in the noise reduction and hence on the reduction of radiation dose. Besides this, the employment of a Gadox scintillator relatively thicker than standard for small animal imaging ($100\ \mu\text{m}$) and a mean photon energy just above the iodine K-edge (35–50 keV in the selected FOV position) were beneficial to keep the dose low enough to allow margins of improvement in the trade-off between the achievable spatial and temporal resolution. The increased scintillator thickness is not an issue for the target spatial resolution of our application, as Gadox thickness up to 120 micron still provide a detector resolution $> 6\ \text{lp/mm}$ at 10% MTF⁵¹. The overall spatial resolution of the tomographic system can be estimated using analytical models⁵²; in our geometry, it will be $< 60\ \mu\text{m}$ FWHM which is fully compatible with cardiac morphometry in small animals.

Apart from dose consideration, the experiment duration is also a limiting factor to be carefully taken into account. The laser repetition rate chosen for our simulation (10 Hz) lead to an experiment duration of 20 minutes in order to get a 4D reconstruction at 3 ms of temporal binning with enough image contrast to perform 3D strain

analysis in mice. Even though thermoregulatory devices are demonstrated to be effective to keep stable the physiological parameters of mice for experiment durations up to 30 min⁵³, longer acquisition times might introduce artifacts due to both myocardial uptake and blood pool washout of the contrast agent⁵⁴. Hence, the total experiment duration should never exceed 30–40 minutes in total. Scaling up the laser rep rate to 100 Hz is fully feasible⁵⁵, even though the present technology of low-noise, high resolution X-ray detector is still restricted to slower frame rates. The temporal characteristics of the selected detectors should be carefully taken into account when planning for such a source-related improvement. Prospective double cardio-respiratory gating appears unfeasible with laser-based sources, at least at actual stage of development, due to the inability to trigger laser shots from external sources and with random rates. Even though the X-ray pulses with fixed rep-rate could be put in AND with a separated physiological trigger signal⁵⁶, in our design we preferred to employ the retrospective gating approach for the sake of experiment shortening, easiness of implementation and flexibility in the post-acquisition spatio-temporal binning. The selected TS-based source implies a scanning geometry with the animal placed on a vertically oriented cradle; even though this is less than optimal in terms of physiological stability of the animal when compared with standard rotating-gantry geometries, vertical positioning of the animal was already employed successfully in several previous works at synchrotron facilities⁵⁷, other laser-based X-ray sources⁵⁸ and even in special designs of micro-CT's based on conventional X-ray tubes⁴⁸.

We recognize that a similar approach to cardiopulmonary imaging in mice may be implemented at existing beamlines of many synchrotron facilities. Nevertheless, it must be understood that the advantage of obtaining comparable results with compact sources (potentially available at most biomedical laboratories or hospitals) is extremely important in almost all preclinical experiments, requiring the proximity to a multidisciplinary environment with biology/veterinary staff and other imaging modalities *in situ*. As a matter of fact, the dynamic cardiac microtomography proposed in this work is likely to remain at the proof-of-principle stage unless more compact and affordable sources, such as the all-optical TS source considered here, become available.

The kind of apparatus described here is currently under development at the Intense Laser Irradiation Laboratory (ILIL) of the CNR in Pisa, Italy, in the framework of the Italian project “PREclinical Laser-based Ultrafast Diagnostics and thErapy (PRELUDE)”. It is worth stressing here that laser-driven electron accelerators have witnessed a tremendous improvement of the final beam quality, in terms of beam divergence/emittance, total charge energy spread, and so on, so that this kind of technology can be considered at the mature level to reach in short times the clinical quality. For instance, the EuPRAXIA project⁵⁹, whose preparatory phase is currently funded by EU in view of the preparation of a Conceptual Design Report, is aimed at developing a plasma-based accelerator with industrial beam quality and user areas for real applications in different fields, including biology and medicine⁶⁰.

Apart from synchrotron sources, the proposed TS source is the only one capable of providing, at the same time, (i) ultra-short X-ray pulses, with (ii) photon energy spectra tunable in the optimal range for small animal imaging, and (iii) with a source size under 10 μm and thus capable of enabling phase contrast edge enhancing, all within a small-scale laboratory infrastructure. A thorough investigation of the possible beneficial effects and possibilities open up by the point (iii) is beyond the scope of the current paper and will be carried out in a future work.

Methods

Ethical statement. All the animal experiments from which data has been retrieved to generate the numerical mouse chest phantom were conducted in compliance to local approved protocols at CNR-IFC, under Italian Law 26/2014 and 2010/63/EU and approved by the Italian Ministry of Health.

Analytical dynamic simulations. Analytical simulation have been performed with a custom developed ray-tracing algorithm, calculating the intersection lengths of rays and ellipsoids arbitrarily oriented in the 3D space. Simulation of finite duration X-ray pulses was done by averaging 10 equally spaced instantaneous ($\Delta T = 0$) pulses in the desired time frame. Because analytical simulations were performed with the main goal of evaluating the effect of pulse duration and of the reconstruction artifacts due to angular sampling non uniformity, the finite source size and the real X-ray spectrum were not simulated. Statistical noise with Poisson probability density function was added to each analytically simulated 2D projection by considering the attenuated number of photons in each detector pixel, normalized to a number of unattenuated photons (detected after just air) of 5000. This number is realistic when taking into account the results of the TS simulated photon output at the center of the detector, at 2500 mm from the e^- -laser interaction where X-rays are originated, and by considering a detector binning with an effective pixel size of $250 \times 250 \mu\text{m}^2$. The attenuation coefficient of air has been neglected. More details on the 4D mouse chest numerical phantom can be found in the Supplementary Materials.

The TS source simulations. The detailed spectral and angular features of the TS source proposed for the present study were retrieved using the *Thomson Scattering Simulation Tools (TSST)* code³². The code evaluates the far-field distribution of the radiation emitted incoherently by the electron bunch. The spectral and angular distribution of the X-rays emitted by a single electron are computed using a semi-analytical approach based on the formulas reported in³². The exact analytical description of the radiation emitted within a single laser cycle is then coherently summed (in a numerical fashion) by taking into account the exact longitudinal pulse profile. A head-on (*backscattering TS*) collision geometry was considered in our case, with the electron bunch and scattering laser figures listed in Table 2. The photon distribution function was sampled using 200 energy bins in the range 1–100 keV, 80 polar angle (ϑ) bins in the range $0 \leq \vartheta \leq 20$ mrad and 64 azimuthal (φ) bins in the range $0 \leq \varphi \leq 2\pi$.

Monte Carlo code for dosimetry and image quality assessment. A Monte Carlo code was developed in order to both model the imaging capability of the TS source and to perform a dosimetric study. The code was based on the Geant4 toolkit^{61–63}. The low-energy physics models based on PENELOPE^{64,65} were used for the simulation of the electromagnetic interactions of X-rays. The primary photons were generated according to the energy and angular distribution provided by TSST code, using a rejection sampling method.

Data Availability

The datasets generated during and/or analysed during the current study are available from the corresponding authors on reasonable request.

References

- Russell, J. C. & Proctor, S. D. Small animal models of cardiovascular disease: tools for the study of the roles of metabolic syndrome, dyslipidemia, and atherosclerosis. *Cardiovasc. Pathol.* **15**, 318–330, <https://doi.org/10.1016/j.carpath.2006.09.001> (2006).
- Zaragoza, C. *et al.* Animal models of cardiovascular diseases. *J. Biomed. Biotechnol.* **2011**, 497841, <https://doi.org/10.1155/2011/497841> (2011).
- Klocke, R., Tian, W., Kuhlmann, M. T. & Nikol, S. Surgical animal models of heart failure related to coronary heart disease. *Cardiovasc. Res.* **74**, 29–38, <https://doi.org/10.1016/j.cardiores.2006.11.026> (2007).
- Menichetti, L. *et al.* MicroPET/CT imaging of $\alpha_v\beta_3$ integrin via a novel ⁶⁸Ga-NOTA-RGD peptidomimetic conjugate in rat myocardial infarction. *Eur. J. Nucl. Med. Mol. Imaging* **40**, 1265–1274, <https://doi.org/10.1007/s00259-013-2432-9> (2013).
- Gambhir, S. S. Molecular imaging of cancer with positron emission tomography. *Nat. Rev. Cancer* **2**, 683–693, <https://doi.org/10.1038/nrc882> (2002).
- Ritman, E. L. Micro-Computed Tomography—Current Status and Developments. *Annu. Rev. Biomed. Eng.* **6**, 185–208, <https://doi.org/10.1146/annurev.bioeng.6.040803.140130> (2004).
- Ritman, E. L. Current Status of Developments and Applications of Micro-CT. *Annu. Rev. Biomed. Eng.* **13**, 531–552, <https://doi.org/10.1146/annurevbioeng-071910-124717> (2011).
- Espe, E. K. S. *et al.* Novel insight into the detailed myocardial motion and deformation of the rodent heart using high-resolution phase contrast cardiovascular magnetic resonance. *J. Cardiovasc. Magn. Reson.* **15**, 82, <https://doi.org/10.1186/1532-429X-15-82> (2013).
- Befera, N. T., Badea, C. T. & Johnson, G. A. Comparison of 4d-microSPECT and microCT for murine cardiac function. *Mol. Imaging Biol.* **16**, 235–245, <https://doi.org/10.1007/s11307-013-0686-z> (2014).
- Hendrikx, G., Bauwens, M., Wierls, R., Mottaghy, F. M. & Post, M. J. Left ventricular function measurements in a mouse myocardial infarction model. Comparison between 3d-echocardiography and ECG-gated SPECT. *Nuklearmedizin* **55**, 115–122, <https://doi.org/10.3413/Nukmed-0776-15-11> (2016).
- Labate, L., Tomassini, P. & Gizzi, L. A. Inverse Compton Scattering X-ray Sources. In *Handbook of X-ray Imaging: Physics and Technology*, 309–323 (CRC Press, 2017).
- Kawase, K. *et al.* Development of a sub-MeV X-ray source via Compton backscattering. *Nucl. Instruments Methods Phys. Res. Sect. A: Accel. Spectrometers, Detect. Assoc. Equip.* **637**, S141–S144, <https://doi.org/10.1016/j.nima.2010.02.042>. The International Workshop on Ultra-short Electron & Photon Beams: Techniques and Applications (2011).
- Egl, E. *et al.* The Munich Compact Light Source: initial performance measures. *J. Synchrotron Rad.* **23**, 1137–1142, <https://doi.org/10.1107/S160057751600967X> (2016).
- Sarri, G. *et al.* Ultrahigh Brilliance Multi-MeV γ -Ray Beams from Nonlinear Relativistic Thomson Scattering. *Phys. Rev. Lett.* **113**, 224801, <https://doi.org/10.1103/PhysRevLett.113.224801> (2014).
- Albert, F. *et al.* Betatron x-ray radiation from laser-plasma accelerators driven by femtosecond and picosecond laser systems. *Phys. Plasmas* **25**, 056706, <https://doi.org/10.1063/1.5020997> (2018).
- Schmüser, P., Dohlus, M., Rossbach, J. & Behrens, C. *Free-Electron Lasers in the Ultraviolet and X-Ray Regime: Physical Principles, Experimental Results, Technical Realization*. Springer Tracts in Modern Physics, 2 edn (Springer International Publishing, 2014).
- Labate, L. *et al.* LESM: a laser-driven sub-MeV electron source delivering ultra-high dose rate on thin biological samples. *J. Phys. D: Appl. Phys.* **49**, 275401, <https://doi.org/10.1088/0022-3727/49/27/275401> (2016).
- Andreassi, M. G. *et al.* Radiobiological Effectiveness of Ultrashort Laser-Driven Electron Bunches: Micronucleus Frequency, Telomere Shortening and Cell Viability. *Radiat. Res.* **186**, 245–253, <https://doi.org/10.1667/RR14266.1> (2016).
- Cole, J. M. *et al.* Laser-wakefield accelerators as hard x-ray sources for 3d medical imaging of human bone. *Sci. Reports* **5**, 13244, <https://doi.org/10.1038/srep13244> (2015).
- Esarey, E., Schroeder, C. B. & Leemans, W. P. Physics of laser-driven plasma-based electron accelerators. *Rev. Mod. Phys.* **81**, 1229–1285, <https://doi.org/10.1103/RevModPhys.81.1229> (2009).
- Faure, J. *et al.* A review of recent progress on laser-plasma acceleration at kHz repetition rate. *Plasma Phys. Control. Fusion* **61**, 014012, <https://doi.org/10.1088/1361-6587/aae047> (2018).
- Leemans, W. P. *et al.* Multi-GeV Electron Beams from Capillary-Discharge-Guided Subpetawatt Laser Pulses in the Self-Trapping Regime. *Phys. Rev. Lett.* **113**, 245002, <https://doi.org/10.1103/PhysRevLett.113.245002> (2014).
- Rousse, A. *et al.* Production of a keV X-Ray Beam from Synchrotron Radiation in Relativistic Laser-Plasma Interaction. *Phys. Rev. Lett.* **93**, 135005, <https://doi.org/10.1103/PhysRevLett.93.135005> (2004).
- Gizzi, L. A. All-Optical X-Ray and γ -Ray Sources from Ultraindense Laser-Matter Interactions. In Giulietti, A. (ed.) *Laser-Driven Particle Acceleration Towards Radiobiology and Medicine*, 183 (Springer, 2016).
- Kneip, S. *et al.* Bright spatially coherent synchrotron X-rays from a table-top source. *Nat. Phys.* **7**, 737, <https://doi.org/10.1038/nphys2093> (2011).
- Döpp, A. *et al.* Quick x-ray microtomography using a laser-driven betatron source. *Optica* **5**, 199–203, <https://doi.org/10.1364/OPTICA.5.000199> (2018).
- Powers, N. D. *et al.* Quasi-monoenergetic and tunable X-rays from a laser-driven Compton light source. *Nat. Photonics* **8**, 28–31, <https://doi.org/10.1038/nphoton.2013.314> (2014).
- Gizzi, L. A. *et al.* Acceleration with self-injection for an all-optical radiation source at LNF. *Nucl. Instruments Methods Phys. Res. Sect. B* **309**, 202–209 (2013).
- Esarey, E., Ride, S. K. & Sprangle, P. Nonlinear Thomson scattering of intense laser pulses from beams and plasmas. *Phys. Rev. E* **48**, 3003–3021, <https://doi.org/10.1103/PhysRevE.48.3003> (1993).
- Cole, J. M. *et al.* High-resolution μ CT of a mouse embryo using a compact laser-driven X-ray betatron source. *PNAS* **115**, 6335–6340, <https://doi.org/10.1073/pnas.1802314115> (2018).
- Albert, F. & Thomas, A. G. R. Applications of laser wakefield accelerator-based light sources. *Plasma Phys. Control. Fusion* **58**, 103001, <https://doi.org/10.1088/0741-3335/58/10/103001> (2016).
- Tomassini, P., Giulietti, A., Giulietti, D. & Gizzi, L. A. Thomson backscattering X-rays from ultra-relativistic electron bunches and temporally shaped laser pulses. *Appl. Phys. B* **80**, 419–436, <https://doi.org/10.1007/s00340-005-1757-x> (2005).

33. Tomassini, P. *et al.* Linear and Nonlinear Thomson Scattering for Advanced X-ray Sources in PLASMONX. *IEEE Transactions on Plasma Sci.* **36**, 1782–1789, <https://doi.org/10.1109/TPS.2008.927428> (2008).
34. Cormier-Michel, E. *et al.* Design principles for high quality electron beams via colliding pulses in laser plasma accelerators. *Phys. Rev. ST Accel. Beams* **17**, 091301, <https://doi.org/10.1103/PhysRevSTAB.17.091301> (2014).
35. Tomassini, P. *et al.* The resonant multi-pulse ionization injection. *Phys. Plasmas* **24**, 103120, <https://doi.org/10.1063/1.5000696> (2017).
36. Leemans, W. P. *et al.* Interaction of Relativistic Electrons with Ultrashort Laser Pulses: Generation of Femtosecond X-Rays and Microprobing of Electron Beams. *IEEE J. Quantum Electron.* **33**, 1925–1934 (1997).
37. Costa, G. *et al.* Characterization of self-injected electron beams from LWFA experiments at SPARC LAB. *Nucl. Instruments Methods Phys. Res. Sect. A: Accel. Spectrometers, Detect. Assoc. Equip.* **118–122**, <https://doi.org/10.1016/j.nima.2018.02.008>. 3rd European Advanced Accelerator Concepts workshop (EAAC2017) (2018).
38. McGuffey, C. *et al.* On the properties of synchrotron-like X-ray emission from laser wakefield accelerated electron beams. *Phys. Plasmas* **25**, 043104, <https://doi.org/10.1063/1.5024547> (2018).
39. Lehe, R., Kirchen, M., Andriyash, I. A., Godfrey, B. B. & Vay, J.-L. A spectral, quasi-cylindrical and dispersion-free Particle-In-Cell algorithm. *Comput. Phys. Commun.* **203**, 66–82, <https://doi.org/10.1016/j.cpc.2016.02.007> (2016).
40. Lundh, O. *et al.* Few femtosecond, few kiloampere electron bunch produced by a laser–plasma accelerator. *Nat. Phys.* **7**, 219, <https://doi.org/10.1038/nphys1872> (2011).
41. Kotaki, H. *et al.* Direct Observation of the PulseWidth of an Ultrashort Electron Beam. *J. Phys. Soc. Jpn.* **84**, 074501, <https://doi.org/10.7566/JPSJ.84.074501> (2015).
42. Sebag, I. A. *et al.* Quantitative Assessment of Regional Myocardial Function in Mice by Tissue Doppler Imaging: Comparison With Hemodynamics and Sonomicrometry. *Circulation* **111**, 2611–2616, <https://doi.org/10.1161/CIRCULATIONAHA.104.474411> (2005).
43. Del Seppia, C. *et al.* Evidence in hypertensive rats of hypotensive effect after mandibular extension. *Physiol. Reports* **6**, e13911, <https://doi.org/10.14814/phy2.13911> (2018).
44. Aarle, W. V. *et al.* Fast and flexible X-ray tomography using the ASTRA toolbox. *Opt. Express, OE* **24**, 25129–25147, <https://doi.org/10.1364/OE.24.025129> (2016).
45. Michail, C. *et al.* Measurement of the luminescence properties of Gd₂O₃:Pr,Ce,F powder scintillators under X-ray radiation. *Radiat. Meas.* **70**, 59–64, <https://doi.org/10.1016/j.radmeas.2014.09.008> (2014).
46. Corde, S. *et al.* Femtosecond x rays from laser-plasma accelerators. *Rev. Mod. Phys.* **85**, 1–48, <https://doi.org/10.1103/RevModPhys.85.1> (2013).
47. Ritschl, L., Sawall, S., Knaup, M., Hess, A. & Kachelriess, M. Iterative 4d cardiac micro-CT image reconstruction using an adaptive spatio-temporal sparsity prior. *Phys Med Biol* **57**, 1517–1525, <https://doi.org/10.1088/0031-9155/57/6/1517> (2012).
48. Badea, C. T. *et al.* A dual micro-CT system for small animal imaging. In *Medical Imaging 2008: Physics of Medical Imaging*, vol. 6913, 691342, <https://doi.org/10.1117/12.772303> (International Society for Optics and Photonics, 2008).
49. Guo, X., Johnston, S. M., Qi, Y., Johnson, G. A. & Badea, C. T. 4d micro-CT using fast prospective gating. *Phys Med Biol* **57**, 257–271, <https://doi.org/10.1088/0031-9155/57/1/257> (2012).
50. Guimarães, C. C., Moralles, M. & Okuno, E. Performance of GEANT4 in dosimetry applications: Calculation of X-ray spectra and kerma-to-dose equivalent conversion coefficients. *Radiat. Meas.* **43**, 1525–1531, <https://doi.org/10.1016/j.radmeas.2008.07.001> (2008).
51. Cha, B. K. *et al.* Design and image-quality performance of high resolution CMOS-based X-ray imaging detectors for digital mammography. *J. Inst.* **7**, C04020–C04020, <https://doi.org/10.1088/1748-0221/7/04/C04020> (2012).
52. Belcari, N. *et al.* Preliminary characterization of a single photon counting detection system for CT application. *Nucl. Instruments Methods Phys. Res. Sect. A: Accel. Spectrometers, Detect. Assoc. Equip.* **576**, 204–208, <https://doi.org/10.1016/j.nima.2007.01.153> (2007).
53. Caro, A. C., Hankenson, F. C. & Marx, J. O. Comparison of Thermoregulatory Devices Used during Anesthesia of C57bl/6 Mice and Correlations between Body Temperature and Physiologic Parameters. *J Am Assoc Lab Anim Sci* **52**, 577–583 (2013).
54. Detombe, S. A., Dunmore-Buyze, J. & Drangova, M. Evaluation of eXIA 160xl cardiac-related enhancement in C57bl/6 and BALB/c mice using micro-CT. *Contrast Media & Mol. Imaging* **7**, 240–246, <https://doi.org/10.1002/cmim.488> (2012).
55. Hwu, Y. *et al.* A viable laser driver for a user plasma accelerator. *Nucl. Instruments Methods Phys. Res. Sect. A: Accel. Spectrometers, Detect. Assoc. Equip.* **909**, 58–66, <https://doi.org/10.1016/j.nima.2018.02.089> 3rd European Advanced Accelerator Concepts workshop (EAAC2017) (2018).
56. Minohara, S., Kanai, T., Endo, M., Noda, K. & Kanazawa, M. Respiratory gated irradiation system for heavy-ion radiotherapy. *Int. J. Radiat. Oncol. Biol. Phys.* **47**, 1097–1103, [https://doi.org/10.1016/S0360-3016\(00\)00524-1](https://doi.org/10.1016/S0360-3016(00)00524-1) (2000).
57. Hwu, Y. *et al.* Synchrotron microangiography with no contrast agent. *Phys Med Biol* **49**, 501–508 (2004).
58. Bech, M. *et al.* In-vivo dark-field and phase-contrast x-ray imaging. *Sci Rep* **3**, 3209, <https://doi.org/10.1038/srep03209> (2013).
59. EuPRAXIA project. www.eupraxia-project.eu.
60. Walker, P. A. *et al.* Horizon 2020 EuPRAXIA design study. *J. Phys.: Conf. Ser.* **874**, 012029, <https://doi.org/10.1088/1742-6596/874/1/012029> (2017).
61. Agostinelli, S. *et al.* Geant4—a simulation toolkit. *Nucl. Instruments Methods Phys. Res. Sect. A: Accel. Spectrometers, Detect. Assoc. Equip.* **506**, 250–303, [https://doi.org/10.1016/S0168-9002\(03\)01368-8](https://doi.org/10.1016/S0168-9002(03)01368-8) (2003).
62. Allison, J. *et al.* Geant4 developments and applications. *IEEE Transactions on nuclear science* **53**, 270–278 (2006).
63. Allison, J. *et al.* Recent developments in Geant4. *Nucl. Instruments Methods Phys. Res. Sect. A: Accel. Spectrometers, Detect. Assoc. Equip.* **835**, 186–225, <https://doi.org/10.1016/j.nima.2016.06.125> (2016).
64. Baró, J., Sempau, J., Fernández-Varea, J. M. & Salvat, F. PENELOPE: An algorithm for Monte Carlo simulation of the penetration and energy loss of electrons and positrons in matter. *Nucl. Instruments Methods Phys. Res. Sect. B: Beam Interactions with Mater. Atoms* **100**, 31–46, [https://doi.org/10.1016/0168-583X\(95\)00349-5](https://doi.org/10.1016/0168-583X(95)00349-5) (1995).
65. Ivanchenko, V., Apostolakis, J. & Bagulya, A. Recent improvements in Geant4 electromagnetic physics models and interfaces. *Prog. Nucl. Sci. Technol.* **898–903** (2011).
66. Panetta, D. *et al.* Temporal weighting and angular rebinning for artifact-free single-rotation retrospectively gated 4d cardiac micro-CT. In *Proceedings of the World Molecular Imaging Congress 2015, Honolulu, Hawaii, September 2-5, 2015, vol. 18 of Molecular Imaging and Biology*, S356–S357, <https://doi.org/10.1007/s11307-016-0969-2> (Springer International Publishing, 2016).
67. Drangova, M., Ford, N. L., Detombe, S. A., Wheatley, A. R. & Holdsworth, D. W. Fast retrospectively gated quantitative four-dimensional (4d) cardiac micro computed tomography imaging of free-breathing mice. *Invest Radiol* **42**, 85–94, <https://doi.org/10.1097/01.rli.0000251572.56139.a3> (2007).
68. Cao, G. *et al.* Prospective-gated cardiac micro-CT imaging of free-breathing mice using carbon nanotube field emission x-ray. *Med Phys* **37**, 5306–5312, <https://doi.org/10.1118/1.3491806> (2010).
69. Dubsky, S., Hooper, S. B., Siu, K. K. W. & Fouras, A. Synchrotron-based dynamic computed tomography of tissue motion for regional lung function measurement. *J R Soc Interface* **9**, 2213–2224, <https://doi.org/10.1098/rsif.2012.0116> (2012).
70. Murrie, R. P. *et al.* Live small-animal X-ray lung velocimetry and lung micro-tomography at the Australian Synchrotron Imaging and Medical Beamline. *J Synchrotron Rad* **22**, 1049–1055, <https://doi.org/10.1107/S1600577515006001> (2015).

Acknowledgements

This work was funded from the Italian MIUR through the PRIN project “Preclinical Tool for Advanced Translational Research with Ultrashort and Ultraintense X-ray Pulse” (prot. 20154F48P9). L.L., L.A.G. and P.T. also acknowledge funding from the European Union’s Horizon 2020 research and innovation programme under grant agreement No. 653782 (EuPRAXIA project), and from the MIUR funded Italian research Network ELI-Italy (D.M.n. 631/16). We would like to thank Dr. Maurizio Varanini for his assistance in the analysis of ECG sequences from rats used to generate the numerical phantom.

Author Contributions

D.P. conceived the proposed application and data acquisition scheme, and conducted the analytical simulations. L.L. conceived the proposed platform and conducted the Monte Carlo simulation of the photon transport and detection. L.B., N.D.L. and F.F. provided the physiological and ultrasound data of mice used for the analytical simulation. P.T. carried out the Thomson scattering simulations. G.E., A.S. and G.M. performed the tomographic reconstruction. L.A.G. reviewed the laser-plasma acceleration scheme and its applicability to the conceptual experiment. D.Pal. contributed to the design of the TS source. L.P., P.P., G.R., P.A.S. and L.A.G. contributed to the design of the system. P.R. contributed to data analysis and interpretation, guarantor of the integrity of the entire study. D.P. and L.L. drafted the manuscript. All authors reviewed the manuscript.

Additional Information

Supplementary information accompanies this paper at <https://doi.org/10.1038/s41598-019-44779-y>.

Competing Interests: The authors declare no competing interests.

Publisher’s note: Springer Nature remains neutral with regard to jurisdictional claims in published maps and institutional affiliations.



Open Access This article is licensed under a Creative Commons Attribution 4.0 International License, which permits use, sharing, adaptation, distribution and reproduction in any medium or format, as long as you give appropriate credit to the original author(s) and the source, provide a link to the Creative Commons license, and indicate if changes were made. The images or other third party material in this article are included in the article’s Creative Commons license, unless indicated otherwise in a credit line to the material. If material is not included in the article’s Creative Commons license and your intended use is not permitted by statutory regulation or exceeds the permitted use, you will need to obtain permission directly from the copyright holder. To view a copy of this license, visit <http://creativecommons.org/licenses/by/4.0/>.

© The Author(s) 2019

Time evolution of stimulated Raman scattering and two-plasmon decay at laser intensities relevant for shock ignition in a hot plasma

G. Cristoforetti¹, L. Antonelli², D. Mancelli^{3,4}, S. Atzeni⁵, F. Baffigi¹, F. Barbato³, D. Batani^{3,6}, G. Boutoux^{3,7}, F. D'Amato¹, J. Dostal^{8,9}, R. Dudzak^{8,9}, E. Filippov^{6,10}, Y. J. Gu^{9,11}, L. Juha^{8,9}, O. Klimo¹², M. Krus⁹, S. Malko^{13,14}, A. S. Martynenko^{6,10}, Ph. Nicolai³, V. Ospina^{13,14}, S. Pikuz^{6,10}, O. Renner^{8,11}, J. Santos³, V. T. Tikhonchuk^{3,11}, J. Trela³, S. Viciani¹, L. Volpe^{13,14}, S. Weber¹¹, and L. A. Gizzi¹

¹National Institute of Optics, CNR, Pisa and Florence, Italy

²York Plasma Physics Institute, University of York, Heslington, York, UK

³Université de Bordeaux, CNRS, CEA, CELIA, Talence, France

⁴Donostia International Physics Center (DIPC), Donostia/San Sebastian, Basque Country, Spain

⁵Dipartimento SBAI, Università di Roma La Sapienza, Roma, Italy

⁶National Research Nuclear University MEPhI, Moscow, Russia

⁷CEA, DAM, DIF, Arpajon, France

⁸Department of Radiation and Chemical Physics, Institute of Physics of the CAS, Prague, Czech Republic

⁹Laser Plasma Department, Institute of Plasma Physics of the CAS, Prague, Czech Republic

¹⁰Joint Institute for High Temperature RAS, Moscow, Russia

¹¹ELI-Beamlines, Institute of Physics of the CAS, Prague, Czech Republic

¹²FNSPE, Czech Technical University in Prague, Prague, Czech Republic

¹³Universidad de Salamanca, Ctr Laseres Pulsados, Salamanca, Spain

¹⁴Centro de Laseres Pulsados (CLPU), Villamayor, Salamanca, Spain

(Received 26 March 2019; revised 19 June 2019; accepted 27 June 2019)

Abstract

Laser–plasma interaction (LPI) at intensities 10^{15} – 10^{16} W · cm⁻² is dominated by parametric instabilities which can be responsible for a significant amount of non-collisional absorption and generate large fluxes of high-energy nonthermal electrons. Such a regime is of paramount importance for inertial confinement fusion (ICF) and in particular for the shock ignition scheme. In this paper we report on an experiment carried out at the Prague Asterix Laser System (PALS) facility to investigate the extent and time history of stimulated Raman scattering (SRS) and two-plasmon decay (TPD) instabilities, driven by the interaction of an infrared laser pulse at an intensity $\sim 1.2 \times 10^{16}$ W · cm⁻² with a ~ 100 μm scalelength plasma produced from irradiation of a flat plastic target. The laser pulse duration (300 ps) and the high value of plasma temperature (~ 4 keV) expected from hydrodynamic simulations make these results interesting for a deeper understanding of LPI in shock ignition conditions. Experimental results show that absolute TPD/SRS, driven at a quarter of the critical density, and convective SRS, driven at lower plasma densities, are well separated in time, with absolute instabilities driven at early times of interaction and convective backward SRS emerging at the laser peak and persisting all over the tail of the pulse. Side-scattering SRS, driven at low plasma densities, is also clearly observed. Experimental results are compared to fully kinetic large-scale, two-dimensional simulations. Particle-in-cell results, beyond reproducing the framework delineated by the experimental measurements, reveal the importance of filamentation instability in ruling the onset of SRS and stimulated Brillouin scattering instabilities and confirm the crucial role of collisionless absorption in the LPI energy balance.

Keywords: plasma simulations; shock ignition; stimulated Raman scattering; two-plasmon decay

Correspondence to: G. Cristoforetti, Istituto Nazionale di Ottica, CNR, Area della Ricerca di Pisa, Via Moruzzi 1, 56124 Pisa, Italy.
Email: g.cristoforetti@cnr.it

1. Introduction

Laser–plasma interaction (LPI) at intensities $\sim 10^{16} \text{ W} \cdot \text{cm}^{-2}$ is a regime of interaction dominated by parametric instabilities, where collisional absorption begins to turn off and non-collisional laser-driven instabilities – mainly stimulated Brillouin scattering (SBS), stimulated Raman scattering (SRS) and two-plasmon decay (TPD) – begin to dominate the scene. The growth of such instabilities results partly in laser absorption in the underdense plasma and partly in energy loss by inelastic light scattering (SBS, SRS). In addition, some of these instabilities (SRS and TPD) generate nonthermal ‘hot’ electrons (HE), capable of escaping the plasma, and carrying a relevant fraction of the laser energy. The strong nonlinearity of these mechanisms, the role of electron kinetic effects in their growth/damping and their mutual interplay, often giving rise to daughter instabilities, make it very hard to accurately depict the interaction scenario. Moreover, this aim is complicated by the impact of local conditions of interaction – varying in lengths of the order of the speckle size ($\sim \mu\text{m}$) – and by the characteristic time of growth/damping – typically shorter than one picosecond – in plasmas which usually have dimensions of the order of 1 mm and are produced by high-energy lasers with duration of $\sim 0.1\text{--}1$ ns.

The interest in this interaction regime mainly concerns the physics of inertial confinement fusion (ICF), where the laser–plasma coupling and the generation of HE can considerably affect the implosion of the fuel pellet. In particular, accurate knowledge of parametric instabilities is crucial in the shock ignition (SI) concept^[1], where ignition is produced by a strong shock driven in a pre-formed millimetre-size plasma corona by a short spike (300–500 ps) at intensity $\sim 10^{16} \text{ W} \cdot \text{cm}^{-2}$. These interaction conditions, in fact, notably enhance the extent of parametric instabilities with respect to conventional direct-drive ICF schemes, where the laser intensity is a factor of ten to twenty lower. A further peculiarity of shock ignition is the role played by HE produced by the shock-driving spike in achieving ignition conditions. In fact, HE produced during the compression phase in conventional (direct-drive) ICF schemes are detrimental, because they preheat the fuel, increasing its entropy and therefore preventing its compression. In contrast, in SI, HE produced by the SI spike are generated at the end of the compression phase, when the target areal density $\langle \rho r \rangle$ is already large enough to stop the less energetic of them; in this way, they deliver their energy in the compressed corona layer, providing an extra pressure, possibly improving the compression^[2–5]. Only the most energetic HE are expected to reach the pre-compressed fuel and enhance the fuel temperature^[6], before the arrival of the shock driven by the laser spike. In order to assess the compression performance in SI, it is therefore decisive to investigate the amount and, above all, the energy distribution of HE. This task is strictly

related to the investigation of the HE sources, mainly SRS and TPD instabilities, which produce HE with different energetic spectra and with different angular distributions. SRS usually generates HE of some tens of keV, with energy mainly depending on the density region where SRS is excited. TPD provides instead a hotter (and potentially detrimental) component, often temperatures in excess of 100 keV, by a staged acceleration mechanism occurring close to the quarter critical density region^[7].

Most of the experiments devoted to investigating LPI for ICF studies have been carried out at intensities of $\lesssim 10^{15} \text{ W} \cdot \text{cm}^{-2}$, mainly by using 351 nm laser light, in conditions relevant for conventional direct- or indirect-drive ICF schemes^[8,9]. Due to the nonlinearity of the processes, extrapolating these results to laser intensities typical of SI is infeasible. On the other hand, the experimental investigation of parametric instabilities in SI conditions is hard, since it requires the interaction of a sub-ns pulse at intensity $\sim 10^{16} \text{ W} \cdot \text{cm}^{-2}$ with a millimetre-size and hot ($T_e > 4$ keV) plasma. Such conditions are presently attainable only at very large laser installations, such as the National Ignition Facility (NIF)^[10] and the Laser MegaJoule (LMJ) facility^[11], which were designed for indirect-drive ICF.

A full numerical investigation of LPI in SI conditions is also impracticable because of the huge computational costs due to the large plasma size; therefore, 2D particle-in-cell simulations of LPI in this regime are presently limited to an interaction time of a few picoseconds (that is, a time much shorter than the duration of the shock ignition spike). It is worth remarking that 2D and 3D simulations are needed to model laser filamentation, spraying, cavitation and side scattering, which can be important in the SI regime. Advanced fully kinetic PIC simulations^[12–14] reveal the importance of nonlinear and kinetic effects, of secondary decay processes and of competition/interplay between parametric instabilities, where all these processes govern the instability growth and make the outcome hard to predict. After a linear stage of growth, electron plasma waves (EPWs) and ionic acoustic waves (IAWs), driven respectively by SRS and SBS, enter in a nonlinear evolution, resulting in consecutive stages of damping and excitation, leading to a burst-like behaviour. In the case of EPWs, this behaviour can be produced by the ponderomotive trapping of thermal electrons or by the bowing and filamentation of EPWs into the laser speckles^[15,16], resulting in a phase detuning of the waves^[17] and finally in an SRS pattern of picosecond or sub-picosecond bursts. Simulations also reveal the possibility of competition between instabilities, usually ruled by laser pump depletion or because they are driven in the same density region. Particularly important is the competition between SRS and TPD in the region close to $n_c/4$, because of its impact on the energy and amount of HE generated. Recent 2D PIC simulations by Xiao *et al.*^[18] and by Weber *et al.*^[19] showed that

SRS and TPD can dominate over each other, depending on the laser intensity, density scalelength and overall plasma temperature. It is shown that the absolute SRS instability begins to dominate the scene at $n_c/4$ density at temperatures higher than ~ 5 keV (that is, in conditions close to SI). Klimo *et al.*^[12, 13] showed also the occurrence of cavitation near $n_c/4$, resulting in a considerable absorption of laser energy and in the damping of TPD instability driven at higher plasma densities. Particular attention should be paid to stimulated Raman side scattering (SRSS), the coupling geometry where light is scattered at angles near 90° , is then refracted towards lower densities, and finally exits the plasma at large angles with respect to laser incidence. It is well known that basic theory predicts that SRSS has the lowest threshold in inhomogeneous plasmas because of the large resonant region along the transverse direction. Despite that, very few experiments have shown evidence of SRSS, which was usually explained by the large collisional absorption of side-scattered light. A recent work by Xiao *et al.*^[20] revisited the theory of SRSS, including the effect of the laser beam width on the threshold of the instability, which could explain the scarcity of experimental evidence of SRSS. According to Xiao *et al.*, SRSS, preferentially driven at low plasma densities where collisional absorption is low, can however be strong and compete with backward SRS at SI intensities, resulting in the scattering of a significant amount of laser energy.

To date, only a few experiments on LPI at SI-relevant intensities have been carried out in moderate kilojoule-class laser facilities, as for example at OMEGA^[2, 3, 21], LULI^[22, 23] and PALS^[24–26]. Due to the lower available energy, typical SI interaction conditions were relaxed, typically resulting in colder (~ 1 – 2 keV) or in shorter ($L = n_e/(dn_e/dx) \sim 100 \mu\text{m}$) inhomogeneous plasmas or otherwise in shorter laser pulses. Such experiments are unable to fully reproduce the expected LPI in the SI regime but are anyway necessary to investigate the effects of different experimental parameters on the growth of parametric instabilities and on HE generation, so that a scaling to real SI conditions becomes more reliable, in view of future full-scale SI experiments. These experiments showed that the energy lost during the interaction – due to laser reflection, SBS and SRS – can reach 40%–50% of the laser energy, depending on the irradiation geometry and on the laser intensity. Among these processes, SBS and laser back-reflectivity are usually of the order of $\sim 10\%$, rising to $\sim 20\%$ when full-aperture scattering is accounted for^[27]. Conversely, the variability of SRS reflectivity is much larger, going from a fraction of a percent, obtained in experiments using a planar geometry of interaction^[22, 27, 28], up to 36%, obtained in spherical irradiation experiments^[3, 21]. Experiments seem to suggest that SRS is the main source of HE, reaching conversion efficiencies up to $\sim 9\%$ of laser energy in spherical irradiation conditions^[3]; recent experiments

carried out at OMEGA showed that such large HE fluxes can significantly contribute to the ablation pressure^[2], providing an extra pressure as large as $\sim 30\%$.

In recent years, we investigated LPI and shock generation at the Prague Asterix Laser System (PALS) facility by using a 300 ps laser pulse at $3\omega_0$ irradiation ($\lambda_0 = 438$ nm). The laser energy of ~ 250 J enabled irradiation of a ~ 2 keV plasma with scalelength $L = n_e/(dn_e/dx) \sim 100 \mu\text{m}$, at a maximum laser intensity of $\sim 6 \times 10^{15} \text{ W} \cdot \text{cm}^{-2}$. Experimental data yielded a detailed description of the extent and timing of parametric instabilities^[29, 30], in particular of SRS, and enabled us to establish a correlation with the measured HE energy distribution.

In this paper we investigate LPI and HE generation of the full energy (~ 650 J) PALS laser pulse at $1\omega_0$ irradiation ($\lambda_0 = 1314$ nm), resulting in a maximum intensity of $\sim 1.2 \times 10^{16} \text{ W} \cdot \text{cm}^{-2}$, a value seldom reached in experiments. In such irradiation conditions the plasma is heated to a temperature in excess of 4 keV, which is crucial for our studies because of the strong temperature dependence of the threshold and the damping of parametric instabilities (and therefore their respective weights), of the density where they are driven, and finally of the HE energy distribution. Moreover, the use of infrared laser light resulted in an even larger value of laser irradiance $I\lambda^2 \approx 2 \times 10^{16} \text{ W} \cdot \mu\text{m}^2 \cdot \text{cm}^{-2}$, enhancing ponderomotive effects on quivering electrons and nonlinear effects in their dynamics. We therefore believe that the interaction regime explored here gives valuable information for the understanding of LPI in SI conditions. Besides, it is worth noting that while conventional ICF schemes make use of ultraviolet (3ω) lasers, in the shock ignition scheme 2ω or even 1ω lasers could in principle be considered for the final irradiation spike driving the strong shock^[31].

2. Experimental setup

The laser pulse (300 ps), used in the fundamental mode ($\lambda_0 = 1314$ nm), was smoothed by a random phase plate and focused at normal incidence on a flat thin target by a $f/\#2$ optical system. Laser energy ranged from 630 to 660 J. Accurate imaging and calorimetry were set up to measure the effective energy enclosed in the $100 \mu\text{m}$ full-width at half-maximum (FWHM) Gaussian focal spot and to calculate the peak laser intensity $I = 1.2 \times 10^{16} \text{ W} \cdot \text{cm}^{-2}$.

Thin multilayer targets were used. The front layer, namely the interaction layer, with thickness ranging from 10 to $180 \mu\text{m}$, was made of Parylene-C plastic, to mimic the low-Z ablation layer in ICF targets. A ‘tracer’ layer of titanium, $10 \mu\text{m}$ thick, was used to characterize the HE propagating into the target through K_α spectroscopy. A final $25 \mu\text{m}$ thick Al layer was used for the measurement of shock breakout time, with the purpose of estimating shock velocity and

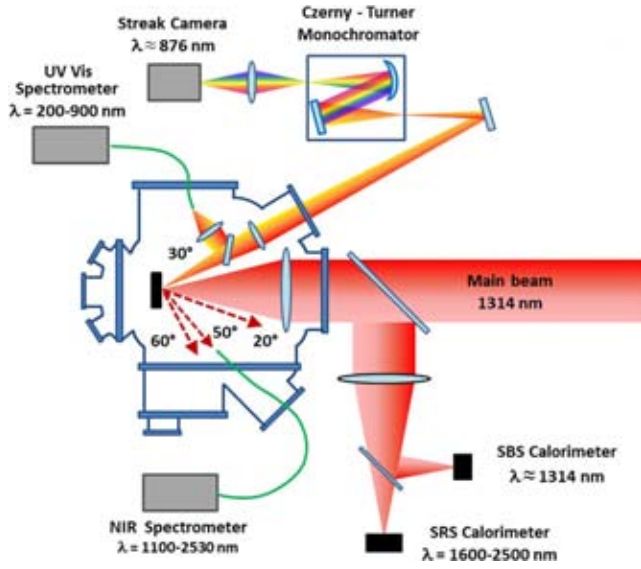


Figure 1. Experimental setup used for the investigation of parametric instabilities.

driving pressure. A companion paper describing results of shock hydrodynamics is in preparation^[32].

A scheme of the optical diagnostics used for investigating the parametric instabilities is reported in Figure 1. The backscattered light collected by the focusing lens was spectrally filtered and characterized by two calorimeters. One of them measured the energy backscattered in the spectral range around $\lambda \approx 1314$ nm, due to laser reflection and SBS, and the other measured the energy in the range 1600–2500 nm, due to SRS. The retrieval of backscattered energy was made possible by an accurate calibration of the spectral transmission of the optical line in the infrared range. Light scattered by SRS outside the cone of the focusing lens was also collected by means of an $f/\#7$ optical system, at angles spanning from $\sim 20^\circ$, close to the backscattering cone, to 62° , and sent to a near-infrared (NIR) spectrometer NIRQuest Ocean Optics via an IR low-OH optical fibre. The spectral range covered by the NIR spectrometer was 1100–2530 nm, thus excluding the $\omega_0/2$ light at $\lambda = 2628$ nm and the longer wavelengths. Light emission in the UV–Vis range, including harmonics and half-harmonics of laser light, was collected by means of an $f/\#8$ optical system at an angle of 30° . A pick-off reflection from this line was conveyed by an optical fibre to an additional Ocean Optics spectrometer, covering the spectral range 200–900 nm. The remaining part of the light was spectrally dispersed by a Czerny–Turner monochromator, and relayed onto the entrance slit of a Hamamatsu C7700 optical streak camera. This setup allowed time-resolution of the $3/2\omega_0$ harmonics, in a spectral window of 60 nm at a maximum temporal resolution of 25 ps, calculated by considering the temporal spread produced by the spectrometer^[33] and the time resolution of the streak camera. As will be shown

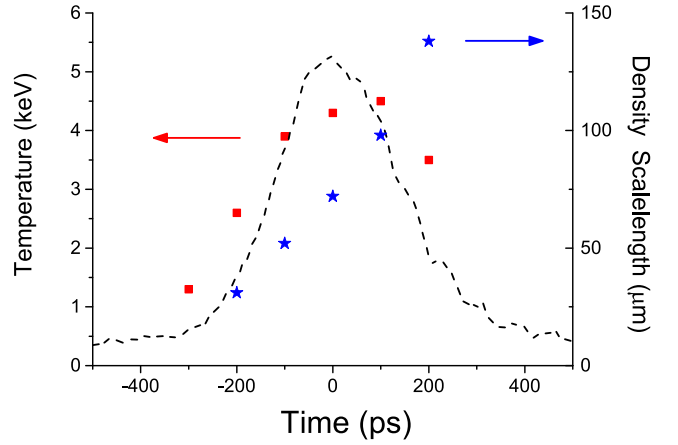


Figure 2. Instantaneous values of electron temperature T_e (red squares) and density scalelength L (blue stars) in the density range $0.05\text{--}0.25 n_c$, as obtained by CHIC hydrosimulations in the experimental conditions of the interaction. The dashed line indicates the laser pulse profile.

below, half-harmonics of laser light reveal information on the timing of both TPD and SRS.

K_α emission of titanium was produced by the collisions of HE with the Ti tracer layer, resulting in the $2p \rightarrow 1s$ K-shell fluorescence. K_α spectroscopy was carried out by using a spherically bent crystal of quartz (211) and image plates (BAS-MS), or alternatively Kodak AA400 X-ray film, as detectors. The spectral resolution of the line profile allowed us to subtract the continuum background emission, mainly due to Bremsstrahlung and recombination continuum. A Bremsstrahlung cannon spectrometer (BCS) using K-edge and differential filtering (14 filters of increasing Z from Al to Pb) was also used with imaging plates to measure the X-ray spectrum and, indirectly, calculate the temperature of the HE distribution. The BCS was looking at the front side of the target at 30° from the laser axis.

3. Interaction conditions

The plasma density where parametric instabilities are driven and their timing depend on local and instantaneous plasma conditions (temperature and density scalelength) and the laser intensity. Interaction conditions were modelled by radiative-hydrodynamic simulations carried out with the codes CHIC^[34] and DUED^[35]. In the CHIC code, the onset of SRS and TPD processes as well as the generation of HE was also implemented^[36] by means of appropriate scaling laws and using local and instantaneous values of laser intensity and plasma parameters. The code, therefore, accounts for the interplay between TPD/SRS and the hydrodynamics of the plasma.

The resulting values of electron temperature and density scalelength $L = n_e/(dn_e/dx)$, in the density range of interest for TPD and SRS instabilities ($0.05\text{--}0.25 n_c$), are plotted in

Figure 2 at different interaction times. While the plasma temperature reaches the maximum value approximately a hundred picoseconds after the laser peak, and successively falls, the density scalelength monotonically increases till the end of the interaction. Simulations show that collisional absorption is only $\sim 9\%$, due to the high intensity and the long wavelength of the laser (high $I\lambda^2$). The energy converted into HE is also a few percent ($\epsilon_{HE}^{TPD} = 1.1\%$, $\epsilon_{HE}^{SRS} = 2.3\%$), suggesting that non-collisional absorption by parametric instabilities is comparable to collisional absorption. It is worth noting that the extent of parametric instabilities is certainly underestimated by the code, as side-scattering SRS, inflationary and secondary scattering processes are neglected. Also, due to the scarcity of experimental results for infrared laser light, scaling laws in this regime should be taken with caution. According to the model implemented in CHIC, the temperature of the two HE populations is 39 keV for SRS and 83 keV for TPD. In the experiment, the HE energy distribution was estimated by the measurements of K_α and Bremsstrahlung X-ray emission. Experimental data of K_α emission could be satisfactorily reproduced with GEANT4 Monte Carlo simulations by using a two-temperature distribution for the HE energy, with temperature values of 40 keV and 85 keV, in agreement with the values given by CHIC simulations. The experimental calibration of the reflectivity of the crystal used for the Ti K_α spectroscopy also allowed us to calculate the energy conversion efficiency of HE, giving $\epsilon_{HE} = 5.3\% \pm 2\%$. Further details on the experimental HE characterization in this experiment can be found in a companion paper, now in preparation^[32].

The plasma conditions, determined by plasma hydrodynamics, and the resulting interaction scenario depicted above, can be significantly modified by considering micrometre-scale variations of temperature and density, which are produced by the profile smoothing of the laser beam. The use of a random phase plate, in fact, limits the longitudinal and the transverse spatial coherence of the beam, subdividing the profile into small beamlets with random phases; according to simple calculations^[37], in our experimental conditions this gives rise to the formation of $\sim 10^4$ speckles of size $3.2 \mu\text{m} \times 3.2 \mu\text{m} \times 14 \mu\text{m}$ in the focal volume. The expected intensity distribution in the speckle ensemble, produced by the interference of the various beamlets^[38], is exponential $f(I) \propto \exp(-I/I_{av})/I_{av}$, where I_{av} is the average laser intensity, which results in a tail of local high intensities reaching $\sim 10^{17} \text{ W} \cdot \text{cm}^{-2}$ in a fraction of the speckles. Local laser power into the speckles is therefore 1–10 GW – that is, well above the critical power for ponderomotive filamentation ($P_c \approx 0.2\text{--}0.6 \text{ GW}$ at relevant plasma temperatures^[39]). This implies that filamentation is rapidly driven into the speckles, further enhancing the local laser intensity and plasma temperature and modifying the plasma density profiles, in times of the order of a few picoseconds. Filamentation instability is therefore expected to strongly affect the

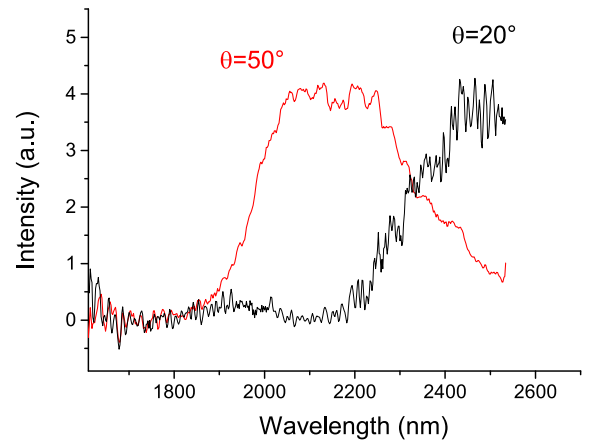


Figure 3. Typical time-integrated SRS spectra acquired at $\theta = 20^\circ$ (BRS) and $\theta = 50^\circ$ (SRSS).

onset and growth of parametric instabilities. Ponderomotive filamentation, not included in the CHIC simulations, is here investigated by particle-in-cell (PIC) simulations of LPI carried out with plasma parameters (density, temperature) defined by hydrosimulations, as shown in the following.

4. Reflectivity, backward- and side-stimulated Raman scattering

Light backscattered in the focusing cone was dominated by laser reflection and SBS light ($\lambda \approx 1314 \text{ nm}$), consisting of 14%–20% of the laser energy, where the relative fractions of SBS and laser light could not be determined. A significant fraction of laser energy $\sim 0.6\%$ –4% consisted also of light back-reflected in the spectral range 1600–2500 nm. This radiation was produced by convective backward SRS (BRS) occurring at densities lower than $n_c/4$. Infrared light at longer wavelengths, including $\omega_0/2$ light due to absolute SRS driven at $n_c/4$ density, could not be quantified because of the poor transmissivity of the backscattering optical line.

Typical time-integrated spectra of SRS scattered light up to $\lambda = 2530 \text{ nm}$ acquired at different angles are reported in Figure 3. Due to the small $f/\#$ of the focusing lens, the spectrum measured at $\theta = 20^\circ$, very close to the focusing cone, is likely comparable to the BRS spectrum. Considering a plasma temperature of $\sim 4 \text{ keV}$, as given by hydrosimulations for times close to the laser peak, the measured emission originates from BRS driven in the range of densities 0.14–0.20 n_c , with a probable maximum emission coming from $n_e \approx 0.17\text{--}0.18 n_c$ (Figure 4). It is worth noting that the spectra acquired by the IR spectrometer do not allow one to determine the highest density where BRS is driven, because of the limited spectral range of our IR spectrometer. However, temperature values of $\sim 4 \text{ keV}$ fix the maximum density to $\sim 0.23 n_c$ – that is, close to the density where absolute TPD/SRS is also driven (see section

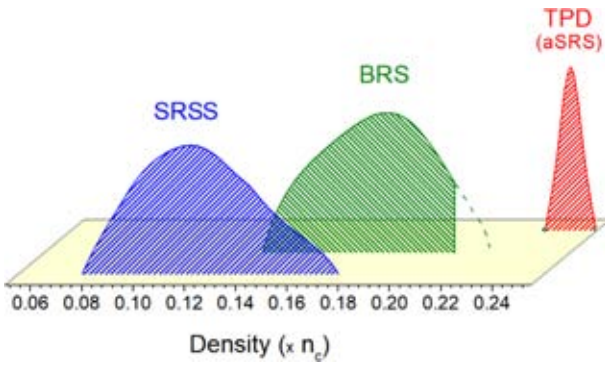


Figure 4. Scheme of regions of density where parametric instabilities are driven.

below). Moreover, streaked spectra shown in Section 6, acquired at a slightly larger angle (30°) confirm that the stronger SRS emission comes from the $n_e \approx 0.17\text{--}0.18 n_c$ region (later in Figure 7). Since the Landau cutoff condition for large damping, $k_e \lambda_D \approx 0.3$, corresponds to densities of $\sim 0.13 n_c$ ($\lambda_{SRSS} \approx 2200$ nm, $k_e = 1.41 \omega_0/c$) and $\sim 0.15 n_c$ ($\lambda_{SRSS} \approx 2350$ nm, $k_e = 1.32 \omega_0/c$), for plasma temperatures of 3 keV and 4 keV, respectively, it is evident that BRS is limited by this effect in the low-plasma-density region. In this way, Landau damping limits the BRS growth to higher densities when plasma temperature is large. This feature agrees with the shift of the BRS peak region from $0.12 n_c$ to $0.18 n_c$, obtained by comparing the results in shots at $3\omega_0$ irradiation^[30], where maximum plasma temperature was 2–2.5 keV, with the ones obtained in the present work.

While the IR spectra acquired at $\theta = 62^\circ$ did not show any appreciable emission, the ones acquired at $\theta = 50^\circ$ (Figure 3) showed evidence of SRSS, suggesting that this instability was driven at lower plasma densities and fell at higher densities where BRS became dominant. According to the spectra, SRSS was driven at densities $0.08\text{--}0.17 n_c$, with a maximum growth rate around $n_e \sim 0.12 n_c$ (Figure 4). Considering light refraction across the density distribution obtained by CHIC simulations, SRSS light was emitted at an angle $65^\circ < \theta' < 90^\circ$, in agreement with the PIC simulations of Xiao *et al.*^[20]. The side-scattered EPWs excited at the lower densities ($\lambda_{SRSS} \approx 2000$ nm, $k_e = 1.12 \omega_0/c$) correspond to $k_e \lambda_D \approx 0.3$ for a plasma temperature $T_e \approx 4$ keV, as expected at times near the laser peak; this suggests that SRSS, as BRS, is limited at lower densities by Landau damping.

A deeper insight into the experimental data can be obtained by calculating the thresholds of BRS and SRSS at the densities of interest. According to Liu *et al.*^[40], the BRS threshold can be expressed by $(v_0/c)^2 > 1/(k_0 L)$, where v_0 is the quiver velocity of an electron in the laser field and L is the density scalelength. Taking $L = 75 \mu\text{m}$, i.e. the expected scalelength value at the laser peak and $k_0 = (\omega_0/c)\sqrt{1 - (\omega_p/\omega_0)^2} \approx 0.98(\omega_0/c)$, corresponding

to the density $n_e/n_c = 0.18$, given by the spectral peak in the BRS spectrum, we obtain the threshold intensity $I_{BRS} > 2.7 \times 10^{15} \text{ W} \cdot \text{cm}^{-2}$. This value is approximately six times lower than the average intensity at the laser peak, and much lower than the local intensity expected from filamentation and in high-intensity speckles. For calculating the SRSS threshold, as pointed out by Xiao *et al.*^[20], we have to account for the finite beam size that limits the instability gain growing in the transverse direction. This mechanism results in a threshold much higher than the classical one and can explain why SRSS is seldom observed in the experiments. According to Ref. [20], in our case the threshold can be expressed as

$$\frac{v_0}{c} > 40 \left(\frac{V_{cs}}{D} \right) \left(\frac{\omega_0 - \omega_p}{\omega_p} \right)^{1/2} \left(\frac{1}{k_e c} \right), \quad (1)$$

where D is the focal spot diameter, k_e is the EPW wavevector and V_{cs} is the convective velocity of scattered light into the transverse direction. In turn $V_{cs} = c^2 k_s / \omega_s$, where the subscript s refers to the scattered light. By taking $D = 100 \mu\text{m}$ and $n_e/n_c = 0.12$, as obtained in the experiment, we obtain an intensity threshold $I_{SRSS} > 6.3 \times 10^{15} \text{ W} \cdot \text{cm}^{-2}$, which is overcome during the interaction. We have to consider that convective SRSS grows while the scattered light propagates transversally through many speckles; it is therefore more correct to consider the average laser intensity and not the local intensity, which can be somewhere higher. This threshold is quite large, suggesting that it was not probably overcome in many of the experiments devoted to ICF, which explains why SRSS was not observed except in very few works. This also suggests that in SI conditions SRSS may result in a significant amount of energy scattered at large angles and should be taken into account. It is interesting also to calculate the SRSS threshold intensity at higher densities, where BRS is observed to dominate in the experiment. By taking the density $n_e/n_c = 0.18$, considered above for the BRS, we obtain an SRSS threshold $I_{SRSS} > 4 \times 10^{15} \text{ W} \cdot \text{cm}^{-2}$. Despite this value being overcome during the interaction, it is clear that the SRSS gain at this density is lower than the BRS gain. Furthermore, while the envelope laser intensity has to be considered for SRSS, the local intensity given by filamentation and by the high-intensity tail into the speckles has to be considered for BRS. This is due to the fact that convective BRS instability grows in the longitudinal direction – that is, along and not across the speckles. These considerations make it clear that, at higher plasma densities, BRS modes are strongly favoured and damp the SRSS modes. This is in agreement with the experimental results.

5. Half-integer harmonic spectra

A valuable tool for investigating TPD and SRS is the observation of half-integer harmonic spectra, produced by the

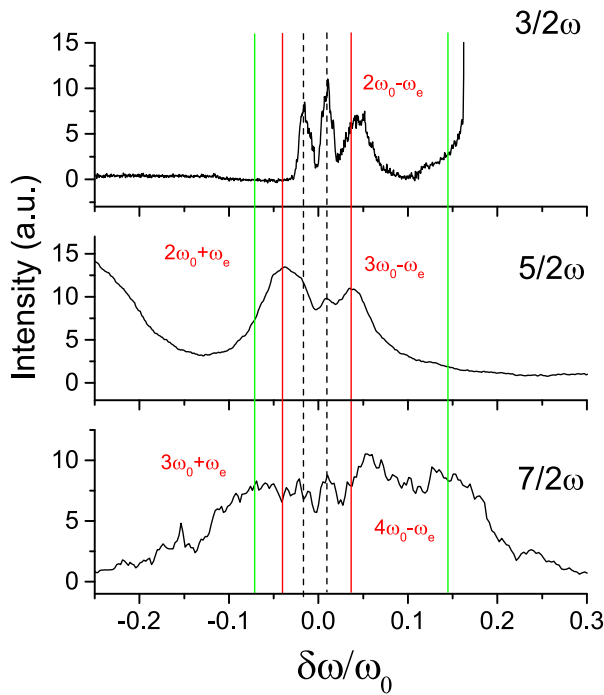


Figure 5. Time-integrated half-integer harmonic spectra plotted versus the shift with respect to their nominal frequency. Dashed, red and green lines correspond to the peaks produced by Thomson scattering with EPWs driven by TPD, BRS and SRSS, respectively.

nonlinear coupling of laser light (ω_0) or integer harmonics ($2\omega_0, 3\omega_0, \dots$) with EPWs driven by the instabilities. A UV–Vis time-integrated spectrometer allowed us to measure $3/2\omega_0$, $5/2\omega_0$ and $7/2\omega_0$ spectra, which will be discussed in the present section. In the next section, the time-resolved spectrum of $3/2\omega_0$, acquired with an optical streak camera, will be discussed.

All the half-integer harmonic spectra exhibited several peaks, produced by different instabilities or by instabilities driven at different densities. In Figure 5 time-integrated half-integer harmonic spectra are plotted versus the shift with respect to their nominal frequency, for a fruitful comparison of the spectral position of the different peaks. Spectra refer to the same shot of the BRS spectrum reported in Figure 3. The two inner peaks (dashed lines), clearly visible in the $3/2\omega_0$ spectrum and just appearing in higher-order half-integer harmonics, are produced by Thomson scattering of the laser light and higher laser harmonics with the EPWs driven by TPD or absolute SRS (aSRS) instabilities at densities close to $n_c/4$. The double-hump structure of the $3/2\omega_0$ emission is usually considered as a spectral signature of the TPD instability. In principle, however, it could also be generated by the presence of both Thomson up-scattering of laser light ($\omega_0 + \omega_e$) and Thomson down-scattering of the $2\omega_0$ light ($2\omega_0 - \omega_e$) with the EPW generated by absolute SRS instability. According to the theory, when driven at $n_e \approx n_c/4$ as in the present experiment (see below), TPD and SRS can also coalesce in

a hybrid TPD/SRS instability^[41], as claimed in the interpretation of some experimental works^[42]. In the conditions of temperature and density profiles expected in this experiment, the threshold of TPD is lower than that of absolute SRS, therefore suggesting a faster growth of the former instability, leading to a prevalence of TPD or eventually to a hybrid instability rather than to a pure aSRS. The frequency shift of TPD blue and red EPWs from the central frequency shift $\omega_0/2$ is given by $|\delta\omega|/\omega_0 = (9/4)(v_{th}^2/c^2)\kappa$, where $\kappa = \mathbf{k}_B \cdot \mathbf{k}_0/k_0^2 - 1/2$, \mathbf{k}_B is the blue EPW wavevector and v_{th} is the thermal velocity. For large plasma temperatures, corrections to this formula should be applied by considering the relativistic modification of the Langmuir wave dispersion relation^[18]. Detailed calculations for a plasma temperature $T_e \approx 3\text{--}4$ keV, as given by hydrosimulations at times close to the laser peak, show that the measured frequency shift of these peaks, $\delta\omega/\omega_0 = (0.5\text{--}1.5) \times 10^{-2}$, corresponds to absolute TPD driven at densities $n_e \approx 0.245 n_c$ (Figure 4). A similar density would be obtained by considering absolute SRS and SRS/TPD hybrid modes, since in all the cases $k_e \approx k_0$. More details on the timing of such instabilities will be provided by time-resolved spectra, discussed in the next section. The peaks at larger shifts cannot be produced by TPD EPWs, since they would be strongly Landau damped at the expected plasma temperatures ($k_e \lambda_D \approx 0.4\text{--}0.8$). The only possibility is that such peaks were produced by Thomson scattering of integer-harmonic light ($2\omega_0, 3\omega_0, 4\omega_0$), strongly visible in the acquired spectra, with the EPWs driven by backward- and side SRS. The generation of $2\omega_0$ and higher harmonics is usually associated to the nonlinear interaction of laser light with plasma waves excited near the critical density, and depends critically on plasma steepness, laser intensity and laser polarization^[43, 44]; the presence of such peaks is therefore indirect evidence that a fraction of laser light reaches the critical density surface. The coupling combinations are reported in Figure 5, where the peaks on the blue side of the nominal half-harmonic frequencies are produced by Thomson down-scattering, while the peaks on the red side are due to Thomson up-scattering processes. It is worth noting that the spectral profile of the different peaks is strongly affected by the geometrical matching conditions, such as the angle of acquisition ($\theta = 30^\circ$), the angle of EPW propagation and the direction of propagation of matching integer-harmonic light. In this way, geometrical parameters result in a distortion of the real spectral distribution of EPWs driven by SRS at different plasma densities. Coupling effects can therefore explain the discrepancies between the corresponding peaks in the different half harmonics. In some cases, a small EPW propagation can improve the matching of light and EPW wavevector; in other cases, Thomson scattering with secondary EPWs produced by Langmuir decay instability (LDI), which could be easily driven in these interaction conditions, could also generate the observed half-harmonic peaks. A typical scheme of

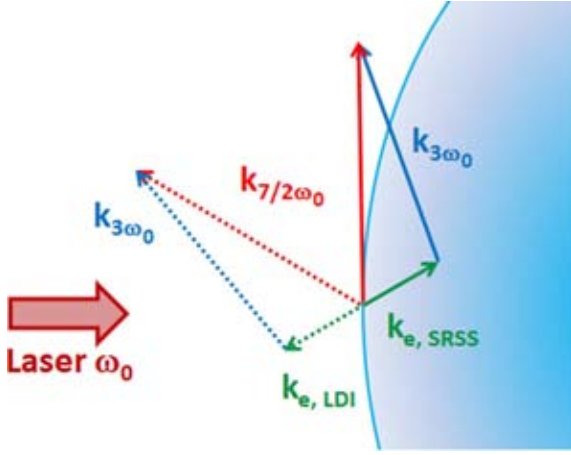


Figure 6. Geometry of the Thomson up-scattering of $3\omega_0$ harmonic light with the EPW driven by SRSS at $n_e \approx 0.12 n_c$. The dotted vectors refer to the up-scattering geometry involving the secondary EPW produced by LDI.

Thomson scattering geometry is sketched in Figure 6; it refers to the up-scattering process of $3\omega_0$ harmonic light with the EPW driven by SRSS at $n_e \approx 0.12 n_c$, resulting in the generation of $7/2\omega_0$ light. In this case, it is evident that the scattering geometry involving the secondary EPW produced by LDI, represented by dotted vectors, easily generates $7/2\omega_0$ light more compatible with the angle of observation of the spectrometer ($\theta = 30^\circ$). The refraction of the light across the density plasma profile, probably also including density fluctuations, could however strongly mitigate the geometrical constraints due to matching conditions, making it quite hard to determine the occurring processes.

The blue-side feature in the $3/2\omega_0$ spectra (right red line) is clearly visible also in $5/2\omega_0$ and $7/2\omega_0$ spectra and is peaked at a shift $\delta\omega/\omega_0 \approx 0.03$ – 0.05 . This feature is produced by Thomson down-scattering of $2\omega_0$ light (and of $3\omega_0$ and $4\omega_0$ light in the corresponding $5/2\omega_0$ and $7/2\omega_0$ spectra) by SRS EPWs with energy $\omega_e \approx 0.45$ – $0.47 \omega_0$. Such EPWs, in turn, correspond to backscattered SRS light peaked at $\lambda \approx 2400$ – 2480 nm, which is exactly the spectral range of the peaks observed by the IR spectrometer (black curve in Figure 3). This is a confirmation that such a peak is produced by the light coupling with BRS EPWs, driven at densities $n_e \approx 0.17$ – $0.18 n_c$. The same EPWs give rise to the left red peak (with the same shift) in the $5/2\omega_0$ spectra (left red line) by Thomson up-scattering of $2\omega_0$ light. It can also be seen that the red peak with the same shift, due to the combination ($\omega_0 + \omega_e$), is not visible in the $3/2\omega_0$ spectrum plotted in Figure 5; in other shots, the peak is visible but it is usually less intense than the corresponding blue one. To be observed at an angle of 30° , SRS EPWs should match with laser light ω_0 propagating almost perpendicularly to the laser incidence direction; the absence or low intensity of this peak can thus possibly be explained by the scarcity of laser light which is side-scattered in the plasma.

The spectrum of $7/2\omega_0$ exhibits light emitted with much larger frequency shift values, $-0.12 < \delta\omega/\omega_0 < 0.18$. This emission, labelled with green lines in Figure 5, is produced by Thomson scattering of $3\omega_0$ and $4\omega_0$ light with EPWs generated by SRS at low plasma densities. The extreme values of frequency shift correspond to EPWs with energy $\omega_e \approx 0.35$ – $0.38 \omega_0$, giving rise to scattered SRS light with $\lambda \approx 2000$ – 2100 nm. These wavelengths correspond to the edge of the red spectrum in Figure 3, suggesting that these features are produced by Thomson scattering with EPWs at low densities (0.08 – $0.17 n_c$) driven by SRSS. Peaks originating from SRSS at low plasma densities are absent in $3/2\omega_0$ and $5/2\omega_0$ spectra. It can be shown that $2\omega_0$ and $3\omega_0$ light propagating in the low-density region at large angles ($\theta > 55^\circ$) is needed to produce such features, while these constraints are relaxed for the formation of $7/2\omega_0$ SRSS peaks. We therefore speculate that the scarcity of large-angle scattered light can explain the experimental results.

6. Timing of TPD and SRS instabilities

Time-resolved spectroscopy of three-halves harmonics is here used for investigating the growth of TPD and BRS along the plasma density profile. Two distinct spectra are reported in Figure 7, showing typical features observed in the various shots. The spectra obtained by the intensity lineout in the different windows reported in the figure clearly exhibit the presence and the temporal evolution of the peaks already discussed in the previous section.

The two peaks produced by EPWs at density close to $n_c/4$ due to TPD (or hybrid TPD/aSRS) with the smaller shift with respect to $\lambda = 876$ nm, begin to grow ~ 100 – 150 ps before the laser peak (yellow dashed line in the figure) – that is, in the leading part of the pulse. An accurate analysis of the splitting of these peaks at early times suggests that such instability begins to grow at a density $n_e \approx 0.247 n_c$ when the temperature is around 2 keV. After the onset of the instability, the distance between the peaks increases with time; this shift is mainly produced by the growth of the plasma temperature and by a migration of TPD (or hybrid TPD/aSRS) to slightly lower densities ($n_e \approx 0.244 n_c$). The maximum splitting of the peaks is compatible with TPD (or hybrid TPD/aSRS) driven at a temperature of ~ 3.5 – 4 keV, which is close to the value given by CHIC simulations at times before the laser peak. The instability is finally damped at times close to the laser peak or a few tens of picoseconds after it, depending on the shot.

At times comparable to the disappearance of the TPD peaks, the peak produced by convective BRS becomes visible. In some shots, as shown in Figure 7 left, absolute instabilities at $\sim n_c/4$ and convective BRS coexist for a few tens of picoseconds. Since Landau damping of TPD/aSRS EPW is here low ($k_e \lambda_D \approx 0.14$), the data suggest that the instability is damped by laser pump depletion due to BRS

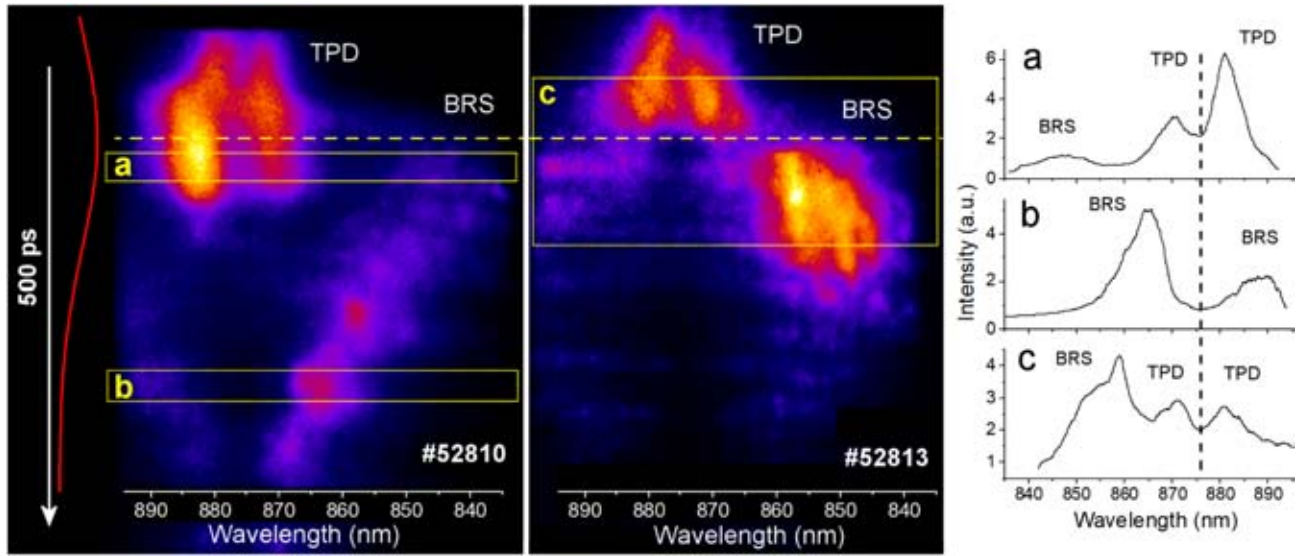


Figure 7. Time-resolved $3/2\omega_0$ spectra. The time spanned across the vertical axis is 500 ps, with a time resolution of 25 ps. The laser pulse profile is indicated by the red curve and the peak time by the yellow dashed line. The spectra on the right are obtained by the lineout in windows a, b and c.

growth at lower densities. In some shots, a corresponding red-shifted peak, produced by $\omega_0 + \omega_e$ coupling, is visible in streaked images; this peak is usually less intense than the blue one, as shown for example by the spectrum b in Figure 7. Time-resolved spectra show also that BRS is present during all the trailing part of the laser pulse, often in visible bursts, and persists at late times. As already discussed in Ref. [30], this is made possible by the increase of the density scalelength of the plasma at late times, which compensates the fall of laser intensity.

Another interesting piece of information is that BRS is initially driven as convective instability at a lower plasma density, corresponding to the lower wavelength edge of the BRS spectrum in Figure 3, and successively moves to higher densities. This can be clearly observed in #52810 and by comparing the blue-shifted peaks in spectra a and b in Figure 7. In the tail of the laser pulse BRS reaches the plasma region close to $n_c/4$ and is finally damped.

Now that local conditions (density, time) where SRS and TPD are driven have been discussed, it is possible to inspect the relation between these instabilities and the experimental HE temperatures.

The energy of HE generated by BRS can be calculated by considering the phase velocity $v_{ph} = \omega_e/k_e$, where ω_e and k_e are the energy and the momentum of the EPW at the density of interest. By taking a maximum BRS reflectivity $\lambda = 2400\text{--}2450$ nm, as given by experimental spectra, corresponding to BRS driven at densities $0.17\text{--}0.18 n_c$, and a plasma temperature of ~ 4 keV, corresponding to the laser peak time, we obtain an HE energy of ~ 40 keV. This value is in very good agreement with the colder HE temperature values given by the experimental data and by CHIC simulations. It is worth noting that HE generated by SRSS at lower

densities, estimated at $n_e \sim 0.12 n_c$ as given by the peak of the SRSS spectrum (red curve in Figure 3), are expected to have a lower temperature ≈ 25 keV. This suggests that low-density SRSS has a weaker impact on LPI and HE generation with respect to high-density BRS.

An estimate of the energy of HE generated by absolute TPD (or hybrid TPD/aSRS) is more tricky and less reliable. By considering the phase velocity of EPWs retrieved by the half-harmonic spectra, we obtain HE temperature values higher than 100 keV. However, it is well known that such an approach is usually not reliable for estimating HE energy, since the acceleration of electrons at $n_c/4$ usually can occur in different stages^[7]; that is, thermal electrons are initially trapped and accelerated at lower densities, and their energy is successively boosted by absolute TPD or hybrid TPD/aSRS modes driven near $n_c/4$. These values suggest, however, that the experimental hotter component of HE could be produced by absolute instabilities driven in the plasma region close to $n_c/4$.

7. PIC simulations

Kinetic simulations of LPI have been performed with the relativistic electromagnetic PIC code EPOCH^[45] in the planar 2D geometry. Absorbing boundary conditions have been applied for the electromagnetic fields leaving the simulation box, while the particles have been thermalized to provide the cold return current. The initial density profile has been taken from the hydrodynamic simulations with the code CHIC corresponding to the peak of the laser pulse on target (time of 0 in Figure 2). The simulation is covering the density region from $0.03 n_c$ to n_c , and thus resonance absorption and

absolute and convective parametric instabilities including filamentation instability, BRS, TPD, SBS and parametric decay are accounted for. The plasma density gradient in the transverse direction is neglected for the sake of simplicity, as its characteristic scale is much smaller than that of the longitudinal density gradient. The initial electron temperature is set to 4.3 keV in the simulation box, in agreement with the hydrodynamic simulation. The average ion model is used to describe the ion species in the plastic (CH) target with an effective charge $Z = 3.5$ and a mass of 6.5 times the proton mass, with ions having an initial temperature of 250 eV. Coulomb collisions are neglected, as collisional absorption is relatively weak in this range of plasma temperatures and densities.

The simulation box has dimensions of $355\lambda_0$ in the longitudinal direction and $200\lambda_0$ in the transverse direction, with 40 cells per laser wavelength (λ_0). Each cell includes 25 particles of each species, with the weight varying according to the local plasma density. The laser pulse has a Gaussian spatial profile with an FWHM of $100\ \mu\text{m}$ and the electric field vector in the simulation plane (p-polarization). It is propagating along the density gradient (normal with respect to the initial target surface). The temporal profile has a 1 ps ramp followed by a constant intensity (9 ps) corresponding to the peak of the laser pulse.

The first five picoseconds of the interaction is significantly influenced by a fast increase in the laser intensity, much faster than in the experiment. Thus we present here the results for the quasi-stationary stage of interaction, corresponding to the time from 5 to 9 ps. The longitudinal profile of the electron energy flux allows one to localize spatial zones where the laser absorption takes place. The electrons propagating into the target behind the critical density are responsible for a transport of about 10% of the incident laser energy flux, which gives the overall collisionless absorption. This electron energy flux is dominated by HE with a distribution which can be best fitted by the sum of two exponential functions with temperatures of 49 and 85 keV. The absorption process takes place in three spatially separated regions. About 1.3% of laser energy is absorbed in a low-density plasma in front of the quarter critical density surface, with the absorption rate being almost constant in this region. This region includes also the region where SRSS is observed in the experiment; however, since SRSS is driven more favourably in the s-polarization plane, the current simulation is not able to quantify this instability. About the same energy fraction (1.3%) is absorbed in a narrow region extending to about $10\lambda_0$ down from the critical density. The remaining part of 7.6% is absorbed in a region extending to $20\text{--}30\ \lambda_0$ around $n_c/4$. This region includes the range of densities where BRS and TPD are observed in the experiment. These numbers correspond to the maximum laser pulse intensity; therefore, the overall absorption into HE may be overestimated for two reasons: laser interaction at times before and after the laser peak

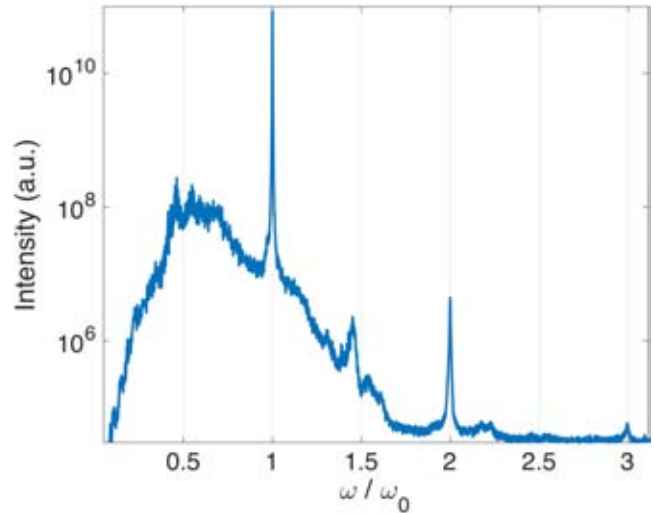


Figure 8. Spectrum of backscattered light recorded in front of the target during the quasi-stationary stage of the interaction (5–9 ps). The frequency is normalized to the laser frequency ω_0 .

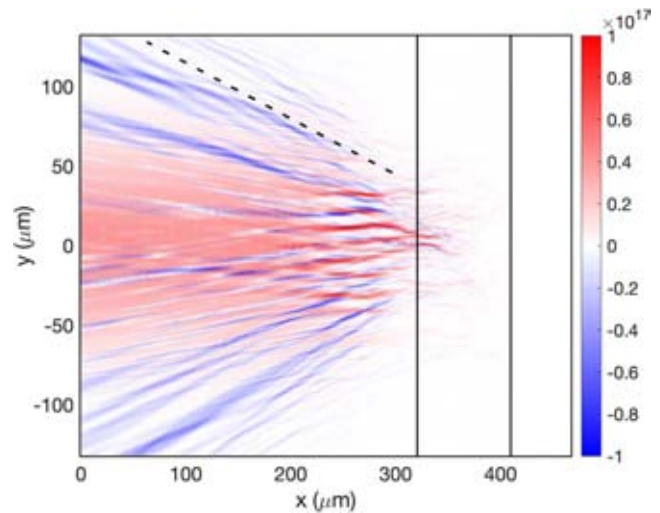


Figure 9. Distribution of the Poynting flux in the laser propagation direction (in units $\text{W} \cdot \text{cm}^{-2}$) averaged temporally over 3 ps during the quasi-steady stage of interaction and spatially over one laser wavelength. Red and blue colours represent therefore incident and backscattered light, respectively. The incident laser beam is propagating from the left and the black vertical lines show the position of the quarter critical and critical density surfaces. The black dashed line is shown to guide the eye for the opening angle of backward propagating light.

may be less efficient in producing HE, and accounting for the third spatial dimension may be less favourable for HE production. Considering these factors, HE conversion efficiency obtained by PIC simulation may be consistent with the value observed in the experiment $\epsilon_{HE} = 5.3\% \pm 2\%$.

Analysis of the simulation results shows that the overall interaction process is dominated by the laser beam filamentation, followed by SBS and SRS (see Figure 9 later). TPD is observed only during the initial transient stage of the interaction, and it is then quickly suppressed and replaced by strong SRS in the filaments, which develop in this

region. These parametric processes manifest themselves in the spectrum of backscattered light shown in Figure 8. It consists of a weakly shifted part near the laser frequency, a broad downshifted wing and narrow features at the three-halves, second and third harmonics, as can be seen in Figure 8. A strong peak near the laser frequency is due to SBS, which develops in filaments over the plasma density profile up to the quarter critical density (see also Figure 9). A broad low-frequency wing in Figure 8 shows a double-hump feature around $0.5\omega_0$ and extends to both higher and lower frequencies. The part of the spectrum to the right from $0.5\omega_0$ corresponds to SRS originating from plasma densities lower than the quarter critical density. The most intense part of the spectrum in the frequency range $0.5\text{--}0.7\omega_0$ corresponds to SRS daughter waves generated in plasma with densities extending from $0.25n_c$ to $0.08n_c$. The left wing at frequencies below $0.5\omega_0$ may be due to the resonance transformation of SRS-driven plasma waves into electromagnetic waves on local density inhomogeneities produced by filamentation^[46]. The harmonics $2\omega_0$ and $3\omega_0$ come from interaction at the critical surface. The peak around $1.5\omega_0$ has also a two-hump structure. It is similar to the feature near $1.5\omega_0$ observed in the experiment (Figure 7), but as TPD was weak in the simulation, electron plasma waves at this stage of interaction are likely produced by SRS or by a secondary parametric decay of SRS-driven plasma waves. The red-shifted component at $1.45\omega_0$, corresponding to the wavelength of 900 nm, can be attributed to Thomson scattering of the laser wave or SBS daughter wave on the electron plasma waves induced by SRS. This component was observed also in some experimental shots. A weaker blue-shifted component ($1.55\omega_0$) is due to the scattering of the second harmonic on electron plasma waves excited near $n_c/4$, and corresponds to the experimental BRS feature shown in Figure 7. All these spectral features observed in simulations are therefore qualitatively similar to the ones observed in the experiment during the trailing part of the laser pulse. The double-hump structure of the $3/2\omega_0$ emission measured in the raising part of the laser pulse and related to TPD could here not be simulated; plasma conditions considered in the simulation, in fact, correspond to the peak intensity, where convective BRS dominates. The overall energy balance in the simulation box is largely dominated by SBS, which is responsible for 60% of laser energy reflected through the front simulation box boundary; the fraction of energy reflected in the back focusing cone is $\sim 30\%$ (that is, larger than the value measured in the experiment), which may be explained by a temporal dependence of SBS on the interaction time. The SRS part of the backscattered light accounts only for 3% of laser energy. This value is in good agreement with the experimental value $\sim 0.6\text{--}4\%$, but it is in contrast to both the experimental data ($5.3\% \pm 2\%$) and the numerical value of energy transferred to HE in the region where SRS is driven ($\sim 7.6\%$). This discrepancy indicates that there are secondary processes (for example,

Table 1. Energy spent in different energy channels during the interaction. The * symbol indicates mechanisms which have been observed but not quantified

	Coll. Abs.	SBS/laser		BRS	SRSS	HE
		Back	All			
Experimental	–	14%–20%	–	0.6%–4%	*	5.3%
PIC results ^a	–	30%	82% ^b	3%	*	10%
CHIC simul.	9%	–	–	–	–	3.4% ^c

^a Simulations do not include collisions. Therefore, these values should be rescaled for the presence of collisional absorption.

^b The value includes the energy scattered through the front (60%) and lateral (22%) boundaries of the simulation box.

^c The value includes the estimated amount of HE driven by TPD and SRS.

parametric decay instability or resonance absorption) able to damp and transform the energy of SRS scattered light waves into plasma waves on local density modulations before they reach the front box boundary. These processes are described in more detail in Ref. [47]. About 22% of laser energy is leaving the simulation box through the lateral boundaries and the lateral energy flux of electrons accounts for less than 1% of laser energy.

For the sake of clarity, a summary of the amount of laser energy spent in different channels, including both experimental and numerical data, is reported in Table 1. It is worth remarking that PIC results simulate ~ 4 ps of interaction at the laser peak intensity. Moreover, collisions are not included in PIC simulations; therefore, all the energy values referring to PIC data should be renormalized, taking into account the extent of collisional absorption.

Distribution of the electromagnetic field intensity in the simulation box averaged over 3 ps during the quasi-steady phase of the interaction is plotted in Figure 9. The laser pulse is propagating from the left (front) boundary and two thick vertical black lines correspond to the positions of the quarter critical and critical density surfaces. It can be seen clearly that the central part is dominated by the forward propagating incident laser (red regions) and the lateral side is dominated by backscattered light (blue regions). Filamentation, with a transverse size of the order of a few microns, similar to the speckle size, is observed for both the incident laser light, beginning at densities around $0.08n_c$, and the backward propagating light in all the backscattering cone. Here, filamentation is excited spontaneously by numerical noise rather than by spatial intensity modulations. However, since the laser power into the speckles significantly exceeds the critical power for ponderomotive filamentation, we do not expect that the description of this process is qualitatively affected by the accurate modelling of speckle intensity statistics. It can be seen that only a small portion of the laser light, around $\sim 20\%$ of the pulse energy, can penetrate behind the quarter critical density surface. The light propagates in narrow filaments with a finite angle with respect to the direction of incidence, and thus the process of resonance absorption at

critical density is also accounted for. On the other hand, this process cannot significantly contribute to the overall energy balance since only $\sim 1\%$ – 2% of laser energy reaches the critical density surface. The light filaments in front of the quarter critical density surface with transverse size of a few microns are also clearly observed. The intensity of the light in these filaments can be locally an order of magnitude higher than the incident pulse intensity (not shown in the figure because of temporal averaging). As our simulation is performed in a 2D planar geometry, the intensity in filaments can be even higher in the real 3D geometry because of filamentation and self-focusing in the third dimension. The black dashed line included in Figure 9 is a guide for the eye showing the backscattering light cone. Its angle is 23° with respect to the target normal. Most of the scattered light in the simulation is enclosed in the cone with this opening angle.

8. Conclusions

In the present experiment, LPI of an infrared laser pulse with a multilayer target at shock ignition intensity was characterized in detail. According to hydrodynamic simulations, the plasma temperature reaches values in excess of 4 keV during the interaction. The combination of laser intensity $\sim 10^{16} \text{ W} \cdot \text{cm}^{-2}$ and temperature $\sim 4 \text{ keV}$ makes this experiment interesting to understand the characteristics of parametric instabilities in the SI regime.

On one hand, the value of plasma temperature determines the density range where convective BRS is driven. When temperature increases, Landau damping of BRS daughter plasma waves pushes the instability towards denser regions. On the other hand, plasma temperature is expected to rule the balance between TPD and SRS, because the threshold of TPD strongly increases in hot plasmas, leading to the damping of the instability. In our experiment, the presence of EPWs in the proximity of $n_c/4$, probably due to TPD or hybrid TPD/aSRS, is observed at early times of interaction when the plasma temperature is still low, and successively is suppressed at times close to the laser peak, when the temperature reaches the maximum value. At a comparable time, experimental spectra show evidence of the convective BRS onset. However, since the BRS is driven at lower densities, and therefore could not compete with absolute TPD, it is possible that TPD at $n_c/4$ is damped by laser pump depletion due to BRS growth at lower densities or in filaments. As expected, PIC simulation carried out at laser peak time shows that TPD rapidly damps and SRS becomes dominant.

We want also to emphasize that a joint observation of $3/2\omega_0$, $5/2\omega_0$ and $7/2\omega_0$ allowed the detection and characterization of TPD (or hybrid TPD/aSRS), BRS and SRSS, driven in different density regions of the plasma.

A meaningful result of the present work is also the measurement of SRSS, which was rarely experimentally observed. This was measured at an angle of $\sim 50^\circ$ which,

considering plasma refraction, corresponds to light scattered at angles of 65° – 90° . According to recent simulations^[18], SRSS is expected to become important at SI laser intensities, leading to laser energy scattered at large angles and to laser pump depletion that can damp TPD and SRS driven in denser plasma regions.

The results of 2D PIC simulations performed in the relevant interaction conditions confirm the framework delineated by the measurements and contribute to shedding further light on LPI and collisionless absorption mechanisms. PIC results show that filamentation instability rules the transport and the absorption of the laser light, in agreement with thresholds of classical theory. Filamentation is driven in the underdense plasma, in front of and slightly beyond the $n_c/4$ region, and results in local laser intensities up to an order of magnitude higher than the value of incident intensity. In this way, filamentation rules the onset of SBS and SRS. Collisionless absorption of laser light by SRS becomes comparable to or even stronger than collisional absorption, and is responsible for the generation of HE with a probable conversion efficiency of the order of several percent. Secondary processes, such as parametric decay and resonance absorption, result in the partial absorption of BRS scattered light, so that calorimetry of the BRS light exiting the plasma could result in an underestimation of the overall collisionless absorbed energy. Inverse resonance absorption of SRS-driven plasma waves, in turn, results in a broad spectral range of infrared scattered light extending to frequencies lower than $0.5\omega_0$.

Finally, experimental data, CHIC hydrodynamic simulations and PIC kinetic simulations suggest the presence of two HE components: the lower energy one, with a temperature around 40 keV, generated by the damping of BRS waves, and the higher energy one, with a temperature of ~ 80 – 100 keV , probably generated by instabilities driven in the proximity of $n_c/4$.

Acknowledgements

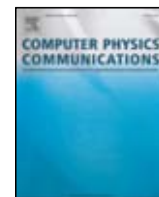
We would like to acknowledge financial support from the LASERLAB-EUROPE Access to Research Infrastructure activity within the ECs seventh Framework Program. This work has been carried out within the framework of the EUROfusion Consortium and has received funding from the Euratom research and training programme 2014–2018 under grant agreement No. 633053. The views and opinions expressed herein do not necessarily reflect those of the European Commission. This work was partially supported by the project ELITAS (ELI Tools for Advanced Simulation) CZ.02.1.01/0.0/0.0/16_013/0001793 and HIFI (High Field Initiative, CZ.02.1.01/0.0/0.0/15_003/0000449), ADONIS (Advanced research using high-intensity laser produced photons and particles, CZ.02.1.01/0.0/0.0/16_019/0000789), and ELITAS (ELI Tools for Advanced Simulations,

CZ.02.1.01/0.0/0.0/16_013/0001793), all from European Regional Development Fund. The Czech participants appreciate financial support from the Czech Ministry of Education, Youth and Sports within grants LTT17015, LM2015083, and CZ.02.1.01/0.0/0.0/16_013/0001552 (EF16_013/0001552). The work of JIHT RAS group was done in the frame of the state assignment of FASO of Russia (topic #01201357846). We acknowledge SciTech Precision and Rutherford Appleton Laboratory Target Fabrication Group for the supplied targets. Finally, we thank the technical staff of PALS for help in running the experiments.

References

- R. Betti, C. D. Zhou, K. S. Anderson, L. J. Perkins, W. Theobald, and A. Solodov, *Phys. Rev. Lett.* **98**, 155001 (2007).
- R. Nora, W. Theobald, R. Betti, F. J. Marshall, D. T. Michel, W. Seka, B. Yaakobi, M. Lafon, C. Stoeckl, J. Delettrez, A. A. Solodov, A. Casner, C. Reverdin, X. Ribeyre, A. Vallet, J. Peebles, F. N. Beg, and M. S. Wei, *Phys. Rev. Lett.* **114**, 045001 (2015).
- W. Theobald, R. Nora, W. Seka, M. Lafon, K. S. Anderson, M. Hohenberger, F. J. Marshall, D. T. Michel, A. A. Solodov, C. Stoeckl, D. H. Edgell, B. Yaakobi, A. Casner, C. Reverdin, X. Ribeyre, A. Shvydky, A. Vallet, J. Peebles, F. N. Beg, M. S. Wei, and R. Betti, *Phys. Plasmas* **22**, 056310 (2015).
- L. J. Perkins, R. Betti, K. N. LaFortune, and W. H. Williams, *Phys. Rev. Lett.* **103**, 045004 (2009).
- A. R. Bell and M. Tzoufras, *Plasma Phys. Control. Fusion* **53**, 045010 (2011).
- J. Trela, W. Theobald, K. S. Anderson, D. Batani, R. Betti, A. Casner, J. A. Delettrez, J. A. Frenje, V. Yu. Glebov, X. Ribeyre, A. A. Solodov, M. Stoeckl, and C. Stoeckl, *Phys. Plasmas* **25**, 052707 (2018).
- R. Yan, C. Ren, J. Li, A. V. Maximov, W. B. Mori, Z.-M. Sheng, and F. S. Tsung, *Phys. Rev. Lett.* **108**, 175002 (2012).
- R. S. Craxton, K. S. Anderson, T. R. Boehly, V. N. Goncharov, D. R. Harding, J. P. Knauer, R. L. McCrory, P. W. McKenty, D. D. Meyerhofer, J. F. Myatt, A. J. Schmitt, J. D. Sethian, R. W. Short, S. Skupsky, W. Theobald, W. L. Kruer, K. Tanaka, R. Betti, T. J. B. Collins, J. A. Delettrez, S. X. Hu, J. A. Marozas, A. V. Maximov, D. T. Michel, P. B. Radha, S. P. Regan, T. C. Sangster, W. Seka, A. A. Solodov, J. M. Soures, C. Stoeckl, and J. D. Zuegel, *Phys. Plasmas* **22**, 110501 (2015).
- R. K. Kirkwood, J. D. Moody, J. Kline, E. Dewald, S. Glenzer, L. Divol, P. Michel, D. Hinkel, R. Berger, E. Williams, J. Milovich, L. Yin, H. Rose, B. MacGowan, O. Landen, M. Rosen, and J. Lindl, *Plasma Phys. Control. Fusion* **55**, 103001 (2013).
- E. I. Moses, R. N. Boyd, B. A. Remington, C. J. Keane, and R. Al-Ayat, *Phys. Plasmas* **16**, 041006 (2009).
- A. Casner, T. Caillaud, S. Darbon, A. Duval, I. Thfouin, J. P. Jadaud, J. P. LeBreton, C. Reverdin, B. Rosse, R. Rosch, N. Blanchot, B. Villette, R. Wrobel, and J. L. Miquel, *High Energy Density Phys.* **17**, 2 (2015).
- O. Klimo and V. T. Tikhonchuk, *Plasma Phys. Control. Fusion* **55**, 095002 (2013).
- O. Klimo, J. Psikal, V. T. Tikhonchuk, and S. Weber, *Plasma Phys. Control. Fusion* **56**, 055010 (2014).
- C. Riconda, S. Weber, V. T. Tikhonchuk, and A. Hron, *Phys. Plasmas* **18**, 092701 (2011).
- L. Yin, B. J. Albright, H. A. Rose, K. J. Bowers, B. Bergen, D. S. Montgomery, J. L. Kline, and J. C. Fernandez, *Phys. Plasmas* **16**, 113101 (2009).
- L. Yin, B. J. Albright, K. J. Bowers, W. Daughton, and H. A. Rose, *Phys. Rev. Lett.* **99**, 265004 (2007).
- G. J. Morales and T. M. O'Neil, *Phys. Rev. Lett.* **28**, 417 (1972).
- C. Z. Xiao, Z. J. Liu, C. Y. Zheng, and X. T. He, *Phys. Plasmas* **23**, 022704 (2016).
- S. Weber and C. Riconda, *High Power Laser Sci. Eng.* **23**, e6 (2015).
- C. Z. Xiao, H. B. Zhuo, Y. Yin, Z. J. Liu, C. Y. Zheng, Y. Zhao, and X. T. He, *Plasma Phys. Control. Fusion* **60**, 025020 (2018).
- W. Theobald, R. Nora, M. Lafon, A. Casner, X. Ribeyre, K. S. Anderson, R. Betti, J. A. Delettrez, J. A. Frenje, V. Yu. Glebov, O. V. Gotchev, M. Hohenberger, S. X. Hu, F. J. Marshall, D. D. Meyerhofer, T. C. Sangster, G. Schurtz, W. Seka, V. A. Smalyuk, C. Stoeckl, and B. Yaakobi, *Phys. Plasmas* **19**, 102706 (2012).
- C. Goyon, S. Depierreux, V. Yahia, G. Loisel, C. Baccou, C. Courvoisier, N. G. Borisenko, A. Orekhov, O. Rosmej, and C. Labaune, *Phys. Rev. Lett.* **111**, 235006 (2013).
- S. Depierreux, P. Loiseau, D. T. Michel, V. Tassin, C. Stenz, P. E. Masson-Laborde, C. Goyon, V. Yahia, and C. Labaune, *Phys. Plasmas* **19**, 012705 (2012).
- P. Koester, L. Antonelli, S. Atzeni, J. Badziak, F. Baffigi, D. Batani, C. A. Cecchetti, T. Chodukowski, F. Consoli, G. Cristoforetti, R. De Angelis, G. Folpini, L. A. Gizzi, Z. Kalinowska, E. Krousky, M. Kucharik, L. Labate, T. Levato, R. Liska, G. Malka, Y. Maheut, A. Marocchino, P. Nicolai, T. O'Dell, P. Parys, T. Pisarczyk, P. Racza, O. Renner, Y. J. Rhee, X. Ribeyre, M. Richetta, M. Rosinski, L. Ryc, J. Skala, A. Schiavi, G. Schurtz, M. Smid, C. Spindloe, J. Ullschmied, J. Wolowski, and A. Zaras, *Plasma Phys. Control. Fusion* **55**, 124045 (2013).
- D. Batani, L. Antonelli, S. Atzeni, J. Badziak, F. Baffigi, T. Chodukowski, F. Consoli, G. Cristoforetti, R. De Angelis, R. Dudzak, G. Folpini, L. Giuffrida, L. A. Gizzi, Z. Kalinowska, P. Koester, E. Krousky, M. Krus, L. Labate, T. Levato, Y. Maheut, G. Malka, D. Margarone, A. Marocchino, J. Nejdil, Ph. Nicolai, T. O'Dell, T. Pisarczyk, O. Renner, Y. J. Rhee, X. Ribeyre, M. Richetta, M. Rosinski, M. Sawicka, A. Schiavi, J. Skala, M. Smid, Ch. Spindloe, J. Ullschmied, A. Velyhan, and T. Vinci, *Phys. Plasmas* **21**, 032710 (2014).
- D. Batani, L. Antonelli, F. Barbato, G. Boutoux, A. Colatis, J. L. Feugeas, G. Folpini, D. Mancelli, Ph. Nicolai, J. Santos, J. Trela, V. Tikhonchuk, J. Badziak, T. Chodukowski, K. Jakubowska, Z. Kalinowska, T. Pisarczyk, M. Rosinski, M. Sawicka, F. Baffigi, G. Cristoforetti, F. D'Amato, P. Koester, L. A. Gizzi, S. Viciani, S. Atzeni, A. Schiavi, M. Skoric, S. Guskov, J. Honrubia, J. Limpouch, O. Klimo, J. Skala, Y. J. Gu, E. Krousky, O. Renner, M. Smid, S. Weber, R. Dudzak, M. Krus, and J. Ullschmied, *Nucl. Fusion* **59**, 032012 (2019).
- D. Baton, M. Koenig, E. Brambrink, H. P. Schlenvoigt, C. Rousseaux, G. Debras, S. Laffite, P. Loiseau, F. Philippe, X. Ribeyre, and G. Schurtz, *Phys. Rev. Lett.* **108**, 195002 (2012).
- M. Hohenberger, W. Theobald, S. X. Hu, K. S. Anderson, R. Betti, T. R. Boehly, A. Casner, D. E. Fratanduono, M. Lafon, D. D. Meyerhofer, R. Nora, X. Ribeyre, T. C. Sangster, G. Schurtz, W. Seka, C. Stoeckl, and B. Yaakobi, *Phys. Plasmas* **21**, 022702 (2014).
- G. Cristoforetti, A. Colatis, L. Antonelli, S. Atzeni, F. Baffigi, D. Batani, F. Barbato, G. Boutoux, R. Dudzak, P. Koester, E. Krousky, L. Labate, Ph. Nicolai, O. Renner, M. Skoric, V. Tikhonchuk, and L. A. Gizzi, *Europhys. Lett.* **117**, 35001 (2017).

30. G. Cristoforetti, L. Antonelli, S. Atzeni, F. Baffigi, F. Barbato, D. Batani, G. Boutoux, A. Colaitis, J. Dostal, R. Dudzak, L. Juha, P. Koester, A. Marocchino, D. Mancelli, Ph. Nicolai, O. Renner, J. J. Santos, A. Schiavi, M. M. Skoric, M. Smid, P. Straka, and L. A. Gizzi, *Phys. Plasmas* **25**, 012702 (2018).
31. S. Atzeni, A. Marocchino, and A. Schiavi, *Phys. Plasmas* **19**, 090702 (2012).
32. L. Antonelli, J. Trela, F. Barbato, G. Boutoux, P. Nicolai, D. Batani, V. Tikhonchuk, D. Mancelli, S. Atzeni, A. Schiavi, F. Baffigi, G. Cristoforetti, S. Viciani, L. A. Gizzi, M. Smid, O. Renner, J. Dostal, R. Dudzak, L. Juha, and M. Krus, submitted to *Phys. Plasmas* (2019).
33. A. Visco, R. P. Drake, D. H. Froula, S. H. Glenzer, and B. B. Pollock, *Rev. Sci. Instrum.* **79**, 10F545 (2008).
34. J. Breil, S. Galera, and P. H. Maire, *Comput. Fluids* **46**, 161 (2011).
35. S. Atzeni, A. Schiavi, F. Califano, F. Cattani, F. Cornolti, D. Del Sarto, T. Liseykina, A. Macchi, and F. Pegoraro, *Comput. Phys. Commun.* **169**, 153 (2005).
36. A. Colaitis, G. Duchateau, X. Ribeyre, Y. Maheut, G. Boutoux, L. Antonelli, Ph. Nicolai, D. Batani, and V. Tikhonchuk, *Phys. Rev. E* **92**, 041101 (2015).
37. D. Batani, C. Bleu, and Th. Lower, *Eur. Phys. J. D* **19**, 231 (2002).
38. H. A. Rose and D. F. Dubois, *Phys. Fluids B* **5**, 590 (1993).
39. D. Pesme, S. Huller, J. Myatt, C. Riconda, A. Maximov, V. T. Tikhonchuk, C. Labaune, J. Fuchs, S. Depierreux, and H. A. Baldis, *Plasma Phys. Control. Fusion* **44**, B53 (2002).
40. C. S. Liu, M. N. Rosenbluth, and R. B. White, *Phys. Fluids* **17**, 1211 (1974).
41. B. B. Afeyan and E. A. Williams, *Phys. Rev. Lett.* **75**, 4218 (1995).
42. W. Seka, B. B. Afeyan, R. Boni, L. M. Goldman, R. W. Short, K. Tanaka, and T. W. Johnston, *Phys. Fluids* **28**, 2570 (1985).
43. F. Baffigi, G. Cristoforetti, L. Fulgentini, A. Giulietti, P. Koester, L. Labate, and L. A. Gizzi, *Phys. Plasmas* **21**, 072018 (2014).
44. L. A. Gizzi, D. Giulietti, A. Giulietti, P. Audebert, S. Bastiani, J. P. Geindre, and A. Mysyrowicz, *Phys. Rev. Lett.* **76**, 2278 (1996).
45. T. D. Arber, K. Bennett, C. S. Brady, A. Lawrence-Douglas, M. G. Ramsay, N. J. Sircombe, P. Gillies, R. G. Evans, H. Schmitz, and A. R. Bell, *Plasma Phys. Control. Fusion* **57**, 113001 (2015).
46. G. Q. Liao, Y. T. Li, C. Li, L. N. Su, Y. Zheng, M. Liu, W. M. Wang, Z. D. Hu, W. C. Yan, J. Dunn, J. Nilsen, J. Hunter, Y. Liu, X. Wang, L. M. Chen, J. L. Ma, X. Lu, Z. Jin, R. Kodama, Z. M. Sheng, and J. Zhang, *Phys. Rev. Lett.* **114**, 255001 (2015).
47. Y. J. Gu, O. Klimo, Ph. Nicolai, S. Shekhanov, S. Weber, and V. T. Tikhonchuk, *High Power Laser Sci. Eng.* **7**, e39 (2019).



A fast and accurate numerical implementation of the envelope model for laser–plasma dynamics

Davide Terzani ^{a,*}, Pasquale Londrillo ^{b,4,5}

^a INO-CNR Sezione di Pisa, Via Giuseppe Moruzzi 1, 56124 Pisa, Italy

^b INAF, Osservatorio Astronomico di Bologna, Via Gobetti 93/3, Bologna, Italy

ARTICLE INFO

Article history:

Received 3 August 2018

Received in revised form 1 March 2019

Accepted 12 April 2019

Available online 18 April 2019

Keywords:

Laser–plasma acceleration

Particle-in-cell

Reduced computational model

Cold fluid plasma numerical integration

ABSTRACT

In laser-driven, plasma wakefield acceleration regimes (LWFA), when relevant scale lengths of the laser envelope and of the driven plasma waves are well separated from the wavelength and frequency of the laser fast oscillating component, a reduced physical model (usually referred to as the envelope model), has been introduced, allowing to formulate the laser–plasma equations in terms of laser cycle-averaged dynamical variables. As a main consequence, physical regimes where this reduced model applies, can be investigated with significant savings of computational resources still assuring comparable accuracy, with respect to standard Particle-In-Cell (PIC) models where all relevant space–time scales have to be resolved.

Here we propose a computational framework characterized by two previously unexplored numerical implementations of the envelope model. The first one is based on explicit second order leapfrog integration of the exact wave equation for laser pulse propagation in a laboratory coordinate system in 3D cartesian geometry, replacing the usually quoted representation in an Eulerian frame moving at the speed of light. Since the laser and driven wakefield wave equations in a laboratory frame are advection dominated, we introduce a proper modification of finite differences approximating longitudinal space derivatives, to minimize dispersive numerical errors coming from the discretized advection operators. The proposed implementation, avoiding semi-implicit procedures otherwise required when dealing with a comoving frame, assures significant saving in computational time and ease of implementation for parallel platforms. The associated equation of motion for plasma particles has been integrated, as in standard PIC codes, using the Boris pusher, properly extended to take into account the specific form of the Lorentz force in the envelope model.

As a second contribution, a novel numerical implementation of the plasma dynamics equations in the cold-fluid approximation, is presented. The scheme is based on the second-order one-step Adams–Bashforth time integrator coupled to upwind non-oscillatory WENO reconstruction for discretized space derivatives. The proposed integration scheme for the Eulerian fluid equations is equivalent to a leapfrog scheme with an added higher order dissipative truncation errors. It can be used either as a much faster, yet of comparable accuracy, alternative to the PIC representation of plasma particle motion, or even in a hybrid fluid–particle combination when kinetic effects and particle injection and acceleration in a wakefield have to be investigated.

© 2019 Elsevier B.V. All rights reserved.

1. Introduction

The general formal setting describing laser–plasma interaction in LWFA, usually referred to as Vlasov–Maxwell system, is represented by the relativistic equation of motion of N_p discrete

plasma particles (electron or positrons) with $(\mathbf{p}_\alpha(t), \mathbf{x}_\alpha(t))$ $\alpha = 1, 2, \dots, N_p$ phase space coordinates and (q, m) charge and mass, respectively, coupled to the Maxwell equation evolving the self-consistent (\mathbf{E}, \mathbf{B}) fields under the mean-field approximation. The Klimontovitch formalism based on delta functions $\delta[\mathbf{x} - \mathbf{x}_\alpha(t)]$, or, as more appropriate when dealing with numerical PIC implementation, using delta-like smoothing shape functions $\hat{S}[\mathbf{x} - \mathbf{x}_\alpha(t)]$, is then applied to connect discrete point particles to continuous fields. In this formalism, particle density $n(\mathbf{x}, t)$ and current density $\mathbf{J}(\mathbf{x}, t)$ are defined, respectively, by

$$n(\mathbf{x}, t) = \sum_{\alpha} \hat{S}[\mathbf{x} - \mathbf{x}_\alpha(t)], \quad \mathbf{J}(\mathbf{x}, t) = q \sum_{\alpha} \mathbf{v}_\alpha(t) \hat{S}[\mathbf{x} - \mathbf{x}_\alpha(t)], \quad (1)$$

* Corresponding author.

E-mail address: davide.terzani@ino.it (D. Terzani).

¹ INO-CNR Sezione di Pisa, Pisa, Italy.

² INFN Sezione di Napoli, Napoli, Italy.

³ Dipartimento di Fisica, Università di Napoli “Federico II”, Italy.

⁴ INAF Sezione di Bologna, Bologna, Italy.

⁵ Dipartimento di Fisica e Astronomia, Università di Bologna, Italy.

and, by converse, the field assignment to each particle position is expressed by:

$$\begin{aligned} \mathbf{E}(\mathbf{x}_\alpha, t) &= \int d\mathbf{x} \hat{S}[\mathbf{x} - \mathbf{x}_\alpha(t)] \mathbf{E}(\mathbf{x}, t), \\ \mathbf{B}(\mathbf{x}_\alpha, t) &= \int d\mathbf{x} \hat{S}[\mathbf{x} - \mathbf{x}_\alpha(t)] \mathbf{B}(\mathbf{x}, t). \end{aligned} \quad (2)$$

The particle equations of motion in dimensionless variables are given by:

$$\begin{aligned} \frac{d\mathbf{p}_\alpha}{dt} &= \frac{q\omega_p}{m} \left[\mathbf{E}(\mathbf{x}_\alpha, t) + \frac{\mathbf{v}_\alpha}{c} \times \mathbf{B}(\mathbf{x}_\alpha, t) \right], \\ \frac{d\mathbf{x}_\alpha}{dt} &= \mathbf{v}_\alpha = \frac{c\mathbf{p}_\alpha}{\gamma_\alpha}, \quad \gamma_\alpha = \sqrt{1 + |\mathbf{p}_\alpha|^2}, \end{aligned} \quad (3)$$

while the evolutionary pair of field Maxwell equation is given by:

$$\partial_t \mathbf{B} = -c \nabla \times \mathbf{E}, \quad \partial_t \mathbf{E} = c \nabla \times \mathbf{B} - \omega_p \mathbf{J}. \quad (4)$$

Here all variables are expressed in dimensionless form, so that charge and mass are normalized respectively to electron charge and mass e , m_e (e.g. the coupling constant in the equations of motion for an electron is $q/m = -1$), particles momenta are normalized to mc , plasma density is normalized to the background electron density n_0 , current is normalized to ecn_0 , electric and magnetic fields are normalized to $E_0 = B_0 = A_0 k_p$, where $A_0 = m_e c^2 / e$ is the normalization unit for the associated $\mathbf{A}(\mathbf{x}, t)$ vector potential and $\omega_p = ck_p = \sqrt{4\pi e^2 n_0 / m_e}$ is the electron plasma frequency.

To introduce the envelope model for the Vlasov–Maxwell equation, one considers that in typical Laser Plasma Accelerator (LPA) configurations, a polarized laser field propagating along the z coordinate, when represented in terms of the normalized vector potential $\mathbf{a}(\mathbf{x}, t) = \mathbf{A}(\mathbf{x}, t) / A_0$, under the Coulomb gauge $\nabla \cdot \mathbf{a} = 0$, can be modeled by an envelope shape function modulated by a fast oscillating monochromatic component

$$\mathbf{a}(\mathbf{x}, t) = \mathcal{R}e \left[\hat{\mathbf{a}}(\mathbf{x}, t) e^{ik_0(z-ct)} \right], \quad (5)$$

where $k_0 = 2\pi/\lambda_0$, $\omega_0 = ck_0$ is the carrier laser space–time frequency. In this representation, the complex envelope function $\hat{\mathbf{a}}(\mathbf{x}, t)$ depends on slower space–time scales, that is the spectral modes of $\hat{\mathbf{a}}(\mathbf{k}, \omega)$ have sizes $\omega/\omega_0 \sim k/k_0 = \mathcal{O}(\varepsilon)$ where ε is a small number. In numerical investigation of LPA regimes, the $\hat{\mathbf{a}}(\mathbf{x}, t)$ field is initialized in vacuum in the form $\hat{\mathbf{a}}(\mathbf{x}, t) = f(z-ct) \mathbf{g}(\mathbf{x})$ where \mathbf{g} has a Gaussian shape along the transverse $r = \sqrt{x^2 + y^2}$ coordinate, characterized by a waist $w_0 \gg \lambda_0$ at the $z = z_f$ focal point and $f(z-ct)$ is a Gaussian-like shape function with scale $L_z \gg \lambda_0$ along the comoving $\xi = z - ct$ longitudinal coordinate. In this configuration, the small parameter measuring scale separation is defined by $\varepsilon = 1/(k_0 w_0) \simeq 1/(k_0 L_z) \ll 1$. To the lowest order approximation, a Gaussian field has a $\mathcal{O}(1)$ field component $\mathbf{a}_\perp = (a_x, a_y)$, where $|a_y| = |a_x|$ for circular polarization, or $a_y = \mathcal{O}(\varepsilon^2)$ for linear polarization along the x coordinate, whereas the longitudinal component has size $a_z = \mathcal{O}(\varepsilon)$. On the assumption that scale separation set by initial conditions is preserved in time during laser propagation, that is scale lengths l_p of the plasma density variations satisfy $1/k_0 l_p = \mathcal{O}(\varepsilon)$, a two-scale perturbative analysis can then be applied [1–3] to reformulate the Vlasov–Maxwell system in terms of laser cycle-averaged dynamical variables depending only on slow space–time coordinates.

By referring to the cited works for a detailed derivation of the envelope model, in Section 2 the resulting set of plasma and field equations of motion, are first shortly reported. Section 3 is devoted to the field solvers, where we present and discuss the details of the implementation of numerical schemes for the laser

envelope and wake fields propagation. In Section 4, the numerical integration of Lagrangian equation of motion for PIC particles, by extending the classical Boris pusher to the envelope model, is then presented and discussed, whereas Section 5 contains the presentation of a numerical integration of the plasma equations in Eulerian fluid variables. Finally, Section 6 contains validations and benchmarks of our schemes.

2. The envelope model equations

The envelope model has been derived using multi-scale perturbative procedures on the equation of motion either in Lagrangian form equation (3), (see [3,4] and references therein) or in Eulerian form for plasma momenta $\mathbf{p}(\mathbf{x}, t)$ derived from the Vlasov equation in the cold-fluid approximation, see [1]. We shortly report here the main results derived in the Eulerian approach, where the formulation appears more convincing and self-contained. These results can then be applied for a system of discrete Lagrangian particles by projection of fluid variables onto the particle phase space coordinates.

In the Eulerian approach, fluid momentum $\mathbf{p}(\mathbf{x}, t)$ (and all related dynamical variables) is split into two components: $\mathbf{p} = \bar{\mathbf{p}} + \delta\mathbf{p}$, where the cycle-averaged part $\bar{\mathbf{p}}(\mathbf{x}_1, t_1)$ depends only on the slow space–time coordinates $t_1 = \varepsilon\omega_0 t$, $\mathbf{x}_1 = \varepsilon k_0 \mathbf{x}$ and the residual part $\delta\mathbf{p}(t_1, \mathbf{x}_1; t_0, z_0)$ depends both on the slow and fast $t_0 = \omega_0 t$, $z_0 = k_0 z$ coordinates. Correspondingly, the plasma current density induced by the plasma fluid motion is split into components $\mathbf{J} = \bar{\mathbf{J}} + \delta\mathbf{J}$. The averaged component acts as a source term of the Maxwell equation expressed by Eq. (4), now evolving the driven wakefield (\mathbf{E}, \mathbf{B}) on the slow space–time scales, whereas the oscillatory part $\delta\mathbf{J}$ acts as a source term of a separate Maxwell equation evolving the laser field, represented by the dominant vector potential components

$$[\partial_{t,t} - c^2 \nabla^2] \mathbf{a}_\perp = \omega_p^2 \delta\mathbf{J}_\perp. \quad (6)$$

In the two-scale perturbative analysis [1] of the momentum equation, the leading order solution for the oscillatory momentum component is given by $\delta\mathbf{p}_\perp = -q\mathbf{a}_\perp/m$, whereas the longitudinal δp_z component has size $\mathcal{O}(\varepsilon)$ smaller. As a first consequence, the particle γ function is approximated by $\gamma = \bar{\gamma} + \mathcal{O}(\varepsilon^2)$, where the cycle-averaged part is $\bar{\gamma} = \left(1 + |\bar{\mathbf{p}}|^2 + q^2 |\hat{a}|^2 / 2m^2\right)^{1/2}$. The oscillatory and averaged current density components can now be expressed, respectively, by

$$\delta\mathbf{J}_\perp = q\bar{n} \frac{\delta\mathbf{p}_\perp}{\gamma}, \quad \bar{\mathbf{J}} = q\bar{n} \frac{\bar{\mathbf{p}}}{\gamma} \quad (7)$$

where \bar{n} is the cycle-averaged plasma density satisfying the continuity equation

$$\partial_t \bar{n} + \nabla \cdot (n\bar{\mathbf{v}}) = 0, \quad \bar{\mathbf{v}} = \frac{c\bar{\mathbf{p}}}{\gamma}. \quad (8)$$

By inserting the $\delta\mathbf{J}_\perp$ relation of Eq. (7) in (6), the fast oscillating phase part of the \mathbf{a}_\perp field is factored out, leading to a closed equation for the envelope function \hat{a} in complex form:

$$[\partial_{t,t} - 2i\omega_0(\partial_t + c\partial_z) - c^2 \nabla^2] \hat{a}(\mathbf{x}, t) = -\omega_p^2 \chi(\mathbf{x}, t, |\hat{a}|) \hat{a}(\mathbf{x}, t), \quad (9)$$

where $\chi(\mathbf{x}, t, |\hat{a}|) = q^2 \bar{n} / \bar{\gamma}$ and all dynamical variables depend only on slow space–time coordinates (here denoted as (\mathbf{x}, t)).

The second main achievement of the envelope modelization is the relation expressing the cycle-averaged laser Lorentz force acting on the plasma fluid (here specialized to linear polarization)

$$\mathbf{F}_L = -\frac{1}{2\bar{\gamma}} \nabla \Phi, \quad \Phi = \frac{q^2 |\hat{a}|^2}{2m^2}. \quad (10)$$

The equation of motion for the averaged plasma momentum $\bar{\mathbf{p}}(\mathbf{x}, t)$, can now be expressed in closed form by

$$[\partial_t + \bar{\mathbf{v}} \cdot \nabla] \bar{\mathbf{p}} = \frac{q\omega_p}{m} \left[\mathbf{E}(\mathbf{x}, t) + \frac{\bar{\mathbf{p}}}{\gamma} \times \mathbf{B}(\mathbf{x}, t) \right] + \mathbf{F}_L(\mathbf{x}, t), \quad (11)$$

where the total Lorentz force is split into a contribution due to the wake fields and a contribution coming from the laser ponderomotive force \mathbf{F}_L .

In the Lagrangian framework, a two-scale perturbative analysis of the equation of motion for particle $[\mathbf{x}_\alpha(t), \mathbf{p}_\alpha(t)]$ phase-space coordinates has been formulated in [3,4], often denoted as ponderomotive guiding center (PGC) modeling, where the cycle-averaged $[\bar{\mathbf{x}}_\alpha(t_1), \bar{\mathbf{p}}_\alpha(t_1)]$ coordinates evolving on slow time scales describe the guiding center motion and the residual components $[\delta\mathbf{x}_\alpha, \delta\mathbf{p}_\alpha]$ describe the oscillatory motion around the guiding center. Using averaged momentum in the Eulerian variables of Eq. (11) and by defining the momentum of the particle guiding center by

$$\bar{\mathbf{p}}_\alpha(t) = \int d\mathbf{x} \hat{S}[\mathbf{x} - \bar{\mathbf{x}}_\alpha(t)] \bar{\mathbf{p}}(\mathbf{x}, t), \quad (12)$$

Eq. (11) can be formulated in a PGC Lagrangian framework as

$$\begin{aligned} \frac{d\bar{\mathbf{p}}_\alpha(t)}{dt} &= \frac{q\omega_p}{m} \left[\mathbf{E}(\mathbf{x}_\alpha, t) + \frac{\mathbf{v}_\alpha}{c} \times \mathbf{B}(\mathbf{x}_\alpha, t) \right] + \mathbf{F}_L(\mathbf{x}_\alpha, t), \\ \mathbf{F}_L &= -\frac{1}{2\gamma_\alpha} \nabla \Phi_\alpha, \quad \gamma_\alpha^2 = 1 + |\mathbf{p}_\alpha|^2 + \Phi_\alpha, \\ \frac{d\bar{\mathbf{x}}_\alpha(t)}{dt} &= \mathbf{v}_\alpha = \frac{c\mathbf{p}_\alpha}{\gamma_\alpha}, \end{aligned} \quad (13)$$

where all field variables have been projected on the particle guiding center following Eq. (12). In this framework, the averaged current density $\bar{\mathbf{J}}(\mathbf{x}, t)$ evolving on slow space–time scales, can be evaluated by:

$$\bar{\mathbf{J}}(\mathbf{x}, t) = \frac{q}{n_0 c} \sum_\alpha \mathbf{v}_\alpha(t) \hat{S}[\mathbf{x} - \mathbf{x}_\alpha(t)], \quad \mathbf{v}_\alpha = \frac{c\mathbf{p}_\alpha}{\gamma_\alpha}, \quad (14)$$

where the shape function $\hat{S}[\mathbf{x} - \mathbf{x}_\alpha(t)]$ now acts as distribution function for particle guiding centers. In the envelope equation (9), the $\chi(\mathbf{x}, t)$ function on the r.h.s is expressed by

$$\bar{\chi}(\mathbf{x}, t) = \frac{q^2}{n_0} \sum_\alpha \frac{\hat{S}[\mathbf{x} - \mathbf{x}_\alpha(t)]}{\gamma_\alpha}. \quad (15)$$

Recasting the oscillatory current component in the PGC formalism appears still an open problem, requiring elaborate perturbative analysis [4].

3. Implementing leapfrog integration scheme for envelope and wake field equations

The dispersion relation in Fourier modes (\mathbf{k}, ω) of Eq. (9) in linear approximation ($\chi \simeq 1$), is expressed by

$$\omega^2 + 2\omega_0\omega = c^2 (2k_0k_z + k^2 + k_p^2), \quad (16)$$

where k_p is related to the plasma frequency as $\omega_p = ck_p$. Since in the envelope model $\omega - ck_z = \mathcal{O}(\varepsilon^2)$, relation (16) can be approximated by

$$\omega = ck_z + \frac{c}{2} \frac{k_\perp^2 + k_p^2}{k_0 + k_z} + \mathcal{O}(k_0\varepsilon^4), \quad (17)$$

giving a group velocity $v_g = c + \mathcal{O}(\varepsilon^2)$ for right propagating modes $k_z > 0$

$$v_g = \frac{\partial\omega}{\partial k_z} = c \left[1 - \frac{1}{2} \frac{\tilde{k}_\perp^2 + \tilde{k}_p^2}{(1 + \tilde{k}_z)^2} \right], \quad (18)$$

where $\tilde{k} = k/k_0$ are the normalized wavenumbers.

In a Galilean frame moving at the speed of light (a *comoving system*), using coordinate transformations $(t, z) \rightarrow (\tau, \xi)$

$$\xi = z - ct, \quad \tau = t, \quad \partial_t = \partial_\tau - c\partial_\xi, \quad \partial_z = \partial_\xi, \quad (19)$$

the laser envelope equation (9), in the time ordering $\partial_\tau = \mathcal{O}(\omega_0\varepsilon^2)$ with neglected second derivative $\partial_{\tau,\tau}$, reduces to

$$[ik_0 + \partial_\xi] \partial_\tau \hat{a} = -\frac{1}{2} [\nabla_\perp^2 - \omega_p^2 \chi] \hat{a} \quad (20)$$

which is the usually quoted form considered in analytical and numerical investigations, (see [3,5–8] and references therein). A main reason underlying this formulation is that a Galilean coordinate transformation induces a frequency shift $\omega \rightarrow \tilde{\omega} = \omega - ck_z$, thus removing the highest frequency $\omega = ck_z$ in Eq. (17). The numerical integration of Eq. (20) is then expected to be free of dispersive effects related to the laser pulse advection.

However, to solve Eq. (20) for time derivative, the $\hat{M} \equiv [ik_0 + \partial_\xi]$ operator on the left has to be inverted and this poses severe limitations on implementation based on finite differences. In fact, the inverse operator

$$\hat{M}^{-1} = -\frac{ik_0 - \partial_\xi}{k_0^2 + \partial_{\xi,\xi}} \quad (21)$$

once discretized on a grid with cell size $\Delta\xi$, is singular at the Nyquist frequency $k_{max} = \pi/\Delta\xi \simeq k_0$, $\Delta\xi \simeq \lambda_0/2$. As a consequence, in explicit integration, grid resolution and Courant number must be severely bounded to assure stability. To overcome these limitations, in published works so far (see for example [9]), a semi-implicit integration scheme, typically a Crank–Nicolson integrator for the linear part, has been applied. This procedure requires inverting a fully 3D Laplacian discretized operator at each time step, with significant increase of computational complexity, also limiting an efficient parallel implementation.

In the cited works, differences arise on the way the envelope field solver relates to the wake field solver and to the plasma dynamical equations. In [3], envelope equation (20) is first integrated in a comoving (τ, ξ) coordinates and then advected back to the laboratory (t, z) coordinates, using $\partial_t + \partial_z = \partial_\tau$. This approach, once implemented by standard finite differences, reintroduces significant dispersive effects coming from the discretized advection operator. In work [6], laser and wakefield equations are all integrated on the comoving (τ, ξ) coordinate system. This entails, in particular, that the wakefield Maxwell equations have to be modified by a backward advection term and a streaming velocity $v_s = -c$ has to be added to the plasma particle motion. As a main consequence, strong anomalous Cherenkov effects are artificially produced, and additional computational costs are then required to control or reduce unphysical current driven instabilities.

3.1. Envelope field solver in the laboratory coordinate system

These arguments suggest that implementing the envelope wave equation directly on a laboratory coordinate system, as expressed in Eq. (9) with second time derivative operator retained, has to be preferred. In fact, Maxwell equation for the laser envelope can be integrated by stable explicit leapfrog schemes with no artificial restriction on CFL condition and on the grid resolution, thus allowing significant improvements in efficiency and simplicity of the implementation procedures. Also consistency arguments favoring this choice have to be considered, since Eq. (9) retains the basic (hyperbolic) structure of the wave equation for scalar fields and of the associated Maxwell equations for the laser driven wakefields. This entails, in particular, that the composite system of envelope, wakefields and particle equation of motion can be integrated on a same unitary numerical framework, as in fully kinetic PIC codes, using a second-order

leapfrog explicit integrator both for particles and fields, under the standard Courant number condition. To integrate Eq. (9) on a grid we use centered first and second finite differences to approximate time derivatives

$$\begin{aligned} \mathcal{D}_t \hat{a} &= \frac{\hat{a}^{n+1} - \hat{a}^{n-1}}{2\Delta t}, \\ \mathcal{D}_{t,t} \hat{a} &= \frac{\hat{a}^{n+1} - 2\hat{a}^n + \hat{a}^{n-1}}{\Delta t^2}, \end{aligned} \quad (22)$$

where index n denotes the time grid point $t^n = n\Delta t$ and Δt denotes the time step. Likewise, centered first and second finite differences on a (non staggered) grid $\mathbf{x}_g = (x_i, y_j, z_k)$ with cell sizes $(\Delta x, \Delta y, \Delta z)$ approximate space derivatives of the field $\hat{a}(x_i, y_j, z_k)$ discretized at integer index grid points:

$$\begin{aligned} \mathcal{D}_z \hat{a} &= \frac{\hat{a}_{k+1} - \hat{a}_{k-1}}{2\Delta z}, \quad \mathcal{D}_{z,z} \hat{a} = \frac{\hat{a}_{k+1} - 2\hat{a}_k + \hat{a}_{k-1}}{\Delta z^2}, \\ \mathcal{D}_{y,y} \hat{a} &= \frac{\hat{a}_{j+1} - 2\hat{a}_j + \hat{a}_{j-1}}{\Delta y^2}, \quad \mathcal{D}_{x,x} \hat{a} = \frac{\hat{a}_{i+1} - 2\hat{a}_i + \hat{a}_{i-1}}{\Delta x^2}. \end{aligned} \quad (23)$$

The Courant number $\sigma \leq 1$, relating Δt to the grid cell sizes is defined, as usual in numerical Maxwell equations, by

$$\sigma = \frac{c\Delta t}{h\Delta z}, \quad \bar{h} = \frac{r}{\sqrt{2+r^2}} \quad (24)$$

where $r = \Delta x/\Delta z = \Delta y/\Delta z$ is the ratio of the transverse to the longitudinal cell sizes ($\bar{h} = 1/\sqrt{3}$ for a uniform 3D grid).

In a laser-wakefield wave system, the discretized $\mathcal{D}_t + c\mathcal{D}_z$ operator entails dominant dispersive numerical errors with size $\mathcal{O}(\Delta t^2) - \mathcal{O}(\Delta z^2)$ given by the difference of second order truncation error in time and space, respectively. In long time integration of LWFA configurations, these errors shorten the dephasing length and affect then electron acceleration efficiency. A simple way to reduce these numerical effects is to modify finite difference operators along the z coordinate using a two-point enlarged stencils of grid points. In this way, still second-order, optimized numerical derivatives can be obtained, related to the standard two-point finite differences (23), by:

$$\begin{aligned} \mathcal{D}_z^{(o)} &= \mathcal{D}_z [1 + \delta_1 \Delta z^2 \mathcal{D}_{z,z}], \\ \mathcal{D}_{z,z}^{(o)} &= \mathcal{D}_{z,z} [1 + \delta_2 \Delta z^2 \mathcal{D}_{z,z}], \end{aligned} \quad (25)$$

where the free parameters (δ_1, δ_2) are chosen in a way to cancel out second order truncation errors of the space-time discretized advection operator. Using the dispersion relation expressed by numerical Fourier components, one obtains $\delta_1 = (\nu^2 - 1)/6 < 0$, and $\delta_2 = (\nu^2 - 1)/12 < 0$, where $\nu = \bar{h}\sigma = c\Delta t/\Delta z < 1$, (see Appendix A for a short derivation).

Modified finite differences is a standard issue in numerical analysis and has been widely used to reduce dispersive effects in FDTD for Maxwell wave equation (see [10]). In particular, a procedure similar to Eq. (25) has been introduced in [11], and, by more elaborate algorithm involving modified stencils also in transverse coordinates [12,13], especially designed to control anomalous Cherenkov effects of relativistic accelerated electron bunches. We point out, that the recipe here proposed involving only the longitudinal coordinate, takes fully advantage of the dominance of the advection operator in the envelope model, as documented in the numerical tests of Section 6.

In terms of finite difference operators, Eq. (9) is then expressed by

$$\begin{aligned} &[\mathcal{D}_{t,t} - 2i\omega_0(\mathcal{D}_t + c\mathcal{D}_z) - c^2\mathcal{D}^2] \hat{a}^n(\mathbf{x}_g) \\ &= -\omega_p^2 \chi(\mathbf{x}_g, t^n, |\hat{a}^n|) \hat{a}^n(\mathbf{x}_g), \end{aligned} \quad (26)$$

where $\mathcal{D}^2 = \mathcal{D}_{z,z} + \mathcal{D}_{\perp}^2$ denotes the 3D numerical Laplacian operator and $\mathcal{D}_{\perp}^2 = \sum_{s=x,y} \mathcal{D}_{s,s}$. In code implementation, either

standard (i.e. Eq. (23)) or optimized (i.e. Eq. (25)) finite differences along the z -coordinate can be activated.

For given $[\hat{a}^n(\mathbf{x}_g), \hat{a}^{n-1}(\mathbf{x}_g)]$ field data at time level $t^n = n\Delta t$ and $t^{n-1} = t^n - \Delta t$, the one step update of Eq. (26) is implemented by first evaluating at the current time level t^n the source term

$$\hat{S}[\hat{a}] = [2ik_0\mathcal{D}_z + \mathcal{D}^2 - \omega_p^2 \chi(\mathbf{x}_g, t^n)] \hat{a}^n(\mathbf{x}_g) \quad (27)$$

and then by solving in explicit form for the updated field data:

$$\begin{aligned} \hat{a}^{n+1} - i\eta \hat{a}^{n+1} &= \tilde{F}[\hat{a}], \\ \tilde{F}[a] &= \Delta t^2 \hat{S}[\hat{a}] + 2\hat{a}^n - \hat{a}^{n-1} - i\eta \hat{a}^{n-1}, \end{aligned} \quad (28)$$

where $\eta = \omega_0\Delta t$. Finally, by separating real and imaginary components $\hat{a} = (a_R, a_I)$, the solution for the updated variables $(a_R, a_I)^{n+1}$ is evaluated by

$$a_R^{n+1} = \frac{F_R - \eta F_I}{1 + \eta^2}, \quad a_I^{n+1} = \frac{F_I + \eta F_R}{1 + \eta^2}. \quad (29)$$

where the source term components are given by

$$\tilde{F}_R = \Delta t^2 \hat{S}_R + 2a_R^n - a_R^{n-1} + \eta a_I^{n-1}, \quad \tilde{F}_I = \Delta t^2 \hat{S}_I + 2a_I^n - a_I^{n-1} - \eta a_R^{n-1}. \quad (30)$$

3.2. Implementation of leapfrog Maxwell solver for driven wakefield

By representing the $(\mathbf{E}, \mathbf{B}, \mathbf{J})$ fields on the standard Yee grid, the leapfrog integrator of Maxwell equations for wakefield equation (4) is expressed by

$$\begin{aligned} [\mathcal{D}_t \mathbf{B}]^n &= -c\mathcal{D} \times \mathbf{E}^n, \\ [\mathcal{D}_t \mathbf{E}]^{n+1/2} &= c\mathcal{D} \times \mathbf{B}^{n+1/2} - \omega_p \mathbf{j}^{n+1/2} \end{aligned} \quad (31)$$

where, as usual in FDTD framework, finite differences in space and time are evaluated at staggered grid points with respect to the collocation of the derived variables.

Since also driven wakefields are advection dominated, dispersive numerical errors can be reduced following the same procedure adopted for the envelope field solver. In the Yee staggered grid, optimized finite differences along the z -coordinate are now defined by

$$\mathcal{D}_z^{(o)} = \mathcal{D}_z [1 + \delta_3 \Delta z^2 \mathcal{D}_{z,z}], \quad \delta_3 = \frac{\nu^2 - 1}{24}, \quad (32)$$

and are then applied to the proper components of both the $(\mathcal{D} \times \mathbf{E})$ and $(\mathcal{D} \times \mathbf{B})$ vector operators.

4. Leapfrog integration of equation of motion of PIC particles

4.1. Boris pusher for particle momentum update

In a leapfrog integration scheme of Eq. (13), the one-step update $\mathbf{p}_\alpha^{n-1/2} \rightarrow \mathbf{p}_\alpha^{n+1/2}$ of particle momentum discretized on the staggered time grid, is expressed by

$$\mathbf{p}_\alpha^{n+1/2} = \mathbf{p}_\alpha^{n-1/2} + \Delta t \left[\frac{q\omega_p}{m} \left(\mathbf{E}_\alpha^n + \frac{\mathbf{v}_\alpha^n}{c} \times \mathbf{B}_\alpha^n \right) - \frac{1}{2\gamma_\alpha^n} \nabla \Phi_\alpha^n \right]. \quad (33)$$

On the right side, grid defined fields $[\mathbf{E}^n(\mathbf{x}_g), \mathbf{B}^n(\mathbf{x}_g)]$ and $[\Phi^n(\mathbf{x}_g), \nabla \Phi^n(\mathbf{x}_g)]$ are evaluated at the current time level t^n by the previous $t^{n-1} \rightarrow t^n$ update expressed in Eqs. (29) and (31), and then assigned to each particle position \mathbf{x}_α^n using splines $\hat{S}_{\mathbf{x}_g}[\mathbf{x}_g - \mathbf{x}_\alpha^n]$ of some order, as routinely defined in the PIC method. To preserve the leapfrog scheme structure and accuracy, all time centered variables, $\mathbf{u}^n \equiv [\mathbf{E}, \mathbf{B}, \Phi, \mathbf{x}_\alpha, \mathbf{v}_\alpha]^n$ on the right hand side are required to be at least second order approximations, $\mathbf{u}^n = \mathbf{u}(t^n) + \mathcal{O}(\Delta t^2)$. To that purpose, in the Boris scheme [14], the

particle velocity is defined by using mid-point rule for centered momentum,

$$\mathbf{v}_\alpha^n = \frac{c\mathbf{p}_\alpha^n}{\gamma_\alpha^n}, \quad \mathbf{p}_\alpha^n = \frac{\mathbf{p}_\alpha^{n+1/2} + \mathbf{p}_\alpha^{n-1/2}}{2}, \quad (34)$$

$$\gamma_\alpha^n = \left[1 + |\mathbf{p}_\alpha^n|^2 + \Phi_\alpha^n \right]^{1/2},$$

but other choices have been proposed as well [15]. In terms of the unknown variables $\mathbf{p} \equiv \mathbf{p}_\alpha^n$, and $\gamma \equiv \gamma^n(|\mathbf{p}|^2)$ as defined in Eq. (34), the momentum equation (33) (particle α index omitted for brevity) can be reformulated as a fully implicit algebraic system

$$\mathbf{p} = \mathbf{p}^{n-1/2} + (\tilde{\mathbf{E}} - \tilde{\mathbf{F}}/\gamma) + \mathbf{p} \times \tilde{\mathbf{B}}/\gamma \quad (35)$$

with $\mathcal{O}(\Delta t)$ coefficients given by

$$\tilde{\mathbf{E}} \equiv \Delta t \frac{q\omega_p}{2m} \mathbf{E}^n, \quad \tilde{\mathbf{B}} \equiv \Delta t \frac{q\omega_p}{2m} \mathbf{B}^n, \quad \tilde{\mathbf{F}} \equiv \frac{\Delta t}{4} \nabla \Phi^n. \quad (36)$$

The Boris procedure to solve (35) is based on the following two main computational steps:

- (i) the exact γ function is reduced to explicit form, by a Taylor expansion to a $\mathcal{O}(\Delta t^2)$ approximation using the same equation (35);
- (ii) the term related to the magnetic field is evaluated in exact explicit form using standard vector algebra (usually interpreted as magnetic rotation).

The main change to be applied in the envelope model refers to task (i), of course, for the presence on the $1/\gamma$ factor in the ponderomotive force. By replacing $\mathbf{p} \rightarrow \mathbf{p}^{n-1/2} + (\tilde{\mathbf{E}} - \tilde{\mathbf{F}}/\gamma) + \mathcal{O}(\Delta t^2)$ in the γ definition equation (34), the approximated $\tilde{\gamma}$ variable is solution of the cubic equation

$$\tilde{\gamma}^2 = \left[\gamma_0^2 + 2(\tilde{\mathbf{E}} - \frac{\tilde{\mathbf{F}}}{\tilde{\gamma}}) \cdot \mathbf{p}^{n-1/2} \right], \quad \gamma_0^2 = \left(1 + \Phi^n + |\mathbf{p}^{n-1/2}|^2 \right), \quad (37)$$

which reduces consistently to the approximation in standard PIC model when $\Phi = 0$, (i.e. $\tilde{\mathbf{F}} = 0$).

By replacing $\gamma \rightarrow \tilde{\gamma}$, the momentum equation (35) can now be solved in explicit form using the Boris procedure indicated in step (ii):

$$\mathbf{p} = \frac{1}{1 + |\mathbf{h}|^2} [\mathbf{u} + \mathbf{u} \times \mathbf{h} + \mathbf{h}(\mathbf{u} \cdot \mathbf{h})], \quad (38)$$

$$\mathbf{p}^{n+1/2} = 2\mathbf{p} - \mathbf{p}^{n-1/2},$$

where $\mathbf{u} = \mathbf{p}^{n-1/2} + \tilde{\mathbf{E}} - \tilde{\mathbf{F}}/\tilde{\gamma}$, $\mathbf{h} = \tilde{\mathbf{B}}/\tilde{\gamma}$.

4.2. Update of particle position in envelope model

The leapfrog scheme to update particle position, is given by

$$\mathbf{x}_\alpha^{n+1} = \mathbf{x}_\alpha^n + \Delta t \mathbf{v}_\alpha^{n+1/2}, \quad \mathbf{v}_\alpha^{n+1/2} = \frac{c\mathbf{p}_\alpha^{n+1/2}}{\gamma_\alpha^{n+1/2}}, \quad (39)$$

$$\gamma_\alpha^{n+1/2} = \left(1 + |\mathbf{p}_\alpha^{n+1/2}|^2 + \Phi_\alpha^{n+1/2} \right)^{1/2},$$

where now the ponderomotive potential $\Phi_\alpha^{n+1/2} = \Phi^{n+1/2}(\mathbf{x}_\alpha^{n+1/2})$ has an implicit dependence on the particle position since $\mathbf{x}_\alpha^{n+1/2} = (\mathbf{x}_\alpha^{n+1} + \mathbf{x}_\alpha^n)/2$. To evaluate Eq. (39) in closed explicit form, still preserving the leapfrog structure and accuracy, we follow the approach first suggested in [16]. In the shorthand notation $\mathbf{p} \equiv \mathbf{p}^{n+1/2}$, $\Phi \equiv \Phi^{n+1/2}$, $\gamma \equiv \gamma^{n+1/2}$ the implicit $\Phi(\mathbf{x}^{n+1/2})$ function

can be linearized by a first order Taylor expansion

$$\Phi(\mathbf{x}^{n+1/2}) = \Phi(\mathbf{x}^n) + \delta \mathbf{x} \cdot \nabla \Phi(\mathbf{x}^n), \quad (40)$$

$$\delta \mathbf{x} = \mathbf{x}^{n+1/2} - \mathbf{x}^n = \frac{\mathbf{x}^{n+1} - \mathbf{x}^n}{2},$$

where the gradient operator can act on the \mathbf{x}_g argument of the shape function $\hat{S}_{\mathbf{x}_g}[\mathbf{x}_g - \mathbf{x}]$ or of the $\Phi(\mathbf{x}_g)$ field. The γ function of Eq. (35) can be evaluated in explicit form by solving the cubic equation (see [16])

$$\tilde{\gamma}^3 = \tilde{\gamma} \gamma_0^2 + \frac{\Delta t}{2} (\mathbf{p} \cdot \nabla \Phi(\mathbf{x}^n)), \quad \gamma_0^2 = 1 + |\mathbf{p}|^2 + \Phi(\mathbf{x}^n), \quad (41)$$

or by a simpler, still second order, explicit approximation

$$\tilde{\gamma}^{-1} = \frac{1}{\gamma_0} \left[1 - \frac{\Delta t}{4\gamma_0^3} (\mathbf{p} \cdot \nabla \Phi) \right]. \quad (42)$$

In this way, the update of the particle position takes finally the explicit form:

$$\mathbf{x}_\alpha^{n+1} = \mathbf{x}_\alpha^n + \Delta t \mathbf{v}_\alpha^{n+1/2}, \quad \mathbf{v}_\alpha^{n+1/2} \equiv \tilde{\gamma}^{-1} c \mathbf{p}_\alpha^{n+1/2}. \quad (43)$$

4.3. The overall integration one-step cycle of the envelope model

At the end of the momentum update step, Eq. (38), the source term $\chi^n(\mathbf{x}_g, t^n, |\hat{a}^n|)$ needed to update the complex envelope field in Eq. (29), is evaluated using the particle $\tilde{\gamma}(\mathbf{x}_\alpha^n)$ function defined in (37), by

$$\chi^n(\mathbf{x}_g) = \frac{q^2}{n_0} \sum_\alpha \hat{S}(\mathbf{x}_g - \mathbf{x}_\alpha^n) [\tilde{\gamma}(\mathbf{x}_\alpha^n)]^{-1}. \quad (44)$$

By mid-point rule, the $\Phi^{n+1/2}(\mathbf{x}_g)$ field is then computed, to update particle positions \mathbf{x}_α^{n+1} and velocities $\mathbf{v}_\alpha^{n+1/2}$ by Eq. (43).

Finally, the current density $\mathbf{J}^{n+1/2}(\mathbf{x}_g)$ in the Maxwell equation for wakefield, (31), is then constructed using particle positions and velocity by

$$\mathbf{J}^{n+1/2}(\mathbf{x}_g) = \frac{q}{cn_0} \sum_\alpha \hat{S}_{\mathbf{x}_g}[\mathbf{x}_g - \mathbf{x}_\alpha^{n+1/2}] \mathbf{v}_\alpha^{n+1/2} \quad (45)$$

where shape function $\hat{S}[\mathbf{x} - \mathbf{x}_\alpha]$ has to be designed in a way to enforce the discretized continuity equation for local charge conservation [17].

In the following, the overall numerical procedure encoding one-step cycle to update particle coordinates, as detailed above, the laser envelope field, Eq. (29) and wakefield solver, (31), will be denoted as ENV/PIC. In the following Section 6, we present a numerical documentation to support error analysis of the proposed schemes.

We have presented in some details the ENV/PIC implementation also because only few works are available on the subject. In work [5], the γ^n function used to implement the Boris algorithm is evaluated by an independent first order integration scheme. In work [3], the Boris procedure to update particle momentum is never explicitly documented, whereas the update of particle position is implemented using a sequence of first order Euler integrations, like a predictor-correction scheme. Moreover, since no error analysis nor convergence test for particle motion has been presented, it is quite difficult to make useful comparisons and cross-checking.

5. Eulerian integration of laser-plasma dynamics in envelope model

Even if the ENV/PIC implementation assures significant saving of computational resources with respect to standard fully kinetic PIC codes (but a precise estimate of speed-up depends crucially

on the chosen number of particle per cell), long time integration of plasma dynamics using particles is still challenging and time consuming. A direct numerical integration of plasma momentum-density equations in Eulerian variables equation (11), coupled to Eqs. (29) and (31), can offer a promising and faster alternative to the ENV/PIC schemes, applicable for several LWFA regimes. In fact, the computational complexity of a discretized fluid model can be evaluated to be roughly equivalent to the corresponding PIC model containing just one particle per cell.

The momentum-density system of Eqs. (11) has the form of a relativistic, pressureless Euler equation with a non-linear forcing coupling momentum advection to the Maxwell field equations. It is clearly challenging since no rigorous numerical analysis results are available. However, accurate and stable integration schemes can still be constructed by taking into account the computational experience in the ordinary Eulerian system for collisional gas dynamics.

A straightforward application of a leapfrog scheme to system (11) using centered numerical derivatives in space and time fails to preserve monotonicity in wave profile (Gibbs pathology) even for modest non-linear steepening, finally leading to numerical instabilities. To prevent or limit this pathology, non-oscillatory (or monotonicity preserving) upwind scheme has been designed and widely applied to simulate compressible fluid dynamics [18]. The implementation we propose here is based on the second order, one-step Adams–Bashforth (AB) scheme for time integration and on second-order Weighted Essentially Non-Oscillatory WENO2 upwind scheme [19] to evaluate space derivatives. We have chosen AB scheme essentially because it is one step and it works as a “modified” leapfrog scheme, and so can be naturally associated to the Maxwell field solvers, thus assuring a unitary computational frame-work for the overall system.

By representing the plasma fluid-dynamics equation (11) in terms of the four-dimensional arrays of fluid variables $u \equiv [\mathbf{p}, n]^T$ (overbar symbols omitted for brevity), one has

$$\partial_t u(\mathbf{x}, t) = F[u, \mathbf{x}, t], \quad (46)$$

where the vector $F \equiv [F_{\mathbf{p}}, F_n]$ has components

$$\begin{aligned} F_{\mathbf{p}} &= -(\mathbf{v} \cdot \nabla \mathbf{p}) + \mathbf{F}_{tot}, \\ F_n &= -\nabla \cdot (n\mathbf{v}), \end{aligned} \quad (47)$$

in which $\mathbf{v} = \mathbf{c}\mathbf{p}/\gamma$ and the total Lorentz force acting on a fluid element is given by

$$\mathbf{F}_{tot}[\mathbf{x}, \mathbf{p}, t] = \frac{q\omega_p}{m} \left[\mathbf{E} + \frac{\mathbf{p}}{\gamma} \times \mathbf{B} \right] - \frac{1}{2\gamma} \nabla \Phi, \quad \Phi = \frac{q^2 |\hat{a}|^2}{2m^2}, \quad (48)$$

with $\gamma(\mathbf{p}, \mathbf{x}, t) = [1 + |\mathbf{p}|^2 + \Phi]^{1/2}$. Here we choose to integrate momentum equation using a non-conservative advection operator $\mathbf{F}_{adv} = (\mathbf{v} \cdot \nabla) \mathbf{p}$, because, in this form, Eq. (46) decouples from the density equation and implementation turns out to be simpler than using the $[n\mathbf{p}]$ momentum variable. We have also implemented momentum equation using a conservative advection flux, but no significant differences between the two implementations have been noticed. On the other hand, there are no general reasons to use conservative advection, since plasma momentum equation has not a general conservation form.

Once discretized on a space–time $[\mathbf{x}_g, t^n]$ grid, the AB update of momentum-density variable $u^n(\mathbf{x}_g)$ is expressed by

$$u^{n+1} = u^n + \frac{\Delta t}{2} [3F^n - F^{n-1}], \quad (49)$$

where $F^n \equiv F[u^n, \mathbf{x}_g, t^n]$. We notice that the update in Eq. (49) is in fact one-step, since F^{n-1} can be evaluated only once at a previous $t^{n-1} \rightarrow t^n$ integration step and then stored. For linear

system, the resulting approximation for time derivative results to be

$$\mathcal{D}_t u = \frac{u^{n+1} - u^n}{\Delta t} = \frac{du}{dt} + c_1 \Delta t^2 \left[\frac{d^3 u}{dt^3} \right] + c_2 \Delta t^3 \left[\frac{d^4 u}{dt^4} \right] \quad (50)$$

showing that the leading order approximation has a dispersive character, as in the associated leapfrog integrator for the envelope and wake field equations, plus a higher order $\mathcal{O}(\Delta t^3)$ dissipative error to balance dissipative numerical errors coming from upwind numerical space derivatives.

Upwind schemes based on the WENO reconstruction procedures offer the following advantages: (i) they assure uniform second (or even higher) order approximation even of steep gradients, and (ii) they provide a robust and accurate numerical approximation of space derivatives, even for non conservative fluid-dynamics systems [20,21].

The numerical procedure encoding the composite [AB – WENO2] scheme for Eq. (46), coupled to field solvers in Eqs. (29) and (31) is here denoted as ENV/Fluid. It turns out to be stable and accurate even for modest grid resolution, for a wide class of problems, covering linear and non-linear conditions, as documented below in the preliminary tests we have considered. For strongly non-linear regimes, when a high intensity laser generates a bubble in the plasma density, a cold-fluid approximation is no longer appropriate.

The ENV/Fluid scheme, where it applies, can fully replace ENV/PIC scheme only in the study of time evolution, structure and propagation properties of the laser-driven wakefield system. When kinetic effects are of interest, like injection and acceleration of electron bunches in a wake field, the ENV/Fluid is no longer appropriate, of course. However, taking advantage of the unitary computational frame-work here proposed, it can still be used in association with the ENV/PIC scheme in a composite hybrid fluid-kinetic computational framework.

6. Numerical benchmark of the envelope approximation

In this section, we test the accuracy of the modified Boris pusher, of the laser envelope solver and the fluid scheme we have introduced in this work. Laser–plasma interaction is in general a strongly nonlinear problem and analytical expressions for the time evolved quantities are only rarely available. Thus, in order to propose a robust benchmark, we first check the correctness of the single particle motion and of laser evolution *in-vacuum*, where it is possible to compare directly the results with the theory, then we investigate the fully nonlinear laser–plasma interaction.

At the current time, we always initialize a laser pulse as the product of a Gaussian transverse profile of given waist at focus w_0 and a Gaussian longitudinal profile with pulse *intensity* duration (Full Width at Half Maximum) τ_{fwhm} , so that $\hat{a}(\mathbf{x}) = a^T(\mathbf{x})a^L(\mathbf{x})$. In particular, the transverse profile is given by

$$a^T(z, r) = \exp \left[-\frac{r^2}{w(z)^2} \right], \quad r^2 = x^2 + y^2, \quad (51)$$

where $w(z)$ is the usual expression for the waist of a Gaussian pulse focalized in $z = z_f$ with a Rayleigh length Z_{Ra} , $w(z) = w_0 \sqrt{1 + \tilde{z}^2}$ and $\tilde{z} = (z - z_f)/Z_{Ra}$, while the longitudinal one is

$$a^L(z, r) = \frac{a_0}{\sqrt{1 + \tilde{z}^2}} \exp(i\varphi) \exp \left[-\frac{(z - z_f)^2}{L_z^2} \right], \quad (52)$$

where, following [2], $\varphi = \arctan(\tilde{z}) - \tilde{z}r^2/w(z)^2$ and L_z is related to the characteristic length $c\tau_{fwhm}$ via $L_z = c\tau_{fwhm}/\sqrt{2 \log(2)}$. From now on, our simulations will refer to a laser pulse of wavelength $\lambda_0 = 0.8 \mu\text{m}$ propagating in a 3D cartesian geometry.

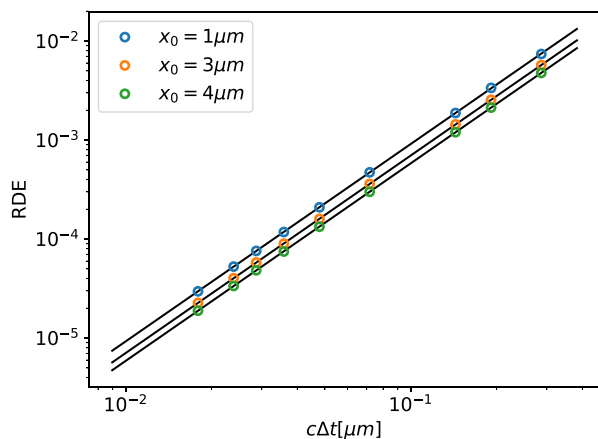


Fig. 1. Relative discretization error of the transverse component of the particle position in function of the resolution (colors online).

6.1. Particle pusher quadratic convergence

We show a grid convergence test performed on particle trajectories interacting with a laser field. In Section 4, we have presented a modified Boris pusher that takes into account the ponderomotive force of the laser expressed in the envelope approximation. Error analysis shows that a second order convergence is expected. To perform this check, we initialized some test particles, distributed with initial zero initial velocity on a plane perpendicular to the laser propagation axis, and four broad laser pulses in vacuum, all of them aligned, that interact via Eq. (13) with the particles. We have chosen a nontrivial field to enhance the effect of the ponderomotive force on the particles. For any test particle, the test has been performed by measuring the final position in function of the resolution and then derived the expected value via a Richardson extrapolation. The Relative Discretization Error (RDE) accumulated along the trajectory scales exactly as $RDE \sim \Delta t^2$, as it is shown in Fig. 1, where every line in LogLog scale has a slope $p = 2$.

6.2. Tests in vacuum

A propagating laser pulse diffracts due to its finite width, that is while moving away from its focal position, *i.e.* defocalizing, the amplitude decreases and the spot size increases to preserve the total energy. In particular, in a linear medium, such as vacuum, it is possible to obtain an analytical expression for the laser pulse evolution by directly solving the electromagnetic wave equation in the paraxial approximation. Rayleigh diffraction thus represents a solid numerical benchmark for any electromagnetic wave solver. Given the amplitude at focus a_0 as the initial condition, the amplitude evolution in time is expressed as $a(t) = a_0 (1 + \tilde{z}^2)$.

In Fig. 2, we study the evolution of the peak amplitude for a $\tau_{fwhm} = 75$ fs and $w_0 = 15$ μm laser pulse starting at the focal point and propagating for 3000 μm , which corresponds to 3.5 Rayleigh lengths. In black, we report the analytical peak amplitude evolution in the paraxial approximation. The measured peak amplitude of the simulated laser pulse during its propagation, represented with the red circles, shows perfect agreement with the theoretical expectations.

The same laser pulse can be initialized before its focal point so that its amplitude has to increase to reach its maximum value exactly at focus. We let the pulse propagate for twice the initial distance from the focus, because, since the electromagnetic field evolution is symmetric, we expect at the end to recover the initial conditions. In a comoving reference frame, longitudinal

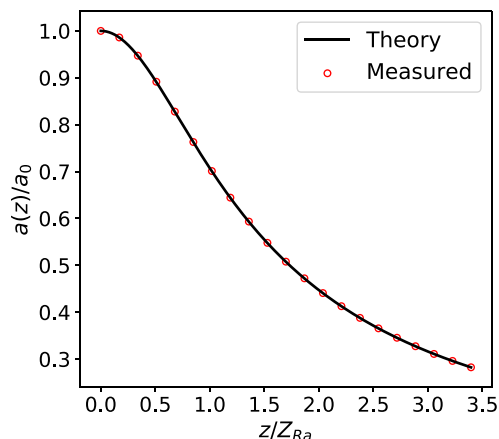


Fig. 2. We show (red circles) the simulated peak amplitude as a function of the propagation distance, for a diffracting laser propagating in vacuum up to a distance of 3000 μm .

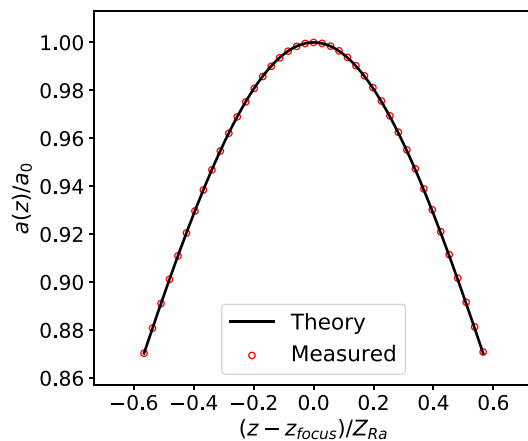


Fig. 3. A laser pulse in vacuum focalizes and then defocalizes so it can be seen that the error is low enough for the initial condition to be recovered.

and transverse laser profiles must therefore overlap after the diffraction process but in numerical simulations, temporal symmetry can only be achieved if numerical dissipation, affecting the total energy, and dispersion, affecting the propagation speed, are kept very low. In particular, in a leapfrog integration scheme, only dispersive error is expected. In Fig. 3, is shown the peak amplitude evolution before and after focusing. In Figs. 4(a) and 4(b), the longitudinal and transverse profiles are overlapped, to verify that the integration scheme presents very low dispersion over long distances. Since the results agree with the expected values, time reversibility is assured. These simulations were run with a resolution of $\lambda_0/\Delta z = 12.5$, with $\Delta y = \Delta x = 8.99\Delta z$ and a CFL $\sigma = 0.7$.

In Section 3, we presented an optimized numerical integration scheme to reduce the dispersive effects affecting wave propagation speed. In the following, we study the envelope solver dispersive error in function of the resolution for a laser pulse with $\tau_{fwhm} = 75$ fs, $w_0 = 30$ μm , $a_0 = 1$ propagating in vacuum, evaluating dispersive effects measured either with the standard FDTD centered scheme or with the optimized one defined in Eq. (25). Then, we compare the outcomes with the results obtained simulating the same laser pulse with a standard PIC code, that is when laser oscillations are retained. It is known that to well reproduce group velocities in a PIC scheme, the highest frequency (*i.e.* laser frequency) has to be well resolved.

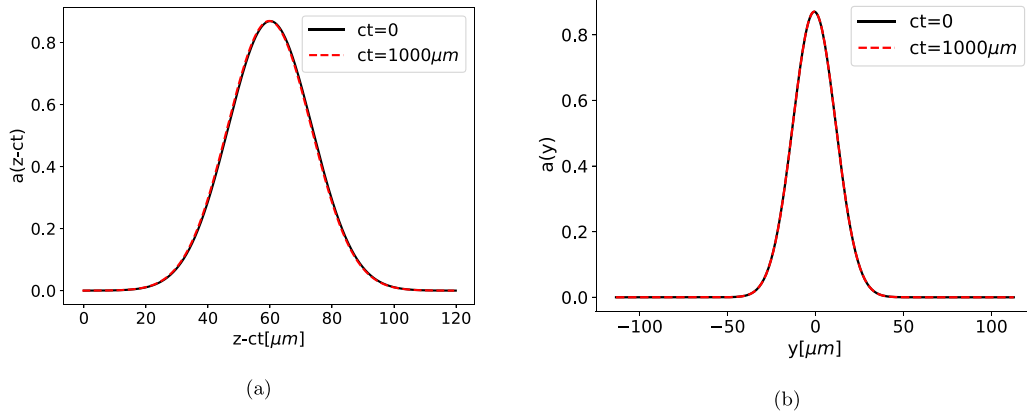


Fig. 4. Superposition of the longitudinal (Fig. a) and transverse (Fig. b) laser profile at the beginning and at the end of the simulation.

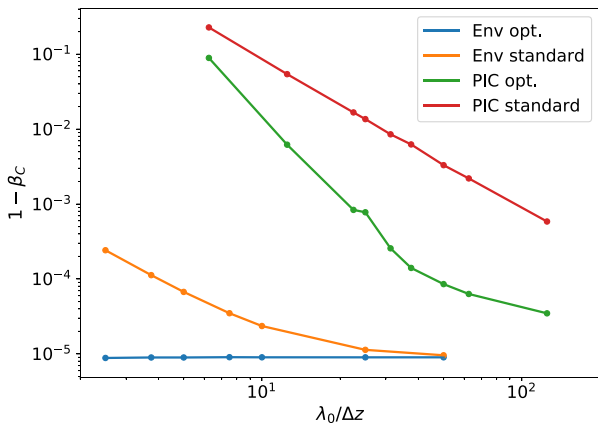


Fig. 5. Comparison between the phase velocities of the laser pulse centroid when it is propagating in vacuum in various computational configurations. In particular, in the ENV/PIC optimized case, $1 - \beta_c$ is lower than the measurement error for every resolution we considered (colors online).

For a laser pulse propagating in vacuum, we define the centroid position as

$$z_c(t) = \frac{\int z |\hat{a}(\mathbf{x}, t)|^2 d\mathbf{x}}{\int |\hat{a}(\mathbf{x}, t)|^2 d\mathbf{x}} = \frac{\sum_{\mathbf{x}_g} z_i \hat{a}_{i,j,k}^n}{\sum_{\mathbf{x}_g} \hat{a}_{i,j,k}^n}, \quad (53)$$

where the sum is extended on all the computational grids, then we numerically derive $z_c(t)$ to get the group velocity. For the two computational frameworks considered (PIC and ENV/PIC), $1 - \beta_c = 1 - v_g/c$ for both the standard centered and the optimized differentiation schemes are represented in Fig. 5. In this run, while varying Δz , we fixed a uniform transverse grid (that is $\Delta y = \Delta x = \Delta z$) and $\sigma = 0.8$. To obtain comparable errors in the PIC scheme, resolution must be increased by at least an order of magnitude, depending on the problem, thus assuring the strong time saving property of the envelope solver. We point out that for optimized derivative in the ENV scheme, discretization error is well below the measurement one, induced by Eq. (53).

6.3. Nonlinear laser–plasma interaction

For a robust test in the nonlinear regime, we follow the “Test 3” reported in [6] where a comparison of the wakefield generated by INF&RNO/Fluid (a fluid 2D cylindrical code based on the envelope description, see [6,9]) and the 1D (broad pulse) analytical nonlinear theory is presented. Performing the simulation with

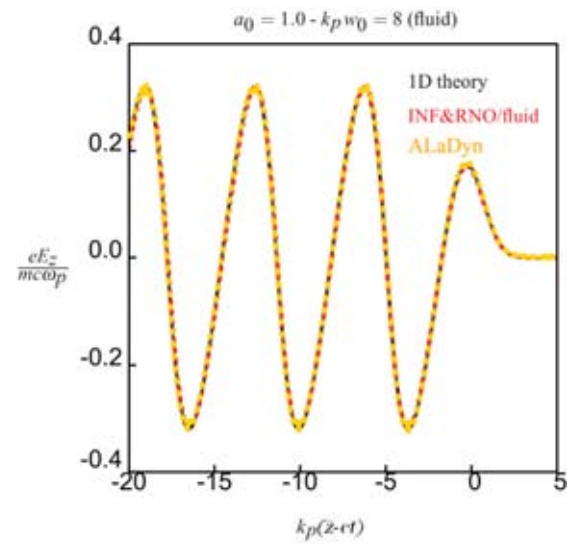


Fig. 6. Wakefield generated by a 1D configuration. We compare it with the theoretical result given by the 1D quasi-static nonlinear theory (black) and the one obtained by INF&RNO/Fluid (colors online).

the same parameters, we obtain perfectly overlapping results with the INF&RNO/Fluid and the analytical value, as shown in Fig. 6, where the propagation distance has been normalized to the plasma wavenumber. Such result shows the correctness of the particle motion for particles self-consistently coupled to the wakefield.

In LWFA experiments, where the acceleration distance can be of the order of many Rayleigh lengths, guiding methods have been proposed to avoid early laser diffractions. In particular, a Gaussian pulse can be matched in a parabolic density plasma channel, where the Rayleigh diffraction is balanced by the focalizing effect due to the medium, and therefore no significant changes in the longitudinal and transverse profile are present for propagation distances $z \gg Z_{Ray}$. In [7,22], a semianalytical model is developed to compute the exact propagation velocity of a laser pulse in a matched plasma channel of given density profile, with $a_0 < 1$. For accurate simulations of LWFA regimes, it is crucial that group and phase laser velocity are well reproduced by the laser solver even when the pulse interacts with a nonlinear medium for long distances. To check the stability of the proposed solver, a laser pulse with $a_0 = 0.1$, $w_0 = 8.9 \mu\text{m}$ and $\tau_{fwhm} = 21.3 \text{ fs}$ is shot through a matched plasma channel with a density on axis $n_0 = 4.25 \times 10^{18} \text{ cm}^{-3}$, then we compare the results

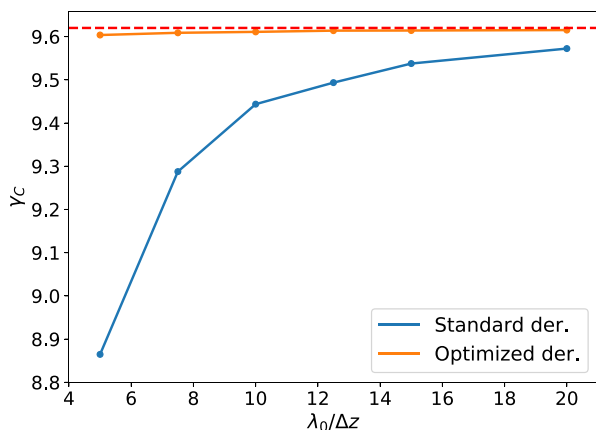


Fig. 7. Relativistic factor γ_c concerning the propagation of a Gaussian laser pulse in a matched plasma channel in function of the resolution. The semianalytical value is shown in red (colors online).

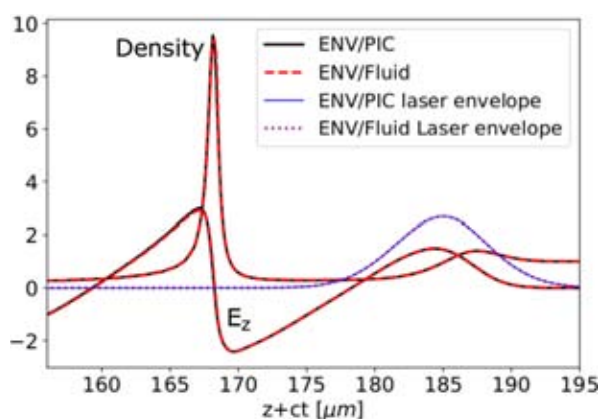


Fig. 8. We show a comparison after $ct = 150 \mu\text{m}$ of propagation between an ENV/PIC and an ENV/Fluid simulation in a mildly nonlinear regime, where we expect the fluid model to hold.

of the measured group velocity obtained with the optimized and standard numerical derivatives. With this choice of the laser and plasma parameters, the expected value for the relativistic factor associated with the laser centroid is $\gamma_c = 9.63$. In Fig. 7 it can be seen that the optimized algorithm shows much faster than quadratic convergence to the exact value even for modest resolutions.

6.4. Benchmark of the Eulerian integrator for the plasma fluid density

It is expected the fluid model to precisely reproduces the same fields as the PIC scheme away from the plasma bubble regime, where wavebreaking happens and the Lorentz–Maxwell system of equations does not provide an adequate description. Such regime is in fact limited by the theoretical foundation of the plasma fluid description and by the practical need to deal with the typical discontinuities that characterize the strongly nonlinear laser plasma interaction. In fact, one should resort to very specific integration schemes, able to avoid instabilities and to enforce the numerical density positivity in the continuity equation. For this reason, simulation of an extremely nonlinear regime in a fluid framework is still a theoretical and computational open problem, even though some comparisons have been provided in [23,24] that show some disagreements in the wakefield generation with respect to a fully kinetic code. In Fig. 8, we report the

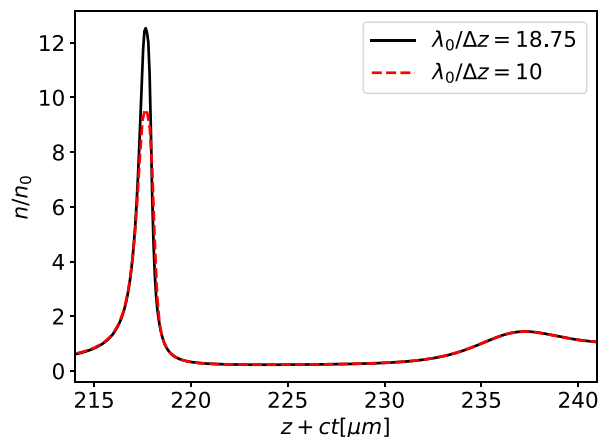


Fig. 9. Dissipation effects in density relative to the AB-WENO2 scheme after $ct = 200 \mu\text{m}$ of laser propagation in a uniform plasma.

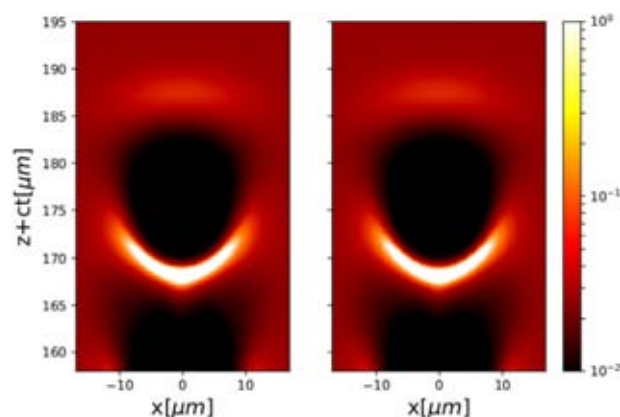


Fig. 10. Log density maps relative to the simulation presented in Fig. 8 obtained in the ENV/PIC (left) and in the ENV/Fluid (right) (colors online).

comparison between an ENV/PIC and an ENV/Fluid simulations when considering the nonlinear laser plasma interaction generated by the propagation of a nonlinear laser pulse with $a_0 = 2.5$, $w_0 = 12.7 \mu\text{m}$ and $\tau_{fwhm} = 20 \text{fs}$ in a uniform plasma of density $n_0 = 4.25 \times 10^{18} \text{cm}^{-3}$. The ENV/PIC simulation was run with a resolution $\lambda_0/\Delta z = 10$, while in this configuration we needed $\lambda_0/\Delta z = 18.75$ with $\sigma = 0.4$ in the ENV/Fluid to reach the perfect agreement. For lower resolutions in the ENV/Fluid configuration, the numerical diffusion induced by discretization errors of the upwind scheme, generated high dissipation of the density profile peak amplitude after $200 \mu\text{m}$ of propagation. The dissipative effect is quite sensitive to the adopted resolution, as shown in Fig. 9 where the same ENV/Fluid configuration is run with a resolution $\lambda_0/\Delta z = 10$. At the end, an overall comparison based on empirical observation, is shown in Fig. 10, where the 2D density maps relative to the ENV/PIC and the ENV/Fluid simulations with the same parameters as in Fig. 8 present a good agreement also for the transverse density distribution.

7. Conclusions

We have presented in detail integration schemes and implementation procedures for numerical simulation of the envelope model for LWFA regimes. The field solver for laser propagation has been implemented in the laboratory coordinate system in 3D cartesian geometry. This unconventional approach allows, in particular, to integrate the exact (to within the model) wave equation

for the envelope field by an explicit leapfrog scheme working under the same CFL stability condition as in the related Maxwell solver for wakefield and PIC particles motion. Since in the physical regimes under consideration, laser-wakefield propagation is advection dominated, that is time evolution is slow, quasi-static in the limit, in a comoving system, numerical space derivatives along the propagation direction have been properly designed to reduce dispersion errors coming from discretized wave operators. This strongly improves grid convergence to the envelope model theoretical predictions for wave propagation speed, as documented in Section 6.

The particle equation of motion has been integrated by a leapfrog scheme using the classical Boris pusher, properly modified to take into account the ponderomotive envelope component in the Lorentz force. Quadratic grid convergence of numerical error in the particle motion, supporting error analysis of the proposed scheme, has been clearly documented in Section 6.

Besides the ENV/PIC implementation, based on PIC particles, a second integration scheme, denoted as ENV/Fluid, where plasma equation of motion is formulated using Eulerian fluid momentum-density variables, has been presented and tested.

The proposed implementations, ENV/PIC and ENV/Fluid, have been designed on a unitary, self-consistent computational framework. The resulting set of all numerical procedures has been encoded in ALADYN-v2018.3 package [25]. The code runs in parallel platforms using standard domain decomposition and MPI procedures. As a preliminary estimate to evaluate the cpu computational resources needed for numerical simulations of realistic LWFA regimes, we take under consideration the ENV/PIC run with $\lambda_0/\Delta z = 10$ and the ENV/Fluid one with $\lambda_0/\Delta z = 18.75$ presented in Fig. 8. We quote a value of $\tau_e \sim 20$ h/mm (run with $N_{p.p.c} = 20$ particles per cell) for ENV/PIC code and $\tau_f \sim 2.5$ h/mm for ENV/Fluid, where both cases were run on 1156 cores on MARCONI (CINECA). Clearly, the comparison has to be made between two converged (in terms of resolution) configurations to correctly estimate the computational time. Anyway, from our measurement, the ENV/Fluid scheme run at $\lambda_0/\Delta z = 10$ takes $\tau_f \sim \tau_e/20$, which confirms that a fluid code is faster by a factor $N_{p.p.c}$ with respect to an ENV/PIC scheme.

Acknowledgments

We would like to thank Carlo Benedetti, for the useful discussions and the precious advices he gave us during the proceeding of this work. We also acknowledge the A. Marocchino grant ISB15_SIPWFA and the P. Londrillo grant IS65_ENV-LWFA under the ISCR initiative at CINECA, for the availability of high performance computing resources and support. Also, we acknowledge support from the European Union's Horizon2020 research and innovation programme under grant agreement No.653782 (EuPRAXIA project), and from the MIUR funded Italian research Network ELI-Italy (D.M.n. 631/16).

Appendix A. Reducing dispersive error in the envelope propagation

To envisage optimal (δ_1, δ_2) parameter values in the modified numerical derivatives equation (25), one first considers the numerical dispersion relation of the linear ($\chi = 1$) equation (9), expressed by the eigenvalues of the numerical operators on a Fourier basis $\sim \exp[i(\mathbf{k} \cdot \mathbf{x}_g - \omega \Delta t)]$:

$$\hat{\Omega}^2 - c^2[\hat{K}_z^2(1 + \delta_2(\Delta z)^2\hat{K}_z^2) + \sum_{c=x,y} \hat{K}_c^2] + 2\omega_0[\hat{\Omega} - c\hat{K}_z(1 + \delta_1(\Delta z)^2\hat{K}_z^2)] = \omega_p^2 \quad (\text{A.1})$$

where

$$\hat{\Omega}^2 \equiv \frac{\sin^2(\omega \Delta t/2)}{(\Delta t/2)^2}, \quad \hat{\Omega} \equiv \frac{\sin(\omega \Delta t)}{\Delta t} \quad (\text{A.2})$$

$$\hat{K}_c^2 \equiv \frac{\sin^2(k_c \Delta c/2)}{(\Delta c/2)^2}, \quad \hat{K}_z \equiv \frac{\sin(k_z \Delta z)}{\Delta z}.$$

Expanding $\sin(u) = u - u^3/6 + \mathcal{O}(u^5)$, one recovers the exact dispersion relation equation (17) to the leading second order approximation:

$$\omega^2 + 2\omega_0(\omega - ck_z) - c^2(k_z^2 + k_x^2 + k_y^2) = TE_1 + TE_2, \quad (\text{A.3})$$

where the truncation errors TE_1 and TE_2 , defined as

$$TE_1 = -\frac{\omega_0}{6}[\omega(\omega \Delta t)^2 - ck_z(k_z \Delta z)^2(1 + 6\delta_1)],$$

$$TE_2 = -\frac{1}{12}[\omega^2(\omega \Delta t)^2 - c^2k_z^2(k_z \Delta z)^2(1 + 12\delta_2) - c^2 \sum_{c=x,y} k_c^2(k_c \Delta c)^2], \quad (\text{A.4})$$

come from the discretized first and second derivatives in time and space, respectively. By expressing the time step size by $\Delta t = \sigma \hbar \Delta z$, where σ is the Courant number, and by taking into account that $\omega = ck_z + \mathcal{O}(k_0 \varepsilon^2)$, the dispersive numerical errors for wave propagation along the z coordinate can be reduced to the $\mathcal{O}(\varepsilon^2)$ size by selecting $\delta_1 = (\nu^2 - 1)/6 < 0$, and $\delta_2 = (\nu^2 - 1)/12 < 0$, where $\nu = \sigma \hbar$.

The numerical dispersion relation for the Maxwell equation (31) has the same form of Eq. (A.1) with $\omega_0 = 0$:

$$\hat{\Omega}^2 - c^2 \left[\hat{K}_z^2(1 + \delta_3(\Delta z)^2\hat{K}_z^2) + \sum_{c=x,y} \hat{K}_c^2 \right] = \omega_p^2. \quad (\text{A.5})$$

Now, if $\mathcal{D}_z^{(o)}$ applies only to $\mathcal{D} \times \mathbf{E}$ terms, $\delta_3 = \delta_2$ whereas if it applies also to $\mathcal{D} \times \mathbf{B}$ terms, $2\delta_3 = \delta_2$, as reported in the main text.

Appendix B. Linear stability analysis for the envelope equation

To evaluate the condition for linear stability, the numerical dispersion relation of the discretized envelope equation (26) multiplied by $\Delta t^2/4$ is now expressed by

$$\sin^2\left(\frac{\omega \Delta t}{2}\right) = c^2 \Delta t^2 \left[\hat{P}_2 + \frac{k_p^2}{4} \right] + \frac{\eta}{2} \hat{P}_1,$$

$$\hat{P}_2 \equiv \sum_c \frac{\sin^2(k_c \Delta c/2)}{\Delta_c^2} + \delta_2 \frac{\sin^4(k_z \Delta z)}{\Delta z^2}, \quad (\text{B.1})$$

$$\hat{P}_1 \equiv \frac{c \Delta t}{\Delta z} \sin(k_z \Delta z)[1 + \delta_1 \sin^2(k_z \Delta z)] - \sin(\omega \Delta t),$$

where $\eta = ck_0 \Delta t = \omega_0 \Delta t$.

Now, by evaluating each spatial wavenumber k_c , $c = x, y, z$ at the Nyquist frequency $[k_c]_{max} = \pi/\Delta c$, one has the upper bound estimate,

$$\sum_c \frac{\sin^2(k_c \Delta c/2)}{\Delta_c^2} + \delta_1 \frac{\sin^4(k_z \Delta z)}{\Delta z^2} < \frac{1}{\hbar^2 \Delta z^2} + \frac{\delta_1}{\Delta z^2}, \quad (\text{B.2})$$

and then, by inserting the relation defining the Courant number relation $c \Delta t = \sigma \hbar \Delta z$,

$$(c \Delta t)^2 [\hat{P}_2 + k_p^2/4] < \sigma^2 [1 + \hbar^2 (\Delta z k_p/2)^2 + \delta_2 \hbar^2]. \quad (\text{B.3})$$

The second term on the right hand side of Eq. (B.1) can be bounded by

$$\hat{P}_1 < \frac{c \Delta t}{\Delta z} [1 + 4\delta_1], \quad (\text{B.4})$$

and the linear stability condition $\sin^2(\omega\Delta t) < 1$ entails the estimate for the Courant number

$$\sigma \leq \left[1 + \bar{h}^2 \left(\frac{\Delta z k_p}{2} \right)^2 + \delta_2 \bar{h}^2 + k_0 \Delta z \bar{h}^{-2} \frac{1 + 4\delta_1}{2} \right]^{-1/2} \quad (\text{B.5})$$

We notice, that the same procedure applied to the linearized Maxwell equation for wake fields, gives the standard condition for stability

$$\sigma_0 \leq \left[1 + \bar{h}^2 \left(\frac{\Delta z k_p}{2} \right)^2 + \frac{\delta_2 \bar{h}^2}{2} \right]^{-1/2} \quad (\text{B.6})$$

showing that the explicit integration of the envelope wave equation requires only a small correction

$$\sigma \leq \sigma_0 \left[1 - k_0 \Delta z \bar{h}^{-2} \frac{1 + 4\delta_1}{4} \right], \quad (\text{B.7})$$

depending on the grid resolution $k_0 \Delta z$ of laser wavenumber. In Eq. (B.7), the longitudinal cell size Δz is necessarily the same as the one in Eq. (B.6), for consistency reasons.

References

- [1] P. Mora, T.M. Antonsen Jr, *Phys. Plasmas* 4 (1) (1997) 217–229.
- [2] B. Quesnel, P. Mora, *Phys. Rev. E* 58 (3) (1998) 3719.
- [3] B. Cowan, D. Bruhwiler, E. Cormier-Michel, E. Esarey, C. Geddes, P. Messmer, K. Paul, *J. Comput. Phys.* 230 (1) (2011) 61–86.
- [4] E.A. Startsev, *Phys. Rev. E* 55 (6) (1997) 7527.
- [5] P. Messmer, D.L. Bruhwiler, *Phys. Rev. ST Accel. Beams* 9 (2006) 031302, <http://dx.doi.org/10.1103/PhysRevSTAB.9.031302>.
- [6] C. Benedetti, C. Schroeder, E. Esarey, C. Geddes, W. Leemans, *AIP Conference Proceedings*, vol. 1299, (1) AIP, 2010, pp. 250–255.
- [7] C. Benedetti, F. Rossi, C. Schroeder, E. Esarey, W. Leemans, *Phys. Rev. E* 92 (2) (2015) 023109.
- [8] A. Helm, J. Vieri, L. Silva, R. Fonseca, *APS Div. Plasma Phys. Meet.* (2016) abstract id. GP10011.
- [9] C. Benedetti, C. Schroeder, C. Geddes, E. Esarey, W. Leemans, *Plasma Phys. Control. Fusion* 60 (1) (2017) 014002.
- [10] M. Kärkkäinen, E. Gjonaj, T. Lau, T. Weiland, Low-dispersion wake field calculation tools, in: *Proc. International Computational Accelerator Physics Conference*, 2006.
- [11] P. Londrillo, C. Benedetti, A. Sgattoni, G. Turchetti, *Nuclear Instrum. Methods Phys. Res. A* 620 (2010) 28–35.
- [12] A. Pukhov, *Proceedings of CAS-CERN Accelerator School: Plasma Wake Acceleration*, 23-29 November 2014, Holzer, CERN-2016-001, (CERN, Geneva Switzerland), 2016, pp. 181–206.
- [13] R. Lehe, A. Lifschitz, C. Thauray, V. Malka, X. Davoine, *Phys. Rev. ST Accel. Beams* 16 (2013) 021301.
- [14] J.P. Boris, *Proceedings of Forth Conference on Numerical Simulation Plasmas*, Naval Research Laboratory, Washington, D.C. 1970, 1970, pp. 3–67.
- [15] J.L. Vay, *Phys. Plasmas* 15 (5) (2008) 056701.
- [16] D. Gordon, W. Mori, T. Antonsen, A Ponderomotive Guiding Center PIC Code for Modeling Laser-Plasma Accelerations, in: *APS Division of Plasma Physics Meeting Abstracts*, 1999.
- [17] T.Z. Esirkepov, *Comput. Phys. Comm.* 135 (2) (2001) 144–153.
- [18] R.J. LeVeque, *Numerical Methods for Conservation Laws*, Springer, 1990, pp. 122–135.
- [19] S.O. Xu-Dong Liu, T. Chang, *J. Comput. Phys.* 115 (1) (1994) 200–212.
- [20] A. Rehman, S. Qamar, *Comput. Math. Appl.* 76 (11–12) (2018) 2648–2664.
- [21] C.-C. Wu, *Geophys. Astrophys. Fluid Dyn.* 101 (1) (2007) 37–61.
- [22] C. Schroeder, C. Benedetti, E. Esarey, J. van Tilborg, W. Leemans, *Phys. Plasmas* 18 (8) (2011) 083103.
- [23] F. Massimo, S. Atzeni, A. Marocchino, *J. Comput. Phys.* 327 (2016) 841–850.
- [24] A. Marocchino, F. Massimo, A. Rossi, E. Chiadroni, M. Ferrario, *Nucl. Instrum. Methods Phys. Res. A* 829 (2016) 386–391.
- [25] S. Sinigardi, D. Terzani, P. Londrillo, A. Marocchino, F. Massimo, F. Mira, A. Sgattoni, *Aladyn/aladyn: Aladyn v2018.3*, 2018, <http://dx.doi.org/10.5281/zenodo.1477315>.

Optical diagnostics for density measurement in high-quality laser-plasma electron accelerators

Fernando Brandi¹ and Leonida Antonio Gizzi^{1,2}

¹*Intense Laser Irradiation Laboratory (ILIL), Istituto Nazionale di Ottica – Consiglio Nazionale delle Ricerche (INO-CNR), Sede Secondaria di Pisa, Via Moruzzi, 1, 56124 Pisa, Italy*

²*Istituto Nazionale di Fisica Nucleare (INFN), Sezione di Pisa, Largo Bruno Pontecorvo, 3, 56127 Pisa, Italy*

(Received 7 August 2018; revised 28 February 2019; accepted 21 March 2019)

Abstract

Implementation of laser-plasma-based acceleration stages in user-oriented facilities requires the definition and deployment of appropriate diagnostic methodologies to monitor and control the acceleration process. An overview is given here of optical diagnostics for density measurement in laser-plasma acceleration stages, with emphasis on well-established and easily implemented approaches. Diagnostics for both neutral gas and free-electron number density are considered, highlighting real-time measurement capabilities. Optical interferometry, in its various configurations, from standard two-arm to more advanced common-path designs, is discussed, along with spectroscopic techniques such as Stark broadening and Raman scattering. A critical analysis of the diagnostics presented is given concerning their implementation in laser-plasma acceleration stages for the production of high-quality GeV electron bunches.

Keywords: gas target; interferometry; laser-plasma; laser wake-field acceleration; Raman scattering; Stark broadening

1. Introduction

Nowadays, research activities in the field of plasma-based particle acceleration are shifting from the investigation of fundamental processes aimed at understanding and optimizing the acceleration mechanism, to the actual practical implementation of such promising technologies. For example, laser wake-field acceleration (LWFA) is foreseen as being implemented in user-oriented facilities to deliver high-quality GeV electron bunches^[1, 2] which are typically obtained from multiple laser-plasma stages (for example, injectors and accelerators), and should be suitable for injection in a free-electron laser (FEL). Also, beam-driven plasma wake-field acceleration is considered as a suitable candidate for 1 GeV injectors in compact FEL facilities^[3].

In this context the definition and deployment of appropriate diagnostic tools for efficient and reliable monitoring of the main process parameters are of paramount importance to fulfill the goal of a functional user-oriented facility. In fact, robust and possibly real-time diagnostic tools are needed for the implementation of the adequate control procedures that are necessary to achieve long-term stable operation of the accelerator.

Concerning the LWFA stages, one of the fundamental parameters is the particle number density in the gas used as the target medium and the free-electron density in the plasma thereby created. The gas can either be pre-ionized to form a plasma^[4] or photo-ionized by the initial part of the main high-intensity ultra-short driving laser pulse itself^[5].

Here, an overview is given of existing optical diagnostics suitable for neutral gas and free-electron number density measurements in laser-plasma accelerator stages (LPA). Both interferometry, in its various configurations, and optical emission spectroscopy (OES), specifically Stark broadening and Raman shift measurements, are discussed. These techniques are analyzed, aimed at their implementation as robust and reliable diagnostics. The sensitivity (that is, the lowest density value that can be reliably measured) and ease of implementation and operation are considered.

All interferometric methods require an appropriate optical line of sight through the sample. In the case of a freely expanding gas jet, interferometry is easy to implement, whereas in the case of confined samples (for example, gas cells and square cross-section capillaries), flat optical side windows are necessary to provide the optical path for transverse interferometry^[4, 6–8]. If a transverse line of sight is not present (as in cylindrical capillaries), then longitudinal interferometry must be adopted, resulting in an average density value along the main laser beam propagation direction.

Correspondence to: F. Brandi, Istituto Nazionale di Ottica – Consiglio Nazionale delle Ricerche (INO-CNR), Sede Secondaria di Pisa, Via Moruzzi, 1, 56124 Pisa, Italy. Email: fernando.brandi@ino.cnr.it

In contrast, optical emission spectroscopy does not require a line of sight through the sample, thus making it easy to implement^[9]. OES can be performed both longitudinally or transversely to the main laser beam and, if imaging spectrometers are used, information on the space-dependent density can be obtained from a single measurement.

Both pure gases and gas mixtures^[10] have been used in laser-plasma acceleration studies, with a very promising medium to obtain high-quality GeV electron bunches being hydrogen^[4, 11]. Therefore, we consider hydrogen gas here, with densities in the range 10^{17} – 10^{19} cm⁻³ being well suited for LWFA. In general, the number density of free electrons in the plasma can be estimated from measurements of the neutral particle number density^[12]. Full ionization of a hydrogen molecule creates a pair of free electrons, and a straightforward relation exists between the neutral hydrogen density and the free-electron density. Thus, estimation and, ultimately, control of the electron density can be implemented through the measurement of the molecular particle density within the target. In the case of a pre-formed plasma – for example, discharged gas-filled capillaries^[13] – a measurement of the actual plasma density has to be performed since, due to plasma dynamics^[4, 13], the local plasma density along the propagation path of the main laser beam is actually different from the background plasma density value obtained by assuming full ionization of the gas.

For the numerical estimates of the interferometric phase shifts given in this work, the fundamental and second harmonic of a Ti:sapphire laser, at 800 nm and 400 nm, respectively, are considered as probe beams. However, the calculations can easily be extended to other gases and different probe beam wavelengths. If gases other than hydrogen are considered there still exists a direct relationship between the neutral gas number density and the background free-electron density in the plasma, which can be estimated by evaluating the degree of ionization using well-known photoionization models^[5]. For instance, helium is another gas suitable for obtaining high-quality 1 GeV electron beams from LWFA^[14, 15], in which more energy is necessary to get full ionization (two electrons per atom) compared to hydrogen molecules. If other lasers are used, the numerical values reported can be scaled easily by considering the wavelength-dependent index of refraction.

2. Interferometric methods

With interferometry, the density of a neutral gas or a plasma is evaluated by measurement of the phase shift acquired by an optical probe beam when passing through the sample relative to a known reference phase. The refractive index $\eta(n)$ of the sample is in fact dependent on the particle number density n , with the refractivity $\eta(n) - 1$ actually being proportional to the particle number density n_g in a gas and of

free electrons n_e in a plasma. For neutral atoms/molecules, as from the Lorentz–Lorenz equation^[16], the refractivity can be expressed as $\eta_g(\lambda, n_g) - 1 = [\eta_0(\lambda) - 1] \times n_g/n_0$, where λ is the wavelength of the light and the reference value $\eta_0(\lambda)$ is the refractive index at a specific number density n_0 . The Loschmidt constant 2.69×10^{19} cm⁻³, being the particle number density of a perfect gas at standard temperature and pressure (STP: 273.15 K and 1 atm), is typically used as a reference value. In an underdense plasma the refractivity is $\eta_e(n_e, \lambda) - 1 = -\frac{n_e e^2 \lambda^2}{8\pi^2 m_e \epsilon_0 c^2}$, where e is the electron charge, m_e is the electron mass, ϵ_0 is the vacuum permittivity and c is the speed of light.

In general, the phase acquired by a light beam when passing through a sample of length L is $\phi = \frac{2\pi}{\lambda} \int_L \eta(l, \lambda) dl = \frac{2\pi}{\lambda} \times L \times \overline{\eta(\lambda)}$, where $\overline{\eta(\lambda)}$ is the average refractive index along the geometrical path. Therefore, with an interferometric measurement the information acquired is related to the line-integrated particle density.

To retrieve the actual density value from interferometric measurements, some assumptions on the spatial density distribution of the sample have to be made. There are two typical cases: cylindrically symmetric samples (for example, pulsed gas jets from circular nozzles) and non-cylindrically symmetric samples (for example, pulsed gas jets with rectangular nozzles). For the simplest case of cylindrically symmetric samples the well-known Abel inversion method is used, which allows one to extract the actual value of the radially dependent density from line-integrated measurements along several chords^[17, 18]. In the case of non-cylindrically symmetric targets, multiple measurements along different lines of sight are necessary to implement a 3D tomographic reconstruction procedure^[19, 20]. Finally, in the case of homogeneous samples, such as uniformly filled gas cells, the density is actually given by the average density measured by means of interferometry^[21].

An interferometric measurement can be performed over a extended area of the plasma using an optical imaging system and camera as the light detector to acquire an image (the so-called interferogram), which enables 2D mapping of the line-integrated density over the light beam cross-section. In such a case, a numerical analysis of the interferogram is necessary to extract the actual phase shift using a phase-retrieval algorithm comprising phase-unwrapping procedures. Such measurements allow one to obtain an actual 2D map of the density, which is necessary to understand and monitor physical phenomena in ultra-fast laser–plasma interactions, especially during alignment and tuning of the LPA stages. As an example of a 2D measurement, in Figure 1 an interferogram of a supersonic gas jet in vacuum acquired by a Nomarski interferometer is shown, along with the density map retrieved from a phase-retrieval algorithm. Conversely, a 1D measurement of the average density along the laser beam path in the sample is performed when the intensity over the entire light beam cross-section is acquired using a

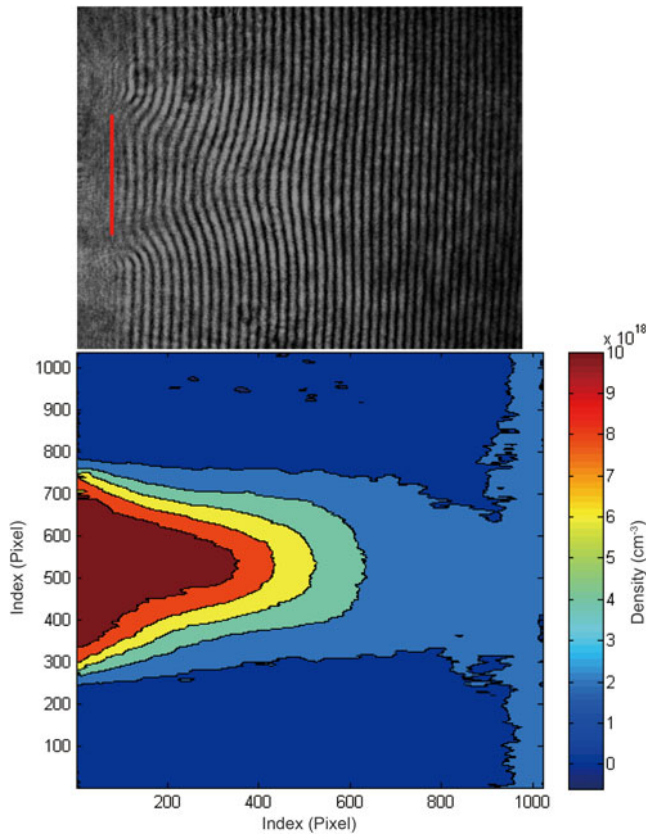


Figure 1. Upper panel: interferogram of a pulsed gas jet in vacuum with a rectangular orifice acquired by means of a Nomarski interferometer; lower panel: corresponding average density map obtained with a phase-retrieval algorithm^[22].

photodiode or a photomultiplier tube (PMT) as the light detector. These 1D measurements are much faster and require less intense data analysis than the 2D measurements, making them potentially more suitable during LPA operation (for example, to monitor in real time the particle number density in the interaction region).

The main interferometric methods used to measure the particle density in LPA targets are schematically summarized in Figure 2 and discussed in the following.

2.1. Two-arm interferometers

In a two-arm interferometer (TAI) the phase shift is measured relative to the phase of a reference optical beam not passing through the sample but typically through a vacuum where the refractive index value is unity. The measured phase shift is then given by $\Delta\phi_{\text{TAI}}(\lambda) = \frac{2\pi}{\lambda} \int_L [\eta(\lambda) - 1] dl$. Two-arm interferometry can be implemented in two main configurations, depending on the optical design adopted.

I *Standard TAI*, such as Mach–Zehnder interferometers, where the light beam is split into two distinct beams following different geometrical paths, called

the reference and measurement arms, which are then recombined and interfere^[7, 23, 24].

II *Modified TAIs*, also called two-arm folded, where the light beam is split into two parts after passing through the sample, and interference takes place between the part of the beam that has passed through the sample and the part of the beam not passing through the sample^[18, 25]. This method provides good control on the fringe spacing and image formation.

The standard TAIs suffer from a very high susceptibility to environmental conditions (for example, mechanical vibration and temperature changes) while the folded TAI is relatively more robust against environmental conditions due to the more compact size of the two-arm section. The typical sensitivity of an ultra-fast imaging TAI can be hundredths of a fringe (~ 0.1 rad). To achieve better sensitivity, on the order of a few milliradians, special care has to be taken during the measurement by making use of a probe beam with very good quality, active mechanical stabilization and averaging^[19]. The latter may hamper implementation of TAIs for real-time measurement and online monitoring applications. However, TAIs may find applications for the characterization, alignment and optimization of LPA stages due to their versatility.

Besides time-domain measurements, also spectral-domain interferometry has been implemented in TAIs for the measurement of the free-electron density in discharged capillaries using ultra-fast laser pulses^[26, 27]. These measurements are based on the density-dependent group velocity of an ultra-short laser pulse when propagating in a plasma channel^[13]. Specifically, the group velocity delay between a laser pulse propagating in vacuum and a laser pulse propagating through the plasma inside the discharged capillary actually depends on the mismatch of the group index of refraction due to the free electrons. However, such a two-arm configuration poses serious challenges which prevent its use in monitoring discharged capillary-based LPA for high-quality accelerators in user-oriented facilities. This limitation can be overcome by instead adopting spectral-domain second-harmonic interferometry, as will be discussed later.

2.2. Nomarski-type interferometers

These are similar in principle to the modified TAI, and the phase measured is exactly the same (reference beam in vacuum and signal beam over the object), but they have a somewhat easier setup, being a quasi-common-path configuration with minimal geometrical separation between the two interfering parts of the beam. Typical configurations are as follows.

I *Standard Nomarski interferometer*, where the two interfering beams are separated by means of a Wollaston

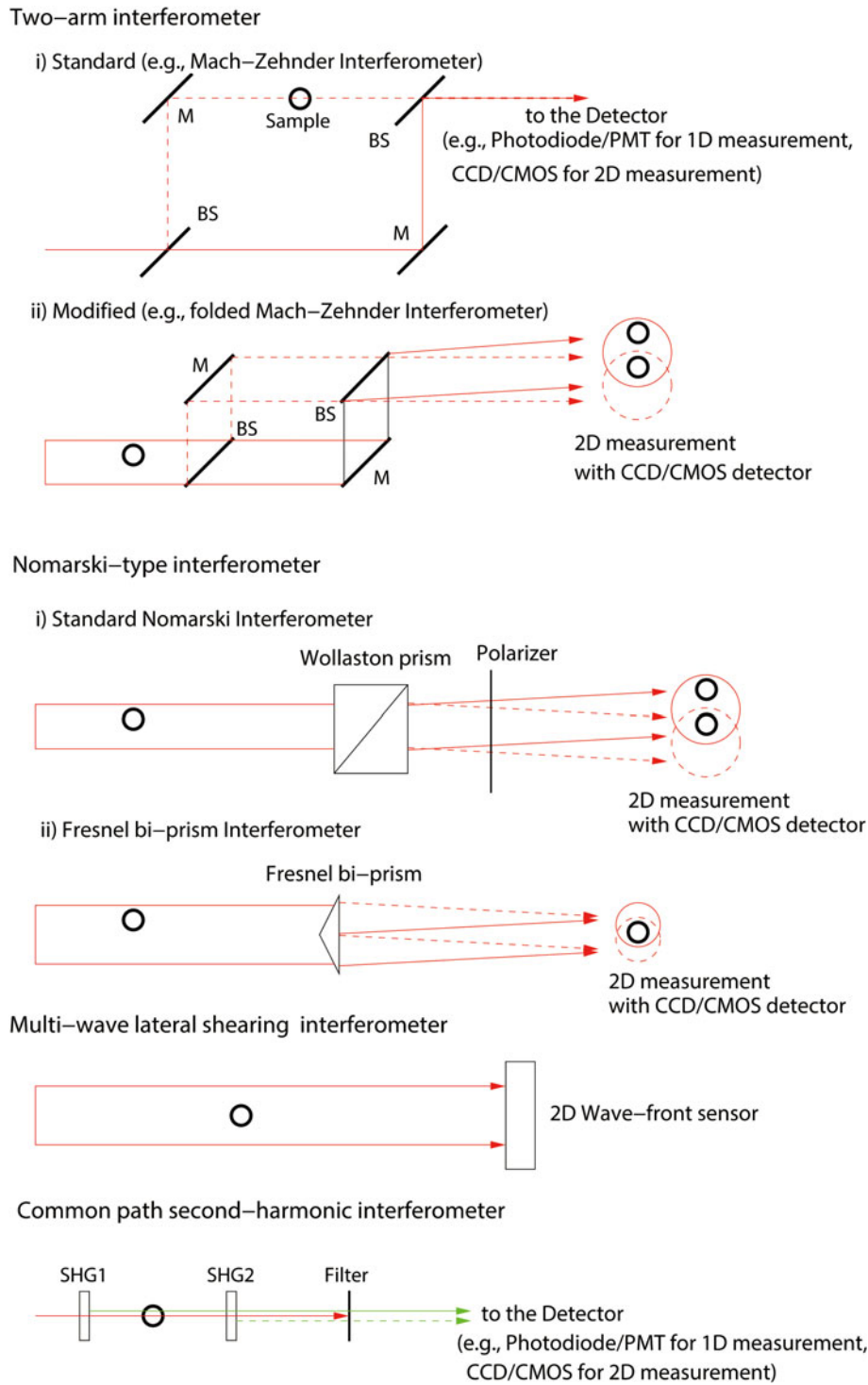


Figure 2. Schematic representation of the most common interferometers used for density measurements in laser-plasma accelerators; M, mirror; BS, beam splitter; SHG, second-harmonic generation unit. Optical elements used for imaging, such as lenses, are omitted for clarity.

beam splitter and interference is recorded after a polarizer^[28–30].

II *Fresnel bi-prism interferometer*, which is based on the use of a Fresnel bi-prism that allows one to overlap directly two different parts of the same input beam^[31].

2.3. Multi-wave lateral shearing interferometer

A versatile and robust method to measure phase variations across a light beam is based on the use of wavefront (WF) sensors (for example, the quadri-wave lateral shearing interferometer^[32]). This instrument measures the phase

difference between two adjacent points of the light beam cross-section by means of a wavefront detector. In fact this method is sensitive to phase gradients of the beam cross-section along two orthogonal directions, and the actual 2D map of the phase is retrieved by analyzing the data with specific software. Finally, the phase shift of interest is calculated by subtracting the phase map of an undisturbed beam acquired in a separate measurement without the sample^[33]. It can be considered a single-arm configuration, since interference takes place only at the detector, and is therefore a very robust method allowing for easy installation with a phase sensitivity which is stated to be <2 nm (that is, <30 mrad at 400 nm)^[34]. A value of 11 mrad has actually been estimated as the root-mean-square over 188 acquisitions using 400 nm laser light^[35]. It must be noted that a single-acquisition value has not been reported to our best knowledge, so a conservative value of 30 mrad at 400 nm is assumed here.

Of note, the wavefront of a laser beam, and the density information contained therein, can be extracted also by numerical beam intensity analysis of standard 2D images from a camera, with a phase resolution of about 80 mrad^[36]. However, the numerical analysis involves multiple images for this approach to be effective, thus limiting its applicability for real-time measurements, but it could be suitable for offline tuning and optimization of LPA stages.

2.4. Second-harmonic interferometer

Another kind of interferometric approach for the measurement of particle density in optically dispersive samples (for example, neutral gas or plasma) is based on the so-called second-harmonic interferometer (SHI), also known as the dispersion interferometer. The SHI has a fully common-path configuration and is sensitive to the phase difference acquired by the fundamental and second-harmonic beams when passing collinearly through the sample^[37, 38]. The measured phase shift is given by $\Delta\phi_{\text{SHI}} = \frac{4\pi}{\lambda} \int_L \Delta\eta(l, \lambda) dl = \frac{4\pi}{\lambda} L \overline{\Delta\eta}(\lambda)$, where $\Delta\eta(\lambda) = \eta(\lambda) - \eta(\lambda/2)$. It is a very robust method against mechanical vibrations and environmental conditions in general, and it can reach a phase sensitivity of less than 1 mrad for 1D measurements without requiring any vibration mitigation system^[39]. Although 2D measurements using the SHI method have been demonstrated^[40, 41], there is no quantitative data available in the literature regarding the sensitivity of the imaging SHI. Here, we assume a conservative value of 10 mrad for quadrature detection^[39, 42]. To date, SHIs have mostly been developed and applied to monitor the free-electron density in magnetically confined large plasma machines^[43, 44]. Recently, due to their versatility and robustness, SHIs have been successfully applied also for the characterization and monitoring of gas targets for

LWFA (namely discharged gas-filled capillaries^[45, 46] and gas cells^[21, 47]).

Specifically, spectral-domain (SD) second-harmonic interferometry^[48] has been adopted instead of spectral-domain TAI to monitor the density inside a discharged gas-filled capillary, due to the much easier implementation and much higher stability of the common-path configuration compared to the two-arm design^[45]. In an SD SHI, the spectral interference takes place between the second-harmonic pulse generated before the sample and the time-delayed second-harmonic pulse generated after the fundamental pulse has propagated through the sample. The time delay ΔT between the two second-harmonic ultra-short pulses arises from the different group velocities in the sample at the fundamental and second-harmonic wavelengths, which is proportional to the density. In terms of phase, the pulse envelope slippage due to the plasma is $\frac{4\pi}{\lambda} c \Delta T$, where λ is the fundamental laser wavelength. The time delay is estimated by measuring the modulation period $\Delta\nu$ in the frequency spectrum of the two interfering pulses ($\Delta T = 1/\Delta\nu$). For laser pulses propagating in a discharged gas-filled capillary with a near-match guided configuration typical for LPA, the relation between the time delay ΔT and the average on-axis plasma density n_e can be approximated very well by assuming free propagation in a plasma with an average density n_e ^[45], resulting in the same phase shift as a function of the electron density (see Table 1). When applying SD interferometry, also the spectral phase of the modulated frequency spectrum can be measured. It is noted that, given a linear response of the plasma, the phase shift due to the different group velocities (group delay) and the phase shift due to the different phase velocities (spectral phase shift) have the same magnitude but opposite sign. Recently, sensitivities of 2.85 rad in group-delay measurements and of 63 mrad for spectral phase measurements have been demonstrated^[46].

The use of a continuous-wave (CW) laser-based SHI has been successfully demonstrated for high-resolution real-time monitoring of the gas density inside a gas flow cell placed in a vacuum chamber^[21, 47]. As an example, Figure 3 reports the results of real-time measurements by a CW 1064 nm second-harmonic interferometer of the Ar gas number density inside a pulsed gas flow cell specifically developed for LWFA (SourceLAB, Model SL-ALC). The measurement is performed transversely over a length of 35 mm for a backing pressure of 600 mbar (1 bar = 100 kPa) and for gas pulse lengths of 100 ms and 500 ms.

A specific issue common to all time-domain interferometric measurements is related to the periodic evolution of the intensity pattern with alternating minima and maxima in the detected light intensity, which gives rise to so-called fringes. This fact implies that measurements of a phase shift that spans multiple fringes may become indeterminate when retrieving the absolute phase shift from the measured

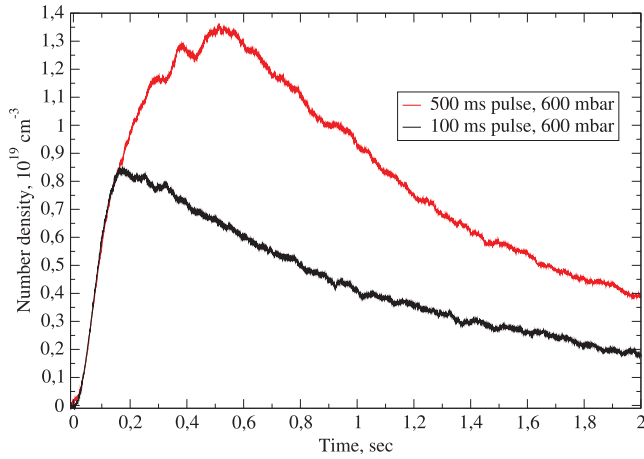


Figure 3. Real-time measurements of the Ar gas number density inside a pulsed gas flow cell by an SHI at 1064 nm: black curve, pulse length 100 ms; red curve, pulse length 500 ms. Backing Ar pressure 600 mbar.

Table 1. Expected phase shifts in TAIs and SHIs for both hydrogen gas and free electrons at 800 nm and 400 nm wavelengths, with L expressed in cm, n_g in 10^{19} cm^{-3} and n_e in 10^{17} cm^{-3} . Note that for SHI the fundamental wavelength used is indicated, while the phase is actually measured at its second harmonic, i.e., 400 nm.

Configuration	Neutral gas	Free electrons
$\Delta\phi_{\text{TAI}}(800 \text{ nm})$	$4.0 \times L \times n_g$	$2.2 \times L \times n_e$
$\Delta\phi_{\text{TAI}}(400 \text{ nm})$	$8.3 \times L \times n_g$	$1.1 \times L \times n_e$
$\Delta\phi_{\text{SHI}}(800 \text{ nm})$	$0.3 \times L \times n_g$	$3.4 \times L \times n_e$

intensity data. Typically, this issue is addressed during the data analysis with specific phase-unwrapping protocols. There are two basic requirements for such phase-unwrapping protocols to be effective. First, the presence of a reference data point with known phase shift, typically zero, with respect to which all other phase shifts are referred. In 2D measurements such data can be a pixel or an area of the image where the two interfering beams have the exact same phase, while in 1D measurements the reference value is typically obtained from the data acquired before the event under investigation has started or by waiting until its completion. Second, the measurements have to resolve all fringes. In 2D measurements this means that the spatial gradient of the phase to be measured must be small enough to avoid fringe jumps between two adjacent pixels of the detector^[49]. In 1D measurements, the detector has to be fast enough to accurately follow the evolution in time of the interference signal in order to count the number of fringes^[50].

When the measured phase shift is small enough to stay within a half-fringe so that it can be determined unambiguously, i.e., $\Delta\phi < \pi$, then fringe jumps are avoided and phase-tracking or phase-unwrapping protocols are not necessary, enhancing the phase measurement sensitivity and speed, and allowing for more robust real-time monitoring. As an example, the maximum density shown in Figure 3 corresponds to

approximately 0.5 bar pressure at room temperature, which would result in a ~ 27 rad phase shift (>4 fringes) in a TAI^[51], while the phase shift read by the SHI is <1 rad^[52], thus sub-fringe, allowing for a real-time measurement.

It is highlighted that a time delay measurement in SD interferometry is inherently immune to the fringe-jump issue, and can be applied to measure plasma densities over relatively long distances, which would result in a signal spanning many fringes in a time-domain measurement. As an example, when adopting SD second-harmonic interferometry to measure the electron density in gas discharged capillary^[46] the group-delay measurement is used to determine the number of fringes, thanks to a sub-fringe phase resolution of 2.85 rad, while the simultaneous determination of the spectral phase allows one to achieve an overall 63 mrad phase resolution over multiple fringes.

2.5. Phase-shift estimates

The actual relation between the measured phase shift and the particle density is different in the case of neutral particles in a gas or free electrons in a plasma. The values of the refractivity of hydrogen at STP for the fundamental and second-harmonic wavelengths of a Ti:sapphire laser are $\eta(800) = 1.374 \times 10^{-4}$ and $\eta(400) = 1.426 \times 10^{-4}$, respectively^[53], thus $\Delta\eta(800) = \eta(400) - \eta(800) = 52 \times 10^{-7}$. So, based on these values and on the known equation for the plasma refractive index as a function of wavelength and electron density, the expected phase shifts can be evaluated and are reported in Table 1. The wavelength reported for SHI is the fundamental wavelength used, while the reported phase refers to the detected second harmonic, i.e., 400 nm wavelength. It is noted that the phase to be measured by Nomarski-type interferometers is actually the same as for the TAI.

The wavefront sensor measures only the gradient of the density, and therefore there is no straightforward analytical relation between the measured quantity and the density which is determined from the phase extracted by dedicated software. A comparison between similar measurements performed with both wavefront-based sensors and a modified TAI revealed a difference in the absolute value of the measured density of 10%–20%^[35]. Indeed, a 15 nm accuracy is stated for the instrument^[34], i.e., 0.24 rad at 400 nm, which can explain the deviation of the absolute value found with respect to the modified TAI measurement. Thus, the WF-sensor-based instrument requires an accurate calibration before being used for the absolute measurement of density. For comparison, the SHI employing quadrature detection can reach an absolute accuracy of 1% or less for 1D measurements^[39].

In Figures 4 and 5 the capabilities of the various interferometric methods are shown graphically for neutral hydrogen and free electrons, respectively: the full lines represent

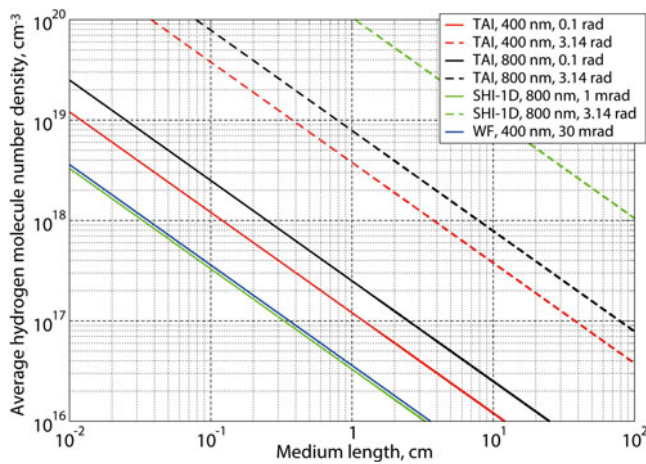


Figure 4. Interferometric capability for neutral hydrogen density measurements. For each methodology considered, the wavelength used and the measured phase are shown. For SHI, the fundamental wavelength used is reported, while the phase shift refers to the actually detected second-harmonic wavelength, i.e., 400 nm. The solid lines correspond to the smallest measurable phase, indicated in the legend, while the dashed lines correspond to measurements within half-fringe.

the lower detection limit set by the sensitivity, while the dashed lines represent the upper limit for measurement within a single fringe, i.e., $\Delta\phi < \pi$. Of course a fringe jump allows one to overcome this upper limit, but at the expense of higher uncertainty in time-domain measurements. As discussed, fringe jumps are not an issue in spectral-domain interferometry, thanks to simultaneous group-delay and spectral phase measurements. In Figure 5 the capabilities in terms of the phase of both group-delay and spectral phase measurements are reported separately.

Interferometry is usually performed transversely to the main laser beam. In such a case, the plasma length covered by the interferometer light beam lies between $10\ \mu\text{m}$ (roughly the dimensions of the main laser beam spot) and hundreds of μm . The transverse neutral gas length can range from $\sim\text{mm}$ typical for pulsed jets^[17] to tens of millimeters in gas flow cells^[21, 24, 54].

For neutral hydrogen measurements, from Figure 4 it is evident that both the SHI and the WF-based sensors are capable of measuring low density values, even for few millimeters path. The 1D measurement with the SHI allows very fast monitoring of the neutral hydrogen density (acquisition time $\sim 1\ \mu\text{s}$) and can be implemented as a sensor in closed-loop gas flow regulation systems. This is very important when gas cells are used. In fact, repetitive shots of the high-power main laser beam will eventually modify the cell's orifice, usually of hundreds of microns diameter, altering the gas flow dynamics and therefore the actual gas number density inside the cell for a pre-set backing pressure^[12]. Online regulation of such a gas supply system is therefore necessary in order to achieve a stable and reproducible laser-plasma acceleration process. The 1D measurement with the SHI

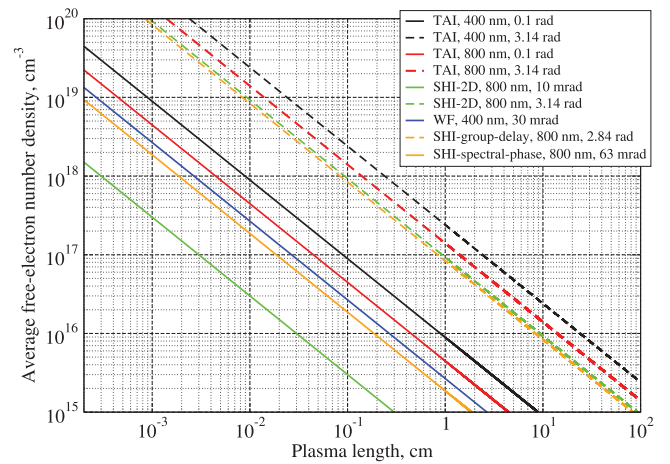


Figure 5. Interferometric capability for free-electron density measurements. For each methodology considered the wavelength used and the measured phase are shown. For SHI, the fundamental wavelength used is reported, while the phase shift refers to the actually detected second-harmonic wavelength, i.e., 400 nm. The solid lines correspond to the smallest measurable phase, indicated in the legend, while the dashed lines correspond to measurements within half-fringe, except for group delay measurements with the SHI.

can achieve a sensitivity of $< 1\ \text{mrad}$, therefore enabling the measurement of densities of about $10^{17}\ \text{cm}^{-3}$ over a 1 mm length^[39]. The WF sensor is indeed suitable for 2D mapping, starting at a few $10^{17}\ \text{cm}^{-3}$ and few millimeters in length. As per the higher values of density and medium length, all the methods can measure within a single fringe for millimeter-sized sample with densities up to $10^{19}\ \text{cm}^{-3}$, except the TAI interferometer at 400 nm.

For free-electron density measurements, Figure 5 shows that only the imaging SHI with 10 mrad sensitivity would be suitable to measure the lowest free-electron density in the range of few $10^{17}\ \text{cm}^{-3}$ for a plasma length $< 100\ \mu\text{m}$. However, such an instrument has not been tested yet and further development is necessary to assess the actual sensitivity achievable with the imaging SHI. An ultra-fast probe beam has to be used to monitor the free electrons during laser-plasma interactions. Ultra-fast SHI has been presented in the literature^[42, 55], but more development is necessary to establish a femtosecond version of the SHI. The WF-sensor-based instrument is suitable for the measurement of free-electron densities $> 10^{18}\ \text{cm}^{-3}$ with plasma paths longer than hundreds of μm , and it can work readily with ultra-fast light sources^[35]. In Figure 5 the capability of SD second-harmonic interferometry is also reported. High-sensitivity spectral phase measurements, combined with group-delay measurements over multiple fringes, are ideal candidates as diagnostics to monitor the electron density inside gas discharged capillaries with relatively large line-integrated densities.

The advantages and disadvantages (pros and cons) of each interferometric method are summarized in Table 2.

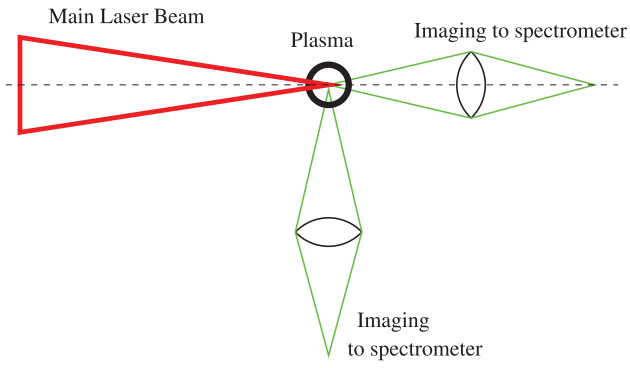


Figure 6. Schematic of the Stark broadening measurement setup, showing both longitudinal and transverse configurations.

Table 2. Qualitative comparison of interferometric methods.

Diagnostics	Pros	Cons
Two-arm	Ultra-fast and 2D capability	Sensitivity to environment Multiple beams
Nomarski-type	Ultra-fast and 2D capability Stability	Signal processing
Second-harmonic	Single-arm, ultra-fast capability Stability, sensibility and accuracy	2D capability to be tested
Lateral shearing	Single-arm, stability Ultra-fast and 2D capability	Accuracy Signal processing

3. Optical emission spectroscopy

All interferometric methods require an appropriate optical line of sight through the sample. In the case of a freely expanding gas jet, interferometry is easy to implement, whereas in the case of confined samples (for example, gas cells, capillaries and tubes), flat optical side windows are necessary to provide the optical path for transverse interferometry. This issue must be considered when designing the actual geometry of the accelerator stage. When a straight optical path through the sample is not available (for example, cylindrical capillary or tubes) optical emission spectroscopy can be considered as a means to monitor the density. Specifically, Stark broadening of hydrogen emission lines and wavelength-shifted Raman scattering of the main laser beam will be considered here.

3.1. Stark broadening

Spectroscopic investigation of hydrogen emission lines (for example, H_α at 656.3 nm and H_β at 486.1 nm) may be implemented to monitor the free electron density with a relatively simple approach^[56]. In fact, the electron density can be estimated from the broadening of the hydrogen emission lines as

$$n_e = 8.02 \times 10^{12} (\Delta\lambda_{1/2} / \alpha_{1/2})^{3/2}, \quad (1)$$

where n_e is in cm^{-3} and $\Delta\lambda_{1/2}$, the full width at half-maximum of the Stark-broadened spectral line, in ångströms. The data analysis in this case depends (slightly) on the actual electron temperature via the tabulated parameter $\alpha_{1/2}$ ^[56], and therefore a measurement (or at least a reliable estimate) of the electron temperature may be necessary in parallel with Stark broadening measurements. Remarkably, the plasma temperature can be estimated from the spectroscopic measurement via the ratio of the emission line to the background underlying continuum^[57, 58]. Stark broadening measurements can be performed both longitudinally^[59–63] and transversely^[9, 64, 65], as shown schematically in Figure 6. Spatially resolved emission spectroscopy can be implemented using an imaging spectrometer, and measurements on the nanosecond time scale can be achieved using a fast camera^[66]. For example, Stark broadening of H_β allows the local electron density with values $< 10^{17} \text{ cm}^{-3}$ to be determined with a medium-resolution spectrometer. An experimental study comparing transverse TAI and longitudinal Stark broadening measurements of H_β ^[63] has demonstrated very good agreement between the two measurement methods.

3.2. Raman scattering

Measurement of the Raman scattering of the main laser beam photons due to the plasma can give information on the local free-electron density^[67]. In fact, the frequency of the Raman scattered signal ω_R is shifted compared to the original laser frequency, ω_L by the plasma frequency ω_p , i.e., $\omega_R = \omega_L - \omega_p$, so that the free-electron density can be estimated as

$$n_e = 1.11 \times 10^8 (1/\lambda_L - 1/\lambda_R)^2, \quad (2)$$

where n_e is expressed in 10^{19} cm^{-3} and the wavelength in nanometers^[68]. Raman scattering can be measured in the forward or backward directions compared to the main laser beam, as schematically shown in Figure 7. The implementation of forward scattering measurements in LWFA experiments requires the use of a mirror with a hole in the center such that the Raman radiation is reflected while the electron bunch can propagate undisturbed^[69], whereas the backward measurement can be performed mainly at wavelengths outside the reflectivity range of the main laser beam mirror^[70].

An experimental study comparing the free-electron density inside a 15-mm-long discharged gas-filled capillary measured by TAI and estimated by the frequency shift between the original TW level main laser wavelength and the forward-scattered Raman light has indicated a good agreement between the two diagnostics up to 10^{19} cm^{-3} ^[69]. However, strong discrepancies in the Raman-based measurement can occur above 10^{19} cm^{-3} ^[70]. On the other

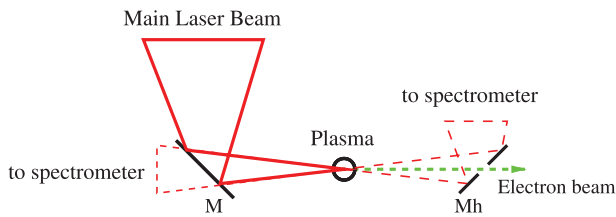


Figure 7. Schematic of the Raman scattering measurement setup, showing both backward and forward configurations. M, mirror, Mh, mirror with a hole in the center to let the electron beam through.

hand, densities $<10^{18} \text{ cm}^{-3}$ are difficult to quantify by this methodology since the wavelength shift and the scattered light intensity may be too low to be accurately measured, due also to the spurious light from the high-intensity main laser beam. So, this methodology is indeed interesting for high-quality LPA due to its relatively simple implementation, but would be useful mainly for free-electron densities in the range 10^{18} – 10^{19} cm^{-3} .

Besides forward and backward Raman scattering, it is worth noting that the measurement of side Raman scattering of the main laser pulse interacting with the plasma can also provide a monitor of the electron number density^[71]. A systematic experimental investigation of the spatial–spectral properties of the side emission scattered out of the polarization plane of the drive intense laser pulse during LWFA has shown a correlation between the wavelength shift of the Stokes line of Raman side scattering and the electron number density^[72]. In the specific case, a detailed analysis of the recorded spectral shifts as a function of the electron number density, measured independently by interferometry in the range 10^{18} – 10^{19} cm^{-3} , revealed a very good agreement with relativistic stimulated Raman scattering theory in plasmas at a high laser intensity, demonstrating the feasibility of Raman side scattering measurements as a density diagnostic tool. From a practical point of view, side Raman scattering measurements, being somehow easier to implement than forward and backward scattering measurements, could provide an online monitor of the accelerator performance as well as a density monitor during alignment, optimization and operation of an LPA once it is calibrated by means of other methodologies (for example, interferometry).

4. Conclusions

For LPA stages in the range 0.1–1 GeV (for example, injector in multi-stage systems) the corresponding electron density is in the range from a few 10^{17} cm^{-3} up to a few 10^{18} cm^{-3} (lower density \rightarrow higher energy), and target configuration may be mm-long gas jets or gas flow cells. The 2D SHI potentially has the capability of accurate diagnostics for the electron density in the low density range, but further development is necessary to validate the ultra-fast and 2D

imaging configuration. At higher density and/or greater plasma lengths the WF-sensor-based instrument provides a good solution for 2D mapping with ultra-fast resolution. Concerning neutral gas density measurements in the range 10^{17} – 10^{19} cm^{-3} , 1D SHI provides a ready solution for real-time monitoring, while the WF sensor is suitable for 2D mapping.

For LPA stage(s) requiring greater acceleration lengths to reach electron energies of several GeV, plasma channels with densities in the range 10^{17} – 10^{19} cm^{-3} provide adequate target structures. In this context, small-diameter plasma channels created with a laser pre-pulse in gas cells are open structures that can allow transverse interferometry: at lower density only the ultra-fast 2D SHI may be useful, while at higher density the WF-sensor-based instrument may be adequate. However, this LPA configuration is difficult to control, involving two separate laser beams, and may pose serious challenges when adopted in user-oriented high-quality accelerators.

Concerning plasma channels created by a discharge in a capillary, they do not allow for transverse interferometry unless a square capillary cross-section is used. Then, Stark broadening/Raman scattering measurements and/or longitudinal interferometry may be adopted. Significantly, spectral-domain second-harmonic interferometry has recently been demonstrated to be an elegant and suitable methodology to monitor discharged gas-filled capillaries longitudinally. Combining simultaneous group-delay and spectral phase measurements, a high phase resolution has been achieved in measurements spanning multiple fringes.

TAI interferometers are in general less suitable for implementation during operation and they may be more useful during alignment/tuning of the system due to their well-established use in research laboratories.

Acknowledgements

This work received support from the European Unions Horizon 2020 research and innovation program under Grant Agreement No. 653782-EuPRAXIA, and the MIUR-funded Italian research Network ELI-Italy.

References

1. P. A. Walker, P. D. Alesini, A. S. Alexandrova, M. P. Anania, N. E. Andreev, I. Andriyash, A. Aschikhin, R. W. Assmann, T. Audet, A. Bacci, I. F. Barna, A. Beaton, A. Beck, A. Beluze, A. Bernhard, S. Bielawski, F. G. Bisesto, J. Boedewadt, F. Brandi, O. Bringer, R. Brinkmann, E. Bründermann, M. Büscher, M. Bussmann, G. C. Bussolino, A. Chance, J. C. Chanteloup, M. Chen, E. Chiadroni, A. Cianchi, J. Clarke, J. Cole, M. E. Couprie, M. Croia, B. Cros, J. Dale, G. Dattoli, N. Delerue, O. Delferriere, P. Delinikolas, J. Dias, U. Dorda, K. Ertel, A. Ferran Pousa, M. Ferrario, F. Filippi, J. Fils, R. Fiorito, R. A. Fonseca, M. Galimberti, A. Gallo,

- D. Garzella, P. Gastinel, D. Giove, A. Giribono, L. A. Gizzi, F. J. Grüner, A. F. Habib, L. C. Haefner, T. Heinemann, B. Hidding, B. J. Holzer, S. M. Hooker, T. Hosokai, A. Irman, D. A. Jaroszynski, S. Jaster-Merz, C. Joshi, M. C. Kaluza, M. Kando, O. S. Karger, S. Karsch, E. Khazanov, D. Khikhlikha, A. Knetsch, D. Kocon, P. Koester, O. Kononenko, G. Korn, I. Kostyukov, L. Labate, C. Lechner, W. P. Leemans, A. Lehrach, F. Y. Li, X. Li, V. Libov, A. Lifschitz, V. Litvinenko, W. Lu, A. R. Maier, V. Malka, G. G. Manahan, S. P. D. Mangles, B. Marchetti, A. Marocchino, A. Martinez de la Ossa, J. L. Martins, F. Massimo, F. Mathieu, G. Maynard, T. J. Mehrling, A. Y. Molodtsov, A. Mosnier, A. Mostacci, A. S. Mueller, Z. Najmudin, P. A. P. Nghiem, F. Nguyen, P. Niknejadi, J. Osterhoff, D. Papadopoulos, B. Patrizi, R. Pattathil, V. Petrillo, M. A. Pocsai, K. Poder, R. Pompili, L. Pribyl, D. Pugacheva, S. Romeo, A. R. Rossi, E. Roussel, A. A. Sahai, P. Scherkl, U. Schramm, C. B. Schroeder, J. Schwindling, J. Scifo, L. Serafini, Z. M. Sheng, L. O. Silva, T. Silva, C. Simon, U. Sinha, A. Specka, M. J. V. Streeter, E. N. Svystun, D. Symes, C. Szwej, G. Tauscher, A. G. R. Thomas, N. Thompson, G. Toci, P. Tomassini, C. Vaccarezza, M. Vannini, J. M. Vieira, F. Villa, C.-G. Wahlström, R. Walczak, M. K. Weikum, C. P. Welsch, C. Wiemann, J. Wolfenden, G. Xia, M. Yabashi, L. Yu, J. Zhu, and A. Zigler, *J. Phys. Conf. Ser.* **874**, 012029 (2017).
2. C. Toth, D. Evans, A. J. Gonsalves, M. Kirkpatrick, A. Magana, G. Mannino, H.-S. Mao, K. Nakamura, J. R. Riley, S. Steinke, T. Sipla, D. Syversrud, N. Ybarrolaza, and W. P. Leemans, *AIP Conf. Proc.* **1812**, 110005 (2017).
 3. M. Ferrario, D. Alesini, M. P. Anania, M. Artioli, A. Bacci, S. Bartocci, R. Bedogni, M. Bellaveglia, A. Biagioni, F. Bisesto, F. Brandi, E. Brentegani, F. Broggi, B. Buonomo, P. L. Campana, G. Campogiani, C. Cannaos, S. Cantarella, F. Cardelli, M. Carpanese, M. Castellano, G. Castorina, N. Catalan Lasheras, E. Chiadroni, A. Cianchi, R. Cimino, F. Ciocci, D. Cirrincione, G. A. P. Cirrone, R. Clementi, M. Coreno, R. Corsini, M. Croia, A. Curcio, G. Costa, C. Curatolo, G. Cuttone, S. Dabagov, G. Dattoli, G. DAuria, I. Debrot, M. Diomedea, A. Drago, D. Di Giovenale, S. Di Mitri, G. Di Pirro, A. Esposito, M. Faiferri, L. Ficcadenti, F. Filippi, O. Frasciello, A. Gallo, A. Ghigo, L. Giannessi, A. Giribono, L. A. Gizzi, A. Grudiev, S. Guiducci, P. Koester, S. Incremona, F. Iungo, L. Labate, A. Latina, S. Licciardi, V. Lollo, S. Lupi, R. Manca, A. Marcelli, M. Marini, A. Marocchino, M. Marongiu, V. Martinelli, C. Masciovecchio, C. Mastino, A. Michelotti, C. Milardi, V. Minicozzi, F. Mira, S. Morante, A. Mostacci, F. Nguyen, S. Pagnutti, L. Pellegrino, A. Petralia, V. Petrillo, L. Piersanti, S. Pioli, D. Polese, R. Pompili, F. Pusceddu, A. Ricci, R. Ricci, R. Rochow, S. Romeo, J. B. Rosenzweig, M. Rossetti Conti, A. R. Rossi, U. Rotundo, L. Sabbatini, E. Sabia, O. Sans Plannell, D. Schulte, J. Scifo, V. Scuderi, L. Serafini, B. Spataro, A. Stecchi, A. Stella, V. Shpakov, F. Stellato, E. Turco, C. Vaccarezza, A. Vacchi, A. Vannozzi, A. Variola, S. Vescovi, F. Villa, W. Wuensch, A. Zigler, and M. Zobov, *Nucl. Instr. Meth. Phys. Res. A* **909**, 134 (2018).
 4. S. M. Hooker, E. Brunetti, E. Esarey, J. G. Gallacher, C. G. R. Geddes, A. J. Gonsalves, D. A. Jaroszynski, C. Kamperidis, S. Knip, K. Krushelnick, W. P. Leemans, S. P. D. Mangles, C. D. Murphy, B. Nagler, Z. Najmudin, K. Nakamura, P. A. Norreys, D. Panasenkov, T. P. Rowlands-Rees, C. B. Schroeder, C. s. Tóth, and R. Trines, *Plasma Phys. Control. Fusion* **49**, B403 (2007).
 5. D. Palla, F. Baffigi, F. Brandi, L. Fulgentini, P. Koester, L. Labate, P. Londrillo, and L. A. Gizzi, *Nucl. Instr. Meth. Phys. Res. A* **829**, 408 (2016).
 6. A. J. Gonsalves, T. P. Rowlands-Rees, B. H. P. Broks, J. J. A. M. van der Mullen, and S. M. Hooker, *Phys. Rev. Lett.* **98**, 025002 (2007).
 7. H. S. Uhm, D. G. Jang, M. S. Kim, and H. Suk, *Phys. Plasmas* **19**, 024501 (2012).
 8. S. M. Hooker, *Nat. Photon.* **7**, 775 (2013).
 9. Z. Qin, W. Li, J. Liu, J. Liu, C. Yu, W. Wang, R. Qi, Z. Zhang, M. Fang, K. Feng, Y. Wu, L. Ke, Y. Chen, C. Wang, R. Li, and Z. Xu, *Phys. Plasmas* **25**, 043117 (2018).
 10. M. Mirzaie, S. Li, M. Zeng, N. A. M. Hafz, M. Chen, G. Y. Li, Q. J. Zhu, H. Liao, T. Sokollik, F. Liu, Y. Y. Ma, L. M. Chen, Z. M. Sheng, and J. Zhang, *Sci. Rep.* **5**, 14659 (2015).
 11. W. P. Leemans, A. J. Gonsalves, H.-S. Mao, K. Nakamura, C. Benedetti, C. B. Schroeder, C. s. Tóth, J. Daniels, D. E. Mittelberger, S. S. Bulanov, J.-L. Vay, C. G. R. Geddes, and E. Esarey, *Phys. Rev. Lett.* **113**, 245002 (2014).
 12. O. Kononenko, N. C. Lopes, J. M. Cole, C. Kamperidis, S. P. D. Mangles, Z. Najmudin, J. Osterhoff, K. Poder, D. Rusby, D. R. Symes, J. Warwick, J. C. Wood, and C. A. J. Palmer, *Nucl. Instr. Meth. Phys. Res. A* **829**, 125 (2016).
 13. C. B. Schroeder, C. Benedetti, E. Esarey, J. van Tilborg, and W. P. Leemans, *Phys. Plasmas* **18**, 083103 (2011).
 14. H. T. Kim, V. B. Pathak, K. H. Pae, A. Lifschitz, F. Syllá, J. H. Shin, C. Hojbota, S. K. Lee, J. H. Sung, H. W. Lee, E. Guillaume, C. Thaury, K. Nakajima, J. Vieira, L. O. Silva, V. Malka, and C. H. Nam, *Sci. Rep.* **7**, 10203 (2017).
 15. N. A. M. Hafz, T. M. Jeong, I. W. Choi, S. K. Lee, K. H. Pae, V. V. Kulagin, J. H. Sung, T. J. Yu, K.-H. Hong, T. Hosokai, J. R. Cary, D.-K. Ko, and J. Lee, *Nat. Photon.* **2**, 571 (2008).
 16. M. Born and E. Wolf, *Principles of Optics* (Cambridge University Press, Cambridge, 1980).
 17. F. Brandi and F. Giammanco, *Opt. Express* **19**, 25479 (2011).
 18. J. Park, H. A. Baldis, and H. Chen, *High Power Laser Sci. Eng.* **4**, e26 (2016).
 19. J. P. Couperusa, A. Köhlera, T. A. W. Wolterink, A. Jochmann, O. Zarinia, H. M. J. Bastiaens, K. J. Boller, A. Irman, and U. Schramma, *Nucl. Instrum. Methods Phys. Res. A* **830**, 504 (2016).
 20. A. Adelman, B. Hermann, R. Ischebeck, M. C. Kaluza, U. Locans, N. Sauerwein, and R. Tarkeshian, *Appl. Sci.* **8**, 443 (2018).
 21. F. Brandi, F. Giammanco, F. Conti, F. Syllá, G. Lambert, and L. A. Gizzi, *Rev. Sci. Instrum.* **87**, 086103 (2016).
 22. P. Tomassini, M. Borghesi, M. Galimberti, A. Giulietti, D. Giulietti, O. Willi, and L. A. Gizzi, *Appl. Opt.* **40**, 35 (2001).
 23. L. A. Gizzi, M. Galimberti, A. Giulietti, D. Giulietti, P. Koester, L. Labate, P. Tomassini, Ph. Martin, T. Ceccotti, P. De Oliveira, and P. Monot, *Phys. Rev. E* **74**, 036403 (2006).
 24. C. Aniculaesei, H. T. Kim, B. J. Yoo, K. H. Oh, and C. H. Nam, *Rev. Sci. Instrum.* **89**, 025110 (2018).
 25. S. Feister, J. A. Nees, J. T. Morrison, K. D. Frische, C. Orban, E. A. Chowdhury, and W. M. Roquemore, *Rev. Sci. Instrum.* **85**, 11D602 (2014).
 26. J. van Tilborg, J. Daniels, A. J. Gonsalves, C. B. Schroeder, E. Esarey, and W. P. Leemans, *Phys. Rev. E* **89**, 063103 (2014).
 27. J. Daniels, J. van Tilborg, A. J. Gonsalves, C. B. Schroeder, C. Benedetti, E. Esarey, and W. P. Leemans, *Phys. Plasmas* **22**, 073112 (2015).
 28. M. Kalal, O. Slezak, M. Martinkova, and Y. J. Rhee, *J. Korean Phys. Soc.* **56**, 287 (2010).
 29. J. Ruiz-Camacho, F. N. Beg, and P. Lee, *J. Phys. D: Appl. Phys.* **40**, 2026 (2007).
 30. A. Gamucci, M. Galimberti, D. Giulietti, L. A. Gizzi, L. Labate, C. Petcu, P. Tomassini, and A. Giulietti, *Appl. Phys. B* **85**, 611 (2006).

31. K. Gao, N. A. M. Hafz, S. Li, M. Mirzaie, G. Li, and Q. Ain, *Plasma Sci. Technol.* **19**, 015506 (2017).
32. J.-C. Chanteloup, *Appl. Opt.* **44**, 1559 (2005).
33. F. Mollica, F. Syllá, A. Flacco, G. Bourgeois, B. Wattellier, and V. Malka, in *Proceedings of 42nd EPS Conference on Plasma Physics* (2010), paper P5.204.
34. <http://phasicscorp.com/product/plasma-density-measurement-using-phase-shift/>.
35. G. R. Plateau, N. H. Matlis, C. G. Geddes, A. J. Gonsalves, S. Shiraishi, C. Lin, R. A. van Mourik, and W. P. Leemans, *Rev. Sci. Instrum.* **81**, 033108 (2010).
36. P. Chessa, M. Galimberti, C. N. Danson, A. Giulietti, D. Giulietti, and L. A. Gizzi, *Laser Part. Beams* **17**, 681 (1999).
37. F. A. Hopf, A. Tomita, and G. Al-Jumaily, *Opt. Lett.* **5**, 386 (1980).
38. K. P. Alum, I. V. Kovalchuk, and G. V. Ostrovskaya, *Sov. Tech. Phys. Lett.* **7**, 581 (1981).
39. F. Brandi and F. Giammanco, *Opt. Lett.* **32**, 2327 (2007).
40. F. C. Jobses and N. L. Bretz, *Rev. Sci. Instrum.* **68**, 709 (1997).
41. E. Abraham, K. Minoshima, and H. Matsumoto, *Opt. Commun.* **176**, 441 (2000).
42. F. Brandi and F. Giammanco, *Opt. Lett.* **33**, 2071 (2008).
43. F. Brandi, F. Giammanco, W. S. Harris, T. Roche, E. Trask, and F. J. Wessel, *Rev. Sci. Instrum.* **80**, 113501 (2009).
44. V. Drachev, Y. Krasnikov, and P. Bagryansky, *Rev. Sci. Instrum.* **64**, 1010 (1993).
45. J. van Tilborg, A. J. Gonsalves, E. H. Esarey, C. B. Schroeder, and W. P. Leemans, *Opt. Lett.* **43**, 2776 (2018).
46. J. van Tilborg, A. J. Gonsalves, E. H. Esarey, C. B. Schroeder, and W. P. Leemans, *Phys. Plasmas* **26**, 023106 (2019).
47. F. Brandi, P. Marsili, F. Giammanco, F. Syllá, and L. A. Gizzi, *J. Phys. Conf. Ser.* **1079**, 012006 (2018).
48. P. T. Wilson, Y. Jiang, O. A. Aktsipetrov, E. D. Mishina, and M. C. Downer, *Opt. Lett.* **24**, 496 (1999).
49. L. A. Gizzi, D. Giulietti, A. Giulietti, T. Afshar-Rad, V. Biancalana, P. Chessa, C. Danson, E. Schifano, S. M. Viana, and O. Willi, *Phys. Rev. E* **49**, 5628 (1994).
50. J. Ju and B. Cros, *J. Appl. Phys.* **112**, 113102 (2012).
51. A. Bideau-Mehu, Y. Guern, R. Abjean, and A. Johannin-Gilles, *J. Quant. Spectrosc. Radiat. Transfer* **25**, 395 (1981).
52. S. P. Velsko and D. Eimerl, *Appl. Opt.* **25**, 1344 (1986).
53. E. R. Peck and S. Hung, *J. Opt. Soc. Am.* **67**, 1550 (1977).
54. T. L. Audet, F. G. Desforges, A. Maitrallain, S. Dobosz Dufrenoy, M. Bougeard, G. Maynard, P. Lee, M. Hansson, B. Aurand, A. Persson, I. Gallardo González, P. Monot, C.-G. Wahlström, O. Lundh, and B. Cros, *Nucl. Instrum. Methods Phys. Res. A* **829**, 304 (2016).
55. K. Minoshima and H. Matsumoto, *Opt. Commun.* **138**, 6 (1997).
56. H. Griem, *Spectral Line Broadening by Plasma* (Academic Press, New York, 1974).
57. A. J. Gonsalves, F. Liu, N. A. Bobrova, P. V. Sasorov, C. Pieronek, J. Daniels, S. Antipov, J. E. Butler, S. S. Bulanov, W. L. Waldron, D. E. Mittelberger, and W. P. Leemans, *J. Appl. Phys.* **119**, 033302 (2016).
58. J. Daniels, A. J. Gonsalves, C. V. Pieronek, C. Benedetti, J. van Tilborg, C. B. Schroeder, and W. P. Leemans, *AIP Conf. Proc.* **1812**, 040008 (2017).
59. G. Gautam and G. C. Parigger, *J. Phys. Conf. Ser.* **810**, 012055 (2017).
60. Z. Qin, W. Li, J. Liu, J. Liu, C. Yu, W. Wang, R. Qi, Z. Zhang, M. Fang, K. Feng, Y. Wu, L. Ke, Y. Chen, C. Wang, R. Li, and Z. Xu, *Phys. Plasmas* **25**, 073102 (2018).
61. M. Liu, A. Deng, J. Liu, R. Li, J. Xu, C. Xia, C. Wang, B. Shen, Z. Xu, and K. Nakajima, *Rev. Sci. Instrum.* **81**, 036107 (2010).
62. A. Deng, M. Liu, J. Liu, X. Lu, C. Xia, J. X, C. Wang, B. Shen, R. Li, Z. Xu, and K. Nakajima, *Plasma Sci. Technol.* **13**, 362 (2011).
63. D. G. Jang, M. S. Kim, I. H. Nam, H. Jang, and H. Suka, *J. Instrum.* **7**, C02045 (2012).
64. J. Ashkenazy, R. Kipper, and M. Caner, *Phys. Rev. A* **43**, 5568 (1991).
65. S. A. Flih, E. Oks, and Y. Vitel, *J. Phys. B* **36**, 283 (2003).
66. S. Y. Oh, H. S. Uhm, H. Kang, I. W. Lee, and H. Suk, *J. Appl. Phys.* **107**, 103309 (2010).
67. N. Pathak, A. Zhidkov, T. Hosokai, and R. Kodama, *Phys. Plasmas* **25**, 013119 (2018).
68. D. Kaganovich, B. Hafizi, J. P. Palastro, A. Ting, M. H. Helle, Y.-H. Chen, T. G. Jones, and D. F. Gordon, *Phys. Plasmas* **24**, 129901 (2017).
69. I. Nam, M. Kim, S.-w. Lee, D. Jang, and H. Suk, *J. Korean Phys. Soc.* **69**, 957 (2016).
70. D. Kaganovich, B. Hafizi, J. P. Palastro, A. Ting, M. H. Helle, Y.-H. Chen, T. G. Jones, and D. F. Gordon, *Phys. Plasmas* **23**, 123104 (2016).
71. A. G. R. Thomas, S. P. D. Mangles, Z. Najmudin, M. C. Kaluza, C. D. Murphy, and K. Krushelnick, *Phys. Rev. Lett.* **98**, 054802 (2007).
72. J. M. Cole, "Diagnosis and application of laser wakefield accelerators," PhD. Thesis (Imperial College London, 2016).

Article

Conceptual Design of a Laser Driver for a Plasma Accelerator User Facility

Guido Toci ¹, Zeudi Mazzotta ^{2,†}, Luca Labate ^{3,‡}, François Mathieu ⁴, Matteo Vannini ¹, Barbara Patrizi ¹  and Leonida A. Gizzi ^{3,*}

¹ Istituto Nazionale di Ottica, Consiglio Nazionale delle Ricerche (CNR-INO), 50019 Sesto F.no, Italy

² Ecole Polytechnique, CNRS, 91120 Palaiseau, France

³ Intense Laser Irradiation Laboratory, Istituto Nazionale di Ottica, 56124 Pisa, Italy

⁴ Laboratoire pour l'Utilisation des Lasers Intenses, CNRS, Ecole Polytechnique, 91128 Palaiseau, France

* Correspondence: la.gizzi@ino.cnr.it

† Current address: Advanced Research Center for Nanolithography (ARCNL), Science Park 106, 1098 XG Amsterdam, The Netherlands

‡ Current address: Istituto Nazionale di Fisica Nucleare, Sezione di Pisa, Largo Bruno Pontecorvo, 3, 56127 Pisa, Italy

Received: 12 June 2019; Accepted: 5 August 2019; Published: 8 August 2019



Abstract: The purpose of the European project EuPRAXIA is to realize a novel plasma accelerator user facility. The laser driven approach sets requirements for a very high performance level for the laser system: pulse peak power in the petawatt range, pulse repetition rate of several tens of Hz, very high beam quality and overall stability of the system parameters, along with 24/7 operation availability for experiments. Only a few years ago these performances were considered unrealistic, but recent advances in laser technologies, in particular in the chirped pulse amplification (CPA) of ultrashort pulses and in high energy, high repetition rate pump lasers have changed this scenario. This paper discusses the conceptual design and the overall architecture of a laser system operating as the driver of a plasma acceleration facility for different applications. The laser consists of a multi-stage amplification chain based CPA Ti:Sapphire, using frequency doubled, diode laser pumped Nd or Yb solid state lasers as pump sources. Specific aspects related to the cooling strategy of the main amplifiers, the operation of pulse compressors at high average power, and the beam pointing diagnostics are addressed in detail.

Keywords: laser driven plasma acceleration; Ti:Sapphire lasers; Chirped Pulse Amplification

1. Introduction

Laser-driven plasma accelerators will require a substantial scale-up of their performance in order to address user applications. In particular, to meet user requirements, a higher repetition rate of petawatt peak power is expected in the 100 Hz range and above, implying several kW of average laser power. Nowadays, such an improvement is made credible by the rapid advancements of the technology in this field. Nonetheless, the possibility of scaling up the existing technology of high peak power lasers to higher average power remains challenging.

Pulsed high energy solid state lasers were recently realized, reaching uninterrupted operation at pulse energy levels of up to approximately 100 J and pulse repetition rates (PRR) of up to 10 Hz e.g., DiPOLE100 (Diode Pumped Optical Laser for Experiments) [1] built by the Rutherford Appleton Laboratory (RAL), and the High-Repetition-Rate Advanced Petawatt Laser System (HAPLS) [2] developed by the Lawrence Livermore National Laboratory (LLNL). Systems reaching the petawatt level with pulse energies in the range of tens of J have been realized [3], such as BELLA (Berkeley Lab

Laser Accelerator) [4], with an average power output of tens of watts. New systems under realization aim to even higher average power levels, such as HAPLS targeting an output power of 300 W. Nonetheless, to address user-level requirements, the average power of ultrafast lasers needs to increase by one or two orders of magnitude.

The purpose of the European project EuPRAXIA [5] is to provide a conceptual design for a compact, user-oriented, plasma accelerator with superior beam quality to enable free electron laser operation in the X-ray range. User requirements for an operational facility imply a significant increase of the laser driver output parameters with respect to systems currently available or under development: pulse peak power in the petawatt range, pulse repetition rate of several tens of Hz, as well as very high beam quality and overall stability of the system parameters.

A description of the architecture of the laser driver was already published in previous work [6], describing the main parameters and technical solutions. This paper complements the previous one by recalling the general lines of the system architecture and addressing some specific points that are particularly critical for the system operation at high average power levels. These aspects are related to the amplifier’s geometrical layout, the cooling solution to address the operation at high average power levels, and the laser beam transport-related issues.

2. Preliminary Laser Design

The development of the EuPRAXIA laser driver relies on Chirped Pulse Amplification (CPA) in Ti:Sapphire (Ti:Sa). The achievement of the required performance and reliability levels poses stark challenges related to several key elements in the system, and requires the most advanced components under development at the industrial level, along with specially devised solutions.

The implementation of the required plasma acceleration schemes involves the simultaneous use of up to three different laser systems, and the time of arrival of their output pulses on the plasma target must be carefully synchronized down to below 10 fs. Moreover, auxiliary laser beams for diagnostics and a photocathode laser are included, tightly synchronized with the main laser pulses.

The overall architecture of the EuPRAXIA laser system is shown in Figure 1. It consists of three different laser chains, with different output pulse parameters matched to meet requirements for the laser-driven plasma injector at 150 MeV (Laser 1), the laser-driven plasma injector at 1 GeV (Laser 2), and the accelerator stage at 5 GeV (Laser 3). They share a common master oscillator for synchronization purposes. Each one consists of a front end segment, an amplification section, a beam shaping segment, a compressor, and the final transport system to the target.

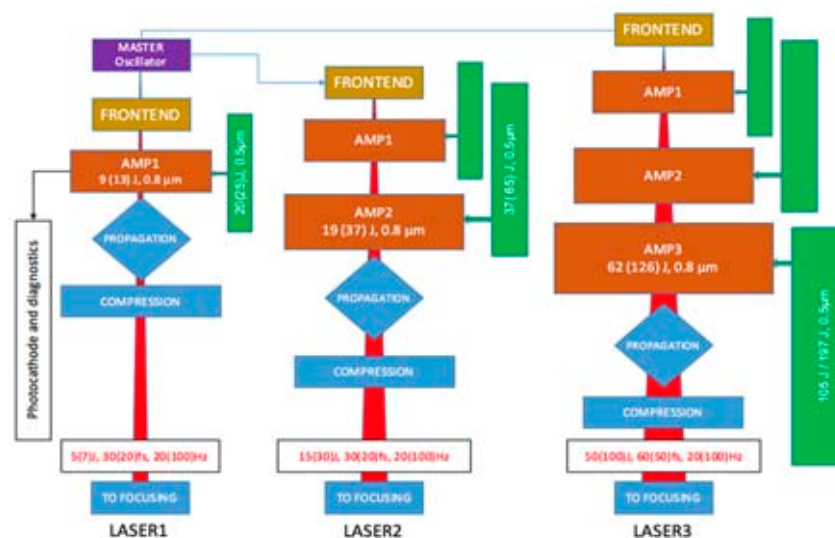


Figure 1. Block diagram of the three laser chains.

In our study, the most critical points in the of design laser systems turned out to be the following:

- (1) the pump lasers for the Ti:Sa amplifiers, in particular regarding the pulse repetition rate (PRR);
- (2) the thermal load management, and the optimization of the extraction efficiency for the Ti:Sa amplifiers;
- (3) the design of the pulse compression system, mainly in relation to the optical damage and the thermal management of the gratings.

For each laser system, two levels of performance have been considered, with different energy output and PRR (see Table 1), as follows:

- (a) Minimum performance level (named P0), featuring lower pulse energy and 20 Hz PRR;
- (b) High performance level (called P1), with higher energy at a PRR of 100 Hz.

Our design shows that the less challenging P0 performance level can be implemented with currently available technologies, requiring mainly integration efforts. Conversely, level P1 lies one step ahead with respect to the current technological capabilities, in particular regarding the PRR of the pump sources. Indeed, the choice of 100 Hz PRR was found to be the trade-off between the need for a sufficiently high repetition rate for user operation of the facility and the high technology readiness level (TRL) of the required components, assuming a 5-year time to construction.

Table 1. Laser emission parameters for the three devices envisaged for laser plasma injection and acceleration, at the levels of performance of P0 and P1. The maximum output energy (before transport and compression) has been calculated from the requirements of energy on target, assuming an overall efficiency of 80% of the compression and the beam transport system. For Laser 1, a further amount of energy output has been considered for the diagnostic beams (2.5 J at P0 and 3.8 J at P1).

Parameter	Label	Laser 1—Injector 150 MeV		Laser 2—Injector 1 GeV		Laser 3 LPA—Driver 5 GeV	
		P0	P1	P0	P1	P0	P1
Wavelength (nm)	λ	800	800	800	800	800	800
Maximum energy on target (J)	E_{target}	5	7	15	30	50	100
Maximum output energy (J)	E_{out}	8.8	12	18.8	40	62.5	130
Energy tuning resolution (% of E_{out})	dE	7	5	7	5	7	5
Shortest pulse length (FWHM *) (fs)	τ	30	20	30	20	60	60
Repetition rate (Hz)	f	20	100	20	100	20	100
Energy stability (RMS **)%	$\sigma_{<E>}$	1	0.6	1	0.6	1	0.6

* FWHM: Full Width Half Maximum, ** RMS: Root Mean Square.

2.1. Front End

The design of the front-end segment, either at the performance level of P0 or P1, is not critical. Several devices that are also commercially available can be adopted. The primary source is a common master oscillator, whose output is shared among the three systems. Then, a first CPA stage amplifies the pulse at the ~1mJ level, in order to efficiently pump an XPW stage immediately downstream. The resulting pulse, with typical energy in the order of 10–100 μ J, is then seeded into the main CPA chain. A regenerative amplifier and two multi-pass amplifiers increase the energy up to approximately >~1 J, which is needed to seed the first stages of the three amplification chains.

During the amplification, the pulse spectrum will be slightly narrowed (few percent of reduction in the FWHM of the spectrum) and red shifted (few nm), due to the higher gain experienced by the leading front of the pulse (which corresponds to the red end of the pulse spectrum due to the chirping). These effects were calculated in the simulations and they will be pre-compensated at the level of the seed pulse by blue-shifting and broadening its spectrum to obtain the desired peak wavelength and

pulse duration at the output of each amplification chain. For this purpose, each chain has its own front end stage. The master oscillator will generate pulses with shorter duration and broader bandwidth than that actually required for the pulse amplification; the pulse sent to each front-end stage will be spectrally filtered to obtain the peak wavelength and bandwidth required by each amplification chain.

Options for Pulse Train Generation

One of the acceleration schemes proposed in order to obtain the high quality electron bunches required for EuPRAXIA is the so-called Resonant Multi-Pulse Ionization injection (ReMPI) scheme [7]. In this scheme, the wakefield is resonantly excited by a train of (relatively low intensity) pulses at the Ti:Sapphire (TiSa) fundamental wavelength, while ionization injection is driven by a shorter wavelength (second or third harmonic) pulse. To this purpose, a small fraction of the laser pulse is picked up and frequency doubled or tripled by a nonlinear crystal, while the most energetic fraction (almost 97% of the total energy, in the case being studied for EuPRAXIA) is shaped temporally as a sequence of sub-pulses. Over the past few years, a few optical schemes were proposed in order to produce a train of ultrashort pulses from a CPA TiSa chain [8–10]. However, in their proposed variants these schemes do not meet the two essential requisites for driving the ReMPI acceleration scheme within EuPRAXIA, namely a high efficiency (energy throughput into the pulse train) and reduced amplitude variations among the different pulses of the train. Within the EuPRAXIA laser design, we are thus exploring other optical schemes able to meet these requirements. Here we sketch the two approaches we are pursuing, briefly outlining their pros and cons.

A first scheme exploits a segmented delay mask, made up of concentric rings of thin fused silica plates with different thicknesses. Full simulations accounting for both the temporal and spatial (that is, focusing) issues were carried out, which were reported in previous work [11]. Of course, the beam propagation optics upstream of the last focusing parabola must be designed taking into account the presence of the delay mask. While very easy to setup, the main drawback of this optical scheme is the small differences among the focal spot sizes and the Rayleigh ranges expected for the different pulses. However, theoretical estimates show that these variations can be tolerated in the ReMPI scheme.

The study of a second approach was undertaken more recently, relying on a slight variant of an optical scheme proposed in a previous study [9]. The concept (named “quasi lossless Train generation by an Early aMplitude dIvision” (TEMPI)) is based upon the usage of birefringent plates of increasing (doubling) thicknesses and crossed polarization. In our scheme the stack of birefringent plates is used early (i.e., upstream) in the laser amplification chain (on the stretched pulse), so that (a) small aperture optics can be used for this purpose and (b) the energy loss (50%) due to the polarization rejection can be recovered at a much smaller price in terms of pump energy (see later). Optical simulations of the amplification process with this scheme have been carried using the MIRO (Mathématiques et Informatique pour la Résolution des problèmes d’Optique—Mathematics and computer science to solve optical problems) code [12] in order to assess the importance of the interference and nonlinear effects occurring along the chain for the EuPRAXIA Laser 1 (see Figure 1), which could possibly be used as the injector with the ReMPI scheme. The simulation is based on a slowly varying envelope approximation computational scheme—the pulse is modeled as an amplitude profile (with dependence on both time and spatial coordinates) and a time varying phase profile modulating a carrier frequency, with the assumption that the variation of the amplitude and phase envelopes are very small on the spatial scale of the wavelength and of the time scale of the optical period. In particular, simulations were carried out for a ReMPI acceleration regime and using four pulses, with duration of 30 fs and separation of the pulses over approximately 103 fs. A detailed discussion of the results of these simulations is beyond the scope of this paper and will be provided elsewhere. Here, we only mention that according to these simulations, the accumulated B-integral for Laser 1 is ~ 0.4 , while the maximum intensity in the chain is $\sim 1.1 \times 10^9$ W/cm², which can be considered as quite safe values; this is due to the original dimensions of the laser amplifier (see later), which, among other issues, were aimed at minimizing nonlinear effects. On the other hand, as it can be easily realized, Kerr nonlinearity in the crystal and

gain saturation and narrowing result (due to the splitting and delaying of the original stretched pulse) in the appearance of pre- and post-pulses between the main pulses of the pulse train (with respect to the desired number of pulses), and to some imbalance in the peak power levels of the amplified pulses. In the case studied for an EuPRAXIA injector, using a ReMPI scheme with a 4-pulse train produced by Laser 1, the maximum intensity of these spurious pulses was ~ 0.2 of the intensity of the main pulses in the train; the overall energy content in the spurious pulses was about 13% of the overall pulse train, with 2% of the total energy located in pre-pulses before the train. The fluctuation between the peak power levels of the main pulses after the amplification was about $\pm 3\%$. Particle in cell (PIC) simulations were recently performed using the actual pulse train temporal profile resulting from the simulations on the amplification (which will be presented elsewhere), and they show no major effects on the plasma wave excitation and final bunch quality from these smaller intensity pulses and the small variation in the peak power of the individual pulses. Nonetheless, these spurious effects can be possibly mitigated by proper temporal, spectral, and phase shaping of the seed pulse train before of the amplification. This will be the subject of future studies. In the case considered here, the cost in terms of additional pump energy (needed to recover the 50% energy loss in the plate/polarizer array, so as to keep the extraction efficiency unchanged) has been estimated to be about 4J, over a total pumping of about 35 J for the front end and the first stage (see below).

2.2. Power Amplification

Pulse amplification relies on CPA in Ti:Sa, requiring pump sources in the visible range (i.e., frequency doubled, solid state Nd, or Yb-based lasers with emission in the range 515–532 nm). Several devices have been realized, achieving amplification of ultrashort (< 20 fs) laser pulses with energy output of up to 100 J or greater, but these devices operate at a very low PRR (< 1 Hz, or single shot). EuPRAXIA requires a much higher PRR, resulting in high average pump power requirements and a severe thermal load on the amplifiers.

Thermal load issues were addressed by means of water cooling at near room temperature of the end surfaces of the amplification crystals, shaped as disks with a relatively large diameter to thickness ratio, as recently proposed [13]. Alternative approaches were considered, such as the cooling of the crystals by means of a high speed gas flow at cryogenic temperatures, as implemented in the DIPOLE Yb:YAG high energy laser system [14,15], or more recently in the Ti:Sapphire high energy amplifier implemented in the ELI-HAPLS system [16]. This cooling method was nonetheless considered not suitable for this design, as it cannot provide a sufficient heat removal for this application, and it can hardly be scaled up to even higher thermal loads, as will be clarified in the following parts. For this reason, this solution was not further studied in the conceptual design.

The optimization of the extraction efficiency was carefully considered to reduce both the requirements on the pump lasers and the overall thermal load. This was addressed by a careful repartition of the amplification between the various stages, and by implementing the Extraction During Pumping (EDP) method to limit the buildup of transverse gain, and thus transverse parasitic lasing [17,18].

Modularity and scalability were addressed in the design—the various laser chains are built by different combinations of a limited set of amplification modules: Laser 1 (see Figure 1) is composed of a single amplification stage (AMP1); Laser 2 consists of two amplification stages (AMP1, featuring the same design and operating parameters as in Laser 1, and AMP2); finally, Laser 3 consists of three stages (AMP1, AMP2, and AMP3), the first two being identical to Laser 2, and the third one featuring a dedicated design. The modules are already dimensioned to operate at the P1 level (Table 1) if a sufficient pump pulse energy is available, as will be clarified in the following sections. This approach is advantageous in view of an industrial development of the system and in view of the scaling up of its performance from P0 to P1 along its lifetime.

2.3. Ti:Sapphire Amplifiers Structure and Geometry

A dedicated analysis was carried out to define the geometrical layout of the multi-pass amplifier based on thin disk crystals. To achieve sufficient pump absorption and energy storage, several disks (from 2 to 4) must be used in each amplification stage, depending on the pump energy and PRR. To achieve efficient amplification and energy extraction the amplified beam must cross the crystal several times (from 4 to 6 depending on the configuration).

As for the cooling strategy and amplification scheme, two possible approaches were considered for the disks: a transmission geometry and a reflection geometry.

In the transmission geometry, the disk-shaped crystal is cooled on both faces; both the pump beams and the amplified beam cross the crystal, the cooling water flow, and the flow containment windows. This solution (proposed in a previous study [13] and analyzed in another study [6] for the Eupraxia system) offers a good performance in terms of heat extraction and allows implementation of a simpler layout from a geometrical point of view, but it presents a potential drawback because the amplified beam is potentially subjected to optical perturbations due to the turbulence of the cooling fluid.

In the reflection geometry, one of the faces of the crystal is highly reflective for the amplification and pump beam. The amplified beam and the pump beams enter the crystal from the front face and are reflected back in the incoming direction on the cooled back surface (Figure 2). As the laser beams do not cross the cooling flow, no optical perturbations are possible. This arrangement allows for less favorable surface/volume ratio for cooling and requires a more complex geometry.

Here, we describe in more detail the design of the amplifiers for the reflection geometry. Both design approaches are still under consideration, as it is difficult to assess the balance of the respective pros and cons only on the basis of theoretical considerations and simulations, and it will be addressed by suitable pilot studies.

The various laser modules were dimensioned by means of numerical simulations using the code MIRO developed by CEA (Commissariat à l'énergie atomique et aux énergies alternatives, France) [12], validated by comparison with similar existing real laser systems [18,19]. As a baseline design, all of the amplifying modules feature a multi-pass amplification architecture with 4 passes. Here, we provide details of the amplifier AMP3 (see Figure 1), as this is the amplifying unit running at the highest energy and power level, and thus is the most challenging in terms of thermal management. The unit consists of 3 equal amplification disks. The main parameters are reported in Table 2 for the performance levels P0 and P1.

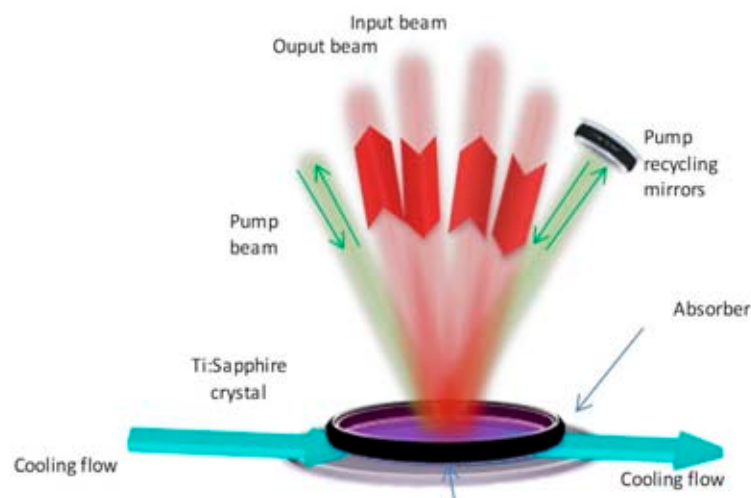


Figure 2. Layout of a single amplifying element in the reflection geometry.

Table 2. Main design and operational parameter for the amplifier AMP3 in the reflection configuration.

Parameter	Value	Parameter	Value (P0–P1)
Crystal diameter (cm)	16	Beam diameter FWHM (cm)	12–13
Crystal clear aperture (cm)	13.2	Pump beam energy (J)	109–189
Crystal thickness (mm)	10.7	Seed pulse energy (J)	18.8–40
Crystal doping (% Wt)	0.045	Output pulse energy (J)	62.0–130
		Pulse bandwidth (nm. FWHM)	27–23

The geometrical layout of the disk arrangement is exemplified in Figure 3, which shows separately the amplified beam path and the pump beam path. The seed pulse enters the first disk of the chain, and it is routed to the second and third disk by a suitable steering mirrors arrangement. After a first pass along the disk sequence, the pulse travels along a delay line and then it is sent backward along the chain meeting the three disks in reverse order. Angular multiplexing is used to separate the forward and the backward beam paths.

The three disks are pumped with the same amount of energy, equally distributed from the same pump pulse by beam-splitters (Figure 3 right). On each disk, the pump energy is completely absorbed in four passes. The path of the pump beams is slanted in the vertical (z) plane to avoid obstruction by the steering mirrors for the amplified beam. The distance between the steering mirrors and the Ti:Sa disks is about 4 m, and the angles of the amplified beam path with respect to the disks’ surfaces are 1.2° and 2.4°.

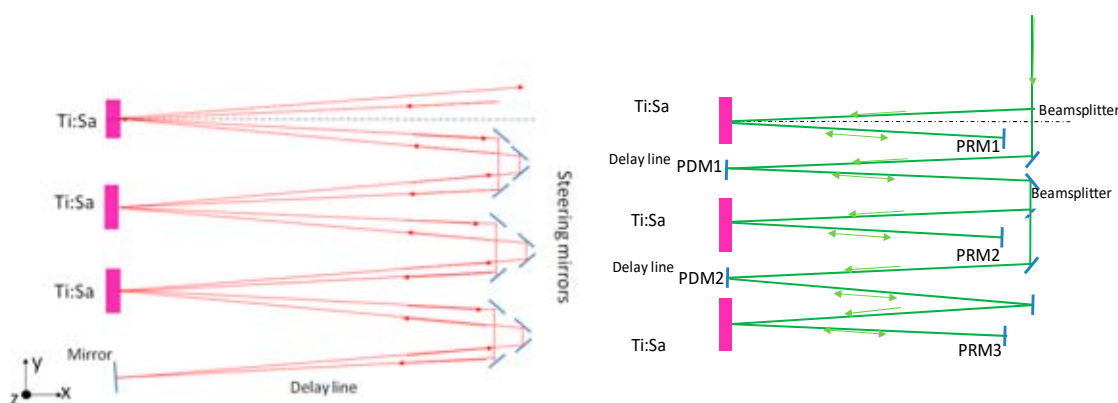


Figure 3. (Left) amplified beam path through the Ti:Sapphire disks. Pump beams are not represented for clarity. (Right) pump beam path. Drawings not in scale, with angles exaggerated for clarity.

The pump beam path includes suitable delay lines so that the arrival of the pump pulse on each disk is synchronized with the arrival of the amplified pulse.

The energy amplification process in AMP3 is described in Figure 4, which reports the pulse energy for increasing numbers of passes, for the performance levels P0 and P1. For the P0 level the module is seeded with 18.8 J and pumped with 109 J, resulting in a output energy of 62 J; for the P1 performance level the output energy is 130 J with a seed pulse energy of 40 J, and a pump energy of 189 J.

The amplification process takes advantage of the fact that in both cases the seed energy is relatively high, so an efficient energy extraction can be realized even though the amplification per bounce on a single disk is relatively low. The different pulse duration and spectral bandwidth between P0 and P1 were found to have a negligible impact on the energy extraction.

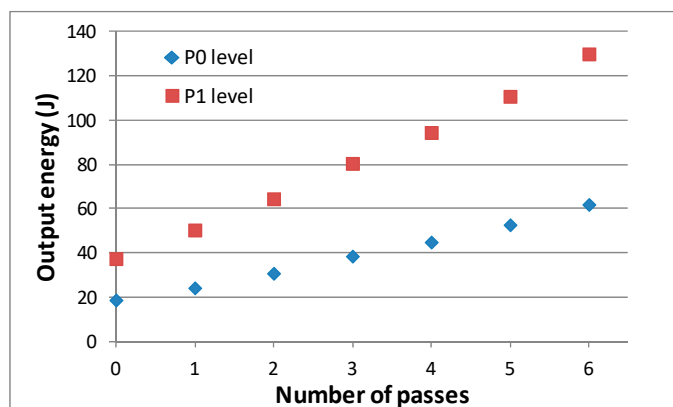


Figure 4. Calculated pulse energy evolution during the propagation in AMP3 at the level of performance of P0 and P1. Each pass corresponds to a single transit of the pulse in the disk (a single reflection consists of 2 passes).

The same concept was applied in the design of all the three modules (AMP1, AMP2, AMP3), as they operate at similar levels of pump pulse fluence, seed pulse fluence, and stored energy density. Therefore, the amplification of the pulse fluence is similar for all the three modules and it scales in the same way when going from P0 to P1 level. Energy scaling from AMP1 to AMP3 was mainly obtained by increasing the beam diameter at about constant fluence. In some cases a small adjustment in the beam diameter was needed to optimize the process either at P0 or at P1.

Regarding the thermal load, the various modules were designed to safely operate at the performance level P1; at the performance level P0 the thermal load is well below the design limits for each stage.

In conclusion, as was mentioned earlier, the output level of the amplifiers can be scaled up from P0 to P1 by increasing the pump and the seed energy without needing major modifications.

The occurrence of parasitic lasing was carefully analyzed in the design. Details about the methodology followed for this subject can be found in previous work [6]. The choice of crystal diameter, beam size, crystal doping, and thickness result from an accurate tradeoff between longitudinal gain, energy storage, cooling considerations, and transverse lasing control and suppression. We notice here that although the multi-slab approach was primarily adopted to provide enough heat exchange surface area, as a side advantage it allows distribution of the stored energy in several crystals, reducing the transverse gain at the pump input face. Increasing the doping level would be favorable from the thermal point of view (as it would allow reduction of the crystal thickness for the same pump absorption), but it would result in an increased parasitic gain.

The implementation of the extraction during pumping (EDP) strategy relies on the proper synchronization between the injection of the seed pulse and of the pump pulse, and on the presence of the delay lines for the pump beam between the various disks.

On each disk, the pump pulse is almost completely absorbed in four passes, using the pump recycling mirrors PRM1, PRM2, and PRM3 to send back in the crystal the fraction transmitted after the first bounce.

The time required to complete the pump absorption process on each disk from the moment when the leading edge of the pump pulse first hits the disk depends on the pump pulse duration and on the distance between the disk and the PRM. As a numeric example, if the pump pulses are roughly rectangular with a duration of 15 ns, and the distance between the disks and the PRM is 2.5 m, the pump absorption will be completed in about 30 ns on each disk.

The seed pulse arrives on the disk before the end of the absorption period, so that the available energy for amplification is only the fraction of the pump pulse absorbed before the arrival of the seed pulse itself; after the first bounce, the seed pulse leaves the disk and it returns back only for the return pass. During this interval the energy absorption is completed and the stored energy remains available

for the amplification in the return pass, as the lifetime of the Ti:Sa is obviously much longer than the overall pulse transit time in the disks sequence.

This sequence of events can be replicated in each disk along the chain by keeping the arrival time of the pump pulse on each disk properly synchronized with the arrival of the seed pulse. For this purpose, the additional pump delay lines between each disk (mirrors PDM1 and PDM2) defer the arrival of the pump pulse on each disk exactly by the time that the seed pulse takes to complete its path through the previous Ti:Sa disks.

This timing scheme is exemplified in the diagram in Figure 5. Through this approach, the stored energy repartition between the first and the second bounce on each disk can be finely tuned by adjusting the injection delay between the pump pulse and the seed pulse, and the length of the intermediate delay lines. As the pump absorption process on each disk takes a time in the order of several tens of ns, a timing accuracy in the range of $\sim 0.3\text{--}0.5$ ns can allow a control of the energy repartition with about 1% accuracy.

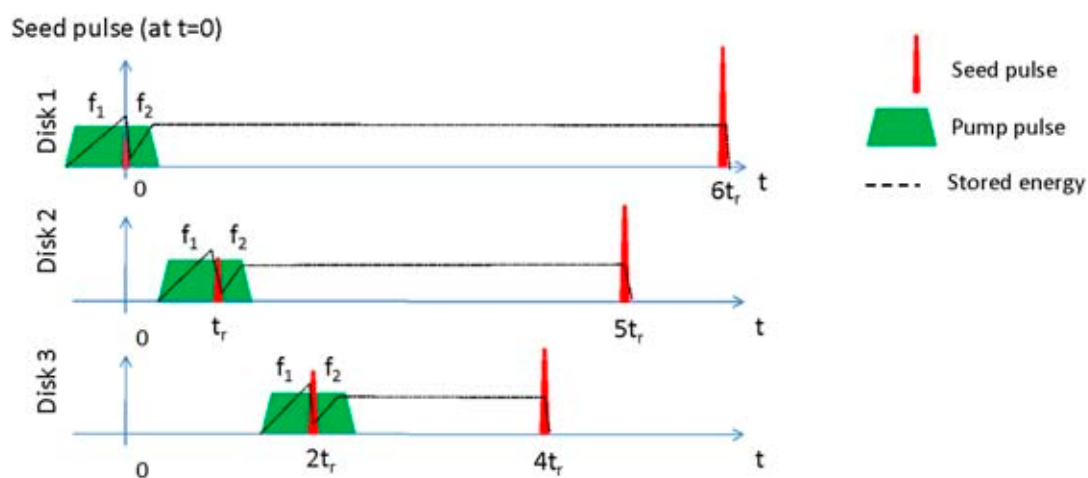


Figure 5. Overview of the synchronization scheme for the implementation of the EDP (Extraction During Pumping) strategy. Red peaks represent the amplified pulses, the green trapezoids represent the arrival of the pump pulses (including recycling), and the dashed line is the stored energy. The time t_r is the transit time from one disk to the next one (about 24 ns for AMP3). The fraction of stored energy f_1 available for the amplification in the first transit can be adjusted by finely tuning the delay between the arrival of the amplified pulse and the pump pulse on each disk, leaving the remaining fraction f_2 available for the amplification of the second transit.

2.4. Fluid Cooling Simulations

A simulation of the temperature distribution and of the thermomechanical stresses affecting the amplifier disks was carried out by means of Finite Element Analysis (FEA) software available in a commercial software package, i.e., LAS-CAD (ver. 3.6.1) developed by LAS-CAD GmbH (www.las-cad.com), to calculate the spatial temperature distribution in the gain material, the resulting stress and deformation distribution induced by the thermal expansion, and finally the thermal aberrations computing the optical path difference (OPD) distribution across the crystal aperture due to both the variation of the refractive index with temperature and the variation in the crystal thickness due to thermal expansion and thermally induced stresses. Thermally induced birefringence [20] was not considered. Detailed results of this approach are described in previous work [6].

A key point to obtain meaningful results from the FEA simulations is the modelling of the heat exchange between the solid and the fluid. This was modelled by means of a film coefficient $k = Q/\Delta T$, where ΔT is the local difference of temperature between the solid surface and the fluid, and Q is the power per unit surface transferred from the solid to the fluid. Although approximate, this approach

is very effective in reducing the computational effort to acceptable levels, in particular with full 3D models.

The fluid–solid heat transfer process was studied by means of dedicated fluidodynamical simulations, in 2D geometry, in order to obtain reliable values for the heat transfer coefficient used in the full 3D simulation. The computational method was a numerical solution of the Navier–Stokes equations for mass and energy transport, using the so-called Low Reynolds k - ϵ method, which is capable of a quite accurate simulation of the behavior of the fluid-solid interface layer with a reasonable computational effort. The fluidodynamics simulations were carried out using a commercial software package (COMSOL Multiphysics Version 5.3a).

An example is shown in Figure 6, depicting the fluid flow in contact with the back (reflective) surface of the disk of Figure 2. The simulation considers a flow of water at 6 m/s entrance speed, in a cooling channel with a thickness of 5 mm. The fluid flow is heated from its bottom side by a constant heat flux of 25 W/cm^2 , corresponding to the heat input generated in the Ti:Sapphire disk under pumping at the P1 performance level. The length of the heated portion of the channel is 160 mm (corresponding to the diameter of the disk of AMP3). Figure 5 shows the calculated fluid velocity distribution. The temperature dependence of the water properties (viscosity, density) was taken into account; buoyancy effects were considered negligible.

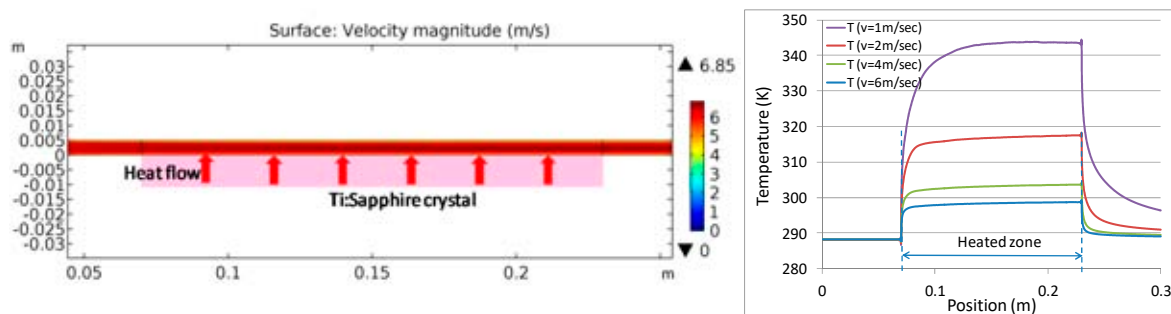


Figure 6. (Left) fluid velocity distribution (in m/sec) in the cooling channel in the simulation conditions specified in the text. The position of the Ti:Sapphire crystal is shown for clarity, but it is considered in the thermal simulation only as a thermal boundary condition for the fluid flow (constant surface heat flux). (Right) Temperature profile along the Ti:Sapphire crystal surface for different flow speeds, at a heat input of 25 W/cm^2 , with an input temperature of 288.15 K ($15 \text{ }^\circ\text{C}$).

Figure 6 also shows the calculated temperature distribution of the boundary layer of the water flow in contact with the Ti:Sapphire surface for different flow speeds. Under fully developed heat transfer conditions the temperature increase of the surface is about proportional to the heat input. This allows calculation of the effective film coefficient $k = Q/\Delta T$, which expresses the cooling capability of the fluid flow. The effective film coefficient resulted independently from of the heat input, and proportional to the flow speed (proportionality constant of about 0.04 J/cm^3). At the maximum flow speed of 6 m/sec the film coefficient was $2.45 \text{ W}/(\text{cm}^2 \text{ K})$.

With the channel configuration shown in Figure 6 (i.e., parallel walls), only a very thin layer of fluid near the surface is actually involved in the heat exchange process. Other channel configurations were also studied, with ridges meant to enhance the fluid turbulence and increase the heat exchange, as shown in Figure 7. Due to turbulence, the fluid speed locally increases (up to about twice the input velocity), thus improving the heat transfer from the lower surface. The temperature increase of the heated surface is thus lower by more than a factor of 2 with respect to the previous case, with a corresponding increase in the film coefficient k .

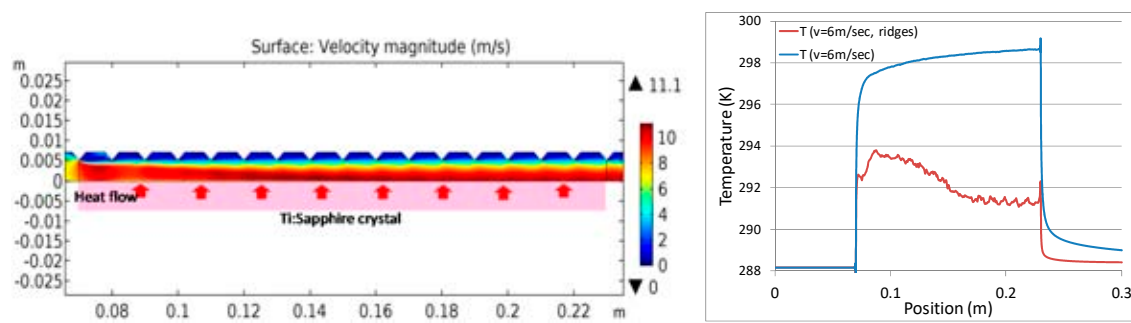


Figure 7. (Left) Fluid velocity distribution in the cooling channel, with triangular ridges on the upper wall. The triangular protrusions on the upper wall have a height of 2 mm, base of 4 mm, and distance of 10 mm. The thickness of the channel between the ridges is 7 mm. Other simulation conditions are the same as in Figure 6. (Right) Temperature profile along the channel position at the interface between the fluid and the Ti:Sapphire, for the smooth channel (blue line) and for the ridged channel (red line).

Such a configuration can be applied for the cooling of the disks in the reflection configuration, as the back face of the cooling channel is not crossed by the light beams, so it can be shaped to optimize heat exchange processes.

It can be noticed that the transversal flow configuration induces a temperature gradient in the cooling flow (and thus in the cooled surface of the Ti:Sa disk) in the flow direction as the fluid is heated along its path. This induces some amount of thermal aberration that is not radially symmetric, as would be desirable. On the other hand, the overall amount of this wavefront distortion is relatively small, at least for the highest flow speeds considered here, as it can be easily estimated. From the graph of Figure 7 it can be seen that the difference in the Ti:Sa surface temperature between the input edge and the output edge is about 1.6 °C. As the transverse heat flow in the Ti:Sa disk is negligible (due to the thin disk geometry), this temperature difference is directly added to the internal temperature distribution in the Ti:Sa. Accounting for the thermal expansion coefficient and for the value of dn/dT of the Ti:Sa ($5 \times 10^{-5}/K$ and $1.5 \times 10^{-5}/K$, respectively), the thermally induced optical path difference is about 0.4 μm over a single pass (i.e., about $\lambda/2$), with a roughly linear variation along the disk diameter. Moreover, this specific contribution to the wavefront aberration is stationary or at worst slowly varying in time, so it can be easily mitigated or canceled both by a proper geometrical arrangement (e.g., by having the flow propagating in alternate opposite directions in the disks) and by active wavefront correction optics, which are already considered in the design.

These investigations are to some extent preliminary, and a significantly broader work is required to obtain an executive design. Particularly relevant are the problems related to the vibrations induced by turbulences and by the pumping system, which could be detrimental for the beam pointing stability, in particular in the reflection geometry. Our major concern here was to assess the effectiveness of the water cooling approach at this unprecedented level of thermal load.

We notice here that according to the data reported in existing literature, gas cooling cannot provide a heat removal rate comparable with water cooling. Implementation of gas cooling would thus require unreasonably large heat exchange surfaces to obtain sufficient cooling, in particular at the envisaged P1 performance level. In more detail, currently the highest cooling performance obtained by this technique in the DiPOLE 100 system corresponds to the removal of about 4 kW of thermal load, with an available cooling surface of about 1450 cm² (six Yb:YAG slabs with a cross-section of 11 × 11 cm², cooled on both sides) [15]; the average heat flow per unit cooling surface is less than 3W/cm², and the film coefficient k was estimated to about 0.17 W/(cm² K) [14]. On the other hand, the overall thermal load expected in the AMP3 module is about 10 kW (i.e., a factor 2.5-times larger than in DiPOLE 100), with an average heat flow per unit cooling surface as high as 25 W/cm² (i.e., an order of magnitude higher); the value of the heat transfer coefficient obtained with water cooling (2.45 W/(cm² K) is more than an order of magnitude larger than in the case of He cooling. We notice here that cryogenic He

cooling was also recently employed for the cooling of a Ti:Sa multi-slab amplifier for the HAPLS system [16]; however, in that case the system runs at 3.3 Hz, with a pump energy of about 60 J, setting the average pump power to about 200 W. This is much lower than the average pump power expected in the Eupraxia system for any of the amplification stages.

3. Pump Laser Requirements and Available Technologies

As outlined above, the laser amplification chains are composed of up to three individual amplifiers, labeled AMP1, AMP2, and AMP3 in the diagram in Figure 1. From the preliminary system design, the following pump energy requirements emerged, as summarized in Table 3.

Table 3. Pump energy requirements for the various amplification stages.

Device	Pump Energy @ P0 (20 Hz) [J]	Pump Energy @ P1 (100 Hz) [J]
AMP1	19.2	25.7
AMP2	37.2	65.2
AMP3	109	189

Pump pulses must have a wavelength around 515–40 nm to match the absorption band of the Ti:Sapphire, and a pulse duration of several nanoseconds. Possible candidates as pump laser systems are the Premiulite-YAG device developed by the French company Amplitude (formerly known as P60) and the DiPOLE 100 developed by the Central Laser Facility, Science and Technology Facility Council (STFC) Rutherford Appleton Laboratory in the United Kingdom.

The Premiulite system is based on a chain of Nd:YAG disk amplifier heads (DAH) based on Nd:YAG, and currently operated with flash lamp pumping, liquid-cooled at room temperature. After conversion of the output to the second harmonic, the system delivers up to 60 J of pulse energy at 532 nm, with a pulse duration of 5–6 ns. The system is modular, i.e., it can be scaled down by reducing the number of active heads. Currently the repetition rate is 10 Hz, possibly limited by thermal management issues related to flashlamp pumping [21].

DiPOLE is a diode-pumped, solid state laser amplifier based on an end-pumped stack of ceramic Yb:YAG slabs, cooled by a flow of low-temperature, high-pressure helium gas. This technology was recently demonstrated at the 1 kW level with the DiPOLE100 system (STFC, UK; HiLASE, CZ), showing 100 J output energy at 10 Hz, 1030 nm, with > 60 J expected conversion at 515 nm [1]. Current development plans are oriented toward a low energy, high repetition rate (10 J at 100 Hz) version of the system, whereas the frequency upscale of the 100 J version is probably challenged by thermal management issues.

4. Pulse Compression and Beam Transport System

The pulse compressor and the beam transport system also pose specific problems because of the high average power level handled by the pulse compressor and the high pointing stability required for the interaction with the plasma target.

A general scheme for this part of the apparatus is depicted in Figure 8. The design of the whole subsystem has to be compliant with the final goal of recompressing the 125 J CPA pulse coming from the last amplification stage down to 20–60 fs on-target (depending on the laser system, see Table 1 for details).

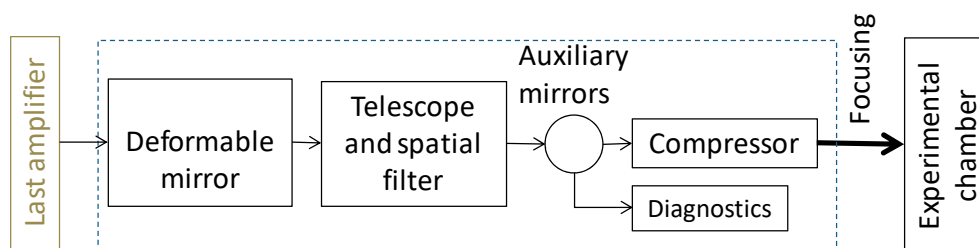


Figure 8. General transport and compression scheme.

The main system elements are:

- a *deformable mirror* for the optimization of the phase front of the beam in a specific plane in the compressor, to keep the phase front compatible with the required compression;
- a beam expander with a given magnification, to relay the image plan on the deformable mirror, which also includes a spatial filter implemented by placing a pinhole at the focal spot;
- a temporal *compression stage*.

The spatial filter is required to remove high spatial frequencies from the beam (due for instance to inhomogeneities in the Ti:Sa crystal), which would otherwise induce hot spots in the beam profile along the transport chain. In any case, the diameter of the pinhole in the spatial filter will be much larger than the spot size (i.e., by a factor between 2 and 10); moreover, the spatial filter is placed downstream with respect to the deformable mirror, which manages both the wave front correction and the pointing stabilization, so that overall there is no risk that the pinhole will be damaged by the laser beam.

Between the spatial filter and the compressor, a possible series of 2 mirrors for polarization rotation or simple beam transport towards the compressor entrance can be considered, also to allow the detection of beam leakage for diagnostics purpose. This stage actually depends on the choice of compressor gratings, and it will be needed for gold gratings, as explained below.

The next section will describe for each point the available technologies and schemes, and the choice of the best option.

4.1. Compressors

At each compressor, the average input power and output pulse parameters will be:

Laser 1: 1.2 kW (12 J @ 100 Hz), needed 20 fs after compression (62 nm bandwidth), spectral acceptance required: 140 nm

Laser 2: 4 kW (40 J @ 100 Hz), needed 20 fs after compression (62 nm bandwidth), spectral acceptance required: 140 nm

Laser 3 13 kW (130 J @ 100 Hz), needed 60 fs after compression (23 nm bandwidth), spectral acceptance required: 60 nm

Laser induced damage threshold (LIDT) of gratings limits the laser fluence arriving on the compressor for each laser system to 100 mJ/cm^2 , and thus the average intensity impinging on the compressors to 10 W/cm^2 . While gratings in air might handle this intensity, it is not at all obvious whether they can do it in a vacuum. The only study available so far on gold grating cooling in air was carried out [22] at LLNL. For these reasons, given the current lack of studies on this issue, the baseline choice for the EuPRAXIA compressor grating material is gold gratings without resin, which requires the study of a cooling strategy. The absence of resin between the gold layer and the substrate might induce less deformation in the gratings, but there is still no established evidence on this and an accurate study is therefore mandatory. Indeed, some new grating technology could make cooling unnecessary, thus simplifying significantly the complexity of the system.

Experimental tests were carried out on heating effects of the gratings of an ultrashort pulse compressor using a kW laser diode as the thermal source. The compressor is installed in the front end

hall of the Apollon laser [23,24] and allows the compression of mJ level pulses at < 17 fs in air. Based on wavelength-dependent wavefront measurements, the spatiotemporal impact on the compressed pulses was evaluated.

The experimental setup is shown in Figure 9. A typical folded gold grating based compressor is used. In order to experimentally reproduce the high average power conditions on the compressor gratings, a 1.2 kW laser diode at 980 nm was used as the thermal source. The heating beam from the diode is first split into twin beams via a polarizer beam splitter (PBS) and each one is directed precisely on the input and output sections of the first compressor grating (G1).

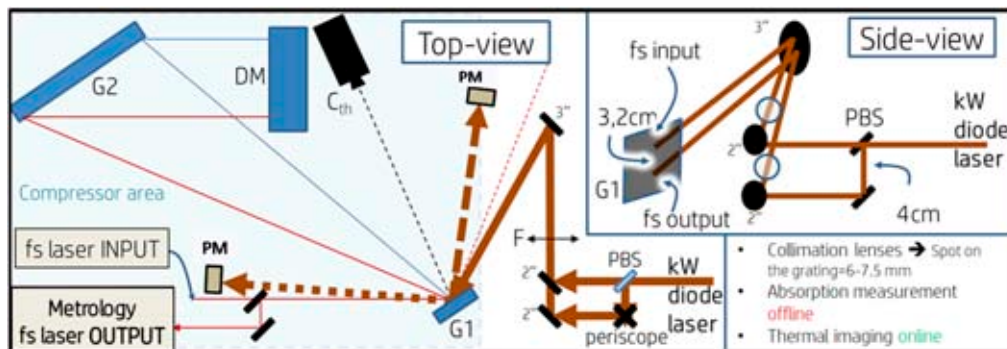


Figure 9. Top-view and side-view of the experimental set-up. Compressor Area: PM = power meter; C_{th} = Thermal camera; G1 = first compressor grating; G2 = second compressor grating (gold, 56°, 1480l/mm); DM = Dihedral Mirror. Diode Area: F = imaging lens; PBS = Polarizing Beam Splitter.

An imaging system allows a perfect overlap of the diode heating beam on the ultrashort beam (Figure 10a). A thermal camera is used in parallel to measure the local spatial distribution of the temperature increase (Figure 10b,c). The metrology used includes a wavefront sensor (Phasics SID4), achromatic near and far field sensors, as well as a single shot autocorrelator and a Wizzler for the estimation of the impact on the pulse duration.

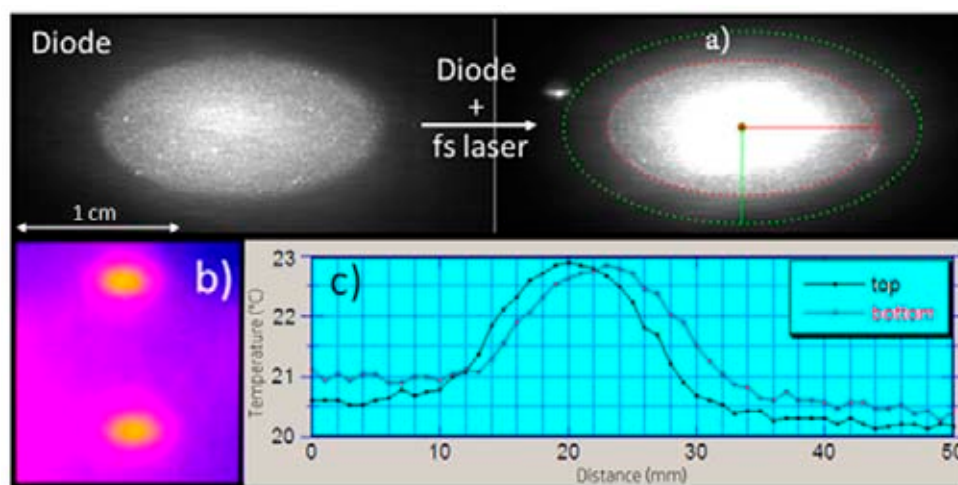


Figure 10. (a) Image of the heating diode laser beam and of the fs laser beam on G1. The laser diode beam has a top hat profile, with a spot size of 0.82 cm × 1.63 cm (surface ~ 1 cm²). The edge of the diode beam is evidenced by a dashed red line, and the edge of the fs beam by a dashed green line. (b) G1 thermal image for 130W sent on each spot (see above). (c) Temperature profiles for the beam spots (b); left profile: input spot; right profile: output spot.

For different values of the average power (0–130 W) sent on G1, the wavefront (peak-to-valley and RMS values in λ units), Strehl ratio, defocus, and all the higher order induced aberrations

were measured. A significant degradation of the spatial profile of the beam was measured, and an accentuated astigmatism was noted, induced by the gratings when they are heated. The focal spot is asymmetrically distorted, and the first measurements suggest a non-negligible difference in this degradation for different wavelengths. (Figure 11c).

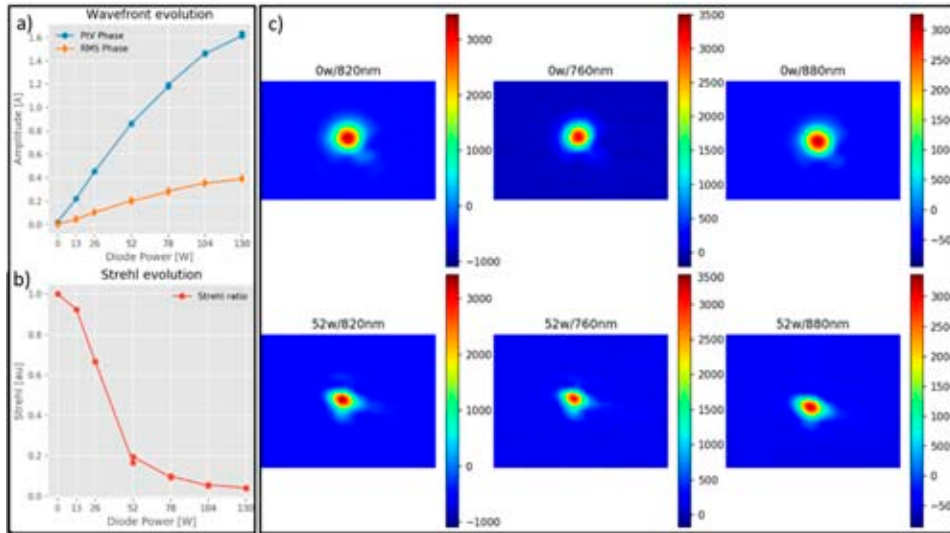


Figure 11. The (increasing) power sent on both input and output spots. (a) Wavefront degradation. (b) Strehl ratio degradation—the graph reports the ratio between the Strehl ratio at a given power and that at zero heating power. (c) Upper line: far field at 760 nm, 820 nm, 880 nm for 0 W heating power. Lower line: far field at 760 nm, 820 nm, 880 nm for 52 W heating power. Pairs of spots at each wavelength are normalized at the same peak intensity to allow a clearer comparison of the spot shapes. Spots at different wavelengths cannot be compared directly due to the different shape of the unperturbed beam.

4.2. Beam at the Interaction Point

In previous work [6] an overview was given of the transport and compression strategy from the compressor output to the interaction point.

A recent work was dedicated to address viable solutions for the interaction point spatial beam diagnostics and the pointing stability diagnostics, which is the final part of the chain until the interaction point (as identified in the scheme in Figure 8). The block diagram in Figure 12 shows the requirements needed to fully characterize and try to correct the beam characteristics in the interaction point.

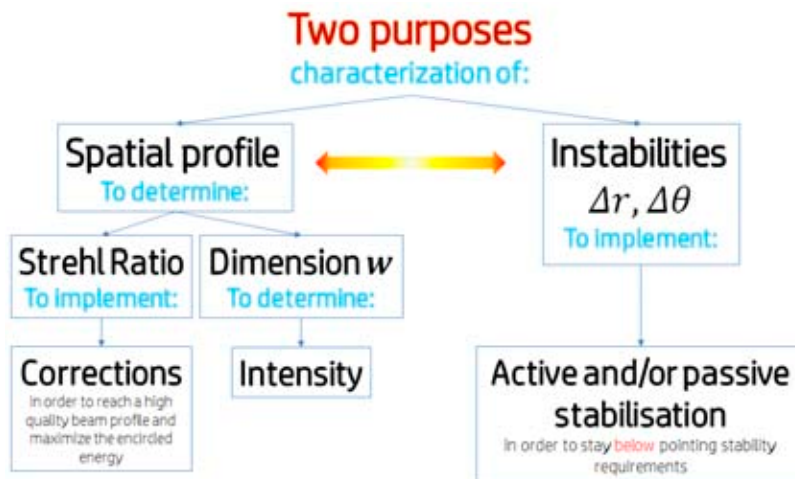


Figure 12. Preliminary flow chart of the laser stability diagnostics and control in the focal point.

Spatial beam diagnostics in the focal plane are necessary in order to measure and improve the beam spatial quality, in a closed loop with the deformable mirror, and in order to estimate the beam intensity achieved during the acceleration experiment.

Focusing conditions on the target require a beam pointing stability of the order of hundreds of nano-radians. This value was set up considering that the pointing instability of the output accelerated electron beam will be influenced by the laser pointing instability. Indeed, focusing of Laser 3 down to a spot of around 100 μm starting from a near field beam diameter of tens of cm requires focal lengths of tens of meters. Moreover, in the case of the 5 GeV acceleration laser, capillaries might be used, and it is important not to damage them during the acceleration phase with unstable pointing on the focal plane. Very long focal lengths cause transverse shifts (hundreds of microns) on the focal plane, even if the laser angular stability is below the micro radiant level (which is normally considered very stable). Several solutions are being investigated to solve this issue, which is still open in all the facilities worldwide. A diagnostic tool is needed in order to measure angular stabilities below the micro radians level, and even more importantly, a diagnostic tool that is able to measure angular fluctuations above 100 Hz frequency. Some facilities have dedicated optical systems for this purpose [25], but only in certain positions along the laser chain. A simple and easy to use diagnostic tool is needed in order to evaluate the entire line of a high-peak, high-average power laser system.

The most used method to measure spatial quality on the far field and pointing stability up to a repetition rate of tens of Hz is to image the focal plane where the laser beam is focused.

In the framework of the Eupraxia activities, a device for the measurement of beam pointing stability and beam shape has been tested (Figure 13).

This module is so compact that it can be placed on the beam path to make a magnified image of the laser spot in the focal plane and around the focal region, to study the laser beam spatial quality and stay in the chamber during laser shots. Its shielding has been studied to survive radiations and EMP during the shots, and special care has been taken in the choice of materials to be complaint with our residual gas analysis criteria so that it will not contaminate the final optics coating. The device can, therefore, stay in the interaction chamber during shots and can be used to make on-shot measurements. The laser system can operate at full energy (thus being subjected to realistic thermal load effects), but the beam after the amplification stage must be attenuated because only a few tens of microjoules can enter the camera module.

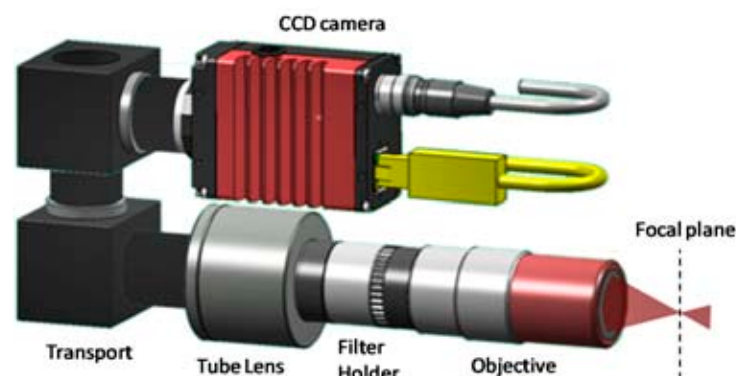


Figure 13. Design and experimental prototype of the module for focal spot quality and stability measurements.

In Apollon, a reflection-type attenuator has been studied to reduce the beam up to 6 orders of magnitude, plus an absorption-type attenuator to be placed just after. Filters are made of Schott VG9 colored glass, which has almost spectrally flat transmission around 800 nm, as seen from the data in Figure 14. Tests have shown that the wavefront distortion induced by the filters is less than $\lambda/10$.

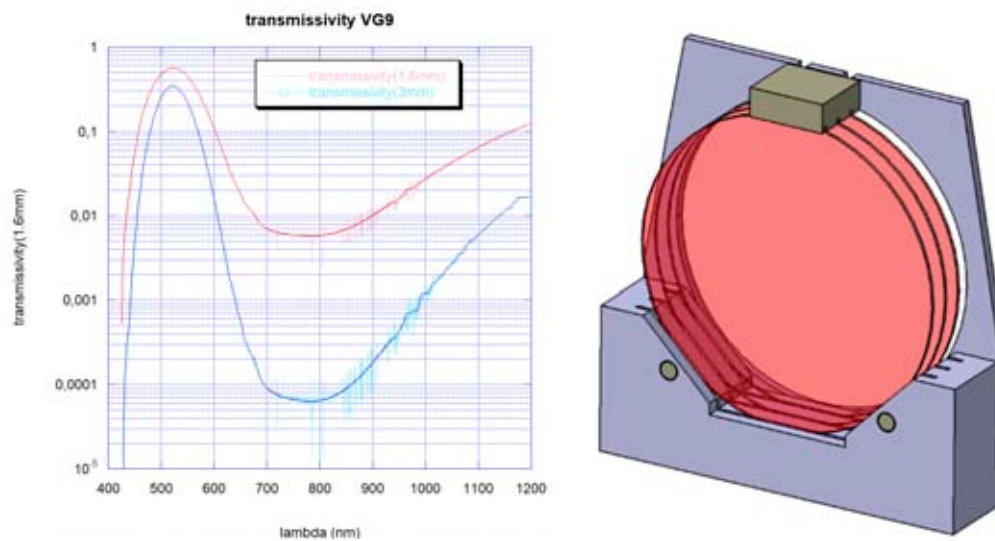


Figure 14. (Left) VG9 transmission spectra, measured with a 3-mm thick sample (blue curve) and a 1.6-mm thick sample (red curve). (Right) Mounting for the VG9 filters. Filter diameter is 160 mm, thickness 1.6 mm.

5. Conclusions

The requirements for the EuPRAXIA laser driver make its design and its realization a very challenging task. These requirements set unprecedented laser performance, never achieved before by any existing laser system worldwide. Nonetheless, recent advancements in laser technology are making the achievement of these performances feasible. On the basis of the requirements, and considering both the available technologies and those at high TRL and reasonable availability in the next few years at an industrial level, a baseline for the system architecture and for the key technologies was devised. The system concept delivered so far combines most, if not all, of the highly advanced and proven technologies and aims to deliver performances well beyond those of systems that already exist, or those currently under construction. Some critical aspects (for instance those related to the amplifiers cooling, the thermal deformation of the gratings, and the pointing stability) have been discussed and are being addressed both by means of simulations and by means of dedicated experimental studies. With this conceptual design, EuPRAXIA will provide a credible step towards reliable operation of a laser-driven plasma accelerator, fostering the development of the European laser industry and launching a disruptive advancement in high power, laser-based sciences and applications.

Author Contributions: Conceptualization, L.G., F.M., G.T., L.L., Z.M.; Investigation, G.T., Z.M., L.L., F.M., M.V., B.P. and L.G.; Supervision, F.M. and L.G.; Writing—original draft preparation, G.T., Z.M. and L.L.; Writing—review & editing, G.T., M.V., B.P., L.L. and L.G. Funding acquisition, F.M. and L.G.

Funding: The research leading to these results has received funding from the European Union Horizon 2020 Research and Innovation Program under Grant Agreement No. 653782 EuPRAXIA. This project has received funding from the CNR funded Italian research Network ELI-Italy (D.M. n. 631 08.08.2016).

Acknowledgments: We gratefully acknowledge P. Mason and K. Ertel of the Central Laser Facility, A. Bayramian, C. Siders, and C. Haefner of the Lawrence Livermore National Laboratory, and F. Falcoz of Amplitude Technologies for fruitful discussion on the laser developments.

Conflicts of Interest: The authors declare no conflict of interest.

References

1. Mason, P.; Divoký, M.; Ertel, K.; Pilař, J.; Butcher, T.; Hanuš, M.; Banerjee, S.; Phillips, J.; Smith, J.; Vido, M.D.; et al. Kilowatt average power 100]-level diode pumped solid state laser. *Optica* **2017**, *4*, 438–439. [[CrossRef](#)]

2. Sistrunk, E.F.; Spinka, T.; Bayramian, A.; Armstrong, O.; Baxamusa, S.; Betts, S.; Bopp, D.; Buck, D.; Charron, K.; Cupal, J.; et al. All diode-pumped, high repetition-rate advanced petawatt laser system (HAPLS). In Proceedings of the CLEO: Science and Innovations 2017, San Jose, CA, USA, 14–19 May 2017.
3. Danson, C.; Hillier, D.; Hopps, N.; Neely, D. Petawatt class lasers worldwide. *High Power Laser Sci. Eng.* **2015**, *3*, e3. [[CrossRef](#)]
4. Nakamura, K.; Mao, H.S.; Gonsalves, A.J.; Vincenti, H.; Mittelberger, D.E.; Daniels, J.; Magana, A.; Toth, C.; Leemans, W.P. Diagnostics, control and performance parameters for the bella high repetition rate petawatt class laser. *IEEE J. Quantum Electron.* **2017**, *53*, 1–21. [[CrossRef](#)]
5. Walker, P.A.; Alesini, P.D.; Alexandrova, A.S.; Anania, M.P.; Andreev, N.E. Horizon 2020 EuPRAXIA design study. *J. Phys. Conf. Ser.* **2017**, *874*, 1–8. [[CrossRef](#)]
6. Gizzi, L.A.; Koester, P.; Labate, L.; Mathieu, F.; Mazzotta, Z.; Toci, G.; Vannini, M. A viable laser driver for a user plasma accelerator. *Nucl. Instrum. Methods Phys. Res. A* **2018**, 58–66. [[CrossRef](#)]
7. Tomassini, P.; De Nicola, S.; Labate, L.; Londrillo, P.; Fedele, R.; Terzani, D.; Gizzi, L.A. The resonant multi-pulse ionization injection. *Phys. Plasmas* **2017**, *24*, 103120. [[CrossRef](#)]
8. Siders, C.W.; Siders, J.L.W.; Taylor, A.J.; Park, S.J.; Weiner, A.W. Efficient high-energy pulse-train generation using a 2n-pulse Michelson interferometer. *Appl. Opt.* **1998**, *37*, 5302–5305. [[CrossRef](#)]
9. Dromey, B.; Zepf, M.; Landreman, M.; O’Keeffe, K.; Robinson, T.; Hooker, S.M. Generation of a train of ultrashort pulses from a compact birefringent crystal array. *Appl. Opt.* **2007**, *46*, 5142–5146. [[CrossRef](#)]
10. Cowley, J.; Thornton, C.; Arran, C.; Shalloo, R.J.; Corner, L.; Cheung, L.; Gregory, C.D.; Mangles, S.P.D.; Matlis, N.H.; Symes, D.R.; et al. Excitation and Control of Plasma Wakefields by Multiple Laser Pulses. *hao* **2017**, *119*, 044802. [[CrossRef](#)]
11. Vantaggiato, G.; Labate, L.; Tomassini, P.; Gizzi, L.A. Modelling of pulse train generation for resonant laser wakefield acceleration using a delay mask. *Nucl. Instrum. Meth. Phys. Res. A* **2018**, *909*, 114–117. [[CrossRef](#)]
12. Morice, O. Miró: Complete modeling and software for pulse amplification and propagation in high-power laser systems. *Opt. Eng.* **2003**, *42*, 1530–1542. [[CrossRef](#)]
13. Nagymihaly, R.S.; Cao, H.; Papp, D.; Hajas, G.; Kalashnikov, M.; Osvay, K.; Chvykov, V. Liquid-cooled Ti: Sapphire thin disk amplifiers for high average power 100-TW systems. *Opt. Express* **2017**, *25*, 6664–6677. [[CrossRef](#)] [[PubMed](#)]
14. Mason, P.D.; Fitton, M.; Lintern, A.; Banerjee, S.; Ertel, K.; Davenne, T.; Hill, J.; Blake, S.P.; Phillips, P.J.; Butcher, T.J.; et al. Scalable design for a high energy cryogenic gas cooled diode pumped laser amplifier. *Appl. Opt.* **2015**, *54*, 4227–4238. [[CrossRef](#)]
15. Banerjee, S.; Mason, P.D.; Ertel, K.; Phillips, P.J.; De Vido, M.; Chekhlov, O.; Divoky, M.; Pilar, J.; Smith, J.; Butcher, T.; et al. 100J-level nanosecond pulsed diode pumped solid state laser. *Opt. Lett.* **2016**, *41*, 2089–2092. [[CrossRef](#)] [[PubMed](#)]
16. Haefner, C.L.; Bayramian, A.; Betts, S.; Bopp, R.; Buck, S.; Cupal, J.; Jarboe, J. High average power, diode pumped petawatt laser systems: A new generation of lasers enabling precision science and commercial applications. In *Research Using Extreme Light: Entering New Frontiers with Petawatt-Class Lasers III*; International Society for Optics and Photonics: Washington, WA, USA, 2017.
17. Chvykov, V.; Nagymihaly, R.S.; Cao, H.; Kalashnikov, M.; Osvay, K. Design of a thin disk amplifier with extraction during pumping for high peak and average power Ti: Sa systems (EDP-TD). *Opt. Express* **2016**, *24*, 3721–3733. [[CrossRef](#)] [[PubMed](#)]
18. Chu, Y.; Liang, X.; Yu, L.; Xu, Y.; Xu, L.; Ma, L.; Lu, X.; Liu, Y.; Leng, Y.; Li, R.; et al. High-contrast 2.0 Petawatt Ti: Sapphire laser system. *Opt. Express* **2013**, *21*, 29231–29239. [[CrossRef](#)] [[PubMed](#)]
19. Gizzi, L.A.; Giove, D.; Altana, C.; Brandi, F.; Cirrone, P.; Cristoforetti, G.; Fazzi, A.; Ferrara, P.; Fulgentini, L.; Koester, P.; et al. New Line for Laser-Driven Light Ions Acceleration and Related TNSA Studies. *Appl. Sci.* **2017**, *7*, 984. [[CrossRef](#)]
20. Ferrara, P.; Ciofini, M.; Esposito, L.; Hostaša, J.; Labate, L.; Lapucci, A.; Pirri, A.; Toci, G.; Vannini, M.; Gizzi, L.A. 3-D numerical simulation of Yb: YAG active slabs with longitudinal doping gradient for thermal load effects assessment. *Opt. Express* **2014**, *22*, 5375–5386. [[CrossRef](#)]
21. Charalambidis, D.; Chikán, V.; Cormier, E.; Dombi, P.; Fülöp, J.A.; Janáky, C.; Lepine, F. The extreme light infrastructure—Attosecond light pulse source (ELI-ALPS) project. In *Progress in Ultrafast Intense Laser Science XIII*; Springer: Basel, Switzerland, 2018; pp. 181–218.

22. Alessi, D.A.; Sistrunk, E.; Nguyen, H.T.; Rosso, P.A.; Spinka, T.; Aasen, M.D.; Herriot, S.; Britten, J.A.; Haefner, C. A Compressor for High Average Power Ultrafast Laser Pulses with High Energies. In Proceedings of the Conference on Lasers and Electro-Optics, San Jose, CA, USA, 14–19 May 2017.
23. Papadopoulos, D.; Zou, J.; Le Blanc, C.; Chériaux, G.; Georges, P.; Druon, F.; Audebert, P. The Apollon 10 PW laser: Experimental and theoretical investigation of the temporal characteristics. *High Power Laser Sci. Eng.* **2016**, *4*, E34. [[CrossRef](#)]
24. Papadopoulos, D.N.; Ramirez, P.; Genevrier, K.; Ranc, L.; Lebas, N.; Pellegrina, A.; Le Blanc, C.; Monot, P.; Martin, L.; Zou, J.P.; et al. High-contrast 10 fs OPCPA-based front end for multi-PW laser chains. *Opt. Lett.* **2017**, *42*, 3530–3533. [[CrossRef](#)]
25. Canuel, B.; Genin, E.; Mantovani, M.; Marque, J.; Ruggi, P.; Tacca, M. Sub-nanoradiant beam pointing monitoring and stabilization system for controlling input beam jitter in gravitational wave interferometers. *Appl. Opt.* **2014**, *53*, 2906–2916. [[CrossRef](#)] [[PubMed](#)]



© 2019 by the authors. Licensee MDPI, Basel, Switzerland. This article is an open access article distributed under the terms and conditions of the Creative Commons Attribution (CC BY) license (<http://creativecommons.org/licenses/by/4.0/>).



InGaN/GaN multiple quantum well for superfast scintillation application: Photoluminescence measurements of the picosecond rise time and excitation density effect



Guido Toci^{a,b,*}, Leonida A. Gizzi^{c,d}, Petra Koester^{c,d}, Federica Baffigi^{c,d}, Lorenzo Fulgentini^{c,d}, Luca Labate^{c,d}, Alice Hospodkova^e, Vitezslav Jary^e, Martin Nikl^e, Matteo Vannini^{a,b}

^a Istituto Nazionale di Ottica - Consiglio Nazionale delle Ricerche CNR-INO Sede di Sesto Fiorentino, Via Madonna del Piano 10, Sesto Fiorentino, FI 50019, Italy

^b Istituto Nazionale di Fisica Nucleare, Sezione di Firenze, Via Giovanni Sansone 1, 50019 Sesto Fiorentino, FI, Italy

^c Intense Laser Irradiation Laboratory, Istituto Nazionale di Ottica - Consiglio Nazionale delle Ricerche, CNR-INO, Sede di Pisa, Via Moruzzi 1, 56124 Pisa, Italy

^d Istituto Nazionale di Fisica Nucleare, Sezione di Pisa, Largo Bruno Pontecorvo 3, 56127 Pisa, Italy

^e Institute of Physics, Academy of Sciences of the Czech Republic, Cukrovarnicka 10, 16200 Prague, Czech Republic

ARTICLE INFO

Keywords:

Multiple quantum wells
InGaN/GaN
Scintillator
Streak camera
Ultrafast rise-time measurements

ABSTRACT

We report the study of the fast rise time and decay time in the ps time scale of the excitonic luminescence of a multiple quantum well (MQW) heterostructure of InGaN/GaN, including the excitation density effect. These structures were proposed as ultrafast scintillators for soft X-ray detectors and particle beam diagnostics. Measurements were carried out with a Hadland Imacon 500 streak camera following excitation of the sample by laser pulses of few tens of μJ at 266 nm and 400 nm, with pulse duration less than 200 fs. The rise time of the detected MQW luminescence was less than 10 ps, with a possible contribution from the detection system and signal collection geometry. The calibration and the signal processing techniques employed to fully exploit the time resolution of the detection system are also described.

1. Introduction

Inorganic scintillators have many applications in various fields as medical imaging, homeland security, high-tech industry and high energy and nuclear physics [1,2]. In particular, strong interest is motivated by the possibility to achieve a high spatial resolution in positron emission tomography (PET) imaging in medicine [3,4] and in electromagnetic calorimetry which are a part of huge detectors installed at high energy physics accelerators detecting particle and photon tracks after beam collisions. In both cases, the so-called time-of-flight (TOF) techniques are used [5] where a key role is played by the timing coincidence resolution parameter that, in today's commercial PET machines, is of the order of 500 ps. Achieving the 10 ps milestone in timing coincidence resolution would allow avoiding reconstruction algorithms in data processing in TOF-PET and increasing the sensitivity by at least one order of magnitude [4,6]. For this application, it is particularly important the rise time of the luminescence signal, following the arrival of the excitation photon, as this eventually determines the limit in the coincidence time resolution. Short decay time of the luminescence is

also relevant to squeeze the generated luminescence photons in a short time window. Despite the importance for applications, until now only few studies addressed the analysis of the scintillation dynamics with sub-10 ps time resolution (see for instance [7,8]). In order to gain access to luminescence rise and decay dynamics in the sub-10 ps time scale, detection schemes typically employ a streak camera.

Scintillators suitable for such a goal must show not only high light yield, but also very fast scintillation response in the time scale of several nanoseconds - few tens of nanoseconds, and with a negligible risetime [6]. The so-called free Wannier exciton emission in wide direct-gap semiconductors could offer such characteristics [9,10], but due to its inevitable small Stokes shift, it is impossible to exploit it in bulk scintillation elements as all the scintillation emission would be re-absorbed [11]. These materials are usually studied in nanocrystalline powder, thin film or nano-composite forms [12]. In the latter case the aim is to provide a transparent bulk optical element with the desired scintillation characteristics which are defined by fine nanocrystallite scintillator phase, homogeneously dispersed in the volume of the host.

Further enhancement of the desirable properties of Wannier exciton

* Corresponding author at: Istituto Nazionale di Ottica - Consiglio Nazionale delle Ricerche CNR-INO Sede di Sesto Fiorentino, Via Madonna del Piano 10, Sesto Fiorentino, FI 50019, Italy.

E-mail address: guido.toci@ino.cnr.it (G. Toci).

<https://doi.org/10.1016/j.jlumin.2018.12.034>

Received 1 October 2018; Received in revised form 4 December 2018; Accepted 17 December 2018

Available online 18 December 2018

0022-2313/ © 2018 Elsevier B.V. All rights reserved.

can be achieved due to so called quantum size effect. This effect results in an enhanced stability and accelerated decay of the exciton state when the exciton motion is confined in one, two or three dimension, in so-called quantum wells, wires and dots, respectively. One of the first examples of 1D (quantum well) confined structure featuring large light output and fast scintillation response was presented by K. Shibuya et al. [13] employing lead-halide-based perovskite-type layers made of $[\text{PbX}_4]^{2-}$ ($X = \text{Br}, \text{I}$), sandwiched between two insulating layers of alkylammonium, resulting in a fast decay time of 390 ps and a risetime in the scale of tens of ps, under excitation of 20 ps electron pulses.

From a practical point of view an interesting option is offered by epitaxial technologies where multiple quantum well (MQW) structures of alternating GaN and InGaN layers, each one a few nanometers thick, are prepared on Al_2O_3 substrates with the lateral dimensions up to several inches. Excitonic emission occurs in InGaN layers in the spectral range 400–450 nm and can achieve subnanosecond photoluminescence decay times [14]. Time-resolved luminescence of these MQW structures was also investigated in [15–17]. Such a nanostructure was found to be an interesting candidate for fast scintillation detector of soft X-ray or low energy particles [18]. Nonetheless, the ultimate quantitative rise time characteristics of luminescence decay in these materials have never been determined so far. In this context, we focus here on the rise time measurements and excitation density effect of a InGaN/GaN MQW scintillator, investigated by means of femtosecond laser excitation and streak camera detection. The appropriate convolution procedures in the data handling have been used to obtain their correct quantitative evaluation.

2. Sample description and preparation

Structure with InGaN/GaN MQWs (see Fig. 1) used in our experiment have been prepared by an Aixtron 3×2 CCS MOVPE system equipped with a Laytec EpiCurve TT apparatus for in situ measurement of reflectivity. The structure contains 6 groups of 5 InGaN QWs in the active region. The In content in $\text{In}_x\text{Ga}_{1-x}\text{N}$ QWs is $x = 0.07 \pm 0.02$, with QW thicknesses 1.4 ± 0.2 nm and GaN barrier thicknesses 5.7 ± 0.2 nm. Thickness was estimated from the simulation of X-ray diffraction data and the In concentration was estimated from SIMS results. Each group of five QWs was followed by a 25 nm thick GaN separation layer with the purpose of decreasing the strain energy in the active region and also to increase the thickness of the scintillator active region.

Trimethylgallium (TMGa) and NH_3 were used as precursors with a hydrogen carrier gas for the growth of buffer layers. Triethylgallium (TEGa), trimethylindium (TMIn), and ammonia with a nitrogen carrier gas were used for the growth of the InGaN QWs and barriers. Structures

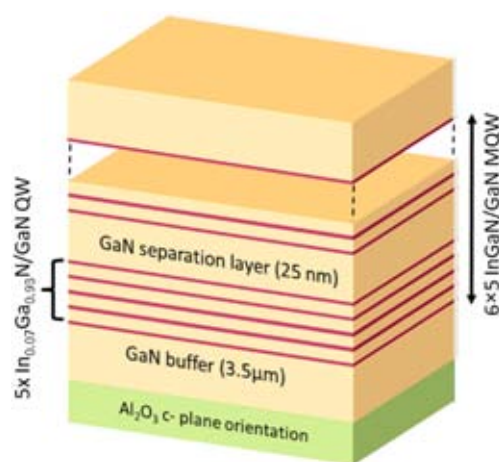


Fig. 1. Schematics of the InGaN/GaN MQW structure used in the experiments.

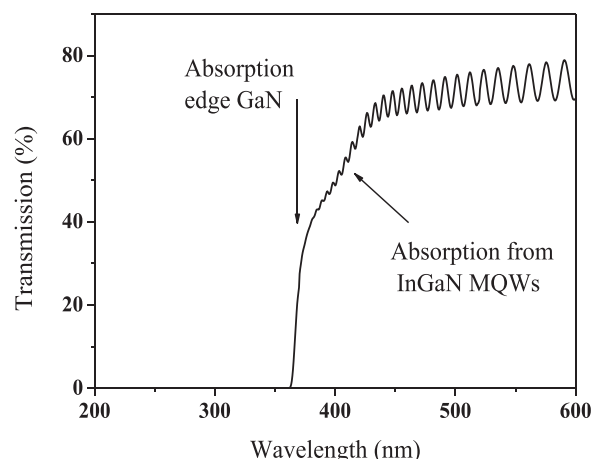


Fig. 2. Transmission spectrum at room temperature of the sample under test.

were grown on sapphire substrates with c-plane orientation. More details about the structure preparation can be found in [18].

The transmission spectrum of the sample used in the experiments is shown in Fig. 2. From this spectrum it can be seen that it is possible to excite selectively the InGaN quantum wells in the band ~ 380 – 420 nm, whereas an excitation below 350 nm will also affect the GaN in the barriers between the InGaN layers and in the separation layers between the individual MQWs groups. The oscillating behavior in the transmission for wavelengths longer than 400 nm is due to etalon effects between the surfaces of the sample.

3. Experimental set-up and data processing

3.1. Experimental set-up

Experiments were carried out at the Intense Irradiation Laser Laboratory (ILIL) of the CNR-INO, in Pisa (Italy) (http://research.ino.it/Groups/ilil/it/about_it/). The sample is excited by laser pulses at about 266 nm and 400 nm obtained as the 3rd and 2nd harmonics respectively, of a Ti:Sapphire amplified laser system, delivering pulses with a duration of 80 fs at 800 nm [19]. After the conversion to the 2nd and 3rd harmonics the pulse duration is less than 200 fs for both wavelengths. The incident energy is of a few tens of μJ , with a spot size on the target of about 2 mm in radius. The experimental set-up is depicted in Fig. 3. The detection is carried out with a Hadland Imacon 500 streak camera (spectral response from 300 nm to 650 nm, peaked at about 450 nm), fitted with an image intensifier. The streak image is acquired by a cooled Electron Multiplying CCD camera (Andor LUCA, 1002×1004 pixels). The streak camera is triggered by a signal derived from the laser pulse; an adjustable delay box allows for the fine tuning of the trigger delay. The streak camera has various scan speeds, from 11.1 ps/mm to 356 ps/mm, corresponding to different values of time resolution and time acquisition window. The sample is illuminated by

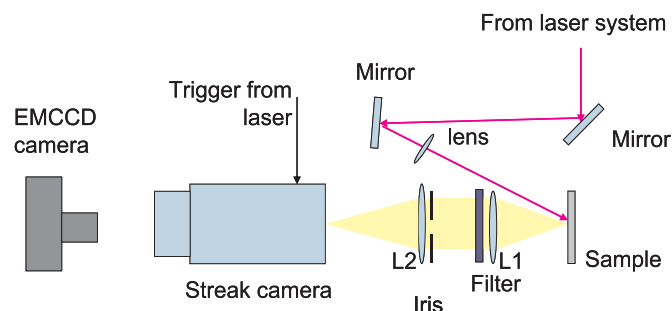


Fig. 3. Schematics of the experimental set-up (not in scale).

the laser pulse with an angle of incidence of about 16° with respect to the optical axis of the collecting optics. The sample surface is placed approximately perpendicular to the optical axis of the collecting optics, with the MQW structure facing the incident beam; the other side (Al_2O_3 substrate) is translucent. The fluorescence of the sample is imaged on the streak camera slit by the lenses L_1 , L_2 , matching the entrance $f/\#$ of the streak camera. The spectral band of interest is selected by a suitable filter placed between the two lenses. An iris between the two lenses is used to adjust the signal intensity reaching the streak camera.

The emission spectra of the sample were collected at the input of the streak camera using a fiber coupled spectrometer (Ocean Optics).

Careful calibration procedures are needed in all the experiments performed with streak camera systems. Attention must be paid to avoid the saturation of both the photocathode of the streak tube, and of the image intensifier, which can lead to severe distortions in the acquired signal.

The intensity response of the streak camera was calibrated to compensate spatial non-uniformities in the photocathode for the streak tube and in the intensifier luminosity. This calibration was carried out by acquiring the decay traces of fluorophores having a decay time of some hundreds of ns, which provide a signal which is temporally uniform (within few %) over a time interval of few ns. The scan speed in the different time scales was calibrated by analyzing the signals obtained from laser pulse pairs with known temporal separation, obtained by reflection on both surfaces of different glass plates with known thicknesses.

The streak traces were acquired on a shot by shot basis. After acquisition the individual traces were processed with the following steps:

- The intensity was corrected using the previously acquired intensity calibration traces, to compensate for spatial non-uniformities in the photocathode for the streak tube and in the intensifier luminosity;
- The time scale was re-sampled at uniform time intervals, using the previously acquired position vs. time calibration curves;
- The traces obtained from different shots (usually 10) were finally synchronized and co-averaged, using the rise front as time marker.

This procedure resulted in a high signal to noise ratio, still not compromising the temporal resolution of the acquisition system. Conversely, a direct averaging of multiple shots would result in a degradation of the temporal resolution of the system, due to the residual jitter between the scan trigger signal and the laser pulse.

The time resolution of the acquisition system has been determined as the FWHM of the response after the excitation with a 200 fs duration laser pulse at 400 nm, and using the same processing protocol adopted for the measurements on the samples. As the laser pulse is much shorter than the time response of the system, these measurements provide the Impulse Response Function (IRF) of the system. In particular we obtained a IRF FWHM of 81.8 ps at the lowest scan speed (356 ps/mm) and of 10.2 ps at the fastest scan speed (29.5 ps/mm). Fig. 4 shows the response of the system under excitation with the laser pulses at 400 nm at the different scan speeds, as obtained after the synchronization and co-averaging procedure described above.

The decay curves were finally approximated by a sum of exponential functions convoluted with the appropriate instrumental response using the software package SpectraSolve (Ametek).

4. Experimental results

4.1. Emission spectra

The emission spectrum of MQW sample described in Section 2, under excitation at 266 nm, is reported in Fig. 5 below. Even though the UV laser emission is cut off by the glass of the collection optics, a bandpass filter (Filter #1, Oriol 5–58, peak wavelength 430 nm, bandwidth 30 nm FWHM) was used to avoid possible spectral

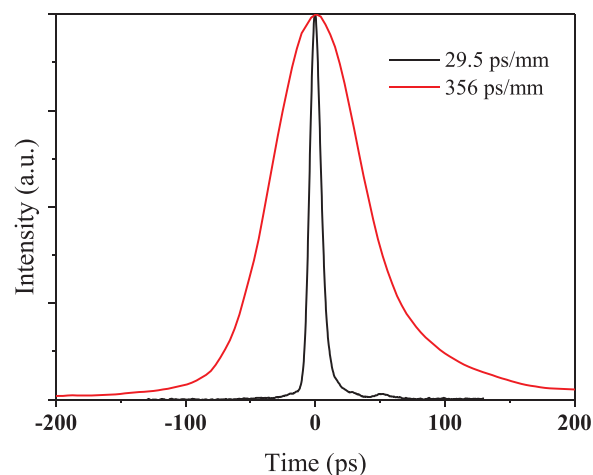


Fig. 4. IRF to the laser pulses at 400 nm at the scan speeds used in the measurements. The traces are normalized to their peak value.

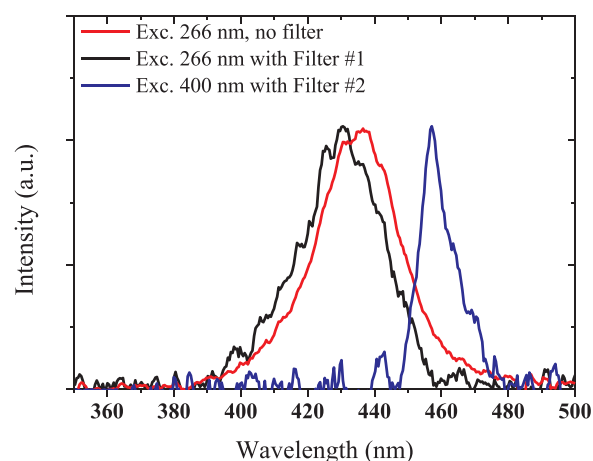


Fig. 5. Excitonic emission of the MQW quantum well structure under 266 nm (with and without the interferential Filter #1) and 400 nm excitation (after the Filter #2 used to reject the excitation radiation). All the plots were rescaled to their peak value. The Filters #1 and #2 are described in the text.

contamination on the signal (such as residual laser 2nd harmonic). A single emission band peaked at 437 nm was observed. We observe that no further band in the yellow region of the spectrum (which was reported in [18,20]) was detected.

When exciting at 400 nm a different bandpass filter (Filter #2, Andover 450FS20–50 peaked at 450 nm, bandwidth 20 nm) was used because the laser was partially superimposed to the emission band. This allowed to collect the MQW exciton emission tail at longer wavelengths.

4.2. Luminescence decay

The temporal dependence of the emission was acquired under excitation at 266 nm and 400 nm. At 266 nm two excitation conditions were used, i.e. lower incident pulse energy (16 μJ , corresponding to approximately $0.4 \text{ mJ}/\text{cm}^2$ of average excitation fluence) and a higher one (29 μJ , i.e. $0.7 \text{ mJ}/\text{cm}^2$). The emission signal was filtered using the Filter #1 (see above). Under excitation at 400 nm the decay behavior was acquired with an incident energy of 30 μJ (about $0.7 \text{ mJ}/\text{cm}^2$ of fluence), using the Filter #2 to select the detection spectral band.

For each excitation, the luminescence signal was acquired with two different settings of the streak camera: the fastest available scan speed, capable to achieve the highest time resolution (i.e. 10.2 ps of IRF FWHM) over a short time window (about 700 ps), and a slower scan

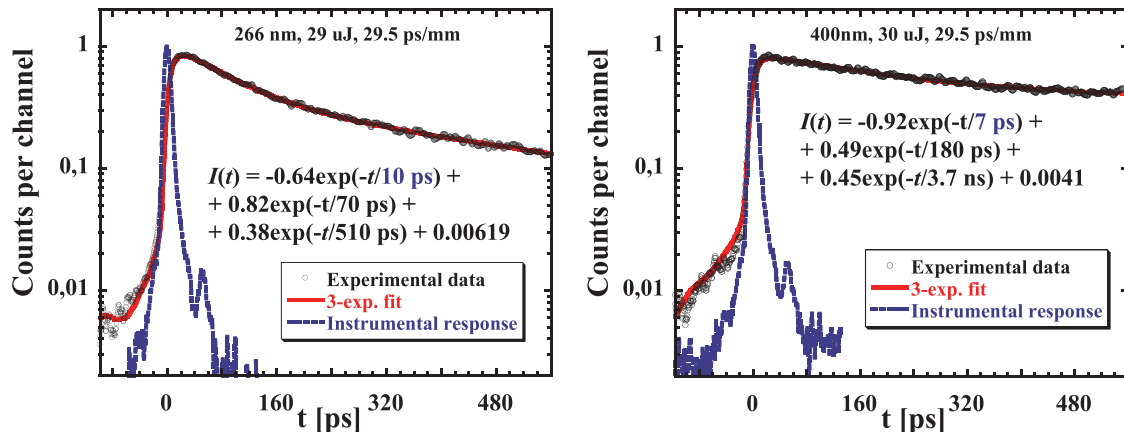


Fig. 6. Luminescence decay with high temporal resolution (nominal scan speed 29.5 ps/mm) and with the same excitation conditions as in Fig. 4. Solid line is convolution of IRF (also in figure) and function $I(t) = A_1 \times \exp(-t/T_1) + A_2 \times \exp(-t/T_2) + A_3 \times \exp(-t/T_3) + \text{Background}$. Fitting parameters are reported in the figure. Detection under excitation at 266 nm is made with Filter #1, under excitation at 400 nm is made with Filter #2 (see Fig. 5).

speed, capable to record a relatively long time interval (about 10 nsec) with a lower time resolution (IRF 81.8 ps, see above). The fast acquisition mode was specifically aimed to determine the rise time of the luminescence response after the excitation, which is the main target of the experiment. The slow acquisition mode addressed the evaluation of the decay behavior, mainly for comparison with previous results [18].

At the fastest scan speeds the rise time could be resolved reliably in the decay curves, over a dynamic range of about 2 decades. The rising edge of the luminescence was analyzed using the fast 29.5 ps/mm scan speed (Fig. 6). The rising part of the curve was fitted by means of a negative exponential function, whose rise time is 10 ps (under excitation at 266 nm) and 7 ps (under excitation at 400 nm). IRF was convoluted with the decay function $I(t)$ to obtain the fit.

The examples of resulting decays are shown in Fig. 7. Apparently, the departure from single exponential behavior is more evident in case of 266 nm excitation. We did not find any substantial difference in the decay shape for two excitation densities of 16 and 29 μJ used in the case of 266 nm excitation.

The decaying part of curve is approximated by different decay times compared with Fig. 6 due to much longer time scale and non-exponential character of the decay (see Section 5).

It must be noticed that the structure of the sample itself introduces a slowdown in the rise time of the luminescence. The MQW structure has an overall thickness of less than 4 μm , which is negligible in terms of propagation delay of the excitation and signal light. On the other hand the sample has an overall thickness of about 0.45 mm, mostly

constituted by the Al_2O_3 substrate, whose back face is diffusing. The group velocity of light in Al_2O_3 at 430 nm (the peak of the emission wavelength) is $c/1.84$. The path difference between the signal generated at the front surface and travelling toward the streak camera, and the signal generated at the front surface travelling toward the back side and reflected back to the streak camera results in a time delay inside the sample of about 5.5 ps (neglecting slanted paths and multiple reflections). This figure is not negligible with respect to the measured rise time, and it is not included in the evaluation of the IRF discussed above (the latter was obtained by sending the laser beam on a surface diffuser in place of the sample, and therefore it is not affected by the optical thickness of the target).

5. Discussion and conclusions

The measurement shown above demonstrate that the luminescence of the MQW under test has a rise time of the luminescence in the sub-10 ps time scale. By using convolution procedure with the measured IRF for the fast streak camera scan (29.5 ps/mm) we have reliably resolved the presence of comparable and very small rise time values on the range 7–10 ps in the luminescence emission mechanism under both the 266 and 400 nm excitations. The former excitation involves also massive charge carrier migration from the GaN nanolayers into InGaN ones where the luminescence process occurs. The obtained results mean that this charge carrier migration does not add any delay in the photoluminescence mechanism. It must be noticed that the actual rise time

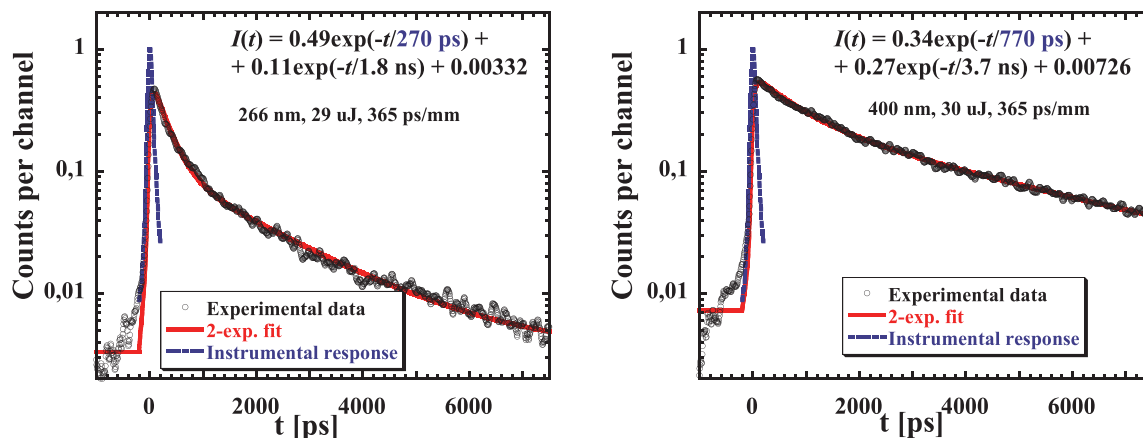


Fig. 7. Decay curves for the excitation at 266 nm (energy 29 μJ) and 400 nm (energy 30 μJ). Solid line is convolution of IRF (also in figure) and function $I(t) = A_1 \times \exp(-t/T_1) + A_2 \times \exp(-t/T_2) + \text{Background}$. Fitting parameters are reported in the figure. Detection under excitation at 266 nm is made with Filter #1, under excitation at 400 nm is made with Filter #2 (see Fig. 5).

could be even shorter, as the calculated rise time is comparable with the detection system IRF, and the luminescence rise time could be affected by light scattering effects at the level of 5 ps.

Regarding the decay behavior, the discrepancy in the value of the decay time resulting from the analysis shown in Figs. 6 and 7 should be understood just as resulting from technical reasons which does not necessarily reflect the physical nature of the process. In particular, the relatively low temporal resolution in the slower acquisition time scale (356 ps/mm) does not allow to obtain a reliable information on the fast component of the decay; conversely, in the fastest scan speed (29.5 ps/mm) it is possible to resolve the rise time and the fastest decay component, but the acquisition time scale is too short to obtain a reliable assessment of the slowest decay component. It must be noticed anyway that the measurement of the slow decay components (in the time scale of several ns) is routinely carried out with more conventional techniques (e.g. time correlated single photon counting [18]).

While single exponential photoluminescence decay was reported only in the case of the measurement of a single InGaN/GaN quantum dot (QD) [21], the measurement over an ensemble of QDs [22] or in MQW structure [23] always shows a non-exponential decay profile, which has been approximated e.g. by a stretched-exponential model and explained by local compositional fluctuations [23].

An interesting aspect, however, is the difference of the decay profiles under 400 nm and 266 nm excitations. Namely, the decay is noticeably accelerated in the latter case. In part, such a difference can be due to the detection of emission in somewhat different spectral parts of excitonic band due the used filters (see Section 4.2 above). However, given the peak power of the excitation laser, the excitation density effects should be also considered. In the context of non-proportionality of scintillator materials, it has been considered that various interactions between elementary closely spaced excitations and charge carriers in the conversion stage of scintillation mechanism (first few picoseconds) induce energy losses [24]. While such a process heavily affects the light yield of a scintillator, it does not show any influence on the luminescence decay itself as it occurs before the relaxed excited state of emission centers is formed. However, noticeable distortion of the decay was noted when high intensity femtosecond pulse laser source at 313 nm (Urbach tail of absorption edge of CdWO₄) was used for the excitation of a CdWO₄ single crystal scintillator [25]. Gradually increasing deviation of the decay from single exponential (acceleration of the decay) with increasing laser power was successfully modeled by the Forster dipole-dipole interaction model which works on the relaxed self-trapped exciton states of CdWO₄. Even if such a process has been forecasted to occur in semiconductors above much higher threshold (compared to ionic crystals as CdWO₄) of the onset of self-quenching due to differences in the mobility of holes, electrons and excitons [26] we tend to explain the above reported difference in the decay shape on the excitation wavelength in the same way: in case of 266 nm excitation the band-to-band absorption transition of GaN is involved and the total absorption coefficient of MQW will be much higher compared to that at 400 nm when only InGaN nanolayers are absorbing, as it was pointed out in Section 2. Thus, total deposited energy in MQW structure will be much higher as well in case of 266 nm excitation. However, all generated electrons and holes in MQW tend to migrate into the InGaN nanolayers which create the lowest-energy band structure for both electrons and holes. In spite of possible migration losses, the density of excitonic states in these regions will be much higher for 266 nm excitation and, consequently, their interaction probability strongly increases. Such interaction of excitons is completely analogous to the above mentioned situation in CdWO₄ and it shows itself qualitatively exactly in the same way. We also note that simple increase of excitation density by factor less than two in case of 266 nm excitation did not show any clear difference in the decay course.

In conclusion, our measurements have demonstrated that InGaN/GaN heterostructures feature a luminescence response with rise time of less than 10 ps; this value can still be lengthened by instrumental and

experimental effects, so that it must be considered as an upper limit of the actual rise time. The timing characteristics of MQW are thus not deteriorated due to rising edge of the luminescence response, which is of great importance for its use in superfast scintillation detectors. Moreover, luminescence decay and in particular the luminescence rise time did not show an appreciable dependence on the excitation density, which is also an important feature in view of practical applications.

Acknowledgments

Financial support of Czech National Foundation grant no. 16-15569S and European project COST, FAST TD1401 are gratefully acknowledged. We also acknowledge funding from the CNR funded Italian research Network ELI-Italy (D.M. n. 631 08.08.2016).

References

- [1] M. Nikl, A. Yoshikawa, Recent R&D trends in inorganic single crystal scintillator materials for radiation detection, *Adv. Opt. Mater.* 3 (2015) 463–481.
- [2] P. Lecoq, Development of new scintillators for medical applications, *Nucl. Instrum. Methods Phys. Res. A* 809 (2016) 130–139.
- [3] M. Conti, Focus on time-of-flight PET: the benefits of improved time resolution, *Eur. J. Nucl. Med. Mol. Imaging* 38 (2011) 1147–1157.
- [4] T. Jones, D. Townsend, History and future technical innovation in positron emission tomography, *J. Med. Imag.* 4 (2017) 011013.
- [5] S. Gundacker, F. Acerbi, E. Auffray, A. Ferri, A. Gola, M.V. Nemallapudi, G. Paternoster, C. Piemonte, P. Lecoq, State of the art timing in TOF-PET detectors with LuAG, GAGG and L(Y)SO scintillators of various sizes coupled to FBK-SiPMs, *J. Instrum.* 11 (2016) P08008.
- [6] P. Lecoq, Pushing the limits in time-of-flight PET imaging, *IEEE Trans. Radiat. Plasma Med. Sci.* 1 (2017) 473–485.
- [7] T. Shimizu, K. Yamanoi, K. Sakai, M. Cadatal-Raduban, T. Nakazato, N. Sarukura, M. Kano, A. Wakamiya, D. Ehrentraut, T. Fukuda, M. Nagasono, T. Togashi, S. Matsubara, K. Tono, A. Higashiya, M. Yabashi, H. Kimura, H. Ohashi, T. Ishikawa, Response time-shortened zinc oxide scintillator for accurate single-shot synchronization of extreme ultraviolet free-electron laser and short-pulse laser, *Appl. Phys. Express* 4 (2011) 062701.
- [8] H. Burešová, L. Procházková, R.M. Turtos, V. Jary, E. Mihóková, A. Beitlerová, R. Pjatkan, S. Gundacker, E. Auffray, P. Lecoq, M. Nikl, V. Čuba, Preparation and luminescence properties of ZnO:Ga – polystyrene composite scintillator, *Opt. Express* 24 (2016) 15289–15298.
- [9] S.E. Derenzo, M. Weber, M.K. Klintonberg, Temperature dependence of the fast, near-band-edge scintillation from CuI, HgI₂, PbI₂, ZnO:Ga and CdS:In, *Nucl. Instr. Meth. Phys. Res. A* 486 (2002) 214–219.
- [10] E.D. Bourret-Courchesne, S.E. Derenzo, M.J. Weber, Development of ZnO:Ga as an ultra-fast scintillator, *Nucl. Instr. Methods Phys. Res. A* 601 (2009) 358–363.
- [11] D. Ehrentraut, H. Sato, Y. Kagamitani, A. Yoshikawa, T. Fukuda, J. Pejchal, K. Polak, M. Nikl, H. Odaka, K. Hatanaka, H. Fukumura, Fabrication and luminescence properties of single-crystalline, homoepitaxial zinc oxide films doped with tri- and tetravalent cations prepared by liquid phase epitaxy, *J. Mater. Chem.* 16 (2006) 3369–3374.
- [12] E.A. McKigney, R.E. Del Sesto, L.G. Jacobsohn, P.A. Santi, R.E. Muenchausen, K.C. Ott, T.M. McCleskey, B.L. Bennett, J.F. Smith, D.W. Cooke, Nanocomposite scintillators for radiation detection and nuclear spectroscopy, *Nucl. Instr. Methods Phys. Res. A* 579 (2007) 15–18.
- [13] K. Shibuya, M. Koshimizu, H. Murakami, Y. Muroya, Y. Katsumura, K. Asai, Development of ultra-fast semiconducting scintillators using quantum confinement effect, *Jpn. J. Appl. Phys.* 43 (2004) L1333–L1336.
- [14] T.S. Ko, T.C. Lu, T.C. Wang, J.R. Chen, R.C. Gao, M.H. Lo, H.C. Kuo, S.C. Wang, J.L. Shen, Optical study of -plane InGaN/GaN multiple quantum wells with different well widths grown by metal-organic chemical vapor deposition, *J. Appl. Phys.* 104 (2008) 093106.
- [15] S. Miasojedovas, S. Juršenas, G. Kurilčik, A. Žukauskas, V. Ivanov, M. Godlewski, M. Leszczyński, P. Perlin, T. Suski, Luminescence in highly excited InGaN/GaN multiple quantum wells grown on GaN and sapphire substrates, *Acta Phys. Pol. A* 106 (2004) 273–279.
- [16] A.N. Cartwright, M.C.-K. Cheung, F. Shahedipour-Sandvik, J.R. Grandusky, M. Jamil, V. Jindal, S.B. Schujman, L.J. Schowalter, C. Wetzel, P. Li, T. Detchprohm, J.S. Nelson, Ultrafast carrier dynamics and recombination in green emitting InGaN MQW LED, *Mater. Res. Soc. Symp. Proc.* 916 (2006) 0916-DDO4-10.
- [17] A. Jaros, J. Hartmann, H. Zhou, B. Szafrański, M. Strassburg, A. Avramescu, A. Waag, T. Voss, Photoluminescence of planar and 3D InGaN/GaN LED structures excited with femtosecond laser pulses close to the damage threshold, *Sci. Rep.* 8 (2018) 11560.
- [18] A. Hospodková, M. Nikl, O. Pacherová, J. Oswald, P. Brůža, D. Pánek, B. Foltynski, E. Hulcius, A. Beitlerová, M. Heuken, InGaN/GaN multiple quantum well for fast scintillation application: radioluminescence and photoluminescence study, *Nanotechnology* 25 (2014) 455501.
- [19] L.A. Gizzi, C. Benedetti, C.A. Cecchetti, G. Di Pirro, G. Gamucci, G. Gatti, A. Giulietti, D. Giulietti, P. Koester, L. Labate, T. Levato, N. Pathak, F. Piastra, Laser

- plasma acceleration with FLAME and ILL ultraintense lasers, *Appl. Sci.* 2013 (3) (2013) 559.
- [20] A. Hospodková, J. Oswald, M. Zíková, J. Pangrác, K. Kuldová, K. Blažek, G. Ledoux, C. Dujardin, M. Nikl, On the correlations between the excitonic luminescence efficiency and the QW numbers in multiple InGaN/GaN QW structure, *J. Appl. Phys.* 121 (2017) 214505.
- [21] M. Winkelkemper, M. Dworzak, T.P. Bartel, A. Strittmatter, A. Hoffmann, D. Bimberg, Origin of the broad lifetime distribution of localized excitons in InGaN/GaN quantum dots, *Phys. Stat. Sol. (b)* 245 (2008) 2766–2770.
- [22] S.F. Chichibu, T. Onuma, T. Aoyama, K. Nakajima, P. Ahmet, T. Chikyow, T. Sota, S. DenBaars, Nakamura, T. Kitamura, Y. Ishida, H. Okumura, Recombination dynamics of localized excitons in cubic In_xGa_{1-x}N/GaN multiple quantum wells grown by radio frequency molecular beam epitaxy on 3C-SiC substrate, *J. Vac. Sci. Technol. B* 21 (2003) 1856–1996.
- [23] S. Khatsevich, D.H. Rich, X. Zhang, P.D. Dapkus, Correlating exciton localization with compositional fluctuations in quantum wells grown on GaN planar surfaces and facets of GaN triangular prisms, *J. Appl. Phys.* 102 (2007) 093502.
- [24] G. Bizarri, W.W. Moses, J. Singh, A.N. Vasil'ev, R.T. Williams, An analytical model of nonproportional scintillator light yield in terms of recombination rates, *J. Appl. Phys.* 105 (2009) 044507.
- [25] S. Markov, V. Nagirnyi, A. Vasil'ev, V. Makhov, R. Laasner, S. Vielhauer, M. Kirm, R. Grigonis, V. Sirutkaitis, Modelling of decay kinetics of self-trapped exciton luminescence in CdWO₄ under femtosecond laser excitation in absorption saturation conditions, *Cent. Eur. J. Phys.* 10 (2012) 1002–1008.
- [26] W.W. Moses, G.A. Bizarri, R.T. Williams, S.A. Payne, A.N. Vasil'ev, J. Singh, Q. Li, J.Q. Grim, W.-S. Choong, The Origins of Scintillator Non-Proportionality, *IEEE Trans. Nucl. Sci.* 59 (2012) 2038–2044.

Petawatt and exawatt class lasers worldwide

Colin N. Danson^{1,2,3}, Constantin Haefner^{4,5,6}, Jake Bromage⁷, Thomas Butcher⁸,
Jean-Christophe F. Chanteloup⁹, Enam A. Chowdhury¹⁰, Almantas Galvanauskas¹¹, Leonida A. Gizzi¹²,
Joachim Hein¹³, David I. Hillier^{1,3}, Nicholas W. Hopps^{1,3}, Yoshiaki Kato¹⁴, Efim A. Khazanov¹⁵,
Ryosuke Kodama¹⁶, Georg Korn¹⁷, Ruxin Li¹⁸, Yutong Li¹⁹, Jens Limpert^{20,21,22}, Jingui Ma²³,
Chang Hee Nam²⁴, David Neely^{8,25}, Dimitrios Papadopoulos⁹, Rory R. Penman¹, Liejia Qian²³,
Jorge J. Rocca²⁶, Andrey A. Shaykin¹⁵, Craig W. Siders⁴, Christopher Spindloe⁸, Sándor Szatmári²⁷,
Raoul M. G. M. Trines⁸, Jianqiang Zhu²⁸, Ping Zhu²⁸, and Jonathan D. Zuegel⁷

¹AWE, Aldermaston, Reading, UK

²OxCHEDS, Clarendon Laboratory, Department of Physics, University of Oxford, Oxford, UK

³CIFS, Blackett Laboratory, Imperial College, London, UK

⁴NIF & Photon Science Directorate, Lawrence Livermore National Laboratory, Livermore, USA

⁵Fraunhofer Institute for Laser Technology (ILT), Aachen, Germany

⁶Chair for Laser Technology LLT, RWTH Aachen University, Aachen, Germany

⁷University of Rochester, Laboratory for Laser Energetics, Rochester, USA

⁸Central Laser Facility, STFC Rutherford Appleton Laboratory, Chilton, Didcot, UK

⁹LULI, CNRS, CEA, Sorbonne Universités, École Polytechnique, Institut Polytechnique de Paris, Palaiseau, France

¹⁰Department of Physics, The Ohio State University, Columbus, USA

¹¹Centre for Ultrafast Optical Science, University of Michigan, Ann Arbor, USA

¹²Intense Laser Irradiation Laboratory, Istituto Nazionale di Ottica (INO), CNR, Pisa, Italy

¹³Institute of Optics and Quantum Electronics, Friedrich-Schiller-University Jena and Helmholtz Institute, Jena, Germany

¹⁴The Graduate School for the Creation of New Photonics Industries, Nishiku, Hamamatsu, Japan

¹⁵Institute of Applied Physics, Russian Academy of Sciences, Nizhny Novgorod, Russia

¹⁶Institute of Laser Engineering, Osaka University, Suita, Osaka, Japan

¹⁷ELI-Beamlines, Institute of Physics, Czech Academy of Sciences, Prague, Czech Republic

¹⁸State Key Laboratory of High Field Laser Physics, Shanghai Institute of Optics and Fine Mechanics, Chinese Academy of Sciences, Shanghai 201800, China

¹⁹National Laboratory for Condensed Matter Physics, Institute of Physics, Chinese Academy of Sciences, Beijing 100190, China

²⁰Institute for Applied Physics (IAP) at Friedrich-Schiller-University Jena, Jena, Germany

²¹Helmholtz Institute Jena, Jena, Germany

²²Fraunhofer Institute for Applied Optics and Precision Engineering (IOF), Jena, Germany

²³Key Laboratory for Laser Plasma (Ministry of Education), School of Physics and Astronomy, Shanghai Jiao Tong University, Shanghai 200240, China

²⁴Centre for Relativistic Laser Science (CoReLS), Institute for Basic Science, Department of Physics and Photon Science, Gwangju Institute of Science and Technology, Gwangju, South Korea

²⁵SUPA, Department of Physics, University of Strathclyde, Glasgow, UK

²⁶Colorado State University, Fort Collins, Colorado, USA

²⁷Department of Experimental Physics, University of Szeged, Szeged, Hungary

²⁸National Laboratory on High Power Laser and Physics, Shanghai Institute of Optics and Fine Mechanics, Chinese Academy of Sciences, Shanghai 201800, China

(Received 10 March 2019; accepted 21 June 2019)

Abstract

In the 2015 review paper ‘Petawatt Class Lasers Worldwide’ a comprehensive overview of the current status of high-power facilities of >200 TW was presented. This was largely based on facility specifications, with some description of their uses, for instance in fundamental ultra-high-intensity interactions, secondary source generation, and inertial confinement fusion (ICF). With the 2018 Nobel Prize in Physics being awarded to Professors Donna Strickland and Gerard Mourou for the development of the technique of chirped pulse amplification (CPA), which made these lasers possible, we celebrate by providing a comprehensive update of the current status of ultra-high-power lasers and demonstrate how the technology has developed. We are now in the era of multi-petawatt facilities coming online, with 100 PW lasers being proposed and even under construction. In addition to this there is a pull towards development of industrial and multi-disciplinary applications, which demands much higher repetition rates, delivering high-average powers with higher efficiencies and the use of alternative wavelengths: mid-IR facilities. So apart from a comprehensive update of the current global status, we want to look at what technologies are to be deployed to get to these new regimes, and some of the critical issues facing their development.

Keywords: exawatt lasers; high-power lasers; petawatt lasers; ultra-high intensity

1. Introduction

There have been two published reviews of ultra-high-power lasers separated by nearly two decades; the first by Backus *et al.*^[1] in 1998, when there was only one petawatt class laser in operation^[2], and the second by Danson *et al.*^[3] some 17 years later, which identified approximately fifty petawatt class lasers either operational, under construction or in the planning phase. These review papers were cited by the Nobel Committee for Physics in its 2018 award to Strickland and Mourou in its Scientific Background paper^[4] ‘Groundbreaking Inventions in Laser Physics’. In addition to these the National Academy of Sciences, Engineering and Medicine in the USA published a report in December 2017 ‘Opportunities in Intense Ultrafast Lasers: Reaching for the Brightest Light’^[5], which summarized the current status of high-power lasers, highlighting the decline in this activity within the USA in recent years, and making recommendations of how this should be remedied.

A special mention should also be made to the work of ICUIL. ICUIL, the International Committee on Ultra-High Intensity Lasers, is an organization concerned with international aspects of ultra-high-intensity laser science, technology and education. This was formed in 2003 following the work of the OECD (Organisation for Economic Co-operation and Development) Global Science Forum^[6] under the International Union of Pure and Applied Physics (IUPAP)^[7]. ICUIL has a very active programme of work and maintains a track of ultra-high-intensity lasers on its website^[8]. It also hosts a biennial conference to bring the community together for the exchange of information on the subject.

1.1. Introduction – historical perspective

The possibility of using lasers to achieve previously unobtainable states of matter in the laboratory gained much attention following the demonstration of the first pulsed

laser in 1960^[9]. In the following few years there was vigorous research activity as attempts were made to increase the peak power and focused intensity in order to reach extreme conditions within the laboratory. Initial jumps of several orders of magnitude in peak power came with the invention of Q -switching^[10], and then mode-locking^[11–15]. Progress slowed, as illustrated in Figure 1, until the late 1980s, with the development of the technique of chirped pulse amplification (CPA) by Strickland and Mourou^[16] at the Laboratory for Laser Energetics (LLE) at the University of Rochester, USA.

A parallel problem existed in radar systems, where short, powerful pulses that were beyond the capabilities of existing electrical circuits were needed. Using dispersive delay lines, the radar pulses could be stretched and amplified prior to transmission, and then the reflected pulse could be compressed, avoiding high-peak powers within the amplifier circuitry^[17]. In the telecommunications industry, work was carried out on the use of prisms^[18] and grating pairs^[19] to compensate for the spectral phase distortions imposed on broad bandwidth laser pulses by long lengths of optical fibre. By putting a telescope inside a grating pair, Martinez produced a method to reverse the sign of the spectral phase that was imparted, thus creating a device that could stretch a pulse and then exactly compress it. These systems were used in stretching pulses prior to propagation along the fibre, then compressing them in order to reduce nonlinear effects.

Strickland and Mourou’s approach was to take the 150 ps output from a commercial mode-locked Nd:YAG oscillator, which was then stretched to 300 ps and spectrally broadened in 1.4 km of optical fibre, using a combination of group velocity dispersion and self-phase modulation. The pulse was then amplified in a Nd:glass regenerative amplifier, and compressed using a Treacy grating pair^[20] which compensated for the second-order spectral phase imposed by the fibre. From the original CPA paper’s conclusion, it states ‘we have shown that by first stretching a chirped optical pulse and then amplifying before compressing, high-peak power pulses

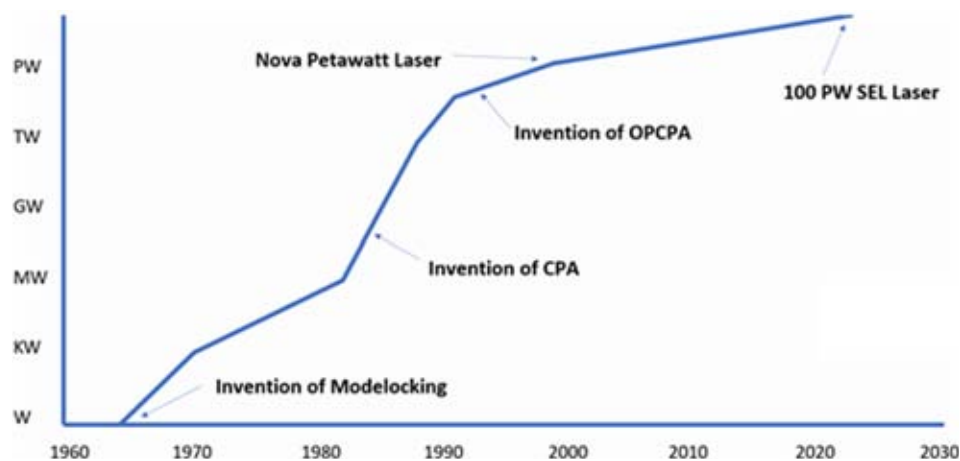


Figure 1. The historical journey to multi-petawatt ultra-short-pulse laser facilities.

can be achieved. To date, we have produced 2 ps pulses with an energy of 1 mJ.

Due to the limitations of mode-locked lasers operating at 1064 nm, early high-power/energy CPA lasers^[21–24] all relied on the use of self-phase modulation to generate enough bandwidth to support pulses of a few picoseconds^[25]. These systems generated large amounts of high-order spectral phase and spectral modulation during the nonlinear process, making optimal compression hard to realize and, moreover, these systems had poor stability due to the nonlinear process. A transformative development was the invention of the transition-metal-doped gain medium titanium-doped sapphire (Ti:Al₂O₃) in 1986 by Peter Moulton at the MIT Lincoln Laboratory^[26]. It has a very large gain bandwidth (~640 to ~1100 nm) that is much larger than other materials and absorbs conveniently at frequency-doubled Nd wavelengths. This naturally led to Ti:sapphire mode-locked oscillators^[27] which allowed much shorter pulses to be produced. These systems could either directly seed Ti:sapphire amplifiers^[28] or, if tuned to 1054 nm^[29], be used to seed existing large-aperture Nd:glass systems. Other developments around this time included a neodymium-based additive-pulse mode-locking system^[30] which could generate pulses at under 0.5 ps at 1054 nm. These new ultra-short-pulse oscillator systems did away with the need to use self-phase modulation to spectrally broaden the pulse. Various geometries of stretcher were then developed, such as the Offner triplet^[31], allowing longer stretches to be realized and hence more energy to be generated.

1.2. Introduction – facility landmarks

The developments described above led to the first well-defined, 100 TW class laser systems being commissioned simultaneously, with the P102 laser at CEA Limeil-Valenton in France (Figure 2)^[32, 33] and on the Vulcan system at STFC



Figure 2. The 100 TW P102 laser system at CEA Limeil-Valenton, France (picture courtesy of CEA).

Rutherford Appleton Laboratory in the UK (Figure 3)^[34, 35], in the early to mid-1990s.

The world's first petawatt laser was put together in 1996 re-purposing one beamline of the existing Nova Nd:glass laser facility based at Lawrence Livermore National Laboratory (LLNL)^[2]. It operated for three years and delivered 1.5 PW with energy up to 680 J to target. By applying chirped-pulse-amplification and stretching pulses from a new, Ti:sapphire based short pulse front-end tuned to 1053 nm centre wavelength to 1 ns, developing metre-scale diffraction gratings for the pulse compressor and using a reflective focusing configuration, the NOVA Petawatt (Figure 4) opened the door to a myriad of high intensity science exploration. In 2004 Vulcan became the first petawatt laser commissioned as a true user facility^[36] at the Central Laser Facility, Rutherford Appleton Laboratory, UK. The first multi-kJ facility, OMEGA-EP, was brought online at LLE in 2008, producing 2.1 kJ at 10 ps pulse duration^[37]. It should be noted that, with the dawn of megajoule-scale Nd:glass



Figure 3. The Vulcan 100 TW laser from the early/mid-1990s showing the first ever single-pass CPA compressor system with one grating in air (centre) and the second in vacuum (bottom right) (picture courtesy of STFC Rutherford Appleton Laboratory).



Figure 4. Inside the Nova Petawatt compressor chamber (picture courtesy of LLNL).

lasers, these facilities are, in their own right, petawatt class lasers, albeit multi-beam facilities. The National Ignition Facility (NIF)^[38], commissioned at LLNL in 2009, was originally specified to deliver 1.8 MJ in 3 ns, giving an output power of 400 TW. Details of all these facilities can be found in the geographical breakdown of current facilities in the next section of this review.

Following the development of the Ti:sapphire oscillator in 1991^[27], extraordinary progress has been made with this medium. The first petawatt class Ti:sapphire laser was commissioned as early as 1999 in the US on the JanUSP system at LLNL. It was pumped by the 1970s JANUS Nd:glass laser and produced 200 TW in 85 fs initially. In Japan at the J-KAREN facility, they produced close to one petawatt (0.85 PW) in 2003^[39]. The next major milestone was the BELLA laser at Berkeley, where in 2013 it produced

the first ever petawatt system operating at 1 Hz^[40]. Only five years later the world's first high average power petawatt laser system HAPLS^[41] developed at Lawrence Livermore National Laboratory was installed at the ELI-Beamlines facility in the Czech Republic. The laser uses a single-aperture, diode-pumped solid-state laser (DPSSL) to pump its Ti:sapphire medium and the laser is designed to deliver >1 PW at 10 Hz, with a commissioning demonstration in 2018 of 0.5 PW at 3.3 Hz. In March 2019 Thales reported the first demonstration of 10 PW operation of their system installed at ELI-NP in Magurele, Romania^[42]. Several other lasers of similar peak power performance are underway in China, France and the Czech Republic. Details of all these facilities are provided in the geographical breakdown of current facilities in this review.

The development of amplifiers capable of supporting broad bandwidths is also required to realize high-peak powers. Early systems relied entirely on dye or Nd:glass amplifiers. While dye lasers could support very large bandwidths, their short lifetimes and low saturation fluences severely limited the amount of energy that could be extracted. Neodymium-based lasers, on the other hand, could provide a large amount of energy but would support only a limited bandwidth. This led to the search for a new laser material that could provide the energy and bandwidth required to support high-energy short pulses. Ti:sapphire oscillators^[26] coupled with optical parametric amplification systems^[43] provided the solution for these problems. These were initially used in the pre-amplification stages of multi-terawatt systems in conjunction with Nd:glass rod or disc amplifiers. They provided many orders of magnitude of gain at high bandwidth before larger amplifiers, generally Nd:glass, added the last few orders and limited the reduction of the bandwidth. As the quality and size of available Ti:sapphire and nonlinear crystals have improved, so has the energy that can be extracted from these systems. An overview of the development of these systems is given in Section 4.1.1 covering 'The journey to 100 PW OPCPA facilities' later in this review.

1.3. Introduction – the future

For this review it was felt appropriate to not only give an historical perspective and the current status of facilities, but also to look to the future, about where facilities are going, and what these might look like in 10–20 years' time. New petawatt laser facilities are embracing a new mission to establish operation of secondary source beamlines and attract users from a much broader range of research fields. A precursor to this approach was Laserlab-Europe, the integrated infrastructure initiative of European Laser Research Infrastructures^[44] that provides access to laser facilities to plasma physicists as well as biologists, chemists and material scientists. This treats lasers in a very similar

way to any other conventional beamline user facility, such as synchrotrons or particle accelerators.

Facilities, currently in their final commissioning phase, like the European Extreme Light Infrastructure (ELI) pillars in the Czech Republic, Romania and Hungary^[45], are pushing forward this concept, providing user access not only to laser beamlines, but also to laser-produced secondary radiation and particle sources, including gamma-ray, proton and electron beams. Facilities currently in their conceptual development phase, like the European EuPRAXIA infrastructure^[46] or the US k-BELLA facility^[47], aim at further advancing this concept, by incorporating step-like changes in the design to enable high-repetition-rate, accelerator-like, high-quality operation of the secondary sources, in a compact size and efficient mode of operation. In light of these developments, the later sections of the review therefore address three areas: ultra-high-power development; high-average-power development; and enabling technologies.

In the ultra-high-power development section we examine the journey to 100 PW OPCPA systems; other developments which could be used to achieve exawatt scale facilities and the potential use of plasma amplifiers as booster amplifiers for these systems.

The high-average-power developments deserve a special mention as they represent the key to the delivery of commercially relevant applications of petawatt lasers. Indeed, research with petawatt lasers has been prolific in terms of results with a high potential for applications in several areas, including medicine, materials and environmental sciences. This applies, for example, to secondary radiation sources for phase-contrast X-ray imaging^[48], for pulsed neutron imaging^[49] or for developments of therapy using very high energy radiation^[50, 51]. The delivery of industrial products in this context has so far been hindered by the lack of high-average-power sources capable of supporting continuous operation at the high repetition rate needed for such uses. Ongoing developments are changing this landscape, with new technologies such as diode laser pumping progressively replacing traditional flashlamp technology, opening the way to efficient and stable operation of petawatt laser-driven secondary radiation and particle sources. We therefore look at the development of new materials for HAP (high average power) technology; new OPCPA schemes; and coherent beam combining in fibre-based systems. This later section covers both spatially multiplexed and temporally multiplexed schemes.

In the final section we examine enabling technologies: where we are; the challenges facing us; and what we believe we will be able to achieve. This will include: the development of mid-IR lasers; the use of plasma optics; grand challenges that face the community in optics, diagnostics and target design; and the issue of temporal contrast techniques to improve the delivered pulse fidelity.

2. Geographic overview of facilities

In the section we give an overview of the current status of petawatt class lasers worldwide. Unlike the 2015 review paper, we have chosen to present this geographically. This was felt appropriate for two main reasons: firstly, the original paper sub-divided the lasers by their classification, but increasingly this is less clear to determine, as many systems are designed using mixed technologies; secondly it graphically illustrates the shift in time of the centre of gravity of ultra-high-intensity facilities from initially the US, through Europe, and currently firmly centred in Asia.

2.1. Geographic overview of facilities – North America

The US, with its combination of national laboratories and university-based systems, had the lead in ultra-high-power laser facilities worldwide until the start of the new millennium. These have ranged from: the first petawatt laser in Nova Petawatt; the only fully operational megajoule facility in NIF; pioneering university-based systems at the University of Rochester with OMEGA and its upgrade OMEGA-EP; and the BELLA facility at Lawrence Berkeley National Laboratory. The pioneering CPA technique also was developed at the University of Rochester. The following section describes the capabilities of these facilities and includes the Advanced Laser Light Source (ALLS) in Canada.

2.1.1. USA

Lawrence Livermore National Laboratory (LLNL) has played a critical and leading role in the development of high-energy and ultra-high-power laser facilities. The building blocks for Nd:glass lasers were developed at LLNL over many years and brought together to construct the Shiva facility in the late 1970s^[52]. The successor laser, Nova, had one of its beamlines reconfigured in the late 1990s to deliver the first-ever petawatt laser worldwide^[2]. A dedicated front end and vacuum compressor were used to deliver 680 J in a 440 fs pulse, giving 1.5 PW. One of the major developments for Nova Petawatt was the capability to manufacture large-aperture diffraction gratings, up to 1 m, for use in the vacuum compressor.

The NIF (National Ignition Facility)^[38] at LLNL, is the first and currently the only fully operational megajoule scale facility. It has 192 40 cm × 40 cm beams that initially delivered a total of 1.8 MJ in a ~3 ns shaped pulse @ 3 ω , 0.6 PW (a true petawatt class laser in its own right, albeit delivered in multiple beamlines) configured for indirect beam drive. It became operational and officially dedicated in March 2009. The facility has been operational for over nine years and delivered data for both the NIC (National Ignition Campaign)^[53] and the US stockpile stewardship programme. In 2018 NIF achieved a record of 2.15 MJ delivered to target, although without increase to the peak power^[54].



Figure 5. NIF ARC compressor gratings during final alignment (picture courtesy of LLNL).

At LLNL, NIF ARC (advanced radiographic capability)^[55] is designed as an advanced X-ray radiography capability for NIF (Figure 5). NIF ARC uses four (one quad) of NIF's beams to obtain a temporal resolution of tens of picoseconds and became operational in 2015. Each beam is split into two, producing eight petawatt class beams delivering between 0.4 and 1.7 kJ at pulse lengths between 1.3 and 38 ps (0.5 PW each) in the infrared. ARC drove many developments for kJ-short pulse lasers forward such as high-efficiency meter-scale dielectric gratings^[56], single shot precision diagnostics^[57], and dispersion management^[58].

Titan^[59] is one of five lasers that make up the Jupiter Laser Facility at LLNL. It is a petawatt class laser coupled to a kilojoule beamline for a broad range of experiments. The short pulse beamline delivers up to 300 J in a sub-picosecond pulse, and offers a 50 J high-contrast green option. It is currently being upgraded to higher peak power and a third beamline added.

There is a long history of using diode-pumped technology at LLNL originally with the Mercury laser facility, a diode-pumped Yb:S-FAP laser. Mercury was developed as a high-average-power laser (HAPL) using diode arrays for laser pumping and pioneered gas cooling as a precursor to an advanced fusion driver and was later considered for a potential pump laser for Ti:sapphire lasers^[60]. This was moth-balled and then dismantled to make way for HAPLS^[41], a 1 PW @ 10 Hz system generating >30 J in 30 fs for ELI-Beamlines discussed later in this paper. The high-power diode array technology was jointly developed by LLNL and LaserTel. The LLNL team has successfully completed the construction of the all-diode-pumped HAPLS laser, and currently it is operated at the ELI-Beamlines in the Czech Republic as the L3 laser, with an initial repetition rate of 3.3 Hz to bring the target area up in steps.

The Laboratory for Laser Energetics (LLE) at the University of Rochester, although university based, is operated more akin to a national laboratory. It has played a critical role in the development of ultra-high-power lasers, from

the original development of CPA^[16] to the first of the multi-kJ petawatt facilities, OMEGA-EP, to be operational. OMEGA-EP is a four-beam system with an architecture very similar to that of the NIF laser and is coupled with the well-proven 30 kJ at 351 nm, 60-beam long-pulse OMEGA laser system^[37]. Two of the EP beams can be operated in short-pulse mode with an OPCPA front end to add high-energy, petawatt class laser performance to provide X-ray backlighting and proton radiography capabilities for inertial confinement fusion (ICF) experiments. The laser can operate between 0.6 and 100 ps, delivering almost 1 PW performance at best compression, and 1.25 to 2.3 kJ performance at pulse widths >10 ps. It has driven the development of high-damage-threshold multi-layer dielectric gratings and their use in tiled geometry.

At Sandia National Laboratory a large-scale kilojoule class petawatt facility provides X-ray radiographic capability to the Z-pinch facility. The laser facility uses Beamlet^[61], which was the original prototype facility for NIF at LLNL that was decommissioned in 1998 before being transferred to Sandia and renamed Z-Beamlet^[62]. The upgrading of the facility to Z-Petawatt^[63] provides enhanced radiographic capability. The beamline, which consists of an OPCPA front end and Nd:phosphate glass amplifiers, delivers 500 J in 500 fs. Updates on the capabilities of the Z-Backlighter facility in its two modes of operation can be found in references from 2016^[64, 65]. There are now two CPA modes of operation based on two different vacuum grating compressors. The beam directly out of the main amplifiers can deliver 100 J/500 fs (200 TW) with a standalone target chamber. The other compressor delivers a 500 J/500 fs, 1 PW, beamline to a new standalone chamber called Chama. Other long pulse modes of operation are available and upgrade to the petawatt capabilities planned.

2.1.2. LaserNet US

Given the numerous smaller-scale facilities in the USA (many described below) the DOE's Office of Science has established a new coordination mechanism for institutes operating ultra-high-power lasers through LaserNet US. This network is designed to provide user access to petawatt class lasers and to foster collaborations. The initial members of LaserNet US are Colorado State University (CSU); Ohio State University (OSU); the Universities of Michigan (UM), Nebraska-Lincoln (UNL) and Texas (UT); the Stanford Linear Accelerator Center (SLAC); and Lawrence Berkeley National Laboratory (LBNL). The network was expanded in 2019 to include lasers from the Jupiter facility at LLNL and the OMEGA-EP at LLE, University of Rochester described above, both of which have already been operating as user facilities. A summary of the capabilities of these LaserNet US^[66] facilities is given in Table 1.

The Advanced Beam Laboratory at Colorado State University (CSU) operates a 0.85 PW Ti:sapphire laser operating at 3.3 Hz, with an option for second-harmonic operation

Table 1. LaserNet US facility capabilities.

Institution	CSU ALEPH	LBNL Bella	LLNL Titan	OSU Scarlet	SLAC MEC	UM Hercules	UNL Diocles	LLE UR Omega EP	UTA Texas Petawatt
Wavelength (nm)	400, 800	815	1053	815	810	815	805	1054	1057
Pulse Energy (J)	10, 26	40	130	10	1	15	20	500	155
Pulse Duration	45, 30 fs	30 fs	0.7 ps	30 fs	45 fs	30 fs	30 fs	0.7 ps	140 fs
Max Repetition Rate	3.3 Hz	1 Hz	1 or 2 per hour	1 per min	5 Hz	1 per min	0.1 Hz	1 per 45 min	1 per hour
Spot Focus Diameter (μm)	1.2, 2.4	65	10, 29	2	7	0.8, 50	1, 20	30 with 80% energy	3.9, 2.2, 60
Contrast	400: 1×10^{-12} @ >25 ps 800: 5×10^{-8} @ >25 ps	1×10^{-8} @ 5 ps	1×10^{-8} @ 200 ps	1×10^{-8} @ 175 ps	1×10^{-10} @ 30 ps 1×10^{-8} @ 5 ps 1×10^{-7} @ 1 ps	1×10^{-8} @ 150 ps	1×10^{-8} @ 175 ps	1×10^{-8} @ 175 ps	1×10^{-8} @ 40 ps

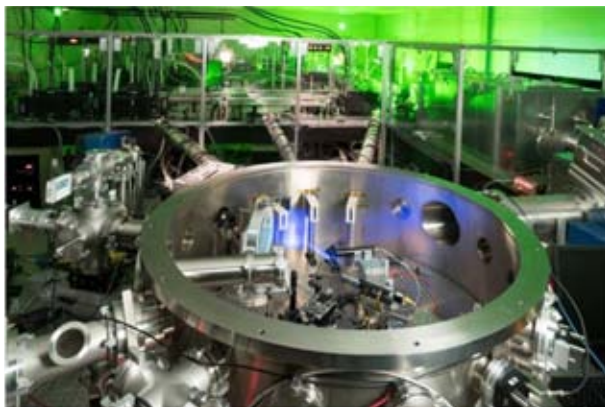


Figure 6. The Advanced Beam Laboratory at Colorado State University (picture courtesy of Colorado State University).



Figure 7. The BELLA laser facility, the world's first 1 Hz petawatt laser (picture courtesy of Lawrence Berkeley National Laboratory).

at ultra-high contrast (Figure 6)^[67]. The pump laser for the Ti:sapphire laser is a novel flashlamp-pumped high-repetition-rate Nd:glass amplifier. The beam propagates in a zigzag path in the amplifier gain medium, aided by total internal reflection in the polished wall of the slabs. Each slab amplifier generates pulses with ~ 18 J energy and 15 ns duration at 1053 nm, with a pulse energy fluctuation of $\sim 1\%$ RMS (root mean square). The amplified beams are frequency-doubled by LBO crystals to generate 11 J pulses at 527 nm to produce a total Ti:sapphire pump energy of 88 J. They have also developed a joule class, all-diode-pumped cryo-cooled Yb:YAG picosecond laser operating at a 0.5 kHz repetition rate^[68] – a technology that is being considered for future high-average-power petawatt class CPA/OPCPA laser pump sources^[48].

The BELLA (BERkeley Lab Laser Accelerator) facility has been operational since 2013 and was built for dedicated experiments on laser plasma acceleration at Lawrence Berkeley National Laboratory, US (Figure 7). BELLA can operate at

peak power levels of 1.3 PW with, at the time, a record-setting repetition rate of 1 Hz^[40]. The Ti:sapphire laser was commercially built by Thales and has demonstrated exceptional pointing stability ($<1.3 \mu\text{rad}$ RMS), shot-to-shot energy stability ($<1\%$ RMS) and pulse duration stability ($<5\%$ RMS). BELLA has demonstrated quasimonoenergetic electron beams of up to 7.8 GeV via laser-plasma wakefield acceleration using a capillary discharge gas target system^[69]. BELLA has also begun construction of i-BELLA, where using an $\sim f/2$ parabola and a new target chamber, they plan to perform ion acceleration experiments at intensities around 10^{22} W/cm^2 . k-BELLA is a proposal for a multi-kW average power laser which would enable high-average-power demonstration experiments of the rapidly advancing laser-plasma accelerator technology; providing a stepping stone to a laser-driven collider. The system performance is planned to be 3 J at 1 kHz operating at 30 fs. So, although not necessarily within the scope of the review in terms of

power (100 TW) this is an important system which will be a technology demonstrator for much higher power systems^[47].

HERCULES (High Energy Repetitive CUos LasEr System) was constructed at the FOCUS Center and Center for Ultrafast Optical Science (CUOS), University of Michigan. In 2004 ultra-high intensities of up to 10^{22} W/cm² in a 45 TW laser could be generated using wavefront correction and an $f/0.6$ off-axis focusing parabola^[70]. By adding a booster amplifier to the system, 300 TW operation was achieved at a 0.1 Hz repetition rate^[71]. Recently, CUOS received funding for upgrading HERCULES to 500 TW. The upgraded pump lasers used for the third and fourth amplification stages of HERCULES are a 5 Hz Gaia 16 J laser and an Atlas 100 J system from Thales Optronique SA. CUOS also houses the lambda-cubed laser, a 500 Hz, 20 mJ, 30 fs laser, that is involved in developing high-repetition-rate electrons, X-rays and ion sources^[72].

The Diocles laser at the Extreme Light Laboratory, University of Nebraska–Lincoln came online at a power level of 100 TW at 10 Hz in 2008, and 0.7 PW at 0.1 Hz in 2012^[73]. It has been modified since to have active feedback spectral phase control^[74], and then with a dual-compressor geometry^[75]. The group recently discovered multi-photon nonlinear Thomson scattering for generating X-rays^[76]. The purpose-built research facility occupies three floors of the Behlen Laboratory Building and operates three separate and independent systems operating at: 0.7 PW peak power at 0.1 Hz; 100 TW at 10 Hz; and 6 TW at 10 Hz.

The Texas Petawatt Laser^[77] based at the Texas Centre for High Intensity Laser Science at the University of Texas at Austin uses a high-energy OPCPA front end with optimized mixed glass to produce shorter pulses than traditional glass petawatt facilities. The OPCPA system amplifies pulses up to the joule level with broad bandwidth, followed by final amplification in mixed glass Nd:glass amplifiers. The first 64 mm rod is silicate with eight-pass angular multiplexing and then four-pass through two pairs of phosphate disc amplifiers. The 1.1 PW beamline produces a bandwidth of 14.6 nm, delivering 186 J in 167 fs. With an $f/1.1$ OAP and an active feedback deformable mirror, the pulses can achieve peak focal intensities up to 2×10^{22} W/cm². In 2015 the front end was upgraded to improve contrast by implementing a picosecond OPCPA stage prior to full pulse stretching in order to reduce parametric fluorescence. Further improvements were made by moving away from lens-based telescopes to an all-reflective geometry, which eliminated a series of pre-pulses.

The Scarlet laser facility^[78] at Ohio State University was built for studies on high-energy density physics and relativistic plasma physics in a dedicated climate and particulate controlled environment in the physics research building. The project began in 2007, with the facility becoming operational in 2012. The dual CPA (DCPA) front end is a kHz Femtopower system (Femtolasers) which goes through a

contrast-enhanced cross polarized wave (XPW) process. The final output operates at 15 J in <40 fs, achieving >400 TW with a shot every minute. The Scarlet laser compressor chamber is vacuum isolated from its target chamber via a Brewster angle ~ 6 μ m thick nitro-cellulose pellicle, and can achieve peak intensities up to 8×10^{21} W/cm². One of the main experimental focuses of the Scarlet facility is ion and electron acceleration from micron-structured targets^[79].

The LCLS (Linac Coherent Light Source) is one of the principal facilities at the SLAC National Accelerator Laboratory. The MEC (Materials in Extreme Conditions) instrument combines the unique LCLS coherent X-ray beamline with a femtosecond laser system. This system has been operational at the 25 TW level, but is planned to be upgraded to the petawatt class level.

2.1.3. Canada

At the University of Quebec, Montreal, Canada the Advanced Laser Light Source (ALLS) is a commercial Ti:sapphire PULSAR system built by Amplitude Technologies operating at 200 TW (5 J, 20 fs, 5–10 Hz PULSAR laser)^[80]. The system has recently been upgraded to deliver 500 TW (10 J, 20 fs)^[81].

2.2. Geographic overview of facilities – Europe

Europe has been pivotal in the development of ultra-high-intensity lasers, with many systems operational in both national laboratories and universities. Many of the developments necessary for the advancement of these systems, including OPCPA, were pioneered in Europe. There is a very strong industrial base, in France in particular, which supplies components, subsystems and even petawatt class facilities to laboratories throughout the world. Looking to the future, ELI (Extreme Light Infrastructure) is a distributed European infrastructure comprising three pillars situated in the Czech Republic, Romania and Hungary, and financed through European Union structural funds. These facilities will transform how researchers gain access to world-leading interaction capabilities, with all three facilities due to start operations in 2019.

Europe has also benefited from the coordination role provided by Laserlab-Europe, bringing together researchers from 38 organizations, as full members, from 16 countries. Its main objective is to provide a sustainable interdisciplinary network of European laser laboratories to: provide training in key areas; conduct research into areas of perceived bottlenecks; and offer access to many of the member facilities to perform world-class research.

2.2.1. United Kingdom

The UK has two national laboratories with facilities which generate ultra-high powers: the STFC Rutherford Appleton Laboratory, which hosts the Central Laser Facility (CLF); and the Atomic Weapons Establishment (AWE). There are

also very active programmes within UK Universities, with petawatt class lasers at the University of Strathclyde and Queen's University Belfast.

Vulcan at the STFC Rutherford Appleton Laboratory was the first petawatt class laser to be used by the international plasma physics community as a dedicated user facility. It is a high-power Nd:glass laser^[36] which has been operational for over 40 years. It enables a broad range of experiments through a flexible geometry^[82, 83]. It has two target areas: one with six 300 J (1053 nm at 1 ns) long-pulse beamlines combined with two synchronized short-pulse beams and a separate target area with high-energy petawatt capability (500 J in 500 fs) synchronized with a single long-pulse beamline.

The Vulcan Petawatt target area will undergo an upgrade with the addition of a petawatt class OPCPA-based beamline delivering pulses with 30 J and 30 fs with a centre wavelength of 880 nm. A new laser area will be created that houses a front end based on a DPSSL-pumped picosecond OPCPA scheme whereby the output from a Ti:sapphire oscillator is amplified to the millijoule level in LBO. These pulses are then stretched to 3 ns before undergoing further stages of amplification in LBO, the final stage employing one of the Vulcan long-pulse beamlines as a pump laser. The pulses will then be compressed in the target area and focused into the same target chamber as the existing petawatt beamline.

The Vulcan 2020 upgrade project is a proposal to increase the peak power of Vulcan to 20 PW (400 J and 20 fs), to enhance its long-pulse capability and to introduce a new target area for interactions at extremely high intensities. The peak power will be increased by the installation of an OPCPA beamline using DKDP crystals pumped by two dedicated 1.5 kJ Nd:glass lasers. The long-pulse provision will be increased by the use of additional 208 mm aperture Nd:glass amplifiers, increasing the output energy of each of the six long-pulse beams to ~ 2 kJ per beam^[84].

Gemini is a Ti:sapphire laser system^[85] operated within the Central Laser Facility. It is operated as an academic user facility that in recent years has seen an increase in the number of industrially focused experiments requested. It has two ultra-high-power beamlines, each delivering 15 J in 30 fs pulses @ 800 nm, giving 500 TW beams to target, generating focused intensities $> 10^{21}$ W/cm². Routine high-contrast operation can be achieved with the use of a double plasma mirror assembly within the target chamber.

AWE, Aldermaston operates the Orion facility which became operational in April 2013 (Figure 8). It is a Nd:glass laser system which combines 10 long-pulse beamlines (500 J, 1 ns @ 351 nm) with two synchronized infrared petawatt beams (500 J in 500 fs)^[86]. One of the petawatt beamlines is operated in ultra-high-contrast mode by frequency doubling two square 300 mm sub-apertures to operate in the green, giving 200 J in < 500 fs, 400 TW, with nanosecond contrast levels of $> 10^{18}$ ^[87].



Figure 8. The Orion laser facility (picture courtesy of AWE).

The TARANIS (Terawatt Apparatus for Relativistic and Nonlinear Interdisciplinary Science) laser in the Centre for Plasma Physics in Queen's University Belfast is a Nd:glass system that can deliver up to 30 J in a nanosecond to ~ 10 J in < 1 ps. TARANIS-X is a major upgrade based around OPCPA to provide ~ 3 J in sub-10 fs pulses representing an ultimate specification of 300 TW in a single beam. The key aim of this upgrade is to improve the near-time contrast of the laser system while at the same time opening the way for few-cycle laser-matter interactions and investigations at relativistic intensities. The unique architecture of TARANIS/TARANIS-X will offer a suite of low- to high-power pulses with durations ranging from a few femtoseconds to nanoseconds, and repetition rates ranging from kHz to once every 10 min, respectively.

University of Strathclyde, Glasgow is home to SCAPA (Scottish Centre for the Application of Plasma-based Accelerators), who operate a commercial Thales Ti:sapphire system commissioned in 2017 (Figure 9). It has 350 TW peak power (8.75 J, 25 fs per pulse) operating at 5 Hz, so with 44 W average power after compression it is currently Europe's highest average power commercial petawatt-scale laser. The front end and vacuum compressor are compatible with an upgrade to petawatt peak power. The laser is used to drive up to four laser-plasma accelerator beamlines: two underdense for GeV-scale wakefield electrons; and two for solid target 50 MeV-scale proton/ion beams. One of the main centre goals is research into coherent radiation production^[88].

2.2.2. France

France has played an important role in the development, construction and operation of ultra-high-power laser facilities in its national laboratories, both academic and defence, and in its universities. A particular strength within France is having a very strong manufacturing base for all aspects of lasers, from components, advanced optics, subsystems and even full-scale petawatt class laser facilities, most notably from Thales and Amplitude Technologies.



Figure 9. The SCAPA facility at the University of Strathclyde (picture courtesy of University of Strathclyde).

At CEA CESTA (Centre d'études scientifique d'Aquitaine), Bordeaux LMJ (Laser Megajoule), a megajoule class laser, is currently being commissioned^[89]. The facility is designed with 176 long-pulse beams with apertures of 40 cm × 40 cm, delivering a total energy of 1.4 MJ @ 351 nm with a maximum power of 400 TW. Five bundles (40 beams) were operational in 2018, with the rest of the beamlines being commissioned over the following years^[90].

A short-pulse capability is also available in LMJ through the PETAL multi-kilojoule glass beamline^[91], which is coupled and synchronized to the long pulses. It uses four independent compressors with the beams phased together. The beamline is specified to operate at 3.5 kJ and was initially commissioned in 2015 with demonstrated performance at 1.15 PW, 700 fs in 850 J^[92]. The performance will be increased when higher-damage-threshold transport optics is deployed. Following an agreement between CEA and the Region Aquitaine, 20%–30% of the time on LMJ/PETAL will be dedicated to academic research access^[93]. In 2017 the first academic campaigns were conducted using both PETAL and the available LMJ long-pulse beams.

Laboratoire de l'Accélérateur Linéaire (LAL), Orsay University is host to the LASERIX facility^[94]. A Ti:sapphire system originally at the University Paris Sud and transferred to LAL, was designed to be a high-repetition-rate multi-beam laser to pump an XUV laser. The laser performance was first demonstrated in 2006, delivering 36 J of energy, although without full compression^[95]. The system is currently operating at low-power mode (30 TW maximum) to pursue experiments with synchronized coherent X-rays with EUV and IR laser sources. It is expected that the facility will return to full operations in 2020/2021. LASERIX is currently being used as a high-intensity laser coupled with an electron gun, producing synchronized photoelectron bunches in the 5–10 MeV range. A plasma accelerating stage, which

will be excited by an amplified pulse from LASERIX in order to reach the 100 MeV range, is being implemented.

Apollon at Orme de Merisiers, Saclay is a next-generation Ti:sapphire 10 PW facility (Figure 10)^[96]. The system is a hybrid OPCPA and Ti:sapphire system, pumped by Nd:glass systems supplied by Thales and Amplitude Technologies to realize short pulses at high energy with a high-contrast front end^[97]. The system is specified to deliver 150 J pulses at 15 fs, giving powers of 10 PW, at a shot rate of one shot per minute. There are two main beamlines delivering 1 PW and 10 PW pulses and two secondary beamlines delivering a 10 TW probe beam and a nanosecond uncompressed beam with energy up to 250 J. All four beam lines can be alternatively directed to two independent experimental areas for high-intensity interactions on either solid or gas targets. Apollon has recently demonstrated^[98] operation at the 1 PW level, with the first commissioning experiments scheduled at the beginning of 2019. The output power of the facility is planned to increase to 4 PW before the end of 2019 (with a 200 J pump) and 9 PW in 2020 (with an upgraded 500 J pump), and finally to 10 PW (with the 600 J designed pump system).

At the Laboratoire d'Optique Appliquée (LOA), Palaiseau there is a commercial 200 TW Ti:sapphire laser delivering 6 J in 30 fs at 1 Hz, originally used as a proton source for medical applications but now used as a multi-particle accelerator for a broader range of applications.

2.2.3. Germany

Many of the laser facilities based in Germany have been brought under the umbrella of the Helmholtz Association. The Association was formed in 2001 and brings together 18 Helmholtz Centres in a broad range of scientific disciplines. The exceptions to this are the lasers operated at CALA in Garching and at the Institute for Laser and Plasma Physics in Dusseldorf. These facilities are described in detail below.

CALA (Centre for Advanced Laser Applications) in Garching is an institute run jointly by the Technical University of Munich (TUM) and the Ludwig Maximilian University of Munich (LMU). It operates the following two lasers.

- ATLAS 3000 consists of a homebuilt 300 TW peak power Ti:sapphire laser and a subsequent 90 J, 1 Hz power amplifier provided by Thales. After compression it is expected to deliver 60 J, 25 fs, 2.4 PW pulses at 1 Hz. The laser serves up to four experimental beamlines for laser-driven electron & ion acceleration; the former also constitutes the basis for well-controlled X-ray sources by undulatory radiation, betatron radiation, and Thomson backscattering in the energy range from keV to multi-MeV. A high-field beam line is available for laser-driven nuclear physics and high-field QED studies.



Figure 10. The Apollon laser at Orme des Merisiers (picture courtesy of Apollon).

- The Petawatt Field Synthesizer (PFS), originally based at the Max-Planck-Institute for Quantenoptik (MPQ), in Garching is a 1 ps, 1 J, 10 Hz diode-pumped thick disk Yb:YAG laser used for pumping a few-cycle OPA chain with unprecedented temporal contrast^[99]. The system, now at CALA, is currently being upgraded to 10 J pump energy at 10 Hz. PFS-pro is a 5 kHz, 200 mJ, 1 ps thin-disk laser, originally intended to pump an OPA chain analogously to PFS (hence the name), but currently examines direct self-phase-modulation (SPM) broadening schemes to create ultra-short pulses for driving a Thomson X-ray source at high efficiency.

At The Institute for Laser and Plasma Physics, Heinrich-Heine University, Dusseldorf, Germany is the Arcturus system^[100]. This is a two-beam Ti:sapphire system where the pulses in each beamline are compressed to ~ 30 fs and transported onto the interaction chamber with $\sim 50\%$ efficiency. Both pulses can be spatially overlapped and temporally synchronized onto the target. Thus, the system can deliver $2 \times 3.5 \text{ J} = 7 \text{ J}$ energy onto the target within a pulse duration of 30 fs, giving a total system power onto target exceeding 200 TW.

The following is a summary of the facilities based at the Helmholtz Centres.

The PHELIX (Petawatt High Energy Laser for heavy Ion eXperiments) kilojoule glass laser system^[101] was constructed at the Helmholtz Centre GSI and is used either in stand-alone or in conjunction with a heavy ion accelerator. The laser can be switched between long- and short-pulse operation and in short-pulse mode is designed to deliver 400 J in 400 fs. Another kilojoule glass laser system is planned at GSI for the Helmholtz Beamline at FAIR (Facility for Antiproton and Ion Research). A repetition rate of one shot per minute is envisioned.

There are two diode-pumped systems POLARIS and PEnELOPE.

- POLARIS (Petawatt Optical Laser Amplifier for Radiation Intensive experiments) is based at the Helmholtz

Institute Jena. It is designed as a fully diode-pumped Yb:glass/Yb:CaF₂ petawatt class laser^[102]. It operates at a central wavelength of 1030 nm with a bandwidth of 18 nm, allowing 98 fs pulse width after compression. The tiled grating compressor limits the peak power on target to about 200 TW, whereas amplification to 54 J has already been demonstrated.

- PEnELOPE (Petawatt, Energy-Efficient Laser for Optical Plasma Experiments) is a rep-rated diode-pumped laser using broadband Yb:glass/Yb:CaF₂ under construction at the Helmholtz-Zentrum Dresden-Rossendorf Laboratory within the ELBE Center (Electron Linac for beams with high Brilliance and low Emittance) for high-power radiation sources^[103]. It will be dedicated to the production of laser accelerated proton and ion beams with energies > 100 MeV, relevant to future cancer treatments. The facility will deliver pulses of 150 J in 150 fs, giving > 1 PW at 1 Hz centred at 1030 nm, with testing of one of the main amplifiers recently demonstrated^[104].

There are also a number of commercial Ti:sapphire lasers based at Helmholtz Centres.

- DRACO (Dresden laser acceleration source)^[105] at the Helmholtz-Zentrum Dresden-Rossendorf Laboratory is a commercially sourced Ti:sapphire laser supplied by Amplitude Technologies. The facility is designed to investigate electron, ion and proton acceleration schemes for radiation therapy as part of the ELBE Center. It is operating at 150 TW at 10 Hz and 1 PW at 1 Hz.
- The commercial Ti:sapphire Jeti200 laser facility at the Helmholtz Institute Jena delivers 17 fs pulses with an energy of up to 5.6 J. The 300 TW system with ultra-high contrast is dedicated to plasma physics and particle acceleration experiments.
- The LUX group at the Center of Free-Electron Laser Science, Department of Physics, University of Hamburg operates a 200 TW commercial Ti:sapphire laser

system ANGUS. The 25 fs pulses produced at a repetition rate of 5 Hz are used for the investigation of plasma accelerators and plasma-driven undulator X-ray generation^[106].

- There is also a 300 TW, 25 fs Ti:sapphire Amplitude Technologies laser currently being constructed for HIBEF (Helmholtz International Beamline for Extreme Fields) at the European XFEL, DESY, Hamburg. The HED (high energy density) end station will couple the XFEL output with laser sources for ultra-intense laser applications^[107].

2.2.4. Russia

The first operational petawatt class OPCPA system was developed at the Institute of Applied Physics, Russian Academy of Science (RAS), Nizhny Novgorod using a homemade pump beam. The laser delivered 0.2 PW in 2006^[108] and was upgraded to 0.56 PW in 2007^[109]. The facility known as PEARL (PEtawatt pARametric Laser) had active elements of DKDP; a wavelength of 910 nm; with pulse durations 43–45 fs. PEARL-X is the next generation of OPCPA facility, with a theoretical limit of 10 PW, but with a more realistic operating limit of 4–5 PW. The technology was also transferred to FEMTA at the Russian Federal Nuclear Center, Sarov, Nizhny Novgorod, using a 2 kJ laser for pumping. This was a potential multi-PW system, but constraints in the pump limited the output to 1 PW, 100 J in 100 fs.

The construction of a high-power megajoule laser facility was started in Russian Federal Nuclear Center, VNIIEF, Sarov, Nizhny Novgorod in 2012 with commissioning expected in the next few years^[110]. The multi-beam Nd:glass facility is designed to deliver 2.8 MJ of energy at 527 nm for inertial confinement fusion (ICF) direct drive target illumination. The target bay, which contains the 10-m-diameter spherical chamber, has two laser bays on either side. The facility has 192 Nd:phosphate glass laser beams, in a four-pass geometry, with each beam delivering 12.5 kJ at the second harmonic, a significant design difference from NIF or LMJ described elsewhere in this review (operating at the third harmonic). An adaptive system, based on deformable mirrors, will allow compensation of large-scale nonuniformities of laser beams. Unlike NIF or LMJ, where a cylindrical indirect drive geometry is used, at the VNIIEF facility scientists will use a spherical indirect drive target geometry. This uses six laser entrance holes, which achieves a very uniform X-ray field distribution on the surface of a DT ice cryogenic target.

2.2.5. Spain

At the Centre for Pulsed Lasers (CLPU), University of Salamanca VEGA is a user facility open for domestic and international researchers (Figure 11). The system is a custom-made Ti:sapphire laser from Amplitude Technologies^[111].

There are three amplification lines, which share the same front end (XPW and Double CPA): VEGA-1 0.6 J, 20 TW at 10 Hz; VEGA-2 6 J, 200 TW at 10 Hz; and VEGA-3 30 J, 1 PW at 1 Hz^[112]. The facility was officially inaugurated by the King of Spain in September 2018.

2.2.6. Italy

In Italy two laboratories have commercial PULSAR Ti:sapphire laser systems from Amplitude Technologies, delivering 200 TW (5 J, 20 fs, 5–10 Hz)^[113].

- The Laboratori Nazionali di Frascati (LNF) is one of the four main laboratories of INFN (National Institute for Nuclear Physics). LNF has also addressed dedicated R&D on advanced accelerator concepts. Born from the integration of a high-brightness photo-injector (SPARC) and of a high-power laser (FLAME); SPARC.LAB is mainly devoted to conducting further development, characterization and application of compact radiation sources (FEL, THz, Compton) driven by plasma-based accelerator modules. This will investigate the techniques of: LWFA (laser wakefield acceleration), which uses short-pulse laser drivers to excite the wake; and PWFA (plasma wakefield acceleration), which uses a high-energy particle bunch to excite the wake^[47].
- The Intense Laser Irradiation Laboratory (ILIL), CNR (Consiglio Nazionale delle Ricerche) National Institute of Optics, Pisa was established in 2001 following more than a decade of experimental activity in the field of high-power laser–plasma interaction, also as a founding member of European collaboration programmes in the field, pioneering access to large-scale facilities and hosting Training Network activities. Today the laboratory is an active member of the Italian Extreme Light Infrastructure initiative and a partner of the EuPRAXIA H2020 collaboration (see 2.2.8) and is also an associate partner of the Eurofusion consortium. ILIL operates a Ti:sapphire laser for laser-driven light ion acceleration, currently operating at the ~ 150 TW level (4 J, 25 fs after compression), with plans to go to >5 J, 25 fs^[114]. The laboratory features active research programmes on laser-plasma electron acceleration, laser-driven light ion acceleration, and atmospheric propagation of intense laser pulses, and has long-standing expertise in medical applications of laser-driven radiation and particle sources^[51].

2.2.7. Romania

At the Centre for Advanced Laser Technologies INFLPR (National Institute for Laser, Plasma and Radiation Physics), Măgurele, Romania the CETAL Ti:sapphire laser is a commercial petawatt laser (25 J in 25 fs at 0.1 Hz) supplied by Thales Optronics^[115]. The laser system allows two modes of operation: 1 PW @ 0.1 Hz and 45 TW @ 10 Hz.

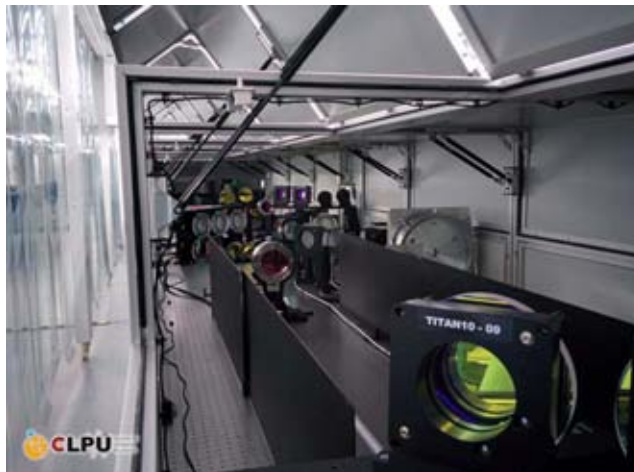


Figure 11. The VEGA 3 laser facility at the University of Salamanca (picture courtesy of the University of Salamanca).

2.2.8. Multi-national European programmes

ELI (Extreme Light Infrastructure) is a distributed European infrastructure comprising three pillars situated in the Czech Republic, Romania and Hungary. ELI^[46] will provide a unique platform for users of ultra-high-power lasers, with each facility providing multiple laser systems delivered to multiple dedicated target interaction areas. The facilities will be operated through a combined multi-national management structure known as ERIC (European Research Infrastructure Consortium). All three facilities are due to be online to users in 2019, with the first systems using kHz lasers going online first in a user-supported commissioning mode.

- ELI-Beamlines, Dolni Brezany, Czech Republic will provide a range of laser systems for research, not only in the fields of physics and material science, but also in biomedical research and laboratory astrophysics. The beamlines use lasers based on either OPCPA, Ti:sapphire, or a combination of the two to produce pulses ranging from hundreds of millijoules at a kHz up to a kJ beamline (flashlamp pumped mixed Nd-doped glass) firing once a minute. These will be coupled to separate interaction areas or beamlines, allowing a wide range of experiments to be performed. The laser systems are: L1: 100 mJ/1 kHz; L2: 1 PW/20 J/10 Hz (laser development beamline); L3: 1 PW/30 J/10 Hz (constructed by LLNL) HAPLS (High-repetition-rate Advanced Petawatt Laser System) uses diode-pumped solid-state laser (DPSSL) pumped Ti:sapphire CPA technology and commissioned in 2018 (Figure 12); L4: 10 PW/1.5 kJ/one shot per minute (constructed by a joint consortium of National Energetics and EKSPLA with contributions from ELI-BL) uses a kJ Nd:glass direct CPA architecture.
- ELI-NP (Nuclear Physics) Magurele, Bucharest, Romania will have two commercial multi-petawatt

systems supplied by Thales with OPCPA front ends and Ti:sapphire power amplifiers (Figure 13). The beamlines will either produce 1 PW at 1 Hz (20 J, <20 fs) or 10 PW at one shot per minute (250 J, 25 fs), capable of producing focused intensities to target of 10^{23} W/cm². The beamlines will be used in the study of photonuclear physics and its applications. The laser beams will be synchronized to a tunable gamma-ray beamline produced by laser light (Yb:YAG green laser) scattered from high-energy electrons. This unique combination will provide a capability for a wide range of nuclear physics applications.

- ELI-ALPS (Attosecond Light Pulse Source) Szeged, Hungary will provide three high-repetition-rate OPCPA beamlines. The high-repetition-rate laser will operate at 100 kHz, providing >5 mJ, <6 fs pulses; a mid-infrared laser operating at 10 kHz, providing >10 mJ, 4–8 μ m pulses; a terahertz pump laser 100 Hz, >1 J, <5 fs and single-cycle (SYLOS) laser 1 kHz, >100 mJ, <5 fs; and a high-field laser 10 Hz, >2 PW, <10 fs. All the beamlines will be used to drive secondary sources (UV/XUV, X-rays, ions, etc.), which will be dedicated to extremely fast electron dynamics in atoms, molecules, plasmas and solids.

The EuPRAXIA (Compact European Plasma Accelerator with Superior Beam Quality) collaboration is the first plasma accelerator collaboration on this scale bringing together 16 European partner laboratories and an additional 24 associated partners from the EU, Israel, China, Japan, Russia and the USA^[116, 117]. EuPRAXIA is a Horizon 2020 project to build a European facility with multi-GeV electron beams based on laser/plasma acceleration. The preliminary design envisions the use of a three-stage system, each driven by a



Figure 12. The L3 HAPLS laser was fully commissioned at LLNL before being shipped and re-installed at ELI-Beamlines (picture courtesy of LLNL).



Figure 13. The two 10 PW lasers installed in the ELI-NP facility (picture courtesy of ELI-NP).

petawatt class Ti:sapphire laser of increasing power/energy running at up to 100 Hz: Stage 1, 7 J, 20 fs; Stage 2, 30 J, 30 fs; Stage 3, 100 J, 50 fs^[118].

2.3. Geographic overview of facilities – Asia

Asia has a long history of operating ultra-high-power laser facilities and has been pioneers in their development and implementation. China, Japan and the South Korea have all had, or have, facilities with world-leading capabilities, described in the sections below. India has only recently commissioned its first petawatt class laser facility.

The Asian Intense Laser Network is an unfunded consortium which uses the ASILS (Asian Symposium on Intense Laser Science) conference series and summer schools to maintain interactions between the various groups throughout Asia. The following is a summary, by country/institute, of the ultra-high-power lasers in Asia.

2.3.1. China

China has seen the greatest growth internationally in the development of ultra-high-power lasers and in their applications. This research is clustered around three main cities: Shanghai, Beijing and Mianyang. In Shanghai there are the following research institutes: SIOM (Shanghai Institute of Optics and Fine Mechanics) National Laboratory on High Power Laser and Physics (NLHPLP); SIOM State Key Laboratory of High Field Laser Physics; there is a further site within ShanghaiTech University operated by SIOM; and the Key Laboratory for Laser Plasma (Ministry of Education) at Shanghai Jiao Tong University. In Beijing there are high-power lasers situated at the Beijing National Laboratory for Condensed Matter Physics, Institute of Physics (IOP), Chinese Academy of Sciences (CAS) and Peking University. Mianyang is the location of the Laser Fusion Research Centre operated by the China Academy of Engineering Physics (CAEP).

At SIOM's National Laboratory on High Power Laser and Physics (NLHPLP) the first Nd:glass petawatt laser in

China was built as an auxiliary beamline to the Shengguang (Divine Light) SG-II high-energy facility^[119] and is still operational. SG-II was an eight-beam Nd:glass laser facility operating at a total of 6 kJ IR or 2 kJ at 3ω . A ninth beam of 4.5 kJ was commissioned and made operational in 2005, and subsequently converted to the SG-II UP PW beamline. SG-II UP also included the building of a separate 24 kJ, 3ω , 3 ns eight-beam facility. A recent paper describes the full scope of the facility^[120].

An additional OPCPA beamline has been recently added to the SG-II facility: the SG-II 5 PW laser facility is designed to deliver 150 J/30 fs pulses and pumped by second harmonic of the 7th and 9th beams of the SG-II facility. Currently, this system is operating at 37 J in 21 fs (1.76 PW) and has successfully been employed for high-energy physics experiments with a focusing intensity exceeding 10^{19} W/cm². The third phase with a high-energy OPCPA stage as the master amplifier is now under construction, and compressed 5 PW pulses will be achieved in the near future^[121].

SIOM's State Key Laboratory of High Field Laser Physics was the home of the first Ti:sapphire petawatt class laser in China which delivered 0.89 PW in 29 fs pulses at 800 nm in 2006^[122]. The 'Qiangguang' (Intense Light) Ti:sapphire laser facility was then upgraded and produced powers of 2 PW (52 J, 26 fs) in 2012, the highest peak powers ever achieved from a laser system at the time^[123]. A high-contrast front end gives contrasts to target of 1.5×10^{11} @100 ps. A further upgraded version of the main amplifier of the facility produces 192.3 J pulse energy and has demonstrated the production of 27 fs pulses at sub-aperture, indicating that 5 PW pulses would be produced if full-aperture beam compression could be achieved^[124]. The laser is located in a building where space limits the option of a large vacuum compressor, and this facility is therefore currently operational at the 1 PW level.

The first multi-TW OPCPA laser in the world was also developed within the laboratory producing 570 mJ/155 fs, giving 3.67 TW in 2002^[125]. In 2012 they started to implement a 10 PW CPA-OPCPA hybrid laser system with the OPCPA booster amplifier based on a 215 mm LBO crystal. The peak power of 0.61 PW was achieved with a pulse energy of 28.7 J in a 33.8 fs pulse at 800 nm in 2013^[126], and then in 2015 they improved the output to 1 PW by using a 100 mm LBO crystal with a pulse energy of 45.3 J in a 32 fs pulse^[127]. However, the final 10 PW (300 J in 30 fs) performance of the laser system is delayed due to the availability of large-aperture LBO crystals.

In the joint laboratory of SIOM and ShanghaiTech University, the team from SIOM's State Key Laboratory of High Field Laser Physics is constructing SULF (Shanghai Superintense Ultrafast Laser Facility), a new standalone Ti:sapphire laser facility in a purpose-built building (Figure 14). The facility will deliver 10 PW, 1 PW, and 100 TW



Figure 14. The SULF Prototype laser during final commissioning before being transferred to the SULF building (picture courtesy of SIOM).

beamlines delivered to three target areas constructed underground. The SULF Prototype was constructed in a neighbouring building but without the room for a target chamber. In 2016 the laser facility achieved powers of 5.4 PW^[128], with an ultimate specification of 10 PW, which is currently limited by the availability of suitable gratings. They also successfully demonstrated the final Ti:sapphire amplifier for 10 PW^[129], delivering 339 J at 800 nm with a 235-mm-diameter Ti:sapphire final amplifier. The pump-to-signal conversion efficiency of the final amplifier was demonstrated to be 32.1%. With the compressor transmission efficiency of 64% and the compressed pulse duration of 21 fs obtained with sub-aperture compression, this laser system would deliver 10.3 PW. New, full-aperture gold-coated gratings from Jobin Yvon were installed when the laser was moved into the purpose-built SULF building. The facility became operational in 2019, with an upgraded pump laser providing 10 PW laser pulses to be delivered to target at one shot per minute^[130].

At the Key Laboratory for Laser Plasmas (LLP), Shanghai Jiao Tong University a commercial PULSAR Ti:sapphire laser from Amplitude Technologies operates at 200 TW, delivering 5 J, 25 fs pulses at repetition rates between 5 and 10 Hz^[131, 132]. They also have a research programme into high-average-power OPCPA systems and plan to construct a 15 PW facility on a small campus they have in Pudong, Shanghai. The facility is single-shot in the first phase and will be eventually upgraded to a high repetition rate with kW average power. The LLP also has a mid-IR OPCPA system operating at 2.2 μ m and 100 TW, which is included in this review as it has been identified as a possible way forward for future petawatt class laser facilities.

At the Laser Fusion Research Centre, CAEP, Mianyang SILEX-I was an early Ti:sapphire petawatt class facility. The facility produced 9 J pulses at 30 fs, giving an output power of 286 TW at a repetition rate of 0.15 Hz^[133]. The facility

was able to produce focused intensities of 10^{20} W/cm² without the need for deformable mirror corrections. This system has been incorporated into their Xingguang (Star Light) XG-III facility (a femtosecond, picosecond and nanosecond beam capability). The three beamlines produce 0.7 PW at 800 nm in 26.8 fs, 0.6 PW at 1053 nm in 0.5–10 ps, and a 527 nm nanosecond beam delivering 575 J^[134].

Shenguang-IV (SG-IV)^[135] is a proposed megajoule facility to be built at the Laser Fusion Research Centre as an ignition demonstrator. The facility is planned to be constructed following the successful commissioning of SG-III, designed to operate with 48 beams at 200 kJ. The initial specification of SG-IV is to be of similar scale to NIF and LMJ, although the design is yet to be finalized. Design options can be tested on SG-IIIP, a separate prototype beamline within the SG-III building.

There is also a 4.9 PW all-OPCPA laser at Mianyang (CAEP-PW) operating at 800 nm delivering 168.7 J after the final amplifier and 91.1 J post-compressor in 18.6 fs^[136]. It is planned that by using larger-aperture LBO crystals, 200 mm × 200 mm, 15 PW will be achieved.

The National Laboratory for Condensed Matter, IOP Beijing operates the Xtreme Light III (XL-III) Ti:sapphire facility which generates 32 J in a 28 fs pulse delivering 1.16 PW to target at focused intensities $>10^{22}$ W/cm²^[137]. It was the first facility to produce more than 1 PW of laser power in China, and has high fidelity pulses with contrasts of 10^{10} @100 ps. This facility was moved to a new building and had its pump lasers upgraded. It is expected the peak power of the system will be 1.5 PW, with a pulse duration shorter than 20 fs and a contrast ratio better than 10^{11} at a time of 10 ps.

At the Institute of Heavy Ion Physics, Peking University CLAPA (Compact Laser-Plasma Accelerator) is a dedicated facility for laser-driven plasma accelerator experiments; it includes a 5 J, 25 fs, 5 Hz, 200 TW commercial Ti:sapphire laser supplied by Thales, a plasma accelerator, proton beam transport line and the application platform^[138]. The XPW technique is used in the system, allowing nanosecond contrasts of 10^9 , and the picosecond contrast can reach 10^{10} 20 ps in front of the pulse. There is also a proposal to install a 2 PW, 1 Hz Ti:sapphire laser for proton acceleration studies.

2.3.2. Japan

The Institute of Laser Engineering (ILE), Osaka University is host to the GEKKO XII Nd:glass facility (Figure 15); the first large-scale (12-beam) laser system employing Nd-doped phosphate laser glasses for inertial confinement fusion research^[139]. Following the development of the first large-aperture 30 TW CPA Nd:glass laser at ILE^[231], the first petawatt class laser in Asia was constructed as part of the high-energy nanosecond capability of the GEKKO XII facility^[140]. This petawatt beamline was composed of an OPCA front end, Nd:glass large-aperture amplifiers and a



Figure 15. The GEKKO XII (right) and LFEX (left) lasers at ILE, Osaka University, Japan (picture courtesy of Osaka University).

double-pass compressor to produce 420 J in 470 fs, giving an output power of 0.9 PW. An $f/7$ off-axis parabola was used to focus the beam to target, giving focused intensities of 2.5×10^{19} W/cm².

Within the GEKKO XII facility, the LFEX (Laser for Fast Ignition Experiment) facility has been commissioned as a fast ignitor^[141] demonstrator for the FIREX project^[142, 143]. The LFEX laser is composed of 2×2 segmented beams. Each beam is 32 cm × 32 cm in size and is compressed with two pairs of dielectric gratings and focused to target with a 4 m focal length off-axis parabola, giving a focal spot of 30–60 μ m in diameter with 2.5 kJ energy/beam. The pulse rise time is 1 ps and the pulse duration is controllable through 1–20 ps, providing petawatt peak powers^[144, 145]. The output power of the compressed beam is currently 2 PW in 1 ps. A full-aperture deformable mirror has been installed in one of the four beams before the pulse compressor to reduce the wavefront distortion. Pulse contrast ratio (pedestal to main peak) has been improved from 10^{10} to better than 10^{11} by using a plasma mirror in front of the target.

At the Kansai Photon Science Institute (KPSI), QST (National Institutes for Quantum and Radiological Science and Technology), Kyoto, Japan (previously Advanced Photon Research Centre (APRC), JAEA (Japan Atomic Energy Agency)), the J-KAREN (JAEA-Kansai Advanced Relativistic ENgineering) Ti:sapphire laser system was the world's first petawatt class Ti:sapphire facility, generating 0.85 PW in 2003 (28.4 J at 33 fs)^[39]. This facility could operate at 50 TW at 10 Hz and at petawatt levels once every 30 min, due to thermal considerations in the final booster amplifier. The upgraded J-KAREN-P (J-KAREN-Petawatt), the first hybrid OPCA/Ti:sapphire system, has a specification of 1 PW (30 J, 30 fs) and 0.1 Hz repetition rate with $f/1.3$ off-axis parabola focusing. This system is currently operated at 0.3 PW, delivering an intensity of 10^{22} W/cm² on target with a high temporal contrast of 10^{12} ^[146].

For laser wakefield electron acceleration, LAPLACIAN (Laser Acceleration PLATform as a Coordinated Innovative ANchor) is being built at RIKEN SPring-8 Centre, Harima, Japan in the framework of a Japanese national project ImPACT (Impulsing PARadigm Change through disruptive Technologies program). This facility is equipped with a Ti:sapphire laser system specially designed to attain stable electron staging acceleration by LWFA. The concept of the laser system was designed by Osaka University and installed by Amplitude Systems. A laser beam from an oscillator is divided into three beams, which are amplified and compressed to provide three beams of 1 J/20 fs at 10 Hz, 2 J/50 fs at 5 Hz and 10 J/100 fs at 0.1 Hz. These beams are then provided to an injector, a phase rotator, and a booster, respectively, with minimum timing jitter. The laser parameters for each stage can be controlled independently to maximize the total performance of the electron acceleration.

At SACLA, the X-ray free electron laser (XFEL) facility, operated by RIKEN SPring-8 Centre, Harima, Japan, there is a Ti:sapphire laser system delivered by Thales Optronique with two 0.5 PW laser beams. This has been commissioned with a maximum energy of 12.5 J in 25 fs at a 1 Hz repetition rate. The laser has been planned as one of the HERMES laser systems, which is coupled to SACLA under a RIKEN-Osaka University collaboration. In 2018 one beam has started operation in combination with SACLA for user experiments at 200 TW (8 J, 40 fs) with a reduced rate of once every few minutes.

The high-power laser community in Japan, led by ILE Osaka, together with KPSI QST, has proposed a concept design of a high-repetition-rate and high-power laser facility J-EPOCH (Japan-Establishment for POver laser Community Harvest). This facility is a 16 kJ/16 Hz/1 ns/160 beam laser system, which is composed of 16 units of ten beams, with each beam providing an energy of 100 J at 100 Hz and a peak power of 1 PW at 50–100 Hz. J-EPOCH will provide laser-accelerated radiation and particle beams (GeV electrons, protons, X-rays, γ -rays and neutrons) and 25 PW beam lines. The 25 PW beam line consists of two 10 PW/20 fs beams with a 10 Hz repetition rate based on Ti:sapphire lasers and one 5 PW/a few ps/5–10 kJ beam with a 10 Hz repetition rate based on ceramic lasers.

2.3.3. South Korea

At the Centre for Relativistic Laser Science (CoReLS), Gwangju, South Korea, a petawatt Ti:sapphire laser facility (Figure 16) has been operational for the exploration of superintense laser–matter interactions by inheriting the petawatt laser facility developed by Advanced Photonics Research Institute (APRI), Gwangju Institute of Science and Technology (GIST). The petawatt laser facility first achieved petawatt capability in 2010 with a 33 J beam in 30 fs, delivering 1.1 PW at a repetition rate of 0.1 Hz^[147], and added the second petawatt beamline of 30 fs, 1.5 PW^[148], which is claimed to be the very first 0.1 Hz Ti:sapphire



Figure 16. The multi-petawatt laser facility at CoReLS, South Korea (picture courtesy of CoReLS).

petawatt laser in the world. After the establishment of the CoReLS, a research centre of the Institute for Basic Science (IBS), in 2012 the 1.5 PW laser beamline was upgraded to a 4 PW laser in 2016, delivering 83 J in 19.4 fs (4.2 PW) at 0.1 Hz with a shot-to-shot energy stability of 1.5%^[149]. The upgraded laser with XPW and OPA front end stages can achieve focused intensities of 10^{23} W/cm², with contrast measured to be 10^{12} up to 150 ps before the main pulse. The measured laser intensity, with an $f/1.6$ off-axis parabola, was 5.5×10^{22} W/cm² with a 3 PW laser pulse^[150].

At ETRI (Electronics and Telecommunications Research Institute) Daejeon, South Korea a 200 TW (5 J in 20 fs) 5–10 Hz PULSAR Ti:sapphire laser system from Amplitude Technologies has been upgraded to 1 PW. The facility is called EXLS (ETRI eXtreme Light Source) and operates at 800 nm, giving 31 J in 22 fs at 0.1 Hz. The 200-mm-diameter beam has $f/1.8$ focusing.

2.3.4. India

The RRCAT (Raja Ramana Centre for Advanced Technology), Indore, Dept of Atomic Energy is the premier Indian institute working in the field of lasers and particle accelerators. In 2012 a 150 TW Ti:sapphire laser operating at 5 Hz was procured from Amplitude Technologies, France. The system provides 3.75 J in 25 fs with a pre-pulse contrast of $\sim 10^{10}$ at 300 ps. This system is mostly used to investigate electron acceleration in gas jets and ion acceleration in thin foil targets. Now RRCAT is in the process of establishing a 1 PW Ti:sapphire laser facility. The laser uses an XPW front end. The final Ti:sapphire laser amplifier is pumped by four Nd:glass pump lasers (ATLAS, Thales, France) providing 100 J at 2ω . The final power is 1.1 PW at 25 J, 25 fs operating at 0.1 Hz.

3. Discussion of fifty years of ultra-high-power lasers

Since the first demonstration of the laser in 1960 by Theodore Maiman^[9], the principal defining characteristic of

lasers has been their ability to focus unprecedented powers of light in space, time and frequency. Shortly after its discovery, the United States Department of Energy's national laboratories aggressively initiated research and development on high-energy, high-peak-power lasers for laser fusion. Similar efforts took place in laboratories in Europe and later in Asia, and saw record peak powers rapidly scaling to the 100 TW level. Twenty years ago, LLNL's petawatt laser based on kilojoule CPA applied to one beamline of the Nova fusion laser^[2] represented a further decadal leap in peak power. 'The PW,' as it was called, opened our eyes to the science frontiers that high-intensity petawatt lasers offered (10^{21} W/cm²).

Beyond achieving its anticipated goals of reaching the threshold to the ultra-relativistic regime, wherein a free electron oscillating in the laser field is accelerated to near the speed of light (peak intensity $>10^{18}$ W/cm²), unexpected discoveries such as the production of ions at multi-MeV energies, which have since become standard probes for high-energy-density science, further enhanced their impact. High-energy, short-pulse laser systems operating at petawatt peak powers (e.g., from 20 J/20 fs to kJ/ps) have in the intervening two decades enabled a wide range of new high-energy (keV–GeV) particle and radiation sources for single-shot discovery science.

An important contribution to enhance the global capabilities is the recycling of components from national laboratories to academic environments, where their implementation is enhanced by university innovators. In the USA, following the closure of the Nova laser, several internationally recognized lasers were born including: PHELIX at GSI Darmstadt, Germany^[101]; Vulcan PW at the Central Laser Facility^[36], UK; LEOPARD at the University of Nevada, Reno, USA^[151]; and Texas PW at the University of Texas at Austin, USA^[77]. In France, following the closure of the Phebus facility at Limeil-Valenton, the LULI-2000 facility was created^[152] at Ecole Polytechnique, with many components also contributing to the Vulcan PW in the UK and PHELIX in Germany.

The physics at the laser–target interaction point is strongly governed by the intensity of the laser, although the reporting of peak power has become the standard in defining laser capability. This might be because a direct measurement of the focal intensity is extremely difficult. Researchers have measured the ionization ratio of atoms in the light field (optical field ionization) to assess the focused peak intensities^[153]. Furthermore, many new high-peak-power laser systems have arisen, and technology has improved over the original petawatt, but the peak focal intensities achieved have only increased from $\sim 10^{21}$ to $\sim 10^{22}$ W/cm². However, the usable intensities for experiments have typically been an order of magnitude less than this, partly due to a lack of emphasis on the integrated capabilities required for practical exploitation, as opposed to academic

demonstration. Notably, peak intensity demonstrations have occurred on specific Nd:glass-based lasers: the Vulcan PW in the UK at 1×10^{21} W/cm² (2004)^[35]; the Ti:sapphire-based HERCULES laser at the University of Michigan, USA at 1×10^{22} W/cm² (2004)^[70], J-KAREN-P in Japan at 1×10^{22} W/cm² (2018)^[146], and most recently, the record intensity of 5.5×10^{22} W/cm² was demonstrated at the CoReLS laser^[150].

It is interesting to note that even the highest-peak-power laser systems (10 PW and beyond) proposed or already in commissioning make no exception to this trend and largely predict intensities of only up to 10^{23} W/cm² (notably L4-ELI^[45], EP-OPAL^[154], SULF^[129] and SEL^[130]). A fundamental physics or engineering limit is not clear; however, material challenges such as imperfect diffraction gratings^[155, 156], optics and gain materials reduce the overall laser focusability in time and space.

Despite this observation, the race to even higher peak power is underway (see Section 4.1 in this review). Figure 17 shows the development of peak power versus year across the world and by region. It can be seen that all early high-power lasers were derivatives of the US inertial confinement fusion (ICF) program and based on Nd:glass for gain media. With the invention of titanium-doped sapphire (Ti:sapphire) in 1982 at MIT Lincoln Lab^[26], which provides $\sim 20\times$ more gain bandwidth at a $\sim 5\times$ lower saturation fluence compared to Nd:glass, the invention of ultra-short pulsed (<100 fs) terawatt and petawatt laser systems became possible. Commercially available 100 TW–10 PW lasers rely on large-aperture Ti:sapphire, with the exception of a product by National Energetics that relies on a mix of Nd:phosphate and Nd:silicate glass to enhance the gain bandwidth in the amplifier chain. Figure 17 also shows that in the US currently no high-power lasers exceeding 1 PW are planned, despite its leadership in the past.

A representation of the operational limits of high-power/high-energy laser systems is demonstrated in Figure 18. The figure includes those facilities that are operational, under construction, or decommissioned globally, with colour indicating the laser media of the final amplifier stage. The diameter of the circles/octagons are logarithmically proportional to the average power of the lasers shown. Vertical and horizontal axes are peak power and integrated pulse energy of a single (coherent) aperture – in the case of multi-beam lasers like the 192-beam NIF laser shown, total system performance is diagonally up and to the right by the number of beams. Diagonal lines indicate the laser pulse width corresponding to the pulse energy divided by peak power. The right vertical axis indicates the peak focal intensity that would be reached if the beam was focused to a spot of a square micron in area, while the upper horizontal axis indicates the energy density corresponding to depositing the laser pulse energy into a cubic millimetre volume. Four operational envelopes are shown, within which laser designs satisfy limits of:

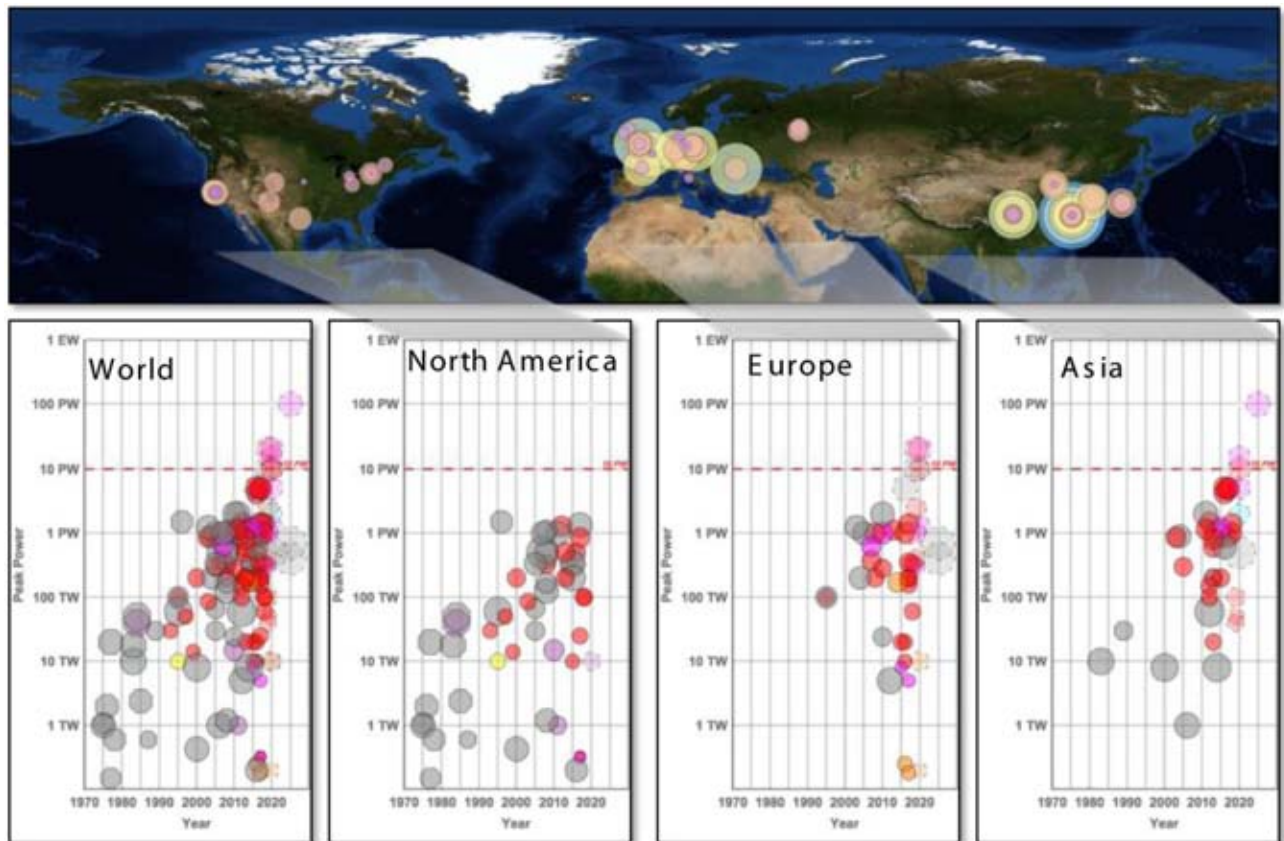


Figure 17. Geographic distribution of high-peak-power lasers (top). Diameter of circle is logarithmically proportional to peak laser power and circle colour is chosen for graphical clarity. Evolution of high-peak-power lasers (>100 GW) in the world over the last fifty years (bottom). Systems that are currently operating are shown as circles with solid borders; systems that were operating in the past but are now de-activated are shown as octagons with solid borders; and systems actively funded and being built are shown as circles with dashed borders. The diameter of the symbol is logarithmically proportional to laser pulse energy and the colour indicates the laser media used in the final amplifiers: Ti:sapphire (red), Nd:glass (grey), Yb:X (orange), Cr:X (yellow), optical parametric amplification (purple-blue), or gas (pink). As of early 2019, no high-power system has exceeded the 10 PW limit, even though there are several funded projects underway in Europe and Asia to break this barrier.

- bandwidth constraints (left diagonal lines);
- aperture size limits (40 cm × 40 cm perpendicular beam size for mirrors, lenses and nonlinear elements such as doublers; and 40 cm × 100 cm optic-normal for diffraction gratings);
- nonlinear B-integral limits; and
- damage fluence limits.

Limits on aperture size and damage fluence limits determine the rightmost edges of the operational zones shown, while the B-integral (intensity) limit and max aperture size limit the peak power laser pulses in NIF-size apertures to <10 TW in the 1 J–10 kJ range, as shown. The damage threshold limits and bandwidth constraints of both gold and multi-layer dielectric metre-scale diffraction gratings are also indicated, as is the similar limits for fused silica. The damage threshold data presented by Stuart *et al.*^[157] were used for the gold grating and fused silica limits as shown.

Figure 18 dramatically illustrates that high-peak-power laser development since the invention of CPA has been fundamentally constrained, especially in the case of Nd:glass lasers based on fusion energy laser technology, by energy limits determined by optic size and damage thresholds, and in the case of Ti:sapphire-based ultrashort-pulse lasers by bandwidth limits. The steady ascent of Ti:sapphire, OPCPA and Nd:glass technologies upward in peak power has, with the construction of several ten to multi-tens of petawatt systems, nearly reached the ~100 PW limit of metre-scale gold diffraction gratings. The continued progress of ultra-intense CPA lasers must therefore take a multi-beam approach. Non-CPA Nd:glass fusion lasers have taken this approach for decades, which is most dramatically demonstrated with the 192-beam NIF laser. This could take the form of either incoherent or coherent beam combination of ~10 PW scale beams. Indeed, the Shanghai SEL facility is already taking that approach to reach the 100 PW scale by combining four multi-tens of petawatt beams. Finally, the pioneering work of the

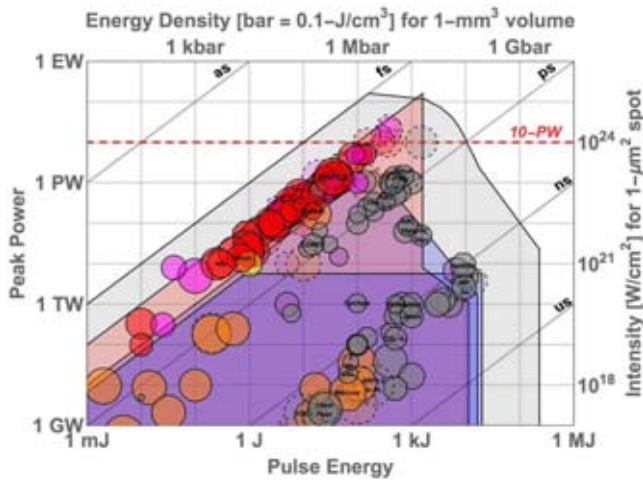


Figure 18. The current high-energy/high-power lasers globally (those that are operational represented by circles with continuous borders; those under construction represented by circles with dashed borders; or those that are decommissioned represented by octagons; with colour indicating the laser media of the final amplifier stage – defined in the legend in Figure 17).

astronomy community should be noted here, who faced very similar challenges of optic size and performance degradation (atmospheric turbulence), which were overcome decades ago with multiple apertures and active beam combination.

The cumulative peak power of high-power laser systems worldwide is shown in Figure 19. In green colour are those that are operational, and in orange colour are those under construction (funded projects). Not shown are conceptual or proposed systems. Europe (including systems in Russia as they are geographically in continental Europe) and North America currently operate approximately the same amount of petawatts as Asia does. However, it can be clearly seen that both Europe and Asia are heavily investing in the installation of several laser systems with very high peak powers, while there is only one high-peak-power laser facility^[55] currently being commissioned in North America.

The increasing number of petawatt class lasers has also resulted in a significant increase in publications on science with petawatt lasers, as described in the recently published NAS Report for Opportunities in Brightest Light^[5], with topics mainly in the areas of secondary source generation, plasma physics and basic science. Practical applications of such petawatt-class-driven capability include the development of proton and ion sources for medical applications, including cancer diagnostics and therapy; high-flux neutron sources for neutron radiography, special nuclear materials detection and materials science; high-brightness X-ray/gamma-ray sources for non-destructive interrogation and evaluation, medical diagnostics, ultrafast imaging at the molecular and atomic level, and nuclear photonics; and electron particle accelerators for next-generation colliders. The prospect of these applications

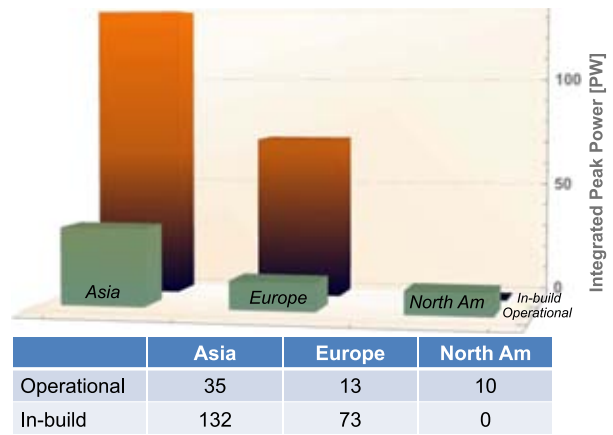


Figure 19. Cumulative peak power of operational (green columns) and in construction (orange columns) high-peak power (>0.1 PW) laser systems worldwide by area.

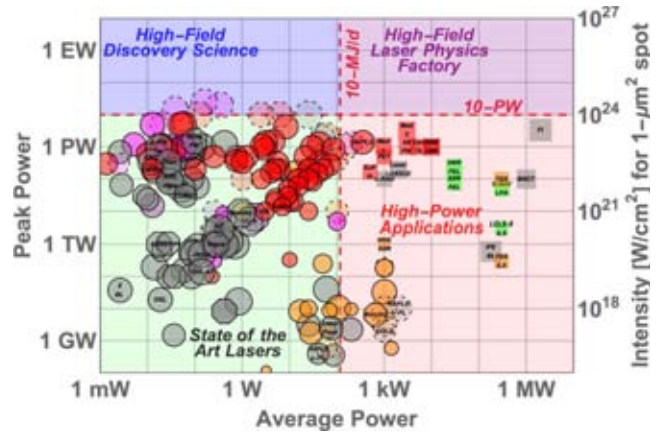


Figure 20. Peak power versus average power of high-peak-power, single-aperture laser systems and its primary pump lasers.

has been demonstrated in proof-of-principle experiments using low-repetition-rate lasers (e.g., high-resolution micro computed tomography^[49]). The ultimate realization of these applications will require petawatt class lasers with photon flux $10 \text{ MJ/day} < \text{flux} < 100 \text{ GJ/day}$, i.e., high repetition rates and higher average powers – beyond the ‘kW barrier’ to 10s of kW, and ultimately 100s of kW (Figure 20 quadrant ‘high-power applications’).

The peak power versus average power of high-peak-power, single-aperture laser systems and its primary pump lasers are shown in Figure 20. Key applications are indicated: a laser-plasma collider 300 kW unit cell (of which there would be ~200 in a TeV-scale collider); positron emission tomography (PET) radioisotope production, hadron and boron-neutron capture (BNCT) therapies; ion and neutron beams for radiography, non-destructive inspection and materials processing; high-harmonic generation (HHG) light sources;

laser-ablation-based space debris clearing; and inertial fusion energy unit cells (of which an IFE plant would require 100–200). Of particular note in this figure is the cluster of systems following a 45-degree upward path. These systems, predominately fusion laser architectures, scale both peak and average powers by scaling aperture and hence pulse energy at constant fluence. The four decades of sustained programmatic investments in fusion laser technology have brought innovations such as multi-beam operation, robust and aggressive thermal management, and novel materials to maintain scaling along this pathway. Future scaling along this well-travelled pathway will lead into the quadrant for applications at extreme peak powers.

An examination of the average powers of the operating and planned petawatt facilities across the world, shown in Figure 20, shows that average powers span from ~100 mW (notionally a kJ shot per hour), where a large amount of global follow-on petawatt capability exists, to state-of-the-art sub-kilowatt, with the operating ~75 W flashlamp pumped Ti:sapphire petawatt laser at the Colorado State University^[67], the ~50 W flashlamp pumped petawatt laser BELLA^[40], the 44 W SCAPA facility at the University of Strathclyde, UK^[88] and LLNL’s 500 W diode-pumped High-repetition-rate Advanced Petawatt Laser System (HAPLS) laser leading the pack^[41].

In fact, the high repetition rate (10 Hz) of the HAPLS system is a watershed moment for the community, as it reaches the point at which sophisticated feedback control systems, as opposed to the feedforward designs of the past, can optimize and maintain the spatial focusing and temporal compression of the laser output to near-diffraction-limit values. At repetition rates >5 Hz they allow for feedback from the sample or target itself (whether in an academic or industrial application) to dynamically optimize the laser system performance based on the end-product performance. Furthermore, the high repetition rate allows the laser system to stay in thermal equilibrium, and therefore offers unprecedented pulse-to-pulse stability. Attributed to its architecture and the diode pumping, HAPLS has already superior stability in pointing (<1 μrad) and energy stability (<0.6% RMS). These modern high-repetition-rate laser systems open up a new arena of precision that gives access to quantitative science.

Comparing the cumulative average power of petawatt class lasers installed and in construction across the world (Figure 21) to the cumulative intensity shown in Figure 19, reveals that Europe is investing strongly in high-average-power technology while Asia focuses its investments in achieving the highest peak power. Europe’s investments, mainly through its ELI (Extreme Light Infrastructure) projects, represent a massive increase in experimental productivity and a focus on development of high-intensity laser applications. Although the US’s LLNL developed the leading DPSSL HAPLS system for the ELI in Europe,

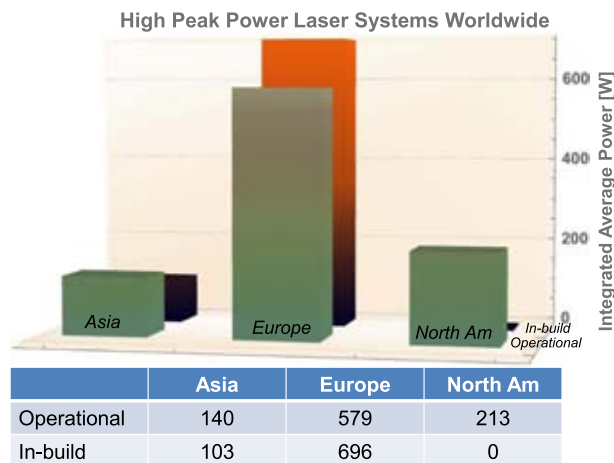


Figure 21. Cumulative average power of operational (green columns) and in construction (orange columns) petawatt class lasers (>0.1 PW) lasers across the world.

currently no other investments in US capability are known. This was also reflected in the NAS Report for Opportunities in Brightest Light^[5].

One of the most compelling applications is the realization of a laser-based free electron laser (FEL). FELs are unique X-ray light sources with unprecedented peak brightness, offering insights into matter, molecules, chemistry, biology and so forth, otherwise not accessible. Shrinking the electron accelerator (typically a few tens of GeV) from several kilometres down to a laser-driven plasma accelerator that occupies only a few metres in real estate would allow a dramatic cost reduction and enlarging the user base of these unique light sources^[45–47].

High-power lasers have, over the preceding five decades, illuminated entirely new fields of scientific endeavour, as well as made a profound impact on society. While the United States pioneered lasers and their early applications, it has been eclipsed in the past decade by highly effective national and international networks in both Europe and Asia.

4. Future technologies

In order to realize petawatt class laser facilities operating at ever shorter pulses, higher energies and higher repetition rates require advanced technologies to be developed. In this section we examine the various technologies which point the way to design these future systems. The section is broken down into three main subsections:

- Ultra-high-power development
- High-average-power development
- Enabling technologies.

4.1. Ultra-high-power development

The drive to deliver ever-increasing powers is driven largely by a desire to achieve ever-increasing intensities to target to achieve focused intensities $>10^{23}$ W/cm². At these focused intensities new regimes of physics could be realized. In this section we therefore examine various techniques which could be used to scale lasers to exawatt class facilities. Three techniques are discussed:

- The journey to 100 PW OPCPA systems
- Alternative 100 PW schemes
- Plasma amplifiers.

4.1.1. The journey to 100 PW OPCPA systems

OPCPA was first demonstrated by Dubietis *et al.*, at Vilnius University, Lithuania in 1992^[44] and the first practical designs for large-aperture systems to generate powers in excess of 10 PW and focused intensities $>10^{23}$ W/cm² were developed by Ross *et al.*, Central Laser Facility, UK^[158]. In this technique the frequency-doubled light from a high-energy Nd:glass laser facility is transferred to a chirped short-pulse laser via parametric amplification in typically BBO, LBO or KDP crystals, depending on beam aperture.

The first terawatt OPCPA laser was demonstrated at the Central Laser Facility in the UK by Ross *et al.* in 2000^[159] with a multi-TW OPCPA laser developed within SIOM's State Key Laboratory of High Field Laser Physics in 2002 producing 570 mJ in 155 fs, giving 3.67 TW^[135]. The limitation for these systems having a relatively long pulse was using KDP as the output crystal, for which the gain bandwidth is narrow.

Further progress towards scaling to the petawatt level was possible after the discovery of ultra-broadband phase-matching at 911 nm wavelength in DKDP crystal^[160]. Even though the difference between the refractive indices of DKDP and KDP is tiny, it drastically impacts the bandwidth of the parametric amplification. Based on this phenomenon, the first petawatt class OPCPA system was developed at the Institute of Applied Physics, Russian Academy of Sciences (RAS), Nizhny Novgorod. The laser, known as PEARL (Figure 22), delivered 0.2 PW in 2006^[116] and was upgraded to 0.56 PW in 2007^[117] using a homemade Nd:glass rod laser (300 J at fundamental wavelength) as a pump.

Later the FEMTA laser was built at the Russian Federal Nuclear Center in Sarov (Nizhny Novgorod region). The scheme was the same as PEARL but the final OPCPA amplifier was pumped by a 2 kJ Nd:glass slab laser LUCH^[161]. The output power was 1 PW (70 J in 70 fs)^[162].

The technique has now moved on with the demonstration, or plans to construct, multi-petawatt OPCPA lasers at a number of institutions in Europe, USA and China, described in the facility review section of this paper. The technique is



Figure 22. The PEARL OPCPA laser facility at the Institute of Applied Physics, Russian Academy of Sciences (picture courtesy of the Institute of Applied Physics).

scalable with plans to use it at several laboratories globally to generate powers of up to 200 PW.

At the Laboratory for Laser Energetics (LLE), University of Rochester, USA, technologies are being developed for using the OMEGA EP beamlines to pump an ultra-intense OPCPA system, called EP-OPAL (Optical Parametric Amplifier Line)^[154]. In this concept, two of the EP beamlines would be used to pump large-aperture DKDP amplifiers with a bandwidth at 920 nm sufficient for 20 fs pulses. The goal at full scale is to deliver two beams each with 30 PW to a target chamber for joint-shot experiments with picosecond and/or nanosecond pulses from the other two EP beamlines. A two-stage focusing scheme with an $f/4.6$ off-axis parabola and an ellipsoidal plasma mirror has been proposed for achieving intensities greater than 10^{23} W/cm². The technical challenges facing EP-OPAL are being addressed in a prototype system, MTW-OPAL, which is a 0.5 PW facility currently under construction to deliver 7.5 J, 15 fs pulses to target using the same all-OPCPA platform^[163]. The primary challenges being developed are, ranked by difficulty:

- (1) Advanced gratings; large-aperture DKDP; specialized optical coatings for large-aperture mirrors.
- (2) Wavefront control, adaptive optics, and two-stage focusing to maximize focused intensity.
- (3) Ultra-short-pulse laser diagnostics and broadband dispersion control.
- (4) Laser subsystem development including broadband front end and OPA gain adjustment.

A common feature of the exawatt scale (>200 PW) facilities is a requirement for coherent pulse combination as a means of generating sufficient power, due to the constraints of individual beam delivery. Precisely overlapping the ultra-short pulses in space and time is going to be extremely challenging. Random spatiotemporal phase noise in one

beam may cause the Strehl ratio of the combined focused pulse to decrease and the temporal contrast on target to degrade. Simulations indicate that phase noise on the beam with peak to valley (P-V) of $\lambda/4$ and $\lambda/3$ results in Strehl ratios of 0.9 and 0.8, respectively. They also show that the higher the frequency of the noise, the poorer the temporal contrast obtained after pulse combination. For high-frequency spatiotemporal phase noise, just $\lambda/5$ P-V could make the temporal contrast drop from 10^{30} (simulation limit) to 10^8 [164].

The original concept of ELI was for there to be a fourth pillar, to study ultra-high field science. This facility was to use a coherent superposition of up to ten 20 PW beamlines to produce 200 PW to target[46]. The facility is still on the agenda but is currently unfunded. All three of the existing pillars are contributing to high-power laser development or nonlinear conversion techniques to generate the baseline technologies to approach the 200 PW level and ultimately generate focused intensities $>10^{25}$ W/cm²[165]. In 2011, the Ministry of Education and Science of France organized the new international institute IZEST (International Institute for Zettawatt-Exawatt Science and Technology) to provide scientific and organizational support of projects aimed at developing exawatt power lasers and their applications.

At the Institute of Applied Physics of the Russian Academy of Sciences in Nizhny Novgorod XCELS (Exawatt Centre for Extreme Light Studies) was proposed as a megascience project. The design is based on phase-locking of 12 laser channels, each of them a copy of the PEARL laser upgraded by additional OPCPA amplification, each delivering up to 15 PW[166]. As a result almost 200 PW will be reached. A ‘double-belt geometry’ has been proposed, which for 12 beams provides an order of magnitude increase in focused intensity compared to the intensity generated when a single 200 PW beam is focused by an $f/1.2$ parabola[167]. It is anticipated that funding from the Russian government will be provided soon in order to start the XCELS project.

An ambitious project led by SIOM, Shanghai, China is the Station of Extreme Light (SEL, Figure 23). SEL is one of the end stations of SHINE (Shanghai High-repetition-rate XFEL aNd Extreme light facility), a hard XFEL currently under construction in Shanghai. The laser will use coherent beam combination generating four 30 PW pulses to deliver 1.5 kJ in 15 fs to target delivering 100 PW. The facility will come online in 2023, firing into a target chamber 20 m underground[140]. The facility is on the site beside ShanghaiTech University in the eastern part of downtown Shanghai, which will be the heart of the Shanghai Zhangjiang Comprehensive Science Centre.

The Institute of Laser Engineering, Osaka University, Japan has proposed a conceptual design of laser delivering 500 J in 10 fs (50 PW), named GEKKO-EXA. The OPCPA chain has three stages generating 1 PW, 10 fs at 100 Hz;

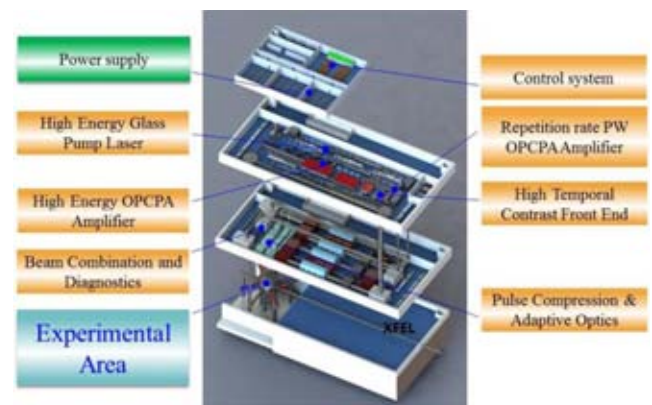


Figure 23. A schematic of the SEL (Station of Extreme Light) 100 PW laser facility under construction in Shanghai (picture courtesy of SIOM).

20 PW, 10 fs at 0.01 Hz and a final stage delivering 50 PW, 10 fs at a shot on demand. The concept is based on laser pumping of p-DKDP crystals, with the first stage pumped by a DPSSL, the second stage by a split disk amplifier producing 2.7 kJ in a sub-ns beam at 532 nm, and the third stage using one of the output beams of the LFEX facility generating 6.4 kJ in a sub-ns beam at 532 nm[168]. Although this concept is not funded yet, development of the major components for GEKKO-EXA is being undertaken at ILE.

To explore exawatt laser physics, a super-intense ultra-short laser project, named SG-II SuperX, is planned at SIOM, China. SG-II SuperX is a multi-beam high-efficiency OPCPA system pumped by the eight 2ω nanosecond beam-lines of the SG-II facility in four implementation phases.

- In phase 1, SG-II 5 PW, the single-beam OPCPA system pumped by the SG-II facility at partial capacity, is used to verify the feasibility of large-aperture efficient and stable OPCPA technology.
- In phase 2, the full capacity of two SG-II beamlines will be used for pumping two OPCPA beams to demonstrate high-power ultrafast coherent beam combining (CBC) technology. The two OPCPA beams will be compressed, coherently combined and focused onto target, yielding 35 PW (350 J/10 fs) peak power and 10^{23} W/cm² focused intensity.
- In phase 3, SG-II facility could be upgraded to deliver 1.8 kJ IR per beam. Two beams will be used to pump early OPCPA stages and six beamlines used to boost the final OPCPA stages of six SG-II SuperX beams. On target, 250 PW (2.5 kJ/10 fs) peak power will be obtained and greater than 10^{24} W/cm² focused intensity will be achieved.
- In the last phase, the OPCPA and CBC techniques can be applied, in principle, to scale up SG-II SuperX system into an exawatt class laser.

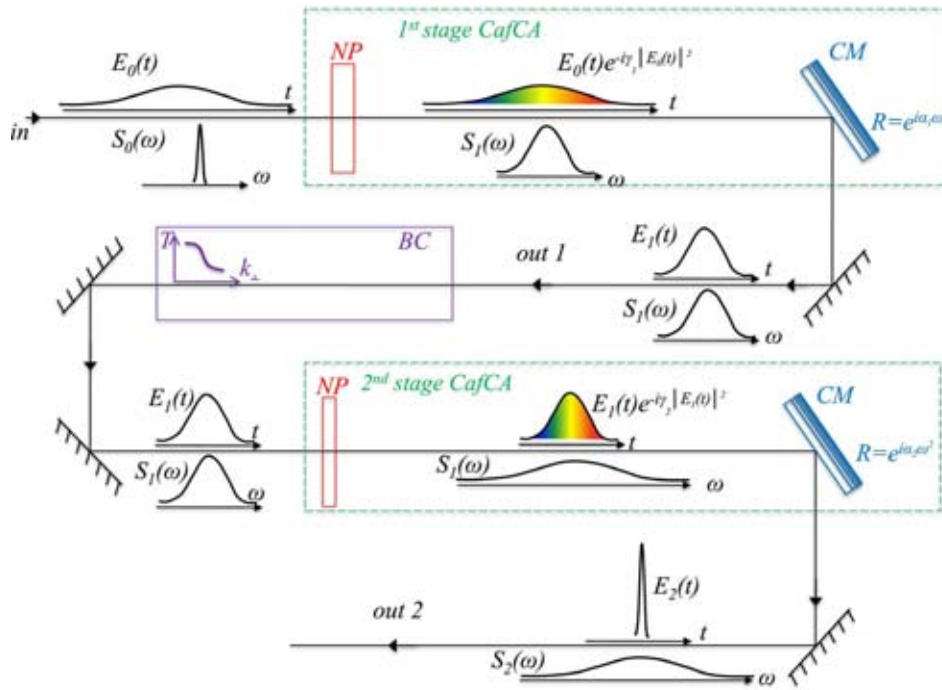


Figure 24. Diagram illustrating the Compression after Compressor Approach (CafCA) (NP – nonlinear plate, CM – chirped mirror, BC – beam cleaner: pinhole spatial filter^[173] or free-space propagation^[174]).

The next decade will see a dramatic increase in development work across the globe for the delivery of >100 PW systems, together with the SEL project expected to come online in 2023. These facilities will open up a new regime in discovery science as focused intensities in excess of 10^{23} W/cm² could be realized. To achieve 100 PW operation of future systems with modest energies, researchers are also endeavouring to reduce the pulsewidth of these lasers towards the single-cycle limit^[169].

4.1.2. Alternative >100 PW schemes

In the previous subsection we discussed the generation of >100 PW using OPCPA as the principal technique. There are also proposals for the generation of this type of pulse using alternative techniques.

4.1.2.1. Compression after Compressor Approach (CafCA).

The main limitation of laser power is the damage threshold and physical size of diffraction gratings. It is not possible to increase the pulse energy after grating compression, but laser power may be increased by pulse shortening. The technique described here is called Compression after Compressor Approach (CafCA) and is based on spectral broadening by self-phase modulation (SPM) in nonlinear plates and eliminating the spectral phase through chirped mirror(s). This idea has been successfully used in mJ pulse energy systems since the 1980s, but power scaling was limited by the aperture of gas-filled capillaries and self-focusing.

In 2009 Mironov *et al.*^[170] proposed a scheme to overcome this limit by using large-aperture nonlinear crystals

instead of capillaries. In recent years CafCA was demonstrated with crystals, glasses, or plastics, in which the most powerful experiment to date was carried out where a 100-mm-diameter 5.5 J pulse was compressed from 57 fs to 22 fs^[171]. At the PEARL laser, Institute of Applied Physics, Russian Academy of Sciences, a pulse with an energy of 17 J was compressed from 70 fs to 14 fs^[172].

The most detailed numerical studies^[173] have shown that the laser power may be increased by a factor of 27 in a single-stage CafCA. In this paper nonlinear phase B was accumulated up to value of $B = 48$. To avoid small-scale self-focusing the beam was cleaned by eight pinhole spatial filters placed in between nine nonlinear elements with $B = 5.3$ in each. This challenging design may be simplified to a practical level by suppression of self-focusing via beam free-space propagation which was proposed and experimentally confirmed in 2012 by Mironov *et al.*^[174], or a multistage CafCA approach as shown in Figure 24. The advantage of multistage CafCA is clearly seen from the simple formulae showing how many times the pulse power may be increased over a single-stage CafCA: $P_{\text{out}}/P_{\text{in}} = 1 + B/2$ ^[175]. According to it $P_{\text{out}}/P_{\text{in}} = 3 \times 3 \times 3 = 27$ may be reached by only three-stage CafCA, with a conservative value $B = 4$ in each stage.

In pulse duration, CafCA is limited by the single-cycle pulse, roughly an order of magnitude shorter than current CPA and OPCPA limits. In energy CafCA is limited by the laser-induced damage threshold of the chirped mirrors,

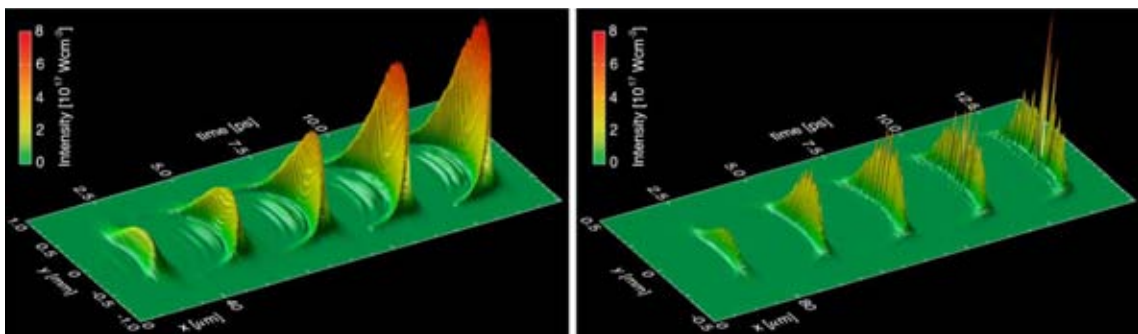


Figure 25. Comparison of Raman amplification for two different parameter configurations, to demonstrate the importance of controlling long-wavelength laser-plasma instabilities. The results displayed are based on numerical simulations originally by Trines *et al.*^[183].

which is much higher than the current grating damage threshold^[176, 177]. CafCA could drastically increase the power of any laser from terawatts to tens of petawatts.

4.1.2.2. Nexawatt. Currently, scaling of petawatt lasers to higher pulse energy and peak powers is limited by several things: intensity-dependent damage thresholds of post-compression and final focusing optics, insufficient stretched pulse durations needed to avoid damage to amplifier and transport optics, and a lack of pre-amplifier bandwidth to support shorter pulse durations.

The Nexawatt concept^[178] proposed at the Lawrence Livermore National Laboratory, US relies on extracting the full potential of the disc amplifiers of a NIF or NIF-like beamline (~ 25 kJ) but using a novel compressor design to confine this energy to a 100 fs pulse, producing pulses with peak powers of over 200 PW. This could be achieved using a typical four-grating compressor; however, two of the gratings would require apertures of 4.5 m. To avoid this, a six-grating compressor design is proposed utilizing gratings with a more achievable 2 m aperture manufactured by stitched lithographic exposure.

The existing main amplifiers do not require any changes to achieve 25 kJ output; however, significant work to the pre-amplifier sections of the beamline must be done to include optical parametric and Nd:silicate amplification stages. This will provide the necessary joule-level seed energy and bandwidth required to support the amplification of 100 fs pulses.

Damage to final optics is avoided by increasing beam area via splitting the beam prior to compression and then coherently recombining the beams prior to focusing, where peak intensities of 10^{26} W/cm² are anticipated.

4.1.3. Plasma amplifiers

Raman (and later Brillouin) scattering was first discovered in solid-state physics^[179] and also found applications in gases and molecular vibrations as well as nonlinear optics. Raman amplification is a pulse compression technique based on Raman scattering^[180]: a long pump pulse with a frequency ω_0 interacts with a short signal pulse with frequency $\omega_1 < \omega_0$ in a medium with characterizing Raman frequency ω_R , and

frequencies are chosen such that $\omega_0 = \omega_1 + \omega_R$. Since the bandwidth of the signal pulse is determined by the growth rate of the Raman scattering process, it can be much larger than the bandwidth of the pump pulse, so the signal pulse can be much shorter than the original pump pulse. If Raman amplification is then carried out in a regime where the pump pulse is significantly depleted, so a significant fraction of its energy ends up in the signal pulse, then the signal pulse's intensity after amplification can be orders of magnitude larger than the original pump pulse intensity. While Raman scattering has been used widely in fibre optics, solid media are not suitable for Raman scattering at truly high powers because of their inherent damage thresholds. For this reason, plasma-based compression and amplification of laser pulses via Raman or Brillouin scattering has been proposed^[181, 182].

Numerical simulations of Raman and Brillouin amplification have been performed using a multitude of models. Examples of Raman amplification modelling are shown in Figure 25, which shows a comparison of Raman amplification for two different parameter configurations, to demonstrate the importance of controlling long-wavelength laser-plasma instabilities^[183]. The left panel shows Raman amplification of a 700 μm FWHM diameter signal pulse in a 2D particle-in-cell (PIC) simulation. Shown here are snapshots of the growing probe pulse ($\lambda = 844$ nm). The x and y scales refer to the local coordinates of the probe pulse itself, and the 'time' scale refers to the probe propagation time. The final probe FWHM intensity, power and duration are 2×10^{17} W/cm², 2 PW and ~ 25 fs after 4 mm interaction length. The energy transfer efficiency is about 35% and the amplified probe has a mostly smooth intensity envelope, as the reduced plasma density ($n_0 = 4.5 \times 10^{18}$ cm⁻³ or $\omega_0/\omega_p = 20$) keeps the probe filamentation in check. The right panel shows Raman amplification of a 350 μm FWHM diameter signal pulse at a plasma density of $n_0 = 1.8 \times 10^{19}$ cm⁻³ or $\omega_0/\omega_p = 10$, all other parameters as in the left frame. For this higher density, uncontrolled filamentation severely compromises the pulse envelope.

In addition to Raman scattering, Brillouin scattering can also be used to amplify and compress laser pulses in plasma

(Brillouin amplification). In order to reach high powers and intensities, Brillouin amplification will take place in the so-called ‘strong coupling’ regime, where the ponderomotive pressure by the EM fields dominates over the thermal pressure of the plasma electrons. The principles of the Brillouin amplification process in plasma have been developed by Andreev *et al.*^[184] and later by Lehmann and Spatschek^[185, 186], and show that it is similar to Raman amplification, even though the scaling is different.

The differences between Raman and Brillouin amplification can be summarized as follows. Raman amplification will achieve the highest intensities, powers and pump-to-signal compression ratios, but requires the frequencies of pump and signal to be separated by the plasma frequency, a separation which depends on the plasma density and may be difficult to achieve in experiments. It is therefore more sensitive to fluctuations in the laser and plasma parameters. Brillouin amplification achieves lower intensities, powers and pump-to-signal compression ratios, but the frequency difference between pump and signal is usually smaller than the signal pulse bandwidth. This means that pump and signal pulses can have the same carrier frequency and thus be generated by the same laser source, making Brillouin amplification experiments easier to design and less sensitive to laser and plasma parameter fluctuations.

Numerous plasma-based Raman amplification experiments have been conducted since the publications by Malkin, Shvets and Fisch^[182] in the late 1990s. Three main campaigns can be highlighted: at Princeton; Livermore; and Strathclyde. Furthermore, there is a campaign to demonstrate Brillouin amplification in plasma by a group at LULI.

The work at Princeton culminated in an experiment by Ren *et al.*^[187], in which a short seed pulse was amplified to an intensity of 2.5×10^{16} W/cm², at 50 fs FWHM duration and 15 μ m FWHM spot diameter, using a pump pulse at 1.5×10^{14} W/cm², 20 ps FWHM duration and 50 μ m FWHM spot diameter. This is the only experimental campaign that provides good temporal and transverse envelope characterization of the amplified signal pulse, so the absolute amplification and compression of the signal pulse can be assessed properly. Again, this experiment showed good amplification of the peak pulse intensity, while this was not matched by a similar increase in total pulse power or energy, mainly because the spot diameter of the seed pulse was much smaller than that of the pump pulse.

The Livermore experimental results report^[188–190] significant ‘spectral amplification’, which is roughly defined as the spectral intensity of the amplified seed divided by that of the initial seed, measured at the Raman backscattering frequency $\omega_0 - \omega_p$, where ω_0 and ω_p denote the pump and plasma frequencies, respectively. However, these experiments cannot be seen separately from the investigations by Kirkwood *et al.* into energy exchange by crossing laser

beams, which started in 1997 and continues into the present day^[191]. The pump-to-signal energy transfer efficiency as measured in these experiments is at or below the 1% level.

The Strathclyde campaign on Raman amplification has been backed up by theoretical and numerical work^[192, 193]. The experiments report high levels of spectral amplification^[194–196], while the pump-to-signal energy transfer efficiency usually hovers around the 1% level.

At LULI research on Brillouin and Raman amplification has consisted of a number of experiments. The early experiments showed significant spectral amplification but the pump-to-signal energy transfer was limited to only 0.1%–0.3% of the total pump energy^[197, 198]. In a more recent milestone experiment laser amplification of subpicosecond pulses above the joule level was demonstrated with a new record for efficiency ($\sim 20\%$)^[199].

On the whole, Raman amplification in plasma has been more successful in theory^[182, 184] and simulations^[183, 200, 201] than even in the best experiments^[187, 197]. This is in contrast to Raman experiments in fibre optics, where this technique is used routinely nowadays^[180]. In particular, the efficiency of plasma-based Raman amplification has to be increased drastically. This can only be achieved if Raman amplification can be maintained over longer interaction distances and larger spot diameters, and future experimental effort will have to concentrate on this. Also, experimental effort needs to move away from maximizing spectral ‘gain’ via reducing the energy content of the initial signal pulse, since this will not lead to any improvement in absolute output power and energy, which are the two yardsticks by which true performance of any laser amplifier needs to be measured.

Furthermore, novel laser amplification techniques such as OPCPA^[174] or diode-pumped solid-state lasers^[202] are threatening to overtake even the theoretical predictions for Raman amplification for near-infrared laser pulses. Thus, Raman amplification needs to find new niches where these competing techniques are not strong:

- (i) scalability to other wavelengths;
- (ii) scalability of signal pulse parameters with pump intensity and duration; and
- (iii) amplification of higher-order laser modes, rather than just Gaussian.

The nature of the Raman backscattering instability allows it to be scaled in various ways. First of all, it can be scaled to various wavelengths, to allow the amplification, for instance, infrared light (for example, the third harmonic of a 1054 nm laser at 351 nm)^[200] or coherent X-ray pulses^[203–205], something that would be hard to achieve using conventional methods. Second, the scaling of the seed pulse duration with pump laser intensity and interaction distance can be exploited to design a tunable Raman amplifier, where the

duration of the amplified signal pulse can be controlled via the pump laser parameters^[200], allowing access to a regime of signal pulse parameters often unavailable to conventional solid-state amplifiers.

Finally, Raman amplification can be used to amplify higher-order laser modes (for example, Laguerre–Gaussian or Hermite–Gaussian). The nonlinearity of the Raman process can be exploited to: (i) create new modes from old ones^[206] and (ii) drive cascades of modes, where a large number of higher-order modes can be generated using just a few lower-order modes in the initial pulses^[207]. These features are not commonly available in present-day solid-state amplifier systems.

4.2. High-average-power development

The petawatt facilities described in Section 2 of this review operate at relatively low repetition rates, generally limited to sub-Hz operation, with only relatively recent facilities able to achieve multi-Hz operation at petawatt power levels. Experiments using these facilities have therefore been limited to fundamental science and proof-of-principle applications. As these experimental techniques have matured, there is a drive to deliver these systems for real-world applications. As can be seen from Figure 20, envisioned applications (shown with rectangles) require average power levels of a few kilowatts to megawatts, with peak power levels of ~ 100 TW to 1 PW. Getting both high-peak and high-average powers simultaneously is therefore becoming increasingly important. Indeed, the first particle acceleration demonstrations^[208] relied on petawatt laser systems with relatively low repetition rates (1 Hz) like BELLA at LNBL, USA^[209], that were energized by multiple, aperture-combined flashlamp pumped Nd:YAG lasers. The HAPLS laser developed by LLNL for ELI-Beamlines is the highest average power diode-pumped petawatt laser capable of delivering up to 300 W of average power for user experiments. However, future particle accelerators would require the laser to operate at repetition rates orders of magnitude higher to reach the hundreds of kW average power requested (see Table 25 in paper by Leemans^[210]). In this section we look at techniques which are making significant advances in the development of systems to deliver high-average-power capabilities:

- HAP gas-cooled architectures
- Scaling petawatt class lasers beyond 10 kW
- Cryo-HAP laser development
- Coherent beam combining
- Time-domain pulse combining
- Temperature-insensitive OPCPA.

4.2.1. HAP gas-cooled architectures

The general recipe for making high-average-power lasers is to significantly reduce the laser gain medium heat intake and optimize the extraction of heat. Furthermore, operating the laser amplifier in a steady-state regime becomes important for stability, repeatability and management of thermal stress in the amplifier. Typical heat-induced, deleterious effects resulting on the system are stress-induced birefringence, thermal lensing or thermo-optic distortion.

Flashlamps energize most of today's Nd-doped pump lasers and are feasible for pumping Ti:sapphire-based petawatt lasers up to 0.1 Hz. Only a fraction of the flashlamp's broadband optical emission is used for optical inversion in the pump laser's gain medium; the other part is directly lost into heat in the amplifier medium. Furthermore, the spectrum from the UV to IR results in a varying loss due to the quantum defect of the gain medium. Therefore, if the repetition rate is increased beyond 0.1 Hz, aperture combining is necessary (i.e., the flashlamp induced heat is distributed over multiple rod amplifiers, effectively increasing the surface area to extract heat). Hence all flashlamp-pumped lasers with repetition rates >0.1 Hz use this technique. However, scaling the repetition rate beyond a few Hz significantly increases the complexity of the system and the electrical power consumed becomes prohibitive (e.g., BELLA at 1 Hz consumes ~ 200 kW of electrical power, including all systems and cooling, for 45 W of optical output).

Therefore, pumping the laser gain medium in its absorption band with a narrowband source such as laser diodes is preferable. Almost all of the optical energy is absorbed – hence only the quantum defect and ASE losses must be accounted for. The electrical-to-optical efficiency for laser diodes is $\sim 60\%$; therefore, replacing the flashlamps with diodes in a Ti:sapphire petawatt laser system leads to a thirteen times increase in efficiency, or the possibility to run the laser system thirteen times faster with a similar heat load.

The second technology advancement required for average power is the removal of heat. Typically, heat is removed through the edges of the amplifier gain medium, resulting in stress patterns perpendicular to the beam propagation direction, and therefore to large distortions. LLNL pioneered the gas-cooling technique in the early 1980s where heat removal is achieved through face-cooling the amplifier with room-temperature helium gas travelling at ultrasonic speeds. In this case the heat gradient is along the beam propagation axis, resulting in minimal distortions. The first high-energy demonstration of this technique was realized in the Mercury laser system^[63], which delivered at its time a record average power of 650 W with 65 J/pulse in the first harmonic, and 225 W from a large YCOB crystal in the second harmonic with $\sim 50\%$ conversion efficiency with a repetition rate of 10 Hz. The Mercury team won 3 R&D100 awards for its innovations. The gas-cooling technique has been successfully adopted by several groups worldwide and extended to cryogenic gas cooling of laser gain materials.

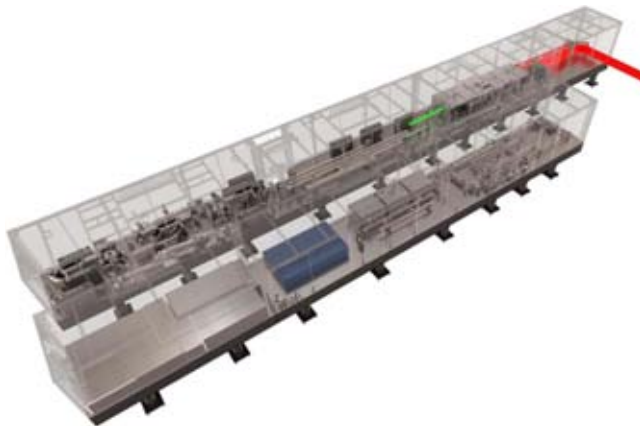


Figure 26. The HAPLS laser is compact and only 17 m long and 4 m wide. The power amplifiers that use helium gas cooling are on the rear table and the front ends are on the front table.

The HAPLS pump laser, shown in Figure 26, is an extension of the Mercury technology. Initially designed for an inertial fusion energy power plant driver^[211], LLNL downscaled their 8 kJ two-head design to a 200 J, DPSSL Nd:glass gas-cooled system, enabling the production of a pump laser pulse from a single aperture at 10 Hz. The power amplifier consists of two amplifier heads that are pumped by four High-Power Intelligent Laser Diode Systems (HILADS), jointly developed by LLNL and Lasertel Inc. Each HILADS provides ~ 800 kW peak power per diode array in a 300 μs pulse width at repetition rates up to 20 Hz and in a 5.6 cm \times 13.8 cm beam. HILADS is the highest-peak-power and brightest pulsed diode light delivery system in the world. The optical-to-optical efficiency is approximately 21%, therefore significantly reducing the heat intake into the amplifier slabs compared to flashlamps. A solid-state edge cladding is used to minimize parasitic amplified spontaneous emission.

A similar technique noteworthy is the thin-disk technology, where conductive cooling through the back-surface of the laser gain medium is achieved. However, the thickness of the disk must be kept small (< 300 μm) so that stress effects do not set in. Hence, the energy storage of such media is typically less than 1 J and unsuitable for high-energy applications.

4.2.2. Scaling petawatt class lasers beyond 10 kW

Scaling the technology of high-peak power lasers to higher average power while maintaining key technological performance requirements is challenging. Operating petawatt class lasers beyond 10 kW average power requires a paradigm shift in laser design. To date, average power increase has been accomplished by scaling: increasing the repetition rate of single-shot laser architectures, in which each shot represents a complete pump/extraction cycle. A new scheme developed by LLNL is multi-pulse extraction (MPE) and is illustrated in Figure 27. In this scheme the gain medium

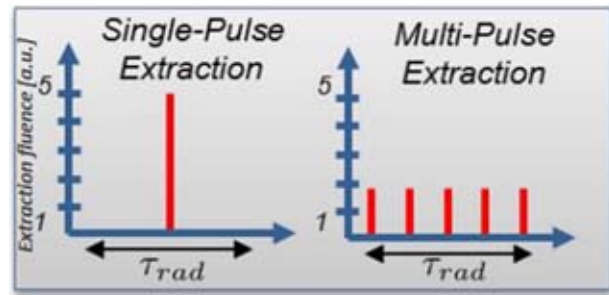


Figure 27. In MPE mode, the same stored energy is extracted from the gain medium over multiple, low-fluence pulses versus extracting the energy in a single, high-fluence pulse. The extraction time in the MPE mode must be less than the storage lifetime.

is pumped continuously, and the upper-state population is extracted over many pulses during the radiation lifetime, allowing access to laser gain media with: long radiation life times; extremely high saturation fluences; and broadband gain spectrum. Hence the method has three primary benefits.

- There is no need to pump within a single inverse lifetime, and therefore more efficient, much cheaper CW pump sources can be used that deliver the pump energy over a longer time.
- Because efficient extraction is not necessary in a single pulse, the extraction fluence is much reduced in the corresponding nonlinear phase as well.
- Broadband gain media that can be directly pumped by diode become accessible, therefore reducing the number of stages, the overall system complexity, and the number of loss stages.

MPE requires that the gain material has an inverse lifetime significantly less than the desired repetition rate. LLNL conducted a study with over 80 known laser gain media and analysed their suitability for maximum net efficiency, for laser diode pumping (long upper-state lifetime) and for lasing properties consistent with achieving high-peak power operation (100 TW to multi-petawatt).

As shown in Figure 28 (left) thulium (Tm)-doped gain media offer significant lifetime advantages over the well-established Yb-doped materials traditionally used for diode-pumped fibre and bulk systems. Thulium MPE becomes efficient at repetition rates $> 3\text{--}5$ kHz (see Figure 28 right). In comparison, ytterbium materials require repetition rates $> 50\text{--}100$ kHz to operate efficiently or must be cryo-cooled. To be relevant for sub-100 fs applications, the gain bandwidth of thulium in the chosen laser host material must be > 50 nm, which is satisfied by most of the host materials.

These considerations led to choosing Tm:YLF as the laser amplifier medium for a laser concept termed big aperture thulium (BAT) laser^[212, 213], shown in Figure 29, consistent with the requirements for secondary source generation, and

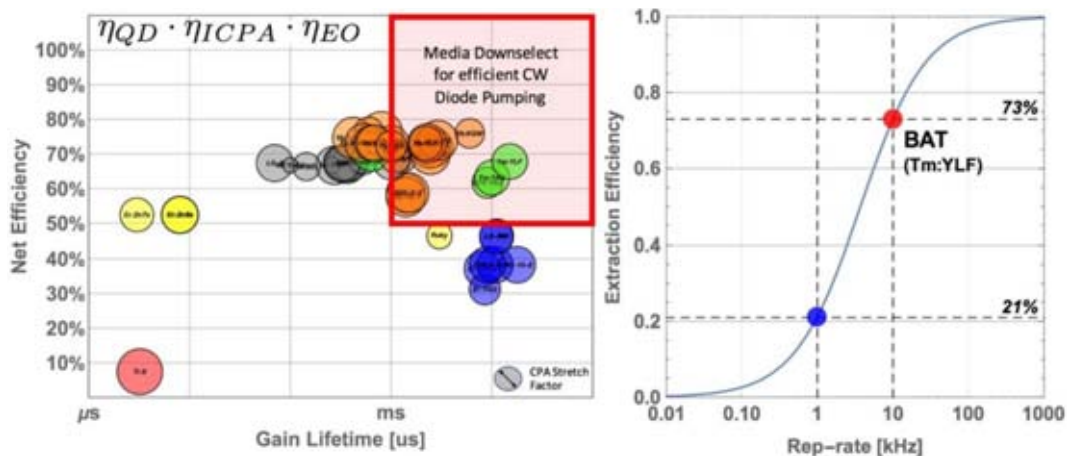


Figure 28. Left: Net efficiency (quantum defect \times indirect CPA efficiency \times electro-to-optical efficiency) versus gain lifetime of various laser gain media. For the Ti:sapphire case, η_{ICPA} is 0.38 while for the other cases, which use direct CPA designs, η_{ICPA} is unity. Laser media were down-selected for net efficiency ($>50\%$) and diode pumping suitability (gain lifetime >1 ms). Right: Extraction efficiency (stimulated emission rate divided by the sum of stimulated emission rate and spontaneous decay rate). In multi-pulse extraction, higher repetition rates (while maintaining the extraction fluence) are beneficial to the overall wall plug efficiency, i.e., the repetition rate determines the overall wall plug efficiency.

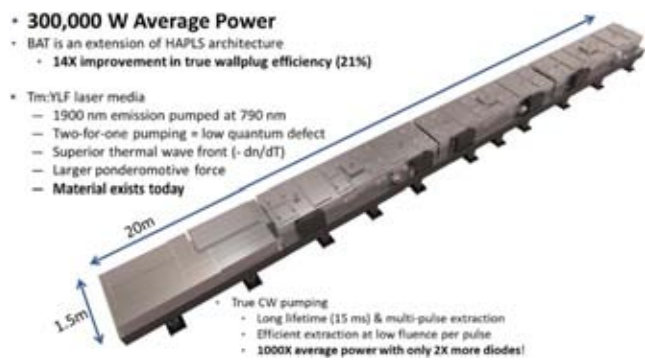


Figure 29. LLNL’s BAT laser is envisioned to be capable of delivering up to 300 kW of 10 kHz, 30 J, 100 fs laser pulses.

specifically for an efficient laser for driving a laser wakefield accelerator (LWFA). The facility will deliver 300 kW at 30 J per pulse, but provides inherent through aperture (energy) and repetition rate (average power) flexibility for a variety of applications. For example, a 3 TW/1 MHz configuration would be of great interest for future high-repetition-rate X-ray FELs. Notably, higher wall-plug efficiencies can be achieved at the greater repetition rates.

The BAT system leverages the HAPLS baseline two-head helium gas-cooled four-pass amplifier design. It amplifies the short pulse directly in the primary laser chain using CPA, avoiding laser-pumped-laser architectures using indirect CPA (diode pumping of the pump laser) that have significantly higher energy loss inherently. Therefore, BAT can operate at electrical-to-optical efficiencies $>30\%$ and true wall-plug efficiencies of $>20\%$. It can be directly pumped by commercially available, standard and inexpensive CW laser diodes at ~ 800 nm, making use of the 2-for-1 excited state quenching in thulium, eliminating the need for an

additional laser system to deliver pump light to the final amplifier. Furthermore, through a cross-relaxation process it is possible to excite two thulium ions with a given pump photon, decreasing the effect of the quantum defect.

Operating directly at 2 μm , BAT operates at reduced accumulated nonlinear phase retardation, or B-integral, which scales as $1/\lambda^2$. Together with the wavelength scaling, the low-gain BAT architecture maintains a total B-integral <0.1 in the amplifier. This low total B-integral, together with the relay-imaged architecture, produces high stability and high beam quality, and contributes to maintaining the high contrast of the front end through the power amplifier. The BAT laser is truly a CW laser: at any given time, there is more energy stored in the laser than extracted; hence the underlying laser and material physics are steady-state and continuous. This transition from pulsed operation to CW has already been exploited in high-average-power fibre lasers for many years.

Significantly, key operating performances of a full-scale (300 kW) BAT can be effectively anchored on the performance of a ten-times-downscaled prototype BAT laser (miniBAT = 30 kW), with lower pulse energy and average power but identical fluences and identical thermal loading per unit area.

In addition to the desired petawatt class secondary source applications, the scalability of the system to higher pulse energy and average power at 2 μm also presents opportunities for additional applications in medicine, non-destructive evaluation, radiation testing, machining and other applications. Development of these new, very high average power technologies is underway at NIF&PS Advanced Photon Technologies Program.

4.2.3. Cryo-HAP laser development

Cryogenic high-average-power (cryo-HAP) laser development is a proven route to meeting the demand for systems that can operate at high average powers while maintaining high energies, a prerequisite for a petawatt class laser system.

Cooling the gain media to cryogenic or close to cryogenic temperatures is a long-standing method for improving a number of critical parameters, including the thermal conductivity^[214, 215] and absorption and emission cross-sections^[216, 217]. In 1998 Fan *et al.* reported^[218] on the improved properties of the then relatively new material, Yb:YAG, operating at cryogenic temperatures. These improvements were discussed between Yb:YAG operating at 300 and 100 K, and included a four-fold increase in thermal conductivity, reducing thermal lensing and stress-induced birefringence; in fact, they estimated that a system operating at 100 K possessed similar thermo-optic properties to one operating at 300 K, but at 1/15 of the average power. Yb:YAG operates as a quasi-3-level laser at 300 K due to the high population of its lower laser level. At cryogenic temperatures the population in this lower level is significantly reduced, resulting in cryogenic Yb:YAG operating as a 4-level laser, reducing the lasing threshold, another significant benefit.

All of these benefits have resulted in a number of groups working on cryo-HAP laser systems based on differing amplifier architectures. For the purposes of this discussion we will define cryo-HAP systems as those that possess the potential to act as a pump or could be scaled to a level suitable for higher-average-power petawatt class operation, and therefore can operate ≥ 1 J and ≥ 10 Hz. The number of systems operating at these levels is not vast, with only a handful of successfully reported systems operating in this arena; the three architectures that have proven successful in this field are active mirror^[73], the so-called TRAM^[219] (total reflection active mirror) and multi-slab-based systems^[220].

Active-mirror and TRAM systems typically populate the lower-energy space in this field, with energy currently limited to ~ 1 J. The active-mirror system is based on thin-disc laser architecture but uses a thick (~ 5 mm) disc that is longitudinally cooled by liquid nitrogen flow across the rear face. This design has been shown capable of operation at 1.5 J, 500 Hz^[68] in a CPA-based scheme producing 5 ps pulses. The system was later tested at 1 J, 1 kHz^[221]; however, at this power level thermal effects dominated, and resulted in a loss of energy after a short period of time. Further work aims to manage this increased thermal load and further scale the average power. The exception to the low-energy trend for active-mirror systems is the LUCIA laser system which is under development at LULI in France. This uses a cryogenically cooled active-mirror design and has been successfully operated at 14 J, 2 Hz^[222].

The TRAM design was proposed in 2009^[219] as an extension to the active-mirror scheme that sees a thin (~ 200 μm)

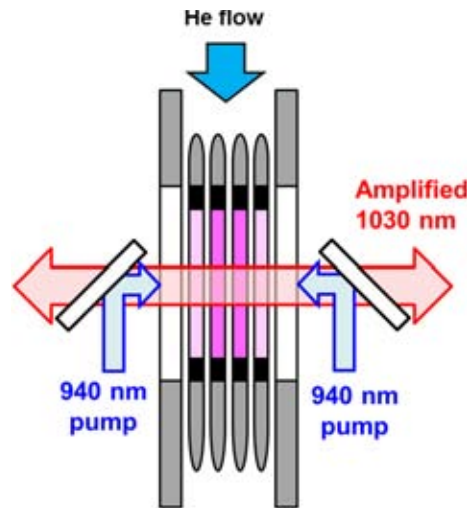


Figure 30. Schematic of the DiPOLE cryo-amplifier concept. Graded index Yb:YAG ceramic slabs are cooled to cryogenic temperatures (150 K) using a high-pressure, high-speed cryogenically cooled helium flow.

layer of Yb:YAG bonded to a trapezoidal undoped YAG prism. The pump and laser light enters the anti-reflection-coated side of the prism and is totally internally reflected at the rear face of the Yb:YAG layer, removing the requirement for a high reflective coating that could become damaged by higher-power operation. As with the active-mirror design, the TRAM is cryogenically cooled directly on the rear face of the Yb:YAG substrate. The TRAM architecture has been reported to operate at 1 J, 10 Hz with a design upgrade to 100 Hz operation well underway^[223]. It is to be used as part of the front end system for the GENBU laser concept developed at ILE, Osaka University in Japan^[224].

To date, the highest reported energy from a cryo-HAP system has been achieved using multi-slab architectures. Of these the DiPOLE 100 system produced by the UK's Central Laser Facility is currently the only one to achieve 1 kW operation, with 100 J pulse energies at 10 Hz^[224]. DIPOLE uses ceramic Yb:YAG amplifier slabs. A general schematic of the interior of the DiPOLE cryo-amplifier head is shown in Figure 30. The gain media slabs are mounted in aerodynamic titanium vanes and housed within a vacuum insulated pressure vessel. The doping concentration of the slabs is graded to provide uniform absorption of the pump energy, resulting in a uniformly distributed thermal load. High-pressure cryogenically cooled helium gas at 150 K flows over the slabs to remove the waste heat.

The PENELOPE laser also uses the He-gas-cooling architecture for cryogenic cooling in its main amplifier^[111]; however, as it is designed as a CPA system the gain media of choice must support a broad bandwidth. As a result Yb:CaF₂ is used in place of Yb:YAG and the system is not cooled below 200 K in order to preserve bandwidth. It should be noted that PENELOPE's design repetition rate is 1 Hz but is included here as by itself is a petawatt class system.

Hamamatsu Photonics has also reported on the successful operation of a 100 J class narrowband multi-slab system^[225]. The main amplifier uses Yb:YAG slabs that are edge-cooled by two cryostats above and below the gain media. This system has achieved output energies of 55 J but is currently not operating at its design repetition rate of 10 Hz.

It should be noted that there are examples of high-average-power systems operating at high pulse energies that do not operate at cryogenic temperatures. The most notable examples are the HAPLS system^[226] developed by LLNL and the POLARIS system^[41] at Jena.

To date, the highest reported performance of a cryo-HAP system is operation at the 1 kW level. This has been achieved by an active mirror, at low energies, and a slab system at high energies. If we consider that a high-average-power petawatt class system would require at least tens of joules of energy then the likely candidate for further increases in average power is the slab-based architecture. Such development work has already started at the Central Laser Facility, on a collaborative project with the HiLASE Centre, Czech Republic to increase the repetition rate of DiPOLE systems to 100 Hz. This would be at the 10 J level, with a view to future scaling of the energy where practicable. Such a system would be capable of driving a short-pulse laser at the 100–200 TW level at 100 Hz.

To summarize, gas-cooled HAP laser systems are already operating well above what flashlamp systems can provide and, in the coming years as the technology matures, they will be capable of significantly increasing the average power.

4.2.4. Coherent beam combining

To achieve both high-peak and high-average powers simultaneously might become a reality thanks to a relatively recent^[227] laser architectural approach called coherent beam combining (CBC). Although underlying advanced technology is necessary, the CBC concept can be described in quite simple words: it basically consists in the spatial splitting of an initial laser beam into N sub-beams prior to amplification, followed by subsequent recombination of the amplified beams. The very large majority of ongoing laser physics research in CBC relies on fibre-based amplifiers. Indeed, the high geometrical aspect ratio of such amplifiers makes it a solution of choice for high-average-power operation requiring extremely efficient thermal management. Fibre-based CBC allows the distribution of power scaling challenges across multiple optical channels to overcome different physical limitations such as average power-related effects like mode instabilities^[228, 229], but also nonlinear pulse-energy- and peak-power-related effects.

To date, the highest peak power (~ 45 GW) was achieved by the IAP-HIJ, Jena, Germany team: 12 mJ pulse energy with 700 W average power and 262 fs pulse duration have been obtained with eight parallel channels and four temporal pulse replicas^[230]. Recently^[231], the same team presented operations at about 2 kW average power with 16 channels

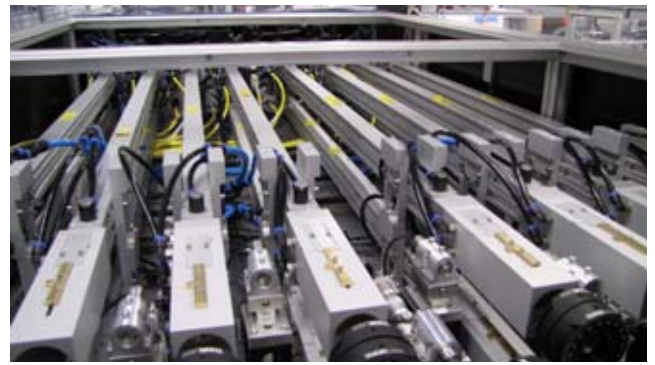


Figure 31. Jena 16-channel filled aperture system.

(2.3 mJ) (Figure 31). Future activities will consider a 32-channel system, also relying on rod-type large-pitch fibre amplifiers^[232]. In addition, a four-channel ytterbium fibre femtosecond CPA system with 3.5 kW average power has been demonstrated^[233]. These performances have been achieved through a filled-aperture configuration, a near-field combination approach allowing a high efficiency (theoretically 100%, in most demonstrations well above 90%) but involving multiple combining elements in cascade, so that the system complexity increases with the number of fibres, somewhat limiting its scalability potential. To overcome this issue, the same team is also exploring multicore fibres with segmented mirror splitters^[234], an interesting approach on the journey to highly parallel CBC systems requiring hundreds/thousands of channels. The idea is to decouple the component count from the channel count, here by a factor of sixteen since this is the number of embedded channels within a single fibre. Future developments will concentrate on increasing the core number per fibre, that will enable joule-class pulse energy at tens of kHz repetition rates from a single fibre.

With this in mind, the highest scalable architecture, XCAN project, Ecole Polytechnique-Thales, Palaiseau, France team is developing a 61-channel prototype (Figure 32) relying on tiled apertures allowing single step far-field combination. The advantage of this method is that there is no actual beam combining element and therefore no power scaling limitation, but the combining efficiency is theoretically limited to about 65% due to the multi-aperture Fourier losses. XCAN recently demonstrated^[235] operation of the first 7 channels with 45% combination efficiency and 70 W average power using 30 μm MFD (mode field diameter) fibre amplifiers. The tiled-aperture approach appears most promising to combine 10,000 channels at unprecedented power levels.

These demonstrations pave the way towards a system required for applications ranging from particle accelerators and nuclear waste transmutation to space debris tracking and mitigation^[236, 237] in the near future.

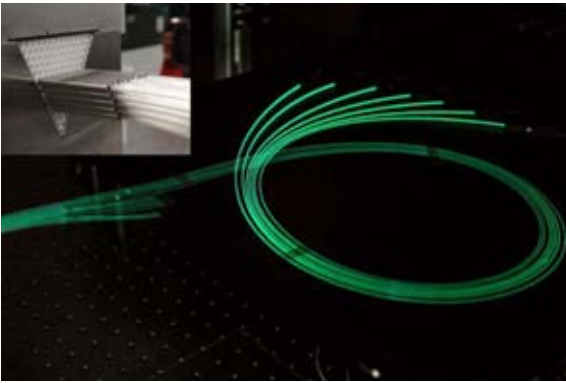


Figure 32. Palaiseau XCAN tiled-aperture system: Yb-doped fibres fluorescence for 19 out of 61 channels. Insert: laserhead with 35 fibres inserted.

4.2.5. Time-domain pulse combining

Coherent spatial beam combining of multiple fibre laser apertures overcomes limitations of individual fibres, and thus enables scaling of the total energy and power, but it does so at the cost of requiring a very large number of parallel channels in a fibre laser array. This is due to the limited energies that are achievable with a fibre-based CPA system. Relatively small beam size and long signal propagation length in a fibre lead to strong nonlinear effects, which confine typical fibre CPA energies to the 100 μJ to 1 mJ range; for fibre core sizes between 30 μm and 100 μm , respectively^[238–240]. Hence, reaching 1 J of pulse energy should need between 1000 and 10,000 fibre amplification channels and combined beams^[241]. Technical challenges and costs associated with such large arrays are very substantial; however, actual stored energies in optical fibres are much higher, exceeding fibre CPA results by approximately two orders of magnitude. This highlights the potential of an approximately hundred times reduction in fibre array size, which would have enormous practical impact on reducing system size, cost and complexity.

Low fibre CPA energies are the result of the fundamental limits on CPA-stretched pulse durations, which cannot exceed a nanosecond range. In solid-state CPA systems, such as Ti:sapphire, large-transverse-aperture crystals can be used to additionally increase CPA energies by a couple of orders of magnitude to reach the full stored energy. Since fibre lasers have constrained transverse apertures, full stored energy can only be accessed by exploiting the time domain – for example, by using coherent pulse combining to artificially extend amplified pulse durations from a nanosecond to at least the hundreds of nanoseconds range.

Recently, a near-complete energy extraction from a fibre amplifier has been achieved using the so-called coherent pulse stacking amplification (CPSA) technique at the University of Michigan, US^[242]. In the latest experiments^[243] a sequence of 81 pulses, each stretched to ~ 1 ns to provide an approximately 80 ns effective pulse duration, was formed,

amplified and coherently time-combined into a single pulse, which was compressed down to ~ 500 fs. This CPSA system, based on an 85 μm core CCC (chirally coupled core) fibre amplifier^[243, 244], achieved 10.5 mJ energy extraction with only 4.5 radians of accumulated nonlinear phase, which is more than 90% of the measured stored energy.

The CPSA approach illustrated in Figure 33 consists of two principal parts: monolithically integrated electronic shaping of the stacking-burst sequence at the system's front; and a compact free-space pulse stacking arrangement at the system's end constructed using Gires–Tournois interferometer (GTI) cavities. The purpose of the electronic shaping is two-fold. First, its phase modulates each individual pulse in the stacking-burst sequence to enable, and to control, its stacking in the GTI-based arrangement at the system's output. Second, since the final amplification stages operate at near-complete energy extraction, it is necessary to control the stacking-burst amplitude profile to offset temporal-shape distortions caused by severe saturation of these stages. This electronic control is implemented using a pair of fibre-pigtailed fast electro-optic modulators, the amplitude modulator in the pair being used to carve out the required burst shape directly from the mode-locked oscillator periodic pulse train, and the phase modulator to imprint the required optical phase on each of the pulses in the burst. Such an arrangement is monolithically integrated, and therefore is very compact. Most importantly, it provides all the degrees of freedom in temporal-shape control needed for completely offsetting the reshaping in strongly saturated amplifiers.

A different time-domain pulse combining technique, the so-called divided pulse amplification (DPA), has also been demonstrated both at Amplitude Systems, France and at the Helmholtz Institute Jena, Germany^[245, 246]. In this DPA technique, illustrated in Figure 34, linear delay lines are used to produce several sequential replicas of the stretched pulse, which after the amplification are recombined back to a single pulse using an identical delay-line arrangement^[245, 246]. DPA is typically used to produce two to four stretched pulse replicas, resulting in a similar improvement in the extracted pulse energies, with experimentally demonstrated energies in the 1–2 mJ range. In conjunction with coherent beam combination of eight parallel fibre amplifiers, this approach allows for the generation of 12 mJ pulses with 262 fs pulse duration^[247]. However, the further enhancement of the energy extraction achievable with DPA is limited, which is mainly associated with the fact that the opto-mechanical arrangement used for pulse splitting offers insufficient degrees of freedom for arbitrary pulse-burst shape control. Thus, the compensation of gain saturation effects of longer sequences of pulses is limited. However, a novel approach named electro-optically controlled DPA, which is based on a fibre-integrated front end for pulse-burst generation, offers sufficient degrees of freedom to arbitrarily scale the number of pulses^[248]. In a first proof-of-principle demonstration,

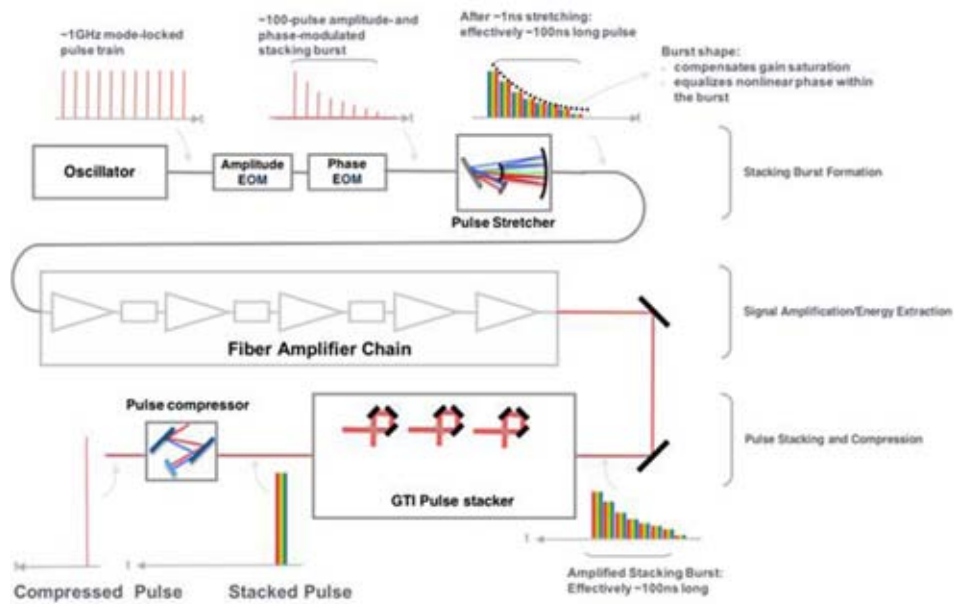


Figure 33. Coherent pulse stacking amplification (CPSA).

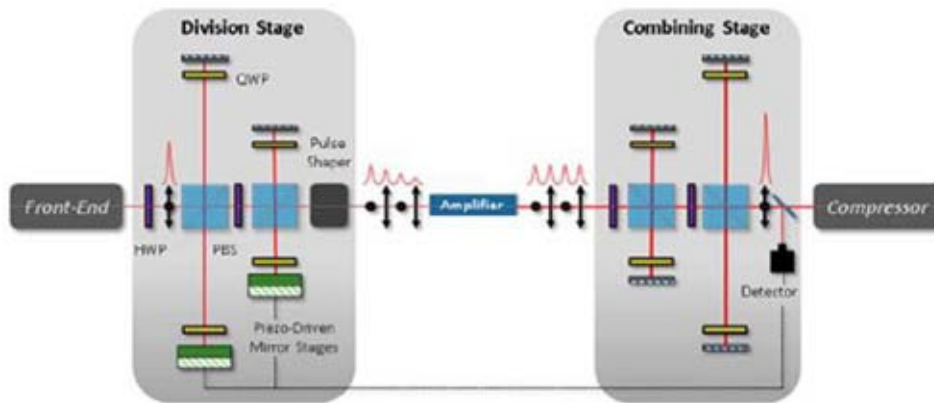


Figure 34. Divided pulse amplification (DPA).

the temporal combination of up to eight pulses allowed high temporal contrast and high combination efficiency of about 90%^[248]. Subsequent experiments with this technique, now involving a high-power ultrafast fibre laser system and an improved low-footprint setup for pulse combination, were carried out recently and have already led to promising initial results at mJ pulse energy levels^[249].

4.2.6. Temperature-insensitive OPCPA

Owing to the inevitable thermal effects at a high repetition rate, OPCPA with simultaneous high-peak and average powers is a challenge to laser technology^[250]. The temperature distortion in an OPCPA crystal will cause thermal dephasing ($\Delta k = k_p - k_s - k_i \neq 0$, where k_p , k_s and k_i are the wave-vectors of the pump, signal and idler waves in Figure 35(a), respectively) and further degrade the con-

version efficiency and the spatiotemporal quality of output pulses. The state-of-the-art OPCPA technique has produced an average power of 88 W in a normal mode^[251], and 112 W in a burst mode^[252]. It is crucial to overcome the thermal dephasing problem in high-average-power OPCPAs.

The phase-matching condition is a major factor that governs nonlinear parametric processes. To enlarge the phase-matching temperature acceptance in second-harmonic generation (SHG), one can select a specific nonlinear crystal with $\partial \Delta k / \partial T = 0$ ^[253] or combine two different crystals with opposite signs of $\partial \Delta k / \partial T$ ^[254]. These methods, however, will not be effective in OPCPA that requires broadband phase-matching simultaneously.

With this in mind a new phase-matching design of OPCPA has been proposed at Shanghai Jiao Tong University,

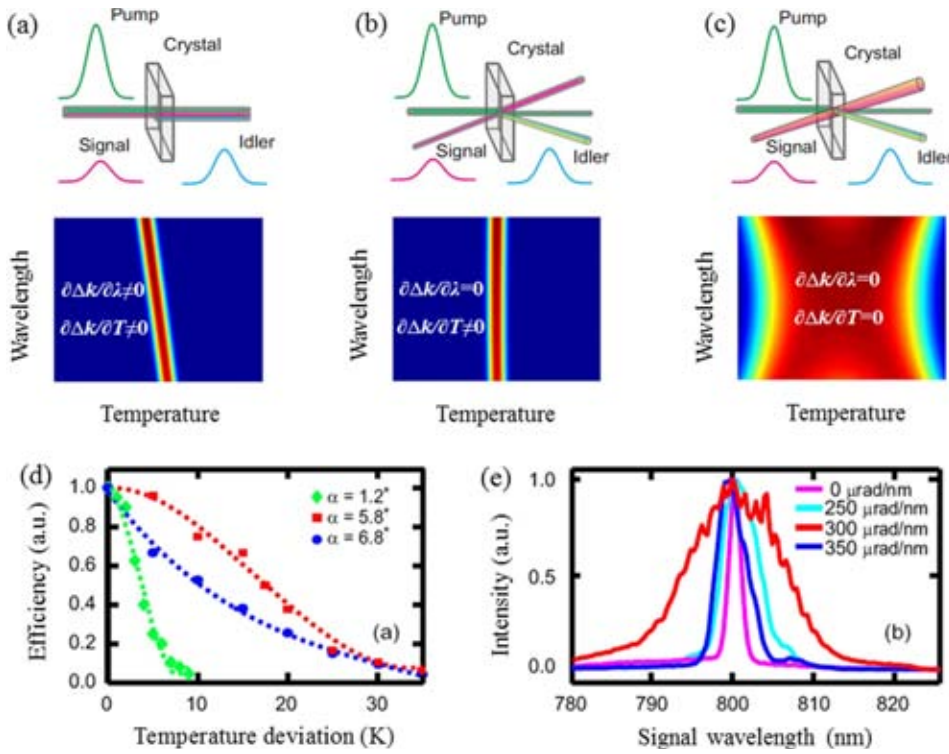


Figure 35. (a) Collinear phase-matching. (b) Conventional wavelength-insensitive non-collinear phase-matching. (c) Temperature-insensitive non-collinear phase-matching with signal angular dispersion. The second rows in (a) to (c) show the normalized gain versus temperature and wavelength. (d) Measured signal efficiency versus temperature deviation for several non-collinear angles. $\alpha = 5.8^\circ$ and 6.8° correspond to non-collinear phase-matching with signal angular dispersion, while $\alpha = 1.2^\circ$ corresponds to wavelength-insensitive non-collinear phase-matching. (e) Measured spectra of amplified signals with different amounts of angular dispersion when $\alpha = 5.8^\circ$.

China. The non-collinear OPCPA configuration was previously devoted to achieving wavelength-insensitive phase-matching ($\partial\Delta k/\partial\lambda = 0$) with a large spectral bandwidth (Figure 35(b)). Notably, it was recently found that the non-collinear phase-matching configuration can also make OPCPA insensitive to temperature ($\partial\Delta k/\partial T = 0$) by setting an appropriate non-collinear angle α ^[255]. In an LBO-crystal-based OPCPA with $\lambda_p = 532$ nm and $\lambda_s = 800$ nm, the non-collinear phase-matching can be designed for either $\partial\Delta k/\partial T = 0$ with $\alpha = 5.8^\circ$ or $\partial\Delta k/\partial\lambda = 0$ with $\alpha = 1.2^\circ$. The non-collinear phase-matching with $\alpha = 5.8^\circ$ has a temperature acceptance six times larger than that at $\alpha = 1.2^\circ$ (Figure 35(d)). As these two non-collinear angles are not equal, angular dispersion on the seed signal must be introduced to ensure $\partial\Delta k/\partial\lambda = 0$ in the temperature-insensitive non-collinear phase-matching with $\alpha = 5.8^\circ$ (Figure 35(c)). In a proof-of-principle experiment with a signal angular dispersion of $350 \mu\text{rad}/\text{nm}$, the spectral bandwidth of temperature-insensitive non-collinear phase-matching can be as large as that of the conventional wavelength-insensitive non-collinear phase-matching (Figure 35(e)).

Furthermore, simultaneous wavelength and temperature-insensitive phase-matching, without the need of additional angular dispersion at seed signal, can be realized if the two

non-collinear angles for $\partial\Delta k/\partial\lambda = 0$ and $\partial\Delta k/\partial T = 0$ coincide with each other. This can be achieved by properly designing the reference temperature for the crystal^[256]. In an LBO-crystal-based OPCPA with $\lambda_p = 355$ nm and $\lambda_s = 550$ nm, the two non-collinear angles for $\partial\Delta k/\partial T = 0$ and $\partial\Delta k/\partial\lambda = 0$ are equal to each other ($\alpha = 3.6^\circ$) at the crystal reference temperature of 337 K. As a result, the spectral bandwidth of such an OPCPA phase-matching design was similar to that ($\Delta\lambda \cong 90$ nm) in conventional wavelength-insensitive non-collinear phase-matching, while the temperature acceptance ($\Delta T \cong 40$ K) was increased by a factor of 4.3. Due to its ability to simultaneously support broadband amplification and large temperature bandwidth, the temperature-insensitive OPCPA design may provide a promising way to generate ultra-intense lasers with kW average powers^[255, 256].

4.3. Enabling technologies

The route to ever-increasing laser powers, coupled with a desire to operate these facilities at higher repetition rates, requires a number of key technologies. In this section we look at some of these technologies and the challenges facing their development.

- The development of mid-infrared lasers
- Improvements in temporal contrast
- Plasma optics
- Grand challenges
 - Advanced optics
 - Laser diagnostics
 - Plasma diagnostics
 - Target fabrication.

4.3.1. The development of mid-infrared lasers

Most ultra-intense lasers available today operate at wavelengths around one micron. The reason is that the shortest pulses are offered by Ti:sapphire lasers whereas the highest pulse energies are possible with neodymium- and ytterbium-doped materials. Moreover, many passive optical materials with high transparency can be found in the near-infrared (NIR) and there is typically no issue from molecular vibration absorption from the normal atmosphere in this range. The classification of the infrared wavelength regions is often inconsistent. Here we will use the term mid-infrared (MIR) for all wavelengths above about $1.7 \mu\text{m}$ to about $15 \mu\text{m}$, even so it is often further split into short- (SWIR), mid- (MWIR) and long-wavelength infrared (LWIR).

Many applications of ultra-intense lasers would greatly benefit from wavelengths longer than those available around one micron. This is not obvious since intensity scales with the wavelength λ as $1/\lambda^3$, the pulse length with $1/\lambda$ and the focusability with $1/\lambda^2$. But laser–matter interaction can only be proportional to intensity I if they are always constrained to the same number of field oscillations. If this is not the case, the interaction length, like the Rayleigh length z_R , assuming diffraction limited focusing, is proportional to λ . Another scaling with λ^2 results from the ponderomotive potential U_p of the free electrons' quiver motion in a electromagnetic field:

$$U_p = \frac{e^2}{8\pi c^3 \epsilon_0 m_e} I \lambda^2, \quad (1)$$

where e is the electron charge, c the speed of light, m_e the electron mass, and ϵ_0 the vacuum permittivity. This cancels the $1/\lambda^3$ scaling of the intensity.

Moreover, the critical plasma density n_e changes with $1/\lambda^2$:

$$n_e = \frac{4\pi c^2 \epsilon_0 m_e}{e^2} \lambda^{-2}, \quad (2)$$

which allows less dense targets to be used for longer-wavelength driving fields. For instance, the maximum energy of laser accelerated ions in the TNSA (target normal sheath acceleration) regime depends on the electron temperature and, by fixing $I\lambda^2$, the lower intensities of longer

wavelengths relax the pulse contrast problem and RPA (radiation pressure acceleration) benefits from the critical density scaling at longer wavelengths. For the wavelength scaling of laser-based acceleration of electrons to maximum energy by LWFA (laser wake field acceleration) the situation is more complicated, since many parameters have to be considered^[257]. Nevertheless it was shown that the larger plasma structures are capable of accelerating bunches of higher charges^[258].

Another application of high laser intensities is the generation of high harmonics (HHG), where the high-energy cutoff also scales with $I\lambda^2$, with the macroscopic scaling $\hbar\omega \sim \lambda^{1.6} - \lambda^{1.7}$. Unfortunately the yield η scales with $\eta \sim \lambda^{-5} - \lambda^{-6}$ ^[247, 259]. From these considerations, HHG with wavelengths longer than about $6 \mu\text{m}$ seems no longer feasible, but MIR laser pulses are nevertheless beneficial.

The generation of THz pulses with high-intensity lasers is also more efficient if the driver is an MIR laser^[260]. The advantage of the lower photon energies is that multi-photon absorption is less likely and higher intensities can be applied.

Similar to THz generation, incoherent X-ray generation with lasers can be more efficient with a longer-wavelength driving laser, as was shown for instance by Weissaupt *et al.*^[261]. There a comparable photon yield using a $0.8 \mu\text{m}$ and a $3.9 \mu\text{m}$ wavelength lasers was observed, whereas the intensity was about two orders of magnitude less in the long-wavelength case.

Not only do direct laser–matter interactions demand longer wavelengths to optimize the effects, the critical plasma density scaling and therefore the plasma refractive index dependence on wavelength requires the tuning of diagnostic laser pulses to suitable wavelengths. The refractive index of the plasma is given by

$$n = \sqrt{1 - \frac{\omega_p^2}{\omega_{\text{probe}}^2}} \quad (3)$$

with the plasma frequency ω_p and the probe frequency ω_{probe} . Therefore, higher-intensity drivers and lower plasma densities need longer-wavelength lasers for diagnostics.

All these considerations show that there is a strong demand for high-peak-power lasers in the MIR. Such lasers should be capable of generating high energies as well as short pulses, preferably pulses consisting of only a few cycles. Moreover, laser diode pumping typically offers operation of such lasers at higher repetition rates and, even more importantly, potentially higher long- and short-term stability. Most of today's petawatt laser designs comprise flashlamp-pumped Nd lasers that are frequency-doubled to pump a Ti:sapphire crystal. Compared to direct diode-pumped short pulse lasers like the POLARIS laser scheme^[110], a two-step approach, where pulse energy in the form of nanosecond pulses is generated without the requirement to produce a broad bandwidth at the

same time, has the advantage of a simpler design. Diode pumping of broad-bandwidth materials that also show a long fluorescence lifetime consequently has a small emission cross-section and a high saturation fluence. The stored energy is therefore difficult to extract. Alternatively, the two-step approach allows the separation of the two problems of generating highly energetic pulses and a large bandwidth. Moreover, it is not possible to find a suitable solid-state laser material for a desired wavelength.

Optic parametric amplifiers (OPAs) are a very versatile solution that offers broad bandwidth without significant thermal limitations. Nevertheless, they require a coherent pump with very high performance and good synchronization with the seed pulse. Moreover, starting at one micron, systems will become less efficient in generating longer wavelengths. With a suitable MIR pump, ultra-intense pulses with even longer wavelengths could be efficiently generated by OPAs.

One problem of diode-pumping MIR lasers is that if the quantum defect needs to be small enough, diode lasers with wavelengths well above $1.8\ \mu\text{m}$ are needed. But all known semiconductor lasers suffer from poor efficiency in the MIR range. Whereas the peak efficiency of diode lasers at 920–980 nm can be more than 75%, 25% is hardly achievable at 1900 nm – a wavelength that, for instance, is useful for pumping Ho-doped materials.

Another approach to achieve efficient diode pumping of MIR lasers is to use a cross-relaxation process where a single pump photon will finally produce two excited states. Such a system is offered by the aforementioned Tm^{3+} -doped laser materials^[262]. It was shown that if the thulium doping level is high enough the cross-relaxation efficiency can be nearly 100%. Nevertheless, the competing energy transfer upconversion (ETU) as a loss mechanism for the desired laser will also rise with the concentration of excited ions. For the optimization of the laser process a balance of doping and pump fluence specific to the properties of the laser material must be found. Moreover, Tm-based laser materials offer a high-energy storage capability because fluorescence lifetimes can be even longer than 10 ms. For Yb:YAG, for instance, cooling to liquid nitrogen temperature levels allows a lifetime of up to 15 ms to be achieved with an increased emission cross-section at the same time, as shown in Figure 36.

The high potential of Tm-doped solid-state lasers for generating coherent radiation around two microns has already been employed for some time in fibre lasers. A *Q*-switched fibre laser producing 2.4 mJ has been demonstrated^[263], as well as the coherent combination of two Tm fibre lasers^[241], that offers high energies and high average power. Ultra-short pulses are also possible, as the reported compression to 13 fs^[264] demonstrates.

Volume lasers with Tm-doped materials have also been investigated. A report of 0.8 J output from a Cr:Tm:YAG laser dates back to 2000^[265]. Nevertheless, this was a

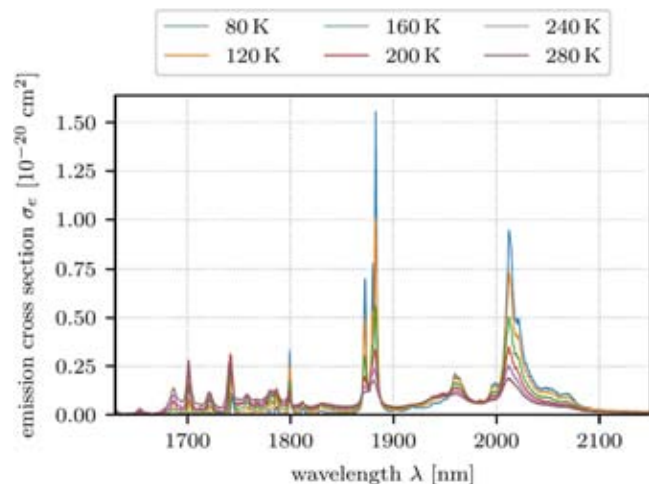


Figure 36. Temperature-dependent emission cross-sections of Tm:YAG.

flashlamp-pumped laser. The highest pulse energy from a diode-pumped Tm:YAG, 128 mJ, was published by Yumoto *et al.*^[266]. An optical-to-optical efficiency of 51% in a *Q*-switched laser was shown using a diode-pumped Tm:YAP^[267], and a record average power of 200 W was demonstrated with Tm:YLF^[268] by the Fraunhofer Institute for Laser Technology.

High average power, pulse energy and efficiency show proof that thulium lasers are promising MIR sources. They allow the production of pulses as short as 380 fs^[269] by themselves and can be used additionally as a pump for another ultra-broadband laser material, which will offer the two-step approach. Suitable materials for such a scheme are the transition-metal-doped zinc chalcogenides^[270–273]. Since the pioneering work of DeLoach *et al.* in 1996^[274] showing a slope efficiency of 22% with Cr:ZnSe, many promising results have been produced.

- 30 W CW output from Cr:ZnSe was achieved by fibre pumping at $1.9\ \mu\text{m}$ wavelength^[270].
- A mode-locked oscillator generating 41 fs was reported by Tolstik *et al.* in 2014^[275].
- The demonstration of a 1 J long pulse from Cr:ZnSe^[276] shows that not only average power but also high pulse energies are possible.
- The amplification of a 27 fs pulse with a spectral width that would even allow 16 fs^[267] shows the capability for the generation of very short pulses and amplification with a gain of 500^[273].

The combination of ultra-broadband transition metal chalcogenides pumped by diode-pumped Tm-doped solid-state lasers offers a promising two-step approach for the generation of ultra-intense laser pulses in the MIR (around

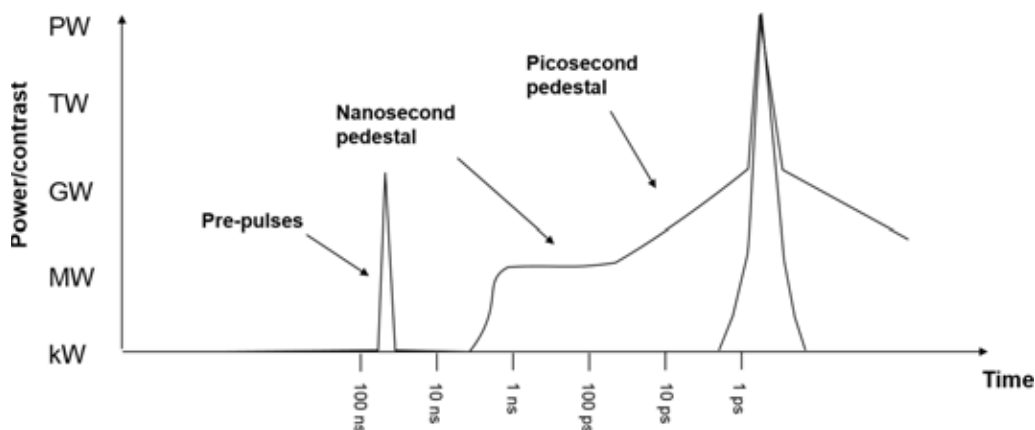


Figure 37. Illustration of sources of contrast issues.

2.5 μm). In contrast to the traditional Ti:sapphire lasers that are pumped by frequency-doubled Nd lasers, no additional nonlinearity is involved. Some attempts can already be found in the literature – for instance, Yumoto *et al.* showed an optical-to-optical efficiency of 44% for a Cr:ZnSe laser pumped by Tm:YAG^[277] and a tuning range of this setup of at least 600 nm^[278].

Transition-metal-doped zinc chalcogenides are not the only option for broadband amplifiers pumped by Tm³⁺-based lasers. Another route may be offered by optically pumping a CO₂-laser. High-peak-power CO₂-lasers that are traditionally discharge-pumped are already being developed nowadays^[279]. It seems that 100 TW and more are achievable in the 10 μm wavelength range. The even longer wavelength and the advantages of being gas lasers make them promising candidates for high-peak-power applications such as particle acceleration^[280, 281].

That optical pumping of CO₂-lasers could be rather efficient, which had already been shown for different wavelengths and pump laser systems in the 1980s^[282]. Among the different wavelengths that can be generated with high-power chemical lasers in the MIR there is also an option to use the output of thulium or holmium solid-state systems. Optical pumping has the advantage that higher-pressure gases and an extended mixture of isotopologues can be applied. The latter is possible since, in contrast to discharge-pumped CO₂-lasers, molecules are not dissociating through optical pumping and the rearrangement of isotopes will therefore not lead to a degradation of the isotopologue mixture^[283, 284]. Moreover, there is no need to pump any isotopologue separately. Targeting one species is sufficient in order to incorporate all of them in the laser process. This finally results in a possible large amplification bandwidth supporting some 100 fs pulses to be amplified, which makes such lasers very attractive for high-intensity applications^[285].

4.3.2. Improvements in temporal contrast

When the first CPA high-power lasers were being built the goal was to deliver the highest focused intensity to target;

temporal contrast was not a major concern. However, it became rapidly apparent that any energy delivered to the target before the main laser pulse arrived could radically change the conditions of the interactions^[286]. The ability to deliver a ‘temporally clean’ laser pulse is now one of the key parameters of any petawatt class laser system, and becomes increasingly important as we move into new regimes at focused intensities in excess of 10^{23} W/cm².

The energy which can precede the main laser pulse results from six principal mechanisms (Figure 37).

- Amplified spontaneous emission (ASE) from conventional laser amplifiers. This lasts for the lifetime of the laser ion used in the amplifier and/or the pump duration, typically hundreds of microseconds. If a regenerative amplifier is used, pedestals of the Q-switch duration of the amplifier (typically hundreds of nanoseconds) and the amplification window (of order ~ 10 ns) are present.
- Parametric fluorescence from optical parametric amplifiers, which lasts for the duration of the pump pulse (usually a few nanoseconds)^[287].
- The coherent pedestal due to scattering from gratings in the stretchers and compressors forms a ~ 100 ps triangular pedestal (on a logarithmic scale) on either side of the main pulse^[288].
- Features within a few picoseconds of the pulse can be formed due to imperfect compression^[289].
- The inherent contrast of the laser (in the absence of any pulse cleaning) is limited by the quantum noise from the seed oscillator^[291].
- Poorly suppressed oscillator pulses or back reflections in multi-passed components can lead to discrete pre-pulses. These may also be formed by nonlinear index effects causing post-pulses to generate pre-pulses^[291].

The final contrast of a petawatt class laser is influenced by the design of many subsystems.

Oscillators: The innate contrast of a range of mode-locked oscillators which form the seed for all petawatt lasers has been characterized by Stuart *et al.* and Alessi *et al.*^[290, 292], revealing unexpected features close to the mode-locked pulses. These features can only be removed using temporally gated amplification (ps-OPA) or nonlinear processes.

Picosecond OPA: The first major improvement to the contrast of Nd:glass-based petawatt lasers was the development of self-pumped picosecond OPAs by Dorrer *et al.* at the University of Rochester^[293]. First fielded on Vulcan by Musgrave *et al.*^[294] and later at OMEGA-EP^[295], Orion^[296], NIF-ARC^[297] and PHELIX^[298], these systems take the output of a mode-locked oscillator and amplify it to the microjoule level in an OPA pumped with a laser seeded by another pulse from the same oscillator. By amplifying the pulse by a factor of 10^4 , while it is weakly stretched, any parametric fluorescence is kept to within a few picoseconds of the pulse. Any subsequent amplifiers (such as an OPA pumped with a nanosecond duration laser) can have their gain reduced significantly and hence reduce the intensity of the parametric fluorescence in the nanosecond regime.

Double CPA: An alternative approach which can be used in conjunction with ps-OPA is the use of double CPA^[299]. Here the seed pulse is stretched, amplified, then compressed and passed through a nonlinear process which inhibits any structure around the main pulse. The cleaned pulse is stretched again and amplified before being compressed and focused onto target.

In systems with short (< 100 fs) pulse durations, crossed polarized wave (XPW)^[300] is the most commonly used nonlinear effect. For systems with longer pulse durations low-gain OPA^[301] is more appropriate.

These processes are similar to ps-OPA in that they generate temporally clean seed pulses for the main amplification stage of a laser. However, these seed pulses still need to be stretched to nanosecond durations for further amplification, which can lead to other effects limiting the contrast.

Stretchers: On all CPA lasers a triangular pedestal exists for a few hundred picoseconds around the main pulse. This is partially due to high-frequency phase errors from the gratings, which form part of the stretchers and compressors. The impact of grating quality was studied by Dorrer *et al.*^[302] and later characterized and improved by Hooker *et al.*^[167]. Reducing this pedestal further is still an area of active research.

Beamline design: Other features within the beamline also have an impact on the contrast. Plane parallel surfaces can generate post-pulses when the main laser pulses pass through them. In the case of OPA crystals this post-pulse will be amplified and sit, slightly delayed, under the main laser pulse. Should the stretched pulse then pass through a

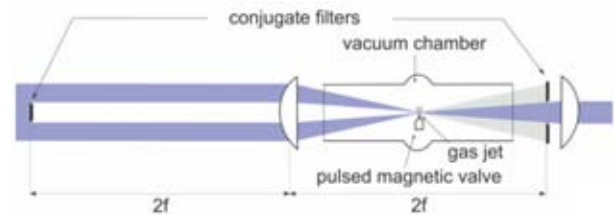


Figure 38. Schematic of the nonlinear Fourier filter.

nonlinear process, such as saturated gain or B-integral build up along the amplifier, a pre-pulse can be generated which mirrors the post-pulse^[291]. This effect can be avoided by using wedged OPA crystals and replacing half-wave plates with reflective polarization rotators^[303].

In multi-passed, imaged amplifiers, ghost foci from the lenses can cause pre-pulses to be formed which lead the main pulse out of the amplifiers. This effect led to the Texas Petawatt system being redesigned by replacing the lenses in their beamline with off-axis parabolic reflectors^[304].

Nonlinear processes post-compression: One of the most dependable methods of improving contrast is to cause the pulse to undergo a nonlinear process after final compression. The most common approach is the use of plasma mirrors^[305]. Here an anti-reflection-coated blank is placed in the converging beam. When the intensity gets high enough a plasma is formed on the surface, which then reflects subsequent light with high ($\sim 70\%$) efficiency. Hence the mirror can be positioned such that any low-intensity pre-pulses leak through and the reflective plasma is only formed by the rising edge of the main pulse. The contrast enhancement of plasma mirrors is limited by the reflectivity of the anti-reflection coating on the blank. Further improvement to contrast can be made by using double plasma mirrors^[306]. By pre-ionizing the surface of the plasma mirror with a controlled pre-pulse, reflectivities of 96% have been realized^[307].

The other approach is frequency-doubling the beam post-compression. This requires very large, thin doubling crystals, to minimize nonlinear phase issues; and a series of dichroic mirrors post-compression to reject the unconverted fundamental. Conversion efficiencies of $\sim 70\%$ have been realized^[308], but the difficulty in manufacturing large, thin crystals limits the energy that can be provided.

Alternative schemes have been developed for short-pulse gas lasers, such as the nonlinear Fourier filter^[309]. Here an annular beam is formed using an apodizing mask. The beam is focused through a gas jet, re-collimated and blocked with a second mask (Figure 38). Nonlinear effects at the focus introduce an intensity-dependent directional modulation of the beam, both in time and space, causing the main pulse and the low-intensity pedestal to become spatially separated.

A huge amount of work has been undertaken to provide the cleanest possible laser pulse, yet as the peak power of lasers increases so does the importance of contrast. Future facilities

could rely on coherent beam combining to achieve the highest possible focused intensities, which gives the possibility of slightly mistimed beams producing interference which could throw energy from the main pulse into satellite pulses. Short pulses at large apertures are susceptible to spectral clipping in compressors, along with localized wavefront and phase errors^[310]. The journey to 100 PW lasers will bring new problems to be solved before these systems can realize their greatest potential.

4.3.3. Plasma optics

As an optical wave propagates from vacuum into plasma it experiences a wavelength- and density-dependent refractive index which acts to refract it away from higher densities (see Equation (3)). Utilizing this effect, in combination with the optical ionization induced when a laser illuminates a solid target, it is possible to generate effective switchable plasma optic^[311]. As the pulse length of high-power lasers reduced to approximately a picosecond by the mid-1990s, the plasma expansion from a solid target during the driving pulse, typically characterized by the distance over which the density reduces by $1/e$, known as the scale length L_s , also decreased. In many laser systems of this era, contrasts of 10^4 – 10^6 a few nanoseconds ahead of the peak of the pulse were common, and scale lengths for interactions at intensities of 10^{15} – 10^{17} W/cm² of the order of only a few times the driving laser wavelength λ became possible for the first time. For short (<ps) pulses and short scale lengths, the plasma does not typically evolve significantly hydrodynamically as the beam travels through it and the refracted output beam leaves the plasma in the specular direction. Also, the reflected fraction of the beam typically becomes more dominant over large-angle scattering at short scale lengths. Thus, novel high-quality plasma ‘reflecting’ optics which operates at high energy densities \sim kJ/cm² becomes feasible.

Initial studies in the early 1990s with nanosecond laser contrasts of $<10^6$ had shown that the reflected laser beam typically ‘broke-up’ at intensities $\geq 10^{16}$ W/cm² due to large scale lengths^[312] effectively producing ripples in the expanding plasma surface where the beam was being refracted. Experimenters in the early 1990s explored the potential for utilizing the plasma as a high-quality active optical switching mirror^[313, 314] and characterized performance^[315, 316] in terms of the potential to deliver reflected pulses for subsequent high-contrast interactions, which became common practice by the early 2000s. Ellipsoidal plasma optics offers the advantage of delivering sub F/1 focusing^[317], enabling intensities^[318] approaching 10^{22} W/cm² with current petawatt class lasers, and the prospect of enhancement of the focused intensities of future systems, illustrated in Figure 39.

Recently, it has been observed that by utilizing a suitable picosecond-scale pre-pulse on the surface of a plasma mirror, the scale length can be optimized^[319] to minimize absorption and give reflectivities of 96% for the main pulse,

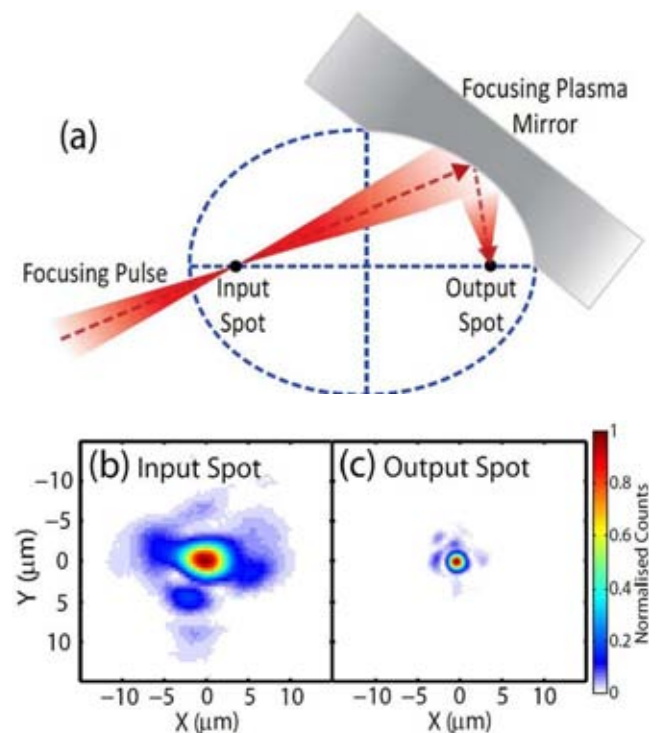


Figure 39. (a) Schematic illustrating the operation principle of an ellipsoidal focusing plasma mirror to increase the intensity by a factor of five. (b) Input laser focal spot spatial-intensity distributions using $f/3$ illumination at 1053 nm and (c) the output spot image obtained, demonstrating a demagnification of $1/3$ in this ellipsoidal geometry^[318].

approaching that of conventional multi-layers. The new generation of high-repetition-rate lasers will require plasma optics that can be fielded at repetition rates of $>$ Hz, and tapes^[320] or liquids are an obvious choice. Liquid plasma mirrors were first investigated in the early 1990s^[321] and high reflectivities were achieved using water^[322], which has minimal associated hazards. More recently, liquid crystals have been studied as their thickness can be readily tuned^[323] to <200 nm and they can be designed to be operated at \gg Hz repetition rates. Such thin plasma mirrors will be ideal for staged acceleration^[324] or beam combination/extraction in the near future, as high-energy photons/electrons/ions will easily pass through a thin plasma mirror without suffering significant absorption or scattering.

At intensities of $\gg 10^{18}$ W/cm² the laser interaction can lead to two additional and significant effects on plasma mirrors^[325]. The light pressure can steepen the density gradient close to critical and the electric field associated with the pulse can drive the plasma electrons/surface, forcing it to oscillate significantly. In such circumstances, a few percent of the incoming beam is converted into the second harmonic, being emitted in the specular reflected beam direction. This work was extended^[326] to intensities of 10^{21} W/cm² by 2011, with the conversion efficiency into second harmonic reaching 20%, equivalent to that achieved

for BBO crystals of the time for such broad bandwidth 35 fs pulses. Due to the short optical path in the plasma, this conversion mechanism should also be suitable for much shorter driving pulses. As well as the second harmonic, higher harmonics have also been observed as the driving intensity is increased. By 1996 the 75th harmonic had been detected^[327] and enhanced driving contrast continued to improve the conversion efficiency^[328] due to the associated sharper density gradients, with the 2000th harmonic being observed^[329] by 2007.

Utilizing the nonlinear plasma response has been used to produce shorter (<picosecond) duration pulses at higher powers than lasers could deliver at the time. Raman scattering in the plasma was used to self-modulate the pulse intensity envelope and self-focusing employed to effectively extend the interaction length over which a pulse propagates and maintains a sufficiently high intensity^[330, 331]. Simple gas jets were initially employed by many in the early 1990s and have been used extensively for laser-driven electron acceleration^[332, 333] studies. However, more complex gas cells with density structures, capillary discharge devices^[334–336] and multi-pulses^[337], have been used to deliver tunable GeV-scale electron beams^[230] over many centimetres of interaction length. The nonlinear plasma response can also be utilized for compressing^[328] and focusing^[338] short ~ 30 fs beams, with expectations that they could readily handle multi-petawatt powers and deliver near-ideal focusing if a suitable density profile is obtained^[319]. More complex phenomena such as plasma compression and diffraction^[339, 340] can also be used to manipulate the beam^[341]. Future plasma components will also utilize relativistic effects to deliver novel optics^[342] with high damage thresholds^[328], such as plasma apertures^[343], waveplates, separators, holograms^[344] and q-plates^[345], and uses in areas such as plasma amplification, discussed in Section 4.1.3, will be further developed to enable new interaction regimes to be reached.

4.3.4. Grand technological challenges

As petawatt/exawatt laser systems are developed in the future there are a number of grand challenges facing the community to realize their potential. In this section we have briefly examined four areas which need to be addressed:

- Advanced optics
- Laser diagnostics
- Plasma diagnostics
- Target fabrication.

4.3.4.1. Advanced optics. The performance limits of optical components are of crucial importance in realizing the potential of petawatt systems. The principal limitation

dictating the energy and power available on target is usually laser-induced damage of the compressor gratings, where energetic short pulses are first exhibited in a beamline^[346]. To realize the highest intensity, one requires gratings with aperture > 1 m, high-efficiency diffraction over bandwidths of hundreds of nanometres and minimal diffracted wavefront errors. For designs using high-angle-of-incidence gratings, the limit may be transferred to the post-compression optics, such as the focusing mirror.

The effective grating aperture may be increased by tiling multiple gratings (and/or other transport optics)^[347]. In this scheme, the gratings must be positioned with interferometric accuracy in five degrees of freedom (only translation parallel to the grooves has a relaxed tolerance). Such a scheme is an inherent feature of the coherent recombination of sub-apertures discussed elsewhere. It has been shown in the case of NIF-ARC, for example, that even when the dispersion in sub-apertures differs slightly, then the overall dephasing between beams in the spectral/temporal regime can be controlled^[348].

Controlling the wavefront through the compressor is important to minimize spatiotemporal coupling and realize the highest intensities. Adaptive optics systems both before and after compression can address this issue.

When operating with high repetition frequencies and high average power, the thermal loading on the optics and optomechanics becomes significant. For example, control of the zero-order beam from gratings is necessary to avoid local heating of components. Absorption within optical components must also be minimized. High-repetition-rate systems also require laser gain media suitable for diode pumping. Materials with a broader gain bandwidth, such as Nd:glass, may be used for direct CPA lasers, or for pumping Ti:sapphire or OPCPA systems. Narrowband systems may only be used as pump sources.

Future OPCPA systems with very high energy will require developments in gain media. For example, highly deuterated ($\sim 90\%$) DKDP crystals, cut for Type-I phase-matching, with high optical quality over a large aperture are required^[173, 349]. Coating development is also necessary to achieve high damage thresholds with very large bandwidths and adequate control of spectral phase^[350].

Improvements in optics performance are expected to plateau unless advances in optical metamaterials^[351] become relevant. Further progress in ultra-high intensity may depend upon alternative schemes, such as the Compression after Compressor Approach (CafCA) and plasma amplifiers, both discussed elsewhere in this paper.

4.3.4.2. Laser diagnostics. While high-power lasers can generate extreme conditions of matter, for the physics to be understood the laser must be well characterized and diagnosed at the point that hits the target. The key parameters required for each experiment differ, but consistency and control of the delivery of energy is essential to reproducible

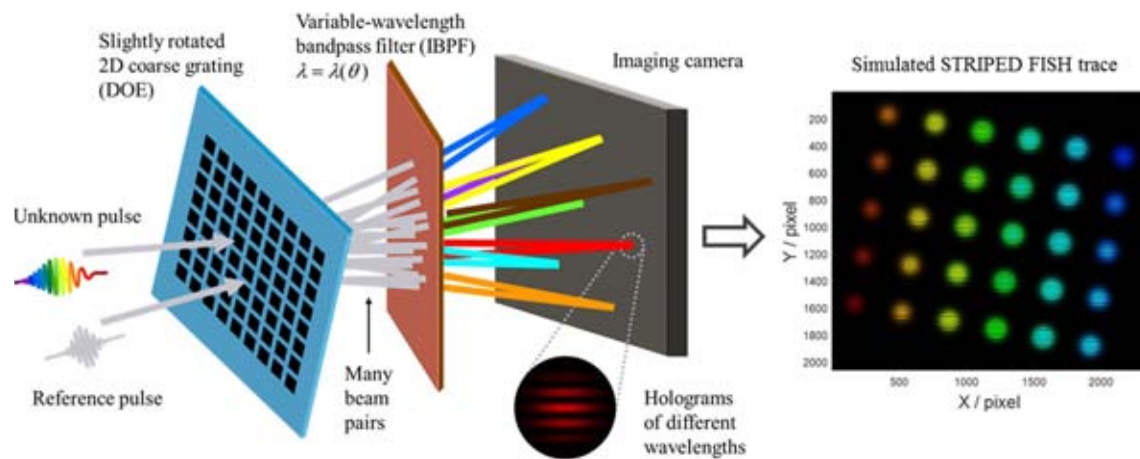


Figure 40. The schematic of a STRIPED FISH apparatus for single-shot complete spatiotemporal pulse measurement (reproduced from Ref. [353]).

science. With the increase in peak and average power of new laser systems, new challenges have come to the fore.

The traditional method of diagnosing a laser is subsampling a beam through a pick off or leak through an optic before reducing it down and sending it to a suite of diagnostics. This becomes increasingly difficult as broad bandwidths and high intensities become the norm. The impact of nonlinear effects on material dispersion means that the diagnostic beam can be radically different from the main beam^[352]. While these effects can be compensated for, the further one goes from measuring the original beam, the more vulnerable to variation in beam properties the diagnostics becomes.

All of the exawatt class facilities currently proposed rely on combining many beams at target to reach the highest intensities. In order to ensure full coherent combination, the full spatiotemporal information of the beams must be measured, including intensity and phase in time and space domains. Advanced diagnostics are therefore required to reconstruct the E-field, such as STRIPED FISH^[353] (Spatially and Temporally Resolved Intensity and Phase Evaluation Device: Full Information from a Single Hologram) shown in Figure 40 or TERMITES^[354] (Total E-Field Reconstruction using a Michelson Interferometer Temporal Scan).

With increased repetition rates the rate at which diagnostic data is produced increases dramatically. Analysis and optimization of the system can be performed in real time and automated^[355] to provide more robust facilities. These techniques can even be applied to the plasma diagnostics themselves, dynamically changing the laser parameters to optimize experimental conditions^[356].

At the other extreme for single-shot facilities the demand for increased information about the pulse as delivered at focus increases. Techniques that had previously been used in a scanning operation, such as high-dynamic-range contrast measurements, now need to be converted to single shot^[141].

All of the aforementioned diagnostics use small optics and are sensitive to wavefront (including pointing) and some

require small time-bandwidth products. On large aperture laser systems those are often a challenge. Furthermore, beam sampling and the beam transport to the diagnostics station are challenging due to B-integral and other nonlinear effects.

Finally, most high intensity laser applications require highest intensities but the community still lacks an online diagnostic that measures intensity directly. None of these challenges are insurmountable, but new techniques will need to be developed and matured to a point that they can leave the lab and become reliable facility diagnostics.

4.3.4.3. Plasma diagnostics. Measuring the radiation, particles, physical states and energy flows present within the broad range of plasmas generated during the interaction of a petawatt class laser with matter^[357] is an ongoing and critical challenge for the future of the field. If the community is to effectively deliver the envisaged wide range of medical^[358], scientific^[359] and industrial^[360] investigations and applications accessible with new high-power, high-repetition-rate lasers, a number of specialized diagnostics will be needed. They must be capable of characterizing not only the primary plasma but also any secondary beams^[361] and their subsequent interactions. High-dynamic-range systems (12–18 bit) capable of differentiating and detecting structures, materials and features will be required from the sub-micron scale through to characterizing large $\sim 10\text{ m}^2$ areas for industrial and medical imaging^[362]. Combining high-resolution sensing and multi-modal capability, utilizing the broad range of particles and radiation (X-rays^[363], THz, ions^[364], electrons^[365], muons, neutrons etc.) available from laser-driven sources will deliver new capability to the community. Efforts on meeting these and similar challenges are underway internationally, not only within the laser plasma community but also at other facilities such as XFELs, Tokamaks, synchrotrons and accelerators, as they face similar challenges in diagnostics, analysis and data management.

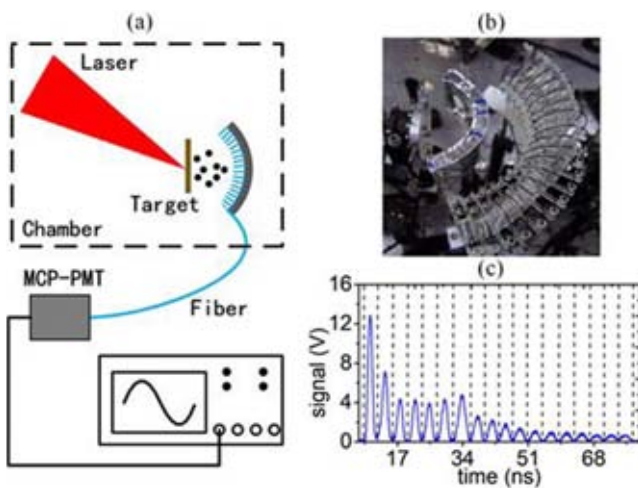


Figure 41. (a) Schematic diagram depicting an angular-resolving escaping electron diagnostic which is based on injecting Cherenkov light^[380] into an optical fibre array surrounding the interaction, as shown in (b). The diagnostic is capable of operating at repetition rates of MHz and, by encoding the electron flux into an optical signal within a fibre, it can be readily transported away from the interaction area, enabling the sensitive detector and digitizing electronics to be located far from the interaction and within an EMP-shielded enclosure giving high-quality data in (c).

The target chamber and environment surrounding a high-intensity interaction^[366] can often be challenging for diagnostic operations, due to the production and escape of:

- (1) large fluxes of energetic particles (primarily electrons^[367], ions^[368] and neutrons);
- (2) the generation of associated electromagnetic pulses (EMP)^[369];
- (3) the emission of broadband radiation at up to multi-GW power levels from THz^[370] through to hard X-rays^[371];
- (4) target debris.

By designing and controlling the interaction geometry to reduce^[372] and mitigate^[373] EMP generation, many general techniques^[374] appropriate for ‘single-shot’ operation^[375] can be delivered at high repetition rates ($\gg 10$ Hz) with suitable retuning/redesign and the replacement of the detector element or by transporting the signal to a more benign environment^[376] before digitization (see Figure 41). Scintillators, phosphors and transducers capable of kHz–GHz rates can be readily coupled to gated or rep-rated high-dynamic-range detectors. Significant efforts are currently underway to increase radiation damage tolerance and component lifetimes when exposed to particles or ionizing fluxes and improve performance in terms of sensitivity, specificity and spatial resolution^[377]. Nuclear activation techniques utilizing isotopes with >10 min half-lives have

been frequently used^[378] to characterize high-energy photons and particles (typically >4 MeV) in the laser-plasma community. At tens of Hz such transitions would become closer to becoming integrating detectors. However, there are much shorter^[379] nuclear transitions which can be adopted so that individual shot measurements are possible for high-repetition-rate systems.

A significant challenge facing the laser-plasma community is to deliver new, matched detectors capable of taking advantage of the short-pulse nature of laser-driven secondary sources to obtain higher-quality, higher-resolution measurements for both scientific studies and applications. This will be an area where development and new approaches and techniques are needed (for instance, efficient hard X-ray detectors with few-ps resolution would enhance backscatter imaging^[381] and provide discrimination against non-ballistic photons for applications such as penetrative imaging). Electronics with sufficient bandwidth to directly digitize signals with temporal resolutions of <20 ps and streak cameras with \sim ps resolutions are currently available, and faster responses are envisaged in the future. Acquiring and transferring multi-megapixel, high-dynamic-range images at $\gg 10$ Hz is becoming routine for scientific-grade digital cameras. Converting, transforming or encoding the desired diagnostic information into an electrical or photonic signal^[382] is already a regularly used technique. However, further developments in this area will enable faster and more complex measurements to be made. Many early studies relied on only a few data points/shots, but new laser systems will offer the possibility of taking significant numbers of repeat shots per configuration, allowing weaker signals to be extracted and statistical techniques to be more fully employed. New paradigms of data acquisition utilizing the high repetition rates of future systems, more in common with particle physics, where ‘near instantaneous’ processing enables significant data reduction and selection to be undertaken, will be necessary for studies involving low-probability events.

State-of-the-art hardware and infrastructure are allowing facilities to take advantage of the many new advances within the electronics/telecommunications industries, where data transfer rates of multi-GHz are now commonly available. Combining such high data flow rates with the broad range of opportunities for encoding and accessing plasma parameters will enable the next generation of laser facilities to greatly extend our diagnostic capabilities, resolutions and understanding of laser-driven interactions. Advanced high-repetition-rate diagnostics and techniques will not only enable new scientific measurements and discoveries to be made, but as laser-driven sources mature, facilities will be able to improve the quality, stability and level of control possible within the plasma and secondary source environment, enabling novel and more advanced studies and applications to be undertaken for the first time.

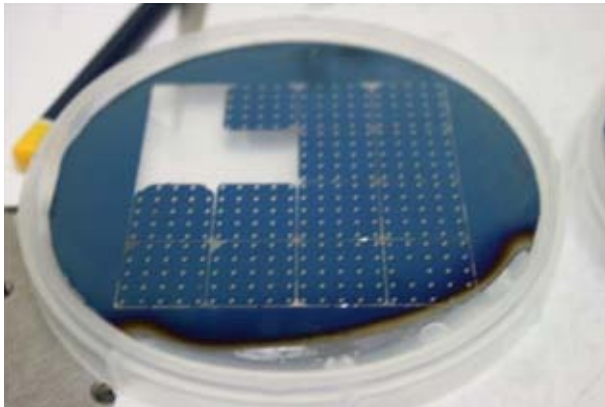


Figure 42. A 100 mm silicon wafer that has been coated with 100 nm low-stress silicon nitride and then processed using optical lithography and silicon etching to produce target arrays for the Gemini laser at RAL. Target flatness characterized to $<2\ \mu\text{m}$ variation over the open apertures. 16 arrays produce 400 targets per wafer (picture courtesy of STFC Rutherford Appleton Laboratory).

4.3.4.4. *Target fabrication.* Future target fabrication challenges can be broadly split into two main areas:

- (1) targets for high-repetition-rate ultra-high-power laser systems;
- (2) complex targets for multi-beam high-energy facilities, usually coupled to petawatt class beam capability.

Each of these areas has challenges to overcome to deliver the highly complex targets that are required by the respective user communities.

The commissioning of new high-repetition-rate facilities such as the ELI pillars will require a significant and fundamental change in the way targets are delivered, due to the large numbers needed to field experiments. With petawatt lasers at shot rates that are of the order of 10 Hz for ELI-BL^[383], and with a petawatt system at ELI-ALPS running at 10 Hz and a terawatt system running at 100 Hz^[384], there is at least two orders of magnitude increase in the number of targets that can be shot; currently there is insufficient capacity to manufacture enough targets using conventional techniques. To overcome this challenge, high-repetition-rate liquid targets have been proposed^[385–387], and recently there has been a demonstration of multi-MeV proton acceleration from sub-micron liquid sheet targets at 1 kHz repetition rates^[388].

The requirements for these and other high-power laser systems, such as the European XFEL, Gemini (UK), CLPU (Spain), Apollon (France), are well defined in a recent review of target fabrication needs^[389] which highlights a range of techniques that are needed to be developed to deliver to such facilities. While some of these facilities are developing a limited range of the capabilities that are required for target manufacture, to deliver a full experimental programme, a



Figure 43. A complex gas target, manufactured by Scitech Precision, UK, for studying counterpropagating radiative shock collisions with X-ray radiography, generated from a petawatt laser beam, as a primary diagnostic used on experiments on SG-II at SIOM, China (picture courtesy of Imperial College London).

suite of integrated technologies is needed. Coordination between each stage of what could be a complex target manufacture process, including their support, base layer coating, and etching is key (Figure 42). Target mounting also needs to be carried out in a streamlined way. This will require experts in many areas of fabrication to work with the user communities and the facilities to develop strategies to reach the most demanding of repetition rates.

In addition to a range of high-repetition-rate laser systems there are many multi-beam high-energy facilities that are open to the academic community to carry out fundamental science experiments. The National Ignition Facility (NIF) has a discovery science program with 41 shots dedicated to this in 2018^[390]. These targets are provided by the extensive capabilities that are available to the NIF for its internal program in inertial confinement fusion, high-energy-density physics and national security applications. Other large-scale facilities such as the Laser MegaJoule (France), Orion (UK) and SG-III (China), while having significant internal capability, require external academic users to provide their own targets (Figure 43). These targets will require access and expertise to the most cutting-edge fabrication and assembly processes, such as diamond point turning, coatings of materials, such as high-density carbon, characterization of properties, such as grain size and orientation, and indeed the ability to change these parameters for experimental needs. These facilities are not available to most small-scale university user groups, and while larger groups such as those at the University of Michigan (US) or the Laboratory for Laser Energetics in Rochester (US) have capability to field experiments, for smaller groups national laboratories such as the Rutherford Appleton Laboratory, or commercial companies such as General Atomics or Scitech Precision, are able to provide targets.

5. Conclusion

This review of petawatt and exawatt class lasers has attempted to provide a snapshot in time of the state-of-the-art of the global capabilities in the ultra-high-power environment. The profusion of these facilities in national laboratories and university departments is largely due to some key developments – not least, the invention of the technique of CPA. Part of the motivation for this review is to provide a tribute to the work of Donna Strickland and Gerard Mourou as the inventors of CPA and to whom the 2018 Nobel Prize in Physics was awarded.

We have presented a comprehensive overview of the current status of petawatt class lasers worldwide. We have described over 50 facilities that are, or have been, operational, under construction, or in the planning/conceptual phase. Many of these facilities are coupled and synchronized to other sources, such as nanosecond lasers, XFELs, particle beams and z-pinchs.

The evolution of such facilities, and the science they have enabled, has been placed in a historical context, describing how the early pioneering work in the US has today been progressed, notably in Europe and Asia. Increasingly, as technology advances, high-average-power machines are being constructed in preference to single-shot facilities. Meanwhile, work continues apace to increase peak powers to the highest possible values.

In looking to the future, we have described some of the technologies that will lead to the next generation of lasers: delivering higher peak powers for fundamental research; and higher average powers relevant to applications. In looking through our crystal ball it is not clear what these facilities will look like 10, 20 or even 50 years from now, but it promises to be a fascinating journey.

Acknowledgements

The authors would like to acknowledge the help and advice from the following researchers in putting this review together; they provided invaluable information on specific facilities and helped validate the information presented: Nathalie Blanchot, CEA, France; Mirela Cerchez, Heinrich-Heine University, Germany; Ioan Dancus, ELI-NP, Romania; Brendan Dromey, Queen's University Belfast, UK; Gilliss Dyer, SLAC, US; Goncalo Figueira, IST, Portugal; Alessandro Flacco, LOA, France; Julien Fuchs, Ecole Polytechnique, France; Yuqiu Gu, Research Center for Laser Fusion, China; Stefan Karsch, CALA, Germany; Junji Kawanaka, ILE Osaka University, Japan; Hiromitsu Kiriya, KPSI, QST, Japan; Seong Ku Lee, APRI, GIST, South Korea; Aurelian Marco, CETAL, Romania; Robin Marjoribanks, University of Toronto, Canada; Mikael Martinez, SLAC, US; Paul Mason, STFC Rutherford Appleton Laboratory, UK; Ian Musgrave, STFC Rutherford Appleton Laboratory, UK;

Moanne Pittman, LASERIX, France; Sergey Popruzenko, MEPHI, Russia; Patrick Rambo, Sandia National Laboratory, US; Luis Roso, University of Salamanca, Spain; Claude Rouyer, CEA, France; Yuji Sano, ImPACT Project, Japan; Stephane Sebban, LOA, France; Wilson Sibbett, University of St Andrews, UK; Hiroyuki Shiraga, ILE Osaka University, Japan; Francisco Suzuki-Vidal, Imperial College London, UK; Zhiyi Wei, IOP Beijing, China; Mark Wiggins, University of Strathclyde, UK; Makina Yabashi, RIKEN, Japan; Kainan Zhou, Research Center for Laser Fusion, China.

References

1. S. Backus, C. G. Durfee, III, M. M. Murnane, and H. C. Kapteyn, *Rev. Sci. Instrum.* **69**, 1207 (1998).
2. M. D. Perry, D. Pennington, B. C. Stuart, G. Tietbohl, J. A. Britten, C. Brown, S. Herman, B. Golick, M. Kartz, J. Miller, H. T. Powell, M. Vergino, and V. Yanovsky, *Opt. Lett.* **24**, 3 (1999).
3. C. Danson, D. Hillier, N. Hopps, and D. Neely, *High Power Laser Sci. Eng.* **3**, e3 (2015).
4. Nobel Prize website: <https://www.nobelprize.org/uploads/2018/10/advanced-physicsprize2018.pdf>.
5. NAP website: <http://nap.edu/24939>.
6. OECD website: <http://www.oecd.org>.
7. IUPAP website: <http://iupap.org>.
8. ICUIL website: <https://www.icuil.org>.
9. T. H. Maiman, *Nature* **187**, 493 (1960).
10. F. J. McClung and R. W. Hellwarth, *J. Appl. Phys.* **33**, 828 (1962).
11. L. E. Hargrove, R. L. Fork, and M. A. Pollack, *Appl. Phys. Lett.* **5**, 4 (1964).
12. M. DiDomenico, Jr., *J. Appl. Phys.* **35**, 2870 (1964).
13. A. Yariv, *J. Appl. Phys.* **36**, 388 (1965).
14. H. W. Mocker and R. J. Collins, *Appl. Phys. Lett.* **7**, 270 (1965).
15. A. J. DeMaria, D. A. Stetser, and H. Heynau, *Appl. Phys. Lett.* **8**, 174 (1966).
16. D. Strickland and G. Mourou, *Opt. Commun.* **56**, 219 (1985).
17. E. Brookner, *Sci. Am.* **252** (1985).
18. R. L. Fork, O. E. Martinez, and J. P. Gordon, *Opt. Lett.* **9**, 150 (1984).
19. O. Martinez, *IEEE J. Quantum Electron.* **23**, 59 (1987).
20. E. B. Treacy, *IEEE J. Quantum Electron.* **5**, 454 (1969).
21. M. Ferray, L. A. Lompré, O. Gobert, A. L'huillier, G. Mainfray, C. Manus, A. Sanchez, and A. S. Gomes, *Opt. Commun.* **75**, 278 (1990).
22. F. G. Patterson and M. D. Perry, *J. Opt. Soc. Am. B* **8**, 2384 (1991).
23. K. Yamakawa, C. P. J. Barty, H. Shiraga, and Y. Kato, *Opt. Lett.* **16**, 1593 (1991).
24. C. Sauteret, G. Mourou, D. Husson, G. Thiell, S. Seznec, S. Gary, and A. Migus, *Opt. Lett.* **16**, 238 (1991).
25. B. Nikolaus, D. Grischkowsky, and A. C. Balant, *Opt. Lett.* **8**, 189 (1983).
26. P. F. Moulton, *J. Opt. Soc. Am. B* **3**, 125 (1986).
27. D. E. Spence, P. N. Kean, and W. Sibbet, *Opt. Lett.* **16**, 42 (1991).
28. C. P. J. Barty, *Opt. Lett.* **19**, 1442 (1994).
29. J. Squier, F. Salin, S. Coe, P. Bado, and G. Mourou, *Opt. Lett.* **16**, 85 (1991).
30. M. W. Phillips, Z. Chang, C. N. Danson, J. R. M. Barr, D. W. Hughes, C. B. Edwards, and D. C. Hanna, *Opt. Lett.* **17**, 1453 (1992).

31. G. Cheriaux, B. Walker, L. F. Rousseau, F. Salin, and J. P. Chambaret, *Opt. Lett.* **21**, 414 (1996).
32. C. Rouyer, G. Mourou, A. Migus, E. Mazataud, I. Allais, A. Pierre, S. Seznec, and C. Sauteret, *Opt. Lett.* **18**, 214 (1993).
33. N. Blanchot, C. Rouyer, C. Sauteret, and A. Migus, *Opt. Lett.* **20**, 395 (1995).
34. C. N. Danson, L. J. Barzanti, Z. Chang, A. E. Damerell, C. B. Edwards, S. Hancock, M. H. R. Hutchinson, M. H. Key, S. Luan, R. R. Mahadeo, I. P. Mercer, P. Norreys, D. A. Pepler, D. A. Rodkiss, I. N. Ross, M. A. Smith, R. A. Smith, P. Taday, W. T. Toner, K. W. M. Wigmore, T. B. Winstone, R. W. W. Wyatt, and F. Zhou, *Opt. Commun.* **103**, 392 (1993).
35. C. N. Danson, J. Collier, D. Neely, L. J. Barzanti, A. Damerell, C. B. Edwards, M. H. R. Hutchinson, M. H. Key, P. A. Norreys, D. A. Pepler, I. N. Ross, P. F. Taday, W. T. Toner, M. Trentelman, F. N. Walsh, T. B. Winstone, and R. W. W. Wyatt, *J. Mod. Opt.* **45**, 1653 (1998).
36. C. N. Danson, P. A. Brummitt, R. J. Clarke, J. L. Collier, B. Fell, A. J. Frackiewicz, S. Hancock, S. Hawkes, C. Hernandez-Gomez, P. Holligan, M. H. R. Hutchinson, A. Kidd, W. J. Lester, I. O. Musgrave, D. Neely, D. R. Neville, P. A. Norreys, D. A. Pepler, C. J. Reason, W. Shaikh, T. B. Winstone, R. W. W. Wyatt, and B. E. Wyborn, *IAEA J. Nucl. Fusion* **44**, S239 (2004).
37. J. H. Kelly, L. J. Waxer, V. Bagnoud, I. A. Begishev, J. Bromage, B. E. Kruschwitz, T. J. Kessler, S. J. Loucks, D. N. Maywar, R. L. McCrory, D. D. Meyerhofer, S. F. B. Morse, J. B. Oliver, A. L. Rigatti, A. W. Schmid, C. Stoeckl, S. Dalton, L. Folsbee, M. J. Guardalben, R. Jungquist, J. Puth, M. J. Shoup, III, D. Weiner, and J. D. Zuegel, *J. Phys. IV* **133**, 75 (2006).
38. G. H. Miller, E. I. Moses, and C. R. West, *Opt. Eng.* **43**, 2841 (2004).
39. M. Aoyama, K. Yamakawa, Y. Akahane, J. Ma, N. Inoue, H. Ueda, and H. Kiriya, *Opt. Lett.* **28**, 1594 (2003).
40. W. P. Leemans, J. Daniels, A. Deshmukh, A. J. Gonsalves, A. Magana, H. S. Mao, D. E. Mittelberger, K. Nakamura, J. R. Riley, D. Syversrud, C. Toth, and N. Ybarrolaza, in *Proceedings of PAC2013* (2013), paper THYAA1.
41. C. L. Hafner, A. Bayramian, S. Betts, R. Bopp, S. Buck, J. Cupal, M. Drouin, A. Erlandson, J. Horáček, J. Horner, J. Jarboe, K. Kasl, D. Kim, E. Koh, L. Koubíková, W. Maranville, C. Marshall, D. Mason, J. Menapace, P. Miller, P. Mazurek, A. Naylor, J. Novák, D. Peceli, P. Rosso, K. Schaffers, E. Sistrunk, D. Smith, T. Spinka, J. Stanley, R. Steele, C. Stolz, T. Suratwala, S. Telford, J. Thoma, D. VanBlarcom, J. Weiss, and P. Wegner, *Proc. SPIE* **10241**, 1024102 (2017).
42. Thales website: <https://www.thalesgroup.com/en/group/journalist/press-release/worlds-most-powerful-laser-developed-thales-and-eli-np-achieves>.
43. A. Dubietis, G. Jonušauskas, and A. Piskarskas, *Opt. Commun.* **88**, 437 (1992).
44. Laserlab-Europe website: <https://www.laserlab-europe.eu/>.
45. ELI white book: <https://eli-laser.eu/media/1019/eli-whitebook.pdf>.
46. EuPRAXIA website: <http://www.eupraxia-project.eu/inf.html>.
47. W. Leemans, 2017. http://www2.lbl.gov/LBL-Programs/atap/Report_Workshop_k-BELLA_laser_tech_final.pdf.
48. J. M. Cole, D. R. Symes, N. C. Lopes, J. C. Wood, K. Poder, S. Alatabi, S. W. Botchway, P. S. Foster, S. Grattan, S. Johnson, C. Kamperidis, O. Kononenko, M. De Lazzari, C. Palmer, D. Rusby, J. Sanderson, M. Sandholzer, G. Sarri, Z. Szoke-Kovacs, L. Teboul, J. M. Thompson, J. R. Warwick, H. Westerberg, M. A. Hill, D. P. Norris, S. P. D. Mangles, and Z. Najmudin, *Proc. Natl Acad. Sci. USA* **115**, 6335 (2018).
49. M. Roth, D. Jung, K. Falk, N. Guler, O. Depfert, M. Devlin, A. Favalli, J. Fernandez, D. Gautier, M. Geissel, R. Haight, C. E. Hamilton, B. M. Hegelich, R. P. Johnson, F. Merrill, G. Schaumann, K. Schoenberg, M. Schollmeier, T. Shimada, T. Taddeucci, J. L. Tybo, F. Wagner, S. A. Wender, C. H. Wilde, and G. A. Wurden, *Phys. Rev. Lett.* **110**, 044802 (2013).
50. V. Moskvina, A. Subiel, C. Desrosiers, M. Wiggins, M. Maryanski, M. Mendonca, M. Boyd, A. Sorensen, S. Cipiccia, R. Issac, G. Welsh, E. Brunetti, C. Aniculaesei, and D. A. Jaroszynski, *Med. Phys.* **39**, 3813 (2012).
51. A. Giulietti, Ed., *Biological and Medical Physics, Biomedical Engineering* (Springer, 2016).
52. D. Speck, E. Bliss, J. Glaze, J. Herris, F. Holloway, J. Hunt, B. Johnson, D. Kuizenga, R. Ozarski, H. Patton, P. Rupert, G. Suski, C. Swift, and C. Thompson, *IEEE J. Quantum Electron.* **17**, 1599 (1981).
53. J. D. Lindl, O. Landen, J. Edwards, E. Moses, and NIC Team, *Phys. Plasmas* **21**, 020501 (2014).
54. Optics.org website: <http://optics.org/news/9/7/20>.
55. C. P. J. Barty, M. Key, J. Britten, R. Beach, G. Beer, C. Brown, S. Bryan, J. Caird, T. Carlson, J. Crane, J. Dawson, A. C. Erlandson, D. Fittinghoff, M. Hermann, C. Hoaglan, A. Iyer, L. Jones, II, I. Jovanovic, A. Komashko, O. Landen, Z. Liao, W. Molander, S. Mitchell, E. Moses, N. Nielsen, H.-H. Nguyen, J. Nissen, S. Payne, D. Pennington, L. Risinger, M. Rushford, K. Skulina, M. Spaeth, B. Stuart, G. Tietbohl, and B. Wattellier, *Nucl. Fusion* **44**, S266 (2004).
56. J. A. Britten, W. A. Molander, A. M. Komashko, and C. P. J. Barty, *Proc. SPIE* **5273**, 1 (2004).
57. C. Hafner, J. E. Heebner, J. Dawson, S. Fochs, M. Shverdin, J. K. Crane, K. V. Kaniz, J. Halpin, H. Phan, R. Sigurdsson, W. Brewer, J. Britten, G. Brunton, B. Clark, M. J. Messerly, J. D. Nissen, B. Shaw, R. Hackel, M. Hermann, G. Tietbohl, C. W. Siders, and C. P. J. Barty, *J. Phys.: Conf. Ser.* **244**, 032005 (2010).
58. C. Hafner, R. Hackel, J. Halpin, J. K. Crane, M. J. Messerly, J. D. Nissen, M. Shverdin, B. Shaw, J. W. Dawson, C. W. Siders, and C. P. J. Barty, in *Conference on Lasers/Electro-Optics and International Quantum Electronics Conference* (2009), paper CMBB4.
59. B. C. Stuart, J. D. Bonlie, J. A. Britten, J. A. Caird, R. Cross, C. A. Ebberts, M. J. Eckart, A. C. Erlandson, W. A. Molander, A. Ng, P. K. Patel, and D. Price, in *CLEO Technical Digest* (Optical Society of America, 2006), paper JTuG3.
60. A. Bayramian, P. Armstrong, E. Ault, R. Beach, C. Bibeau, J. Caird, R. Campbell, B. Chai, J. Dawson, C. Ebberts, A. Erlandson, Y. Fei, B. Freitas, R. Kent, Z. Liao, T. Ladrán, J. Menapace, B. Molander, S. Payne, N. Peterson, M. Randles, K. Schaffers, S. Sutton, J. Tassano, S. Telford, and E. Utterback, *Fusion Sci. Technol.* **52**, 383 (2007).
61. B. M. Van Wonterghem, J. R. Murray, J. H. Campbell, D. R. Speck, C. E. Barker, I. C. Smith, D. F. Browning, and W. C. Behrendt, *Appl. Opt.* **36**, 4932 (1997).
62. P. K. Rambo, I. C. Smith, J. L. Porter, Jr., M. J. Hurst, C. S. Speas, R. G. Adams, A. J. Garcia, E. Dawson, B. D. Thurston, C. Wakefield, J. W. Kellogg, M. J. Slattery, H. C. Ives, III, R. S. Broyles, J. A. Caird, A. C. Erlandson, J. E. Murray, W. C. Behrendt, N. D. Neilsen, and J. M. Narduzzi, *Appl. Opt.* **44**, 2421 (2005).
63. J. Schwarz, P. Rambo, M. Geissel, A. Edens, I. Smith, E. Brambrink, M. Kimmel, and B. Atherton, *J. Phys.: Conf. Ser.* **112**, 032020 (2008).

64. J. Schwarz, P. Rambo, D. Armstrong, M. Schollmeier, I. Smith, J. Shores, M. Geissel, M. Kimmel, and J. Porter, *High Power Laser Sci. Eng.* **4**, e36 (2016).
65. P. Rambo, J. Schwarz, M. Schollmeier, M. Geissel, I. Smith, M. Kimmel, C. Speas, J. Shores, D. Armstrong, J. Bellum, E. Field, D. Kletecka, and J. Porter, *Proc. SPIE* **10014**, 100140Z (2016).
66. LaserNetUS website: <https://www.lasernetus.org/>.
67. Y. Wang, S. Wang, A. Rockwood, B. M. Luther, R. Hollinger, A. Curtis, C. Calvi, C. S. Menoni, and J. Rocca, *Opt. Lett.* **42**, 3828 (2017).
68. C. Baumgarten, M. Pedicone, H. Bravo, H. Wang, L. Yin, C. S. Menoni, J. Rocca, and B. A. Reagan, *Opt. Lett.* **41**, 3339 (2016).
69. A. J. Gonsalves, K. Nakamura, J. Daniels, C. Benedetti, C. Pieronek, T. C. H. de Raadt, S. Steinke, J. H. Bin, S. S. Bulanov, J. van Tilborg, C. G. R. Geddes, C. B. Schroeder, Cs. Tóth, E. Esarey, K. Swanson, L. Fan-Chiang, G. Bagdasarov, N. Bobrova, V. Gasilov, G. Korn, P. Sasorov, and W. P. Leemans, *Phys. Rev. Lett.* **122**, 084801 (2019).
70. S. W. Bahk, P. Rousseau, T. A. Planchon, V. Chvykov, G. Kalintchenko, A. Maksimchuk, G. A. Mourou, and V. Yanovsky, *Opt. Lett.* **29**, 2837 (2004).
71. V. Yanovsky, V. Chvykov, G. Kalintchenko, P. Rousseau, T. Planchon, T. Matsuoka, A. Maksimchuk, J. Nees, G. Cheriaux, G. Mourou, and K. Krushelnick, *Opt. Express* **16**, 2109 (2008).
72. B. Hou, J. Nees, J. Easter, J. Davis, G. Petrov, A. Thomas, and K. Krushelnick, *Appl. Phys. Lett.* **95**, 3 (2009).
73. C. Liu, S. Banerjee, J. Zhang, S. Chen, K. Brown, J. Mills, N. Powers, B. Zhao, G. Golovin, I. Ghebregziabher, and D. Umstadter, *Proc. SPIE* **8599**, 859919 (2013).
74. C. Liu, J. Zhang, S. Chen, G. Golovin, S. Banerjee, B. Zhao, N. Powers, I. Ghebregziabher, and D. Umstadter, *Opt. Lett.* **39**, 1 (2014).
75. C. Liu, G. Golovin, S. Chen, J. Zhang, B. Zhao, D. Haden, S. Banerjee, J. Silano, H. Karwowski, and D. Umstadter, *Opt. Lett.* **39**, 14 (2014).
76. W. Yan, C. Fruhling, G. Golovin, D. Haden, J. Luo, P. Zhang, B. Zhao, J. Zhang, C. Liu, M. Chen, S. Chen, S. Banerjee, and D. Umstadter, *Nat. Photonics* **11**, 514 (2017).
77. E. W. Gaul, M. Martinez, J. Blakeney, A. Jochmann, M. Ringuette, D. Hammond, T. Borger, R. Escamilla, S. Douglas, W. Henderson, G. Dyer, A. Erlandson, R. Cross, J. Caird, C. Ebberts, and T. Ditmire, *Appl. Opt.* **49**, 9 (2010).
78. P. L. Poole, C. Willis, R. L. Daskalova, K. M. George, S. Feister, S. Jiang, J. Snyder, J. Marketon, D. W. Schumacher, K. U. Akli, L. Van Woerkom, R. R. Freeman, and E. A. Chowdhury, *Appl. Opt.* **55**, 4713 (2016).
79. S. Jiang, L. L. Ji, H. Audesirk, K. M. George, J. Snyder, A. Krygier, P. Poole, C. Willis, R. Daskalova, E. Chowdhury, N. S. Lewis, D. W. Schumacher, A. Pukhov, R. R. Freeman, and K. U. Akli, *Phys. Rev. Lett.* **116**, 085002 (2016).
80. S. Formaux, S. Payeur, A. Alexandrov, C. Serbanescu, F. Martin, T. Ozaki, A. Kudryashov, and J. C. Kieffer, *Opt. Express* **16**, 11987 (2008).
81. ALLS website: <http://inf.emt.inrs.ca/?q=en/ALLS>.
82. C. Hernandez-Gomez, P. A. Brummitt, D. J. Canny, R. J. Clarke, J. Collier, C. N. Danson, A. M. Dunne, B. Fell, A. J. Frackiewicz, S. Hancock, S. Hawkes, R. Heathcote, P. Holligan, M. H. R. Hutchinson, A. Kidd, W. J. Lester, I. O. Musgrave, D. Neely, D. R. Neville, P. A. Norreys, D. A. Pepler, C. J. Reason, W. Shaikh, T. B. Winstone, and B. E. Wyborn, *J. Phys. IV* **133**, 555 (2006).
83. I. O. Musgrave, A. Boyle, D. Carroll, R. Clarke, R. Heathcote, M. Galimberti, J. Green, D. Neely, M. Notley, B. Parry, W. Shaikh, T. Winstone, D. Pepler, A. Kidd, C. Hernandez-Gomez, and J. Collier, *Proc. SPIE* **8780**, 878003 (2013).
84. C. Hernandez-Gomez, S. P. Blake, O. Chekhlov, R. J. Clarke, A. M. Dunne, M. Galimberti, S. Hancock, R. Heathcote, P. Holligan, A. Lyachev, P. Matousek, I. O. Musgrave, D. Neely, P. A. Norreys, I. Ross, Y. Tang, T. B. Winstone, B. E. Wyborn, and J. Collier, *J. Phys.: Conf. Ser.* **244**, 032006 (2010).
85. C. J. Hooker, J. L. Collier, O. Chekhlov, R. J. Clarke, E. J. Divall, K. Ertel, P. Foster, S. Hancock, S. J. Hawkes, P. Holligan, A. J. Langley, W. J. Lester, D. Neely, B. T. Parry, and B. E. Wyborn, *Rev. Laser Engng* **37**, 443 (2009).
86. N. Hopps, K. Oades, J. Andrew, C. Brown, G. Cooper, C. Danson, S. Daykin, S. Duffield, R. Edwards, D. Egan, S. Elsmere, S. Gales, M. Girling, E. Gumbrell, E. Harvey, D. Hillier, D. Hoarty, C. Horsfield, S. James, A. Leatherland, S. Masoero, A. Meadowcroft, M. Norman, S. Parker, S. Rothman, M. Rubery, P. Treadwell, D. Winter, and T. Bett, *Plasma Phys. Control. Fusion* **57**, 064002 (2015).
87. S. Parker, C. Danson, D. Egan, S. Elsmere, M. Girling, E. Harvey, D. Hillier, D. Hussey, S. Masoero, J. McLoughlin, R. Penman, P. Treadwell, D. Winter, and N. Hopps, *High Power Laser Sci. Eng.* **6**, e47 (2018).
88. D. A. Jaroszynski, B. Ersfeld, M. R. Islam, E. Brunetti, R. P. Shanks, P. A. Grant, M. P. Tooley, D. W. Grant, D. Reboredo Gil, P. Lepipas, G. McKendrick, S. Cipiccia, S. M. Wiggins, G. H. Welsh, G. Vieux, S. Chen, C. Aniculaesei, G. G. Manahan, M.-P. Anania, A. Noble, S. R. Yoffe, G. Raj, A. Subiel, X. Yang, Z. M. Sheng, B. Hidding, R. C. Issac, M. H. Cho, and M. S. Hur, in *Proceedings of 40th International Conference on IRMMW-THz* (2015), paper H2E-1.
89. J. Ebrardt and J. M. Chaput, *J. Phys.: Conf. Ser.* **244**, 032017 (2010).
90. M. Nicolaizeau and P. Vivini, *Proc. SPIE* **10084**, 1008402 (2017).
91. N. Blanchot, G. Behar, T. Berthier, E. Bignon, F. Boubault, C. Chappuis, H. Coïc, C. Damiens-Dupont, J. Ebrardt, Y. Gautheron, P. Gibert, O. Hartmann, E. Hugonnot, F. Laborde, D. Lebeaux, J. Luce, S. Montant, S. Noailles, J. Néauport, D. Raffestin, B. Remy, A. Roques, F. Sautarel, M. Sautet, C. Sauteret, and C. Rouyer, *Plasma Phys. Control. Fusion* **50**, 1240045 (2008).
92. N. Blanchot, G. Béhar, J. C. Chapuis, C. Chappuis, S. Chardavoine, J. F. Charrier, H. Coïc, C. Damiens-Dupont, J. Duthu, P. Garcia, J. P. Goossens, F. Granet, C. Grosset-Grange, P. Guerin, B. Hebrard, L. Hilsz, L. Lamaignere, T. Lacombe, E. Lavastre, T. Longhi, J. Luce, F. Macias, M. Mangeant, E. Mazataud, B. Minou, T. Morgaint, S. Noailles, J. Neauport, P. Patelli, E. Perrot-Minnot, C. Present, B. Remy, C. Rouyer, N. Santacreu, M. Sozet, D. Valla, and F. Lanieste, *Opt. Express* **25**, 16957 (2017).
93. 'LMJ Users Guide' and 'LMJ-PETAL scientific case': <http://www-lmj.cea.fr/en/ForUsers.htm>.
94. D. Ros, K. Cassou, B. Cros, S. Daboussi, J. Demailly, O. Guilbaud, S. Kazamias, J.-C. Lagron, G. Maynard, O. Neveu, M. Pittman, B. Zielbauer, D. Zimmer, T. Kuhl, S. Lacombe, E. Porcel, M. A. duPenhoat, P. Zeitoun, and G. Mourou, *Nucl. Instrum. Methods. Phys. Res. A* **653**, 76 (2011).
95. F. Ple, M. Pittman, G. Jamelot, and J. P. Chambaret, *Opt. Lett.* **32**, 3 (2007).
96. D. N. Papadopoulos, J. P. Zou, C. Le Blanc, G. Chériaux, P. Georges, F. Druon, G. Mennerat, P. Ramirez, L. Martin,

- A. Fréneaux, A. Beluze, N. Lebas, P. Monot, F. Mathieu, and P. Audebert, *High Power Laser Sci. Eng.* **4**, e34 (2016).
97. D. N. Papadopoulos, P. Ramirez, K. Genevriér, L. Ranc, N. Lebas, A. Pellegrina, C. LeBlanc, P. Monot, L. Martin, J. P. Zou, F. Mathieu, P. Audebert, P. Georges, and F. Druon, *Opt. Lett.* **42**, 3530 (2017).
 98. D. N. Papadopoulos, J. P. Zou, C. Le Blanc, L. Ranc, F. Druon, L. Martin, A. Fréneaux, A. Beluze, N. Lebas, M. Chabanis, C. Bonnin, J. B. Accary, B. L. Garrec, F. Mathieu, and P. Audebert, in *Conference on Lasers and Electro-Optics* (Optical Society of America, 2019), paper STu3E.4.
 99. A. Kessel, V. E. Leshchenko, O. Jahn, M. Krüger, A. Münzer, A. Schwarz, V. Pervak, M. Trubetskov, S. A. Trushin, F. Krausz, Z. Major, and S. Karsch, *Optica* **5**, 434 (2018).
 100. M. Cerchez, R. Prasad, B. Aurand, A. L. Giesecke, S. Spickermann, S. Brauckmann, E. Aktan, M. Swantusch, M. Toncian, T. Toncian, and O. Willi, *High Power Laser Sci. Eng.* **7**, e37 (2019).
 101. V. Bagnoud, B. Aurand, A. Blazevic, S. Borneis, C. Bruske, B. Ecker, U. Eisenbarth, J. Fils, A. Frank, E. Gaul, S. Goette, C. Haefner, T. Hahn, K. Harres, H.-M. Heuck, D. Hochhaus, D. H. H. Hoffmann, D. Javorková, H.-J. Kluge, T. Kuehl, S. Kunzer, M. Kreutz, T. Merz-Mantwill, P. Neumayer, E. Onkels, D. Reemts, O. Rosmej, M. Roth, T. Stoehlker, A. Tauschwitz, B. Zielbauer, D. Zimmer, and K. Witte, *Appl. Phys. B* **100**, 137 (2010).
 102. M. Hornung, H. Liebetrau, S. Keppler, A. Kessler, M. Hellwing, F. Schorcht, G. A. Becker, M. Reuter, J. Polz, J. Körner, J. Hein, and M. C. Kaluza, *Opt. Lett.* **41**, 22 (2016).
 103. M. Siebold, F. Roeser, M. Loeser, D. Albach, and U. Schramm, *Proc. SPIE* **8780**, 878005 (2013).
 104. D. Albach, M. Loeser, M. Siebold, and U. Schramm, *High Power Laser Sci. Eng.* **7**, e1 (2019).
 105. K. Zeil, S. D. Kraft, S. Bock, M. Bussmann, T. E. Cowan, T. Kluge, J. Metzkes, T. Richter, R. Sauerbrey, and U. Schramm, *New J. Phys.* **12**, 045015 (2010).
 106. N. Delbos, C. Werle, I. Dornmair, T. Eichner, L. Hübner, S. Jalas, S. W. Jolly, M. Kirchen, V. Leroux, P. Messner, M. Schnepf, M. Trunk, P. A. Walker, P. Winkler, and A. R. Maier, *Nucl. Instr. Meth. Phys. Res. A* **909**, 318 (2018).
 107. HIBEF website: <https://www.hzdr.de/db/Cms?pOid=50566&pNid=694&pLang=en>.
 108. V. V. Lozhkarev, G. I. Freidman, V. N. Ginzburg, E. V. Katin, E. A. Khazanov, A. V. Kirsanov, G. A. Luchinin, A. N. Mal'shakov, M. A. Martyanov, O. V. Palashov, A. K. Poteomkin, A. M. Sergeev, A. A. Shaykin, and I. V. Yakovlev, *Opt. Express* **14**, 446 (2006).
 109. V. V. Lozhkarev, G. I. Freidman, V. N. Ginzburg, E. V. Katin, E. A. Khazanov, A. V. Kirsanov, G. A. Luchinin, A. N. Mal'shakov, M. A. Martyanov, O. V. Palashov, A. K. Poteomkin, A. M. Sergeev, A. A. Shaykin, and I. V. Yakovlev, *Laser Phys. Lett.* **4**, 421 (2007).
 110. V. B. Rozanov, S. Gus'kov, G. Vergunova, N. Demchenko, R. Stepanov, I. Doskoch, R. Yakhin, S. Bel'kov, S. Bondarenko, and N. Zmitrenko, in *IFSA-2013* (2013), paper O.TuA15.
 111. L. Roso, *Proc. SPIE* **8001**, 800113 (2011).
 112. L. Roso, *EPJ Web Conf.* **167**, 01001 (2018).
 113. L. A. Gizzi, C. Benedetti, C. Alberto Cecchetti, G. Di Pirro, A. Gamucci, G. Gatti, A. Giuliètti, D. Giuliètti, P. Koester, L. Labate, T. Levato, N. Pathak, and F. Piastra, *Appl. Sci.* **3**, 559 (2013).
 114. L. A. Gizzi, D. Giove, C. Altana, F. Brandi, P. Cirrone, G. Cristoforetti, A. Fazzi, P. Ferrara, L. Fulgentini, P. Koester, L. Labate, G. Lanzalone, P. Londrillo, D. Mascali, A. Muoio, D. Palla, F. Schillaci, S. Sinigardi, S. Tudisco, and G. Turchetti, *Appl. Sci.* **7**, 984 (2017).
 115. CETAL website: www.cetal.inflpr.ro.
 116. P. A. Walker, P. D. Alesini, A. S. Alexandrova, M. P. Anania, N. E. Andreev, I. Andriyash, A. Aschikhin, R. W. Assmann, T. Audet, A. Bacci, I. F. Barna, A. Beaton, A. Beck, A. Beluze, A. Bernhard, S. Bielawski, F. G. Bisesto, J. Boedewadt, F. Brandi, O. Bringer, R. Brinkmann, E. Bründermann, M. Büscher, M. Bussmann, G. C. Bussolino, A. Chance, J. C. Chanteloup, M. Chen, E. Chiadroni, A. Cianchi, J. Clarke, J. Cole, M. E. Couprie, M. Croia, B. Cros, J. Dale, G. Dattoli, N. Delerue, O. Delferriere, P. Delinikolas, J. Dias, U. Dorda, K. Ertel, A. Ferran Pousa, M. Ferrario, F. Filippi, J. Fils, R. Fiorito, R. A. Fonseca, M. Galimberti, A. Gallo, D. Garzella, P. Gastinel, D. Giove, A. Giribono, L. A. Gizzi, F. J. Grüner, A. F. Habib, L. C. Haefner, T. Heinemann, B. Hidding, B. J. Holzer, S. M. Hooker, T. Hosokai, A. Irman, D. A. Jaroszynski, S. Jaster-Merz, C. Joshi, M. C. Kaluza, M. Kando, O. S. Karger, S. Karsch, E. Khazanov, D. Khikhlikha, A. Knetsch, D. Kocon, P. Koester, O. Kononenko, G. Korn, I. Kostyukov, L. Labate, C. Lechner, W. P. Leemans, A. Lehrach, F. Y. Li, X. Li, V. Libov, A. Lifschitz, V. Litvinenko, W. Lu, A. R. Maier, V. Malka, G. G. Manahan, S. P. D. Mangles, B. Marchetti, A. Marocchino, A. Martinez de la Ossa, J. L. Martins, F. Massimo, F. Mathieu, G. Maynard, T. J. Mehrling, A. Y. Molodozhentsev, A. Mosnier, A. Mostacci, A. S. Mueller, Z. Najmudin, P. A. P. Nghiem, F. Nguyen, P. Niknejadi, J. Osterhoff, D. Papadopoulos, B. Patrizi, R. Pattathil, V. Petrillo, M. A. Pocsai, K. Poder, R. Pompili, L. Pribyl, D. Pugacheva, S. Romeo, A. R. Rossi, E. Roussel, A. A. Sahai, P. Scherkl, U. Schramm, C. B. Schroeder, J. Schwindling, J. Scifo, L. Serafini, Z. M. Sheng, L. O. Silva, T. Silva, C. Simon, U. Sinha, A. Specka, M. J. V. Streeter, E. N. Svystun, D. Szymes, C. Szawaj, G. Tauscher, A. G. R. Thomas, N. Thompson, G. Toci, P. Tomassini, C. Vaccarezza, M. Vannini, J. M. Vieira, F. Villa, C.-G. Wahlström, R. Walczak, M. K. Weikum, C. P. Welsch, C. Wiemann, J. Wolfenden, G. Xia, M. Yabashi, L. Yu, J. Zhu, and A. Zigler, *J. Phys.: Conf. Ser.* **874**, 012029 (2017).
 117. L. A. Gizzi, F. Baffigi, F. Brandi, G. Bussolino, G. Cristoforetti, A. Fazzi, L. Fulgentini, D. Giove, P. Koester, L. Labate, G. Maero, D. Palla, M. Romé, and P. Tomassini, *NIM A* **902**, 160 (2018).
 118. L. A. Gizzi, P. Koester, L. Labate, F. Mathieu, Z. Mazzotta, G. Toci, and M. Vannini, *Nucl. Instrum. Methods Phys. Res. A* **909**, 58 (2018).
 119. G. Xu, T. Wang, Z. Li, Y. Dai, Z. Lin, Y. Gu, and J. Zhu, *Rev. Laser Eng.* **36**, 1172 (2008).
 120. J. Zhu, J. Zhu, X. Li, B. Zhu, W. Ma, X. Lu, W. Fan, Z. Liu, S. Zhou, G. Xu, G. Zhang, X. Xie, L. Yang, J. Wang, X. Ouyang, L. Wang, D. Li, P. Yang, Q. Fan, M. Sun, C. Liu, D. Liu, Y. Zhang, H. Tao, M. Sun, P. Zhu, B. Wang, Z. Jiao, L. Ren, D. Liu, X. Jiao, H. Huang, and Z. Lin, *High Power Laser Sci. Eng.* **6**, e55 (2018).
 121. J. Zhu, X. Xie, M. Sun, J. Kang, Q. Yang, A. Guo, H. Zhu, P. Zhu, Q. Gao, X. Liang, Z. Cui, S. Yang, C. Zhang, and Z. Lin, *High Power Laser Sci. Eng.* **6**, e29 (2018).
 122. X. Liang, Y. Leng, C. Wang, C. Li, L. Lin, B. Zhao, Y. Jiang, X. Lu, M. Hu, C. Zhang, H. Lu, D. Yin, Y. Jiang, X. Lu, H. Wei, J. Zhu, R. Li, and Z. Xu, *Opt. Express* **15**, 15335 (2007).
 123. Y. Chu, X. Liang, L. Yu, Y. Xu, L. Ma, X. Lu, Y. Liu, Y. Leng, R. Li, and Z. Xu, *Opt. Express* **21**, 24 (2013).
 124. Y. Chu, Z. Gan, X. Liang, L. Yu, X. Lu, C. Wang, X. Wang, L. Xu, H. Lu, D. Yin, Y. Leng, R. Li, and Z. Xu, *Opt. Lett.* **40**, 5011 (2015).

125. X. Yang, Z. Xu, Y. Leng, H. Lu, L. Lin, Z. Zhang, R. Li, W. Zhang, D. Yin, and B. Tang, *Opt. Lett.* **27**, 1135 (2002).
126. L. Xu, L. Yu, X. Liang, Y. Chu, Z. Hu, L. Ma, Y. Xu, C. Wang, Xi. Lu, H. Lu, Y. Yue, Y. Zhao, F. Fan, H. Tu, Y. Leng, R. Li, and Z. Xu, *Opt. Lett.* **38**, 22 (2013).
127. L. Yu, X. Liang, L. Xu, W. Li, C. Peng, Z. Hu, C. Wang, X. Lu, Y. Chu, Z. Gan, X. Liu, Y. Liu, X. Wang, H. Lu, D. Yin, Y. Leng, R. Li, and Z. Xu, *Opt. Lett.* **40**, 3412 (2015).
128. Z. Gan, L. Yu, S. Li, C. Wang, X. Liang, Y. Liu, W. Li, Z. Guo, Z. Fan, X. Yuan, L. Xu, Z. Liu, Y. Xu, J. Lu, H. Lu, D. Yin, Y. Leng, R. Li, and Z. Xu, *Opt. Express* **25**, 5169 (2017).
129. W. Li, Z. Gan, L. Yu, C. Wang, Y. Liu, Z. Guo, L. Xu, M. Xu, Y. Hang, Y. Xu, J. Wang, P. Huang, H. Cao, B. Yao, X. Zhang, L. Chen, Y. Tang, S. Li, X. Liu, S. Li, M. He, D. Yin, X. Liang, Y. Leng, R. Li, and Z. Xu, *Opt. Lett.* **43**, 5681 (2018).
130. E. Cartlidge, *Science* **359**, 382 (2018).
131. Y. Wang, J. Ma, J. Wang, P. Yuan, G. Xie, X. Ge, F. Liu, X. Yuan, H. Zhu, and L. Qian, *Sci. Rep.* **4**, 3818 (2014).
132. Key Laboratory for Laser Plasmas website: <http://lpl.sjtu.edu.cn>.
133. H. S. Peng, W. Y. Zhang, X. M. Zhang, Y. J. Tang, W. G. Zheng, Z. J. Zheng, X. F. Wei, Y. K. Ding, Y. Gou, S. P. Zhou, and W. B. Pei, *Lasers Part. Beams* **23**, 205 (2005).
134. Q. Zhu, K. Zhou, J. Su, N. Xie, X. Huang, X. Zeng, X. Wang, X. Wang, Y. Zuo, D. Jiang, L. Zhao, F. Li, D. Hu, K. Zheng, W. Dai, D. Chen, Z. Dang, L. Liu, D. Xu, D. Lin, X. Zhang, Y. Deng, X. Xie, B. Feng, Z. Peng, R. Zhao, F. Wang, W. Zhou, L. Sun, Y. Guo, S. Zhou, J. Wen, Z. Wu, Q. Li, Z. Huang, D. Wang, X. Jiang, Y. Gu, F. Jing, and B. Zhang, *Laser Phys. Lett.* **15**, 015301 (2018).
135. W. Y. Zhang and X. T. He, *J. Phys.: Conf. Ser.* **112**, 032001 (2008).
136. X. Zeng, K. Zhou, Y. Zuo, Q. Zhu, J. Su, X. Wang, X. Wang, X. Huang, X. Jiang, D. Jiang, Y. Guo, N. Xie, S. Zhou, Z. Wu, J. Mu, H. Peng, and F. Jing, *Opt. Lett.* **42**, 2014 (2017).
137. Z. Wang, C. Liu, Z. Shen, Q. Zhang, H. Teng, and Z. Wei, *Opt. Lett.* **36**, 16 (2011).
138. X. Q. Yan, C. Lin, H. Y. Lu, K. Zhu, Y. B. Zou, H. Y. Wang, B. Liu, S. Zhao, J. Zhu, Y. X. Geng, H. Z. Fu, Y. Shang, C. Cao, Y. R. Shou, W. Song, Y. R. Lu, Z. X. Yuan, Z. Y. Guo, X. T. He, and J. E. Chen, *Front. Phys.* **8**, 577 (2013).
139. C. Yamanaka, Y. Kato, Y. Izawa, K. Yoshida, T. Yamanaka, T. Sasaki, M. Nakatsuka, T. Mochizuki, J. Kuroda, and S. Nakai, *IEEE J. Quant. Electron.* **QE-17**, 1639 (1981).
140. Y. Kitagawa, H. Fujita, R. Kodama, H. Yoshida, S. Matsuo, T. Jitsuno, T. Kawasaki, H. Kitamura, T. Kanabe, S. Sakabe, K. Shigemori, N. Miyanaga, and Y. Izawa, *IEEE J. Quantum Electron.* **40**, 281 (2004).
141. M. Tabak, J. Hammer, M. E. Glinsky, W. L. Kruer, S. C. Wilks, J. Woodworth, E. M. Campbell, and M. D. Perry, *Phys. Plasma* **1**, 1626 (1994).
142. K. Mima, H. Azechi, Y. Johzaki, Y. Kitagawa, R. Kodama, Y. Kozaki, N. Miyanaga, K. Nagai, H. Nagatomo, M. Nakai, H. Nishimura, T. Norimatsu, H. Shiraga, K. A. Tanaka, and Y. Izawa, *Fusion Sci. Technol.* **47**, 662 (2005).
143. H. Shiraga, S. Fujioka, M. Nakai, T. Watari, H. Nakamura, Y. Arikawa, H. Hosoda, T. Nagai, M. Koga, H. Kikuchi, Y. Ishii, T. Sogo, K. Shigemori, H. Nishimura, Z. Zhang, M. Tanabe, S. Ohira, Y. Fujii, T. Namimoto, Y. Sakawa, O. Maegawa, T. Ozaki, K. A. Tanaka, H. Habara, T. Iwawaki, K. Shimada, H. Nagatomo, T. Johzaki, A. Sunahara, M. Murakami, H. Sakagami, T. Taguchi, T. Norimatsu, H. Homma, Y. Fujimoto, A. Iwamoto, N. Miyanaga, J. Kawanaka, T. Jitsuno, Y. Nakata, K. Tsubakimoto, K. Sueda, N. Morio, S. Matsuo, T. Kawasaki, K. Sawai, K. Tsuji, H. Murakami, T. Kanabe, K. Kondo, R. Kodama, N. Sarukura, T. Shimizu, K. Mima, and H. Azechi, *High Energy Dens. Phys.* **8**, 227 (2012).
144. H. Azechi, K. Mima, Y. Fujimoto, S. Fujioka, H. Homma, M. Isobe, A. Iwamoto, T. Jitsuno, T. Johzaki, R. Kodama, M. Koga, K. Kondo, J. Kawanaka, T. Mito, N. Miyanaga, O. Motojima, M. Murakami, H. Nagatomo, K. Nagai, M. Nakai, H. Nakamura, T. Nakamura, T. Nakazato, Y. Nakao, K. Nishihara, H. Nishimura, T. Norimatsu, T. Ozaki, H. Sakagami, Y. Sakawa, N. Sarukura, K. Shigemori, T. Shimizu, H. Shiraga, A. Sunahara, T. Taguchi, K. A. Tanaka, and K. Tsubakimoto, *Nucl. Fusion* **49**, 104024 (2009).
145. H. Azechi and FIREX Project Team, *J. Phys.: Conf. Ser.* **717**, 012006 (2016).
146. H. Kiriya, A. S. Pirozhkov, M. Nishiuchi, Y. Fukuda, K. Ogura, A. Sagisaka, Y. Miyasaka, M. Mori, H. Sakaki, N. P. Dover, K. Kondo, J. K. Koga, T. Zh. Esirkepov, M. Kando, and K. Kondo, *Opt. Lett.* **43**, 2595 (2018).
147. J. H. Sung, S. K. Lee, T. J. Yu, T. M. Jeong, and J. Lee, *Opt. Lett.* **5**, 3021 (2010).
148. T. J. Yu, S. K. Lee, J. H. Sung, J. W. Yoon, T. M. Jeong, and J. Lee, *Opt. Express* **20**, 10807 (2012).
149. J. H. Sung, H. W. Lee, J. Y. Yoo, J. W. Yoon, C. W. Lee, J. M. Yang, Y. J. Son, Y. H. Jang, S. K. Lee, and C. H. Nam, *Opt. Lett.* **42**, 2058 (2017).
150. J. W. Yoon, C. Jeon, J. Shin, S. K. Lee, H. W. Lee, I. W. Choi, H. T. Kim, J. H. Sung, and C. H. Nam, *Opt. Express* **27**, 20412 (2019).
151. P. P. Wiewior, A. Astanovitskiy, G. Aubry, S. Batie, J. Caron, O. Chalyy, T. Cowan, C. Haefner, B. Le Galloudec, N. Le Galloudec, D. Macaulay, V. Nalajala, G. Pettee, S. Samek, Y. Stepanenko, and J. Vesco, *J. Fusion Energy* **28**, 218 (2009).
152. J. P. Zou, C. L. Blanc, P. Audebert, S. Janicot, A. M. Sautivet, L. Martin, C. Sauteret, J. L. Paillard, S. Jacquemot, and F. Amiranoff, *J. Phys.: Conf. Ser.* **112**, 032021 (2008).
153. Y. Akahane, J. Ma, Y. Fukuda, M. Aoyama, H. Kiriya, J. Sheldakova, A. Kudryashov, and K. Yamakawa, *Rev. Sci. Instrum.* **77**, 023102 (2006).
154. J. D. Zuegel, in *CLEO* (2014), paper JTh4L.4.
155. J. Bromage, C. Dörner, and R. K. Jungquist, *J. Opt. Soc. Am. B* **29**, 1125 (2012).
156. C. Hooker, Y. Tang, O. Chekhlov, J. Collier, E. Divall, K. Ertel, S. Hawkes, B. Parry, and P. P. Rajeev, *Opt. Express* **19**, 2193 (2011).
157. B. C. Stuart, M. D. Feit, S. Herman, A. M. Rubenchik, B. W. Shore, and M. D. Perry, *J. Opt. Soc. Am. B* **13**, 459 (1996).
158. I. N. Ross, P. Matousek, M. Towrie, A. J. Langley, and J. L. Collier, *Opt. Commun.* **144**, 125 (1997).
159. I. N. Ross, J. L. Collier, P. Matousek, C. N. Danson, D. Neely, R. M. Allott, D. A. Pepler, C. Hernandez-Gomez, and K. Osvay, *Appl. Opt.* **39**, 2422 (2000).
160. N. F. Andreev, V. I. Bespalov, V. I. Bredikhin, S. G. Garanin, V. N. Ginzburg, K. L. Dvorkin, E. V. Katin, A. I. Korytin, V. V. Lozhkarev, O. V. Palashov, N. N. Rukavishnikov, A. M. Sergeev, S. A. Sukharev, G. I. Freidman, E. A. Khazanov, and I. V. Yakovlev, *J. Exp. Theor. Phys. Lett.* **79**, 144 (2004).
161. S. G. Garanin, A. I. Zaretskii, R. I. Il'kaev, G. A. Kirillov, G. G. Kochemasov, R. F. Kurunov, V. M. Murugov, and S. A. Sukharev, *Quantum Electron.* **35**, 299 (2005).
162. A. A. Shaykin, G. I. Freidman, S. G. Garanin, V. N. Ginzburg, E. V. Katin, A. I. Kedrov, E. A. Khazanov, A. V. Kirsanov, V. V. Lozhkarev, G. A. Luchin, L. V. L'vov, A. N. Mal'shakov, M. A. Martyanov, V. A. Osin, O. V. Palashov, A. K. Poteomkin, N. N. Rukavishnikov,

- V. V. Romanov, A. V. Savkin, A. M. Sergeev, S. A. Sukharev, O. V. Trikanova, I. N. Voronich, L. V. Yakovlev, and B. G. Zimalin, in *CLEO/EUROPE-EQEC* (2009).
163. J. Bromage, S.-W. Bahk, I. A. Begishev, C. Dorrer, M. J. Guardalben, B. N. Hoffman, J. B. Oliver, R. G. Roides, E. M. Schiesser, M. J. Shoup, III, M. Spilatro, B. Webb, D. Weiner, and J. D. Zuegel, *High Power Laser Sci. Eng.* **7**, e4 (2019).
 164. P. Zhu, Shanghai Institute of Optics and Fine Mechanics, China. Private communication.
 165. E. Cartlidge, *Science* **24**, 785 (2017).
 166. XCELS website: www.xcels.iapras.ru.
 167. A. V. Bashinov, A. A. Gonoskov, A. V. Kim, G. Mourou, and A. M. Sergeev, *Eur. Phys. J. Special Topics* **223**, 1105 (2014).
 168. J. Kawanaka, K. Tsubakimoto, H. Yoshida, K. Fujioka, Y. Fujimoto, S. Tokita, T. Jitsuno, N. Miyanaga, and Gekko-EXA Design Team, *J. Phys.: Conf. Ser.* **688**, 012044 (2016).
 169. Z. Li and J. Kawanaka, *OSA Continuum* **2**, 1125 (2019).
 170. S. Y. Mironov, V. V. Lozhkarev, V. N. Ginzburg, and E. A. Khazanov, *Appl. Opt.* **48**, 2051 (2009).
 171. S. Y. Mironov, V. N. Ginzburg, I. V. Yakovlev, A. A. Kochetkov, A. A. Shaykin, E. A. Khazanov, and G. A. Mourou, *Quantum Electron.* **47**, 614 (2017).
 172. V. Ginzburg, I. Yakovlev, A. Zuev, A. Korobeinikova, A. Kochetkov, A. Kuzmin, S. Mironov, A. Shaykin, I. Shaikin, and E. Khazanov, in *Ultrafast Optics XII Conference* (2019).
 173. A. A. Voronin, A. M. Zheltikov, T. Ditmire, B. Rus, and G. Korn, *Opt. Commun.* **291**, 299 (2013).
 174. S. Y. Mironov, V. V. Lozhkarev, V. N. Ginzburg, I. V. Yakovlev, G. Luchinin, A. A. Shaykin, E. A. Khazanov, A. A. Babin, E. Novikov, S. Fadeev, A. M. Sergeev, and G. A. Mourou, *IEEE J. Sel. Top. Quantum Electron.* **18**, 7 (2012).
 175. V. N. Ginzburg, A. A. Kochetkov, I. V. Yakovlev, S. Y. Mironov, A. A. Shaykin, and E. A. Khazanov, *Quantum Electron.* **46**, 106 (2016).
 176. K. Kafka, N. Talisa, G. Tempea, D. R. Austin, C. Neacsu, and E. A. Chowdhury, *Opt. Express* **24**, 28858 (2016).
 177. K. R. P. Kafka, N. Talisa, G. Tempea, D. R. Austin, C. Neacsu, and E. A. Chowdhury, *Proc. SPIE* **10014**, 100140D (2016).
 178. C. P. J. Barty, *J. Phys.: Conf. Ser.* **717**, 012086 (2016).
 179. C. V. Raman and K. S. Krishnan, *Ind. J. Phys.* **2**, 399 (1928).
 180. C. Headley and G. P. Agrawal, Eds., *Raman Amplification in Fiber Optical Communication Systems* (Academic Press, 2005).
 181. M. Maier, W. Kaiser, and J. A. Giordmaine, *Phys. Rev. Lett.* **17**, 1275 (1966).
 182. V. M. Malkin, G. Shvets, and N. J. Fisch, *Phys. Rev. Lett.* **82**, 4448 (1999).
 183. R. M. G. M. Trines, F. Fiúza, R. Bingham, R. A. Fonseca, L. O. Silva, R. A. Cairns, and P. A. Norreys, *Nature Phys.* **7**, 87 (2011).
 184. A. A. Andreev, C. Riconda, V. T. Tikhonchuk, and S. Weber, *Phys. Plasmas* **13**, 053110 (2006).
 185. G. Lehmann, K. H. Spatschek, and G. Sewell, *Phys. Rev. E* **87**, 063107 (2013).
 186. G. Lehmann and K. H. Spatschek, *Phys. Plasmas* **20**, 073112 (2013).
 187. J. Ren, W. Cheng, S. Li, and S. Suckewer, *Nature Phys.* **3**, 732 (2007).
 188. R. Kirkwood, A. E. Charman, E. Dewald, N. J. Fisch, R. Lindberg, C. Niemann, V. M. Malkin, N. Meezan, E. O. Valeo, S. C. Wilks, J. Wurtele, D. W. Price, and O. L. Landen, *Phys. Plasmas* **14**, 113109 (2007).
 189. Y. Ping, R. K. Kirkwood, T.-L. Wang, D. S. Clark, S. C. Wilks, N. Meezan, R. L. Berger, J. Wurtele, N. J. Fisch, V. M. Malkin, E. J. Valeo, S. F. Martins, and C. Joshi, *Phys. Plasmas* **16**, 123113 (2009).
 190. R. K. Kirkwood, P. Michel, R. A. London, D. Callahan, N. Meezan, E. Williams, W. Seka, L. Suter, C. Haynam, and O. Landen, *Phys. Rev. E* **84**, 026402 (2011).
 191. R. K. Kirkwood, D. P. Turnbull, T. Chapman, S. C. Wilks, M. D. Rosen, R. A. London, L. A. Pickworth, A. Colaitis, W. H. Dunlop, P. Poole, J. D. Moody, D. J. Strozzi, P. A. Michel, L. Divol, O. L. Landen, B. J. MacGowan, B. M. Van Wousterghem, K. B. Fournier, and B. E. Blue, *Phys. Plasmas* **25**, 056701 (2018).
 192. B. Ersfeld and D. Jaroszynski, *Phys. Rev. Lett.* **95**, 165002 (2005).
 193. J. P. Farmer, B. Ersfeld, and D. Jaroszynski, *Phys. Plasmas* **17**, 113301 (2010).
 194. G. Vieux, A. Lyachev, X. Yang, B. Ersfeld, J. P. Farmer, E. Brunetti, R. C. Issac, G. Raj, G. H. Welsh, S. M. Wiggins, and D. A. Jaroszynski, *New J. Phys.* **13**, 063042 (2011).
 195. X. Yang, G. Vieux, E. Brunetti, B. Ersfeld, J. P. Farmer, M. S. Hur, R. C. Issac, G. Raj, S. M. Wiggins, G. H. Welsh, S. R. Yoffe, and D. A. Jaroszynski, *Sci. Rep.* **5**, 13333 (2015).
 196. G. Vieux, S. Cipiccia, D. W. Grant, N. Lemos, P. Grant, C. Ciocarlan, B. Ersfeld, M. S. Hur, P. Lepipas, G. Manahan, G. Raj, D. Reboredo Gil, A. Subiel, G. H. Welsh, S. M. Wiggins, S. R. Yoffe, J. P. Farmer, C. Aniculaesei, E. Brunetti, X. Yang, R. Heathcote, G. Nersisyan, C. Lewis, A. Pukhov, J. M. Dias, and D. A. Jaroszynski, *Sci. Rep.* **7**, 2399 (2017).
 197. L. Lancia, J.-R. Marquès, M. Nakatsutsumi, C. Riconda, S. Weber, S. Hüller, A. Mančić, P. Antici, V. T. Tikhonchuk, A. Héron, P. Audebert, and J. Fuchs, *Phys. Rev. Lett.* **104**, 025001 (2010).
 198. L. Lancia, A. Giribono, L. Vassura, M. Chiaramello, C. Riconda, S. Weber, A. Castan, A. Chatelain, A. Frank, T. Gangolf, M. N. Quinn, J. Fuchs, and J.-R. Marquès, *Phys. Rev. Lett.* **116**, 075001 (2016).
 199. J.-R. Marquès, L. Lancia, T. Gangolf, M. Blecher, S. Bolaños, J. Fuchs, O. Willi, F. Amiranoff, R. L. Berger, M. Chiaramello, S. Weber, and C. Riconda, *Phys. Rev. X* **9**, 021008 (2019).
 200. R. M. G. M. Trines, F. Fiúza, R. Bingham, R. A. Fonseca, L. O. Silva, R. A. Cairns, and P. A. Norreys, *Phys. Rev. Lett.* **107**, 105002 (2011).
 201. G. M. Fraiman, N. A. Yampolsky, V. M. Malkin, and N. J. Fisch, *Phys. Plasmas* **9**, 3617 (2002).
 202. P. Mason, M. Divoký, K. Ertel, J. Pilař, T. Butcher, M. Hanuš, S. Banerjee, J. Phillips, J. Smith, M. De Vido, A. Lucianetti, C. Hernandez-Gomez, C. Edwards, T. Mocek, and J. Collier, *Optica* **4**, 438 (2017).
 203. V. M. Malkin, N. J. Fisch, and J. S. Wurtele, *Phys. Rev. E* **75**, 026404 (2007).
 204. V. M. Malkin and N. J. Fisch, *Phys. Rev. E* **80**, 046409 (2009).
 205. J. D. Sadler, R. Nathvani, P. Oleśkiewicz, L. A. Ceurvorst, N. Ratan, M. F. Kasim, R. M. G. M. Trines, R. Bingham, and P. A. Norreys, *Sci. Rep.* **5**, 16755 (2015).
 206. J. Vieira, R. M. G. M. Trines, E. P. Alves, R. A. Fonseca, J. T. Mendonça, R. Bingham, P. Norreys, and L. O. Silva, *Nature Commun.* **7**, 10371 (2016).
 207. J. Vieira, R. M. G. M. Trines, E. P. Alves, R. A. Fonseca, J. T. Mendonça, R. Bingham, P. Norreys, and L. O. Silva, *Phys. Rev. Lett.* **117**, 265001 (2016).
 208. W. P. Leemans, B. Nagler, A. J. Gonsalves, Cs. Tóth, K. Nakamura, C. G. R. Geddes, E. Esarey, C. B. Schroeder, and

- S. M. Hooker, *Nature Phys.* **418**, 696 (2006).
209. K. Nakamura, H. S. Mao, A. J. Gonsalves, H. Vincenti, D. E. Mittelberger, J. Daneils, A. Magana, C. Toth, and W. P. Leemans, *IEEE J. Quantum Electron.* **53**, 1200121 (2017).
 210. W. P. Leemans, *ICFA Beam Dyn. Newsl.* **56**, 10 (2011).
 211. A. C. Erlandson, S. M. Aceves, A. J. Bayramian, A. L. Bullington, R. J. Beach, C. D. Boley, J. A. Caird, R. J. Deri, A. M. Dunne, D. L. Flowers, M. A. Henesian, K. R. Manes, E. I. Moses, S. I. Rana, K. I. Schaffers, M. L. Spaeth, C. J. Stolz, and S. J. Telford, *Opt. Mater. Express* **1**, 1341 (2011).
 212. C. Haefner, Lawrence Livermore National Laboratory, Advanced Photon Technologies, DESY Hamburg (2017).
 213. C. Haefner, DOE Office of Science Report on Workshop on Laser Technology for k-BELLA and Beyond. 1-64, LLNL-AR-733300 (2017).
 214. G. A. Slack and D. W. Oliver, *Phys. Rev. B* **4**, 592 (1971).
 215. R. L. Aggarwal, D. J. Ripin, J. R. Ochoa, and T. Y. Fan, *J. Appl. Phys.* **98**, 103514 (2005).
 216. J. Dong, M. Bass, Y. Mao, P. Deng, and F. Gan, *J. Opt. Soc. Am. B* **20**, 1975 (2003).
 217. D. C. Brown, R. L. Cone, Y. Sun, and R. W. Equal, *IEEE J. Sel. Top. Quantum Electron.* **11**, 604 (2005).
 218. T. Y. Fan, T. Crow, and B. Hoden, *Proc. SPIE* **3381**, 200 (1998).
 219. H. Furuse, J. Kawanaka, K. Takeshita, N. Miyanaga, T. Saiki, K. Imasaki, M. Fujita, and S. Ishii, *Opt. Lett.* **34**, 3439 (2009).
 220. P. D. Mason, M. Fitton, A. Lintern, S. Banerjee, K. Ertel, T. Davenne, J. Hill, S. P. Blake, P. J. Phillips, T. J. Butcher, J. M. Smith, M. De Vido, R. J. S. Greenhalgh, C. Hernandez-Gomez, and J. L. Collier, *Appl. Opt.* **54**, 4227 (2015).
 221. B. A. Reagan, C. Baumgarten, E. Jankowska, H. Chi, H. Bravo, K. Dehne, M. Pedicone, L. Yin, H. Wang, C. S. Menoni, and J. J. Rocca, *High Power Laser Sci. Eng.* **6**, e11 (2018).
 222. T. Gonçalves-Novo, D. Albach, B. Vincent, M. Arzantsyan, and J.-C. Chanteloup, *Opt. Express* **21**, 855 (2013).
 223. M. Divoky, S. Tokita, S. Hwang, T. Kawashima, H. Kan, A. Lucianetti, T. Mocek, and J. Kawanaka, *Opt. Lett.* **40**, 855 (2015).
 224. J. Kawanaka, N. Miyanaga, K. Tsubakimoto, T. Jitsuno, M. Nakatsuka, Y. Izawa, R. Yasuhara, and T. Kawashima, *NIFS-937* (2008).
 225. T. Sekine, Y. Takeuchi, T. Kurita, Y. Hatano, Y. Muramatsu, Y. Mizuta, Y. Kabeya, Y. Tamaoki, and Y. Kato, *Proc. SPIE* **10082**, 100820U (2017).
 226. M. Hornung, H. Liebetrau, A. Seidel, S. Keppler, A. Kessler, J. Körner, M. Hellwing, F. Schorch, D. Klöpfel, A. K. Arunachalam, G. A. Becker, A. Sävert, J. Polz, J. Hein, and M. C. Kaluza, *High Power Laser Sci. Eng.* **2**, e20 (2014).
 227. T. Y. Fan, *IEEE J. Sel. Top. Quantum Electron.* **11**, 567 (2005).
 228. A. V. Smith and J. J. Smith, *Opt. Express* **19**, 10180 (2011).
 229. C. Jauregui, J. Limpert, and A. Tünnermann, *Nat. Photonics* **7**, 861 (2013).
 230. M. Kienel, M. Müller, A. Klenke, J. Limpert, and A. Tünnermann, *Opt. Lett.* **41**, 3343 (2016).
 231. M. Mueller, A. Klenke, H. Stark, J. Buldt, T. Gottschall, A. Tünnermann, and J. Limpert, *Proc. SPIE* **10512**, 1051208 (2018).
 232. J. Limpert, F. Stutzki, F. Jansen, H.-J. Otto, T. Eidam, C. Jauregui, and A. Tünnermann, *Light Sci. Appl.* **1**, e8 (2012).
 233. M. Müller, A. Klenke, A. Steinkopff, H. Stark, A. Tünnermann, and J. Limpert, *Opt. Lett.* **43**, 6037 (2018).
 234. A. Klenke, M. Müller, H. Stark, F. Stutzki, C. Hupel, T. Schreiber, A. Tünnermann, and J. Limpert, *Opt. Lett.* **43**, 1519 (2018).
 235. A. Heilmann, J. Le Dortz, L. Daniault, I. Fsaifes, S. Bellanger, J. Bourderionnet, C. Larat, E. Lallier, M. Antier, E. Durand, C. Simon-Boisson, A. Brignon, and J.-C. Chanteloup, *Opt. Express* **26**, 31542 (2018).
 236. G. Mourou, B. Brocklesby, T. Toshiki, and J. Limpert, *Nat. Photonics* **7**, 258 (2013).
 237. M. N. Quinn, V. Jukna, T. Ebisuzaki, I. Dicaire, R. Soulard, L. Summerer, A. Couairon, and G. Mourou, *Eur. Phys. J. Spec. Top.* **224**, 2645 (2015).
 238. A. Galvanauskas, G. C. Cho, A. Hariharan, M. E. Fermann, and D. Harter, *Opt. Lett.* **26**, 935 (2001).
 239. F. Röser, T. Eidam, J. Rothhardt, O. Schmidt, D. N. Schimpf, J. Limpert, and A. Tünnermann, *Opt. Lett.* **32**, 3495 (2007).
 240. T. Eidam, J. Rothhardt, F. Stutzki, F. Jansen, S. Hädrich, H. Carstens, C. Jauregui, J. Limpert, and A. Tünnermann, *Opt. Express* **19**, 255 (2011).
 241. C. Gaida, M. Kienel, M. Müller, A. Klenke, M. Gebhardt, F. Stutzki, C. Jauregui, J. Limpert, and A. Tünnermann, *Opt. Lett.* **40**, 2301 (2015).
 242. T. Zhou, J. Ruppe, C. Zhu, I.-N. Hu, J. Nees, and A. Galvanauskas, *Opt. Express* **23**, 7442 (2015).
 243. H. Pei, J. Ruppe, S. Chen, M. Sheikhsofla, J. Nees, Y. Yang, R. Wilcox, W. Leemans, and A. Galvanauskas, in *OSA Laser Congress, Advanced Solid State Lasers (ASSL) Conference* (2017), paper AW4A.4.
 244. X. Ma, C. Zhu, I.-N. Hu, A. Kaplan, and A. Galvanauskas, *Opt. Express* **22**, 9206 (2014).
 245. Y. Zaouter, F. Guichard, L. Daniault, M. Hanna, F. Morin, C. Hönninger, E. Mottay, F. Druon, and P. Georges, *Opt. Lett.* **38**, 106 (2013).
 246. M. Kienel, A. Klenke, T. Eidam, S. Hädrich, J. Limpert, and A. Tünnermann, *Opt. Lett.* **39**, 1049 (2014).
 247. B. R. Galloway, D. Popmintchev, E. Pisanty, D. D. Hickstein, M. M. Murnane, H. C. Kapteyn, and T. Popmintchev, *Opt. Express* **24**, 21818 (2016).
 248. H. Stark, M. Müller, M. Kienel, A. Klenke, J. Limpert, and A. Tünnermann, *Opt. Express* **25**, 13494 (2017).
 249. H. Stark, J. Buldt, M. Müller, A. Klenke, A. Tünnermann, and J. Limpert, *Proc. SPIE* **10897**, 108971B (2019).
 250. J. Rothhardt, S. Demmler, S. Hädrich, T. Peschel, J. Limpert, and A. Tünnermann, *Opt. Lett.* **38**, 763 (2013).
 251. K. Mecseki, M. K. R. Windeler, A. Miahnahri, J. S. Robinson, J. M. Fraser, A. R. Fry, and F. Tavella, *Opt. Lett.* **44**, 1257 (2019).
 252. H. Höppner, A. Hage, T. Tanikawa, M. Schulz, R. Riedel, U. Teubner, M. J. Prandolini, B. Faatz, and F. Tavella, *New J. Phys.* **17**, 053020 (2015).
 253. C. E. Barker, D. Eimerl, and S. P. Velsko, *J. Opt. Soc. Am. B* **8**, 2481 (1991).
 254. H. Zhong, P. Yuan, H. Zhu, and L. Qian, *Laser Phys. Lett.* **9**, 434 (2012).
 255. D. Tang, J. Ma, J. Wang, B. Zhou, G. Xie, P. Yuan, H. Zhu, and L. Qian, *Sci. Rep.* **6**, 36059 (2016).
 256. D. Tang, J. Wang, J. Ma, B. Zhou, P. Yuan, G. Xie, and L. Qian, *IEEE Photon. J.* **10**, 3200211 (2018).
 257. E. Esarey and W. P. Leemans, in *Proceedings of the 1999 Particle Accelerator Conference* (1999), p. 3699.
 258. D. Woodbury, L. Feder, V. Shumakova, C. Gollner, R. Schwartz, B. Miao, F. Salehi, A. Korolov, A. Pugžlys, A. Baltuška, and H. M. Milchberg, *Opt. Lett.* **43**, 1131 (2018).

259. T. Gaumnitz, A. Jain, Y. Pertot, M. Huppert, I. Jordan, F. Ardana-Lamas, and H. J. Wörner, *Opt. Express* **25**, 27506 (2017).
260. J. A. Fülöp, G. Polónyi, B. Monoszlai, G. Andriukaitis, T. Balciunas, A. Pugzlys, G. Arthur, A. Baltuska, and J. Hebling, *Optica* **3**, 1075 (2016).
261. J. Weisshaupt, V. Juvé, M. Holtz, S. Ku, M. Woerner, T. Elsaesser, S. Ališauskas, A. Pugžlys, and A. Baltuška, *Nat. Photonics* **8**, 927 (2014).
262. J. Körner, T. Lühder, J. Reiter, I. Uschmann, H. Marschner, V. Jambunathan, A. Lucianetti, T. Mocek, J. Hein, and M. C. Kaluza, *J. Lumin.* **202**, 427 (2018).
263. F. Stutzki, F. Jansen, C. Jauregui, J. Limpert, and A. Tünnermann, *Opt. Lett.* **38**, 97 (2013).
264. M. Gebhardt, C. Gaida, T. Heuermann, F. Stutzki, C. Jauregui, J. Antonio-Lopez, A. Schulzgen, R. Amezcua-Correa, J. Limpert, and A. Tünnermann, *Opt. Lett.* **42**, 4179 (2017).
265. C. Li, J. Song, D. Shen, Y. Cao, N. S. Kim, and K.-I. Ueda, *Opt. Rev.* **7**, 58 (2000).
266. M. Yumoto, N. Saito, Y. Urata, and S. Wada, *IEEE J. Sel. Top. Quantum Electron.* **21**, 364 (2015).
267. B. Cole, L. Goldberg, and A. D. Hays, *Opt. Lett.* **43**, 170 (2018).
268. J. Li, S. H. Yang, A. Meissner, M. Hofer, and D. Hoffmann, *Laser Phys. Lett.* **10**, 055002 (2013).
269. A. Wienke, D. Wandt, U. Morgner, J. Neumann, and D. Kracht, *Opt. Express* **23**, 16884 (2015).
270. S. B. Mirov, V. V. Fedorov, D. Martyshkin, I. S. Moskalev, M. Mirov, and S. Vasilyev, in *Advanced Solid State Lasers* (2015), paper AW4A.1.
271. S. Vasilyev, I. Moskalev, M. Mirov, S. Mirov, and V. Gapontsev, *Opt. Express* **24**, 1616 (2016).
272. S. Vasilyev, I. Moskalev, M. Mirov, V. Smolsky, S. Mirov, and V. Gapontsev, *Laser Tech. J.* **13**, 24 (2016).
273. S. Vasilyev, I. Moskalev, M. Mirov, V. Smolski, S. Mirov, and V. Gapontsev, *Opt. Mat. Express* **7**, 2636 (2017).
274. L. D. DeLoach, R. H. Page, G. D. Wilke, S. A. Payne, and W. F. Krupke, *IEEE J. Quantum Electron.* **32**, 885 (1996).
275. N. Tolstik, A. Pospischil, E. Sorokin, and I. T. Sorokina, *Opt. Express* **22**, 7284 (2014).
276. V. V. Fedorov, M. S. Mirov, S. B. Mirov, V. P. Gapontsev, A. V. Erofeev, M. Z. Smirnov, and G. B. Altshuler, in *Frontiers in Optics 2012/Laser Science XXVIII* (2012), paper FW6B.9.
277. M. Yumoto, N. Saito, U. Takagi, T. Tomida, and S. Wada, in *CLEO* (2013), paper CTu3D.2.
278. M. Yumoto, N. Saito, U. Takagi, and S. Wada, *Opt. Express* **23**, 25009 (2015).
279. M. N. Polyanskiy, M. Babzien, and I. V. Pogorelsky, BESTIA (Brookhaven Experimental Supra-Terawatt Infrared at ATF) laser: a status report 2017, 110007 (2017).
280. Y.-h. Chen, M. Helle, A. Ting, D. Gordon, N. Dover, O. Ettliger, Z. Najmudin, M. Polyanskiy, I. Pogorelsky, and M. Babzien, *AIP Conf. Proc.* **1812**, 090002 (2017).
281. I. V. Pogorelsky, M. Babzien, M. N. Polyanskiy, and W. D. Kimura, *AIP Conf. Proc.* **1812**, 040001 (2017).
282. K. Stenersen and G. Wang, *IEEE J. Quantum Electron.* **25**, 147 (1989).
283. J. D. Brandner and H. C. Urey, *J. Chem. Phys.* **13**, 351 (1945).
284. L. Y. Yeung, M. Okumura, J. T. Paci, G. C. Schatz, J. Zhang, and T. K. Minton, *J. Am. Chem. Soc.* **131**, 13940 (2009).
285. R. N. Campbell, United States Patent US8897333 (2014).
286. M. Natel, J. Itatani, A. Tien, J. Faure, D. Kaplan, M. Bouvier, D. Buma, P. Van Rompay, J. Nees, P. P. Pronko, D. Umstadter, and G. A. Mourou, *IEEE J. Sel. Top. Quantum Electron.* **4**, 449 (1998).
287. N. H. Stuart, D. Bigourd, R. W. Hill, T. S. Robinson, K. Mecseki, S. Patankar, G. H. C. New, and R. A. Smith, *Opt. Commun.* **336**, 319 (2015).
288. V. Bagnoud and F. Salin, *J. Opt. Soc. Am. B* **16**, 188 (1999).
289. J. Tan, N. Forget, A. Borot, D. Kaplan, P. Tournois, A. Muschet, and L. Veisz, *Opt. Express* **26**, 25003 (2018).
290. D. Alessi, T. Spinka, S. Betts, V. K. Kanz, R. Sigurdsson, B. Riordan, J. K. Crane, and C. Haefner, in *Conference on Lasers and Electro-Optics* (Optical Society of America, 2012), paper CM4D.5.
291. N. V. Didenko, A. V. Konyashchenko, A. P. Lutsenko, and S. Yu, Tenyakov. *Opt. Express* **16**, 3178 (2008).
292. N. Stuart, T. Robinson, D. Hillier, N. Hopps, B. Parry, I. Musgrave, G. Nersisyan, A. Sharba, M. Zepf, and R. A. Smith, *Opt. Lett.* **41**, 3221 (2016).
293. C. Dorrer, I. A. Begishev, A. V. Okishev, and J. D. Zuegel, *Opt. Lett.* **32**, 2143 (2007).
294. I. Musgrave, W. Shaikh, M. Galimberti, A. Boyle, C. Hernandez-Gomez, K. Lancaster, and R. Heathcote, *Appl. Opt.* **49**, 6558 (2010).
295. C. Dorrer, A. Consentino, D. Irwin, J. Qiao, and J. D. Zuegel, *J. Opt.* **17**, 094007 (2015).
296. D. I. Hillier, S. Elsmere, M. Girling, N. Hopps, D. Hussey, S. Parker, P. Treadwell, D. Winter, and T. Bett, *Appl. Opt.* **53**, 6938 (2014).
297. R. L. Acree, J. E. Heebner, M. A. Prantil, J. M. Halpin, T. S. Budge, L. A. Novikova, R. Sigurdsson, and L. J. Pelz, *Proc. SPIE* **10084**, 1008406 (2017).
298. F. Wagner, C. P. João, J. Fils, T. Gottschall, J. Hein, J. Körner, J. Limpert, M. Roth, T. Stöhlker, and V. Bagnoud, *Appl. Phys. B* **116**, 429 (2014).
299. M. P. Kalashnikov, E. Risse, H. Schonnagel, and W. Sandner, *Opt. Lett.* **30**, 923 (2005).
300. A. Jullien, O. Albert, F. Burgy, G. Hamoniaux, J. P. Rousseau, J.-P. Chambaret, F. Auge-Rochereau, G. Cheriaux, J. Etchepare, N. Minkovski, and S. M. Satiel, *Opt. Lett.* **30**, 920 (2005).
301. R. C. Shah, R. P. Johnson, T. Shimada, K. A. Flippo, J. C. Fernandez, and B. M. Hegelich, *Opt. Lett.* **34**, 2273 (2009).
302. C. Dorrer and J. Bromage, *Opt. Express* **16**, 3058 (2008).
303. S. Keppler, M. Hornung, R. Bödefeld, M. Kahle, J. Hein, and M. C. Kaluza, *Opt. Express* **20**, 20742 (2012).
304. E. Gaul, T. Toncian, M. Martinez, J. Gordon, M. Spinks, G. Dyer, N. Truong, C. Wagner, G. Tiwari, M. E. Donovan, T. Ditmire, and B. M. Hegelich, *J. Phys.: Conf. Ser.* **717**, 012092 (2016).
305. C. Thaury, F. Quéré, J.-P. Geindre, A. Levy, T. Ceccotti, P. Monot, M. Bougeard, F. Réau, P. D'Oliveira, P. Audebert, R. Majoribanks, and P. H. Martin, *Nat. Phys.* **v3**, 424 (2007).
306. A. Lévy, T. Ceccotti, P. D'Oliveira, F. Réau, M. Perdrix, F. Quéré, P. Monot, M. Bougeard, H. Lagadec, P. Martin, J.-P. Geindre, and P. Audebert, *Opt. Lett.* **32**, 310 (2007).
307. G. G. Scott, V. Bagnoud, C. Brabetz, R. J. Clarke, J. S. Green, R. I. Heathcote, H. W. Powell, B. Zielbauer, T. D. Arber, and P. McKenna, *New J. Phys.* **17**, 033027 (2015).
308. D. Hillier, C. Danson, S. Duffield, D. Egan, S. Elsmere, M. Girling, E. Harvey, N. Hopps, M. Norman, S. Parker, P. Treadwell, D. Winter, and T. Bett, *Appl. Opt.* **52**, 4258 (2013).
309. S. Szatmári, R. Dajka, A. Barna, B. Gilicze, and I. B. Földes, *Laser Phys. Lett.* **13**, 075301 (2016).
310. M. Kalashnikov, A. Andreev, and H. Schönnagel, *Proc. SPIE* **7501**, 750104 (2009).

311. U. Teubner, U. Wagner, and E. Forster, *J. Phys. B* **34**, 2993 (2001).
312. A. S. Pirozhkov, I. W. Choi, J. H. Sung, S. K. Lee, T. J. Yu, T. M. Jeong, I. J. Kim, N. Hafz, C. M. Kim, K. H. Pae, Y.-C. Noh, D.-K. Ko, J. Lee, A. P. L. Robinson, P. Foster, S. Hawkes, M. Streeter, C. Spindloe, P. McKenna, D. C. Carroll, C.-G. Wahlström, M. Zepf, D. Adams, B. Dromey, K. Markey, S. Kar, Y. T. Li, M. H. Xu, H. Nagatomo, M. Mori, A. Yogo, H. Kiriya, K. Ogura, A. Sagisaka, S. Orimo, M. Nishiuchi, H. Sugiyama, T. Zh. Esirkepov, H. Okada, S. Kondo, S. Kanazawa, Y. Nakai, A. Akutsu, T. Motomura, M. Tanoue, T. Shimomura, M. Ikegami, I. Daito, M. Kando, T. Kameshima, P. Bolton, S. V. Bulanov, H. Daido, and D. Neely, *Appl. Phys. Lett.* **94**, 241102 (2009).
313. H. C. Kapteyn, M. M. Murnane, A. Szoke, and R. W. Falcone, *Opt. Lett.* **16**, 490 (1991).
314. D. M. Gold, *Opt. Lett.* **19**, 2006 (1994).
315. C. Ziener, P. S. Foster, E. J. Divall, C. J. Hooker, M. H. R. Hutchinson, A. J. Langley, and D. Neely, *J. Appl. Phys.* **93**, 768 (2003).
316. G. Doumy, F. Quere, O. Gobert, M. Perdrix, P. Martin, P. Audebert, J. C. Gauthier, J. P. Geindre, and T. Wittmann, *Phys. Rev. E* **69**, 026402 (2004).
317. M. Nakatsutsumi, A. Kon, S. Buffechoux, P. Audebert, J. Fuchs, and R. Kodama, *Opt. Lett.* **35**, 13 (2010).
318. R. Wilson, M. King, R. J. Gray, D. C. Carroll, R. J. Dance, C. Armstrong, S. J. Hawkes, R. J. Clarke, D. J. Robertson, D. Neely, and P. McKenna, *Phys. Plasmas* **23**, 033106 (2016).
319. D. F. Gordon, A. B. Stamm, B. Hafizi, L. A. Johnson, D. Kaganovich, R. F. Hubbard, A. S. Richardson, and D. Zhigunov, *Phys. Plasmas* **25**, 063101 (2018).
320. T. Sokollik, S. Shiraishi, J. Osterhoff, E. Evans, A. J. Gonsalves, K. Nakamura, J. van Tilborg, C. Lin, C. Toth, and W. P. Leemans, *AIP Conf. Proc.* **1299**, 233 (2010).
321. S. Backus, H. C. Kapteyn, M. M. Murnane, D. M. Gold, H. Nathel, and W. White, *Opt. Lett.* **18**, 134 (1993).
322. D. Panasenko, A. J. Shu, A. Gonsalves, K. Nakamura, N. H. Matlis, C. Toth, and W. P. Leemans, *J. Appl. Phys.* **108**, 044913 (2010).
323. P. L. Poole, A. Krygier, G. E. Cochran, P. S. Foster, G. G. Scott, L. A. Wilson, J. Bailey, N. Bourgeois, C. Hernandez-Gomez, D. Neely, P. P. Rajeev, R. R. Freeman, and D. W. Schumacher, *Sci. Rep.* **6**, 32041 (2016).
324. S. Steinke, J. van Tilborg, C. Benedetti, C. G. R. Geddes, C. B. Schroeder, J. Daniels, K. K. Swanson, A. J. Gonsalves, K. Nakamura, N. H. Matlis, B. H. Shaw, E. Esarey, and W. P. Leemans, *Nature* **530**, 190 (2016).
325. R. Horlein, B. Dromey, D. Adams, Y. Nomura, S. Kar, K. Markey, P. Foster, D. Neely, F. Krausz, G. D. Tsakiris, and M. Zepf, *New J. Phys.* **10**, 083002 (2008).
326. M. J. V. Streeter, P. S. Foster, F. H. Cameron, M. Borghesi, C. Brenner, D. C. Carroll, E. Divall, N. P. Dover, B. Dromey, P. Gallegos, J. S. Green, S. Hawkes, C. J. Hooker, S. Kar, P. McKenna, S. R. Nagel, Z. Najmudin, C. A. J. Palmer, R. Prasad, K. E. Quinn, P. P. Rajeev, A. P. L. Robinson, L. Romagnani, J. Schreiber, C. Spindloe, S. Ter-Avetisyan, O. Tresca, M. Zepf, and D. Neely, *New J. Phys.* **13**, 023041 (2011).
327. M. Zepf, S. Moustazis, A. P. Fews, J. Zhang, P. Lee, M. Bakarezos, C. N. Danson, A. Dyson, P. Gibbon, P. Loukakos, D. Neely, F. N. Walsh, J. S. Wark, A. E. Dangor, and P. A. Norreys, *Phys. Rev. Lett.* **76**, 1832 (1996).
328. C. Ren, B. J. Duda, R. G. Hemker, W. B. Mori, T. Katsouleas, T. M. Antonsen, and P. Mora, *Phys. Rev. E* **63**, 026411 (2001).
329. B. Dromey, S. Kar, C. Bellei, D. C. Carroll, R. J. Clarke, J. S. Green, S. Kneip, K. Markey, S. R. Nagel, P. T. Simpson, L. Willingale, P. McKenna, D. Neely, Z. Najmudin, K. Krushelnick, P. A. Norreys, and M. Zepf, *Phys. Rev. Lett.* **99**, 085001 (2007).
330. T. M. Antonsen and P. Mora, *Phys. Fluids B* **5**, 1440 (1993).
331. T. M. Antonsen and P. Mora, *Phys. Rev. Lett.* **69**, 2204 (1992).
332. T. Tajima and J. M. Dawson, *Phys. Rev. Lett.* **43**, 267 (1979).
333. E. Esarey, C. B. Schroeder, and W. P. Leemans, *Rev. Mod. Phys.* **81**, 1229 (2009).
334. Y. Ehelich, C. Cohen, A. Zigler, J. Krall, P. Sprangle, and E. Esarey, *Phys. Rev. Lett.* **77**, 4186 (1996).
335. A. Butler, D. J. Spence, and S. M. Hooker, *Phys. Rev. Lett.* **89**, 185003 (2002).
336. D. J. Spence, A. Bulter, and S. M. Hooker, *J. Opt. Soc. Am. B* **20**, 138 (2003).
337. C. G. Durfee and H. M. Milchberg, *Phys. Rev. Lett.* **71**, 2409 (1993).
338. J. P. Palastro, D. Gordon, B. Hafizi, L. A. Johnson, J. Penano, R. F. Hubbard, M. Helle, and D. Kaganovich, *Phys. Plasmas* **22**, 123101 (2015).
339. H. C. Wu, Z. M. Sheng, Q. J. Zhang, Y. Cang, and J. Zhang, *Phys. Plasmas* **12**, 113103 (2005).
340. S. Suntsov, D. Abdollahpour, D. G. Papazoglou, and S. Tzortzakis, *Appl. Phys. Lett.* **94**, 251104 (2009).
341. S. Monchoce, S. Kahaly, A. Leblanc, L. Videau, P. Combis, F. Reau, D. Garzella, P. D'Oliveira, P. Martin, and F. Quere, *Phys. Rev. Lett.* **112**, 145008 (2014).
342. G. A. Mourou, T. Tajima, and S. V. Bulanov, *Rev. Mod. Phys.* **78**, 309 (2006).
343. B. Gonzalez-Izquierdo, R. J. Gray, M. King, R. J. Dance, R. Wilson, J. McCreadie, N. M. H. Butler, R. Capdessus, S. Hawkes, J. S. Green, C. D. Murphy, L. C. Stockhausen, D. C. Carroll, N. Booth, G. G. Scott, M. Borghesi, D. Neely, and P. McKenna, *Nature Phys.* **12**, 505 (2016).
344. A. Leblanc, A. Denoed, L. Chopineau, G. Mennerat, P. Martin, and F. Quere, *Nature Phys.* **13**, 440 (2017).
345. K. A. Qu, Q. Jia, and N. J. Fisch, *Phys. Rev. E* **96**, 053207 (2017).
346. N. Bonod and J. Neauport, *Adv. Opt. Photon.* **8**, 156 (2016).
347. T. Zhang, M. Yonemura, and Y. Kato, *Opt. Commun.* **145**, 367 (1998).
348. D. Homoelle, J. K. Crane, M. Shverdin, C. L. Haefner, and C. W. Siders, *Appl. Opt.* **50**, 554 (2011).
349. X. Liang, X. Xie, C. Zhang, J. Kang, Q. Yang, P. Zhu, A. Guo, H. Zhu, S. Yang, Z. Cui, M. Sun, and J. Zhu, *Opt. Lett.* **43**, 5713 (2018).
350. O. Razskazovskaya, F. Krausz, and V. Pervak, *Optica* **4**, 129 (2017).
351. V. Shalaev, *Nat. Photonics* **1**, 41 (2007).
352. I. Musgrave, M. Galimberti, A. Boyle, C. Hernandez-Gomez, A. Kidd, B. Parry, D. Pepler, T. Winstone, and J. Collier, *High Power Laser Sci. Eng.* **3**, e26 (2015).
353. P. Zhu, R. Jafari, T. Jones, and R. Trebino, *Opt. Express* **25**, 24015 (2017).
354. G. Pariente, V. Gallet, A. Borot, O. Gobert, and F. Quéré, *Nat. Photonics* **10**, 547 (2016).
355. S. J. Telford, A. J. Bayramian, K. Charron, R. N. Fallejo, E. S. Fulkerson, G. W. Johnson, D. Kim, E. S. Koh, R. K. Lanning, C. D. Marshall, J. D. Nissen, D. E. Petersen, T. M. Spinka, C. Haefner, M. A. Drouin, K. Kasl, T. Mazanec, J. Naylor, and B. Rus, in *International Conference on Accelerator and Large Experimental Physics Control* (2015).

356. M. J. V. Streeter, S. J. D. Dann, J. D. E. Scott, C. D. Baird, C. D. Murphy, S. Eardley, R. A. Smith, S. Rozario, J.-N. Gruse, S. P. D. Mangles, Z. Najmudin, S. Tata, M. Krishnamurthy, S. V. Rahul, D. Hazra, P. Pourmoussavi, J. Hah, N. Bourgeois, C. Thornton, C. D. Gregory, C. J. Hooker, O. Chekhlov, S. J. Hawkes, B. Parry, V. A. Marshall, Y. Tang, E. Springate, P. P. Rajeev, A. G. R. Thomas, and D. R. Symes, *Appl. Phys. Lett.* **112**, 244101 (2018).
357. M. Roth, *J. Instrum.* **6**, R09001 (2011).
358. F. Albert, A. G. R. Thomas, S. P. D. Mangles, S. Banerjee, S. Corde, A. Flacco, M. Litos, D. Neely, J. Vieira, Z. Najmudin, R. Bingham, C. Joshi, and T. Katsouleas, *Plasma Phys. Control. Fusion* **56**, 084015 (2014).
359. D. Riley, *Plasma Phys. Control. Fusion* **60**, 014033 (2018).
360. C. M. Brenner, S. R. Mirfayzi, D. R. Rusby, C. Armstrong, A. Alejo, L. A. Wilson, R. Clarke, H. Ahmed, N. M. H. Butler, D. Haddock, A. Higginson, A. McClymont, C. Murphy, M. Notley, P. Oliver, R. Allott, C. Hernandez-Gomez, S. Kar, P. McKenna, and D. Neely, *Plasma Phys. Control. Fusion* **58**, 014039 (2016).
361. P. R. Bolton, M. Borghesi, C. Brenner, D. C. Carroll, C. De Martinis, A. Flacco, V. Floquet, J. Fuchs, P. Gallegos, D. Giove, J. S. Green, S. Green, B. Jones, D. Kirby, P. McKenna, D. Neely, F. Nuesslin, R. Prasad, S. Reinhardt, M. Roth, U. Schramm, G. G. Scott, S. Ter-Avetisyan, M. Tolley, G. Turchetti, and J. J. Wilkens, *Phys. Medica-Eur. J. Med. Phys.* **30**, 255 (2014).
362. R. A. Lewis, *Phys. Med. Biol.* **49**, 3573 (2004).
363. P. A. Norreys, M. Santala, E. Clarke, M. Zepf, I. Watts, F. N. Beg, K. Krushelnick, M. Tatarakis, A. E. Dangor, X. Fang, P. Graham, T. McCanny, R. P. Singhal, K. W. D. Ledingham, A. Creswell, D. C. W. Sanderson, J. Magill, A. Machacek, J. S. Wark, R. Allott, B. Kennedy, and D. Neely, *Phys. Plasmas* **6**, 2150 (1999).
364. H. Daido, M. Nishiuchi, and A. S. Pirozhkov, *Rep. Prog. Phys.* **75**, 056401 (2012).
365. M. Downer, in *Conference on Lasers and Electro-Optics* (2013).
366. I. Turcu, F. Negoita, D. A. Jaroszynski, P. McKenna, S. Balascuta, D. Ursescu, I. Dancus, M. O. Cernaianu, M. V. Tataru, P. Ghenuche, D. Stutman, A. Boianu, M. Risca, M. Toma, C. Petcu, G. Acbas, S. R. Yoffe, A. Noble, B. Efersfeld, E. Brunetti, R. Capdessus, C. Murphy, C. P. Ridgers, D. Neely, S. P. D. Mangles, R. J. Gray, A. G. R. Thomas, J. G. Kirk, A. Ilderton, M. Marklund, D. F. Gordon, B. Hafizi, D. Kaganovich, J. P. Palastro, E. D'Humieres, M. Zepf, G. Sarri, H. Gies, F. Karbstein, J. Schreiber, G. G. Paulus, B. Dromey, C. Harvey, A. Di Piazza, C. H. Keitel, M. C. Kaluza, S. Gales, and N. V. Zamfir, *Rom. Rep. Phys.* **68**, 145 (2016).
367. M. M. Gunther, K. Sonnabend, E. Brambrink, K. Vogt, V. Bagnoud, K. Harres, and M. Roth, *Phys. Plasmas* **18**, 083102 (2011).
368. M. Borghesi, A. Bigongiari, S. Kar, A. Macchi, L. Romagnani, P. Audebert, J. Fuchs, T. Toncian, O. Willi, S. V. Bulanov, A. J. Mackinnon, and J. C. Gauthier, *Plasma Phys. Control. Fusion* **50**, 124040 (2008).
369. M. J. Mead, D. Neely, J. Gauoin, R. Heathcote, and P. Patel, *Rev. Sci. Instrum.* **75**, 4225 (2004).
370. G. Liao, H. Liu, G. G. Scott, Y. Zhang, B. Zhu, C. Armstrong, E. Zemaityte, P. Bradford, Z. Zhang, Y. Li, D. Neely, P. G. Huggard, P. McKenna, C. M. Brenner, N. C. Woolsey, W. Wang, Z. Sheng, and J. Zhang, *Proc. Natl. Acad. Sci.* **116**, 3994 (2019).
371. D. R. Rusby, C. D. Armstrong, C. M. Brenner, R. J. Clarke, P. McKenna, and D. Neely, *Rev. Sci. Instrum.* **89**, 073502 (2018).
372. P. Bradford, N. C. Woolsey, G. G. Scott, G. Liao, H. Liu, Y. Zhang, B. Zhu, C. Armstrong, S. Astbury, C. Brenner, P. Brummitt, F. Consoli, I. East, R. Gray, D. Haddock, P. Huggard, P. J. R. Jones, E. Montgomery, I. Musgrave, P. Oliveira, D. R. Rusby, C. Spindloe, B. Summers, E. Zemaityte, Z. Zhang, Y. Li, P. McKenna, and D. Neely, *High Power Laser Sci. Eng.* **6**, e21 (2018).
373. J. L. Dubois, P. Raczka, S. Hulin, M. Rosinski, L. Ryc, P. Parys, A. Zaras-Szydłowska, D. Makaruk, P. Tchorz, J. Badziak, J. Wolowski, J. Ribolzi, and V. Tikhonchuk, *Rev. Sci. Instrum.* **89**, 103301 (2018).
374. R. H. Huddleston and S. L. Leonard, *Plasma Diagnostic Techniques* (Academic Press, 1965).
375. I. H. Hutchinson, *Principles of Plasma Diagnostics*, 2nd ed. (Cambridge University Press, 2005).
376. J. S. Green, M. Borghesi, C. M. Brenner, D. C. Carroll, N. P. Dover, P. S. Foster, P. Gallegos, S. Green, D. Kirby, K. J. Kirkby, P. McKenna, M. J. Merghant, Z. Najmudin, C. A. J. Palmer, D. Parker, R. Prasad, K. E. Quinn, P. P. Rajeev, M. P. Read, L. Romagnani, J. Schreiber, M. J. V. Streeter, O. Tresca, C. G. Wahlstrom, M. Zepf, and D. Neely, *Proc. SPIE* **8079**, 807919 (2011).
377. M. J.-E. Manuel, J. Strehlow, J. S. Green, D. Parker, E. L. Alfonso, J. Jaquez, L. Carlson, D. Neely, F. N. Beg, and T. Ma, *Nucl. Instrum. Methods Phys. Res.* **913**, 103 (2019).
378. A. Gamucci, N. Bourgeois, T. Ceccotti, S. Dobosz, P. D'Oliveira, M. Galimberti, J. Galy, A. Giulietti, D. Giulietti, and L. A. Gizzi, *IEEE Trans. Plasma Sci.* **36**, 1699 (2008).
379. R. J. Clarke, K. W. D. Ledingham, P. McKenna, L. Robson, T. McCanny, D. Neely, O. Lundh, F. Lindau, C. G. Wahlstrom, P. T. Simpson, and M. Zepf, *Appl. Phys. Lett.* **89**, 141117 (2006).
380. H. Liu, G.-Q. Liao, Y.-H. Zhang, B.-J. Zhu, Z. Zhang, Y.-T. Li, G. G. Scott, D. R. Rusby, C. Armstrong, E. Zemaityte, D. C. Carroll, S. Astbury, P. Bradford, N. C. Woolsey, P. McKenna, and D. Neely, *Rev. Sci. Instrum.* **89**, 083302 (2018).
381. R. M. Deas, L. A. Wilson, D. Rusby, A. Alejo, R. Allott, P. P. Black, S. E. Black, M. Borghesi, C. M. Brenner, J. Bryant, R. J. Clarke, J. C. Collier, B. Edwards, P. Foster, J. Greenhalgh, C. Hernandez-Gomez, S. Kar, D. Lockley, R. M. Moss, Z. Najmudin, R. Pattathil, D. Symes, M. D. Whittle, J. C. Wood, P. McKenna, and D. Neely, *J. X-ray Sci. Technol.* **23**, 791 (2015).
382. S. Karsch, A. D. Debus, M. Bussmann, U. Schramm, R. Sauerbrey, C. D. Murphy, Z. Major, R. Hoerlein, L. Veisz, K. Schmid, J. Schreiber, K. Witte, S. P. Jamison, J. G. Gallacher, D. A. Jaroszynski, M. C. Kaluza, B. Hidding, S. Kiselev, R. Heathcote, P. S. Foster, D. Neely, E. J. Divall, C. J. Hooker, J. M. Smith, K. Ertel, A. J. Langley, P. Norreys, J. L. Collier, and S. Karsch, *Phys. Rev. Lett.* **104**, 084802 (2010).
383. B. Rus, P. Bakule, D. Kramer, G. Korn, J. T. Green, J. Novák, M. Fibrich, F. Batysta, J. Thoma, J. Naylor, T. Mazanec, M. Vítek, R. Barros, E. Koutris, J. Hřebíček, J. Polan, R. Baše, P. Homer, M. Košelja, T. Havlíček, A. Honsa, M. Novák, Ch. Zervos, P. Korouš, M. Laub, and J. Houžvička, *Proc. SPIE* **8780**, 87801T (2013).
384. S. Kühn, M. Dumergue, S. Kahaly, S. Mondal, M. Füle, T. Csizmadia, B. Farkas, B. Major, Z. Várallyay, E. Cormier, M. Kalashnikov, F. Calegari, M. Devetta, F. Frassetto, E. Månsson, L. Poletto, S. Stagira, C. Vozzi, M. Nisoli, P. Rudawski, S. Maclot, F. Campi, H. Wikmark, C. L. Arnold, C. M. Heyl, P. Johnsson, A. L'Huilier, R. Lopez-Martens, S. Haessler, M. Bocoum, F. Boehle, A. Vernier, G. Iaquaniello, E. Skantzakis, N. Papadakis, C. Kalpouzos, P. Tzallas, F. Lépine, D. Charalambidis, K. Varjú, K. Osvay, and G. Sansone, *J. Phys. B: At. Mol. Opt. Phys.* **50**, 132002 (2017).

385. G. Korn, A. Thoss, H. Stiel, U. Vogt, M. Richardson, T. Elsaesser, and M. Faubel, *Opt. Lett.* **27**, 866 (2002).
386. M. Gauthier, C. B. Curry, S. Göde, F.-E. Brack, J. B. Kim, M. J. MacDonald, J. Metzkes, L. Obst, M. Rehwald, C. Rödel, H.-P. Schlenvoigt, W. Schumaker, U. Schramm, K. Zeil, and S. H. Glenzer, *Appl. Phys. Lett.* **111**, 114102 (2017).
387. K. M. George, J. T. Morrison, S. Feister, G. Ngirmang, J. R. Smith, A. J. Klim, J. Snyder, D. Austin, W. Erbsen, K. D. Frische, J. Nees, C. Orban, E. A. Chowdhury, and W. M. Roquemore, *High Power Laser Sci. Eng.* **7**, e50 (2019).
388. J. T. Morrison, S. Feister, K. D. Frische, D. R. Austin, G. K. Ngirmang, N. R. Murphy, C. Orban, E. A. Chowdhury, and W. M. Roquemore, *New J. Phys.* **20**, 069501 (2018).
389. I. Prencipe, J. Fuchs, S. Pascarelli, D. W. Schumacher, R. B. Stephens, N. B. Alexander, R. Briggs, M. Buscher, M. O. Cernaianu, A. Choukourov, M. De Marco, A. Erbe, J. Fassbender, G. Fiquet, P. Fitzsimmons, C. Gheorghiu, J. Hund, L. G. Huang, M. Harmand, N. J. Hartley, A. Irman, T. Kluge, Z. Konopkova, S. Kraft, D. Kraus, V. Leca, D. Margarone, J. Metzkes, K. Nagai, W. Nazarov, P. Lutoslawski, D. Papp, M. Passoni, A. Pelka, J. P. Perin, J. Schulz, M. Smid, C. Spindloe, S. Steinke, R. Torchio, C. Vass, T. Wiste, R. Zaffino, K. Zeil, T. Tschentscher, U. Schramm, and T. E. Cowan, *High Power Laser Sci. Eng.* **5**, e17 (2017).
390. LLNL website: <https://lasers.llnl.gov/for-users/nif-target-shot-metrics>.

Laser-driven strong shocks with infrared lasers at intensity of 10^{16} W/cm²

Cite as: Phys. Plasmas **26**, 112708 (2019); doi: 10.1063/1.5119697

Submitted: 12 July 2019 · Accepted: 8 October 2019 ·

Published Online: 19 November 2019



L. Antonelli,¹ J. Trela,² F. Barbato,² G. Boutoux,² Ph. Nicolai,² D. Batani,² V. Tikhonchuk,^{2,3} D. Mancelli,^{2,4} A. Tentori,² S. Atzeni,⁵ A. Schiavi,⁵ F. Baffigi,⁶ G. Cristoforetti,⁶ S. Viciani,⁶ L. A. Gizzi,⁶ M. Smid,^{3,7} O. Renner,³ J. Dostal,³ R. Dudzak,³ L. Juha,³ and M. Krus³

AFFILIATIONS

¹York Plasma Institute, Department of Physics, University of York, York YO10 5DQ, United Kingdom

²Université de Bordeaux, CNRS, CEA, CELIA (Centre Lasers Intenses et Applications), UMR 5107, F-33405 Talence, France

³Institute of Plasma Physics, Czech Academy of Sciences, Prague, Czech Republic

⁴Donostia International Physics Center (DIPC), Donostia/San Sebastian, Basque Country, Spain

⁵Dipartimento SBAI, Università degli Studi di Roma "La Sapienza," Via Antonio Scarpa 14, 00161 Roma, Italy

⁶Intense Laser Irradiation Laboratory, INO CNR (National Council of Research), Pisa, Italy

⁷Helmholtz-Zentrum Dresden-Rosendorf, Dresden, Germany

ABSTRACT

We present the results of an experiment on laser-driven shock waves performed at the Prague Asterix Laser system (PALS), where the fundamental frequency of the laser (1315 nm) is used to launch a strong shock in planar geometry. The experiment aims to characterize both shock waves and hot electrons generated at intensities of $\approx 10^{16}$ W/cm². It is shown that, in these interaction conditions, hydrodynamics is strongly impacted by noncollisional mechanisms, and the role of the hot electrons, generated by parametric instabilities, is essential in determining shock dynamics.

Published under license by AIP Publishing. <https://doi.org/10.1063/1.5119697>

I. INTRODUCTION

The shock ignition approach to inertial confinement fusion (SI)¹ presents several advantages compared to the standard central ignition approach,² such as a lower implosion velocity in the compression phase, which makes SI less sensitive to hydrodynamic instabilities, and a lower amount of energy needed to achieve ignition.^{3,4} In the SI scheme, ignition is triggered by a strong shock (>300 Mbar) launched by a laser spike of duration a few hundred picoseconds close to the end of the compression phase, with intensity between 10^{15} and 10^{16} W/cm². Interaction of the laser spike is expected to be strongly affected by parametric instabilities such as Stimulated Brillouin Scattering (SBS), Stimulated Raman Scattering (SRS), and Two Plasmon Decay (TPD), which reduce the laser energy coupled with the target and can also produce suprathermal electrons.^{5,6}

Several works have pointed out the essential role of such hot electrons (HEs) not only toward target preheating (a well-known effect in inertial fusion research)⁷ but also in the process of shock generation and in determining shock dynamics.^{8,9} It appears that if the energy of HEs is not too high, they could actually improve the laser-plasma

coupling and increase the shock strength, while at the same time, they would not be able to penetrate deeply into the target and preheat the fuel.^{8,10} Therefore, experiments have recently addressed the study of HE, parametric instabilities, and shock generation in the SI interaction regime. These include experiments done at OMEGA¹¹ in planar¹² and spherical geometries,^{13–15} at LIL,¹⁶ and at the Prague Asterix Laser system (PALS).^{17,18} All of them made use of UV laser light, which is expected to result in a stronger coupling with denser plasma regions. The use of short wavelength laser light is essential for compressing inertial fusion targets because it guarantees a better hydrodynamics efficiency and a lower level of parametric instabilities. However, assuming that HEs have a beneficial effect for the generation of the final shock, it could be possible to think about mixed irradiation schemes where compression is performed at 3ω , and the final spike is realized at 1ω or 2ω . The advantage of using longer wavelength radiation is a lower level of damage to the optics for beam transport and the availability of larger energy. For example, at PALS,¹⁹ the laser can routinely deliver 300 J in the third harmonic ($\lambda_0 = 438$ nm) but up to 700 J in the first harmonic ($\lambda_0 = 1.315$ μm). Using phase plates to

produce a uniform focal spot of $100\ \mu\text{m}$, the full width at half maximum (FWHM) provides an intensity of $\approx 1.5 \times 10^{16}\ \text{W cm}^{-2}$ on the target. If we consider the irradiance $I\lambda^2$, which is the physical quantity governing the onset of parametric instabilities, we reach $I\lambda^2 \approx 3 \times 10^{16}\ \text{W}\ \mu\text{m}^2\ \text{cm}^{-2}$, an order of magnitude higher compared to the third harmonic.

Such nonlinear interaction conditions may result in stronger SRS and TPD and consequently larger HE production, which should strongly affect shock dynamics. In addition, studying parametric instabilities and HE generation at high intensity and longer wavelengths will allow for a better understanding of the physical processes that take place and for retrieving quantitative information on thresholds and conversion efficiencies. Such information is essential for developing advanced numerical models and validating them.¹⁰

II. EXPERIMENTAL SETUP

Streaked-optical-pyrometry (SOP) was used to characterize dynamics of the shock waves, while focusing spectroscopy with spatial resolution (FSSR) and spherical crystal imaging (SCI) were used to characterize K_α emission generated by interaction of hot electrons²⁰ with tracer layers buried in the target. Parametric instabilities were studied by collecting light backscattered within the cone of the focusing lens and characterizing it by time integrated optical spectroscopy (OS) and calorimetry (Cal).^{21,22} Bremsstrahlung emission was recorded using a bremsstrahlung cannon placed in front of the target (BC). A sketch of the experimental setup is shown in Fig. 1.

In this work, we focus on hydrodynamics and hot electron effects by analyzing SOP results through comparison with numerical simulations. Other diagnostics provided complementary information on laser-plasma interaction, which reinforces the proposed interpretation of the experiment and allows constraining simulation parameters. For some of them, the detailed analysis is developed in an associated article.²³

PALS is a single beam laser delivering 700 J at a fundamental wavelength ($\lambda = 1.315\ \mu\text{m}$) in an ~ 300 ps, full width half maximum (FWHM), Gaussian pulse. The beam was smoothed with a Random Phase Plate (RPP) providing a Gaussian focal spot of $\sim 100\ \mu\text{m}$

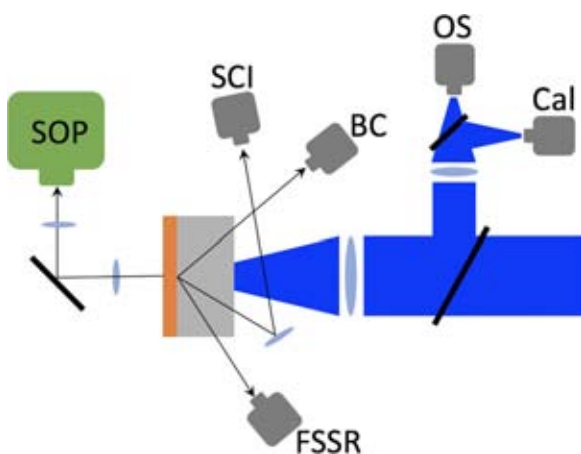


FIG. 1. Experimental setup.

(FWHM). The RPP diameter was 30 cm, and its focal length was 60 cm, leading to an $f/\#2$ optical system. By performing accurate calorimetric measurements, we determined that only $\sim 50\%$ of the nominal energy was contained in the $100\ \mu\text{m}$ spot. Therefore, the effective laser energy inside the focal spot was 350 J. Figure 2 shows laser power as a function of time (right) and intensity distribution as a function of radius (left). Solid lines are horizontal and vertical line-outs of a time integrated image of the laser focal spot. The dashed line represents the smoothed profile used in simulations. The peak power of 1.10 TW results in a peak intensity on axis of $0.97 \times 10^{16}\ \text{W/cm}^2$ and in an interaction parameter $I\lambda^2 = 1.68 \times 10^{16}\ \text{W}\ \mu\text{m}^2\ \text{cm}^{-2}$, which is largely above the threshold for laser plasma instabilities. Hence, a significant amount of hot electrons is expected to be produced. The PALS beam was used to irradiate two-layer targets with a front layer of Polystyrene (CH) of variable thicknesses, ranging from $10\ \mu\text{m}$ to $180\ \mu\text{m}$, followed by $5\ \mu\text{m}$ of Titanium. The targets were embedded into an aluminum washer, and the inner diameter was 2 mm. The use of different plastic thicknesses allowed us to obtain information on both shock waves and HE heating.

III. EXPERIMENTAL RESULTS

A. X-ray measurements

Figure 3 shows a typical 2D-resolved image of the Ti K_α emission produced by hot electron interaction with a target (in this case, a $5\text{-}\mu\text{m}$ Ti layer covered by $10\ \mu\text{m}$ of plastic). The elliptical shape of the emitting area corresponds to the oblique line of sight of the imager observing the target surface at an angle of about 45° . The measurement of the number of photons emitted by Titanium at this energy gives information on the flux of hot electrons. This flux depends on the thickness of the CH layer. Taking, for example, targets with $50\ \mu\text{m}$ of CH, it can be found that only hot electrons with energies of $\geq 50\ \text{keV}$ reach the

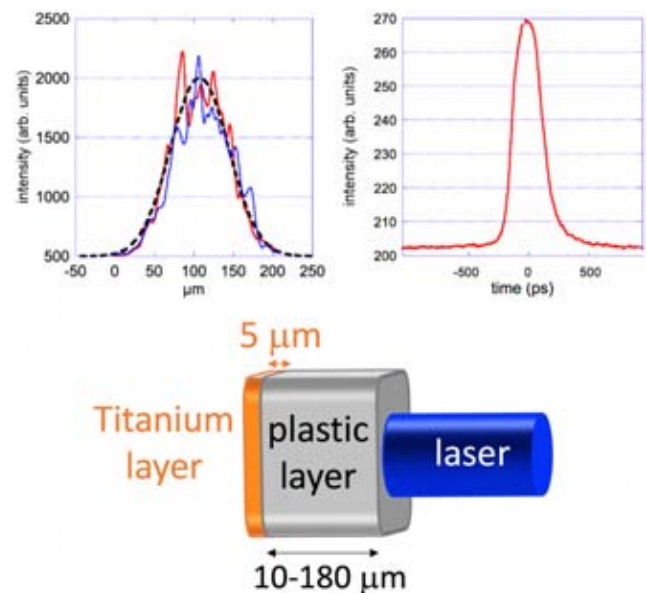


FIG. 2. (top-left) PALS laser focal spot (see the text) and (top-right) laser power as a function of time for a total energy of 700 J. Target scheme (bottom).

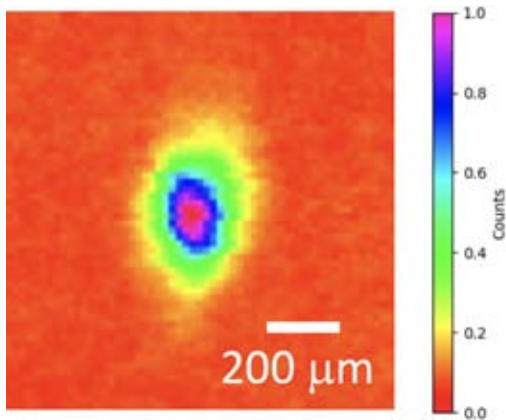


FIG. 3. Distribution of K_{α} emission from the 1ω -irradiated $5\text{-}\mu\text{m}$ -Ti foil covered by $10\ \mu\text{m}$ of plastic, visualized by monochromatic imaging.

titanium layer. For targets with a thicker CH layer, this cut-off energy increases, which results in a reduction of hot electrons reaching the Ti layer and therefore a lower K_{α} signal. However, we observed the K_{α} signal even for the largest plastic thickness, implying the presence of a HE component at high energy. Figure 4 presents the analysis of the K_{α} signal as a function of the thickness of the CH layer. Squares represent the measured average fluxes at each thickness (these data refer to FSSR; however, data from the SCI provide similar results), while spheres represent simulations of hot electron fluxes. The analysis has been performed with the Monte Carlo code GEANT4²⁴ simulating propagation of hot electrons and the K-shell emission inside the studied target. The K-shell ionization cross sections were provided by the PENELOPE physics library.²⁵ The Monte Carlo simulation, which best-fits the experimental data, uses two Maxwellian hot electron populations—a dominant one with the temperature of $\approx 40 \pm 5\ \text{keV}$ and a hotter one with the temperature

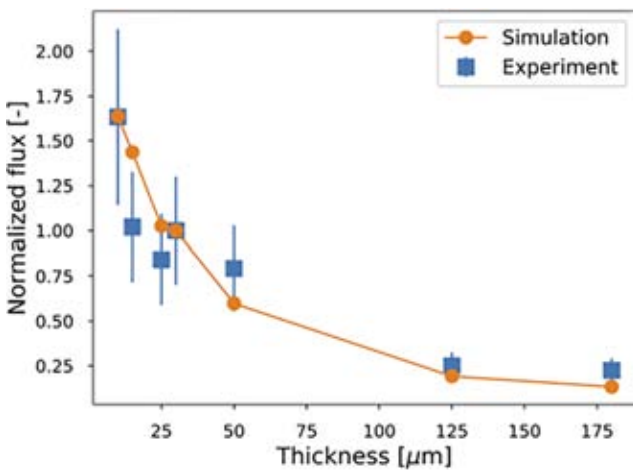


FIG. 4. Integrated K_{α} emission vs plastic thickness obtained using the FSSR spectrometer. Experimental points are averaged over several shots. Simulation points include the contribution of two Maxwellian hot electron populations, a dominant one with a temperature of $\approx 40 \pm 5\ \text{keV}$ and a hotter distribution with a temperature of $\approx 85 \pm 5\ \text{keV}$.

of $\approx 85\ \text{keV} \pm 5\ \text{keV}$. In agreement with known scaling laws (and with the results of Ref. 23), we attribute the first component to hot electrons produced by SRS and the second one to TPD. The total conversion efficiency from the laser to hot electrons is $\eta = 5.3 \pm 0.58\%$, distributed as 2/3 and 1/3 for SRS and TPD, respectively. Note that, in previous campaigns at PALS, using 300 J energy at the third harmonic ($\lambda_0 = 438\ \text{nm}$), the measured conversion efficiency was below 1% with the hot electron temperature of $25 \pm 7.5\ \text{keV}$.^{9,10}

B. Bremsstrahlung cannon

A bremsstrahlung cannon (BC) provides information on the high-energy photon distribution and hence indirectly allows us to estimate the hot electron energy distribution. The typical results from this diagnostic are shown in Fig. 5.

Monte Carlo simulations have been used in two steps to infer hot electron temperature. First, the BC structure has been fully simulated to obtain, at the entrance, the photon spectrum yielding signals in each image plate. In a second step, the MC code has been run to find the electron population, leading to the photon spectrum at the position of diagnostic. The best results were systematically obtained using a Maxwellian distribution at an electron temperature of $45 \pm 10\ \text{keV}$.

C. Streaked optical pyrometer

Information on the shock wave dynamics was obtained thanks to Streaked Optical Pyrometry (SOP) that measures the breakout time of

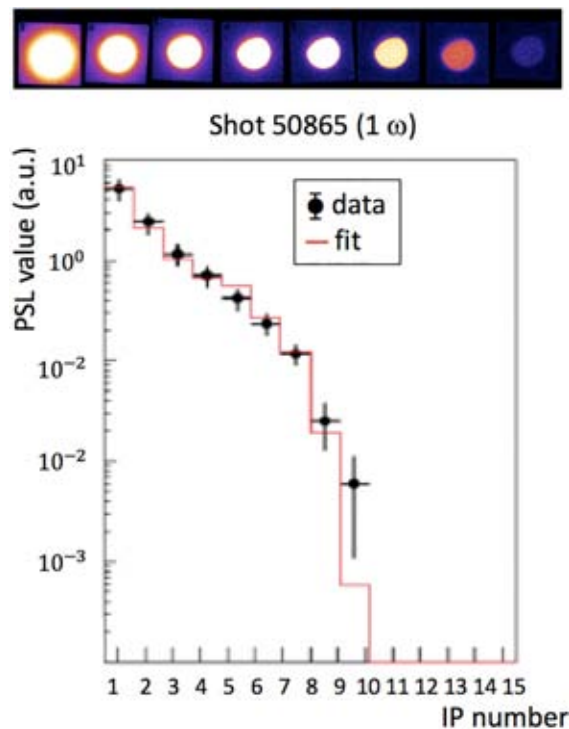


FIG. 5. Raw data from BC (each circle corresponds to a different IP) and fit related to a photon spectrum at the entrance of the diagnostic.

the shock at the rear side of the target. The target is imaged on the slit of a streak camera that records the self-emission of the Titanium layer in the visible range of the electromagnetic spectrum. Figure 6 presents the SOP signal for three representative plastic thicknesses: 15, 50, and 125 μm . Line-outs of the SOP signal as a function of time are also displayed. The peak of emission observed at early times is due to preheating of the rear surface by hot electrons reaching the Titanium layer after crossing the plastic layer. Practically, it occurs at the time of the maximum laser intensity. Due to such significant preheating, the target rear side expands rapidly, cooling down, which implies a rapid reduction of the emitted thermal radiation. For 50 μm and 125 μm plastic thicknesses, a second peak of emission is clearly visible. It is induced by the shock produced at the front side of the target that crosses the whole target, heating and compressing it and finally reaching the rear side. For the target with 125 μm of CH, the delay between the peak due to hot electrons and the signal rising due to shock breakout is $4.1 \pm 0.2 \text{ ns}$. For the target with 50 μm , this delay is $1.0 \pm 0.1 \text{ ns}$. For

the target with 15 μm of CH, there is no signal rise, and so the delay cannot be defined. This does not mean that there is no shock but simply that the hot electron heating dominates the shock heating, hiding its arrival at the rear side. The signal due to hot electron preheating decreases with the plastic thickness, as expected. This is due to the fact that when the propagation thickness increases, fewer electrons arrive at the Ti layer, reducing its heating. At the same time, the signal corresponding to shock breakout also decreases because for larger propagation distances, the shock pressure reduces. However, for large thicknesses, although reduced, it becomes larger than the initial peak due to hot electrons.

D. Parametric instabilities

The impact of noncollisional processes in this interaction regime, giving rise to HEs, is confirmed by spectroscopic and calorimetric measurements of scattered light. In our setup, due to the low spectral

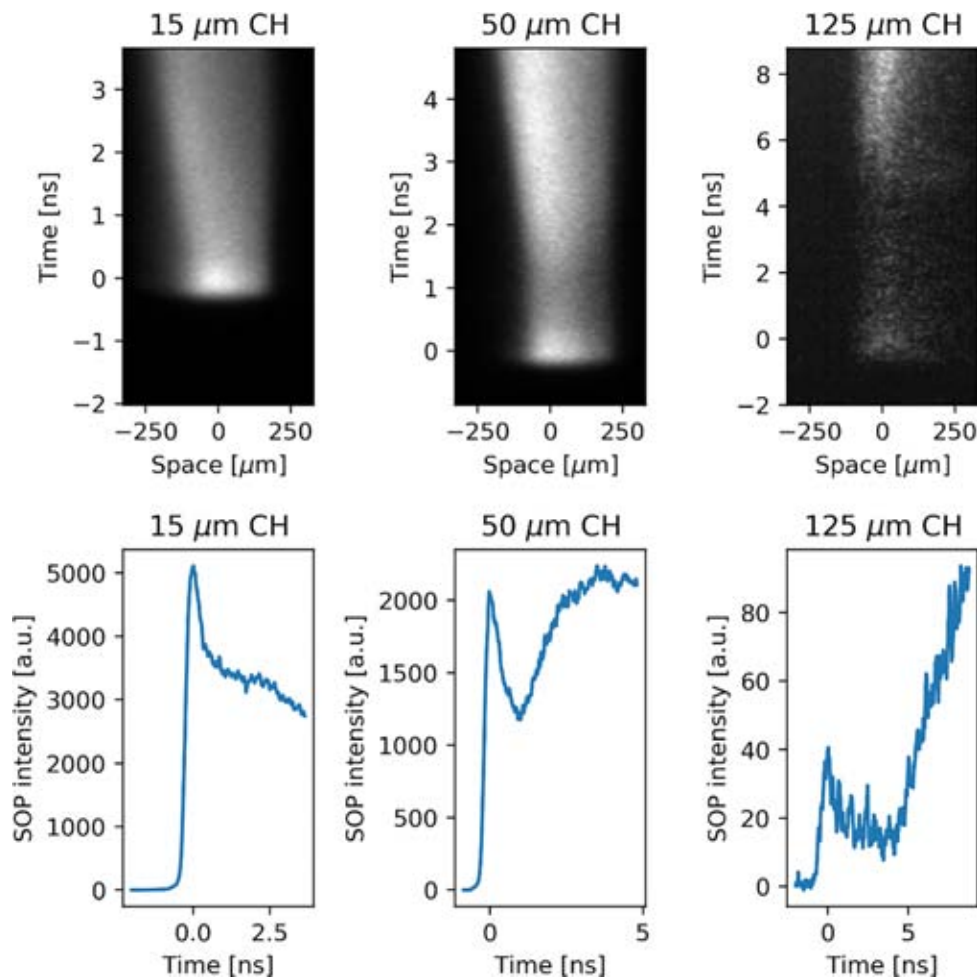


FIG. 6. Streak images of rear side emission for different thicknesses of the CH layer (top row) and corresponding line-out as a function of time (bottom row). The time $t = 0$ is defined by the peak of the emission due to the electrons. For the target with a 125 μm thick CH layer, the signal rises at $t = 4.1 \pm 0.2 \text{ ns}$ due to shock breakout. For the target with 50 μm of CH, this rises at $t = 1.0 \pm 0.1 \text{ ns}$. For the target with 15 μm of CH, the shock breakout time cannot be precisely measured.

resolution of the optical diagnostics, we were not able to distinguish SRS from laser light simply reflected from the target. The reflectivity due to SRS, in the lens cone, was 0.6–4% of laser energy. Comparing such results to our previous measurements performed at 3ω ,^{21,22} we observe a large increase in SRS, which can be explained by the increase in the irradiance parameter ($I\lambda^2$), which determines the convective gain in the resonance region. The measured increase in SRS is consistent with the rise in the hot electron signal, suggesting that the main HE component is generated by SRS. This is further confirmed by the spectral characterization of SRS back reflectivity, showing a maximum in the spectral range of 2400–2450 nm,²³ implying that SRS is preferentially emitted at densities of 0.17–0.19 n_c . In this case, assuming a background plasma temperature to be ~ 4 keV (as extracted from simulations and as expected from simple scaling laws), we can estimate that the energy of electrons accelerated by the plasma waves produced by SRS is ~ 40 keV, in fair agreement with our experimental findings.

IV. DISCUSSION

E. The numerical tool

Numerical simulations of the experiment were performed with the hydrodynamic code CHIC,²⁶ which includes a model¹⁰ accounting nonlinear laser-plasma interaction (LPI), the generation of hot electrons, and their propagation into the plasma. The description of the laser propagation is based on the Paraxial Complex Geometrical Optics (PCGO): the laser beam is described by a bunch of thick Gaussian rays. Unlike models based on ray tracing, the PCGO model calculates laser intensity in plasma and allows computing parametric instabilities and subsequent hot electron production. The electron transport model is described in the continuous slowing down approximation considering electron-ion and electron-electron collisions. The hot electrons are described by an exponential distribution function in energy that is logarithmically discretized in a series of monoenergetic beamlets. This multigroup model for HE beam transport in plasmas has been validated by comparison with a reference code.²⁷ The free parameters defining the hot electron source are initial energy flux, mean temperature, angular distribution, and direction. These parameters are determined from laser and plasma characteristics, thus coupling parametric instabilities and hot electron sources. In CHIC, they are computed using scaling laws obtained from extensive PIC simulations or experimental data.¹⁰ For TPD HE, flux (W/cm^2) and temperature (keV) are defined as

$$F^{TPD} = 2.6 \times 10^{-2} I \left\{ 1 - \exp \left[- \left(\xi^{TPD} - 1 \right)^{1/2} \right] \right\}, \quad (1)$$

$$T^{TPD} = 15.5 + 17.7 \xi^{TPD}, \quad (2)$$

where $\xi^{TPD} = I/I^{TPD}$ is the ratio of the local intensity to the threshold intensity $I^{TPD} = 8.2 T_{\text{keV}} / (L_{\mu\text{m}} \lambda_{\mu\text{m}}) \text{ PW}/\text{cm}^2$, with $L_{\mu\text{m}}$ being the density scale length in μm . The electron plasma waves are excited by TPD in a broad range of directions within the cone $\pm 45^\circ$ with respect to the pump. Multiplicity of configurations for the pump and daughter waves produces a uniform hot electron emission in the $\pm 45^\circ$ cone with respect to the PCGO ray direction.

The energy of hot electrons produced by SRS is linked to the phase velocity of the electron plasma wave at the point of resonance. It is supposed that the hot electrons are produced at the density of $n_e = 0.2n_c$, and their temperature reads $T^{\text{SRS}} = 34 + 1.5T_{\text{keV}}$.¹⁰ The hot electron flux reads

$$F^{\text{SRS}} = 12.5 \times 10^{-2} I \left\{ 1 - \exp \left[- \left(\xi^{1/3} - 1 \right) \right] \right\} \text{ W}/\text{cm}^2, \quad (3)$$

where $\xi = I/I^{\text{SRS}}$ is the ratio of the local intensity to the threshold intensity. The threshold intensity can be calculated using the absolute or convective threshold formulas, $I_{\text{abs}}^{\text{SRS}} = 99.5 / (L_{\mu\text{m}}^2 \lambda_{\mu\text{m}})^{2/3} \text{ PW}/\text{cm}^2$ or $I_{\text{conv}}^{\text{SRS}} = 220 / \left(L_{\mu\text{m}} \lambda_{\mu\text{m}} \sqrt{1 - n_e/n_c} \right) \text{ PW}/\text{cm}^2$, respectively. From experimental observations, it is known that SRS electrons are more directional than TPD electrons relative to the laser direction. In CHIC simulations, it is assumed that SRS electrons propagate in the laser beam direction. The model describing coupling between the laser beam, plasma dynamics, hot electron generation, and propagation has been used to better simulate experiments in the intensity range of 10^{15} – $10^{16} \text{ W}/\text{cm}^2$ with $\lambda = 351 \text{ nm}$.¹⁰ Nevertheless, for longer laser wavelengths, the scaling laws used to define the hot electron sources from TPD and SRS have to be validated/tuned by comparison with experimental measurements.

F. Simulation without the hot electron

We performed CHIC simulations using the PCGO description of the laser beam, including or not the hot electron effects on hydrodynamics. The three plastic thicknesses, 15, 50, and 125 μm , have been tested. All the simulations share a common time scale. The zero time corresponds to the beginning of the laser pulse and differs from experimental zero time used in Figs. 2 and 6 defined at the maximum laser intensity. Comparisons between experiment and simulation concern the delay time between emission induced by hot electrons and emission induced by the shock breakout and so are independent of the choice of zero time. A focus is made on the interpretation of the thickest CH layer, characterized by a longer distance traveled by the shock wave. Figure 7 presents the results from the simulation without hot electrons. In this simulation, only 9.3% of the laser energy has been absorbed through inverse Bremsstrahlung. This low absorption is due to the short pulse, long wavelength, and high intensity of the laser pulse. 2D maps of pressure and density 800 ps after the beginning of the simulation show a well-defined shock front with a pressure of ~ 12 Mbar. The maximum pressure, 14–15 Mbar, is reached just after the peak of laser intensity. This relatively low pressure, for a laser intensity of $\sim 10^{16} \text{ W}/\text{cm}^2$, can be explained by two main reasons. First, at the first harmonic, laser-plasma coupling is weak. The laser absorption is less than 10% and takes place at a density of $6.5 \times 10^{20} \text{ cm}^{-3}$. Locally, plasma temperature is high but pressure due to a low density is small. The second reason is a small focal spot diameter of $\sim 100 \mu\text{m}$. Lateral losses are important and strongly reduce the pressure. A one dimensional simulation or a spherical geometry leads to higher pressure. However, this pressure is large enough to compress the plastic up to 3.6 times its initial density. Pressure and density maps as a function of time and space show that the shock propagates through the two layers and breaks out at the rear side of the target 4.45 ns after the beginning of the simulation.

Synthetic SOP images have been produced by looking at the total radiation escaping from the target rear side in the range of 1–4 eV accounting for the spectral acceptance of the SOP diagnostic (streak camera sensitivity plus transport optics). In addition, we have taken into account the spatial (80 μm) and temporal resolution (80 ps) of the diagnostics.

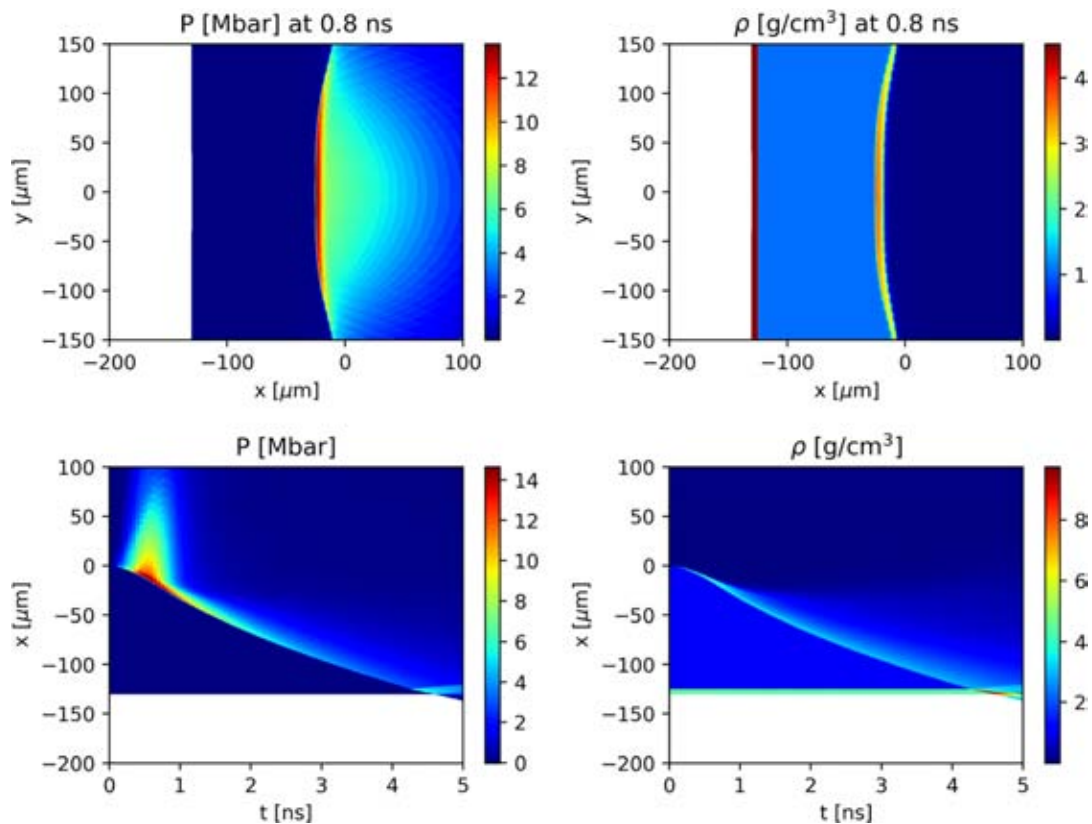


FIG. 7. Simulation without hot electrons. 2D map of pressure at 800 ps (top left), 2D map of density at 800 ps (top right). Pressure as a function of time and space (bottom left). Density as a function of time and space (bottom right).

As expected, in Fig. 8, only heating induced by the shock appears on the SOP signal, and the first emission induced by hot electrons is not reproduced by this simulation. Note that the X-ray emission produced by the laser-plastic interaction is not strong enough to heat the Ti layer and to be registered on the SOP signal.

At this step, an important remark has to be done concerning simulations and comparisons with experimental data. The CHIC code is a two dimensional hydro-code. Two geometries can be used: slab or cylindrical. The latter may be very close to 3D simulation in a case of cylindrical laser beam illuminating a target perpendicularly to the target surface. This geometry correctly represents the laser in terms of intensity, power, and energy. In planar geometry, the focal spot is a stripe with an intensity distribution, which is correct in one direction but invariant in the other one. To keep the same laser intensity on the target, the laser power has to be modified. For short hydrodynamic simulations or large focal spot dimension, both geometries lead to the same results. In this PALS experiment, the laser focal spot size was only $100\ \mu\text{m}$ at FWHM, the pulse duration was short, and the shock was traveling distances longer than $100\ \mu\text{m}$ during several nanoseconds. The geometry effect on shock propagation without hot electrons can be tested for the different plastic thicknesses using the model based on ray tracing (the PCGO model is for the moment implemented in planar geometry only). For the thickest layer, $125\ \mu\text{m}$, the shock

breakouts 600 ps later in the cylindrical case compared to that in the slab one. This is mainly due to different lateral losses during the shock creation and its propagation. Indeed, if in the cylindrical case, these losses are correctly calculated, in slab geometry, the invariance by translation in one direction reduces losses, leading to a higher pressure and finally to a faster shock. This effect is smaller for thinner targets. For the $50\ \mu\text{m}$ thickness, the delay between the two geometries is only 50 ps, and no difference is observed for the $15\ \mu\text{m}$ thickness.

G. Simulation with hot electrons

When simulating the case of the $125\ \mu\text{m}$ target with hot electrons, we have assumed that the difference between planar and axisymmetric geometries still results in a shock breakout difference of 600 ps. All the following simulations have been performed in slab geometry.

Figure 9 presents hydrodynamics with hot electrons. Both SRS and TPD electrons have been considered. The temperatures and conversion efficiencies of the electron sources are given by Eqs. (1) and (3). For the SRS electrons, the time averaged temperature and conversion efficiency are 39 keV and 9.2%, respectively. We used for this run the absolute intensity threshold. For the TPD electrons, these parameters are 83 keV and 1.9%. The SRS hot electrons have no initial divergence, while the TPD hot electrons have a $\pm 45^\circ$ divergence.

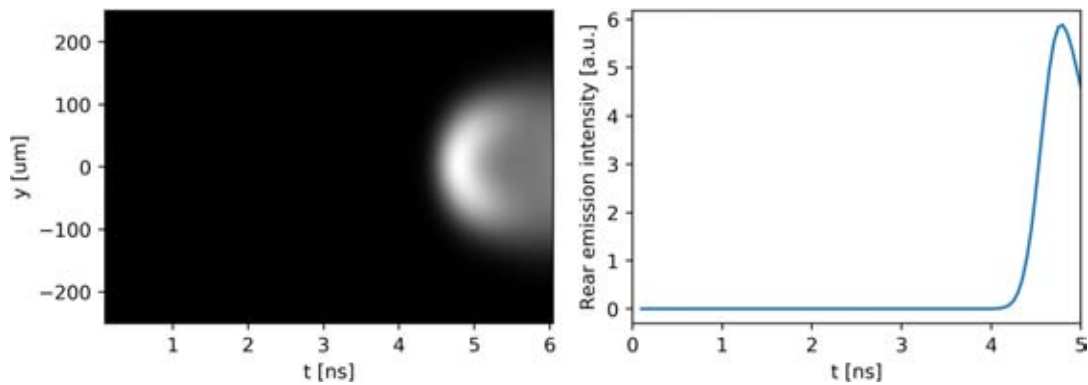


FIG. 8. Synthetic SOP image obtained by postprocessing the results of CHIC simulations, without HE (left) and line-out of this results along the axis $y = 0$ (right).

Additionally, 8.2% of the laser energy is absorbed through inverse Bremsstrahlung. Hence, collisional absorption is smaller than absorption by parametric instabilities. 2D maps of pressure and density 800 ps after the beginning of the simulation (Fig. 9, top row) show the effects of hot electrons on hydrodynamics of the target. Hot electrons heat the target both upstream and downstream of the shock front. In the unshocked plastic, this heating increases the pressure up to a

maximum value of about 110 Mbar. We must notice, however, that in this case, the pressure profile is not sharp, as the one obtained without hot electron, but is characterized by a slow spatial decay. In this simulation, because of a high upstream pressure, due to preheat, the shock wave compresses the plastic only by a factor of 1.15. The pressure increase due to the hot electron energy deposition also leads to expansion of the target from both sides. At the rear side, the heated

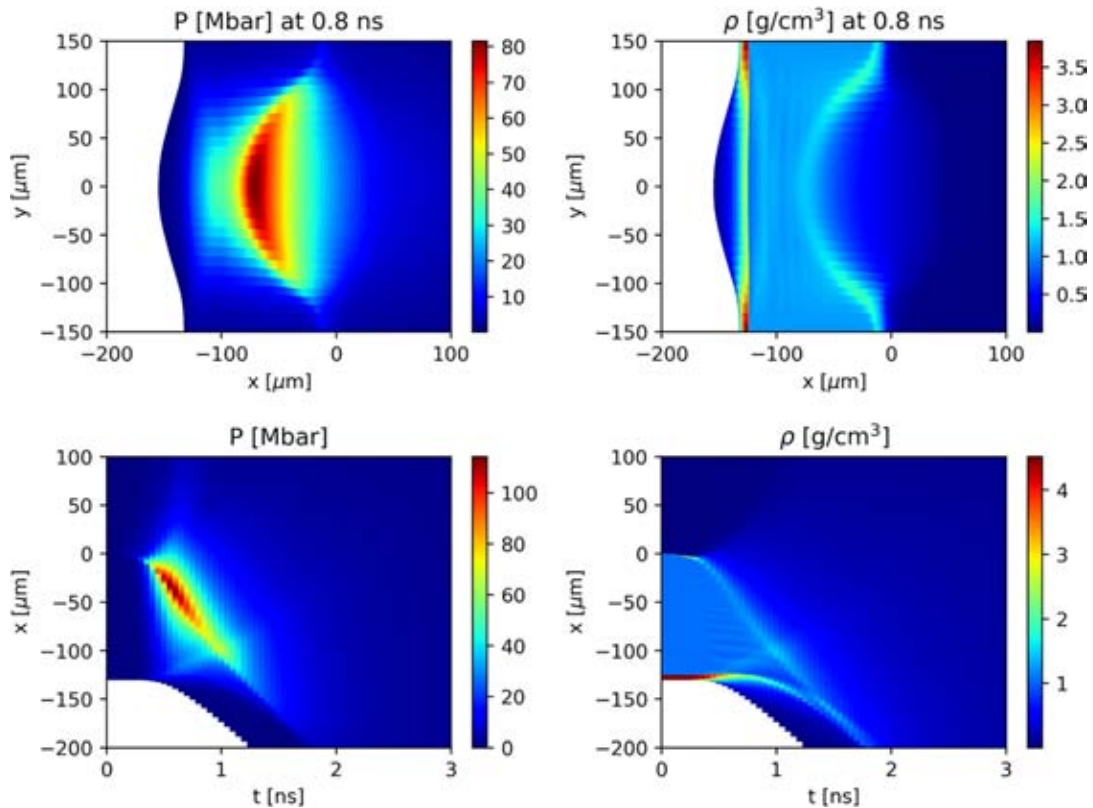


FIG. 9. Simulation with hot electrons. 2D map of pressure at 800 ps (top left). 2D map of density at 800 ps (top right). Pressure as a function of time and space (bottom left). Density as a function of time and space (bottom right).

Titanium layer expands into vacuum, creating a decreasing density gradient. Due to the directionality of the SRS hot electrons, this heating is localized close to the laser symmetry axis ($y = 0$). As a consequence, the shock front curvature is larger in the simulation with hot electrons. The pressure and density as a function of time and space (bottom row) show the dynamics of the target. The shock is faster in the simulation with hot electrons, and it reaches the Titanium layer at 1.6 ns, against 4.2 ns in the simulation without hot electrons. However, due to the large expansion of the Titanium layer, the breakout at the rear side of the target is not well defined. Figure 10 shows the synthetic SOP image obtained from this simulation. The emissivity of the rear side shows a behavior similar to the experiment. During laser matter interaction (before 800 ps), there is a peak of emissivity due to direct heating of the Titanium layer by the hot electrons. This signal then decreases with time as the layer expands and cools down. Then, the shock breaks out at the rear side of the target, leading to a second increase in the emissivity. In this simulation, the delay between the rising of the signal due to shock breakout and the peak of emission due to hot electrons is 1.6 ± 0.1 ns. Even considering 600 ps delay due to planar geometry, this is much shorter than the experimental delay (4.1 ± 0.2 ns). The disagreement between simulation and experiment is due to overestimation of the amount of hot electrons in the computation. Indeed, in this simulation, 9.2% of the laser energy is converted into SRS HE with a temperature of 39 keV. While the temperature is close to the measurements, the conversion efficiency is much larger in the simulation. In another simulation (not shown), the SRS intensity threshold has been changed from the absolute to the convective one. The latter intensity is higher, which leads to a smaller SRS electron flux but not small enough to reproduce experimental data. This inaccuracy in the scaling laws used to estimate HE source parameters is not surprising since these have mainly been determined from experiments and simulations at a shorter wavelength (typically $0.351 \mu\text{m}$) and smaller $I\lambda^2$.

H. Effects of reduced hot electron fluxes

We therefore performed another set of simulations adjusting the HE flux and angular spreading with the goal of reproducing all experimental measurements (shock breakout time, hot electron temperature, and conversion efficiency). It is important to notice that the goal of this study is not to discuss in detail the origin of hot electrons but is to

quantitatively characterize the hot electron amount and temperature required to reproduce their effects on hydrodynamics. This is of course more critical for SRS, which is the main source of hot electrons in our conditions. In particular, we compared the hot electron flux needed to reproduce experimental results to what predicted by scaling laws, either considering the intensity threshold for absolute SRS or that for convective SRS. Since the absolute SRS threshold is lower than the convective SRS threshold, it means that absolute SRS is triggered earlier in the laser pulse and acts for a longer time. Therefore, we get a higher hot electron flux from absolute SRS as compared to convective SRS. In both cases, we need to apply a reduction to the flux predicted by scaling laws in order to get the flux required to reproduce experimental results. This is a factor of about 4 if we consider absolute SRS and about 2 if we consider convective SRS. Physically, the reduction of hot electron fluxes needed for both SRS and TPD could be equivalent to modify the scaling laws for the fluxes by adding a wavelength dependence, but this reduction could also highlight a missing physical effect in simulations, for instance, related to the presence of strong magnetic fields close to the hot electron sources or other reasons. For both SRS and TPD sources, the temperatures and initial divergences have not been modified.

Figure 11 shows the effects of reduced hot electron fluxes on hydrodynamics. The conversion efficiencies of SRS and TPD are now 2.3% and 1.1%, respectively. Additionally, 9.3% of the laser energy has been absorbed through inverse Bremsstrahlung. 2D maps of pressure and density 800 ps after the beginning of the simulation (Fig. 11, top row) show that despite the flux reductions, hot electrons still heat the target. However, their effects are significantly reduced. Expansion of the Titanium layer is clearly less significant, and the shock is slower. The maximum pressure in the target has also been reduced to ~ 51 Mbar. This can also be observed in the pressure and density as a function of time and space (Fig. 11, bottom row). The shock now reaches the Titanium layer at ~ 2.2 ns. However, similar to the precedent simulation, expansion of the Titanium layer prevents from determining the shock breakout time. Figure 12 presents the numerical SOP image postprocessed from the hydrodynamic simulation, and it shows that the rising of the signal due to the shock breakout arrives later. In the time line-out (Fig. 12, right), the delay between the peak due to hot electrons and the signal due to the shock breakout is 3.1 ± 0.15 ns. Adding 600 ps due to the planar geometry gives 3.7 ± 0.14 ns, which is

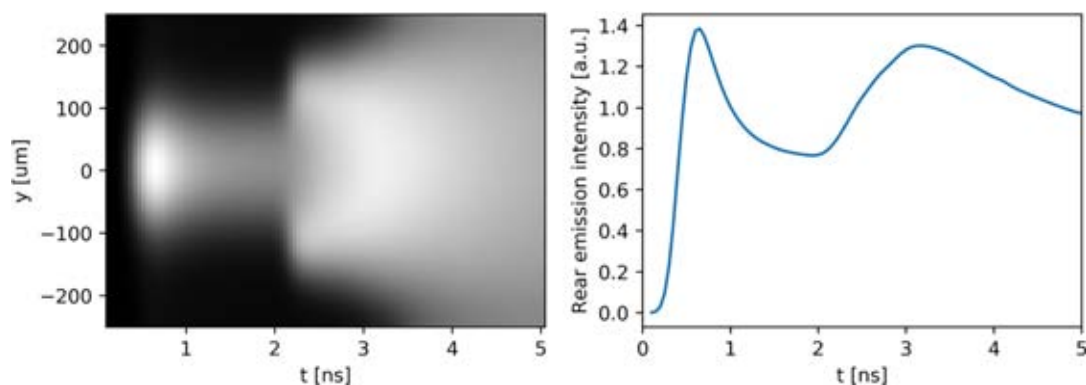


FIG. 10. Synthetic SOP image obtained by postprocessing the results of the CHIC simulation presented in Fig. 9 (left) and line-out of this results along the axis $y = 0$ (right).

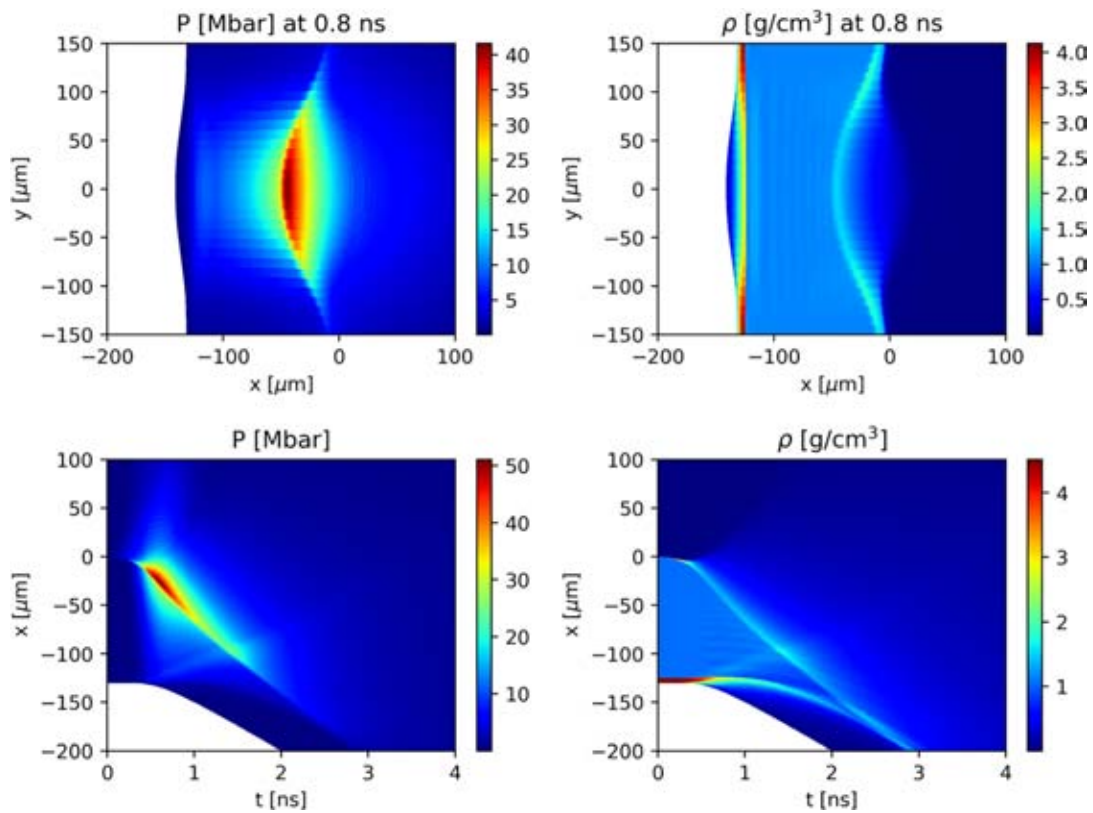


FIG. 11. Simulation with reduced hot electron fluxes. 2D map of pressure at 800 ps (top left). 2D map of density at 800 ps (top right). Pressure as a function of time and space (bottom left). Density as a function of time and space (bottom right).

much closer to the measured delay. Emissivity of the rear side as a function of time and space (Fig. 12, left) shows that the shock breaks out earlier away from the central axis (the earliest being for $y \simeq 150 \mu\text{m}$). Indeed, expansion of the Titanium layer is more significant near the axis, $y = 0$, and so at this position, the shock propagates a longer distance before breaking out. This effect is also

visible in the simulation with the nonreduced fluxes, but in this case, the shock is faster, and therefore, the titanium layer has less time to expand, reducing the difference between the center and the edges of the emission. This effect is not observed in the experimental image, which suggests that in experiment, hot electrons are less directional than what is assumed in the simulation.

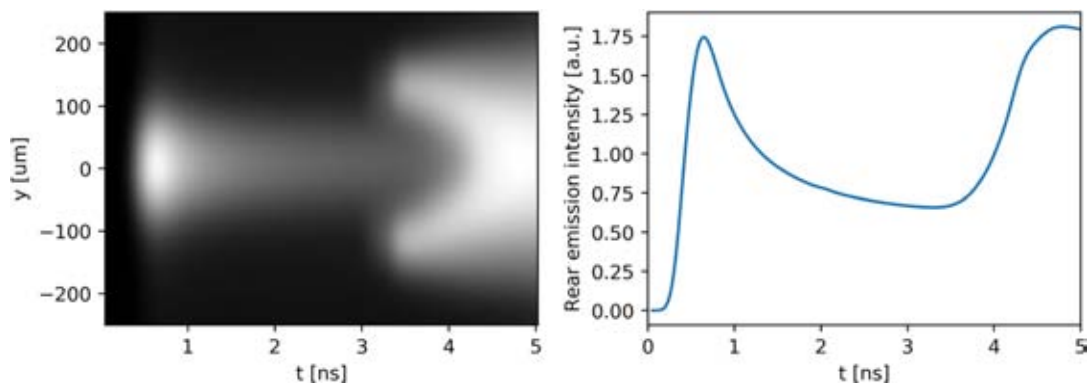


FIG. 12. Synthetic SOP image obtained by postprocessing the results of the CHIC simulation presented in Fig. 11 (left) and line-out of this results along the axis $y = 0$ (right).

I. Effects of angular spreading

We repeated the simulation with reduced fluxes and with $\pm 20^\circ$ initial divergence for the SRS electron source. While the temperature and conversion efficiency for SRS and TPD hot electrons are kept unchanged, electron heating shown in 2D maps of pressure and density at 0.8 ns, in Fig. 13, is much less directional. This results in a flatter shock front and a decrease in the pressure in both shocked plastic and the corona, the heated volume being larger, for the same injected energy. A lower pressure and cooler unshocked material produces a slower shock. The heated surface zone at the rear side is larger, which reduces the time difference of the shock breakout between the center and edges. Figure 14 shows the numerical SOP image. The curvature of the shock breakout signal is still visible but is strongly reduced. Such a curvature in the experimental image is not apparent but might be blurred due to the low level of the signal. The line-out of the central part of the rear side emission image shows a slightly later shock breakout compared to that in the simulation without initial divergence. The delay between the peak of emission due to hot electrons and the second bump due to the shock breakout is 3.35 ± 0.1 ns. Taking into account 600 ps induced by the planar geometry of simulation leads to a delay of 3.95 ± 0.1 ns, in agreement with the measured delay within error bars. The maximum pressure in the target is now reduced to about 40 Mbar.

The last simulation better reproduces the experimental SOP data, while remaining close to the experimental constraints concerning the measured characteristics of hot electrons. Yet, an increase in the signal due to the shock breakout is steeper in the simulation, and it also starts to decrease after ~ 4.2 ns. This behavior differs from the experimental signal that slowly increases with time. This difference has already been observed in interpretation of other experiments.²⁸ Among possible explanations, we mention the equation of state and opacity of Titanium, which might be inaccurate in the regime of low density (below 1 g/cc) and moderate temperature (a few electron volts), induced by rear side expansion.

J. Other plastic thicknesses

Parameters used to reproduce the experimental data for 125 μm targets have also been used to simulate the cases of different plastic thicknesses (50 and 15 μm). Figures 15 and 16 present synthetic SOP images for both cases. The numeric SOP signals are close to the measured ones. For the 50 μm thick CH (Fig. 15, right), the delay between the peak of emission due to hot electrons and the signal due to shock breakout is 1.15 ± 0.10 ns. Adding 50 ps from the planar geometry correction brings this delay in fair agreement with the measured delay (1.0 ± 0.1 ns). Concerning the 15 μm thick CH, the shock breakout does not lead to a significant increase in rear side emissivity. It slightly

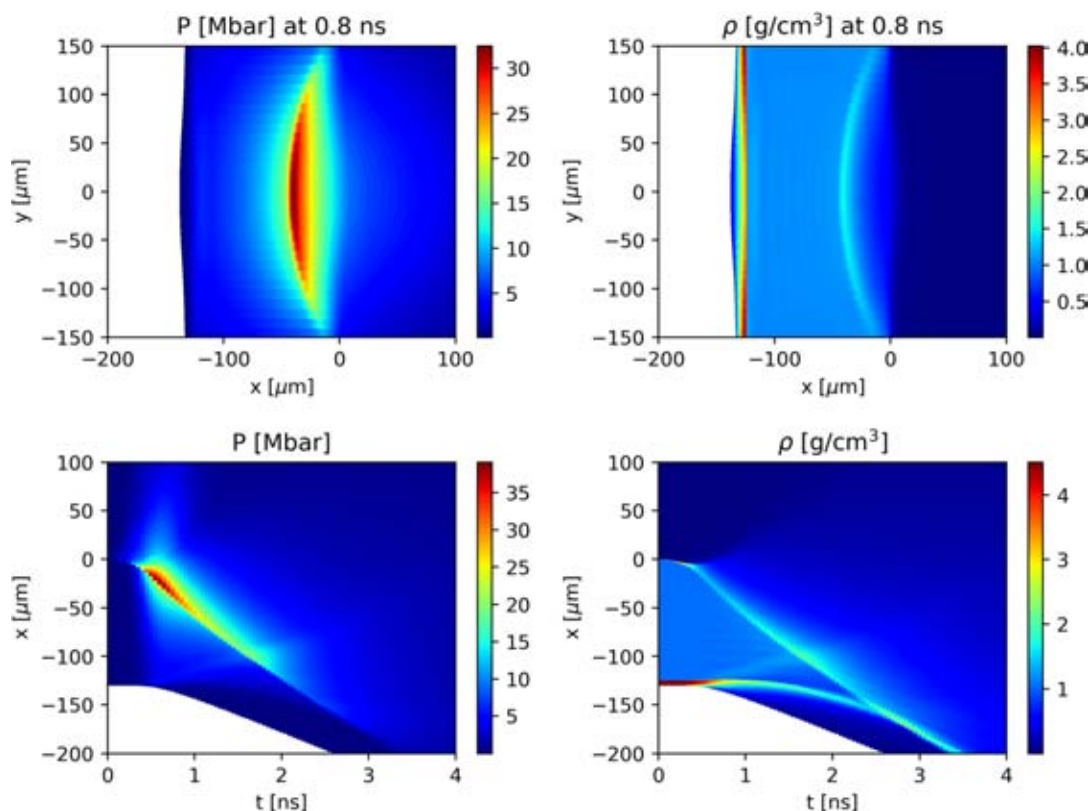


FIG. 13. Simulation with reduced hot electron fluxes and with a $\pm 20^\circ$ initial divergence of the SRS electron source. 2D map of pressure at 800 ps (top left). 2D map of density at 800 ps (top right). Pressure as a function of time and space (bottom left). Density as a function of time and space (bottom right).

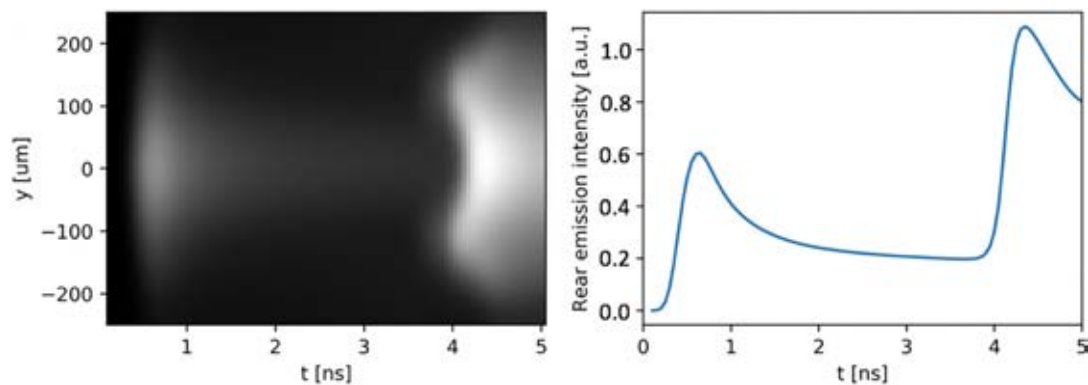


FIG. 14. Synthetic SOP image obtained by postprocessing the results of the CHIC simulation presented in Fig. 13 (left) and line-out of this results along the axis $y=0$ (right).

changes the slope of the rear side cooling down after being heated by hot electrons. This numerical SOP signal evolution looks similar to the experimental image. Moreover, the overall shape of SOP images and, specifically, the relative brightness of induced-hot electrons and -shock emissions are correctly reproduced. As shock propagates, it compresses and heats matter and loses in strength. So one could expect to obtain a lower emission for the thickest target. This is indeed the case, but heating induced by hot electrons decreases even more rapidly with the thickness. For $15 \mu\text{m}$, heating of the Titanium layer exceeds 40 eV during the laser pulse, whereas it is of 28–30 eV and 12–15 eV for target thicknesses of 50 and $125 \mu\text{m}$, respectively. This is directly correlated with the electron ranges. The distance of $15 \mu\text{m}$ of plastic can be crossed by 25 keV electrons, but distances of 50 and $125 \mu\text{m}$ require energies larger than 50 and 90 keV, respectively. Since hot electron distributions are exponential functions of temperature, the number of electrons at high energy is much smaller, thus reducing the Titanium temperature accordingly. The line-outs presented in Figures 14–16 use the same scale and can be directly compared.

V. CONCLUSION

This work presents experimental results obtained at high intensities and long laser wavelength, $\lambda = 1.315 \mu\text{m}$. These conditions

dramatically increase hot electron generation and decrease the role of collisional absorption. A significant fraction of the laser energy absorption is due to parametric instabilities, which are responsible for hot electron generation. Consistent experimental data have been interpreted with the hydrodynamic code CHIC, which accounts for laser-plasma coupling, the generation of hot electrons by SRS and TPD, and their energy depositions. Compared to a previous PALS experiment performed at the short laser wavelength (3ω of the iodine laser), experimental data can be interpreted only if the hot electron parameters are modified. Specifically, the angular spreading of SRS electrons had to be increased, and the hot electron fluxes had to be reduced by a factor between 2 and 4 (depending on whether we consider the threshold for absolute or for convective SRS). Such modifications of the fluxes could be interpreted as the signature of an additional wavelength dependence in the scaling laws for hot electron fluxes. However, they could also be produced by some missing effects in the simulations, eventually enhanced due to the long wavelength used in the experiment: 3D geometry, the presence of a strong magnetic field near the hot electron source, and strong filamentation locally modifying the laser intensity.

Spectroscopic data, data from crystal imagers and from bremsstrahlung cannon, demonstrate the presence of a significant number of hot electrons, a fraction of which can penetrate deeply into the

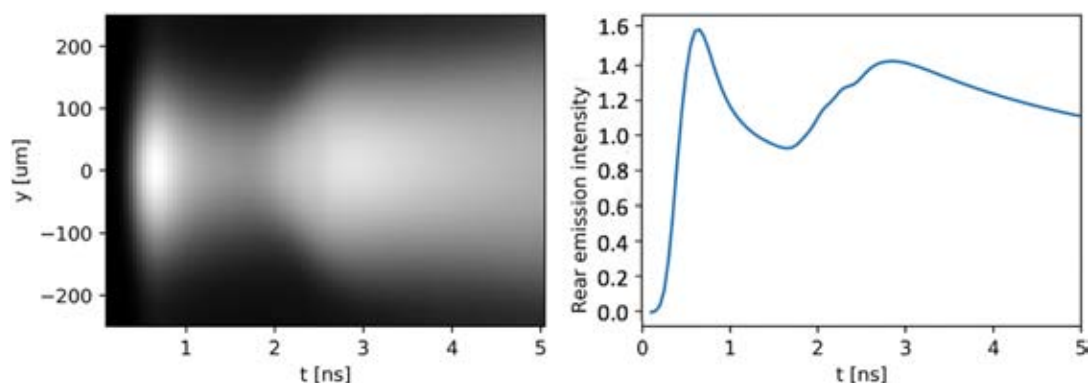


FIG. 15. Synthetic SOP image obtained by postprocessing the results of the CHIC simulation for a $50 \mu\text{m}$ plastic target (left) and line-out of this results along the axis $y=0$ (right).

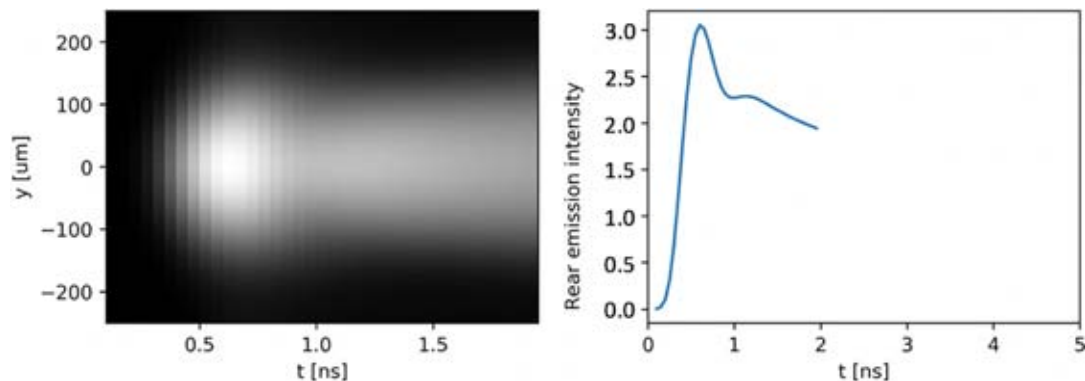


FIG. 16. Synthetic SOP image obtained by postprocessing the results of the CHIC simulation for a $15\ \mu\text{m}$ plastic target (left) and line-out of this results along the axis $y=0$ (right).

target, suggesting energies beyond 90 keV. Our experimental results and the simulations show a dramatic impact of hot electron preheating on shock dynamics. Energy deposition from hot electrons is clearly visible in the experimental and synthetic SOP images.

Hot electrons strongly increase the shock pressure.³⁰ The previous experiment performed at PALS, at the third harmonic, showed a pressure increase of 40%.¹⁰ The pressure increase in the present experiment is larger than 250%. This difference comes not only from an enhancement of the hot electron number but also from a weaker laser-matter coupling by collisional absorption. Hot electrons also have a significant impact on shock velocity owing to preheat of the unshocked plastic.

The pressure increase due to hot electrons could be a beneficial factor for shock ignition²⁹ if one can suppress the strong preheat upstream of the shock front. In our experiment, we used thin targets characterized by a small areal density of $\sim 0.01\ \text{g}/\text{cm}^2$, which are unable to stop electrons with energies larger than a few tens of kilo electron volts. In the SI scenario, one should get values of areal density larger than unity for the compressed shell. This could be sufficient to stop all hot electrons downstream of the shock. Therefore, in future shock ignition experiments, hot electrons could turn out to be beneficial for shock amplification, and long wavelength lasers could be a possible alternative for the spike irradiation.

ACKNOWLEDGMENTS

This work was carried out within the framework of the EUROfusion Enabling Research Project: AWP17-ENR-IFE-CEA-01 Preparation and Realization of European Shock Ignition Experiments and received funding from the Euratom Research and Training Program 2014–2018 under Grant Agreement No. 633053. The views and opinions expressed herein do not necessarily reflect those of the European Commission. This work was also supported by the European Union under the Laserlab IV Program (PALS2196); by the Czech Ministry of Education, Youth and Sports, Projects LTT17015, LM2010014, CZ.02.1.01/0.0/0.0/16013/0001552, CZ.02.1.01/0.0/0.0/16013/0001793; and within targeted support of Large Infrastructures, ELI Beamlines Project LQ1606 of the National Program of Sustainability II. Finally, the authors are grateful to the PALS staff for help in running the experiments.

REFERENCES

- R. Betti, C. Zhou, K. Anderson, L. Perkins, W. Theobald, and A. Solodov, *Phys. Rev. Lett.* **98**, 155001 (2007).
- R. Craxton, K. Anderson, T. Boehly, V. Goncharov, D. Harding, J. Knauer, R. McCrory, P. McKenty, D. Meyerhofer, J. Myatt *et al.*, *Phys. Plasmas* **22**, 110501 (2015).
- S. Atzeni, X. Ribeyre, G. Schurtz, A. Schmitt, B. Canaud, R. Betti, and L. Perkins, *Nucl. fusion* **54**, 054008 (2014).
- D. Batani, S. Baton, A. Casner, S. Depierreux, M. Hohenberger, O. Klimo, M. Koenig, C. Labaune, X. Ribeyre, C. Rousseaux *et al.*, *Nucl. Fusion* **54**, 054009 (2014).
- W. L. Krueer, *The Physics of Laser Plasma Interactions*, Frontiers in Physics Vol. 73 (Addison-Wesley, 1988).
- R. Drake, R. Turner, B. Lasinski, K. Estabrook, E. Campbell, C. Wang, D. Phillion, E. Williams, and W. Krueer, *Phys. Rev. Lett.* **53**, 1739 (1984).
- J. Trela, W. Theobald, K. Anderson, D. Batani, R. Betti, A. Casner, J. Delettrez, J. Frenje, V. Y. Glebov, X. Ribeyre *et al.*, *Phys. Plasmas* **25**, 052707 (2018).
- P. Nicolai, J.-L. Feugeas, T. Nguyen-Bui, V. Tikhonchuk, L. Antonelli, D. Batani, and Y. Maheut, *Phys. Plasmas* **22**, 042705 (2015).
- D. Batani, L. Antonelli, F. Barbato, G. Boutoux, A. Colaiitis, J.-L. Feugeas, G. Folpini, D. Mancelli, P. Nicolai, J. J. Santos *et al.*, *Nucl. Fusion* **59**(3), 032012 (2019).
- A. Colaiitis, G. Duchateau, X. Ribeyre, Y. Maheut, G. Boutoux, L. Antonelli, P. Nicolai, D. Batani, and V. Tikhonchuk, *Phys. Rev. E* **92**, 041101 (2015).
- T. Boehly, D. Brown, R. Craxton, R. Keck, J. Knauer, J. Kelly, T. Kessler, S. Kumpan, S. Loucks, S. Letzring *et al.*, *Opt. Commun.* **133**, 495 (1997).
- M. Hohenberger, W. Theobald, S. Hu, K. Anderson, R. Betti, T. Boehly, A. Casner, D. Fratanduono, M. Lafon, D. Meyerhofer *et al.*, *Phys. Plasmas* **21**, 022702 (2014).
- W. Theobald, R. Betti, C. Stoeckl, K. Anderson, J. Delettrez, V. Y. Glebov, V. Goncharov, F. Marshall, D. Maywar, R. McCrory *et al.*, *Phys. Plasmas* **15**, 056306 (2008).
- W. Theobald, R. Nora, M. Lafon, A. Casner, X. Ribeyre, K. Anderson, R. Betti, J. Delettrez, J. Frenje, V. Y. Glebov *et al.*, *Phys. Plasmas* **19**, 102706 (2012).
- R. Nora, W. Theobald, R. Betti, F. Marshall, D. Michel, W. Seka, B. Yaakobi, M. Lafon, C. Stoeckl, J. Delettrez *et al.*, *Phys. Rev. Lett.* **114**, 045001 (2015).
- S. Baton, M. Koenig, E. Brambrink, H. Schlenvoigt, C. Rousseaux, G. Debras, S. Laffite, P. Loiseau, F. Philippe, X. Ribeyre *et al.*, *Phys. Rev. Lett.* **108**, 195002 (2012).
- T. Pisarczyk, S. Gus'kov, O. Renner, N. Demchenko, Z. Kalinowska, T. Chodukowski, M. Rosinski, P. Parys, M. Smid, J. Dostal, J. Badziak, D. Batani, L. Volpe, E. Krousky, H. Turcicova, J. Hrebicek, M. Pfeifer, J. Skala, A. Zaras-Szydłowska, L. Antonelli, Y. Maheut, S. Borodziuk, A. Kasperczuk, and P. Pisarczyk, *Laser Part. Beams* **33**, 221 (2015).
- D. Batani, L. Antonelli, S. Atzeni, J. Badziak, F. Baffigi, T. Chodukowski, F. Consoli, G. Cristoforetti, R. De Angelis, R. Dudzak *et al.*, *Phys. Plasmas* **21**, 032710 (2014).

- ¹⁹K. Jungwirth, A. Cejnarova, L. Juha, B. Kralikova, J. Krasa, E. Krousky, P. Krupickova, L. Laska, K. Masek, T. Mocek *et al.*, *Phys. Plasmas* **8**, 2495 (2001).
- ²⁰O. Renner, M. Šmíd, D. Batani, and L. Antonelli, *Plasma Phys. Controlled Fusion* **58**, 075007 (2016).
- ²¹G. Cristoforetti, A. Colaitis, L. Antonelli, S. Atzeni, F. Baffigi, D. Batani, F. Barbato, G. Boutoux, R. Dudzak, P. Koester *et al.*, *EPL (Europhys. Lett.)* **117**, 35001 (2017).
- ²²G. Cristoforetti, L. Antonelli, S. Atzeni, F. Baffigi, F. Barbato, D. Batani, G. Boutoux, A. Colaitis, J. Dostal, R. Dudzak *et al.*, *Phys. Plasmas* **25**, 012702 (2018).
- ²³G. Cristoforetti, L. Antonelli, D. Mancelli, S. Atzeni, F. Baffigi, F. Barbato, D. Batani, G. Boutoux, F. D'Amato, J. Dostal, R. Dudzak, E. Filippov, Y. J. Gu, L. Juha, O. Klimo, M. Krus, S. Malko, A. Martynenko, P. Nicolai, V. Ospina, S. Pikuz, O. Renner, J. Santos, V. T. Tikhonchuk, J. Trela, S. Viciani, L. Volpe, S. Weber, and L. A. Gizzi, *High Power Laser Sci. Eng.* **7**, e51 (2019).
- ²⁴J. Sempau, E. Acosta, J. Baro, J. Fernandez-Varea, and F. Salvat, *Nucl. Instrum. Methods Phys. Res.* **132**, 377 (1997).
- ²⁵F. Salvat, J. Fernandez-Varea, and J. Sempau, in PENELOPE: A code system for Monte Carlo simulation of electron and photon transport, NEA/NSC/DOC (2015).
- ²⁶J. Breill, S. Galera, and P.-H. Maire, *Computers Fluids* **46**, 161 (2011).
- ²⁷M. Touati, J.-L. Feugeas, P. Nicolai, J. J. Santos, L. Gremillet, and V. T. Tikhonchuk, *New J. Phys.* **16**, 073014 (2014).
- ²⁸J. J. Santos, B. Vauzour, M. Touati, L. Gremillet, J.-L. Feugeas, T. Ceccotti, R. Bouillaud, F. Deneuille, V. Floquet, C. Fourment, M. Hadj-Bachir, S. Hulin, A. Morace, P. Nicolai, P. d Oliveira, F. Reau, A. Samake, O. Tcherbakoff, V. T. Tikhonchuk, M. Velcheva, and D. Batani, *New J. Phys.* **19**, 103005 (2017).
- ²⁹W. Shang, R. Betti, S. Hu, K. Woo, L. Hao, C. Ren, A. Christopherson, A. Bose, and W. Theobald, *Phys. Rev. Lett.* **119**, 195001 (2017).
- ³⁰S. Gus'kov, N. Demchenko, A. Kasperczuk, T. Pisarczyk, Z. Kalinowska, T. Chodukowski, O. Renner, M. Smid, E. Krousky, M. Pfeifer, J. Skala, J. Ullschmied, and P. Pisarczyk, *Laser and Particle Beams* **32**, 177 (2014).

High-quality 5 GeV electron bunches with resonant multi-pulse ionization injection

P Tomassini² , D Terzani, F Baffigi, F Brandi, L Fulgentini, P Koester, L Labate¹, D Palla and L A Gizzi¹

Intense Laser Irradiation Laboratory, INO-CNR, Pisa, Italy

E-mail: paolo.tomassini@ino.it

Received 24 July 2019, revised 4 September 2019

Accepted for publication 18 September 2019

Published 24 October 2019



CrossMark

Abstract

The production of high-quality electron bunches in laser wakefield acceleration relies on the possibility of injecting ultra-low emittance bunches in the plasma wave. A new bunch injection scheme (resonant multi-pulse ionization, ReMPI) has been conceived and studied, in which electrons extracted by ionization are trapped by a large-amplitude plasma wave driven by a train of resonant ultrashort pulses. Such a train of pulses can be obtained in a very efficient, compact and stable way, by phase manipulation in the laser front-end. The ReMPI injection scheme relies on currently available laser technology and is being considered for the implementation of future compact x-ray free electron laser schemes. Simulations show that high-quality electron bunches with an energy of up to 5 GeV and a peak current exceeding 2 kA, with normalized emittance of below $0.1 \text{ mm} \times \text{mrad}$ and a slice energy spread of below 0.1%, can be obtained with a single stage.

Keywords: laser-plasma acceleration, high-brightness beams, resonant multi-pulse ionization injection, multi-pulse laser wake field acceleration, free electron lasers, high-quality electron beams

(Some figures may appear in colour only in the online journal)

1. Introduction

Laser wakefield accelerators (LWFA) are nowadays approaching the 10 GeV energy scale [1], with accelerating gradients in the order of 40 GeV m^{-1} . Several applications of those electron bunches, including staging [2–6], LWFA-based colliders [7–9] and high-quality secondary sources [10–16] can now be envisaged. Therefore, a viable laser wakefield accelerator producing GeV scale, high-quality, electron bunches should operate with a flexible and stable injection mechanism capable of producing very low emittance bunches.

Several electron injection schemes have been proposed and tested so far. Among them, ionization injection [17–25] opens up the possibility of experimental control of the injection mechanism. Injection via density downramp [26–30] has been proven to be capable of generating very low

emittance bunches [28], though it is not easy to disentangle the mean energy, the energy spread, the charge and the emittance of the produced bunch.

The need for a flexible scheme capable of generating very low emittance bunches led to the introduction of the two-color ionization injection [31]. The two-color ionization scheme needs the use of two laser systems. The ‘driver’ pulse excites the plasma wave and is delivered by a long-wavelength (e.g. CO_2) system, while a synchronised pulse (the ‘ionization’ pulse) from a Ti:Sa system extracts the electrons from the dopant by tunnel field-ionization. To date, however, long-wavelength ($\lambda > 5 \mu\text{m}$), high-power ($P > 100 \text{ TW}$) and ultrashort ($T \ll 100 \text{ fs}$) laser systems are lacking and hopefully will be available in the near future.

The new resonant multi-pulse ionization injection scheme (ReMPI) [32] is capable of generating very low emittance bunches in a flexible way, yet using a single Ti:Sa laser system. In ReMPI, the long-wavelength driver pulse of the two-color injection is substituted by a train of pulses that excites the wakefield through the multi-pulse LWFA

¹ Also at INFN, Sect. of Pisa, (Italy).

² Author to whom any correspondence should be addressed.

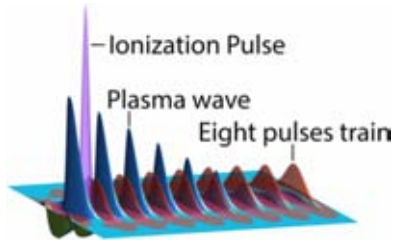


Figure 1. The ReMPI scheme. The incoming pulse passes through a beam splitter; a portion is time shaped as a train of eight pulses (red, transparent surface), while a smaller portion in fourth harmonics is tightly focused in the rear of the train (purple surface) and extracts electrons from the argon dopant. The driver train resonantly excites a high-amplitude plasma wave (black line) that traps and accelerate the electrons.

mechanism [33–36], maintaining each pulse’s electric field under the ionization threshold for the selected dopant (e.g. nitrogen or argon). Subsequently, a tightly focused, low amplitude, pulse in second, third or fourth harmonics in the tail of the train ionizes the dopant, thus injecting the electrons into the wakefield with an ultra-low emittance (see figure 1). While the ReMPI scheme has been already (numerically) tested for producing low-charge ($Q \simeq 5\text{pC}$) high-quality beams [32, 37, 38], relatively high-charge ($Q \simeq 30\text{pC}$) high-quality explorations of the scheme were still lacking.

In this paper we report on numerical simulations about the trapping and acceleration of a 5 GeV electron bunch, with a beam-quality high enough to drive a free electron laser (FEL), as envisaged in the EuPRAXIA project [39]. FELs are extremely demanding in terms of beam quality [40, 41], especially at their high energy end, where radiation with wavelength $\lambda_R \simeq \lambda_U/2\gamma^2 \approx 1\text{Å}$ (here $\lambda_U \approx 2\text{cm}$ is the undulator period) can be generated. In addition to standard beam-quality parameters, the so-called ‘slice quality’ parameters should be evaluated for a bunch aiming at driving a FEL. Slice parameters refer to the phase space quality of each transverse slice of the bunch, and give us relevant information on which slice will participate in FEL lasing. In the case of the EuPRAXIA envisioned FEL, the required global and slice parameters at the undulator entrance are summarized in the ‘requested’ row of table 1.

The working configuration shown here is based on a 1PW Ti:Sa laser system, temporally shaped into a train of eight pulses in the fundamental harmonics, each delivering 6.3J in 55 fs. Moreover, a 45 fs long pulse in the fourth harmonics, obtained by an amplified portion of the same master pulse of the train, is tightly focused behind the driver, thus constituting the ionization pulse. The experimental arrangement can deal either with multiplexing techniques after the amplification chain [34–36, 42] or with the new TEMPI scheme, recently proposed by Labate *et al* and tested with start-to-end simulations [43, 44]. TEMPI is based upon the usage of birefringent plates of increasing thicknesses and crossed polarizations, which produce delayed replicas of the original pulse, and linear polarizers [45]. In contrast to the arrangement described in [45], in TEMPI such a stack is used, on the stretched pulse, early in the CPA amplification chain,

thus allowing for a recovering of the pulse energy at a relatively small price in terms of additional pump energy. The TEMPI scheme should result in a more compact and stable setup with respect to the above mentioned schemes, yet be able to generate a train of pulses with almost constant peak intensity along the train and with an energy conversion efficiency approaching unity. Finally, we stress that being the driving train and the ionization pulse amplified replicas of the same master pulse, no synchronization jitter issues are raised. Nonetheless, μm sized mechanical vibrations can induce some fluctuations in the ionization pulse-to-driver train delay, but those fluctuations can be safely maintained at (some) femtoseconds level, i.e. to a very small fraction of the plasma period. The laser train and ionization pulse parameters have been collected in table 2.

The plasma target consists of a two adjacent sections stack. In the first section, made by a gas-cell filled with a mixture of argon (50%) and helium, electrons are extracted by field ionization and subsequently trapped by the plasma wave. Finally, electrons experience a longitudinal phase-rotation that reduces their overall energy spread to a percent level. In this first section the laser pulse is still focusing, therefore a guiding parabolic channel is not necessary here. The second section is placed as close as possible to the cell and consists of a gas capillary filled by pure helium. In the capillary the laser pulse remains focused and can excite the plasma wave for about 25 cm [1]. In both stages, background plasma density is set to $n_e = 2.1 \times 10^{17}\text{cm}^{-3}$, which sustains a plasma wave of wavelength 75 μm .

Simulations of about 25 cm of propagation in the plasma have been performed with the hybrid fluid/PIC code QFluid [46]. The QFluid simulations assume a 2D cylindrical symmetry of the fields, while particles of the bunch move in a full 3D space. The bunch is sampled with $N_b \approx 10^6$ equal-weighted macroparticles and the simulation box (a cylinder, actually) has radius 320 μm and length 690 μm . QFluid is equipped with a mesh-refining technique, which is activated in the longitudinal portion of the cylinder where the bunch is placed. The fields are solved by quasi-static approximation [47] by using the coarse resolution of $dz_{\text{coarse}} = 0.47\mu\text{m}$ (longitudinal) and $dr_{\text{coarse}} = 0.93\mu\text{m}$ (radial), while the refined grid spacing are $dz_{\text{fine}} = 0.0125\mu\text{m}$ and $dr_{\text{fine}} = 0.1\mu\text{m}$.

We remark that the evolution of the laser pulse’s complex envelope [48] has been performed maintaining the second order derivative in the time evolution, thus ensuring the most accurate description of the (very long) pulse’s evolution.

2. Driving pulse train evolution

The evolution of the driver train as a whole is highly non-trivial, due to propagation of the pulses in a nonuniform plasma. A detailed analysis of this evolution is beyond the scope of the present work and will be presented elsewhere [49]. However, as the first pulse propagates in a steady, uniform plasma, it starts exciting the wakefield, which is reinforced by the subsequent pulses via a resonant process. We point out

Table 1. Requested beam quality ('R' raw) and quality parameters obtained by means of the simulations reported in the paper ('O' raw). The overall and slice relative energy spread $\sigma(E)/E$ and normalised emittance ϵ_n , as well as the total charge Q and peak current I , are shown.

Param.	$\sigma(E)/E$	ϵ_n	$\sigma(E)/E_{slice}$	$\epsilon_n _{slice}$	Q	I
R	<1, %	$\ll 1 \mu\text{mrad}$	<0.1%	$\ll 1 \mu\text{mrad}$	$\geq 30 \text{ pC}$	>1 kA
O	0.9%	0.085 μmrad	0.03% (min)	0.085 μmrad	30 pC	2.5 kA

Table 2. Relevant parameters set for the driving train and the ionization pulse. The total delivered energy (E), the FWHM pulse(s) duration (T), the minimum waist (w_0), the pulse-to-pulse delay (the ionization pulse refers to the last pulse of the train) and the normalized pulse amplitude (a_0) are shown.

Laser	E	T	w_0	Delay	a_0
Driver	50 J	55 fs	90 μm	250 fs	0.63
Ionization	0.06 J	45 fs	5.9 μm	85 fs	0.25

that in such a framework, all the driver pulses behind the first one interact with a perturbed plasma density which can strongly affect their evolution. Therefore, different portions of a given driver pulse, depending on its length and phase in the plasma wave, could be refracted away or focused. Moreover, the energy exchange from the pulse and the wave can vary significantly from the usual scenario.

In the simulation shown here, some optimization procedure has been employed to stabilize the evolution of the pulses in the tail of the driving train. Nevertheless, a sizable fluctuation of the peak intensity is still present during the 25 cm of propagation, as is shown in figure 2(a). The severe pump depletion of about 70% of laser energy is mostly due to erosion of the last pulses in the train, as is now apparent in figure 2(b), while not only the first pulse shows a depletion of just a 10 % (not shown there) but also experiences a strong self-focusing. Nonetheless, the train is capable of exciting a large-amplitude plasma wave for most of its propagation distance, as will be shown in the next section.

3. Tunnel field-ionization of bunch electrons

In the first target section containing argon, it is supposed that the laser prepulse and the first few cycles of the first driver pulse are able to ionize the gas up to the eighth level. This is because the ionization energies of the first eight electrons are relatively low, with the highest being about 144 eV. In the passage to the K-shell (i.e. to the ninth electron), however, a large jump in the ionization energy occurs ($U_{i,9} \simeq 422 \text{ eV}$), thus realizing the optimal conditions for a controlled extraction of the electrons with an ad hoc large-amplitude electric field. This is accomplished by focusing the fourth harmonic 'ionization' pulse behind the train, in such a way that its electric field is close to its threshold for the $\text{Ar}^{8+} \rightarrow \text{Ar}^{9+}$ transition. It is worth noting that the electric field amplitude of a laser pulse is proportional to its normalized amplitude $a_0 = eA_0/mc^2$ and to its wavevector $k_0 = 2\pi/\lambda_0$, λ_0 and a_0

being the pulse wavelength and vector potential amplitude, respectively. Therefore, a large electric field amplitude can be realized with a moderate normalized amplitude a_0 but with a very short wavelength. If a Ti:Sa pulse is chosen ($\lambda \simeq 800 \text{ nm}$), a fourth harmonics conversion is an efficient, yet cumbersome, option. In the following, a fourth harmonics converted pulse will be considered, along with the resulting normalized amplitude $a_{0,ion} = 0.25$ and a minimum waist of $w_{0,ion} = 5.8 \mu\text{m}$.

Once the electron leaves the atom, it starts to quiver in the oscillating pulse electric and magnetic fields and, after the ionizing pulse has overpassed it, a residual secular transverse momentum along the polarization axis is left, thus constituting a source of bunch emittance. Analytical results and simulations in [50], show that the minimum normalized emittance achievable by using a linearly polarized pulse can be as low as

$$\epsilon_{n,\min} \simeq \frac{1}{\sqrt{2}} w_{0,ion} \cdot a_{0,ion} \cdot \Delta^2 = \frac{1}{\sqrt{2}} w_{0,ion} \cdot a_{0,ion}^2 / a_c, \quad (1)$$

with $\Delta \equiv \sqrt{a_{0,ion}/a_c}$, $a_c = 0.108 \cdot \lambda_{ion}(U_i/U_H)^{3/2}$ ($U_H \simeq 13.6 \text{ eV}$; see equation (26) in [50] and (4) in [32]). Having selected the transition $\text{Ar}^{8+} \rightarrow \text{Ar}^{9+}$, along with the above mentioned ionizing pulse, we derive from equation (1) a minimum achievable 'thermal' emittance of $\epsilon_{n,\min} \simeq 0.05 \mu\text{mrad}$. We mention, however, that other mechanisms can be responsible for an emittance increase. Though the ponderomotive forces are a good linear approximation in the transverse coordinate and consequently do not contribute to the transverse emittance (see [50]), the transverse kick on the low-energy electrons increases the beam radius just after the pulse passage and causes a fraction of the beam lying in a region of nonlinear transverse force. Those electrons, therefore, will oscillate with a lower betatron frequency, thus partially spoiling out the transverse quality. Moreover, as bunch charge increases, space charge and beam loading can contribute to increasing the beam emittance. In our simulations a final emittance of $\epsilon_{nx} = 0.08 \mu\text{mrad}$ in the first section has been obtained, which should be compared with the minimum value of $0.05 \mu\text{mrad}$ obtained with equation (1).

4. Bunch trapping and energy boosting up to 5 GeV

Once the newborn electrons are extracted by the ionizing pulse, they slip back in the wake while they are accelerated by the electric field. Those electrons are trapped by the wave, provided that they reach the wake (phase) velocity prior to entering into its decelerating region. The trapping, therefore, occurs if the wake accelerating field exceeds some threshold

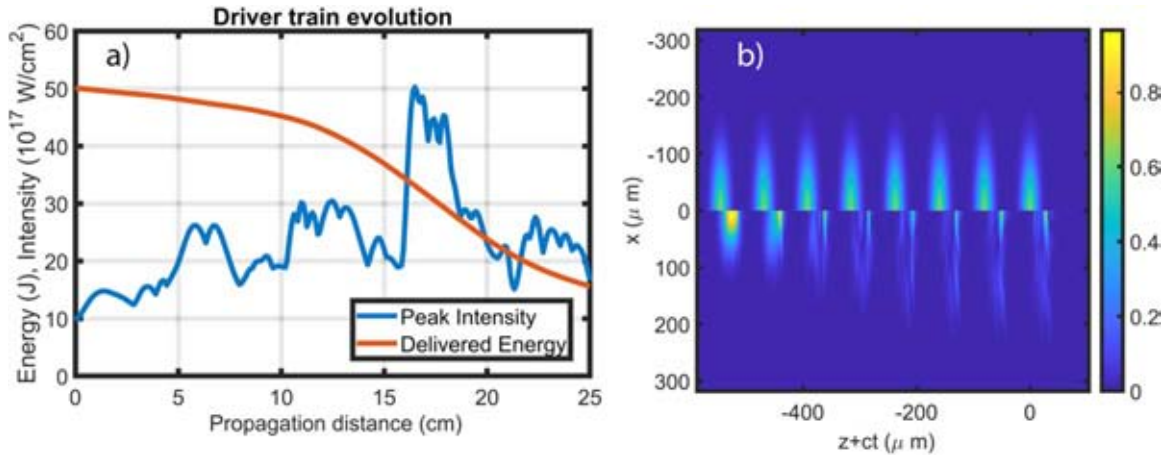


Figure 2. Driver train evolution. (a) Peak intensity and overall pulse energy evolution. (b) Initial (upper) and final (lower) maps of the pulse envelope. Pulses move towards the left.

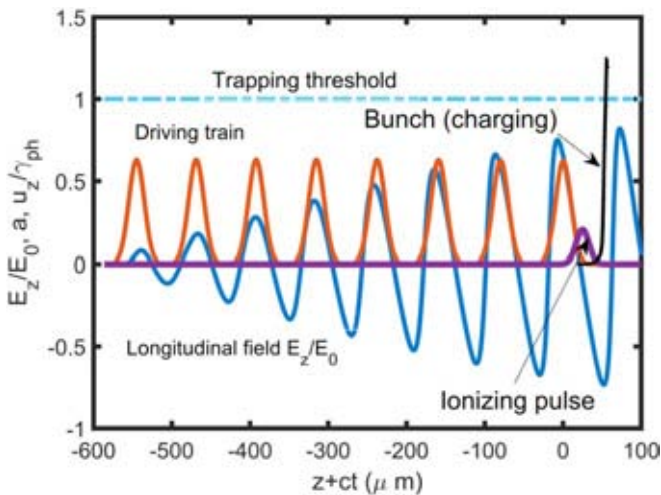


Figure 3. An axis snapshot at the early stage of bunch trapping. Lineout of the driving train (red line) and of the ionizing pulse (purple line) normalized amplitudes, as well as the lineout of the longitudinal normalized electric field E_z/E_0 are shown. The Lorentz factor γ associated with the wakefield is $\gamma_{ph} \approx 90$. The longitudinal phase space of the bunch (black dots) is $(z + ct[\mu\text{m}], u_z/\gamma_{ph})$, where $u_z = -p_z/mc$. Particles with $u_z/\gamma_{ph} \geq 1$ are trapped by the wave.

that depends on the exact phase of the wake where the the electrons are frozen. In our simulations electrons reach the wake's speed well before its node, which means that trapping occurs within the standard trapping and the 'strong' trapping [32] condition boundaries. In figure 3 a snapshot of the bunch longitudinal phase-space is shown, at a time in which electrons are still being extracted from the dopant. The bunch (black dots) is already partially trapped, while most of the particles still have a longitudinal momentum $u_z = -p_z/mc$ well below the trapping threshold $\gamma_{ph} = 1/\sqrt{1 - \beta_{ph}^2} \approx 90$, $\beta_{ph} = v_{ph}/c$ being the phase speed of the wake. In figure 3 the driving pulse train (red line) and ionization pulse (purple line) are also shown. After the last train pulse, a nonlinear wave (blue line) with amplitude $E_z/E_0 \approx 0.7$ has been excited (here

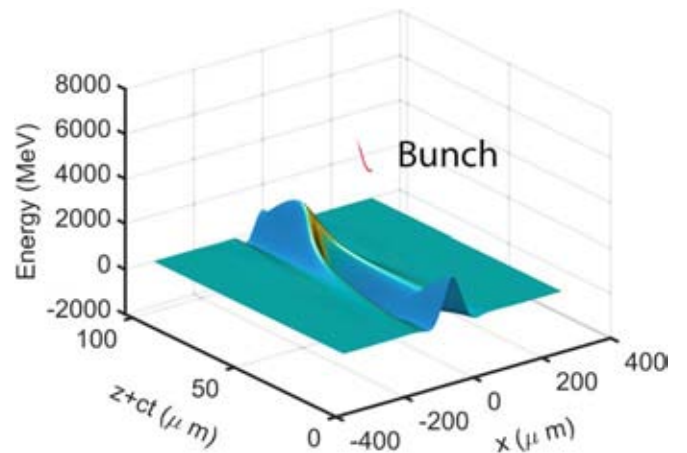


Figure 4. The phase-space $((z + ct)[\mu\text{m}], x[\mu\text{m}], E[\text{MeV}])$ of the bunch at the end of the 25 cm (approx.) long capillary. The longitudinal electric field map is also shown.

$E_0 = mc \omega_p/e$ is the nonrelativistic wavebreaking limit and ω_p is the plasma frequency). As the bunch is fully trapped by the wave, a longitudinal phase-space rotation occurs. Moreover, transverse focusing forces remain linear inside the bunch, which is adiabatically squeezed down to a (quasi round) beam of about $0.8 \mu\text{m}$ diameter.

After the phase-space rotation, the train and the bunch enter into the helium-filled capillary, which guides the laser for more than 20 cm. Notwithstanding the nontrivial evolution of the laser pulses (as shown in section 2), the bunch always experiences linear focusing forces, though the accelerating fields varies considerably during the propagation. Yet, a mean accelerating gradient of $\approx 45 \text{ GV m}^{-1}$ has been obtained, which corresponds to a mean normalized field $E_z/E_0 \approx 0.45$. At the end of the capillary, the driving train is depleted by its 70% and the bunch energy is about 5 GeV, with a marginal increase of the normalized emittance up to $\epsilon_{nx} = 0.085 \mu\text{mrad}$ and $\epsilon_{ny} = 0.080 \mu\text{mrad}$. The final beam phase-space, along with the longitudinal electric field in its bucket, are shown in figure 4.

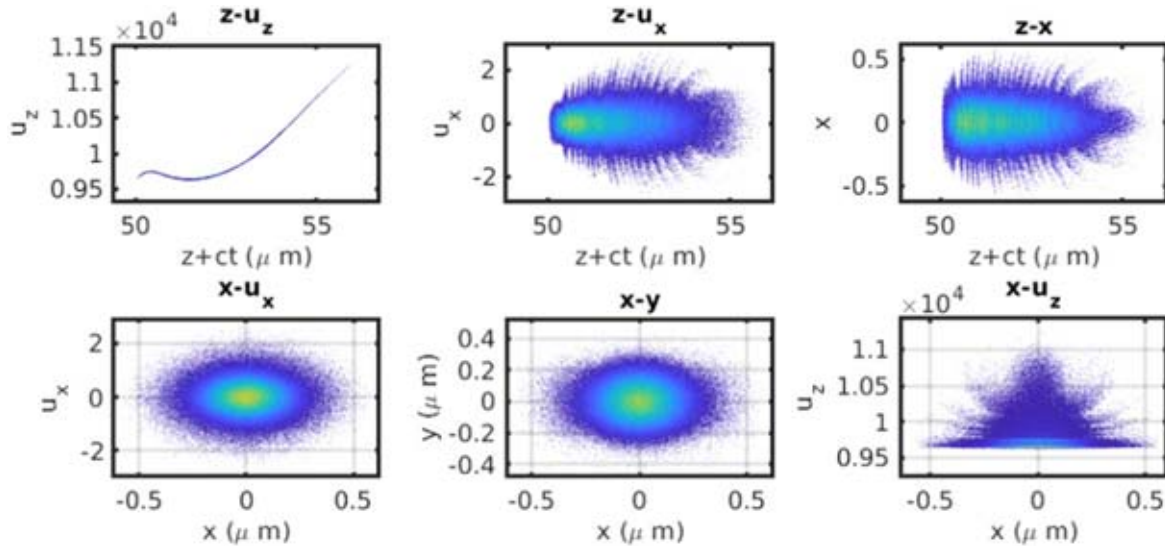


Figure 5. Phase-space cuts of the final beam. Here $u_{x,y} = p_{x,y}/mc$ and $u_z = -p_z/mc$. The bunch moves towards the left.

5. Final bunch quality

As we pointed out in the introduction, a FEL oriented beam should be analyzed in both the overall and slice perspectives. While the projected (overall) one gives us relevant information about quality degradation during the beam transport lines [51, 52], a slice inspection of the phase space will definitely show us which (and how) portions of the bunch will participate in lasing [40, 41]. In figure 5 some cuts of the 6D final phase space are shown. As is apparent from cuts in the $x - y$ and $x - u_x$ planes, a (quasi) round and matched beam has been obtained. The $z - u_z$ plane, however, shows us that a higher energy tail is present. This tail partially spoils the longitudinal beam quality, the overall energy spread being about 1.8%. A better inspection of the longitudinal phase-space cut, however, reveals that only a small fraction of the beam charge (about 8%, actually) is responsible for the high-energy tail and of the subsequent large energy spread (see figure 6). The tail is therefore easily removed with a simple tuning of the transfer line energy acceptance. The transported beam (with about 92% of the total charge, i.e 30 pC) complies with all the (projected) requirements of the ‘requested’ raw in table 1, its overall energy spread being $\sigma_E/E = 0.9\%$.

Slice analysis of the bunch phase space has been performed with a slice thickness of $0.1 \mu\text{m}$, which is compatible with the cooperation length of the envisioned FEL setup [40]. In figure 7(a) the slice current profile, as well as brightness-5D ($B_{5D} \equiv 2I/(\pi^2 \epsilon_{nx} \times \epsilon_{ny})$) and brightness-6D ($B_{6D} \equiv B_{5D}/(\sigma_E/E/10^3)$) are shown. Remarkably, at least brightness-5D is about a factor of three above the one recently obtained with a two-stage LWFA/PWFA hybrid approach (see [53], where a definition of brightness without the π 's has been used). Moreover, the current distribution shows a gentle-varying profile with peak value of 3.7 kA. In figure 7(b) the normalized emittances along the x (ionization) and y (driver) polarization axis are reported. At peak current, i.e at a longitudinal position of about $-1 \mu\text{m}$ from the bunch center-of-mass, emittances of $0.065 \mu\text{mrad}$ and $0.04 \mu\text{mrad}$ along the

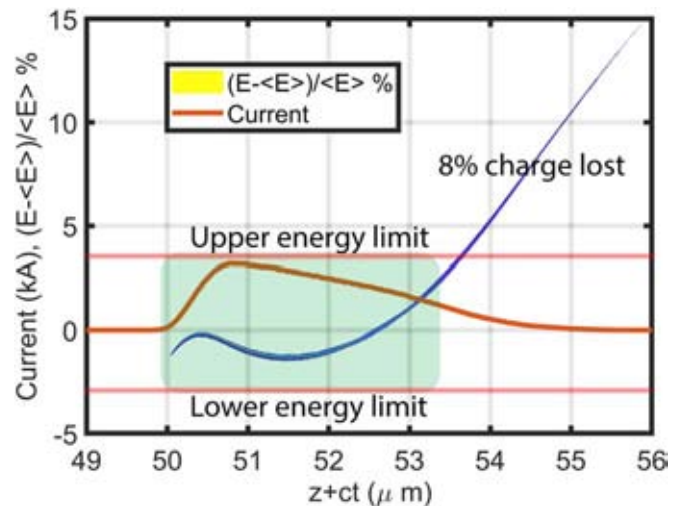


Figure 6. Longitudinal phase-space plot ($(z + ct)[\mu\text{m}]$, $(E - \langle E \rangle) / \langle E \rangle$) and current profile of the final beam. By selecting a standard beam optics with maximum energy below $1.3 \times \langle E \rangle$, about 92% of the bunch charge is transported to the final undulator stage for lasing.

x - and y -axis are reported. Remarkably, the slice energy spread reported in figure 7(c) shows an excellent distribution, with more than 80% of the bunch charge in slices having an energy spread of less than the required upper limit of 0.1%. Finally the minimum slice energy spread is attributed to a slice in the head of the bunch and in position $-1.4 \mu\text{m}$. That slice possesses the highest brightness, having extremely low emittances of $0.045 \mu\text{mrad}$ and $0.03 \mu\text{mrad}$, an energy spread of 0.03% and a current 2 kA.

6. Sensitivity to parameter fluctuations

Several laser and plasma parameters can affect the final beam quality. Fluctuations on the delivered laser pulse energy, for example, is directly linked to variation on both the

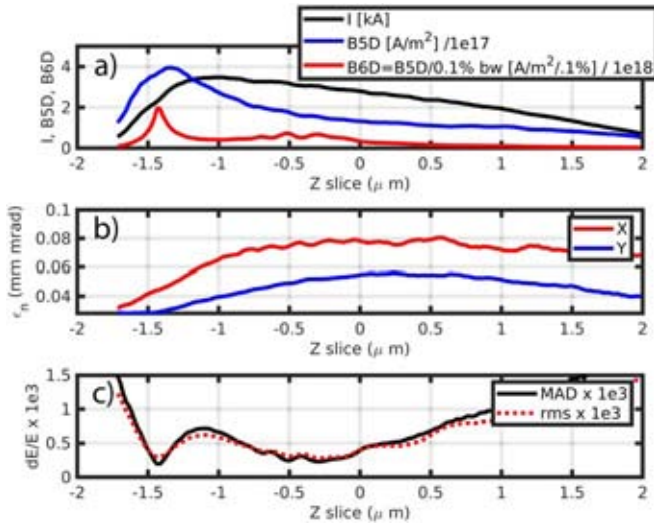


Figure 7. Slice analysis with slice thickness $0.1 \mu\text{m}$. The longitudinal axis corresponds to the slice position with respect to beam center-of-mass. (a) Current (black), brightness-5D $B_{5D} \equiv 2I/(\pi^2 \epsilon_{nx} \times \epsilon_{ny})$ (blue) and brightness-6D $B_{6D} \equiv B_{5D}/(\sigma_E/E/10^3)$ (red). (b) Emittances in the x (red) and y (blue) directions. (c) Energy spread using the *rms* estimator (red, dashed) and the mean absolute deviation robust indicator (black).

accelerating field amplitude and phase (due to nonlinear plasma wavelength increase), while variations in the background density mostly affect the resonance condition for the wave excitation. A full evaluation of the final beam parameters' stability against most of the working point parameters has been performed for a setup related to a 150 MeV injector for the EuPRAXIA 5 GeV line [54], where a background density of about $1 \cdot 10^{18} \text{cm}^{-3}$ was used. There, we found that the selected working point is stable, provided that 'reasonable' conditions for the upper limit of the experimental conditions fluctuations were satisfied. As an example, a 1% level of maximum admissible delivered pulse energy should be assured so as to limit the mean final energy fluctuation to about 1%. Pulse-to-pulse delay T_D (timing) jitter can be responsible of a resonance condition loss, therefore inducing a fluctuation in the wakefield amplitude (and phase) unless $N\delta(\omega_p \cdot T_D)/(\omega_{p,ref} \cdot T_{D,ref}) \ll 1$, where $N = 8$ is the number of pulses of the train and the subscript *ref* refers to the reference value of the parameter. Therefore, the experimental scheme that generates a time modulation in the laser pulse must possess a very good stability ($\delta T_D/T_{D,ref} \ll 1/N$). The TEMPI scheme, which was selected for the experimental demonstration of the ReMPI, shows a virtually null pulse-to-pulse jitter: the replicas of the stretched pulse (about 1 ps long) are produced by a mechanically stable stack of birefringent crystals and polarizers and overlap until they leave the compressor. We also mention that the time jitter between the pulse train and the ionizing pulse possesses potential detrimental effects on beam quality. However, being both the driving train and the ionization pulses amplified replicas of the same master pulse, the time jitter between them is only due to mechanical vibrations and can be safely limited to a few μm , which should be compared with the plasma

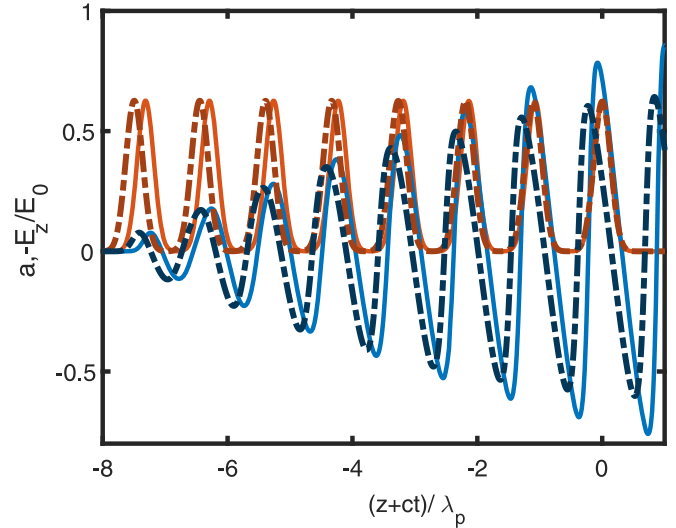


Figure 8. Sensitivity of the accelerating field (blue lines) on the resonance condition mismatch. The horizontal axis refers to the number of plasma periods and in the vertical axis both the accelerating field and pulses amplitude (orange) are shown. While in the optimized case (full lines) the peak accelerating field reaches the value of $E_{z,ref} = 0.7E_0$, the wakefield excited in a plasma with a background density increased by 5% (dashed lines) has peak value $E_z = 0.55E_0$, showing a reduction of more than 20%.

wavelength $\lambda_p \simeq 75 \mu\text{m}$. Plasma density fluctuations result in the most severe source of beam-quality fluctuations. The resonance condition refers to the plasma period, which depends on the local background density $n_0 = n_{0,ref} + \delta n_0$. Since the efficient resonant excitation of the wave can be rewritten as $\delta n_0/n_{0,ref}/2 + \delta T_D/T_{D,ref} \ll 1/N$, extremely low (of percent size) background density fluctuations can be acceptable. This can be made clearer by figure 8, where the pulse train and its excited wakefield is shown in two different cases: the optimized case with the couple of parameters $(T_{D,ref}, n_{0,ref})$ (full lines) and a case with the couple $(T_{D,ref}, n_{0,ref} + \delta n_0)$, being $\delta n_0 = 5\% n_{0,ref}$ (or, alternately, the couple $(T_{D,ref} + 2.5\% T_{D,ref}, n_{0,ref})$, shown with the dashed lines). From figure 8 we can infer that a variation of 5% of the plasma density, or equivalently, a variation of about 2.5% of the time delay of all the pulses, will cause a reduction of more than 20% in the wakefield amplitude, thus reinforcing the claim that the background plasma density must be controlled at about one percent level.

7. Conclusions

We have shown, by means of hybrid fluid/PIC simulation, that a FEL-quality 5 GeV electron bunch can be obtained with a single-stage LWFA. In order to employ the ReMPI injection scheme, the 1PW Ti:Sa laser system is equipped with a longitudinal pulse-shaper that modulates the pulse envelope in a sequence of eight pulses which drive a large amplitude plasma wave. Just after the pulse train, a low-intensity fourth harmonic converted portion of the initial pulse is tightly focused, so as to act as an 'ionization pulse'. The argon

K-shell electrons are extracted by tunnel ionization in the ionizing pulse field and are subsequently trapped by the wakefield. Finally, after about 25 cm of propagation in a capillary filled with helium, they are accelerated up to the desired energy of 5 GeV. The pulse train evolution is highly nontrivial and will be further investigated in a future work. Despite this, a 30 pC electron bunch with an energy spread of below 1% can be obtained after a standard selection of the beam transport energy range. The normalized emittance, being below 0.1 μmrad , is about on order of magnitude below the one usually obtained at those energies. Moreover, slice analysis reveals an excellent quality of a large fraction of the slices, with about 80% of the charge in slices having an energy spread below the threshold of 0.1%. We finally mention that a record brilliance-5D of $4 \times 10^{17} \text{ A m}^{-2}$, along with outstanding properties of the best slice of $\sigma_E/E = 0.03\%$, $\epsilon_{nx} = 0.045 \mu\text{mrad}$, $\epsilon_{ny} = 0.03 \mu\text{mrad}$ and current of 2 kA, can be obtained. The experimental demonstration of the scheme should face mechanical stabilization at (some of) μm size of the laser system, the pulse beamline and the interaction area, as usual in high energy LWFA experiments. Moreover, an additional constraint of stable control of the plasma background density at the 1% level is necessary, so as to assure an efficient resonant excitation of the plasma wave.

Acknowledgments

The research leading to these results has received funding from the EU Horizon 2020 Research and Innovation Program under Grant Agreement No. 653782 EuPRAXIA. This project has received financial support from the CNR funded Italian research Network ELI-Italy.

ORCID iDs

P Tomassini  <https://orcid.org/0000-0002-8106-8917>

References

- [1] Gonsalves A J *et al* 2019 Petawatt laser guiding and electron beam acceleration to 8 GeV in a laser-heated capillary discharge waveguide *Phys. Rev. Lett.* **122** 084801
- [2] Dopp A, Guillaume E, Thaurya C, Lifschitz A, Ta Phuoc K and Malka V 2015 Energy boost in laser wakefield accelerators using sharp density transitions *Phys. Plasmas* **23** 056702
- [3] Steinke S *et al* 2016 Staging of laser-plasma accelerators *Phys. Plasmas* **23** 056705
- [4] Audet T L *et al* 2016 Electron injector for compact staged high energy accelerator *Nucl. Instrum. Methods Phys. Res. A* **829** 304–8
- [5] Golovin G, Banerjee S, Chen S, Powers N, Liu C, Yan W, Zhang J, Zhang P, Zhao B and Umstadter D 2016 Control and optimization of a staged laser-wake field accelerator *Nucl. Instrum. Methods Phys. Res. A* **830** 375–80
- [6] Zhang Z *et al* 2016 Energy spread minimization in a cascaded laser wakefield accelerator via velocity bunching *Phys. Plasmas* **23** 053106
- [7] Schroeder C B, Esarey E, Geddes C G R, Toth C and Leemans W P 2009 *Advanced Accelerator Concepts* (vol 1086) ed C B Schroeder, E Esarey and W Leemans (New York: AIP) pp 208–14
- [8] Schroeder C B, Esarey E, Geddes C G R, Benedetti C and Leemans W P 2010 Physics considerations for laser-plasma linear colliders *Phys. Rev. Spec. Top. Accel. Beams* **13** 101301
- [9] Muggli P and Cros B 2018 ALEGRO, the advanced linear collider study group IX *International Particle Accelerator Conf. IPAC* (<https://accelconf.web.cern.ch/AccelConf/ipac2018/papers/tupml036.pdf>)
- [10] Nakajima K 2008 Few femtosecond, few kiloampere electron bunch produced by a laser-plasma accelerator *Nat. Phys.* **4** 92–3
- [11] Petrillo V *et al* 2013 Observation of time-domain modulation of free-electron-laser pulses by multi-peaked electron-energy spectrum *Phys. Rev. Lett.* **111** 114802
- [12] Loulergue A, Labat M, Evain C, Benabderrahmane C, Malka V and Couprie M E 2015 Beam manipulation for compact laser wakefield accelerator based free-electron lasers *New J. Phys.* **17** 023028
- [13] Esarey E, Ride S K and Sprangle P 1993 Nonlinear Thomson scattering of intense laser pulses from beams and plasmas *Phys. Rev. E* **48** 3003
- [14] Tomassini P, Giulietti A, Giulietti D and Gizzi L A 2005 Thomson backscattering x-rays from ultra-relativistic electron bunches and temporally shaped laser pulses *Appl. Phys. B* **80** 419–36
- [15] Corde S, Ta Phuoc K, Lambert G, Fitour R, Malka V, Rousse A, Beck A and Lefebvre E 2013 Femtosecond x rays from laser-plasma accelerators *Rev. Mod. Phys.* **85** 1
- [16] Micieli D, Drebot I, Bacci A, Milotti E, Petrillo V, Rossetti Conti M, Rossi A R, Tassi E and Serafini L 2016 Compton sources for the observation of elastic photon-photon scattering events *Phys. Rev. Spec. Top. Accel. Beam.* **19** 093401
- [17] Chen M, Sheng Z-M, Ma Y-Y and Zhang J 2006 Electron injection and trapping in a laser wakefield by field ionization to high-charge states of gases *J. Appl. Phys.* **99** 056109
- [18] Pak A, Marsh K A, Martins S F, Lu W, Mori W B and Joshi C 2010 Injection and trapping of tunnel-ionized electrons into laser-produced wakes *Phys. Rev. Lett.* **104** 025003
- [19] McGuffey C *et al* 2010 Ionization induced trapping in a laser wakefield accelerator *Phys. Rev. Lett.* **104** 025004
- [20] Thauray C *et al* 2015 Shock assisted ionization injection in laser-plasma accelerators *Sci. Rep.* **5** 16310
- [21] Clayton C E *et al* 2010 Self-guided laser wakefield acceleration beyond 1 GeV using ionization-induced injection *Phys. Rev. Lett.* **105** 105003
- [22] Chen M, Esarey E, Schroeder C B, Geddes C G R and Leemans W P 2012 Theory of ionization-induced trapping in laser-plasma accelerators *Phys. Plasmas* **19** 033101
- [23] Zeng M, Chen M, Yu L L, Mori W B, Sheng Z M, Hidding B, Jaroszynski D A and Zhang J 2015 Multichromatic narrow-energy-spread electron bunches from laser-wakefield acceleration with dual-color lasers *Phys. Rev. Lett.* **114** 084801
- [24] Zeng M, Luo J, Chen M, Mori W B, Sheng Z-M and Hidding B 2016 High quality electron beam acceleration by ionization injection in laser wakefields with mid-infrared dual-color lasers *Phys. Plasmas* **23** 063113
- [25] Audet T L *et al* 2016 Investigation of ionization-induced electron injection in a wakefield driven by laser inside a gas cell *Phys. Plasmas* **23** 023110

- [26] Bulanov S, Naumova N, Pegoraro F and Sakai J 1998 Particle injection into the wave acceleration phase due to nonlinear wake wave breaking *Phys. Rev. E* **58** R5257
- [27] Suk H, Barov N, Rosenzweig J B and Esarey E 2001 Plasma electron trapping and acceleration in a plasma wake field using a density transition *Phys. Rev. Lett.* **86** 1011–4
- [28] Tomassini P, Galimberti M, Giulietti A, Giulietti D, Gizzi L A, Labate L and Pegoraro F 2003 Production of high-quality electron beams in numerical experiments of laser wakefield acceleration with longitudinal wave breaking *Phys. Rev. Spec. Top. Accel. Beams* **6** 121301
- [29] Geddes C G R, Cormier-Michel E, Esarey E, Nakamura K, Plateau G R, Schroeder C B, Toth C, Bruhwiler D L, Cary J R and Leemans W P 2008 Plasma gradient controlled injection and postacceleration of high quality electron bunches *Proc. of the Thirteenth Advanced Accelerator Concepts Workshop* 1086
- [30] Buck A *et al* 2013 Shock-front injector for high-quality laser-plasma acceleration *Phys. Rev. Lett.* **110** 185006
- [31] Yu L-L, Esarey E, Schroeder C B, Vay J-L, Benedetti C, Geddes C G R, Chen M and Leemans W P 2014 Two-color laser-ionization injection *Phys. Rev. Lett.* **112** 125001
- [32] Tomassini P, De Nicola S, Labate L, Londrillo P, Fedele R, Terzani D and Gizzi L A 2017 The resonant multi-pulse ionization injection *Phys. Plasmas* **24** 103120
- [33] Umstadter D, Esarey E and Kim J 1994 Nonlinear plasma waves resonantly driven by optimized laser pulse trains *Phys. Rev. Lett.* **72** 1224
- [34] Hooker S M, Bartolini R, Mangles S P D, Tunnermann A, Corner L, Limpert J, Seryi A and Walczak R 2014 Multi-pulse laser wakefield acceleration: a new route to efficient, high-repetition-rate plasma accelerators and high flux radiation sources *J. Phys. B* **47** 234003
- [35] Shaloo R J, Corner L, Arran C, Cowley J, Cheung G, Thornton C, Walczak R and Hooker S M 2016 Generation of laser pulse trains for tests of multi-pulse laser wakefield acceleration *Nucl. Instrum. Methods Phys. Res. A* **829** 383–5
- [36] Cowley J *et al* 2017 Excitation and control of plasma wakefields by multiple laser pulse *Phys. Rev. Lett.* **119** 044802
- [37] Tomassini P, Labate L, Londrillo P, Fedele R, Terzani D and Gizzi L A 2017 High-quality electron bunch production for high-brilliance Thomson Scattering sources *Proc. vol 10240, Laser Acceleration of Electrons, Protons, and Ions IV102400T* (<https://doi.org/10.1117/12.2266938>)
- [38] Tomassini P, De Nicola S, Labate L, Londrillo P, Fedele R, Terzani D, Nguyen F, Vantaggiato G and Gizzi L A 2018 High-quality GeV-scale electron bunches with the resonant multi-pulse ionization injection *Nucl. Inst. Meth. Phys. Res. A* **909** 1–4
- [39] Walker P A *et al* 2017 Horizon 2020 EuPRAXIA design study *J. Phys.: Conf. Series* **874** 012029
- [40] Dattoli G, Ottaviani P L and Pagnutti S Booklet for FEL Design (http://fel.enea.it/booklet/pdf/Booklet_for_FEL_design.pdf)
- [41] Dattoli G, Renieri A and Torre A 1993 *Lectures on Free Electron Laser Theory and Related Topics* (Singapore: World Scientific)
- [42] Siders C W, Siders J L W, Taylor A J, Park S-G and Weiner A M 1998 *Appl. Opt.* **37** 5302–5
- [43] Toci G, Mazzotta Z, Labate L, Mathieu F, Vannini M, Patrizi B and Gizzi L A 2019 Conceptual design of a laser driver for a plasma accelerator user facility *Instruments* **3** 40
- [44] Labate L *et al* Efficient pulse train generation in Ti:Sa CPA systems in preparation
- [45] Dromey B, Zepf M, Landreman M, Okeeffe K, Robinson T and Hooker S M 2007 Generation of a train of ultrashort pulses from a compact birefringent crystal array *Appl. Opt.* **46** 5142–6
- [46] Tomassini P and Rossi A R 2016 Matching strategies for a plasma booster *Plasma Phys. Control. Fusion* **58** 034001
- [47] Sprangle P, Esarey E and Ting A 1990 Nonlinear theory of intense laser-plasma interaction *Phys. Rev. Lett.* **64** 2011–4
- [48] Sprangle P, Esarey E and Krall J 1996 Self-guiding and stability of intense optical beams in gases undergoing ionization *Phys. Rev. E* **54** 4211
- [49] Tomassini P *et al* Evolution of pulse trains in long-range propagation MP-LWFA in preparation
- [50] Schroeder C B, Vay J-L, Esarey E, Bulanov S, Benedetti C, Yu L-L, Chen M, Geddes C G R and Leemans W P 2014 Thermal emittance from ionization-induced trapping in plasma accelerators *Phys. Rev. Spec. Top. Accel. Beams* **17** 101301
- [51] Migliorati M, Bacci A, Benedetti C, Chiadroni E, Ferrario M, Mostacci A, Palumbo L, Rossi A R, Serafini L and Antici P 2013 Intrinsic normalized emittance growth in laser-driven electron accelerators *Phys. Rev. Spec. Top. Accel. Beams* **16** 011302
- [52] Li X, Chancé A and Nghiem P A P 2019 Preserving emittance by matching out and matching in plasma wakefield acceleration stage *Phys. Rev. Accel. Beams* **22** 021304
- [53] Martinez de la Ossa A *et al* 2019 Hybrid LWFA PWFA staging as a beam energy and brightness transformer: conceptual design and simulations *Phil. Trans. Royal Soc. A* **377** 20180175
- [54] Tomassini P, Terzani D, Labate L, Toci G, Chance A, Nghiem P A P and Gizzi L A 2019 High quality electron bunches for a multi-stage GeV accelerator with the Resonant Multi-Pulse Ionization injection *Phys. Rev. Accel. Beams* submitted for publication

Leonida Antonio Gizzi

Ralph Assmann

Petra Koester

Antonio Giulietti *Editors*

Laser-Driven Sources of High Energy Particles and Radiation

Lecture Notes of the “Capri” Advanced
Summer School



Springer

Preface

New ultra-intense laser facilities with unique specifications, like the Extreme Light Infrastructure, will soon be on-line and will deliver laser performances never achieved before, based on the Chirped Pulse Amplification (CPA) concept [1]. It is worth mentioning that the extraordinary importance of CPA was recognised with the Nobel Prize in Physics in 2018, giving rise to a wave of interest from both the academic world and the general public for this novel science and technology. A number of dedicated laser installations are being built or upgraded across the world to enter new regimes of laser-matter interaction for particle acceleration and applications to generation of ionizing radiation. The major achievements in this field are now motivating the development of an entirely new generation of compact accelerator machines. This is a major leap that requires a new approach, similar to the approach followed by other pioneering enterprises like the development of radio-frequency accelerators occurred more than fifty years ago.

In this rapidly evolving context there is a compelling need of advanced training for the community of young researchers involved in the various aspects of this research, requiring theoretical, numerical and experimental skills.

The concept of the Advanced Summer School on *Laser-Driven Sources of High Energy Particles and Radiation* originates from the need of delivering advanced training in the field of novel acceleration techniques, gathering experts in optics, lasers, plasmas, accelerators and particle beams. The community of laser-plasma accelerator physics has traditionally been focusing on the extraordinary innovation emerging from ever-increasing laser intensities and performances and the advanced understanding of the physics of high-intensity laser-plasma interaction. Indeed, the School was also intended to provide tutorials on these fundamental physics aspects, introducing the theoretical framework and addressing the numerical approach to laser-plasma acceleration.

The School was conceived to bring together distinguished scientists and motivated young researchers, postdoc and Ph.D. students engaged or willing to enter this field, to promote advanced training in the key areas of ultraintense lasers,

interaction with matter at ultra-high field and laser-plasma acceleration, with a focus on emerging, new, ground-breaking initiatives based on novel particle acceleration techniques, like the EuPRAXIA project aiming at the construction of the first ever industrial plasma-based particle accelerator. Novel accelerator techniques indeed were one of the highlights of the School, where the best expertise from the accelerator science was present to deliver fundamental notions and extraordinary achievements of modern light sources based on the latest acceleration technology, with a perspective view on novel accelerators. Also, specialists in generation of advanced radiation provided the latest update on applications to major multidisciplinary fields, including medicine and biology, material science and space industry.

Beam quality and reliability in this context call for a wide range of skills to be applied to overcome current issues in all aspects of laser-driven sources, from the laser driver, to the target plasma, developing appropriate diagnostic techniques for laser pulses, plasmas and beams and adopting appropriate stabilization and control techniques. All this goes through modelling of all components, from start to end, including all the relevant physical processes. This design approach, routinely followed by conventional accelerators, synchrotron and free-electron laser facilities, is now being extended to laser-plasma acceleration, defining a common knowledge base and promoting advanced training.

A special attention goes to the impressive developments of laser technology, now moving rapidly towards high average power systems, capable of higher repetition rate and gradually integrating efficient pumping technology. Progress has been very fast in this area, with laser labs promoting approaches ranging from evolution of existing technology, to entirely new schemes, based on laser materials capable of overcoming current limitations and aiming at performances compatible with the most advanced power drivers of RF accelerators. The School aims at delivering training in all these key areas of ultraintense lasers and laser-plasma interactions, having in mind the development of novel accelerator machines.

In summary, the scientific programme of the course covered all aspects of plasma acceleration, including fundamental laser-plasma interaction at high intensity, beam driven and laser-driven electron acceleration and different flavours of laser-driven ion acceleration. Leading experts guided participants through a journey across the science and technology of intense lasers, including advanced laser schemes for future high average power sources, fundamental aspects of laser-plasma interactions, electron beam dynamics and advanced configurations of radiation emission, from Thomson scattering to X-ray free electron laser. Ultrafast measurements and ultimate diagnostic techniques for laser and plasma characterization were a key part of the course, with step-by-step training on laser pulse amplification and compression, pulse duration and temporal contrast measurement, phase control and frequency conversion, electron and ion detection. Basic and advanced concepts of numerical modelling of laser-plasma interaction physics, radiation emission and particles and radiation transport were presented in view

of the development of full start-to-end simulation of radiation sources. An overview was also given of the main laser facilities featuring the most advanced high power and high energy laser sources.

The School took place at the Conference Facility of the Consiglio Nazionale delle Ricerche (CNR) in Anacapri, on the island of Capri, in the south of Italy, off the coast of the beautiful peninsula of Sorrento. The conference facility is located at the premises of the former Solar Observatory of the Swedish Royal Academy, now owned by the Italian National Research Council. Capri is a famous destination in the Tyrrhenian Sea on the south side of the Gulf of Naples in the Campania region of Italy. Anacapri is located on the slopes of Mount Solaro at a higher elevation than Capri town. Points of interest include The Blue Grotto, the greatest attraction of the island, Villa San Michele, the Villas of Tiberius and the Chairlift for Mount Solaro which takes to the highest peak of the island from which you can enjoy the most stunning panoramas.

Pisa, Italy

Hamburg, Germany

Pisa, Italy

Pisa, Italy

Leonida Antonio Gizzi

Ralph Assmann

Petra Koester

Antonio Giulietti

Reference

1. D. Strickland, G. Mourou, Compression of amplified chirped optical pulses. *Opt. Commun.* **56**(3), 219–221 (1985)

Contents

1	Laser-Driven Sources of High Energy Particles and Radiation	1
	Leonida Antonio Gizzi	
2	Basics of Laser-Plasma Interaction: A Selection of Topics	25
	Andrea Macchi	
3	Laser Wakefield Accelerators: Plasma Wave Growth and Acceleration	51
	Zulfikar Najmudin	
4	LWFA Electrons: Staged Acceleration	71
	Masaki Kando	
5	Fundamentals and Applications of Hybrid LWFA-PWFA	95
	Bernhard Hidding, Andrew Beaton, Lewis Boulton, Sebastián Corde, Andreas Doepp, Fahim Ahmad Habib, Thomas Heinemann, Arie Irman, Stefan Karsch, Gavin Kirwan, Alexander Knetsch, Grace Gloria Manahan, Alberto Martinez de la Ossa, Alastair Nutter, Paul Scherkl, Ulrich Schramm and Daniel Ullmann	
6	Introduction to High Brightness Electron Beam Dynamics	121
	M. Ferrario	
7	Ion Acceleration: TNSA and Beyond	143
	Marco Borghesi	
8	Ultrafast Plasma Imaging	165
	Malte C. Kaluza	
9	Particles Simulation Through Matter in Medical Physics Using the Geant4 Toolkit: From Conventional to Laser-Driven Hadrontherapy	187
	G. A. P. Cirrone, G. Cuttone, L. Pandola, D. Margarone and G. Petringa	

10 Lectures About Intense Lasers: Amplification Process	209
Bruno LeGarrec	
11 Diagnostics of Ultrafast and Ultraintense Laser Pulses	227
Luca Labate	
Index	251

Contributors

Andrew Beaton Department of Physics, University of Strathclyde, Glasgow, UK;
Cockcroft Institute, Sci-Tech Daresbury, Daresbury, Cheshire, UK

Marco Borghesi Centre for Plasma Physics, Queen's University Belfast, Belfast,
UK

Lewis Boulton Department of Physics, University of Strathclyde, Glasgow, UK;
Cockcroft Institute, Sci-Tech Daresbury, Daresbury, Cheshire, UK;
Deutsches Elektronen-Synchrotron DESY, Hamburg, Germany

G. A. P. Cirrone INFN-LNS, Catania, Italy;
ELI-Beamline Project, Institute of Physics, ASCR, PALS Center, Prague, Czech
Republic

Sebastián Corde LOA, ENSTA ParisTech, CNRS, Ecole Polytechnique,
Université Paris-Saclay, Palaiseau, France

G. Cuttone INFN-LNS, Catania, Italy

Alberto Martinez de la Ossa Deutsches Elektronen-Synchrotron DESY,
Hamburg, Germany

Andreas Doepp Ludwig-Maximilians-Universität München, Garching, Germany;
Helmholtz-Zentrum Dresden-Rossendorf, Institute of Radiation Physics, Dresden,
Germany

M. Ferrario Frascati National Laboratory, National Institute for Nuclear Physics,
Rome, Italy

Leonida Antonio Gizzi Istituto Nazionale di Ottica, Consiglio Nazionale delle
Ricerche, Pisa, Italy;
Sezione di Pisa, Istituto Nazionale di Fisica Nucleare, Pisa, Italy

Fahim Ahmad Habib Department of Physics, University of Strathclyde,
Glasgow, UK;
Cockcroft Institute, Sci-Tech Daresbury, Daresbury, Cheshire, UK

Thomas Heinemann Department of Physics, University of Strathclyde, Glasgow, UK;

Cockcroft Institute, Sci-Tech Daresbury, Daresbury, Cheshire, UK;
Deutsches Elektronen-Synchrotron DESY, Hamburg, Germany

Bernhard Hidding Department of Physics, University of Strathclyde, Glasgow, UK;

Cockcroft Institute, Sci-Tech Daresbury, Daresbury, Cheshire, UK

Arie Irman Max Planck Institut ü Quantenoptik, Garching, Germany

Malte C. Kaluza Institute of Optics and Quantum Electronics, Jena, Germany;
Helmholtz-Institute Jena, Jena, Germany

Masaki Kando Kansai Photon Science Institute, National Institutes for Quantum and Radiological Science and Technology, Kizugawa, Kyoto, Japan

Stefan Karsch Ludwig-Maximilians-Universität München, Garching, Germany;
Helmholtz-Zentrum Dresden-Rossendorf, Institute of Radiation Physics, Dresden, Germany

Gavin Kirwan Department of Physics, University of Strathclyde, Glasgow, UK;
Cockcroft Institute, Sci-Tech Daresbury, Daresbury, Cheshire, UK;
Deutsches Elektronen-Synchrotron DESY, Hamburg, Germany

Alexander Knetsch Deutsches Elektronen-Synchrotron DESY, Hamburg, Germany

Luca Labate Istituto Nazionale di Otticam, Consiglio Nazionale delle Ricerche, Pisa, Italy;

Sezione di Pisa, Istituto Nazionale di Fisica Nucleare, Pisa, Italy

Bruno LeGarrec LULI, Ecole Polytechnique, Palaiseau, France

Andrea Macchi National Institute of Optics, National Research Council (CNR/INO), Adriano Gozzini laboratory, Pisa, Italy;

Enrico Fermi Department of Physics, University of Pisa, Pisa, Italy

Grace Gloria Manahan Department of Physics, University of Strathclyde, Glasgow, UK;

Cockcroft Institute, Sci-Tech Daresbury, Daresbury, Cheshire, UK

D. Margarone ELI-Beamline Project, Institute of Physics, ASCR, PALS Center, Prague, Czech Republic

Zulfikar Najmudin Blackett Laboratory, Department of Physics, The John Adams Institute for Accelerator Science, Imperial College London, London, UK

Alastair Nutter Department of Physics, University of Strathclyde, Glasgow, UK;
Cockcroft Institute, Sci-Tech Daresbury, Daresbury, Cheshire, UK;

Max Planck Institut ü Quantenoptik, Garching, Germany

